A 226 815

Sixth International Conference on Modulated Semiconductor Structures

DTIC ELECTE MAR 17 1994 S B D

94-08508

August 23 - 27, 1993
Garmisch-Partenkirchen
Germany

Workbook

DISTRIBUTION STATEMENT A
Approved for public release;
Distribution Unlimited

94 3 16 012

Best Available Copy

Best
Available
Copy

Preface

This workbook contains unrefereed manuscripts of papers which will be presented at the 6th International Conference on Modulated Semiconductor Structures to be held in Garmisch-Partenkirchen, Germany from August 23 to August 27, 1993. Abstracts are included for those manuscripts not received in time. The papers will be refereed and accepted papers will be published in a special issue of Solid State Electronics.
We expect roughly 300 participants from 20 countries, presenting approximately 180 papers. More than 200 papers had to be rejected in order to keep the conference reasonably small with no parallel sessions. This was not an easy task for the program committee but we believe nevertheless that the papers chosen are representative of some of the best current work in the area of Modulated Semiconductor Structures.

The organisation of the conference was made possible by the financial support of

Deutsche Forschungsgemeinschaft
Bayerisches Staatsministerium für Unterricht, Kultus, Wissenschaft und Kunst
Commission of the European Communities
European Research Office United States Army
AIXTRON Semiconductor Technologies
Alcatel Hochvakuumtechnik
Balzers Hochvakuum
Bruker
Coherent
Cryovac
Daimler Benz
DILOR
FISONS Instruments
IBM Deutschland
Instruments S.A.
Intevac
Leybold
L.O.T.
Oxford Instruments
Siemens

On behalf of the organizing committee I would like to express my gratitudes to all sponsors.
The conference was organized at the Walter Schottky Institut, Technische Universität München, Garching with telephone and fax-numbers familiar to many participants now. I want to mention especially the many contributions to the local organisation by the secretaries Veronika Enter, Claudia Hartel and Sirkku Piminainen as well as Ulrich Bockelmann, Max Bichler, Sepp Brunner, Werner Dondl, Christoph Engelhardt, Joachim Nützel, Dirk Többen, Robert Strenz, Adi Ziegltrum and others.
In addition we had the pleasure of working with very capable and cooperative staff at the conference center in Garmisch-Partenkirchen.

Gerhard Abstreiter
Chairman of MSS6
July 1993

Organizing Committee

G. Abstreiter (TUM, Garching)	Chairman
E. Gornik (TUM, Garching)	Program
K. von Klitzing (MPI, Stuttgart)	
P. Vogl (TUM, Garching)	Finances
A. Zrenner (TUM, Garching)	Arrangements

Program Committee

G. Bastard (ENS, Paris)
G. Bauer (Universität Linz)
S. J. Bending (University of Bath)
H. Dämbkes (Daimler, Ulm)
A. Forchel (Universität Würzburg)
E. Göbel (Universität Marburg)
E. Gornik (TU München, Garching)
J. P. Kotthaus (LMU, München)
E. Molinari (CNR, Roma)
H. Oppolzer (Siemens, München)
K. Ploog (PDI, Berlin)

Advisory Committee

Z. J. Alferov (Ioffe Inst., St. Petersburg)
F. Briones (CSIC, Madrid)
L. L. Chang (IBM, Yorktown Heights)
G. H. Döhler (Univ. Erlangen)
L. Esaki (Univ. Tsukuba)
A. Fasolino (SISSA, Trieste)
T. Foxon (Univ. of Nottingham)
A. C. Gossard (Univ. of California)
D. Heitmann (Univ. Hamburg)
S. Hiyamizu (Univ. of Osaka)
E. Kasper (Daimler, Ulm)
M. J. Kelly (Univ. of Surrey)
F. Koch (TUM, Garching)
D. J. Lockwood (NRC, Ottawa)
P. Lugli (Univ. of Roma)
J. C. Maan (Katholieke Univ. Nijmegen)
B.D. McCombe (SUNY at Buffalo)
H. Ohno (Hokkaido Univ.)
H. Okamoto (Chiba Univ.)
J. F. Palmier (CNET, Bagneux)
A. Pinczuk (AT&T Bell Labs, Murray Hill)
F. H. Pollak (CUNY, Brooklyn)
J. Robert (USTL, Montpellier)
H. Sakaki (RCAST, Univ. of Tokyo)
S. C. Shen (Shanghai Inst. of Tech. Physics)
Y. Shiraki (RCAST, Univ. of Tokyo)
C. Tejedor (Univ. Autonoma de Madrid)
D. C. Tsui (Univ. of Princeton)
B. Vinter (Thomson, Orsay)
M. Voos (ENS, Paris)
G. Weimann (TUM, Garching)
C. Weisbuch (Thomson, Orsay)
J. M. Worlock (Univ. of Utah)
Xie Xide (Fudan Univ., Shanghai)
W. Zawadzki (Polish Academy of Sci., Warsaw)

MSS6 PROGRAM

Monday, August 23, 1993

Conference Opening 8:30 - 8:50

MoA Growth of ...ce and Dots 8:50 - 10:20

MoA1 8:50	**Fabrication of Quantum Wires and Dots by MOCVD Selective Area Growth** Y. Arakawa (invited)	1
MoA2 9:20	**Polarization Spectroscopy of Modulated GaAs/GaAlAs Quantum Wells Grown on Vicinal Surfaces: Anisotropic Islands or Ordered Growth?** J.I. Bloch, U. Bockelmann, F. Laruelle	9
MoA3 9:40	**Preparation of Low-dimensional Structures by Molecular Beam Epitaxy-regrowth on Patterned AlGaAs Buffer Layers** K. Eberl, A. Kurtenbach, P. Grambow, A. Lehmann, D. Heitmann, K. von Klitzing, M. Dilger, M. Hohenstein	13
MoA4 10:00	**Fabrication of SiGe/Si Quantum Wire Structures on a V-groove Patterned Si Substrate by Gas-source Si Molecular Beam Epitaxy** N. Usami, T. Mine, S. Fukatsu, Y. Shiraki	17

Coffee break 10:20 - 10:50

MoB Transport Properties in Low-dimensional Systems (10:50-12:40)

MoB1 10:50	**Evidence of Directional Electron Heating in Doped GaAs** B. Brill, M. Heiblum, H. Shtrikman (invited)	21
MoB2 11:20	**High-mobility Transport along Single Quasi 1-Dimensional Quantum Wires Formed by Cleaved Edge Overgrowth** W. Wegscheider, W. Kang, L. N. Pfeiffer, K. W. West, H. L. Störmer, K. W. Baldwin	23
MoB3 11:40	**Observation of Knudsen and Gurzhi Transport Regimes in a Two-dimensional Wire** L.W. Molenkamp, M. J. M. de Jong	29
MoB4 12:00	**Quantized Conductance and its Effects on Non-linear Drain Current Observed at 80 K in Mesa-etched InAs Quantum Wires with Split-Gate** K. Yoh, A. Nishida, M. Inoue	35

MoB5 12:20	**Transport Properties of Lateral Superlattices Grown on Vicinal GaAs (100) Surfaces** S. A. Lorke, P. M. Petroff	44

Lunch break 12:40 - 14:00

Poster Session:

MoP Growth, Characterisation, Transport (14:00 - 16:00)

MoP1	**MBE Fabrication of GaAs Quantum Wire Structures on Mesa Stripes Along the [001] Direction** M. López, T. Ishikawa, I. Matsuyama, N. Tanaka, Y. Nomura	48
MoP2	**Alternate Method to Produce Quantum Wires Using Dislocation Slipping** C. Guasch, F. Voillot, M. Goiran, J. P. Peyrade, E. Bedel, C. Fontaine, H. Atmani, A. Rocher	54
MoP3	**Formation of N-AlGaAs/GaAs Edge Quantum Wire on (111)B Micro Facet by MBE and Magnetic Depopulation of Quasi-One-Dimensional Electron Gas** Y. Nakamura, M. Tsuchiya, J. Motohisa, H. Noge, S. Koshiba, H. Sakaki	60
MoP4	**Lateral Potential Modulation in InAs/AlSb Quantum Wells by Wet Etching** T. Utzmeier, K. Ensslin, J. P. Kotthaus, C. Bolognesi, C. Nguyen, H. Kroemer	68
MoP5	**Optical Properties of GaAs Quantum Dots Fabricated by MOCVD Selective Growth** Y. Nagamune, M. Nishioka, S. Tsukamoto, Y. Arakawa	73
MoP6	**Fabrication of Nanometer-Scale Conducting Silicon Wires with a Scanning Tunneling Microscope** P. M. Campbell, E. S. Snow, P. J. McMarr	80
MoP7	**Selective Growth of SiGe Nanostructures by Low Pressure VPE** G. Schmidt, W. Langheinrich, K. Heime	88
MoP8	**Direct Epitaxial Growth of (AlGa)As/GaAs Quantum Wires by Orientation-Dependent Metal Organic Vapour Phase Epitaxy** D. Bertram, B. Spill, W. Stolz, E. O. Göbel	94

Availability Codes
Dist | Avail and/or Special
A-1

MoP9 **GaAs/Al$_{0.3}$Ga$_{0.7}$As Quantum Wire Structure Fabricated by Cleaving Angle Molecular Beam Epitaxy on Reverse-Mesa-Etched GaAs (100) Substrates** 102
S. Shimomura, K. Inoue, M. Tanaka, A. Adachi, M. Fujii, T. Yamamoto, T. Watanabe, N. Sano, K. Murase, S. Hiyamizu

MoP10 **Coverage Dependence of Migration Potential of Cation Adatoms on GaAs(001)-(2x4) Surface** 104
F. Shirashi, T. Ito, T. Ohno

MoP11 **Raman Scattering Investigation on the Ordered Incorporation of Si Dopant Atoms on (001) GaAs Vicinal Surfaces During MBE Growth** 110
M. Ramsteiner, J. Wagner, G. Jungk, D. Behr, L. Däweritz, R. Hey

MoP12 **Disorder-Induced Raman Scattering of Folded Phonons in Quantum Wells and Superlattices** 119
T. Ruf, V. I. Belitsky, J. Spitzer, V. F. Sapega, M. Cardona, K. Ploog

MoP13 **FTIR Spectroscopy of Longitudinal Confined Phonons and Plasmon-Phonon Vibrational Modes in GaAs$_m$/AlAs$_m$ Superlattices** 123
Yu. Pusep, A. Milekhin, A. Toropov

MoP14 **Raman Scattering Study of Longitudinal Acoustic and Optic Phonons in InSb/In$_{1-x}$Al$_x$Sb Strained-Layer Superlattices** 124
V. P. Gnezdilov, D. J. Lockwood, J. B. Webb

MoP15 **Optical Phonon Probes of Interface Roughness: A Theoretical Investigation** 131
S. de Gironcoli, E. Molinari

MoP16 **Infrared Reflectivity of Strained GaSb/AlSb Superlattices** 199
G. Scamarcio, C. Gadaleta, A. Tagliente, L. Tapfer, K. Ploog, Y. Ohmori, H. Okamoto

MoP17 **Quantitative Analysis of Strain Relaxation and Mosaicity in Short Period Si$_m$Ge$_n$ Superlattices Using Reciprocal Space Mapping by X-ray Diffraction** 144
E. Koppensteiner, P. Hamberger, G. Bauer, V. Holy, H. Kibbel, H. Presting, E. Kasper

MoP18 **Evidence of Non-commutativity of Band Discontinuities in InP-Al(In)As Ga(In)As Heterostructures** 151
E. Lugagne-Delpon, J. P. André, P. Voisin

MoP19 **Above Barrier Exciton Confinement in InGaAs/GaAs Multiple Quantum Well Structures** 157
M. Capizzi, A. Frova, A. Polimeni, F. Martelli, K. B. Ozanyan, T. Worren, M. R. Bruni, M. G. Simeone

MoP20 **Spectroscopic Study of Piezo-electric Field Effects in InGaAs/GaAs Multi-Quantum Wells Grown on (111)B Oriented GaAs Substrates** 165
T. A. Fisher, R. A. Hogg, A. R. K. Willcox, D. M. Whittaker, M. S. Skolnick, D. J. Mowbray, J. P. R. David, A. S. Pabla, C. J. Rees, R. Grey, J. L. Sanchez-Rojas, J. Woodhead, G. Hill, M. A. Pate, P. N. Robson

MoP21 **Optical Properties of AlP-GaP Short-period Superlattices** 170
A. Morii, T. Takano, J. Kitamura, K. Hara, H. Kukimoto, J. Yoshino, T. Yasuda

MoP22 **InGaAs/InP Quantum Wells with Periodic Thickness Variation** 175
A. A. Bernussi, M. J. S. P. Brasil, J. A. Brum, M. A. Cotta, R. A. Hamm, T. W. Staley, S. N. G. Chu, L. R. Harriot, M. B. Panish, H. Temkin

MoP23 **Determination of Built-in Electric Fields in Delta-doped GaAs Structures by Phase-sensitive Photoreflectance** 181
V. L. Alperovich, A. S. Jaroshevich, H. E. Scheibler, A. S. Terekhov

MoP24 **Advantages of a Piezoelectric Field in a Quantum Well** 182
U. Ekenberg, D. Richards

MoP25 **Determination of the Basic Parameters of Pseudomorphic GaInAs Quantum Wells by means of Simultaneous Transport and Optical Investigations** 188
E. Litwin-Staszewska, F. Kobbi, D. Dur, C. Skierbiszewski, M. Kamal-Saadi, H. Sibari, K. Zekentes, V. Mosser, A. Raymond, W. Knap, J. L. Robert

MoP26 **The Conduction Band Spin Splitting in Type-I Strained and Unstrained (GaIn)As/InP Quantum Wells** 192
P. Omling, B. Kowalski, B. K. Meyer, D. M. Hofmann, C. Wetzel, V. Harle, F. Scholz

MoP27 **Binding Energies of D$^-$ Ion in GaAs Quantum Well** 200
Y. H. Chang, J. J. Yeh, Y. M. Sheu, C. C. Wang, T. C. Chen, K. H. Chang, C. P. Lee

MoP28 **Correlations of the Remote Impurity Charges - A Method of 2DEG Mobility Tuning in GaAs/AlGaAs Heterostructures** 206
T. Suski, P. Wisniewski, L. H. Dmowski, I. Gorczyca, J. Smoliner, E. Gornik, G. Böhm, G. Weimann

MoP29 **Three-dimensional Boltzmann-Bloch Theory of Miniband Transport in Superlattices with Elastic Scattering** 213
R. R. Gerhardts

MoP30 **Domain Formation in Modulation-doped GaAs/$Al_xGa_{1-x}As$ Heterostructures** 220
R. Döttling, E. Schöll

MoP31 **Inside a 2D Electron System: Images of Potential and Dissipation** 228
R. Knott, U. Klass, W. Dietsche, K. von Klitzing, K. Eberl, K. Ploog

MoP32 **DC Transport in Intense, In-PlaneTeraHertz Electric Fields in $As_xGa_{1-x}As$ Heterostructures at 300 K** 234
N. G. Asmar, A. G. Markelz, E. G. Gwinn, P. F. Hopkins, A. C. Gossard

MoP33 **Microwave Miniband NDC in GaInAs/AlInAs Superlattices** 238
J. F. Palmier, J. C. Harmand, C. Minot, H. Le Person, E. Dutisseuil, H. Wang, G. Leroux

MoP34 **Quasi-one-dimensional Ballistic Electron Transport in In-Plane-Gated Channels at Liquid Nitrogen Temperature** 244
D. K. de Vries, K. Ploog, A. D. Wieck

MoP35 **The Dependence of Boundary Scattering in Split-gate Quantum Wires on the Transverse Mode Number** 248
M. Yamamoto, S. Nakata, K. Aihara, T. Mizutani

MoP36 **Experimental Studies of Electronic Transport in Semiconductor Quantum Dot Structures** 252
J. P. Bird, K. Ishibashi, Y. Aoyagi, T. Sugano

MoP37 **Photovoltaic Effect in Quasiballistic Electron Interferometer** 261
A. A. Bykov, Z. D. Kvon, L. V. Litvin, Ju. V. Nastaushev, V. G. Mansurov, V. P. Migal, S. P. Moschenko

MoP38 **Dimensional Transition of Weak Localization Effects in Lateral Surface Superlattices** 262
P. E. Selbmann, M. Suhrke

MoP39 **Luminescence Studies of Resonant Tunneling in a Triple Barrier Structure with Strongly Coupled Quantum Wells** 268
T. S. Turner, P. M. Martin, L. Eaves, H. B. Evans, P. A. Harrison, M. Henini, O. H. Hughes, D. M. Whittaker, P. D. Buckle, T. A. Fisher, M. S. Skolnick, G. Hill

MoP40 **Correlation Effects in Magnetoluminescence Spectra from Dense Quasi 2D Electron Gas in Selectively Doped InGaAs/GaAs Quantum Wells** 275
V. D. Kulakovskii, L. V. Butov, I. E. Itskevich, L. V. Kulik, T. G. Anderson, W. Shumin, A. Lomsadze

MoC Growth, Characterization and Phonons
(16:10 - 18.50)

MoC1 16:10 **MBE Growth of GaAs Nanometer-scale Ridge Quantum Structures and their Structural and Optical Characterizations** 281
S. Koshiba, H. Noge, Y. Nakamura, H. Akiyama, T. Inoshita, T. Someya, K. Wada, A. Shimizu, H. Sakaki

MoC2 16:30 **Control of Interface Composition in InAs/GaSb Superlattices** 290
B. R. Bennett, B. V. Shanabrook, R. J. Wagner, J. L. Davis, J. R. Waterman, M. E. Twigg

MoC3 16:50 **Lateral Piezoelectric Fields - an Universal Feature of Strained III-V and II-VI Semiconductor Heterostructures** 298
M. Ilg, A. Heberle, K. H. Ploog

MoC4 17:10 **Band Discontinuity and Effects of Si-Insertion Layer at (311)A GaAs/AlAs Interface** 302
T. Saito, Y. Hashimoto, T. Ikoma

MoC5 17:30 **X-Ray Diffraction Analysis of GaAs/AlAs Multilayer Structures Grown by Molecular Beam Epitaxy on (311) and (210) GaAs Surfaces** 307
M. A. Tagliente, L. De Caro, L. Tapfer, R. Nötzel, A. Fischer, K. Ploog

MoC6 17.50 **Folded Acoustic Phonons in GaAs/AlAs Superlattices Grown on Non-(100)-Oriented Surfaces** 314
J. Spitzer, Z. V. Popovic, T. Ruf, M. Cardona, R. Nötzel, K. Ploog

MoC7 18:10 **Vibrational Properties of Si/Ge Superlattices: Theory and In-plane Raman Scattering Experiments** 319
R. Schorer, G. Abstreiter, S. de Gironcoli, E. Molinari, H. Kibbel, E. Kasper

MoC8 18:30 **Phonons and Electron-phonon Interaction in GaAs Quantum Wires** 324
F. Rossi, C. Bungaro, L. Rota, P. Lugli, E. Molinari

Tuesday, August 24, 1993

TuA Quantum Wells - Electrical Properties (8:30 - 10:20)

TuA1 8:30 **Strained Si/SiGe Heterostructures for Device Applications** 333
F. Schäffler (invited)

TuA2 9:00 **Capture and Emission of Electrons in Quantum Wells under Applied Electric Field** 338
B. Vinter, F. Luc, P. Bois, L. Thibaudeau, E. Rosencher

TuA3 9:20 **Observation by Spin-Resolved Resonant Magnetotunneling of Oscillatory Landé Factor in Two-dimensional Electron Systems** 347
E. E. Mendez, J. Nocera, W. I. Wang

TuA4 9:40 **Wire-like Incorporation of Dopant Atoms during MBE Growth on Vicinal GaAs(001) Surfaces** 354
L. Däweritz, C. Muggelberg, R. Hey, H. Kostial, M. Höricke

TuA5 10:00 **Size Effects in the Transport Properties of Thin $Sc_{1-x}Er_xAs$ Epitaxial Layers Buried in GaAs** 360
R. Bogaerts, A. De Keyser, F. Herlach, F. M. Peeters, F. DeRosa, C. J. Palmstrøm, D. Brehmer, S. J. Allen Jr.

Coffee break 10:20 - 10:50

TuB Vertical Transport - Resonant Tunneling (10:50 - 12:40)

TuB1 10:50 **Single-electron Tunneling and Coulomb Charging Effects in Double Barrier Resonant Tunneling Diodes** 365
M. Tewordt, V. J. Law, J. T. Nicholls, L. Martín-Moreno, D. A. Ritchie, M. J. Kelly, M. Pepper, J. E. F. Frost, R. Newbury, G. A. C. Jones (invited)

TuB2 11:20 **Hydrostatic Pressure Sensors Based on Solid State Tunneling Devices** 377
H. Brugger, U. Meiners, R. Diniz, T. Suski, E. Gornik, A. Förster, H. Lüth

TuB3 11:40 **Realization of a Novel Resonant-tunneling Hot-electron Transistor: Competition of Ultrafast Resonant-tunneling and Energy Relaxation** 383
C.-H. Yang, R. A. Wilson

TuB4 12:00 **Γ-X Electron Transfer in Type II Tunneling Bi-Quantum Wells** 389
A. Tackeuchi, U. Strauß, W. W. Rühle, T. Inata, S. Muto

TuB5 12:20 **Valley Mixing Effects on Electron Tunneling Transmission in GaAs/AlAs Heterostructures** 396
E. L. Ivchenko, A. A. Kiselev, Y. Fu, M. Willander

Lunch break 12:40 - 14:00

TuC Quantum Wells, Superlattices - Optical Properties (14:00 - 16:10)

TuC1 14:00 **Luminescence Investigation on Strained $Si_{1-x}Ge_x/Si$ Coupled Quantum Wells** 403
S. Fukatsu (invited)

TuC2 14:30 **Fermi Sea Shake-up in Quantum Well Luminescence Spectra** 411
K. J. Nash, M. S. Skolnick, D. J. Mowbray, T. A. Fisher, D. W. Peggs, D. M. Whittaker, M. K. Saker, S. J. Bass, R. S. Smith

TuC3 14:50 **Optical Investigation of Superlattice Orbits and Impurity States in InGaAs/GaAs** 416
R. J. Warburton, J. G. Michels, P. Peyla, R. J. Nicholas, K. Woodbridge

TuC4 15:10 **Miniband Formation in Graded-Gap Superlattices** 424
H. T. Grahn, F. Agulló-Rueda, A. D'Intino, K. Schmidt, G. H. Döhler, K. Ploog

TuC5 15:30 **Stark-Ladder Transitions in GaAs/AlGaAs Superlattices** 431
M. Yamaguchi, M. Morifuji, H. Kubo, K. Taniguchi, C. Hamaguchi, C. Gmachl, E. Gornik

TuC6 15:50 **Modulated Blue Shift of the Quantum Well Electroluminescence in a GaAs/AlAs-Superlattice Resonant Tunnelling Device** 435
O. Kuhn, D. K. Maude, J. C. Portal, M. Henini, L. Eaves, G. Hill, M. Pate

Poster Session:
TuP Transport Optics (16:30 - 18:30)

TuP1 A Metastable State in Self-Electro-Optic Effect Devices using Stark Ladder Transitions — 442
M. Hosoda, K. Kawashima, K. Tominaga, K. Fujiwara

TuP2 "Spin"-Flip of Holes in Asymmetric Quantum Wells — 446
R. Ferreira, G. Bastard

TuP3 Interactions between Wannier-Stark States — 454
R. Ferreira, P. Voisin, G. Bastard

TuP4 Resonant Coupling between Buried Single-Quantum-Well and Wannier-Stark Localization States in a GaAs/AlAs Superlattice — 460
I. Tanaka, M. Nakayama, H. Nishimura, K. Kawashima, K. Fujiwara

TuP5 Fermi Edge Singularities in Doped Quantum Wires and Quantum Wells — 466
F. J. Rodríguez, C. Tejedor

TuP6 Excitonic Enhancement of the Fermi Edge Singularity and Recombination Kinetics of Photogenerated Electrons in p-type δ-doped GaAs/δ/$Al_xGa_{1-x}As$ Double-Heterostructures — 471
J. Wagner, D. Richards, H. Schneider, A. Fischer, K. Ploog

TuP7 Free to Bound Exciton Relaxation in [001] and [111] GaAs/GaAlAs Quantum Wells — 479
L. Muñoz, L. Viña, N. Mestres, W. I. Wang

TuP8 Resonant Quenching of Exciton Photoluminescence in Coupled GaAs/AlAs Quantum Wells: Effect of Exciton Binding Energy — 485
H. Schneider, J. Wagner, K. Ploog

TuP9 Pressure Dependence of Photoluminescence in $In_xGa_{1-x}As/Al_yGa_{1-y}As$ Strained Quantum Wells with Different Widths — 492
Z-X. Liu, G-H. Li, H-X. Han, Z-P. Wang

TuP10 Optical Transitions in GaAs/AlAs Superlattices with Different Miniband Widths — 496
K. Fujiwara, K. Kawashima, T. Yamamoto, K. Ploog

TuP11 Electromodulation Spectroscopy Study of a GaAs/GaAlAs Asymmetric Triangular Quantum Well Structure — 502
H. Qiang, F. H. Pollak, Y-S. Huang, D. Mathine, G. N. Maracas

TuP12 Spectroscopic Studies of Ultra-thin Quantum-Wells of GaAs and GaInAs in InP grown by MOVPE — 509
D. Hessman, X. Liu, M. E. Pistol, L. Samuelson, W. Seifert

TuP13 Optical Properties of Symmetrically Strained (GaIn)As/Ga(PAs) Superlattices Grown by Metalorganic Vapour Phase Epitaxy (MOVPE) — 515
S. Lutgen, T. F. Albrecht, T. Marschner, W. Stolz, E. O. Göbel

TuP14 Impurity-Bound Excitons in Selectively Doped Strained-Layer Quantum Wells in High Magnetic Fields — 522
A. B. Dzyubenko, A. Yu. Sivachenko

TuP15 Optically Detected Magnetic Resonance Study of the Transition from Pseudodirect Type II to Type I GaAs/AlAs Superlattices — 525
N. G. Romanov, P. G. Baranov, I. V. Mashkov, P. Lavallard, R. Planel

TuP16 Valence-subband Level Crossing in GaAs/GaAsP Strained-barrier Quantum Well Structures Observed by Circularly Polarized Photoluminescence Excitation Spectroscopy — 537
H. Yaguchi, K. Ota, K. Onabe, Y. Shiraki, R. Ito

TuP17 Magneto-optics of Dense Electron Plasmas in Modulation-doped GaInAs/AlInAs Single Quantum Wells — 533
Y.-H. Zhang, J. L. Merz, M. Potemski, J. C. Maan, K. Ploog

TuP18 High Magnetic Field Effects on the Dynamics of Excitons in a GaAs Quantum Well — 541
S. Haacke, A. P. Heberle, M. Potemski, J. C. Maan, W. W. Rühle, G. Weimann

TuP19 Linear Optical Properties of Pseudomorphic Si/Ge Superlattices — 548
C. Tserbak, G. Theodorou

TuP20 Band-edge Photoluminescence of SiGe/Strained-Si/SiGe Type-II Quantum Wells on Si(100) — 553
D. K. Nayak, N. Usami, H. Sunamura, S. Fukatsu, Y. Shiraki

TuP21 On the Two-dimensional Character of Absorption Spectra of Si/Ge Superlattices — 558
H. M. Polatoglou

TuP22 **Systematic Study of the Intersubband Absorption in Modulation Doped p-type $Si/Si_{1-x}Ge_x$ Quantum-Wells** 559
T. Fromherz, M. Helm, M. Seto, G. Bauer, J. F. Nützel, G. Abstreiter

TuP23 **Characterization of Valence Band Offset in p-$Si/Si_{1-x}Ge_x$/Si by Space Charge Spectroscopy** 565
K. Schmalz, H. G. Grimmeiss, B. Dietrich, H. Rhan-Lenfeld, J. Klatt, G. Lippert, W. Mehr, H. J. Osten, P. Schley

TuP24 **High Mobility 2D Hole Gases in Strained Ge Channels on Si Substrates Studied by Magnetotransport and Cyclotron Resonance** 572
C. M. Engelhardt, D. Többen, M. Aschauer, F. Schäffler, G. Abstreiter, E. Gornik

TuP25 **Magnetotransport and Microwave Photoresistivity of Two-dimensional Hole Gases in $Si/Si_{1-x}Ge_x$ Heterostructures** 576
Y. Guldner, J. M. Berroir, J. P. Vieren, M. Voos, I. Sagnes, P. Warren, D. Dutartre

TuP26 **Photoluminescence and Magnetotransport of 2D Hole Gases in Si/SiGe/Si Heterostructures** 581
R. Loo, R. Apetz, L. Vescan, U. Zastrow, A. Hartmann, A. Leuther, T. Schäpers, H. Lüth

TuP27 **A New Technique for Directly Probing the Intrinsic Tristability and its Temperature Dependence in a Resonant Tunneling Diode** 585
M. L. F. Lerch, A. D. Martin, P. E. Simmonds, L. Eaves, M. L. Leadbeater

TuP28 **Mesoscopic Effects in Resonant Tunneling Diodes** 593
J. W. Sakai, N. La Scala P. H. Beton, T. J. Foster, M. Henini, P. C. Main, L. Eaves, G. Hill

TuP29 **Schottky Barrier Tunneling Spectroscopy of a 2D Electron System in Delta-doped Si(100) Layers** 600
J. Lindolf, B. Klehn, U. Kunze, W. Klunke, I. Eisele

TuP30 **Photohole-induced Resonant Tunneling of Electrons in Selectively Etched Small Area GaAs/AlAs Double Barrier Diodes** 605
H. Buhmann, P. H. Beton, J. Wang, L. Eaves, M. Heath, M. Henini

TuP31 **Interface Effects, Band Overlap and the Semimetal to Semiconductor Transition in InAs/GaSb Interband Resonant Tunneling Diodes** 613
U. M. Khan-Cheema, P. C. Klipstein, D. G. Austing, J. M. Smith, N. J. Mason, P. J. Walker, G. Hill

TuP32 **InAs/Antimonide-Based Resonant Tunneling Structures with Ternary Alloy Layers** 617
J. N. Schulman, D. H. Chow, T. C. Hasenberg

TuP33 **Thermally Deactivated Resonant Current in High Peak to Valley Current Ratio (69:1) GaAs/GaAlAs Resonant Tunneling Structures: A Spectroscopic View of the Emitter Density of State** 628
F. Laruelle, G. Faini

TuP34 **Theoretical Analysis of Resonant Magnetotunneling Spectroscopy of Holes** 629
G. Goldoni, A. Fasolino

TuP35 **Control of Electron Populations in the Quantum Well Levels of GaAs-AlGaAs Double Barrier Resonant Tunneling Structures** 634
P. D. Buckle, J. W. Cockburn, M. S. Skolnick, D. M. Whittaker, R. Grey, G. Hill, M. A. Pate, G. W. Smith

TuP36 **Single-Electron Transistors Realized in In-Plane-Gate and Top-Gate Technology** 638
R. J. Haug, H. Pothier, J. Weis, K. von Klitzing, K. Ploog

TuP37 **Quasi One-dimensional In-Plane-Gate Field-Effect-Transistor** 640
U. Meiners, H. Brugger, B. E. Maile, C. Wölk, F. Koch

TuP38 **Reflection of Ballistic Electrons by Diffusive 2D Contacts** 645
A. K. Geim, P. C. Main, R. Taboryski, H. Carmona, C. V. Brown, T. J. Foster, R. B. S. Oakeshott, E. Veje

TuP39 **Giant Temperature Resonances of Noise in Submicron Quantum Well Structures** 652
S. T. Stoddart, A. K. Geim, S. J. Bending, J. J. Harris, A. J. Peck, K. Ploog

TuP40 **Non-linear Transport Properties of Miniband Conduction in Presence of a Crossed Electric and Magnetic Fields: A Semi-classical Approach** 658
F. Aristone, J. F. Palmier, A. Sibille, D. K. Maude, J. C. Portal, F. Mollot

Wednesday, August 25, 1993

WeA Metal/Semiconductor and Type II Interfaces (8:30 - 10:20)

WeA1 8:30 — **Electronic Interactions at Superconductor-semiconductor Interfaces** — 665
H. Krömer, C. Nguyen, E. L. Hu (invited)

WeA2 9:00 — **Direct Observation of the Semimetal to Semiconductor Transition in Crossed Band Gap Superlattices at Magnetic Fields up to 150T** — 675
D. J. Barnes, R. J. Nicholas, R. J. Warburton, N. J. Mason, P. J Walker, N. Miura

WeA3 9:20 — **Magnetotransport Properties of MBE-Grown Magnetic Superlattices of Mn-Based Intermetallics on GaAs Heterostructures** — 680
M. Tanaka, J. P. Harbison, T. Sands, J. DeBoeck, T. L. Cheeks, V. G Keramidas

WeA4 9:40 — **Studies of GaSb capped InAs/AlSb Quantum Wells by Resonant Raman Scattering** — 687
J. Wagner, J. Schmitz, M. Maier, J. D. Ralston, P. Koidl

WeA5 10:00 — **Luminescence Up-conversion by Auger Process at InP-AlInAs Type II Interfaces** — 694
A. Titkov, W. Seidel, J. P. André, P Voisin, M. Voos

Coffee break 10:20 - 10:50

WeB Atomic Scale Characterization (10:50 - 12:20)

WeB1 10:50 — **High Resolution TEM of Heterostructures** — 700
H. Cerva (invited)

WeB2 11:20 — **Cross Sectional STM on Heterostructures** — 712
H. L W. Salemink (invited)

WeB3 11.50 — **The Surface Evolution and Kinetic Roughening during Homoepitaxy of GaAs (001)** — 714
B G Orr, J. Sudijono, M. D Johnson, A. W. Hunt (invited)

Excursion 13:00

Conference Dinner 19:00

Thursday, August 26, 1993

ThA II-VI, IV-VI and Magnetic Structures (8:30 - 10:20)

ThA1 8 30 — **Zeeman Tuning of II-VI-based Diluted Magnetic Semiconductor Superlattices** — 729
J. K. Furdyna (invited)

ThA2 9:00 — **Novel Magnetic Phase Transition Behaviour in Short Period EuTe/PbTe Superlattices** — 738
J. J Chen, Z. H. Wang, M. S. Dresselhaus, G. Dresselhaus, G. Springholz, G. Bauer

ThA3 9:20 — **Band Offsets and Electronic Structures of (ZnCdHg)(SSeTe) Strained Superlattices** — 742
T. Nakayama

ThA4 9:40 — **Light Induced Inversion of Magnetic Hysteresis in CdTe/(Cd,Mn)Te Superlattices** — 749
V P. Kochereshko, I. A. Merkulov, G. R. Pozina, I N. Uraltsev, D. R. Yakovlev, W. Ossau, A. Waag, G. Landwehr

ThA5 10 00 — **Photomodulation Spectroscopy and Cyclotron Resonance of $Cd_{1-x}Mn_xTe/CdTe$ Semimagnetic and Strained Multi-Quantum Well Structures** — 756
S. C. Shen, L. J. Zhang, W. Lu, R. N. Bicknell

Coffee break 10:20 - 10:50

ThB Dots and Wires - Optical Properties (10:50 - 12.40)

ThB1 10:50 — **Optical Properties o Etched GaAs/GaAlAs Quantum Wires and Dots** — 763
J. Y. Marzin, A. Izrael, L. Birotheau (invited)

ThB2 11:20 — **Radiative Recombination in Pseudomorphic InGaAs/GaAs Quantum Wires Grown on Nonplanar Substrates** — 773
M Grundmann, V. Tuerck, J. Christen, E. Kapon, D M Hwang, C. Caneau, R. Bhat, D. Bimberg

ThB3 11:40 — **Optical Characterisation of InGaAs/GaAs Quantum Dots Defined by Lateral Top Barrier Modulation** — 777
A. Schmidt, A. Forchel, F. Faller, I. Itskevich, A. Vasiliev

ThB4 12.00 — **Electron-Phonon Scattering Rates in Quantum Wires** — 783
P. A Knipp, T. L. Reinecke

ThB5 12:20 — **Relaxation and Radiative Decay of Excitons in GaAs Quantum Dots** — 790
U Bockelmann, K. Brunner, G Abstreiter

Lunch break 12:40 - 14:00

Poster Session:

ThP Optics, Magnetic Structures, Infrared, Devices
(14:00 - 16:00)

ThP1 Determination of Band Edge Offset by Weak Field Hall Measurement on MBE PbSe/PbEuSe Multi-Quantum Well Structures on KCL — 796
Z. Shi, A. Lambrecht, M. Tacke

ThP2 Static and Dynamical Properties of the Bound Magnetic Polaron in $CdTe/Cd_{1-x}Mn_xTe$ Quantum Wells — 803
P. Boudicket, G. Bastard

ThP3 Time-resolved Optical Study of Vertical Transport in $Cd_{0.22}Mn_{0.18}Te/CdTe$ Superlattices — 810
Ph. Roussignol, J. Martinez-Pastor, A. Vinattieri, C. Delalande, B. Lunn

ThP4 Electron Subband Structure of HgCdTe Metal-Insulator-Semiconductor Heterostructures — 815
J. Chu, R. Sizmann, K. Liu, I. Nachev, F. Koch

ThP5 Zeeman Studies of $CdTe-Cd_{1-x}Mn_xTe$ Multiquantum Wells — 821
S. Jackson, S. R. Bardorf, T. Stirner, W. E. Hagston, P. Harrison, J. E. Nicholls

ThP6 Time-resolved Photoluminescence Studies of Stimulated Emission and Exciton Dynamics in $ZnSe/ZnS_{0.18}Se_{0.82}$ Superlattices — 825
C. J. Stevens, R. A. Taylor, J. F. Ryan, M. Dabbicco, M. Ferrara, R. Cingolani, Y. Kuroda, I. Suemeune

ThP7 Strain, Confinement, Carrier Dynamics, and High Density Effects in ZnSe/ZnMnSe-Quantum Structures — 829
F. Kreller, A. Schülzgen, J. Puls, F. Henneberger

ThP8 PbSrS MQW Lasers and the Effect of Quantum Well on Operation Temperature — 834
A. Ishida, N. Sakurai, K. Aikawa, H. Fujiyasu

ThP9 Electronic Structure of Thin Si Layers in CaF_2: Hybridization Versus Confinement — 841
A. Fasolino, S. Ossicini, F. Bernardini

ThP10 Coulomb Attraction in the Optical Spectra of Quantum Discs — 846
B. Adolph, S. Glutsch, F. Bechstedt

ThP11 Electronic Properties and Electron-Phonon Interaction in an Array of Anisotropic Parabolic Quantum Dots in the Presence of a Magnetic Field — 853
R. Haupt, L. Wendler

ThP12 Monte-Carlo Calculation of Few-Electron Systems in Quantum Dots — 859
F. Bolton

ThP13 Spectral Luminescence Enhancement in Three-dimensional Optical Microcavities Formed by GaAs Microcrystals — 865
S. Juen, K. F. Lamprecht, R. Rodrigues, R. A. Höpfel

ThP14 Tayloring of the Carrier Capture Efficiency of a Quantum Well — 875
J. M. Gerard, B. Deveaud

ThP15 Stark-Wannier States in Nanostructures — 879
E. A. M. Fagotto, P. A. Schulz, J. A. Brum

ThP16 Multi-phonon Relaxation of Electrons in a Semiconductor Quantum Dot — 885
T. Inoshita, H. Sakaki

ThP17 Ground State Properties of Interacting Electrons in Semiconductor Quantum Dots: Exact and Unrestricted Hartree-Fock Results — 889
L. Martín-Moreno, J. J. Palacios, C. Tejedor, G. Chiappe, E. Louis

ThP18 Strong Lateral Quantization Effects in the Luminescence of InGaAs/InP Quantum Wires — 894
P. Ils, M. Michel, A. Forchel, I. Gyuro, M. Klenk, E. Zielinski

ThP19 GaAs/AlGaAs Quantum Well Infrared Photodetectors — 899
T. Miyatake, S. Honhata, T. Ezaki, H. Kubo, N. Mori, K. Taniguchi, C. Hamaguchi

ThP20 New Type of Photoconductivity Induced by Continuum-Confined States in Intersubband Transitions — 903
C. Sirtori, J. Faist, F. Capasso, D. L. Sivco, A. Cho

ThP21 Landau Levels of Bragg Confined Electrons and Holes — 904
M. Zahler, E. Cohen, J. Salzmann, E. Linder, L. N. Pfeiffer

ThP22 Long Lived Photoexcited Electron-Hole Pairs in Modulation Doped GaAs/AlGaAs Quantum Wells Studied by Intersubband Spectroscopy — 909
Y. Garini, E. Ehrenfreund, E. Cohen, A. Ron, K-K. Law, J. L. Merz, A. C. Gossard

ThP23 **Electron Transport in InAs-$Ga_{1-x}In_xSb$ Superlattices** 915
C. A. Hoffman, J. R. Meyer, E R. Youngdale, F. J. Bartoli, R. H. Miles, L. R. Ram-Mohan

ThP24 **Comparison of Far-Infrared- and dc-Conductivity of Electron-Systems Laterally Patterned by Low-energy Ion Beam Exposure** 916
C. Lettau, M. Wendel, A. Schmeller, W. Hansen, J. P. Kotthaus, G. Böhm, G. Weimann, M. Holland

ThP25 **Novel Tunable Far Infrared Detector Based on a Quantum Ballistic Channel** 922
L. E. Fedichkin, V. I. Ryzhii, V. V. V'yurkov

ThP26 **Cyclotron FIR Emission from Hot Electrons in GaAs-GaAlAs Heterostructures** 927
W. Zawadzki, C. Chaubet, D. Dur, W. Knap, A. Raymond

ThP27 **Resonant Magneto-Polarons in Strongly-Coupled Superlattices** 928
F. M. Peeters, J. M. Shi, J T. Devreese, J. P. Cheng, B. McCombe, W. Schaff

ThP28 **Far Infrared Response of Quantum Dots: From Few Electron Excitations to Magnetoplasmons** 934
D. Pfannkuche, V. Gudmundsson, P. Hawrylak, R R. Gerhardts

ThP29 **Cyclotron and Intersubband Resonance Studies in [100] and Piezoelectric [111] InAs(Ga,In)Sb Superlattices** 943
M. Lakrimi, T. A. Vaughan, R. J. Nicholas, D. M. Symons, N. J. Mason, P. J. Walker

ThP30 **Magnetic Field Tuned Transition of Aharonov-Bohm Oscillations from hc/e TO nc/2e Periodicity in the Array of AlGaAs/GaAs Rings** 949
G. M. Gusev, P. Basmaji, D I Lubyshev, J. C Portal, L V. Litvin, Yu. V. Nastaushev, A. I. Toropov

ThP31 **Negative Conductance at THz Frequencies in Multi-well Structures** 955
W. S Truscott

ThP32 **Perpendicular Transport Through Rough Interfaces in the Metallic Regime** 962
A. Brataas, G. E. W. Bauer

ThP33 **Giant Third-order Nonlinear Susceptibilities for In-Plane Far-Infrared Excitation of Single InAs Quantum Wells** 970
A. G. Markelz, E. G. Gwinn, M. S. Sherwin, C. Nguyen, H. Kroemer

ThP34 **Enhancement of Free-to-bound Transitions due to Resonant Electron Capture in Be-doped AlGaAs/GaAs Quantum Wells** 974
K. Muraki, Y. Takahashi, A. Fujiwara, S. Fukatsu, Y. Shiraki

ThP35 **Constructive Superposition of Field- and Carrier Induced Absorption Changes in Hetero-n-i-p-i Structures** 978
M. Kneissl, K. H. Gulden, P. Meisel, A. Luczak, S. Malzer, G. H. Döhler, X. Wu, J. S Smith

ThP36 **Polarization of the Spontaneous Radiation of Stressed Laser Heterostructures** 983
A. A. Ptashchenko, M. V. Deych, N. B. Mironchenko, F. A Ptashchenko

ThP37 **Bi-Stability Effect in Laser-Transistor Resonant-Tunneling Structure** 992
V. Ryzhii, I. Khmyrova

ThP38 **Optoelectronic Properties of (001) and (111) Lattice-Matched and Strained Quantum Wire Lasers - Comparison with Quantum Well Lasers** 1000
I Vurgaftman, J. Singh

ThP39 **Photomodulation Spectroscopy of Narrow Minibands in the Continuum of Multi Quantum Wells** 1009
J. Oiknine-Schlesinger, E. Ehrenfreund, D. Gershoni, D Ritter, R. A. Hamm, J. M. Vandenberg, S-N G. Chu

ThC Electronic Excitations - Superlattices
(16.10 - 18.30)

ThC1 16.10 **Intersubband Lifetime in Quantum Wells with Transition Energies Above and Below the Optical Phonon Energy** 1015
J. Faist, F. Capasso, C. Sirtori, D L Sivco, A Y. Cho, L. N. Pfeiffer, K. W. West

ThC2 16.30 **Miniband Dispersion, Critical Points and Impurity Bands in Superlattices: an Infrared Absorption Study** 1016
M Helm, W Hilber, T. Fromherz, F. M Peeters, K Alavi, R N Pathak

ThC3 16.50 **Inelastic Light Scattering by Electrons in GaAs Quantum Wires: Spin-Density, Charge-Density and Single-Particle Excitations** 1022
A. Schmeller, A. Pinczuk, J. S Weiner, B. S. Dennis, J. M. Calleja, A. Goñi, L. N Pfeiffer, K. W West

ThC4 17.10 **Tunable Far Infrared Absorption in Logarithmically Graded Quantum Wells** 1029
P. F Hopkins, M. Sundaram, K. L. Campman, G. Bellomi, E. L. Yuh, S. J. Allen Jr., A. C. Gossard

ThC5 17:30 **Widely Tunable Quantum Wire Arrays in MISFET-type Heterojunctions with a Stacked Gate** 1033
G. Hertel, H. Drexler, W Hansen, A. Schmeller, J. P. Kotthaus, M. Holland, S. P. Beaumont

ThC6 17:50 ***Infrared Spectroscopy of Lateral-Density Modulated 2DES in InAs/AlSb Quantum Wells*** 1039
M Sundaram, S J. Allen Jr , C. Nguyen, B. Brar, V. Jayaraman, H. Kroemer

ThC7 18:10 **Middle Infrared (l≈2-5.5 μm) High Quantum Efficiency Luminescence in GaSb/InAs II-type Multi-Quantum Well Structures** 1066
S. V. Ivanov, B. K. Kurinkiev, N. N. Ledentsov, B. Ya. Meltser, A. A. Monakhov, A. A. Rogachev, S V Shaposhnikov, P S. Kop'ev

Friday, August 27, 1993

FrA Optical Properties - Lasers (8.30 - 10:20)

FrA1 8 30 **Microdisk Lasers** 1049
A F. J Levi (invited)

FrA2 9:00 ***GaAs-AlAs and Si-SiGe Quantum Well Structures for Applications in Nonlinear Optics*** 1058
M J. Shaw, K. B. Wong, M Jaros

FrA3 9:20 **Charge Transfer and Electroabsorption in an Electric Field Tunable Double Quantum Well Structure** 1059
K. Bernhard, A. Zrenner, G. Bohm, G. Trankle, G. Weimann

FrA4 9:40 **Strained InAs/$Ga_{0.47}In_{0.53}As$ Quantum-well Heterostructures grown by Molecular-beam Epitaxy for Long-wavelength Laser Applications** 1064
E. Tournié, P. Grunberg, C. Fouillant, A. Baranov, A. Joullié, K. Ploog

FrA5 10:00 **Feasibility of Room Temperature Operation of Tunable Coupled-Quantum-Well Lasers** 1068
M. Ogawa, E. E. Mendez

Coffee break 10:20 - 10:50

FrB Ultrafast Processes - New Optical Phenomena (10:50 - 12.40)

FrB1 10 50 **Detection of Bloch Oscillations in a Semiconductor Superlattice by Time-Resolved Terahertz Spectroscopy and Degenerate Four-Wave Mixing** 1075
C Waschke, P. Leisching, P. H. Bolivar, R. Schwedler, F. Brüggemann, H. G Roskos, K. Leo, H. Kurz, K. Köhler (invited)

FrB2 11:20 **Femtosecond Degenerate Four-wave Mixing on Unstrained (InGa)As/InP Multiple-Quantum Wells using an Optical Parametric Oscillator** 1081
T. F. Albrecht, J. H. H. Sandmann, S. T. Cundiff, J. Feldmann, W Stolz, E. O Göbel

FrB3 11.40 **Time Resolved Spectroscopy of Electron Decay in Coupled Quantum Wells - Observation of Relaxation Induced Slow-Down** 1089
I. Bar-Joseph, G. Cohen, B Deveaud, P. Bergman, A. Regreny

FrB4 12.00 **Modulation of Wannier-Stark Transitions by Miniband Franz-Keldysh Oscillations in Strongly Coupled GaAs-AlAs Superlattices** 1094
K H Schmidt, W. Geißelbrecht, N Lindner, G. H. Dohler, H T. Grahn, K Ploog, H. Schneider

FrB5 12.20 **Photonic Bandgap of Two-dimensional Dielectric Crystals** 1100
J M Gérard, A. Izraël, J. Y. Marzin, R. Padjen

Conference Closing 12.40 - 13.00

Monday, August 23

MoA Growth of Wires and Dots

MoB Transport Properties in Low-dimensional Systems

MoP Growth, Characterisation, Transport

MoC Growth, Characterisation, Phonons

MoA1

Fabrication of Quantum Wires and Dots by MOCVD Selective Growth

Yasuhiko Arakawa

Institute of Industrial Science, University of Tokyo
7-22-1 Roppongi, Minato-ku, Tokyo 153, Japan

Abstract

We discuss fabrication of GaAs quantum wires and quantum dots using an *in-situ* MOCVD selective growth technique on SiO2 patterned substrates, including the optical properties of those nano-structures. As for the GaAs quantum wires, triangular-shaped GaAs quantum wires with a lateral width less than 10 nm were obtained. The photoluminescence (PL) and magneto-PL measurements clearly demonstrate the existence of the quantum wire effects in the structures. In addition, InGaAs strained quantum wires were also fabricated. Using a similar but slightly different selective growth technique, GaAs dots with a dimension of 25nmx25nmx12nm surrounded by AlGaAs regions were prepared.

1. Introduction

A reduction of dimensionality of the electron motions in quantum nano-structures brings new phenomena in semiconductor physics. Moreover, it allows new device concept to be considered and permits improvements in performance of the transistors and lasers. In 1980, the quantum wire was discussed for application to extremely high electron mobility channels[1]. In addition, in 1982, the quantum wire laser and the quantum dot laser were proposed, predicting significant improvement of lasing characteristics[2]. These proposals and discussions triggered the efforts toward semiconductor devices with lower-dimensional systems. Particularly, in the optical devices, the electronic states can be fully quantized, in contrast to the situation in transport devices, where the electrons need propagate along the channels.

Recently full confinement of photons (or optical wave) has been also discussed for the future zero-threshold lasers in which the electron-hole pairs are coupled with only a single spontaneous emission mode. Consequently, as for the semiconductor lasers, the full-quantization of both electrons and photons is the ultimate direction forward[3]. The goal is, however, far away because the fabrication technology for such low-dimensional structures is still under development. In order to explore the frontier of the new physics experimentally and develop new optical and electronic devices, sufficiently small and uniform nano-structures need to be obtained so that all carriers are populated at the lowest subband for both the conduction band and the valence band. In addition, a three-dimensional optical cavity with extremely high reflectivity must be also prepared.

In this paper, after brief discussion of carrier relaxation phenomena in the quantum dot structures from the view point of laser applications, fabrication of the quantum wires using a developed *in-situ* MOCVD growth technique is investigated[4-6]. Using this technique, triangular-shaped GaAs quantum wires with the lateral width less than 10 nm are obtained. The optical properties of the quantum wires including photoluminescence (PL) and magneto-PL are studied in order to confirm the existence of the two-dimensional quantum confinement in the quantum wires. Strained quantum wires with a laser structure are also fabricated[7]. Using a similar but slightly different selective growth technique, GaAs quantum dot structures of 25nmx25nmx12nm are successfully prepared[8,9].

2. Bottleneck in Quantum Dots

Recently carrier relaxation phenomena from barrier region into the quantum dots have been discussed, predicting significant reduction of carrier relaxation rate due to the increasing energy separation between the barrier region and the quantized energy level of the quantum dots. In the full quantized system, the transitions of electrons to lower energy levels can occur only when the phonon energy is resonant with the energy difference between the two energy levels. Weisbuch *et al.*[10] discussed this issue and attributed the decreased PL intensity with the reduction of the lateral size of the quantum dots to this bottleneck. Moreover, they predicted that this bottleneck leads to drastic increase of the threshold current in the quantum dot lasers. Although the simple model shows us serious problems for the quantum dot lasers, the question whether this bottle neck problem really exists should be clarified by experiments. As discussed later, even from the quantum dots with the lateral size of 25nm, PL can be observed. Moreover, even if the bottleneck exits, there are several ways to avoid this bottleneck in the quantum dot lasers by designing carefully the quantum dot arrays, as discussed below.

Figure 1 illustrates one example of the structures where the bottleneck problem can be reduced. In Fig.1 (a), the size of the quantum dots is determined so that the energy separation between the barrier region and the quantized energy level is two times larger than the longitudinal optical phonon energy (i.e., $\Delta E = 2\hbar\omega_{LO}$). In this case, the relaxation time is very fast because the energy difference is in resonance with the two LO phonon energy. Although some carriers are populated in the barrier region, the threshold current due to the population in the barrier region is increased by a factor of just two. By taking account of the fact that the threshold current can be improved by a factor of ten compared to that of the quantum wire lasers, the advantages of the use of the quantum dots definitely exist in the semiconductor lasers. The second example is shown in Fig.2(b). In this structure, the resonant tunnelling is utilized. It is, however, necessary that the quantum dot array is precisely fabricated so that the resonant condition is satisfied.

3. Fabrication of GaAs Quantum Wires [4,5]

In order to fabricate the quantum nano-structures, wet chemical etching, reactive ion etching[9], ion beam implantation and ion beam milling have been investigated. These methods, however, suffer from free surface effects, creation of a damage field during implantation, or a loss of interface control due to the random nature of the disordering mechanism. To avoid these problems, growth techniques on masked substrates and non-planer substrates[11-13]] have been also investigated. Here, we discuss an in-situ fabrication technique for the quantum wires and quantum dots by utilizing MOCVD selective growth on a SiO2 patterned substrate on which the V-groove structures are formed by the growth.

The MOCVD growth was performed in a low pressure, horizontal, rf-heated MOCVD reactor, using trimethylgallium (TMG), trimethylaluminum (TMA) and arsine (AsH_3) as group III and V sources, respectively. The ratio of group V tp group III was 100. The growth temperature was 700 °C. Purified H_2 with a 6 liter/min flow rate was used as a carrier gas. The growth pressure was 100 torr.

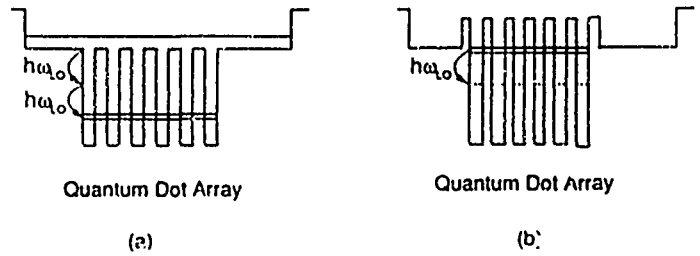

Fig 1: Examples of the quantum dot laser structures where the bottleneck problem can be reduced.

Fabrication procedure for the quantum wires is as follows[4]. First, a SiO_2 layer with the thickness of 20nm is formed by plasma chemical vapor deposition on a semi-insulating (100) GaAs substrate. PMMA was then patterned on the SiO_2 layer by electron beam lithography technique, followed by a wet chemical etching to pattern the SiO_2. After this procedure, the triangular shaped GaAs with (111)A facet sidewalls were grown on the masked substrate by MOCVD growth. The formation of the triangular structure is due to the large growth rate difference between (100) orientation and (111)B or (111A). Further continuation of the growth leads to the lateral growth above SiO_2 mask, making the gap between the triangular prisms small. The gap between the triangular prisms was then filled up with $Al_{0.4}Ga_{0.6}As$ layer by switching the growth layer from GaAs to $Al_{0.4}Ga_{0.6}As$. In contrast to GaAs, orientation dependence of the growth rate is weak in AlGaAs materials, although the dependence is strongly affected by temperature and Al content. As a result, a sharp corner at the bottom of the V-groove between the triangular prisms is formed by the growth of AlGaAs layer. At this point the growing layer is again switched to GaAs. Since at the V-groove corner there is a small point which has (100)-orientation, triangular-shaped quantum wires can be grown at the V-groove corner. This quantum wire is connected to thin quantum wells on {111}A-sidewalls of large triangular GaAs prisms. Thus, GaAs quantum wires which are coupled with thin quantum wells are formed between the triangular prisms without being exposed to air. Figure 2 shows a high-resolution a cross sectional

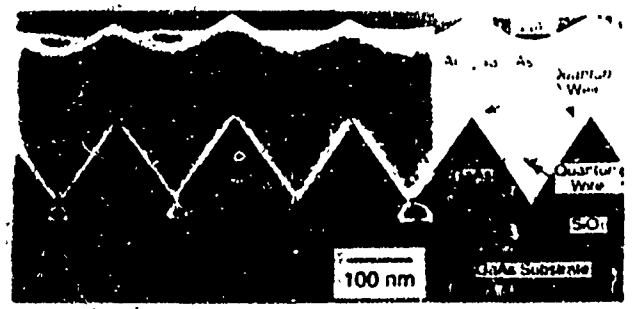

Fig. 2: A high-resolution scanning electron micrograph of GaAs triangular-shaped quantum wire array structure with the lateral width of ~15nm and its illustration.

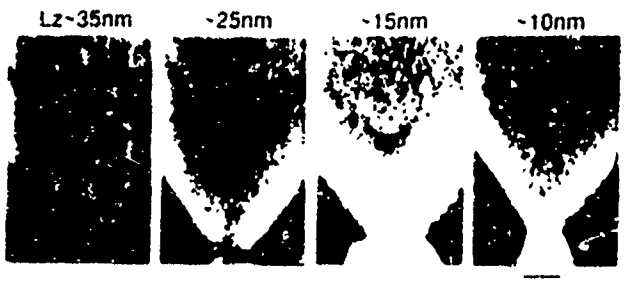

Fig. 3: high-resolution scanning electron micrographs of the part of the quantum wires with lateral widths of ~10 ~15, ~25, ~35 nm, respecuvely.

SEM image of the quantum wire array with 20nm period and its illustration. As shown in this photograph, even though there is ~30% lateral size fluctuation in SiO_2 mask, the quantum wires are uniformly formed, which is due to the relaxation of the size deviation by the lateral selective growth of the triangular prisms.

By changing the growth time of GaAs material for the quantum wires, we obtained the quantum wires with various lateral widths. Figure 3 shows high-resolution SEMs of the quantum wires region with lateral widths of ~10, ~15, ~25, ~35nm, respectively. Each quantum wire smoothly connects to quantum well layers with ~2, ~3, ~5, ~7nm thickness. As shown in this photograph, the quantum wire with Lx~10nm was obtained by systematic change of the growth time.

4. Photoluminescence and Magneto-Photoluminescence of Quantum Wires [5,6]

Photoluminescence (PL) spectra from the quantum wire structures are measured at 20K as a function of the lateral widths of 0, ~7, ~10, ~15, ~25, ~30, ~35nm as shown in Fig. 4(a). In this figure, the hatched PL peaks are corresponding to the quantum wires. Figure 4(b) shows the energy shift ΔE of the PL peak of the quantum wires versus the lateral width Lx. The ΔE is defined as the energy difference between the PL peaks of the GaAs bulk and the quantum wires As shown in these figures, systematic blue shifts are observed with decreasing Lx, which is due to enhancement of the two-dimensional quantum confinement effect. The solid calculation curve in the figure is based on a simple one band model. These results indicate that a strong lateral confinement is achieved in the present structures.

PL measurements are a useful tool in order to confirm the quantum wire effects in the structures. However, it is necessary to obtain additional clear evidences. When the lateral potential exists in the quantum wires, the behavior of the Landau shift should depend on the direction of the applied magnetic fields. Therefore measurements of magneto-PL spectra were performed for the quantum wires with the lateral width of 20nm using pulsed magnetic fields at 4.2 K. The pulse duration of the magnetic field was 10 msec and the maximum field was about 40 T. PL spectra were detected with an optical multi-channel analyzer system installed at the exit of the monochromator through the optical fiber.

The PL peak position from the quantum wires and the bulk at the three configurations (i.e., $B//x$,$B//y$,$B//z$) are plotted as a function of applied magnetic fields in Fig.5. As shown in this figure, the behavior of the PL peak shift ΔE is different between the bulk and the quantum wires. The bulk PL peak shifts at various magnetic fields are almost equally independent on the configurations throughout the magnetic field region. In contrast, PL peak shift of the quantum wires is clearly depending on the configuration. When the magnetic field is applied in parallel with the quantum wires ($B//x$), the energy shift with the increase of the magnetic field is the smallest. This can be explained by a classical picture in which the cyclotron motion on the plane perpendicular to the magnetic field is restricted by the two dimensional lateral potentials of the quantum wires. On the other hand, there is also anisotropic effect when the magnetic field is applied in the two directions perpendicular to the quantum wires. The results indicate that the cross sectional shape of the quantum wires are not isotropic.

In order to analyze these behaviors, we analyzed the experimental results assuming that the quantum wire potential is expressed by the following harmonic potential f(x,y,z).

$$\phi(x,y,z) = \frac{1}{2} m^* \omega_{0y}^2 y^2 + \frac{1}{2} m^* \omega_{0x}^2 x^2 \qquad (1)$$

In this case, the energy shift ΔE due to the magnetic filed applied perpendicularly to the quantum wires can be expressed as follows.

$$\Delta E = \frac{1}{2} \hbar \sqrt{\omega_c^2 + \omega_{0y}^2} \quad : B//y \qquad (2)$$

$$\Delta E = \frac{1}{2} \hbar \sqrt{\omega_c^2 + \omega_{0x}^2} \quad : B//x \qquad (3)$$

Where ω_c is equal to eB/m. By fitting the curve to the measured data using above relationship, the value of ω_{0x}/ω_{0y} are 2.9. It should be noted that the w_x is approximately proportional to $1/L_x^2$ (

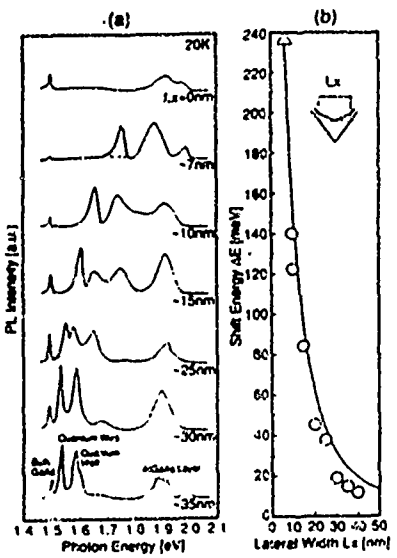

Fig. 4: (a) Photoluminescence(PL) spectra from the quantum wire structures measured as a function of the lateral wire widths at 20K. (b) The energy shift ΔE of the PL peak of the quantum wires versus the lateral width Lx.

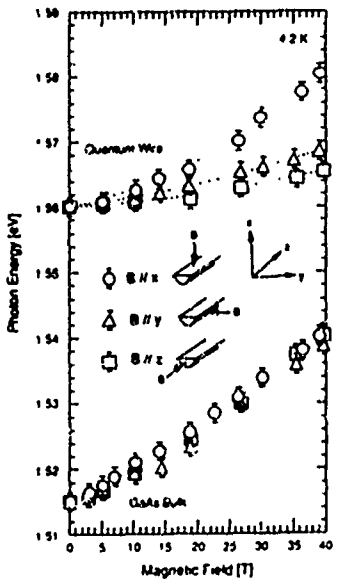

Fig. 5. PL peak positions from the quantum wires and the bulk as a function of applied magnetic field for various configurations. Circles, triangles and squares represent the data for *B//x*,*B//y*, and *B//z* , respectively.

≈ x or y), where L_i is the thickness of the quantum well. Since the SEM observation showed that Lx and Ly are about 12 nm and 20 nm, the value of $(L_x/L_y)^2$ is in good agreement with the value of ω_{0x}/ω_{0y}.

5. Fabrication of Strained InGaAs Quantum Wires and Laser Structures [7]

In the search for new materials useful in semiconductor lasers, strained systems have received great attention. In fact, low threshold current and high modulation frequency have been achieved in the semiconductor lasers with the strain effects. In addition, recent theoretical studiespredicted that the strain effects lead to additional improvements of the lasing characteristics in the quantum wire lasers[14]. Thus it is important to fabricate such strained quantum wire structures.

Here we fabricated InGaAs strained quantum wires using the same technique as that for the GaAs quantum wires because the growth behavior of InGaAs is quite similar to GaAs[15]. Figure 6 shows the PL spectra of the sample at 14 K for various In compositions. The sample was pumped by a CW Ar^+ laser. In this figure, the hatched spectral regions corresponds to PL from the quantum wires. As shown in this figure, the PL peak positions of the quantum wires are

systematically shifted toward to lower energy side with increasing In composition. Here, we assume that In composition of these quantum wire structures is the same as that of InGaAs bulk grown under the same conditions. The lateral width of the quantum wire is estimated to be in the range of 10 and 13 nm.

A laser structure was fabricated with these InGaAs strained quantum wires. Figure 7(a) shows a schematic illustration of the cross section of the structure. Before the deposition of SiO_2, an $Al_{0.4}Ga_{0.6}As$ cladding layer was grown. After the InGaAs quantum wire structures were grown, the structures were embedded by GaAs in order to realize flat surface which can not be obtained with thin AlGaAs layers because of differences of the growth behavior. Then finally an Al0.4Ga0.6As cladding layer is formed again. The wafer were cleaved into 800 mm-long cavity chip. The lasing property of this sample was measured at 10 K, using optical pumping method with a mode-locked Nd^{3+}:YAG laser. Figure 7(b) shows output power of light from the sample plotted as a function of power of the pumping light .

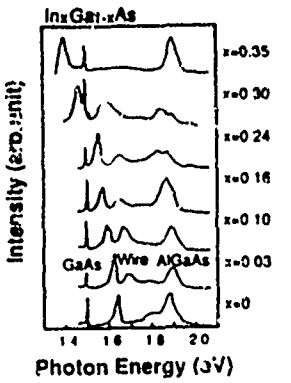

Fig. 6: PL spectra from the InGaAs strained quantum wires with various In content.

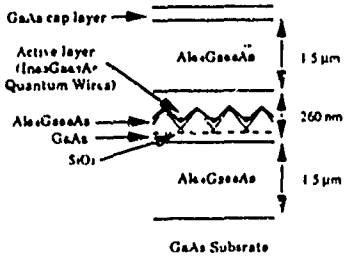

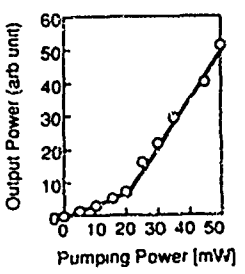

Fig 7: (a) Illustration of a laser structure with the strained quantum wires (b) Light output characteristics the laser structure pumped by Nd3+-YAG lasers.

6. Fabrication of Quantum Dots [8,9]

Fabrication trials of quantum dot structures using masked substrate have been intensively investigated by several groups. Here the GaAs quantum dots were fabricated by the MOCVD selective growth technique on SiO2 patterned (100) GaAs substrates[8]. The masks are consisted of 100nmx100nm nm^2 windows with a period of 140nm. First, $Al_{0.4}Ga_{0.6}As$ plinths are formed on the SiO2 masks. Then, the GaAs is grown on the top of the AlGaAs plinths, followed by the growth of $Al_{0.4}Ga_{0.6}As$ so that the GaAs quantum dots are embedded by $Al_{0.4}Ga_{0.6}As$.

Figure 8 is the cross sectional view of the GaAs surrounded by AlGaAs and its illustration. The photograph indicates that the lateral with of the quantum dots is 25nmx25nm. We believe that this lateral width is the smallest so far as for the GaAs quantum dots embedded by AlGaAs materials.

Even from this small structures, PL can be observed. Figure 9 shows PL spectra of the quantum dot structures excited by an CW argon lasers. In this case electron-hole pairs are excited in the barrier region and then relaxed into the quantum dot region. The energy shift of the PL peak from the quantum dot region is about 18meV. We believe that this energy shift is resulting from the lateral confinement of electrons. The full width of half maximum (FWHM) of the PL peak is

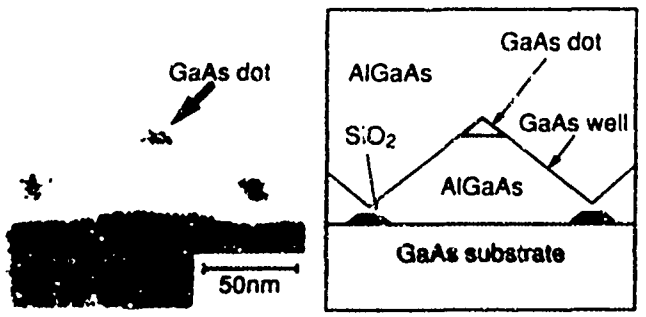

Fig. 8: The cross section of the GaAs quantum dot with a lateral width of 25nm nm as illustration.

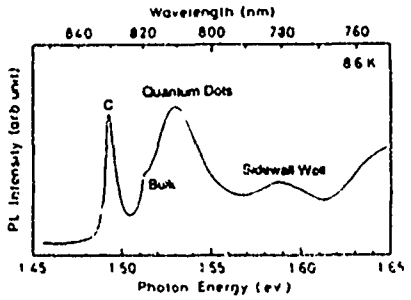

Fig. 9 Photoluminescence spectra of the GaAs quantum dot structures.

broad compared to those of the quantum wires. However, the tail of the luminescence at the low energy side disappears at the photon energy of the bulk GaAs. This indicates that the broadening is not due to strain and defect effects but due to size variation of the quantum dots. In the measurement, more than 100,000 quantum dots are simultaneously excited. Excitation of smaller number of quantum dots are discussed elsewhere.

7. Conclusion

We discussed fabrication of GaAs quantum dots and quantum wires using an *in-situ* MOCVD selective growth on SiO2 patterned substrates. The optical properties of these nano-structures has been also presented. Triangular-shaped GaAs quantum wires with a lateral width less than 10 nm have been obtained. The PL and magneto-PL measurement clearly demonstrate the existence of the quantum wire effects in these samples. In addition, the strained quantum wires with laser structures were also reported. Using a similar but slightly different selective growth technique, GaAs quantum dots with a lateral dimension of 25nm were successfully obtained.

The author expresses his thanks to Dr. Y. Nagamune for the fabrication of quantum dot and his excellent work on the electron beam lithography, to Dr. Tsukamoto for the fabrication of the GaAs quantum wires, to T. Arakawa for the fabrication of the InGaAs quantum wires and the laser structures, to Mr. H. Nishioka for his excellent MOCVD growth work, respectively. He also expresses his thanks to Dr. Weisbuch of Thomson CSF for the discussion on the bottleneck problem and to Professors Y. Fujii, T. Ikoma and H. Sakaki of University of Tokyo for their encouragement and support. We would also like to give our thanks for the support to the University-Industry Joint Project on Mesoscopic Electronics. This work is also supported in part by TEPCO Research Foundation.

References

[1] H. Sakaki, Jpn. J. of Appl. Phys. 19, L735 (1980)
[2] Y. Arakawa and H. Sakaki, Appl. Phys. Lett., 40, 939 (1982).
[3] For example, Y. Arakawa, Extended Abstracts of 1990 International Conference on Solid State Devices and Materials, Sendai, 745, Japan (1990)
[4] S. Tsukamoto, Y. Nagamune, M. Nishioka, and Y. Arakawa, J. of Appl. Phys. 71, 533 (1992).
[5] Y. Nagamune, Y. Arakawa, S. Tsukamoto, and M. Nishioka, Phys. Rev. Lett., 69, 2963 (1992)
[6] S. Tsukamoto, Y. Nagamune, M. Nishioka, and Y. Arakawa, Appl. Phys. Lett., 63, 310 (1993)
[7] T. Arakawa, .Y. Nagamune, S. Tsukamoto, M. Nishioka, Y. Arakawa, 1993 International Conference on Solid State Devices and Materials, Makuhari (1993), submitted to Jpn. J. of Appl. Phys.
[8] Y. Nagamune, S. Tsukamoto, M. Nishioka, Y. Nagamune, J. of Crystal Growth 126, 707
[9] Y. Nagamune, S. Tsukamoto, M. Nishioka, Y. Arakawa, 1992 Gallium Arsenide and Related Compounds, Karuizawa, Inst. Phys. Conf. Ser., 129, 335 (1992)
[10] H. Benisty C.M. Sotomayor,-Torres and C. Weisbuch, Phys. Rev. B 44 10945 (1991)
[11] R. Bhat, E. Kapon, D. M. Hwang, M. A. Koza, and C. P. Yun, J. Cryst. Growth, 93, 850 (1988).
[12] J. A. Lebens, C. S. Tsai, and K. J. Vahala, Appl. Phys. Lett., 56, 2642 (1990).
[13] T. Fukui, S. Ando, and Y. K. Fukai, Appl. Phys. Lett., 57, 1209 (1990).
[14] T. Yamauchi, T. Takahashi, J. Schulman and Y. Arakawa, IEEE, J. of Quantum Electron. QE-29, June Issue (1993)
[15] M. Nishioka, S. Tsukamoto, Y. Nagamune, and Y. Arakawa, J. of Cryst. Growth, 124, 502

MoA2

Polarization spectroscopy of modulated GaAs/GaAlAs quantum wells grown on vicinal surfaces : anisotropic islands or ordered growth ?

J. Bloch, U. Bockelmann* and F. Laruelle

Laboratoire de Microstructures et de Microélectronique, CNRS, B P 107,

92225 Bagneux Cedex, France.

*Walter Schottky Institut, Technische Universität München, D-85748 Garching, Germany.

Abstract

We have investigated the anisotropy of optical properties in quantum wells grown on vicinal surfaces and modulated by a fractional AlAs layer inserted in their middle. Photoluminescence linear polarization is systematicaly measured as a function of terrace length and of AlAs terrace coverage. Our results highlight the influence of anisotropic islands on optical properties.

1. Introduction

In the past decade, a growing interest has been devoted to quantum size effects due to the low dimensionality achievable in semi-conductor nanostructures, both from the viewpoint of fundamental solid state physics and of optical and electronical devices. To fabricate Quantum Well (QW) Wires with lateral dimensions less than 10 nm, direct growth on the atomic step array of a vicinal surface was proposed by Petroff et al. [1]. During idealized step-flow growth, adatoms are intended to diffuse on the terrace and incorporate at the upper step edge. By alternate submonolayer deposition of GaAs and AlAs, it is possible to grow laterally modulated structures. Among other effects, the lateral modulation induces valence band mixing which implies a polarization dependence of the inter-band optical matrix element, a characteristic which has been searched for in early experiments. Anisotropic optical properties of such structures have already been reported for fractional layer superlattices grown by organometallic-vapor-phase epitaxy [2], for serpentine superlattice quantum wires [3] and grid-inserted quantum wells [4] grown by Molecular Beam Epitaxy (MBE). Although ordered growth has been undoubtedly evidenced by structural studies [1-3], the dependence of the electronic properties (linear polarization, spectral shift) on the lateral periodicity remains to be experimentally proved. Here we report on systematic linear polarization measurements of inter-sub-band optical transition in modulated QW. The modulation results from the growth of a fractional AlAs Monolayer (ML) in the middle of the 36 ML GaAs QW. We compare the experimental results with a calculation of the polarization dependent band to band absorption in laterally modulated QW's.

2. Growth

Our samples are grown by Molecular Beam Epitaxy (MBE) simultaneously on three vicinal substrates to allow for a valuable comparison. We used misoriented GaAs substrates (purchased from Sumitomo) tilted from the (001) plane toward [110] by an angle $\alpha = 2°$, 1° and 0.5° ± 0.1° (surface As dimers are parallel to the step edges). This corresponds to a terrace length of 8, 16 and 32 nm respectively. We investigate three different growth conditions. For sample A, we run conventional MBE at 640°C without growth interruption. At lower temperatures (580°C in sample B and 520°C in sample C), we choose Migration Enhanced Epitaxy (MEE) [5]. In this growth mode, elements III and V are alternatively supplied on the surface to improve the adatom mobility. In order to preserve good optical properties, we deposited one fourth of a ML in each MEE sequence [6] and interrupt growth for 3 minutes at both QW interfaces. To let the step array become more periodic, we grow first a 0.5 µm GaAs buffer and 10 periods of a 25Å GaAs/25Å AlAs superlattice. Then a 36 ML GaAs QW with half an AlAs ML in the middle is embedded between two 300 Å $Ga_{0.67}Al_{0.33}As$ barriers. For MBE, growth rates are set to 1 Å/s for GaAs and 0.3 Å/s for AlAs whereas MEE is performed with elemental III fluxes half as large as in MBE.

3. Theory

In this section, we discuss what physical dependencies are expected for the theoretical case of a perfectly ordered lateral structure. Ideally the half monolayer of AlAs incorporated in the QW should form a lateral superlattice with a periode L_y equal to the terrace length. We describe the resulting modulation of the QW energy levels by a periodic lateral potential of the form:

$$V(x) = V_1 \left[\cos\left(\frac{2\pi . x}{L_y}\right) - 1 \right] \qquad (1)$$

The amplitudes V_1 are adjusted for the different 2D subbands and are of opposite sign for electrons and holes. In the present case, they are given by one half of the energy shift induced by one monolayer of AlAs in the middle of the 36 ML (10 nm) wide GaAs/GaAlAs QW. To calculate the polarization dependence of the interband transitions in laterally modulated structures, it is necessary to solve the Γ_8 valence band Hamiltonian which includes the effects of heavy-hole (hh) light-hole (lh) mixing [7-11]. A detailed description of the theory and more results on energy dispersions and absorption spectra for QW's with a periodic lateral modulation are given in ref. 11. In fig 1 (bottom part), we present absorption spectra calculated for a 10 nm wide QW with half a ML of AlAs that forms a lateral superlattice of period $L_y = 32$ nm. Spectra are given for a linear polarization in the QW plane, perpendicular (x) and parallel (y) to the step edges and for a polarization oriented along the QW growth axis (z). In z-polarization only the lh part of the valence band wavefunction contributes to the absorption spectrum. In the upper part the normalized difference between the x and y spectra is given (the polarization P is defined in eq 2 below). A positive (negative) value of the polarization P identifies a transition that involves a valence band state of dominant lh (hh) character. The magnitude of the lateral anisotropy is determined by the amount of hh-lh mixing. It is quite small in the present case because the confinement by the quantum well dominates over the one caused by the lateral superlattice.

Both energy and polarization of the absorption peaks depend on the period L_y. The onset of the absorption shifts by 8 meV to higher energies with L_y decreasing from 32 nm to 8 nm. Parallel to that, the magnitude of P of the lowest absorption peak decreases from 0.15 to 0.03 due to increasing tunneling through the lateral barriers. The lowest transition is always polarized along the y-axis and the variation of the polarization effect over the energy range of the peak is very small.

4. Optical experiments

Photoluminescence (PL) and photoluminescence excitation (PLE) spectroscopy are performed with a tunable Ti:Sapphire laser (exciting power density : 1 Wcm^{-2}) pumped with an Ar^+ laser. PL is dispersed through a double monochromator and detected with a cooled GaAs photomultiplier and a gated photon counting system. The polarization anisotropy of PL and PLE spectra is measured with a photoelastic modulator (PEM). This apparatus introduces a periodic phase shift $\Phi = \Phi_0 \sin(2\pi f t)$ (f = 50 kHz) between orthogonal components (along the PEM optical axis) in the transmitted light beam. To measure linear polarization, Φ_0 is chosen equal to π and the photon counter gate A (B), synchronized at the 2f PEM reference frequency, is open around $t = 0$ ($t = 1/4f = 5$ µs) during 1.7 µs. Data are accumulated for 1 s. We have checked that polarization measurements give similar results with shorter gate length.

Samples are mounted so that the [1 1 0] direction (step edges direction) is parallel to the horizontal line and makes a 45° angle with the PEM optical axis. We checked thoroughly that all optical elements (lenses, cryostat windows,...) have no optical activity. The experimental set up is the following :

a) PL polarization spectrum : the PEM is placed between the sample and the monochromator and is followed by a Glan-Thompson polarizer parallel to the horizontal line. In this configuration, gate A (B) counts the PL intensity $I_{\parallel}$ ($I_{\perp}$) polarized parallely (perpendicularly) to the step edges. The sample has to be precisely oriented perpendicularly to the monochromator optical axis in order to avoid PL polarization induced by refraction at the GaAs/air interface. As already underlined in ref.[12], the light which enters the spectrometer is always polarized along the same direction so that the grating polarization does not matter.

b) PLE polarization spectra : the PEM is placed between the laser (whose polarization is horizontal) and the sample. Gate A (B) counts the PL intensity $I_{\parallel}$ ($I_{\perp}$) corresponding to an absorbed light polarized parallely (resp. perpendicularly) to the step edges. The sample is then oriented perpendicularly to the exciting light beam and not to the monochromator optical axis.

In both configurations the polarization value is defined by the quantity:

$$P = \frac{I_{\perp} - I_{\parallel}}{I_{\perp} + I_{\parallel}} \qquad (2)$$

The PEM allows a typical accuracy of 0.5% in the polarization measurements with a 1 s counting time. It is limited by the signal to noise ratio. The PEM measures PLE polarization anisotropy without moving the exciting light beam as is the case when rotating Glan-Thompson polarizers. One also notices that the gated photon counter measures directly $I_{\perp}$ and $I_{\parallel}$. The evaluation of P does not need any normalisation procedure but requires fewer electronic than used by Wassermeier et al. [12]

5. Results

All samples with half an AlAs monolayer in the middle of the QW present good optical properties at 2 K : PL linewidth and Stokes-shift do not exceed 4 meV. The spectral position of the hh excitonic transition corresponds in average to the 1.576 eV calculated gap (corrected by a 9 meV exciton binding energy) of a 36 ML GaAs QW with half a homogeneous AlAs ML in the middle. This fractional layer introduces a PL blue-shift of 27 meV relative to the bare QW.

To compare polarization anisotropy in PL and in PLE, we chose a temperature of 77 K so that excited QW levels are thermally populated. We have verified that polarization PLE spectra weakly depend on temperature between 2K and 77 K. Figure 2 shows PL and corresponding polarization spectra of samples A, B and C for a terrace length of 8 nm. Sample A and B exhibit similar polarization spectra : the low energy side of the fundamental transition is polarized along the step edges whereas the high energy side shows a pronounced polarization peak perpendicularly to the step edges. The lh like transition is well resolved and is polarized parallely to the step edges. These results do not agree with theoretical predictions.

Figure 3 presents PL and PLE polarization spectra of sample B : the same inhomogeneous polarization in the fundamental transition is evidenced in PLE. Polarization spectra are the same whether we modulate the polarization of the absorbed light in PLE or the polarization of the emitted light in PL. This indicates that both experiments measure the polarization anisotropy of the optical matrix element.

To determine the hh-lh mixing through circular polarization selection rules, we have realized optical pumping experiments with the PEM and a quarter-wave plate. Circular polarization spectra are the same whether there is or not AlAs in the middle of the QW. As is well established [13], the hh like excitonic line is homogeneously and strongly polarized whereas the lh transition shows a pronounced dip in the polarization PLE spectrum. In our samples, the linear polarization direction does not allow the precise identification of heavy or light hole predominence in a given optical transition as optical pumping does.

Sample C grown at a lower temperature (520 °C instead of 640 or 580°C) does not present any polarization anisotropy either in the PL or in the PLE spectrum (shown in fig 2). This demonstrates that the polarization anisotropy we measure on sample A and B is due to a thermally activated organization of the Al adatoms into anisotropic islands when they are deposited on the GaAs surface. At 520 °C, the surface mobility is considerably reduced so that Al ada-

lasers are randomly distributed and AlAs anisotropic islands do not form.

We studied the evolution of the PL polarization spectra with the AlAs terrace coverage θ. Some typical PL spectra are shown in figure 4 for samples grown by MBE at 640 °C. The PL line energy of the QW with 0 or 1/2 AlAs ML correspond to the 1.565 and 1.571 eV calculated gap within the experimental precision. For the QW with 1 and 3/2 AlAs ML, we measure the PL at an energy of 1.605 and 1.626 eV. These values are larger than the calculated ones (1.591 and 1.604 eV). This is probably due to a Ga flux lower than intended. Due to an increased disorder, PL line widths are getting larger when we rise the AlAs terrace coverage.

When no Aluminium is deposited in the middle of the QW, no polarization anisotropy is measured. Then when θ is increased, the polarization peak rises and is maximum for θ = 1/2. It goes down to zero for θ = 1 and rises again for θ = 3/2. We can notice that the P versus θ curve displayed in figure 5 is not symmetrical about θ = 1/2. The polarization peak is much weaker for θ = 3/4 than for θ = 1/4 suggesting that the AlAs islands distribution is more disordered for 3/4 ML than for 1/4 ML. In the same way, 1/2 AlAs ML deposited on a GaAs surface seems to form more anisotropic islands than when deposited on a surface where 1 ML AlAs has already been grown (θ = 3/2).

Another effect expected from the lateral periodicity is the variation of the QW effective band gap, shifting to higher energies for shorter periodicities. To allow for a valuable comparison between the PL energy of different samples, we chosen pieces which were close to one another during the simultaneous growth. In order to avoid energy shifts due to molecular beams inhomogeneities across the wafers. Therefore, shifts smaller than ± 2.5 meV are not considered as reliable for the investigated structures. We have not detected any significant PL energy dependence on terrace length in our samples grown by MBE or MEE. Moreover similar polarization spectra were measured for all the terrace lengths we investigated (8 ,16 and 32 nm), and even on a (001) oriented substrate (oriented with a 0.05° precision). This evidences that steps do not play a crucial role in the polarization anisotropy we measure and this suggests that anisotropic AlAs islands form independently of the step array. The island shape reflects the surface anisotropy between [110] and [1$\bar{1}$0] directions during the growth. Both surface diffusion [14] and step attachment of element III adatoms [15] strongly differ between these two directions. This picture of random AlAs islands is in agreement with preliminary results obtained with transmission electron microscopy cross-section of our samples. When disorder is introduced and anisotropy is preserved, previous theoretical works [10–11] indicate that polarization remains whereas the spectral effect vanishes. This argument has been put forward to explain similar results obtained by Dawson et al. [16] whereas ref. [4] reports no linear polarization for a nominal surface. This discrepancy might originate from different growth conditions.

6. Conclusion

We have evidenced a linear polarization anisotropy in modulated QW which strongly depends on growth conditions and on the fractional AlAs coverage introduced in the middle of the QW. Our systematic theoretical study shows that in the case of a perfect ordered growth, we would expect a strong dependence of electronic properties on the lateral periodicity between 32 and 8 nm. In our samples, we did not measure any significant variation of the PL energy or of the PL linear polarization with the terrace length. This indicates that, in our growth conditions, the AlAs half ML introduced in the middle of the GaAs QW, is weakly ordered by the step array. When it is grown at 520°C, the AlAs half ML is homogeneously distributed, whereas for growth at higher temperature (580 or 640°C), polarization measurements suggest that it is made of anisotropic islands. These results highlight the influence of anisotropic islands on optical properties and the sensitivity of polarization measurements using modulation techniques.

Acknowledgements

We wish to thank B. Etienne and R. Planel for many fruitful and stimulating discussions. We are also very grateful to J.Y. Marzin for his collaboration and to C. Vieu for his contribution in electronic microscopy. We express our thanks to N. Launois for her support.

References

1. P.M. Petroff, A.C. Gossard, and W. Wiegmann, Appl. Phys. Lett. 45, 620 (1984).
2. M. Kasu, H. Asahi, H. Saito, and T. Fukui, Appl. Phys. Lett. 59, 301 (1991).
3. M.S. Miller, H. Weman, C.E. Pryor, M. Krishnamurthy, P.M. Petroff, H. Kroemer, and J.L.Merz, Phys. Rev. Lett. 68, 3464 (1992).
4. M. Tanaka and H. Sakaki, Appl. Phys. Lett 54, 1326 (1989)
5. Y. Horikoshi, M. Kawashima, and H. Yamaguchi, Jpn. J. Appl. Phys 25, L868 (1986)
6. P. Lavallée and J. Bloch, J. Cryst. Growth 127, 774 (1993) and references therein.
7. P. C. Sercel and K. J. Vahala, Phys. Rev B44, 5681 (1991)
8. U. Bockelmann and G. Bastard, Europhys. Lett. 15, 215 (1991)
9. D.S. Citrin and Y.C. Chang, Phys. Rev. B 43, 11703 (1991)
10. G. E.W. Bauer and H. Sakaki, Phys. Rev. B 44, 5562 (1991)
11. U. Bockelmann and G. Bastard, Phys. Rev. B 45, 1688 (1992)
12. M. Wassermeier, H. Weman, M.S. Miller, P.M. Petroff and J.L. Merz, J. Appl Phys 71, 2397 (1992)
13. R.C. Miller, W.T. Tsang and W.A. Nordland, Phys Rev B 21, 1569 (1980)
14. K. Ohta, T. Kojima, and T. Nakagawa, J Cryst Growth 95, 71 (1989)
15. T. Shitara, D.D. Vvedensky, M.R. Wilby, J. Zhang, J H. Neave, and B A Joyce, Phys Rev B 46, 6825 (1992); T. Shitara, J.H. Neave, and B.A. Joyce, Appl Phys Lett 62, 1658 (1993)
16. P. Dawson, D.J. Wentink and G. Bauer, private communication

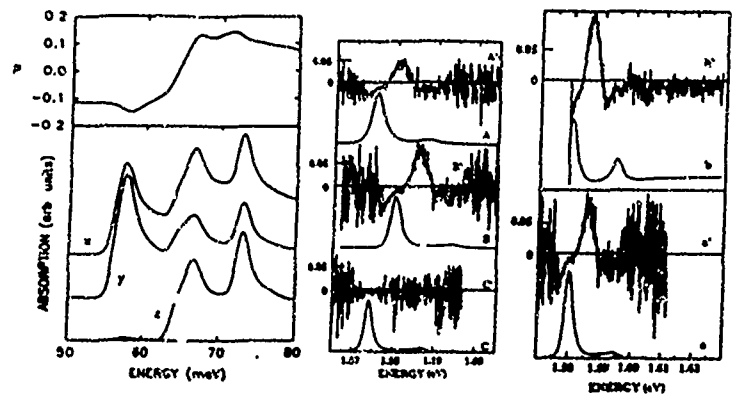

Figure 1 : Calculated absorption spectra of a GaAs/$Ga_{0.75}Al_{0.25}As$ QW (L_z = 10 nm) subjected to a lateral band gap modulation of period L_x=32 nm for three different linear light polarizations. Zero energy corresponds to the band gap of bulk GaAs (1.519 eV at 2 K, 1.514 eV at 77 K). In the upper part, the normalized linear anisotropy is given (P is defined in eq. 2).

Figure 2 : PL spectra measured at 77 K of sample A, B and C described in the text. Labels correspond to the sample names. Each spectrum has been shifted vertically for clarity. PL intensity is plotted in linear scale and arbitrary units. A', B', C' are the corresponding linear polarization spectra. Each base line is shown as well as a five percent reference marker.

Figure 3 : bottom : PL spectrum (a) and associated polarization spectrum (a') of sample B. Top: PLE spectrum (b) and associated polarization spectrum (b') of sample B. Spectra are measured at 77 K. In PLE, the PL detection energy is set to 1.579 eV. PL intensities are plotted in linear scale and arbitrary units. For polarization spectra, the base line is shown as well as a five percent reference marker.

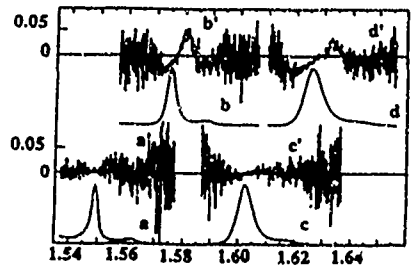

Figure 4 : PL spectrum of a 36 ML QW grown by MBE at 640°C with a) no AlAs, b) 1/2 (sample B described in the text), c) 1, d) 3/2 AlAs ML in the middle. PL intensities are plotted in linear scale and arbitrary units. Curves a', b', c' and d' are the respective linear polarization spectra. Each base line is shown as well as a five percent reference marker.

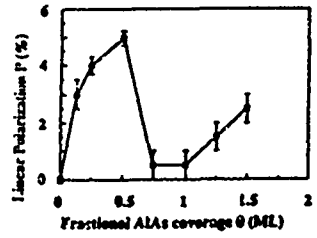

Figure 5 : PL linear polarization of a 36 ML QW grown by MBE at 640°C as a function of the AlAs terrace coverage.

MoA3

Preparation of low dimensional structures by molecular beam epitaxy-regrowth on patterned AlGaAs buffer layers

K. Eberl, A. Kurtenbach, P. Grambow, A. Lehmann and K.v. Klitzing
Max-Planck-Institut für Festkörperforschung, 70569 Stuttgart, Germany
D. Heitmann
Max-Planck-Institut für Festkörperforschung, 70569 Stuttgart and Institut für Angewandte Physik, 20355 Hamburg, Germany
M. Dilger and M. Hohenstein
Max-Planck-Institut für Metallforschung, Institut für Physik, 70569 Stuttgart, Germany

Abstract

We studied the preparation of low dimensional structures by molecular beam epitaxy (MBE)-regrowth on patterned AlGaAs buffer layers. The detailed interface and surface structure was investigated by scanning electron microscopy and transmission electron microscopy. The active area on the patterned $Al_{0.33}Ga_{0.67}As$ buffer layer was passivated by a thin GaAs cap layer which is thermally desorbed in the MBE-system prior to overgrowth. Small (111)A and larger (311)A facets dominate the surface structure after MBE-regrowth on the etched ridges along the $[0\bar{1}1]$ direction within the (100) surface plane. Hall effect measurements demonstrate that an electron concentration of $8x10^{11}cm^{-2}$ is achieved in a 20nm wide modulation doped quantum well with a regrown AlGaAs buffer layer thickness of only 65nm. No free carriers are detected in the overgrown quantum well within the region where the etched $Al_{0.33}Ga_{0.67}As$ surface was exposed to air.

Epitaxial growth of GaAs/AlGaAs heterostructures on patterned GaAs substrates and AlGaAs buffer layers opens the possibility to synthesize one and zero dimensional structures. Planar devices have been demonstrated based on regrowth after lithography and etching processes [1-5]. It is known, that different facets evolve during molecular beam epitaxy growth on non planar substrates [5-9]. The detailed surface structure depends mainly on the orientation of the etched pattern and the growth parameters.

In this contribution we study the MBE-regrowth on mesa etched lines in $[0\bar{1}1]$ direction within the (100) surface on $Al_{0.33}Ga_{0.67}As$ buffer layers. The 300nm thick $Al_{0.33}Ga_{0.67}As$ buffer layer and a 10nm GaAs cap layer are deposited in a first MBE-growth step. It is difficult to grow directly on AlGaAs which was exposed to air, because of the formation of very stable aluminiumoxide. On the other hand, it was demonstrated that a clean AlGaAs surface can be achieved by covering the active area of the AlGaAs buffer with a thin passivating GaAs layer, which can be thermally desorbed in the MBE-system prior to regrowth [2,10]. We used both, disrupted growth in the exposed AlGaAs area and perfect MBE-regrowth in the active area on the ridges to prepare modulation doped quantum wire structures [11].
The wafers are patterned by holographic lithography and subsequent reactive ion etching with a $SiCl_4$-process. Figure 1a shows the patterned $Al_{0.33}Ga_{0.67}As$ buffer layer on GaAs (100) substrate. The step height of the mesa etched lines is about 100nm. The period length of the etched grating is 1µm. The lines are oriented in $[0\bar{1}1]$ direction. The area on top of the ridge is passivated by a thin GaAs cap layer. After a careful cleaning procedure, the patterned wafers are introduced into the MBE-system. The cleaning involves the following steps: Repeated stripping of the photoresist with a resist remover, oxygen plasma, and 15 minute rinse in concentrated H_2SO_4 followed by a di-water rinse. Just before starting the MBE regrowth the 10nm thick GaAs passivation layer is desorbed by annealing the sample at 720°C for 10 minutes in As_4 atmosphere.

Figure 1b to 1e shows a series of samples with increasing thickness of the overgrown layer sequence from 34nm to 220nm. The samples 1b and 1d are grown on identically patterned GaAs substrates. The growth was carried out in an Intevac GEN II system at a substrate temperature between 560°C to 580°C and with continuous wafer

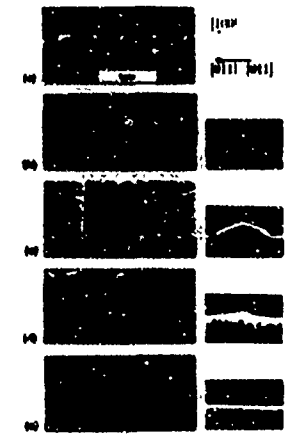

Figure 1.
SEM pictures. Patterned AlGaAs buffer layer with the ridges along $[0\bar{1}1]$ on (100) GaAs substrate (a). After MBE-regrowth 34nm (b), 90nm (c), 132nm (d), and 220nm (e). The lateral period length of the patterning is 1µm for all samples.

rotation at 12rpm. The growth rate for GaAs was 0.1nm/s with an As/Ga ratio of 4:1. For the sample shown in 1b, the total thickness of the overgrown layer (8nm $Al_{0.33}Ga_{0.67}As$ / 8nm GaAs / 8nm $Al_{0.33}Ga_{0.67}As$ / 10nm GaAs) is less than the etch depth. The etched grooves are partly filled. On top of the ridges we observe mainly (311) facets and a small (100) flat.
The thickness of the overgrown layer for the sample shown in Figure 1c is 90nm. The same sample is shown in more detail in the TEM micrograph in Figure 2. The overgrown layer sequence is: 0.56nm GaAs marker layer / 40nm $Al_{0.33}Ga_{0.67}As$ / 10nm GaAs / 30nm $Al_{0.33}Ga_{0.67}As$ /10nm GaAs cap layer.
The interface between GaAs substrate and AlGaAs buffer layer on the bottom, and the profile of patterning is clearly observable in the TEM picture. The surface of the overgrown structure on the ridge is dominated by the Ga terminated (311)A, and (111)A facets. The 10nm thick GaAs quantum well is marked in the area of the etched groove and on top of the ridge. The surface of the patterned $Al_{0.33}Ga_{0.67}As$ buffer layer was passivated on the ridge, consequently we achieve perfect epitaxial regrowth in this region. It is however quite remarkable that there are also no extended defects observable in the TEM picture at the interface in the etched region where the $Al_{0.33}Ga_{0.67}As$ was exposed to air.
Figure 1d and 1e show samples where the thickness of the overgrown layer sequence was 132nm and 220nm respectively. The growth rate on the (100) surface is obviously much larger than on the (311)A and (111)A facets, so that the surface patterning is completely buried after 220nm thick overgrowth. Figure 1d is also shown in more detail in the TEM micrograph in Figure 3. In this sample we deposited a sequence of six times alternating 11nm $Al_{0.33}Ga_{0.67}As$ / 11nm GaAs grown on a patterned GaAs substrate without $Al_{0.33}Ga_{0.67}As$ buffer layer. Before starting the regrowth the patterned wafer was heated to 620°C for 15 minutes to remove the oxide. The interface between the patterned GaAs substrate and the first overgrown 11nm thick AlGaAs layer indicates, that there is already a (311)A facet formation on the edges of the GaAs ridge. This is not observed for

Figure 2.
Cross sectional TEM micrograph of the sample shown in Figure 1c. The overgrown layer sequence is: 0.56nm GaAs marker layer / 40nm $Al_{0.33}Ga_{0.67}As$ / 10nm GaAs / 30nm $Al_{0.33}Ga_{0.67}As$ /10nm GaAs cap layer. The structure was grown on a patterned 300nm thick $Al_{0.33}Ga_{0.67}As$ buffer layer.

Figure 3:
Cross sectional TEM micrograph of the sample shown in Figure 1d. The overgrown layer sequence is six times 11nm $Al_{0.33}Ga_{0.67}As$ / 11nm GaAs grown on a patterned GaAs substrate without AlGaAs buffer layer

the patterned $Al_{0.33}Ga_{0.67}As$ buffer layer as one can clearly see on Figure 2 even though the $Al_{0.33}Ga_{0.67}As$ samples have been annealed to 720°C for 10 minutes. The small {311}A facets on the patterned GaAs surface with lines along the $[0\bar{1}1]$ direction obviously evolve during the annealing process. Otherwise we did not observe significant differences in the regrowth behavior of AlGaAs/GaAs heterostructures for patterned $Al_{0.33}Ga_{0.67}As$ buffer layers or GaAs substrates. Figure 3 demonstrates how the surface morphology develops as the thickness increases. The main aspects are:

- The deposition rate on the {311}A planes is significantly smaller than on (100). Therefore the {111}A facets become dominant on the ridges. After the etched grooves are filled up the (100) plane between the ridges start to overgrow the {311}A facets, and finally a smooth surface is regained (see also Figure 1c)
- The {111} facets play a minor role as compared to regrowth on [011] oriented lines of the patterned substrates (see for example Ref. [9])
- On {111}A the AlGaAs layers are significantly thicker than the GaAs layers
- The GaAs layers are thicker than the AlGaAs layers on the small (100) flat in the middle of the ridge. Ga migration on the {311} facets increase the growth rate on the (100) planes [6]

These points in turn allow to prepare extremely narrow quantum wires on top of the ridge which are completely embedded in a finally planarized structure. In the sample shown in Figure 3 the second GaAs quantum well forms a triangular shaped wire with a lateral width of about 30nm.

For the characterization of the electronic properties of the MBE-regrown layers we performed Hall effect measurements. Both the active region on the ridge where the $Al_{0.33}Ga_{0.67}As$ buffer was passivated and the area which was etched and exposed to air were investigated. Therefore we prepared a Van der Pauw geometry of 4x4mm in an unpatterned area of the wafer and in a large 100nm deep mesa etched section. The overgrown layer sequence was: 15nm $Al_{0.33}Ga_{0.67}As$ / 30nm $Al_{0.33}Ga_{0.67}As$ (Si doped) / 20nm $Al_{0.33}Ga_{0.67}As$ spacer / 20nm GaAs quantum well / 10nm $Al_{0.33}Ga_{0.67}As$ spacer / 30nm $Al_{0.33}Ga_{0.67}As$ (Si doped) / 10nm GaAs cap layer. The structure was grown on a 300nm $Al_{0.33}Ga_{0.67}As$ buffer layer with a 30nm GaAs cap layer which was desorped prior to regrowth. The curve (a) in Figure 4 shows the two dimensional (2D) electron density and the mobility for this sample. At room temperature we measure a density of $1.8x10^{11}cm^{-2}$ with a mobility of 3000 cm^2/Vs. The carrier density drops to less the $10^{10}cm^{-2}$ region at 77K.
In sample (b) we replaced the first 15nm $Al_{0.33}Ga_{0.67}As$ layer by a superlattice with five periods of 1nm AlAs / 2nm GaAs. Thus, the total thickness of the regrown buffer below the 20nm GaAs quantum well is again 345nm. 2D electron density and mobility at room temperature increase to $8x10^{11}cm^{-2}$ and 5120 cm^2/Vs for this sample. The curve (c) shows the data for a reference sample were the 300nm thick $Al_{0.33}Ga_{0.67}As$ buffer layer including the overgrown layer sequence like for sample (a) were deposited in one MBE process. The electron density at room temperature in the reference sample is $1.25x10^{12}cm^{-2}$ with a mobility of 8300 cm^2/Vs. For the overgrown samples shown in Figure 4 (a) and (b) we did not detect free carriers within the etched region where the $Al_{0.33}Ga_{0.67}As$ buffer layer was exposed to air.

Figure 4:
Hall effect measurement on modulation doped quantum well structures regrown on a 300nm thick $Al_{0.33}Ga_{0.67}As$ buffer layer. Overgrown layer sequence: 15nm $Al_{0.33}Ga_{0.67}As$ / 30nm $Al_{0.33}Ga_{0.67}As$ (Si doped) / 20nm $Al_{0.33}Ga_{0.67}As$ spacer / 20nm GaAs quantum well / 10nm $Al_{0.33}Ga_{0.67}As$ spacer / 30nm $Al_{0.33}Ga_{0.67}As$ (Si doped) / 10nm GaAs cap layer
(a) 10 minutes thermal annealing at 720 C in As_4 atmosphere before overgrowth
(b) like (a) however 5periods of 2nm GaAs / 1nm AlAs instead of the 15nm $Al_{0.33}Ga_{0.67}As$ layer
(c) reference sample. 300nm $Al_{0.33}Ga_{0.67}As$ buffer layer and overgrown layer sequence are deposited in one MBE run without an intermediate patterning process

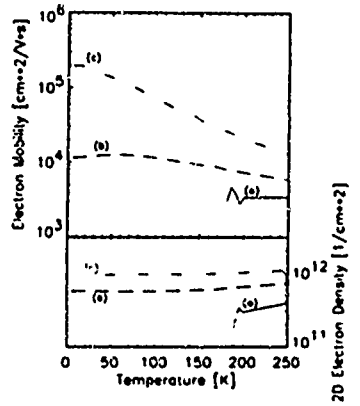

Therefore we can assume, that active quantum well structures with free electrons are formed on the ridges, which are electrically isolated by the inactive regions in the etched sections of the sample. Far-infrared spectroscopy on similar samples support this conclusion. The results have been presented in Ref. [11]. They strongly indicate that a quasi 1D electron gas is formed on top of the overgrown ridge.

In conclusion, we demonstrated that extremely narrow completely encapsulated modulation doped quantum wire structures can be prepared in a very controlled way by MBE-regrowth on $[0\bar{1}1]$ oriented mesa etched lines on AlGaAs buffer layers. This method allows to prepare low dimensional electronic device structures which are defined and separated by the etched areas which are electrically inactive.
We wish to thank M. Hauser, B. Schönherr, C. Lange, A. Gollhard and M. Rieck for expert technical assistance.

References

[1] W. Tsang and A. Y. Cho, Appl. Phys. Lett. 30, 293 (1977)
[2] H. Tanaka and M. Mushiage, J. Crystal Growth 111, 1043 (1991)
[3] I. Kapon, S. Simhony, J.P. Harbison, L.T. Florez and P. Worland, Appl. Phys. Lett. 56, 1825 (1990)
[4] W.Q. Li, Y.J. Chan, P.K. Bhattacharya, J. Vac. Sci. Technol. B10, 1035 (1992)
[5] J. S. Smith, P. L. Derry, S. Margalit, and A. Yariv, Appl. Phys. Lett. 47, 712 (1985)
[6] H. P. Meier, J. Van Gieson, P. W. Epperlein, C. Harder, W. Walter, M. Krahl and D. Bimberg, J. Crystal Growth 95, 66 (1989)
[7] J. Brockenhoff and H. Beneking, J. of Crystal Growth 114, 619 (1991)
[8] T. Takebe, M. Fujii, T. Yamamoto, K. Fujita, and K. Kobayashi, J. of Crystal Growth 127, 937 (1993)
[9] Y. Nakamura, S. Koshiba, M. Tsuchiya, H. Kano and H. Sakaki, Appl. Phys. Lett. 59, 760 (1991)
[10] M. Walther, J. Rohr, G. Bohm, G. Trankle and G. Weimann, J. of Crystal Growth 127, 1045 (1993)
[11] K. Eberl, C. Grambow, A. Lehmann, A. Kurtenbach, K.v. Klitzing, D. Heitmann, M. Dilger and M. Holzenstein, Appl. Phys. Lett. in press

MoA4

Fabrication of SiGe/Si quantum wire structures on a V-groove patterned Si substrate by gas-source Si molecular beam epitaxy

N Usami, T.Mine* S Fukatsu, and Y Shiraki

Research Center for Advanced Science and Technology (RCAST)
The University of Tokyo
4-6-1 Komaba Meguro-ku Tokyo 153 Japan

Fabrication of SiGe Si quantum wire (QWR) structures on a V-groove patterned Si substrate by gas source Si molecular beam epitaxy (GS SiMBE) is reported. Cross sectional image of transmission electron microscope (TEM) clarified a crescent shaped SiGe layer at the bottom of the V groove. Existence of the quantized state in QWR was evidenced by photoluminescence (PL) spectra of the QW grown by selective epitaxial growth (SEG) technique.

1. Introduction

Modulated semiconductor structures with reduced dimension have attracted considerable attention for the possibility of obtaining new and novel optical properties due to the quantum confinement effect. Among various techniques to obtain quantum wire (QWR) structures, growth on non planar substrates is promising since it is free from damage during processing. Recently, Kapon *et al.* reported the successful growth of GaAs/AlGaAs QWR arrays on a V-groove patterned GaAs substrate by metal organic chemical vapor deposition (MOCVD) [1] and demonstrated room temperature operation of QWR laser [2]. Pan *et al.* fabricated GaAs/GaAsP QWR by also MOCVD and clearly showed the existence of quantized state in QWR by cathodeluminescence (CL) [3]. These reports are actually some parts of great progress in the *in situ* fabrication of QWR in III-V material system [4]-[7]. However, SiGe/Si QWR has not been obtained yet in spite of recent rapid progress in research on luminescence properties of this material system. Therefore, we report the successful fabrication of SiGe/Si QWR arrays on a V-groove patterned Si substrate using gas source Si molecular beam epitaxy (GS SiMBE). A crescent-shaped SiGe layer was clearly seen in cross sectional image of transmission electron microscopy (TEM). Photoluminescence (PL) spectra of the QWR grown by selective epitaxial growth (SEG) technique showed phonon resolved luminescence which might come from QWR region.

2. Experimental

Figure 1 shows the fabrication process of SiGe/Si QWR. At first, a 1350Å SiO_2 film was uniformly grown on a Si(100) substrate by thermal oxidation technique (a). Subsequently, standard electron beam lithography was carried out in order to generate line (0.3μm) and space (0.3μm) patterns along the [110] direction (b). After removing resist completely by O_2 plasma irradiation, the substrate was dipped in N_2H_4-based solution in order to create a V-groove pattern with Si(111) facets (c). The top SiO_2 layer acts as a mask for the chemical etching. QWR growth was performed in a GS SiMBE (Daido Hoxan VCE S2020) system using disilane (Si_2H_6) and germane (GeH_4) as gaseous sources. The detail of the system reported elsewhere [8]. In some cases, the SiO_2 layer was removed with hydrofluoric acid (d) before introduction into loading chamber. Prior to growth, the substrate temperature was raised up to 850 °C and kept for 10 minutes so as to thermally desorb the contaminants and to obtain a clean surface. Then, the substrate temperature was lowered to 740 °C. In order to obtain a high quality surface while maintaining geometry of the V-groove sharp, the thickness of the Si buffer layer was reduced to less than 1000Å. It is noted that we should take three different regions into account when discussing the structure of the sample. One of them is a SiGe QWR layer formed at the bottom of the V groove as shown in the bottom of Fig.1. The others are quantum well (QWL) structures on Si(100) flat region and Si(111) sidewall. In order to facilitate PL peak assignment, SEG was also performed. In this case, the Si (100) flat region between neighboring grooves was kept being covered with the SiO_2 layer. Under appropriate growth condition, no growth occurs on this SiO_2 layer. Hence, QWL on Si(100) flat region is not formed. PL spectra were measured in standard lock-in configuration and detected by a liquid nitrogen-cooled Ge photo-detector (North Coast EO-817L). Excitation was provided by a defocused argon-ion laser with an optical power density of 10-100mW/cm^2.

3. Results and Discussion

Figure 2 (a) shows a typical cross sectional transmission electron microscopy (TEM) image of $Si_{0.82}Ge_{0.18}$/Si QWR grown on a V-groove patterned Si substrate. Ge atomic composition was estimated by x-ray diffraction of QWL which was grown on a Si(100) substrate using the same growth conditions. A very sharp V-form is seen as a dark band which represents the interface between the substrate and the Si buffer layer. At the bottom of the groove, excellent crescent shape can be clearly seen in this micrograph. We believe that this is the first successful fabrication of QWR like SiGe layer. Any traces of misfit dislocation were not found. From a simple estimation by the nominal growth rate (5.4 Å/sec) and the growth time (6 sec), the vertical wire width of this sample is expected as about 32.4 Å. However, this micrograph shows that the vertical wire width is as thick as 100 Å. On the other hand, well width of QWL fabricated on Si(111) facets is much smaller than the expected value. Hence, the unexpected large value of vertical wire width might be brought by the surface migration of adatoms on Si(111) to the bottom of the V groove. Figure 2 (b) shows a typical cross sectional TEM image of a QWR fabricated by SEG technique. Epitaxial growth occurs only between the groove, and no polycrystalline Si layer can be found on the SiO_2 layer. Figure 3 shows PL spectra of Si/SiGe/Si heterostructures grown on (a) on-axis Si(100) substrate, (b) a V-groove patterned Si substrate without SiO_2 layer, and (c) with SiO_2 layer. These three different samples were grown using strictly same growth conditions. The thickness of a Si buffer layer and the SiGe well width of this sample is nominally ~40 Å and 32.4 Å for Si (100) flat region, respectively. In the spectra (a), No phonon (NP) transition due to symmetry breaking allow

---

* *On leave from Hitachi Central Research Laboratory*
1-280 Higashi-koigakubo, Kokubunji-shi Tokyo 185 Japan

disorder in the SiGe well layer and its transverse optical (TO) phonon replica can be clearly identified. The peaks labeled Si around 1097 meV come from the Si substrate with assistance of TO phonon. In the spectra (b), phonon resolved spectra can be seen. The intense part is thought to come from the QWL formed on the Si (100) flat region between the grooves. Spectral blue shift can be seen compared to the spectra (a) which comes from a reduced well width. This might be brought by a reduced effective source gas flux due to a large surface area and/or the diffusion of adatoms to the groove. Since we can hardly identify the emission from the QWR at the bottom of the groove due to the intense luminescence from the QWL on Si (100), we carried out PL measurement of the QWR grown by SEG. The result is shown in Figure 3 (c). At the lower energy side of the emission from the Si substrate, we can observe a pair of two peaks. The energy separation (98meV) between the two peaks is in good agreement with Si-Si TO phonon energy. One can say that these peaks are NP and its TO phonon replica of a quantized state. The QWL region on the (111) facet is a candidate which attribute to the emission. However, a QWL on Si (111) grown at the temperature selected here is known not to exhibit PL [9]. Moreover, the peak energy is much lower than the estimation by a numerical calculation using the well width on Si(111) obtained by TEM measurement. Hence, this quantized state can be attributed to the QWR layer fabricated at the bottom of the V-groove.

4. Conclusion

We succeeded in growing SiGe/Si QWR arrays on a V-groove patterned Si substrate by GS-SiMBE. Excellent crescent shaped SiGe layer was evidenced by TEM cross sectional image. PL spectra of the QWR formed by selective epitaxial growth technique showed the existence of the quantized state in QWR.

Acknowledgement

We would like to acknowledge A. Nishida, I. Sakama and K. Suzuki for their expert technical support. H. Oku, T. Ohnishi and S. Okumura are gratefully acknowledged for developing the GS-SiMBE system. We thank H. Sunamura and S. Ohtake for their technical support. One of the authors (N.U.) was financially supported by Japan Science Promotion Society (JSPS) Fellowships for Japanese Junior Scientists.

References

1. E. Kapon, K. Kash, E.M. Clausen Jr., D.M. Hwang, and E. Colas, Appl. Phys. Lett. 60, 477 (1992).
2. S. Simhony, E. Kapon, E. Colas, D.M. Hwang, N.G. Stoffel, and P. Worland, Appl. Phys. Lett. 59, 2225 (1991).
3. W. pan, X. Ma, Z. Fu, H. Yaguchi, K. Onabe, Y. Shiraki, and R. Ito (unpublished).
4. S. Tsukamoto, Y. Nagamune, M. Nishioka, and Y. Arakawa, Appl. Phys. Lett. 62, 49 (1993).
5. M. Walther, E. Kapon, K. Kash, J. Christen, D.M. Hwang, and R. Bhat, Appl. Phys. Lett. 60, 521 (1992).
6. J. Christen, M. Grundmann, E. Kapon, E. Colas, D.M. Hwang, and D. Bimberg,

Appl. Phys. Lett. 61, 67 (1992).
7. Y. Nagamune, Y. Arakawa, S. Tsukamoto, M. Nishioka, S. Sasaki, and N. Miura, Phys. Rev. Lett. 69, 2963 (1992).
8. S. Fukatsu, H. Yoshida, N. Usami, A. Fujiwara, Y. Takahashi, Y. Shiraki, and R. Ito, Jpn. J. Appl. Phys. 31, L1359 (1992).
9. S. Fukatsu, Y. Kuki, N. Usami, H. Sunamura, and Y. Shiraki (unpublished).

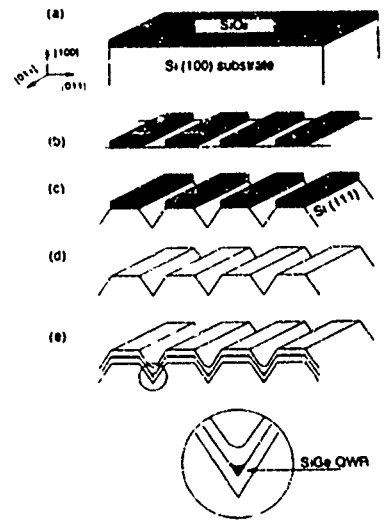

Fig. 1 Fabrication step of SiGe/Si QWR

Fig. 2 Cross-sectional TEM image of SiGe/Si QWR grown on a V-groove patterned Si (b) by SEG

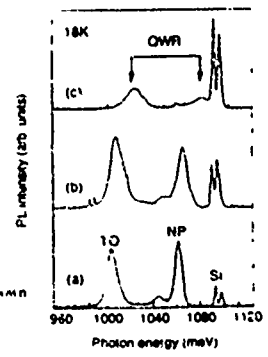

Fig. 3 Comparison of PL spectra of Si/SiGe/Si grown (a) on an unprocessed Si (100), (b) on a V-groove patterned Si substrate, (c) by SEG.

MoB1

Evidence of Directional Electron Heating in Doped GaAs

B. Brill, M. Heiblum, and H. Shtrikman

Braun Center for Submicron Research, Weizmann Institute of Science, Rehovot, Israel

As electrons gain energy or heat up their energy relaxation rate via phonon or electron scattering increases. This is mostly due to the available phase space that opens up for their final states after scattering. For very long samples, the electrons and the lattice reach thermal equilibrium with equal temperatures, however, when the transport region is very short, the electrons' and phonons' temperatures can be quite different. In extreme situations their distributions may be far from equilibrium and the electron temperature cannot be defined. Moreover, when the path length is on the order of the electron's wavelength, quantum size effects are expected to modify the cooling rate of the electrons.

We report of initial experimental results, via transport measurements, in narrow wells of doped GaAs, showing strong evidence of heated electron distribution with net momentum along the injected current direction. The measurements were done with a Hot Electron Device (THETA), having a 30 nm long transport region (*base*) doped to (1, 1.5, 2)x10^{18} cm^{-3}. Hot, non-equilibrium electrons were injected into the transport region utilizing a biased GaAs-AlGaAs-GaAs tunnel barrier and were collected above another barrier (*collector barrier*) that terminated the narrow base region. The collector barrier was designed to be only some 10-20 meV above the Fermi energy in the base, so that it prevented the collection of cold electrons while allowing forward moving hot electrons with *normal energy* higher than the collector barrier to be collected. In past works, when the collector barrier was higher, the differential transfer ratio, α=d(collected current)/d(injected current), approached unity, indicating the large fraction of ballistic electrons that *had made it* across the base. Measurements performed now, with the low-collector-barrier devices, resulted, surprisingly, with α values peaking much above unity. Increasing the doping levels in the base or lowering the collector barrier height results with a higher α.

We suggest that directional electron heating takes place, namely, that the collected current has two contributions, resulting from the injected ballistic electrons and from electrons that were heated above the Fermi sea by the ballistic electrons. A simple model that assumes the heated electrons have a Fermi distribution with an electron temperature of some 20 K, while the lattice temperature is maintained at 4.2 K, can partially account for the experimental results. However, it is expected that the distribution may not be fully equilibrated and thus a more rigorous treatment is warranted. These results suggest a way to obtain three terminal devices with extremely high current gains (for α=1, $\beta=\alpha/(1-\alpha) \rightarrow \infty$)

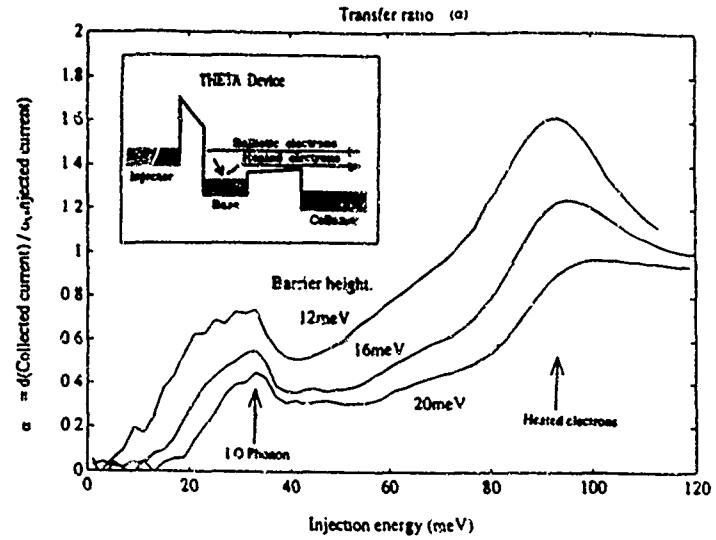

Differential transfer ratio of the ballistic electrons through a 2x10^{18} cm^{-3} doped base as a function of the injection energy. As the Collector barrier height decreases (from 20 to 12 meV), α increases with a distinct peak around 95 meV, where α exceeds unity. We attribute this peak to heated electrons with momentum along the direction of the injected ballistic electrons. The peak around 36 meV is due to the onset of LO phonon emission.

MoB2

High–mobility transport along single quasi one–dimensional quantum wires formed by cleaved edge overgrowth

W. Wegscheider, W. Kang, L. N. Pfeiffer, K. W. West, H. L. Stormer, and K. W. Baldwin
AT&T Bell Laboratories, Murray Hill, New Jersey 07974, USA

Abstract

We report on a novel contact scheme which for the first time makes possible magnetotransport measurements on individual quasi one–dimensional quantum wires prepared by cleaved edge overgrowth. Contacting is achieved via two isolated 2–dimensional electron systems that are connected to one another by the quantum wire under study. Two–terminal magnetoresistance measurements along our modulation–doped quantum wires exhibit electron mobilities in excess of 2×10^5 cm^2/Vs and show pronounced Shubnikov–de Haas oscillations. Clear evidence for confinement of the electrons in two dimensions is deduced from the retarded depopulation of Landau levels at low magnetic fields. The results are in close agreement with a calculation of the magnetic field dependence of the number of occupied subbands in a narrow channel.

Introduction

Quantum sized semiconductor structures in which free carrier motion is restricted to one dimension, so–called quantum wires, are expected to show unique electrical transport properties such as extremely high electron mobilities [1], and quantized conductances that are independant of the wire length. These predictions have attracted considerable attention and motivation for the fabrication and the experimental investigation of these structures. While conductance quantization through narrow constrictions in a two–dimensional electron gas (2DEG) has been demonstrated [2,3], corresponding quantization in long one–dimensional (1D) wires has been elusive. This has been attributed to size fluctuations along the length of the quantum wires, and to the appearance of universal conductance fluctuations which wash out the effects associated with the reduced dimensionality. So far, the fabrication of quantum wire structures for transport measurements has mostly relied on lithographic techniques [4], which allow the fabrication of wires of widths well below 100 nm but are subject to considerable fluctuations of the wire width. Recently a molecular beam epitaxy (MBE) growth technique called cleaved edge overgrowth (CEO) has been developed, which involves regrowth on the sidewall of an *in situ* cleaved GaAs/AlGaAs heterostructure [5]. CEO is able to generate atomically precise quantum wires with minimum fluctuation of the wire width, however, the study of such highly uniform 1D wires via electronic transport has been hampered by inability to make reliable low–resistance electric contacts.

In this paper we introduce a new method to reliably contact CEO structures and in particular one–dimensional wires. Our technique makes use of the presence of two isolated 2DEGs defined by a shadow mask during the first CEO growth step. The transport properties of the quantum wires whose widths are defined on an atomic scale by the MBE growth process can be studied by

connecting current and voltage probes to the 2DEGs. Contacting can be achieved by conventional means, thereby avoiding complicated lithographic processing steps. Since the 2DEGs lie in a plane perpendicular to the (110) cleavage plane, magnetotransport characterization of the quantum wires becomes indepedent of the contacting 2DEGs by proper orientation of the magnetic field.

Experimental procedures

Our technique is a variation of the CEO technique described in detail elsewhere [6]. First, a modulation–doped quantum well of thickness d embedded between $Al_{0.32}Ga_{0.68}As$ layers is grown on a GaAs(001) substrate. The relevant layer thicknesses as well as the location of additional buffer and cap layers are indicated in Fig. 1. During deposition of the Si dopant ($n \approx 10^{12}$ cm^{-2}) a shadow mask is positioned in close vicinity of the substrate surface. This mask blocks Si incorporation in the MBE film along stripes typically $\approx$ 40–100 μm wide, resulting in two spatially seperated 2DEGs in the (001) plane. After the first MBE growth the substrate is removed from the machine, mechanically thinned from the backside and reinserted into the MBE growth chamber where an *in situ* cleave is performed. Within seconds after the cleave the second MBE overgrowth is started on the fresh (110) surface. The post–cleave sequence consists of a $Al_{0.32}Ga_{0.68}As$ spacer layer, a Si dopant spike ($n \approx 3\times10^{12}$ cm^{-2}) and finally a $Al_{0.32}Ga_{0.68}As$ cap. As visualized in the perspective drawing of Fig. 1, this results in the formation of a quasi one–dimensional quantum wire connected over the corner to the two 2DEGs. While the width of the low–dimensional structure is given by the width of the quantum well d (70–1000 nm) of the first MBE growth, the wire length is defined by the width of the shadow mask which was in our case typically 40–100 μm.

For the shadow mask we use Ta wires etched in HNO_3:HF (1:1) to the desired diameter. These are mounted on a Ta frame which, in turn, is attached to a hinge permanently connected to the sample holder block. Sample rotation by an angle of 180° in the vertical growth position moves the mask either in front of, or away from the sample surface aided by gravitation. Since the Si dopant cell is not a point source, a close proximity between the mask and the sample surface is required in order to guarantee complete shadowing. In addition, due to the sensitivity of the sample to contamination during MBE growth, extreme requirements are imposed on the mask as to the cleanliness so as to avoid outgassing as it is heated by the substrate during use. For that reason we prebake the chemically–cleaned empty substrate holder block and mask in a 10^{-11} Torr vacuum at a temperature of about 900°C before mounting the GaAs substrate and insertion into the growth chamber. This is followed by the usual outgassing procedure. As another precaution we terminate the $Al_{0.32}Ga_{0.68}As$ spacer layer by 3 monolayers of GaAs to protect the highly reactive $Al_{0.32}Ga_{0.68}As$ during mask manipulation.

Magnetotransport measurements were performed with standard lock–in techniques at a temperature of 300 mK. Four In–diffused contacts were made to each of the 2DEGs connected to the ends of the quantum wire. This allows us to perform two–probe magnetoresistance measurements along the quantum wire and after tilting the sample with respect to the magnetic field, to independently characterize each 2DEG region by four–probe Hall measurements.

Results and discussion

In order to verify the usefulness of the described contact scheme we characterized the properties

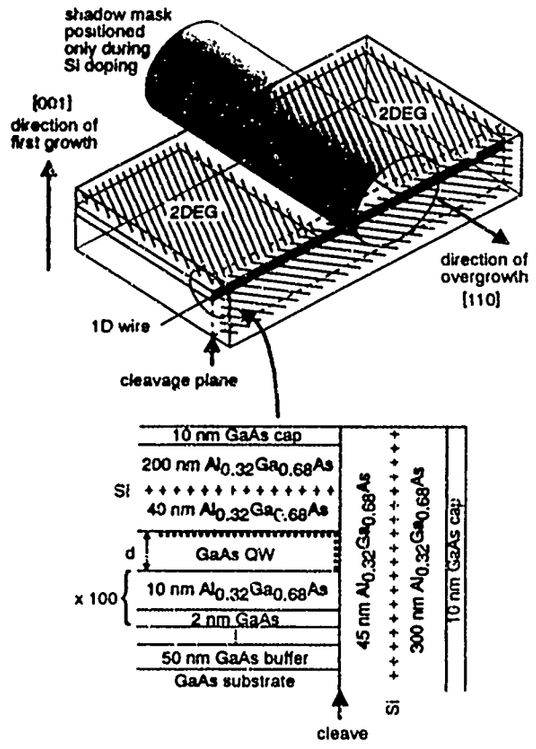

Figure 1: Schematic diagram of MBE overgrowth of a modulation–doped quantum wire structure on a cleaved interface (bottom) and perspective drawing of the location of the quantum wire and the 2DEGs with respect to the shadow mask (top). Hatched areas indicate Si dopant layers; dots locate two and quasi one–dimensional electron gases.

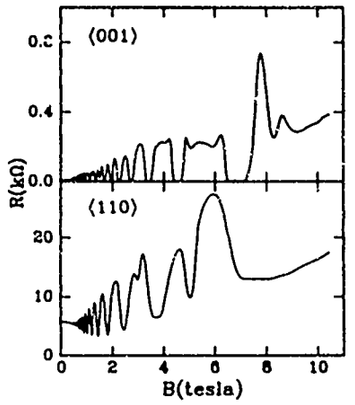

Figure 2: Four–probe magnetoresistance data in the 2DEG contact regions (top) and two–probe magnetoresistance across the 1 μm wide channel (bottom) of a CEO quantum wire sample.

of the resulting quantum well structure before the cleave and its overgrowth took place. Van der Pauw measurements of the modulation–doped quantum well regions reveal typical electron mobilities in the dark after exposure to light in the range of 1 to 3×10^5 cm^2/Vs at a carrier density of 3.6×10^{11} cm^{-2}, comparable to our conventional quantum well samples. The resistance across the undoped quantum well stripe is found to be higher than 10 MΩ provided that a breakdown voltage of about 1 V is not exceeded.

Figure 2 shows the magnetoresistances of a *fully processed* CEO sample with a GaAs wire width of $d = 1$ μm. The (001) data in the upper panel are taken on one side of the contacting 2DEG with the magnetic field normal to the 2DEG plane. The high quality of the 2DEG in the (001) contact region is evident from the observation of the $\nu = 5/3$ fractional quantum Hall state at about 8.2 T in addition to the integral quantum Hall states. For the electron density and the mobility of these contacting 2DEGs in the (001) plane we obtain 3.2×10^{11} cm^{-2} and 2×10^6 cm^2/Vs, respectively. The data in the bottom panel are taken on the 1 μm wide wire with the magnetic field normal to the "plane" of the wire [(110) plane] and parallel to the plane of the contacting 2DEGs [(001) plane]. The electric current proceeds from the first 2DEG through the wire into the second 2DEG and the voltage is measured at seperate contacts between both 2DEGs. Although this constitutes a four–probe geometry it is not a truly four–probe electrical transport measurement, since the current and voltage probes are not truly independent. One current and one voltage contact is attached to each of the 2DEGs and each 2DEG in turn contacts the wire along a common edge. This

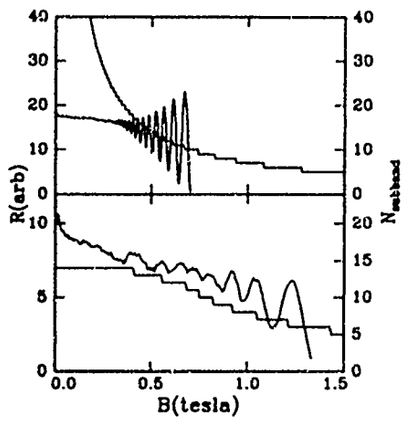

Figure 3: Comparison of low–field magnetoresistance across 1 μm (top) and 300 nm wide channels (bottom). The number of occupied subbands calculated after Eqs. (1) and (2) for both cases are also indicated.

unusual geometry leads to the mixing between magnetoresistance and Hall resistance observed in Fig. 2, reminiscent of two–probe messurements on 2DEGs. Such a mixing can be avoided by contacting four 2DEGs to the wire in future implementations. Under any circumstances the transport around the edge and into a true quantum wire opens interesting opportunities for future studies. Using an aspect ratio of 1:100 for the 100 μm long wire ($d = 1\mu$m) we obtain a zero–field mobility of 2.8×10^5 cm^2/Vs. This underestimates the true electron mobility in the wire since the resistances of the junctions from the 2DEGs to the wires have not been included. The deviations of the measured Hall plateaus from the quantized values at high magnetic fields indeed suggest a junction resistance of about 2–3 kΩ which is a considerable fraction of the total resistance of about 10 kΩ.

Low–field magnetoresistance data across 1 μm and 300 nm wide wires are shown in Fig. 3 together with the theoretically expected 1D subband population. The number of occupied subbands N at the Fermi energy E_f for a square well confining potential of width d is given approximately by [4(b)].

$$N \approx \mathrm{Int}\left[\frac{2}{\pi}\frac{E_f}{\hbar\omega_c}\left(\arcsin\frac{d}{2l_c}+\frac{d}{2l_c}\left[1-\left(\frac{d}{2l_c}\right)^2\right]^{1/2}\right)\right], \quad \text{if } l_c > \frac{d}{2} \qquad (1)$$

$$N \approx \mathrm{Int}\left[\frac{1}{2}+\frac{E_f}{\hbar\omega_c}\right], \quad \text{if } l_c < \frac{d}{2}. \qquad (2)$$

where $l_c = \hbar k_F/eB$ is the cyclotron radius at the Fermi energy and $\hbar\omega_c = \hbar eB/m$ is the Landau level separation. The onset of the SdH oscillations in the 1 μm wide wire is about 0.3 T, so that it is not possible to observe any one–dimensional behaviour which will appear only below the 1D to 2D crossover field of about 0.2 T. In the 300 nm wide wire, the crossover field is about 0.7 T and the quasi–one dimensional subbands can be resolved. Below 0.7 T we observe the retarded depopulation of Landau levels characteristic for lateral confinement of a 2DEG. The SdH oscillations are no longer periodic in 1/B, confirming the presence of carrier confinement in two dimensions. At higher fields (> 0.7 T) the 1/B periodicity is restored. Using the electron density n obtained from the high–field SdH data we achieve excellent agreement between the experimentally observed and the theoretically after Eqs. (1) and (2) calculated population of 14 electronic subbands. This close agreement confirms the implementation of a 300 nm wide quantum wire and the viability of our contacting scheme.

Conclusions

The contact scheme we reported here provides a simple and reliable way to probe individual quasi one–dimensional quantum wires fabricated by CEO. The high potential of this novel technique is demonstrated by the clear 1D subband population behaviour observed in 300 nm wide quantum wires with electron mobilities in excess of 2×10^5 cm^2/Vs. However, in order to investigate narrower, ballistic channels whose length are comparable with the electron mean free path the dimensions of the shadow mask have to be further reduced. We expect that this can be achieved with lithographically prepared masks.

Acknowledgements

One of us (W. W) gratefully acknowledges financial support from the Deutsche Forschungsgemeinschaft (DFG).

References

1. H. Sakaki, Jpn. J. Appl. Phys. **19**, 94 (1980).
2. B. J. van Wees, H. van Houten, C. W. J. Beenakker, J. G Williamson, L. P. Kouwenhoven, D. van der Marcel, and C. T. Foxon, Phys. Rev. Lett. **60**, 848 (1988).
3. D. A. Wharam, T. J. Thornton, R. Newbury, M. Pepper, H. Ahmed, J. E. F. Frost, D. G. Hasko, D. C. Peacock, D. A. Ritchie, and G. A. C. Jones, J. Phys. C **21**, L209 (1988).
4. For reviews see, (a) *Nanostructures Physics and Fabrication*, edited by M. A. Reed and W. P. Kirk (Academic, New York, 1989); (b) C. W. J. Beenakker and H. van Houten, in *Solid State Physics: Advances in Research and Applications*, edited by H. Ehrenreich and D. Turnbull (Academic, New York, 1991), Vol. 44, pp. 1–228.
5. L. N. Pfeiffer, K. W. West, H. L. Stormer, J. P. Eisenstein, K. W. Baldwin, D. Gershoni, and J. Spector, Appl. Phys. Lett. **56**, 1897 (1990).
6. L. Pfeiffer, H. L. Stormer, K. W. Baldwin, K. W. West, A. R. Goñi, A. Pinczuk, R. C. Ashoori, M. M. Dignam, and W. Wegscheider, J. Crystal Growth **127**, 849 (1993).

MoB3

Observation of Knudsen and Gurzhi transport regimes in a two-dimensional wire

L. W. Molenkamp and M. J. M. de Jong*
Philips Research Laboratories, 5656 AA Eindhoven, The Netherlands

Abstract

We have observed electronic Knudsen and Poiseuille flow in a current heating experiment on electrostatically defined wires in (Al,Ga)As heterostructures. Current heating induces an increase in the number of electron-electron collisions in the wire, leading first to an increase (Knudsen regime) and subsequently to a decrease (due to Poiseuille electron flow, and known as the Gurzhi effect) of the resistance of the wire.

In his famous 1909 paper on gas flow through a capillary, Knudsen [1] demonstrated that the pressure drop over the capillary first increases and then decreases with increasing density. The mechanism is that with increasing gas particle density, the number of inter-particle collisions also increases. At low densities (what is now known as the Knudsen transport regime) this leads to increasing dissipation of forward molecular momentum at the capillary walls, while at higher densities laminar Poiseuille flow sets in, which decreases the effective particle-wall interaction.

Because of the analogy between classical diffusive transport of electrons and gas particles, one may anticipate that a similar transition from Knudsen to Poiseuille also occurs in electron transport, where normal electron-electron scattering events (NEES) are the analogue of gas particle collisions. This issue has indeed been pursued since the early 1950's. However, it proved difficult to obtain reliable data [2], because the electron-phonon interaction is much more important than the electron-electron interaction.

So far, only preliminary indications of electronic Knudsen- and Poiseuille transport effects have been found [3]. Most experiments were performed on potassium, as an exemplary simple metal. However, the observed changes in the resistance as a function of lattice temperature were limited to about 0.01 % of the total resistance, because of the limited impurity mean free path l_{imp} and the onset of electron-phonon scattering. Observations of a positive temperature derivative of the resistivity $d\rho/dT$ in potassium wires [4] could be assigned by Moyshovitz and Wiser [5] as a Knudsen-like behaviour due to the combination of relatively infrequent normal electron-electron and electron-phonon collisions. However, until now there has been no observation of electronic Poiseuille flow.

Electronic Poiseuille flow should lead to a negative $d\rho/dT$, a phenomenon predicted by Gurzhi in 1963 [6], and generally known as the Gurzhi effect.

Here we present a study of Knudsen and Gurzhi phenomena in two-dimensional wires, fabricated from high-mobility (Al,Ga)As heterostructures. Using this material to study NEES effects offers several advantages, allowing a clear and unambiguous observation of the Knudsen and Poiseuille flow regimes. The resistance changes caused by NEES processes can be larger than 10 % of the total resistance. A full discussion of this work, as well as a detailed theoretical framework for calculations of NEES effects on the resistance for arbitrary electron temperature will be given elsewhere [7].

The wires used for the experiments are defined electrostatically in the two-dimensional electron gas (2DEG) of (Al,Ga)As heterostructures. The lay-out of the Ti/Au gates is given schematically in Fig. 1. We report here on two wires, both fabricated from an (Al,Ga)As wafer with electron density $n = 2.7 \times 10^{11}$ cm^{-2} and $l_{imp} = 19.7$ μm. Both wires have a width $W = 1.0$ μm, but they differ a factor of two in length L. $L = 6.17$ μm in one wire, and $L = 12.73$ μm in the other. For transport measurements, the samples are kept in a cryostat at 1.5 K, and at zero magnetic field. The differential resistance is measured with standard low-frequency lock-in techniques, using a 100 μV ac voltage.

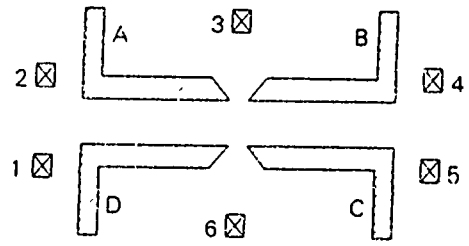

FIG. 1. Lay-out of the gates defining the wires used in the experiments. Current is passed between Ohmic contacts 2 and 1, and the voltage drop is measured between contacts 4 and 5. Ohmic contacts 3 and 6 can be used for measuring the thermovoltages across the point contacts in the wire boundaries. The wires studied here both have a width $W = 1$ μ, but differ in length ($L = 6.17$ and 12.73 μm).

In order to be able to study the effects of NEES separately from electron-phonon scattering effects, we utilize a peculiarity of (Al,Ga)As two-dimensional electron gases at low temperatures. In these materials, the coupling between hot electrons and the lattice is orders of magnitude smaller than the coupling within the electron system. This allows one to achieve selective Joule heating of the electron gas in the wires by passing a dc current I through the wire. This technique has proven to be very, very useful for the study of thermoelectric phenomena in nanostructures [8]. The wires studied here are equipped with opposing pairs of point contacts in their boundaries, allowing us to determine the electron temperature T as a function of I, using the the quantized thermopower of a point contact, as described in Ref. [9]. A typical example of such a measurement of T vs. I is shown in Fig. 2. We find that for $|I| \lesssim 20$ μA, and a lattice temperature $T_L \lesssim 2$ K, the

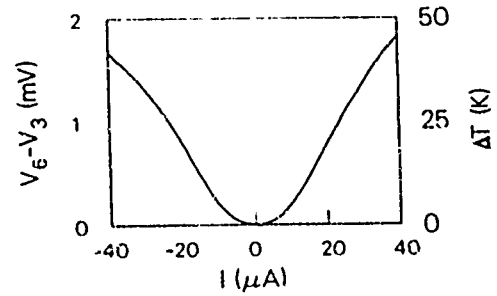

FIG. 2. Transverse voltage $V_6 - V_3$ as a function of heating current I. In this experiment, point contact AB is adjusted between the $N = 1$ and $N = 2$ for maximum quantized thermopower, and the thermopower of point contact CD can be neglected. The electron temperature in the channel can now be deduced from the size of the transverse voltage. See Refs [8]b and [9] for details.

electron temperature T in our wires is approximately given by

$$T = T_i + (I/W)^2 \rho C', \tag{1}$$

where ρ is the resistivity of the channel. The constant C' is of order $C' \approx 0.05$ m^{2}K/W.

In Fig. 3 we show our data (drawn lines) on the differential resistance (dV/dI) of both wires. The top trace was obtained from the longer, the bottom trace from the shorter wire. For both wires we observe first an increase, followed by a decrease of dV/dI with I. At low currents, where Eq. (1) applies, we observe a remarkable behaviour of dV/dI: an initial increase, followed by a *decrease* in dV/dI with increasing $|I|$ [10].

To see whether NEES could in principle be responsible for this behaviour, let us estimate the electron-electron scattering mean free path l_{ee} at $T \approx 10$ K (which, according to Eq. (1), is the electron temperature in the wire at $I = 15\ \mu$A and $T_i = 1.5$ K). We have $l_{ee} = v_F \tau_{ee}$, where v_F is the Fermi velocity, and τ_{ee} the electron-electron scattering time, given by [11]

$$\frac{1}{\tau_{ee}(T)} = \frac{E_F}{\hbar}\left(\frac{k_B T}{E_F}\right)^2 \left[\ln\left(\frac{E_F}{k_B T}\right) + \ln\left(\frac{2q}{k_F}\right) + 1\right] \tag{2}$$

Here q is the 2D Thomas-Fermi screening wave vector ($q = me^2/2\pi\varepsilon_0\varepsilon\hbar^2$). We find $l_{ee} \approx 0.8\ \mu$m, which is much smaller than W. In this limit the electrons undergo a random motion due to frequent NEES events, and we assign the decrease in dV/dI to the Gurzhi effect. For currents below 5 μA, dV/dI is positive. As $l_{ee} \approx W$ for $|I| = 8\ \mu$A and $T_i = 1.5$ K, this additional feature occurs in the right current range for the electron-Knudsen effect. Moreover, we see that the total increase in dV/dI in the long wire is twice the increase in the short wire. This proportionality to L rules out a contact-resistance effect as an explanation for the anomalies.

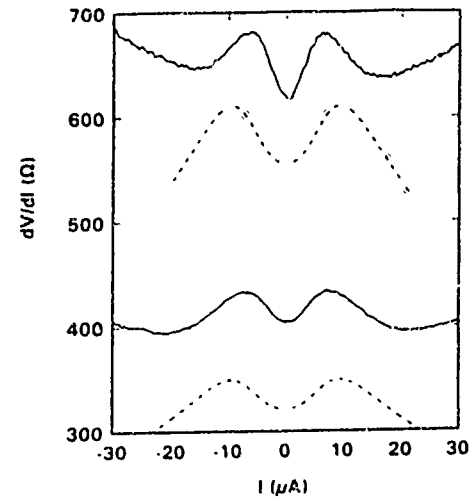

FIG. 3. Drawn curves: experimental dependence of dV/dI on heating current I for the $L = 127.1\ \mu$m (top curve) and $L = 61.7\ \mu$m wire (bottom curve), respectively. The dashed curves are the result of our calculations obtained using boundary scattering parameter a as 0.7, and width $W = l_{mp}/5.5$.

In order to substantiate our assignment of the anomalous behaviour of dV/dI to hydrodynamic phenomena, we have performed model calculations of the effects of NEES on the differential resistance of a two-dimensional wire. We have included NEES events in an electron path tracing method originally due to Chambers [12], and obtained a solution for arbitrary l_{ee}, l_{mp} and W. In this method one follows the path of an electron until it relaxes at an impurity or the boundary of the system, and then determines a weighted average of the path lengths. The resulting effective mean free path l_M is related to the resistivity ρ of the wire by

$$\rho^{-1} = \frac{ne^2}{mv_F} l_M \tag{3}$$

We assume that a fraction p of the incident electrons is reflected specularly at the boundary, the remainder being scattered diffusively, and obtain for the effective mean free path at position x along the width of the wire

$$l_{\rm eff}(x) = l - \frac{ll}{\pi}\int_0^1 du\,\sqrt{1-u^2}\frac{(1-p)e^{-x/lu}}{1-pe^{-W/lu}} + \frac{2}{\pi l_\infty}\int_0^1 du\,\frac{\sqrt{1-u^2}}{u}\int_0^W dx'\,[l_{\rm eff}(x')+l_{\rm eff}(W-x')]\left[e^{-|x-x'|/lu}\Theta(x-x')+\frac{pe^{-(x+x')/lu}}{1-pe^{-W/lu}}\right]$$

where $l^{-1} \equiv l_{\rm imp}^{-1} + l_{ee}^{-1}$, and $\Theta(x)$ is the unit step function. The average effective mean free path can now be obtained from $l_{\rm eff} = (1/W)\int_0^W dx\, l_{\rm eff}(x)$. Eq. (4) is solved self consistently using numerical methods.

For a comparison with the experiments, we relate l_∞ to l using Eqs. (1) - (4). The resistance of the wire is obtained from $R \equiv 1/I = h\pi/2e^2k_{\rm F}W + \rho L/W$, where the first term is the two-dimensional Sharvin contact resistance [11]. Subsequently dV/dI is evaluated numerically. The dotted lines in Fig. 3 are the results of our calculation. In both cases, the calculated dV/dI values are 60 – 80 Ω smaller than the experimental values. This is due to the resistance of the wide 2DEG leading to the wires, which is not included in the calculations. In addition, we did not include the lattice heating for currents $|I| > 20\,\mu$A in our modelling. Apart from this the agreement between experiment and theory is very good. Two remarks must be made regarding the parameters used in our modelling. Firstly, one expects that due to depletion the electronic width of the wires is slightly smaller than the lithographic width; we have set $W = l_{\rm imp}/5.5$ for both wires. In addition, we noticed that using a constant value of p for all angles of incidence leads either to a too large value for dV/dI at zero heating current or a too small Knudsen effect. It is well known from metal wires that in reality p depends on the angle of incidence θ, such that $p \to 1$ for grazing incidence ($\theta \to \pm\pi/2$). According to Ref. [14],

$$p(\theta) = \exp[-(a\cos\theta)^2] \qquad (5)$$

Using this expression in Eq. (4) – where $u \equiv \cos\theta$ – we obtain the numerical results of Fig. 4. Good agreement with the experimental data is found with $a \equiv 0.7$, which implies that some 80% of all boundary collisions are specular. A high specularity for boundary scattering in split gate wires was previously found in magnetoresistance experiments [15].

In summary, we have found convincing evidence of the occurrence of electronic Knudsen and Poiseuille transport regimes in the non linear differential resistance of split gate defined wires in a two dimensional electron gas. Our results verify speculations on hydrodynamic flow phenomena in solids that date back to the 1930's and 60's, which only came within reach of the experimentalist after the development of metals of sufficiently high mobility, and nano lithography techniques.

The heterostructures were grown by C. T. Foxon at the Philips Research Laboratories in Redhill (Surrey, UK). L. W. M. acknowledges the kind hospitality he enjoyed during a visit to the Laboratory for Quantum Materials, RIKEN, Saitama, Japan, where this research was initiated. M. J. M. de J. is supported by the Dutch Science Foundation NWO/FOM.

REFERENCES

* Also at: Instituut-Lorentz, University of Leiden, 2300 RA Leiden, The Netherlands.
[1] M. Knudsen, Ann. Phys. **28**, 75 (1909).
[2] J. M. Ziman, *Electrons and Phonons*, (Oxford Univ. Press, Oxford, England, 1960).
[3] M. Kaveh and N. Wiser, Adv. in Phys. **33**, 257 (1984).
[4] J. Zhao, W. P. Pratt, Jr., H. Sato, P. A. Schroeder, and J. Bass, Phys. Rev. B **37**, 8718 (1988).
[5] D. Moshovitz and N. Wiser, J. Phys.: Condens. Matter **2**, 8053 (1990).
[6] R. N. Gurzhi, Zh. Eksp. Teor. Fiz. **44**, 771 (1963) [Sov. Phys. JETP **17**, 521 (1963)]; Usp. Fiz. Nauk **94**, 689 (1968) [Sov. Phys. Usp. **11**, 255 (1968)].
[7] L. W. Molenkamp and M. J. M. de Jong, submitted.
[8] B. L. Gallagher, J. Galloway, P. Beton, J. P. Oxley, S. P. Beaumont, S. Thoms, and C. D. W. Wilkinson, Phys. Rev. Lett. **64**, 2058 (1990); L. W. Molenkamp, H. van Houten, C. W. J. Beenakker, R. Eppenga, and C. T. Foxon, Phys. Rev. Lett. **65**, 1052 (1990).
[9] L. W. Molenkamp, Th. Gravier, H. van Houten, O. J. A. Buyk, M. A. A. Mabesoone, and C. T. Foxon, Phys. Rev. Lett. **68**, 3765 (1992).
[10] The approximately quadratic increase in dV/dI for $|I| > 20\,\mu$A depends on the cooling capacity of the cryostat, and can be attributed to heating of the lattice.
[11] G. F. Giuliani and J. J. Quinn, Phys. Rev. B **26**, 4421 (1982).
[12] R. G. Chambers, Proc. R. Soc. London Ser. A **202**, 378 (1950).
[13] M. J. M. de Jong, submitted.
[14] S. B. Soffer, J. Appl. Phys. **38**, 1710 (1967).
[15] T. J. Thornton, M. L. Roukes, A. Scherer, and B. P. Van der Gaag, Phys. Rev. Lett. **63**, 2128 (1989).

MoB4

Quantized Conductance and Its Effects on Non-linear Current-Voltage Characteristics at 80K in Mesa-Etched InAs/AlGaSb Quantum Wires with Split-Gate

Kanji Yoh, Akira Nishida and Masataka Inoue

Department of Electrical Engineering, Osaka Institute of Technology,
5-16-1 Omiya, Asahi-ku, Osaka 535

Abstract

We report electrical characteristics of InAs/(AlGa)Sb quantum wire devices based on deep mesa-etched structures with split gate. Quantized current and conductance has been observed at around 80K for the first time. Current quantization analysis revieled that the quantized conductance showed constant value with the drain voltages up to ≈180mV suggesting that the Landauer's formula in one dimensional electron systems in finite voltages holds up to ≈105mV. The 3650Å-wide, 3525Å long InAs quantum wire showed non linear I-V characteristics with fixed gate voltage. The drain current dependence on matrix of gate and drain voltages revieled that the current increase at high drain voltages is caused by the so called drain-induced-barrier-lowering: sublevels at the point contact are actually lowered by the application of high drain voltage which has a same effect as positive gate voltage application. Overall drain current saturation tendency is caused presumably by the saturation velocity effect in the high field region between the point contact and rest of the wire under high drain voltage.

Introduction

There have been extensive amount of work on the quantum wire transport mostly on (AlGaAs/GaAs hetrostructures[1-4] and on silicon based materials[5]. However, most of these phenomena were observed at 4.2K or much lower temperatures[6]. InAs quantum-effect devices[7] are potentially superior to the GaAs counterpart[8] in high temperature operation for their higher low-field mobility[9-11], higher conduction band discontinuities, and higher energy separation of sublevels. Because of this strong confinement nature and the low effective mass of electrons in the InAs well, quantum effects of the confined electron systems are expected to be oserved at relatively high temperatures[7]. However, there have only been results measured at much lower temperatures than expected for several reasons[13-14] One of the major reasons is that the lateral confinement is limited with the Schottky split-gate method. Reduction of the upper barrier is limited by the trade-off between confinement strength andtunneling currents. In this paper, we report the fabrication and characterization of deeply etched quantum wires on an (AlGa)Sb/InAs heterostructure with split-gate by utilizing electron beam lithography and wet-chemical etching. In order to avoid the inherent gate leakage current in heterostructures based on antimonides[11], deeply etched wire structures have been investigated.

Experimental

The heterostructures have been grown by molecular beam epitaxy using ANELVA MBE-620 system. The growth techniques of the InAs/(AlGa)Sb are similar to what has been used to fabricate high performance heterojunction field-effect transistors[11,14].

The heterostructure of the device(#231) is shown in Fig.1, consisting of 2000Å of GaAs layer grown on undoped GaAs substrates, 1.0 μm AlSb buffer layer, 2000Å (Al_4Ga_5)Sb buffer layer, 70Å of AlSb layer, 150Å of InAs, 150Å of (Al_3Ga_5)Sb, and 100Å of GaSb cap layer. The inserted 70Å of AlSb was intended to prevent leakage currents through (AlGa)Sb buffer layer which becomes appreciable at high temperatures under high gate bias voltages. The carrier concentration and electron mobility of the present sample measured at 77K by Hall effect measurement were $1.07 \times 10^{12} cm^{-2}$ and 20,200 cm^2/Vs, respectively.

Device fabrication has been performed by electron beam lithography and wet chemical etching with phosphoric-acid-based etchant and photoresist developper. Phosphoric-acid-based etchant was used to etch arsenides and antimonides isotropically whereas photoresist developper was used as a selective etchant for antimonides[15]. Fabrication of deeply etched quantum wire structures using electron beam lithography and wet chemical etching is similar to what has been used to make ungated quantum wires[7,15]. Ti/Au was used as non-alloyed ohmic metal which is directly deposited on InAs layer after selective etching of antimonides. The nominal etch-depth were 1500Å. The JEOL multi-purpose Scanning Electron Microscope system, JSM840A, was used as the electron beam source. The width of the device was determined to be approximately, 3650Å by measuring the SEM and AFM images.

The conductance of the devices have been measured using HP4145B semiconductor parameter analyser. In order to collect as much data as possible in a wide range of drain and gate voltages a single shot of measurements, drain voltage step was taken to be 100mV. This relatively large drain voltage bias extracting the conductance data has been justified by the current voltage analysis which will be discussed in the results section. Voltage of only one of the split-gates, whichever has better Schottky quality than the other, was modulated and the other member of the split-gates is connected to the common ground and source terminal. This configuration was chosen to keep as much gate voltage range as possible by minimizing the total gate leakage current.

Results

Current voltage characteristics of the split-gated quantum wire measured at 80K is shown in Fiure 2. Clear current steps can be soen in the figure. Conductance dependence on gate voltage is shown in Figure3 in various temperatures. A clear quantized conductance steps of three, four and five fold multiples of ($2e^2/h$) were observed at temperatures between 55K and 80K. Beyond 104K, although clear conductance steps were observed up to 120K, conductance plateau did not agree with multiples of ($2e^2/h$), suggesting the existance of a current leakage path other than the quantum point contact. This is probably due to parasitic MESFET effect which turns on very weakly at high temperatures.

Drain current increment at each current step in Figure 1 where wave mode number increases by unity. Thus, from this figure, one can extract the current increment data at each increment of the wave-mode by unity. The current increment dependence on drain voltage is plotted in Figur 4. The slope corresponds to device conductance increment at each wave-mode

increment point. It clearly shows that the conductance increment is equal to ($2e^2/h$) with the drain voltages from 0V up to ~180mV, suggesting that the Landauer's formula in one dimension in finite voltages[16] holds within this voltage range. This result gives foundation on the validity of our conductance measurements at finite drain voltage of 100mV. Beyond 180mV, quantized current seems to saturate with increasing the drain voltage suggesting the resistance increase at high field region of the quantum wire between the point contact (source edge where the sublevels have peaks) and the drain edge of the wire as shown in Figure 5. This topic will be elaborated in detail in the next section.

At much higher drain voltage conditions, the drain current increment starts to rise again. Drain current dependence on the matrix of gate voltage and drain voltage is shown in Figure 6. It clearly shows that the trace of the current increment (mode-change) point moves toward reduced gate voltages as the drain voltage is increased. The effect becomes most appreciable in the high end of the drain voltage axis when the drain voltage is 1.1V or higher. This effect is similar to what is observed in the short channel MOSFET : the drain-induced-barrier-lowering(DIBL)[17] In short channel MOSFET, these effects cause high output conductance and it gradually becomes severer at higher drain voltages. In case of short channel "and" narrow wire as is the present case, DIBL occurs in such a way that it(V) leaves a bunndle of lower electron wave mode and switches to a higher mode bundle as shown in Figure 7. This is a quantum wire version of drain-induced barrier-lowering effect which must be overcome eventually if quantum wires are to be applied to high performance field-effect transistors.

Discussion

Current voltage characteristics of a different sample(#223) in a wider drain voltage region is shown in Figure 8. This sample had very low efficiency in modulating drain current by the split-gate voltage application indicating low efficiency in modulating sublevels at the point contact by the gate voltage presumably because of the imperfect Scottky contact of split-gates. However, we were able to measure current voltage characteristics in a wide range of drain voltage without suffering from severe gate leakage current by exactly the same reason. Sudden increase of the drain current is observed at drain voltages of approximately 1V and 2V as indicated in the arrows in the figure. The sudden gate leakage current at around 2V of drain voltage contribute only partially to the drain current increase. The ohmic contact can be shown to have no effect on non-linearities in a separate four terminal measurement on the present sample and other sample (#252). Drain current non-linearities can be divided into two parts: namely sudden current increase and gradual saturation tendency of the drain current as a function of drain voltage. The sudden increase of the drain current at high drain voltage bias points are presumably assigned to DIBL effect. No gate leakage effect nor ohmic contact resistance are responsible of the non-linearity. There remains a question of the physical origin of the current saturation tendency overlapped with the sudden increase caused by DIBL in the "quasi-ballistic point contact" structure. The schematic energy band diagram under high drain bias of Figure 5 well illustrates the situation. At low drain bias, the device is reasonablly well described as a 1D quantum wire and drain voltage has small effect on pulling down the 1D sublevels. At high drain bias, the energy band is strongly pulled down by the drain voltage as shown in the figure and the device is pretty well described as a quantum point contact (0D) connected in series with a quantum wire under high bias. The electrical properties of the 1D and 0D point contact are basically the same. But the series resistance of the rest of the wire region under high field comes in to alter the electrical properties of the device under high bias. Since present (#231) device is quasi-ballistic regime with the mean free path of 3450Å, which is comparable to the device

length (3625Å), extremely high field would possibly cause slight current saturation. Estimated saturation current agrees reasonably well with the experiment using the data from the separate velocity saturation experiments on the same heterostructure system[18]. This result supports the above model. The other possibility of non-parabolicity effects of InAs conduction band is eliminated by the separate experiment on the ballistic electrons in InAs which will be reported elsewhere

Conclusion

We have reported electrical characteristics of InAs/(AlGa)Sb quantum wire devices based on deep mesa-etched structures with split gate. Quantized current and quantized conductance have been clearly observed at around 80K for the first time. The non-linear drain current characteristics with fixed gate voltage were shown to be explained by the drain-induced-barrier-lowering: sublevels at the point contact are actually lowered by the application of high drain voltage which has a same effect as positive gate voltage application. Overall drain current saturation tendency has been shown to have been caused by the saturation velocity effect in the high field region between the point contact and rest of the wire under high drain voltage.

Acknowledgements

The authors are grateful to H.Kawahara for the technical assistance in the device fabrication and measurements. This work was partially supported by Grant-in-Aid for Scientific Research on Priority Area (Electron Wave Interference Effects in Mesoscopic Structures) from The Ministry of Education, Science and Culture. One of the authors, KY, also appreciates the partial support from The Murata Science Foundation

References

[1] K.-F. Berggren, T.J.Thornton, D.J Newson and M.Pepper: Phys. Rev. Lett. 57 (1986) 1769.
[2]M.L.Roukes, A.Scherer, S.J.Allen Jr., H.G.Craighead, R.M.Ruthen, E.D.Beebe and J P Harbison: Phys.Rev Lett. 59 (1987) 3011.
[3] K -F.Berggren, G. Roos and H. van Houten: Phys.Rev B 37 (1988) 10118
[4] C C.Eugster and J A. del Alamo: Phys. Rev. Lett. 67 (1991) 3586.
[5] H.Matsuoka, T.Ichiguchi, T.Yoshimura and E.Takeda: IEEE Electron Device Lett. EDL-13 (1992) 20.
[6] There is a report on quantized conductance observed at 30K, but the quantized conductance can be just bearly seen at 30K showing how difficult it is to cofine electrons by Schottky split-gate. G.L.Snider et al. Appl.Phys.Lett 59 (1991) 2727
[7] K.Yoh, H.Taniguchi,K.Kiyomi,M.Inoue and R.Sakamoto: IEEE IEDM Tech Dig. (IEEE, New York, 1991) p813.
[8] B.J van wees, H van Houten, C.W.J Beenecker, J.G.Williamson, L.P.Kouwenhoven, D.van der Marel, and C.T.Foxen, Phys Rev Lett. 60, p 848, 1988
[9] G.Tuttle, H Kroemer and J.H.English: J. Appl Phys. 65 (1989) 5239.
[10] G Tuttle, H Kroemer and J H.English: J.Appl.Phys.15 (1990) 3032.
[11] K.Yoh,T Moriuchi and M.Inoue: IEEE Electron. Device Lett.11 (1990) 526.
[12]M.Inoue, K Yoh, K Kiyomi, A.Nishida, and T.Maemoto, Extended Abstracts of Second International Symposium on New Phenomena in Mesoscopic Structures, p.64, 1992

[13] S.J.Kreater, C.R Bolognesi, M.J.Rooks, E.L.Hu, and H Kroemer, Extended Abstracts of Second International Symposium on New Phenomena in Mesoscopic Structures, p.56, 1992
[14] K.Yoh, K.Kiyomi, H.Taniguchi and M.Inoue, Jpn.J.Appl.Phys.vol.30, No.12B(1991) 3833
[15] K.Yoh, K.Kiyomi, A.Nishida and M.Inoue, JpnJ Appl.Phys. vol.31, No.12B(1992) 4515
[16] P.F.Bagwell and T.P.Orlando, Phys Rev B40 (1989)1456
[17] R.R.Troutman, IEEE Trans.Electron.Devices, ED-26, No 4 (1979) 461
[18] K.Yoh, T.Moriuchi and M.Inoue, Jpn.J.Appl.Phys.vol 29,No 12(1990) 12445

FIGURE CAPTIONS

Figure 1. Schematic diagrams of deep mesa-etched split-gated InAs quantum wire device of sample #231.

Figure 2 Current voltage characteristics of the split-gated InAs quantum wire device (#231). Gate voltage is taken from -5V to 3V and drain voltage is taken from 0V to 1.5V by 0.1 V step.

Figure 3. Conductancedependence on split-gate voltage at various temperatures of sample #231.

Figure 4. Current increment dependence on drain voltage of sample #231 measured at 80K The slope corresponds to the conductance increment when the electron wave mode increases by unity

Figure 5. Schematic diagram of lowest sublevels of electrons confined in 2-D (source and drain) and 1-D (wire) freedom of motion. Quantized current flows through 1-D sublevels in the present system when each sublevel crosses Fermi level by drain-induced barrier-lowering (DIBL). (a) represent the energy band diagram under zero bias and (b) represent the situation with high drain bias voltage.

Figure 6. Drain current dependence on the matrix of gate voltage and drain voltage. The trace of the current increment (mode-change) point moves toward reduced gate voltages as the drain voltage is increased.

Figure 7. Current voltage characteristics of the sample #231 measured at 80K. The gate voltage is taken from -5V to 3V by 0.5V step. Each curve can be seen to leave a bunndle of lower electron wave mode and switches to a higher mode bundle as the drain voltage isincreased. This is a quantum wire version of drain-induced-barrier-lowering effect.

Figure 8. Current voltage characteristics of a different sample#2231 in a wider drain voltage region. This sample had very low efficiency in modulating drain current by the split-gate voltage application indicating imperfect Scottky contact of split-gates. Current voltage characteristics in a wide drain-voltage range were measured without suffering from severe gate leakage current by the same reason. Sudden increase of the drain current is observed at drain voltages of approximately 1V and 2V as indicated in the arrows in the figure.

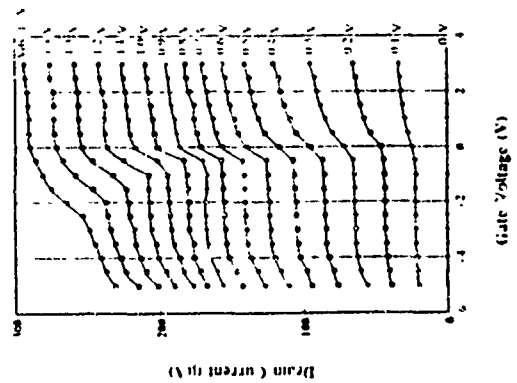

Figure 2

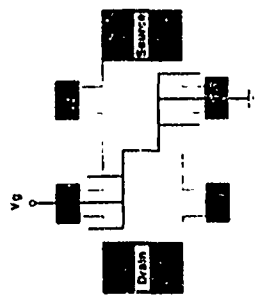

top view of a split gate device

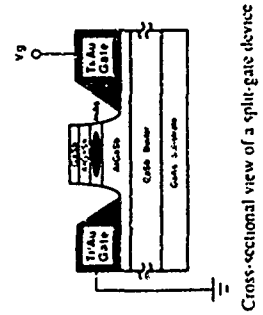

Cross-sectional view of a split-gate device

Figure 1

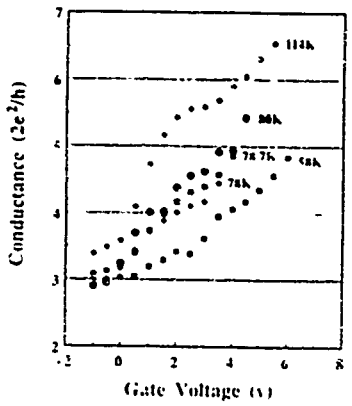

Figure 3

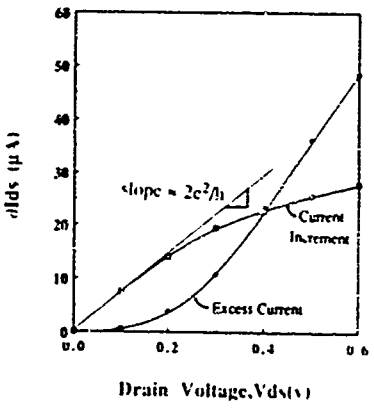

Figure 4

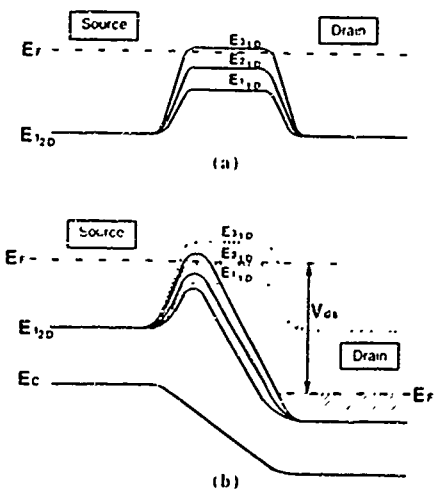

Figure 5

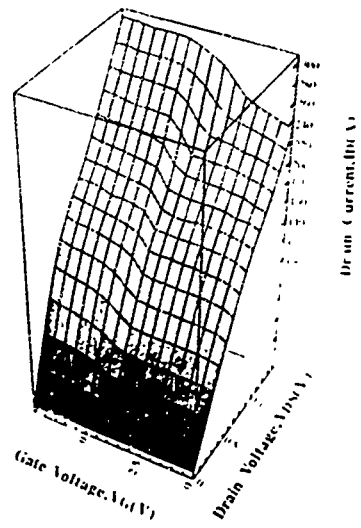

Figure 6

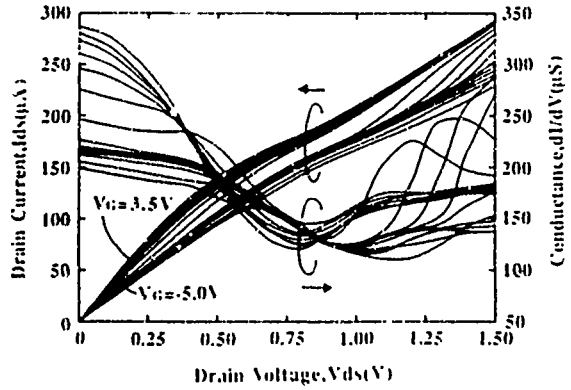

Figure 7

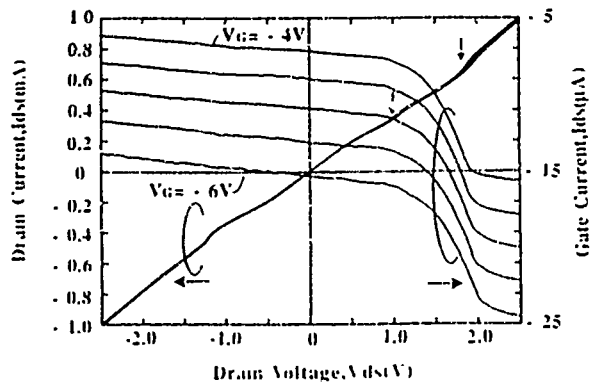

Figure 8

MoB5

Transport Properties of Lateral Superlattices Grown on Vicinal GaAs (100) Surfaces

Axel Lorke and Pierre M. Petroff
Materials Department, University of California, Santa Barbara, CA 93106, USA

Abstract

We report on the growth and the transport characterization of sub-monolayer inserted quantum wells grown on vicinal GaAs (100) surfaces. The deposition conditions were carefully adjusted to ensure an ordered array of steps on the surface during growth. In magneto-transconductance we observe that the Shubnikov-de Haas oscillations of the samples vanish at intermediate gate-voltages. In the same regime, the resistance across the steps exhibits a pronounced plateau-like increase whereas the resistance along the steps remains essentially unchanged. Lateral miniband formation as well as the presence of a limited number of traps are discussed as possible explanations for the experimental findings.

Introduction

After the idea of vertical semiconductor superlattices was introduced in 1970 in the seminal paper by Esaki and Tsu [1], the concept soon was extended to lateral superlattices (LSL) [2]. In these systems, a two-dimensional electron gas (2DEG) is subjected to an in-plane (lateral) periodic potential with a period corresponding approximately to the Fermi wave length of the free carriers. Although the fabrication of LSL constitutes a great technological challenge, they are appealing under both technological and theoretical considerations. They provide for model systems in which basic solid state properties can be studied on a variable length scale. Furthermore, they allow one to apply electric and magnetic fields which can compete with the built-in potentials, a situation which is not, or only poorly, achievable in "real" solids.

First attempts to realize LSLs were undertaken by fabricating metal-oxide-semiconductor (MOS) field effect transistors on semiconductor substrates which were cut slightly off a major crystal axis ("vicinal substrates"). Many essential observations, establishing the existence of an artificial miniband structure, were made on these devices [3-6]. In MOS systems, however, the superlattice potential and the carrier density cannot be independently controlled. Furthermore, even for smooth or randomly corrugated oxide-semiconductor interfaces, intervalley scattering can lead to quasi-superlattice effects [4].

Epitaxially grown LSL on III-V semiconductors are expected to offer a number advantages over MOS systems: (1) a considerably higher mobility, (2) a wide tunability of the lateral potential amplitude, largely independent of the carrier density, and (3) only small contributions to the minigap from the intervalley scattering [7]. A number of epitaxially grown LSL structures have been proposed and realized [7-11]. They are commonly fabricated by decorating (once or repeatedly) the regular step structure on a vicinal semiconductor substrate (e.g. GaAs) with a submonolayer of a different semiconductor (e.g. AlAs). Even though the preparation of a smooth and regularly stepped surface, as well as the submonolayer control of the growth, are of great difficulty, a number of novel physical properties have been reported on epitaxially grown LSL [8-11].

In the present work, we study the transport properties of submonolayer-inserted AlGaAs heterostructures at low temperatures with and without a magnetic field applied perpendicular to the plane of the LSL.

Design and Growth

The samples are grown by molecular beam epitaxy on GaAs (100) substrates, tilted towards the nearest (111)A plane by 0.5°. Such small tilt angles make the growth of a regularly stepped surface extremely difficult. The large terraces (average width l = 320 Å) require a large diffusion length of the impinging group III atoms to achieve "step-flow", necessary for step equalization. However, there are several advantages in choosing small angle vicinal substrates: Scanning tunneling microscopy shows that the raggedness of the step edges is given by the basic 2×4 reconstruction cell of length 16 Å [12], which is already 20% of the terrace width l of a 2° vicinal substrate. Also, the randomness of the deposition process leads to a fluctuation of the terrace width $\Delta(l) = \sqrt{a \cdot l}$ (with a

being the lattice constant of the semiconductor) in favor of large terraces [13]. The greatest advantage in choosing low angle substrates lies in the electronic energy dispersion. The strongest superlattice effects are expected when the Fermi energy E_F of the 2DEG lies in or above the energetic position E_g of the minigap. The carrier density $n_{s,g}$ at which $E_F = E_g$ is given by $n_{s,g} = \pi/2\ell^2$, independent of the semiconductor material. For the GaAs/AlGaAs system, with typical carrier densities of 3×10^{11} cm^{-2} this requires tilt angles well below 1°.

To assure step-flow mode, the samples are grown at a substrate temperature of = 605 °C and at growth rates below 0.2 µm/hr for both GaAs and AlAs. The As flux is held at 3×10^{-6} torr. The step-flow condition is controlled by monitoring the absence of RHEED oscillations during growth. Shortly before depositing the AlAs submonolayer, a clear splitting of the specular RHEED spot is observed, indicating a regularly stepped surface. The complete growth sequence is as follows. On semi-insulating substrates are deposited: A smoothing superlattice of 20 periods of 40 Å GaAs + 40 Å AlAs; 2500 Å GaAs buffer layer; 2500 Å short period superlattice consisting of 50 Å $Al_{0.4}Ga_{0.6}As$ + 50 Å GaAs; a 130 Å thick, AlAs inserted quantum well; 880 Å short period superlattice (40 Å AlAs + 40 Å GaAs); and a 100 Å thick cap layer. The short period superlattice is Si δ-doped to 5×10^{12} cm^{-2}, 230 Å from the interface. The growth of the quantum well layer is interrupted after 70 Å for 60s, and 0.5 monolayers AlAs are deposited to form a grating as schematically depicted in Fig. 1. The low temperature mobility of the samples, as determined from van der Pauw measurements, is = 80 000 cm^2/Vs. Two perpendicular Hall bars (cf. inset in Fig. 1) are defined by standard lithography.

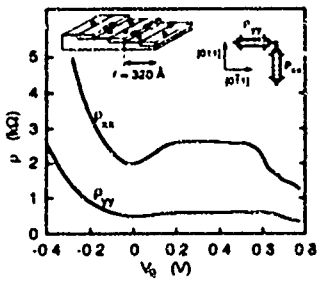

Fig. 1. Anisotropic resistivity of a LSL grown on (100) substrate tilted by 0.5° towards [111]A.

Experimental Results

All experiments are carried out at liquid He temperatures. Figure 1 shows the resistivity of a grating-inserted quantum well as a function of gate voltage, with the current (1 µA) flowing across (ρ_{xx}) or along (ρ_{yy}) the steps. Close to the threshold voltage V_t = -0.4 V, in both directions the usual drop in resistance proportional to = $1/(V_g - V_t)$ is observed. Between V_g = 0 V and V_g = 0.5 V, the resistance across the grating (ρ_{xx}) exhibits a pronounced increase of more than 30 %. In the same regime, ρ_{yy} stays almost constant with only a small increase. At gate voltages above 0.6 V, both ρ_{xx} and ρ_{yy} decrease again with increasing gate voltage. Up to V_g = 0.8 V, only negligible gate leakage current < 10^{-8} A is observed.

Figure 2 displays the magneto-transconductance of the same sample at different magnetic fields. Again, three distinct gate voltage regimes can be identified. Below V_g = 0 V (region I) equidistant Shubnikov-de Haas oscillations are present. Their period is in agreement with the gate voltage - carrier density dependence derived from the geometric capacitance of the sample. Between V_g = 0 V and V_g = 0.6 V (region II), the SdH oscillations completely vanish and a sharp, step-like structure at V_g = 0.2 V appears. For V_g > 0.6 V (region III), again SdH oscillations appear with a period which is almost identical with the one below V_g = 0 V. In both regions I and III the period of the SdH oscillations shows the usual linear dependence on the magnetic field.

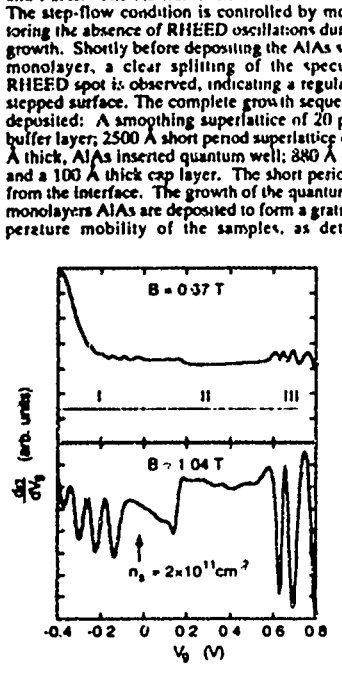

Fig. 2. Transconductance of a LSL at different magnetic fields. Between V_g = 0 V and V_g = 0.6 V, the SdH oscillation disappear

The (100) surface of GaAs does not have a 4-fold symmetry, and even for just substrates anisotropic resistivity is commonly observed (for a systematic study of anisotropic island formation see, e.g. [15]). To investigate the possible influence of this inherent anisotropy on the observed transport features, we have grown a LSL on (100) substrate, tilted by 1° towards [11$\bar{0}$]. The resistance of this sample as a function of gate voltage is shown in Fig. 3. It can be seen that the overall anisotropy is much smaller than in the above sample and a plateau-like increase in ρ is observed in *both* current directions. We therefore conclude that the anisotropic transport feature in Fig. 1 is a direct consequence of the AlAs decorated steps along the [011] direction.

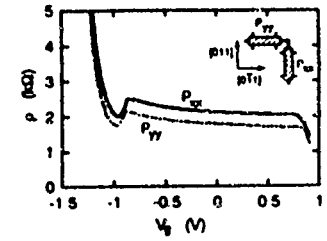

Fig. 3. Resistivity as a function of gate voltage of a LSL grown on (100) substrate tilted by 1.0° towards [11$\bar{0}$].

It has been proposed [14] that the surface structure of (100) substrates tilted towards [11$\bar{0}$] may give rise to a *two-dimensional* periodic lateral modulation with much stronger superlattice effects. However, apart from the difference in anisotropy, we find quite similar transport and magnetotransport characteristics for both tilt orientations. We can therefore not confirm a two-dimensional lateral modulation in the sample tilted towards [11$\bar{0}$].

Discussion

Many of the above experimental observations can be understood as resulting from an artificial mini-band structure caused by the periodic potential of the AlAs-decorated steps. Figure 4 schematically displays the Fermi surfaces expected for a 2DEG subjected to a one-dimensional periodic potential. For Fermi energies well below the gap (Fig. 4(b)), the Fermi surface is only little affected by the lateral modulation. In this regime, the LSL is expected to behave like an ordinary 2DEG. For $E_F \approx E_g$, the Fermi surface is strongly modified as shown in Fig. 4(c). Here, no closed orbits in k-space are possible, and hence no SdH oscillations are expected. In the gap, the states at the Fermi energy carry only little momentum along the x-direction, leading to an increase in ρ_{xx}. For $E_F >> E_g$, the second mini-band is occupied, closed orbits become possible again, and states with large k_x are available (Fig. 4(d)). Following this picture, the regions I, II, and III in Fig. 1 can directly be associated with the situations depicted in Fig. 4(b), (c), and (d), respectively. The increase in resistance and the vanishing of the SdH oscillations between $V_g \approx 0$ V and $V_g \approx 0.6$ V are then understood as a consequence of the Fermi energy being in the minigap of the LSL. Using the SdH oscillations in Fig. 2 as an energy scale, a rough estimate of the size ΔE_g of the gap can be made. The value obtained in this way is $\Delta E_g \approx 12$ meV, in agreement with the potential modulation achieved in similarly grown island-inserted quantum wells [15]. It should be pointed out that in the whole regime I, $E_F << \Delta E_g$, a situation which can not be obtained in MOS structures. This might explain why we do not observe magnetic breakdown [5, 6] up to B = 2 T, the highest magnetic field where more than one SdH oscillation can clearly be identified in regions I and III. Semiclassical theory gives an estimated breakdown field of more than 4 T.

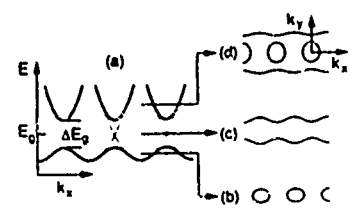

Fig. 4. Schematic representation of the dispersion (a) and different Fermi surfaces (b) - (d) of a lateral miniband

Even though many of the observed experimental features can well be understood within the framework of lateral miniband formation, a number of observations question this explanation For example, the second miniband with its large curvature in *k*-space (cf. Fig 4(a)) should exhibit more widely spaced SdH oscillations than the lowest miniband [5, 6] Clearly, this is not the case in Fig. 2. A possible explanation is that the presence of higher quantum well subbands influences the dispersion of the second miniband and lower its curvature [16]. Also, above $V_g = 0.6$ V, not the second miniband but the second subband might become occupied. Two-dimensional, self-consistent calculations of the band structure expected for our samples are presently under way to clarify these points

A more important argument against the formation of a lateral miniband structure is the apparent insensitivity of the experimental observations on both the substrate vicinal angle and the vertical position of the AlAs submonolayer in the quantum well. Recently, a number of samples were grown with vicinal angles up to 4°. Even though for these structures the miniband gap is expected to lie well above Fermi energies that can be achieved in the (AlGa)As system, their transport properties closely resemble those of the 0.5° vicinal samples. At present, we do not have an explanation for this unusual behavior. On vicinal GaAs (110) surfaces, it has been observed that step bunching can lead to a local misorientation of 0.5°, independent of the macroscopic miscut angle [17]. However, such a process is highly unlikely for the present structures, and no indication for step bunching has been observed in the RHEED pattern during growth.

As an alternate explanation for the transport anomalies, the presence of a limited number ($\approx 5\times10^{11}$ cm^{-2}) of traps in the samples might be considered, with the inserted AlAs submonolayer as a possible source. At intermediate gate voltages, these traps would become occupied, leading to a constant density of electrons in the 2DEG and hence to the absence of SdH oscillations. However, a number of experimental observations are incompatible with this explanation. (1) Illumination of the samples at low temperatures has only little effect on the transport properties of the samples. Both the increase in resistance and the vanishing of the SdH oscillations remain essentially unchanged. (2) A number of LSL samples were grown with differing doping schemes, growth temperatures, and growth interruptions before AlAs deposition. All these parameters have only little influence on the observed transport features. (3) Reference samples grown on just (100) substrates, with and without inserted AlAs, do not exhibit the above resistance anomalies. (4) In capacitance - gate voltage measurements, no indication for charge shifting within in the samples could be observed.

Acknowledgments
We would like to thank A. Gossard, H. Sakaki, and K. Ensslin for stimulating discussions Financial support by AFOSR and the NSF Science and Technology Center for Quantized Electronic Structures (QUEST), grant #DMR 92-20007 is gratefully acknowledged

References

1. L. Esaki and R. Tsu, IBM J. Res. and Dev. **14**, 61 (1970).
2. H. Sakaki, K. Wagatsuma, J. Hamasaki, and S. Saito, Thin Solid Films **36**, 497 (1976)
3. T. Cole, A. Lakhani, and P. Stiles, Phys. Rev. Lett. **38**, 722 (1977)
4. L. J. Sham, S. J. Allen, Jr., A. Kamgar, and D. C. Tsui, Phys. Rev. Lett. **40**, 472 (1978).
5. T. G. Matheson, R. J. Higgins, Phys. Rev. B **25**, 2633 (1982).
6. T. Evelbauer, A. Wixforth, and J. P. Kotthaus, Z. Phys. B **64**, 69 (1986)
7. L. J. Sham, Appl. Phys. Lett. **59**, 2010 (1991).
8. M. Tanaka and H. Sakaki, Jpn. J. Appl. Phys. **27**, L2025 (1988)
9. M. Tanaka and H. Sakaki, Appl. Phys. Lett. **54**, 1326 (1989)
10. J. Motohisa, M. Tanaka, and H. Sakaki, Appl. Phys. Lett. **55**, 1214 (1989)
11. K. Tsubaki, T. Honda, H. Saito, and T. Fukui, Appl. Phys. Lett. **58**, 376 (1991)
12. K. Pond *et al*, J. Vac. Sci. Technol. July/August 1993, in press
13. D. R. M. Williams and M. Krishnamurthy, Appl. Phys. Lett. **62**, 1350 (1993).
14. K. Yamaguchi and K. Okamoto, Jap. J. of Appl. Phys. **30**, L231 (1991); O. Brandt, L. Tapfer, and K. Ploog, Surf. Sci. **267**, 204 (1992)
15. T. Noda, J. Motohisa, and H. Sakaki, Surface Science **267**, 187 (1992)
16. H. Sugawara, J. N. Schulman, and H. Sakaki, J. Appl. Phys. **69**, 2722 (1991).

MoP1

MBE Fabrication of GaAs Quantum Wire Structures on Mesa Stripes along the [001] Direction

M. Lopez, T. Ishikawa, I. Matsuyama, N. Tanaka, and Y. Nomura
Optoelectronics Technology Research Laboratory
5-5 Tohkodai, Tsukuba, Ibaraki 300-26, JAPAN

Abstract

We propose a novel mesa geometry for the fabrication of nanostructures by molecular beam epitaxy We have found that (110) and (1$\bar{1}$0) facets can be formed by GaAs growth on [001] oriented mesa structures. Smooth surface morphology and extremely low growth rate on the (110) facets are the advantages of using this mesa direction over the conventional [0$\bar{1}$1]- and [01$\bar{1}$]-cleaved directions The width of the mesa top (100) plane, which is limited by the (110) facets, can be narrowed to the nanometer scale by GaAs growth Quantum wire-like structures, as narrow as ~30nm with a thickness of ~30nm at its center, were succesfully fabricated

1 Introduction

Fabrication of quantum wire and quantum dot structures, in which charge carries are confined in two and three dimensions, respectively, has attracted considerable attention recently These low dimensional structures are expected to exhibit new physical properties which could be used for the development of new optical and electronic devices[1,2].

Crystal growth by metalorganic chemical vapor deposition on patterned or masked substrates has been used to fabricate the above structures[3,4,5]. Also, there have been several attempts for fabricating nanostructures by molecular beam epitaxy (MBE). For example, the MBE growth on (100) substrates patterned with mesa stripes along the (0$\bar{1}$1) or [01$\bar{1}$] direction has been extensively investigated[6,7], however, the sidewalls formed during growth on these mesa stripes are often rough[8], thus complicating the fabrication of quantum wire structures

In this work we have studied the growth mechanism of GaAs on [001] oriented mesa stripes The growth of GaAs led to the formation of smooth

(110) and (1$\bar{1}$0) facets. It was found that the growth rate on these facets is extremely low. This is explained by the particular surface reconstruction of the {110} planes. Reducing the width of the (100) mesa top plane to the nanometer scale by GaAs growth, quantum wire like structures were fabricated.

2 Experimental

Mesa stripes aligned along the [001] direction were patterned on GaAs (100) substrates by conventional photolitography and wet chemical etching by $NH_4OH:H_2O_2:H_2O$ = 1:1:20. The pattern comprised mesas of different widths having a depth of ~1μm. The profile of the mesa stripe before growth is shown in the inset of Fig. 1. For a comparison, [0$\bar{1}$1]- and [01$\bar{1}$]-patterned substrates with (111)A and (111)B exposed sidewalls, respectively, were also prepared and mounted side by side with the [001] patterned substrate on a molybdenum block. GaAs layers were grown under a variety of MBE growth conditions with a constant growth rate of 0.25μm and a substrate rotation of 10 rpm.

3 Results and Discussion

The growth of GaAs on [001] oriented mesa stripes led to the formation of (110) and (1$\bar{1}$0) facets in all the growth conditions used in this work. The surface of these facets were very smooth as compared with the facets formed on the [0$\bar{1}$1]- and [01$\bar{1}$]-mesa stripes[9].

Figure 1 shows (011) cross-section SEM photographs of 4000Å-thick GaAs layers grown on [001] oriented mesa stripes under different growth conditions. 150Å-thick AlAs layers were introduced as markers and are observed as dark lines in the photographs. The inset show the shape of the mesa stripe before growth. GaAs growth led to the formation of (110) and (1$\bar{1}$0) facets in all cases, however, (310) and (3$\bar{1}$0) facets were also formed at low growth temperatures or high As pressures. These facets were formed in cases where bump like regions (indicated by arrows in Fig. 1) appeared on the (100) plane. The bump-like regions, formed by the diffusion of Ga atoms from the {110} facets, were not observed at high temperatures and/or low As pressures; growth conditions where the Ga migration length is expected to be large. Therefore, the development of the {310} facets seems to be associated to a reduction of the Ga migration length on the (100) plane at low growth temperatures and/or high As pressures.

Figure 2(a) shows the GaAs growth rate on the {110} facets relative to that on the (100) plane. The measurements were performed using ~1μm wide {110} facets of 10μm wide mesa stripes in order to minimize the effects of a possible diffusion of Ga atoms from the (1$\bar{1}$0) to the (1$\bar{1}$0) facet, and vice versa. The GaAs growth rate on the {110} facets drastically decreased by decreasing the As pressure and/or increasing growth temperature. Figure 2(b) show the width, W, of the {110} facets after one hour of GaAs growth. The {110} facets were wider when the growth was performed under low As pressures and/or high temperatures. In general, the formation of facets during growth is caused by the different growth rates on different crystallographic planes. Facets on which the GaAs growth rate is low are preferentially formed therefore, as observed in Figs. 2(a) and (b), the {11$_A$} facets were more easily formed when the growth rate on these planes was minimized. The {110} facets were narrow when the growth on these facets increased such that could become comparable to that of other shallow angle facets like the {310}. As shown in Fig. 2(a), at 620°C under an As pressure of 0.9×10^{-5} Torr, the growth rate on the {110} facts was two orders of magnitude lower than that on the (100) plane. The low growth rate on the {110} planes could be caused by the stable nature of the (110) surface.

Although the (110) plane is composed of an equal number of Ga and As atoms, the surface reconstructs in such a way that As atoms rotate ~27° out of the surface and the Ga atoms inwards. Each As surface atom moves towards an s^2p^3 arrangement with three p electrons forming bonds with its three nearest neighbors and two s electrons forming filled s^2 orbitals. Each Ga atom moves toward an sp^3 configuration and uses all of its three electrons to bond with its nearest neighbors[10]. Since the s^2 orbitals of As surface atoms are satisfied, Ga atoms impinging on the {110} planes find few nucleation sites, and are expected to have a large migration length. On the other hand, the low chemical activity of the surface Ga atoms forming the sp^3 configuration yields to a low sticking coefficient of As on the {110} surface; thus a high As flux is therefore necessary in order to obtain significant growth on the {110} facets.

At high growth temperatures or low As pressures, the mobility of Ga atoms on the {110} facets is further increased and most of the Ga atoms impinging these facets can thus more easily diffuse to the adjacent (100) plane. As a result, the width of the mesa top (100) plane, which is limited by the (110) and (1$\bar{1}$0) facets, can be reduced by the GaAs growth using such migration effects. Using an As pressure of 0.9×10^{-5} Torr and a growth temperature of 600°C, we fabricated quantum wire like structures. The width of the (100) facet was narrowed to about 50nm and then an AlAs/GaAs quantum well was grown. Figure 3 is a cross sectional SEM photograph of the resulting wire structure formed on the top of the mesa stripe. The quantum wells on the {110} facets are very thin due to the low GaAs growth rate on these facets, while the AlAs barrier layers, with a considerable thickness, cover them due to shorter migration length of Al atoms. In this figure the wire structure is observed along the [0$\bar{1}$1] cleaved direction, which is deviated by 45° from the [001] direction, the real size of this structure being as narrow as ~30nm with a thickness of ~30nm at its center.

4 Conclusions

The growth mechanism of GaAs by MBE on [001] mesa stripes was described

We found that smooth {110} facets can be formed on this novel mesa geometry, and that the GaAs growth rate on these facets is extremely low. Using these unique characteristics, we fabricated quantum wire-like structures along the [001] direction.

Acknowledgements

The authors would like to acknowledge stimulating discussions with Dr. Y. Katayama, Dr. M. Tamura, and Dr. T. Hayashi.

References

1. Y. Arakawa, K. Vahala, A. Yariv, Appl. Phys. Lett. 45, 950(1984).
2. H. Sakaki, Jpn. J. Appl. Phys. 19, L735(1980).
3. E. Kapon, K. Kash, E. M. Clausen Jr., D. M. Hwang, and E. Colas, Appl. Phys. Lett. 60, 477(1992).
4. T. Fukui, S. Ando, Y. Honda, and T. Toriyama, Surf. Sci. 267, 233(1992).
5. Y. Nagamune, S. Tsukamoto, M. Nishioka, and Y. Arakawa, J. Cryst. Growth, 126, 707(1993).
6. F. S. Turco, S. Simhony, K. Kash, D. M. Hwang, T. S. Ravi, E. Kapon, and M. C. Tamargo, J. Cryst. Growth, 104, 766(1990).
7. Y. Nakamura, S. Koshiba, M. Tsuchiya, H. Kano, and H. Sakaki, Appl. Phys. Lett. 59, 700(1991).
8. T. Takamori, K. Watanabe, and T. Kamijoh, Electron. Lett. 28, 2208(1992).
9. M. Lopez, T. Ishikawa, and Y. Nomura, submitted to Jpn. J. Appl. Phys.
10. S. Y. Tong and W. N. Mei, J. Vac. Sci. Technol. B2, 393(1984).

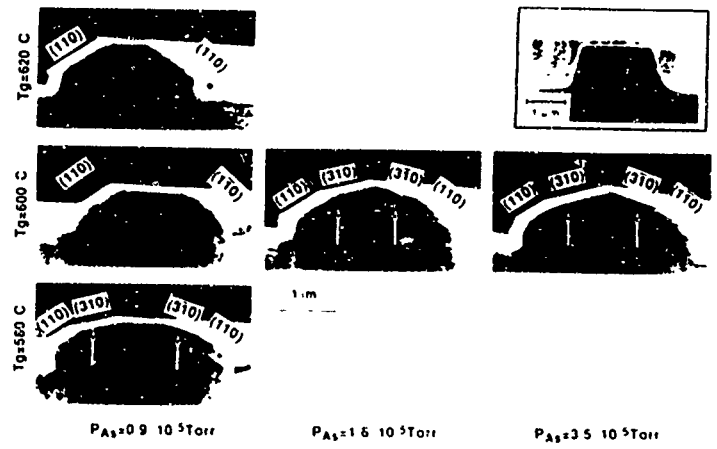

Fig. 1 Cross-sectional SEM photographs, taken along the [0$\bar{1}$1] direction, of 4000Å GaAs layers grown under different conditions on [001]-oriented mesa stripes. 150Å-thick AlAs layers were introduced as markers and observed as dark lines in the photographs. The arrows indicate the bump-like shaped regions which are formed by diffusion of Ga atoms from the {110} facets. The photograph in the inset shows the shape of the mesa stripe before growth.

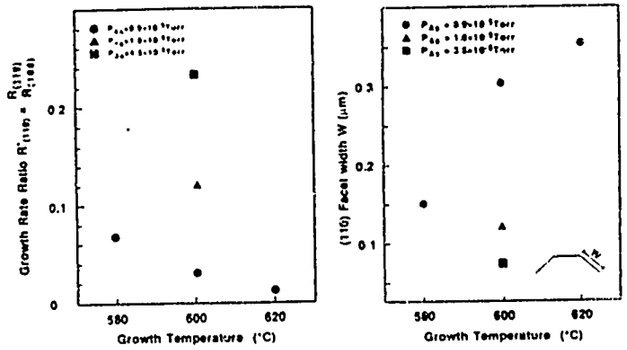

(a) (b)

Fig2 Growth temperature and As pressure dependence of (a) GaAs growth rate on the (110) facet relative to that on the (100) facet. (b) width of the (110) facet after one hour of GaAs growth.

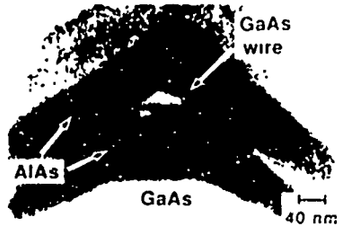

Fig.3 Cross-sectional SEM photograph, taken along the [0$\bar{1}$1] direction, of a quantum wire-like structure.

MoP2

ALTERNATE METHOD TO PRODUCE QUANTUM WIRES USING DISLOCATION SLIPPING

C. GUASCH* - F. VOILLOT* - M. GOIRAN* - J.P. PEYRADE* - E. BEDEL* - C. FONTAINE* - H. ATMANI* - A. ROCHER*
*Laboratoire de Physique des Solides, LA074, 31077 TOULOUSE Cedex
*LAAS du CNRS 7, av du Colonel Roche, 31077 TOULOUSE Cedex
*CEMES-LOE, BP 4347, 31055 TOULOUSE Cedex

ABSTRACT

We propose to generate quantum wires by a new method based on single crystal plasticity properties. In this method the shift induced by the controlled dislocation slipping is used to cut a 2D structure in 1D structures. This method is not material specific and can be applied to any structure grown on crystalline substrates. We have used deformation by bending to control dislocation motion at high temperature on a 5 nm GaAs single quantum well MBE grown on a (001) GaAs substrate. Experimental observations show the efficiency of the method. PL spectra of the deformed structure exhibits a blue shift in regard to the single quantum well PL spectra, corresponding to an additional lateral confinement.

INTRODUCTION :

In many fields of physics the reduction of dimensions has become a challenge. This is particularly true for semiconductors where the nanometer scale is now considered since control of layer deposition by molecular beam epitaxy (MBE) is now nearly perfect. Although many techniques have been proposed either to pattern existing two dimentional (2D) strutures or grow directly 1D or 0D structures, none has reached such a degree of perfection. We propose a new technique applicable to any crystalline system to obtain a sharp lateral confinement without loss of material. If used with appropriate conditions it leaves the active region free of damage and thus keeps the optical and transport properties of the system unaltered.

PRINCIPLE :

In principle the process is very simple : if we submit a single crystal to a stress higher than its elastic limit it will be plastically deformed. For adapted experimental conditions of temperature and strain rate it deforms by dislocation slipping. As observed by "in situ" transmission electron microscopy (TEM), randomly distributed dislocation

sources in the volume or near the surface generate loops in the active slip planes [1]. The size of the loop increases in this slip plane until it reaches the surface where it creates a slip trace, i. e. a step, characterized by its Burgers vector $\vec{b}$. During this process the crystal periodicity is restored in the volume (Fig 1). When a source has emitted n loops a slip trace having a height $n\vec{b}$ is created at the surface. If we consider an epilayer of thickness e in the crystal it will be cut in fact shifted by this process if $e \leq nb_{eff}$ (where b_{eff} is the component of $\vec{b}$ along the growth direction). So, if one can control the slip by choosing crystal orientation, stress conditions (temperature and source density (by artificial creation for example) one obtains the perfect tool to pattern a 2D structure in 1D or even 0D keeping all the active layer. We should mention here that these very straight and long slip traces at the surface can also be used as an alternative to patterned or misoriented substrates for direct growth techniques [2].

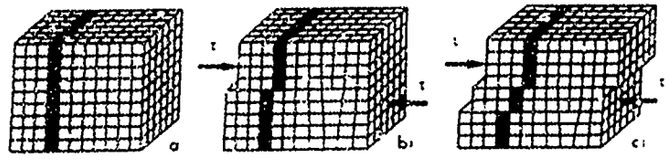

Fig 1 : Simple scheme for dislocation slipping across a perfect cubic crystal : a buried one monolayer of different composition is represented in dark (starting structure : a - one (b) and two (c) dislocation slippings). A wire is produced in figure 1c.

DIFFERENT DEFORMATION CONDITIONS

The simplest configuration to realize this principle in sphalerite structure is the uniaxial compression.

The edges of the parallelepipedic test-bar are cut along $<\bar{1}23>$, $<1\bar{1}1>$ and $<54\bar{1}>$ directions. A compressive stress is applied along the $[\bar{1}23]$ direction of the test-bar, in order to achieve a simple slip condition for deformation. In this configuration, the Schmidt factor of the $[\bar{1}01](111)$ system is the highest, thus it will be the more efficient [2].

When the single crystal is stressed, dislocation sources emit loops formed by six dislocation segments : two screw dislocations, two 60° α and two 60° β. These loops increase with the stress and propagate through out the crystal. When the dislocation loop reaches the edges of the sample, a (111) plane slips along the $[10\bar{1}]$ direction, leaving on the $(54\bar{1})$ surfaces a step characterised by the Burgers vector of the dislocation. The direction of this step is $<56\bar{1}>$.

So we have used n type GaAs single crystals elaborated by horizontal Bridgman in = 10^{15} cm^{-3}; The mean residual dislocations density is 10^8 m^{-2}. The sample size is 12 mm X 2.7 mm X 3.5 mm. All faces are mechanically polished. In order to perform T E M on

surface replica, the $(54\bar{1})$ face is mechanochemically polished. The choosen temperature is 673 K and the rate is 2 10^{-7} s^{-1}.

Replica of such $(54\bar{1})$ surface is observed by TEM. Fig. 2 shows a relatively homogeneous region over 20 µm^2 area, in which the height value is 200 Å and the step width 400 Å. In some less homogeneous regions steps with height between 200 Å and 400 Å and width between 400 Å and 600 Å are observed.

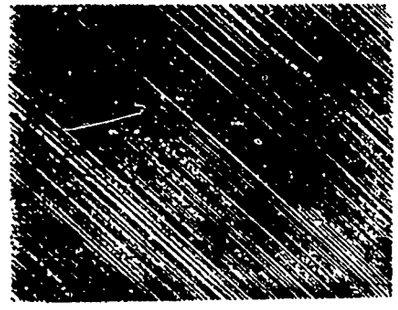

Fig 2 : TEM observation of the $(54\bar{1})$ surface.

Those results confirm that deformation of GaAs single crystal, in simple slip conditions, can generate step-like surfaces with geometrical characteristics compatible with quantum confinement. Step heights are about 10 times greater than the lattice width, so subsequent deposition by M B E on such surfaces would lead to the generation of quantum lines in an easy way.

The main problem in this deformation process is the heterogeneity of the steps size distribution on the surface on a large scale due to secondary slip, sources distribution and local hardening, so these structures will be useable only with local characterisation techniques.

This very simple situation can not be used since only MBE growth on (001) substrates are available [3]. This case is more complicated but it is possible to choose two favourable stress orientations in which four slipping systems are activated which have in each case parallel traces on the (100) surface : a stress applied along $[\bar{1}10]$ favours $(\bar{1}11)$ [101], $(\bar{1}11)$ $[01\bar{1}]$, $(1\bar{1}1)$ $[0\bar{1}\bar{1}]$ and $(1\bar{1}1)$ $[10\bar{1}]$ slip systems ; in the same way, a stress along {110} will favour (111) $[\bar{1}01]$, (111) $[01\bar{1}]$, $(11\bar{1})$ [011] and $(11\bar{1})$ {101} slip systems.

We have used a pure bending tests which is a simple way to apply tensile stress : in pure bending no cutting stress is involved, only a bending moment exists at the surface. In addition from the (001) face to the $(00\bar{1})$ one, the stress varies linearly from tension to compression. This situation will activate dislocation sources at the surface or close to the surface. Moreover the neutral plane at the center of the sample acts as a barrier for dislocation slipping which is a more favourable case to avoid inhomogeneities. The stress

orientation chosen is [111] in order to favour the development of 60° dislocations sources from the surface on which the active layer is grown. The temperature is 673 K and the surface strain rate is about 10^{-5} s^{-1} in order to favour slipping deformation mechanisms [4]. We have tried both homogeneous four point bending and inhomogeneous three point bending.

SAMPLE CONFIGURATION

Single quantum wells (SQW) were grown by MBE on a (001) GaAs semi-insulating substrate. They present a GaAs 18 Å monolayer between two $Ga_{1-x}Al_xAs$ (x = 0.3) barriers of thickness d and a cap layer of thickness e. d varies from 30 nm to 100 nm and e is typically 20 nm.

RESULTS

Atomic Force Microscopy (AFM)

Fig. 3a displays a three dimensional image of a sample deformed by four point bending by an amount of 1.5 %. The terraces created are defined by very parallel straight lines which continue throughout the sample as observed by optical microscopy. The average step height is 2.5 nm corresponding to 7 elementary slipping steps of the (111) plane. Two different slipping planes from the (111) family with parallel slip traces have been involved in this process. This explains why the surface does not present the aspect of a simple monotonic staircase.

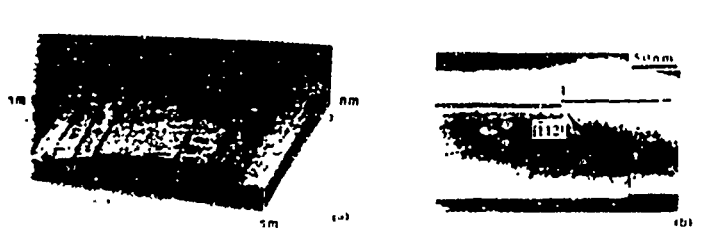

Fig. 3 : (a) Tridimensional AFM image of the (001) GaAs surface after four point bending deformation. (b) (220) XTEM dark field micrograph of a 7 nm SQW after four point bending deformation.

Transmission Electron Microscopy cross section (XTEM)

Fig. 3b is an XTEM micrograph of a deformed SQW. A sharp shift A (38 Å) is clearly revealed. A corresponding V shift is observed at the barrier - buffer interface. The AV direction is [1 1 2] which confirms that the slipping planes belong to the (111) family. It should be mentioned that no dislocation is left inside the MBE 2D structure : dislocations are only observed at about 1.5 µm from the surface.

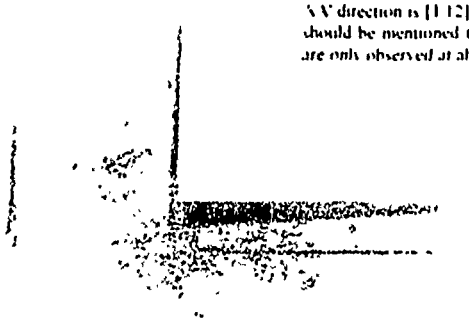

Photoluminescence (PL) measurements

PL spectra were taken at 1.7 K on SQW before and after deformation with a 700 nm laser line excitation. After deformation the exciton peak intensity is only slightly decreased. No blue shift is detected on samples with deformation smaller than 2 %, which is expected due to the distance between two cuts inducing very large wires (> 150 nm). For larger deformations on three points bending we observed a blue shift which increases with the deformation according to calculations on the expected wire width for a given deformation. Typical spectra before and after deformation are presented on Fig. 4.

Preliminary X Ray diffraction results allow us to evaluate the maximum tensile stress close to the surface at 30 MPa along the [1̄10] direction. The effect of uniaxial tensile stress is to reduce the energy gap value [5]. Thus the measured PL spectra could be the result of two opposite contributions : a uniaxial tensile stress along [1̄10] and an additional lateral confinement with a 25 nm period along the same direction.

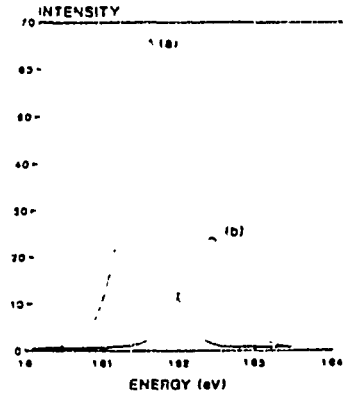

Fig. 4 : 1.7 K PL spectra before (a) and after (b) a three point bending deformation.

ADVANTAGES OF THE METHOD

The different results exposed here confirm that quantum wires have been obtained by the proposed method and show that plasticity can be an alternate for quantum wires or quantum dots production. Our method has many advantages : theoretically the lateral roughness is no more than the atomic step ; in principle there is no limitation in the size of the wire : neither in width nor in length ; its simplicity and low cost : quantum wires are obtained by having a 2D structure with an atomic scale tool (the dislocation) so there is absolutely no loss of active material ; a very large field of application : since only dislocation slipping is used this method is basically applicable to any material or structure as

long as we are dealing with a crystalline substrate only its plasticity properties have to be known and its plastic deformation has to occur at reasonable temperature

Nevertheless it has to be pointed out that plasticity studies are still strongly needed in order to control the homogeneity and the location of dislocations sources

REFERENCES

[1] Zafrani M , Veuillot E Pevrade J P Caillard D Couret A and Coquille R Phil Mag A 65 (1) (1992) 195
[2] Veuillot E Guiran M , Guasch C Pevrade J P Dinh L , Rocher A Bedel H special issue of Journal de Physique III Microelectronique et Optoelectronique III-V", 1993 to be published
[3] Karmouda M Thesis University of Lille (France), 1984
[4] Bouya P Thesis University of Poitiers (France) 1988
[5] Pollak F H and Cardona M Phys Rev 172 (1968) 816

MoP3

Formation of N-AlGaAs/GaAs Edge Quantum Wire on (111)B Micro Facet by MBE and Magnetic Depopulation of Quasi-One-Dimensional Electron Gas

Y Nakamura, M Tsuchiya, J Motohisa, H Noge, S Koshiba, and H. Sakaki

Quantum Wave Project, JRDC, 4-3-24-302 Komaba, Meguro-ku, Tokyo 153, Japan, and Research Center for Advanced Science and Technology, University of Tokyo, 4-6-1 Komaba, Meguro ku, Tokyo 153, Japan

Abstract

An edge quantum wire (EQWI) structure with a feature width of 120 nm was successfully prepared on (111)B micro facets; the structure was fabricated by an ensemble of several growth modes in molecular beam epitaxy (MBE) on a patterned (001) substrate without resorting to any advanced lithographic technique A clear deviation from the linear relationship is observed in a Landau plot of magnetoresistance at low magnetic fields, providing the first evidence of magnetic depopulation of one dimensional subbands in a facet EQWI The sheet electron concentration measured is 5.4×10^{11} cm^{-2}, which corresponds to the linear concentration of 4.8×10^{6} cm^{-1}, and mobility is 3×10^{4} cm^{2} V^{-1} s^{-1} or higher. These values indicate a high crystal quality of the facet EQWI thus prepared.

The edge quantum wire (EQWI) scheme provides a feasible way of forming very fine wire structures without requiring advanced fine lithographic technique [1] The achievable lateral dimensions are expected to be far below 100nm and will allow large separation of subband levels, leading to the various novel electronic properties predicted in the strongly confined quantum wire regime [1] Fabrication of such EQWI requires two basic steps; the formation of edge surfaces in undoped quantum well (QW) layers (1), and the subsequent

overgrowth of an electron supply layer onto the edge surface (2). Several methods have been proposed for those two processes.

The use of cleavage for the edge formation was first demonstrated by Pfeiffer et al. They fabricated a planar superlattice [2, 3] on a (011) surface using molecular beam epitaxial (MBE) overgrowth. Motohisa and Sakaki have formed an EQWI by this method and observed the magnetic depopulation (MD) of one-dimensional subbands [4], providing the first clear proof for quasi-one-dimensional electron gas (1DEG) formed in an EQWI. In this approach, however, the area of cleavage plane is extremely small, which makes the subsequent processing rather difficult, particularly for future device application.

As an alternative method, Fukui et al proposed the use of an epitaxially grown (001)-(111)B facet structure and demonstrated the formation of an EQWI by crystallographically anisotropic metalorganic chemical vapor deposition (MOCVD) [5]. Unlike the cleaved-edge-overgrowth (CEO) method this facet approach has advantages in that a large number of quantum wires can be prepared over the entire wafer by one consecutive run of epitaxial growth and the electrodes to the wires can be prepared much more easily by using standard lithography. In their sample, however, it was difficult to prevent the formation of a two-dimensional electron gas (2DEG) at (001) hetero-interface, and the parallel conduction of the 2DEG masked key features of 1DEG on (111)B interfaces.

It was earlier suggested that a high surface selectivity of growth rates in MBE on a patterned substrate may be used to form a facet EQWI [6]. This MBE approach may have an advantage over the MOCVD method since, in addition to the crystallographic anisotropy, one can control the position and concentration of dopants by the oblique deposition technique and thereby prevent an undesirable parallel conduction outside an EQWI channel. In this paper, we report a successful fabrication of a EQWI by MBE and the first observation of MD in a facet EQWI. We describe a rather sophisticated ensemble of various MBE growth techniques employed to form the EQWI whose structure is schematically shown in Fig. 1 (a).

First, a line-and-space geometry of 2μm depth was prepared on a SiO_2-clad Cr-O doped semi-insulating (001) GaAs substrate by photolithography and $SiCl_4$ reactive ion etching [7]. The line width and spacing were both 5μm. The stripes were set 2~3 degrees off from the [110] direction to provide eventually off-oriented (111)B facet surfaces where both morphology and Si donor activation are known to be better [8, 9]. After degreasing the

patterned substrate, the SiO2 mask layer was removed to expose the mesa plateau. The substrate thus patterned was mounted on a Mo holder together with two flat (001) substrates. Those flat substrates were used to prepare the sample to monitor transport properties of electrons along the (001) interfaces.

Next, MBE growth of GaAs, AlAs, and AlGaAs layers was performed on the mesas in the following way to form the EQWI structure by paying attentions for crystallographic anisotropy and beam flux geometry (see Fig. 1 (a)). The growth rate of GaAs on flat (001) was set at 0.26 μm/h by monitoring the oscillation of reflective high energy electron diffraction on unpatterned (001) substrates. The As4/Ga flux ratio measured with a flux monitor was 26 on (001). Aluminum content x in $Al_XGa_{1-X}As$ was 0.32 on (001) if grown with the Mo holder in rotation. The substrate was always rotated except in the last phase, where the oblique deposition was used to prepare GaAs QW and AlGaAs spacer, and to perform the δ-doping of Si. Substrate temperature (T_{sub}) was varied in the range of 580°C~665°C.

MBE was started with the deposition of undoped GaAs layer (260nm) at T_{sub} =580°C to form a trapezoidal GaAs structure of Fig. 1 (a), which consists of (001) and two (111)B facets. This temperature is suitable to obtain a sharp facet corner at the boundary of (111)B and (001) planes. Then, a GaAs layer of 74nm was deposited, while T_{sub} was raised up to 665°C with the rate of 5°C/min to achieve good surface morphology. At 665°C, 50nm GaAs and 200nm AlGaAs were grown further. Although the growth at this temperature leads to somewhat rounded facet corners, it is effective to improve the quality of AlGaAs and also to reduce the outgassing from the substrate heater during the subsequent growth. Next, T_{sub} was gradually reduced to 580°C with the rate of 5°C/min, while 108nm AlGaAs was grown giving a rather sharp facet corner. Then to complete the bottom barrier, 100nm AlGaAs was grown. The (111)B surface was kept smooth in the growth of these AlGaAs layers. These AlGaAs layers are thick enough to prevent the accumulation of 2D electrons at the first AlGaAs / GaAs heterojunction.

Then the whole structure was covered with two-monolayer GaAs to prevent the oxidation of AlGaAs surface. Next, the substrate holder was adjusted so that the As beam was incident almost parallel (~0°) to the left facet plane of (111)B as shown in Fig. 1(a). After this adjustment 100nm GaAs layer was deposited to form a GaAs QW layer on the trapezoidal base as shown in Fig. 1 (a) and (b). Because of its low incident angle, the flux of As beam on the

(111)B surface was extremely low. Under this condition, the migration of Ga adatoms from the (111)B facet to the adjacent (001) surface is very efficient, resulting in an extremely low growth rate (~9nm/hr) on (111)B surfaces, which is 1/30 of that on the (001) surface [6]. As a result, the GaAs layer grown on the (111)B gets narrow (~3nm) enough to prevent the accumulation of the 2D electrons. On this structure an undoped AlGaAs of 120nm was deposited as a thick spacer layer primarily on (001) plane, while the thickness of the AlGaAs spacer on the (111)B plane is about 20nm. Although the incident As flux and GaAs growth rate were both very low on the (111)B, it was found that the concentration of contaminating impurities at the (111)B surface was tolerably low and the crystal quality near the (111)B surface was rather high. This is possibly because the effective As4/Ga flux ratio on the (111)B is almost equal to that on the (001) plane as the effective population of Ga atoms is reduced by the inter-surface diffusion.

After the formation of the AlGaAs spacer two-monolayer GaAs was deposited to passivate the surface. Then δ-doping of Si donors was done with the oblique deposition technique, in which Si beam was adjust to be incident almost normal (70~75 degrees) to the left (111)B plane but almost parallel (15~20 degrees) to the top (001) plane, as shown in Fig. 1 (a). In this geometry, the areal density of Si donors on the left (111)B facet is ~2.5×10^{12} cm^{-2} and is about three times as high as that (~8×10^{11} cm^{-2}) on the (001) plane. During the process of Si δ-doping, T_{sub} was raised up to 620°C to enhance the activation of Si donors on (111)B [9]. Because of the thick spacer layer and the low Si concentration on the top (001) plane, the formation of 2D electrons on (001) heterointerface was successfully prevented, while the supply of 1D electrons in the EQWI on (111)B plane was achieved. Finally, a 100nm undoped AlGaAs layer, a 44nm N-AlGaAs with Si dopants of 3×10^{18} cm^{-3}, and an 30nm undoped GaAs cap layer were successively grown. This N-AlGaAs layer was inserted to prevent the surface depletion effect. During the growth of AlGaAs layer Al mole fraction x was maintained between 0.3~0.5 on both the left (111)B plane and the top (001) plane to avoid both parallel conduction of electrons and excessive oxidation in the air. For this purpose, the AlGaAs layers were grown at T_{sub} of 620°C where the inter-surface migration of Ga adatoms is relatively small. Figure 1 (c) shows a cross-sectional image taken by scanning electron microscope (SEM) for the edge-exposed QW structure thus prepared. The width W of the QW in (111)B is ~120nm. Its schematic structure is also shown in Fig. 1 (b).

To study the electron transport in this EQWI structure, we formed two AuGe ohmic electrodes using the lift-off technique by which fifty wires were connected in parallel. The electrode spacing L was 10μm. The sample was conductive without light illumination at 4.2K. The reference samples grown on (001) planes were almost insulating at 77K in dark, indicating the absence of 2D electrons in the (001) plane. We measured the transverse magnetoresistance of the EQWI sample by applying a field B from different angles with respect to the (111)B plane. A Clear Shubnikov de Haas (SdH) oscillation was observed for B>1.7T as shown in Fig. 2 (a). The oscillation is found to be determined almost by the magnetic field component $B_\perp$ normal to the (111)B plane, indicating that the conductivity is due to the electrons accumulating at the (111)B heterojunction. The Landau plot for B normal to the (111)B is shown in Fig. 2 (b). A clear deviation from the linear relationship is seen for B less than 3T. This is due to the magnetic depopulation of 1D subbands and proves the quasi-one-dimensionality of electrons in our facet EQWI. The electron concentration N_{2D} derived from the Landau plot at high field was 5.4×10^{11} cm^{-2}, which corresponds to the dashed line in Fig. 2 (b). Electron mobility μ estimated from the two-terminal resistance R (850Ω) was 3×10^4 cm^2 V^{-1} s^{-1} or higher. Note that R is $L/(eN_{2D}\mu nW_{eff})$, where n (=50) is the number of EQWIs and W_{eff} the effective wire width [10].

Finally, we analyze the Landau plot and estimate the effective width W_{eff}. If a parabolic potential is assumed along the lateral direction, the position of magnetoresistance maxima can be easily calculated [10]. The Landau plot of Fig. 2 (b) was best explained when we set the linear electron concentration N_{1D} to be 4.8×10^6 cm^{-1} and the quantized energy separation $\hbar\omega_0$ to be 3meV as shown by the cross marks in Fig. 2(b). The effective width W_{eff} of the wire evaluated from N_{1D}/N_{2D} is 90nm, which is a little smaller than the width W (~120nm) determined by SEM. The origin of this small discrepancy is not clear but may be related to the fact that our EQWI has a wedge-like structure of Fig. 1, where the effective confinement size may differ from the geometrical size. The calculation based on the square potential, which seems more suitable in our EQWI, has shown that non-linear features of the observed Landau plot are not significantly altered even when the square potential is used. This point will be clarified in the future work, in which Fermi level is varied systematically by the gate voltage.

In summary, a 120nm wide edge quantum wire has been successfully prepared by MBE

on a (111)B facet. The magnetic depopulation of one-dimensional subbands has been demonstrated in the facet EQWI for the first time.

Quantum wire samples were prepared at Process Center of RCAST, University of Tokyo We thank Dr. S. Fukatsu, Mr Y Kadoya, Dr. H Kano, Prof T Ikoma, Dr T. Saito, and Mr. H. Yano of Sumitomo Electric Industries for their cooperations A part of this work is supported by Grant-in-Aid for Scientific Research from the Ministry of Education, Science and Culture

References

[1] H. Sakaki, Jpn. J. Appl. Phys 19, L735 (1980).

[2] L. Pfeiffer, K. W. West, H. L. Stormer, J P Eisenstein, K W Baldwin, D Gershoni and J Spector, Appl Phys Lett 56, 1697 (1990)

[3] H. L. Stormer, L. N Pfeiffer, K. W. Baldwin, K W. West and J Spector, Appl. Phys Lett 58, 726 (1991).

[4] J. Motohisa and H Sakaki, in Proceedings of the 21st International Conference on the Physics of Semiconductors (World Scientific, to be published)

[5] T. Fukui and S Ando, Electron Lett 25, 410 (1989).

[6] Y. Nakamura, S. Koshiba, M. Tsuchiya, H Kano and H Sakaki, Appl Phys Lett. 59, 700 (1991).

[7] Y. Nakamura, M Tsuchiya, S. Koshiba, H. Noge, H. Kano and H. Sakaki, Jpn J. Appl. Phys 32, L383 (1993).

[8] L. Vina and W. I. Wang, Appl. Phys Lett 48, 36 (1986)

[9] K Tsutsui, H Mizukami, O Ishiyama, S. Nakamura and S. Furukawa, Jpn J. Appl. Phys 29, 468 (1990)

[10] K. F. Berggren, G Roos and H van Houten, Phys Rev. B37, 10118 (1988).

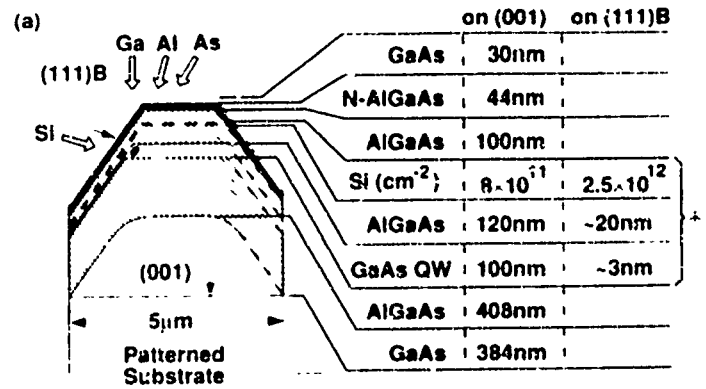

Fig 1 Cross-sectional views of an edge quantum wire. In (a) the direction of each incident beam is shown by open arrows under the conditions for the oblique deposition modes (a) In (b) magnified view of the facet EQWI is shown The SEM photograph is shown in (c)

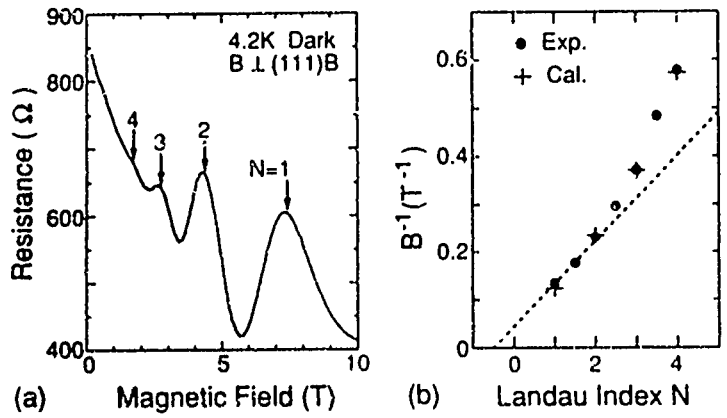

Fig 2 Magnetoresistance of the EQWI measured at 4 2 K for the magnetic field B almost normal to the (111)B facet (a) The Landau plot of the SdH oscillation (b), showing a clear deviation from the linear relationship for $B<3$T This is due to the magnetic depopulation of 1D subbands Closed circles indicate observed peaks and valleys, whereas crosses show peaks calculated for $N_{1D} = 4.8\times10^{6}$ cm^{-1} and $\hbar\omega_0 = 3$meV From the slope of the dashed line, N_{2D} was estimated to be 5.4×10^{11} cm^{-2}

MoP4

Lateral Potential Modulation in InAs/AlSb Quantum Wells by Wet Etching

T Utzmeier, T Schlösser, K Ensslin, and J P Kotthaus
Sektion Physik, LMU München, Geschw. Scholl Platz 1, D-80539 München, Germany
and
C. R Bolognesi, C. Nguyen, and H Kroemer
Materials Department, University of California, Santa Barbara, Ca 93106, USA

Lateral superlattices are fabricated on InAs/AlSb quantum wells using wet chemical etching For magnetic fields where the cyclotron diameter matches an integer multiple of the superlattice period commensurability oscillations in the magnetoresistance are observed. The spin-splitting of the Landau levels can be resolved for high magnetic fields In this regime the height of the maxima in the magnetoresistance depends on the direction of current flow with respect to the superlattice orientation

Introduction

High quality semiconductor heterostructures constrain the free motion of carriers in the plane of the hetero-interface where a so-called two-dimensional electron gas (2DEG) is formed A variety of technological methods has been applied to impose a lateral potential modulation onto the two-dimensional electron system [1] In general the fabrication of lateral superlattices on semiconductors starts from GaAs/AlGaAs heterostructures, a material system that offers large electron mobilities and well established technological procedures Here we present experimental results obtained on InAs/AlSb quantum wells that provide a number of advantageous features [2,3]

The huge conduction band offset of 1 35 eV between InAs and AlSb permits carrier densities of several 10^{12} cm^{-2} in the well The small effective mass of $m^*/m_0 = 0.023$ at the conduction band edge favors large confinement energies in quantum structures for a given geometrical feature size Without intentional doping in general the wells contain mobile electrons that dominantly originate from surface states [3,4] This fact lends itself to intentionally manipulate the surface and induce a lateral potential modulation We show that wet etching being a straight forward technique can be used in combination with holographic lithography to instigate a lateral potential modulation onto the 2DEG in InAs/AlSb quantum wells The high quality of our samples as signified by the large electron mobilities $\mu > 1.500{,}000$ cm^2/Vs leads to a large mean free path λ_l of the carriers much longer than typical periods p of the lateral superlattice The Fermi wavelength λ_F is more than an order of magnitude smaller than the lattice period Electron transport in such systems can thus safely be regarded as operating in the classical ballistic regime

We have realized lateral superlattices being periodic in one and two spatial directions with strong and weak potential modulation Here we focus on the presentation of experimental results as obtained on one dimensional weakly modulated potentials For current flow along the superlattice axis (i e perpendicular to the wires) maxima are observed in the magnetoresistance that are related to the commensurability of the lattice period and the classical cyclotron diameter at the Fermi energy [5,6] The magnitude of the potential modulation can be extracted from the positive magnetoresistance following the magnetic field regime of the commensurability oscillations and qualitative agreement with screening calculations is obtained For high magnetic fields where the spin-splitting of the Landau levels can be resolved a pronounced anisotropy in the magnetoresistance is observed depending on the direction of current flow with respect to the superlattice orientation A tentative explanation is based on the modification of the edge states caused by the interplay of Zeeman splitting and the potential modulation

Fabrication and Samples

The InAs-AlSb quantum wells are grown by molecular-beam epitaxy on GaAs substrates. As a buffer a sequence of layers of AlSb, GaSb as well as superlatuces of these two materials is grown to minimize the detrimental effects of the lattice mismatch with respect to GaAs. The InAs quantum well itself is imbedded between AlSb barriers and the capping material is GaSb or InAs. Two perpendicular Hall geometries are defined by wet etching onto the substrate. This enables us to measure simultaneously with current directions parallel and perpendicular to the wire-like superlattice. Ohmic contacts to the channel are made by annealing In in reducing atmosphere. The low-frequency (ν = 30Hz) transport experiments are performed in a superconducting magnet (0 - 12 T) and the samples are cooled by the exchange gas at temperatures 0.5 K < T < 4.2 K. The magnetic field is oriented perpendicular to the plane of the electron gas.

One of the most spectacular features of InAs quantum wells imbedded between AlSb barriers is the high density of mobile carriers without intentional doping. It has been shown that the electrons originate from three different parts of the sample. Firstly from donors in the AlSb barriers, secondly from interface states at the InAs-AlSb interface and thirdly and most importantly from surface states that lie about 0.85 eV below the AlSb conduction band edge. [3,4] The third mechanism can be used in two different ways.

One possibility is to change the surface material and therefore the Fermi level pinning at the surface. It has been shown by Nguyen et al [7] that for a constant thickness of the cap layer the carrier density in the well depends on the material on the very top of the sample. In particular if the surface material is replaced from GaSb to InAs (a thin layer of InAs such that bound states are above the Fermi level) the carrier density is reduced by about a factor of two. The details of this approach are described in Ref.7. Here we investigate a sample where the 2DEG is capped by a 30 nm AlGaSb layer and a 3nm InAs layer. Using holographic lithography and suitable development conditions a one-dimensional periodic photoresist pattern is created on the sample surface as an etch mask. Using a selective etch the InAs is locally removed leaving stripes of InAs on the sample surface. [8] This is schematically depicted in Fig 1 (a). The lateral potential modulation is expected to be such that the potential is lowered below the InAs stripes.

An alternative approach relies on the observation that for samples that have a uniform AlSb/GaSb cap the carrier density significantly depends on the cap thickness. [9] Using a photoresist pattern fabricated in the same way as described before wet etching can be used to transfer the wire pattern onto the AlSb/GaSb cap. The laterally varying cap thickness will then induce a lateral potential modulation as sketched in Fig 1 (b). In the following we will present experimental data on two samples each fabricated by one of the two methods

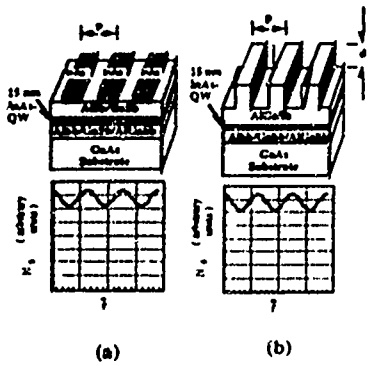

Fig. 1: Schematic for the two alternative procedures to fabricate lateral superlattices via wet chemical etching. On the left hand side (a) the thickness of the InAs cap layer is negligible. It is the lateral modulation of the Fermi level pinning caused by the lateral variation of the surface material that leads to a modulation of the carrier density. On the right hand side (b) the actual distance from quantum well to the surface laterally modulated. Thus the amount of mobile carriers that originate from surface states depends on the vertical dimension. The bottom parts of the figure indicate where the carrier density is expected to be raised and lowered

Experimental Results

We will first concentrate on a sample whose fabrication relies on the first method, namely the lateral variation of Fermi level pinning at the surface. In Fig. 2 the magnetoresistance ρ_{xx} for current flow across the wire-like barriers is presented for a sample with period p = 530 nm. The inset shows ρ_{xx} in an enlarged scale. Two maxima occur for low magnetic fields (as indicated by the arrows in the inset) that are related to the commensurability of the classical cyclotron diameter and the lattice period. This phenomenon has been studied in GaAs/AlGaAs heterostructures [5,6] and can be classically explained by the magnetic-field-induced modulation of the drift velocity [10] in a lateral superlattice. The fact that commensurability oscillations can be observed in our InAs-AlSb quantum wells is another indication about the quality of the material as well as the fabrication procedure.

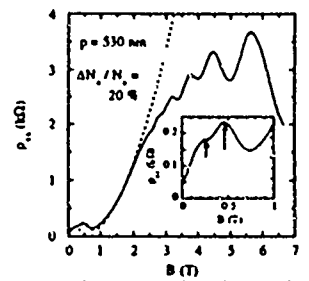

Fig. 2: Magnetoresistance for current flow across the wires of the lateral superlattice (full line) at T= 4.2 K. The dashed line marks the result of the fitting procedure to ρ_{xx} in the regime 0 T < B < 2 T as described in the text. The inset presents ρ_{xx} in an enlarged scale. The arrows mark the positions of the maxima that correspond to cyclotron orbits across one and two superlattice periods.

In order to estimate the effective potential modulation in the system the positive magnetoresistance following the regime of the commensurabiltiy oscillations is investigated. From the formulas as derived in the literature [6,10,11] for the magnetoresistance a parabolic increase is expected and was observed in the experiments [5,6,12]. We went one step beyond Ref. 12 and fitted the magnetoresistance in the regime 0T < B < 2T with the theoretical expression including the Bessel function that describes the low-field maxima. The dashed line in Fig. 2 depicts the results of this fitting procedure. The position and shape of the highest lying maximum that corresponds to an electron orbit of the size of the lattice period is nicely described by the theory. The lower lying maxima are less pronounced in the experiment probably because the scattering time in reality acquires a spatial dependence which is not taken into account in the theory. Nevertheless we can extract a value for the effective carrier density modulation from the behavior at higher magnetic fields 1T < B < 2T of $\Delta N_s / N_s \approx 20\%$.

Two homogeneous samples without lateral potential modulation where measured, one sample with the unstructured InAs cap layer and another sample with a completely removed InAs cap layer. We can thus estimate the bare potential modulation to be 50 %. The effective potential modulation is reduced with respect to the bare potential because of screening of the mobile electrons. Furthermore the closer the 2DEG to the surface of the sample the stronger the effective potential modulation in the electron channel will be. Both effects are taken into account according to Ref. 13 and a theoretical value of 28% for the carrier density modulation is found. The screening length [13] in InAs is 15 nm, much larger than in GaAs or Si. We conclude that the observed experimental features that occur at low magnetic fields and are related to the lateral superlattice are reasonably explained within the existing theoretical framework.

We also fabricated lateral superlattices by using the second fabrication method where the distance of the electron gas to the surface is periodically modulated. Again we clearly observe commensurability oscillations but now the oscillations are less pronounced and an overall negative magnetoresistance is observed that is not understood so far. The potential modulation that can be induced with this method is probably much smaller than in the experiment described before. Nevertheless an unexpected phenomenon is detected that we like to address in the following

The bare g-factor in InAs is very large g=15 and spin splitting of the Landau levels can easily be resolved in a magnetotransport experiment Figure 3 presents the components of the resistivity tensor for the current direction along the wires (ρ_{yy}) and across the wires (ρ_{xx}). The spectra are only shown in the magnetic field range 5T < B < 10 T at low temperatures T=0 5 K. The wide minima are related to the Landau splitting at even integer filling factors as indicated in the figure. The filling factor is defined as the number of occupied Landau levels below the Fermi energy. Every pair of maxima neighbors a minimum that is related to the spin splitting of a Landau level, i.e. an odd integer filling factor. The vertical arrows mark the magnetoresistance maximum on the low-field side of the spin-splitting. For current flow across the wires (b) the left maximum is always lower than the right maximum, for current flow along the wires (a) the situation is reversed. In the following we will refer to this effect by AMOF (anisotropy in the maxima neighboring an odd-integer filling factor)

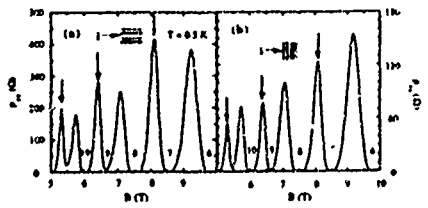

Fig 3: Magnetoresistance along (ρ_{yy}) and across (ρ_{xx}) the wires in the magnetic field regime 5 T < B < 10 T at T = 0 5 K. The integers in the minima signify the number of occupied Landau levels The vertical arrows mark maxima that lie on the low-field side of minima that reflect the position of the Fermi energy between two spin-split Landau levels (odd integers)

The AMOF was observed on more than ten samples with different superlattice periods fabricated by different fabrication technologies and never depended on cooling cycle or other external parameters of the experiment. On a homogeneous sample without a lateral superlattice the experiments revealed the same behavior for the magnetoresistance maxima as in the case of Fig 3 (b) independent of the direction of current flow. We conclude that the AMOF is not related to possible anisotropies in the growth kinetics along the different crystal axis. In homogeneous samples it was observed that the height of a maximum in the magnetoresistance depended on the current level. [14,15] In our experiment the measurement current is changed over 4 orders of magnitude and the qualitative behavior of AMOF is not changed. The AMOF is identical under reversal of the magnetic field. As a function of decreasing temperature the minimum in the magnetoresistance related to the spin-splitting of Landau levels becomes more pronounced but the anisotropy of the neighboring maxima does not change qualitatively. The anisotropy is most pronounced for intermediate cases where the minimum related to an odd-integer filling factor is close to zero For very low temperatures, high magnetic fields and high mobility samples where the Landau levels are well separated the AMOF becomes less pronounced. In the opposite limit where the spin-splitting of the Landau levels can barely be resolved the AMOF also becomes weaker. In general spin-splitting in GaAs-AlGaAs heterostructures is harder to resolve because of the smaller g-factor However, after the observation of AMOF in InAs-AlSb quantum wells we were able to detect similar behavior in weakly modulated one-dimensional superlattices as well as in rectangular antidot latices on GaAs

For an explanation of AMOF it is important to remember that the height of the maxima neighboring a minimum in the magnetoresistance is modified with respect to a homogeneous sample in case the current flows parallel to the wires in the superlatuce (Fig 3. (a)) It is therefore this current direction that deviates from "usual" two-dimensional behavior. The fact that the magnetoresistance vanishes if the Fermi energy lies in between Landau levels can be understood in terms of absence of back-scattering in the quantum Hall regime. [16] The maxima in the magnetoresistance are supposed to arise from scattering from edge states into the bulk. If the current flows along the wires a Landau level will exhibit the minima and maxima of the potential modulation in the direction across the current direction This situation is presented schematically

in Fig. 4. For two Landau levels that are energetically close to each other as in the case of spin-split Landau levels the Fermi energy may thus cross a Landau level several times. The scattering from an edge state into the bulk could therefore be greatly modified. This is completely different if the current flows across the wires In that case a Landau level will be flat across the direction of current flow and scattering from an edge state into the bulk should be the same as for an unmodulated sample. This simple model explains the direction dependence of the AMOF. It further suggest that the scattering rate from an edge state into the bulk could be modified if the current flows along the wire direction which would influence the shape of the respective maximum in the magnetoresistance. Nevertheless a more refined theoretical analysis is required to understand this phenomenon in more detail.

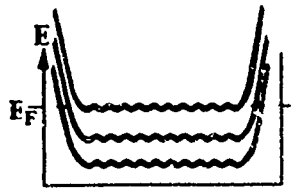

Fig. 4: Schematic fo. a series of spin-split Landau levels across the direction of the wires in the lateral superlattice. The dashed line marks the position of the Fermi energy. The wiggles of the Landau levels reflect the lateral potential modulation The size of the cyclotron energy, Zeeman energy and potential modulation are not drawn to scale but to clarify the idea behind the explanation in the text.

We have presented two fabrication techniques that enable us to produce lateral superlattices on InAs-AlSb quantum wells. Commensurability oscillations occur in the low-field magnetoresistance which reflects the high quality of our samples. For high magnetic fields and low temperatures the spin-splitting of Landau levels can be detected in the magnetoresistance. The two spin-split Shubnikov-de Haas maxima reveal a pronounced anisotropy being related to the current direction with respect to the superlattice orientation. A simple model is presented that suggests a mechanism in terms of scattering from edge states into the bulk of the sample

It is a pleasure to thank A Wixforth for valuable discussion Financial support from the Volkswagen-Stiftung is gratefully acknowledged

References

[1] for a review see: W Hansen, U. Merkt, and J P. Kotthaus, in Semiconductors and Semimetals, ed. R. K Willardson, A C Beer, E. R Weber,Vol. 35, ed M. Reed, (Academic Press, San Diego 1992) p. 279.
[2] G. Tuttle, H. Kroemer, and J H. English, J Appl Phys. 65, 5239 (1989)
[3] C. Nguyen, B Brar, H Kroemer, and J H English, Appl Phys Lett 60, 1854 (1992)
[4] C. Nguyen, B. Brar, H. Kroemer, and J. H. English, J. Vac Sci. Technol. B10, 898 (1992)
[5] D. Weiss, K. v. Klitzing, K. Ploog, and G. Weimann, in "High Magnetic Fields in Semiconductor Physics II", edited by G Landwehr, Springer Series in Solid State Science 87, 357 (1988)
[6] R. W. Winkler, J P Kotthaus, and K Ploog, Phys. Rev Lett 62, 1177 (1989)
[7] C. Nguyen, B Brar, and H. Kroemer, to be published
[8] C Nguyen, B Brar, V. Jayaraman, A. Lorke, and H Kroemer, to be published
[9] C. Nguyen, B. Brar, and H Kroemer, to be published
[10] C. W. J. Beenakker, Phys Rev. Lett 62, 2020 (1989)
[11] R. R. Gerhardts, D. Weiss, and K v Klitzing, Phys Rev. Lett 62, 1173 (1989)
[12] A. K. Geim, R. Taboryski, A. Kristensen, S. V. Dubonos, and P. E. Lindelof, Phys Rev. B46, 4324 (1992)
[13] J. P. Kotthaus and D Heitmann, Surf Science 113, 481 (1982)
[14] R J. Haug, K v Klitzing, and K Ploog, Phys Rev B35, 3933 (1987)
[15] P. Svoboda, P Streda, G Nachtwei, A Jaeger, M Cukr, and M Lazncka, Phys Rev. B45, 8763 (1992)
[16] M Buttiker, Phys Rev B38, 9375 (1988)

MoP5

Optical Properties of GaAs Quantum Dots Fabricated by MOCVD Selective Growth

Y. Nagamune[1], M. Nishioka[2], S Tsukamoto[1], and Y. Arakawa[1,2]

[1]Research Center for Advanced Science and Technology, University of Tokyo
4-6-1 Komaba, Meguro-ku, Tokyo 153, Japan
[2]Institute of Industrial Science, University of Tokyo
7-22-1 Roppongi, Minato-ku, Tokyo 106, Japan

Abstract

In spite of a bottle-neck prediction, strong photoluminescence intensity was observed from nanometer-scale GaAs quantum dot structures *in situ* fabricated by selective growth technique using metal-organic chemical vapor deposition. The dot structures showed a large PL peak by excitation above AlGaAs barrier from 8 K to room temperature, while its intensity largely decreased by excitation below the barrier. This demonstrates that carrier diffusion smoothly occurs into the dots from the barrier region.

Introduction

Three-dimensional (3D) confinement of carriers in semiconductor quantum dots (QDTs) has much attention for quantum device applications[1,2] as well as for fundamental study in quantum physics. Many workers have intensively investigated for fabricating structures inducing the predicted quantum effects[3-8], and estimated optical properties of the fabricated samples by spectrally resolved photoluminescence (PL) experiment, which directly depict radiative transition between density of states of the reduced dimensionality.

However, there have been facts that fabricated zero-dimensional (0D) or 1D nanostructures lead to almost diminished PL intensity[5,9]. This poor radiative efficiency in QDTs was thought to be due to non-radiative recombination at surfaces or interfaces damaged by etching or other processings. But, recently it is pointed that the poor efficiency is intrinsic effect rather than the extrinsic effect caused by processing, so-called bottle-neck prediction[10], so that such the undesired effect is unescapable even in QDTs fabricated by improved techniques.

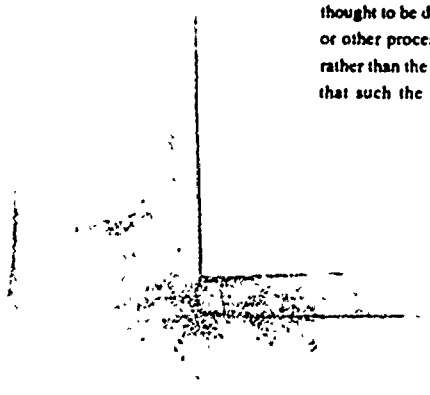

On the other hands, large efforts for making high quality nanostructures have been continuously made, in particular, to *in situ* fabrication techniques, which can largely reduce impurity and damages at hetero-interfaces. In *in situ* fabrication techniques, selective epitaxial growth on masked substrates by metal-organic chemical vapor deposition (MOCVD) is promising for fabrication of quantum wire (QWR) structures[7] or QDT[8,11]. More recently large PL intensity was observed even from very narrow (7 nm) QWR structures[12]. Then, possibility for obtaining large PL intensity from QDTs is generated.

In this paper, we report PL spectra of nanometer-scale GaAs QDT structures fabricated by MOCVD selective growth. The QDT structures showed a clear blue-shifted PL peak with high quantum efficiency not only at low temperature but also at room temperature. In addition, we discuss carrier diffusion into the QDTs from the barrier region based on the result of PL excitation (PLE) spectra.

Fabrication Procedure

Samples were prepared by selective growth technique using MOCVD, which was carried out on (100) GaAs substrates with a low-pressure (100 torr) horizontal MOCVD reactor, where the substrates were masked by 20 nm thick SiO_2 films with square windows of about 700 x 700 nm^2 size made by plasma CVD, electron beam lithography and wet chemical etching. The sides of the windows were oriented in the direction of <0$\bar{1}$1> and <011> of the substrates. The whole pattern was composed of 2000 x 2000 windows placed in the period of 1 μm and their sizes were 2 x 2 mm^2. Concerning the condition of MOCVD growth, partial pressure of arsine (AsH_3), trimethylgallium (TMG) and trimethylaluminium (TMA) were kept at 4.4×10^{-4}, 4.4×10^{-6} and 1.5×10^{-6} atm, respectively. The group V/III ratio was 100 for GaAs growth, and the total gas flow rate including carrier gas H_2 was 6 liter/min. Before the MOCVD growth at 700 °C, thermal etching was performed at 800 °C for 5 min in order to exclude an oxide film or a contaminated surface of the substrate.

Under this growth condition, GaAs or AlGaAs are selectively grown in the windows on the substrates, and a few hundred nanometer size GaAs QDT structures surrounded by $Al_{0.4}Ga_{0.6}As$ can be made by switching the suppling material at the proper stage of the growth process. A scanning electron micrograph of the cross section of the fabricated GaAs

QDT structure for (011) are shown in Fig. 1(a), where dark parts are corresponding to GaAs and a little light ones to AlGaAs as shown in Fig. 1(b). The QDT structure have disk-shaped structure of which the dimension is 190 x 160 x 12 nm, and are three-dimensionally surrounded by the AlGaAs barrier. This structures was made using the surface migration mechanism and difference of growth rate between (100) and other planes[8].

PL Spectra and Temperature Dependence

Figure 2 shows PL spectra of the sample including QDT structures at various temperatures between 8 and 300 K, where the PL spectra was obtained by use of Ar^+ laser light with multi-lines, of which the energies are larger than the band gap of AlGaAs barrier. Here, laser beam diameter was about 0.2 mm and the power 10 mW. In Fig. 2, a PL peak at 805 nm of spectra measured at 8 K is corresponding to GaAs QDT structures while that at 817 nm is to GaAs bulk transition, probably (D_0, X)[13,14], and that at 830 nm is to the transition at carbon impurities. A broad peak at 775 nm is considered to be corresponding to thin GaAs quantum wells with a thickness of about 5 nm grown on (311)A and mostly on (110) sidewalls of the AlGaAs plinths shown in Fig. 1, and that at 730 - 610 nm in the inset is to AlGaAs with various compositions.

The energy shift of the PL peak position of the QDTs from that of the GaAs bulk is about 25 meV. This energy shift is considered to be induced almost by the longitudinal confinement of the disk-shaped dot-structures as is almost equal to that of a normal quantum well with the same thickness. However, the large intensity of the PL spectra in spite of small filling factor of the dots is expected to be caused by the zero-dimensional nature such as large interface-to-recombination volume rate, carrier diffusion from the outside.

As well as PL peak of GaAs QDTs is larger than that of GaAs bulk and sidewall wells, the PL peak survive until higher temperatures. This is in contrast to the case that the PL peaks by the transition in GaAs bulk and that at carbon impurities disappear at comparatively lower temperatures. This weak temperature dependence of GaAs QDTs is considered to be caused also by the three-dimensional confined structures.

Excitation laser power dependence of PL spectra of GaAs QDTs at room temperature is shown in Fig. 3. A PL peak of the QDTs is clearly observed even at room temperature, and the peak intensity increases in proportion to the excitation power below about 50 mW, showing linear response within this excitation power range.

Figure 4 shows PL spectra by excitation wavelength of 710 nm by a wavelength-tunable Ti:Sapphire laser, and PLE spectra detected at 805 nm by the tunable laser. In comparison with the case by the Ar^+ laser light, PL intensity of the GaAs QDTs is much smaller and it is in a factor of 10^{-2}. This small intensity is according to its small spatial filling factor, while the large intensity by Ar^+ laser light is mostly owing to carrier diffusion into the QDTs from the barrier region. This situation is also observed in PLE spectra. PLE intensity at PL peak position of the QDTs is almost zero, but it increases with increasing excitation energy. Therefore, it should be noted that PLE measurement is not equivalent to absorption measurement for GaAs QDTs, but that the PLE spectra include effect of carrier diffusion. It is considered that the PL intensity of the QDTs is caused by carrier diffusion from the sidewall well regions, and that carrier diffusion from outside of the dots smoothly occurs.

Conclusion

In conclusion, we fabricated GaAs QDT structures three-dimensionally surrounded by $Al_{0.4}Ga_{0.6}As$ by MOCVD selective growth, and observed a clear blue-shifted PL peak with high quantum efficiency not only at low temperature but also at high temperature. By PLE measurement smooth carrier diffusion into the dots from the barrier region was observed in spite of the bottle-neck prediction. These results demonstrate availability for the fabrication of QDTs by MOCVD selective growth technique and possibility of optical devices such as quantum dot laser using QDT structures.

Acknowledgement

We wish to thank Prof. T. Ikoma and H. Sakaki for their instructive discussion and encouragement. We would like to give our thank for supporting to the University-Industry Joint Project on Mesoscopic Electronics. This work was also supported in part by a Grant-in-Aid for Scientific Research on Priority Area, "Electron Wave Interference Effects in Mesoscopic Structures" from the Ministry of Education, Science and Culture, TEPCO Research Foundation, and Kanagawa Academy of Science and Technology Foundation.

References

[1] Y. Arakawa, and H. Sakaki, Appl. Phys. Lett 40, 939 (1982).
[2] Y. Arakawa, Y. Vahala, and A. Yariv, Appl. Phys. Lett. 45, 950 (1984)
[3] H. Asai, S. Yamada, and T Fukui, Appl. Phys. Lett. 51, 1518 (1987).
[4] T. F. Kuech , M. A. Tischler, and R. Potemski, Appl. Phys Lett. 54, 910 (1989)
[5] J. A. Lebens, C. S. Tsai, and K. J. Vahala, Appl. Phys. Lett. 56, 2642 (1990)
[6] T. Fukui, S. Ando, Y. Tokura, and T. Toriyama, Appl. Phys. Lett. 58, 2018 (1991)
[7] S. Tsukamoto, Y. Nagamune, M. Nishioka, and Y. Arakawa, J. Appl. Phys. 71, 533 (1992).
[8] Y. Nagamune, S. Tsukamoto, M. Nishioka, and Y. Arakawa, J. Crys. Growth, 126, 707 (1993).
[9] H. Temkin, G. J. Dolan, M. B. Panish, and S. N. G. Chu, Appl. Phys. Lett. 50, 413 (1987).
[10] H. Benisty, C. M Sotomayor-Torres, and C. Weisbuch, Phys. Rev. B 44, 10945 (1991).
[11] Y. D. Galeuchet, H Rothuizen , and P. Roentgen, Appl Phys. Lett. 58, 2423 (1991).
[12] S. Tsukamoto, Y. Nagamune, M. Nishioka, and Y. Arakawa, to be published in Appl. Phys. Lett. (1993).
[13] E. H. Bogardus and H B. Bebb, Phys. Rev. 176, 993 (1968)
[14] H. Künzel and K. Ploog, Appl. Phys Lett. 37, 416 (1980).

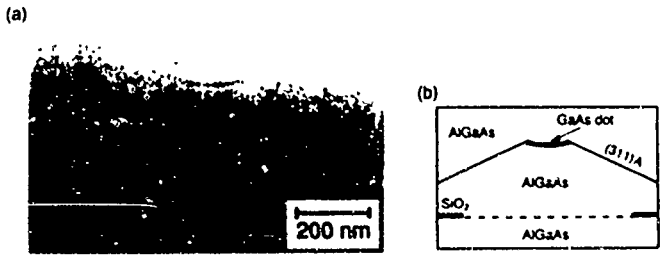

Fig 1 (a) A cross section for (011) of disk-shaped GaAs dot structures surrounded by AlGaAs, and (b) its schematic illustration.

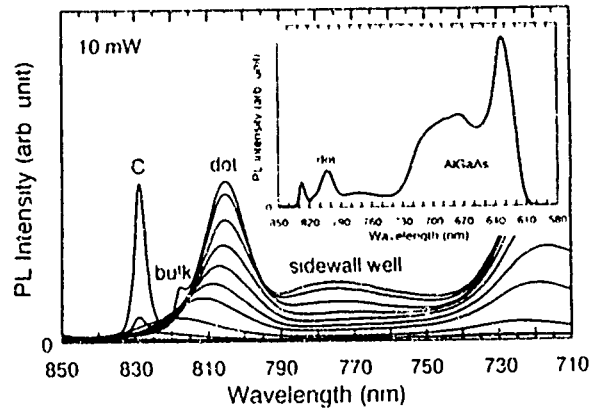

Fig 2 Photoluminescence spectra at various temperatures between 8 and 300 K of the sample shown in Fig. 1 Measurement temperatures of each of the spectra are 8, 20, 40, 60, 80, 100, 120, 160, 200, 250 and 300 K, respectively from the topmost of the spectra The inset shows spectra of large wavelength scale at 8 K

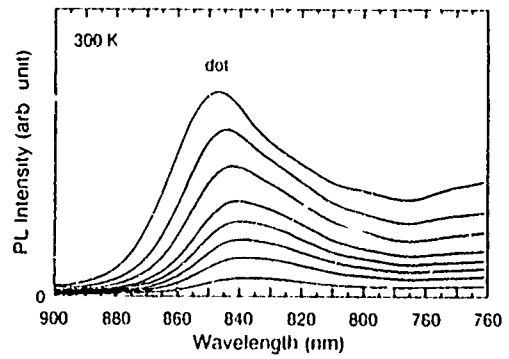

Fig 3 Excitation power dependence of photoluminescence spectra of GaAs dot structures at 300 K Powers corresponding to each spectrum are 10, 20, 30, 40, 50, 75, 100, and 150 mW, respectively from the lowest one.

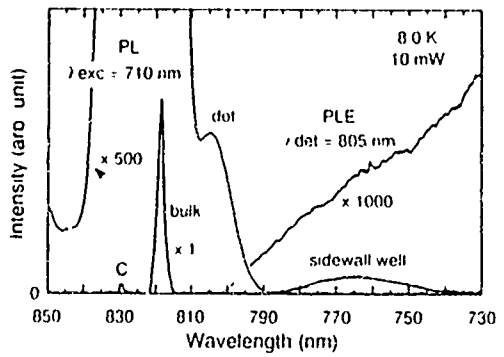

Fig 4 Photoluminescence and photoluminescence excitation spectra of GaAs dot structures at 8 K, where excitation wavelength of the photoluminescence spectra is 710 nm and detection wavelength of the photoluminescence excitation spectra 805 nm

MoP6

Fabrication of Nano meter-Scale Conducting Silicon Wires with a Scanning Tunneling Microscope

P. M. Campbell, E. S. Snow, and P. J. McMarr*
Naval Research Laboratory
Washington, DC 20375-5000

ABSTRACT

We repo.t the fabrication of nanometer-scale conducting silicon wires through the STM-induced modification of a passivated silicon < 100 > surface followed by a selective liquid etch . The modified surface layer is a thin oxide a few monolayers thick which acts as a mask against subsequent liquid etching of the unexposed portions of the silicon Silicon wires as narrow as 30 nanometers have been fabricated with this technique More complicated patterns can be written selectively by pulsing the STM bias to a suitable writing voltage pixel-by-pixel during a low-bias (hence non-exposing) scan. The maximum pattern size is limited by the range of the piezoscanners, which for our system is in excess of 100 micrometers. Conducting silicon wires between contact pads were fabricated on a silicon layer on top of a buried insulating layer of SiO_2 formed by oxygen implantation and subsequent anneal (SIMOX). Backgating of these structures permits the biasing of these wires into accumulation or inversion, thus allowing independent control of the conductivity of the wires. The techniques described here allow the simple, easy, and reliable fabrication of nanometer-scale device structures using relatively inexpensive and widely available equipment

*Sachs-Freeman Associates

1 INTRODUCTION

The physics of nanometer-scale structures and their fabrication are topics of intense current interest Various techniques have been employed to generate sufficiently small patterns and transfer them into the material of interest. The most widely used pattern-generation technique is electron-beam lithography of polymer resists, which is followed by pattern transfer techniques such as etching and metallization While electron-beam lithography can generate patterns with features in the 10 nanometer range and below, the purchase and operation of a state-of-the-art electron-beam lithography system represents a large financial investment

The scanning tunneling microscope (STM) has been proposed as a simpler and lower-cost alternative to electron-beam systems for the generation of nanometer-scale patterns Originally developed as a means of surface characterization, the STM has been used to modify the properties of surface layers [1] Recently, the STM was used to manipulate and position single atoms on a surface [2] This potential for atomic-scale surface modification suggests that the STM may equal or surpass the electron-beam system size limit for pattern generation

One method of STM lithography uses the STM tunneling current to expose a layer of polymer resist, in a manner analogous to electron-beam lithography [3]. An alternate approach is to use the STM to modify the surface directly in such a way that the modified surface layer itself acts as a resist for pattern transfer. Dagata et al. demonstrated that the H-passivated Si < 111 > surface could be selectively oxidized by STM exposure [4]. This thin oxide layer was sufficiently robust to serve as a mask for the selective MBE growth of GaAs on the unexposed portion of the surface [5], but was only partially able to withstand a liquid etch of the unexposed surface [6].

We recently demonstrated that the H-passivated Si < 100 > surface can, in a manner similar to Dagata et al., be selectively oxidized by STM [7]. The etch rate of the Si < 100 > surface in conventional etches is much larger than that of the < 111 > surface [8]. The selectivity against degradation of the oxide mask during the liquid etch is consequently enhanced by a similar factor, which allows the controlled etching into silicon of useful nanometer-scale structures from patterns written directly on the silicon surface by the STM. The highly local nature of the STM tip-surface interaction, and the fact that the oxide mask is approximately 1 nanometer thick, suggest that this technique may ultimately approach near-atomic scale resolution.

In this paper we demonstrate that this technique of localized STM oxidation of a passivated < 100 > silicon surface, combined with the enhanced etch selectivity of this surface, can be used to fabricate nanometer-scale conducting silicon wires between metal contact pads. These wires, separated from the substrate by a buried insulating layer of SiO_2 formed by ion implantation, can by backgating be biased either into accumulation or into inversion. This allows independent control of the conductivity and carrier type of the wires. Such wires form the basic building blocks for more complex nanometer-scale silicon devices which are expected to play a central role in new generations of electronics technology.

2. STM PATTERNING AND ETCHING TECHNIQUES

The full details of the exposure and etching techniques have been treated in Reference 7 and will be summarized here. A < 100 > Si sample to be patterned is first passivated by a 60 second immersion in 10% HF and then blown dry. This process strips the native oxide from the silicon surface and replaces the oxide with a passivating dihydride layer [9]. Passivated samples were attached to a STM sample stage with a conducting mechanical clip. An etched tungsten STM tip operated in air was scanned over the passivated Si surface. Typical tunneling conditions to write patterns were tip bias of 3.5 to 4 V (tip negative relative to sample) and tunneling current maintained by feedback control at 0.2 nA. The tip was scanned across the surface at a speed of 1 to 10 micrometers/sec. Under these conditions, the regions exposed to the STM tip experienced modification of the surface. This was confirmed by subsequent atomic force microscopy (AFM) imaging of the scanned regions which showed that each line scan of the STM tip had generated a raised line on the order of 1 nanometer high. The width of these latent image lines can be as small as 15 nanometers, depending upon tunneling conditions and scan speed. We attribute this latent image to the growth of a local surface oxide formed when the STM tip interaction with the surface locally removes the H-passivation and the exposed region oxidizes. Although we have no direct evidence to confirm this view, the properties of these films are consistent with those of a thin oxide [7]. Dagata et al. argued a similar oxidation mechanism on < 111 > Si [4].

There exist several liquid etches which etch silicon but do not etch silicon oxide (e.g., hydrazine [10]) or etch silicon oxide slowly (aqueous KOH solutions [11]). The STM-modified surface oxide layer should therefore act as a selective mask against etching. Figure 1 shows an AFM image of a .008 Ohm-cm n-type < 100 > Si sample onto which has been patterned a 50 nanometer period grating under the conditions described above and etched in an 11 molar KOH solution at a temperature of 60 C. The top half of the pattern was exposed at 3.5 V, while the bottom half was written at 4 V. The localized regions modified by the STM have withstood the etch, producing silicon wires approximately 30 nanometers wide at the top for the 3.5 V lines. The 4 V lines are slightly wider. The average etch depth is approximately 15 nanometers. Much deeper etches have shown that while the surface layer etch mask can be undercut by a long etch, it is not attacked by the hydrazine: the RMS roughness of the STM-modified region after a deep hydrazine etch is the same as before the etch. In contrast, a deep etch performed with a solution of KOH shows eventual degradation of the mask layer, which we attribute to the fact that KOH solutions etch silicon oxide, although at a rate several orders of magnitude slower than they etch silicon [11].

Another consideration for the formation of effective etch masks is dose. The slower the scan speed at a given bias, the larger the dose received by a given region. We find that an effective etch mask can be formed at virtually any tip-sample bias if a large enough dose is given. Conversely, a low bias at a high scan speed may not provide sufficient exposure to form an effective etch mask. This suggests that selective writing can be achieved by scanning a region at a sufficiently low bias and high speed in those areas where one does not wish to write, and pulsing the bias to a higher (exposing) value in those areas where one does wish to write. Performing this pixel-by-pixel in an area should allow the generation of arbitrarily complex patterns. We observe that it is quite easy to find conditions which will allow one to scan without writing a mask for KOH etches but somewhat more difficult for hydrazine. We attribute this to the fact that KOH will etch silicon oxide slowly but hydrazine will not. Therefore, a sufficiently low bias may generate a weak oxide layer on the surface which the KOH can dissolve but the hydrazine, owing to its extreme selectivity against silicon oxide, will not attack.

3. DEVICE FABRICATION AND RESULTS

While the etching of free-standing wires on the surface of bulk silicon constitutes a proof of principle of the technique, a more interesting structure would be a conducting wire connected at both ends to contact pads but electrically isolated from the substrate. Such a structure is one of the building blocks for more complicated dimensionally-confined devices. For this purpose we select as our starting material a piece of 1 Ohm-cm n-type < 100 > silicon which has been ion-implanted with a heavy dose of oxygen and annealed to form a buried layer of SiO_2 approximately 250 nm below the surface. This results in a thin layer of the host silicon being

electrically isolated by an insulating dielectric from the underlying substrate. This type of material, referred to as SIMOX, is used extensively in radiation-hardened electronics and is described elsewhere in more detail [12].

The sample was first coated with photoresist and patterned by standard photolithography to form open windows. This was followed by a deposition of 2 nanometers of Cr and 60 nanometers of Au which by liftoff formed metal contact pads separated by distances of 5 to 40 micrometers. The sample was then thoroughly cleaned to remove all residual photoresist. The sample was next passivated for 60 seconds in 10% HF. As described above, the STM was used to write (at 4 V, 0.2 nA) lines of oxide between pairs of contact pads. These were then etched in hydrazine at room temperature to remove all the unprotected silicon down to the buried SiO_2 layer formed by oxygen ion implantation, which acted as an etch stop for the hydrazine. As soon as the etch reached this layer, the sample was removed from the hydrazine to avoid undercutting of the wires masked by the thin surface oxide.

Figure 2 shows an AFM image of one end of a wire where it joins the contact pad. The wire is 250 nanometers high and 250 nanometers wide at the top. The flat plane at the base of the wire is the SIMOX oxide layer exposed by the etch. At the very top of the image one can see the metal contact pad. Extending out from the pad for a distance of approximately 300 nanometers is a region of unetched silicon. Rather than undercutting the metal contact pad (which is itself unaffected by the etch), the etch leaves a projection of silicon to which the silicon wire connects. The resistances of these contact pads, while greater than might have been obtained with a more complex contacting process, are still several orders of magnitude below the resistance of the fabricated wire devices and hence not a limiting factor in the electrical characteristics of the completed devices.

Several factors must be considered in the STM fabrication of conducting wires between contact pads, as well as more complex device structures derived from them. The first issue is surface cleanliness. Unlike the surfaces used to make free-standing wires in bulk silicon, which were relatively clean from contaminants, the process of writing lines between lithographically-defined metal pads implies that the surface has undergone considerable prior exposure to organic processing compounds, including photoresist, developer, resist remover, etc. Any remnant of these can interfere with the H-passivation of the surface and result in a poor pattern and hence an uneven etch. This is especially true if the etch used is hydrazine, which cannot cut through organic layers as easily as KOH does. The result in such cases is a rough etch with islands of unetched material, which would not occur with KOH. However, KOH is not appropriate for use with material which contains a SiO_2 insulating layer for electrical isolation because of the tendency for potassium to penetrate the oxide and compromise its dielectric properties [13]. Therefore, hydrazine is preferred over KOH for the fabrication of wires isolated by oxide, especially if backgating will be used to modulate the conductivity.

An additional factor to be considered is the joining of the wire to the metal contact. The wire pattern is usually written by starting the scan with the STM tip on one contact pad and scanning across to the other pad. When the tip leaves the edge

of the metal pad, the feedback control will lower the tip from the metal to the silicon surface. One must be certain that the tip is scanning slowly enough, or that the feedback loop time constant is fast enough, to lower the tip to the surface and expose it before the tip moves a distance greater than the exposure radius. If these conditions are not satisfied, the wire will not form a good connection to the metal contact pad. In practice, the unetched region surrounding the metal contact pad shown in Figure 2 aids in establishing continuity between the wire and the contact.

The silicon wires fabricated as described above are more than simple wire resistors. Because they sit on a high-quality dielectric layer of SiO_2 which itself rests on an underlying silicon substrate, one can by application of an appropriate bias to the substrate use the field effect to drive the wire into accumulation or alternately into inversion [14]. Figure 3 shows the curve tracer characteristics of one such wire under both accumulation and inversion. This backgated FET action, although extremely weak from the standpoint of electronic gain, is useful because it affords independent control over the conductivity (and even carrier type) of the wire.

The physical properties of semiconductor wires of this type are interesting from the standpoint of studying dimensionally-confined systems. In addition, such wires form the basic building blocks for fabricating more complex structures. The addition of a side gate to constrict a narrow portion of the wire would constitute a narrow-gate field-effect transistor. In the appropriate size limit, such a structure could be operated as a ballistic point contact for the study of basic transport phenomena in dimensionally-confined semiconductors. The addition of several closely-spaced gated regions would allow the fabrication of lateral resonant tunneling structures and coupled quantum dots. The full realization of such structures will require the fabrication between conducting pads of wires much narrower than the 250 nanometer width shown in Figure 2. The limiting factor in the width of the wires described here is the thickness of the isolated top silicon surface of the SIMOX wafer. Because of undercutting, one cannot expect liquid etching to preserve features of width smaller than the depth to be etched. The wire shown in Figure 2 is at the limit of the one-to-one aspect ratio of width-to-depth. We have demonstrated that lines as narrow as 30 nanometers can be defined by STM and etched into silicon [7]. The fabrication of electrically isolated wires of this width on SIMOX will require material with an oxide buried 30 nanometers below the surface. This can be achieved by a shallower oxygen implant or by thinning the top layer of silicon to the desired value. We are currently pursuing work on thinner SIMOX material.

The ultimate limit on the size of structures achievable with this type of lithography will be determined by several factors. One factor is the thickness of the oxide mask (approximately 1 nanometer), since in general one cannot expect the lateral size of a feature to be much smaller than the thickness of the mask. Another consideration is the size of the smallest region of a silicon surface which can be selectively stripped of its passivating hydrogen layer by a STM tip. Recent work has shown that this can be as small as 10 atomic surface sites [15]. Therefore, the ultimate size limit of this technique may approach near-atomic scale pattern sizes. Because only the top few monolayers are modified, the bulk properties underneath should not be harmed. There are no proximity effects from backscattered beams; hence very

densely packed patterns can be fabricated. Finally, nanostructure fabrication becomes accessible through simple, easy, reliable techniques using relatively inexpensive equipment and widely available equipment.

REFERENCES

1. R. Wiesendanger, Applied Surface Science 54, 271 (1992).
2. D. M. Eigler and E. K. Schweizer, Nature 344, 524 (1990).
3. M. A. McCord and R. F. W. Pease, J. Vac. Sci. Technol. B6, 293 (1988).
4. J. A. Dagata, J. Schneir, H. H. Harary, C. J. Evans, M. T. Postek, and J. Bennett, Appl. Phys. Lett. 56, 2001 (1990).
5. J. A. Dagata, W. Tseng, J. Bennett, C. J. Evans, J. Schneir, and H. H. Harary, Appl. Phys. Lett. 57, 2437 (1990).
6. J. A. Dagata, J. Schneir, H. H. Harary, J. Bennett, and W. Tseng, J. Vac. Sci. Technol. B 9, 1384 (1991).
7. E. S. Snow, P. M. Campbell, and P. J. McMarr, to be published in Appl. Phys. Lett.
8. E. D. Falik, V. M. Bermudez, and O. J. Glembocki, J. Electrochem. Soc. 132, 871 (1991).
9. S. R. Kasi, M. Liehr, P. A. Thiry, H. Dallaporta, and M. Offenberg, Appl. Phys. Lett. 59, 108 (1991).
10. R. M. Finne and D. L. Klein, J. Electrochem. Soc. 114, 965 (1967).
11. E. D. Palik, O. J. Glembocki, and R. E. Stahlbush, J. Electrochem. Soc. 135, 3126 (1988).
12. P. J. McMarr, B. J. Mrstik, M. S. Barger, G. Bowden, and J. R. Blanco, J. Appl. Phys. 67, 7211 (1990).
13. E. H. Nicollian and J. R. Brews, MOS(Metal Oxide Semiconductor) Physics and Technology, p. 759. Wiley Interscience, New York (1982).
14. Sorin Cristoloveanu and Stephen Williams, IEEE Electron Device Lett. 13, 102 (1992).
15. R. S. Becker, G. S. Higashi, Y. J. Chabal, and A. J. Becker, Phys. Rev. Lett. 65, 1917 (1990).

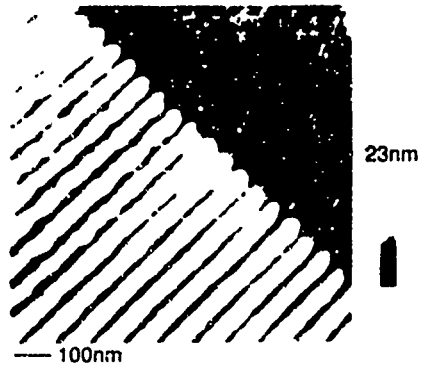

Figure 1. AFM image of 50 nanometer period grating written on <100> Si with STM and etched in 11 M KOH. Etch depth is 15 nanometers.

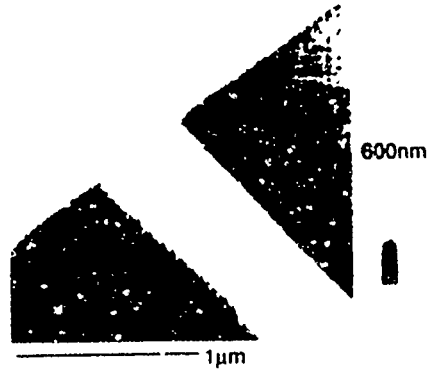

Figure2. AFM image of a Si wire (written with STM and etched in hydrazine) where it joins contact pad. Wire width and height are 250 nanometers. Wire sits on insulating SiO_2 layer formed by oxygen ion implantation.

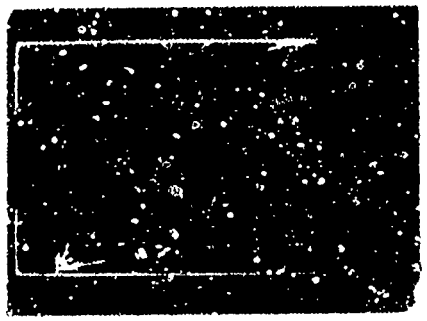

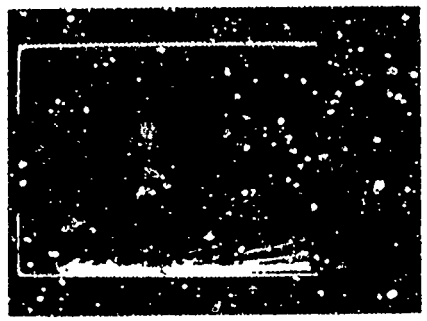

Figure 3. Curve tracer I-V characteristics of conducting Si wire (as shown in Figure 2) backgated into a) accumulation and b) inversion. Wire length is 8 micrometers.

MoP7

Selective growth of SiGe nanostructures by low pressure VPE

C. Schmidt, W. Langheinrich and K. Heime

Institut für Halbleitertechnik, RWTH Aachen, Templergraben 55, D-52056 Aachen, Germany

Tel.: ++49/241/80 77 45 Fax: ++49/241/80 77 51

For the investigation of optical effects in low dimensional silicon germanium heterostructures it is necessary to transfer patterns into silicon germanium with a lateral scaling of less than 100nm. We use electron beam lithography and a special resist system to transfer the pattern into an SiO_2 mask. By selective low pressure vapour phase epitaxy small silicon germanium structures can then be grown. By this method surface damage resulting from subsequent etching can be avoided and an immediate coverage with silicon is possible. The process and first results are presented in this paper.

Introduction

In recent years Si/SiGe heterostructures have gained importance. In high speed electronics SiGe devices achieve a performance preserved up to now to III/V semiconductors [1]. Also SiGe heterostructures were expected to allow the application of silicon technology for optoelectronics especially light emitting devices [2,3].

Many experiments and theoretical computations have shown, that even by the use of superlattices light emission is restricted to very low efficiency [4]. A new approach to this subject is the investigation of low dimensional systems like quantum wires or even quantum dots. Since SiGe quantum wells show an increase of radiative recombination in photoluminescence [5], an additional spatial restriction should limit the movement of excitons and so exclude non radiative recombination paths.

As these effects are expected to appear in structures of a scale well below 100nm, lateral structuring in this range is required. Satisfactory tools to reach this aim are electron beam lithography and reactive ion etching. These methods have proved to be able to produce silicon structures down to some tens of nanometers [6,7].

As a great part of the volume of quantum dots has to be considered as surface, the processes in these structures are very sensitive to surface effects or defects induced by the structuring. So direct patterning of semiconductors by dry etching diminishes any radiative quantum effects due to the radiation induced defects, as many experiments with III/V semiconductors have already shown [8]. For silicon germanium the effect should be even stronger because of the smaller dimensions required for quantum effects in this material.

We use an indirect way of patterning by selective growth of small SiGe structures. This way,

lateral dimensions in the range of 100nm and probably less can be achieved. In selective growth only the mask consisting of SiO_2 is affected during the patterning. Since the dots were grown only after patterning their surface is unaffected by the processing. An other point to be considered is the limited growth area. The very small lateral dimensions lead to higher critical layer thickness and allow much higher germanium concentrations than in large area growth without the formation of misfit dislocations [9]. Thus ideal conditions for optical effects should be given. In addition an in-situ coverage of the dots surface with pure silicon can be done. In this way any contact to air and any free lying SiGe surface can be avoided. This process will be described in this paper.

Resist system

The substrates we used were boron doped 100 oriented silicon substrates with a resistance of 10Ωcm. After an RCA cleaning the substrates were thermally oxidized at a temperature of 1050°C for 15 minutes. This way a high quality SiO_2 layer of 170nm thickness was produced.

Since the desired lateral dimensions are ≤ 100nm, a high aspect ratio has to be achieved. Hence an anisotropic RIE-process is required for patterning the SiO_2 layer. RIE of SiO_2 can be performed using fluorine-containing plasmas. A sufficiently high anisotropy and a high etch rate as well is achievable by using CHF_3 as an etch gas. However, this process is critical, especially if the resist covered area is large. In this case a shift of the chemical equilibrium of the RIE-process may occur and a passivation of the uncovered SiO_2 surface by carbonization is the consequence. Whether carbonization or etching dominates, mainly depends on the oxygen content within the plasma. A mixture of CHF_3 and O_2 for instance avoids carbonization but one has to take into account the enhanced etch rate of the resist (e. g. PMMA) in an oxygen containing plasma.

The main idea of the approach used in this work is the insertion of a thin titanium layer on top of the resist system. Although this titanium layer is etched by CHF_3, the metal layer influences the etching in a way that carbonization is suppressed. One reason for this effect could be the presence of a thin TiO_x layer on top of the Ti surface. This TiO_x layer is believed to adjust the equilibrium during the initial stage of CHF_3-RIE.

Figure 1.a describes the four level resist system. It consists of a double layered bottom polymer (50nm PMMA and 170nm polyimide), the titanium intermediate layer and finally on top the electron beam resist PMMA [10]. Electron beam lithography has been performed using a modified STEM with 100keV electron energy [11]. The critical exposure dose for squares larger than 100nm was 500μC/cm² whereas the dose for a single dot was 12fC.

After development in a mixture of 70% methanol and 30% ethylglycol (Figure 1 b) the titanium is etched using BCl_3-RIE (p=2.6Pa, P=0.28W/cm²) for 3 minutes (Figure 1.c). Subsequently, the double bottom polymer is patterned (Figure 1 d). Thereby the titanium acts as a mask, and as O_2-RIE is used, a thin TiO_x film is formed. The parameters for O_2-RIE are p=1.9Pa, P=0.32W/cm² and etch time 2.3 minutes. Now the critical SiO_2 etch process follows (Figure 1 e). The parameters for this CHF_3-RIE are p=0.66P, P=0.16W/cm² and the etch time 8.5 minutes. The advantage of the double leveled bottom polymer is the easy removal of the complete resist system by lift off (Figure 1.f), since the lower PMMA layer is soluble in organic solvents like ethylglycol.

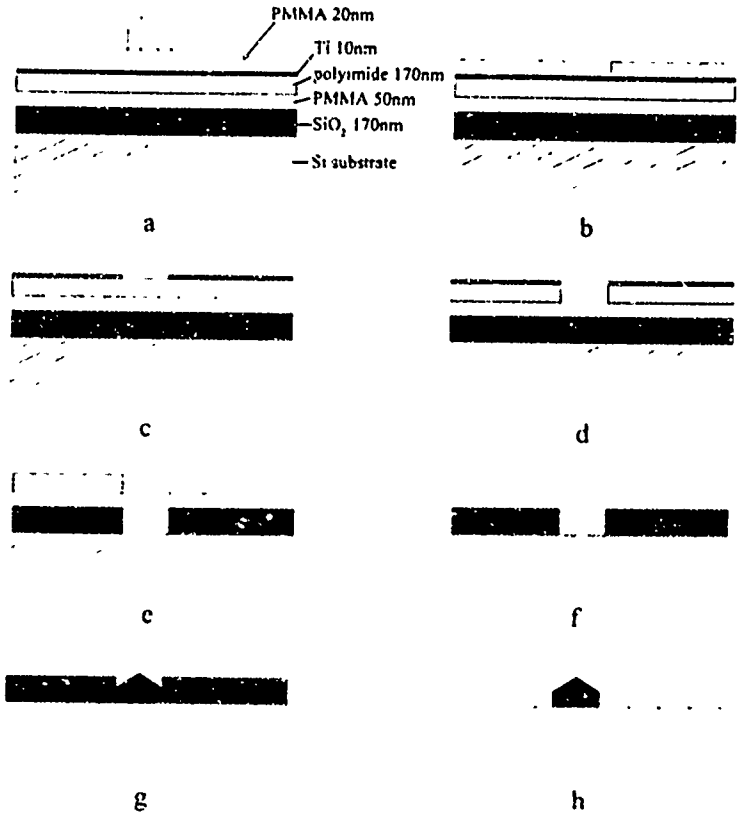

Figure 1: Process steps for fabrication of selectively grown SiGe nanometer structures. The SiO_2 layer is patterned using a multilayer resist system in order to avoid carbonization during RIE (See text).

Epitaxy

An established process for selective growth of silicon germanium layers is low pressure VPE [12] The system we use consists of a horizontal radiantly heated cold wall reactor with a graphite substrate holder The tube can be evacuated to a pressure of 0 1Pa Further description was done elsewhere [13]

After the removal of the resist the samples were first cleaned in a mixture of H_2O, NH_4OH, and H_2O_2. Next they were put for 15 minutes in H_2SO_4/H_2O_2 Finally a short dip in HF/H_2O 1:100 was done. This dilution allows us to remove only some atomic layers of native oxide leaving the mask nearly unaffected. After a final rinse in deionized water the samples were introduced in the reactor.

At the beginning of the deposition process the reactor is heated up to a temperature of 900°C at a constant pressure of 14 hPa of pure hydrogen. The temperature is then lowered to 820°C and a buffer layer of pure silicon is grown to produce a perfect starting surface for the following SiGe deposition The silicon germanium deposition (Figure 1 g) was performed at a temperature of 700°C or 650°C The latter temperature is more suitable for device applications allowing sharp interfaces. The partial pressures during the deposition are as follows: Hydrogen 100 Pa, SiH_2Cl_2 6Pa, GeH_4 0 to 0.3 Pa depending on the germanium content that shall be achieved. At a growth temperature of 650°C a small amount of HCl is added to the gas stream, to achieve perfect selectivity.

If needed a silicon layer may be grown on top to protect the surface of the structures. After growth the SiO_2 is removed by hydrofluoric acid (Figure 1 h) and an additional silicon layer can be grown to bury the dots, in order to keep surface depletion away from the Si/SiGe interface

Results

Figure 2 shows an array of well defined dots with a diameter of 200nm and 50nm spacing. All sidewalls show facets with the (311)-plane At the edge of a <110>-oriented structure no atoms can be added to the (100)-plane as the chemical bonds necessary for this reaction are not available After growth of some (100)-monolayers near the SiO_2 sidewalls (311)-facets begin to form Also dots grown in circular holes always show these facets For edges along the <100>-orientation this problem is avoided and vertical sidewalls without facets can be produced

The diameter of the smallest structures we have grown up to now is about 80nm (Figure 3) with a height of 130nm In large area growth using the same process, layer thickness was 160nm In these small structures the facets mentioned before form at the beginning of the growth process So the growth rate of the crystal plane, on which growth occurs, is reduced. Due to the aspect ratio of 1 7, these structures show vertical sidewalls, whereas the facets have formed on their top The period of the array is 200nm The SiO_2 layer had a thickness of 170nm

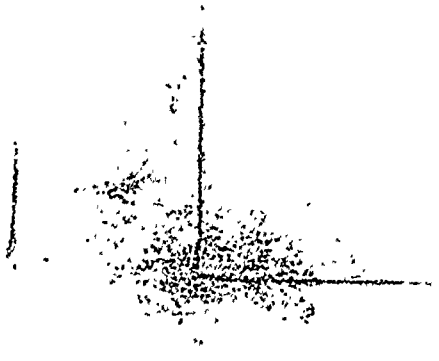

Figure 2: Selectively grown SiGe structures. Diameter 200nm with 50nm spacing All sidewalls show facets with (311)-planes.

Figure 3: Array of selectively grown SiGe dots 80nm diameter with a height of 130nm

Conclusion

We have produced SiGe nanostructures by selective low pressure VPE Using a special resist system and reactive ion etching very small patterns can be transferred into SiO, Up to now lateral dimensions go down to 80nm, a further diminuation should be possible Oxide layers of 50nm thickness or less will allow a higher precision in pattern transfer and thus lead to smaller structures Also optimization of the aspect ratio would allow a decrease of the lateral dimensions For photoluminescence studies large arrays of dots are necessary Even with an array of thousands of dots only less than 1 % of a laser beam with a diameter of 100µm would be used for excitation. In the case of high efficiency this should be no problem, but for low luminescence intensities it will be necessary to work with arrays of about 100,000 to 1,000,000 dots. Using our electron beam lithography system 30,000 dots have been exposed in 10 minutes.

Acknowledgment

The authors wish to thank B Spangenberg for the RIE processing and H P Bochem from Forschungszentrum Jülich for the SEM photographs

1. A. Gruhle, H. Kibbel, U. Erben, E. Kasper, ELECTRONICS LETTERS 29 (4), 415 (1993)
2. G. Abstreiter, Thin Solid Films, 183, 1 (1989)
3. N. L. Rowell, J.-P. Noel, D. C Houghton, M. Buchanan, Appl. Phys Lett. 58 (9), 957 (1991)
4. U. Menczigar, G. Abstreiter, Physical Review B, 47 (7), 4099 (1993)
5. L. Vescan, A. Hartmann, K. Schmidt, C. Dieker, W. Jäger, H Lüth, Appl. Phys. Lett., 60 (18), 2183, (1992)
6. P. B. Fischer, S Y. Chou, Appl Phys. Lett. 62 (12), 1414 (1993)
7. H. I. Liu, N. I Maluf, R. F. W. Pease, D K. Biegelsen, N. M. Johnson, F. A. Ponce J. Vac. Sci. Technol. B 10 (6), 2846 (1992)
8. B. E. Maile, A Forchel, R. Germann, A Menschig, H P Meier, D. Grützmacher J Vac. Sci. Technol B 6 (6), 2308 (1988)
9. T Stoica, L. Vescan, Journal of Chrystal Growth, (to be published 1993)
10. W. Langheinrich, H Beneking, Microelectron. Eng., 13, 225 (1991)
11. E. Kratschmer, D Stephani, H. Beneking, Proc of Microcircuit Engineering 83, 15 (1983)
12. Y. Zhong, M C. Öztürk, D T Grider, J J Wortman, M A Littlejohn, Appl. Phys. Lett. 57 (20), 2092 (1990)
13. L Vescan, H Beneking, Journal of Chrystal Growth, 76, 63 (1986)

MoP8

Direct Epitaxial Growth of (AlGa)As/GaAs Quantum Wires by Orientation-Dependent Metal Organic Vapour Phase Epitaxy

D Bertram*, B. Spill, W. Stolz, E.O. Göbel
Wiss. Zentrum für Materialwissenschaften (WZMW) und Fachbereich Physik, Philipps-Universität, D-35032 Marburg, Germany

Abstract

The direct growth of (AlGa)As/GaAs quantum wire structures using metalorganic vapour phase epitaxy (MOVPE) is investigated. The present concept takes advantage of the different growth rates of GaAs and (AlGa)As on (100) and {111} planes to transfer a trapezoidal GaAs starting structure with dimensions in the µm-range into a quantum wire structure in the nm-range. For stripe dimensions below 500 nm significant changes in growth behaviour (enhanced growth rates and for special cases also the formation of other crystallographic facets) are observed by using scanning electron microscopy (SEM) studies. Based on these findings (AlGa)As/GaAs quantum wire structures are realized with lateral structure sizes of 30 nm as proved by SEM. The luminescence properties of these structures, which are determined by standard and polarization-dependent photoluminescence excitation spectroscopy, are presented and discussed in comparison to the properties of quantum well structures.

Introduction

Semiconductor heterostructures with carrier confinement in two and three dimensions (one-dimensional (1d-) and zero-dimensional (0d-) systems, respectively) have gained increasing interest in recent years due to their unique physical properties, e.g. the fundamental changes in the density of states distribution or in the Coulomb interaction of carriers in these systems [1-5]. Two principle approaches have been investigated in order to realize these modulated semiconductor structures. The first one is the lateral structuring of a 2D carrier system by using various submicrometer lithography techniques in combination with subsequent dry or wet chemical etching processes [6-15]. Because of defect formation problems of the dry etching techniques, direct epitaxial growth is becoming more and more interesting. Both molecular beam epitaxy (MBE) as well as metalorganic vapour phase epitaxy (MOVPE) have been used for growth studies to realize 1D- and 0D-systems by applying the fractional layer superlattice (FSL) process [16,17] as well as epitaxial growth on various kinds of prestructured substrate surfaces [18-27].

Recently, we have presented a new approach of direct epitaxial growth of quantum wire structures by MOVPE in the (AlGa)As/GaAs material system [27]. This approach takes advantage of the different growth rates on (100) and {111} planes as a function of substrate temperature [28,29], to transfer a trapezoidal GaAs stripe structure (stripe width in the µm-range), defined by simple photolithography and selective wet chemical etching, into an (AlGa)As/GaAs trapezoidal or triangular quantum wire structure in the nm-range. A growth rate enhancement on the top (100) stripe plane has been observed for a stripe width reduction below about 1 µm, presumably due to an increased diffusion of Ga-species from the {111} side planes to the (100) top plane From this observation, which is of key importance for a precisely designed realization of quantum wire structures, it can be concluded that the epitaxial growth mechanism on narrow stripe structures is different from standard growth on plain (100) substrates. It is assumed that this change in growth behaviour takes place, if the geometrical extension of the growth planes becomes smaller as compared to typical surface diffusion lengths of ad-atom species on this plane.

Therefore, after a brief description of our concept for realization of quantum wire structures, we concentrate in the present report on the investigation of the MOVPE growth on crystallographic planes with lateral dimensions in the nm-range. In the studied stripe structures, MOVPE growth proceeds on the (100) top stripe plane as well as on $(111)_{As}$ or $(111)_{Ga}$ side planes, depending on whether the stripe is oriented in [011]- or in [0$\bar{1}$1]-direction, respectively The growth behaviour for both GaAs and (AlGa)As is investigated

as a function of substrate temperature by scanning electron microscopy (SEM) studies of cross-sectional cleavage planes of the deposited heterostructures. Finally, the optical properties of (AlGa)As/GaAs quantum wire structures, realized by the present approach, are briefly summarized.

Experimental

The MOVPE growth experiments have been performed in a commercial equipment (Aix 200, Aixtron Corp.) at a reactor pressure of 50 mbar. The substrate temperature has been varied in the range of 650°C to 750°C. In order to study the growth rate dependence of both GaAs and (AlGa)As on crystallographic planes in the nm-range, periodic (AlGa)As/GaAs multilayer structures have been deposited on prestructured GaAs trapezoidal stripe structures. Additional details of the MOVPE growth as well as the preparation of the trapezoidal GaAs starting structure using conventional contact photolithography and selective wet chemical etching ($NH_4OH:H_2O_2:H_2O$ etching solution) have already been published [27].

The structural investigations have been performed using SEM studies on cross-sectional (01$\bar{1}$)- and (0$\bar{1}$1) cleavage planes of the deposited heterostructures. These cleavage planes have been selectively etched for contrast enhancement between the individual GaAs and (AlGa)As layers. A standard luminescence set-up has been used for the optical photoluminescence (PL) and photoluminescence excitation spectroscopy (PLE) investigations. In the optical experiments only one quantum wire is excited, because of the chosen stripe separation of 80 to 125 μm. Thus, inhomogeneous broadening by interwire width fluctuations as well as grating effects in polarization dependent experiments are avoided.

Results and discussion

The principle of the present approach to realize quantum wire structures is schematically illustrated in Fig. 1. In a first MOVPE growth step an (AlGa)As/GaAs double layer is deposited. The (AlGa)As etch stop layer has a thickness of typically 0.5 μm, while the thickness of the GaAs layer is in the range of about 1 to 3 μm. This GaAs layer is structured by photolithography and the material as well as orientation selective $NH_4OH:H_2O_2:H_2O$ etching solution. In this etching process trapezoidal GaAs stripes are prepared with near $\{111\}_{As}$ side wall planes. The resulting stripe structure with stripe widths in the μm-range is schematically depicted in Fig. 1.a) for a stripe orientation along [011]-direction. This stripe width is reduced to values in the nm-range in the second MOVPE growth step (Fig. 1.b)), by taking advantage of the different growth rates of GaAs and/or (AlGa)As on the (100) top and $\{111\}$ side planes. In a continuous process the quantum wire structure is then deposited on top of the stripe (Fig. 1.c)). For the other stripe orientation in [0$\bar{1}$1]-direction, the shape of the GaAs starting trapezoid is reversed, with the narrower side formed at the GaAs/(AlGa)As interface [27]. For this stripe orientation growth proceeds on (100) top and $\{111\}_{Ga}$ side planes. The principle, however, is not changed.

In the following, the temperature dependence of the second MOVPE growth step is presented for structures with submicrometer stripe widths extending the growth experiments reported elsewhere [27]. The SEM micrographs of 10 period (AlGa)As/GaAs multilayer structures are summarized in Fig. 2, for the two stripe orientations ([011]-stripe orientation (left column) and [0$\bar{1}$1]-stripe orientation (right column)) as a function of increasing growth temperature (from top to bottom of Fig. 2) in the range of 650°C and 750°C. Because of the selective etching of the GaAs layers in the respective cleavage planes, GaAs layers appear darker as compared to (AlGa)As layers. For the samples with [011]-stripe orientation the full trapezoidal GaAs starting structure is shown, while for the samples with [0$\bar{1}$1]-stripe orientation only the top part of the trapezoid is displayed in the SEM micrographs.

First the MOVPE growth temperature dependence for the samples with [011]-stripe orientation (Fig. 2, left column) is considered. Here, we would like to concentrate on the growth behaviour on top of the GaAs starting trapezoid. As can be seen from the SEM micrographs, the principle concept, as illustrated in Fig. 1, can be applied for all growth

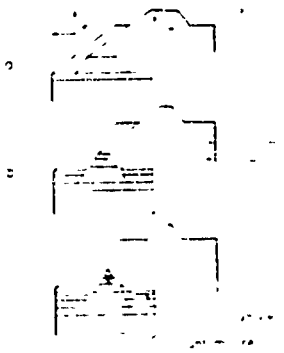

Fig. 1 Schematic sequence of realization of trapezoidal or triangular quantum wire structures. a) trapezoidal GaAs starting structure after photolithography and selective wet chemical etching, b) transfer of stripe widths in the μm-range to stripe widths in the nm-range by MOVPE growth of GaAs and (AlGa)As under appropriate growth conditions on (100) top and {111} side wall surfaces, c) growth of trapezoidal or triangular GaAs quantum wire structure.

temperatures using this stripe orientation. This is due to the almost negligible growth rate of GaAs and the small growth rate of (AlGa)As on the $\{111\}_{As}$ side wall planes. For growth temperatures above 700°C an increase in growth rate on the top (100) plane in the transition range to the $\{111\}_{As}$ side planes is observed. This is indicated by the small hump on the (100) plane at the left and right edge to the triangular side plane. The lateral extension of the humps on the (100) top plane are on the order of about 300 nm. It is assumed that this hump is caused by the additional diffusion of ad-atom species from the $\{111\}_{As}$ side planes onto the (100) top plane and/or an increase of the local gas phase concentration due to species desorbing from the $\{111\}_{As}$ side planes. Irrespective of the microscopic mechanism, this behaviour has to be taken into account in the design of the quantum wire structure. This becomes in particular true for (100) top stripe widths below about 500 nm, when the humps from the left and right corner of the trapezoid overlap, as can be seen in the top part of the triangle for the sample, grown at 700°C. So far, the formation of other crystallographic facets has not been observed for the [011]-stripe orientation and the corresponding (100) and $\{111\}_{As}$ growth planes.

For the other stripe orientation in [0$\bar{1}$1]-direction the growth temperature dependence is shown in the right column of Fig. 2, in the range of 650°C to 750°C. In these structures, growth proceeds on the (100) top plane as well as $\{111\}_{Ga}$ side planes. Because of the temperature dependent growth rate on $\{111\}_{Ga}$ planes in contrast to the $\{111\}_{As}$ planes, the realization of the quantum wire structures is different as compared to the other stripe orientation. While for low substrate temperatures (650°C) the width of the stripe is becoming slightly larger, a narrowing of the stripe width with continuing growth is

Fig. 2 Scanning electron microscopy (SEM) micrographs of cleavage planes of (AlGa)As/GaAs multilayers deposited on stripe structures oriented in [011]-direction (left column) and in [0$\bar{1}$1] direction (right column) as a function of growth temperature in the range of 650°C to 750°C. For contrast enhancement the GaAs layers have been selectively etched, thus GaAs layers appear darker as compared to (AlGa)As layers.

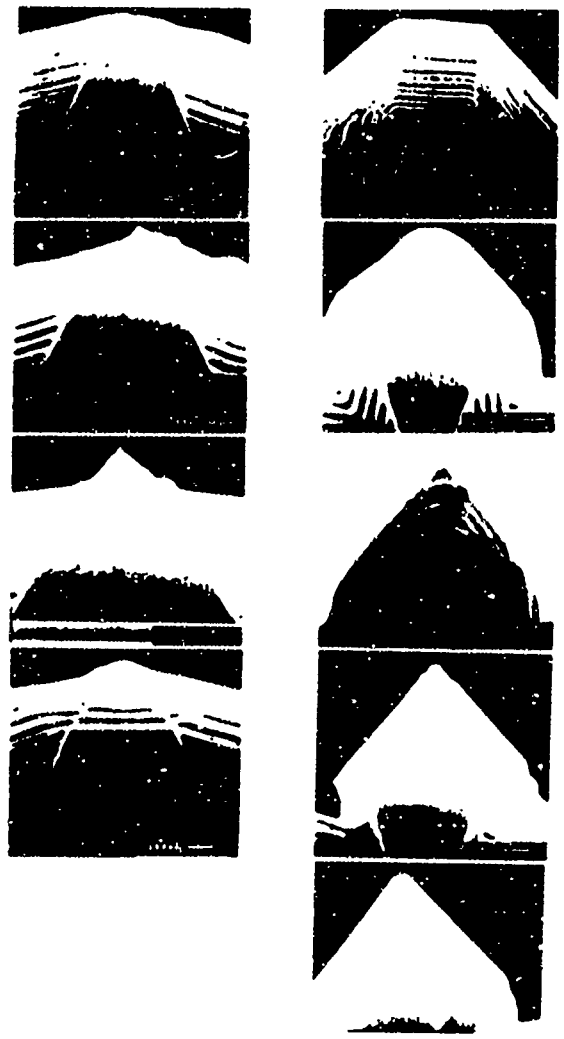

observed for all the higher temperatures. This is caused by the reduction in growth rate on the $\{111\}_{Ga}$ planes with increasing growth temperature, as can be seen in the SEM micrographs. Also for this stripe orientation an increase in growth rate on the (100) top plane near the transition to the $\{111\}_{Ga}$ side planes is observed. However, for this stripe orientation additional crystallographic planes develop for stripe widths below about 300 nm for growth temperatures of 700°C and above. This behaviour is identified most clearly for the sample, grown at a temperature of 700°C. From the SEM micrograph one can deduce the occurence of other crystallographic facets in the transition region of the (100) top and $\{111\}_{Ga}$ side wall plane during the growth of GaAs (darker part in the SEM micrograph). The angle between this plane and the (100) top surface of around 25° indicates that {311} planes have been formed in this growth step for stripe widths below 500 nm. A similar facet formation has been observed recently also in overgrowth experiments using (AlGa)As for the formation of arrow-head quantum wire structures on GaAs partially masked with SiO_2 stripes in the [011]-direction [26].

The formation of {311} facets, which seems to be characteristic for MOVPE growth on stripes oriented in [011]-direction with dimensions below about 500 nm, can be seen in more detail in Fig. 3. In this figure, the SEM micrographs of a series of stripes with decreasing stripe widths (Fig. 3.a) through c)) are shown. These stripes have been overgrown first by a GaAs layer at a temperature of 700°C to realize stripe widths in the range of 600 nm to 400 nm. The humps in deposited material at the right and left edge of the (100) top plane and the respective $\{111\}_{Ga}$ side planes is clearly seen in Fig 3.a). For slightly narrower stripe widths these two humps overlap and the {311} facets are formed together with a (100) top surface (Fig. 3.b)). Finally, for even narrower stripe widths only the {311} facets remain (Fig. 3 c)) during growth of GaAs at 700°C.

In order to establish whether or not the {311} facets are stable also at lower growth temperature, once the facets have developed at high temperature, the substrate temperature has been reduced to 650°C after the deposition of the GaAs layer. Then, the stripe structure has been overgrown by an (AlGa)As/GaAs multilayer structure at 650°C. As can be seen in Fig. 3.b) and c) the {311} facets are not stable at this lower growth temperature. With continuing overgrowth the (100) top and $\{111\}_{Ga}$ side wall plane are reestablished. Thus, it should be possible also for the [011]-stripe orientation to realize trapezoidal or triangular as well as arrow-head quantum wire structures depending on the deposition temperature.

It is important to note, that the overgrowth in the top of the stripe depends very much on the actual geometrical stripe width. This is manifested by comparing the growth experiments for a growth temperature of 650°C as a function of the stripe width, i.e. the SEM micrographs in Fig. 2 (top, right column) and in Fig. 3 b) and c). For stripe widths

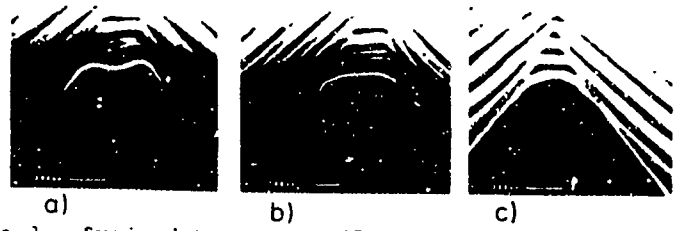

Fig. 3 Scanning electron microscopy (SEM) micrographs of cleavage planes of (AlGa)As/GaAs multilayers deposited at 650°C on stripe structures oriented in [011]-direction with decreasing wire width (a) through c)). The stripe structures have been realized by growing a GaAs layer at a temperature of 700°C. For contrast enhancement the GaAs layers have been selectively etched, thus GaAs layers appear darker as compared to (AlGa)As layers

of about 500 nm (Fig. 2 (top, right column)) the stripe width is slightly increased during growth of the (AlGa)As/GaAs multilayer structure, while for a stripe width of about 600 nm (Fig. 3.b)) the width is slightly reduced during growth of the first three multilayer periods. For a slightly narrower stripe width of about 450 nm (Fig. 3.c)), however, a strong reduction in stripe width is observed, leading to a triangular quantum wire structure with a structure size of about 60 nm after deposition of three multilayer periods. These observations prove that the growth rate depends on the geometrical widths of the respective plane. It is assumed that this behaviour is directly correlated to the increased growth rate due to the diffusion of ad-atom species from the {111} side wall planes. The growth behaviour is changed significantly, if the geometrical widths of the crystallographic planes become smaller than typical surface diffusion lengths on these planes. Therefore, further growth experiments for structure sizes below 200 nm are necessary to understand the growth dependences on nm-sized planes in detail.

For the optical experiments in the final part of this report we concentrate on quantum wire structures which are realized on {011} oriented stripe structures, because of the complication due to the formation of the crystallographic {311} facets for the other stripe orientation. The deposition of (AlGa)As at a growth temperature of 700°C has been used to realize the reduction in the top trapezoidal stripe widths to the nm-range. Trapezoidal or triangular GaAs quantum wire layers have been grown and covered directly by (AlGa)As layers. Series of samples with wire dimension in z-direction of L_z = 8 nm and L_z = 5 nm have bee realized with varying wire widths down to L_y = 30 nm, as proved by SEM microscopy [27] and presumably below. Additional high-resolution SEM- and TEM-investigations are underway to precisely determine the geometrical parameters of the realized quantum wire structures. The PL spectra of one of the realized quantum wire structures with L_z = 8 nm (full line) together with the respective reference sample, grown simultaneously on a plain (100) substrate (dashed line) are shown in Fig. 4, on a logarithmic intensity scale. The marks on the scale indicate the orders of magnitude in PL intensity. The samples were excited using a photon energy of 2.41 eV (80 W/cm²) at a sample temperature of 5 K. For thereference sample the luminescence recombination lines of the (AlGa)As cladding layers are observed at wavelengths of 618.6 nm (line A, bound

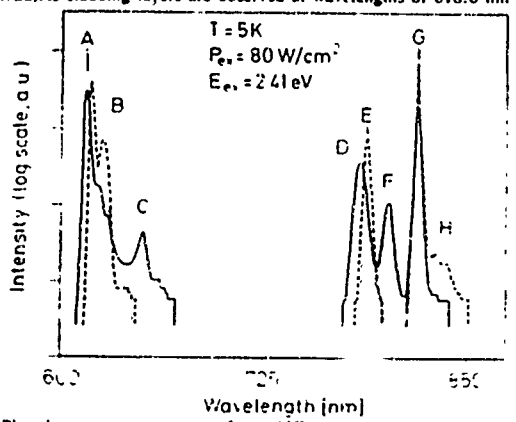

Fig. 4. Photoluminescence spectra of an (AlGa)As/GaAs quantum wire heterostructure (full line) and of a corresponding reference sample (dashed line) on a logarithmic intensity scale. For details see text

exciton and/or (D^0,h)) and 625.8 nm (line B, (e,A^0C)). These recombination processes of the GaAs buffer layer are detected at 819.0 nm (line G) and 830.1 nm (line H). The luminescence of the single quantum well structure with a well width of L_z = 8 nm is observed at 788 nm (line E). For the quantum wire sample, realized on the structured surface, similar energetic positions of the luminescence of the (AlGa)As cladding layers, the GaAs buffer and the GaAs quantum well (line D) are observed as in the reference sample.In addition luminescence lines at 650.3 nm (line C) and 801.7 nm (Line F) are detected. The luminescence line C is ascribed to the recombination in the GaAs (111) side wall quantum well, while line F is assigned to the recombination in the GaAs quantum wire structure deposited in the top of the trapezoid stripe structure. It is important to note that the quantum wire luminescence (line F) is red-shifted with respect to that of the quantum well layer deposited simultaneously in between the stripes. This red-shift is caused by the increased growth rate in z-direction on the narrow (100) top stripe plane, as described above. With a reduction in wire width a blue shift of line F is observed.

The assignment of the quantum wire luminescence line F is based on spatially-resolved PL as well as standard and polarization-dependent PLE investigations, which are presented in more detail elsewhere [27]. The PLE spectra of the quantum wire structures are always shifted in energy with respect to the corresponding spectra of the quantum well structures, proving the intrinsic character of luminescence line F. In addition, the wire luminescence intensity shows a distinct dependence on the orientation of the electric field vector of the linear-polarized light with respect to the quantum wire axis, while no such dependence is observed for the quantum well luminescence. As also reported in the literature [21], no evidence for an excitonic resonance or a peaked density of states is detected in the PLE spectra. Inhomogeneous broadening effects of the excitonic resonance due to wire width fluctuations along the wire axis and the reduced Sommerfeld-factor in 1D-systems [30] might cause the present experimental observations.

Summary

A new approach to realize trapezoidal or triangular (AlGa)As/GaAs quantum wire structures on (100) stripe facets by direct epitaxial growth using metalorganic vapour phase epitaxy (MOVPE) is presented. This concept takes advantage of the different growth rates on (100) and (111) planes as a function of substrate temperature to transfer a trapezoidal GaAs stripe structure (stripe width in the μm-range), defined by simple photolithography and selective wet chemical etching, into an (AlGa)As/GaAs trapezoidal or triangular quantum wire structure in the nm-range. Growth investigations for GaAs and (AlGa)As in particular for facet dimensions in the submicrometer range as a function of growth temperature are presented using scanning electron microscopy (SEM) investigations. A growth rate enhancement on the (100) top stripe plane for submicrometer widths is observed for both GaAs as well as (AlGa)As, presumably due to the diffusion of ad-atom species from {111} side planes. Therefore, the growth rate strongly depends on the width of the growing plane, if the geometrical dimensions of the respective growth plane become smaller than typical diffusion lengths on plain surfaces. Further growth experiments on nm-scale crystallographic planes are necessary to clarify the respective growth mechanism in detail. The present approach can be applied for growth temperatures above about 675°C, thus, leaving a wide range of growth conditions for optimization of both the structural (geometrical width, fluctuations) as well as the optical properties (interface quality) of the respective quantum wire structure. Using high-resolution SEM investigations, the realization of (AlGa)As/GaAs quantum wire structures with lateral strutures sizes of about 30 nm is proven. PL and PLE studies reveal the intrinsic character of the quantum wire luminescence. A distinct difference in the polarization dependence of this 1d-structures as compared to quantum well systems is found.

Acknowledgment

The authors are indebted to T. Ochs for expert technical support, to F. Schartner and H.U. Habermeier (Max-Planck Institut fur Festkorperforschung, Stuttgart) for preparation of the optical stripe masks. The expert support by A. Schaper during SEM investigations and by

T.F. Albrecht during optical experiments is gratefully achnowledged. Part of this work has been sponsored by the Deutsche Forschungsgenmeinschaft (DFG, Bonn).

* present address: Max-Planck-Institut für Festkörperforschung, D-70000 Stutgart, Germany

References

(1) Y. Arakawa and H. Sakaki, Appl. Phys. Lett. 40, 939 (1982).
(2) Y. Arakawa, K. Vahala and A. Yariv, Appl. Phys. Lett. 45, 950 (1984).
(3) I. Suemune and L.A. Coldren, IEEE J. Quantum Electron. QE-24, 1778 (1988).
(4) A. Forchel, H. Leier, B.E. Maile and R. Germann, in: "Advances in Solid State Physics" Vol. 28, p. 99, Ed. U. Rössler, Pergamon-Vieweg, Braunschweig (1988).
(5) D. Heitmann, T. Demel, P. Grambow and K. Ploog, in: "Advances in Solid State Physics" Vol. 29, p 285, Ed. U. Rössler, Pergamon-Vieweg, Braunschweig (1989).
(6) Y Hirayama, S. Tarucha, Y. Suzuki and H Okamoto, Phys. Rev. B37, 2774 (1988).
(7) J Cibert, P M Petroff, G.J. Dolan, S.J. Pearton, A.C Gossard and J.H. English, Appl. Phys. Lett. 49, 1275 (1986)
(8) K. Brunner, U. Bockelmann, G. Abstreiter, M. Walther, G. Böhm, G. Tränkle and G. Weimann, Phys. Rev. Lett. 69, 3216 (1992).
(9) M. Kohl, D. Heitmann, P. Grambow and K. Ploog, Phys. Rev. Lett. 63, 2124 (1989).
(10) R. Germann, A. Forchel, M. Bresch and H.P. Meier, J. Vac. Sci. Technol. B7, 1475 (1989).
(11) H. Temkin, G.J. Dolan, M.B. Panish and S N.G. Chu, Appl. Phys. Lett 50, 413 (1987).
(12) D. Gershoni, H. Temkin, G.J. Dolan, J Dunsmuir, S.N.G Chu and M.B. Panish, Appl. Phys. Lett. 53, 995 (1988).
(13) K. Kash, J.M. Worlock, M.D Sturge, P. Grabbe, J.P. Harbison and A. Scherer, P.S.D. Lin, Appl. Phys. Lett. 53, 782 (1988).
(14) K. Kash, J.M Worlock, D D. Marhoney, A.S. Gozdz, B.P. van der Gaag, J.P Harbison, P.S.D. Lin and L.T. Florez, Surf. Sci. 229, 245 (1990).
(15) C. Gréus, A. Forchel, G. Mauckner, M. Emmerling, J. Straka and K. Pieger, Surf Sci. 267, 263 (1992).
(16) J. M. Gaines, P M. Petroff, H. Krömer, R.J. Simes, R.S. Geels and J.H. English, J Vac. Sci. Technol. B6, 1378 (1985).
(17) T. Fukui and H. Saito, Jap J. Appl Phys. 29, L731 (1990) and references therein.
(18) H.M. Cox, P.S. Lin, A. Yi-Yan, K. Kash, M. Seto and P. Bastos, Appl. Phys. Lett. 55, 472 (1989).
(19) E. Colas, E. Kapon, S. Simhony, H.M. Cox, R. Bhat, K. Kash and P.S. Lin, Appl Phys. Lett. 55, 867 (1989)
(20) E. Kapon, S. Simhony, R Bhat and D.M. Hwang, Appl. Phys. Lett 55, 2715 (1989).
(21) M. Walther, E. Kapon, D M. Hwang, E. Colas and L. Nunes, Phys Rev B45, 6333 (1992).
(22) S Tsukamoto, Y. Nagamune, M. Nishioka and Y. Arakawa, J Appl Phys 71, 533 (1992).
(23) K. Kojima, K. Mitsunaga and K. Kyuma, Appl. Phys. Lett. 56, 154 (1990).
(24) R. Nötzel, N.N. Ledentsov, L. Daweritz, K. Ploog and M. Hohenstein, Phys. Rev. B45, 3507 (1992).
(25) F.E.G. Guimaraes, B. Elsner, R Westphalen, B. Spangenberg, H J Geelen, P Balk and K. Heime, J. Cryst. Growth 124, 199 (1992).
(26) S. Tsukamoto, Y. Nagamune, M. Nishioka and Y. Arakawa, Appl. Phys Lett 62, 49 (1993).
(27) D. Bertram, W. Stolz, E O. Göbel, J. Crystal Growth, to be published
(28) R A. Logan, F K. Reinhart, J Appl. Phys 44, 4172 (1973)
(29) S.D. Hersee, E. Barbier, R Blondeau, J Cryst. Growth 77, 310 (1986).
(30) T. Ogawa and T Tagahara, Phys Rev. B44, 8138 (1991).

MoP9

GaAs/$Al_{0.3}Ga_{0.7}As$ Quantum Wire Structure Fabricated by Glancing Angle Molecular Beam Epitaxy on Reverse-Mesa-Etched GaAs (100) Substrates

S. Shimomura[a], K. Inoue[a], M. Tanaka[a], A. Adachi[b], M. Fujii[c], T. Yamamoto[c], T. Watanabe[c], N. Sano[d], K. Murase[e,f], and S. Hiyamizu[a,f]

[a] Faculty of Engineering Science, Osaka University, Toyonaka, Osaka 560, Japan
[b] Nissin Electric Co Ltd ,Umezu-Takase-cho, Ukyo-ku, Kyoto 615, Japan
[c] ATR Optical and Radio Comm. Res. Labs., Soraku-gun, Kyoto 619-02, Japan
[d] Faculty of Science, Kwansei Gakuin University, Nishinomiya, Hyogo 662, Japan
[e] Faculty of Science, Osaka University, Toyonaka, Osaka 560, Japan
[f] Research Center for Extreme Materials, Osaka University, Toyonaka Osaka 560, Japan

Selective growth of molecular beam epitaxy (MBE) on channeled substrates is one of the key technologies to fabricate laterally modulated structures with atomic-scale control Glancing angle incident molecular beam enhances the growth rate dependence on different facets. In this paper, we report the fabrication of the quantum wire (QWR) structures by glancing angle MBE (GA-MBE) on reverse-mesa-etched GaAs (100) substrates (stripes // [011]) and their characterization of optical properties by cathodoluminescence (CL)

10 periods of GaAs/AlAs (50 nm/50 nm) layers were grown by GA-MBE at 580°C under V/III= 26 (pressure ratio) Growth rates were 1 μm/h (GaAs) and 0 43 μm/h (AlAs) Substrates were not rotated during the growth (111)B facets were preferentially grown for an epitaxial layer on the (100) top of the reverse-mesa structure in the [011] direction, when the incident molecular beams of the group III elements had a glancing angle of 42° from the (100) substrate surface In this case, Ga and Al atoms do not impinge directly on the (111)B facet sufaces by the self shadowing effect. After the growth of the GaAs/AlAs (50 nm/50 nm) multi-layers, an AlAs layer (200 nm) and GaAs cap layer (20 nm) were grown on both the (111)B facet and (100) face after rotating the substrate by 180 ° Fig 1 shows the cross sectional SEM photograph of the sample. The dark layers are AlAs and the bright are GaAs. The edge of each layer appears on the (111)B facet surface Thus, this growth mode can be used for fabricating QWR structures $GaAs/Al_{0.3}Ga_{0.7}As$ T-shape QWRs were made using GA-MBE as shown in Fig 2. The T-shape QWR consist of $GaAs/Al_{0.3}Ga_{0.7}As$ (4.5 nm / 20 nm) multi quantum wells (MQW) on the (100) plane and a 5-nm-thick GaAs layer covered by an $Al_{0.3}Ga_{0.7}As$ barrier layer (30 nm). CL measurements at 78 K for the cleaved face of the sample showed spatially resolved two peaks at 771 nm and 784 nm The higher energy CL peaks comes from MQW on the (100) plane and the lower energy peak comes from the T-shape QWRs The intensity of the lower energy peak gradually increased with approaching the excited position by the electron beam to the T shape QWR region This shows that carriers excited by the electron beam in MQW region flew into the T-shape QWR region which have a lower energy state, indicating carriers were successfully confined within the very narrow T-shape QWR structures

GaAs/$Al_{0.3}Ga_{0.7}As$ Quantum Wire Structure
Fabricated by Glancing Angle Molecular Beam Epitaxy
on Reverse-Mesa-Etched GaAs (100) Substrates

S. Shimomura[a], K. Inoue[a], M. Tanaka[a], A. Adachi[b], M. Fujii[c], T. Yamamoto[c], T. Watanabe[c], N. Sano[d], K. Murase[b,d], and S. Hiyamizu[a,d]

Fig. 1

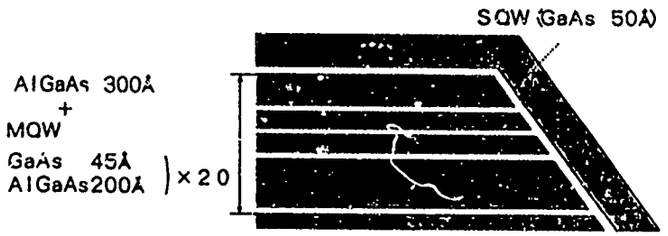

Fig. 2

MoP10

Coverage Dependence of Migration Potential
of Cation Adatoms on GaAs(001)-(2×4) Surface

Kenji Shiraishi[a,b], Tomonori Ito[a,b], and Takahisa Ohno[a,b]
[a]NTT Basic Research Laboratories, Musashinoshi, Tokyo 180, Japan
[b]NTT LSI Laboratories, Atsugi-shi, Kanagawa 243-01, Japan

We theoretically investigate the migration potential of cation adatoms on reconstructed As-rich GaAs(001)-(2×4) surface by *ab initio* calculation. By increasing the number of cation adatoms, we also study how migration potential depends on coverage. The calculated results for Ga adatoms suggest that the long bridge sites are energetically the most favorable at the initial stage of crystal growth. However, as the Ga coverage increases, the missing dimer row sites become the most favorable. Migration potentials strongly depend on the adatom coverage. Similar results were obtained for Al adatom migration. Furthermore, based on these migration potentials, we demonstrate the dynamical behaviors of cation adatoms on GaAs(001) surface including AlAs-GaAs binary systems by performing Monte Carlo simulations at finite temperatures.

1. Introduction

Adatom migration on solid surfaces is a fundamental problem in surface science. Also, adatom migration has been found to be a key mechanism in epitaxial growth. It is essential to increase adatom migration in order to obtain high quality samples when using epitaxial growth techniques. This is because adatoms migrate over a wide area, leading to a flat surface during the growth [1]. Consequently, the synthesized interfaces become sharp. Therefore, numerous experiments have been carried out to clarify the mechanism of adatom migration during epitaxial growth [2, 3]. However, the migration parameters obtained by these experiments are usually macroscopic, containing both intrinsic migration and reactions at the steps. It is not easy to obtain information on intrinsic adatom migration by experiment; thus theoretical calculations are necessary in order to study the microscopic processes of adatom migration. Various theoretical works have been carried out. BCT theory [4], molecular dynamics (MD) [5], and Monte Carlo (MC) [6, 7] simulations are the most popular approaches and have been widely studied. In these theoretical studies, the basic parameters are usually chosen to reproduce the experimental results. Therefore, the microscopic foundation of these parameters are not clear.

In order to study the microscopic parameters, we reported the *ab initio* calculation of the adiabatic potential surface of Ga adatoms on an As-stabilized GaAs(001) surface [8]. However, the surface unit cells used in Ref. 8 were not large enough. Consequently, the results described Ga migration at high Ga coverage. In this paper, we use a very large surface unit cell and study the migration potential for low Ga coverage. Furthermore, we investigate the dependence of the migration potential on adatom coverage by increasing the number of Ga adatoms. The migration potentials of Al adatoms are also investigated. In order to qualitatively investigate dynamical behavior of adatoms, we performed the Monte Carlo (MC) simulation of crystal growth including GaAs-AlAs binary systems based on these migration potentials.

2. Method

We use the *ab initio* pseudopotential method on the basis of local density functional formalism (LDF) [9]. We adopt Kleinman-Bylander-type separable pseudopotentials and the kinetic energy cut-off value was carefully chosen so as not to produce ghost bands [10]. The electron exchange-correlation potential is approximated by Wigner's interpolation formula. To simulate the GaAs(001) surface, the usual repeated slab geometry is employed. The unit supercell consists of five atomic layers of GaAs, one atomic layer of hydrogen H atoms, and a vacuum region equivalent to about five atomic layers in thickness. The validity of the thickness of this repeated slab model is carefully checked. Surface termination with the hydrogen H atoms is a very powerful method for eliminating the interaction of the surface states of both sides of the slab, and this method is discussed in detail elsewhere [12].

To calculate the migration potential $E(x, y)$, we optimize the z coordinate of an adatom and the positions of substrate atoms, whereas the (x, y) coordinates of an adatom are fixed. The present

study uses a (4×6) surface unit cell (Fig. 1 (a)). This surface unit cell contains two (2×6) GaAs surface superstructures and is four times larger than that of our previous report [8]. In the present calculation after one adatom is adsorbed on the surface unit cell adatom coverage becomes 0.0625.

Coverage dependence of the potential surfaces is investigated by increasing the number of adatoms in the surface unit cell. In this process we fixed previously adsorbed adatoms to the most stable sites and the migration potential of the adatom that arrives next is then calculated.

In this calculation we used the missing dimer model for the GaAs(001) surface which consists three surface T_4 dimers and one missing dimer in a (2×6) unit cell. Fahta *et al.* recently proposed a different model for the (2×6) GaAs surface where two of the six surface As atoms are exchanged by two Ga atoms [11]. We calculated the relative stability of Fahta models compared with the usual missing dimer model. The results show that Fahta's models are energetically unstable compared with the usual missing dimer model for a wide range of As chemical potential [13]. Therefore investigating migration potentials using the missing dimer model is realistic and reliable.

In the stochastic Monte Carlo (MC) simulation kinetic rates are assumed to be of Arrhenius form

$$R = R_0 \exp(-\Delta E/k_B T) \qquad (1)$$

where R_0 is the diffusion prefactor in hops per second and ΔE is the activation energies which are determined from the obtained migration potential. Coverage dependence of the migration potential is also taken into account. In this study the diffusion prefactor of Ga R_0(Ga) is adjusted to the value used in ordinary MC simulation [14] for the predominant migration path and the prefactor of Al is set to be R_0(Al)=1.67R_0(Ga) based on our *ab initio* molecular dynamics calculation [15]. MC formalism is described in detail elsewhere [7].

3. Calculated Results and Discussions

3.1 Migration Potentials

We first address the adsorption potential surface of Ga adatom migration on an As stabilized GaAs(001) surface. In Fig. 1 (a) adsorption sites in the surface unit cell are indicated by the alphabet and Fig. 1 (b), (c), (d) and (e) show the migration potential surface of Ga adatoms at Ga coverage (θ) of 0.0625, 0.125, 0.1875 and 0.25, respectively. As seen in Fig. 1 (b) the most stable adsorption site at θ=0.0625 is a long bridge site (F site) which is located between two As dimer rows. Missing dimer region sites (A, B, C sites) are not stable in this figure. This shows that Ga adatoms tend to be adsorbed on the dimer region at the initial stage of epitaxial growth. The favorable migration path is along the [1$\bar{1}$0] direction on the dimer region.

After one As atom is adsorbed on the surface migration potential changes. As seen in Fig. 1 (c) migration potential at θ=0.125 shows that another long bridge site is the most stable as Fig. 1 (b). The most noticeable change in this figure is that the missing dimer region becomes more stable after one long bridge site (F site) is occupied.

As the number of adsorbed Ga atoms increases (Ga coverage increases) this tendency becomes more clear. As seen in Fig. 1 (d) the Ga bridge site in the missing dimer region (B site) becomes the most favorable at θ=0.1875. The B site is energetically more stable than the second favorite site (FB site) by about 0.3 eV. From this figure, the most favorable migration path is along the missing dimer row. After the two long bridge sites (F sites) are occupied, Ga atoms tend to be adsorbed in the missing dimer rows and migrate through the missing dimer rows.

At the Ga coverage of 0.25, the missing dimer regions are much more stable than the dimer regions and the migration path clearly lies in the missing dimer rows (Fig. 1(e)). Detailed structures of this migration potential at θ=0.25 are different from those in our previous report [8] which corresponds to θ=0.27, however the basic characteristics are very similar. A detailed comparison between these two migration potentials will be given elsewhere [16].

As explained above, migration potentials of a Ga adatom strongly depend on the Ga coverage and the characteristics of Ga migration change essentially as Ga coverage increases. Therefore to study epitaxial growth by Monte Carlo simulations, it is essential to take into account the above coverage dependence of migration potentials.

We also calculate the migration potential of an Al adatom on the As stabilized GaAs(001) surface. The calculated results show that the basic characteristics of Al migration potential are the same as those of Ga migration potential, but the absolute value of the activation barrier is about 1.4 times larger than that of Ga. Coverage dependence of Al migration potentials is also similar to that of Ga migration potentials.

3.2 Monte-Carlo Simulations

To investigate the dynamical behavior of adatoms qualitatively, we performed the MC simulations. Figures 2 (a) and (b) give the growth profiles at Ga coverage θ=0.1 and θ=0.25, where the MC simulation was carried out at 873 K with growth rate 2 ML/sec on an As stabilized GaAs(001)-(2×6) surface. As seen in Fig. 2 (a), randomly impinged Ga atoms predominantly occupy the lattice sites on the dimer region at θ=0.10.

As the coverage increases, the favorable lattice sites for Ga adatoms changes from those on the dimer region to those along missing dimer rows as seen in Fig. 2 (b). This reflects the migration potentials where the energetically stable site is located at long bridge sites (F site) in the dimer region at θ=0.125, while the Ga bridge site (B site) in the missing dimer region becomes favorable at θ=0.25.

In Figs. 3 (a) and (b), we show the growth profiles of GaAs-AlAs binary systems under the same conditions as the above pure GaAs systems. Figure 3 (a) and (b) correspond to the MC results at the cation coverage θ=0.1 and θ=0.25, respectively. The white circles, black circles and shaded circles indicate the Ga adatoms, Al adatoms and surface As atoms, respectively. The basic characteristics of the growth profile are very similar to those of pure GaAs systems. The noticeable fact is that movement of Al atoms with the increase of adatom coverage is much slower than that of Ga atoms. This reflects that migration barrier for Al atoms is larger than that for Ga atoms. In these calculations for the binary systems, the resultant growth profile show that Ga and Al atoms are randomly distributed over the surface without any segregation observed in the experiment [17].

4. Conclusion

We investigated the migration potential of cation adatoms by the *ab initio* pseudopotential method and based on the results, we performed a Monte Carlo (MC) simulation of epitaxial growth.

The following characteristics are obtained from the calculated migration potentials. The most stable sites of cation adatoms are located in the dimer region at the initial stage of epitaxial growth. However, stable sites change from the dimer region to the missing dimer region as the cation adatom coverage increases. Migration potentials of cation adatoms strongly depend on the adatom coverage.

MC simulation reflects the coverage dependence of migration potential. At the cation coverage of 0.1, impinged cation atoms predominantly occupy the dimer region. However, the missing dimer region is occupied when the cation coverage is 0.25. This preliminary MC simulation for a GaAs-AlAs binary system does not reveal any experimentally observed segregation.

In the next step, we plan to investigate other processes such as the reactions at the step sites and elsewhere. When these processes are taken into account, our theoretical simulation will become more realistic and reliable.

Acknowledgments

We would like to thank Dr. Yoshio Bando, Dr. Shintaro Miyazawa and Kazuto Hirata for their beautiful comments and continuous encouragement throughout this work.

References

[1] Y. Horikoshi, M. Kawashima and H. Yamaguchi, Jpn. J. Appl. Phys. **25**, L868 (1986); Appl. Phys. Lett. **50**, 1686 (1986).

[2] J H Neave *et al* Appl Phys Lett 47 100 (1985)

[3] T Nishinaga and K J Cho Jpn J Appl Phys 27 L12 (1988)

[4] A K Myers Beaghton *et al* Phys Rev B 42 5511 (1991)

[5] D K Choi *et al* J Cryst Growth 85 9 (1987)

[6] S Clark and D D Vvedensky J Cryst Growth 95 28 (1989)

[7] T Ito T Ohno and K Shiraishi *Proc 21st Int Conf Phys Semicond* (Beijing 1992) p 550

[8] K Shiraishi Appl Phys Lett 60 1363 (1992); Appl Surf Sci 60/61 210 (1992)

[9] D R Hamman *et al* Phys Rev Lett 43 1494 (1979)

[10] T Ohno Phys Rev Lett 70 631 (1993)

[11] J Falta *et al* Phys Rev Lett 69 3068 (1992)

[12] K Shiraishi J Phys Soc Jpn 59 3455 (1990)

[13] K Shiraishi and T Ohno unpublished

[14] S V Ghaisas and A Madhukar Phys Rev Lett 56 1066 (1986)

[15] T Ohno K Shiraishi and T Ito submitted to 1993 Fall Meeting of the MRS

[16] K Shiraishi T Ito and T Ohno unpublished

[17] M Tsuchiya *et al* Appl Phys Lett 54 1690 (1989)

Figure Captions

Fig. 1 Surface unit cell used in our calculation and the calculated migration potentials for several Ga coverages. (a) (1×4) surface unit cell. Adsorption sites are indicated by the alphabet. (b) migration potential at θ=0.0625. (c) θ=0.125. (d) θ=0.1875 and (e) θ=0.25.

Fig. 2 Calculated growth profiles for Ga adatoms at the coverage of (a) θ=0.10 and (b) θ=0.25. The profiles were obtained by MC simulation at a growth temperature of 873 K.

Fig. 3 Calculated growth profiles for GaAs-AlAs binary systems at the coverage of (a) θ=0.10 and (b) θ=0.25. The profiles were obtained by MC simulation at growth temperature of 873 K.

Fig. 1

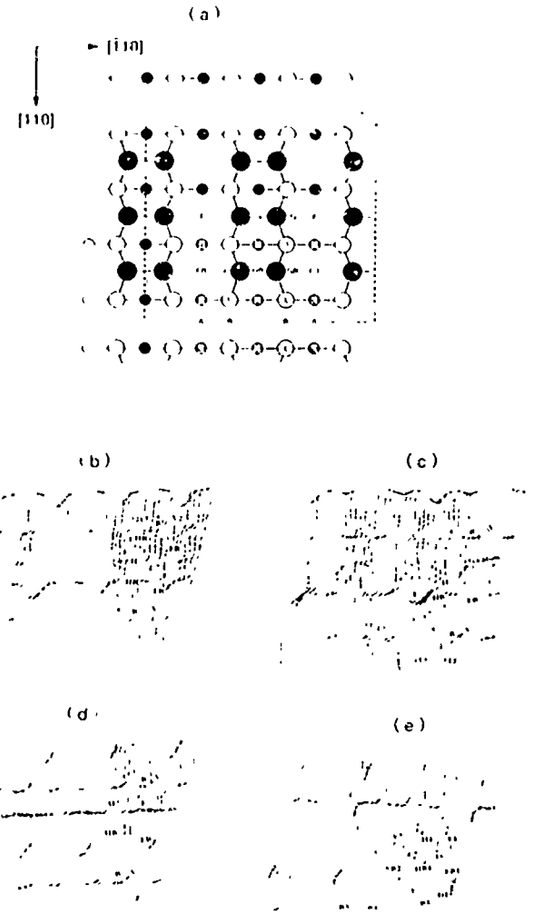

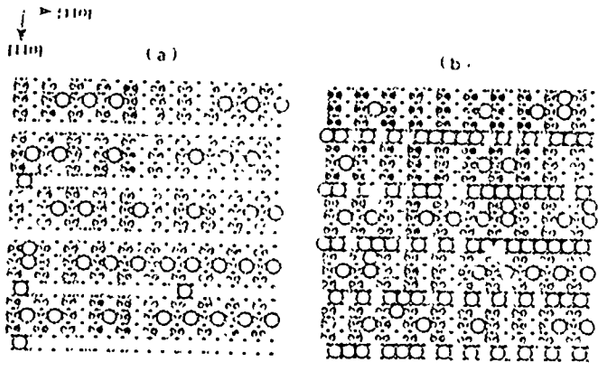

Fig. 2

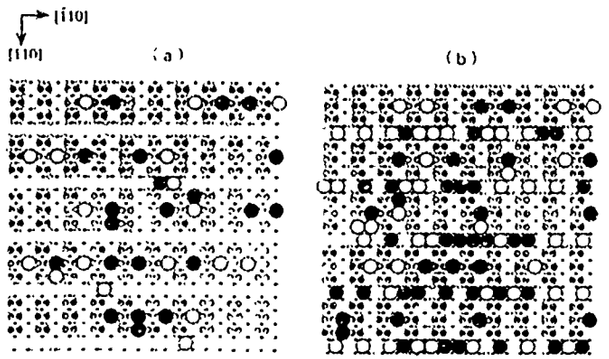

Fig. 3

MoP11

Raman scattering investigation on the ordered incorporation of Si dopant atoms on (001) GaAs vicinal surfaces during MBE growth

M Ramsteiner [1], J Wagner [2], G Jungk [1], D Behr [2], L Daweritz [1], and R Hey [1]

[1] *Paul-Drude-Institut fur Festkorperelektronik, Hausvogteiplatz 5-7, D-10117 Berlin, Germany*

[2] *Fraunhofer-Institut fur Angewandte Festkorperphysik Tullastrasse 72, D-79108 Freiburg, Germany*

Abstract

Using Raman scattering by local vibrational modes (LVM) and collective electronic excitations we have investigated the ordered incorporation of Si dopant atoms on vicinal GaAs(001) surfaces. LVM spectra revealed for a sequence of δ-doped samples grown by molecular beam epitaxy (MBE) under specific conditions that the Si dopant atoms are *predominantly* incorporated on Ga-sites even at a doping concentration as high as 1.8×10^{13} cm^{-2}. For a sample grown under conditions established by real-time high-energy electron diffraction (RHEED) to be favourable for the wire-like Si incorporation, a polarization asymmetry in the Raman scattering intensity of collective intersubband plasmon-phonon modes arising from the δ-doping layer has been found

1. Introduction

A combination of lattice step growth with δ-doping on GaAs(001) vicinal surfaces has been shown to be a promising technique to prepare doping wires [1,2]. Thereby, under certain growth conditions, a preferential attachment of Si atoms at misorientation steps leads to an ordered array of dopant atom strings. A scheme of the growth model is shown in Fig. 1. So far, evidence for this self-organization during Si incorporation has been traced only from reflection high-energy electron diffraction (RHEED) measurements. Therefore, it is desirable to have other characterization methods at hand to confirm the above results. Raman spectroscopy is such a method. To investigate the lattice sites occupied by the Si dopant atoms in MBE layers Raman scattering by local vibrational modes (LVM) has been shown to very useful [3]. In addition, Raman scattering by plasmon excitations has been successfully used to characterize the two dimensional electron gas in δ-doped GaAs [4] as well as the one dimensional electron gas in quantum wire structures [5].

We have studied heavily Si doped samples grown by molecular beam epitaxy (MBE) on GaAs(001) substrates tilted towards the (111)Ga plane. The growth conditions to obtain the desired self-organization during Si incorporation have been established by in-situ RHEED measurements [2]. In order to proof the wire-like Si incorporation, Raman scattering by electronic excitations has been studied.

2. Experimental

Raman scattering is in general sensitive to the inequivalence of the orthogonal crystallographic directions [110] and [$\bar{1}$10] in polar semiconductors like GaAs [6,7]. Therefore, to study polarization asymmetries introduced by doping-wires aligned along the [$\bar{1}$10] direction, a comparison with reference samples having a random arrangement of the dopant atoms is neccessary. Therefore, three samples grown by solid-source MBE have been studied (see Tab. 1). For samples B and C we used GaAs(001) substrates misoriented 2° toward the (111)Ga plane, resulting in a misorientation step separation of 8 nm. Sample C has been grown using conditions favourable for a wire-like Si incorporation along the [$\bar{1}$10] direction [2]. For sample B the substrate temperature during Si deposition was decreased, making the formation of doping wires less probable due to the smaller diffusion length of the Si atoms. Sample A was grown side by side with sample C on a perfectly oriented GaAs(001) substrate, where the absence of an ordered arrangement of misorientation steps prevents the formation of doping-wires. In all samples a single Si δ-doped layer with an intended dopant concentration of 1.8×10^{13} cm^{-2} was placed at a nominal depth of 10 nm below the surface. The growth details are described in Ref. 8.

	δ-doping with Si	misorientation steps	appropriate Si diffusion
sample A	x	–	–
sample B	x	x	
sample C	x	x	x

Tab. 1. Growth characteristics of sample C and reference samples A and B. Favourable conditions for the wire-like Si incorporation along the [$\bar{1}$10] direction have been used for sample C.

Raman measurements were carried out in backscattering from the epilayer surface with the sample cooled by He exchange gas in a continuous-flow variable-temperature He cryostat. Optical excitation was performed at 3.00 eV or 3.05 eV with a Kr ion laser in resonance with the GaAs E_1 band gap [3,4,9]. The optical probing depth $l/(2\alpha)$ for these photon energies is about 10 nm, which is matched to the nominal depth of the δ-doping layers [3]. For Raman spectra of LVM a depolarized scattering configuration $x(y,z)\bar{x}$ was used, where x, $\bar{x}$, y and z denote [001], [00$\bar{1}$], [010] and [100] crystallographic directions. Polarized Raman spectra were recorded in the $x(z',z')\bar{x}$ and the $x(y',y')\bar{x}$ scattering configurations, where y' and z' denote [$\bar{1}$10] and [110] crystallographic directions.

3. Results and Discussion

Fig. 2 shows low-temperature (77 K) Raman spectra of sample A [Fig. 2(a)], B [Fig. 2(b)] and C [Fig. 2(c)] excited at 3.00 eV. All spectra show the LVM from Si on Ga site (Si_{Ga}) at the expected frequency of 384 cm^{-1} [10] superimposed on the second-order phonon spectrum of GaAs [9]. An additional contribution to the background arises from electronic excitations which are discussed below. LVM from the acceptors Si on As site (Si_{As}) at 399 cm^{-1} or the Si-X defect centre at 369 cm^{-1} [10] have not been resolved, which indicates a low electrical compensation of the Si donors (Si_{Ga}) in the present samples in spite of the high doping concentration in the δ-layer. This supports the RHEED results from which it has been concluded that most of the Si dopant atoms are incorporated on Ga site. In more recent RHEED studies it has been shown that the Si dopant atoms in sample C should be incorporated as Si_{Ga}-Si_{Ga} second-next neighbour pairs [8]. The present Raman data show the LVM of $^{28}Si_{Ga}$ donors, however, it is not clear to what extend the formation of Si_{Ga}-Si_{Ga} second-next neighbour pairs should affect the LVM spectra.

For excitation at 3.05 eV scattering by collective intersubband plasmon-phonon modes (ω^*_A and ω^*_B) is observed in the polarized spectra besides scattering by one (1LO) and two (2LO) longitudinal optical phonons. This is shown in Fig. 3 for the scattering configuration $x(z',z')\bar{x}$. As discussed for similar Si δ-doped GaAs layers, these collective modes are assigned to excitations involving various electron subbands [4,11]. The scattering by collective intersubband plasmon phonon modes was found to be strongly resonant with the E_1 band gap of GaAs [4]. The collective mode frequency ω^*_B increases from 980 cm^{-1} to 1110 cm^{-1} when going from sample B [Fig. 3(b)] to sample C [Fig. 3(c)]. This effect can be discussed in terms of an additional lateral confinement and/or an locally increased carrier density because of the segregation of the dopant atoms at the misorientation steps. However, a quantitative analysis of the peak positions and widths for the collective mode spectra is complicated by the fact that several subbands are populated in the present structures, which leads to a coupling of the individual modes [11]. For sample C where wire-like Si incorporation is expected, self-consistent, two-dimensional, solutions of the Schrödinger and Poisson equations are required to calculate the spectra of collective intersubband excitations. For the present separation of the misorientation steps, and thus the Si doping wires, of 8 nm the individual wires are expected to be strongly electronically coupled [12] forming a lateral n-i-n-i superlattice. Nevertheless, the observation of the collective modes in the present sample structures indicates a high carrier density of $\geq 10^{13}$ cm^{-2} [4]. Otherwise, at lower carrier densities, the δ-doped region placed only 10 nm underneath the sample surface would be almost entirely depleted with no individual intersubband excitations resolved [4]. This estimate of the carrier density is consistent with the low compensation ratio indicated by the above LVM data.

In order to investigate polarization asymmetries in the scattering intensities, polarized Raman spectra were recorded under the same conditions as described for Fig. 3 but with the scattering configuration $x(y',y')\bar{x}$, i.e. with the sample rotated by 90°. As a measure for polarization asymmetries we computed the difference spectra $I(z',z')-I(y',y')$ between the spectra polarized along $z' = [110]$ and those polarized along $y' = [\bar{1}10]$. As can be seen in Fig. 4 the collective mode at the frequency ω^*_A shows an increasing polarization asymmetry when going from sample A [Fig. 4(a)] to sample B [Fig. 4(b)] and to sample C [Fig. 4(c)], i.e. in the direction of an increasing probability for the formation of doping wires. The asymmetries observed for sample A are entirely due to the intrinsic inequivalence of the [110] and [$\bar{1}$10] crystallographic directions. The enhanced asymmetry observed for sample C can be explained by an ordered incorporation of the Si dopant atoms along misorientation steps, leading to a lateral modulation of the potential confining the

two-dimensional electron gas at the δ-doping layer. This supports the results obtained by RHEED measurements [2].

The origin for the polarization asymmetry induced by the wire-like incorporation of the dopant atoms is an additional polarization dependence in the efficiency for scattering by the collective mode at the frequency ω_+ caused by a lateral modulation of the electron potential, which is attributed to a change of the lateral confinement potential in the conduction band. For the collective mode at the frequency ω_- such an increased polarization asymmetry in sample C was not found. This can be explained assuming a larger contribution of transitions involving higher lying subbands to this collective mode, which are less sensitive to the lateral potential modulation. Preliminary results obtained from Raman measurements using optical excitation in resonance with the $\Gamma_0+\Delta_0$ band gap of GaAs confirm the above results.

4. Conclusions

We have used Raman scattering by local vibrational modes (LVM) and by collective intersubband plasmon-phonon modes to study Si δ-doped GaAs layers grown by MBE on GaAs(001) vicinal surfaces. LVM Raman spectra indicate a low compensation of the Si on Ga-site donor for the present δ-doped samples in spite of the high doping level of 1.8×10^{13} cm^{-2}. For samples grown under certain conditions such as to promote the formation of Si doping wires, polarized Raman spectra of collective electronic excitations indicate a lateral electron potential modulation. This gives support to results obtained by real-time high-energy electron diffraction (RHEED) measurements from which a wire-like incorporation of the Si dopant atoms has been inferred.

Acknowledgements

We would like to thank P. Koidl and H.S. Rupprecht as well as K. Ploog for continuous support of the work at the Fraunhofer-Institut für Angewandte Festkörperphysik and the Paul-Drude-Institut für Festkörperelektronik.

References

1. C.E.C. Wood, J. Appl. Phys. 71, 1760 (1992).
2. L. Däweritz, K. Hagenstein and P. Schützendübe, J. Cryst. Growth 127, 1051 (1993).
3. J. Wagner, Mat. Science Forum Vols. 65 - 66, p. 1 (1990) and references therein.
4. J. Wagner, M. Ramsteiner, D. Richards, G. Fasol, and K. Ploog, Appl. Phys. Lett. 58, 143 (1991).
5. T. Egeler, G. Abstreiter, G. Weimann, J. Demel, D. Heitmann, P. Grambow, and W. Schlapp, Phys. Rev. Lett. 65, 1804 (1990).
6. J. Ménendez and M. Cardona, Phys. Rev. Lett. 51, 1297 (1983).
7. J. Menendez and M. Cardona, Phys. Rev. B 31, 3696 (1985).
8. L. Däweritz, C. Muggelberg, R. Hey, H. Kostial, and M. Höricke, this conference.
9. R. Trommer and M. Cardona, Phys. Rev. B 17, 1865 (1978).
10. R. Newman, in *Proc. of the Int. Conf. on the Science and Technology of Defect Control in Semiconductors*, ed. by K. Sumino, p. 65 (North Holland, Amsterdam, 1990) and references therein.
11. D. Richards, J. Wagner, M. Ramsteiner, U. Ekenberg, G. Fasol, and K. Ploog, Surf. Sci. 267, 61 (1992).
12. G.E.W. Bauer and A.A. van Gorkum, in *Science and Engineering of One- and Zero-Dimensional Semiconductors*, ed. by S.P. Beaumont and C.M. Sotomayor Torres, p. 133 (Plenum, New York, 1990).

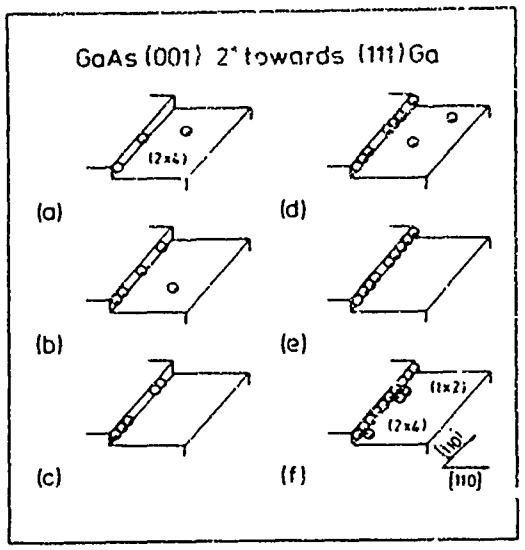

Fig. 1. Schematic model illustrating the ordered incorporation of Si dopant atoms at misorientation steps along the [$\bar{1}$10] direction on a GaAs(001) vicinal surface [2] with the Si coverage increasing from (a) to (f).

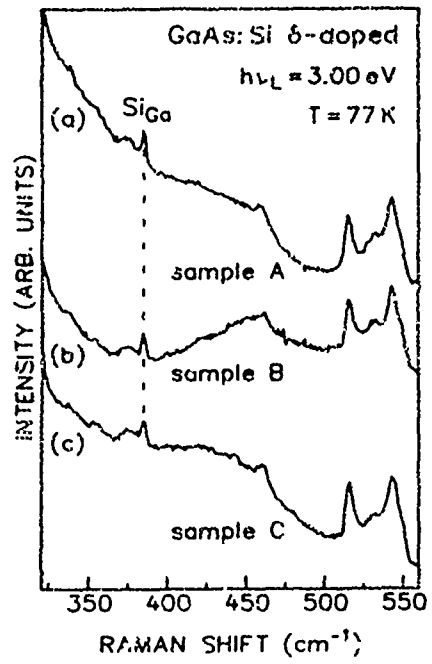

Fig. 2. Low-temperature (77 K) Raman spectra of Si δ-doped GaAs grown on perfectly oriented [(a)] and misoriented [(b) and (c)] GaAs(001) substrates. Optical excitation was at 3.00 eV close to resonance with the GaAs E_1 band gap.

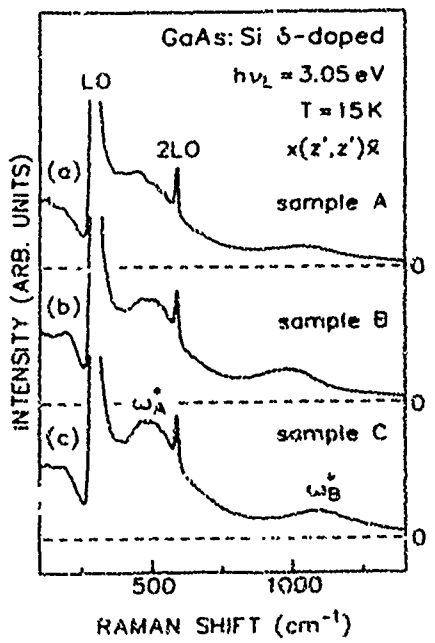

Fig. 3. Polarized low-temperature (15 K) Raman spectra of Si δ-doped GaAs grown on perfectly oriented [(a)] and misoriented [(b) and (c)] GaAs(001) substrates. Optical excitation was at 3.05 eV in resonance with the GaAs E_1 band gap.

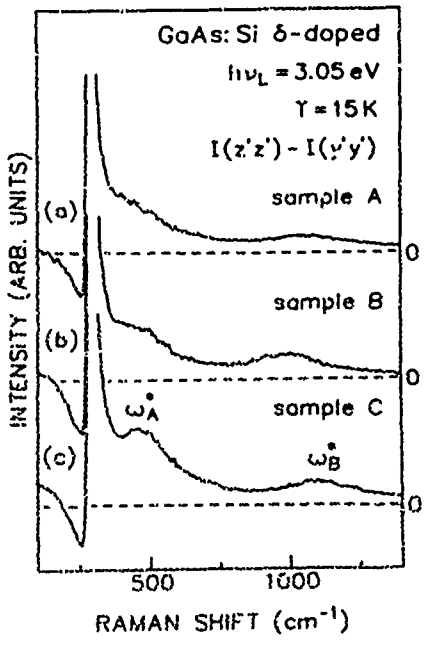

Fig. 4. Difference spectra [I(z'z')–I(y'y')] between polarized low-temperature (15 K) Raman spectra recorded in the x(z',z')x̄ and the x(y',y')x̄ configurations, respectively, where y' and z' denote [110] and [1̄10] crystallographic directions. Optical excitation was at 3.05 eV in resonance with the GaAs E_1 band gap.

MoP12

Disorder-Induced Raman Scattering of Folded Phonons in Quantum Wells and Superlattices

T. Ruf, V. I. Belitsky*, J. Spitzer, V. I. Sapega*, M. Cardona and K. Ploog
Max Planck Institut für Festkörperforschung, Heisenbergstr. 1, D-7000 Stuttgart 80, Federal Republic of Germany

In addition to the well known folded modes Raman spectra of GaAs AlAs superlattices and multiple quantum wells show in the low energy regime a continuous acoustic phonon background related to scattering processes where crystal momentum q_z along the growth direction is not conserved. Such a situation may occur when excitons become localized due to layer thickness fluctuations. This causes resonant Raman scattering from a random distribution of isolated wells. Superimposed on this background we find pronounced peaks and dips in the Raman intensity. These peculiarities occur at gaps of the folded longitudinal acoustic (LA) phonon dispersion and at energies where LA and transverse acoustic (TA) branches cross. The observations are explained by the dependence of the Raman efficiency on phonon crystal momentum.

I. INTRODUCTION

In Raman experiments from semiconductor superlattices (SL) or multiple quantum wells (MQW) doublets of acoustic phonons are observed which reflect the back folding of bulk dispersions into a mini Brillouin zone [1,2]. The doublets arise from a coherent superposition of contributions to the scattering intensity from individual wells. This superposition is also the origin of crystal momentum conservation both along the growth direction (q_z) and perpendicularly ($q_\parallel$) in the scattering process.

Recently additional features apart from the allowed folded phonon doublets, have been observed which cannot be accounted for by standard selection rules. These structures consist of a *continuous emission background* and pronounced *intensity anomalies (peaks and dips)*. Due to its close vicinity to the exciting laser line the background has not attracted particular attention but was attributed to insufficient spectrometer stray light rejection. Recent magneto-optical experiments, however, demonstrated that the continuum emission exhibits oscillatory intensity variations corresponding to interband resonances between Landau levels [3–5]. It was noticed that the peaks and dips coincide with folded phonon gaps [1,3,6–8] but no explanation for their relation to the phonon dispersion and to mechanisms for Raman scattering has been given. The features were tentatively attributed to antiresonances associated with acoustic phonons at the reduced Brillouin zone edge [1] to disorder induced or q_z non conserving scattering [6,7] or to local modes near the dispersion gaps [3].

In this report we present a model for Raman scattering by acoustic phonons from individual quantum wells due to interface roughness and layer thickness fluctuations. The dependence of the Raman intensity on phonon wave vector explains most of the observations. They are caused by a partial breakdown of crystal momentum conservation.

II. THEORY

The intensity I of Raman scattering from acoustic phonons in semiconductor MQW and SL is given by a coherent superposition of the scattering contributions from all individual layers within the penetration depth of the incident light

$$I \sim \sum_{q_z} |M(q_z)|^2 \; \delta(\omega_i - \omega_s \mp \omega_j) \; \Big| \sum_m \frac{e^{iq_z md}}{(\Delta(m) + i\Gamma)(\Delta(m) - \omega_i \pm \omega_j + i\Gamma)} \Big|^2 \qquad (1)$$

$M(q_z)$ is a matrix element containing details of the optical absorption at electron phonon interaction mediated steps of the Raman process. All the modes $\omega(q_z)$ for which energy is conserved contribute to scattering of incident photons ω_i at a particular frequency ω_j. The resonance behavior of the scattering is contained in the two denominators in which a phenomenological lifetime broadening Γ has been included. Resonances are determined by the energy detuning $\Delta(m)$ of incident or scattered photons with respect to critical points of the electronic structure. Ideally confinement energies in all wells of thickness d are identical. In this case the detuning Δ does not depend on layer index m. The summation over an infinite number of layers then ensures conservation of crystal momentum. As a consequence doublets corresponding to modes $\omega(q_z)$ of the folded phonon dispersion with a certain fixed wave vector q_z are observed in Raman spectra.

In real structures electronic confinement energies can vary from one layer to another and even within one layer due to growth inhomogeneities and imperfections. The explicit dependence of the detuning energy $\Delta(m)$ on layer index in the resonance denominators has a random component and thus causes a partial breakdown of crystal momentum conservation. The scattering intensity at frequencies other than those of the folded phonon doublets does not vanish anymore. In the approximation of bulk phonons a *continuous emission background* is obtained. This case is illustrated in Figure 1. The solid line shows the Raman spectrum of a sequence of 11 GaAs quantum wells with $d \approx 100$Å embedded in AlAs layers with the same thickness. For simplicity the wave vector of incident and scattered light has been set to zero. Strong scattering only occurs at Raman shifts corresponding to zone center modes of the folded dispersion. The solid line was calculated with a constant detuning of $\Delta = 10\,\mathrm{cm}^{-1}$ for all wells. Due to the finite size of the system the intensity between the zone center modes does not vanish completely. Note the relative increase of the Raman signal due to outgoing resonance at a shift of $10\,\mathrm{cm}^{-1}$. The dotted line in Fig. 1 was calculated under the assumption that the central one of the eleven layers has a larger confinement energy than the others by $10\,\mathrm{cm}^{-1}$, e.g. due to a slightly smaller well width. In this case the exciting laser light is exactly in resonance with that one well whereas all other wells are slightly off resonant. The effect of such a perturbation is an increase of the Raman intensity near the laser line by almost two orders of magnitude.

The relative intensity of background and folded phonon doublet scattering is determined by the homogeneous width of the electronic structure and its inhomogeneous broadening due to layer thickness fluctuations and interface roughness. An interpretation of recent experiments along these lines has been given in Ref. [9].

While these considerations are valid for bulklike acoustic phonons, a treatment of superlattice effects has to take the influence of folded phonon dispersion gaps at the center and edge of the mini Brillouin zone into account. In a superlattice transmission and reflection at each interface cause the displacement field $u(\omega(q_z))$ of acoustic phonons along the growth direction to be a linear combination of two counterpropagating plane waves

$$u(\omega(q_z)) = A_+(q_z)e^{ikz} + A_-(q_z)e^{-ikz} \qquad (2)$$

The wave vectors k_z are given by the bulk dispersions of the constituent layers and the amplitude coefficients $A_\pm$ are determined from periodicity and matching boundary conditions at the interfaces. We find that the Raman intensity for a mode $\omega(q_z)$ is proportional to the amplitude difference

$$\delta = |A_+(q_z) - A_-(q_z)|^2 \qquad (3)$$

in the wells. Qualitatively this result can be easily understood for the special case of dispersion gaps. There the phonon displacement field is either symmetric or antisymmetric with respect to the center of the well, i.e. the coefficients $A_\pm$ are equal in magnitude but either equal or opposite in sign. The associated strain field which determines deformation potential electron phonon interaction with acoustic phonons [3,10], as given by the first derivative of $u(\pm(q_z))$ with respect to the coordinate z and has therefore just the opposite symmetry. Thus the Raman intensity vanishes at one side of a dispersion gap whereas it has a non zero value at the other side. This leads to characteristic *peaks and dips* in the spectrum. For phonons away from the gaps intermediate situations occur. This behavior is closely related to the oscillatory changes of dispersion gaps studied in Ref. [11].

At energies where LA and TA dispersions cross, interaction gaps open for phonons with a non zero in plane crystal momentum component $q_\parallel$ [12,13]. In backscattering Raman experiments $q_\parallel$ is conserved. A way to circumvent this selection rule is provided by impurity mediated second order Raman processes [14]. In quantum wells and superlattices interface roughness provides an elastic scattering mechanism in analogy to that of impurities. Therefore phonons $\omega(q_z, q_\parallel)$ also contribute to the Raman intensity. From the width of *internal gap structures* and their strength compared to that of peaks and dips associated with *zone edge dispersion gaps* information on length scales of interface roughness can be obtained.

III. EXPERIMENT

Figure 2c shows the Raman spectrum of a symmetric GaAs-AlAs superlattice with a layer thickness of 16 monolayers. The resonant enhancement of the continuum emission intensity in a magnetic field was exploited to obtain these data: $T = 10\,\mathrm{K}$, $B = 11\,\mathrm{T}$, $\hbar\omega_i = 1.727\,\mathrm{eV}$ excitation in resonance with the $n = 1$ Landau level of the first subband transition) [3]. In Figure 2a the LA phonon dispersion for this structure is given vs. superlattice wave vector. Figure 2b displays the amplitude difference factor δ. Superimposed on the continuous emission background Fig. 2c shows a series of characteristic intensity anomalies. By comparison with Fig. 2a the coincidence of most of these features with phonon dispersion gaps becomes evident. The character of the intensity anomalies as in complete agreement with the behavior of δ on either side of the various gaps. The remaining features can be attributed to internal gaps. Most pronounced is the lowest LA–TA anticrossing dip at $8\,\mathrm{cm}^{-1}$. In a detailed analysis we find that in plane scattering from growth islands with a diameter of about 450 Å yields best agreement with the experiment.

The influence of roughness-mediated in plane scattering processes is further highlighted in Fig. 3b. The experimental spectrum from a symmetric GaAs-AlAs superlattice with layer thicknesses of 6.7 monolayers (top) is compared to the best theoretical description within our model (bottom). The spectrum was measured at a temperature of 77 K without magnetic field in resonance with the direct $1 - \Gamma$ transition of the superlattice. The folded phonon dispersion for all modes is shown in Fig. 3a at a non-vanishing value of crystal momentum $q_\parallel = 0.8\,\pi/d$. For propagation at arbitrary angles with respect to the (001) growth direction, the longitudinal branch interacts with one of the transverse branches. Depending on wave vector and energy, their character is only quasi-longitudinal (QL) or quasi transverse (QT). The second

transverse branch remains unaffected (T) The dispersion in Fig 3a was obtained by solving the Christoffel equation for the constituent materials [15] and matching of the appropriate boundary conditions for the phonon displacement and stress fields [12] By comparison the QL-gap at about 25 cm^{-1} can be identified in the spectrum The prominent feature at 20 cm^{-1} originates from the internal QL QT gap A kink is observed at 15 cm^{-1} which can be attributed to the zone edge gap of the QT-dispersion Due to the vicinity of an internal gap, QT phonons in this region still have enough longitudinal character to give a small contribution to the spectrum To obtain best agreement with experiment the integration over $q_\parallel$ was performed up to $q_\parallel = 0.5\pi/d$ This corresponds to an island size of about 150 Å which is rather close to typical exciton radii in such systems [16] Since excitons enter into Raman scattering as intermediate states, the value obtained for this sample might be limited by the sensitivity of the experimental method to length scales of this order In the integration over $q_\parallel$ a three-dimensional phonon density of states, modified by zone folding effects along the growth direction, is considered This manifests itself in the vanishing of the Raman intensity for small shifts in agreement with experimental observations

The behavior of the Raman intensity factor δ as a function of relative layer thicknesses $\alpha = d(AlAs)/d$ is shown in Fig 4 for GaAs-AlAs superlattices with a total period of about 30 monolayers In analogy to the oscillatory behavior of the dispersion gaps [2] no changes are predicted for the lowest zone edge gap over the whole range of layer thicknesses The second zone edge gap has two zeroes of α near 0.4 and 0.7 Consequently two changes of δ occur For the zone center gaps, one and three zeroes are expected for the lowest ($\alpha \simeq 0.55$) and next higher gap ($\alpha \simeq 0.3, 0.55, 0.8$), respectively The intensity factor δ changes its character once and three times accordingly The experimental verification of this behavior would provide a further test of the model presented

IV. CONCLUSIONS

In Raman spectra of GaAs-AlAs multiple quantum wells and superlattices we have observed a characteristic emission background and pronounced intensity anomalies in the acoustic phonon regime We find that Raman scattering from isolated quantum wells due to interface roughness and layer thickness fluctuations provides a mechanism for a partial breakdown of crystal momentum conservation both parallel and perpendicular to the growth direction This accounts for the observed features and provides a new way to obtain information on length scales of interface roughness

V ACKNOWLEDGMENTS

Two of us (V I B and V F S) acknowledge support from the Max Planck Gesellschaft Thanks are due to M P Chamberlain for a critical reading of the manuscript We would like to thank H Hirt, M Siemers and P Wurster for expert technical assistance

* on leave from the A F Ioffe Physico-Technical Institute Russian Academy of Sciences 194021 St Petersburg, Russia

[1] C Colvard T A Gant M V Klein R Merlin R Fischer, H Morkoc, and A C Gossard Phys Rev B 31 2080 (1985)
[2] B Jusserand, and M Cardona in *Light Scattering in Solids V* Vol 66 of *Topics in Applied Physics* edited by M Cardona and G Güntherodt, (Springer Heidelberg 1989), p 61
[3] V F Sapega, V I Belitsky, T Ruf, H D Fuchs M Cardona, and K Ploog, Phys Rev B 46 (6005 (1992)
[4] P S Kop ev, D N Mirlin, V F Sapega and A A Sirenko, Pis ma Zh Eksp Teor Fiz 51 624 (1990) [Sov Phys JETP Lett 51, 708 (1990)]
[5] T Ruf V F Sapega, J Spitzer, V I Belitsky, M Cardona and K Ploog, in *Phonons in Semiconductor Nanostructures* NATO ASI Series edited by J P Leburton et al (Kluwer Amsterdam 1993) p 61
[6] J Sapriel J Charfagnon, F Alexandre and R Azoulay Phys Rev B 34 7119 (1986)
[7] A B Talochkin V A Markov, I G Neizvestnyi O P Pchelyakov M P Sinyukov, and S I Stenin Pis'ma Zh Eksp Teor Fiz 50, 21 (1989), [Sov Phys JETP Lett 50, 24 (1989)]
[8] D J Mowbray private communication (1990)
[9] D N Mirlin I A Merkulov V I Perel' I I Reshina and A A Sirenko Solid State Commun 84, 1093 (1992)
[10] A Pinczuk and E Burstein in *Light Scattering in Solids I* Vol 8 of *Topics in Applied Physics* edited by M Cardona (Springer, Heidelberg, 1983) p 23
[11] P V Santos L Ley, J Mebert, and O Koblinger, Phys Rev B 36 4858 (1987)
[12] S Tamura and J P Wolfe Phys Rev B 35, 2528 (1987)
[13] E Calle M Cardona E Richter and D Strauch, Solid State Commun 72 1153 (1989)
[14] A A Gogolin and E I Rashba, Solid State Comman 19, 1177 (1976)
[15] B A Auld in *Acoustic Fields and Waves in Solids* Vol I (Wiley New York 1973) p 210
[16] M A Herman, D Bimberg and J Christen, J Appl Phys 70 R1 (1991)

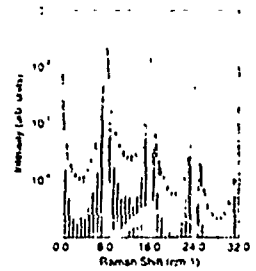

FIG 1 Influence of disorder on the acoustic phonon Raman spectrum for a superlattice with 11 quantum wells The excitation energy was chosen to be 10 cm^{-1} above an electronic resonance The solid line was calculated assuming that all confinement energies are identical the dashed line shows the enhancement obtained for the case when one of the wells has a confinement energy which is larger than that of the others by 10 cm^{-1}

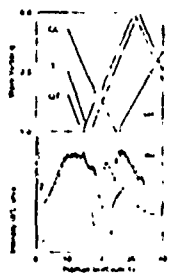

FIG 3 (a) Folded phonon dispersion for a symmetric GaAs AlAs superlattice with a period of 13 monolayers calculated for an in plane wave vector of $q_\parallel = 0.4\pi/d$ (b) Comparison of experimental Raman spectrum (top) with the best theoretical description (bottom) obtained by $q_\parallel$ integration

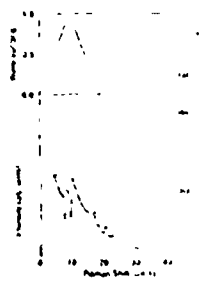

FIG 2 (a) Folded LA phonon dispersion for a symmetric GaAs AlAs superlattice with a layer thickness of 16 monolayers (b) Raman intensity factor δ showing the origin of anomalies near dispersion gaps in wave vector non conserving scattering processes (c) Experimental spectrum with background continuum and superimposed peaks and dips

FIG 4 Dependence of the intensity factor δ on the layer thickness ratio α (given next to each curve) for GaAs AlAs superlattices with a total period of 30 monolayers Intensity anomalies show different oscillatory behavior for the various zone edge (ZE) and zone center (ZC) gaps

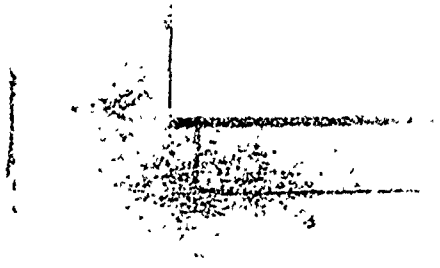

MoP13

FTIR SPECTROSCOPY OF LONGITUDINAL CONFINED PHONONS AND PLASMON-PHONON VIBRATIONAL MODES IN $GaAs_n/AlAs_m$ SUPERLATTICES.

Yu.Pusep, A.Milekhin, A.Toropov
Institute of Semiconductor Physics, 630090,
Novosibirsk, Russia

The longitudinal optical (LO) and plasmon-phonon (L^+) vibrational modes have been investigated in $(GaAs)_n/(AlAs)_m$ superlattices (SL's) grown by MBE on (100) GaAs:Si substrates by Fourier-transform infrared (FTIR) spectroscopy. To measure the longitudinal modes of SL's the p-polarized reflection spectra with incidence angle $\simeq 70°$ were recorded in the spectral range of GaAs and AlAs optical phonons. In the short period SL's the modes originates from confined LO phonons have been observed (Fig.1); the dispersion of LO phonons obtained by means of FTIR spectra is in good agreement with the Raman data.

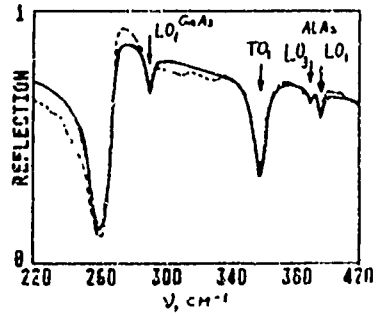

Fig.1. P- polarized reflection spectra of the $(GaAs)_3/(AlAs)_3$ SL at T= 80K; LO1, LO3 are the confined longitudinal modes. Broken line is the measured spectrum.

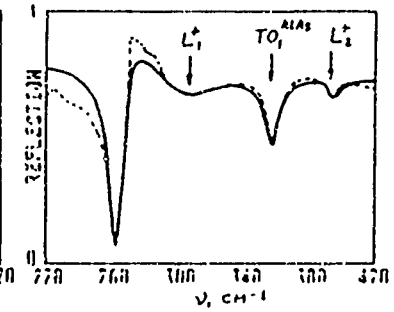

Fig.2. P- polarized reflection spectra of the doped $(GaAs)_{40}/(AlAs)_2$ SL at T=80 K. Broken line is the measured spectrum

In order to study the plasmon-phonon vibrational modes the doped long period SL's with thin barriers were investigated. In this case at appropriate polarization of the light (p- polarization) the LO phonons are coupled with electrons moving in a half-filled miniband and thus the "vertical" transport of electrons can be studied. The fitting of calculated spectra to experimental ones allowed us to measure the "vertical" mobility of electrons that for the sample shown in Fig.2. was 890 cm /v-s.

MoP14

Raman Scattering Study of Longitudinal Acoustic and Optic Phonons in $InSb/In_{1-x}Al_xSb$ Strained-Layer Superlattices

V.P. Gnezdilov,[1] D.J. Lockwood, and J.B. Webb
Institute for Microstructural Sciences, National Research Council, Ottawa, Ontario K1A 0R6 Canada
[1]Institute for Low Temperature Physics & Engineering, Ukrainian Academy of Sciences, 47 Lenin Avenue, 310164 Kharkov, Ukraine

Abstract

Detailed Raman scattering studies of $InSb/In_{1-x}Al_xSb$ ($0.15 < x < 0.5$) strained-layer superlattices grown by magnetron sputter epitaxy on (001)InSb substrates are reported for the first time. A number of folded acoustic phonons appear in the Raman spectra and their frequencies are accurately predicted by Rytov's theory of acoustic vibrations in layered media. The longitudinal optic phonons in the $In_{1-x}Al_xSb$ layers exhibit two-mode behavior and their shift due to the intralayer strain is discussed. Resonant Raman scattering was used to probe the electronic structure in the region of the E_1 and $E_1 + \Delta_1$ optical gaps. The two sets of peaks observed in the plots of the Raman cross section versus photon energy are shown to originate from the independent electronic transitions in the alternating layers. Estimates of the strain and confinement effects were made and these agree with the observed differences from bulk material.

Introduction

Semiconductor superlattices (SLs) have now been of interest for nearly 20 years. Such interest has been stimulated by the thin film epitaxial growth techniques that show stable and reproducible behavior at the atomic level and through potential device application of new artificial materials. Raman spectroscopy has been one of the most widely employed experimental tools in the study of SLs and in the characterization of the materials used in devices [1]. The most extensively studied superlattices have been those composed of III-V compounds such as $GaAs/Ga_{1-x}Al_xAs$. Recently, high-quality $InSb/In_{1-x}Al_xSb$ strained-layer SLs have been grown by magnetron sputter epitaxy (MSE) [2]. This system is particularly interesting since information regarding InSb-based alloys is very limited and the high electron mobility and small effective mass associated with InSb would suggest superior performance of devices based on this system. The aim of this work was to perform a detailed study of $InSb/In_{1-x}Al_xSb$ ($0.15 < x < 0.5$) strained-layer SLs using Raman scattering.

All 20 period SLs used in this study were grown by MSE on (001)InSb substrates and had different InSb and $In_{1-x}Al_xSb$ layer thicknesses d_1 and d_2, respectively. The top layer of the samples was InSb. The compositions of the ternary layers were determined from double-crystal x-ray diffractometer scans of single layer test structures and by fitting the x-ray diffractometer scans of the superlattices. The excellent crystalline quality of the epilayers was evaluated using x-ray diffraction and transmission electron microscopy. The individual layer thicknesses and ternary composition were chosen to ensure that the superlattices did not relax, as evidenced by x-ray line widths, transmission electron microscopy, and optical phase contrast microscopy.

The light scattering measurements were carried out using the quasi-backscattering geometry $z(y'y'+y)\bar{z}$ (x,y, and z coincide with principal cubic axes, and z is perpendicular to the superlattice layers). The spectrum was excited with various line of Ar^+ and Kr^+ lasers, and a

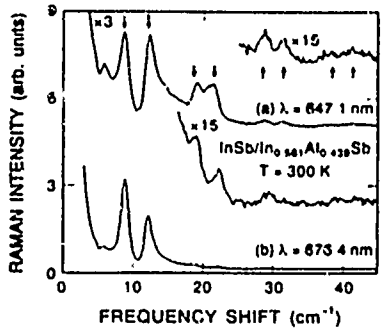

Figure 1. Room temperature Raman spectra of acoustic phonons in the InSb/$In_{1-x}Al_xSb$ (x = 0.439) superlattice excited with (a) 647.1 nm and (b) 676.4 nm laser light. The arrows indicate the calculated peak frequencies of the folded acoustic modes. The experimental resolution is 0.8 cm^{-1}.

rhodomine-6G dye laser pumped with all the lines of the Ar^+ laser. The scattering light was frequency analyzed with a Spex 14018 double monochromator, detected with a cooled RCA 31034A photomultiplier, and recorded under computer control. All measurements were carried out at room temperature in a helium-gas atmosphere. For the resonant investigations, the intensity data were normalized to the Raman intensity of pure silicon [3] in order to correct them for the instrumental response function and for the frequency to the fourth power law of the Raman cross section.

Acoustic Phonons

Low frequency Raman spectra obtained from an InSb/$In_{1-x}Al_xSb$ (x = 0.439) superlattice is shown in Fig. 1. The spectra are typical of the other superlattices investigated in that all gave three or four well-resolved doublets, which are indicative of the high interface and surface quality of the MSE-grown samples.. These sharp pairs of lines are attributed to the longitudinal acoustic (LA) phonons folded into the new Brillouin zone, which arises from the additional periodicity ($d = d_1 + d_2$) of the superlattice. According to the elastic continuum theory of Rytov [4] for layered media, the folded acoustic phonon dispersion well away from the zone center $q = 0$ and boundary $q = \pi/d = q_{max}$ is given by

$$\omega_m = V_{SL}\,|(2\pi m/d \pm q)| \qquad (1)$$

where

$$q = [4\pi n_{SL}(\lambda)/\lambda][1-(1/4)[n_{SL}(\lambda)]^2)] \qquad (2)$$

is the component of the light scattering wave vector perpendicular to the layers, m = 0,1,2,... the zone folding index, λ the incident laser light wavelength, n_{SL} the refractive index of the superlattice at that wavelength, and V_{SL} the average superlattice sound velocity, which is a function of the component layer thicknesses, densities, and sound velocities. The predictions of the Rytov model are given by the arrows in Fig. 1 and are in excellent agreement with experiment. The layer thicknesses d_1 = 72.5 Å and d_2 = 41.0 Å were obtained from the x-ray diffraction study; the following values for the sound velocity $V_{SL} = 3.581 \times 10^5$ cm/s and refractive index n_{SL} (647.1 nm) = 4.278 were used in the calculation.

The Raman intensity in the photoelastic coupling model for acoustic phonons is given by [5]

$$I \propto m^{-2} \sin^2 (m\pi d_1/d)\omega_m(n_m + 1), \qquad (3)$$

where n_m is the Bose factor. Equation (3) may be used to determine the InSb layer thickness d_1. For example, the ratio of the intensity of the m = 1 peak to that of m = 2 peak for the lower curve (b) in Fig. 1 gives the value of d_1 = 66.8 Å for the superlattice with x = 0.439. This is in good agreement with the value of d_1 = 72.5 Å obtained from the x-ray diffraction measurements. In using the experimental intensity data to obtain quantitative information about the layer thickness, it is necessary to note that under resonant conditions the intensity of the folded phonon scattering can be considerably altered [5]. An example is the upper curve (a) in Fig. 1, which was measured with excitation close to resonance with a superlattice electronic transition.

Optic Phonons

The Raman spectrum of semiconductor superlattices at higher frequencies usually exhibits a number of first-order features characteristic of the two materials comprising the alternating layers. Figure 2 shows the high frequency region of the Raman spectrum of the InSb/$In_{1-x}Al_xSb$ (x = 0.364) superlattice obtained using 530.9 nm Kr^+ laser exciting light. The peak labeled "A" corresponds to the longitudinal optic (LO) of the InSb layers, while the peaks labeled "B" and "C" correspond to the two LO phonons (InSb-like and AlSb-like, respectively) due to the two-mode behavior of optic phonons in $In_{1-x}Al_xSb$ alloys. The frequency positions of the A, B, and C phonons in the Raman spectra for several SLs are summarized in Fig. 3, where the solid lines are the least-squares fit of a straight line to the frequency data. These fits yielded the concentration dependences

$$\omega_{InSb} = 187.2 + 2.9x\ (cm^{-1}) \qquad (4)$$

for the InSb line,

$$\omega_{InSb\text{-}like} = 186.8 - 23.7x\ (cm^{-1}) \qquad (5)$$

for the InSb-like alloy line, and

$$\omega_{AlSb\text{-}like} = 291.3 + 10.6x\ (cm^{-1}) \qquad (6)$$

for the AlSb-like alloy line.

The lattice mismatch in the superlattice composed of alternate layers of two materials with different lattice constants is elastically accommodated, i.e., the materials inside the superlattice are epitaxially strained in order to match the substrate in-plane lattice parameter a. The lateral biaxial strain can be described as a biaxial stress. This is equivalent to a hydrostatic pressure and a uniaxial stress of opposite sign perpendicular to the interface. In the Raman scattering geometry, the stress causes a shift in the LO-phonon frequency ω by [6]

$$\Delta\omega = (1/\omega_o^{LO})[pS_{12} + q\,(S_{11} + S_{12})]\tau \qquad (7)$$

where ω_o^{LO} is the phonon frequency of the unstrained cubic lattice, p and q are phenomenological parameters (known for AlSb [7] but not for InSb), S_{11} and S_{12} are the elastic compliances, and τ is the stress factor (positive for tensile and negative for compressive stress).

The higher frequency AlSb-like line lies well below the bulk AlSb LO-phonon frequency [8] of 340 cm^{-1}. Assuming a linear relationship between the two end points of 291.3 cm^{-1} (Eq. (6) at x = 0) and 340 cm^{-1}, it is possible to predict the concentration dependence of the AlSb-like mode in bulk (relaxed) $In_{1-x}Al_xSb$

$$\omega^{bulk}_{AlSb\text{-}like} = 291.3 + 48.7x\ (cm^{-1}) \qquad (8)$$

Using the linear fits to $\omega_{AlSb\text{-}like}$ and $\omega^{bulk}_{AlSb\text{-}like}$ (Eqs. (6) and (8)) and a linear interpolation of

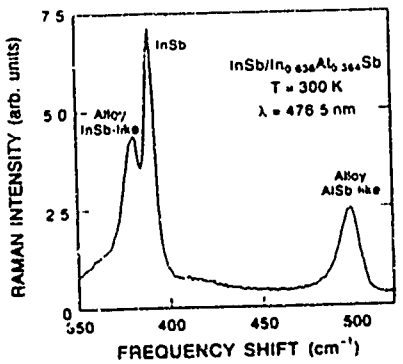

Figure 2 The room temperature Raman spectrum of optical phonons in the $InSb/In_{1-x}Al_xSb$ ($x = 0.364$) superlattice excited with 476.5 nm laser light. The experimental resolution is 4.3 cm^{-1}

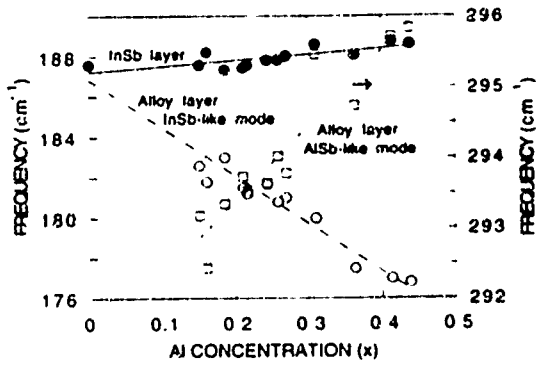

Figure 3 Concentration dependences of the peak frequencies of the InSb, AlSb-like, and InSb-like lines in the Raman spectrum of $InSb/In_{1-x}Al_xSb$ superlattices at room temperature

the compliances S_{11} and S_{12} [7,9] and lattice constants [9] of pure InSb and AlSb, an estimate for the AlSb-like mode stress factor for the $In_{1-x}Al_xSb$ alloy may be obtained:

$$\tau_{AlSb\ like} \approx 0.17x^2 - 3.8x + 11.3\ (cm^{-1}/GPa). \qquad (9)$$

The stress X, in the alloy layers can be calculated from $\Delta\omega = -\tau X$ using Eqs. (6), (8), and (9) for AlSb-like mode. At $x = 0.5$, $X = 2.0$ GPa. As expected, the strain is mostly accommodated in the SL alloy layer, but the slight shift of the InSb line indicates that a small compensating strain

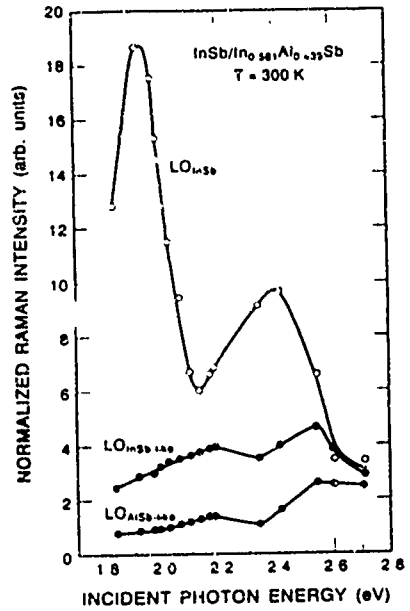

Figure 4. Resonant Raman profiles for the three main LO vibrations of the $InSb/In_{1-x}Al_xSb$ ($x = 0.439$) superlattice. The lines are guides for the eye.

appears in the InSb layers. It is significant that the high strain in the alloy layers for larger x values results in a small compressive biaxial strain in the InSb layers, as this indicates a slight relaxation has occurred in the superlattices. The mechanism for this relaxation is not clear at present.

Resonant Raman

The significance of resonant Raman scattering as a spectroscopic tool for obtaining information on the electronic states of superlattices is now well known [1]. Although this method does not allow for exact determination of transition energies, it provides information on whether the electronic states under study are confined within the quantum wells or if they extend through the whole structure. This possibility is due to the exploitation of the modulation produced in the electronic states by the optical lattice vibrations that are characteristic of each type of layer and that are not significantly affected by the periodicity of the superlattices [10,11].

Most resonant Raman scattering work has been performed on direct band gap semiconductors in the vicinity of the Brillouin zone center and, although it is well recognized that Raman scattering investigations can provide a great deal of information about the E_1 and $E_1 + \Delta_1$ transitions in superlattices [1], only two reports are known in which Raman scattering has been used to study the

resonance at the E_1 gap in zinc-blende superlattices [12,13]. In these studies the resonant behavior of the longitudinal optical (LO) phonons of only one of the two alternating layers was analyzed.

Figure 4 shows the resonant Raman profiles for the LO phonons in the InSb/$In_{1-x}Al_xSb$ (x = 0.439) superlattice. The shapes and interpretation of the resonances in bulk InSb are well understood [14]. As might be expected, the shapes and energy positions of both peaks in the resonant profile of the InSb phonon (see Fig. 4) are in good agreement with those found for bulk InSb [14]. The superlattice effect, which shifts the peak positions towards higher energies due to strain and confinement [1], is small. The strain dependent shift can be neglected for the InSb layers [1], while the possible shift for the confinement effect is expected to be less than 0.01 eV [8] and this is too small to resolve in a room temperature experiment. Contrary to the findings of Ref. 12, two weak but distinct resonant features are observed for the InSb-like mode. In addition, similar resonances are observed for the AlSb-like mode. The resonances at high energy are stronger than those at lower energy. It is also seen from Fig. 4 that the enhancements in the LO phonons originating in the alloy layers are smaller than those ones in the LO phonon originating in the pure InSb layers. Peak positions of the resonant profiles for InSb-like and AlSb-like phonon modes in Fig. 4 are shifted to higher energy relative to the positions of the corresponding peaks of InSb by values approximately equal to the differences in the E_1 and $E_1 + \Delta_1$ gaps of InSb and $In_{1-x}Al_xSb$ [15]. The observation of the separate resonant enhancements in the InSb and $In_{1-x}Al_xSb$ layers at energies close to the E_1 and $E_1 + \Delta_1$ gap energies in the respective bulk materials means that the electronic transitions that produce the resonances in the Raman scattering are independent, or nearly independent [1], for both materials in the superlattice.

Bulk material gaps have counterparts in superlattices and the energies of resonant peaks observed in both types of materials are related to each other by [12]

$$E_R(\epsilon,d) = E_R^{bulk} + \Delta_s(\epsilon) + \Delta_c(d), \qquad (10)$$

where $\Delta_s(\epsilon)$ and $\Delta_c(d)$ are energy shifts produced by strain and confinement, respectively. The strain shift is calculated to be $\Delta_s(\epsilon) = 0.043$ eV using the dependence $\Delta_s(\epsilon) = 3.016\epsilon$ (Δ_s in eV) for InSb from Ref. 12 and strain ϵ evaluated from Ref. 16. The confinement shift is found to be $\Delta_c(d) = 0.011$ eV from the experimental dependence [12] of the position of the resonant maximum (corrected for strain) versus d^{-2} for the InSb/$In_{1-x}Al_xSb$ superlattice of well width d. Thus, the shift of 0.05 eV (see Fig. 4) between the position of the experimentally observed resonant peak near the E_1 gap energy in the superlattice and that deduced for the bulk alloy with the same Al content is very close to the calculated one of $\Delta_s(\epsilon) + \Delta_c(d) = 0.054$ eV.

Conclusion

In summary, strained layer superlattices of InSb/$In_{1-x}Al_xSb$ have been prepared by magnetron sputter epitaxy. Superlattices with periods of less than 16 nm and alloy compositions $x < 0.5$ have been studied by Raman spectroscopy. The observed frequencies of the zone-folded longitudinal acoustic phonons are in good agreement with calculations based on Rytov's theory of acoustic vibrations in layered media. The higher frequency regions of the Raman spectra consist of the confined LO phonons in the InSb and $In_{1-x}Al_xSb$ layers. The two-mode behavior of the $In_{1-x}Al_xSb$ alloy layer phonons was clearly confirmed. A linear frequency-shift behavior was observed for all LO modes with increasing Al content. Resonant Raman experiments reveal the existence of two sets of interband transitions in the region of the E_1 and $E_1 + \Delta_1$ optical gaps of the InSb and $In_{1-x}Al_xSb$ host materials. The existence of these two separate sets of resonances indicates that the electronic energy levels of the respective layers are essentially independent, i.e., the superlattice comprises a double set of multiple quantum wells for the E_1 and $E_1 + \Delta_1$ transitions. The resonance positions for the $In_{1-x}Al_xSb$ layers show the effects of both strain and confinement.

Acknowledgment

We would like to thank H.J. Labbé for expert technical assistance.

References

1. B. Jusserand and M. Cardona, in *Light Scattering in Solids V*, edited by M. Cardona and G. Güntherodt, Topics in Appl. Phys., Vol. 66, p. 49. Springer-Verlag, Berlin (1989)
2. J.B. Webb, G.H. Yousefi, and R. Rousina, *Appl. Phys. Lett.* **60**, 998 (1992).
3. A. Compaan and H.J. Trodahl, *Phys. Rev. B* **29**, 793 (1984)
4. S.M. Rytov, *Akust. Zh.* 2, 71 (1956) [*Sov. Phys. - Acoust.* 2, 68 (1956)]
5. C. Colvard, T.A. Gant, M.V. Klein, R. Merlin, R. Fischer, H. Morkoç, and A.C. Gossard, *Phys. Rev. B* **31**, 2080 (1985).
6. G. Abstreiter, H. Brugger, T. Wolf, R. Zachai, and Ch. Zeller, in *Two-Dimensional Systems: Physics and New Devices*, edited by G. Bauer, F. Kuchar, and H. Heinrich, p. 130. Springer-Verlag, Berlin (1986)
7. E. Anastassakis and M. Cardona, *Solid State Commun.* **63**, 893 (1987).
8. S. Ves, K. Strössner, and M. Cardona, *Solid State Commun.* **57**, 483 (1986)
9. *Landolt-Börnstein, Numerical Data and Functional Relationships in Science and Technology*, New Series, edited by O. Madelung, Group III, Vol. 22a. Springer-Verlag, Berlin (1987)
10. G. Abstreiter, E. Bauser, A. Fischer, and K. Ploog, *Appl. Phys.* **16**, 345 (1978)
11. J.E. Zucker, A. Pinczuk, D.S. Chemla, A. Gossard, and W. Wiegmann, *Phys. Rev. B* **29**, 7065 (1984)
12. F. Cerdeira, A. Pinczuk, T.H. Chiu, and W.T. Tsang, *Phys. Rev. B* **32**, 1390 (1985)
13. C. Tejedor, J.M. Calleja, F. Meseguer, E.E. Mendez, C.A. Chang, and L. Esaki, *Phys. Rev. B* **32**, 5303 (1985)
14. M. Cardona, in *Light Scattering in Solids II*, edited by M. Cardona and G. Güntherodt, Topics in Appl. Phys., Vol. 50, p. 19. Springer-Verlag, Berlin (1982).
15. S. Isomura, F.G.D. Prat, and J.C. Woolley, *Phys. Stat. Sol.* **65**, 213 (1974)
16. V.P. Gnezdilov, D.J. Lockwood, and J.B. Webb, to be published

MoP15

Optical phonon probes of the lateral scale of interface roughness: a theoretical investigation

S de Gironcoli
INFM - Institute of Condensed Matter Theory (FORUM),
Scuola Normale Superiore, Piazza dei Cavalieri 7, I 56100 Pisa, Italy

E Molinari
Dipartimento di Fisica, Università di Modena, Via Campi 213/a, I 41100 Modena, Italy

Abstract

We study the effect of the different lateral scale of interface roughness on the optical phonon spectrum of thin Si/Ge (001) superlattices We find that the *first* Si like confined optical mode does localize either in the thinest or in the thickest part of the Si well already for relatively small lateral sizes of the interface terraces, contrary to the corresponding behaviour in GaAs/AlAs structures We show that this gives rise to distinct changes in the Raman lineshape, which should be useful to discriminate between short range intermixing and long range interface corrugation in Si/Ge superlattices We finally discuss the optimal conditions to allow experimental observation of this effect

Introduction

A number of important contributions have been recently devoted to the determination of the *lateral scale* of interface disorder in semiconductor superlattices (SL's), particularly GaAs/AlAs [1-13] Early interpretations of optical experiments had led to the conclusion that structures with atomically sharp interfaces over very large regions ($\sim 1\mu m$) had been achieved The observed splittings of exciton recombination lines were attributed to discrete (1 monolayer) variations in the well width and flat interface regions (terraces) much larger than the exciton diameter [1, 2] However a less optimistic view is now coming from experiments using different probes, including Raman spectra of optical modes [3-5], as well as more conventional structural characterization techniques (high resolution transmission electron microscopy (HRTEM) [6-8], x ray diffraction and also scanning tunneling microscopy [9]) Moreover the existence of systematic photoluminescence (PL) [1 2 10 11] and vibrational light scattering [3-5] studies on GaAs/AlAs samples grown in a wide range of conditions allows to conclude that the "optimal growth parameters" (i e parameters yielding minimal disorder effects) depend strongly on the probe used to characterize On one hand, the observed excitonic transition lineshape splittings suggest that largest terraces are favoured by relatively high substrate temperatures T_s and growth interruption [10]. On the other hand, optical phonon features —which are expected to be especially sensitive to short scale roughness [14]— indicate that intermixing exists even in the best samples, and it decreases for low-T_s growth while remaining quite insensitive to growth interruption [3, 4]

The most natural way to reconcile this set of results is the idea, independently supported by HRTEM data [6, 8], that interface disorder must occur over different lateral lengthscales, so that its spectrum in reciprocal space is at least bimodal [11], with different Fourier components depending differently upon the growth parameters and affecting the possible probes in different ways A critical reexamination of PL spectra [11-13] has been crucial to reach this conclusion. The above interpretation is thus becoming increasingly accepted for GaAs/AlAs SL's.

A thorough work on similar issues has not been undertaken for Si/Ge structures sofar one of the reasons certainly being that a systematic photoluminescence line shape study is impossible there. A probe which could be mostly sensitive to "long range" terraces seemed thus unavailable in this case.

In the present paper, we focus on the vibrational properties and show that in thin Si/Ge SL's optical phonons may be such a probe, i.e phonon spectra should allow to discriminate between "large terrace" and "short scale intermixing" behaviors much more easily than in GaAs/AlAs [15] In particular, we discuss the effect of disorder with different lateral lengthscales on the Si like confined vibrations, and identify the sample geometry and the experimental conditions under which Raman spectroscopy may be most effective for this type of characterization

Theoretical approach

As in previous studies of AlGaAs based heterostructures [14], we use accurate interatomic force constants which are calculated from first principles within density functional theory in the local density approximation by means of a linear response scheme The ability of such force constants to reproduce the bulk vibrational properties of Si and Ge was demonstrated in [16] In order to extend this approach to Si/Ge heterostructures, however one has to face the additional difficulty of including strain effects in the *ab initio* force constant scheme This has been recently achieved [17], by introducing higher order corrections, due to the different bond lengths, to the interatomic force constants

To model SL's with disordered layers, an additional periodicity in the (xy) plane parallel to the interfaces has been assumed In order to keep the size of the calculation tractable, we introduce an in plane periodic corrugation only along the x direction, with alternating terraces and barriers p and q atomic layers wide The lateral period is thus $(p+q)a/4$ and the three dimensional unit cell needed to treat a SL with a period of $2n$ atomic layers contains $2n(p+q)$ atoms For comparison, we have also simulated short range interface intermixing [18] In that case Si and Ge atoms in the allowed planes are distributed at random in a 18 atom two dimensional unit cell according to the assumed concentration and the calculated properties are averaged over ~ 10 different configurations

Phonon spectra (frequencies and displacement profiles) are then obtained by direct diagonalization of the dynamical matrix, and the corresponding Raman strengths are estimated assuming the same bond polarizability in both materials [19].

Confined Si-like phonons
the effect of short- and long-scale interface disorder

It is by now well known that in ideal Si/Ge SL's (i.e. SL's with perfectly abrupt interfaces) Si-like phonons are strongly confined in the Si region [20]. In particular for longitudinal (L) vibrations, which are allowed in the standard Raman backscattering configuration, it has been shown [21] that the confined mode frequencies ω_m are related to the bulk Si dispersion $\omega_{Si}(q)$ by the condition $\omega_m = \omega_{Si}(q_m)$, with

$$q_m = \frac{m\pi}{[(n+1)a/4]} \qquad (1)$$

n being the number of atomic planes in the Si layer and a the bulk lattice parameter. It has therefore become customary to plot the experimental SL phonon frequencies "unfolded" onto the bulk Brillouin Zone (BZ) according to (1), and to compare them with the appropriate bulk dispersion (in the same strain configuration [22]). Deviations between "unfolded SL" and bulk dispersions are thus attributed to disorder effects. We have recently been able to show [18,23] that for high m confined modes (or large q_m unfolding) such deviations are accounted for by assuming a thin intermixed layer of SiGe at the interfaces, which is also responsible for the observed SiGe-like interface mode around 400 cm^{-1} [24].

In Fig. 1 we now show results for two different sets of $Si_{n/4}/Ge_{4/4}$ (001) SL's grown on $Si_{0.5}/Ge_{0.5}$ alloy substrate with "nominal" thicknesses $n=4$ and $n=8$ respectively, and variable in-plane corrugation periodicity ($p+q$ = 12, 24, 36 and $x = \pm p/(p+q)$). The symbols represent calculated SL Raman peaks of increasing intensity with increasing darkness in the grey scale, while the solid line is the bulk L dispersion. Focusing on the first half of the bulk BZ, it is apparent that some splitting of the first confined mode peak is always present for the thinnest ($n = 4$) SL even for the smallest terrace periodicity ($p+q = 12$, $x = 1/2$), although both split peaks have comparable intensity only to the largest $p+q$ values. This is not the case for the $n = 8$ SL, where an in-plane periodicity $p+q = 12$ is clearly not sufficient to induce a splitting of the first confined Raman line. At larger values of $p+q$ some splitting Δ_m does appear, although still small in frequency ($\Delta_m \geq 1 - 3$ cm^{-1}).

To examine the origin of these splittings, in Figs. 2a and 3a we show the displacement amplitude corresponding to the individual frequencies for two particular SL's having $p+q = 12$ and $n = 4$ and 8. The two split modes obtained for $n = 4$ (Fig. 2b) clearly appear to derive from confined phonons which are localized either in the thickest or in the thinnest part of the Si layer. It is therefore not surprising that their frequency turns out to be approximately consistent with confinement in a well of width 3 or 4 monolayers respectively. The displacement amplitude of Fig. 3a ($n = 8$) is instead quite delocalized over the Si layer, consistent with the antiphase lineshape of the corresponding peak (Fig. 3b). A similar analysis can be performed for all frequencies of Fig. 1, leading to the conclusion that the first Si-like confined

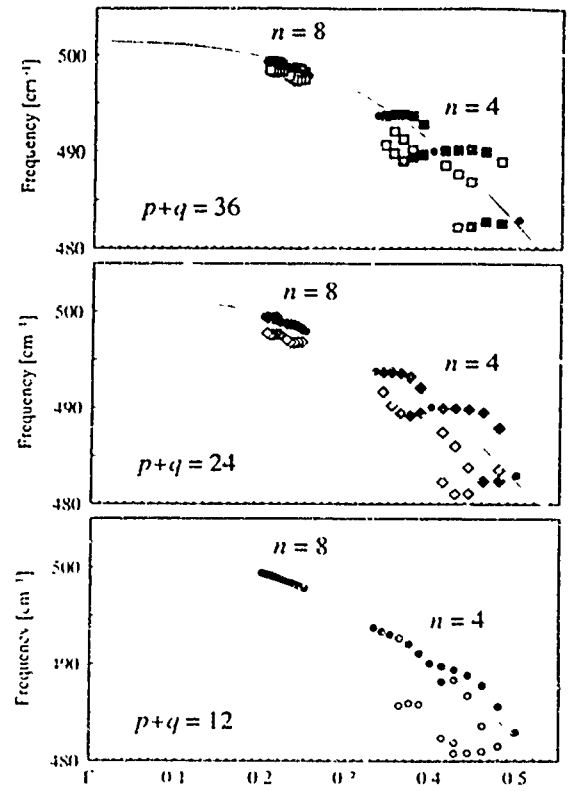

Fig. 1 - Effect of in-plane terraces on the calculated SL frequencies. Symbols: first Si-like confined modes, unfolded onto the first half of the bulk BZ, for strain-symmetrized Si_n/Ge_4 (001) SL's with nominal thicknesses $n = 4$ and $n = 8$ respectively, and variable in-plane corrugation periodicity ($p+q$ = 12, 24, 36 and $x = \pm p/(p+q)$). Increasing darkness of the symbols indicates increasing calculated intensity of the corresponding Raman peaks. Solid line: calculated L dispersion for bulk Si in the same strain configuration as in the SL's.

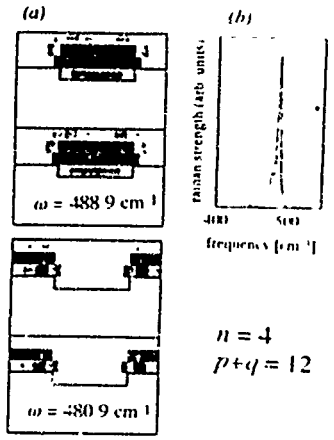

Fig. 2. *(a)* Spatial distribution in the (z,x) plane of the squared displacement amplitude corresponding to the two split frequencies of the first Si like confined mode for a $n = 4$ SL with $p + q = 12$. The confined phonons localized in the thickest and thinnest parts of the Si well fall at frequencies $\omega_1^{(Si)} = 488.9$ cm^{-1} and $\omega_1^{(Si)} = 480.9$ cm^{-1} respectively. *(b)* Calculated Raman strength in the Si like frequency range of the same SL

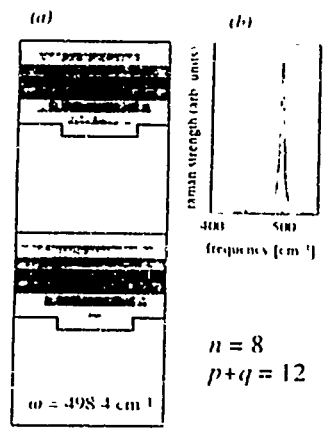

Fig. 3. Same as Fig. 2 for a $n = 8$ SL. *(a)* Spatial distribution in the (z,x) plane of the squared displacement amplitude of the first Si like confined mode for $p + q = 12$. In this case the Raman peak is essentially unsplit (see *(b)*) and the displacement pattern is quite delocalized over the Si layer. (Note that the grey scale is the same as in the previous figure.)

mode in Si/Ge SL's may indeed give rise to monolayer splittings similar to those hypothesized for exciton lines [1].

It is thus meaningful to design a situation where this effect is expected to be most apparent in order to suggest an actual experimental application. By comparing a few sample geometries, we have found that SL's with $n = 6$ should show at the same time relatively large splittings ($\Delta\omega \geq 1 \div 3$ cm^{-1} for $p + q$ in the range 24–36) together with comparable intensities of the split lines, so that the spectrum corresponding to terraced interfaces would differ significantly from that of broadened interfaces (Fig. 1). In particular, it appears that the linewidth of the Si like peak is only slightly affected by homogeneous broadening, which instead may induce significant frequency shifts (lowest curves in Fig. 1). On the contrary, an increasing splitting of the Raman lines (which might result in a broadened peak in the experimental spectra) originates from lateral corrugation with increasing period. This result suggests that a meaningful experiment would consist in monitoring the Si like lines in nominal $Si_n Ge_n$ SL's grown under different substrate temperature and interruption conditions. Any splitting or

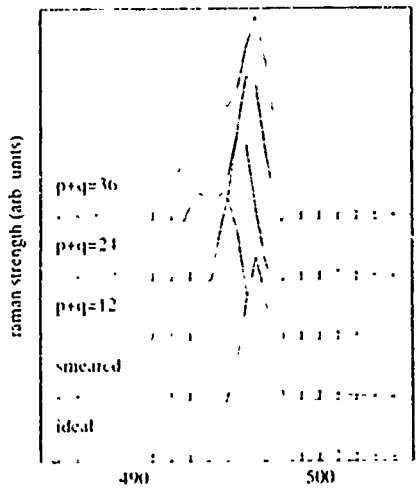

Fig. 4. Raman intensity profiles in the frequency range of the first Si like L confined mode for a nominal Si_6Ge_6 SL with different interface profiles. The two lowest curves correspond to ideally abrupt interfaces and to interfaces with two intermixed layers of Si_3Ge_3. The three upper curves are for SL's with a "terraced" interface and variable in plane corrugation periodicity ($p + q = 12, 24, 36$).

marked broadening of the Raman lines would then indicate a transition from a regime dominated by homogeneous intermixing to a regime with more important terrace effects.

We finally come to the comparison with similar studies previously performed by B. Jusserand for GaAs/AlAs SL's [15]. In that case, no splitting of the first confined mode frequency was found in the calculated spectra, even for the largest terraces and the thinnest wells that could be examined [23]. This was attributed [15] to the non analytic properties of phonon dispersions close to BZ center, arising from long range Coulomb forces in polar materials. The very different behaviour of Si/Ge SL's confirms this interpretation. Unlike in GaAs/AlAs, we indeed find that in Si/Ge the minimum terrace width Λ needed to induce well defined phonon modes confined in the Si regions of different thickness is roughly consistent with the expression proposed for the same transition of confined electrons [26, 15], namely

$$\Lambda \geq d d / 2\Delta d)^{1/2}, \qquad (2)$$

d and Δd being the nominal thickness and its fluctuation (eq. (2) of Ref. [15] with the assumption of isotropic phonon dispersion).

In conclusion we have performed *ab initio* calculations of the effects of interface disorder with different lateral scale on the phonon spectrum of Si/Ge SLs. The results indicate that — unlike in GaAs/AlAs — the first confined Si like mode is quite sensitive to the size of interface terraces. Thus candidates optical phonons as possible tools for a more detailed structural characterization of interfaces.

Acknowledgements. We acknowledge partial financial support by CNR under grant 92.01598.PF69.

References

[1] R.F. Kopf, E.F. Schubert, T.D. Harris, and R.S. Becker, Appl. Phys. Lett. 58, 641 (1991).
[2] B. Deveaud, A. Regreny, J.Y. Emery, and A. Chomette, J. Appl. Phys. 59, 1643 (1986).
[3] J. Grant, J. Menendez, V. Pinczuk, E.N. Pfeiffer, K.W. West, F. Molinari, and S. Baroni, Appl. Phys. Lett. 59, 2859 (1991).
[4] B. Jusserand, F. Mollot, F. Molinari, and S. Baroni, Surf. Sci. 267, 171 (1992).
[5] D. Gammon, B.V. Shanabrook, and D.S. Katzer, Phys. Rev. Lett. 67, 1547 (1992).
[6] A. Ourmazd, D.W. Taylor, J. Cunningham, and C.W. Tu, Phys. Rev. Lett. 62, 933 (1989).
[7] P.M. Petroff, A.C. Gossard, W. Wiegmann, and A. Savage, J. Cryst. Growth 44, 5 (1978).
[8] N. Itakashi, M. Tanaka, H. Sakaki, and K. Ishida, Appl. Phys. Lett. 60, 1460 (1992).
[9] O. Albrektsen, H.P. Meier, D.J. Arent, and H.W. Salemink, Appl. Phys. Lett. 62, 2605 (1993).
[10] P. Kozlowski, S. Munnix, D. Bimberg, D.E. Mars, and J.N. Miller, J. Vac. Sci. Technol. B8, 798 (1990).
[11] C.A. Warwick, W.Y. Jan, A. Ourmazd, and T.D. Harris, Appl. Phys. Lett. 60, 588 (1992).
[12] C.A. Warwick and R.F. Kopf, Appl. Phys. Lett. 60, 486 (1992).
[13] B. Orschel, G. Odegard, R. Houdre, M. Proctor, and D.E. Reinhart, Appl. Phys. Lett. 62, 813 (1993).
[14] F. Molinari, S. Baroni, P. Giannozzi, and S. de Gironcoli, Phys. Rev. B45, 4280 (1992).
[15] B. Jusserand, Phys. Rev. B42, 7256 (1990).
[16] P. Giannozzi, S. de Gironcoli, S. Baroni, and P. Pavone, Phys. Rev. B43, 7231 (1991).
[17] S. de Gironcoli, Phys. Rev. B46, 2412 (1992).
[18] S. de Gironcoli, F. Molinari, R. Schorer, and G. Abstreiter, Phys. Rev. B (1993), in press.
[19] This approximation is acceptable because we always compare Raman intensities of modes having the same origin.
[20] A. Lascialfari and F. Molinari, Journal de Physique C5, 569 (1987); F. Molinari and A. Lascialfari, Appl. Phys. Lett. 54, 1920 (1989).
[21] A. Lascialfari, F. Molinari, and A. Qteish, in *Condensed systems of low dimensionality*, edited by J.L. Beeby et al. (Plenum, New York, 1991), p. 197.
[22] A. Qteish and F. Molinari, Phys. Rev. B42, 7090 (1990).
[23] R. Schorer, G. Abstreiter, S. de Gironcoli, F. Molinari, H. Kibbel, and E. Kasper, this conference, and to be published.
[24] H. Brugger, F. Cross, G. Abstreiter, E. Kasper, and H. Kibbel, Semicond. Sci. Technol. 3, 1166 (1988); S.S. Iyer, J.C. Tsang, M.W. Copel, P.R. Pukite, and R.M. Tromp, Appl. Phys. Lett. 54, 219 (1989); M. Ospelt, W. Barsa, J. Henz, K.V. Mader, and H. von Känel, Superlatt. Microstruct. 5, 71 (1989); J. Menendez, V. Pinczuk, J. Bevk, and J.P. Mannaerts, J. Vac. Sci. Technol. B6, 1306 (1988).
[25] Splittings were instead predicted for higher order confined modes, on which long range fields have a much smaller effect.
[26] D. Paquet, Superlatt. Microstruct. 2, 429 (1986).

MoP16

INFRARED REFLECTIVITY OF STRAINED GaSb/AlSb SUPERLATTICES

G Scamarcio C Gadaleta
Dipartimento di Fisica G N E Q P Università di Bari via Orabona 4 I 70126 Bari Italy

A Tagliente L Tapfer
C R S M Mesagne I 72023 Brindisi Italy

K Ploog
Paul Drude Institut für Festkörperelektronik O 1086 Berlin Germany

Y Ohmori
Electronics Engineering Osaka University 2 1 Yamada Oka Suita Osaka 565 Japan

H Okamoto
Chiba University Faculty of Engineering 1 33 Yayoi Cho Chiba Shi Chiba 260 Japan

The careful analysis of far infrared reflectivity spectra of GaSb AlSb superlattices allows us to obtain information on intermixed $Al_xGa_{1-x}Sb$ layers at the heterointerfaces namely average chemical composition and thickness Complementary information on structural properties and strain relaxation processes are obtained from x ray diffraction

I INTRODUCTION

Far infrared spectroscopy is well known to be a primary tool for the investigation of vibrational properties of solids Nevertheless only very recently its usefulness for the study of semiconductor superlattices (SL) has been exploited [1-4] The ability of far infrared reflectivity (FIR) to probe confined phonons in SLs has been documented even in the case of ultrathin layers [4] The influence of the spatial configuration on the SL dielectric function is the origin of the high sensitivity of FIR to the structural properties of multiple heterostructures [5] Particularly the simultaneous analysis of far and mid infrared reflectivity spectra, in the framework of the effective medium approximation, allows the assessment of the individual layer thicknesses with an accuracy comparable to that of double crystal x ray diffraction [5] To the best of our knowledge, no FIR investigation of strained layer SLs has been reported

GaSb/AlSb superlattices have attracted attention for their possible application in laser diodes emitting in the 1 3-1 7 μm range [6] Their structural properties are influenced by the moderate (0 65%) lattice mismatch between the constituent materials Strain and confinement effects have been previously investigated by means of ion channeling, x ray diffraction [9] and Raman spectroscopy [10,11] Strain relaxation takes place for total AlSb thickness greater than the critical value $h_c \approx 11 \pm 3$ nm [9] We report here far ir reflectivity and x ray diffraction of GaSb AlSb superlattices Our results show that a satisfactory description of FIR spectra can be obtained provided that not only strain and phonon confinement but also strain relaxation processes are considered

II EXPERIMENTAL

GaSb/AlSb superlattices were grown by molecular beam epitaxy either on GaAs or n doped GaSb (001) oriented substrates Undoped buffer layers 0 8 μm thick were grown on n doped GaSb wafers The optimized growth procedure reported in Ref [12] was used

Structural data on the samples were obtained from x ray diffraction Diffraction patterns were recorded with a high resolution double crystal diffractometer using CuKα radiation close to the symmetric (400) and asymmetric (511) reflections in order to obtain the lattice mismatch and strain fields normal and parallel to the crystal surface Structural parameters were obtained through comparison with the results of computer simulation based on the dynamical scattering theory [13] The best fit values are listed in Table I

IR measurements were performed under near normal incidence at 10 K by using a Fourier transform spectrophotometer operating under vacuum

III RESULTS AND DISCUSSION

Figure 1 shows the FIR reflectivity spectrum representative of the series grown on n doped GaSb substrates The high reflectivity band extending in the low energy part of the spectrum up to about 266 cm^{-1} and the broad band around 400 cm^{-1} originate from plasma oscillations in the doped substrate The intense structure extending in the range 200-300 cm^{-1} is due to the combined effect of "Reststrahlen" (RS) from GaSb either in the SL or in the substrate The edge at 229 5 cm^{-1} coincides in energy with the bulk GaSb TO and is ascribed to the

TABLE I Structural parameters of GaSb/AlSb superlattices Here N = number of periods d = superlattice period, d_j = individual layer thicknesses measured by x rays (samples 1-3) or FIR (samples 4 5), $(\frac{\Delta d}{d})_\perp, (\frac{\Delta d}{d})_\parallel$ = lattice mismatch parallel and normal to the (001) plane, respectively, values in < > brackets indicate mean values

sample	substrate	N	d (nm)	layer	d_j (nm)	$(\frac{\Delta d}{d})_\perp$	$(\frac{\Delta d}{d})_\parallel$
1	GaSb	50	16 04	GaSb	13 26	$-3\ 6\times10^{-3}$	$< 3\ 96\times10^{-3}>$
				AlSb	2 89	$+3\times10^{-3}$	
2	GaSb	100	5 53	GaSb	3 75	$< 4\ 1\times10^{-3}>$	
				AlSb	1 80		
3	GaSb	200	2 78	GaSb	1 74	0	0
				AlSb	1 04	$1\ 29\times10^{-3}$	0
4	GaAs	285	4 9	GaSb	3 1	$< 3\ 13\times10^{-3}>$	$< 6\ 5\times10^{-3}>$
				AlSb	1 8		
5	GaAs	146	5 6	GaSb	4 2	$< 6\ 14\times10^{-3}>$	$< 6\ 68\times10^{-3}>$
				AlSb	1 4		

substrate The weak shoulder at 227 cm^{-1} appearing on the low energy side of the bulk GaSb RS band can be ascribed to GaSb-like TO phonons in the SL The structure appearing in the range 300-330 cm^{-1} is due to RS from AlSb-like phonons in the SL

Figure 2 shows the FIR spectrum of sample 5 which is grown on GaAs Due to the different substrate, several changes can be observed with respect to the spectrum of sample 1 In particular no plasmon like reflectivity features related to the substrate are present The GaAs substrate manifests itself in the range 270-300 cm^{-1} where the bulk like RS band is modulated by the interference of radiation in the epilayer In this case, the GaSb-like and AlSb-like RS bands around 230 and 320 cm^{-1}, respectively, are well separated from that of the substrate A complete assignment of the spectral features of Figs 1 and 2 will be discussed later after detailed comparison with calculations

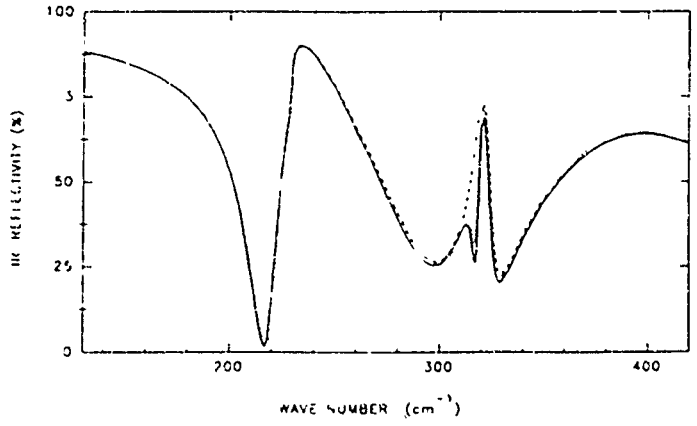

FIG 1 FIR spectrum of $(GaSb)_{13\ 2nm}/(AlSb)_{2\ 89nm}$ SL (sample 1) grown on a doped GaSb substrate Continuous line experimental data Dashed line spectrum calculated as explained in the text for abrupt interfaces Dotted line spectrum calculated considering 5%intermixing at the interfaces

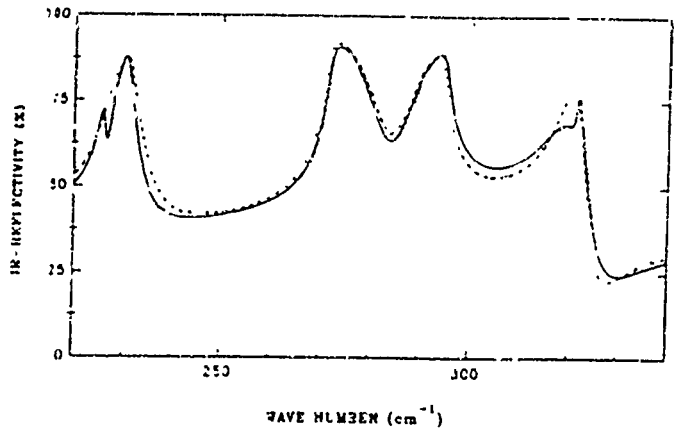

FIG. 2 FIR spectrum of $(GaSb)_{3.2nm}(AlSb)_{3.2nm}$ SL (sample 3) grown on GaAs substrate. Continuous line: experimental data. Dashed line: spectrum calculated for abrupt interfaces. Dotted line: spectrum calculated for a $Al_{0.3}Ga_{0.7}Sb/Al_{0.7}Ga_{0.3}Sb$ SL as explained in the text.

The theory of refs [2, 14] gives a very satisfactory description of FIR for an "ideal" SL grown onto a semi-infinite substrate. The SL dielectric function is written in the effective medium approximation as the average of the dielectric function of the constituent layers weighted with the layer thicknesses [7]. For layers thinner than about 10 monolayers the confinement induced shift of phonon energies has to be considered [13]. In the case of strained layers the influence of lattice distorsion on phonon energies needs to be evaluated, too.

The dashed lines in Fig. 1 and 2 have been calculated according to the above model considering an ideal GaSb/AlSb SL with abrupt interfaces. For sample 1 the substrate doping has been properly considered by introducing a plasmon oscillator in the substrate dielectric function. In the calculations we have taken the layer thicknesses of Table I. The following parameters have been adjusted for best reproduction of the experimental data: the plasmon frequency and damping ω_p and γ_p, the phonon frequency and damping in the j-th layer, ω_{TO_j} and Γ_j. Although a good overall agreement was obtained, several important structures cannot be reproduced at all. In particular, there is no way to reproduce the dip at 316.7 cm^{-1} in Fig. 1. The same is true for the structured GaSb-like and AlSb-like RS bands in Fig. 2. This discrepancy will be corrected by taking into account strain induced structural deformation, as explained in the following.

Strain relaxation. A superlattice structure manifests itself by non-zero values of the in plane lattice mismatch or by negative strain values in the GaSb layers. The values of Table I show a partial degree of relaxation for samples 1-3 grown on GaSb substrate, which increases at increasing the AlSb layer and the total superlattice thicknesses. This expected behaviour is related to the individual layer and total AlSb thicknesses by far exceeding the critical values in GaAs/AlSb structures [9]. Lattice relaxation occurs through the formation of defects, misfit dislocations and intermixed layers at the heterointerfaces. This causes interface roughness and local fluctuations of strain fields in the layers. In fact, a satisfactory agreement between the calculated and experimental x-ray diffraction patterns of samples 1-3 was obtained only if 0.1-0.2 nm thickness fluctuations and $\sim 10^{-3}$ strain fluctuations were considered. Hence, the simplistic assumption of homogeneous and abrupt interfaces has to be abandoned. Considering moderate thickness fluctuations in the model of FIR, does not give substantial improvement to the reproduction of the experimental features in Fig. 1. On the other hand, the existence of an intermixed layer at the GaSb/AlSb interface can have a strong influence on the SL "Reststrahlen" profile mainly because of the additional phonon resonances and the modification in the spatial configuration. Hence, we have included in the model of FIR the presence of an $Al_xGa_{1-x}Sb$ layer of thickness t at the interface. In this way we are considering one SL period as constituted by three layers of thicknesses d_1 (GaSb), d_2 (AlSb) and t ($Al_xGa_{1-x}Sb$)

TABLE II Data on the intermixing in GaSb/AlSb SL samples deduced by the fitting of FIR spectra. Here t and x indicate the average thickness and Al mole fraction of the $Al_xGa_{1-x}Sb$ layer at the interface. The percentage of intermixing is evaluated as $100\frac{t}{d_2+t}$.

sample	t (nm)	x	%
1	0.67	0.15	5
2	0.40	0.40	14
3	0.10	0.32	3

The sum $(d_1' + d_2' + t)$ and the ratio $\frac{d_1'+t}{d_2'+t}$ are fixed at the x-ray values of the period a and the ratio $\frac{d_1}{d_2}$ between the layer thicknesses, whereas the Al mole fraction x is left as a fitting parameter. The last parameter fixes also the alloy phonon frequencies according to the known dependence from the chemical composition [6]. The dotted line in Fig. 1 was calculated considering a 0.67nm thick $Al_{0.15}Ga_{0.85}Sb$ layer at each heterointerface. All spectral features of Fig. 1 are now satisfactory reproduced. A similar improvement is obtained also for samples 2 and 3. The best fit values of SL TO phonon frequencies are consistent with the moderate confinement and strain induced shifts calculated considering the measured structural parameters. Similar findings on the combined effects of strain and confinement on the LO phonon frequencies have been obtained from Raman scattering experiments [10, 11]. A detailed description of the fitting procedure will be reported elsewhere in a more extensive form. For the sake of the present discussion it is worth to list in Table II the fitting parameters concerning the intermixing.

The values of the Al mole fraction of Table II are close to the ratio $\frac{t}{d_2+t}$ between the x-ray thickness values. A simple explanation for this is that the chemical composition of the intermixing alloy layers is determined by the relative abundance of the Al and Ga atoms. Further a correlation appears between the percentage of intermixing and growth parameters such as the AlSb overall thickness, and the relative thickness between GaSb and

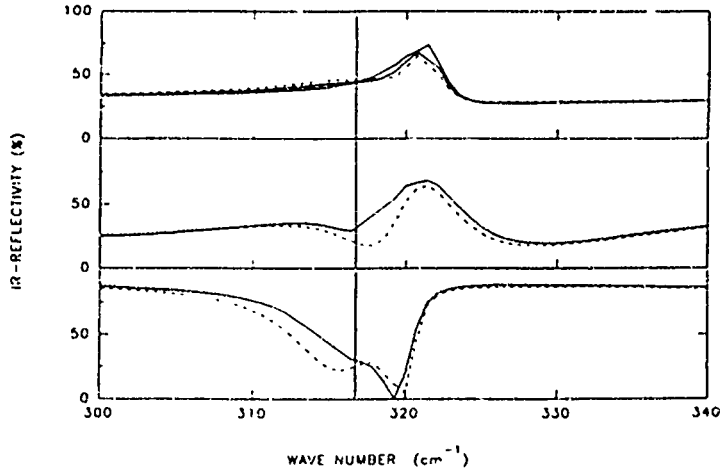

FIG. 3 AlSb-like "Reststrahlen" bands calculated for different values of plasmon frequencies (a) $\omega_p = 0$ (b) $\omega_p = 400cm^{-1}$ (c) $\omega_p = 800cm^{-1}$. Continuous lines: abrupt interfaces. Dashed lines: 5% intermixing at the interfaces. Dotted lines: 10% intermixing at the interfaces. The vertical line marks the AlSb-like TO frequency of the alloy.

AlSb layers For drawing more quantitative conclusions on this point the investigation of a larger number of samples is needed

Our previous analysis shows that intermixed layers as thin as a few tenths of nanometers intercalated in the SL matrix reveal themselves as clearly detectable structures in the reflectivity spectra of Fig 3. Indeed, the presence of a doped substrate, whose reflectivity behaviour resembles that of a metal, strongly enhances weak phonon resonances of the superlattice Figures 3a,b,c show the AlSb-like RS spectra calculated for different values of the substrate plasma frequency ω_p and the $Al_xGa_{1-x}Sb$ layer thickness, t The remaining parameters in the calculations are the same used for the fitting of the spectrum of sample 1 In Figure 3a we see that only very weak differences exist among the spectra corresponding to $\varepsilon_\infty = 0.3$, 2d 1.6 cm when $\omega_p \approx 0$, i.e for an undoped substrate In contrast, the "Reststrahlen" band lineshape changes dramatically in Fig 4b where a metallic behaviour is switched on by setting $\omega_p \approx 400 cm^{-1}$, close to the actual value of ω_p in sample 1 A strong dip appears on the low energy side of the AlSb-like band close to the TO frequency of the alloy By further increasing the doping level, i.e setting $\omega_p \approx 800 cm^{-1}$ causes a stronger modification of the whole spectrum which becomes absorptive-like in Fig 4c This behaviour closely resembles the reflectivity of a thin dielectric film deposited onto a metallic substrate [7]

In the case of samples 4 and 5, by considering the presence of only a thin intermixed layer at the interface gives no significant improvement in the reproduction of experimental data

The diffraction patterns of the superlattices deposited on GaAs substrate (samples 4 and 5) are characterized by much broader and weaker satellite peaks This indicates a large amount of defect formation and, particularly, a strong intermixing The structural deterioration in the above samples is mainly caused by the huge (~ 8%) lattice mismatch between GaAs and GaSb or AlSb layers

The above structural data induced us to model the SL as a sequence of two alternating $Al_xGa_{1-x}Sb$ and $Al_yGa_{1-y}Sb$ layers, with the Al mole fractions x and y close to the nominally pure layer values 0 and 1 The dotted curve in Fig 2 was calculated with x=0.1 and y=0.7 Since the spectral quality of the x-ray diffraction patterns is not good enough to allow the determination of the individual layer thicknesses in this case, they were fixed to the values of Table 1 which give the best reproduction of FIR spectra In spite of the roughness of the considered model a very satisfactory reproduction of all the spectral features is obtained In particular, the dips at 226.7 cm^{-1} and at 319.7 cm^{-1} which are peculiar of the GaSb-like and AlSb-like SL "Reststrahlen" bands, are now properly reproduced by the theory

IV CONCLUSION

Our results show that FIR is a powerful tool for the investigation of vibrational and structural properties of strained layer GaSb/AlSb superlattices In addition to strain and confinement effects on SL phonons, our analysis allows to obtain important information on the interface deterioration Taking advantage from the enhancement of weak SL phonon resonances induced by the metallic behaviour of the doped substrate, the chemical composition and the average thickness of $Al_xGa_{1-x}Sb$ alloy layers formed at the interfaces are determined X ray diffraction is insensitive to thickness and strain fluctuations in the structure It clearly emerges the close complementarity of the two techniques for the study of strain relaxation processes.

This work is partially supported by MURST and CNR

[1] K A Maslov, T J Parker, N Ray, D R Tilley, P J Dobson, D Hilton and C T B Foxon Solid State Commun 60 (6), (1986)
[2] Bo Lee, R.Sudharsanan, S Perkowitz, Phys Rev B38 2012 (1988)
[3] G.Scamarcio, L Tapfer, W König, and K Ploog Appl Phys A 51 282 (1990)
[4] G Scamarcio, L Tapfer, W Konig A Fisher K Ploog C. McLean, S Barosi P Giannozzi and S de Gironcoli Phs Rev B43, 14754 (1991)
[5] G Scamarcio,G Gonzalez M Silvestri and K Ploog, Solid State Commun 66, 757 (1988)
[6, B Samson T Dumelow A A Hamilton, T J Parker S R P Smith D R Tilley C T Foxon, D Hilton K J Moore Phys Rev B 46 2375 (1992)
[7] V M Agranovich and V E Kravtsov, Solid State Commun 55, 85 (1985)
[8] T Ohmori, Y Suzuki and H Okamoto, Jpn J Appl Phys 26 L637 (1988) J Appl Phys 66 6733 (1989)
[9] H , Goosman B A Davidson C J Gaultieri, G P Schwartz A F Macrander, S E Slusky, M H Grabow, and W A Sunder, J Appl Phys 66 1687, (1989)
[10] P V Santos, A K Sood M Cardona and K Ploog, Y Ohomori and H Okamoto Phys Rev B 37 6181 (1988)
[11] G P Schwartz, G J Gualtieri and W A Sunder,L A Farrow, Phys Rev B 38 4078 (1988) and references therein
[12] Y Suzuki Y Ohomori and H Okamoto, J Appl Phys 59 3760 (1986)
[13] L Tapfer Physica Scripta T25, 65 (1989)
[14] O E Pua Phys Rev B 38, 3637 (1987)
[15] see e.g B Jusserand and M Cardona in Topics in applied Physics vol 66 edited by M Cardona and G Guntherodt Springer Verlag Berlin
[16] Landolt Bornstein Numerical Data and Functional Relationships in Science and Technology ed O Madelung (Springer Verlag, Berlin 1982) Vol III 17 a
[17] D V Bert sse, Phys R v 130 2193 (1.63).

MoP17

Quantitative Analysis of Strain Relaxation and Mosaicity in Short Period Si_mGe_n Superlattices using Reciprocal Space Mapping by X-Ray Diffraction

E Koppensteiner[1], P Hamberger[1], G Bauer[1], V Holy[2], H.Kibbel[3], H.Presting[3], E.Kasper[3]
[1] Institut für Halbleiterphysik Johannes Kepler Universität, A-4040 Linz, Austria
[2] Department of Solid State Physics, Masaryk University, 61137 Brno, Czech Republic
[3] Daimler Benz AG, Forschungszentrum, D-7900 Ulm, Germany

Abstract

Double crystal and triple axis x ray diffractometry was used to characterize in detail the structural properties of several short period Si_9Ge_6 and Si_6Ge_4 superlattices grown by molecular beam epitaxy on thick step-graded SiGe alloy buffers resulting in reduced dislocation densities Precise strain data were extracted from two-dimensional reciprocal space maps around (004) and (224) reciprocal lattice points. Due to the much higher instrumental resolution of triple axis diffractometry Bragg reflection peaks from buffers and superlattices, which often overlap in such almost free-standing superlattices, have been clearly separated experimentally, and minute changes in strain status and mean Ge content are determined. From the distribution of diffusely scattered intensity around reciprocal lattice points the correlation function of the deformation field due to structural defects has been calculated using a model based on the kinematical theory of x-ray diffraction and on a formalism well known from statistical optics.

Introduction

The unique electronic properties [1-3] of ultrathin Si_mGe_n SLS's depend strongly on their structural perfection and the strain adjustment of the SLS's by a $Si_{1-x}Ge_x$ alloy buffer. A number of investigations was devoted to a study of the structural quality and stability of Si/Ge structures using mainly double crystal x-ray diffractometry (DCD) e.g [4]. Recently, the use of triple axis diffractometry (TAD) has been introduced for the structual analysis of complex epitaxial multilayer structures, which allows the determination of the distribution of diffusely scattered x-ray intensity around reciprocal lattice points (RELP's) [5,6]. If graded buffers are used, a reduction of the number of threading dislocations by 3 to 4 orders of magnitude has been reported to occur [7,8] employing transmission electron microscopy (TEM). As a consequence in such samples the luminescence efficiency is higher [1-3].

It is the purpose of this paper to investigate structural parameters in three nominally Si_9Ge_6 and one nominally Si_6Ge_4 short period SLS's grown on a 650 nm thick step graded SiGe alloy buffers, followed by an alloy buffer with constant Ge content (40%, 550 nm thick), with nominally the same structural parameters. We want to point out that the relative positions of the RELP maxima alone reflect the strain status and the Ge content in the corresponding layer, while the distribution of the intensity scattered diffusely around the RELP maximum yields detailed information on structural imperfections like strain gradients [9], mosaicity [10,11] and interface roughness [12]

A method has been developed for calculating the correlation function of the random deformation field due to structural defects in heteroepitaxial layers and SLS's from measurements of diffuse x-ray scattering (DXS) [11,12] This method is applied to the DXS from Si/Ge SLS's by calculating the correlation function, and estimating the parameters of the defects. Calculated results based on a mosaic block model are compared to estimates of the size of regions which scatter coherently [13] and to estimates of the total dislocation densities [14] For the latter, the FWHM's of x-ray diffractograms are used, whereas in the new approach the entire DXS distribution around the RELP maxima is compared to calulated data

Strain analysis based on reciprocal space mapping

The principle of reciprocal space mapping as well as the procedure for a precise determination of the strain status of the buffer and SLS layers and of the thicknesses of the SLS constituating layers is described briefly, following Ref [6]. A reciprocal space map is performed by measuring a number of $\omega/2\Theta$ scans (along the vector $q_{\parallel}[hkl]$ for a (hkl) reflection) for different ω offsets (ω-scan direction: near RELP perpendicular to $q_{\parallel}[hkl]$ in reciprocal space, where ω denotes the angle between sample surface and incident beam, and 2Θ the angle between incident and diffracted beams). The center of the [001] oriented Si substrate reflection is used as an internal standard, since the thick substrate is assumed to be unstrained and undistorted. If an SLS grows pseudomorphically on the substrate, in both symmetric (001) and asymmetric (hkl) reflections the central SLS RELP SL0 lies along the line $q_{\parallel}[00l]$ through the substrate RELP maximum in reciprocal space. If the superlattice is completely free-standing from underlying layers (i.e., strain-symmetrized, theoretical critical SLS thickness is infinite), the relative position of the SL0 RELP maximum lies along the direction $q_{\parallel}[hkl]$ through the substrate RELP maximum for both symmetric and asymmetric reflections. Finally, if a SLS is partially relaxed, the position of the SL0 RELP maximum lies in between the two extreme positions described above in reciprocal space, and from its angular deviations from the (known) position of the substrate RELP maximum in ω and $\omega/2\Theta$ scan direction, both the inplane lattice constant $a_{p,SL}$ and the vertical lattice constant $a_{n,SL}$ in growth direction are determined independently from each other and without any assumptions on elastic constants. In a Si/Ge SLS, where the individual layer thicknesses are below the critical layer thicknesses, the assumption $a_{p,SL} = a_{p,Si} = a_{p,Ge}$ holds. Since the strain status of the individual layers in a Si/Ge superlattice is obtained as described, and the SLS period is determined form the angular deviation of higher order SLS peaks (denoted by SL+1, SL-3, etc.), the only free parameter in a simulation of a diffractogram from this structure is the relative thickness ratio of the Si and Ge layers in the SLS, which thus can be determined unambiguously.

The samples studied in this work are three nominally Si_9Ge_6 SLS's grown at T_g=500°C (sample A), 470°C (sample B) and 450°C (sample C), and one nominally Si_6Ge_4 SLS (sample D, T_g=500°C), which are all grown on nominally the same buffers consisting of two parts. The first part is a graded SiGe alloy layer (graded buffer B1: Ge content increases by 3% each 50 nm up to 39%, 650 nm thick, T_g reduced cotinuously from 650 to 520°C), and the second part consists of a $Si_{0.6}Ge_{0.4}$ alloy layer (buffer B2, 550 nm thick, T_g=500°C). In the case of almost free-standing superlattices grown on almost fully relaxed buffers B2 on top of fully relaxed graded buffers B1, as it is the case for samples A-D (see Tab.I), the SL0 and B2 RELP's are lying very close together in reciprocal space. In order to separate these RELP's experimentally, which is essenual for avoiding uncertainities in the strain analysis outlined above, it is *necessary* to use triple axis diffractometry which offers an about 15 times higher instrumental resolution as compared to DCD (see Figs. 1 and 2). The diffractometer (Philips MRD) uses $CuK_{\alpha 1}$ radiation, a Bartels-type 4-crystal monochromator in the Ge(220) monochromator setting in the primary beam, and in the diffracted beam either a slit with a detector opening angle of *180* arcsec (DCD optics) or a two-reflection Ge(220) channel-cut analyser crystal (TAD optics, detector opening angle *12* arcsec).

Figure 1 clearly shows the peak separation between SL0 (smaller peak) and buffer B2 Bragg reflecuons in $\omega/2\Theta$ scans using TAD in comparison to DCD measurements of the three Si_9Ge_6 samples A-C. The reflections from the graded buffer part B1 are extended over the angular region between B2 and Si substrate. In the TAD reciprocal space maps shown in Fig 2 the reflections from B1 are not visible because of their low intensity and the higher scan speed (0.5 seconds per 0.003 degree step) used for two-dimensional reciprocal space mapping compared to one-dimensional TAD measurements (2-4 s / step). In Fig 2 symmetrical (004) (a) and asymmetrical (224) (b) reciprocal space maps are shown, in which the different distances of SL0 and B2 from the Si RELP indicate slight changes both in strain status and mean Ge content in the three samples. Mere inspection of the relative positions of the Si, B2 and SL0 RELP extrema in the (224) map indicates that not only the Ge content of the SLS in sample C is different from that of

the buffer B2. B2 is fully almost relaxed (see Tab I, $a_p = a_n$), however, since the center of SL0 does not coincide with the line $q_{\parallel}[224]$ through the Si RELP maximum, the whole SLS stack is under slight biaxial compression. The in-plane lattice constants of the SLS's are a useful measure for the degree of strain-symmetrization within the SLS's. The higher the values of a_p, the better the strain-distribution in these structures: a perfect strain-symmetrized Si_9Ge_6 as well as a perfect Si_6Ge_4 SLS would have a in-plane lattice constant of 5.514 Å (calculated from minimum of elastic energy stored, using values for elastic constants from Ref.[15]), the measured in-plane lattice constants in the structures investigated are 5.509 Å (sample A), 5.502 Å (B), 5.503 Å (C), and 5.504 Å (D), respectively. Further structural parameters determined from (004) and (224) TAD reciprocal space maps are listed in Tab I

Tab I: Structural parameters, layer strains and relative thicknesses in samples A to D.

sample	T_g (°C)	layer	a_p (Å)	$\varepsilon_{p(SL)}$ (%)	a_n (Å)	$\varepsilon_{n(SL)}$ (%)	$a_{n,SL}$ (Å)	mono-layers	t(Si/Ge	xGe	D_{SL} (Å)
A	500	Si	5.509	+1.44	5.371	-1.11	5.526	9.18	1.58	0.386	22.02
100x	"	Ge	5.509	-2.63	5.770	+1.98		5.82			
Si_9Ge_6	"	B2	5.509	-	5.526	-	-	-	-	0.386	5500
B	470	Si	5.502	+1.31	5.376	-1.01	5.528	9.40	1.63	0.380	23.57
100x	"	Ge	5.502	-2.75	5.775	+2.07		5.70			
Si_9Ge_6	"	B2	5.501	-	5.519	-	-	-	-	0.370	5500
C	450	Si	5.503	+1.32	5.375	-1.03	5.531	9.15	1.56	0.385	23.96
100x	"	Ge	5.503	-2.74	5.774	+2.05		5.85			
Si_9Ge_6	"	B2	5.502	-	5.518	-	-	-	-	0.370	5500
D	500	Si	5.504	+1.34	5.375	-1.03	5.520	7.5	1.74	0.364	15.87
100x	"	Ge	5.504	-2.72	5.774	+2.05		4.3			
Si_6Ge_4	"	B2	5.504	-	5.519	-	-	-	-	0.364	5500

Correlation function of the deformation field

Assuming the kinematical approximation and the two-wave case, the following equation for the diffusely scattered intensity I as a function of the coordinates q_x and q_z was derived [11] for a point in the plane of diffraction in reciprocal space:

$$I(q_x,q_z) = |D_{inc}\, \pi\, K / \gamma_h|^2 \int_{-\infty}^{+\infty} d(X\text{-}X') \int_0^t dz \int_0^t dz'\, \chi_h(z)\, \chi_h(z')^* \times$$
$$\times \exp\{2\pi i[q_x(X\text{-}X') + q_z(z\text{-}z')]\} \exp[-\mu(z+z')]\, G(X\text{-}X', 0, z\text{-}z') \qquad (1)$$

The coordinate system choosen in real space (x, z, x_1, x_2) and in reciprocal space (q_x, q_z, q_1, q_2) is shown in Fig 3, where 0 is the origin (000) of reciprocal space, H is a reciprocal lattice point with the Miller indices (hkl), $\mathbf{k_0}$ and $\mathbf{k_h}$ are the wave vectors of the incident and the diffracted beams, and h is the diffraction vector. In Eq.1 D_{inc} is the amplitude of the incident wave, K is the length of wave vector in vacuum ($1/\lambda$, λ: x-ray wavelength), $\gamma_h = \cos(\varphi_h)$ and $\gamma_0 = \cos(\varphi_0)$ are the direction cosines of the incident and the diffracted waves with respect to the internal surface normal n. χ_h and χ_0 are the h-th and 0 th Fourier components of the polarizability of the perfect crystal including the polarization factor, the asterisk denotes the complex conjugate. For an SLS, $\chi_h(z)$ is a periodic function of z which can be expanded into a Fourier series [12].

$$\chi_h(z) = \sum_H \chi_{hH} \exp(-2\pi i\, H\, z) \qquad (2)$$

where H = m/D, m is an integer (the diffraction satellite order) and D is the SLS period The term which depends opn the effective absorption coeffic-ent $\mu = \pi K\ Im(\chi_0)(1/\gamma_h - 1/\gamma_0)$ describes the influence of absorption . The first integral is performed for the distance in the x-coordinates X and X´ of two observation points R = (X,Y,0) and R´ = (X´,Y´,0) lying on the crystal surface along the lines $I_h(R)$ and $I_h(R')$ (Fig 3a). The latter are parallel to k_h and connect r = (x, y, z) and r´= (x´, y´, z´) within the layer (thickness t). r and r´ mark the positions from which the two scattered beamlets originate G denotes the correlation function of the random deformation field on the crystal surface [10] Using this optical coherence approach, for volume defects like mosaic blocks we assume the random deformation field in the layer to be statistically homogeneous, and $G(r,r') = G(r - r')$ holds Assuming a certain defect model, Eq.1 is used to simulate the measured DXS intensity distribution in the vicinity of RELP's

In the following we show that this correlation function of the atomic displacements u can be calculated *directly* from the measured DXS intensity This procedure represents a significant simplification of the numerical analysis Calculating the Fourier transformation $I(x_0, z_0)$ of $I(q_x, q_z)$ we obtain

$$I(x_0, z_0) = G(x_0, 0, z_0)\, R(z_0), \tag{3}$$

where $R(z_0)$ represents the Fourier transformation of the reflection curve of the perfect structure Equation 3 means that the correlation function G of the random deformation field due to defects equals the Fourier transformation of the (measured) distribution of the diffusely scattered intensity near a RELP *divided* by the Fourier transformation of the reflection from the perfect structure This approach is similar to the Patterson analysis well known from statistical optics, with the Fourier transformation of the DXS intensity treated as the Patterson function In the case, where mosaic blocks are the main reason for the defect deformation field G, the DXS does not depend on the satellite order, and the DXS intensity is centrosymmetric with respect to the RELP We assume the coherence of crystallographic net planes to be completely destroyed, if two points r and r´ are lying in two different blocks, and that the mosaic blocks are rotated with respect to each other Then

$$G(r - r') = P(r - r') \exp[-2/3\ (\pi h \Delta (x_2 - x_2'))^2], \tag{4}$$

where $P(r - r')$ is the probability of finding both points r and r´ in the same block (which depends on the block size), Δ is the root mean square misorientation of the blocks For the derivation of Eq 4 we have assumed that the static Debye-Waller factor is much smaller than unity In the case of blocks with diameter 2R, both the contours of the DXS distribution as well as the contours of constant G are ellipses with the main axes q_1, x_1 and q_2, x_2, respectively

If the mosaic blocks are the dominant defects, then the block size 2R should not depend on the Bragg angle Θ of the particular RELP around which the DXS intensity has been measured A random elastic deformation within different mosaic blocks (i.e. microstrain) would lead to smaller values for 2R for RELP's measured at larger Bragg angles Θ [11] The true block diameter is then obtained by extrapolating to $\Theta = 0$ If random elastic deformation dominates in comparison to mosaic blocks, then in asymmetric Bragg reflections (i.e. for lattice planes tilted with respect to the sample surface) the main axes of the ellipses arising from DXS are no longer perpendicular and parallel to h, however, the DXS intensity is still centrosymmetric We want to emphasize, that the DXS intensity around a central superlattice peak (SL0) is not sensitive to interface roughness

Discussion

The whole analysis of the structural defects and the strain status described so far is based on the assumption that RELP contours or at least RELP maxima arising from different portions of the heterostructure are well separated experimentally in the plane of diffraction in reciprocal space

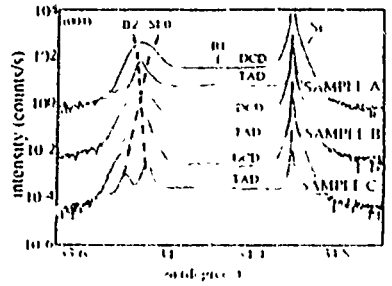

Fig 1 Double crystal (DCD) and triple axis (TAD) (004) $\omega/2\Theta$ scans of samples A, B and C For B and C, DCD and TAD measurements were shifted along the intensity axis by a factor of 100, respectively

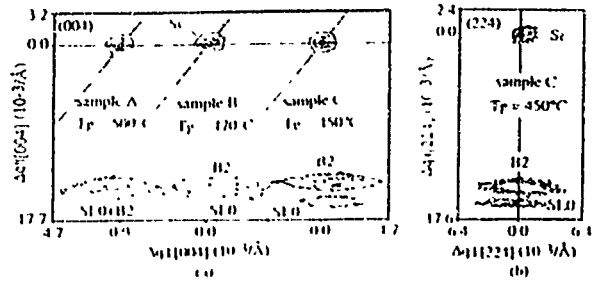

Fig 2 Triple axis reciprocal space maps in the vicinity of (004) (a) and (224) (b) substrate (Si), top buffer (constant Ge content, B2) and central superlattice (SL0) reciprocal lattice points of samples A to C as indicated Iso intensity contours are plotted at 1, 2, 5, 10, 20, 50,100, and 1000 counts / s The reflection from the graded buffer B1 is not visible because of the low intensity

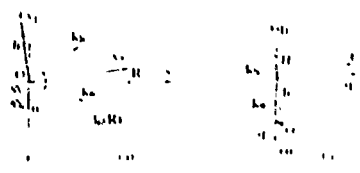

Fig 3 Definition of the coordinate axes in real space (a) and reciprocal space (b)

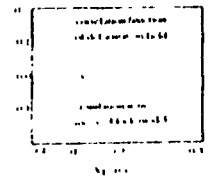

Fig 4 Calculated correlation function and simulation assuming a mosaic block model for central superlattice peak SL0 in sample C

The samples studied here consist of almost free-standing superlattices grown on almost fully relaxed buffers B2, the reflections of which are lying very close together in reciprocal space and are separated experimentally much better from each other in TAD than in DCD measurements.

The shape of iso-intensity contours around these RELP's is centrosymmetric (if the RELP's do not overlap, e.g.in sample C), and therefore no strain gradient exists [9] in the top buffer part B2 and the SLS. The distribution of diffusely scattered intensity in the vicinity of the B2 and SL0 RELP maxima is similar in all samples (as evident from the FWHM's, which are the same within the accuracy of ±10 arcsec), indicating similar defect structures, but only in sample C the SL0 and B2 intensity distributions are *fully* separated from each other. For sample C the intensity distribution around both the (004) SL0 and B2 RELP's measured by TAD has been used to calculate the correlation function of the deformation field (Fig.4), which has been simulated on the basis of the mosaic block model explaining the shape of the contour maps. For the SLS and the buffer with constant Ge content B2, the mean block size turns out to be of the order of 310 and 390 nm in diameter, respectively, and the mean misorientation of the mosaic blocks with respect to growth direction is 370 and 360 arcsec, respectively. Using the measured FWHM's of 110 arcsec and 140 arcsec to estimate the size of coherently scattering regions using Scherrer's equation [13], values of 313 nm and 246 nm are obtained for B2 and SLS, which is in good agreement with the values found for 2R assuming the mosaic block model. The resulting dislocation density from the FWHM values would be 2.2×10^7 and 3.5×10^7 cm^{-2} following the approximation in Ref.[14] and using a Burger s vector of 3.8Å. This dislocation density is about one order of magnitude larger than that found by TEM [16].

Assuming the mosaic block model for a simulation of the correlation function G in these structures, it turns out that the average size of mosaic blocks would be larger than the thickness of the SLS, and that a wall between mosaic blocks (with a dislocation density of about 10^9cm^{-2}, calculated from the mean Δ) would consist of only one dislocation over the SLS and only a few dislocations would pile up over the buffer B2 thickness. The pile-up of dislocations having the same Burger's vector (i.e., originating from the same dislocation source), which leads to a mosaic block-like structure, has been observed previously [5,8]. We conclude therefore that the more pronounced mosaicity of the underlying graded buffer B1, which is evident from the about 50% larger values of the FWHM in the direction perpendicular to q‖[004] of the B1 RELP compared to that of the B2 [6], still influences the defect structure of the layers above. However, the mosaic block model is just one possible explanation for the shape of the DXS intensity. Another model is based on a random elastic deformation field, which may play a role in the buffer B2 in these samples. This is indicated by a slight deviation of the main axes of the elliptical contours of the DXS intensity around the asymmetrical (224) B2 RELP from being parallel and perpendicular to q‖[224] (Fig.2b). Such an effect should not occur if the defect structure would be determined entirely by mosaicity. If this slight tilt is ignored and if the validity of the mosaic block model is asumed, the (224) Bragg reflection RELP data for buffer B2 were fitted. The values of 2R=350 arsec and Δ=360 arsec were obtained. The value for 2R increases slightly with decreasing Bragg angle Θ which indicates a certain influence of random deformation on the results. Unfortunately the diffracted intensity from the (224) SL0 RELP was too low for performing such an analysis. The TEM data of sample A show that in the SLS for distances which are one μm apart from each other a few dislocations appear [16], which is not too different from the average values found here (for each 350 nm one dislocation) for sample C.

Conclusions

We show that triple axis diffractometry gives precise information on the strain status in complex multilayer structures, especially in the case of overlapping Bragg-diffraction peaks from MBE grown, strain-symmetrized Si_9Ge_6 and Si_6Ge_4 short period superlattices and from underlying buffers. In addition, reciprocal space maps yield the shape of isointensity contours of scattered radiation, from which - for the first time for Si/Ge structures - information on the correlation function of the deformation field due to structural defects is obtained. The latter can be expressed in terms of two statistical parameters assuming a defect model.

Acknowledgements: Work supported by ESPRIT Basic Research Action 7128, FWF Project No 9119PHY and Jubiläumsfonds der Österreichischen Nationalbank Project No 4542

References

1. For a recent review see e.g. W. Press1ng, A. Kibbel, M. Jaros, R.M.Turton,U.Menczigar, G Abstreiter, and H G.Grimmeiss, Semicond.Sci.Technol. 7, 1127 (1992)
2. J.Olajos, J.Engvall, H.G Grimmeiss, U.Menczigar, G Abstreiter, H Kibbel, E.Kasper, and H Presting, Phys Rev.B 46, 12857 (1992).
3. J Engvall, J Olajos, H.G.Grimmeiss, H.Presting, H Kibbel, E.Kasper, Appl.Phys Lett. in print.
4. D C.Houghton, D.D Perovic, J M Baribeau, and G.Weatherly, J Appl.Phys. 67,1850 (1990).
5. P F Fewster, J Appl.Cryst. 22, 64 (1989); 24, 178 (1991)
6. E.Koppensteiner, P.Hamberger, G Bauer, A Pesek, H Kibbel, H Presting, and E Kasper Appl.Phys.Lett 62 (15) 1783 (1993).
7. E A Fitzgerald, Y.-H.Xie, M L.Green, D.Brasen, A R Kortan, J Mschel, Y -J. Mii, and B E.Weir, Appl.Phys.Lett. 59 811 (1991).
8. W Jäger, D Stenkamp, P Ehrhardt, K.Leifer, W.Sybertz, H Kibbel, H Presting, and E Kasper, Thin Solid Films, 222(1992) 221.
9. E.Koppensteiner, G.Springholz, P.Hamberger, and G Bauer, J.Appl Phys., submitted
10. V Holy, J.Kubena, E.Abramof , A Pesek and E.Koppensteiner, J.Phys.D· Appl Phys 26 A146 (1993).
11. V Holy, E Koppensteiner, K Wolf, and M.Kastner, J.Appl.Crystallography submitted
12. V Holy , J Kubena and K Ploog, Superlattices and Microstruct. 12, 25 (1992)
13. D Scherrer, Göttinger Nachrichten, 3, 98(1918)
14. P Gay, P B.Hirsch, A Kelly, Acta Metall 1, 315 (1953).
15. A Segmüller and M Murakami, "Treatise on Materials Science and Technology", eds K N Tu, R Rosenberg, Academic Press, N Y. 1988, Vol.27, pp113
16. W Jäger, E Kasper, private communication

MoP18

Evidence of non-commutativity of band discontinuities in InP-Al(In)As-Ga(In)As heterostructures

E. Lugagne-Delpon*, J.P. André**, and P. Voisin*

*Laboratoire de Physique de la Matière Condensée de l'Ecole Normale Supérieure
24 rue Lhomond F 75005 Paris, France

**Laboratoire d'Electronique Philips
22 Avenue Descartes, F 94453 Limeil-Brévannes Cedex, France

Abstract

In spite of the spatial separation of electrons and holes associated with its type II nature, the InP-Al(In)As system has excellent optical properties. In particular, it is possible to measure the photo-luminescence excitation and photo-current spectra in single hetero-junctions. In addition, the bandgap of a type II heterostructure varies linearly with the discontinuity of the conduction bands. This system thus offers a unique opportunity for a detailed experimental study of the band offsets. We find that offsets at InP-Al(In)As and Al(In)As-InP heterojunctions are quite reproducible, but differ by (100 ± 20 meV). It also appears that the average band offset is not transitive in the Ga(In)As-InP-Al(In)As family of heterostructures.

The basic problem of band discontinuities at a semiconductor-to-semiconductor contact has been a hotly contested topic [1-3] for the last twenty years. On one hand, there exist "global" approaches based on the assumption of a reference energy level, absolute like the vacuum level in the old electron affinity rule or the valence band extremum in Harrison's tight binding theory [4], or relative to the bulk material like the "charge neutrality level" introduced by Tejedor et al. [5] and by Tersoff [6]. Such approaches have built-in properties of commutativity and transitivity. More recently, super-computers have allowed a number of ab-initio calculation methods in which the redistribution of electronic charges at interface chemical bonds is evaluated for the actual atomic distribution [2,3,7]. In these approaches, band offset commutativity and transitivity are not imposed, but may actually appear as a de-facto result of numerical calculations. Also, it was proved already long ago that the deliberate (or non) introduction of a dipole layer, for instance by localized doping or addition of a chemical layer, will modify the measured band offset in a given system [8], which implies that in some circumstances, band offsets might not be an intrinsic property of an heterojunction. Finally, evidences of band offset asymmetry were recently reported by Landesman et al. [9] for the InP-$Ga_{0.47}In_{0.53}As$ interfaces from photo emission studies. However, there are considerable difficulties in characterizing properly the composition of ultra-thin semiconductor layers involved in such measurements, and more complete investigations are certainly necessary. In fact the experimental difficulty of measuring band offsets is such that until recently the commutativity of band offsets, ie the equivalence of the intrinsic A-B and B-A interfaces, has not been seriously questionned by the community of quantum well physicists who generally consider that semiconductor quantum wells are reasonably symmetric. The main reason why such a basic question remains open is that the majority of heterolayers which have been investigated in some details are of the type I, ie electron and holes are confined within the same layers. In this case, interband optical properties are rather insensitive to the value of the band offset ratio $\Delta E_c/\Delta E_v$, the consideration of uncertainties in the material or quantum well parameters and of the limited accuracy of theoretical models themselves explains surprising large fluctuations in the reported values. On the opposite, the band gap of a type II heterostructure (in which electrons and holes are confined in the adjacent layers) depends nearly linearly on the value of the conduction band offset,

and simple optical measurements should allow a direct and precise evaluation of the band offsets. Unfortunately, the type II systems investigated earlier in some details, the InAs-GaSb and Ge-GeSi systems and the GaAs-AlAs short period superlattices, have a number of intricate characteristics which make the analysis of a single heterojunction rather difficult.

Recently, we realized that the almost unexplored InP-Al(In)As system [10-12], which presents a regular type II configuration with electrons confined in InP and holes in Al(In)As, has excellent optical properties which allow direct spectroscopic measurements on single interfaces [13], using various experimental methods like photoluminescence (PL), photoluminescence excitation (PLE) or photo-current (PC) spectroscopies. Here we report a set of observations on the "direct" InP-Al(In)As and "inverse" Al(In)As-InP heterojunctions, as well as on multiquantum well structures. These results evidence that direct and inverse band-offsets are quite reproducible, but differ by as much as 100 meV, which contradicts recently reported theoretical results [3,14,15]. We finally discuss the issue of band offset transitivity in the trilogy of the Ga(In)As-InP, Ga(In)As-Al(In)As and InP-Al(In)As systems.

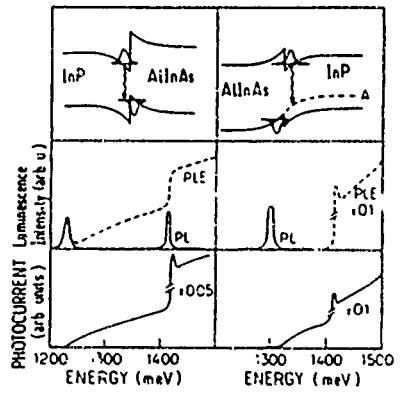

Fig. 1 (a)Low temperature PL, PLE and PC spectra for the "direct" InP-Al(In)As interface sketched in the insert. (b) same spectra for the "inverse" Al(In)As-InP interface.

All our samples were grown by atmospheric pressure metal-organic chemical vapor deposition (MOCVD) on n-doped InP substrates. They were characterized by X-ray double diffraction, which yields the precise value of $Al_xIn_{1-x}As$ composition x, a crucial parameter for this study since the bandgap of this alloy varies quite rapidly: $E_g^{Al_xIn_{1-x}As}$ (meV) = 1520 + 27 $(x-x_0)$, where x_0=0.48 is the composition of the alloy lattice matched to InP. Electrical measurements on thick layers show that Al(In)As (InP) has a n-type residual doping in the 10^{16} cm^{-3} (10^{14} cm^{-3}) range. Figure 1a shows low temperature (2K) PL, PLE and PC spectra of a sample consisting in a single 1000Å thick $Al_{0.53}In_{0.47}As$ layer (4.8 % Al-rich compared to the lattice-matched alloy) grown on undoped epitaxial InP. The luminescence consists in a single line, remarkably intense, ≈30 meV broad and centered at 1.23 eV, well below both InP (1.42 eV) and Al(In)As (1.65 eV) bandgaps. This luminescence has a short decay time (a few ns) and gives rise to an absorption gap at nearly the same energy, as can be observed in both the PLE and PC [16] spectra. Absorption occurs between valence states localized in Al(In)As and conduction states localized in InP, as shown schematically in the insert. In fact, these states are confined close to the interface by the band bending resulting from the charge transfer of electrons from Al(In)As to InP, which probably helps the absorption. The smooth absorption profile is thought to result from the combination of i) absence of parity selection rule for the absorption thence, many different

subbands can contribute to the absorption), ii) ≈30 meV inhomogeneous broadening mainly due to ≈1% long range fluctuations of alloy composition, and iii) weakness of exciton binding energy due to electron hole spatial separation. It is noteworthy that our excitation source is an halogen lamp followed by a grating monochromator, with a maximum power of 50 μW only, and that estimates of the wavefunction overlap indicate an absorption of a few 10^{-4}. Observation of a PLE spectrum in these conditions witnesses the very high radiative efficiency of this type II system. The heterojunction bandgap is equal to the Al(In)As bandgap $E_g^{Al(In)As}$ (1.65 eV, as observed directly in extended PLE and PC spectra) minus the conduction band offset ΔE_c plus the sum of electron and hole confinement energies E1 and H1. Precise estimates of these confinement energies in the absence of complete electrical characterization are impossible, but 50 ± 20 meV should be a representative figure and a comfortable error bar for H1+E1 [17]. Hence, these data give a rather precise value of ΔE_c for this system, ΔE_c = 460 ± 20 meV.

Figure 1b shows the same PL, PLE and PC spectra observed on a different structure consisting of a 1000 Å thick $Al_{0.52}In_{0.47}As$ layer grown on a GaInAs buffer (to avoid the presence of the direct interface), and topped with a thick InP layer. An intense luminescence line is also observed in this sample, but at a significantly larger energy, 1.3 eV, and with a completely different qualitative behavior: it has a very long decay time (non-exponential, with a characteristic time of 1μs), and does not give rise to any absorption below InP bandgap. This luminescence is in fact most likely associated with the presence of a deep acceptor which appears systematically in InP grown by MOCVD on thick As-based alloys. We have observed a similar luminescence in InP grown on thick GaInAs layers. Yet, the fact that no luminescence related to the interface can be observed is strange enough, and indicates that the interface transition is at a somewhat higher energy. Indeed, the PC spectrum shows a well defined absorption gap at 1.32 eV, with a lineshape and an absolute value of the photo-current similar to those of Fig. 1a. This absorption gap, certainly associated with the interface transition, indicates that the offset at this inverse interface is considerably larger than the one at the direct interface. Since the Al(In)As composition is nearly the same for the two samples, and since band-bending effects cannot account for such a large difference, these data are a rather strong evidence that the direct offset (≈460 meV) and the inverse offset (≈360 meV) are intrinsically different. We would like to stress that these behaviors of direct and inverse interfaces, both qualitatively and quantitatively, are observed in all the samples (eight) that we have investigated so far.

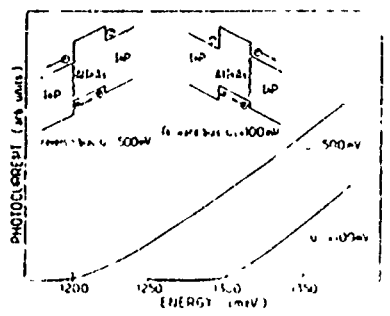

Fig 2. Low temperature PC spectra for a InP-Al(In)As-InP heterostructure. As illustrated in the insert, the direct interface is observed in reverse bias, and the inverse one in forward bias. In both cases, above a bias threshold of a few hundred mV, the PC spectrum becomes independent of the applied voltage.

An additional evidence is obtained from photocurrent spectra of a structure consisting in a 3000 Å thick $Al_{0.5}In_{0.5}As$ layer embedded between thick epitaxial InP layers, displayed in Fig. 2. As illustrated in the insert, in the forward bias the inverse interface contributes directly to the photocurrent, while the contribution of the direct interface is inhibited by the large potential barrier

that carriers have to overcome, and vice versa for the reverse bias: we thus expect, and do observe the direct interface in reverse bias and the inverse one in forward bias. Here, the Al(In)As layer is the same, and electrical properties of the interfaces cannot differ significantly. From this, and from the general consistency of the whole set of data, we thus conclude that the 100 meV difference between the two interface transitions directly reflects a reproducible difference of the band offsets. Recently, the offset at the inverse interface has been measured by photo-emission spectroscopy [18], a method which has been rather successful in measuring band offsets in contested cases [19]. In these experiments, the ultra-thin InP layer was grown by MBE, and the reported offset is quite consistent with our result for the inverse interface. Conversely, our data for the direct interface and for multi quantum wells (see below) agree with the recently reported photo-luminescence data [11,12], which indicate an offset ΔE_c≈400 meV.

The microscopic reason for this strong asymmetry is still unknown, and we can only add a few heuristic remarks. As discussed by several groups [3,15], the driving force for a strong intrinsic asymmetry is that chemical bonds at the two interfaces are completely different because the materials share no common atom. Ideally, the direct interface is predominantly built with P-(Al,In) bonds (shorter than the regular bonds), while the inverse one is primarily built with As-In bonds (longer than the regular bonds). Therefore, strain and chemical-dipole contributions to the band offset may differ appreciably, and for instance Foulon and Priester [15] do predict an offset asymmetry of 50 meV for this system. However, it has been shown that exchange mechanisms [20] occur at the growing interface, and in particular that P atoms at the surface, due to their smaller sticking coefficient, may be replaced by As atoms as soon as AsH_4 is substituted to PH_4 in the reactor atmosphere [21]. If such a mechanism prevails, it should at first symmetrize the interfaces! On the other hand, if several monolayers are affected by these exchange mechanisms (as suggested by Brasil et al. [12]), this may result in non-symmetric interface non-stoechiometries. Conversely, it could be argued that the observed asymmetry is rather due to the reproducible presence of different defects at the interfaces. The observation of a specific deep acceptor level in InP grown on As-based layers indicates the possibility of such differences. However, since the long recombination time indicates a rather low density, it is unlikely that the dopant density may be large enough to affect the band offset. We rather expect that only a moderate increase of the band-bending effect would result from this possible p-type doping [22]. Another important issue is the interface sharpness. X-ray diffraction data for short period InP-Al(In)As superlattices [13] indicate that the composition modulation is quite sharp, and the observation of quantitatively comparable PC signals from the two interfaces (see Fig. 2) proves that the electron-hole wavefunction overlaps are similar, which rules out a strong sharpness asymmetry.

The offset asymmetry has important consequences for the optical properties of InP-Al(In)As superlattices. As illustrated in the insert of Fig. 3, to avoid the building-up of a macroscopic potential, the system has to create a built-in electric field by accumulating electric charges near the terminating planes, a classical mechanism which cancels the quantum potential difference associated with the sum of band offset differences [23]. Calculations of the energy band structure and optical absorption for the structure depicted in the insert show that for reasonably narrow quantum wells, everything behaves nearly as if the offsets were symmetric, with the average value. We have examined the optical properties of a number of superlattices, grown in slightly different conditions and having slightly different alloy compositions. From the fit of their observed bandgaps we determine the variation of the average offset with $Al_xIn_{1-x}As$ composition, as shown in Fig. 3. With a remarkably small dispersion of the data points we get $\langle\Delta E_c\rangle$ (meV) = (410±20 +1500 δx), where δx is the deviation from the lattice-matched composition x_0= 0.48. These results thus give a precise value of $\langle\Delta E_c\rangle$ = 410 ± 20 meV for the lattice-matched system.

There exists a general consensus for the offsets in the GaInAs-InP ($\langle\Delta E_c\rangle$ = 260 ± 20 meV) and GaInAs-AlInAs ($\langle\Delta E_c\rangle$ = 500 ± 50 meV) systems which have been extensively studied because of their technological importance [24]. Both core level emission and electrical measurements on single heterojunctions, and optical properties of quantum well structures (which, as underlined above, are sensitive to the average band offset) seem to agree in these cases, although some recent measurements contradict this unanimity [9]. Our results indicate that band offsets are

not transitive in this group of materials, since transitivity requires $<\Delta E_c>$ = 240 meV for the InP-AlInAs system

Finally, it should be noted that the average offset dependence observed in short period SLs does not perfectly fit the data in single heterojunctions, for which the average offset is somewhat smaller. We recently studied [25] a structure with 4% In-rich Al(In)As. This structure shows exactly the same qualitative behavior as the Al-rich sample of Figs. 1 and 2, and we find that the measured composition dependence of the average offset for single heterojunctions would be well fitted by the 15 meV/% law, but with $<\Delta E_c>$ = 370 ± 20 meV for the lattice-matched system. This ≈40meV difference with respect to superlattices remains within the error bars, but could also be significant and reflect a physical effect. Among possible causes for this observation, the role of plastic relaxation should be considered: for the lattice mismatch and layer thicknesses involved in our Al-rich heterojunctions, the plastic relaxation of the layers is almost complete (as proved by the comparison of X-ray and optical data of the hosts), while for our short period superlattices, the small lattice mismatch is accommodated by elastic strain. For a given composition, the offsets might be slightly different for strained and relaxed layers.

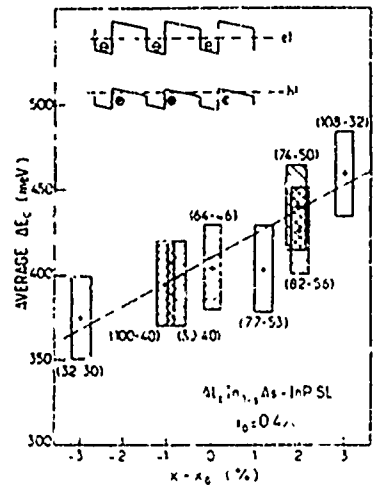

Fig. 3 Measured average offset for a series of short period Al(In)As-InP superlattices. Respective Al(In)As and InP layer thicknesses (as indicated for each sample) are in the 30-100 Å range, which ensures that band bending corrections are negligible. Calculations for the potential profile shown in the insert prove that optical properties are essentially sensitive to the average band offset.

In conclusion, from a number of highly consistent observations, we find that band offsets are simultaneously reproducible and non-commutative in the InP-Al(In)As heterojunctions, and non-transitive in the InP-Al(In)As, Ga(In)As-InP, and Ga(In)As-Al(In)As family of heterostructures. The microscopic origin of these effects is not fully established, and a more detailed knowledge of the chemical and structural properties of these interfaces is certainly needed to assert whether the leading term is the difference in strain and dipole contributions or the effect of non-stoechiometric interfaces. Yet, these properties are established with an unprecedented accuracy thanks to the type II nature of the InP-Al(In)As system, which allow, for the first time, direct spectroscopic investigations of single heterojunctions. This should stimulate a new interest in the comparison of theoretical and experimental results on heterojunction band discontinuities. The direct observation of single heterojunction optical properties also opens new areas of investigations like the dependence on the growth method or the effect of intermixing on the band offsets, for which there exists contradictory and unverified theoretical predictions.

Acknowlegements: LPMC-ENS is Unité Associée at CNRS N° 1437. This work is supported by PIRMAT / DRET / DRED.

References

1 For a review, see "heterojunctions band discontinuities: physics and applications", edited by F. Capasso and G. Margaritondo, North-holland, 1987
2 C. Priester, J. Phys. III, 1, 481 (1991), and references therein
3 R.G. Dandrea, C.B. Duke and A. Zunger, J. Vac. Sci. Technol. B 10, 1744 (1992), and references therein
4 W.A. Harrison, J. Vac. Sci. Technol. 14, 1016 (1977)
5 C. Tejedor, F. Flores and E. Louis, J. Phys. C 10, 2163 (1977)
6 J. Tersoff, Phys. Rev. Lett. 52, 465 (1984) and Phys. Rev. B 30, 4874 (1984)
7 M. Hybertsen, Phys. Rev. Lett. 64, 555 (1990) and references therein
8 G. Margaritondo, Surf. Sci. 168, 439 (1986)
9 J.P. Landesman, J.C. Garcia, J. Massies, P. Maurel, G. Jezequel, J.P. Hirtz and P. Ainot, Appl. Phys. Lett. 60, 1241 (1992)
10 E.J. Caine, H. Subbanna, H. Kroemer, J.L. Merz and A.Y. Cho, Appl. Phys. Lett. 45, 1123 (1984)
11 I. Aina, M. Mamingly and L. Stecker, Appl. Phys. Lett. 53, 1620 (1988)
12 M.J.S.P. Brasil, R.E. Nahory, W.E. Quinn, M.C. Tamargo and H.H. Farrel, Appl. Phys. Lett. 60, 1981 (1992)
13 E. Lugagne-Delpon, P. Voisin, J.P. Vieren, M. Voos, J.P. André and J.N. Patillon, Semicond. Sci. Technol. 7, 524 (1992); E. Lugagne-Delpon, J.P. André and P. Voisin, Solid State Comm. 86, 1 (1993)
14 M. Hybertsen, Appl. Phys. Lett. 58, 1759 (1991)
15 Y. Foulon and C. Priester, Phys. Rev. B 45, 6259 (1992); Y. Foulon et al., J. Vac. Sci. Technol. B 10, 1754 (1992)
16 Photocurrent spectra are obtained in the "vertical" geometry, with the electric field applied parallel to the growth axis
17 E1+H1=50 meV and a sheet electron density of 2 10^{11} cm^{-2} are the figures coming out of the usual self consistent calculation of the heterojunction (see ref. 1) for a n-type doping level of 2 10^{16} cm-3 in Al(In)As and a band offset of 450 meV. Increasing this doping level up to 10^{17} cm-3 doubles the electron density and yields E1+H1= 71 meV.
18 J.R. Waldrop, E.A. Kraut, C.W. Farley and R.W. Grant, Appl. Phys. Lett. 69, 372 (1991)
19 R.W. Grant, E.A. Kraut, J.R. Waldrop and S.P. Kowalczyk, in ref. 1
20 J.M. Moison, F. Houzay, F. Barthe, J.M. Gérard, B. Jusserand, J. Massies and F. Turco-Sandroff, J. Crystal Growth 111, 141 (1991)
21 T.Y. Wang, E.H. Reihlen, H.R. Jen and G.B. Stringfellow, J. Appl. Phys. 66, 5376 (1989)
22 For a review of energy levels in heterostructures, see G. Bastard, "wave mechanics applied to semiconductor heterostructures", les Editions de Physique (Les Ulis), 1988
23 This 'macroscopic edge effect" screening a quantum (mesoscopic or microscopic) potential occurs in a variety of physical circumstances, like the "quantum photovoltaic effect" (Brum et al., Phys. Rev. B 33, 1063 (1986), or the built in piezoelectric field in strained superlattices (Smith and Mailhiot, Phys. Rev. Lett. 58, 1264 (1987)), or the simple fact that there is no permanent voltage across a polar semiconductor or a piezo-electric material..
24 M. Quillec, SPIE vol. 1361, edited by M. Razeghi (Bellingham, 1991), p. 34
25 W. Seidel, P. Voisin, M. Sacilotti, T. Benyattou and G. Guillot, unpublished

MoP19

Above Barrier Exciton Confinement in InGaAs/GaAs Multiple-Quantum-Well Structures

M Capizzi, A Polimeni, and A Frova
Dipartimento di Fisica, Università di Roma "La Sapienza", Piazzale A. Moro 2, I-00185 Roma Italy

F Martelli
Fondazione Ugo Bordoni, via B. Castiglione 59, I-00142 Roma, Italy

K B Ozanyan and J Worren
Department of Physics, Norwegian Institute of Technology, N-7034 Trondheim, Norway

M R Brunt and M G Simeone
ICMAT CNR, Area della Ricerca di Roma, c.p. 10, I-00016 Monterotondo Stazione, Italy

Abstract

Exciton confinement in the GaAs barriers of InGaAs/GaAs multiple quantum well structures is demonstrated by luminescence self-absorption and photoluminescence excitation spectroscopies. The confinement energy and absorption linewidth depend on the barrier width as predicted by a plain quantum mechanical model. For thin barriers, a splitting in the experimental lineshape is accounted for by including into the theoretical model the interaction among excitons confined in individual barriers. Evidence for a transition between a hole state in the well and an electron state confined in the barrier is also reported, which provides a direct way for estimating the band offsets.

The discovery of confined states in the energy continuum (i.e., above the top of the barrier potential) of modulated semiconductor structures has given new impulse to fundamental studies of these systems [1-5]. From a theoretical point of view, above-barrier carrier confinement (or resonances) can be easily modeled [6], its first discovery can be traced back to the independent reports by Ramsauer and Townsend, in the early twenties, that electrons colliding with noble-gas atoms have a minimum in the scattering cross section for very low kinetic energies, as described in most textbooks of quantum mechanics [7]. From an experimental point of view, an effective carrier localization has been achieved by means of electronic Bragg reflection in suitably designed superlattices [1,2]. In more simple structures, such as single- and multiple quantum wells (MQW), it has been shown, instead, that interference effects due to quantum reflection at the barrier/well interfaces give rise to a sizeable confinement of excitons in the quantum-barrier region [3-5]. In particular, electrons in the conduction band, and holes in the valence band, travelling in the GaAs barrier clad between two InGaAs wells, experience some reflection at the InGaAs/GaAs interfaces, thus undergoing partial confinement in the barrier region. Coulomb interaction between confined electrons and holes leads to the formation of excitons confined in the barrier, C-FE, with energy higher than that of the bulk free excitons, 3D-FE. This model has been verified by comparing the estimated values of the confinement energy with those obtained at 80 K by using a non-conventional, *ad hoc* designed, absolute absorption method, called "luminescence self-absorption" (LSA), as well as conventional photoluminescence (PL) [4,5].

In this work, LSA performed at 5 K, photoluminescence excitation spectroscopy (PLE) performed at 12 K, and PL performed mainly at 80 K provide additional evidence of exciton confinement in the GaAs barriers of InGaAs/GaAs strained MQW structures. The increased resolution achieved at low temperature allows a better determination of the C-FE lineshape and linewidth. These have been successfully compared with the theoretical model, extended to include interactions among excitons confined in different barriers. Furthermore, earlier undetected absorption steplike structures have been observed in PLE spectra at energies below the GaAs 3D-FE. These structures have been interpreted in terms of a transition involving electrons confined in the quantum barriers and holes confined in adjacent quantum wells, thus allowing a direct way of estimating the band offsets.

The structures of all the samples studied in this work, $In_{0.09}Ga_{0.91}As/GaAs$ MQWs grown by molecular beam epitaxy (MBE) on GaAs substrates, are reported in Table I. Buffer layers, quantum wells, and quantum barriers were all nominally undoped; the small linewidth of the QW-ground-state PL at 5 K (about 1 meV) indicated a high quality material. All sample substrates are n doped to $1 - 4 \times 10^{18}$ cm^{-3} except those of samples S52-S55, which are semiinsulating.

The luminescence self-absorption method is described in the following. Excitation by a Ti-Sapphire laser, at energy slightly above the GaAs band gap, creates electron-hole pairs in the whole multilayer structure, and in the substrate. At low temperatures PL from epitaxial GaAs is virtually absent, compared to the broad band emitted from the degenerate substrate and centered around the band gap value of GaAs, which dominates the PL spectra. In the backscattering

geometry, used in conventional PL experiments, the substrate emission is detected after crossing the epitaxial layers' absorption in the buffer layer and in the quantum barriers shows up therefore as dips in the PL spectra (a more detailed discussion of this technique can be found elsewhere [4,5]). On the other hand, a sizeable PL signal from both buffer layer and quantum barriers can be obtained at all temperatures in the backscattering geometry by using an Ar^+ laser to favor near-surface excitation. Conventional PLE is performed by monitoring the QW ground-state luminescence intensity.

Sample	N	L_b	L_w	L_B
S93	4	30	5	500
S102	6	35	5	80
S92	4	40	5	80
S89 S95 S96	4	40	5	500
S103	4	50	5	80
S97, S98	2	50	2.5 + 25	500
S111	4	60	5	80
S52	5	40	15	500
S53	4	20	15	500
S54	4	10	15	500
S55	4	5	15	500

Table 1. Characteristics of the $In_{0.095}Ga_{0.905}As/GaAs$ MQW structures used in this work. L_b, L_w and L_B indicate the thickness (in nm) of quantum barriers, quantum wells, and buffer layers, respectively. N gives the number of quantum wells and barriers. The sample parameters have been determined by means of RHEED oscillations.

A series of absorption dips is observed in the LSA spectra of all samples described in Table 1, which have been grown on a degenerate GaAs substrate, at energies higher than that of 3D-FE (1.515 eV). This is illustrated in Fig. 1 for three samples, *S111*, *S103*, and *S102*, which nominally differ only for the barrier thickness (60, 50 and 35 nm respectively). These dips, with the only exception of the doublet structure observed for the first time at 5 K in sample *S102*, confirm the previous LSA measurements at 80 K, which have been interpreted in terms of transitions between states of excitons confined in the barrier region, C-FE [4,5]. The arrow in the figure points to the $n = 2$ state of C-FE in sample *S111* [5].

As already discussed, in the perfectly abrupt ideal case, particle confinement in the barriers can be obtained whenever the constructive interference condition is satisfied

$$k_b L_b = n\pi \qquad (1)$$

where $k_b = (2m^*\Delta E/\hbar^2)^{1/2}$ is the particle wave vector in the barrier region, m^* is its effective mass, ΔE is the confinement energy defined as the difference between the confined and bulk particle energies, and n is an integer. The same result can be obtained by calculating the quantum-transmission coefficient for a particle incident onto a single quantum barrier [6,7], an approach formally equivalent to the determination of the optical transmission coefficient of a dielectric slab.

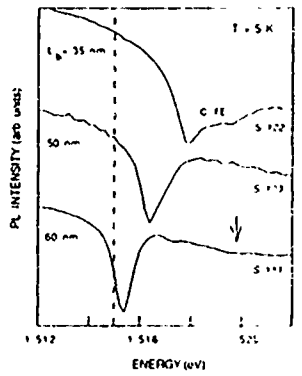

Fig. 1. LSA spectra at $T = 5$ K, for three $In_{0.095}Ga_{0.905}As/GaAs$ multiple quantum-well structures, *S111*, *S103* and *S102*. All samples have the same buffer thickness, 80 nm, and well width, 5 nm, but differ for barrier thickness L_b (60, 50 and 35 nm, respectively). The dashed line gives the position of the bulk-free exciton, 3D-FE, measured in samples with a thick buffer layer. The arrow indicates the position of the $n = 2$ state of the confined exciton, C-FE, in sample *S111*. The excitation wavelength is 801 nm.

In both cases, an inverse quadratic relationship between ΔE and L_b, where ΔE is the sum of confinement energies for an electron with mass m_e and a heavy hole with mass m_{hh}, can be derived,

$$\Delta E = \frac{h^2\pi^2}{2L_b^2}\left(\frac{1}{m_e} + \frac{1}{m_{hh}}\right) = \frac{h^2\pi^2}{2L_b^2}\frac{1}{m^*}, \qquad (2)$$

shown as a dashed line in Fig. 2, in excellent agreement with the experimental results. This is shown in the figure, where the values of the confinement energy ΔE, as determined from the LSA, PL, and PLE spectra taken at different temperatures and averaged over several samples with the same quantum structure, have been reported. The theoretical line has been drawn considering a separate confinement of electrons and heavy holes in a GaAs barrier [8]. The good agreement between experiment and theory, as far as the slope is concerned, indicates that the confined exciton is formed by the Coulomb interaction among separately confined free carriers. Confinement of the exciton as a whole would imply the use of the exciton center-of-motion mass (m_e+m_{hh}) [9], thus resulting in much smaller confinement energies than those observed experimentally. On the other hand, the lack of agreement for what concerns the absolute values stresses the important role of deviations from ideality (real potential profiles, changes in the Coulomb interaction with barrier thickness, interaction between barriers, et cetera).

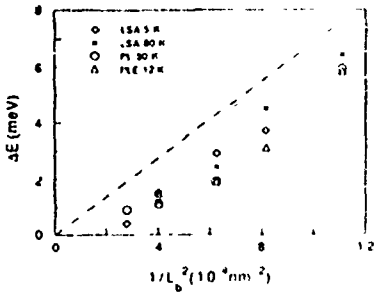

Fig 2 Values of the experimental confinement energy ΔE, as determined at different temperatures by different photoluminescence techniques, together with the values evaluated from Eq (2) (dashed line), vs the reciprocal L_b squared

In particular, the importance of the wavefunction overlap between electron states located at different barriers is shown in Fig 3 In this figure, the PLE spectrum of sample *S102* is compared with the absorption coefficient α of the GaAs buffer layer and barriers, extracted from the LSA spectrum in Fig 1 for the same sample In order to get the I_0 baseline which appears in Lambert's law $\alpha d = \ln (I_0/I)$, where d is the total GaAs epilayer thickness we adopted an approach already successfully used in a previous case [10] the PL level has been linearly extrapolated assuming $\alpha = 0$ at the energy of 1 513 eV, where the nominally undoped epilayers are virtually transparent, and assuming $\alpha = 1 \times 10^4$ cm^{-1} at the energy of 1 525 eV, i e , above the exciton line, a value well established in the literature [11] The close agreement between the lineshape obtained by the two different experimental techniques rules out trivial artifacts

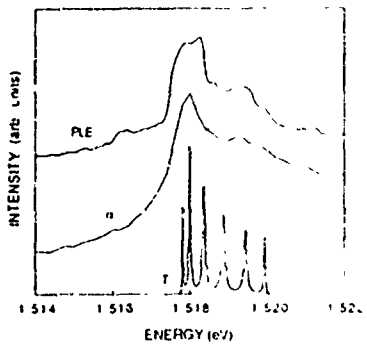

Fig 3 Comparison of the PLE spectrum taken in sample *S102* at 12 K with the the absorption coefficient α estimated from the LSA spectrum of the same sample (see text) The theoretical estimate of the electron transmission coefficient in a similar six barrier structure is also shown

The experimental curves have been then compared with the transmission coefficient calculated for an electron in a structure like *S102*, where the termination at the surface has been simulated by a step 50 meV high and 5 nm wide The theoretical curve, which has to be convoluted with that obtained for the heavy holes (confined a few tens of a meV), agrees almost perfectly with the experimental ones with respect to both its absolute energy and basic lineshape It is worth noting that the doublet-like lineshape is dictated by the presence of a barrier at the surface (without it, all the individual split resonances would have a transmittance equal to one) Therefore, the above agreement has not to be overemphasized the simulation of the surface being quite crude and needing further work However, it already appears that the main features of the experimental lineshape can be successfully accounted for by the plain transmission model, despite the exclusion of hole contributions and Coulomb interaction [12] In particular, the peculiar square-wave like lineshape with the abrupt rise and fall observed in the highly resolved PLE spectrum of sample *S102* shown in Fig 3, is characteristic of interacting resonance levels

The above conclusions are further substantiated by the analysis of the experimental values of the full width at half maximum (FWHM) determined from the LSA spectra at 5 K (open circles) and reported as a function of barrier width on a log-log scale in Fig 4 The experimental FWHM increases for decreasing barrier thickness L_b as the inverse cube This behavior is quite well reproduced, with respect to its slope by the electron transmission model (crosses in the figure)

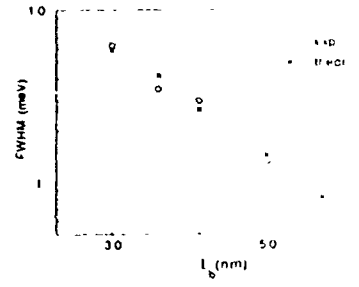

Fig 4 Experimental FWHM for the C-HE absorption dip measured at 5 K (open circles) vs L_b on a log-log scale The corresponding theoretical values (crosses, multiplied by a factor 1 9 for ease of comparison) are obtained from the electron transmission model

The structure of the different samples has been taken explicitely into account while the surface has been simulated as done for the transmission spectrum shown in Fig 3 (sample *S102*) For what concerns the absolute values those obtained from the theoretical model have been multiplied by a factor 1 9, for ease of comparison (convolution with the hole band has not been considered, as well as other broadening factors)

Electrons confined in the quantum barriers give also rise to transitions different from those responsible of the C-HE state In Fig 5 we report the PLE spectra, below the GaAs gap, of

samples *552*, *553*, and *554*. These samples have all the same well width, 15 nm, but different barrier thickness, 40, 20, and 10 nm, respectively. In the spectrum of sample *552*, a signal is observed with a threshold at 1.498 eV, shifted to higher energy in sample *553* and missing in sample *554*. This feature is the only one, in the below GaAs gap PLE spectra of samples *552* and *553*, which shifts in the opposite direction as *e1 hh1*, the transition from the $n = 1$ electron state to the $n = 1$ heavy hole state in the well. Moreover, it is not observed in samples with narrower barriers, such as *554* and *555* (the latter not shown in the figure).

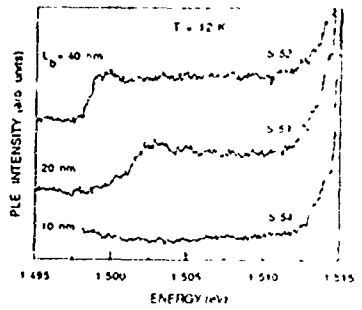

Fig. 3. Steplike features in the energy region below the GaAs gap of the 12-K-PLE spectra for samples *552*, *553*, and *554*. All samples have the same well-width, 15 nm, but different barrier thickness, 40, 20, and 10 nm, respectively.

We believe that this transition involves an electron confined in the quantum barrier and a hole confined in the adjacent quantum well (hereafter called $e_1 hh_1$). The steplike lineshape of the PLE signal suggests that the two dimensional continuum of the hole density of state is involved in the transition, most likely the heavy hole from a first qualitative analysis. In samples *554* and *555*, this transition is not observed because it would take place at energies resonant with the buffer/barrier GaAs transition energies, and be too weak to be distinguished. The shift of the transition to higher energy, for narrowing barrier width, can be interpreted in terms of an increased confinement energy for the electron, as indicated by a comparison with the C.T.E. shift, corrected for the shift of the ground-state energy of the QW. For more quantitative results, one would need to know with adequate precision the In concentration x, which is slightly different in the two samples and causes the above mentioned difference in the QW ground state emission. Therefore, the band offsets can be in principle derived from the comparison of $e_1 hh_1$ with ground state transitions in samples grown with large Δx's, measurable by PL.

In conclusion, luminescence self absorption, plain photoluminescence and photoluminescence excitation spectroscopies appear to be suitable techniques to study detailed aspects of exciton confinement in the GaAs barriers of InGaAs/GaAs multiple quantum well. A plain quantum

mechanical model, where the interaction between different barriers has been taken into account, is able to predict the lineshape of the experimental spectra as well as its dependence on barrier thickness. Finally, a transition between a hole state in the well and an electron state in the barrier has been observed, which can be used for estimating band offsets.

It is a pleasure to acknowledge useful and stimulating discussions with C. Prestilla. This work has been partially supported by Ministero dell'Universita e della Ricerca, and by Progetti Finalizzati "MADESS" and "Materiali Speciali", both of CNR, and by the Norwegian Research Council. The work at Fondazione Ugo Bordoni has been carried out in the frame of the agreement between FUB and the Italian P.T. Administration.

1. M. Zahler, I. Brener, G. Lenz, J. Salzman, E. Cohen, and L. Pfeiffer, *Appl. Phys. Lett.* **61**, 949 (1992).
2. F. Capasso, C. Sirtori, J. Faist, D. L. Sivco, S. N. G. Chu, and A. Cho, *Nature* **358**, 565 (1992).
3. F. C. Zhang, N. Dai, H. Luo, N. Samarth, M. Dobrowolska, J. K. Furdyna, and L. R. Ram Mohan, *Phys. Rev. Lett.* **68**, 3220 (1992); H. Luo, N. Dai, F. C. Zhang, N. Samarth, M. Dobrowolska, J. K. Furdyna, C. Parks, and A. K. Ramdas, *ibid.* **70**, 1307 (1993).
4. F. Martelli, M. Capizzi, A. Frova, A. Polimeni, F. Sarto, M. R. Bruni, and M. G. Simeone, *Phys. Rev.* **B48**, 15 July (1993).
5. F. Martelli, M. Capizzi, A. Frova, A. Polimeni, F. Sarto, M. R. Bruni, and M. G. Simeone, *SPIE Proc.* **1985**, *Physical Concepts and Materials for Novel Optoelectronic Device Applications II - part II*, in the press.
6. G. Bastard, *Wave Mechanics Applied to Semiconductor Heterostructures*, p. 86ff, Les Editions de Physique, Les Ulis (1988).
7. See, for example, D. Bohm, *Quantum Theory*, p. 568ff, Prentice Hall Inc., Englewood Cliffs, N.J. (1960).
8. The electron mass has been taken equal to $0.067\ m_0$, the heavy hole mass to $0.62\ m_0$ (S. Adachi, *J. Appl. Phys.* **53**, 8775 (1982)).
9. J. C. Kusano, Y. Segawa, M. Mihara, Y. Aoyagi, and S. Namba, *Proc. of the 20th International Conference on the Physics of Semiconductors*, edited by E. M. Anastassakis and J. M. Joannopoulos, World Scientific, Singapore (1992), p. 1935.
10. F. Sarto, M. Capizzi, and A. Frova, *Semic. Science and Technol.* **8**, 1231 (1993).
11. J. M. Dell, M. J. Joyce, B. F. Usher, G. W. Yoffe, and P. C. Kemeny, *Phys. Rev.* **B42**, 9496 (1990); D. D. Sell, *ibidem*, **B6**, 3750 (1972).
12. It may be worth noting that, for increasing temperature, the doublet lineshape gradually evolves into the single broad dip observed in the LSA spectrum at 80 K (see Refs. 4 and 5), the narrower low energy component of the doublet weakening down to zero. No simple explanation of this behaviour has been yet found.

MoP20

Spectroscopic Study of Piezoelectric Field Effects in InGaAs/GaAs Multi-Quantum Wells Grown on (111)B Oriented GaAs Substrates

T A Fisher, R A Hogg, A R K Wilcox, D M Whittaker, M S Skolnick and D J Mowbray
Department of Physics, University of Sheffield, Sheffield S3 7RH, UK
J P R Davenport, G J Rees, R Grey, J L Sanchez-Rojas*, J Woodhead, G Hill, M A Pate and P N Robson
Department of Electronic and Electrical Engineering, University of Sheffield, Sheffield S1 3JD, UK

An optical study of a series of high quality piezo-electric (PZ) (111)B GaAs-(InGa)As strained multi-quantum wells is reported. Well defined $\Delta n=0$ transitions (E1HH2, E1HH3 and E2HH1) are observed with comparable strength to the $\Delta n=0$ transition, as a result of the asymmetric well profile induced by the piezo electric field. In PLE the onset of the E1HH1 continuum is clearly seen, allowing the deduction of an exciton binding energy of 9 meV. Applying a bias to oppose the PZ field reduces the field in the well, which decreases the quantum confined Stark shift and weakens the $\Delta n\neq 0$ transitions. At high bias, corresponding to flat band in the well, strong lifetime broadening is observed. Good agreement between theory and experiment is found only by using a value for the PZ constant ~30% smaller than the commonly accepted value.

There has been considerable recent interest in the optical and electronic properties of strained layer quantum well (QW) structures grown in the (111) polar direction [1-7]. Due to the lack of inversion symmetry in the zinc-blende structure, strain in the (111) direction produces a significant piezo-electric (PZ) field in the wells (~ 2×10^5 V/cm in $In_{0.1}Ga_{0.9}As$/GaAs QWs)[1]. As a result, a strong quantum confined Stark effect (QCSE) is experienced in these structures without any external field [2]. This has been demonstrated both by the application of an opposing bias, producing a large blue-shift of the transition energies [3-5], and by non-linear optical behaviour when photo-excited carriers screen the internal fields [4,5].

In this paper we present an experimental and theoretical investigation of the optical properties of a series of high quality samples in which a number of PZ (InGa)As/GaAs multi-QWs (MQWs) are embedded in the intrinsic region of a p-i-n structure. Both photoluminescence excitation (PLE) and photocurrent (PC) spectroscopies are used to measure the low temperature (T=4K) absorption characteristics as a function of applied bias. Up to four prominent optical transitions are observed in the spectra, including $\Delta n\neq 0$ lines [6] of comparable strength to the $\Delta n=0$ transition. In the highest quality PLE spectra of the series both the excitonic transitions and the onset of the associated continuum transitions are observed allowing an exciton binding energy of 9±1 meV for E1HH1 to be deduced. As the applied bias opposing the PZ field is increased, the QCSE is reduced, weakening the $\Delta n\neq 0$ transitions, until only E1HH1 remains strong when the well profile is flat [2,7]. However, the field in the barriers is still large, leading to significant lifetime broadening of the exciton peak. Solutions to Schrodinger's equation support our interpretation of the results and show that the growth parameters are close to their nominal values. However, the fits suggest a value for the PZ constant e_{14} (0.097 ± 0.014 C/m^2) considerably smaller than previously determined [8].

The samples were fabricated by molecular beam epitaxy and grown on (111)B semi-insulating GaAs substrates oriented 2 degrees towards (001). The layers, in order of growth, consist of 2.5 μm n+ GaAs (dopant, Si), an intrinsic region in which the $(In_xGa_{1-x})As$-GaAs MQWs of nominal width 100Å are incorporated centrally in GaAs, and 0.3 μm p+ GaAs (dopant Be). The number of QWs in a structure ranged in the series from 1 to 25 [9-11]. In this paper we concentrate on two structures: sample M25 has 25 QWs (x=0.13), with barrier widths of 150Å in an intrinsic region of width 6150Å and sample M5 has 5 QWs (x=0.15) with barrier widths of 900Å and an intrinsic region 6250Å wide. Transmission electron microscopy (TEM) measurements indicate well widths close to 100Å with variations of ± 10 % for different structures in the series. The samples were processed into 400μm diameter annular diodes with 200μm optical access.

Fig. 1(a) shows PL (dotted) and PLE (full line) spectra obtained from the unprocessed sample M25. The sample is of high quality, comparable to the best (100) structures [11]. This is indicated by the narrow PL and lowest energy PLE linewidths of 3.5 and 3.0 meV respectively, and by the negligible Stokes shift between the PL and the lowest energy PLE peak. The PC spectra from the processed sample M5 is shown in Fig. 2(a) at an applied bias of V_a = -2V. In general, for the series, the PC spectra show linewidths broader than in the PLE spectra (5.4meV for lowest energy transition in PC of sample M5 in Fig. 2(a)). For example, in a 17 MQW structure (x=0.15) the lowest energy transition has a linewidth of 6.5meV in PC at low bias and 3.2meV in PLE [9]. In PLE as the excitation energy is varied only one recombination energy within the inhomogeneous linewidth is being detected. Therefore it is plausible that linewidth narrowing occurs in PLE due to the selective nature of the PL detection process. On the other hand, for PC the measured current is due to photocreated carriers being swept out of the wells, so that the observed PC linewidth will generally be an average over all inter and intra-well fluctuations in width, and hence will have broader lines than for PLE. The series of samples all show PLE and PC spectra of similar quality to sample M25 and M5. These are discussed in more detail in Ref. 9 at low temperature and at room temperature in Ref. 10. The measurements were taken using 100 mW/cm^2 of radiation, but varying the power from 10 mW/cm^2 to ~5 W/cm^2 does not affect the observed spectra, showing that photo-excited carrier screening effects are negligible.

Four prominent excitonic transitions are observed in the PLE of Fig. 1. The identifications are confirmed by the solutions of Schrodinger's equation (discussed in detail further on). The lowest energy transition (E1HH1) involves absorption between the first heavy-hole state (1HH) and the first electron state (1E). The transitions to higher energy are E1HH2, E1HH3 and E2HH1. A similar PC spectrum is observed for sample M5 at V_a = -2V (Fig. 2(a)), the calculated transition energies (shown by arrows) are in good agreement with experiment. For all of the series the strain is expected to cause the light hole transitions to become type II. Therefore they will be upshifted by ~30 meV and are expected to be weak [7,11] and as a result do not appear in the PLE of Fig. 1 or PC of Fig. 2(a). In Fig. 1(a) the $\Delta n\neq 0$ transitions E1HH2, E2HH1 and E1HH3 are of comparable strength to the allowed transition E1HH1. This arises from the strong internal PZ field [1,2] which removes the usual selection rules in a flat well. The $\Delta n\neq 0$ transitions are prominent in all of the processed structures measured near V_a = 0V [9], as shown in the PC spectra of sample M5 at V_a = -2V (Fig. 2(a)).

In addition to the prominent E1HH1 and E1HH2 excitonic transition observed in the PLE of Fig. 1(a) for sample M25 at ~9 meV to higher energy clearly defined absorption onsets are seen. The absorption onset is composed of 2s and higher excitonic transitions broadened into the continuum edge. The E1HH1 exciton binding energy is deduced to be 9±1 meV from Fig. 1 by taking the energy difference between the E1HH1 exciton peak and the continuum onset marked by the downward pointing arrow. This value is very close to that found by Moore et al [12] for a (100) $In_{0.1}Ga_{0.9}As$/ GaAs 50Å QW. This agreement is somewhat surprising considering the high electric field in the present structures and the narrower QW in the work of Moore et al [12].

PC spectra as a function of applied bias V_a, are shown in Fig. 2 for sample M5. A strong increase in the energy of the excitonic transitions of 16 meV is seen as the bias is increased from V_a = -2V to V_a = -8V. This is also shown in the plot of the PC transition energies (filled circles) against bias in Fig. 3. As the field in the well is reduced the QCSE [15,16] is reduced causing the observed blue shift. The turning point in the graph corresponding to flat band in the well occurs at V_a = -8V. At low bias, V_a = -2 V (Fig. 2 (a)) the $\Delta n\neq 0$ transitions E1HH2 and E1HH3 are of similar strength to the $\Delta n=0$ transition E1HH1 [6]. Increasing the reverse bias leads to a clearly observed reduction in the strength of $\Delta n\neq 0$ transitions E1HH2 and E1eHH3 as the field in the well is reduced. By V_a = -8V E1HH2 is not observable and E1HH3 is very weak, as expected for flat band in the well. A further trend observed with increasing bias above V_a = -5V is for all excitonic transitions to undergo a strong broadening with only very broad features apparent at V_a = -9V (Fig. 2(f)).

In order to interpret the experimental results in more detail the transition energies and oscillator strengths have been calculated as a function of V_a using numerical solutions to Schrodinger's equation. Since there is a significant probability of tunnelling out of the well especially at high reverse biases the states are treated as resonances rather than true bound states. In the calculations standard interpolated values of the elasticity parameters and deformation potentials [8] were used to evaluate the effects of the strain on the band structure and to calculate the PZ field [16]. The (InGa)As electron mass was taken to be $0.067m_e$ [17] and the heavy hole mass along (111) to be m_{hh} = $(\gamma_1 - 2\gamma_2)^{-1} m_e$ = 0.7 m_e [6,13]. This gives a good fit to the spacings of the observed heavy hole transitions.

Fig. 4 shows a typical potential profile for one of the wells in sample M5, calculated at V_a = -2V along with energy levels and associated wavefunctions of the first few states. At this bias the heavy hole states 1HH2 and 1HH3 and electron state 1E2 penetrate into the sloping barriers [7] which means that the continuum potential is effectively wider for 1HH3 than the lower hole states. As a consequence, at low bias

the energy separation of E1HH1 and E1HH2 is greater than that of E1HH2 and E1HH3, while at V_a = -8V the spacing is reversed (Fig 3)

Three fits to the experimental transition energies (circles) as a function of V_a for sample M5 are shown in Fig 3, using various values of the PZ constant, e_{14}, well width and Indium concentration 9 meV has been subtracted from all the calculated energies to allow for the exciton binding energy The short dashed line uses the standard value of e_{14} = 0 143 C/m^2 [8], linearly interpolated for the alloy, with nominal values of well width (100A) and Indium concentration (x = 0 15), giving a piezoelectric field, E_p = 227kV/cm [3] The agreement with experiment is very poor In order to improve the fit, e_{14} and x were varied using this well width: reducing e_{14} moves the curves towards zero bias, while reducing x shifts the transition energies upwards The value of x is determined by fitting to the E1HH1 energy (1 410 eV) around V_a = -8V, where the bottom of the well is flat and the transition energy is relatively insensitive to the other parameters [18] An optimum fit, shown by the long dashes, is obtained for e_{14} = 0 088 C/m^2 and x=0 145 (E_p = 140 kV/cm) Although this gives good agreement for E1HH1, the energies of the higher transitions are still well below the experimental values The best fit (solid lines), which agrees very well with experiment was obtained by reducing the well width to 90A and using e_{14} = 0 097 C/m^2 with x=0 15 (E_p = 155 kV/cm) The error in the e_{14} determination is estimated to be ±10%, most of the uncertainty arising from the precision with which the flat band voltage can be located in Fig 3

The values of e_{14} used in the better fits are much smaller than the standard value of 0 143 C/m^2 The lower values of e_{14} are necessary in order to make the bias which gives flat wells agree with the experimentally observed maximum in the transition energies However, a similar result would be obtained if the intrinsic region were narrower than its nominal width of 6250A Although capacitance-voltage measurements suggest that this is not the case, there is sufficient uncertainty to prevent the fits being a definitive determination of e_{14} [19] Very similar variations of transition energy against bias are observed for other samples in the series, except for a shift along the voltage axis This shift can be well explained using the same values of e_{14} as for the 5 well sample M5 and taking into account the larger number of wells [9, 10]

The calculated lifetime broadening only becomes significant in comparison with inhomogeneous broadening at biases beyond about V_a = -6V where the barrier fields are high, but the well profile is close to flat band (inset Fig 3) At V_a = -9V (Fig (2f)), where features can still be seen, the calculated broadening is 4 5 meV The experimental linewidth changes from 6 meV at V_a = -2V to 16 meV at V_a = -9V, an increase of 10 meV This is considered as good agreement, since the calculations are very sensitive to the input parameters Increases in linewidth due to field variations in the structure at high V_a are not a likely explanation for the results of Fig 2(f) since near V_a = -8V the transition energy does not vary greatly with bias (Fig 3) At V_a = -8V, for sample M5, the calculations predict that, because the bottom of the well is flat, E1HH2 and E2HH1 are very weak and E1HH3 has only 3% of the strength of E1HH1, in agreement with the spectra of Fig 2(e) As the reverse bias is reduced and the field in the well becomes larger, the diagonal transitions are predicted to become stronger, until at V_a = -2V E1HH2 and E1HH3 are of comparable strength to E1HH1, again in good qualitative agreement with the spectra of Fig 2(a)

In conclusion, the variation of transition energies and oscillator strengths with applied bias has been investigated in a series of high quality InGaAs-GaAs MQWs Good agreement between theory and experiment is found, but only by using a value for the piezoelectric constant ~ 30% smaller than the commonly accepted value Strong lifetime broadening is observed close to flat band conditions in the well This result contrasts strongly with that in non-piezoelectric structures where the fields in the wells and barriers are equal, and lifetime broadening is observed at high fields in the wells An exciton binding energy of 9±1 meV is deduced for E1HH1

Acknowledgement - We would like to thank G Duggan for helpful discussions This work was supported by SERC (grant number GR/I20925)

References

* Permanent address Departamento de Ingeniera Electronica, Universidad Politecnia de Madrid, Madrid, Spain

1 D L Smith Solid State Commun 57 919 (1986)
2 C Mailhiot and D L Smith, J Vac Sci & Technol A7, 609 (1989)
3 E A Canda, T Y Chang, K W Goossen and L F Eastman, Appl Phys Lett 56, 659 (1990)
4 I Sela, D E Watkins B K Laurich, D L Smith, S Subbanna and H Kroemer, Appl Phys Lett 58, 684 (1991)
5 K Nishi and T Anan J Appl Phys 70, 5004 (1991)
6 G Duggan, K J Moore, A Raukema, G Th Jaarsma and K Woodbridge, Phys Rev B 45, 4494 (1992)
7 B K Laurich, K Elcess, C G Fonstad, J B Beery, C Mailhiot and D L Smith, Phys Rev Lett 62, 649 (1989)
8 Landolt-Bornstein, Vol 22a Semiconductors, Ed O Madelung (Springer-Verlag, New York, 1986)
9 R A Hogg T A Fisher, A R K Willcox, D M Whittaker, M S Skolnick, D J Mowbray, J P R David, A S Pabla, G J Rees R Grey J Woodhead G Hill, M A Pate and P N Robson, submitted to Phys Rev (Rapid Commun)
10 A S Pabla, J L Sanchez-Rojas J Woodhead, R Grey, J P R David, G J Rees, G Hill, M A Pate, P N Robson R A Hogg, T A Fisher, A R K Willcox, D M Whittaker, M S Skolnick and D J Mowbray, Appl Phys Lett, 1993
11 M K Saker, D M Whittaker, M S Skolnick, M T Emeny C R Whitehouse, Phys Rev B 43, 4945 (1991)
12 K J Moore, G Duggan, K Woodbridge C Roberts, Phys Rev B 41, 1090 (1990)
13 L W Molenkamp, R Eppenga, G W t'Hooft, P Dawson, C T Foxon and K J Moore, Phys Rev B 38 4314 (1988)
14 D A B Miller, J S Weiner and D S Chemla, IEEE J Quantum Electron QE-22, 1816 (1986)
15 W Chen and T G Andersson Semicond Sci Technol 7 828 (1992)
16 E Anastassakis Phys Rev B 46 4744 (1992)
17 R People and S K Sputz, Phys Rev B 41, 8431 (1990)
18 For example a 10A change in well width, the maximum variation from the TEM measurement, would lead to a 5 meV shift in the transition energy, a 1% change in x changes the transition energy by 9 meV
19 The relatively low value of E_p =155 kV/cm corresponding to e_{14} =0 097C/m^2 could also arise if the strain in the structures were relaxed by 30% ! the reduction of E_p from 227 kV/cm to 155 kV/cm) However, such large strain relaxation would lead to a downshift of the E1HH1 transition energy by 26 meV leading to predicted energies for x = 0 15 in strong disagreement with experiment

Figure Captions

Fig 1 (a) PL (dotted line) and PLE (full line) spectra from sample M25 at T=4K The spectra show Δn= 0 transitions E1HH2, E1HH1 and E2HH1 of comparable strength to E1HH1 At ~9 meV to higher energy the associated continuum onsets for the E1HH1 and E1HH2 excitonic transitions are clearly observed

Fig 2 PC as a function of applied bias for sample M5 With increasing reverse bias the strength of the Δ n=0 transitions decreases, until at flat band in the well, V_a = -8V (e) only E1HH1 is strongly observed

Fig 3 Experimental transition energies (circles) as a function of applied bias for sample M5 The lines are theoretical fits using various sets of parameters (see text for details) The inset shows the band profile at V_a = -8V where the well is flat

Fig 4 Potential profile for one of the wells in sample M5 calculated at V_a = -2V, along with energy levels and associated wavefunctions of the first few states

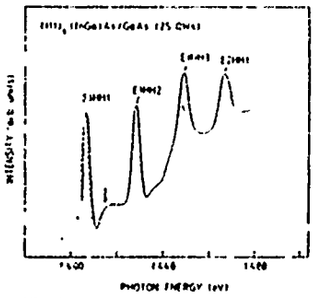

Fig. 1

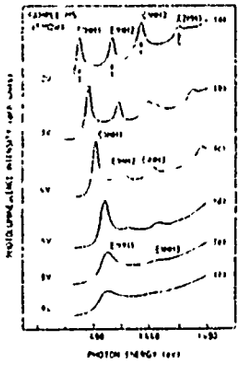

Fig. 2

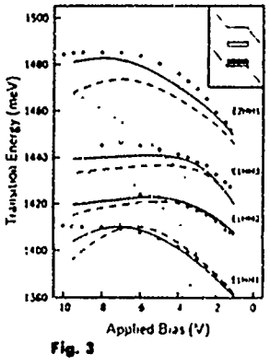

Fig. 3

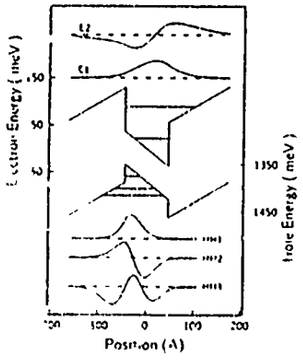

Fig. 4

MoP21

Optical Properties of AlP-GaP Short-Period Superlattices

A. Morii, T. Takano, J. Kitamura, K. Hara, H. Kukimoto
Imaging Science and Engineering Laboratory, Tokyo Institute of Technology,
4259 Nagatsuda, Midori-ku, Yokohama 227, Japan
J. Yoshino
Department of Physics, Tokyo Institute of Technology,
2-12-1, O-okayama, Meguro-ku, Tokyo 152, Japan
and T. Yasuda
Photodynamic Research Center, The Institute of Physical and Chemical Research
Naga-machi, Aoba-ku, Sendai 982, Japan

Abstract

We present several optical properties of $(AlP)_n(GaP)_n$ short-period superlattices grown by metalorganic vapor phase epitaxy (MOVPE), which include the low temperature photoluminescence of samples with a shorter period, low temperature photoluminescence lifetime, and refractive indexes of the superlattices at room temperature. The photoluminescence characteristic of the superlattice with n=3 has been clearly observed. The radiative lifetime of the excited carriers in the superlattice is fairly long against expectation. It has been found that the refractive indexes of $(AlP)_n(GaP)_n$ superlattices are similar to that of AlGaP alloys.

Introduction

The AlP-GaP short-period superlattices composed of two indirect-gap semiconductors of AlP and GaP, with appropriate periods, are expected to have direct-gaps due to the folding of the indirect conduction band minima at the X point to the center of the Brillouin zone (Γ), and the mixing of the electronic states of both materials [1]. We pay attention to this system for two reasons. One is that AlP and GaP can be nearly lattice-matched to each other with a small lattice mismatch of about 0.2 %. The other is that the bandgap energy of the AlP-GaP superlattices corresponds with visible light in the red to green spectral region. Therefore, they are expected to offer potential for use in novel laser diodes operating in the yellow to green region.

The first optical study of $(AlP)_n(GaP)_n$ short-period superlattices has revealed blue shift and intensity enhancement of the characteristic photoluminescence with decreasing the number of sublayer, n [2]. More recent electrical and optical measurements have indicated that the band lineup of the AlP/GaP heterojunction is of the type II [3, 4], which is consistent with the photoluminescence peak shift, and that the observed photoluminescence is due to the electronic transition from the zone-folded conduction band at the Γ point to the valence band maximum [5, 6].

We have already observed the characteristic photoluminescence in the $(AlP)_n(GaP)_n$ superlattices with n ranging from 4 to 10, which were grown at 780 °C by metalorganic vapor phase epitaxy (MOVPE) [7]. One of our present concerns is with the characteristic photoluminescence to appear in the superlattices of much shorter periods. The other is with fundamental optical properties including radiative transition rate and refractive index, in conjunction with an application of this superlattice system for laser diodes.

In this paper we present the first observation of a dominant photoluminescence peak in a shorter-period superlattice of $(AlP)_3(GaP)_3$. Also, we show that the radiative lifetime of the excited carriers in this superlattice system is fairly long, against expectation, and that the

refra... ...e indexes of $(AlP)_n(GaP)_n$ superlattices with n ranging from 4 to 9 are similar to that of AlGaP alloys.

Photoluminescence of Shorter Period Superlattices

Growth of superlattice samples was carried out by MOVPE using the same growth system of the previous study [7]. The growth conditions were also the same as before except that the growth temperature was changed from the previous temperature of 780°C to 720°C. X-ray diffraction satellite lines were clearly observed for the superlattices with n=2, 3 and 4 as shown in Fig. 1. It is noted that the satellite peak intensity for the sample of n=3 grown at 720°C was about 4 times higher than for the previous sample of the same n grown at a higher temperature of 780°C. Also noted is that the clear satellite diffraction was observable even for the sample of n=2, when the growth temperature was decreased to 720°C. These observations are ascribed to an improved abruptness at the AlP/GaP heterointerfaces of superlattices by reducing growth temperature, i. e., by suppressing a thermal interdiffusion of Al and Ga atoms within one or two monolayers adjacent to the AlP/GaP heterointerface during growth.

Low temperature photoluminescence spectra for three samples of different numbers of sublayer are shown in Fig. 2. Emission lines characteristic of the superlattices can be clearly seen for samples with n=3 and 4, in contrast with the previous case, where the spectrum for the sample with n=3 were similar to that for a typical AlGaP alloy sample [7]. This is also attributed to the improved abruptness at the AlP/GaP heterointerfaces of superlattices by reducing growth temperature.

The emission peak energy for the sample with n=3 is definitely determined from this spectrum, while one of the emission bands in the photoluminescence spectrum for a gas source molecular beam epitaxy grown sample was ascribed to the superlattice emission band by Asami *et al* [5]. Our peak energy is different from theirs, and is located on the extrapolated line in the relation between photon energy and n.

Photoluminescence Lifetime

The samples used for the photoluminescence lifetime measurements were $(AlP)_n(GaP)_n$ superlattices ranging from 5 to 9 previously grown at 780 °C, an $(AlP)_3(GaP)_3$ grown at 720 °C, and a nitrogen-doped bulk GaP grown by liquid phase epitaxy. Samples were excited by 20-nsec pluses from a 308-nm KrF excimer laser at about 2 K. The time resolution of the measurement system was about 100 nsec for superlattice samples and about 10 nsec for a GaP:N sample. The luminescence decay for the superlattice samples with n=3, 5, 6 and 7 consisted of a single-exponential component, while that for n=8 and 9 double components. Figure 3 shows the decay time of photoluminescence peak intensity for different numbers of sublayer. The decay times ranging from 0.2 to 1.0 μsec are one or two orders of magnitude longer than that of GaP:N which is about 0.023 μsec at around 2.30 eV. These decay times for the superlattices are fairly long against expectation. Further studies are necessary for understanding the mechanism of luminescence decay and for fabricating superlattice samples of better quality in terms of periodicity and interface abruptness.

Refractive Index

The samples used for the refractive index measurements were those previously grown at 780 °C. A 0.2 μm-thick GaP was grown on the n-type GaP nominally (100) orientated substrate, followed by an about 1.0 μm-thick $(AlP)_n(GaP)_n$ superlattice layer with n = 4 to 9 or an about 1.5 μm-thick $Al_{0.63}Ga_{0.37}P$ alloy layer.

In the wavelength region where optical absorption in layers is negligibly small, a reflection oscillation appears in the spectrum due to the multiple-internal-reflection interference effect. The conventional method of estimating the refractive index takes an advantage of this oscillation. That is, if layer thickness, d, is known from a separate experiment, the average refractive index, $\bar{n}$, is estimated from the wavelengths of two adjacent maxima or minima in the reflectance spectrum, λ_1 and λ_2 ($\lambda_1 > \lambda_2$), by

$$2\bar{n}d = \left(\frac{1}{\lambda_2} - \frac{1}{\lambda_1}\right)^{-1} \qquad (1)$$

Based on this method, Asami *et al*. estimated the refractive indexes of $(AlP)_n(GaP)_m$ superlattices (m+n=14), and concluded that the refractive index of superlattices is larger than that of alloys [6].

We have found that this method essentially involves a large error when applied to the layers which have refractive indexes with wavelength dispersion, as is the present case. We confirmed this by estimating the refractive index of an AlP layer on a GaP substrate. The refractive index evaluated from the oscillatory reflectance spectrum calculated using the reported wavelength-dependent refractive indexes of AlP and GaP [8], was about 20 % larger than the refractive index of AlP which was initially used in the calculation of the reflectance spectrum. In the present study, therefore, we have used an alternative method reported by Heavens [9]. Suppose that a sample consists of a film with refractive index n_f and a substrate with refractive index n_s. On condition that either the reflection minima or maxima coincides with the reflectance of the substrate, the refractive index n_f is given by

$$n_f = \left(n_s \frac{1+\sqrt{R}}{1-\sqrt{R}}\right)^{1/2}, \qquad (2)$$

where R is reflectance maxima or minima of the reflectance spectrum depending on n_f is larger or smaller than n_s, respectively.

Figure 4 shows the reflectance spectrum of an $(AlP)_7(GaP)_7$ superlattice layer on the GaP substrate together with that of a GaP substrate itself. The reflectance of GaP substrate is accurate within 1 % of the published value [8]. From the figure we find that the refractive index of the superlattice layer is smaller than that of GaP.

The refractive indexes of an $(AlP)_7(GaP)_7$ superlattice layer and an $Al_{0.63}Ga_{0.37}P$ alloy layer, obtained using eq. (2) and the reflectance minima, are shown in Fig. 5. Refractive indexes of superlattices did not depend on the superlattice period, locating between those of AlP and GaP as is the case of AlGaP alloys. The results is surprising in view of the photoluminescence peak shift which depends largely on the superlattice period.

Summary

The low temperature photoluminescence characteristic of the superlattice with n=3 has been clearly observed by decreasing the growth temperature in MOVPE. It has been found that the radiative lifetime of the excited carriers in the superlattice is fairly long against expectation, and that the refractive indexes of $(AlP)_n(GaP)_n$ short period superlattices are similar to that of AlGaP alloys. These results should be taken into account for designing the laser diodes utilizing this superlattice system as an active layer.

One of authors (A. Moritani) acknowledges support from the Japan Society for the Promotion of Science.

References

[1] U. Gnutzmann and K. Clausecker, *Appl. Phys.* 3, 9 (1974).
[2] A. Morii, I. Ohno, A. Kanda, K. Arai, K. Tokudome, K. Hara, J. Yoshino and H. Kukimoto, *Japan. J. Appl. Phys.* 30, L1244 (1991).
[3] A. Morii, H. Okagawa, K. Hara, J. Yoshino and H. Kukimoto, *Japan. J. Appl. Phys.* **31**, L1161 (1992).
[4] K. Adomi, N. Noto, A. Nakamura and T. Takenaka, *J. Crystal Growth* **124**, 570 (1992).
[5] K. Asami, H. Asahi, T. Watanabe, S. Gonda, H. Okumura and S. Yoshida, *Surf. Sci.* **267**, 450 (1992).
[6] K. Asami, H. Asahi, T. Watanabe, M. Enokida, S. Gonda and Sg. Fujita, *Appl. Phys. Lett* **62**, 81 (1993).
[7] A. Morii, H. Okagawa, K. Hara, J. Yoshino and H. Kukimoto, *J. Crystal Growth* **124**, 772 (1992).
[8] T. Takagi, *Japan J. Appl. Phys.* 21, L167 (1982).
[9] O. S. Heavens, *Phys. Thin Films* 2, 193 (1964).

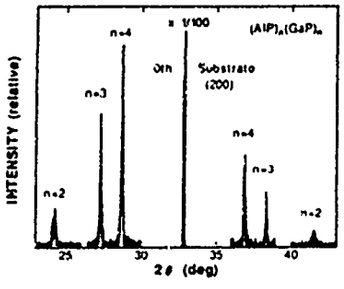

Fig. 1. X-ray diffraction satellite lines for $(AlP)_n(GaP)_n$ superlattice samples

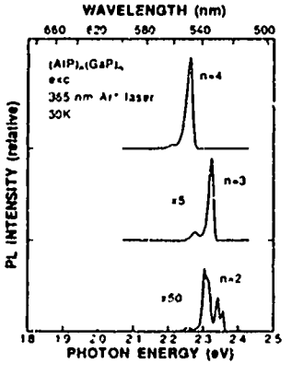

Fig. 2 Photoluminescence spectra at 30 K in $(AlP)_n(GaP)_n$ superlattice samples grown at 720°C Excitation was made by an argon ion laser operating in the ultraviolet at about 350 nm

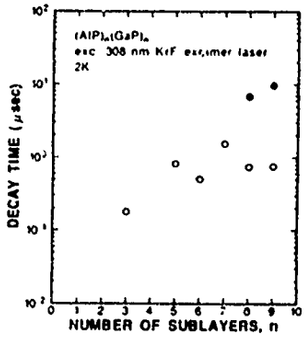

Fig. 3. Photoluminescence decay time at about 2 K for $(AlP)_n(GaP)_n$ superlattice samples.

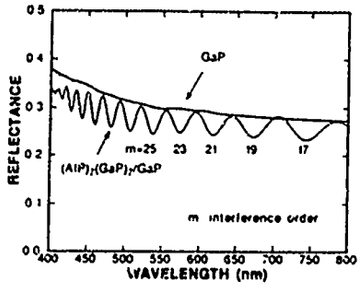

Fig 4. Reflectance spectra for an $(AlP)_7(GaP)_7$ superlattice sample and a GaP substrate at room temperature.

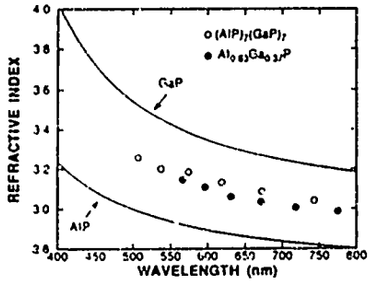

Fig. 5. Dispersion of the refractive indexes for an $(AlP)_7(GaP)_7$ superlattice sample and an $Al_{0.63}Ga_{0.37}P$ sample, which were estimated from the minima in reflectance spectra

MoP22

InGaAs/InP quantum wells with periodic thickness variation

A A Bernussi[1], M J S P Brasil[1], J A Brum[2], M A Cotta[2], R A Hamm[3], I W Stalev[1], S N G Chu[3], L R Harriot[3], M B Panish[3], H Temkin[3]

[1]CPqD - Telebras, Campinas, SP 13088-061, Brazil
[2]Instituto de Fisica, UNICAMP, Campinas, SP 13081-970, Brazil
[3]AT&T Bell Laboratories, Murray Hill NJ 07971, USA
[4]Electrical Engineering Dept., Colorado State University, Fort Collins, CO 80523, USA

We investigated the optical and structural properties of lattice-matched InGaAs/InP quantum wells grown by metalorganic molecular beam epitaxy. The growth conditions were chosen to provide a patterned InP buffer layer surface with elongated features aligned in the [011] direction. The morphology of the patterned surface was revealed by transmission electron and scanning force microscopy measurements. Low temperature photoluminescence results are correlated with the structural properties of the samples. The observation of multiple emission lines indicates the presence of elongated terraces with different thicknesses at the interface of the single quantum well. Information about the carrier dynamics between these elongated terraces is obtained from the photoluminescence temperature dependence.

I - INTRODUCTION

The investigation of semiconductor heterostructure interfaces is of great interest because of its strong influence on the electro-optical properties of these systems. The understanding of the detailed characteristics of the interfaces is not only crucial for obtaining high quality semiconductor heterostructure devices, but it is the first step to use the interface control as a new tool to design special systems. In this work, we investigated a series of InP/InGaAs quantum wells where the InP buffer layer was specially prepared to build-up periodic elongated features along the [011] direction [1]. This new growth technique may become a useful tool to obtain quantum wires eliminating intermediate ex-situ steps used in other methods [2, 3].

The observation of excitons confined in quantum wells is a powerful tool to investigate heterointerfaces and it can easily be performed by using photoluminescence spectroscopy (PL). Since the effective probe of this technique is the exciton, which diameter is of the order of 300 Å, it gives information about features at the interface with sizes comparable to this value.

II - EXPERIMENT

The samples were grown by Metalorganic Molecular Beam Epitaxy. They consist of single InGaAs quantum wells (QWs) with nominal thicknesses of the order of 15 Å lattice-matched to InP. Samples with InP buffer layers varying from 4000 to 10000 Å were grown o nominal (100) and 2° off the (100) plane InP Fe substrates using trimethylindium (TMI), methylgallium (TEG), cracked As_2 and P_2, as the material sources.

Fig 1 - Transmission electron micrograph ([011] cross section) of InGaAs quantum well (dark) on top of InP film with elongated features along the [011] direction.

Investigations on the InP growth [1] showed that the roughness increases and the surface evolves from a smooth two-dimensional growth to a pattern with features along the [011] direction. These structures can be observed on the Transmission Electron Microscopy picture presented in Fig. 1 for a single InGaAs/InP QW. This effect was attributed to an anisotropic diffusion of the In species along the crystallographic directions. For the present work, different morphologies of the InP surface were obtained varying the PH_3 flux and the thickness of the InP buffer layer, but maintaining both the temperature (510 C) and the growth rate constants. The InGaAs layers were grown on top of these specially prepared surfaces and follow the InP profile. These parameters give some control on the basic characteristics of the InP surface, the height and period of the elongated terraces. Microroughnesses are also present on top of this anisotropic surface and they also depend on the growth parameters.

The PL measurements were performed using the 5145 Å line of an Ar^+ laser as the excitation source and analyzed by a 0.5m single spectrometer coupled to a nitrogen cooled Ge photodetector. The measurements were carried out at the temperature range of 2 to 300 K using a liquid helium Janis Supervaritemp cryostat.

III. RESULTS AND DISCUSSION

To analyze the PL spectra, we have to compare its effective probe, the exciton, with the roughness scale. When the roughness scale is small compared to probe dimensions, the exciton experiences a fast varying thickness and a single PL broad emission is expected. When the roughness scale is relatively large excitons from different regions probe different thicknesses giving rise to multiple PL lines. A realistic interface is probably a combination of roughnesses with different frequencies.

Figure 2 shows the PL spectra at 2 K from four InGaAs/InP single QW samples

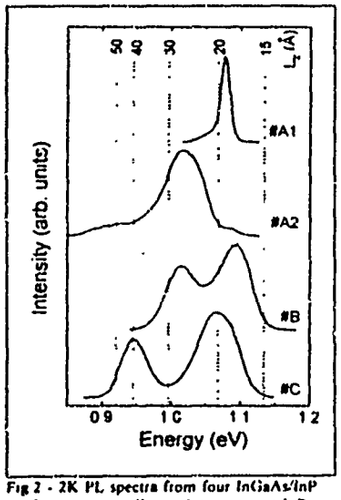

Fig 2 - 2K PL spectra from four InGaAs/InP single quantum well samples grown on InP surfaces with different morphologies

corresponding to different InP surface morphologies Sample #A1 corresponds to a QW with a very smooth InP surface grown on (100) InP substrate at conditions in which the elongated terraces have not been developed yet This result is in strong contrast with sample #A2 that was grown simultaneously with sample #A1 but with a slightly misoriented InP substrate As it can be seen from this figure, the roughness development is very sensitive to the substrate orientation Scanning Force Microscopy (SFM) measurements show that in the case of sample #A2 the terraces already started building up but they are still quite aleatory These results also show that the microroughness for sample #A2 is enhanced as compared to sample #A1 This is in agreement with the PL data that show a single narrow (FWHM~16 meV) line for sample #A1 and broad emission bands for sample #A2 (FWHM~65 meV)

Samples #B and #C were grown on (100) InP substrates with slightly different parameters SFM measurements confirm the presence of elongated terraces along the [011] direction for both samples These measurements give an estimation of the height (H~50 Å), the length (6000<L<30000Å) and the distance between adjacent terraces (D~20000 Å) The two PL peaks observed for these samples are attributed to fundamental excitonic transitions in the QW from two regions with different thicknesses The origin of these regions is related to the growth on the patterned InP buffer layer

Figure 2 also presents the results of a three band envelope function calculation for the energy transitions on InGaAs/InP QWs with different thicknesses using a conduction band offset value of 0.4Eg [4, 5] The high energy peaks correspond to quantum well thicknesses of the order of 15-20 Å that is close to the nominal value The low energy bands of the doublet correspond however to relatively thicker QWs, of the order of 25-40 Å This thickness variation is expected because of the inhomogeneous growth rates on the anisotropic InP surface

Figure 3 shows the temperature evolution of the PL spectra from samples #B and #C As the temperature increases, the intensity of the higher energy band of these doublet like spectra decreases faster than the lower energy one At room temperature the higher band is

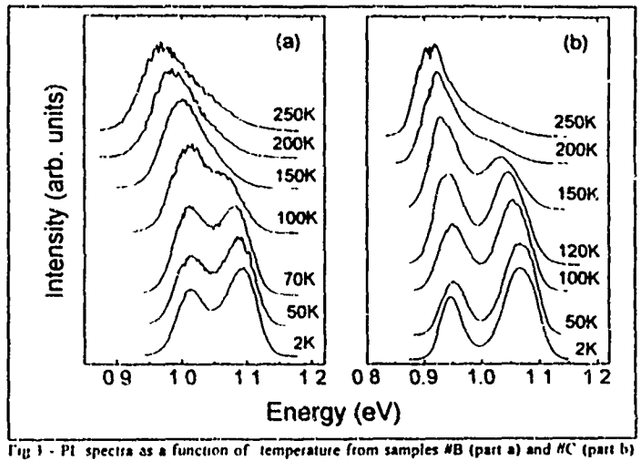

Fig 3 - PL spectra as a function of temperature from samples #B (part a) and #C (part b)

completely suppressed The quenching of the high energy band occurs at different temperatures for these two samples This is clearly observed at 100 K where the higher energy band from sample #B has almost disappeared, while the corresponding one for sample #C remains almost unchangeable Nevertheless the ratio intensity between the two bands at 2 K is very similar

The total integrated PL emission intensity for samples #B and #C is almost constant up to 120 K and decreases exponentially for higher temperatures This can be explained by the relative increase of competitive processes, mainly the thermal emission of the carriers out of the InGaAs well to the InP barriers followed by non-radiative recombination [6, 7]

As we discussed above, the PL band emissions, for samples #B and #C, originate from contiguous regions with different thicknesses and dimensions bigger than the exciton diameter The PL intensity corresponding to each region should then reflect the relative area of each region and the carriers diffusion between these regions The first parameter is a constant for each sample [8] The second one is probably responsible for the variation of the intensity ratio between the PL bands as a function of the temperature The exciton transfer from a region with a higher energy level to a lower one depends basically on the ratio between the excitonic diffusion constant and the dimensions of the regions, which is also a constant for each sample The fact that the intensity ratio between the PL bands is constant for low temperatures and decreases exponentially above a given temperature suggests a

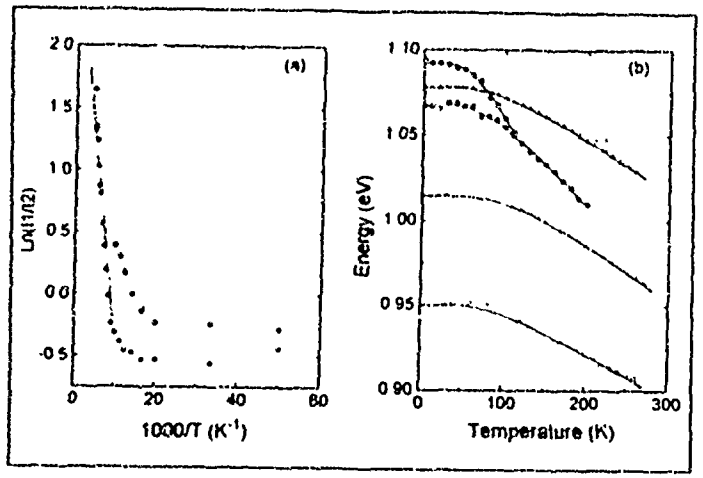

Fig. 4 - (a) Ratio between the intensity of the low over the high PL band for samples #B (●) and #C (■) versus the inverse of the temperature. (b) Peak energies from samples #A1 (▲), #B (● and ○) and #C (■ and □). Open (full) symbols represent low (high) energy bands

mobility edge for the excitons. This edge has been observed by various authors and it was interpreted as a transition from localized to mobile excitons with relatively higher energy levels [9, 10]. This effect is attributed to microscopic statistical variations of the well width and the alloy composition that creates local fluctuations of the potential which localizes the exciton. However, it is difficult to quantitatively evaluate these effects. Experimentally, they result in an "effective activation energy" obtained from the dependence of the intensity ratio between the two PL bands for samples #B and #C as shown in Fig. 4(a). The energies obtained from linear square fittings on fig.4(a) are 33 meV for sample #C and 7 meV for sample #B. This "activation energy" should reflect the barrier height that the localized excitons have to overcome to become mobile excitons. We observe that this "activation energy" can assume relative high values and it is extremely sensitive to the sample parameters, making it difficult to correlate to the fundamental characteristics of the QW.

Finally, we present in Fig. 4(b) the variation of the PL peak energies as a function of the temperature for samples #A1, #B and #C. Sample #A1 shows the behavior of a typical uniform QW, following the band gap energy of the well material. Similar energy dependence is presented by the low energy bands of samples #B and #C. In contrast, the high energy PL bands from these samples show a markedly different dependence with temperature. The

position of the high energy emission bands follows the band gap of InGaAs at low energies in the temperature range where the intensity ratio between the bands is almost constant. However, as the temperature is further increased, the peak of the high energy bands decrease in a much faster rate than the InGaAs band gap and become closer to the lower band. To understand this effect we have to take into account that the emission from each PL band does not originate from a single level, but from a set of levels due to the present roughness. The PL linewidth reflects an average occupation of these set of states. The "activation energy" for the transition localized-to-mobile experienced by the excitons should be relatively smaller for the higher energy levels. These excitons should then overcome the barrier to become mobile at relatively smaller temperatures, resulting in a PL peak shift to lower energies as the band intensity decreases.

IV - CONCLUSIONS

In conclusion, we have investigated InGaAs QWs grown by metalorganic molecular beam epitaxy on specially prepared InP surfaces with elongated terraces along the [0$\bar{1}$1] direction. The build-up roughness results in periodic thicknesses of the InGaAs wells. The periodicity was observed by SFM measurements and reflects on doublets observed in the PL spectra at low temperatures. The PL experiments as a function of temperature give some insight on the dynamics of excitons in the regions created by long range roughness with a superimposed microroughness.

ACKNOWLEDGEMENTS: The authors gratefully acknowledge the financial assistance from CNpQ and FAPESP.

REFERENCES

1 M A Cotta, R A Hamm, T W Staley, S N Chu, L R Harriott, M B Panish and H Temkin, *Phys Rev Lett*, in press.
2 K Kash, *J of Lumin* 46, 69 (1990).
3 D V Lang, M B Panish, F Capasso, J Allan, R A Hamm, A M Sergent and W T Tsang, *Appl Phys Lett* 50, 736 (1987).
4 H Kawanishi and H Ikeda, *Jap J Appl Phys* 30, 27 (1991).
5 K Fujiwara, K Kanamoto and N Tsukada, *Phys Rev B* 40, 9698 (1989).
6 G Bacher, J Kovac, K Streubel, H Schweizer and F Scholz, *Phys Rev B* 45, 9136 (1992).
7 X Liu, S Nilsson, I Samuelson, W Seifert and P L Souza, *Phys Rev B* 47, 2203 (1993).
8 J Hegarty, L Goldner and M D Sturge, *Phys Rev B* 30, 7346 (1984).
9 G Bastard, C Delalande, M H Meynadier, P M Frijlink and M Voos, *Phys Rev B* 29 7042 (1984).

MoP23

DETERMINATION OF BUILT-IN ELECTRIC FIELDS IN DELTA-DOPED GaAs STRUCTURES BY PHASE-SENSITIVE PHOTOREFLECTANCE

V.L.Alperovich, A.S.Jaroshevich, H.E.Scheibler, and A.S Terekhov

Institute of Semiconductor Physics, 630090 Novosibirsk, Russia

Photoreflectance (PR) technique, which in most cases is essentially a contactless form of electroreflectance, is based on the screening of built-in fields by photogenerated charged carriers created by the modulated illumination. One of the problems of the PR spectroscopy is that several regions of a sample may simultaneously contribute to PR, thus hindering the interpretation and quantitative analysis of the resulting spectra. In this paper we developed a technique for separation of contributions originating from different regions of a layered semiconductor structure. This technique explores differences in the temporal responses of the PR signal, which stem from differences in relaxation kinetics of screening of the built-in fields. As a result, the phase shifts of PR contributions with respect to the light pump are different. Therefore, proper selection of modulation frequency and of the phase angle of the synchronous detector allows us to suppress one of the contributions and to extract the other (or the superposition of the other contributions, if more than two interfaces contribute to a PR spectrum).

Using the proposed technique of phase suppression, the Fourier analysis of Franz-Keldysh oscillation, and the precise step-by-step etching of GaAs, we studied the built-in fields in the following MBE-grown structures: (i) GaAs with a single delta-doped layer, (ii) delta-doped n-i-p-i superlattices with a "sawtooth" potential; (iii) GaAs SIN$^+$ structure, which contained 100-nm undoped GaAs layer separated from the n$^+$-substrate by a 1-μ n$^+$-GaAs buffer layer. Along with the well-known above-bandgap Franz-Keldysh oscillations originating from the regions with homogeneous built-in field, we observed sharp near-bandgap features in the PR spectra of delta-doped structures. It was shown that these features stem from the built-in fields of buffer layers and are not associated with quantum-confined optical transitions. Built-in electric field at the interface of highly doped n$^+$-GaAs buffer layer with n$^+$-substrate was observed in a GaAs SIN$^+$ structure. The interface band diagram was determined, with the Fermi level being fixed within the range of 0.1 - 0.2 eV below the bottom of the conduction band. The observed Fermi level fixing is due to the interface defects, which arise at the initial stages of the molecular beam epitaxy. Thus, the development of photoreflectance spectroscopy performed in the present work enabled us to probe the built-in electric fields in layered semiconductor structures and, therefore, to evaluate the concentration of charged defects at surfaces and interfaces.

MoP24

Advantages of a piezoelectric field in a quantum well

U. Ekenberg
Department of Theoretical Physics
Royal Institute of Technology, S-10044 Stockholm, Sweden
and
D. Richards
Cavendish Laboratory, Madingley Road, Cambridge CB3 0HE, UK

We have compared the properties of strained quantum wells grown along the (001) and (111) directions. In the latter case a piezoelectric field is created which we have found to have several advantages. We have analyzed in some detail quantum wells n-doped on one side by performing self-consistent subband structure calculations in the local density approximation and calculating scattering times due to remote ionised impurity scattering, which is an important limiting factor for the mobility. We find that the scattering times can be increased considerably by increasing the separation between the electrons and the ionised donors. We also predict electron densities in excess of $3 \cdot 10^{12} cm^{-2}$, which should be useful for improving High Electron Mobility Transistors (HEMT's).

1. Introduction

So far layered semiconductor heterostructures have usually been grown along the (001) direction, but in the last few years other growth directions have also been used. This in particular applies to the (111) direction where the initial growth problems have been overcome to a large extent. Hayakawa et al. [1] showed that good crystal quality can be achieved by tilting the substrate. (111)-grown $GaAs$ quantum well lasers were found to have lower threshold current densities compared to (001)-grown ones [1], which was explained by the lower parallel hole mass for (111) growth [2]. More recently, the critical layer thickness for strained layers was found to be larger [3] for (111) growth than for (001) growth. In $GaAs/AlGaAs$ heterostructures grown along (311) the dopant Si turns out to be an acceptor, which has lead to considerably enhanced hole mobilities [4].

It was pointed out by Smith [5] that a built-in longitudinal piezoelectric field (i.e. directed perpendicular to the layers) is created if a strained heterostructure is grown along anything but the (001) or (110) directions. For a given amount of strain this longitudinal piezoelectric field has its maximum for growth along the (111) direction. In this paper we will only consider (111)-grown samples and compare them with the corresponding (001)-grown samples. We will consider quantum wells n-doped on one side only in which the piezoelectric field concentrates the electrons to the interface region near the undoped barrier.

In a preliminary report [6] we examined the possibility of taking advantage of the piezoelectric field in such structures. Then, we only considered the often studied combination of $InGaAs$ quantum wells and $GaAs$ barriers and made some conclusions concerning sample design. With a well width of 200 Å one can have 1 % strain without forming dislocations [3, 7] and simultaneously the charge distribution can respond considerably to the piezoelectric field. We also compared different background doping in finite and semi-infinite buffer layers and found some advantage of having a wide n-type buffer layer as the "undoped" barrier. Hence, we only consider this case here. We take the background donor concentration to be $10^{14} cm^{-3}$ and the intentional donor concentration N_d to be $2 \cdot 10^{18} cm^{-3}$. We have found that the results are remarkably insensitive to N_d. This can be explained by a simple argument. We consider two samples with intentional donor concentrations N_{d1} and N_{d2}, spacer layer widths d_1 and d_2 and depletion layer widths a_1 and a_2. We further assume that the carrier concentration N_s is the same for the samples. This implies

$$N_{d1}a_1 = N_{d2}a_2 \qquad (1)$$

The line up of the Fermi level in the electron gas and the doped barrier implies that the band bending in the barrier is the same for both the samples.

$$\frac{1}{2}N_{d1}a_1^2 + N_{d1}a_1d_1 = \frac{1}{2}N_{d2}a_2^2 + N_{d2}a_2d_2. \qquad (2)$$

Together with eq (1) this gives

$$\frac{1}{2}a_1 + d_1 = \frac{1}{2}a_2 + d_2 \qquad (3)$$

Thus the distance from the interface to the middle of the depleted layer and thereby the average electron-donor separation are the same in both the samples. We can then expect similar scattering times.

In this paper we have made a more systematic study and have considered several material pairs in which the compressive or tensile strain is 1 %. $In_{0.15}Ga_{0.85}As$ quantum wells surrounded by $GaAs$ or $Al_{0.3}Ga_{0.7}As$ barriers and $In_{0.68}Ga_{0.32}As$ or $In_{0.39}Ga_{0.61}As$ quantum wells (under biaxial compression or tension, respectively) between InP or $Al_{0.48}In_{0.52}As$. Among the material pairs considered a good choice seems to be $In_{0.68}Ga_{0.32}As/Al_{0.48}In_{0.52}As$, partly due to the large conduction band offset. We have also calculated scattering times due to remote ionised impurity scattering which gives a measure of the potential improvements of the mobility.

2. Calculations

We have performed self-consistent subband structure calculations in the envelope function approximation. Using a modified variational approach we apply current-conserving boundary conditions [8] and the numerical work mainly consists of diagonalisation of 21 x 21 matrices. Exchange and correlation have been included in the local density approximation [9]. As a measure of the shift of the electron distribution we have determined the average position (z) numerically. The strength of the piezoelectric field is given by simple analytical expressions involving the lattice mismatch and experimentally determined material constants [5]. We have considered different values of the 2D electron density N_s and the spacer layer width d_s.

Using the results of these calculations as input we have also calculated scattering times for remote ionised impurity scattering. This we do within the Born approximation, determining the screened Coulomb interaction between an electron and the ionised donors within the random phase approximation [10]. The scattering time we consider is that for electrons at the Fermi wavevector, which is appropriate for low temperatures, as it is only electrons at the Fermi level which are then involved in transport. The mobility μ is related to the total scattering time τ by $\mu = e\tau/m^*$, where m^* is the electron mass. In this paper we only calculate the contribution from remote ionised impurity scattering to the total scattering time and only for cases with one occupied subband.

3. Results

a. Shift of electron distribution

For (001) growth, the electrons in a one-side doped quantum well are shifted towards the doped barrier because of the attraction to the ionised donors. This shift decreases the average electron-donor separation and increases the remote ionised impurity scattering. A typical example is given in fig 1a. This effect can be opposed by a piezoelectric field, which causes the electrons to be strongly displaced towards the undoped barrier (fig. 1b).

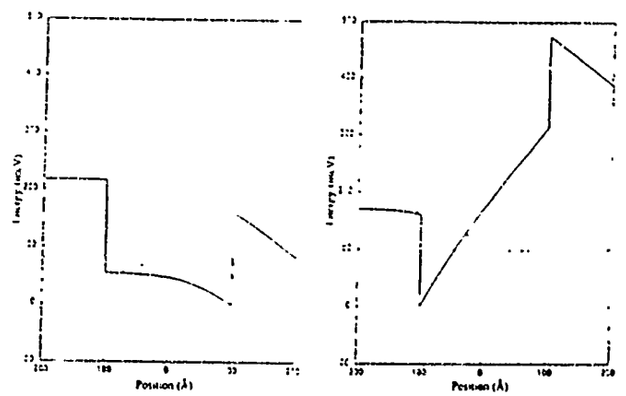

Potential (solid lines) and charge density (dashed lines) in a 200 Å $In_{0.15}Ga_{0.85}As$ quantum well surrounded by GaAs barriers for two different growth directions: (a) (001) growth, no piezoelectric field, d = 92 Å, and (b) (111) growth, piezoelectric field = 2.23 10^5V/cm, d = 391 Å. In both cases the electron density is $6 \cdot 10^{11}cm^{-2}$. Only the right barrier is intentionally doped.

The impurity scattering is decreased by this effect as well as by the effects described below. The appropriate sign of the piezoelectric field can be influenced by three factors: (i) the sample can be grown along the inequivalent directions called (111)A or (111)B, (ii) the quantum well can be under either compressive or tensile strain, and (iii) the doped barrier can be grown before or after the quantum well. We do not specify which case we have but only assume that the flexibility with these factors is used such that the piezoelectric field moves the electrons away from their parent donors.

It should be noted that the strong concentration of the electrons near the undoped barrier can lead to enhanced interface roughness scattering. This effect can be expected to vary from sample to sample and it is beyond the scope of the present article to evaluate it. Here we just try to minimise the effect of remote impurity scattering. But it should be noted that in designing the optimal structure a possible difference between (111) growth and (001) growth with respect to other scattering mechanisms should be taken into account.

b. Enhanced electron concentration

The piezoelectric field does not only influence the distribution of the electrons in the quantum well but also increases their number [6, 11, 12]. A similar idea was suggested by Snow et al. [13] who used a piezoelectric field in a barrier to produce a 2D electron gas without intentional doping in the barrier. We assume that the intentionally doped layer is thick enough that it is not completely depleted. Then the width of the depleted

layer is increased by the piezoelectric field and N_s, the number of electrons per unit area, increases. In the case of $InGaAs/GaAs$, N_s can be increased from $6.0 \cdot 10^{11} cm^{-2}$ to $1.18 \cdot 10^{12} cm^{-2}$ in a typical case [6]. If N_s is already rather large for the (001) grown samples, the relative increase due to the piezoelectric field is smaller. For example if we use $Al_{0.3}Ga_{0.7}As$ barriers but keep the spacer layer width fixed, the corresponding increase is from $1.5 \ 10^{12} cm^{-2}$ to $1.84 \cdot 10^{12} cm^{-2}$. The reason why this increase is smaller than for $GaAs$ barriers, even on an absolute scale, is that here we have two filled subbands

As discussed in c) below the maximal value of N_s is obtained if the spacer layer is zero It is also found that a large conduction band offset leads to a high N_s if the other factors are kept constant In the optimal case with $In_{0.68}Ga_{0.32}As/Al_{0.48}In_{0.52}As$ we predict that an N_s value of $3.2 \cdot 10^{12} cm^{-2}$ can be achieved provided that the conduction band offset, that we use as an input parameter, is correct. We have taken this to be 615 meV for this system. This is based on an interpolation between the calculated band offsets for lattice matched materials [14]. It is larger than what we would obtain from ref [15] but smaller than the experimental value in ref. [16].

To our knowledge such high electron densities have not previously been achieved in standard modulation-doped structures. Above we have considered an Al content of 30 % because then the $AlGaAs$ still has a direct band gap. It is likely that higher Al contents will improve the results further, but it is dubious to use the one-valley envelope function approximation when one material has its conduction band minimum away from the Γ point. We have therefore refrained from such calculations.

c. Increased spacer layer widths

A thin ($\sim$ 100 Å) undoped spacer layer of the barrier material is often grown between the doped layer and the quantum well. The purpose is to reduce the impurity scattering by increasing the electron-donor separation. However, a spacer layer also increases the band bending in the barrier and thereby decreases the carrier concentration N_s, which vanishes if d_{sp} is too large. We saw above in b) that considerably higher electron concentrations can be obtained in (111)-grown samples than (001)-grown ones which are identical except for the growth direction. Thus, it is possible to increase d_{sp} in the (111)-grown sample until N_s has been lowered to the same level as in the (001)-grown sample. In this way we can compare samples with the same electron densities N_s but with different spacer layer widths d_{sp} and electron distributions, as shown in fig. 1. Here we keep N_s at $6.0 \cdot 10^{11} cm^{-2}$.

In table 1 we compare samples for both the growth directions and different material pairs The results for different material pairs depend on the effective masses and dielectric constants as well as the piezoelectric field and the conduction band offset, but we have found that the latter two are the most important factors. For each case we include both the scattering time due to remote impurity scattering, τ, and the average electron donor separation given by

$$\langle L \rangle = \frac{L_z}{2} + d_{sp} + \frac{a}{2} - \langle z \rangle \qquad (1)$$

Here L_z is the quantum well width, a is the depletion layer width and $\langle z \rangle$ is the average electron position relative to the middle of the quantum well We note that both $\langle L \rangle$ and τ are increased considerably by the piezoelectric field. They are also larger for larger conduction band offsets. In general τ is increased more than $\langle L \rangle$ by these factors If other scattering mechanisms could be ignored, the increase in scattering time, because of the piezoelectric field, from 55 fs to 2ps for the case of $In_{0.15}Ga_{0.85}As/GaAs$ corresponds to an increase in the mobility from $2.6 \ 10^3 cm^2/Vs$ to $1.0 \ 10^7 cm^2/Vs$. Even if other scattering mechanisms are taken into account it is easy to verify that important improvements to the low-temperature electron mobilities are possible

Table 1. Average electron donor separation $\langle L \rangle$ in Å and scattering time τ in ps due to remote ionised impurity scattering for different material pairs The conduction band offset ΔE_c in meV and the piezoelectric field ϵ_p in kV/cm ((for (111) growth) are also given

Quantum well	Barrier	ΔE_c	ϵ_p	$\langle L \rangle$ (001)	$\langle L \rangle$ (111)	τ (001)	τ (111)
$In_{0.15}Ga_{0.85}As$	$GaAs$	161	223	92	391	0 055	2.21
$In_{0.15}Ga_{0.85}As$	$Al_{0.3}Ga_{0.7}As$	439	223	389	669	1.18	6.87
$In_{0.39}Ga_{0.61}As$	InP	158	171	81	288	0 045	1.04
$In_{0.39}Ga_{0.61}As$	$Al_{0.48}In_{0.52}As$	498	171	478	687	1.75	5.93
$In_{0.68}Ga_{0.32}As$	InP	275	115	202	322	0.233	0.941
$In_{0.68}Ga_{0.32}As$	$Al_{0.48}In_{0.52}As$	615	115	606	739	2 68	5.22

d. Higher N_s limit for filling of second subband

We have investigated how high carrier densities can be achieved for the different cases before the second subband starts to fill. For $In_{0.68}Ga_{0.32}As/Al_{0.48}In_{0.52}As$ we have found that this limiting N_s-value is $8.25 \ 10^{11} cm^{-2}$ in the (001) case and somewhat higher, $8.75 \ 10^{11} cm^{-2}$, in the (111) case. The corresponding scattering times are 1.2 and 2 0 ps, respectively If the main purpose is to achieve high mobilities one should probably try to stay slightly below this limiting N_s-value, as for higher carrier concentrations intersubband scattering becomes important. This occurs in the case mentioned above with $N_s = 3.2 \ 10^{12} cm^{-2}$. Calculations including this scattering mechanism will be presented elsewhere In the present paper we have only calculated scattering times for samples with only one filled subband.

4. Discussion and conclusions

We have calculated subbands, electron distributions and remote ionised impurity scattering times for strained quantum wells doped on one side. We have compared (001)-grown samples with (111)-grown ones, where the main difference is the quite strong built-in piezoelectric field, which gives many advantages. The optimal design depends on what properties we want to improve. If we want to achieve high electron mobilities at low temperatures for studies of fundamental effects like the fractional quantum Hall effect, we should increase the electron donor separation, in order to reduce remote ionised impurity scattering in the quasi-2D electron gas The piezoelectric field yields two effects contributing to this. The electron distribution is displaced towards the undoped barrier and one can increase the width of the undoped spacer layer by several hundred Å.

For studies of the fractional quantum Hall effect, especially in the Wigner solid regime, it is often an advantage to have a low carrier density In high electron mobility transistors (HEMT's), on the other hand, one often strives for very high carrier concentrations which, among other things, give rise to strong screening For devices operating at room temperature, where phonon scattering is important, the saturation velocity can be more important than the impurity scattering limitation of the mobility at low temperatures and small current densities In this respect we believe that the possibility of using the piezoelectric field to raise N_s above $3 \ 10^{13} cm^{-2}$ can be very valuable.

In all the cases considered here the quantum well material is a ternary alloy and so the mobility is influenced by alloy scattering In future work we plan to consider strained binary $GaAs$ quantum wells between suitable barrier materials Even if these structures are not optimal with respect to impurity scattering it is conceivable that the well developed GaAs technology and the absence of alloy scattering can make such structures promising for applications

Acknowledgements

U E is grateful to the Swedish Natural Science Research Council for economic support and D R wishes to thank St. John's College, Cambridge, UK, for support

References

[1] T Hayakawa, M Kondo, T Suyama, K Takahashi, S Yamamoto and T Hijikata, Jpn J. Appl Phys 26, L302 (1988)

[2] W Batty, U. Ekenberg, A. Ghiti and E P O'Reilly, Semicond. Sci Technol 4, 901 (1989)

[3] T Anan, K Nishi and S. Sugou, Appl Phys. Lett 60, 3159 (1992)

[4] J. J Heremans, M. B Santos and M. Shayegan, Appl. Phys. Lett. 61, 1652 (1992)

[5] D L. Smith, Solid State Commun. 57, 919 (1986)

[6] U Ekenberg and D. Richards, Surf Sci 263, 580 (1992).

[7] T G Andersson, Z G Chen, V D Kulakovskii, A Uddin and J. T Vallin, Appl Phys Lett 51, 752 (1987)

[8] M Altarelli, Phys Rev B 28, 842 (1983)

[9] T Ando and S Mori, J. Phys Soc Jpn 47, 1518 (1979)

[10] T Ando, A B Fowler and F. Stern, Rev Mod. Phys. 54, 437 (1982).

[11] X Li, K F Longenbach and W I Wang, Appl Phys. Lett 60, 1513 (1992)

[12] J Sánchez-Dehesa, J L Sánchez-Rojas, C Lopez and R J. Nicholas, Appl Phys Lett. 61, 1072 (1992)

[13] E S Snow, B V Shanabrook and D Gammon Appl. Phys Lett 56, 758 (1990)

[14] M. S Hybertsen, Appl Phys Lett 58, 1759 (1991).

[15] M P C M Krijn, Semicond. Sci Technol 6, 27 (1991)

[16] J-H Huang, T Y Chang and B Lalevic, Appl Phys Lett 60, 733 (1992)

MoP25

Determination of the band structure parameters of pseudomorphic GaInAs quantum wells by means of simultaneous transport and optical investigations

E. Litwin - Staszewska[*], F. Kobbi, M.Kamal-Saadi, D. Dur, C.Skierbiszewski[*], H.Sibari, K. Zekentes*, V. Mosser**, A. Raymond, W. Knap, J. L. Robert

Groupe d'Etude des Semiconducteurs Université Montpellier II
Place E Bataillon, 34095 Montpellier Cedex 05, FRANCE
** FORTH Institute of Electronic Structure and Laser. P O. Box 1527,*
Heraklion,71110 Crète,Greece.
*** Schlumberger Montrouge Recherche*
50, av. Jean Jaurès, BP 620-05, F-92542 Montrouge, France

Abstract

Combined studies of GaAlAs/GaInAs/GaAs pseudomorphic structures have been performed by means of transport under hydrostatic pressure, luminescence and cyclotron resonance emission experiments. The structures investigated were 130 Å quantum wells. They were δ-doped outside the quantum well, with the spacer thickness ranging between 20 and 60 Å. These structures allowed us to study the influence of the carrier concentration on the mobility and on the position of the Fermi level above the first electrical sub-band. By using pressure and illumination, we changed the carrier concentration N_s from 0.5 to 1.8 10^{12} cm^{-2}. In this range, only the first electrical sub-band is populated. A strong decrease of mobility at higher concentrations was shown and depended essentially on correlation effects. High magnetic field transport measurements confirmed that only the lowest sub-band was populated. Moreover, cyclotron resonance emission gave the effective mass as a function of the carrier density in the well. On this basis, the importance of the non parabolicity effect was estimated. All these results were interpreted within the framework of the variational method leading to a determination of the most important physical parameters describing this system

High quality pseudomorphic heterostructures can be grown epitaxially provided the thickness of the strained layer are small enough to avoid the generation of dislocations and defects. These structures, quantum wells and superlattices, have been studied intensively in the last years because of the wider range in the confinement related effects which they make possible. We focused our work on pseudomorphic GaInAs quantum wells which were δ-doped outside the well.

A combination of electrical transport and optical experiments have been performed to characterize these structures and to determine the parameters describing their electronic properties and their relation to the carrier concentration N_s.

The samples investigated were Si-δ doped $Al_xGa_{1-x}As/Ga_{1-y}In_yAs/GaAs$ structures grown by molecular beam epitaxy. The Al mole fraction, x=0.32, was checked by double X-ray diffraction as was the Indium content, y=15%. The quantum well of thickness 130 Å was separated from the δ-doping plane by a spacer S_p ranging between 20 to 50 Å. The values of the effective doping density N_s amounted to 1.7 10^{12} cm^{-2} and 2.5 10^{12} cm^{-2} .The samples were patterned in a Hall-bar geometry with six AuGeNi contacts

Electrical characterizations

Hall measurements were performed between 4 and 400K using a helium continuous flow cryostat, reversing both the current and the magnetic field

In order to study the behaviour of the structures as a function of the carrier concentration N_s, the metastable properties of the DX-Si centres present in the GaAlAs were used. The combined effects of illumination [1] (by red LED), pressure (He-gas compressor system is used to change

the pressure even at low temperature) and temperature were used to produce different populations depending on the preparation cycles [2,3] (high pressure freeze out technique HPFO and persistent photoconductivity PPC). It should be noted that all the measurements were actually made at atmospheric pressure by means of this technique

In figure 1-a, we show the Hall mobility μ_H measured at 4.2K in the dark as a function of N_s. As expected, the carrier concentration in the well was increasing with the δ doping density N_δ and was a decreasing function of the spacer thicknesses S_p. In figure 1-b the variation of μ_H at 77K is presented for two samples having the same N_δ but different S_p. It should be noted that the mobility passes through a maximum in both cases. The increase of μ_H with N_s has already been observed in heterojuctions and can be well explained taking into account the effect of screening by free carriers [4].

To explain the maximum and the decrease of the mobility [5] observed on our samples, we must consider the effect of spatial correlation of remote impurity charges in the Si δ-doped plane[6,7]. Indeed, other effects as the influence of the higher sub-band could not be involved since N_s in the well was too small (see SdH experiments). The role of alloy scattering certainly could not explain the strong decrease of μ_H observed. The effect of correlation could be seen by measuring the mobility after different preparation cycles. In ref [8], it was demonstrated that depending on the way the remote impurity charges are distributed among the donor sites, different values of electron mobility were obtained for the same N_s and in the same sample, which confirmed this hypothesis.

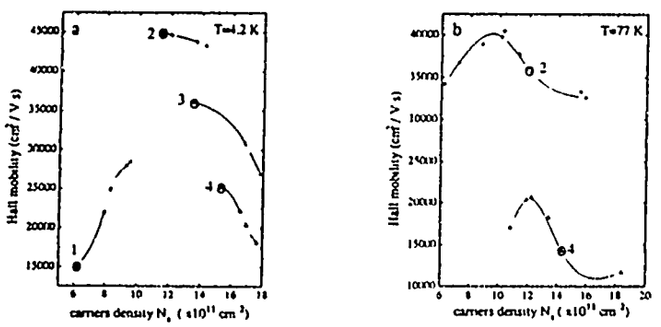

Fig.1: Hall mobility μ_H versus carrier concentration N_s for various samples. 1 (N_δ=1.7 10^{12} cm^{-2}, S_p=40 Å), 2, 3 and 4 (N_δ=1.7 10^{12} cm^{-2} and respectively S_p=60, 40, 20 Å). The points inside the circles are obtained under equilibrium conditions

Fig 1-a) T=4.2 K. ●, ●, Δ, x are obtained after illumination (PPC)

Fig 1-b) T=77 K, P=1atm. ● Δ are obtained after different HPFO preparation cycles. Points for the highest concentrations are obtained after illumination (PPC)

Cyclotron resonance experiments

Cyclotron resonance emission was observed in the same samples. In these measurements, electrons heated by electric pulses to occupy higher Landau levels, relaxed by emitting photons of the cyclotron energy. The emitted radiation was detected by means of a selective GaAs detector operating at an energy of 4.43 meV. A detailed description of the experimental set up can be found in ref.[9]. An increase of the cyclotron mass with N_s was observed as shown in figure 2.

The cyclotron resonance peak shifted towards higher magnetic fields with increasing N_s in the quantum well. This effect was interpreted in term of the variations of effective mass with energy in conduction band (non parabolicity effects) [10].

Shubnikov-de Haas experiments (SdH)

Carrier concentrations in the well were deduced from the period of ρ_{xx} magnetoresistance oscillations (SdH effects) [11]. The values deduced from these experiments were the same as those determined by Hall effect measurements. These results confirmed that in our samples only the lowest sub-band of the quantum well was populated (see electrical characterization)

Thus it's possible, using the values of the effective masses deduced from cyclotron resonance experiments, to determine the position of the Fermi level above the conduction band minimum as a function of the carrier density. The results are shown in figure 3.

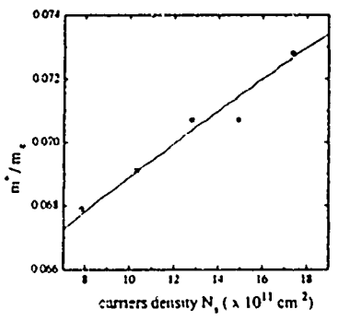

Fig 2 : Cyclotron resonance effective mass as a function of the carrier concentration N_s. The solid line is the theoretical curve

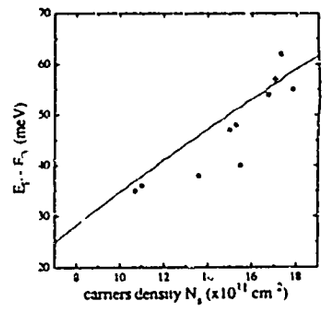

Fig 3. The difference between Fermi energy E_F and the first electrical sub-band E_0 as a function of N_s. ● are deduced from SdH experiments, + is obtained from photoluminescence spectra. The solid line represents theoretical results.

Luminescence experiments

Photoluminescence spectra [11, 12] were obtained at 12K using an He-Ne source operating at 632.8 μm with an intensity of 0.5 W/cm². The signal was detected using a Si photodetector. Under these experimental conditions, the concentration measured by the Hall effect was practically the same for each sample. The Fermi level position above the conduction band minimum was deduced from the Fermi edge singularity observed in the spectra. Its value is in good agreement with those deduced by SdH experiments (see figure 3)

Modeling

Using the variational method [13], we determined the Fermi level energy E_F and the first electrical sub-band E_0 as a function of N_s. By calculating the wave function of the electron at the Fermi level we determine its mean position z_0 in the well. and the corresponding energy $E(z_0)$ above the bottom of the conduction band. The Kane model was used to calculate the effective mass at the energy $E(z_0)$:

$$m^*(E(z_0)) = m^*_0 (1 + 2\, E(z_0)/E_g)$$

A good agreement with the experimental results (E_F and $m^*(E_F)$) was found by taking the following parameters Eg=1.355 eV, m^*_0=0.060 m_e and the trial functions given in ref.[13].
We wish to stress that good agreement between experimental and theory requires a full variational calculation and cannot be deduced from simple models of triangular or rectangular wells This was due to the high values of N_s we have in our system and to the existence of the second barrier (InGaAs/GaAs).

Conclusion

Electrical and optical experiments performed on our AlGaAs/InGaAs/GaAs structures have shown that only the first sub-band was populated up to N_s=1.8 10^{12} cm^{-2}. Correlation effects must be invoked to explain the maxima and the decrease of the mobility when N_s was increasing Cyclotron resonance experiments allowed us to establish the effect of non parabolicity by measuring the electron effective mass as a function of N_s. PPC and HPFO techniques were used to change N_s in the well. Whatever the method used to change the carrier concentration N_s in the range of 0.5 to 1.8 10^{12} cm^{-2}, accounts for the energy structure of the well. This also allows us to estimate the effect of non parabolicity on the effective mass. This establishes the experimental method which we believe can be used to determine the properties of InGaAs quantum wells with different thicknesses and others growth parameters.

(x) Permanent address: UNIPRESS, Polish Academy of Sciences, 01-142 Warszawa, POLAND.

References:

[1] M.Van der Burgt, A.Van Esch, F.M Peeters, M.Van Hove, G Borghs and F Herlach, Physica B 184 p 211 (1993).
[2] R.Piotrzkowski, E.Litwin-Staszewska, T.Suski, L.Konczewicz and J.L Robert, Jpn J. Appl Phys. Vol 32 (1993) suppl. 32-1.
[3] S Contreras, L.Konczewicz, V Mosser, J L Robert and K.Zekentes, Proc 21 Int. Conf. of Physics Semicond., Beijing (1992).
[4] H Okico, J.K.Luo, K.Matsuishi and Hasegawa, Appl. Phys Lett 54(1), p 36 (1989).
[5] G M.Yang, S G Park, K.S Seo and B D Choe, Appl Phys. Lett., 60(19), p 2380 (1992).
[6] R.Piotrzkowski, E.Litwin-Staszewska and J L Robert, 17 Int Conf of Defects in Semicond., Gmunden (1993).
[7] T.Suski, P.Wisniewski, L.H.Dmowski, I Gorczyca, J.Smoliner, E Gornik, G Böhm and G Weimann, MSS 6 Conference.
[8] E.Litwin-Staszewska, T.Suski and J.L.Robert (to be published)
[9] W Knap, D Dur, A.Raymond, C Meny, J Leotin, S Huant and B Etienne, Rev Sci. Instrum 63(6), p 3293 (1992)
[10] W.Zawadzki, C Chaubet, D Dur, W Knap and A Raymond, MSS-6 Conference.
[11] H Brugger, H Mässing, C.Wölk, H Kern and D Heitmann, Appl. Phys. Lett 59(21), p 2739 (1991)
[12] J M Gilpérez, J L.Sanchez-Rojas, E.Munoz, E.Calleja, J P R David, G Hilland and J Castagne, Appl Phys. Lett. 61(10), p 1225 (1992).
[13] G Bastard, Wave mechanics applied to semiconductor heterostructures, Edition de Physique (1988)

MoP26

The conduction band spin splitting in type-I strained and unstrained (GaIn)As/InP quantum wells

P. Omling, B. Kowalski
Solid State Physic Department, University of Lund, Box 118, S-22100 Lund, Sweden

B.K. Meyer, D.M. Hofmann, C. Wetzel
Physik-Department, E 16, Technische Universität München, D-85747 Garching bei München, Germany

V. Härle, F. Scholz
1. Physikalisches Institut, Universität Stuttgart, Pfaffenwaldring 57, D-7000 Stuttgart, Germany

Abstract

We present the first successful optically detected magnetic resonance experiments (ODMR) on strained and unstrained $Ga_xIn_{1-x}As$/InP type I quantum wells. The resonances attributed to electrons are in general anisotropic and detailed results are given for the composition range $0.4 < x < 0.6$ Extrapolating to the binary end points i.e. InAs and GaAs close agreement with existing results is found. The anisotropy is explained within a simple model using subband calculations. It also explains why one sided p-type modulation doping reduces the electron-hole wavefunction overlap, increases the radiative life times and allows for optical detection of magnetic resonance. A detailed discussion why hole resonances can be ruled out is given.

Introduction

Optical detection of electron spin resonance (CESR, ODMR) is an ideal technique to determine the Lande factor g^* of conduction electrons [1]. The g-factor can be calculated by $\vec{k}\cdot\vec{p}$ theory and thus provides a test of band structure parameters and theoretical concepts. This is of special interest for the technologically important type-I quantum wells (QW) systems such as GaAs/(GaAl)As or (GaIn)As/InP However, the measurement of g-factors in these structures is not an easy task, since the radiative recombination times occur on a nanosecond time scale. A prerequisite to observe optically detected magnetic resonance (ODMR) is, however, to induce microwave transitions within the life-time of a decaying system. For the standard cw-ODMR technique life-times must be longer than 0.1 μs. Therefore it is no wonder that the few experimental results on two dimensional structures using the ODMR technique were applied on type II quantum wells Here the electrons and holes are separated in real space, e.g. with the electrons in the barrier material and the holes in the quantum well or vice versa. This separation leads to increased recombination times into the microsecond range. In type I quantum wells type-II behaviour, i.e. longer life-times can be achieved by the presence of an external electrical field applied perpendicular to the quantum well plane [2]. A built in electrical field as achieved by a one-sided modulation doping can play an equivalent role We will demonstrate that one sided p-modulation doping allows for the first successful identification of electron g-values in strained and unstrained InGaAs/InP quantum wells.

Experimental

Our measurements were performed on $Ga_xIn_{1-x}As$ single quantum well (SQW) and multiple single quantum wells (MQW). The structures were grown by metal organic vapour phase epitaxy (MOVPE) either lattice-matched ($x_{Ga} = 0.47$) to InP, having different well thicknesses or with varying composition ($0.4 < x_{Ga} < 0.6$) but fixed QW thickness ($d = 15$ nm). The characteristic layer sequence was the same in all samples. The QW on top of several 100 nm of InP is followed by a single sided p-modulation doping, a 10 nm layer with an acceptor concentration of typically $2 \cdot 10^{18}$ cm^{-3}. It is separated from the QW by a 5 nm spacer. All structures were grown in a low pressure MOVPE system at 80 mbars and at a growth temperature of 620 °C on semi insulating InP:Fe substrates. The quality of the samples was controlled by Hall effect, photoluminescence and magneto-luminescence. Hall effect measurements (77 K) showed mobilities around 100 cm^2/Vs for the composition range studied ($0.6 < x < 0.4$).

For the ODMR experiments the sample was placed in an open TE_{011} resonator itself located in the center of split-coil superconducting magnet (Magnex, 0 – 4 T) allowing for excitation with unpolarized light from the 514 nm line of an Ar^+ (typically 100 mW) laser. The luminescence emitted was focussed on the entrance slit of a f/4 48 cm double monochromator (Spex) and detected by a LN_2 cooled Ge diode (North Coast). For the resonance experiments the circularly polarized components of the emission in Faraday configuration were analized by a combination of a linear polarizer and photo-elastic stress modulator (HINDS) working at 42 kHz. The spin resonance transitions were induced by applying microwaves at 21 or 36 GHz delivered from a Gunn diode or a klystron. The magnetic field was varied to tune to resonance.

Experimental Results

A typical photoluminescence spectrum from the $Ga_xIn_{1-x}As$/InP QW series is shown in the inset of fig 1. A single line with a half width of 8 meV is observed, the peak maximum is at $E = 0.83$ eV ($x = 0.47$, $d = 15$ nm). It is due to band to band recombination between the first electron and heavy hole subband (e_1hh_1). The emission is circularly polarized (magnetic circular polarized emission, MCPE) with a degree depending on temperature and the applied magnetic field. This behaviour reflects an unequal spin-occupation in the Zeeman split states and is a necessary condition to perform magnetic resonance experiments. The difference in occupation, in our case not a Boltzmann equilibrium, can be changed by resonant microwaves and the magnetic resonance signal is observed as a decrease of the MCPE signal (see fig.1). For the magnetic field parallel to QW plane (001) we obtain a g-value of $g_\parallel = -3.27 \pm 0.04$, for clarity the field dependent background signal of the MCPE has been subtracted (the sign of the g-value has been checked independently [3]). The resonance signal has a Lorentzian line shape characteristic for homogeneous broadening. When rotating the sample from (001) towards the [011] direction the resonance position changes, the g-value decreases significantly. (see fig 2). A complete 90 degrees rotation pattern could not be performed, since the MCPE signal on which we detect the ODMR decreased with increasing angle. The angular dependence was analized with the usual expression for the g-tensor in axial symmetry [4]

$$g(\vartheta) = (g_\parallel^2 \cos^2\vartheta + g_\perp^2 \sin^2\vartheta)^{1/2} \qquad (1)$$

where ϑ is the angle between the magnetic field and the quantum well plane. $g_\perp$ is the only fitting parameter and the solid line in fig.2 results from equ.1 when using $g_\parallel = -3.27 \pm 0.04$ and $g_\perp = -1.88 \pm 0.01$ (see also table 1).

As a function of composition the $g_\parallel$-values decrease for higher Ga-content, also the $g_\perp$-components follow this trend (see fig. 3 and table 1). The anisotropy ratio $g_\parallel/g_\perp$ more or less remains the same for constant well width of $d = 15$ nm and varying composition. The data points lie on a straight line (see fig 3), except for the values of the lattice-matched composition ($x_{Ga} = 0.47$). The reason is at present not understood, but this interesting observation deserves future investigations. The influence of size quantisation was studied in SQW's for $x_{Ga} = 0.47$. It was possible to observe resonances for a 100 nm (quasi-3-dimensional, 3D) QW down to thicknesses of 6 nm (see table 2). One notes that the anisotropy ratio decreases with increasing well width. For the quasi-3D QW no anisotropy is found, the g-value of -4.1 ± 0.01 is substantially smaller than reported by Johnson et al [5] of $g = 5.6 \pm 0.3$ (same composition and well width). Electrically detected spin resonance experiments gave values between 4 and 4.5, the authors [6] suggested that the bare or bulk spin splitting factor is $g = 4.1$, close to our experimental value.

Discussion and Interpretation

For an assignment of the resonances we first take a look on the band structure of the (GaIn)As/InP system. Strain and confinement considerably influence the ordering of the electron and hole levels in the QW's [7]. For $x_{Ga} < 0.17$, that means under compression of the layer, the radiative recombinations involve the conduction band and the $|J, J_z| = |3/2 \pm 3/2\rangle$ heavy hole valence band states, under tension ($x_{Ga} > 0.47$) the light hole $|3/2 \pm 1/2\rangle$ has to be considered. Including the mass dependent confinement energy the cross over point of the heavy and light hole energy as a function of Ga-content shifts. Calculations show that for x_{Ga} up to 0.5 the heavy hole is highest in energy for a QW width of 15 nm.

The large anisotropy of the g-tenser could on first sight suggests that the resonances could be due to holes. For the holes the Zeeman Hamiltonian in the Luttinger formalism can be written as [8]:

$$H_A = -2\mu_B \sum \left(\kappa J_{A,i} + q J_{A,i}^3\right), \qquad i = x, y, z \qquad (2)$$

with κ and q the Luttinger parameters and z parallel to [001]. In our samples the heavy hole band is separated from the light hole band by several 10 meV and it is highest in energy for $x_{Ga} < 0.5$. The heavy and light hole bands can thus be treated separately. Diagonalization of Eq. 2 gives the g-values for the heavy holes in the effective spin $J' = \frac{1}{2}$ formalism: $g'_{AA,\parallel} = 6\kappa + 13.5q$, $g'_{AA,\perp} = 3q$. q is usually very small (< 0.1), since it represents a correction due to 3rd order spin terms. Hence one expects a $g_\parallel \cos\vartheta$ behavior for the heavy hole resonances, as found in the systems $Si_{1-x}Ge_x$/Si [9] and AlAs/GaAs (type II superlattices) [10]. In both cases $|g_\perp|$ is close to zero. Also the $g_\parallel$-value should be less influenced when changing the composition, since on the In-rich side the Kohn-Luttinger parameters do not change considerably. Clearly, this is not in agreement with our experimental data, and therefore the assignment of the resonances to the spin splitting of the valence band is ruled out.

Furthermore all the spin split hole states near $\kappa = 0$ are occupied due to the two dimensional hole gas. Its Fermi energy E_0 between 5 and 20 meV has to be compared with a

spin splitting of 0.1 meV. We conclude, that spin resonance is not possible at the valence band edge. This is supported by the fact, that we detect the spin resonance on the band-edge-PL ($k \approx 0$).

We attribute the resonances to electrons at the edge of the lowest conduction subband. Extrapolating the g-values to the binary end points (see fig.3), i.e. InAs/InP and GaAs/InP supports this interpretation. For GaAs we have values close to zero, the bulk g-value is $g^* = -0.44$ [10]. The extrapolated value on the InAs side is 7.2, for a 100 nm InAs/GaSb quantum well values between 7.8 and 8.7 were observed [11].

The spin splitting for the 100 nm lattice-matched QW (quasi 3D) is calculated using Roth three band formula [12]

$$\frac{g^*}{g_0} = \frac{2}{m} p^2 \frac{\Delta}{3E_g(E_g + \Delta)} \qquad (3)$$

where p is the interband matrix element, $p^2/2m$ is 25.5 eV, the bandgap energy E_g is 0.813 eV and the spin-orbit splitting energy Δ is 0.356 eV. With equ.3 we calculate $g^* = -4.34$ in reasonable agreement with the experimental value of 4.01.

For the 2-D-system the band edge energy E_g and the lowest subband energies of the electrons E_{e1}, light E_{lh1}, heavy E_{hh1} and spin orbit split of holes E_{sh1} are needed. $g_\parallel$ is given by

$$\frac{g_\parallel}{g_0} = 1 - \frac{2}{3m} p^2 \left(\frac{3}{2(E_g + E_{e1} - E_{hh1})} - \frac{1}{2(E_g + E_{e1} - E_{lh1})} - \frac{1}{E_g + E_{e1} - E_{sh1}} \right) \qquad (4)$$

and $g_\perp$ by

$$\frac{g_\perp}{g_0} = 1 - \frac{2}{3m} p^2 \left(\frac{1}{E_g + E_{e1} - E_{lh1}} - \frac{1}{E_g + E_{e1} - E_{sh1}} \right) \qquad (5)$$

From eq. 4 and 5 the composition dependence as well as the anisotropy ratio $g_\parallel/g_\perp$ can be calculated, provided all parameters are known. In most cases the subband energies need to be calculated. Moreover, this calculations only hold for a flat bandprofile and the effects of the one side p-modulation doping on the bandstructure and subband energies are not considered. Preliminary selfconsistent calculations showed, that the energies of espacially the hole states deviate considerably from the flat band case. The electron states in the conduction band seemed to be less affected.

Calculated g-values in the flat band assumption deviate from the experimental ones by 30%.

For the GaAs/(AlGa)As material system a theoretical model has been put forward by Ivschenko et al [13] which could explain the large anisotropy as well as the well width dependence. It has to be adopted to the GaInAs/InP system. Strain and the influence of the electrical field have to be included. These theoretical calculations are currently under way.

The recombination life-time in type I QW's is on the nanosecond scale, the observation of ODMR is an indication that the radiative life-time must be larger than 0.1 μs. The reason is, that the one-sided p-modulation doping changes the band structure. In fig.4 the calculated band edges are shown for a 15 nm QW with lattice matched composition. The subband edges of the first quantized states (e_1, hh_1, lh_1) are indicated. The holes from the asymetric Zn-acceptor modulation doping on the left side are transfered into the deep quantum well ($Ga_{0.47}In_{0.53}As$: $\delta E_V = 383$ meV).

There is a strong electrical field between the dopant layer and the two-dimensional hole-gas. It peaks at the interface between barrier and QW with $E \approx 1.7 \cdot 10^5$ V/cm. The field causes a spatial separation of hole states from electrons along the growth direction z. This is shown by the square of the wavefunctions χ, for the electrons χ_{e1} and heavy holes χ_{hh1}. Due to the spatial separation of electrons and hole the overlap intergral entering into Fermi's Golden Rule is reduced and hence the recombination life-time increases. For the order of magnitude of the electrical field a reduction of a factor 100 is calculated.

With increasing size quantization the separation is suppressed, the radiative life-times get shorter and shorter. This happens to be the case for $d < 6.0$ nm, resonance experiments so far failed for $d \approx 4$ nm. We currently set up time-resolved measurements to verify this estimate.

Conclusion

We have measured the conduction band spin splitting in type I (InGa)As/InP QW's with varying composition and well width. It was possible due to a built-in electrical field by a p-modulation doping enhancing recombination life-times. A influence of the confinement energies on the g values is described theoretically.

Acknowledgement

This work was supported by the Deutsche Forschungsgemeinschaft via SFB 348.

References

[1] C. Herman and C. Weisbuch, Phys. Rev. B 15 (1977) 823
[2] H.J. Polland, L. Schultheis, J. Kuhl, E. Göbel and C. Tu, Phys. Rev. Lett. 55 (1985) 2610
[3] B. Kowalski, Diploma Thesis, Munich 1993
[4] C.P. Slichter, Principles of magnetic resonance, Harper and Row Publ. New York 1963
[5] G.R. Johnson, A. Kana-ha, B.C. Cavenett and S.J. Bass, Semicond. Sci. Technol. 2 (1987) 182
[6] M. Dobers, J.P. Vieren, V. Guldner, P. Bove and M. Razhegi, Phys. Rev. B 40 (1989) 8075
[7] D. Gershoni and H. Temkin, J. Lum. 44 (1989) 381
[8] H.W. v.Kesteren, E.C. Cosman, W.A.J.A. VanderPoel and C.T. Foxon, Phys. Rev. B 41 (1990) 5283
[9] E.R. Glaser, J.M. Trombetta, T.A. Kennedy, S.M. Prokes, O.J. Glembock, K. Wang and C.H. Chern, Phys. Rev. Lett. 65 (1990) 1247
[10] J.M. Trombetta, T.A. Kennedy, D. Gammon and S.M. Prokes, ed. by E.M. Anastassakis, J.M. Joannopoulos, 20. Int. Conf. of Semicond. Phys., World Scientific, Singapore, 1990 Vol. 2, p1361
[11] Landolt Börnstein, Semiconductors, edited by O. Madelung, M. Schulz and H. Weiss, Vol. 17a, Springer, Berlin 1982
[12] L.M. Roth, B. Lax and S. Zwerdling, Phys. Rev. 114 (1959) 90
[13] E.L. Ivschenko, A.A. Kiselev, Sov. Phys. Semicond. 26 (1992) 827

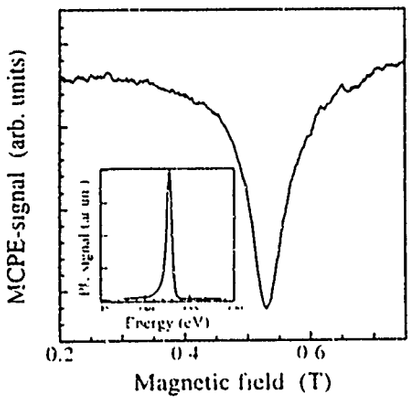

Fig 1: Optically detected magnetic resonance spectrum of a 15 nm $Ga_xIn_{1-x}As/InP$ single quantum well ($x = 0.47$) at $T = 1.6$ K, and a microwave frequency of 21 GHz. The inset shows the corresponding photoluminescence signal

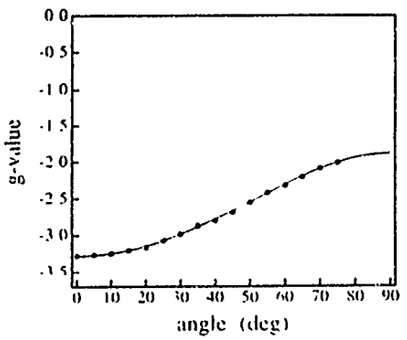

Fig 2 The anisotropy of the g factor for a rotation of the sample from the (001) plane towards the [110] direction with respect to the static magnetic field (solid circles: experimental points, the solid line is a fit to the experimental values with the help of equ 1, parameters: $d = 15$ nm, $x_{Ga} = 0.47$)

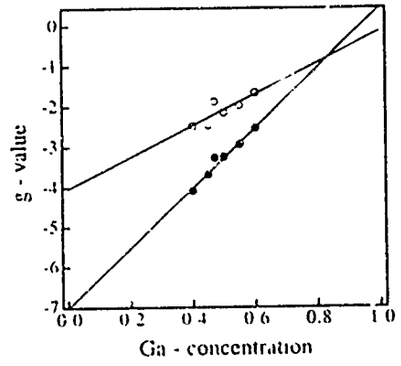

Fig 3 The parallel (full circles) and perpendicular (open circles) components of the g values for the different Ga compositions in $Ga_xIn_{1-x}As/InP$ single quantum wells. The solid lines are linear extrapolations

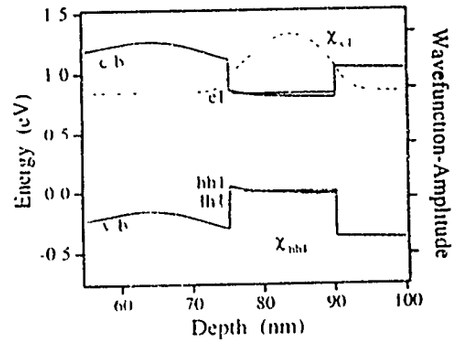

Fig 4 Bandstructure and subband energies for a 15 nm single quantum well considering the influence of the one sided p modulation doping. The amplitudes of the electron (dashed curve) and heavy hole (dotted curve) wavefunctions are indicated

x_{Ga}	$g_{\parallel}$	$g_{\perp}$
0.40	-1.08 ± 0.01	-2.19 ± 0.06
0.45	-3.68 ± 0.03	-2.16 ± 0.06
0.47	-1.27 ± 0.01	-1.88 ± 0.01
0.50	-1.21 ± 0.03	-2.15 ± 0.01
0.55	-2.91 ± 0.02	-1.98 ± 0.05
0.60	-2.53 ± 0.02	-1.67 ± 0.01

Table 1 The g values for $Ga_xIn_{1-x}As/InP$ quantum wells with different Ga contents and a constant well width $d \sim 15$nm

d(nm)	$g_{\parallel}$	$g_{\perp}$
100	-1.01 ± 0.01	-1.01 ± 0.05
15	-1.27 ± 0.01	-1.8 ± 0.01
10	-3.27 ± 0.01	-1.80 ± 0.01
8	-2.91 ± 0.01	-1.05 ± 0.01
6	-2.62 ± 0.02	-0.65 ± 0.05

Table 2 The g values for $Ga_xIn_{1-x}As/InP$ quantum wells with different thicknesses and a constant Ga composition $x_{Ga} = 0.47$

MoP27

Binding Energies of D Ion in GaAs Quantum Well

Y H Chang, J J Yeh*, Y M Sheu, C C.Wang, and T.C.Chen

Department of Physics, National Taiwan University, Taipei, Taiwan, Republic of China

K H Chang * P Lee

Institute of Electronics National Chiao-Tung University, Hsinchu, Taiwan, Republic of China

Abstract

Magnetic field dependent binding energies of D ion in the center of a 210 Å GaAs quantum well are determined from temperature dependent magneto-transport measurements The binding energies increase from 2 1 meV at 2T to 4 meV at 8T, and are consistently higher than the transition energies obtained from magneto optics measurements performed with the same sample We conclude from these data that in magneto-optics measurement the observed transitions are between ground and excited D states.

The properties of D ions in GaAs quantum wells have attracted much attention recently [1-9] A D ion is a shallow impurity that binds two electrons with binding energy lower than neutral impurity (D^0) because of Coulomb repulsion between electrons This is a simple many electron system and is an analogue of the H ion in atomic physics. D ion can be created much easier in a quantum well system than in a three-dimensional system [10]. With shallow impurities placed both in GaAs quantum wells and in AlGaAs barriers the impurity atoms in the wells can capture an extra electron released from barrier

impurities to form a D ion. Because of the effect of quantum confinement, the binding energy of D ion in quantum well is enhanced over corresponding three dimensional D ion. For example, the binding energy of a D ion in bulk GaAs is 0.24 meV, while the binding energy of a D ion in the center of a 100 Å GaAs quantum is about 1.7 meV. In the presence of magnetic fields, the energy levels of D ion are strongly modified. From optical measurements, transitions between D ground state to other states can be observed. But there is still some controversy over whether the final states in the observed optical transitions are free electron Landau levels or excited states of D ion. In the former case, the binding energy of D ion can be easily determined from optical transition energies, while in the latter case, the binding energy of D ion can not be deduced from the transition energies directly. Here, we report our study on the activation energies of D ion in a 210Å GaAs quantum well in the presence of magnetic field determined from transport measurements.

The sample used in this study is grown by molecular beam epitaxy with 20 layers of 210 Å quantum wells and 21 layers of 150 Å $Al_xGa_{1-x}As$ barriers. The center 70 Å of the wells are doped with n-type impurities of concentration $2 \times 10^{18} cm^{-3}$ and the center 100 Å of the barriers are doped with n-type impurities of concentration $1 \times 10^{18} cm^{-3}$. Hall pattern is defined by standard photo-lithography technique and contacts are made by alloying In dots into the sample. The sample, after being cooled down in the dark to 5K is illuminated with red LED for about one minute. The purpose of light illumination is to eject all the electrons trapped in AlGaAs into GaAs quantum well [11]. After the sample is illuminated with LED, there are $1.4 \times 10^{11} cm^{-2}$ neutral impurity and $1.0 \times 10^{11} cm^{-2}$ excess electrons in each quantum well if the sample is uncompensated. Because there are not enough excess electrons, not all the neutral impurities can capture an excess electron to form D ion. At low temperature, when thermal equilibrium is reached, there are $1.0 \times 10^{11} cm^{-2}$ D ions and $0.4 \times 10^{11} cm^{-2}$ D^- in each quantum wells. After LED is turned off, the sample resistance reaches a constant value in a couple of minutes. Data were then taken with constant current flowing through the sample in sweeping magnetic field and fixed

temperature. Far infrared photo-conductivity response of this sample has been published else where [6]. Both D^- and D related transitions can be clearly identified.

Typical dependence of longitudinal and transverse resistivities, ρ_{xx} and ρ_{xy}, with magnetic field applied along crystal growth (z-) direction are depicted in Fig-1. Strong temperature dependence of ρ_{xx} and ρ_{xy} is a clear indication of activated transport. Since electron mobility in low magnetic field and low temperature is found to be around $2 \times 10^4 cm^2/V\text{-}sec$, the condition $\mu B > 1$ is satisfied and the free electron concentration (n_e) can be given approximately [12,13] by

$$n_e \approx \frac{1}{e} \frac{\rho_{xy}}{\rho_{xx}^2 + \rho_{xy}^2} B \qquad (1)$$

But we also know that for thermally activated transport, n_e is given by $n_e = A \times \exp(-E_a/kT)$, here A is a constant, k is Boltzman constant and E_a is the activation energy. The free carrier concentration calculated according to equ. (1) for different temperature and magnetic fields, are plotted against inverse temperature in Fig-2. It is clear that ln n_e depends linearly on 1/T from 2 to 8T, and from the slopes of the curves magnetic field dependent activation energy can be determined. These activation energies are assigned as the magnetic field dependent binding energies of D ion in GaAs quantum wells. The justification of this assignment is that the binding energies of D ion is much lower than the binding energy of D^- impurity. Thus, in the temperature range studied, the conducting electrons mostly come from the process $D \rightarrow D^+ + e$. The number of free electrons released from the process $D^- \rightarrow D^+ + e$ are too small and can be ignored. A detailed calculation taking into account the statistics of occupation of D^-, D and free electron states is currently under study. Preliminary results indicate that the free electrons are indeed mostly come from electrons released from D ions.

The dependence of binding energies of a D ion in the center of a 210Å GaAs quantum

well on magnetic fields are shown in Fig-3 Also shown in the figure are transition energies between D ground state ($|1S^2>$) and first excited state ($|1S^1 2P^1>$) [14] obtained from magneto-photoconductivity measurements performed with sample cut from the same wafer Here the notation of ref. 9 is used. As can be seen from Fig-3, the binding energy of D ion increases monotonically with magnetic fields and at low magnetic field region D binding energy increases faster than that in the high field region These results are qualitatively consistent with theoretical calculation. For a quantitative comparison, we can only compare our results with available calculations for D ion in bulk GaAs and D ion in the center of 100 Å GaAs quantum well At B = 6.7T, the binding energies of D ion at the center of a 100 Å GaAs quantum well is 4 1 [9] ~ 4 5 [2] meV, and the binding energy of a D ion in bulk GaAs is 1.9 meV [2] At same magnetic field, the binding energy obtained from our data is 3.8 meV which is close to the binding energy of D ion in the center of a 100 Å GaAs quantum well and is apparently quite reasonable.

From Fig-3 we can see quite clearly that the binding energies determined from transport measurements are different from the transition energies obtained from optical measurements. The optical transition energies are always higher than the transport binding energies. The differences are particularly evident in low magnetic fields.. These results clearly indicate that in the optical measurements, the observed transitions are from ground to excited D states, i.e., $|1S^2>$ to $|1S^1 2P^1>$ transition, and not from ground D state to free electron Landau level. For if the latter is true, the binding energies obtained from optical and transport measurements will be the same. From these data, we can also conclude that the energy level of the first excited state of a D ion in a 210 Å quantum well is higher than the lowest free electron Landau level for magnetic field below 8T

In conclusion, we have obtained the binding energies of a D ion in the center of a GaAs quantum well for magnetic field from 2 to 8T and the result is quite consistent with theoretical calculation. From comparing the transport and optical data, we conclude that the transitions observed in optical measurements are between D ground and excited states We also show that for a D ion in a center of a 210 A GaAs quantum well, the first excited

state of such an ion has an energy higher than the energy of ground state Landau level when the magnetic field is smaller than 8T.

This work is supported by National Science Council of the Republic of China under contract NSC-82 0208-M002-68

References

* permanent address: AT&T Bell Lab, Murray Hill, NJ 07974 , U.S.A.

1 S Huant and S P Najda, Phys Rev. Lett. 68, 1486 (1990)

2. T. Pang and S G. Louie, Phys Rev Lett. 65, 1635 (1990).

3 D M. Larsen and S.Y. McCann, Phys. Rev B 45, 3485 (1992).

4 E R Muller, D M Larsen, J Waldman, and W D Goodhue, Phys. Rev. Lett. 68,204(1992)

5. A.H. MacDonald, Solid State Commun. 84, 109 (1992).

6 Y H Chang, T.C. Chen, C J Chen and Y.F. Chen, Phys. Rev. Lett. 69, 2256 (1992)

7 S. Holmes, J P. Cheng and B D McCombe, Phys. Rev. Lett. 69, 2571 (1992).

8 A Mandray, S. Huant, and B Etienne, Europhys. Lett. 20, 182 (1992).

9 X Xia and J.J. Quinn, Phys. Rev. B 46, 12530 (1992).

10 S.P Najda,C J.Armstead,C.Trager,and R.A Stradling,Semicond.Sci.Technol 4,439(1989)

11 N.C Jarosik B.D McCombe B.V. Shanabrook, J. Comas, J. Ralston, and G.Wick, Phys. Rev Lett. 54, 1283 (1985)

12. R Ransfield, J Phys. C 4, 2084 (1971)

13. J L. Robert, A Raymond, L Konczewicz, C Bousquet, Z. Zawadzki, F Alexandre, J M. Masson, J P. Andre and P M Frijlink, Phys Rev B 33, 5935 (1986).

14 to be published

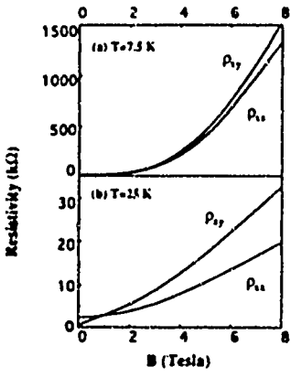

Figure-1 Magnetic field dependence of ρ_{xx} and ρ_{xy} at a) 7.5K and b) 2.5K.

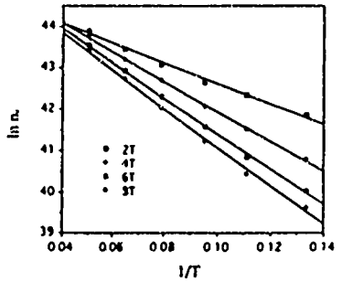

Figure-2 Temperature dependence of carrier concentration for different magnetic fields.

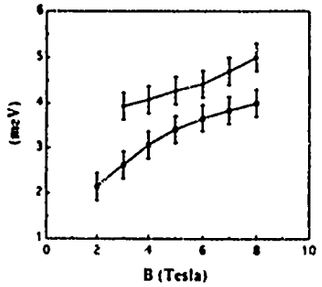

Figure-3 D-Binding energies obtained from transport measurements and ● transition energies obtained from optical measurements for a D ion at the center of a 210 Å GaAs quantum well.

MoP28

Correlations of the Remote Impurity Charges- a Method of 2DEG Mobility Tuning in GaAs/AlGaAs Heterostructures

T. Suski, P. Wiśniewski, L.H. Dmowski, I. Gorczyca,
UNIPRESS, Polish Academy of Sciences, 01-142 Warszawa, POLAND
J. Smoliner, E. Gornik, G. Böhm, and G. Weimann,
Walter Schottky Institut, TUM, D-8046 Garching, GERMANY

Abstract

Low temperature 2DEG mobility and carrier concentration measurements made on two modulation doped GaAs/AlGaAs heterostructures are described. We demonstrate that, depending on the method which is used to populate the metastable donor states of Si-remote impurity, different values of electron mobility can be obtained for the same 2DEG density and in the same heterostructure. Concept of the correlation in the spatial distribution of the impurity chargee (i.e. positively and negatively charged states of Si donor), caused by the Coulomb interactions is employed to explain our experimental finding. The invoked effect induces a strong reduction of the 2DEG scattering and can produce the mobility enhancement by as much as a factor of two over its value with a random distribution of impurity charges.

Introduction

Many attempts have been undertaken in order to improve a performance of electronic devices based on GaAs/AlGaAs heterostructures. High mobility of electrons and their high densities represent the major features important for applications. The first requirement has been achieved by means of modulation doped heterostructures (MDH) [1]. A spatial separation of donors located in AlGaAs barrier from the channel of two dimensional electron gas, 2DEG, situated in GaAs at the interface between two semiconductors, causes a substantial enhancement of electron mobility, μ. This originates in a strong reduction of efficiency of electron scattering by ionized impurities which constitutes the main mechanism limiting μ at low temperatures. With increasing a thickness of the undoped spacer , i.e. a AlGaAs layer incorporated between ionized remote donors and 2DEG, the impurity scattering is reduced (see e.g. [2]). There are two factors which determine the resulting effect: the falloff in Coulomb fields generated by individual impurities and drastic decrease of short-wavelength (large-wave-vector) potential fluctuations, which is the source of scattering by ionized impurities. However, at the same time the increase in the spacer thickness gives rise to a reduction in the concentration of 2DEG, n. The latter effect represents a drawback for many applications. Therefore, a particular design of high performance devices based on MDH, requires finding a compromise between the values of μ and n.

The purpose of this paper is to point out an existence of a new mechanism which contributes significantly to the additional reduction in electron scattering by ionized impurities. It originates in a correlations in a remote-impurity-charges arrangement among the impurity sites in the doped region of AlGaAs barrier.

It is well established now that donors in GaAs and AlGaAs form either positively charged substitutional d^+ centers or after trapping two electrons they transform to the interstitial DX^- states [3]. The latter states represent negatively charged centers. Both states of the donor take part in electron scattering by ionized impurities. Moreover, it has been demonstrated for uniformly doped bulk GaAs [4-7] and AlGaAs [8,9] crystals as well as for GaAs with δ doping [10] that the spatial arrangement of these two charge states of the donor in a dipole-like pairs of d^+-DX^- causes a gain of crystal energy with respect to the uncorrelated arrangement of d^+ and DX^- centers. This energy gain results from minimization of Coulomb interactions between the two considered charge states of the donor. On the other hand creation of close dipoles d^+-DX^- within the impurity region induces a strong reduction in the efficiency of electron scattering with respect to the situation when both charge states of the donor are distributed randomly.

It is natural to expect that the effect of spatial correlations in the system of remote impurity charges in GaAs/AlGaAs MDH's can cause also the effect of enhancement of μ [11]. Moreover, since an appearance of this phenomenon requires high density of impurities (empty donor centers d^+ and occupied DX^- ones should coexist in the system), a high concentration of 2DEG can be achieved in such MDH's. Concerning 2DEG mobility enhancement, it is suggestive to predict larger effect when more d^+-DX^- dipoles appear in the doped region and smaller is a distance between d^+ and DX^- centers. We will show that this intuitive picture can be applied to the results of experiments performed on different MDH's. The decrease in efficiency of electron scattering caused by the correlations produces an increase of low temperature mobility of 2DEG as much as a factor of two over its value with a random distribution of charges.

Experiment

Experimental testing of the existence of the spatial correlation related contribution to the 2DEG transport, consists in examining of μ as a multivalued function of the 2DEG concentration, n. We will demonstrate that depending on the method of the "preparation" of the same heterostructure, various values of μ can be obtained for the same density of 2DEG. These preparation procedures utilize DX center metastable properties related to the existence of thermodynamic barriers for electron emission from and capture to the localized state of the donor. For Si-donor (the impurity used for doping of MDH's) the barriers block the electron transfer between two dimensional channel and DX^- states at temperatures below about 100K-160K [12]. Thus, below this temperature range the spatial arrangement of remote impurity charges, i.e. arrangement of d^+ and DX^- states, among the impurity sites freezes. Our experimental finding of different values of μ for the same n and for the same heterostructure, we interpret (by analogy with the situation for bulk GaAs and AlGaAs [7-9]) as originating from various distributions of charges among the donor sites within the AlGaAs barrier. In particular, we compare low temperature 2DEG mobilities measured for the maximum amount of spatial correlations with μ values corresponding to the situation with reduced correlations. This situation enables us to concentrate on the electron scattering by ionized impurities distributed differently in the region of the heterostructure barrier.

To alter 2DEG density (i.e., an amount of occupied DX centers) and μ we employed two procedures (the first one, Fig. 1, a-d, shows strong correlations, the second one, Fig. 1e and f, represents weak correlations):

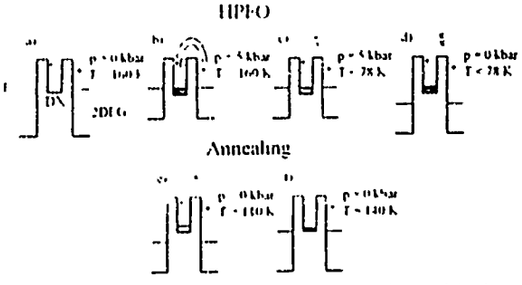

Figure 1. Schematic illustration of the procedures leading to changes in the spatial distribution of donor centers d^+ and DX^-. (a) to (d) represent high pressure freezeout of electrons onto DX^- states (HPFO) and (e) (f) correspond to the annealing of heterostructures at different temperatures. Note the solid and dotted arrows which stand for free and hindered transfer of electrons between the conduction band and DX^--system due to barriers for electron emission and capture. The dashed arrows correspond to partially transparent barriers.

a) *high pressure freezeout* (HPFO) [12,13] of electrons on the metastable DX^- states. This procedure consists in applying hydrostatic pressure at temperatures above 160K and releasing it at T<100K. After applying hydrostatic pressure the donor levels corresponding to DX^- states penetrate deeper to the energy gap of AlGaAs which results in the enhanced transfer of electrons from the 2DEG to the donor states provided that the electron thermal energy exceeds the energy barrier (Fig. 1b). At temperatures below about 100K releasing the pressure does not change n because the trapped electrons cannot overpass the energy barrier between DX^- and the band states (Fig. 1c and 1d). Therefore in these pressure-induced processes of arrangement of impurity charges the minimization of their Coulomb interactions is achieved. The HPFO procedure allows to achieve the maximum value of μ for each value of n (determined by the magnitude of the freezeout pressure). This effect was proved to reproduce μ_{max} versus n for bulk GaAs [7] and bulk AlGaAs [9].

b) *annealing*. Employing HPFO procedure makes it possible to form a reservoir of localized electrons which, at atmospheric pressure, are frozen in a metastable manner on DX^- states. Then a temperature increase in a controlled manner can modify n and the arrangement of donor charges. This consists of a subsequent annealing of the sample to temperatures above about 100K and then cooling down to 4.2K or to 78K for performing measurements of n and μ. Each successive annealing step requires heating of the heterostructure to a higher temperature. Increasing temperature induces transfer of electrons from a metastable DX^- states to the two dimensional conducting channel (Fig. 1e). In the range of annealing temperatures between 110K and 140K, changes in the impurity-charges distribution are caused by the electron emission from randomly "chosen" DX^- centers. At this temperature range retrapping of electrons onto DX^- centers and thus rearrangement of their spatial positions minimizing Coulomb interactions is hindered by capture barrier. This results in a reduction in the amount of the correlations. A higher annealing temperatures causes ionization of a higher amount of DX^- states to d^+ states as

well as induction of correlations in spatial positions of impurity charges since a capture barrier becomes partially transparent (Fig. 1f). In other words, during the annealing processes both, the Fermi energy and electron kinetic energy increase leading to the decrease of the effective capture barrier. In addition, since the concentration of d^+ and 2D electrons raise significantly, the transfer of carriers from 2DEG to DX^- states is enhanced. One can see that the conduction band "mediates" the transfer of electrons between different DX^- centers leading to the appearance of the correlation effects. This situation requires that the both barriers become transparent (Fig. 1f). We have used two heterostructures with low and high value of μ (about 0.25 and $1.2*10^6$ cm^2/Vs at T=4.2K , respectively). Table I gives a description of the employed samples.

Table I Parameters of the GaAs/Al_x Ga_{1-x}As modul- -doped heterostructures

Sample	n (T=4.2K) [$10^{12}cm^{-2}$]	μ (T=4.2K) [$10^6cm^2/Vs$]	spacer [nm]	x [%]	doping layer thickness [nm]	doping layer density [$10^{18}cm^{-3}$]
H01	0.56	0.26	5	35	5	4
H70	0.365	1.16	24	29	36	2.8

Results

First, we will describe results of applying HPFO procedure to the H70 sample characterized by the higher value of μ. Open circles on Fig. 2 represent the obtained results. Increasing freeze-out pressure during subsequent sample cooling-down processes (highest pressure 5 kbar) results in the decrease of both n and μ measured at T=4.2K or at T=78K. An interplay between two effects determines the observed lowering of μ: a modification of the correlations and a decrease in efficiency of the scattering potential screening by 2DEG (lower concentration of carriers). Filled diamonds illustrate variation of μ with increasing n obtained after annealing of the sample. The first cycle of the annealing (T is raised up to about 110K) induces a decrease of μ. The origin of the μ reduction which accompanies the increase of n lies in a decrease in the amount of spatial correlations of d^+ and DX^- states. Thermal ionization of DX^- states occurs in a random manner. Consequently it leads to a more efficient 2DEG scattering due to remote impurities. The effect found here resembles behavior observed in bulk GaAs and AlGaAs [7-9]. Further annealing processes performed at higher temperatures cause a mobility increase although the "annealing branch" of the μ vs n dependence gives the mobility values lower than those obtained during HPFO. With increasing annealing temperature contributions from two additional factors influence μ value. i) increase in the 2DEG screening efficiency, ii) a process of equilibrium redistribution of electrons among the donor states. The second mechanism leads to a decrease of the crystal energy caused by inter-impurity Coulomb interactions and this results in a reestablishing of the correlations.

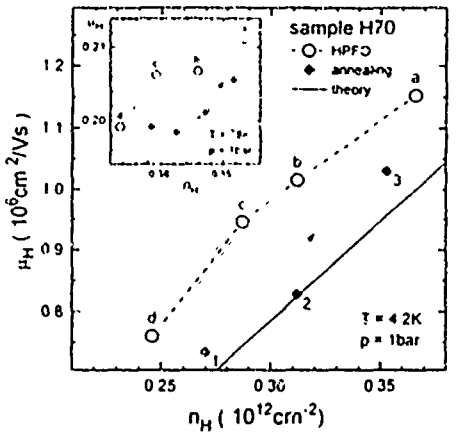

Figure 2 2DEG mobility variation with electron concentration measured at T=4.2K in the sample H70. The a, b, c branch of the plot represents a strong correlation path achieved by HPFO procedure performed at different freezeout pressures, whereas filled diamonds correspond to a weak correlation path produced by the sample subsequent annealing. Solid lines represent results of theoretical calculations performed under the assumption of absence of the spatial correlations. The insert shows the corresponding dependence of μ versus n measured at T=78K.

Some information about the magnitude of the effect leading to mobility enhancement and originating in the spatial correlation of the donor charges can be deduced from a comparison of two μ values corresponding to the same 2DEG density. The maximum difference in the mobility values on the two branches of μ is about 30% which sets the lower limit of the examined effect. The solid line in Fig. 2 represents μ vs n for the examined heterostructure calculated under the assumption of absence of the spatial correlations [14].

To determine whether the correlation contribution to μ could be seen at higher temperatures we have repeated the same sequence of the sample preparation as described above but all measurements have been performed at 78K. The results obtained (Insert in Fig. 2) clearly show that μ at 78K is approximately 6 times smaller that the value measured at T=4.2K. The gain in μ value corresponding to correlations of impurity charges at T=78K decreases in a similar manner as the absolute value of μ. This behavior results from the following effect. At higher temperatures electron scattering by phonons contributes more significantly to processes limiting 2DEG mobility. The latter effect raises the background scattering and therefore it masks changes of ionized impurity scattering processes caused by the spatial correlation of impurity charges. At T=78K, one can expect much higher mobility gain due to this effect when MDH with a thinner spacer is employed.

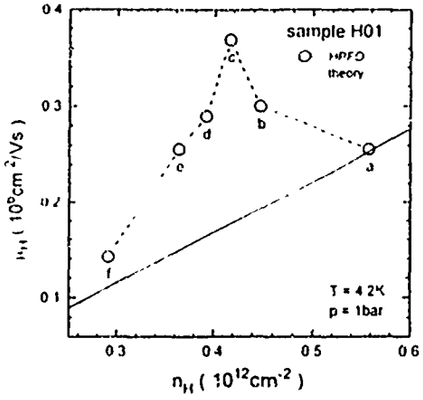

Figure 3 2DEG mobility variation with electron concentration for the sample H01 The dashed line corresponds to the strong correlation path obtained by HPFO method The solid line gives the results of calculations assuming that spatial correlations are absent

The additional experimental test of correlation-related effects in GaAs/AlGaAs has been performed on the sample H01 which has the thin spacer and the low mobility value Contrary to the usual behavior, a decrease in 2DEG concentration induced by the employed HPFO procedure causes an increase of μ in the initial stage, after which μ decreases gradually (Fig. 3). The observed enhancement allows μ to reach value of $0.37*10^6$ cm^2/Vs compared with $0.26*10^6$ cm^{-2}/Vs obtained after cooling of the sample to T=4.2K, at p=0kbar. Again we associate the origin of the μ enhancement with the spatial correlations of d^+ and DX^+ states. We found a mobility increase of about 50% of its value detected after sample cooling at ambient pressure At this early stage of HPFO the correlation related contribution to mobility increase overcompensates a decrease in the screening efficiency. The latter effect is due to the lowering of n and leads to the mobility decrease. This usual behavior of MDH is illustrated by the results of calculations neglecting correlations (see the solid line on Fig 4). Comparison of experimentally determined μ value (maximum of correlations) with the calculated one (no correlations) gives the increase of μ by factor of two Moreover, the result obtained for the sample H01 demonstrates that the spatial correlation induced enhancement of μ could reach its maximum value for the distribution of electrons between 2DEG and DX^- states different from that existing in the "as grown" heterostructure (i.e. during cooling at ambient pressure)

Conclusions

In conclusion, we examined variation of 2DEG mobility with carrier concentration in two different heterostructures of GaAs/AlGaAs. We have shown that depending on the way the impurity charges are distributed among the donor sites in the AlGaAs barrier, different values of μ can be achieved for the same 2DEG density. This distribution depends in turn on a thermal treatment of the sample. The observed behavior of μ can be qualitatively attributed to changes in spatial correlation of the remote donor charges. This effect is responsible for very strong reduction of the 2DEG scattering by ionized remote impurities. The presented finding gives an important correction to understanding the electron transport in low dimensional structures [14-17]. It is very important to establish a theoretical description which gives the proper model of 2DEG scattering by ionized impurities. It would enable to incorporate the spatial correlation of impurity charges in processes of choosing parameters of the produced MDH (spacer thickness, doping density and doping profile). As it can be deduced from the results of papers by Sobkowicz et al. [10], better correlations can be achieved in a doping system of lower dimensionality. Accordingly, δ-like doping of the barrier would introduce larger reduction in a scattering efficiency due to ionized remote impurities.

Acknowledgements: We acknowledge valuable discussions with Drs. R. Piotrzkowski, Z. Wilamowski and Prof. J. Kossut This work was supported by the National Scientific Research Committee (Poland) under Project 20160 9101.

References

[1] L. Stormer, R. Dingle, A.C Gossard, and W Wiegmann, Inst. Conf. Ser London, 43, 557 (1978).
[2] G. Weimann and W. Schlapp, Appl Phys Lett 44, 411 (1985)
[3] D.J. Chadi and K J. Chang, Phys. Rev Lett. 61, 873 (1988), Phys Rev. B39, 10063 (1989).
[4] E P. O'Reilly, Appl. Phys. Lett. 55, 1409 (1989)
[5] T. Suski, P. Wiśniewski, E. Litwin-Staszewska, J. Kossut, Z. Wilamowski, T. Dietl, K. Świątek, K.Ploog, and J. Knecht, Semicond Sci. Technol. 5, 261 (1990).
[6] J. Kossut, Z. Wilamowski, T. Dietl, and K. Świątek, *Proc. 20th Int. Conf. on the Physics of Semiconductors*, ed. E.M Anastassakis and J.D. Joannopoulos (World Scientific, Singapore, 1990) p. 613.
[7] D K. Maude, L. Eaves, and J.C. Portal, Appl. Phys. Lett. 60, 1993 (1992), L.H. Dmowski, B. Goutiers, D.K. Maude, L. Eaves, J.C. Portal, and J.J. Harris, Japan. J. Appl. Phys. 32, Suppl. 32-1, 221 (1993).
[8] P.L. Coz, C. Ghezi, and A. Parisini, Semicond. Sci. Technol. 8, 13 (1993).
[9] R. Piotrzkowski, E. Litwin-Staszewska, and J.L. Robert, to be published.
[10] P. Sobkowicz, Z. Wilamowski, and J Kossut, Semicond. Sci. Technol. 7, 1155 (1992) and J. Phys.: Cond. Matter, in press
[11] A.L. Efros, F.G. Pikus, and G.G. Samsonidze, Phys. Rev. B41, 8295 (1990).
[12] Suski, E. Litwin-Staszewska, P. Wiśniewski, L.H. Dmowski, W.H. Zhuang, G.B Liang, D.Z. Sun, and Y.P. Zun, J. Appl Phys. 63, 2307 (1988)
[13] R. Piotrzkowski, J.L. Robert, E. Litwin-Staszewska, J.P. Andre, Phys. Rev.B37, 1031 (1988)
[14] Gorczyca, C. Skierbiszewski, E. Litwin-Staszewska, T. Suski, J. Krupski, and K Ploog, Semicond. Sci. Technol. 6, 461 (1991)
[15] T. Ando, J. Phys Soc. Japan 51, 3900 (1982).
[16] F. Stern, Appl. Phys. Lett. 43, 974 (1983)
[17] W Walukiewicz, H E Ruda, J Lagowski, and H.C. Gatos, Phys Rev. B30, 4571 (1984).

MoP29

Three-Dimensional Boltzmann-Bloch Theory of Miniband Transport in Superlattices with Elastic Scattering

Rolf R. Gerhardts

Max-Planck-Institut für Festkörperforschung, Heisenbergstr. 1, D-70569 Stuttgart, Germany

Elastic scattering couples the quasi one dimensional (1D) motion of electrons responding to an applied electric field in growth direction of a semiconductor superlattice effectively to the lateral degrees of freedom. We describe the superlattice by a simple miniband and elastic scattering explicitly by an appropriate collision term in Boltzmann's equation. As a function of the applied field, we calculate the heating of the electron system and its drift velocity, which shows pronounced negative differential conductance.. Our results are qualitatively different from those of previous 1D theories, but compare favorably with results of recent experiments and balance-equation calculations.

72.20.Ht, 72.10.Fg, 73.20.Dx

Quasi-classical dynamics of Bloch electrons predicts fascinating phenomena such as Bloch oscillations and regimes with negative differential conductance (NDC), if the electrons can be forced by an applied electric field to follow the periodic band structure through a considerable region in k-space before being scattered. Whereas large Brillouin zones and wide energy bands prohibit these phenomena in natural bulk crystals, Esaki and Tsu [1] predicted a long time ago that they should become observable in semiconductors with artificial superlattices of sufficiently large lattice constants a. The prediction was that the drift velocity v_D of electrons responding to an electric field F applied in the growth (z) direction of the superlattice will decrease with increasing F, once F becomes larger than a critical value $F_{max} = h\nu/ea$, at which the scattering rate ν equals the Bloch-oscillation frequency eaF/h. Here $-e$ is the electron charge. A characteristic feature of this prediction is that the critical field F_{max} does not depend on the miniband width Δ. Previous generalizations of the Esaki-Tsu prediction to finite temperatures using the Boltzmann-Bloch equation in relaxation time approximation [2,3] confirmed this feature. Also Monte Carlo calculations of the drift velocity [4,5] produced no significant Δ-dependence of F_{max} and essentially confirmed the Esaki-Tsu prediction, long before it could be verified experimentally.

So far only two groups have claimed that their experiments reveal the Esaki-Tsu mechanism of miniband transport, and not hopping of electrons between localized states in adjacent wells of the superlattice. Sibille et al. [6] systematically studied stationary transport in several superlattices with different miniband widths and periods. They reported qualitative agreement with the Esaki Tsu predictions, however, their F_{max} values seemed to decrease systematically with increasing Δ. The first direct observation of a v_D-F characteristic corresponding to NDC up to F-values far beyond the maximum, has been achieved in time-of-flight experiments by Grahn et al. [7]. They found a good agreement with the finite-temperature version of the Esaki-Tsu theory [2,3], at least for higher temperatures, $k_BT > \Delta$.

These experiments, especially the unexpected Δ dependence of F_{max}, stimulated a renewed theoretical interest in the problem [8-10]. Lei et al. [8] applied a balance equation approach [11] to the superlattice model and reported an impressive agreement with the experimental results of Ref. [6]. Similar to the Monte Carlo calculations [4,5], their calculation included explicitly the interaction of the electrons with acoustical and optical phonons as well as with randomly distributed impurities, and, in addition, the screening of these interactions. Although the ansatz of Ref. [8] is very general, it lacks transparency and does not clarify which particular interaction mechanism is responsible for the qualitative differences from the predictions of the Boltzmann-Bloch theories, notably for the Δ-dependence of F_{max}.

In order to clarify the situation and to gain a deeper physical understanding of the apparent insufficiencies of the previous Boltzmann-Bloch theories, we consider explicitly the role of elastic scattering. The basic idea is that elastic scattering by impurities or interface roughness will transfer energy, gained by the electron during its motion in the field direction, to the lateral degrees of freedom. Thus, elastic scattering will effectively render the problem a really three-dimensional one, and should be treated explicitly. In order to do this in the most simple and transparent way, we describe it by a simplified collision term in the Boltzmann-Bloch equation, in addition to the inelastic relaxation considered previously [2,3]

As in previous work [1-5,8-10], we take the tight-binding energy

$$E_1(k_z) = \frac{1}{2}\Delta(1 - \cos ak_z) \tag{1}$$

in z direction and free motion with effective mass m in the lateral directions,

$$E(\mathbf{k}) = \frac{\hbar^2 k_\perp^2}{2m} + E_1(k_z), \tag{2}$$

with $k_\perp^2 = k_x^2 + k_y^2$.

The stationary Boltzmann-Bloch equation is written as

$$-\frac{eF}{\hbar}\frac{\partial}{\partial k_z} f(\mathbf{k}) = -\nu_{in}\,[f(\mathbf{k}) - f_0(E(\mathbf{k}))] + C_{el}(f, \mathbf{k}), \tag{3}$$

where the inelastic scattering rate ν_{in} describes relaxation towards the equilibrium distribution function f_0. If elastic scattering is neglected, $C_{el} = 0$, and if non-degenerate statistics is assumed, one obtains the well known result for the drift velocity [2,3],

$$v_D = v_0 \frac{F/F_0}{1 + (F/F_0)^2}\, Q\left(\frac{k_BT}{\Delta}\right). \tag{4}$$

where $v_0 = -a\Delta/2\hbar$, and $Q(t) = I_1(1/2t)/I_0(1/2t)$ with modified Bessel functions I_ν. For $C_{el} = 0$, this theory is effectively one-dimensional, since the transverse motion ($k_\perp$) enters Eq. (3) only parametrically and drops out from Eq. (4). The maximum of v_D occurs at the electric field $F_0 = h\nu_{in}/ae$, which is independent of Δ, whereas the amplitude factor Q is independent of F. The original Esaki-Tsu result follows in the limit $T \to 0$, with $Q(0) = 1$.

In order to simulate elastic scattering, we introduce in the Boltzmann equation (3) the collision term

$$C_{el}(f, \mathbf{k}) = -\nu_{el}\,[f(\mathbf{k}) - \Phi_f(E(\mathbf{k}))]\,. \tag{5}$$

Here

$$\Phi_f(E) = \alpha \int d^3k'\, \delta(E - E(\mathbf{k}'))\, f(\mathbf{k}') / D(E) \qquad (6)$$

is the average of the distribution function taken over surfaces of constant energy, $E(\mathbf{k}') = E$, $D(E)$ is the density of states, and $\alpha = 2/(2\pi)^3$. This ansatz describes forth and back scattering with equal weights between the state $\mathbf{k}$ and all states $\mathbf{k}'$ of the same energy. It effectively couples the motion in superlattice direction to the lateral degrees of freedom. Before proceeding, we stress that our 3D model is qualitatively different from the corresponding 1D model discussed by Ignatov et al. [9] (IDS). The IDS model couples the motion in z direction only to that in $-z$ direction, but not to the lateral degrees of freedom. As a consequence, the drift velocity can be calculated analytically. The result can be written in the form of Eq. (4), if one replaces v_0 with $v_0^{IDS} = v_0\delta^{1/2}$ and F_0 with $F_0^{IDS} = \delta^{1/2}\hbar\nu_{tot}/ea$, where $\nu_{tot} = \nu_{in} + \nu_{el}$ is the total scattering rate and $\delta = \nu_{in}/\nu_{tot}$. This model yields a suppression of the drift velocity below the value of Eq. (4). It can, however, not explain a Δ-dependence of F_{max}. Moreover, it predicts the same temperature dependence of the drift velocity as Eq. (1), namely a simple scaling factor which does not change the shape of the v_D-F curve.

For our 3D model, the drift velocity cannot be calculated analytically. With the dimensionless quantities $\varepsilon = E/\Delta$ and $\xi = F/F_0$ where $F_0 = \hbar\nu_{tot}/ea$, our Boltzmann equation subjected to the boundary condition $f(k_\perp, k_z + 2\pi/a) = f(k_\perp, k_z)$ has the formal solution

$$f(k_\perp, k_z) = \frac{a}{\xi} e^{a k_z/\xi} \int_{k_z}^{\infty} dk_z'\, e^{-a k_z'/\xi}\, g_f(\varepsilon(k_\perp, k_z')), \qquad (7)$$

where

$$g_f(\varepsilon) = (1 - r_\varepsilon)\, f_0(\varepsilon) + r_\varepsilon \Phi_f(\varepsilon\Delta) \qquad (8)$$

and $r_\varepsilon = \nu_{el}/\nu_{tot}$. Inserting (7) into the definition (6), we obtain an integral equation for g_f which can be written in the form

$$g_f(\varepsilon) - (1 - r_\varepsilon)\, f_0(\varepsilon) = \frac{r_\varepsilon}{z(\varepsilon)} \int_{-z(\varepsilon)}^{z(\varepsilon)} dz \int_0^\infty du\, e^{-2u}\, g_f\left(\varepsilon - \sin^2 z + \sin^2(z + \xi u)\right) \qquad (9)$$

Here, we have inserted the density of states, $D(E) = (2m/\pi^2 a\hbar^2)\, z(E/\Delta)$, with $z(\varepsilon) = \arcsin(\sqrt{\varepsilon})$ if $0 < \varepsilon \le 1$, and $z(\varepsilon) = \pi/2$ if $\varepsilon \ge 1$. In view of the low electron densities in the experiments [6,7], we present numerical results only for non-degenerate statistics, $f_0(\varepsilon) = \exp(-\varepsilon/t)$, where $t = k_B T/\Delta$ is the reduced temperature. Figure 1 shows Φ_f for different situations. As compared with the equilibrium case ($\xi = 0$), in a stationary state with applied field ($\xi > 0$) electrons are redistributed from states with lower energy to states with higher energy. This 'heating' of the electron system is even increased, if part of the scattering is elastic. Apparently, this heating cannot be described by the equilibrium distribution at an elevated electron temperature $T_e > T$, since this would lead to a straight line in Fig. 1, because $\Phi_f = f$ if f depends on $\mathbf{k}$ only via the energy. The cusp behavior at $\varepsilon = 1$ is, of course, closely related to the van Hove singularity of the density of states.

The drift velocity is defined by

$$v_D = \alpha \int d^3k\, v_z(k_z)\, f(\mathbf{k}) / n_e\,, \qquad (10)$$

with $v_z(k_z) = \hbar^{-1} dE_z/dk_z$. The normalization constant is the electron density,

$$n_e = \alpha \int d^3k\, f(\mathbf{k}) = \int_0^\infty dE\, D(E)\, \Phi_f(E). \qquad (11)$$

Since n_e in the stationary state has the same value as in the equilibrium state without applied electric field, we may replace in Eq. (11) Φ_f with f_0. We used this sum rule for Φ_f to check our numerical results. With the formal solution (7) the integral in Eq. (10) can be evaluated to yield v_D again in the form of Eq. (4), but now with

$$Q(r_\varepsilon, \xi, t) = \int_0^1 d\varepsilon\, g_f(\varepsilon)\sqrt{\varepsilon(1-\varepsilon)} \Big/ \int_0^\infty d\varepsilon\, z(\varepsilon)\, f_0(\varepsilon)\,. \qquad (12)$$

In the absence of elastic scattering, $r_\varepsilon = 0$, one has $g_f = f_0$, and Q is independent of ξ. With $f_0(\varepsilon) = \exp(-\varepsilon/t)$ one exactly recovers Eq. (4). For degenerate statistics this factor $Q(t)$ is, of course, different. For $r_\varepsilon > 0$, Q depends via ξ on the electric field. Then the shape of the v_D-F curves is different from the Esaki-Tsu result and changes with changing temperature. Two limits can easily be discussed analytically. The first is the linear response regime, $\xi \ll 1$. Here one obtains from Eq. (9) $g_f = f_0 + O(\xi^2)$. Thus, up to first order in ξ, the distribution function and the drift velocity depend only on the total scattering rate, and $Q(0, 0, t)$ is a sufficient approximation. A distinction between elastic and inelastic scattering is irrelevant in the linear response regime. The other trivial limit is that of extremely high temperatures, where $f_0(\varepsilon)$ becomes a constant independent of ε. In this limit the solution of Eq. (9) is the constant $g_f = f_0$, and again $Q(0, 0, t)$ is sufficient. Thus, our result should approach the 1D form (4) in the linear response regime and, for arbitrary values of ξ, in the limit of high temperatures, provided we define the scaling field as $F_0 = \hbar\nu_{tot}/ea$.

In Fig. 2 we present typical results of our numerical calculations for three values of the temperature and for three values of the ratio $r_\varepsilon = \nu_{el}/\nu_{tot}$, keeping ν_{tot} fixed. For $r_\varepsilon = 0$ (dashed lines) we get the results of the 1D theories [1,9], with increasing temperature the curves are reduced by an F-independent factor, but their shape does not change. For fixed reduced temperature and increasing r_ε, the shape of the curves changes, the maxima are reduced and shifted to smaller values of F. This behavior is qualitatively similar to, but *quantitatively* different from the results of Ref. [9]. For fixed $r_\varepsilon > 0$, the position of the maximum shifts with increasing temperature (or decreasing Δ) to larger values of F, so that the effect of elastic scattering is largest at low temperatures and becomes small at high temperatures. This result is *qualitatively* different from that of the 1D model of Ref. [9]. It is, however, in qualitative agreement with that of Ref. [8]. Systematic results for the dependence of the position F_{max} and the height $(v_D)_{max}$ of the maxima on the scattering-rate ratio r_ε and the reduced band width $\Delta/k_B T$ are presented in Fig. 3. The results of the 1D model of Ref. [9] would appear in Fig. 3a as horizontal straight lines at $(F/F_0)_{max} = (1 - r_\varepsilon)^{1/2}$ and in Fig. 3b as curves with the same shape as that for $r_\varepsilon = 0$ (top curve), but rescaled by a constant factor $(1 - r_\varepsilon)^{1/2}$.

In order to calculate the heating of the electron system, we consider the mean energy $\langle E \rangle_\xi$ in the stationary state, given by Eq. (10) with $v_z(k_z)$ replaced by $E(\mathbf{k})$. The result can be written as

$$\frac{\langle E \rangle_\xi}{\Delta} = \frac{\int_0^\infty d\varepsilon\, g_f(\Delta\varepsilon)\, \varepsilon z(\varepsilon)}{\int_0^\infty d\varepsilon\, f_0(\Delta\varepsilon)\, z(\varepsilon)} + \frac{1}{2}\frac{\xi^2}{1 + \xi^2}\, Q(r_\varepsilon, \xi, t)\,. \qquad (13)$$

In thermal equilibrium, $\xi = 0$, only the first term on the r.h.s. survives, yielding $\langle E\rangle_0 = k_BT + (\Delta/2)[1 - Q(0,0,t)]$. In the absence of elastic scattering, $r_e = 0$, only the second term contributes to the heating, since $g_f = f_0$. Then the increase of the internal energy density $n_e(\langle E\rangle_t - \langle E\rangle_0)$ is just given by the Joule heating jF/ν_{in} during the inelastic scattering time $1/\nu_{in}$, with $j = -en_e v_D$ the current density. It is interesting to note that this remains true if inelastic scattering is taken into account by the 1D model of Ref. [9]. For our 3D model the first term on the r.h.s. of Eq. (13) also contributes to the heating, and no analytic results are available. Numerical results are presented in Fig. 4. In all cases the heating saturates at high values of the applied field F. It is most effective for strong elastic scattering, $(1 - r_e) \ll 1$, and for low (lattice) temperature. We may define an electron temperature in the stationary state as the temperature of that equilibrium state with the same mean energy per electron.

In conclusion, we have emphasized the fact that elastic scattering makes the miniband transport through a 1D superlattice in a 3D semiconductor effectively to a 3D problem. Incorporating this into Boltzmann's equation in a simple relaxation time approximation, we obtain qualitative deviations from the results of the previously studied 1D theory. Our results are in good qualitative agreement with the very sophisticated calculation of Lei et al. [8]. Quantitative agreement cannot be expected, since our model does not contain any detailed information about scattering matrix elements or screening, and even assumes the scattering rates to be independent of energy. In principle such detailed informations could be incorporated into a Boltzmann-Bloch treatment. But this would be at the expense of transparency, and, perhaps more important, these details are not well known for semiconductors with superlattices. For a meaningful comparison with the experimental results of Sibille et al. [6], we would have to assume that, at a given temperature, the scattering rates are the same for superlattices with different miniband widths Δ. Then we conclude from Fig. 3a that the electric field F_{max} at maximum drift velocity should decrease with increasing Δ. This is in agreement with the data of Ref. [6], but these data scatter by about 30 per cent, so that the assumption about the scattering rates becomes questionable. Therefore, we do not attempt a quantitative fit. From a rough estimate, we conclude that in their experiment the elastic scattering rate must be more than an order of magnitude larger than the inelastic one. This conclusion also applies to a very recent time-of-flight experiment by Minot et al. [12] with results which are in satisfactory agreement with our theory. Considering the experiments of Grahn et al. [7], is seems not surprising that at the relatively high temperature good agreement with the result of the 1D theory [3] is obtained, although this indicates that elastic scattering is not so predominant in this situation.

Stimulating discussions with Wolfgang Müller and Holger Grahn are gratefully acknowledged.

[1] L. Esaki and R. Tsu, IBM J. Res. Dev. 14, 61 (1970).
[2] F.G. Bass and E.A. Rubinshtein, Fiz. Tverd. Tela (Leningrad) 19, 1379 (1977) [Sov. Phys. Solid State 19, 800 (1977)].
[3] R.A. Suris and B.S. Shchamkhalova, Fiz. Tekh. Poluprovodn. 18, 1178 (1984) [Sov. Phys. Semicond. 18, 738 (1984)].

[4] D.L. Andersen and E.J. Aas, J. Appl. Phys. 44, 3721 (1973).
[5] M. Artaki and K. Hess, Superlattice Microstruct. 1, 489 (1985).
[6] A. Sibille, J.F. Palmier, H. Wang, and F. Mollot, Phys. Rev. Lett. 64, 52 (1990).
[7] H.T. Grahn, K. von Klitzing, K. Ploog, and G.H. Döhler, Phys. Rev. B 43, 12094 (1991).
[8] X.L. Lei, N.J.M. Horing, and H.L. Cui, Phys. Rev. Lett. 66, 3277 (1991).
[9] A.A. Ignatov, E.P. Dodin, and V.I. Shashkin, Mod. Phys. Lett. B 5, 1087 (1991).
[10] K. Huang and B. Zhu, Phys. Rev. B 45, 14404 (1992).
[11] X.L. Lei and C.S. Ting, Phys. Rev. B 32, 1112 (1985).
[12] C. Minot, H. Le Person, J.F. Palmier, and F. Mollot, Phys. Rev. B 47, 10024 (1993).

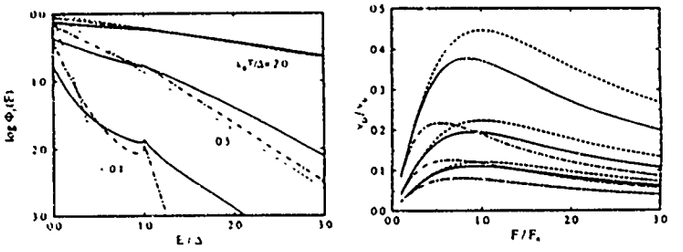

FIG. 1. Average of the distribution function over surfaces of constant energy, as defined in Eq. (6), versus energy for three values of the reduced temperature and, in each case, for thermal equilibrium $f_0(\varepsilon)=\exp(-\varepsilon/k_BT)$ ($F=0$, thin broken lines), for a stationary state with purely inelastic scattering ($F=F_0$, $r_e=0$, dash dotted lines), and for the stationary state with partly elastic scattering ($F=F_0$, $r_e=0.75$).

FIG. 2. Calculated drift velocity v_D versus electric field F for $r_e = 0.0$ (dashed lines), 0.5 (solid lines), and 0.9 (dash dotted lines), and, in each case, for $k_BT/\Delta = 0.1$, 0.5, and 1.0 (from top to bottom). The units are $v_0 = -a\Delta/2\hbar$ and $F_0 = \hbar\nu_{tot}/ea$, where ν_{tot} is fixed.

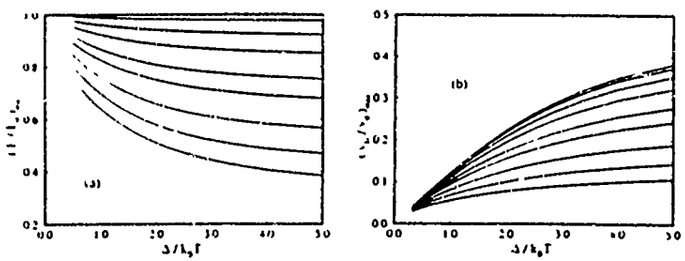

FIG. 3. Values of (a) the electric field and (b) the drift velocity at the maxima of curves as shown in Fig. 2 versus reduced miniband width for r_s= 0.975, 0.95, 0.9, 0.8, 0.7, 0.5, 0.3, 0.1, and 0.0 (from bottom to top). For r_s=0 the curve in (a) is $(F/F_c)_{max}$ =1.0. Symbols have the same meaning as in Fig. 2.

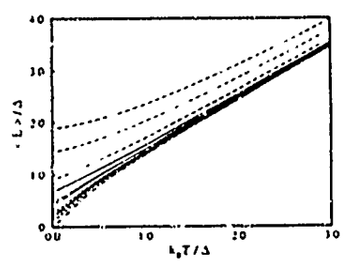

FIG. 4. Mean energy per electron vs. reduced temperature in stationary states with r_s= 0 (dashed lines), 0.5 (solid lines), and 0.95 (long dashed lines), in each case for $\xi = Fea/\hbar\omega_{LO}$= 0.5, 1.0, and 3.0 (from bottom to top), and in the thermodynamic equilibrium (dash-dotted line).

MoP30

Domain Formation in Modulation-doped $GaAs/Al_xGa_{1-x}As$ Heterostructures

R. Döttling and E. Schöll
Institut für Theoretische Physik
Technische Universität Berlin
Hardenbergstr. 36
D-10623 Berlin, Germany

Abstract

We develop a theory of self-organized domain formation arising in charge transport parallel to the layers of a modulation doped $GaAs/Al_xGa_{1-x}As$ heterostructure in the regime of real space transfer from the high-mobility undoped $GaAs$ layer into the low-mobility doped $Al_xGa_{1-x}As$ layer. We predict the existence of solitary travelling high-field domains associated with packets of real space transferred electrons propagating parallel to the layers with velocities of the order of $v \approx 2\times10^5 m/s$. This leads to transit time oscillations of $f \approx 2GHz$ for typical device dimensions of $l \approx 100\mu m$ above fields of about $2kV/cm$. Chaotic domain motion can occur under ac driving conditions.

Introduction

Negative differential conductivity (NDC) and electrical instabilities associated with parallel transport in modulation-doped semiconductor heterostructures have received much interest recently [1]-[13]. The occurrence of N-shaped current-voltage characteristics (NNDC) is due to real space transfer of hot electrons from undoped $GaAs$ to n-doped $Al_xGa_{1-x}As$ layers. At low bias U_0 applied parallel to the layers the electrons reside in the $GaAs$ channel, where they are separated from their parent donors. Therefore the mobility μ_1 of the electrons in the $GaAs$ channel will be high because of strongly reduced impurity scattering. A small electric field $E_\parallel$ ($< 1kV/cm$) will result in a current mainly due to the electrons in the $GaAs$ layer, because the carrier density and mobility in the $GaAs$ channel is much higher than in the $Al_xGa_{1-x}As$ layer. A high electric field ($\approx 2kV/cm$) parallel to the layers induces carrier heating, and the electrons are thermionically emitted into the low-mobility (μ_2) n-doped $Al_xGa_{1-x}As$-layer, thus producing NNDC.
A physical mechanism for self-generated oscillatory instabilities under dc conditions in the real space transfer regime has been proposed in [9, 14]. The idea is based on the coupled nonlinear dynamics of real space electron transfer, the dielectric relaxation of the parallel electric field and of the space charge in the $Al_xGa_{1-x}As$ layer, which controls the interface potential barrier Φ_B [14, 15]. The spatially uniform system has been predicted to display hysteretic switching transitions between oscillatory and stationary states [16] and periodic or chaotic self-generated oscillations at frequencies of 20 – 100 GHz [9, 14, 15].
The formation of travelling field domains has recently been predicted under current bias and an analytical description using methods of singular perturbation theory has been presented [17, 18]. In this paper we will theoretically develop the idea of domain formation due to real space transfer of hot electrons with a particular emphasis on the *voltage controlled* case, and present additional results on periodically *driven* heterostructures.

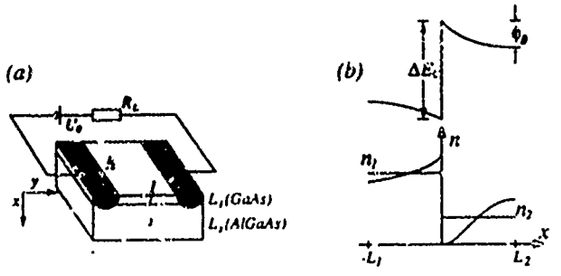

Figure 1: (a) Schematic sample and circuit configuration of a modulation doped $GaAs/Al_xGa_{1-x}As$ heterostructure with heterolayer widths L_1 and L_2, respectively, and lateral dimensions h, l. (b) Energy-band diagram (top) and carrier density (bottom) versus the perpendicular coordinate x of the heterolayer (schematic).

Experimental evidence of spontaneous current oscillations of 1 GHz and static or slowly propagating high field domains in modulation-doped multilayer heterostructures has been reported recently under dc conditions [1].

Model

In our simple analytical model we describe the heterostructure by a set of local variables, whose time evolution is given by nonlinear transport equations coupled to Maxwell's equations. On a mesoscopic level we use a set of nonlinear partial differential equations for the carrier densities n_1, n_2 in the two layers of widths L_1, L_2, for the dielectric relaxation of the applied lateral field $\mathcal{E}_y$ and for the potential barrier Φ_B in the $Al_xGa_{1-x}As$ layer as a function of the lateral coordinate y (the direction parallel to the layer interface) and the time t (see Fig. 1). The differential equations can be obtained by integrating the equation of continuity and the momentum and energy transport equations over the space coordinate x in transverse direction and neglecting spatial dependence in the z direction [17, 18]. The spatially averaged carrier density in the $GaAs$ layer $n_1(y,t) \equiv \int_{-L_1}^{0} n(x,y,t)\,dx/L_1$ as a function of t and y is then governed by the averaged continuity equation

$$\frac{\partial n_1}{\partial t} = \frac{1}{eL_1}(j_{1\to 2} - j_{2\to 1}) + \mu_1 \frac{\partial}{\partial y}(n_1 \mathcal{E}_y) + D_1 \frac{\partial^2 n_1}{\partial y^2} \tag{1}$$

where we have assumed that the carrier concentration and the parallel electric field are smoothly varying functions in the direction perpendicular to the layer interface. Eq. (1) is correct only within a finite distance from the heterojunction barrier which is comparable to the mean free distance of collisionless flight of the electrons. Far from the semiconductor barrier the average velocity of the carriers in the x direction is much smaller due to enhanced collisions with phonons, and the assumption of a nearly constant carrier concentration in transverse direction breaks down [19]. To simplify matters we have further assumed the mobility μ_1 and the diffusion coefficient D_1 in the $GaAs$ to be constant, i.e. independent of the other variables. In (1)

$$j_{1\to 2} = -en_1\sqrt{\frac{k_B T_1}{2\pi m_1^*}}\exp\left(-\frac{\Delta E_c}{k_B T_1}\right) \tag{2}$$

$$j_{2\to 1} = -en_2\sqrt{\frac{k_B T_2}{2\pi m_2^*}}\exp\left(-\frac{\Phi_B}{k_B T_2}\right) \tag{3}$$

are the thermionic emission current densities (m_i^* are the electron effective masses) given by Bethe's theory [19], ΔE_c is the conduction band discontinuity (Fig. 1b), and T_i ($i = 1, 2$) are the carrier temperatures. The thermionic emission theory corresponds to the following physical picture. Electrons in the $GaAs$ with energy less than ΔE_c cannot penetrate into the adjacent $Al_xGa_{1-x}As$ layer; all electrons with higher energy are emitted across the barrier without collisions. This assumption is correct only within a certain regime that is of the order of the mean free paths of electrons. If the $GaAs/Al_xGa_{1-x}As$ layers are wider, the thermionic emission current represents the current only close to the interface, and perpendicular diffusion (transverse dissipation of carriers in the $Al_xGa_{1-x}As$ layer) will play a major role [2].

Intervalley transfer has been shown [20, 21] to be negligible compared to real space transfer at electric fields $\leq 4kV/cm$. This means that the transport processes are dominated by the Γ-valley in our case. At higher electric fields ($\approx 8kV/cm$) intervalley scattering will become more important.

Quantum effects like the quantum-transmission coefficient or tunnelling through the barrier are also disregarded, cf. discussion in Ref. [20]. Size quantization effects, which arise if the layer widths are smaller than 100 Å, are also neglected, since the current-voltage characteristic is not essentially affected by the quasi-two dimensional subbands below the barrier, except that the critical field for the onset of real space transfer is shifted to higher values [5].

As shown in Ref. [17] the dielectric relaxation of the parallel electric field is given by the balance of displacement current, total current, and conduction current:

$$\varepsilon_0\varepsilon_r \frac{\partial \mathcal{E}_y}{\partial t} = j_B - \frac{1}{L_1 + L_2}\left((en_1\mu_1 L_1 + en_2\mu_2 L_2)\mathcal{E}_y + eD_1 L_1 \frac{\partial n_1}{\partial y} + eD_2 L_2 \frac{\partial n_2}{\partial y}\right) . \tag{4}$$

where ε_0, ε_r are the absolute and relative permittivity, and the spatially averaged carrier concentration $n_2(y,t) \equiv \int_0^{L_2} n(x,y,t)dx/L_2$ in the $Al_xGa_{1-x}As$ layer can be expressed by the averaged Poisson eq. $\varepsilon_0\varepsilon_r \partial\mathcal{E}_y/\partial y = e((N_D - n_2)L_2 - n_1 L_1))/(L_1 + L_2)$ where N_D is the donor concentration in the $Al_xGa_{1-x}As$. In (4) $j_B(t) \equiv \int_{L_1}^{L_2} j_{ms}(\vec{x},t)dx/(L_1 + L_2)$ is a first integral equal to the current density flowing through the external circuit and is determined by the particular external circuit used in the experiment. For a resistive circuit as shown in Fig. 1a $j_B(t)$ is determined by Kirchhoff's law such that the applied bias voltage $U_0 = \mathcal{E}_0 l$ is a constant: $j_B(t) = \sigma_L(\mathcal{E}_0 - \int_0^l \mathcal{E}_y(y,t)\,dy/l)$ where l is the sample length, $\sigma_L \equiv l/(A R_L)$ is connected to the load resistance R_L, and A is the cross section of the current flow. Voltage bias means that $1/\sigma_L$ can be chosen arbitrarily small which reduces Kirchhoff's law to an

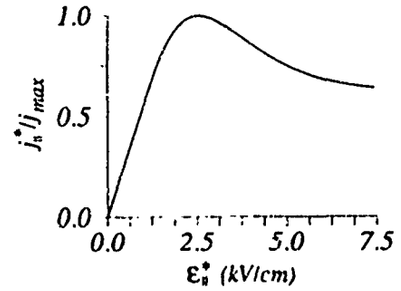

Figure 2: Static current density-field characteristic. The numerical parameters are listed in Table 1

integral constraint for $\mathcal{E}_n(y,t)$:

$$U_0 = \int_0^l \mathcal{E}_n(y,t)\,dy\,. \tag{5}$$

The dielectric relaxation of the interface potential barrier $\Phi_n(y,t) = -e\int_0^{l_2} \mathcal{E}_z(x,y,t)\,dx$ is governed by the space-charge dynamics in the $Al_xGa_{1-x}As$ layer and the resulting internal electric field $\mathcal{E}_z(x,y,t)$. As discussed in [17] the dynamic eq. for $\Phi_n(y,t)$ can be obtained by integrating the dielectric relaxation eq. for the perpendicular electric field $\mathcal{E}_z$ together with Poisson's eq. and the boundary conditions $\mathcal{E}_z(-L_1,y,t) = \mathcal{E}_z(L_2,y,t) = 0$:

$$\frac{\partial \Phi_n(y,t)}{\partial t} = -\frac{e n_2 N_D}{\varepsilon_0 \varepsilon_r}\Phi_n + \frac{\eta\mu_2}{2}\left(\frac{e}{\varepsilon_0\varepsilon_r}(N_D - n_2)L_2 - L_2\frac{\partial \mathcal{E}_n}{\partial y}\right)^2 + \mu_2\Phi_n\frac{\partial \mathcal{E}_n}{\partial y} \tag{6}$$

The steady uniform state (denoted by an asterisk) of (6) is given by $\Phi_0^* = e^2L_1^2n_1^{*2}/(2\varepsilon_0\varepsilon_r N_D) = e^2N_DL_2^2/(2\varepsilon_0\varepsilon_r)$ which corresponds to the depletion approximation in the $Al_xGa_{1-x}As$ layer within the effective depletion width $L_2 = n_1^*L_1/N_D$.
The energy transfer between the heterolayers is described by the energy-balance equation containing Joule heating, convective, diffusive, and electron-pressure induced heat flow, and energy loss due to polar-optical-phonon scattering [9]. Adiabatic elimination of the mean energy and neglecting spatial derivatives yields in a first order approximation

$$T_1 = T_L + \frac{2}{3k_B}\tau_{\varepsilon_1}e\mu_1\mathcal{E}_n^2 \quad , \quad T_2 = T_L + \frac{2}{3k_B}\tau_{\varepsilon_2}e\mu_2\mathcal{E}_n^2 \tag{7}$$

with the lattice temperature T_L and the energy relaxation times τ_{ε_1} in the GaAs-channel and τ_{ε_2} in the $Al_xGa_{1-x}As$ layer.
The model equations (1), (4) and (6) represent a simplified description of the complex transport phenomena between the semiconductor layers at high electric fields. These

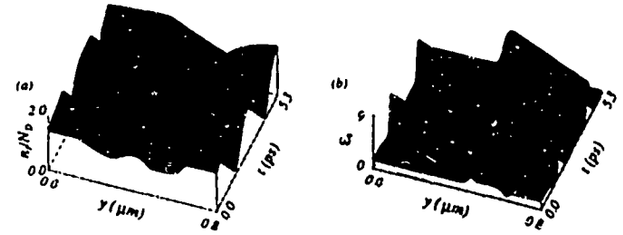

Figure 3 Travelling domain under voltage bias ($\mathcal{E}_0 = 2.1\,kV/cm$, $R_L = 0$) and periodic boundary conditions (a) Carrier density distribution in the GaAs layer. (b) Corresponding high field domain of the parallel electric field. The lateral electric field is in units of kV/cm. (Calculated with the Parameters of Table 1).

equations have to be solved on a segment $0 < y < l$, with suitable boundary conditions that depend on the nature of the metal-semiconductor contact [22].

Travelling Domains

The homogeneous stationary states of the system are obtained by setting the spatial and temporal derivatives in (1),(4) and (6) equal to zero. The resulting static current-density-field characteristic is shown in Fig 2. Real space transfer of hot electrons leads to a N-shaped characteristic with a regime of negative differential conductivity [17, 18]. The critical field for the onset of NDC is of the order of $2\,kV/cm$.
The uniform dynamical system which is obtained by neglecting the spatial derivatives in (1),(4) and (6) shows spontaneous current and voltage oscillations at frequencies of $100\,GHz$ for a large enough load resistance R_L [17]. In the voltage controlled regime ($R_l \to 0$), however, no temporal instabilities occur.
The numerical solution of the full coupled partial differential equations (1),(4) and (6) with periodic boundary conditions under voltage controlled conditions exhibits spatio-temporal instabilities and is shown in Fig 3. We have modelled the semiconductor by identical sections of length d joint by periodic boundary conditions neglecting the influence of the metal-semiconductor contacts at $y = 0$ and $y = l$. Nevertheless our solutions are expected to represent reasonable approximations of the full problem away from the contacts.
In Fig 3a an initial small perturbation develops into a propagating depletion pulse of real space transferred electrons in the GaAs-channel. In the $Al_xGa_{1-x}As$ the emitted carriers form an accumulation pulse moving with the same velocity as the depletion pulse in the GaAs. This can be explained by the following physical picture: A large enough local fluctuation of the electric field leads to real space transfer of hot electrons into the $Al_xGa_{1-x}As$ layer. Because of the different mobilities in the semiconductor layers, the

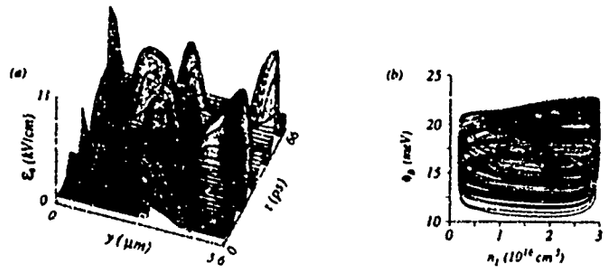

Figure 4: Chaotic domain for a driven system with $\mathcal{E}_0 = 1.8 kV/cm$, $\mathcal{E}_a = 1.188 kV/cm$ and $f_d = 75.41$ Ghz. (a) High field domain of the lateral electric field (b) Phase plot of Φ_B vs n_1 at $y = d/2$. Parameters as in in Table 1 except for $L_1 = 100$ Å, $L_2 = 600$ Å, $N_D = 10^{16} cm^{-3}$, $\mu_1 = 10^4 cm^2/Vs$, $\tau_{E_1} = 2 \times 10^{-12} s$ and $\tau_{f_1} = 15 \times 10^{-12} s$.

carrier fluctuation in the *GaAs*-channel moves fast with the electric field and is readily damped out due to lateral diffusion, while the emitted carrier fluctuation in the $Al_xGa_{1-x}As$ layer remains almost unchanged. The local increase of the carrier density in the $Al_xGa_{1-x}As$ diminishes the positive space charge controlling the band bending. The potential barrier Φ_B decreases therefore with some delay due to the finite dielectric relaxation time. This leads to an increased backward thermionic emission current, which decreases the carrier density and increases the space-charge and the potential barrier Φ_B in the $Al_xGa_{1-x}As$. This local process of real space transfer of hot electrons in the $Al_xGa_{1-x}As$ layer and backward emission into the *GaAs* channel can lead to a stable disturbance of carriers which cycle between the two semiconductor layers while the solitary pulse moves with constant velocity from the cathode to the anode.

In Fig.3b the corresponding high field domain is shown under voltage bias for periodic boundary conditions The velocity v of the propagating domain is of about $2 \times 10^5 m/s$ and the pulse width is of the order of $0.2 \mu m$. For different parameters as in Table 1 we obtain similiar results for the velocity of the travelling domains. These domains lead to transit time oscillations of $f \approx 2 GHz$ for typical device dimensions of $l = 100 \mu m$ above fields of $2 kV/cm$. As compared to the case of current bias [17, 18], the depletion pulse is less pronounced and narrower, but the domain propagation velocity is similiar.

More complex nonlinear phenomena occur when the semiconductor heterojunction is connected to a periodically driven voltage bias. In this case eq. (5) becomes

$$U_0 + U_A \sin(2\pi f_d t) = \int_0^l \mathcal{E}_h(y,t)\, dy \qquad (8)$$

where U_A is the amplitude and f_d is the frequency of the driving force. Depending on U_A and f_d we find quasiperiodic, frequency locked and chaotic states Fig 4 shows the spatio-temporal dynamics of a chaotic domain. The chaotic attractor has been generated

Table 1: The numerical parameters used in the simulation

N_D	10^{17} cm^{-3}
L_1	100 Å
L_2	200 Å
μ_1	8000 cm^2/Vs
μ_2	50 cm^2/Vs
T_L	300 K
ΔE_c	250 meV($\lambda = 0.3$)
m_1^*	0.067 m_0 (m_0 free electron mass)
m_2^*	$(0.067 + 0.083 \times x)\, m_0$
τ_{E_1}	1.8×10^{-12} s
τ_{f_1}	6.4×10^{-12} s
h	1 mm
ϵ_r	12 ϵ_0

by an intermittency catastrophe of a torus. The topological property of this catastrophe is that the torus (which exists before the bifurcation event) lies inside the chaotic attractor (which exists after the bifurcation) [23].

Conclusion

The spatio-temporal self-organization due to real space transfer of hot electrons in modulation-doped heterostructures has been investigated theoretically on the basis of a system of nonlinear transport equations.

Our model predicts stable solitary travelling domain solutions under voltage bias as well as under current bias. The high-field domains are connected with moving *packets* of real space transferred electrons, and propagate with velocities of about $2 \times 10^5 m/s$ which typically correspond to oscillations in the *GHz* regime. These propagating domain solutions may serve as an explanation for the current oscillations observed at electric fields below the onset of intervalley transfer in semiconductor heterostructures [1, 2].

References

[1] N Balkan, B.K Ridley and A. Vickers (eds.), Negative Differential Resistance and Instabilities in 2-D Semiconductors. Plenum, New York (1993).

[2] B.K Ridley, Rep Progr Phys. 54, 169 (1991).

[3] Z S Gribnikov, Sov. Phys. Semicond 6 1204 (1973).

[4] F Pacha, F. Paschke, Electron Commun. 32, 215 (1978).

[5] K Hess, H Morkoc, H Shichijo, and B G Streetman, Appl. Phys Lett 35, 469 (1979)

[6] H Shichijo, K. Hess, and B G. Streetman, Sol State Electron 23, 817 (1980).

[7] P.D. Coleman, J Freeman, H. Morkoc, K. Hess, B.G. Streetman, and M. Keever, Appl Phys Lett 40, 493 (1982)

[8] R Sakamoto, K Akai, and M Inoue, IEEE Trans Electron Devices 36, 2344 (1989)

[9] K Aoki, K. Yamamoto, N. Mugibayashi, and E. Schöll, Sol. State Electron 32, 1149 (1989).
[10] A. Kastalsky, M. Milshtein, L.G. Shantharama, J. Harbison, and L. Florez, Sol. State Electronics 32, 1841 (1989).
[11] A.J. Vickers, A. Straw, and J.S Roberts, Semicond. Sci. Technol. 4, 743 (1989)
[12] P. Hendriks, E.A E. Zwaal, J G A Dubois, F.A.P. Blom, and J H. Wolter, J. Appl Phys. 69, 302 (1991).
[13] S Luryi and M R Pinto, Phys Rev Lett 67, 2351 (1991).
[14] E. Scholl and K. Aoki, Appl. Phys. Lett. 58, 1277 (1991).
[15] E Scholl and K. Aoki, Proc. 20th Int. Conf. Physics of Semiconductors, ed E H. Anastassakis and J.D. Joannopoulos, p 1125 World Scientific, Singapore (1990).
[16] R. Döttling and E. Scholl, Phys Rev. B 45, 1935 (1992).
[17] R. Döttling and E. Scholl, Physica D (1993) in press.
[18] R Döttling and E. Scholl in: Negative Differential Resistance and Instabilities in 2-D Semiconductors eds N Balkan, B K Ridley and A. Vickers. Plenum, New York (1993)
[19] K Hess, Advanced Theory of Semiconductor Devices Prentice Hall, New Jersey (1988).
[20] K F. Brennan and D.H. Park, J Appl. Phys. 65, 1156 (1989).
[21] T H. Glisson, J R Hauser, M A. Littlejohn, K. Hess, B G. Streetman and H Shichijo, J Appl. Phys 51, 5445 (1980)
[22] L.L. Bonilla and S W. Teitsworth, Physica D 50, 545 (1991).
[23] J M T Thompson and H.B. Stewart, Nonlinear Dynamics and Chaos. J. Wiley, Chichester (1986).

MoP31

Inside a 2D Electron System: Images of Potential and Dissipation

R Knott, W Dietsche, K v Klitzing, K Eberl, K Ploog[§]
MPI fur Festkörperforschung, 70506 Stuttgart, FRG

ABSTRACT

Lateral potential distributions in two-dimensional electron systems are imaged under magnetotransport conditions with an electrooptic method. In low mobility δ-doped samples, the results agree with a classical picture in the ohmic regime. For high currents, a uniform breakdown is found. In high-mobility modulation-doped heterostructures, the change in the potential distribution at breakdown is strongly asymmetric upon current reversal.

INTRODUCTION

Two-dimensional electron systems (2DES) are established as the basis of various practical devices. In semiconductor heterostructures, remarkable microscopic qualities have been achieved. In addition, macroscopic homogeneity of the layers is also regarded essential for successful applications. Relative resistivity gradients around 0.005/mm have been reported on 3" wafers [1].

In basic research, there has been much magnetotransport work on 2DES. Alloyed contacts are employed to feed the current and to sense the voltages. Global resistances can be extracted from these experiments, but their connection to the local resistivities has been unclear for some time [2]. Currently, there is a lot of discussion on the validity and usefulness of global and local descriptions of magnetotransport.

Alloyed contacts in the interior of a piece of 2DES have yielded some local information [3]. However, they are not flexible enough to yield a comprehensive picture of the potential distribution inside the 2DES. Furthermore, it is possible that these internal contacts will act as reservoirs or inject current. Clearly, a contactless spatially resolving method is desireable to investigate the previously marked degrees of freedom in the transport.

EXPERIMENTAL METHOD

Fortunately, optical measurements of electric potentials are possible by virtue of the linear electrooptic (Pockels) effect. In the present context, the electrooptic method has been introduced by Fontein et al. [4].

The following optical setup (figure 1) is used. Subbandgap light from a collimated laser diode (850 nm, 2 mW) is circularly polarized by the calcite polarizer P and the appropriately set Soleil-Babinet compensator SBC. As it passes through the GaAs sample, it acquires some ellipticity [5]. We look at the light reflected from the gold coated rear side of the sample S, which also serves as a reference electrode. The front side electrode is provided by the structured and contacted 2DES itself. The

[§] now at PDI fur Festkorperelektronik, 10117 Berlin, FRG.

reflected light is separated from the incident beam by the beam splitter BS and analyzed by the calcite analyzer A.

A silicon photodiode PD serves as a detector. Its photocurrent is analyzed synchronously with the AC current through the sample (f≈1kHz). For a plane incident wave and a homogenous electric field the AC photocurrent is then proportional to the electrostatic potential difference between the front and the rear side of the crystal.

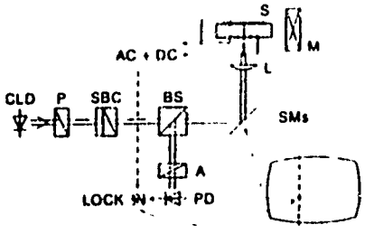

Figure 1. Schematic of the experimental setup. Symbols are mentioned in the text. The sample S and the lens L are immersed in superfluid helium in the bore of the superconducting magnet M.

To obtain spatial resolution, the laser beam is raster scanned across the sample surface by the galvanometer scanners SMs under computer control and focussed onto the sample by the adjacent lens L. The AC photocurrent measured at each sample spot is displayed as the brightness a pixel on the computer screen.

In our setup, we deduce a spatial resolution of 20 µm. The potential resolution is around 3 mV/√Hz, depending on the received optical power. These experimental values are sufficient for investigation of the Quantum Hall effect in the low current regime.

In practice, it is important to avoid any parallel channel bypassing the 2DES. Such a bypass would act as a undesired frontgate altering the electrostatic boundary conditions in the structure. Since electrooptics measures the potential difference between the front and back side of the sample, a parallel channel will mask the potential distribution in the 2DES.

LOW MOBILITY SAMPLES

Delta-doped layers [6] are an example of low mobility 2DES which intrinsically avoid parallel channels. We have prepared such layers by molecular beam epitaxy on [100] GaAs substrates. Upon a 500nm buffer layer a Si doping layer of ≈ $7*10^{11}cm^{-2}$ was accumulated, which was in turn capped with 100nm GaAs. A Hall bar structure with dimensions $0.5*1.5mm^2$ was defined using photolithographic techniques. Ohmic contacts were processed by alloying AuGe-Ni. On the polished rear side of the wafer, a

200nm Au layer was evaporated onto a 10nm Cr seed layer.

When cooled in the dark to 1.6K, no conductivity was measureable. Upon illumination in the cold by a broadband visible source (intensity $10mW/cm^2$) however, a (quasi) 2DES was established with a density of $5.5*10^{11}cm^{-2}$ and a mobility of $2000\ cm^2/Vs$, as deduced from Hall measurements.

Such δ-doped layers are known to exhibit the Quantum Hall Effect at low integer filling factors [7]. Experimentally, we find a broad plateau centered around 11T in the magnetotransport trace, which is quantized to better than 1% at currents below 10µA. It is accompanied with a minimum in the longitudinal resistance of ≈500Ω. This rather large value clearly reflects the short elastic scattering times in the δ-layer.

A set of electrooptic images taken at T=1.6K is depicted as unprocessed data in figure 2. The current contacts are situated at the left and at the right hand side of the indicated 2dES area. Four additional voltage probe contacts are also discernible at the top and at the bottom side of the hall bar. The measured potential difference between the front and rear side of the sample is brightness coded.

The upper picture was obtained without an applied magnetic field (B=0). The AC current amplitude was 35µA. On the whole, a linear potential drop is recognized from the left to the right. This is just the result expected for a homogenous conductor. A closer look at the image reveals, however, deviations from the ideal potential picture. They may be either due to uncorrected transmission inhomogeneities in the optical system or due to inhomogeneities in the conducting sheet. This point will be worked out further in connection with the measurements in a magnetic field.

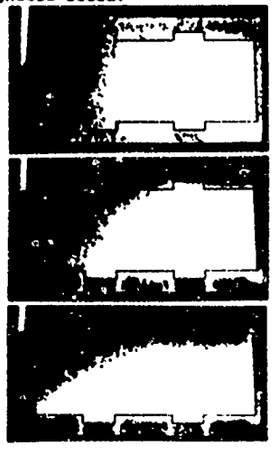

Figure 2.

Electrooptic images of the potential distribution in a δ-doped layer. I_{AC}≈30µA, T=1.6K.

B=0.

B=7T.

B=10.8T.

The central picture was taken in a magnetic field of 7T (filling factor 3.1) corresponding roughly to $\omega_c\tau=1$, where τ is the the zero field scattering time. The current amplitude was 27μA. The potential distribution expected is reproduced quite nicely in the measurement: In the central part of the sample the equipotential lines intersect the sample boundaries with an angle of 45°. This is consistent with homogenous current flow in this region and a Hall angle of 45°. Approaching the current contacts, the equipotentials tilt towards the injecting boundary to match the potential distribution in the contacts [8].

In the bottom picture of figure 2, the magnetic field was increased to 10.8T, which is the center value of the broad Hall plateau. From $\omega_c\tau=1.5$ a Hall angle of ≈56° is expected. Experimentally, however, an angle close to 90° is found in the central part of the sample assuming a homogenous current flow in this area. This angle is in agreement with the minimum in the longitudinal resistance, which is typical for the QHE. Close to the current contacts the equipotentials converge towards a corner. Such a pattern is necessary to fit the potential distribution in the low resistivity contact.

The Hall potential drop, which is uniform and linear in the center of the sample, is confined to a narrow range close to the current contact. The whole current also has to transverse this narrow range. Therefore, the dissipating region is highly localized, as revealed by previous thermography experiments [9].

A closer look at the image reveals that the Hall bar cannot be perfectly homogenous. Especially, the electric field vector between the voltage probes on the right side is not parallel to that in the center of the sample. This behaviour was even more pronounced in nonlinear transport experiments.

As an example, a bias current of 90 μA was applied in figure 3 (B=10.8T). Transport measurements yield an increase of the longitudinal resistance from 500Ω to 3kΩ. On the left of the image, the potential pattern is now very similar to that at B=7T. Obviously the conductivity is increased. On the right of the image the equipotential lines experience an odd distortion, which also depends on the bias polarity. Evidently, the current distribution in the sample is strongly inhomogenous making the extraction of a Hall angle from the potential distribution alone impossible. We take this as an indication of a small density inhomogeneity in the sample.

Figure 3.

Potential distribution in the δ-layer at large current.
B=10.8T, I_{DC}=90μA, T=1.6K.

HIGH MOBILITY SAMPLES

To compare the findings with experiments on high mobility 2DES, we have prepared samples of modulation-doped heterostructures by MBE. An undoped $Al_{.3}Ga_{.7}As$ spacer upon the GaAs buffer seperates the ionized Si donors from the 2D channel to achieve high mobility. All other sample processing steps were done as mentioned above for the δ-layers.

The sample for the electrooptic experiments was selected to show no conduction bypassing the 2DES under a variety of illumination conditions. When cooled in the dark, no conductivity was found in the heterostructure. Exposure to ambient light (Intensity ≈ .1mW cm^{-2}) yielded a carrier density of $3.7*10^{11}cm^{-2}$ with a mobility of 500000 cm^2/Vs. Magnetotransport traces show pronounced quantized Hall plateaus and accompanying zeros of the SdH voltage, as usual in samples of high quality. Critical current densities for breakdown of the QHE were around .5 A/m for filling factors 2 and 4 and for channel widths between 50 and 400 μm.

In figure 4, electrooptic images are shown for filling factor 2 at T=1.6K. The boundaries of the 2DES (width 200 μm) are indicated. Only a part of the structure is shown, with one current contact at the left of the images and a connection to a larger 2DES at the right. Current polarities refer to that contact. In figure 4a, there is a DC bias of 140 μA with a square wave modulation amplitude of 30 μA. In figure 4b, the bias polarity is reversed. The current values are switched between just below breakdown and far above it to enhance the contrast.

Contrary to the I-V characteristics, there is a large asymmetry in the potential distribution. With positive bias, the breakdown voltage drop occurs immediately after the current contact. The Hall potential drop then gradually moves from the upper to the lower side of the bar. On the right of the picture, the potential profile is homogenous. With negative bias, the Hall potential drop always remains on the upper side of the sample, while the longitudinal drop occurs on the right of the strip. The overall behaviour of the potential distribution is obviously entirely different from the low mobility case discussed above. Its understanding will require a more elaborate picture than e.g. [8].

The dissipative current entry/exit point is always in the upper left corner of the sample. But since the potential landscape in its surroundings is different for both bias polarities, the asymmetry in the power dissipation reported in [9] is understandable.

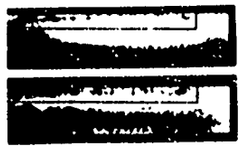

Figure 4.

Potential distribution in a heterostructure sample.
Filling factor 2, T=1.6K.
(upper) I_{DC}=+140μA,
(lower) I_{DC}=-140μA.
Polarity with respect to left current contact.

SUMMARY

The electrooptic technique has thus proven to be powerful in revealing the potential distributions in 2DES under magnetotransport conditions. In the low mobility δ-layers, the change in the potential landscape from zero to quantizing magnetic field has been analyzed and found to accord with conventional descriptions. Images of breakdown situations have revealed a reduction of the Hall angle back to 45° and a pronounced tendency towards density inhomogeneities. In high mobility heterostructure, potential distributions not envisiged previously have been encountered. They demonstrate the variability of the internal degree of freedom in two-dimensional magnetotransport.

REFERENCES

1. G. Böhm et al., J. Crystal Growth 127, 81 (1993).
2. J. Nakabayashi and S. Kawaji, J. Phys. Soc. Japan 44, 1839 (1978).
3. G. Ebert et al., J. Phys. C 18, L257 (1985).
4. P. Fontein et al., Phys. Rev. B 43, 12090 (1991).
5. A. Yariv and P. Ye, Optical Waves in Crystals, Wiley, New York (1984).
6. K. Ploog, J. Crystal Growth 81, 304 (1987).
7. A. Zrenner et al., Semicond. Sci. Technol. 2, 1132, (1988).
8. B. Neudecker and K. Hoffmann, Solid State Comm. 62, 135 (1987).
9. U. Klaas et al., Z. Phys. B 82, 351 (1991).

MoP32

DC Transport in Intense, in-Plane Terahertz Electric Fields in $Al_xGa_{1-x}As$ Heterostructures at 300 K

N. G. Asmar, A. G. Markelz, and E. G. Gwinn
Center for Free-Electron Laser Studies and Department of Physics,
University of California, Santa Barbara California 93105

P. F. Hopkins and A. C. Gossard
Department of Electrical and Computer Engineering,
University of California, Santa Barbara California 93106

We report 300 K studies of the dependence of the in-plane, dc conductivity, $\sigma_{dc}(E_\omega)$, of a quasi-2D electron gas on the amplitude E_ω and frequency of intense far-infrared fields ($\omega/2\pi = 0.24 - 3.5$ THz). We measure $\sigma_{dc}(E_\omega \| E_{dc})$ where E_{dc} is a small sensing field, and observe a monotonic decrease in σ_{dc} with increasing E_ω. Although a simple scaling ansatz collapses the measured $\sigma_{dc}(E_\omega)$ data onto a single curve for frequencies from 0.25-3.45 THz (at low to moderate scaled fields), the decrease in conductivity is substantially more rapid than expected from comparison to similar data taken by Masselink *et al*[1] at 35 GHz. We tentatively attribute this difference to effects of a high frequency modulation in the electron temperature.

Development and application of high-speed devices made from modulation-doped semiconductor heterostructures require a better understanding of transport in large, rapidly varying electric fields. Electronic transport under *static* high-field conditions in bulk GaAs has long been known to greatly differ from linear, low-field transport; for example, when an applied d.c. field is sufficiently large, GaAs exhibits Gunn oscillations due to negative differential mobility. Because high-speed devices are approaching the THz regime, it has become important to understand high-field transport in fields that vary periodically on the time scale of the fundamental energy and momentum relaxation processes. Currently, very little is known about electronic transport in this regime[2]. In order to probe high-field, high-frequency transport, we have studied the dependence of the d.c. conductivity of a quasi-two-dimensional electron gas (2DEG) in a modulation-doped heterojunction on the frequency and amplitude of applied, THz-frequency electric fields.

We have measured the 300 K, dc conductivity $\sigma_{dc}(E_\omega)$ of the 2DEG in far infrared (FIR) fields at frequencies from 0.25 to 3.5 THz. The FIR radiation is supplied by the UCSB Free Electron Laser (FEL), which provides intense, linearly polarized fields from 0.12 THz to 4.8 THz[3]. As shown in Fig. 1, the FIR radiation propagates in air and is directed onto the sample at normal incidence with a focussing mirror. A beam splitter couples a small fraction of the light to a fast pyroelectric reference detector. The attenuators used to vary the FIR intensity are mounted on the FEL beam port to avoid stray reflections. In the data shown here, the FIR radiation was polarized parallel to the small dc sensing field that biases the sample, an MBE-grown GaAs/Al$_{0.3}$Ga$_{0.7}$As heterojunction with an electron sheet density of 2.75×10^{11} cm^{-2} and a mobility of 8,500 cm^2/V-sec at T=300K. This mobility yields a low-field momentum relaxation time, τ_m, of 0.32 ps, so that $\omega\tau_m$ varies from 0.45 at 0.24 THz to 6.5 at 3.6THz.

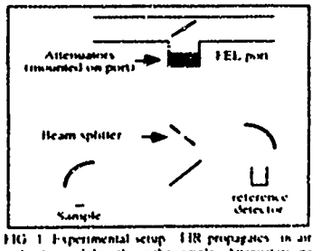

FIG 1 Experimental setup FIR propagates in air and is focused directly on the sample Attenuators are used to vary its intensity and a real prism rotates its polarization A small fraction of the light is focused onto a reference detector

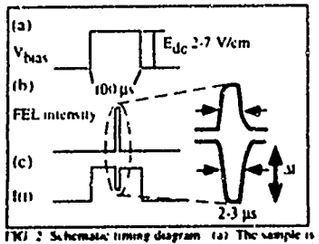

FIG 2 Schematic timing diagram (a) The sample is biased with a 100μs dc pulse which provides a small sensing field (E_{dc} < 7kV/cm) (b) The FIR pulse typically 2 μs, coincides with the center of the dc pulse (c) We observe a decrease in the current through a load resistor coincident with the FIR

The sample is a mesa-etched, 3 mm x 0 5mm bar with Ni-Au-Ge contacts We voltage-bias the sample in series with a load resistor R_L, and measure the sample current from the voltage drop across R_L The FIR electric field, which is polarized parallel to the direction of the dc sample current and in the plane of the electron gas, produces a decrease in the current throught the load resistor due to an increase in the sample's resistance As shown in Fig 2, the 2-3 μsec FIR pulse arrives at the center of the small (E_{dc} <7 V/cm), 100 μsec dc voltage bias We have varied the length of the FIR pulse to confirm that the observed increase in the sample resistance is not due to gross heating of the lattice

We measure the total power incident on the sample with a photothermophore energy meter (Thomas Keating Ltd) that is electrically calibrated We measure the spot size using a micrometer-driven pyroelectric detector with a small aperture, and use a Gaussian fit to obtain the spot radius The electric field E_ω at the electron gas is different from the incident field due to interference between the parallel faces of the sample We correct for this by using the measured FIR transmission of the sample to calculate the field inside. To determine the dc conductivity ratio, $\sigma_{dc}(E_\omega)/\sigma_{dc}(0)$, from the sample resistance, we use the measured spot size and a simple numerical algorithm to correct for the spatial variation of the conductivity due to the nonuniform(Gaussian) sample illumination[3].

Figure 3 shows the dependence of $\sigma_{dc}(E_\omega)/\sigma_{dc}(0)$ on the terahertz field E_ω, at representative frequencies from 0 25 to 3 5 THz At fixed ω, we observe a monotonic decrease in $\sigma_{dc}(E_\omega)/\sigma_{dc}(0)$ with increasing E_ω As ω increases, $\sigma_{dc}(E_\omega)/\sigma_{dc}(0)$ decreases less rapidly with increasing E_ω. This ω-dependence reflects the increasing phase shift between the high-frequency current and E_ω, which decreases the power absorbed by the electron gas

To analyze the frequency dependence of the data in Fig 3, we make the ansatz that the d c. conductivity is an (unspecified) function of P_{abs}, the power absorbed by the electron gas $\sigma_{dc} = \sigma_{dc}(P_{abs})$ We further assume that the absorbed power has a Drude form, $P_{abs} \propto E_\omega^2/(1+\omega^2\tau_m^2)$, where τ_m is the *low-field* momentum relaxation time determined from the mobility If these assumptions were valid, then plotting σ_{dc} versus the scaled field $E' = E_\omega/(1+\omega^2\tau_m^2)^{1/2}$ would collapse the data in Fig 3 onto a single curve Figure 4 shows that the data do indeed scale roughly with this ansatz over more than a decade in frequency, for

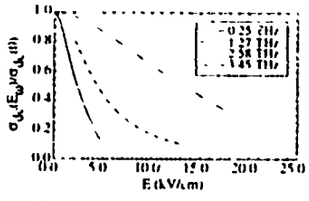

FIG 3 dc conductivity ratio, $\sigma_{dc}(E\omega)/\sigma_{dc}(0)$ v THz field, E_ω We observe a monotonic decrease in $\sigma_{dc}(E\omega)/\sigma_{dc}(0)$ with increasing E_ω for The decrease is more slow at the higher frequencies

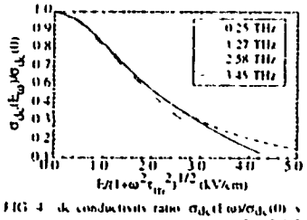

FIG 4 dc conductivity ratio $\sigma_{dc}(E\omega)/\sigma_{dc}(0)$ v rescaled terahertz field, $E' = E_\omega(1+\omega^2\tau_m^2)^{1/2}$, where τ_m is the low field momentum relaxation time obtained from the mobility For our sample τ_m was 0 32 ps The rescaled data coincide well at low fields but depart signifi cantly when E_ω is large

fields below ~ 2 kV/cm there τ_m has been adjusted slightly to obtain coincident curves at the lowest fields).

This good scaling over a wide frequency range leads one to expect the scaled data in Fig. 4 to agree with the $\sigma_{dc}(E_\omega)$ curves measured in the presence of much lower frequency, microwave fields by Masselink and co-workers, who have studied bulk, n-GaAs and GaAs/AlGaAs 2DEG samples driven by a 35 GHz field[1] Thus, Their bulk and 2DEG samples had mobilities of ~8000 cm^2/V-sec, comparable to that of the sample discussed here At 35 GHz, $1+\omega^2\tau_m^2 \approx 1$, and $E' \approx E_\omega$ The 35 GHz data show that the 300 K $\sigma_{dc}(E')$ curves for both bulk and 2DEG samples are nearly identical for fields below ~ 2 kV/cm

At 35 GHz, the decrease in $\sigma_{dc}(E')$ from $\sigma_{dc}(0)$ is ~ 5% at $E' = E_\omega = 1$ kV/cm, and ~ 20% at $E' \approx 2$ kV/cm[1]. In contrast, in our scaled data in Fig. 4, $\sigma_{dc}(E')$ is reduced by ~20% from $\sigma_{dc}(0)$ at $E' = 1$ kV/cm, and by ~50% at $E' \approx 2$ kV/cm The reason for this substantially more rapid fall-off in σ_{dc} with E' in our data is unclear. Although it is possible that this discrepancy between $\sigma_{dc}(E')$ at 0 25-3 45 THz and $\sigma_{dc}(E')$ at 35 GHz reflects a frequency-dependent error of a factor of 2 to 3 in our calibration of E_ω, this exceeds any generous estimate of the random and systematic errors involved in finding the field at the plane of the 2DEG It also seems unlikely that the slightly higher mobility of our sample could be responsible for the difference between the microwave and terahertz-frequency data

More interesting possibilities for the discrepancy between the 35 GHz data and our high frequency results for $\sigma_{dc}(E')$ are effects of modulation, at high frequencies, of the electron temperature, and of modification of the hot phonon population In the 35 GHz data, $\omega\tau_m << 1$ and $\omega\tau_\varepsilon << 1$, where τ_ε is the low-field energy relaxation time, so that both the current and the electron temperature T_e of the gas follow E_ω adiabatically Furthermore, at 35 GHz the period of the microwave field is substantially longer than the lifetime of a non-equilibrium optical phonon, which ranges from ~0 5 psec to ~3 5 psec at 300 K in GaAs/AlGaAs quantum wells, depending on interface roughness[5] In our data, $\omega\tau_\varepsilon$ ranges from ~1 6 at 0 25 THz to ~22 at 3 45 THz, assuming τ_ε ~ 1 psec Thus, the electron temperature T_e cannot follow the drive, and should oscillate about its time average value at frequency of 2ω, with an amplitude that decreases with increasing ω This oscillation in T_e should lead to enhanced optical phonon emission twice per drive cycle. Because the optical phonon lifetime is comparable to or longer than the half period of the FIR drive for all of our

data, an enhanced, non-drifting population of non-equilibrium phonons may occur at the high frequencies we have explored. This would tend to decrease the time-average conductivity $\sigma_{dc}(E')$ in terahertz-frequency fields relative to the d.c. conductivity at microwave frequencies.

It is somewhat surprising that the very simple scaling ansatz above, which assumes a Drude form for the power absorption, works well to such high fields in Fig. 4. The deviation from this simple scaling with increasing E' may reflect the frequency-dependent effects discussed above. It would be very interesting to extend the balance-equation calculations[2] of $\sigma_{dc}(E_{eff})$ that have been carried out for bulk n-GaAs at 35 GHz (which appear to agree fairly well with the 35 GHz data of Masselink *et al*) to the frequency regime explored here, to explore in detail the origins for the behavior shown in Fig. 4.

The authors acknowledge useful discussions with S. J. Allen Jr. and M. S. Sherwin, and the support of the staff at the Center for Free Electron Laser Studies. Work at the Center for Free Electron Laser Studies was supported by Office of Naval Research (N00014-92-J-1452). Clean room use was supported in part by the NSF Science and Technology Center for Quantized Electronic Structures, Grant No. DMR88-10450.

[1]W. T. Masselink, N. Braslau, D. LaTulipe, W. I. Wang, and S. L. Wright, *Solid State Electronics* 31, 337 (1988).
[2] W. Cai and M. Lax, in *Physics of Hot Electron Transport in Semiconductors*, edited by C. S. Ting, World Scientific, London, (1992), and *Int. J. of Mod. Phys.* B6, 1007 (1992).
[3] G. Ramian, *Nuclear Instr. Meth. Phys. Res.* A318, 225 (1992).
[4] N. G. Asmar et al, to be published.
[5]R. Gupta, N. Balkan, and B. K. Ridley, *Phys. Rev.* B46, 7745 (1992).

MoP33

MICROWAVE MINIBAND NDC IN GaInAs/AlInA SUPERLATTICES

J.F. Palmier, J.C. Harmand, C.Minot, H.Le Person,
E. Dutisseuil, H. Wang and G. Leroux
France Telecom, CNET/PAB 196 av. Ravera 92220 Bagneux (Fr)

Abstract

The negative differential conductance originating from electron Bragg scattering in miniband transport is demonstated in a series of five GaInAs/AlInAs superlattices having miniband width from 18 to 81 meV. Sharp resonances or broad band amplification (0-55 Ghz) are obtained according to the miniband width. The experimental values of the peak velocities deduced from the microwave resonances, and, to some extent, the DC values are satisfactorily compared with semi-classical theory based upon the complete Boltzmann Transport Equation.

Introduction

Recent progress has been performed in the non-linear Esaki-Tsu [1] NDC in semiconductor superlattices [2-5]. This effect is different from the Wannier-Stark resonances, as the critical electric field does not depend at the first order upon the miniband width and, in principle, could be reduced to very low values. Most of these results have been obtained in the GaAs/AlAs system, and very few in other systems. Beltram et al have inserted a GaInAs/AlInAs superlattice in the collector of a npn HBT and have concluded to the existence of the NDC [6] in terms of Wannier-Stark localization. In the present communication, we give an other convincing evidence of the Esaki-Tsu NDC in a series of 5 GaInAs/AlInAs superlattices having different minibands, from 18 to 81 meV. Our demonstration is based on two facts. The first one is the comparison of the static DC current-voltage characteristics with a semi-classical Boltzmann miniband transport numerical solution. The second one is based upon the microwave S-parameters measurements which is directly related to the carrier transit-time though the whole SL structure, and therefore to the drift velocity. In our first publications dealing with the miniband transport NDC in GaAs/AlAs superlattices, we were somewhat embarrassed by the proximity of X and L minibands from the first Γ one, and we argued that, even though a significant part of the electron distribution were "absorbed" in an inefficient X-miniband hopping transport, the observed effects were undoubtedly due to the Γ miniband. With GaInAs/AlInAs superlattices and for electric fields less than a few ten kV/cm, the contribution of X and L bands is negligible as their lowest extrema are almost resonant with the continuum above the InAlAs barriers. For that reason, and owing to the surprisingly good microwave performances of this first preliminary series of samples, GaInAs/AlInAs SLs may be of great interest in the development of futher millimeter wave applications of SL devices.

Sample fabrication.

The epilayer have been grown by MBE on semi-insulating Fe-doped InP wafers. It consist of Si-doped (N_d = 2 10^{18} cm^{-3}) $In_{0.53}Ga_{0.47}As$ / $Al_{0.48}In_{0.52}As$ SL layer of total thickness L = 1 µm sandwiched between two n^+ layers (N_d = 2 10^{18} cm^{-3}). Graded MWQ layers with very thin barriers are inserted between the n^+ layers and the active SL in order to provide a continuous variation of the lowest conducting state between the contact and the active layer. The five samples have been designed with a constant well thickness (45 Å) and different barrier thicknesses, as listed in table (1). Wide microwave bandwidth devices have been obtained by means of an SiO_2 insulated mesa technique, in a process very similar to the GaAs/AlAs recently published results[7]. The final step is particularly the same, consisting in a coplanar 50 Ω Ti-Au interconnection suitable to the 0-40 Ghz Microtech Cascade probes used in S parameter measurements. In figure (1) the cross section of the sample and a schematic representation of the technology are drawn for indication. The mesa lateral dimensions are 14x12 µm.

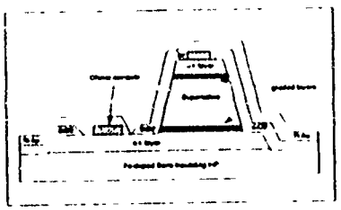

Figure 1 cross section of the SL device

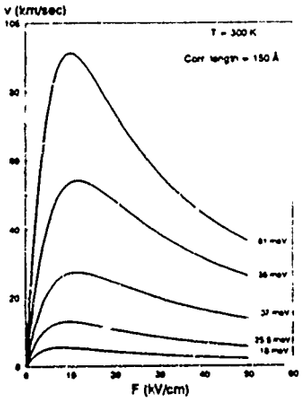

Figure 2 Theoretical variations of the drift velocity versus F for the five miniband widths corresponding to the studied SLs

reter	a (Å)	b (Å)	a + b (Å)	period X rays	Δ meV	E_1 meV
297W	45	40	85	84 8	17 7	140
304W	45	35	80	78 8	25 5	136
298W	45	30	75	74 5	37 1	131
303W	45	25	70	69 8	5' 8	124
299W	45	20	65	64 7	80 6	114

Table 1 Superlattice geometrical and band parameters a and b are respectively the well and barrier aimed thicknesses The period d=a+b is compared to the measured one by X rays Δ is the lowest electron miniband width and E_1 the position of the miniband origin from the Ga In$_{0.47}$As Γ band

Characterization.

In table (1), the nominal periods are compared with the results as given by X-rays, one can note that the "error" is 0.5 Å in the worst case, resulting in a mean error less than 1% on the period Up to four diffraction secondary peaks near (HKL) = (002) have been observed with about the same relative ratio to the main diffraction peak that provided by the diffraction model We therefore consider that the crystallographic quality of the present SL series is sufficiently good

to assure the coherence of the Bloch wave function in the miniband The miniband parameters Δ and E_1, also listed in table (1) are, respectively, the miniband width and the position of the miniband origin from the GaInAs Γ minimum These parameters are obtained from a Kronig-Penney-Bastard derivation using 60% of the gap's difference for the band offset in the conduction band

The static current voltage characteristics of all samples can be directly compared to the semi classical drift-velocity versus electric field law , v(F), at least in the positive differential conductance range ($F < F_v$) The very coarse relations used in that direct comparison are $J = q N_d v$ and $V = FL$ This has been done in figures (2) and (3), respectively for the theory and the experiment, taking N_d as the nominal doping value One can remark from that coarse comparison that the experimental peak velocities are systematically higher than the theoretical ones. We advance the following explanations

- The actual N_d value is higher than wanted

The graded layers are doped $N_d = 2\ 10^{17}$ cm^{-3}, and may electrically diffuse excess carriers in the active layer One can remark an apparent shift of Fc for the widest minibands This is due to a parasitic resistance caused by the n+ buffer layer (see fig 1). An estimated value of 12 Ω is in agreement with a separate TLM measurement of the buffer layer resistance per square and the observed shift of 0.5 volt for a current of the order of 50 mA

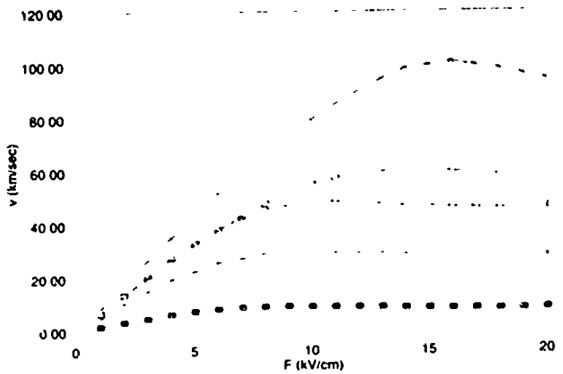

Figure 3 Experimental drift velocities deduced from the I(V) at 300K

Anyway in spite of a significant discrepancy for narrowest minibands the agreement is quite good owing to the simplicity of the method In the numerical simulation shown in fig (2) only one parameter has been used The complete BTE has been numerically solved with only two dominant scattering mechanisms at T=300K the electron PO phonon scattering and the interface roughness scattering (IR) The treatment of IF scattering follows Dharssi-Butcher's approach [8], numerous details are given in [9 10] for its application to the complete BTE numerical solution The IF scattering intensity is represented by only one parameter Λ which is the correlation length of the fluctuation on one monolayer at interfaces Λ has been chosen equal to

150Å for all samples in order to give the best fit of F_c for most samples. It is clear that the monolayer fluctuation for the present kind of SL could not be seriously maintained in a more conspicuous approach. On the other hand the agreement of the measured F_c with the semi-classical model of a rigid miniband discards the Wannier-Stark approach ($qdF_c = \Delta$) in favor to the Esaki-Tsu approach ($qdF_c = \hbar/\tau$). The mean collision time is represented here by a more detailed BTE solution, but the mean collision time order of magnitude is also an interesting parameter, about 10^{-13} sec in applying the simple formula. One of the major interest of AC measurements when NDC occurs is to provide a more complete analysis beyond the critical field than given by DC measurements.

Microwave measurements.

Microwave measurements on these samples have been performed by a Wiltron 360 network analyser in one port configuration in order to obtain the complex reflection coefficient S_{11}. In figure (4a) and (4b) are represented the variations of S_{11}, respectively for the narrowest miniband (17meV) and the largest one (81meV), at different applied voltages, in the frequency range 01-40 Ghz. Intermediate cases are not represented to shorten the text. Let us first consider the narrowest miniband result. fig (4a)

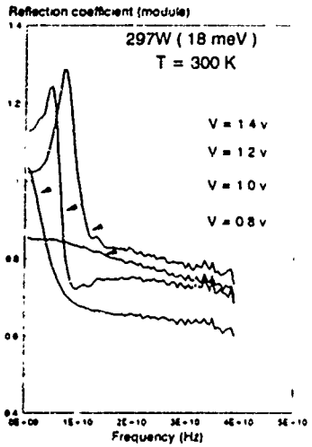

Figure 4a Variations of the reflexion coefficient module between 0.01 and 40 Ghz for different applied voltages (sample 297W, miniband = 18 meV)

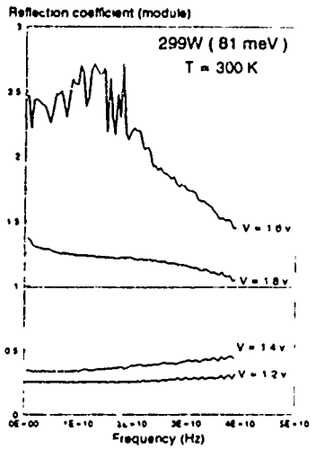

Figure 4b Same than fig 4a but for the widest miniband (81 meV) sample 299W

At a voltage somewhat higher than the critical one (V=1volt) a sharp resonance occurs, with a significant central frequency at f_m = 7 Ghz. The reflection gain is a direct consequence of the NDC and similar to the Gunn amplifiers already described [11]. Another point is interesting to note, the cutoff point corresponding to $|S_{11}| = 1$, we note as f_c f_c rapidly drops when the voltage is increased for sample 297W and also for all the intermediate samples. We interpret this by a decrease of the mean drift velocity versus F, whereas the DC current varies little, due to a static distorsion of the band diagram near the anode. In fig (4b) the widest miniband results show much broader resonances, with f_c higher than 40 Ghz. In table 2 we compare the results for all five samples through four velocity values : the theoretical peak velocity (fig 2), the DC peak velocity (fig 3), $v_m = L \cdot f_m$ and $v_c = L \cdot f_c$ for the applied voltage at which f_c is maximum. The f_c value is extrapolated when it is higher than 40 Ghz. It is interesting to note that v_m and the theoretical peak velocities are very coherent for the three lowest miniband samples. This reinforce the interpretation in terms of a bulk NDC due to the miniband non-linear transport in the frame of the Esaki-Tsu model. For samples 303W and 299W the microwave performances are not limited by the electron transport in the miniband, but merely by the sample capacitance on about 60 Ω (load plus access). The present series of SL samples have not been designed in order to obtain great microwave performances, but merely to extend earlier results to another class of materials. In spite of this significant microwave reflexion gain values have been obtained, owing to the moderated value of N_d in the SL.

ref	Δ	v_{peak} km/sec	v_{DC} km/sec	v_m km/sec	v_c km/sec
297W	18 meV	10	5.52	7	10
304W	25.5 meV	28	13	12	21
298W	37 meV	48	27.4	25	29
303W	55 meV	62	54.2	broad	38
299W	81 meV	100	92	broad	>40

Table 2 Comparison of different values of the drift velocity : v_{peak} the peak velocity from DC measurements, v_{DC} the peak velocity form BTE, and v_m and v_c from microwave data

Conclusions.

The present results constitute a clear experimental demonstation of miniband NDC in GaInAs/AlInAs superlattices giving more credit to the Esaki-Tsu semi-classical approach, already validated with GaAs/AlAs SLs. We point out the remarkable agreement between the time of flight resonance occuring at v/L and the value predicted through BTE solution, whereas the DC values of the drift velocity obtained by a thumb rule do qualitatively follow the experimental ones within 50%. Such SLs have also interesting optical properties, in blocking contact structures and in the Wannier Stark localization conditions [12]. The broad band NDC amplifier demonstrated here, far from optimized, nevertheless opens a new class of millimeter wavelength active devices.

Acknowledgements.

The authors are endebted to J.C. Esnault, O. Dolac and C. Besombes for their contribution to device fabrication, and J.P. Medus for microwave measurements. Paul Voisin has impulsed the preliminary studies on GaInAs/AlInAs SLs from which the present series has been designed. The authors would like to thank M. Hadjazi, A. Sibille and G. Etemadi for stimulating discussions.

References.

1. L. Esaki and R. Tsu, IBM J. Res. Dev., 14, 61 (1970).
2. A. Sibille, J.F. Palmier, H. Wang and F. Mollot, Phys. Rev. Lett., 64,52 (1990).
3. J. Feldmann et al, Phys. Rev. B, 46, 7252 (1992).
4. C. Waschke, H.G. Roskos, R. Schwedler, K. Leo, H. Kurtz and K. Kohler, Phys. Rev. Lett. 70,3319(1993).
5. A.A. Ignatov, K.F. Renk and E.P. Dodin, Phys. Rev. Lett. 70,1996(1993).
6. F. Beltram, F. Capasso, D.L. Sivco, A.L. Hutchinson, S.G. Chu and A.Y. Cho, Phys. Rev. Lett. 64,3167(1990).
7. M. Hadjazi, J.F. Palmier, A. Sibille, H. Wang, E. Paris and F. Mollot, Electr. Lett. 29,648(1993).
8. I. Dharssi and P.N. Butcher, J. Phys. Condens. Matter,2,319 (1990).
9. J.F. Palmier,G. Etemadi, A. Sibille,M. Hadjazi,F. Mollot and R. Planel, Surf. Science, 267, 574(1992).
10. G. Etemadi and J.F. Palmier, to apperar in Solid State Comm.
11. B. Hakki, J. Appl. Phys. 38,4080(1967).
12. E. Bigan, M. Allovon, M. Carre and P. Voisin, Appl. Phys. Lett. 57, 327(1990).

MoP34

Quasi-one-dimensional ballistic electron transport in In-Plane-Gated channels at liquid nitrogen temperature

D.K. de Vries, K. Ploog[1], and A.D. Wieck

Max Planck-Institut fur Festkorperforschung, Heisenbergstraße 1, D 70569 Stuttgart
[1]Paul Drude-Institut fur Festkorperelektronik, Hausvogteiplatz 5-7, D 10117 Berlin

Abstract

In-Plane Gated quantum point contacts were fabricated in a pseudomorphic GaAs/InGaAs/AlGaAs heterostructure by focused ion beam implantation of 100 keV Ga^+ ions. We see an intricate conductance quantization structure at 4.2 K. As the temperature is increased, the quantization becomes less pronounced but clear remnants are observed even at liquid nitrogen temperature and above.

Introduction

After the discovery of quantized conductance in split gated point contacts in GaAs/GaAlAs heterostructures [1, 2], ballistic electron transport has been shown in devices of several kinds. Solid state devices modulate either the two-dimensional electron density by illumination or a (surface/back) gate or the "width" of the one dimensional channel by a split surface gate or in plane gate. Devices of both the electron density modulation type as well as the channel width tuning type can be made using focused ion beam (FIB) implantation to define the channel [3, 4]. A FIB fabricated device in which the channel width can be tuned is the In-Plane Gated field effect transistor [4].

Most experiments on quantized conductance have been performed at temperatures below liquid helium temperature, 4.2 K. These temperatures are too low for most device applications. Considering the mean free path of electrons in high mobility heterostructures, it should be feasible to find remnants of quantization at higher temperatures. Such remnants were indeed found at up to 30 K in GaAs/AlGaAs [5] and InAs/GaSb [6] split gate devices. In these devices, the gates were brought close to the electron gas to increase the energy spacing of the one-dimensional bands.

In a GaAs/InGaAs/AlGaAs heterostructure where the electron gas is contained in a strained InGaAs layer, high transconductance in plane gated transistors have already been realized. [7] We consider GaAs/InGaAs/AlGaAs a promising structure for quantized conductance above 4.2 K because of its high electron density. Although the electron mobility is smaller than in GaAs/AlGaAs, the mean free path remains approximately 0.5 μm up to 100 K, above which the mobility is reduced by optical phonon scattering.

Experimental setup

A GaAs/InGaAs/AlGaAs modulation doped heterostructure was grown by molecular beam epitaxy on a semi-insulating GaAs (100) substrate. The two-dimensional electron gas is contained within the 12 nm thick strained $In_{0.1}Ga_{0.9}As$ layer. The doped layer is a 40 nm thick Si doped $Al_{0.21}Ga_{0.79}As$ layer ($Si \sim 2 \times 10^{12}$ m^{-2}) separated from the 2DEG by a 3 nm thick undoped spacer layer. At room temperature, the electron sheet density is 1.3×10^{16} m^{-2} at a mobility of

0.57 m^2/Vs. At 77 K, electron mobility in the dark is 2.8 m^2/Vs, hardly lower than the 4.2 K value of 3.0 m^2/Vs. The sheet density at these temperatures is around 1.0×10^{16} m^{-2}.

The samples were mesa etched to obtain electrically insulated areas with contact pads. By focused ion beam implantation of 100 keV Ga^+ ions, nominally 100 nm wide insulating lines were directly written at normal incidence with a dose of 1×10^{16} m^{-2} to define in-plane gated channels. The inset of Fig. 1 shows the geometry, for which only two FIB written lines are necessary. The channel between source (S) and drain (D) can be depleted or enhanced by applying a voltage to the in-plane gate (IPG) area. The channel width at zero gate voltage equals the geometrical width w_{geo}, minus the implanted line width of 100 nm, minus twice the width of the depletion zone between the implanted lines (p-type) and the conductive areas (n-type). The geometrical widths were varied between 0.1 and 1.0 μm. After rapid thermal annealing at 700°C for 15 s, ohmic contacts were made with a AuGe/Ni alloy.

Transport measurements

Transport measurements were performed in the dark, with no magnetic field applied. With an HP 4142B parameter analyzer, current-voltage measurements were made at a finite drain-source bias voltage in order to measure the conductance. The derivative of the conductance with respect to the gate voltage V_g was determined numerically. We also measured the AC voltage response to a 1 nA alternating current (81 Hz) through the channel by standard lock-in techniques, leading to ballistic structures at the same conductance values.

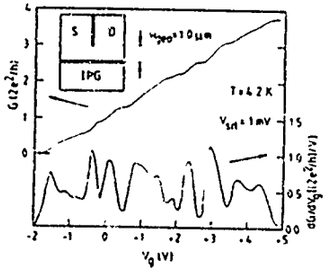

Fig. 1. Conductance G and dG/dV_g vs gate voltage at 4.2 K. The sample was cooled and measured in the dark. The inset shows the geometry of the channel. Thick lines denote insulating lines written directly by FIB implantation.

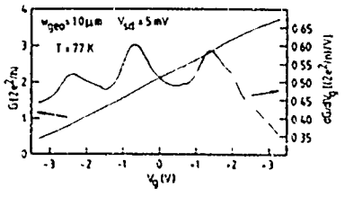

Fig. 2: G and dG/dV_g vs gate voltage at 77 K for the same channel as in Fig. 1.

Figure 1 shows the conductance G of an in-plane gated channel at 4.2 K at a source-drain voltage V_{sd} of 1 mV, and its derivative with respect to the gate voltage. In calculating the conductance we neglected the series resistance. The gate leakage current is in the pA range. We observe a large number of plateaus in the conductance in the range of 0 to 4 times $2e^2/h$. The derivative shows corresponding minima, and some extra structure which is not quite apparent in the graph of the conductance. A similar complex structure has also been observed in strained InGaAs channels below 1 K by Mace et al. [8].

The observed conductivity structure is independent of sweep direction. It is reproducible after thermal-thermal cycling, although the threshold voltage tends to drift. This drift has no structural effect on the measurement results.

On devices with smaller geometrical channel widths, we get qualitatively the same picture. This shows that an explanation of the complex structure in terms of states bound to a single impurity [9] does not apply here.

That the finite bias plateaus are relatively well-defined opens the way to measurements at higher temperatures. Figure 2 shows the conductivity of the same channel at liquid nitrogen temperature (77 K). The visible kinks in the conductance plot correspond to clear minima in the derivative dG/dV_g. In the case of ideal ballistic transport, we expect minima to occur at integer multiples of $2e^2/h$. The minima in Fig. 2 occur at somewhat higher values of G. Nevertheless they give direct evidence of quasi-ballistic transport at 77 K.

The peak-to-peak change in the derivative is well over 10 %, or $> \mu S/V$ on an average value of 40 μS/V. This change can be increased to 25 % in channels with smaller w_{geo} at the cost of tunability. Our narrower channels could not be enhanced to conductance values as high as the 1 μm channels.

To show that the peaks in dG/dV_g at 77 K are remnants of the 4.2 K peaks, we have measured the development of the conductance as a function of the temperature. We used a liquid helium flow cryostat in the temperature range 20 K to room temperature. In Fig. 3 we see how the intricate structure in the low temperature limit is averaged to less pronounced but still well defined structures at temperatures up to 100 K.

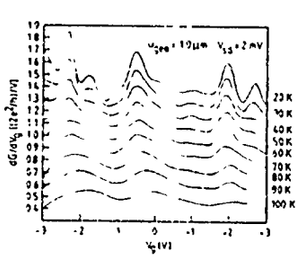

Fig. 3 dG/dV_g versus V_g as a function of temperature. For clarity, subsequent curves are offset 0.1 units with respect to the graph at 100 K.

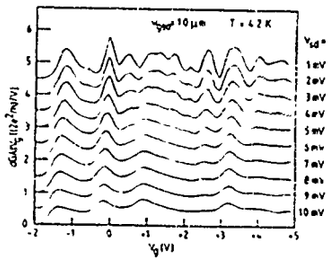

Fig. 4 dG/dV_g versus V_g as a function of source-drain bias at 4.2 K. Subsequent curves are offset 0.5 units with respect to the 10 mV curve.

For not too high temperatures, the averaging width of thermal smearing is $4k_BT$, centered around the Fermi energy E_F, which is the inverse slope of the Fermi-Dirac distribution function at E_F. A similar averaging, over a range of eV_{sd}, is attained by measuring at a finite drain-source voltage. Figure 4 shows the effect of such different source-drain voltages. To compare curves from

Figs. 3 and 4, we note that at 4.2 K (Fig. 4) the channel could be tuned over a wider range than at higher temperatures. The peak at $V_g = -0.1$ V in Fig. 4 corresponds with the leftmost peak in Fig. 3. In comparing curves where $4k_BT = eV_{sd}$ (10 K≙3.4 meV), we observe that in the finite voltage curves, the structure of the peaks is less pronounced than in the curves at the corresponding temperatures.

Conclusions

The presence of ballistic properties in FIB written In Plane-Gated transistors at liquid nitrogen temperature is a large step towards device application of one dimensional transport phenomena. By making the channel width smaller, we expect that these phenomena will persist to even higher temperatures. The problem of decreasing tunability could be tackled by better control of the lateral doping profile, i.e. the ion beam focusing.

Acknowledgments

We thank Hans-Peter Schönherr for growing the InGaAs samples. This work was supported by the Bundesministerium für Forschung und Technologie of the Federal Republic of Germany.

References

[1] B.J. van Wees, H. van Houten, C.W.J. Beenakker, J.G. Williamson, L.P. Kouwenhoven, D. van der Marel, and C.T. Foxon, *Phys. Rev. Lett.* **60**, 848 (1988).

[2] D.A. Wharam, T.J. Thornton, R. Newbury, M. Pepper, H. Ahmed, J.E.F. Frost, D.G. Hasko, D.C. Peacock, D.A. Ritchie, and G.A.C. Jones, *J. Phys. C: Solid State Phys.* **21**, L209 (1988).

[3] Y. Hirayama and T. Saku, *Appl. Phys. Lett.* **54**, 2556 (1989).

[4] A.D. Wieck and K. Ploog, *Appl. Phys. Lett.* **56**, 928 (1990).

[5] G.L. Snider, M.S. Miller, M.J. Rooks, and E.L. Hu, *Appl. Phys. Lett.* **59**, 2727 (1991).

[6] S.J. Koester, C.R. Bolognesi, M.J. Rooks, E.L. Hu, and H. Kroemer, *Appl. Phys. Lett.* **62**, 1373 (1993).

[7] A.D. Wieck and K. Ploog, *Appl. Phys. Lett.* **61**, 1048 (1992).

[8] D.R. Mace, M.P. Grimshaw, D.A. Ritchie, A.C. Churchill, M. Pepper, and G.A.C. Jones, *J. Crystal Growth* **127**, 601 (1993).

[9] E. Tekman and S. Ciraci, *Phys. Rev. B* **43**, 7145 (1991).

MoP35

The Dependence of Boundary Scattering in Split-Gate Quantum Wires on the Transverse Mode Number

M. Yamamoto, S. Nakata, K. Aihara and T. Mizutani
NTT LSI Laboratories
3-1, Morinosato Wakamiya, Atsugi-shi 243-01, Japan

Abstract

Boundary scattering in quantum wires is investigated as a function of the transverse mode number, N, using a split-gate configuration. It is found that the specularity factor, p, of boundary scattering increases toward 1 with decreasing N. Taking into consideration that the boundary roughness in the split gate quantum wires, which is caused by the random positions of the ionized impurity ions in the doped layer, increases as the split-gate voltage decreases, then the increase in the specularity indicates decreased intersubband scattering due to the reduction of the mode number.

1. INTRODUCTION

The quantum interference phenomena in microstructures offer the possibility of constructing viable three-terminal devices with a large transconductance and novel functional devices[1-5]. To realize quantum interference devices with a large on/off ratio and well-designed control characteristics, it is required to maintain the phase coherence length and the elastic scattering length much longer than the device length. In this sense, it is indispensable to suppress diffuse boundary scattering in quantum wires with which quantum interference devices are constructed.

The purpose of the present study is to clarify the guidelines that ensure the suppression of diffuse boundary scattering. This study experimentally investigates boundary scattering in quantum wires as a function of the transverse mode number, N, using split-gate quantum wires. It was found that the specularity of boundary scattering increased toward 1 with decreasing N. This result suggests that the diffuse boundary scattering is sufficiently suppressed by reducing the mode number.

2. EXPERIMENTAL METHOD

The samples investigated were split-gate quantum wires. The split-gate structures were made on high-mobility AlGaAs/GaAs heterostructures grown by molecular beam epitaxy (MBE). The carrier concentration and mobility of the two-dimensional electron gas (2DEG) were 4.2×10^{11} cm^{-2} and 2.1×10^5 cm^2/V s at 4.2 K, respectively. The split gates were fabricated by electron beam lithography and a Ti/Au lift-off technique. The lithographic gap width between the split gates and device length were 0.5 μm and 2.0 μm, respectively. In this device, the two-dimensional electron gas beneath the split gate was depleted at the split-gate voltage $V_g = 0.26$ V. By further decreasing V_g, the one dimensional channel could be completely pinched off at $V_g = -0.65$ V.

Magnetoresistance was measured using a low frequency four-terminal ac technique with a lock-in amplifier at 4.2 K in a magnetic field up to 8T.

3. EXPERIMENTAL RESULTS AND DISCUSSION

3.1 Magnetoresistance

Typical magnetoresistances, $R(B)$, are shown for various values of V_g, in Fig. 1, in which a positive magnetoresistance peak at around 0.2 T and saturation of $R(B)$ at around $B = 1$ T were

observed. These structures in $R(B)$ are characteristic of diffuse boundary scattering[6-8]. Furthermore, the magnetic field value corresponding to the positive $R(B)$ peak, B_p, was in good agreement with the theoretical value of $B_p(th) = 0.55\ \Phi_0/W_{eff}\lambda_F$ for diffuse boundary scattering[6] where $\Phi_0 = h/e$ is the flux quantum, W_{eff} is the effective channel width, and λ_F is the Fermi wavelength.

The experiments revealed a characteristic feature : the resistance ratio $\Delta R/R_i = (R_{eff}(0) - R_i)/R_i$ decreased with decreasing V_g, as shown in Fig. 2. Here, $R_{eff}(0)$ represents the extrapolated value of $R(B)$ at $B = 0$ from the positive peak at $B = B_p$, as indicated in Fig. 1, which corresponds to approximately subtracting the contribution from the weak localization, and R_i represents the resistance value at the plateau region around $B = 1$T, where diffuse boundary scattering is sufficiently suppressed.

Assuming Mathiessen's rule, that is, the bulk (impurity) and edge scattering (diffuse boundary scattering) rate are additive, the effective scattering time for $B = 0$, $\tau(B=0)$, is given using the probability of specular boundary scattering (specularity factor), p, as[6,7],

$$\frac{1}{\tau(B=0)} = \frac{1}{\tau_0} + v_F\left(\frac{1-p}{W_{eff}}\right) \qquad (1)$$

where v_F is the Fermi velocity and τ_0 is the bulk scattering time. Furthermore, the effective scattering time for $B = B_i$ where diffuse boundary scattering is sufficiently suppressed, $\tau(B=B_i)$, is simply given by τ_0, that is,

$$\tau(B=B_i) = \tau_0. \qquad (2)$$

For the present sample, it is shown below that $L_{eff} > L_e$, where L_{eff} is the effective wire length including the length of the depletion region along the wire direction, and $L_e = v_F\tau_0$ is the bulk mean free path. Therefore, the conductivity is represented by the Drude expression. Using the relationships of eqs. (1) and (2) for the Drude expression, the ratio, $\Delta R/R_i$ is given as

$$\frac{\Delta R}{R_i} = \left(\frac{L_e}{W_{eff}}\right)(1-p). \qquad (3)$$

To deduce the intrinsic parameter, p, from the experimental values of $\Delta R/R_i$ [9] as a function of the mode number, how W_{eff}, N and L_e vary with V_g were evaluated, as described in 3.2 and 3.3.

3.2. Evaluation of W_{eff} and N as a function of V_g

The values of W_{eff} and the mode separation energy, ΔE, were obtained from the analysis of a plot of the Landau index n versus $1/B$ for Shubnikov-de Haas (S-dH) oscillations using a parabolic potential model[10]. The empirical dependences of W_{eff} and ΔE on V_g were expressed as follows,

$$W_{eff}(\mu m) = 0.275 + 0.255V_g - 0.115V_g^2, \qquad (4)$$

$$\Delta E(meV) = 0.975 - 0.664V_g \qquad (5)$$

The Fermi energy, E_F, was obtained from the slope of a linear region of a plot of n versus $1/B$ and is empirically expressed as

$$E_F(meV) = 15.47 + 15.0V_g - 12.8V_g^2. \qquad (6)$$

The transverse mode number, N, was estimated using the relation $N = E_F/\Delta E$ and varied from 21 to 3 corresponding to V_g values from 0.2 V to -0.5 V.

3.3 Evaluation of L_e

As shown below, the present sample was in the one-dimensional diffusive transport region in the sense that $L_e < L_{eff}$ and $W_{eff} << L_e$. Therefore, the resistance is expressed with the Drude rule and Ohm's law as

$$\sigma_1 = n_1 e\mu, \qquad (7)$$

$$R = (1/\sigma_1)L_{eff}, \qquad (8)$$

where σ_1 and n_1 are the one-dimensional conductivity and electron density, respectively, and μ is the mobility.

The experimental dependence of $L_e = v_F\tau_0$ was evaluated from the saturated resistance value, R_i, at $B = B_i$. By using the approximation of $n_1 = n_2W_{eff}$ in eq. (8) where n_2 is the two-dimensional electron density, R_i is given as

$$R_i = \left(\frac{1}{n_1 e\mu}\right)L_{eff} = \left(\frac{1}{n_2 e\mu}\right)\left(\frac{L_{eff}}{W_{eff}}\right) \qquad (9)$$

The obtained values of L_e as a function of V_g are shown in Fig. 3 in comparison to L_{eff} and W_{eff}. From these comparisons, the applicability of the one-dimensional Drude relation and Ohm's law was confirmed for the present sample, that is, $L_e < L_{eff}$ and $W_{eff} << L_e$.

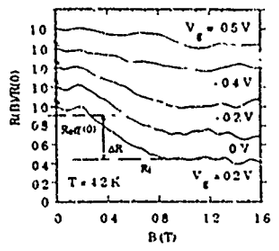

Fig.1. Magnetoresistances for various V_g. $R(0) = 6.5$, 3.8, 2.1, 1.5 and 1.2 kΩ from top to bottom, respectively.

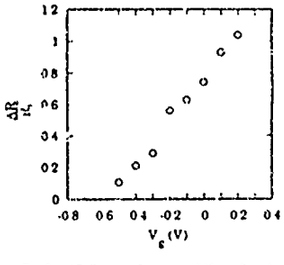

Fig 2. $\Delta R/R_i$ as a function of V_g. ΔR and R_i are indicated in Fig 1.

3.4 Specularity, p, as a function of the mode number

It was found that the obtained values of p increased toward 1 with decreasing N, as shown in Fig. 4. The results of the quantum mechanical calculation of boundary roughness scattering in quantum wires, based on the model in which the boundary roughness is characterized by the root mean square deviation, Δ, and the correlation length, Λ, depend on the various parameters such as Δ/λ_F, Λ/λ_F, the mode number, N, and the unperturbed potential model, that is, the hardwall or softwall potential[11]. Therefore, comparison of the present results, characterized by the single phenomenological parameter, p, with the theoretical results is not straightforward. Here, it should be noted that N varied substantially from 21 to 3 while λ_F varied only from 0.035 μm to 0.069 μm in the experimental range of V_g. Furthermore, according to the calculated results[12], the boundary roughness of the quantum wires defined by a split gate, which is caused by the random positions of ionized impurity ions in the doped layer, becomes more pronounced with decreasing V_g. Thus, the observed increase in specularity with decreasing V_g,

in spite of the increased roughness, is probably attributed to the decrease of the intersubband scattering due to the reduction of the transverse-mode number

4. CONCLUSION

In conclusion, it was experimentally shown that the specularity of boundary scattering in a quantum wire defined by a split gate increased toward 1 with a decreasing transverse-mode number. The increase in the specularity was attributed to the decreased intersubband scattering due to the reduction of the mode number. The present results indicate that the diffuse boundary scattering in a quantum wire, which is a deteriorating factor for quantum wire-based devices such as quantum interference devices, is sufficiently suppressed by decreasing the mode number

REFERENCES

1. S Datta, M. R. Melloch, S Bandyopadhyay and M S Lundstrom, *Appl Phys. Lett* 48 (1986) 487, and S. Bandyopadhyay, M R Melloch, S Datta, B. Das J A. Cooper Jr and M. S. Lundstrom, *IEDM* 86, p. 76
2. F. Sols, M. Macucci and K. Hess, *Appl Phys Lett* 54, 350 (1989)
3. S. Datta, *Superlattices and Microstruct* 6, 83 (1989)
4. K. Aihara, M Yamamoto and T Mizutani, *Jpn J Appl Phys* 31, 1916 (1992)
5. K. Aihara, M Yamamoto and T. Mizutani, *IEDM* 92, p. 491
6. T J. Thornton, M L. Roukes, A Scherer and B P Van de Gaag, *Phys Rev Lett.* 63, 2128 (1989)
7. T. J Thornton, M L. Roukes, A. Scherer and B P Van de Gaag, *Granular Nanoelectronics* (Edited by D. K Ferry, J R. Barker and C. Jacoboni), p. 165 Plenum Press, New York (1990).
8. E. Ditlelsen and J Lothe, *Philos Mag* 14, 759 (1966)
9. M. Yamada, K. Hirakawa, T Odagiri, T J Thornton and T Ikoma, *Superlattices and Microstruct.*, 11, 261 (1992)
10. K -F Berggren, G Roos and H van Houten, *Phys Rev* B37, 10118 (1988).
11. H Akera and T. Ando, *Phys Rev* B43, 11676 (1991)
12. J. A Nixon and J. H Davies, *Phys Rev.* B41, 7929 (1990)

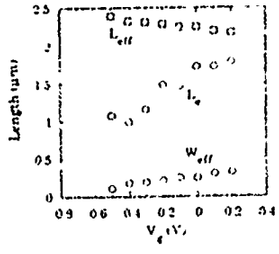

Fig 3 L_e, L_{eff} and W_{eff} as a function of V_g

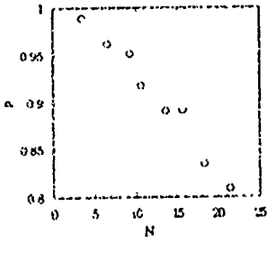

Fig 4 Specularity vs transverse mode number

MoP36

Experimental Studies of Electronic Transport in Semiconductor Quantum Dot Structures

JP Bird, K Ishibashi, Y Aoyagi, and T Sugano
Nanoelectronics Materials Laboratory, Frontier Research Program, RIKEN, 2-1 Hirosawa, Wako, Saitama 351-01, JAPAN.

Abstract

We have studied the low temperature electrical properties of semiconductor quantum dot structures at high magnetic fields. The devices consisted of lithographically defined aluminium gates deposited on to the surface of a GaAs AlGaAs heterojunction substrate and the dot structures were formed on the application of a suitable negative bias to the gates. At high magnetic fields electronic transport occurred via edge states and we were able to use the well known properties of these states to study transmission through the dot structures. In particular we observed large resistance resonances superimposed on the quantised magnetoresistance plateaux of the dot. These resonances were found to persist with reduced amplitude to above a degree Kelvin and showed a sensitive dependence on the applied gate voltage. We associate them with the increased edge state interaction introduced by the dot and discuss our results in terms of the various scattering mechanisms inherent to quantum dot structures

The study of semiconductor quantum dot structures, in which electronic motion in all three dimensions is confined on the scale of the Fermi wavelength, is currently an area of strong theoretical and experimental interest [1]. Since the energy spectrum of such structures is quantised in to a series of discrete levels geometrical considerations are expected to exert a strong influence on the resulting device performance and several recent theoretical studies have predicted the existence of novel geometry dependent resonances in the corresponding electrical properties [2-3]. In this paper we demonstrate the presence of scattering resonances in quantum dots at high magnetic fields such that transport is in the edge state regime [4-5]. In particular we use the well known properties of these states to directly relate the measured electrical behaviour to the transmission of electrons through quantum dots. The resonances were found to weakly persist to temperatures above a degree Kelvin and also showed a sensitive dependence on the applied gate voltage. We associate them with the increased edge state interaction introduced by the dot and discuss our results in terms of the various scattering mechanisms inherent to quantum dot structures.

Probably the most versatile technique for the realisation of quantum dot structures employs lithographically defined metal gates deposited on to the surface of a suitable semiconductor substrate; a negative bias applied to the gates then depletes electrons from underneath them leaving only a small conducting structure whose geometry is determined by both the lithographic design of the gates *and* the magnitude of the applied bias [6]. In this paper we discuss the results obtained in gated quantum dot structures geometrically defined using electron beam lithography and deposited on to the surface of a GaAs AlGaAs heterojunction [7]. The aluminium gates were patterned into a stub structure which employed single quantum point contacts as the entrance and exit ports to a $4\mu m^2$ central dot (figure 1). The wafer was etched in to a standard Hall bar geometry and had a typical low temperature carrier density $n_s \approx 3.5\ 10^{15}$ cm^{-2} and mobility $\mu \approx 350{,}000$ cm^2/Vs. After being mounted on a ceramic header the sample was attached to the mixing chamber of a dilution refrigerator and audio frequency magnetotransport measurements were made at temperatures below 10 mK. Great care was taken to ensure good thermal contact to the sample and spurious heating effects were minimised by using a source to drain excitation of under 1 μV. The measurements typically employed a geometry in which current was passed between probes 1 and 4 while the voltage drop across the dot was measured between probes 2 and 5. As has been described in the literature this corresponds to a two-terminal measurement in which all contact resistances are eliminated [1].

With the gates grounded at the drain potential the electron gas underneath them was undepleted and the device structure consisted of a two dimensional electron gas system. Spin-resolved quantum Hall plateaux were clearly observed in the magnetoresistance and were quantised to better than 0.1%, the experimental accuracy of the measurement. With a suitable negative bias applied to the gates the dot structure was formed and as can be seen in figure 1

the resulting magnetoresistance showed very different behaviour to the two dimensional system. In particular the plateau quantisation was found to be significantly reduced and reproducible resonant like features were observed on the plateaux (figure 1). As the negative bias applied to the gates was increased the plateau quantisation was found to be further reduced while the resonant features became increasingly prominent (figure 2). An important feature of these resonances was that they occurred on plateau and not in the transition region between successive plateaux (although we point out that additional structure was also observed in the transition regions). Measurements at higher temperatures revealed the amplitude of the resonances to be temperature independent below approximately 400 mK and residual structure could still be resolved above a degree Kelvin (figure 3).

As is now well understood the observation of quantised plateaux in the magnetoresistance results from the perfect transmission of a finite number of edge states at high magnetic fields [1-5]. In the case of a simple two dimensional electron gas system there is a direct correspondence between the number of such edge states and the number of occupied Landau levels N. The resistance of the device can then be calculated by a Landauer-Büttiker approach and for the measurement geometry we employ [4]

$$R = (1/N)(h/e^2) \quad (1)$$

which is quantised and depends only on N. Equivalently the observation of quantised plateaux in the magnetoresistance of the dot also indicates perfect transmission of a finite number of edge states through the dot. In this case the situation is somewhat different from the bulk however since the point contacts of the dot are able to selectively transmit and reflect edge states [8]. The number of states fully transmitted through the dot is therefore no longer simply determined by N and under these conditions the magnetoresistance of the dot shows a different series of quantised resistance plateaux to that of the bulk (figures 2 and 3). Equation 1 must then be written as

$$R = (1/N_T)(h/e^2) = (1/[N-N_r])(h/e^2) \quad (2)$$

where N_T is the number of edge states perfectly transmitted through the dot and N_r is the number of completely reflected edge states ($N_T+N_r=N$). While the resistance in equation 2 is still clearly quantised, departures from quantisation will occur once one or more of the edge states become only partially transmitted through the dot. Associating a transmission probability t_n with the nth edge state ($t_n<1$) we must then write

$$R = (1/T)(h/e^2) > (1/[N-R])(h/e^2) \quad (3)$$

where $T=\sum_n t_n$ is the overall edge state transmission probability and R is the overall edge state reflection probability ($T+R=N$). Clearly this resistance is no longer necessarily quantised.

The important feature of the above equations is that they enable us to directly relate the measured magnetoresistance to the edge state transmission probability through the quantum dot. We have already shown that as the negative gate voltage was increased the plateau features of the dot shifted to resistance values larger than those predicted by equation 2 (figure 1 and 2). For the highest gate voltages this shift corresponded to a 20% increase above the expected quantised value and so indicates a corresponding reduction in the overall edge state transmission probability. This reduction presumably resulted from the increased interaction between oppositely propagating edge states as the width of the quantum point contacts was reduced and has previously been reported in smaller dot structures [9].

More interesting however are the large resistance resonances observed on plateau. The resonances correspond to an increase in the resistance above the quantised plateaux and we associate them with a magnetic field induced increase in the edge state backscattering. As can be seen from figure 2 the magnetic field position and amplitude of the resonances was found to alter as the gate voltage was increased indicative of some dependence on the precise device geometry. The most likely origin of the resonances is that they arise from the interaction between localised and extended edge states within the dot. In particular under conditions such that N_T (<N) edge states are perfectly transmitted through the dot additional edge states will also be localised within the dot. An electron in a transmitted edge state may then scatter into one of the localised states and finally backscatter out of the dot. Since this scattering loop encloses a finite magnetic flux its associated phase change modulates the overall scattering probability and can be shown to give rise to a series of backscattering resonances as the magnetic field is varied [2]. In a similar fashion as the gate voltage is varied the associated

change in the edge state paths causes the resonances to occur at different magnetic field values.

The magnetic resonances described above were first observed in studies of small quantum dot structures in which the Hall resistance was found to dip unexpectedly to zero at certain magnetic field values [10]. In contrast we have demonstrated the presence of resonances which correspond to an increase in the magnetoresistance above the plateau value. While this feature may at first seem contradictory we point out that it is merely a consequence of the different measurement geometries employed in the experiments. In particular from equation 3 it can be seen that for the probe configuration describe above an increase in the edge state backscattering probability will give an associated rise in the magnetoresistance. However we could equally measure the magnetoresistance using a geometry in which current is passed between probes 1 and 4 and in which the voltage drop across the dot is now measured across probes 3 and 6. Under these conditions equation 3 takes the form [4]

$$R = (1/[N-2R])(h/e^2) \quad (4)$$

and in this case an increase in the backscattering probability actually gives rise to a reduction in the measured resistance. In figure 4 we compare the results of measurements in the geometries of equations 3 and 4 and show the clear relationship between them. In the geometry of equation 4 the resonances now occur as a series of dips below the magnetoresistance plateau reminiscent of the Hall dips described above. Furthermore it can also be seen that in agreement with theory the resonances have the same amplitude in both geometries and are symmetric about the plateau value.

A surprising feature of the Hall resonances mentioned above was their persistence with almost unattenuated amplitude to temperatures in excess of a degree Kelvin [10]. This robustness to thermal averaging was actually predicted by theory and basically results from the fact that thermal smoothing of the Fermi function is ineffective in averaging out the resonances, which can only be upset by inelastic scattering [2]. We in fact observe a stronger dependence of the resonance amplitude on temperature in our experiment and we associate this with the increased diameter of the dot which we study [10]. As can be seen from figure 3 the amplitude of the resonances was temperature independent below 400 mK. Since the maximum path length around the circumference of the dot was 8 μm we suspect that at temperatures below 400 mK the inelastic scattering length of the electrons was comparable to or longer than this length. At higher temperatures however the reduced amplitude of the resonances suggests that the inelastic length became significantly shorter than 8 μm. In other words, even though electrons in high field edge states can propagate over hundreds of microns without equilibration [4-5] their phase is clearly only conserved over much shorter lengths. This is an an important result and suggests that "quantum dot interferometers" may provide a useful system for the study of electron phase breaking at high magnetic fields [2].

We have already mentioned that the dot geometry studied here is significantly larger than that employed in previous experiments. This increased size is actually advantageous since the edge state population of a larger dot is expected to be well approximated by that of the bulk [11]. As a result we note that the resonances often occur at magnetic field values simultaneous with the depopulation of an edge state from the dot. For example consider the resonances at 4.1 Tesla in figure 1 and at 5.3 Tesla in figure 2, both of which appear to be enhanced by an associated edge state depopulation. However, since other resonances are also observed at magnetic fields not in any way correlated to a specific edge state depopulation it is difficult to make any quantitative conclusions with regards to this matter and here we merely note the coincidence for the sake of completeness.

While the edge state scattering mechanism described above is able to account for many of the features we observe experimentally, before concluding we make some comment on other possible origins of the resonances. In particular it is well known that aperiodic structure is often observed in the magnetoresistance in single point contacts [12]. However, in these experiments the structure is typically always observed in the transition between successive quantised plateaux and features have not yet been reported on plateau. In contrast, we have demonstrated the presence of striking, on plateau resonances and since we have observed the same generic features in measurements on three different devices we conclude that the resonances are indeed an intrinsic feature of quantum dots.

In conclusion we have studied the magnetoresistance of gated quantum dot structures in the edge state regime. Large resonant features were observed on the resistance plateaux and

we associate these with an interference effect between localised and extended edge states within the dot. The resistance plateaux were also found to be shifted above their expected quantised values consistent with increased edge state interaction within the dot. Studies of the temperature dependence of the resonances indicate that the inelastic scattering length of electrons in high field edge states is very much smaller than their associated equilibration length. The observation of large resonant features on plateau and away from the transition region between successive plateau provides support that the features we observe are intrinsic to quantum dot structures.

The authors would like to acknowledge invaluable discussions with C Barnes, M Stopa, RP Taylor, Y Ochiai, DK Ferry, and J Spector.

References

[1] For a recent review of theoretical and experimental aspects of quantum dot structures see DK Ferry, Prog. Quant. Electr. **16** (1992), 251.
[2] G Kirczenow, Phys Rev B **42** (1990), 5357, and G Kirczenow and E Castano, Phys. Rev. B **43** (1991), 7353.
[3] H Xu, Z Ji, and KF Berggren, Superlatt. Microstruct. **12** (1992), 237, GW Bryant, Phys. Rev. B **44** (1991), 12837, Y Takagaki and DK Ferry, Phys. Rev. B **44** (1991), 8399, PF Bagwell, Phys. Rev. B **41** (1990), 10354, and DG Ravenhall, HW Wyld, and RL Schult, Phys. Rev. Lett. **62** (1989), 1790.
[4] H van Houten, CWJ Beenakker, and BJ van Wees, in Semiconductors and Semimetals **35** (Ed MA Reed), Academic Press, 1992.
[5] RJ Haug, Semicond. Sci. Technol. **8** (1993), 131.
[6] CG Smith, M Pepper, H Ahmed, JEF Frost, DG Hasko, DC Peacock, DA Ritchie, and GAC Jones, J. Phys. C **21** (1988), L893
[7] K Ishibashi, JP Bird, Y Aoyagi, and T Sugano, to appear in Jap. Journ. Appl. Phys
[8] BJ van Wees, LP Kouwenhoven, EMM Willems, CJPM Harmans, JE Mooij, H van Houten, CWJ Beenakker, JG Williamson, and CT Foxon, Phys. Rev. B **43** (1991), 12431.
[9] RP Taylor, AS Sachrajda, JA Adams, P Zawadzki, PT Coleridge, and M Davies, Surf. Sci **263** (1992), 247.
[10] CJB Ford, S Washburn, R Newbury, CM Knoedler, and JM Hong, Phys. Rev. B **43** (1991), 7339.
[11] RP Taylor, AS Sachrajda, JA Adams, PT Coleridge, and P Zawadzki, Phys. Rev B **47** (1993), 4458.
[12] BJ van Wees, LP Kouwenhoven, CJPM Harmans, JG Williamson, CET Timmering, MEI Broekaart, CT Foxon, and GJ Harris, Phys Rev. Lett **62** (1989), 2523.

Figure Captions

Figure 1: Magnetoresistance of the quantum dot structure measured both with the gates grounded and with an applied bias such that the dot was well defined. The inset shows a schematic of the gate geometry as well as the numbering scheme of the measurement probes. The central dot had a lithographic area of $4\mu m^2$ and the corresponding length and width of the point contacts was 0.1 μm and 0.4 μm respectively.

Figure 2: The evolution of the resonant structure for several well defined gate voltages. The corresponding magnetoresistance with the gates grounded is also shown for comparison.

Figure 3a: Temperature dependence of the resonance amplitude. For this gate voltage the dot was only just formed and over the magnetic field range shown two spin resolved edge states were occupied in both the bulk and the quantum dot. No resonant structure was observed in the corresponding bulk magnetoresistance trace however. For the sake of clarity, the curves at 105 mK, 480 mK, and 1200 mK have been offset by +2kΩ, +4kΩ, and +6kΩ respectively.

Figure 3b: Temperature dependence of two of the resonant features observed in figure 3a.

Figure 4: The dependence of the resonant structure on the measurement geometry. The probe combinations used in the two different measurements are shown as labels to the resulting magnetoresistance traces. In both measurements the resonances occur at the same magnetic field values, indicating their common origin.

JP Bird et al Fig 1

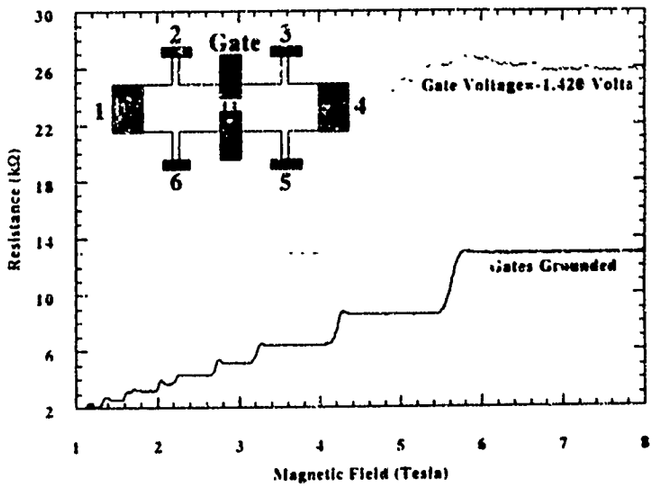

JP Bird et al Figure 2

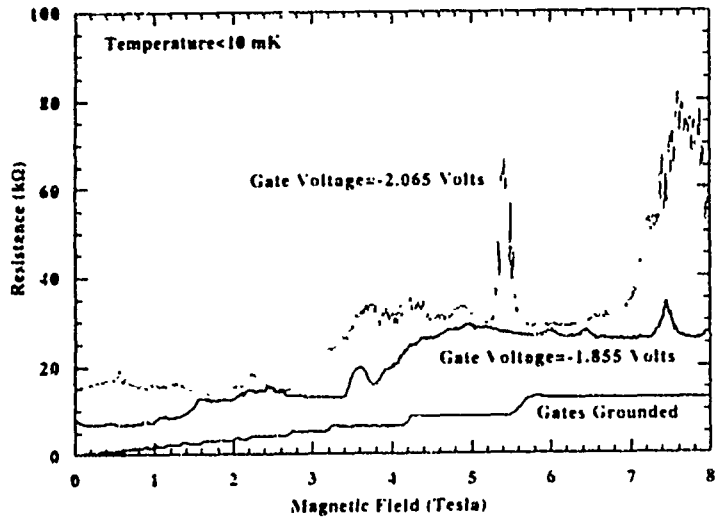

JP Bird et al Figure 3a

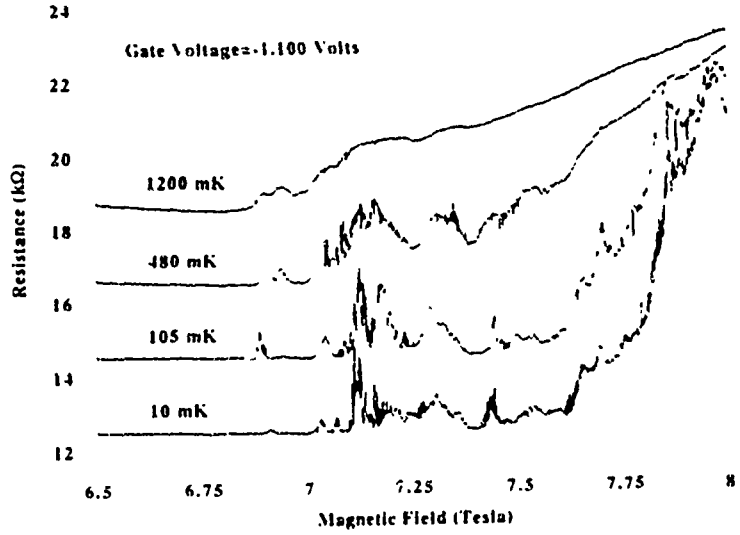

JP Bird et al Figure 3b

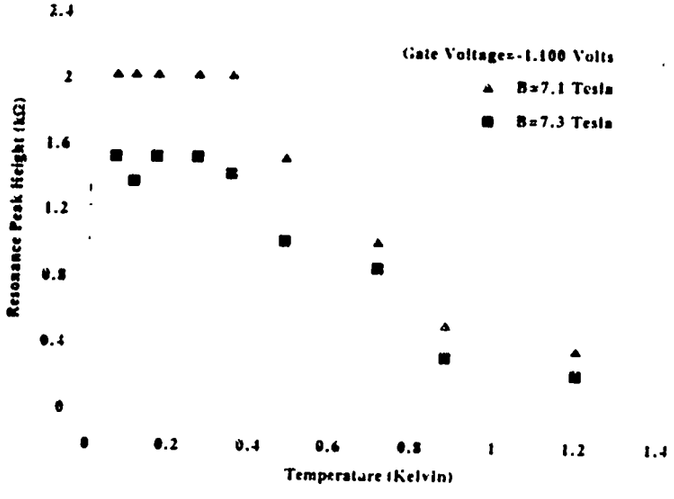

JP Bird et al Figure 4

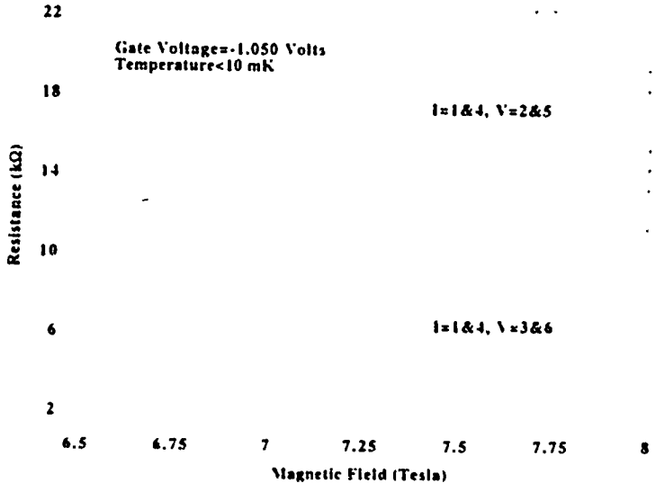

MoP37

Photovoltaic effect in quasiballistic electron interferometer

A.A.Bykov, J.C.Kwon, L.V.Litvin, Ju.V.Nastaushev,
V.G.Mansurov, V.P.Migal, S.P.Moschenko

Institute of Semiconductor Physics, Russian Academy of Sciences,
Siberian Branch, Novosibirsk 630090, Russia

It has been shown [1], that the lack of inversion symmetry in mesoscopic samples should give rise to a photovoltaic effect in the presence of microwave radiation. Later this effect was observed and studied experimentally in various mesoscopic samples of single-connected geometry [2].

In this work we report the first observation of the photovoltaic effect in a quasiballistic electron interferometer exposed to microwave radiation with frequency lying in the range from 9 GHz to 140 GHz.

The experimental samples had a loop-shaped geometry and were fabricated by means of electron lithography with subsequent reactive ion etching. The 2D-electron gas parameters in the original AlGaAs/GaAs heterostructures at 4.2 K were as follows: $n_s \approx 3 \cdot 10^{11}$ cm^{-2}, $\mu \approx 10^5$ cm^2/V·s. The effective ring diameter was about 0.6–0.7 μm.

At T≤4.2 K the application of microwave radiation to the interferometer results in appearance of a microwave emf oscillating with magnetic field. This emf has two constituents. The first one originates from the electron interference in one of the loop's channels and is analogous to those studied previously [1]. The second component of the microwave emf oscillates only with magnetic flux change through the area of the ring. As supposed that the component periodical with magnetic field is caused by the asymmetry of electron wave interference through both channels of the ring with respect to the ring center. At magnetic fields larger than 1 T these microwave emf oscillations disappear.

1. V.I.Fal'ko, D.E.Khmel'nitskii, J.E.Phys.JETP 68, (1989).
2. A.A.Bykov et al., In search of the influence of the asymmetry properties of 2D system (1989), JETP Lett. 49, (1989).

MoP38

Dimensional transition of weak localisation effects in lateral surface superlattices

Peter E. Selbmann[a)] and Michael Suhrke[b)]

a) Max-Planck-Arbeitsgruppe Halbleitertheorie, O-1086 Berlin, Germany
b)Institut für Theoretische Physik, Universität Regensburg, D-8400 Regensburg, Germany

Weak localization is investigated for a two-dimensional electron gas subject to a cosine-potential in one direction. With decreasing Fermi energy the system gradually develops into an array of almost isolated quantum wires of finite width. Interference effects are reduced in dimensionality if the coherent motion of the electrons between adjacent wires is suppressed. The weak-localization correction to the conductivity is remarkably enhanced then and changes its dependence on the phase coherence length from a logarithmic to a linear one. In the 1D limit the system shows a transition from weak to strong localization with increasing phase coherence length. The localization length changes from an exponential to a linear dependence on scattering length at the dimensional transition. Numerical results are presented for GaAs structures in dependence on Fermi energy.

1 Introduction. In addition to studies of two-dimensional systems weakly modulated by a periodic potential there exists a growing number of experimental investigations of carrier transport in strongly modulated structures which represent an array of quantum wires if the Fermi energy becomes smaller than the potential amplitude [1–5].
An interesting topic isthe influence of interference effects such as weak localization in these systems. The 1D-2D transition of weak localization in a single quantum wire takes place if the phase coherence length becomes smaller than the wire width [6]. Subband effects and the transition to strong localization in a wire have been studied in Refs. [7, 8]. Weak localization in lateral surface superlattices has been investigated within a tight binding scheme [9]. In this calculation only one subband exists in each quantum wire which does not correspond to the experimental situation.
Our aim is to investigate the 2D-1D transition in weak localization in lateral surface superlattices with a more realistic model of the periodic potential. In semiconducting structures the total scattering length is usually much larger than the potential period of some hundred nanometers . The same applies to the phase coherence length which results in a transition from 2D to 1D behavior of weak localization if the Fermi energy becomes smaller than the potential amplitude. The mechanism of the transition has to be distinguished from that in a single wire due to the coupling of different wires via tunneling. It is expected to take place if coherent tunneling of the electrons from one wire to another is suppressed. In the limit of isolated wires a rapid transition to strong localization takes place with increasing phase coherence length. This will be taken into account approximately via a self-consistent treatment of the interference effects and will be used to estimate the localization length in dependence on Fermi energy. Details of the calculations will be published elsewhere [10].

2 Model of the system. We describe the uni-directional modulation of the 2DEG located in the x-y plane by a cosine-potential $V(y) = V_0 \cos(2\pi y/a)$. The solution of Schrödinger's equation yields a parabolic band in x-direction with the effective mass m^* and minibands in y-direction characterized by the band index n and the wave vector k_y which is restricted to the first Brillouin zone $(-\pi/a, \pi/a)$.

Investigating weak localization one has to consider elastic and inelastic scattering mechanisms, respectively. Elastic scattering is described within the model of Gaussian White Noise which corresponds to short-ranged scatterers in real space. Inelastic scattering limiting the phase coherence of electrons is assumed here for simplicity to be short-ranged, too. The total coupling constant $g = g^{el} + g^{in}$ is then the sum of the elastic and inelastic ones and given by the mobility μ_{2D} of the 2DEG. The inelastic coupling constant can be related to the phase coherence length L_ϕ via $\Delta_\phi \equiv g^{in}/g \equiv l_e^2/L_\phi^2$ [8]. l_e is the total scattering length in x-direction.

For weak enough scattering ($E_F \gg \Gamma$) we can neglect interference effects in the equilibrium properties of the system and restrict ourselfes to the self-consistent Born approximation [11]. The self-energy is averaged over the period a of the modulation potential which makes it independent of the quantum numbers n and k for short-range scattering. Numerical results for the density of states $\varrho(E_F)$ which is related to the scattering rate via $\Gamma(E_F) = \pi g \varrho(E_F)$ are shown in Fig. 1 in dependence on Fermi energy for a modulation potential corresponding to usual experimental values [1-5]. Here and in the following figures the arrow indicates the position of the potential maximum.

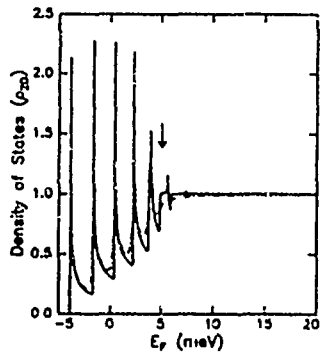

Fig. 1: Density of states in units of its value ϱ_{2D} in a two-dimensional system in dependence on Fermi energy for a modulation potential of amplitude $V_0 = 5meV$ and period $a = 200nm$. The two different scattering strengths correspond to mobilities of the 2D reference system $\mu_{2D} = 5 \times 10^6 cm^2/Vs$ (solid line) and $\mu_{2D} = 5 \times 10^4 cm^2/Vs$ (dashed-dotted line).

For energies well below the maximum at $5meV$, $\varrho(E_F)$ behaves essentially as in one dimension. For stronger scattering the peaks are broadened by lifetime effects. Above the potential maximum the density of states approaches quickly its two-dimensional value which is energy independent. Close to the threshold the spectrum shows already dispersion in y-direction but the bands are still well separated by gaps. This leads to a step-like onset of the density of states at the lower band edge and a logarithmic divergency at the upper band edge for negligible scattering as usual for a band of finite width in two dimentions.

3 Conductivity. Regarding electron transport properties it is essential to include interference of electron waves leading to weak localization even if $E_F \gg \Gamma$ [11,12]. This means that in addition to diagramms with non-crossed interaction lines corresponding to the self-consistent Born approximation those with maximally crossed impurity lines have to be taken into account. We have done this by use of the non-equilibrium Green function technique [8,10]. First, we evaluate the conductivity of the system in self-consistent Born approximation. Without magnetic field and at zero temperature the diagonal tensor of band conductivities is given by

$$\sigma_{ii}^B(E_F) = \frac{e^2}{h} \sum_{nk} \hbar^2 v_i^2 A_{nk}^2(E_F) \quad , \quad v_i = \frac{\partial E_{nk}}{\partial \hbar k_i} \tag{1}$$

with the group velocity v_i and $i = x, y$. Here we have omitted the non-diagonal elements of the velocity matrix element in y-direction which correspond to scattering-induced intersubband transitions. The anisotropy of the system enters via the differing group velocities for both directions. Obviously, the group velocity in y-direction vanishes in the 1D limit since the spectrum shows no dispersion in this direction.

From the conductivity tensor one can obtain the tensor of diffusion coefficients with help of the Einstein relation $D_{ii}(E_F) = \sigma_{ii}^B(E_F)/e^2\varrho(E_F)$. The diffusion coefficients are related to the scattering lengths $l_i(E_F)$ by $l_i^2(E_F) = \hbar D_{ii}(E_F)/\Gamma(E_F)$. The latter are shown in Fig. 2 in dependence on Fermi energy.

The scattering length l_y along the equipotential lines is seen to be much larger than the potential period and subband effects are well resolved. This results in the pronounced oscillations of l_y in the one-dimensional region ($E_F < V_0$). Above the treshold it behaves as in two dimensions $l_y \sim \sqrt{E_F}$. The scattering length l_x in direction of the potential modulation is extremly small in the 1D region as expected. Contrary, for $E_F > V_0$ it shows a 2D energy dependence as l_y but is smaller in amplitude due to the lower density of electrons which can move freely into this direction. At the treshold one recognizes the influence of the finite band width due to the enhanced tunneling between adjacent potential wells both on l_x and on l_y which becomes finite there.

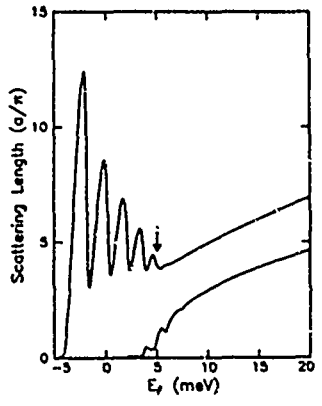

Fig. 2: Scattering lengths l_y (upper curve) and l_x (lower curve) in units of a/π in dependence on Fermi energy for $\mu_{2D} = 5 \times 10^6 cm^2/Vs$ and otherwise the same parameters as in Fig. 1.

Within the non-equilibrium Green function technique [8,10] a self-consistent treatment of the Cooperon allows to investigate the transition from weak to strong localization and to estimate the localization length. For a modulated 2DEG the resulting conductivity is for zero temperature

$$\sigma_{ii}(E_F) = \frac{e^2}{h} \sum_{nk} \hbar^2 v_i^2 A_{nk}^2(E_F) (1 + F_{nk}(E_F))^{-1} \tag{2}$$

with

$$F_{nk}(E_F) = g^{st} C(E_F) A_{nk}(E_F)/\Gamma(E_F) \qquad (3)$$

In Eq. (3) $C(E_F)$ represents the Cooperon averaged over the potential period as it has been done for the self-energy. Note that the Cooperon term appears in the denominator of the relation for the conductivity as a result of self-consistency. The solution for the Cooperon reduces to the expressions derived in Ref. [8] in the limit of an isolated quantum wire if the spectrum shows no dispersion in y-direction and to the usual expression for a 2D system for vanishing modulation potential. For $L_\phi \gg a$, the result is

$$C(E_F) \approx \frac{1}{4\pi l_x l_y} \int_\tau^\infty \frac{dt}{t} erf\left[\frac{\pi l_y}{a}(t/\tau)^{1/2}\right] e^{-t/\tau_\phi} \qquad (4)$$

after an expansion for small q ($L_\phi \gg l_x$). Here, $\tau_\phi = \hbar/\Gamma_\phi$ is the phase coherence time, l_x and l_y are the scattering lengths defined above, and the total scattering time $\tau = \hbar/\Gamma$ has been used as the necessary short-time cutoff [12]. The limiting cases of Eq. (4) are $C(E_F) = L_\phi/2l_y^2$ a for $L_\phi^y \ll a$ and $C(E_F) = (1/2\pi l_x l_y)\ln(L_\phi/l_x)$ for $L_\phi^y \gg a$ where we have introduced the phase coherence length in y-direction $L_\phi^y = \sqrt{D_{yy}\tau_\phi}$. The Cooperon acquires its one-dimensional form for $l_y \to 0$ and behaves as in two dimensions for $l_y \sim l_x \gg a$. This means that the 1D-2D transition in weak localization effects takes place in coupled wires when the electrons can tunnel between adjacent wires without loosing phase coherence, i.e. if L_ϕ^y becomes *larger* than the modulation period. This has to be distinguished from the usual 1D-2D transition in an isolated wire discussed e.g. in Ref. [6] which takes place if the phase coherence length becomes *smaller* than the wire width. For weak interference effects, i.e. not too large phase coherence length, one can expand the denominator in Eq. (2) which yields the usual perturbational relation $\sigma_{xx}(E_F) \approx \sigma_{xx}^B(E_F) - \Delta\sigma_{xx}(E_F)$ with the limits $\Delta\sigma_{xx}^{1D}(E_F) = (3/2)(e^2/\pi\hbar)(L_\phi/a)$ and $\Delta\sigma_{xx}^{2D}(E_F) = (3/2)(e^2/\pi^2\hbar)\ln(L_\phi/l_x)$. The small parameter for this expansion is $\delta = 4g^{st}C(E_F)/\Gamma^2(E_F) \approx 4\Delta\sigma_{xx}(E_F)/3\sigma_{xx}^B(E_F)$ [8]

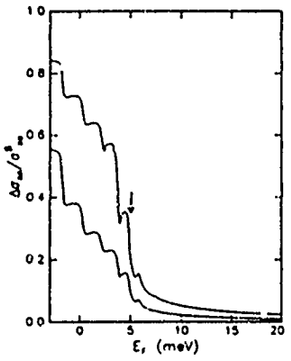

Fig. 3: Relative correction $\Delta\sigma_{xx}(E_F)/\sigma_{xx}^B(E_F)$ in dependence on Fermi energy for $\Delta_\phi = 0.1$ (lower curve) and $\Delta_\phi = 0.01$ (upper curve). The other parameters are the same as in Fig. 2

If δ becomes larger with increasing phase coherence length and for low electron densities the conductivity Eq. (2) approaches zero which describes the transition to strong localization. Now, the weak localization correction acts additive in the *resistivity*. The relative correction $\Delta\sigma_{xx}(E_F)/\sigma_{xx}^B(E_F)$ is shown in Fig. 3. The different ratios of elastic to inelastic scattering strengths, Δ_ϕ, correspond to phase coherence lengths of about $1\mu m$ (lower curve) and $3\mu m$ (upper curve). The population of 1D subbands with increasing Fermi energy leads to a stepwise decrease of $\Delta\sigma_{xx}/\sigma_{xx}^B$. For low electron densities and weak inelastic scattering interference effects contribute considerably to the total conductivity and the usual perturbative result is not applicable. If the Fermi energy becomes larger than the potential amplitude the conductivity correction is much smaller and only weakly dependent on energy as expected for a 2DEG. The minima close to the treshold are due to the finite widths of the minibands leading to 2D behavior of weak localization. They become more pronounced for larger L_ϕ when 1D behavior is preserved to larger Fermi energies.

The expansion parameter δ can be used to estimate the localization length l_{loc} in our system from the assumption that the interference effects begin to dominate the conductivity if L_ϕ becomes larger than l_{loc}, $\delta(L_\phi = l_{loc}) = 1$

The localization length obtained from this assumption fulfills the correct limiting relations $l_{loc}^{1D} = Nl_x$ and $l_{loc}^{2D} \propto l_x \exp(\pi k_F l_x/4)$ where N is the number of occupied subbands in the 1D limit and k_F is the Fermi wave vector. It is shown in Fig. 4 its dependence on Fermi energy. Below $3.5meV$ the localization length behaves essentially as in one dimension. Above the potential maximum l_{loc} rises exponentially with Fermi energy as usual for a two-dimensional system. For $E_F \sim 4meV$ the system undergoes a transition from being effectively one-dimensional to the 2D regime as the electrons become allowed to tunnel coherently between adjacent wires in the last subband below l_0

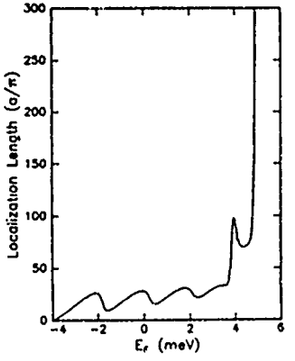

Fig. 4: Localization length l_{loc} in units of a/π in dependence on Fermi energy for the parameters of Fig. 2.

4 Conclusions. A study of interference effects in a 2DEG subject to a uni-directional periodic modulation has been presented. With decreasing ratio of Fermi energy and potential amplitude the system turns from a weakly modulated 2DEG into an array of quantum wires which are coupled by tunneling. A transition from 2D to 1D behavior of the weak localization correction to conductivity is found if the coherent propagation of the electrons between adjacent wires is suppressed. This occurs when the period of the potential exceeds the transversal phase coherence length related to the diffusion coefficient in the direction perpendicular to the wires. We have presented numerical results for transport properties in dependence on Fermi energy showing a smooth transition from the 2D to the 1D limit.

respectively. Furthermore, we have estimated the localization length of the system which changes from an exponential to a linear dependence on scattering length.

M.S. acknowledges financial support by the DFG (Sonderforschungsbereich 348 - Teilprojekt YD). P.E.S. wishes to thank the GOS e V.,Berlin.

References

[1] K. Ismail, W. Chu, D. A. Antoniadis, and H. I. Smith, Appl Phys. Lett. **52**, 1071 (1988).
[2] J. Alsmeier, Ch. Sikorzky, and U. Merkt, Phys. Rev. B**37**, 4314 (1988)
[3] F. Brinkop, W. Hansen, J. P. Kotthaus, and K. Ploog, Phys. Rev. B**37**, 6547 (1988)
[4] P. H. Beton, E. S. Alves, P. C. Main, L. Eaves, M. W. Dellow, M Henini, O. H Hughes, S. P. Beaumont, and C. D. W. Wilkinson, Phys. Rev. B**42**, 9229 (1990)
[5] G. Berthold, J Smoliner, W Demmerle, F. Hitler, E. Gornik, W Ettmüller, G. Böhm. and G. Weimann, Semicond. Sci Technol. **6**, 709 (1991).
[6] M. J. Kearney and P N Butcher, J. Phys C· Solid State Physics **21**, 2539 (1988)
[7] M. Suhrke, S. Wilke, and R Keiper, Solid State Commun. **76**, 551 (1990).
[8] M. Suhrke and S. Wilke, Phys Rev. B **46**, 2400 (1992)
[9] W. Szott, C. Jendrzejek, and W. P. Kirk, Superlattices and Microstructures **11**, 199 (1992).
[10] M. Suhrke and P E. Selbmann, submitted to Phys Rev. B.
[11] B. L. Altshuler, A.G Aronov, D. E Khmelnitskii, and A. I. Larkin, in *Quantum Theory of Solids*, edited by I M. Lifshits (Mir Publishers, Moscow, 1982), p 130
[12] G. Bergmann, Phys Rep **107**, 1 (1984)

MoP39

LUMINESCENCE STUDIES OF RESONANT TUNNELING IN A TRIPLE BARRIER STRUCTURE WITH STRONGLY COUPLED QUANTUM WELLS

T S Turner, P M Martin, L. Eaves, H B Evans, P A. Harrison, M Henini and O H Hughes
Department of Physics, University of Nottingham, Nottingham NG7 2RD

D M Whittaker, P D Buckle, T A Fisher, M S Skolnick, and G Hill*
Department of Physics, University of Sheffield, Sheffield S3 7RH

Abstract

The electrical and optical properties of an n doped triple barrier resonant tunneling diode are investigated A thin central AlAs barrier provides strong coupling between the two GaAs quantum wells which have equal widths Photoluminescence (PL) arises from both spatially direct and spatially indirect transitions in the quantum wells The intense spatially indirect transition shows a pronounced red shift with increasing bias. A strong intrinsic bistability effect is observed in one of the three resonant peaks in the current-voltage curve This effect is also seen in the photon energy and intensity of the PL from the wells Photoluminescence excitation spectroscopy is used to identify the optical transitions and the strength of the tunneling interaction

The optical properties of coupled quantum wells separated by a thin tunnel barrier have been intensively investigated in recent years [1-3] An interesting feature of these structures is that the thin central barrier leads to a strong quantum mechanical coupling between the two states in the quantum wells In a device in which the two quantum wells have the same width, an applied electric field reduces this coupling and at sufficiently high electric fields the electron (and hole) wavefunctions become largely confined to one or other of the two quantum wells. A coupled quantum well structure comprising a thin central barrier and two wider outer barriers can be incorporated in the undoped, intrinsic (i) region of an n-i-n diode to form a modified version of the standard double barrier resonant tunneling device [4] When a voltage is applied to this structure, resonant tunneling of electrons can occur from the doped contact regions into the quantum wells and peaks are observed in the current-voltage characteristics, I(V);

Photoluminescence spectroscopy has proved to be a powerful tool for studying double barrier resonant tunneling devices [5-9] and provides detailed information about the charge buildup in the bound states of the quantum well [10-12] and of the energy relaxation and recombination processes In this paper, we use photoluminescence (PL) and photoluminescence excitation (PLE) spectroscopy to investigate a triple barrier resonant tunneling structure with coupled quantum wells Spectra were obtained over a wide range of bias and compared with the resonance effects observed in the current-voltage characteristics, I(V) Electron hole recombination in the quantum wells gives rise to two intense PL lines The line corresponding to spatially indirect recombination has the much higher intensity and its photon energy is tunable with applied bias A very pronounced intrinsic bistability effect is observed in one of the resonances in the I(V) characteristics due

to a space charge buildup process This involves resonant electron tunneling into one of the wells, followed by a sequential tunneling process across the thin central barrier, accompanied by the emission of a longitudinal optic phonon

Figure 1 shows a schematic band diagram of the device at a bias of around 0 6 V The device consists of two GaAs quantum wells, each of width 6 0 nm, separated by a thin central barrier of AlAs, of nominal width 0 85 nm (3 monolayers) The two outer AlAs barriers are 5 1 nm wide Two undoped GaAs spacer layers of width 7 6 nm separate the barriers and quantum wells from the Si-doped contact regions in which the doping is graded from 1×10^{17} cm^{-3} to 2×10^{18} cm^{-3} The top n$^+$ contact region incorporates an $Al_{0.33}Ga_{0.67}As$ window layer to transmit light to and from the region of the quantum wells The devices are in the form of circular mesas of diameter 100 μm, with an annular Au/Ge top contact which provides optical access

Figure 2(a) shows the I(V) curve with the substrate biased negative A similar curve is obtained in the opposite bias direction Three resonant peaks are observed, corresponding to resonant tunneling into the three quasi-bound states of the conduction band quantum wells shown in Figure 1 Tunneling occurs from a two-dimensional electron gas in the accumulation layer adjacent to the left-hand barrier The second peak (E2) exhibits a pronounced intrinsic bistability effect which, as discussed below, also appears in the PL emission spectra Interestingly, this second peak has a higher maximum current in I(V) than the third (E3), even though it occurs at about half of the applied voltage Such behaviour is not observed in conventional double barrier resonant tunneling devices in which the current passed at successive resonances increases with increasing bias [see for example ref 13]

Photoluminescence from the device was excited using a He-Ne laser (λ = 633 nm) Photoexcited holes created in and around the electron depletion layer between the quantum wells and the positively biased contact layer are swept towards the tunnel barrier by the applied electric field (see Figure 1) They can then tunnel into the quantum well where they undergo recombination with electrically injected electrons, giving rise to PL Figure 3 shows a series of spectra taken with an excitation power density of ~0 5 W/cm^2, at a lattice temperature of 4 K No change in the I(V) curve is observed at these relatively low laser power densities The PL spectra consist of three distinct features the feature at around 1 5 eV corresponds to recombination of photo excited holes in the n-type GaAs contact layers and will not be discussed in detail in this paper, the two lines, QW1 and QW2, arise from electron-hole recombination in the quantum well region Their intensities as a function of bias are shown in Figure 2(b) and reveal resonant features which can be related to those in I(V) For most biases above about 0 1 V the QW1 line has an intensity which is comparable to that of the near-band edge recombination (see Figure 3) It shows a pronounced peak in intensity at a bias corresponding to the peak of the E1 resonance in I(V) A weak peak in the intensity of this line (peak H) is also observed at a lower bias (0 135 V) which we ascribe to resonant tunneling of the photo created holes into the quantum well regions The intensity of the QW1 line is bistable in the region of the second (E2) resonance in I(V) Interestingly on the high current section of the bistable loop the intensity of QW1 is low its intensity is about a factor of two higher on the low current section of the loop An additional weak peak is observed in the intensity of QW1 at around 0 7 V A corresponding broad feature is also observed in I(V) and we ascribe both to electron tunneling into the E2 state of the quantum

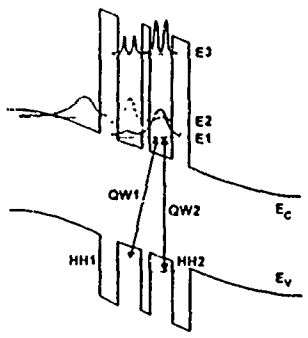

Figure 1
Schematic band diagram of the device under a bias of ~0 6 V

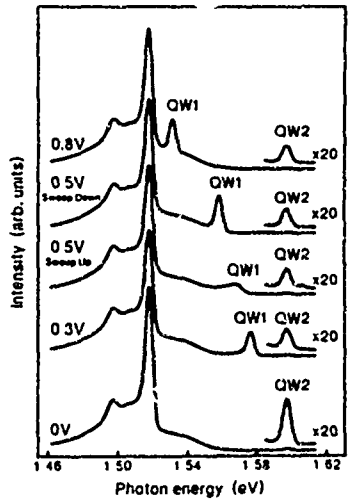

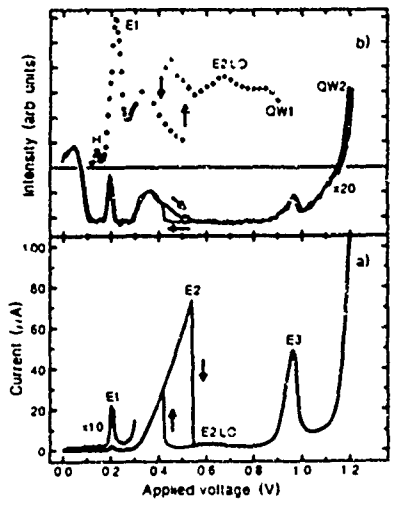

Figure 3
Photoluminescence spectra, taken at 4 K and various bias conditions The spectra at V = 0 5 V were obtained in the high and low current sections of the bistability loop

Figure 2
(a) The current voltage characteristics, I(V), taken at 4 K (b) The variation, as a function of bias, of the intensity of the two photoluminescence lines, QW2 and QW1

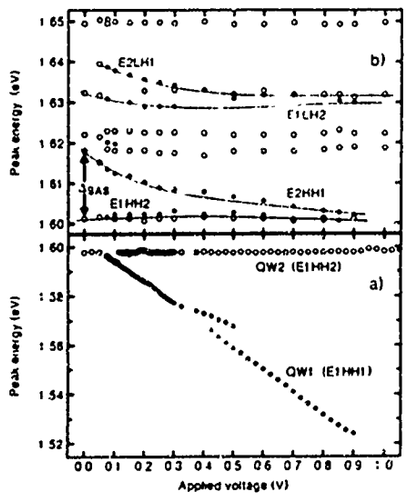

Figure 4
Variation with applied bias of the photon energy of the (a) PL and (b) PLE lines
For (a) filled circles correspond to the indirect QW1 line and open circles to the direct QW2 line Triangles represent data from the low current loop of the bistable region
For (b) filled circles correspond to PLE observed when detecting on the QW1 line and open circles correspond to PLE observed when detecting on the QW2 line

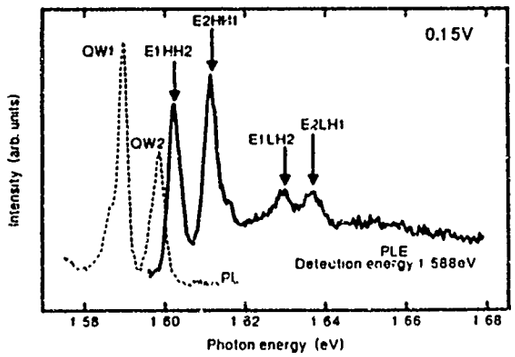

Figure 5
A typical PLE spectrum and its associated QW PL spectrum at 0 15 V

well, accompanied by the emission of a longitudinal optic (LO) phonon As shown in Figure 4(a) the QW1 line undergoes a significant red shift with increasing bias, shifting from 1 60 eV at 0 1 V to 1 525 eV at 0 9 V, where it merges with the band gap emission from the contact region The weaker line, QW2, at 1 60 eV does not shift in energy with bias Its intensity is typically ~ 20 times weaker than QW1 The variation of the intensity of the QW2 line with bias shows distinct peaks at the E1 and E3 resonances in I(V) There is also a peak at 0 325 V, at the onset region of the E2 resonance, a weak bistability is also observed at slightly higher voltages At low bias between 0 and 0 1 V, the QW1 and QW2 lines merge and have a weak intensity relative to the PL from the GaAs contact regions

We can understand the qualitative behaviour of the I(V) characteristics and of the PL spectra by considering the effect of the applied voltage on the confined electron and hole states in the quantum wells The thin central barrier couples the two quantum wells which in this device have the same thickness At zero bias, the electron (and hole) wavefunction of the two lowest states E1 and E2 of the conduction (and valence) band quantum wells are of the familiar symmetric and antisymmetric type, extending over both wells Increasing bias causes the electron wavefunctions to become increasingly localized in one or other of the two conduction band quantum wells as shown schematically in Figure 1 This effect is even more pronounced for holes because of their larger effective mass The three peaks in I(V) correspond to resonant tunneling into states E1 and E2 and into the lower energy state E3 of the upper pair of coupled QW states, E3 and E4 No E4 resonance is observed, however

We ascribe both PL lines to transitions involving electrons in the E1 state of the conduction band quantum wells The QW2 line is due to a transition between E1 and HH2, the lowest hole state of the right hand well The QW1 line arises due to a spatially indirect transition between E1 and HH1 (see Figure 1) The voltage-induced confinement effect leads to the pronounced red shift of transition QW1 with increasing bias In contrast, the shift of QW2 is small as it effectively corresponds to a spatially direct transition The relative weakness of the spatially direct QW1 line indicates that the hole population is much higher in the left hand quantum well

This identification of the transitions corresponding to the QW1 and QW2 lines is confirmed by the PLE measurements which were obtained with a Ti-sapphire laser pumped by an Ar ion laser, detecting on either the QW1 or QW2 emission lines A typical PLE spectrum at a bias of 0 15 V is shown in Figure 5 and reveals four clear QW transitions. The spectrum was obtained at a detection energy of 1 588 eV corresponding to the QW1 PL line The QW PL spectrum at this bias is also shown in Figure 5 The variation of the principal PLE lines with bias is shown in Figure 4(b) These data give a value of the symmetric antisymmetric splitting (electron + hole) of Δ = 17 meV under flat band conditions at zero bias, in reasonable agreement with the value obtained from an effective mass model The PLE measurements also confirm the identification of the QW1 and QW2 emission lines as E1 HH1 and E1 HH2 respectively each of which involves the lowest heavy hole (HH) states of the respective quantum wells Note that the E1 HH2 and E2 HH1 lines in PLE do not move symmetrically with increasing bias the downward shift of E2 HH1 is considerably larger than the upward shift of E1 HH2 We attribute this to an excitonic effect in which the exciton binding energy decreases with increasing bias due to the increasing electron localization in the individual QWs

The observation of an intense QW1 line even when the device is biased on the E2 resonance implies that electrons which resonantly tunnel into E2 relax their energy and scatter into E1 prior to recombination. The energy separations of the E2 HH1 PLE line and the E1 HH1 PL line indicate that the energy separation between the E2 and E1 levels exceeds the optical phonon energy in GaAs ($\hbar\omega_{LO}$ = 36 meV) at bias voltages above about 0.38 V. Hence LO phonon emission is energetically possible over most of the bias range of the E2 resonance. Further evidence for this relaxation process is provided by the strong peak in PLE due to the E2 HH1 transition for detection on the QW1 (E1 HH1) transition.

Using magneto-tunneling measurements [12] we estimate that the electron sheet density in the right hand quantum well is $n_s \approx 1 \times 10^{11}$ cm^{-2} on the peak of the E2 resonance at 0.525 V. The linewidth of the QW1 line also provides us with an estimate of the charge density in the E1 state. The linewidth varies with applied voltage, showing peaks at all three electron resonances in I(V). From the linewidth at 0.525 V we obtain an estimate of n_s = 1.3×10^{11} cm^{-2}. Using the relation $J = n_s e/\tau_{tunn}$, and the measured value of the current density J = 8.6 kA m^{-2}, we estimate the tunneling out time to be 25 ns at this voltage. Both this time and the expected radiative recombination time of the spatially indirect QW1 transition $\tau_{rad} \geq 1$ ns are much longer than the LO phonon emission time $\tau_{LO} \approx 0.3$ ps. Hence the absence of any observable PL from electrons in the E2 state is not surprising since the relative population of E1 to E2 is given by $\tau_{LO}(\tau_{rad}^{-1} + \tau_{tunn}^{-1}) \geq 10^3$ [14].

The red shift of the QW1 PL with increasing bias (see Figure 4(a)) shows an interesting dependence in the region of the E2 resonance. On the high current section of the bistability loop the rate of red shift of QW1 with increasing bias is smaller than on the low current section. A similar but less pronounced behaviour is also observed on the E1 resonance around 0.2 V and on the LO phonon related peak at around 0.7 V. This effect is associated with the build up of space charge in the quantum well at resonance. When the device is biased on a resonance, the voltage drop across the emitter barrier remains constant and the additional voltage necessary to sweep through the resonance gives rise to charge buildup in the quantum well. This additional voltage is then dropped mainly across the collector barrier and depletion layer beyond. In this device, the red shift of the QW1 line is effectively due to the increasing voltage drop across the two quantum wells with increasing bias. On the E2 resonance, the built up charge resides in the right hand quantum well and therefore the rate of red shift with increasing voltage is much smaller than it is for regions of bias voltage in which there is no resonant charge buildup.

In conclusion, we have shown that photoluminescence and photoluminescence excitation experiments as a function of bias can provide detailed information about the energy levels and inter well transitions in a coupled well system under resonant tunneling conditions. The origin of the strong intrinsic bistability observed in the I(V) characteristics is explained in terms of a charge build up effect involving a sequential tunneling process, with LO phonon emission across the central barrier.

This work is supported by the Science and Engineering Research Council and the European Community.

*G. Hill is at the Department of Electronic Engineering, University of Sheffield, Sheffield S3 7RH, U.K.

References

[1] A. Alexandrou, J. A. Kash, E. E. Mendez, M. Zachau, J. M. Hong, T. Fukuzawa and Y. Hase, Phys. Rev. B 42 (14), 9225 (1990).

[2] T. Fukuzawa, E. E. Mendez and J. M. Hong, Phys. Rev. Lett. 64 (25), 3066 (1990).

[3] Y. J. Chen, E. S. Koteles, B. S. Elman and C. A. Armiento, Phys. Rev. B 36 (8), 4562 (1987).

[4] L. L. Chang, L. Esaki and R. L. Tsu, Appl. Phys. Lett. 24 (1974).

[5] J. F. Young, B. M. Wood, G. C. Aers, R. L. S. Devine, H. C. Liu, D. Landheer, M. Buchanan, A. J. SpringThorpe and P. Mandeville, Phys. Rev. Lett. 60, 2085 (1988).

[6] N. Vodjani, D. Cote, D. Thomas, B. Sermage, P. Bois, E. Costard and J. Nagle, Appl. Phys. Lett. 56, 33 (1990).

[7] M. S. Skolnick, D. G. Hayes, P. E. Simmonds, A. W. Higgs, G. W. Smith, H. J. Hutchinson, C. R. Whitehouse, L. Eaves, M. Henini, O. H. Hughes, M. L. Leadbeater and D. P. Halliday, Phys. Rev. B 41, 10754 (1990).

[8] C. R. H. White, M. S. Skolnick, L. Eaves, M. L. Leadbeater, M. Henini, O. H. Hughes, G. Hill and M. A. Pate, Phys. Rev. B 45, 6721 (1992).

[9] C. van Hoof, J. Genoe, R. Mertens, G. Borghs and E. Goovaerts; Appl. Phys. Lett. 60, 77 (1992).

[10] V. J. Goldman, D. C. Tsui and J. E. Cunningham, Phys. Rev. Lett. 58, 1256 (1987).

[11] E. S. Alves, L. Eaves, M. Henini, O. H. Hughes, M. L. Leadbeater, F. W. Sheard, G. A. Toombs, G. Hill and M. A. Pate, Elect. Lett. 24, 1190 (1988).

[12] M. L. Leadbeater, E. S. Alves, F. W. Sheard, L. Eaves, M. Henini, O. H. Hughes and G. A. Toombs, J. Phys. Condens. Matter 1, 10605 (1989).

[13] E. S. Alves, M. L. Leadbeater, L. Eaves, M. Henini and O. H. Hughes, Solid State Electronics 32, 1627 (1989).

[14] J. W. Cockburn, P. D. Buckle, M. S. Skolnick, D. M. Whittaker, W. I. E. Tagg, R. A. Hogg, R. Grey, G. Hill and M. A. Pate, Phys. Rev. B 45, 13757 (1992).

MoP40

CORRELATION EFFECTS IN MAGNETOLUMINESCENCE SPECTRA FROM DENSE QUASI 2D ELECTRON GAS IN SELECTIVELY DOPED InGaAs/GaAs QUANTUM WELLS

V.D. Kulakovskii, V.V. Bu'ov, I.E. Itskevich, L.V. Kulik
Solid State Physics Inst. Russian Academy of Sciences, 142432, Chernogolovka, Russia

T.G. Andersson, W. Shumin
Department of Physics, Chalmers University of Technology, Gothenburg, Sweden

A.V. Lomsadze
High Pressure Physics Inst. Russian Academy of Sciences 142092, Troitsk, Russia

Abstract

Low temperature magnetoluminescence from a quasi-2D electron gas in n-AlGaAs/InGaAs/GaAs quantum well with a partially filled n_z=2 subband has been investigated. For n_z=1 electrons, the energy of interband Landau level transitions has been found to demonstrate an oscillating magnetic field dependence, and an additional structure in the emission lines has been revealed. The former is related with oscillations in the energy gap between the n_z=1 and n_z=2 subbands due to the redistribution of electrons between the subbands, while the latter indicates a strong enhancement of shake-up processes that allows different final states in the photoemission transition.

I. INTRODUCTION

High carrier density effects in quasi 2D (two dimensional) semiconductor quantum well (QW) heterostructures are of considerable interest from a fundamental point of view to test many-particles theories of structures with reduced dimensionality [1-4]. Most publications deal with the shrinkage of the fundamental energy gap, referred to as band gap renormalization which is due to exchange and correlation interaction.

In charged systems, the dynamic response of an electron Fermi sea to the optically generated holes is known to give rise to an enhanced interaction of correlated electron-hole pairs near the Fermi level. It results in an enhanced oscillator strength for optical transitions at the Fermi edge [5-8], referred to as Fermi-edge singularity. However, in the 2D magnetoplasma with the single occupied electron subband, the interband Landau level (LL) transition energies turn out to be almost linear in a magnetic field and separated by the electron cyclotron energy, $\hbar\omega_{ce}$.

In the present paper we study peculiarities in the low temperature radiative recombination of the n_z=1 electrons in QWs with a partial filling of the next, n_z=2, subband in high magnetic fields under low excitation level. We have found that, first, the dependence of the LL transition energy on magnetic field becomes nonmonotonic and, second, an additional well resolved structure appears in the emission spectra. The latter cannot be described in a simple approximation that the n_z=1 electron-hole recombination leaves the free quasihole in the first conduction subband. With increasing temperature these effects become negligible at T≈10-12 K. The oscillations of the transition energy with magnetic field are supposed to be related with oscillations in the energy gap between the first and second subbands. The latter is due to the redistribution of electrons between the subbands when their Landau levels cross each other [9,10]. The additional emission lines indicate a strong enhancement of the shake-up processes that give rise to different final states of the photoemission transition.

II. EXPERIMENTAL

Selectively doped single QW heterostructures were grown by MBE using solid source evaporation material. We used (001)-oriented substrates of semi-insulating GaAs. The layers were grown in the following succession - an 500 nm GaAs buffer layer, an undoped 25 nm thick $In_{0.18}Ga_{0.82}As$ QW, an undoped 5 nm $Al_{0.25}Ga_{0.75}As$ spacer, a δ-layer of Si (N_s ~2 5.10^{12} cm^{-2}), and a 50 nm $Al_{0.25}Ga_{0.75}As$ layer. The 2DEG concentration was n_{2D}~$2.4.10^{12}$ cm^{-2}.

Photoluminescence measurements were carried out with the use of a cw He-Ne-laser with λ=632.8 nm. The sample was placed in a cryostat with a superconducting coil. It was immersed in liquid helium (T=1.8 or 1.2 K) or located in helium vapors (T>4.2 K). To control the electron concentration in the QW we have used the quasihydrostatic pressure up to 3 GPa. In this case the sample was located in a low-temperature fixed pressure cell with diamond anvils, one of which was used as an optical window.

The plane of the QW was oriented normally to the magnetic field. A 0.6 mm quartz fiber was used to transmit both the excitation and luminescence light. The latter was dispersed by a grating monochromator and detected by a cooled photomultiplier.

III. EXPERIMENTAL RESULTS AND DISCUSSION

1. Emission spectra from 2DEG

To investigate the influence of the second subband filling on the emission spectra, we start from the case when it is empty. Figure 1 displays low excitation 2DEG emission spectra from a selectively doped n-AlGaAs/InGaAs/GaAs 25 nm thick QW under 3 GPa for different magnetic fields at 1.8 K. Without external pressure a 2DEG density is $2.4.10^{12}$ cm^{-2}, and electrons occupy two subbands. The pressure of 3 GPa decreases n_{2D} down to 8.10^{11} cm^{-2} that results in depopulating of the second subband. The magnetoluminescence spectra consist of a few lines J^1_e-0^1_h corresponding to the transitions between occupied LLs in the first (1) subbands of conduction (J_e) and valence (0_h) bands. In addition, there is a weak 1^1_e-1^1_h line that appears due to slow relaxation of photoexcited holes. The dipole-forbidden transitions J^1_e-0^1_h with J≠0 appear mainly due to the defect induced carrier scattering. Both the small relative intensity of these transitions and the small halfwidth of the lines indicate the high quality of the QW investigated.

Figure 1 shows that the J^1_e-0^1_h transition energies, E^1_J, are nearly linear in H. In the present paper only the recombination of holes from the $j=0^1_h$ LL is discussed, and we indicate only the numbers of the electron LL and subband. The energy gap between the near-by transitions, $\Delta^1_J=E^1_{J+1}-E^1_J$, corresponds to a cyclotron energy of electrons with effective mass m_e=0.084m_0, where m_0 is the free electron mass. This value is close to the calculated one (0.078m_0) in the framework of Kane's model. These features are typical for the emission spectra from 2DEG with a single occupied subband.

Figure 2 shows an example of the magnetic field dependence of the emission spectra at higher 2DEG density, with the second subband partly filled. It displays the spectra from the same sample as Fig.1 but under pressure of 1.8 GPa, when n_{2D} increases to ~ $1.3.10^{12}$ cm^{-2} that results in the population of the second subband. As a consequence, there appears a strong emission line 0^2_e-0^1_h corresponding to the recombination of electrons from the 0^2_e LL. A high intensity of this line, I^2_0, is due to the strong overlapping of the n_z=1 hole and n_z=2 electron wave functions resulting from the electric field normal to the QW plane because of selective doping.

Comparison of Figs. 1 and 2 shows that the 2DEG magnetoluminescence spectra from QWs with electrons in one and two subbands are markedly different. In the latter case the emission lines are significantly broader and reveal an additional structure. Magnetoluminescence studies of the sample under different pressure have shown that both the line width and additional structure are very sensitive to magnetic field and to filling of the second subband.

Comparison of the dependence of the LL transition energies on magnetic field for P=1.5, 1.8 and 3 GPa (σ_{2D}=8, 13 and 15.10^{12} cm^{-2}, respectively) is presented in Figs. 3 and 4. It shows that the filling of the second subband gives rise to the qualitative change in magnetic field dependence of n_z=1 transition energies. It becomes nonlinear and even nonmonotonic, whereas that for the 0_e^2-0_h^1 transition demonstrates only very small deviations from linear. Dashed lines in Fig. 3 show the magnetic field dependence of the n_z=1 LL transition energies expected in the case of the empty second subband. To draw them, it is taken into account that at 1.8 GPa the second subband is depopulated at 14 T, and there were used the measured values of E_0^1 at 14 T and the slope of the E_j^1 (H) dependences in QW with the empty second subband (at 3 GPa).

Figures 3 and 4 show that the filling of the 0_e^2 LL results in the lowering of energy of the main emission line from the first subband. In some cases, the magnitude of this lowering exceeds a half of $\hbar\omega_{ce}$. Note, however, that there is a discrepancy between the position of extrema in the transition energies E_0^1 (H) and in the 0_e^2-0_h^1 line intensity. In particular, at 1.5 GPa the maximum of I_0^2 is at H=11 T whereas the minimum of E_0^1 is at 12.2 T (Fig. 4).

Figure 2 shows that for 2DEG with two occupied subbands, the broad emission band 0_e^1-0_h^1 consists of a few half-resolved lines. Their energetic position and intensity have quite different magnetic field dependences. The additional structure of the emission band is most pronounced at 8-14 T, that is the range of crossing of the 0_e^2 LL with the first and second LLs from the n_z=1 subband. At H=8 T, when the intensity of the 0_e^2-0_h^1 line has a minimum, a line marked A' dominates in the emission spectra from the first subband. With increasing H till 10.4 T, the luminescence peak moves to lower energies, and simultaneously it broadens. This range of H corresponds to the high intensity of the 0_e^2-0_h^1 line.

At 10.2-10.8 T, a pronounced shoulder appears at the high energy side of the band A'. At higher H, when the intensity of the 0_e^2-0_h^1 line strongly decreases, it transforms into the peak marked A. This peak becomes dominating at H=11-11.8 T, whereas the peak A' weakens and disappears. Fig. 2 shows also that at H=10-12 T there is another well pronounced shoulder at the high energy side of the peak A. At higher H it increases strongly and transforms into the line B which is relatively narrow. When the 0_e^2 LL becomes empty only that peak remains in the spectrum.

2. Discussion

When 2D-electrons transfer from the first to the second subband the lowering of the 0_e^1-0_h^1 transition energy is due to the change of the electric field normal to the 2DEG plane. The latter is caused by the redistribution of electron density in this direction. In the frame of a simple approximation, this transition energy should lower with the filling of the second subband. However, the experiment shows that the largest lowering of the 0_e^2-0_h^1 transition energy does not coincide with maxima in the 0_e^2-0_h^1 line intensity. The discrepancy might be related with incorrect determination of the transition energy as a spectral position of a maximum of the broad asymmetric 0_e^1-0_h^1 emission line that reveals, in addition, the multicomponent structure.

The multicomponent structure of the emission band indicates that in the initial or final state of the photoemission transition there are a few different states. The excited initial states are to be excluded because of very low temperature of investigated 2DEG. The random potential fluctuations that are known to modify strongly the emission spectra of 2DEG in QW should mainly result in the line shift and broadening. They can be hardly responsible for majority of the observed peculiarities. Therefore we would like to discuss the contribution from the different final states in photoemission transition.

The radiative recombination of electron from a LL below Fermi level leaves the 2DEG in an excited state. Therefore one can write that the photon energy $\hbar\omega = E_0 - E_{exc}$, where E_0 is the energy of the transition to the 2DEG ground state, and E_{exc} is the energy of an additional excitation in the 2DEG if it arises with electron-hole recombination.

The excitation generated in the optical transition has a momentum k~0. For 2DEG with electrons in one subband, it can be described in terms of intrasubband magneto-excitons or magnetoplasmons, with their energies coinciding at k=0. In 2DEG with n_z=2 electrons there is an additional possibility to leave the system with excitations belonging to intersubband magnetoplasmon branches. Two of them are expected to interact strongly at the resonance of their energies. These are the principal mode (corresponding to hole in the n_z=1 LL below the Fermi level) and the Bernstein one (corresponding to the excitation of electron from the n_z=2 LL to one of the n_z=1 LLs above the Fermi level) [11]. The generation of the Bernstein mode in the optical transition is related with shake-up processes. It can be hardly expected far from the resonance. However near the resonance the mixing of these modes should result in arising of an additional line. With increased H the emission intensity redistributes between two components, and the lower energy one becomes smaller and disappears, being transformed into the Bernstein mode. The arising high energy component transforms into the principal mode and becomes dominating. This is in qualitative agreement with observed behavior of the components in the emission spectra, i.e. the peaks A' and A near 11 T and the peaks A and B as well as the peaks C and D near 12 T.

Acknowledgements. We would like to thank A. V. Petinova and J.-M. Lefeuvre for assistance in measurements. The Swedish National Board for Technical Development (STU) and the Fundamental Research Foundation of Russia are acknowledged for their financial support.

REFERENCES

[1] S.Shmitt-Rink, C.Ell, and H.Haug, Phys. Rev. B 33, 1183 (1986).
[2] G.Tränkle, H.Leier, A.Forchel, H.Haug, C.Ell, and G.Weimann, Phys. Rev. Lett., 58, 419 (1987).
[3] Das Sarma, R.Jalabert, and S.-R.Eric Yang, Phys. Rev. B 41, 8288 (1990).
[4] T.Uenoyama and L.J.Sham, Phys. Rev. Lett., 65, 1048 (1990).
[5] G.Mahan, Many Particle Physics, 2nd ed. (Plenum, N.Y., 1990).
[6] A.E.Ruckenstein, S.Shmitt-Rink and R.C.Miller, Phys. Rev. Lett., 56, 504 (1986).
[7] W.Chen, M.Fritze, A.Nurmikko, C.Colvard, D.Ackley and H.Lee, Phys. Rev. Lett., 64, 2434 (1990).
[8] P.Hawrylak, Phys. Rev. B 44, 11236 (1991). P.Hawrylak, N.Pulsford, K.Ploog, Phys. Rev. B 46, 15193 (1992).
[9] P.E.Simmonds, M.S.Skolnick, L.L.Taylor, S.J.Bass, K.Nash, Solid State Commun. 67, 1151 (1988).
[10] T.Rifger, J.C.Maan, P.Wyder, F.Meseguer, K.Ploog, J.Phys. (Paris) 48, 387 (1987).
[11] L.Wendler, R.Pechstedt, J.Phys.Condens.Matter 2, 8891 (1990).

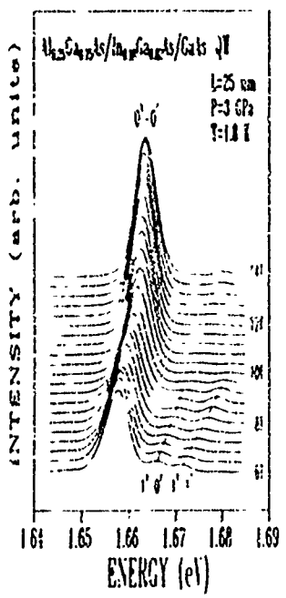

FIG 1 Emission spectra from n-AlGaAs/InGaAs/GaAs heterostructure in strong magnetic fields at 3 GPa

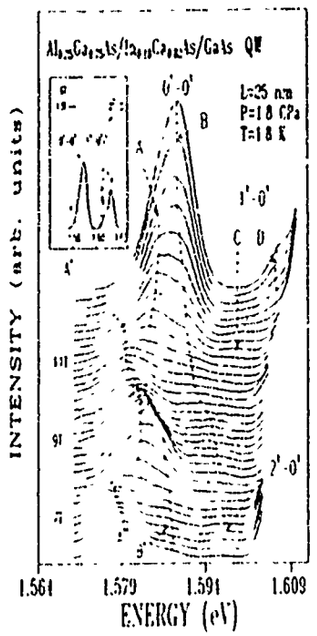

FIG 2 Emission spectra from n-AlGaAs/InGaAs/C heterostructure at 1 8 GPa corresponding to recombination of electrons from the first subband strong magnetic fields
Inset illustrates the full spectra recorded at 6 and 13

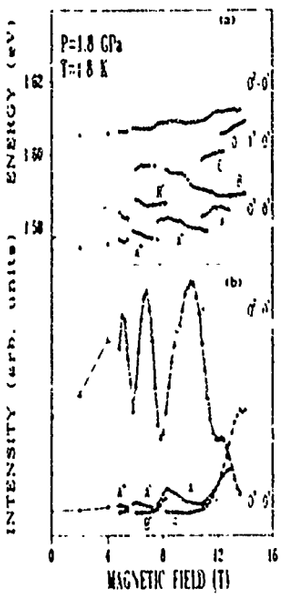

FIG.3. The energy (a) and the intensity (b) of transitions versus magnetic field at 1.8 GPa Dashed lines show LL transitions energies expected in the case of the empty second subband

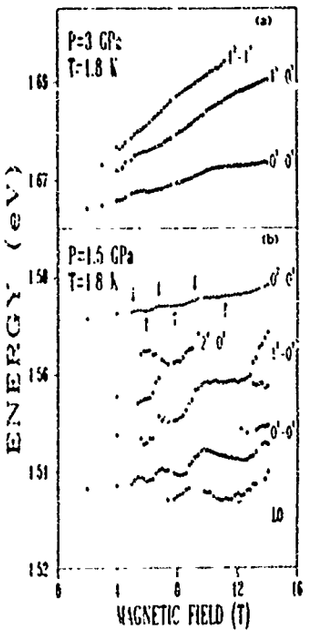

FIG 4 The transition energies versus magnetic field at 3GPa (a) and 1 5 GPa (b) For 1 5GPa up and down arrows indicate the maxima and minima of the second subband line intensity

MoC1

MBE Growth of GaAs Nanometer-Scale Ridge Quantum Wire Structures and Their Structural and Optical Characterizations

S. Koshiba*, H. Noge*, H. Ichinose***, H. Akiyama*, Y. Nakamura*, T. Inoshita*, F. Someya**, K. Wada***, A. Shimizu* and H. Sakaki***

* *Quantum Wave Project, JRDC, 4-3-24-302 Komaba, Meguro-ku, Tokyo 153, Japan*

** *Reserch Center for Advanced Science and Technology, University of Tokyo, 4-6-1 Komaba, Meguro-ku, Tokyo 153, Japan*

*** *NTT LSI Laboratories, 3-1 Morinosato Wakamiya, Atsugi-shi, Kanagawa Pref. 243-01, Japan*

**** *University of Tokyo, 4-6-1 Hongo, Bunkyou-ku, Tokyo 153, Japan*

Abstract ---- A novel method for fabrication of the quantum wire structures has been investigated by which a quantum wire has been successfully fabricated on top of a (111)B facet structure with a very sharp ridge. Electron microscope study has shown that GaAs wires with the effective lateral width of 16 ~ 18 nm and with the thickness of 6 ~ 9 nm are formed at the ridge top. Photoluminescence and cathodoluminescence measurements indicate that one dimensional quantum confinement of electrons is realized at the ridge top and its blue shift agrees with the quantum confined energy calculated for the observed wire structure.

1. INTRODUCTION

Quantum wire (QWI) structures with feature size comparable with de Broglie wavelength (~ 10 nm) of electrons are predicted to have unique electronic and photonic properties [1-3]. To realize them, various epitaxial methods have been tried such as, selective growth on a vicinal surface [4-6], over growth on the cleaved edge surface of quantum wells (QWs) [7, 8], and selective epitaxy on patterned substrates. As a result, QWIs are being formed at the bottom of V-grooves [9, 10], at the top of ridges [11-13], or on facet edges [14, 15]. In this work, we report molecular beam epitaxy (MBE) growth on a patterned substrate to form a novel QWI structure on top of a GaAs ridge structure consisting of a very narrow (001) top surface and two (111)B side facets.

The advantages of facet growth used here are that the carrier confinement is achieved by smooth facet planes, and that the incorporation of damages and impurities can be minimized due to the continuous nature of facet growth. Selective epitaxy on patterned substrates to form such facet structures has been performed so far, mainly by means of organometallic vapor phase epitaxy, since the selectivity of its growth chemistry can be employed [9-12, 14]. In contrast, our method based on MBE utilize the dependence of surface migration processes on crystalline orientation. Although

MBE has been considered less suited for facet growth because of inefficiency of desorption process, we have recently shown that well-defined facet structures consisting of (001) - (111)B planes can be grown by MBE on mesa structures [22].

In the MBE growth Ga ad-atom migration from the (111)B to the top (001) surface plays important role [16-19]. The width W of the top (001) surface or ridge region is narrowed as the growth of a (001) - (111)B facet progresses owing to the Ga migration. When the width W reaches some critical width, it can not decrease any further, because substantial portion of Ga atoms coming into the ridge region leave again by their frequent migration or desorption. To control the lateral width of the QWI, we have investigated the factor which defines this critical width, and found that the ridge can be as narrow as 10 nm when formed at 580 °C. On the basis of these investigations, we have successfully fabricated GaAs QWIs on top of the ridge structures. We have studied their structure by electron microscopy and also their electronic states by luminescence spectroscopy and compared them with theoretical calculation.

2. SAMPLE FABRICATION

In our experiment a (001) GaAs substrate with reverse mesa stripes was prepared by photolithography and reactive ion etching using $SiCl_4$. The mesa stripes running along the [110] direction were less than 2 μm in width, and about 2 ~ 3 μm in depth. On top of these mesas, a GaAs layer was grown by MBE at the substrate temperature Ts of 570 °C with the growth rate of 0.75 μm/h and the flux ratio of J_{As}/J_{Ga} of 3 if measured on a flat (001) substrate. During this growth, the substrate holder was rotated so that the As and Ga flux were uniformly supplied. As the growth progressed, the width of (001) top surface decreased, resulting in the facet structure consisting of a (001) top surface and two (111)B side surfaces, and eventually in a sharp ridge consisting of two (111)B faces. After the ridge is formed, a thin AlAs layer was grown as a lower barrier with the growth rate of 0.1 μm/h. Then a thin GaAs QW layer was deposited at Ts = 550 °C. Here two type of samples (A and B) with the different well thicknesses were prepared. Sample A has a 10 nm thick AlAs lower barrier layer, a 7 nm thick GaAs QW layer, a 150 nm thick $Al_{0.3}Ga_{0.7}As$ upper barrier layer, and a 30 nm thick GaAs cap layer. Sample B has a 5 nm thick AlAs lower barrier layer, a 5 nm thick GaAs QW layer, a 10 nm thick AlAs upper barrier layer and a 20 nm thick GaAs cap layer. All the layer thicknesses are defined as those measured when the layers are grown on a flat (001) surface.

3. EXPERIMENTAL RESULTS AND DISCUSSION

Figure 1(a) shows the cross sectional lattice image of the ridge region of sample A taken by transmission electron microscope (TEM), where a dark GaAs QW layer is seen on top of the bright AlAs layer. The thickness of this QW layer is position dependent and is largest (8 ~ 9 nm) at the top of the ridge because the incident flux of Ga atoms gets maximum at the top of the ridge and also the Ga migration from (111)B facet further enhances the growth on the ridge. On the other hand, the observed thickness of the side QW (S-QW) (= 4 nm) is about $1/\sqrt{3}$ (= cos 54.7°) of the

integrated flux (≈ 7 nm) on the flat (001) surface. We expect that carriers in this ridge structure are confined two - dimensionally, since two side QWs are thinner and act as barriers for in the lateral direction. Note that the width W at the ridge is different for the three interfaces; W at the AlAs on GaAs interface formed at Ts = 570 °C is 20 nm, while W at the GaAs on AlAs interface formed at Ts = 570 °C is 16 nm. The width W on the GaAs QW surface formed at Ts = 550 °C is 15 nm. This indicates that the lateral width of the QWI is dependent on growth conditions and compositions. The effective lateral width of the QWI is estimated to be about 17 ~ 18 nm.

Figure 1(b) shows the cross sectional TEM image of sample B. Thin bright layers are the AlAs barriers. The thickness of this QWI structure is about 6 nm whereas the thickness of S-QW on the (111)B facets is found to be about 2 ~3 nm. The effective lateral width of the QWI sandwiched by the AlAs barrier layers is about 16 nm.

Photoluminescence (PL) measurements were carried out on sample A at various temperature by focusing 3 mW He - Ne laser light (632.8 nm) into 500 μm spot size. Measured PL spectra are shown in Fig. 2, where five peaks (a) - (d) and (QWI) are clearly seen. The origins of these PL peaks were identified by cathodoluminescence (CL) measurement at 15K [22, 23]. The luminescence generated by a 3 ~ 40 keV electron beam with 1 nA current was collected by a mirror and its spectrum was analyzed as a function of position over the epitaxial layer. The magnetic field of 0.2 T was applied to suppress the carrier diffusion and improve spacial resolution [20]. A close examination of the CL data suggests that peak (QWI) comes from the top region of the ridge, peak (b) comes mainly from S-QW, and peak (a) originates mainly from the QW formed on the bottom of trench region between two mesas (B-QW).

Peak (QWI) has the full width at half maximum of 11 meV at 77 K, and keeps its shape up to 220 K which shows the stability of 1D excitons in the QWI. It is also noteworthy that despite the small wire volume which occupies only the 1% of the patterned area, the intensity of peak (QWI) is as strong as other peaks. These facts mean the good quality and uniformity of this QWI structure and the efficient diffusion of electrons and holes from the AlGaAs barrier or S-QW into the QWI. Time resolved PL measurement for this sample revealed the smaller temperature dependance of radiative lifetime ($\tau \propto T^{1/2}$) than that of a reference QW ($\tau \propto T$), which is attributed to the sharp density-of-state function of 1D excitons [24].

We have examined the shape of the ridge structure and the quantum levels in the respective QWI and QWs. The detailed discussion is given in Ref. [23]. The conclusion is that the lowest state of QWI is lower than that of S-QW because of the enhanced growth rate at the ridge region. The observed thickness of S-QW (≈ 4 nm) is close to the value expected from PL energy. For the B-QW, incoming Ga flux to the bottom of the trench is partially interrupted by the adjacent mesas. Hence, the lowest energies B-QW is expected to be higher than that of S-QW.

For the quantitative discussion, we have calculated the energy levels of electrons and heavy holes for the QW structure formed on the ridge by using the finite element method. The structure was approximated as the region bounded by the two functions $F(z)$ and $G(z)$, where $F(z) = \sqrt{2}\, b \log_e\{\cosh(z/b)\}$, $G(z) = F(z) + L_z$. The parameter b defines the sharpness of the ridge and is assumed to be 8, 10, 12 nm. Figure 3 shows the calculated total quantization energies for the lowest states of QWI (open circles), S-QW (solid line), and QW (dashed line) on a flat (001) plane as a function of the QW width L_z in the direction of (001). Here the excitonic effects are ignored. Note that the 1st quantized level of QWI is lower than that of the S-QW and this supports reasonable lateral confinement in ridge QWI structures. On the other hand, these levels are above those of the QW on flat (001) substrate which indicate that the quantized state by the narrow effective ridge width W_z. The shape of the ridge affect the level of QWI. The level of QWI decreases with the increase of W_z, which is indirectly set by value of b and L_z, and gradually approaches the level of QW on flat (001). The calculated value of 63 meV was obtained for L_z = 9 nm and b = 10 nm (W_z = 17 nm), and these sizes are estimated from the TEM (fig. 1(a)). This agrees well with the energy 64 meV of the peak (QWI) measured relative to the GaAs bulk. The detailed discussion will be found in Ref. [21].

For sample B, PL measurements were carried out at 77 K by focusing Ar$^+$ laser light into 200 μm spot size. Measured PL spectrum is shown in Fig. 4(a), where the large peak at 1.62 eV and the small peak at 1.51 eV from GaAs bulk are clearly seen. As a reference, the PL spectrum from the QW grown simultaneously on a flat (001) substrate is shown by the dashed line with its peak located at 1.65 eV. The energy of the dominant peak is 30 meV lower than that of the reference QW. The origin of this PL peak has been also identified by CL measurement. Figure 4(b) shows the cross-sectional scanning electron microscope (SEM) image of sample B. Figure 4(c) shows the super imposed mapping of CL intensities on the SEM image of fig. 4(b), measured at the photon energy corresponding to the 1.62 eV PL peak. Figure 4 (b) and (c) clearly indicate that the peak comes exactly from the top region of the ridge, where the QWI is formed. The quantization energy of this QWI is 110 meV, which is larger than that of sample A. In contrast to sample A, we observed no PL from S-QW nor B-QW. This is because the width of those QWs get so thin that the lowest states of the QWs exceed the X valley energy in the conduction band of AlAs (type II QW). In fact, the lowest state of the S-QW of 2 ~ 3 nm thick is expected to be about 300 meV above the GaAs band edge which is higher than the X - valley energy in AlAs [25, 26]. The lowest state of B-QW is expected to be higher than or at least equal to that of S-QW, because the width of the B-QW should be thinner than that of S-QW as in sample A. Furthermore, fast diffusion of electrons and holes from S-QWs to the adjacent QWI may explain the absence of PL from S-QW [27]. The full width at half maximum of the peak from the B-QWI of sample B is 21 meV at 77 K, and is larger than that of sample A. This is likely because the fluctuation of wire size affects the energy levels strongly in the narrower QW.

4. CONCLUSION

We have demonstrated that the MBE growth on a patterned substrate provide a very sharp ridge structure and results in a QWI by which two-dimensional confinement of carriers is achieved.

We express our sincere thanks to Mr. H Yano of Sumitomo Electric Industries and Mr Y Kadoya of Quantum Wave Project for their support in SiO_2 deposition, and Prof M Tsuchiya for stimulate discussions. We also thank to Professor Y. Shiraki and Dr. S. Fukatsu for their collaboration at the Processing Center of RCAST A part of the work is supported by Grant-in-Aid for Scientific Research from the Ministry of Education, Science, and Culture, Japan

References:

1. H Sakaki, K. Wagatsuma, J Hamasaki, and S Saito, Thin Solid Films 36 497(1976)
2. H Sakaki, Jpn. J. Appl. Phys 19, L735(1980)
3. H. Sakaki, Surf Sci 267, 623(1992)
4. P. M. Petroff, A C Gossard, and W Wiegmann, Appl. Phys Lett 45, 620(1984)
5. T. Fukui and H Saito, J. Vac Sci Technol B4, 1373(1988)
6. M Tanaka and H Sakaki, Jpn J Appl Phys 27, L2025(1988).
7. L. Pfeiffer, K W West, H L Stormer, J P Eisenstein, K W Baldwin, D Gershoni, and J Spector, Appl Phys. Lett. 56, 1697(1990)
8. J Motohisa and H. Sakaki, to be pub. in the Proc of 21st Int Conf on Phys of Semicond., Beijing, August, 1992 (World Scientific)
9. E. Kapon, D M Hwang, and R. Bhat, Phys Rev Lett 63, 430(1989)
10. S Tsukamoto, Y Nagamune, M Nishioka, and Y Arakawa, J Appl Phys 71, 533(1992)
11. C S Tsai, J A Lebens, C C Ahn, A Nouhi, and K J Vahala, Appl Phys Lett. 60, 240(1992)
12. S Tsukamoto, Y Nagamune, M Nishioka and Y Arakawa, Appl Phys. Lett. 62, 49(1993)
13. K Kojima, K Mitsunaga, and K Kyuma, Appl Phys. Lett 55, 882(1989)
14. T Fukui and S Ando, Electron. Lett. 25, 410(1989)
15. Y Nakamura, S Koshiba, M Tsuchiya, H Kano, and H Sakaki, Appl Phys Lett 59, 700(1991)
16. S Koshiba, Y Nakamura, M. Tsuchiya, and H Sakaki, unpublished
17. X Q Shen, M Tanaka, and T Nishinaga, Proc Alloy Semiconductor Physics and Electronics Symposium, Japan (ASPEcs)-11, 333(1992)
18. M Hata, T Isu, A. Watanabe, and Y Katayama, J Vac Sci Technol B8, 692(1990)
19. M Kawashima and Y. Horikoshi, Jpn J Appl Phys. 27, L483(1988)
20. K. Wada, A Koren, H Fushimi, and N Inoue, Jpn J Appl Phys 27, L1952(1988)
21. T Inoshita, S Koshiba, H Akiyama, H. Noge, and H Sakaki, unpublished
22. S Koshiba, H Noge, H Akiyama, Y Nakamura, A Shimizu, and H Sakaki, Inst Phys Conf. Ser 129 (IOP Publishing, Bristol, 1993), p 931
23. S Koshiba, H Noge, H Akiyama, T Inoshita, Y Nakamura, A Shimizu, H Sakaki and K Wada, unpublished. (submitted to APL)
24. H. Akiyama, S Koshiba, T Someya, K. Wada, H Noge, Y Nakamura, T Inoshita, A Shimizu and H. Sakaki, unpublished. (submitted to PRL)
25. S H Wei and A Zunger, J Appl Phys 63, 5794(1988)
26. G Bastard, J A Brum, and R Ferreira, Solid State Phys 44 229(1991)
27. M Walther, E Kapon, D M Hwang, E Colas, and L. Nunes, Phys Rev B 45 6333(1992)

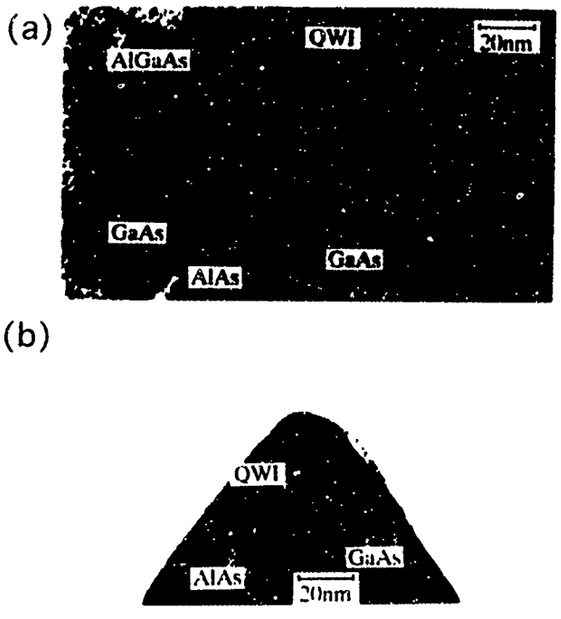

FIG. 1. Transmission electron micrographs of the cross-section of the ridge structures of sample A (a) and sample B (b) The dark line running obliquely in the upper right corner in fig (a) is a dislocation

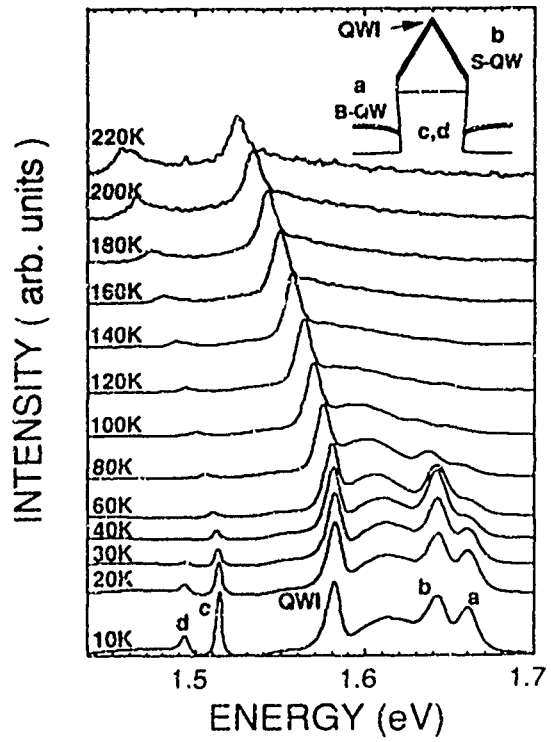

FIG. 2. Photoluminescence spectra measured at various temperatures excited by He-Ne laser for the QWI and QWs formed on ridge structure (sample A). The peaks are assigned as PL from ridge quantum wires (QWI), bottom quantum well (B-QW) (a) side quantum well (S-QW) (b) and bulk GaAs (c,d)

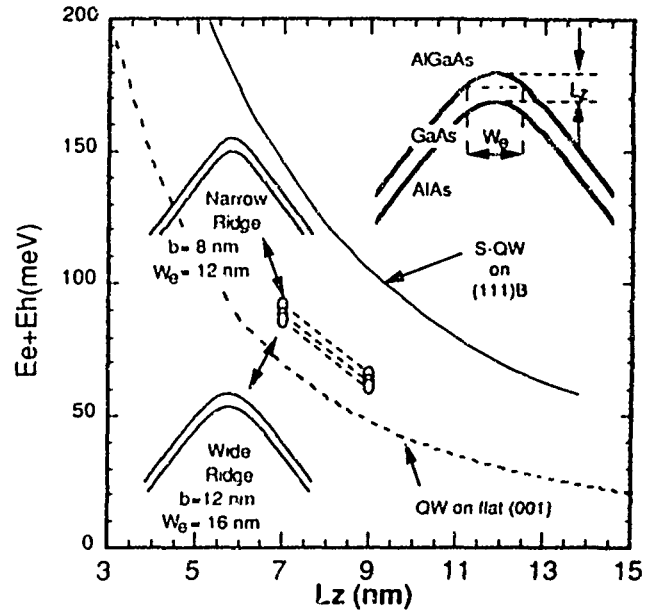

FIG. 3. The total quantization energies of electrons and heavy holes calculated for the lowest states in QWI are shown by open circles, those of S-QW by solid line, and those in reference QW by dashed line as a function of the QW thickness L_z and the width W_e (in lateral direction)

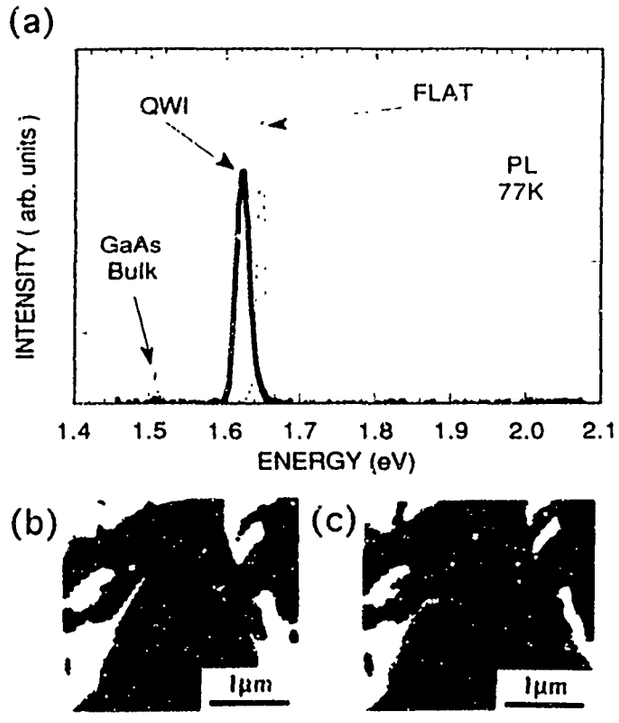

FIG. 4. (a) Photoluminescence spectrum of sample B measured at 77K. Shown by the dashed line is the spectrum of the reference QW grown on a flat (001) wafer. (b) Cross-sectional SEM image of the ridge structure of sample B. (c) Super imposed CL intensity mapping on the SEM image of fig. (b).

MoC2

Control of Interface Composition in InAs/GaSb Superlattices

B.R. Bennett, B.V. Shanabrook, R.J. Wagner,
J.L. Davis, J.R. Waterman, and M.E. Twigg
Naval Research Laboratory,
Washington, DC 20375-5347

ABSTRACT

The GaSb/InAs materials system, with two species of both cations and anions, permits the construction of heterostructures with either InSb- or GaAs-like interfaces. As a result, this system provides a unique opportunity to explore the limits of interfacial control that can be achieved by vapor phase growth techniques. We have characterized a series of superlattices (SL's) prepared with both types of interfaces by x-ray diffraction, Raman spectroscopy, transmission electron microscopy, and photoconductivity. The large differences in bond lengths, electronic properties, and vibrational properties of InSb and GaAs interfaces allow these techniques to be sensitive probes of interfacial structure. By carefully measuring and minimizing the group V cross contamination in the SL layers, we are able to unambiguously demonstrate the growth of SL's with almost pure InSb-like or GaAs-like interfaces.

INTRODUCTION

Semiconductor heterostructures containing both As and Sb are of increasing interest for device applications. For example, the combination of a large conduction band offset for AlSb/InAs heterojunctions and the high mobility of InAs has been exploited in the design of high speed transistors [1]. In addition, the staggered band line up and resulting small effective energy gap of InGaSb/InAs strained layer superlattices (SL's) may make this system suitable for use in infrared detectors [2, 3]. Very thin layers are often required to achieve the desired absorption characteristics in the SL's. Hence, interfaces will be a substantial fraction of the heterostructures and are expected to strongly affect optical and electrical properties.

In the case of heterojunctions in which both the cation and anion change, the interfacial structure can be varied. For example, in an InAs/GaSb structure, interfaces with either InSb-like bonds or GaAs-like bonds (or a mixture) can be envisioned. Hence, these material systems are excellent candidates for basic studies of interfacial control in epitaxial growth. In this article, we report studies of InAs/GaSb superlattices grown by molecular beam epitaxy (MBE). By carefully measuring and minimizing the group V cross contamination in the SL layers, we are able to prepare SL's with almost pure InSb-like or GaAs-like interfaces. The differences in interfacial stoichiometry are shown to affect the structural, vibrational, and electronic properties of the SL's.

EXPERIMENTAL PROCEDURES

Epitaxial growth was carried out on a solid source MBE system equipped with a valved As cracker. The substrates were 50 mm, epi ready semi insulating, (001) GaAs wafers. After oxide desorption, about 0.3 μm of GaAs was grown at 580 C using As_4. Next, the substrate temperature was lowered to 430 C and a 1.0 μm buffer layer of GaSb was grown with the temperature increasing to 500 C during growth [1]. Then, the substrate temperature was decreased to 400 C and the InAs/GaSb superlattice was grown using As_2 and Sb_4. Growth temperatures were determined by infrared transmission thermometry and are believed accurate to within 20 C [1]. Growth rates were calibrated by reflection high energy electron diffraction (RHEED) oscillations. As explained below, for most samples we chose growth rates of 0.35 monolayers (ml)/s for GaSb and 0.14 ml/s for InAs.

We grew 40 period superlattices with nominal structures of 8 ml InAs/ 12 ml GaSb, and 1 ml InSb or GaAs (designated as 8/12/1), as well as 8/8/1 and 12/8/1. The nominal interface type was varied by using the techniques of migration enhanced epitaxy [5, 6]. For example, to obtain a GaAs interface on GaSb, the Sb shutter is closed at the end of the GaSb layer. The Ga shutter remains open for another 2.2 s to deposit an additional monolayer of Ga. Next, the Ga shutter is closed and the As shutter opened for a 4 s soak to saturate the Ga with As. Then, the In shutter is also opened and InAs is grown.

Structural properties of the SL's were measured by x-ray diffraction (XRD), using theta/two theta scans and Cu $K\alpha_1$ radiation. Raman spectroscopy (RS) was applied to evaluate the vibrational properties. RS measurements were taken at ~10 K in the Z(X,X)Z and Z(Y,X)Z configurations where Z and Z are the directions of the incident and scattered light. (',') denote their polarizations, and X, Y, and Z denote the [100], [010] and [001] crystallographic directions, respectively. Radiation from an Ar ion laser operating at 514.5 nm was employed in the measurements. Specimens were prepared for high resolution transmission electron microscopy (HRTEM) by mechanically thinning a cross sectional sample which is then subjected to Ar^+ beam milling on a stage cooled by liquid nitrogen. Both [100] and [110] oriented cross sections were imaged on a Hitachi H-9000NAR microscope operating at 300 kV.

RESULTS AND DISCUSSION

Due to transients, the flux of an element incident on a sample will not immediately drop to the background levels when its shutter is closed. Based upon ion gauge beam equivalent pressure (BEP) measurements, this problem is most severe for As. In the case of InSb like interfaces on InAs, there is a total of 12.7 s (7.7 s of In and 5 s of Sb) between the closing of the As shutter of InAs and the opening of the Ga shutter for GaSb. In the case of GaAs like interfaces, however, there is only a 2.2 s interval (deposition of 1 ml of Ga) between As and GaSb. To reduce GaSb contamination by As flux transients, we interrupted growth for 40 s after the As shutter was closed during each InAs to GaSb transition for sample A, an 8/8/1 SL with GaAs like interfaces. Except for the growth interrupt, sample B was grown under identical conditions. The (001) diffraction peaks for the n = 1, 0, and −1 SL satellites as well as the GaSb buffer layer are shown in fig. 1. The position of the n=0 peak is related to the average lattice constant of the SL via Bragg's law. The fact that sample A has a smaller Bragg angle than sample B means that its average lattice constant is larger. The average lattice constant of the SL is a function of the InAs and GaSb layer thicknesses,

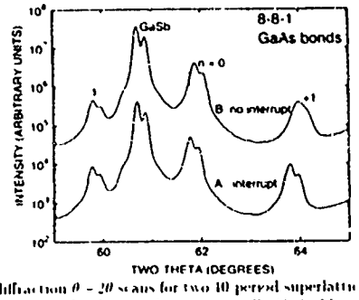

Figure 1. X-ray diffraction $\theta - 2\theta$ scans for two 40 period superlattices. Each period consists of 8 ml InAs and 8 ml GaSb, along with two nominally GaAs like interfaces. Sample A was grown with a 40 s growth interrupt (see text). Sample B was grown without the interrupt. SL satellite peaks and the GaSb buffer peak are visible. The curves are offset for clarity.

the composition of the interfacial layers, and the actual composition of the nominally InAs and GaSb layers. It seems unlikely that the layer thicknesses or InAs composition would be a function of growth interrupts. The nominally GaSb layer, however, could contain As. If so, we would expect more As contamination in sample B (no interrupt). The lattice constant of GaAs is 5.6533 Å compared to 6.0954 Å for GaSb. Hence, As contamination of the GaSb will reduce the average SL lattice constant, as observed. Based upon these results, we used the 40 s interrupt on all subsequent GaAs bonded SL's.

Cross contamination can also result from the background pressure of the group V elements. The background pressure of an element is related to its cell temperature as well as the pumping efficiency of the MBE system. As a test, we grew two 8/8/1 SL's with nominally InSb like interfaces. Different antimony cell temperatures were used, resulting in BEPs of 7 and 11 × 10^{-7} for samples C and D, respectively. Sample D has an n=0 SL Bragg angle (not shown) which is 470 arc sec smaller than C's, translating to a lattice constant which is 0.024 Å larger. This can be explained by "InAs" layers in D with a composition of $InAs_{0.9}Sb_{0.1}$. The cross-contamination of As in GaSb layers was even more severe. To reduce it, we grew our SL structures at relatively slow growth rates and used the lowest As and Sb cell temperatures which provided anion rich surfaces. Based upon RHEED reconstruction patterns and uptake oscillations, we estimate our V/III flux ratios to be between 1.0 and 1.5. Using XRD measurements of thick layers of InAs and GaSb grown under SL conditions, we estimate that the As contamination in GaSb is about 1% (e.g. $GaSb_{0.99}As_{0.01}$), and the Sb contamination in InAs is 0.5% or less [7].

With group V cross contamination minimized, we are now in a position to quantify our ability to control interface type. In fig. 2 we show the XRD data for two superlattices with 40 periods of 8 ml InAs and 12 ml GaSb. Sample E was grown with nominally GaAs like interfaces and F was grown with InSb like interfaces. First, we note that both samples exhibit several SL satellite peaks, indicating reasonably good crystalline quality. $K\alpha_1$, $K\alpha_2$ splitting is observed for some peaks. For simplicity, we reference the SL peak positions to

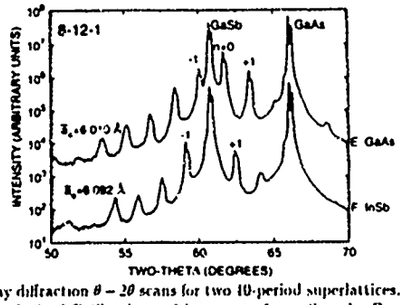

Figure 2. X ray diffraction $\theta - 2\theta$ scans for two 40-period superlattices. Each period consists of 8 ml InAs and 12 ml GaSb, along with two interfaces. Samples E and F were grown with nominally GaAs like and InSb-like interfacial bonds, respectively. SL satellite peaks, as well as the GaSb buffer and GaAs substrate peaks, are visible. The curves are offset for clarity.

the GaSb buffer peak. (Almost identical results are obtained if the GaAs substrate peak is used as the reference.) The n=0 SL peak for sample E is at a relative Bragg angle, $\Delta\theta$, of +1728 arc sec, giving an average lattice constant of 6.018 Å. For sample F, the n=0 peak is obscured by the GaSb buffer peak. However, we can estimate its position from the n= -1 and n= +1 peaks. We obtain $\Delta\theta$ = +68 arc sec, corresponding to 6.092 Å. We can also determine the SL period from the separation between satellite peaks [8]. For samples E and F, we obtain a period of 60.82 Å and 62.80 Å, respectively. These values are somewhat smaller than the theoretically predicted periods: 61.62 Å (E) and 63.95 Å(F).* The discrepancies of 3-5% may result from flux non-uniformities across the wafer.

We now compare our observed changes in lattice constant with interface type to theoretical predictions. In table 1, we list our measured $\Delta\theta$'s along with the theoretical values for all six structures studied. The $\Delta\theta_{th}$ values are based upon the dynamical theory of x-ray diffraction[9], assuming the nominal thicknesses and interface types, no cross-contamination, and no lattice relaxation in the SL with respect to the GaSb buffer. Our experimental values are always higher than the theory. These discrepancies can be reduced if we assume $GaSb_{0.97}As_{0.03}$ layers instead of pure GaSb. To estimate changes in interfacial composition we can look at the amount by which $\Delta\theta$ changes with bond type. In table 1, we show the differences in $\Delta\theta$ for the two types of interface bonds along with the percent change in bond type which we define as

$$\%\ change = \frac{\Delta\theta_{expt\,GaAs\text{-}like} - \Delta\theta_{expt\,InSb\text{-}like}}{\Delta\theta_{theo\,GaAs\text{-}like} - \Delta\theta_{theo\,InSb\text{-}like}} \times 100 \qquad (1)$$

The measured SL period was always less than or equal to the predicted period, with differences as large as 4 Å. By definition, each of the interfacial layers cannot be less than 0.5 ml thick. The InAs and GaSb layers, however, could be somewhat thinner than the nominal

* These predictions are based upon linear elastic theory, assuming coherent layers with the in-plane spacing fixed by the relaxed GaSb buffer layer.

Table 1. Comparison of experimental and theoretical n=0 SL peak position in XRD of InAs/GaSb superlattices. $\Delta\theta$ values are in units of arc seconds.

Sample	Structure	$\Delta\theta_{th}$(")	$\Delta\theta_{expt}$(")	% Change[1]	% Change[2]	% Change[3]
F,P	8-12-1 InSb	100	+68			
E	8-12-1 GaAs	+1470	+1728			
	Difference	1570	1660	106	100	103 ±6
C	8-8-1 InSb	130	36			
A	8-8-1 GaAs	+1820	+1926			
	Difference	1950	1962	101	95	98 ±6
O	12-8-1 InSb	+180	+238			
N	12-8-1 GaAs	+1770	+1890			
	Difference	1590	1652	101	99	101 ±6

[1] Assumes all monolayers are present (e.g. 8-8-1)
[2] Assumes one monolayer is missing (e.g. 7-8-1 or 8-7-1)
[3] Average value; error bar includes experimental errors in $\Delta\theta$

values. If, for example, the InAs thickness in a nominal 8-8-1 structure is really only 7 ml, then the interfaces are a larger fraction of the SL, and the predicted change in $\Delta\theta$ will be larger. We assumed a missing ml (or 3 Å) in determing $\Delta\theta_{th}$ for the % Change[2] column in table 1. The % Change[3] column is an average of the other two values, with estimated errors in $\Delta\theta_{expt}$ included in the uncertainties. For all three structures (8-8-1, 8-12-1 and 12-8-1), we are able to change the interfacial bonding by about 100%.

Raman scattering spectra for five 8-8-1 SL's, taken in the Z(Y,N)Z configuration at ~10 K, are shown in fig. 3. The large peaks at about 236 cm^{-1} result from the quasi-confined longitudinal optic (LO) phonon modes of InAs and GaSb [10]. In sample A (nominal GaAs bonds), we observe a second peak at 254 cm^{-1}. We see no evidence of this peak in the SL with nominally InSb like interfaces, sample K. The 253 cm^{-1} feature is also present in the 8-12-1 and 12-8-1 SL's with GaAs bonds, and absent in the 8-12-1 and 12-8-1 SL's with InSb bonds [5]. We attribute this peak to GaAs interfacial vibrational modes. We conclude that, to within the resolution of our Raman measurements, GaAs bonds are not present in the nominally InSb samples.

Although it is not obvious in fig. 3, we always observe a weak shoulder near 213 cm^{-1} when higher resolution Raman data is taken on our SL's. We associate this peak with the 1% As contamination in the GaSb layers. XRD data taken on sample J, grown under an excess As background, yields about 2% As in the GaSb. In fig. 3, we see that the contamination peak is the largest feature and has shifted to higher energies, as expected for the two mode behavior of GaAsSb [11].

Superlattice H was grown with no attempt to control the interface stoichiometry. The Ga and Sb shutters were closed at the same time the In and As shutters were opened and vice versa. The XRD data shows an n=0 SL peak between that of sample A (GaAs bonds) and sample K (InSb bonds), suggesting a mixture of interfacial bonds for sample H. This result is confirmed by the Raman measurement which reveals a GaAs interfacial mode which is shifted toward lower energies. A study of a series of samples with controlled but mixed interfaces revealed a clear correlation between the energy of the GaAs interfacial mode and

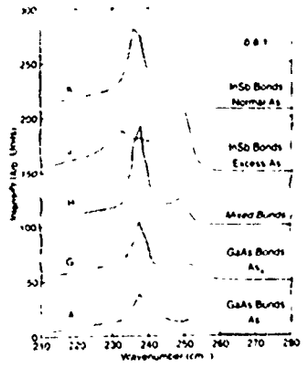

Figure 1 Raman scattering data at ~10 K with the Z(X,Y)Z geometry for five 8 8 1 superlattices. The curves are offset for clarity.

the interface composition [12].

Normally, we use a temperature of 875 C for the As cracker zone, resulting in primarily As_2. For sample G, however, the As zone was set at 800 C, resulting in an As_4 beam on the sample. The nominal bond type was GaAs. Several satellites are visible in the XRD data, demonstrating that a superlattice was achieved. The Raman scattering data are almost identical to those of sample A. We conclude that InAs/GaSb SLs can be grown with uncracked As_4, contrary to an earlier report [13].

Raman measurements taken in the Z(X,X)Z configuration (not shown) reveal both LO phonons at higher energies (200–300 cm^{-1}) and folded longitudinal acoustic phonons at lower energies (< 100 cm^{-1}). These Satter modes result from the additional periodicities imposed by the superlattice. SL period, calculated from their energies are in good agreement with the XRD results [6].

Using HRTEM, we observed apperent differences in the interfaces in sample N (12 8 1 GaAs bonds) and sample O (12 8 1 InSb bonds). To ensure that the differences were not an artifact of imaging conditions, we grew sample L, a 30 period 8 8 1 structure with InSb interfaces for the GaSb to InAs transition and GaAs interfaces for the InAs to GaSb transition. A [110] oriented cross sectional image is shown in fig. 4. About three periods of the SL are visible. The GaAs interfaces are consistently brighter than the InSb interfaces. We also note that the GaAs interfaces appear to extend over about three monolayers. We speculate that this results from the fact that we are imaging through many atomic planes. Any roughness or steps in the structure would broaden the observed interfaces.

Interfacial bond type has also been reported to influence electronic properties in the InGaSb/InAs[5] and AlSb/InAs[14] materials systems. We performed photoconductivity measurements at 77K on seven InAs/GaSb SLs. The effective band gaps were estimated from the photocurrent turn on point. The results are shown in table 2. For each of the three

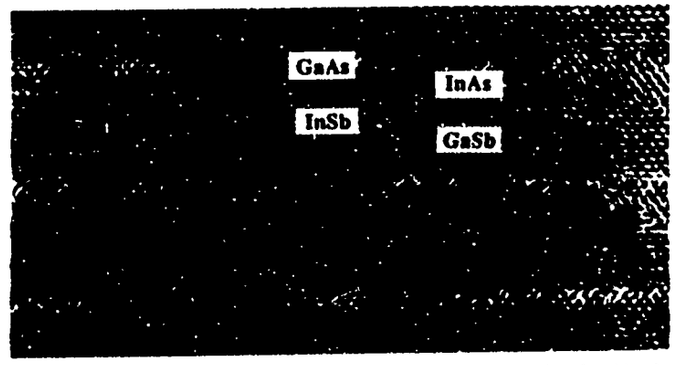

Figure 4 Cross sectional [110] TEM image of sample L with alternating interfacial bonds. The GaAs like interfaces always appear brighter than the InSb-like interfaces.

structures, the InSb bonded SL has a smaller band gap than the GaAs-bonded sample, as expected. The differences range from 18-20 meV (8 12-1 and 12 8-1) to 40 meV (8 8 1).

CONCLUSIONS

Using migration enhanced epitaxial techniques, we varied the interface composition of InAs/GaSb superlattices. After minimizing group V cross contamination, we demonstrated that structures with almost pure InSb like and GaAs like interfaces were achieved. The interface composition strongly affects the structural, optical, and electrical properties of these superlattices.

Table 2 Effective energy gaps for InAs/GaSb superlattices, measured by photoconductivity.

Sample	Structure	Interface	77K Energy Gap (eV)
N	8 8 1	GaAs	0.253
L	8 8 1	InSb	0.236
M	8 8 1	InSb	0.209
N	12 8 1	GaAs	0.161
O	12 8 1	InSb	0.141
E	8 12 1	GaAs	0.281
F	8 12 1	InSb	0.266

Acknowledgments. This work was done while B R B held a National Research Council NRL Research Associateship. The work was supported in part by the Office of Naval Research. The authors thank M. Tatum for the use of an x-ray diffractometer.

References

[1] C. R. Bolognesi, J. D. Werking, E. J. Caine, H. Kroemer, and E. L. Hu, *IEEE Electron Dev. Lett.* **14**, 11 (1993).

[2] D. L. Smith and C. Mailhiot, *J. Appl. Phys.* **62**, 2545 (1987).

[3] D. H. Chow, R. H. Miles, J. N. Schulman, D. A. Collins, and T. C. McGill, *Semicond. Sci. Technol.* **6**, C47 (1991).

[4] B. V. Shanabrook, J. R. Waterman, J. L. Davis, and R. J. Wagner, *Appl. Phys. Lett.* **61**, 2338 (1992).

[5] D. H. Chow, R. H. Miles, and X. F. Hunter, *J. Vac. Sci. Technol.* **B10**, 888 (1992).

[6] J. R. Waterman, B. V. Shanabrook, R. J. Wagner, M. E. Yang, J. L. Davis, and J. P. Omaggio, *Semicond. Sci. Technol.* **8**, S406 (1993).

[7] B. R. Bennett, B. V. Shanabrook, R. J. Wagner, J. L. Davis, and J. R. Waterman, *Appl. Phys. Lett.* **63**, (16 Aug 1993).

[8] V. Swaminathan and A. T. Macrander, *Materials Aspects of GaAs and InP Based Structures*, p. 205, Prentice Hall, Englewood Cliffs, NJ (1991).

[9] Program RADS from Bede Scientific, using the following values of lattice constant and Poisson's ratio: GaAs 5.65325 Å, 0.311; InAs 6.0583 Å, 0.352; GaSb 6.0951 Å, 0.313; InSb, 6.4788 Å, 0.353.

[10] C. López, R. J. Spreeuw, R. J. Nicholas, P. J. Walker, N. J. Mason, and W. Hayes, *Surface Science* **267**, 176 (1992); I. Sela, E. A. Samoska, C. R. Bolognesi, V. C. Gossard, and H. Kroemer, *Phys. Rev. B* **46**, 7200 (1992), and M. Inoue, M. Yano, H. Furuse, N. Nasu, and Y. Iwai, *Semicond. Sci. Technol.* **8**, S121 (1993).

[11] D. W. Taylor in *Optical Properties of Mixed Crystals*, p. 35, Elsevier Science, The Netherlands (1988).

[12] B. V. Shanabrook, B. R. Bennett, and R. J. Wagner, submitted for publication.

[13] R. Lasher, T. F. Zhorowski, T. D. Golding, H. D. Shih, P. C. Chow, K. Matsuuchi, B. C. Covington, X. Chu, J. Zheng, and H. F. Schnake, *J. Cryst. Growth* **111**, 677 (1991).

[14] G. Tuttle, H. Kroemer, and J. H. English, *J. Appl. Phys.* **67**, 3032 (1990).

MoC3

Lateral piezoelectric fields - a universal feature of strained III-V and II-VI semiconductor heterostructures

Matthias Ilg and Albert Heberle
Max Planck Institut für Festkörperforschung, D-70506 Stuttgart, Germany

Klaus H. Ploog
Paul Drude Institut für Festkörperelektronik, D-10117 Berlin, Germany

Strained II-VI and III-V semiconductor heterostructures in general are expected to have a piezoelectric polarization with a non-zero component in the plane of the interfaces which generates lateral piezoelectric fields. We use InAs structures synthesized on vicinal (110) GaAs surfaces as a model system to study such fields for the first time. These lateral fields manifest themselves in strong blueshifts of the photoluminescence peaks and an energy dependence of the radiative lifetime. Our experiments unambiguously prove the existence of these electric fields and furthermore demonstrate their tremendous impact on the electronic and optical properties of our InAs/GaAs samples.

Strong piezoelectric fields have been shown to exist in strained III-V and II-VI semiconductor heterostructures with non-(100) orientation[1,2,3]. These fields are generated by interface charges due to an internal polarization $\vec{P}$ which in general is expected to have a component $P_\perp$ in the plane of the interface as well as a component $P_\parallel$ along the growth axis[4]. In an **ideal** quantum well structure only $P_\parallel$ persists, the interfaces and creates piezoelectric fields whereas $P_\parallel$ remains without influence on the electronic properties of the well. A **real** heterostructure however always exhibits interface fluctuations and therefore a non-zero $P_\parallel$ will also introduce charges and thus create piezoelectric fields. Figure 1 illustrates different scenarios for the special case of a (110) oriented heterostructure. These lateral fields are present with varying magnitude in heterostructures of any orientation with the sole exceptions of the (100) and (111) cases ($\vec{P} = \vec{0}$ and $P_\perp = 0$ respectively) and therefore constitute a truely universal phenomenon. Their importance is two fold. First they significantly influence or alter the electronic properties of the above mentioned heterostructures and second they provide a means to create huge piezoelectric field effects via an appropriate lateral patterning of the interfaces. As a model system to study such effects we select the InAs/GaAs system with [110] growth axis. For this direction $\vec{P}$ is strictly perpendicular[11] to the growth axis, and therefore theoretically no piezoelectric field effects should occur. Furthermore in this case $|\vec{P}|$ has a maximum[14] and is capable of generating electric field strengths of the order of $10^6 V/cm$. We therefore expect pronounced electric field effects and simultaneously are assured that any observed effects are due to lateral piezofields only. In order to introduce a lateral structure, our samples are prepared on vicinal (110) GaAs surfaces. We first present a structural analysis of our set of (110) and (100) reference samples by high resolution double crystal X-ray diffraction (HRDXD). Then by means of an optical study using cw and time resolved photoluminescence (PL) spectroscopy we unambiguously demonstrate the presence of these lateral piezofields and their strong impact on the optical properties of our samples.

We use solid source molecular beam epitaxy (MBE) to synthesize our structures on (110) GaAs n^+ substrates with 2° misorientation towards the [111] direction. Simultaneously grown on-axis (100) structures on semi-insulating GaAs substrates serve as reference samples. The growth process is monitored *in situ* by reflection high energy electron diffraction (RHEED). Details about the growth procedure will be reported elsewhere.

the inset of Fig. 2 gives the sample structure. X-ray diffraction is performed with a double crystal x-ray diffractometer in Bragg geometry. The diffraction patterns are recorded in the vicinity of the symmetrical GaAs (220) and (004) reflections.

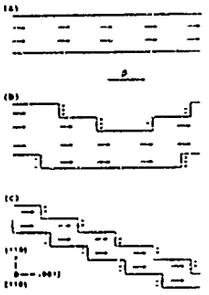

Figure 1: Impact of a lateral polarization on different quantum well geometries illustrated for the case of a (110) oriented strained heterostructure with the polarization vector $\vec{P}$ pointing in [001] direction. In an ideal heterostructure (a) we have no interface fluctuations and therefore $\vec{P}$ cannot create any interface charges. In a real heterostructure (b) however interface fluctuations always exist and therefore surface charges are introduced. Since for a strained heterostructures with general orientation $\vec{P}$ is expected to have a lateral component[4] lateral piezofields are an universal phenomenon in strained semiconductor heterostructures made from III-V and II-VI semiconductors. (c) finally demonstrates the controlled introduction of interface charges by the use of vicinal surfaces and illustrates in an idealized way the situation realized in the samples under investigation.

For the PL experiments the samples are excited at 6K by the red line (647.6 nm) of a Kr^+ laser. The emitted light is detected by a photomultiplier in the photon counting mode. Time-resolved PL experiments are carried out under pulsed excitation with an Ar^+-laser pumped Ti:sapphire laser. The emission is dispersed by a 32 cm spectrometer followed by a Hamamatsu 2D streak camera with a time-resolution of 10 ps.

We report on a set of three typical samples with different In contents. The parameters of the (110)- and the corresponding (100) reference samples are given in table I. First we direct our attention to the HRDXD spectra of the (110) samples together with reference sample #1(100) displayed in Fig. 2. For all samples we observe well defined *Pendellosung* fringes indicative of high structural quality. The increase in In content from sample #1(110) to #3(110) results - as expected - in more pronounced and a larger number of observable fringes. Finally we even observe a clearer and better defined pattern for sample #3(110) than for #3(100). Although a final assessment has to wait for a theoretical simulation of the diffraction patterns this observation clearly underlines the structural excellence of our (110) samples.

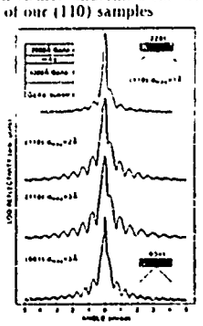

Figure 2: HRDXD patterns of all (110)- and one (100) sample taken in the vicinity of the GaAs (220) and (004)-reflections.

In order to find the first fingerprints of the expected strong internal electric fields we show in Fig. 3 the PL spectra of all investigated samples. The spectra of the (110) samples exhibit an extremely strong dependence on the excitation density whereas the (100) spectra remain virtually independent of this parameter. Therefore two spectra at different excitation densities are shown for the (110)- and only one spectrum for the (100) samples. Due to the low In content of samples #1(100) and #1(110) the respective spectra are dominated by the GaAs free exciton emission at 1.515 eV and a broad band originating in the n^+ doped GaAs substrate respectively. In addition we observe in both cases carbon related features at about 1.49 eV. For the samples with higher In content the InAs related emission is the dominating feature. The energy and linewidth of all (100) reference samples agrees very well with studies carried out previously on such structures[7].

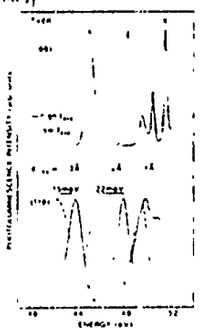

Figure 3: PL spectra for (110)- and (100) samples. For the (110) samples the spectra are taken at an excitation density of 3 mW/cm² and 30 W/cm²[5].

In which way do the internal fields manifest themselves in the PL spectra? For all (110) samples we see a clear blue-shift of the PL peak with increasing excitation density. This blue-shift ranges from a few meV in sample #1(110) where no definite value can be given due to partially superimposed carbon- and InAs related peaks - to striking 22 meV for sample #3(110). This observation contrasts with a shift of zero in the (100) reference samples and can be understood by the presence of strong internal electric fields in the (110)-samples which at larger excita-

TABLE I: Parameters of the investigated single quantum well (110)- and (100) InAs/GaAs samples. High and low excitation densities are 30W/cm² and 3 mW/cm² for samples #2 and #3[5].

sample	d_{InAs}/Å	E_{PL}/eV	low I_{PL}	high I_{PL}	FWHM/meV	low I_{PL}	high I_{PL}
#1(110)	1		1.498				
#1(100)	1		1.504	1.504		3.2	3.2
#2(110)	2		1.457	1.479		25	13.7
#2(100)	2		1.484	1.484		4.1	4.1
#3(110)	3		1.423	1.438		26.3	15
#3(100)	3		1.450	1.450		9	9

tion densities are screened out by photogenerated carriers[1]. Since lateral fields can act across larger distances than perpendicular fields they create larger potential differences and thus have a larger impact on the electronic structure. This is underlined by the fact that comparable (211)- and (311)-InAs/GaAs structures with perpendicular fields across a few Å instead of lateral fields across tens of Å as in the present case exhibit blue-shifts which range from unobservable[7] to at most a few meV [8,9]. Contrary to the case of perpendicular fields, the observed blue-shift does not increase with the quantum well thickness which indicates that the detailed microscopic configuration of the sample plays a major role.

Second - again in strong contrast to the (100) case - we observe a reduction of the PL linewidth with increasing excitation density. Since an increase of the PL linewidth with increasing electric field strength is a familiar feature of standard (100)-heterostructures under external electric fields[10] it is reasonable to assign the linewidth reduction observed here also to the screening of the internal piezoelectric fields by photogenerated carriers. With blueshift and linewidth reduction upon increase of the excitation density we thus observe two features which strongly imply the presence of internal electric fields in our (110) samples.

Because external fields are known to induce an enhancement of the radiative lifetime in (100)-heterostructures[10], it is an interesting test for our hypothesis of lateral piezofields to investigate the temporal emission characteristics of our (110) structures. Figure 4 displays the temporal evolution of the PL peak of sample #3(110) after pulsed excitation at 1.530 eV. We see a pronounced spectral diffusion of about 10 meV to the red. This finding is again in striking contrast to InAs/GaAs structures on vicinal (100) surfaces where under comparable conditions a spectral diffusion by about 2 meV to the blue was observed[6].

Two sources can contribute to this spectral red shift. The first influence certainly is the number of carriers which decreases in the course of time and leads to a less efficient screening of the internal fields. But the onset of the PL demonstrates a strong dependence of the radiative lifetime on the PL energy which also contributes to the observed spectral diffusion. For the low energy part of the PL emission we observe a purely exponential decay as it is normally seen in (100) In/Ga/As structures[6] with a decay time of 750 ps whereas for the high energy part a biexponential decay with an initially much shorter decay time of only 250 ps is observed. This difference in decay time can be understood the wavefunctions of the low energy states to be distorted by the internal electric fields. Therefore the electron hole overlap for low energy states is reduced compared to the high energy states for which the internal fields are screened out. A decrease of the overlap however increases the radiative lifetime and results in the observed variation of the lifetime with energy.

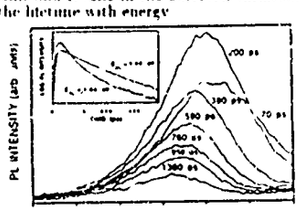

Figure 1. Transient photoluminescence spectra of the MA (110) sample after pulsed excitation at 1.51 eV. The spectra are taken at different delay times after excitation as indicated in the figure. The inset shows the time dependence of the emission spectrum integrated over the low energy ($E_{PL} < 1$ HeV) and the high energy part of the PL line ($E_{PL} > 1$ HeV) in order to reveal the energy dependence of the radiative lifetime.

The time resolved measurements thus strongly support our conclusions given above. The combination of the two spectroscopic methods therefore is a clear demonstration of the existence and importance of lateral piezoelectric fields. We point out however that at this stage we cannot give more than this qualitative demonstration. By their very nature lateral piezoelectric fields depend strongly on the actual geometry of the quantum well structure and therefore a quantitative analysis - in contrast to the case of perpendicular fields - is extremely intricate.

In conclusion we have presented spectroscopic evidence for the existence of lateral piezoelectric fields in strained III-V heterostructures. Our results demonstrate the strong and dominating impact such fields can have on the electronic properties and the relaxation kinetics of a strained III-V heterostructure with arbitrary orientation. They furthermore open up the way to novel monolithic optoelectronic devices based on piezoelectric fields introduced into a strained heterostructure by lateral patterning. Our conclusions also hold for II-VI heterostructures where even stronger effects are expected due to the one order of magnitude larger piezoelectric fields.

We would like to acknowledge the expert help of A. Fischer with MBE growth. Part of this work was sponsored by the Bundesministerium für Forschung und Technologie of the Federal Republic of Germany.

[1] C. Mailhiot and D.L. Smith, Phys. Rev. B 35, 1242 (1987).

[2] F.A. Ponce, G.B. Anderson, J.C. Chang, K.W. Goossen and J.F. Eastman, Appl. Phys. Lett. 56, 659 (1990).

[3] M.P. Halsall, J.E. Nicholls, J.E. Davies, B. Cockayne and P.E. Wright, J. Appl. Phys. 71, 307 (1992).

[4] D.L. Smith and C. Mailhiot, J. Appl. Phys. 63, 2717 (1988).

[5] For samples #1 we used 1W/cm² and 10 mW/cm² because the low In content of these samples does not allow the observation of a well defined PL peak outside of this range.

[6] O. Brandt, L. Tapfer, K. Ploog, R. Bierwolf, M. Hohenstein, F. Phillipp, H. Lage and A. Heberle, Phys. Rev. B 44, 8043 (1991).

[7] M. Hg, M.E. Alonso, A. Fehmann, K.H. Ploog and M. Hohenstein, unpublished results.

[8] M. Hg, O. Brandt, A. Ruiz and K. Ploog, Phys. Rev. B 45, 8825.

[10] H.J. Polland, L. Schultheis, J. Kuhl, E.O. Göbel and C.W. Tu, Phys. Rev. Lett. 55, 2610 (1985).

MoC4

Band Discontinuity and Effects of Si-Insertion Layer at (311)A GaAs/AlAs Interface

T. Saito, Y. Hashimoto, and T. Ikoma
Institute of Industrial Science, University of Tokyo,
7-22-1 Roppongi, Minato-ku, Tokyo 106, Japan

Abstract - We present a theoretical analysis of the valence-band discontinuity (ΔE_V) at the (311)A GaAs/AlAs interface and a possibility of ΔE_V control by Si-insertion layers. The calculation is carried out by the self-consistent tight-binding method in a $(GaAs)_8/(AlAs)_5$ (311) superlattice. ΔE_V at the (311)A interface is calculated to be 0.50 eV, while it is 0.51 eV at the (100) and (110) interfaces. The orientation independence of the ΔE_V holds for the (311)A interface. The result is consistent with our experimental results. At the (311)A interface, inserted Si double-layers can have two possible layer spacings, one is $a/4\sqrt{11}$ on an As-terminated GaAs and the other $3a/4\sqrt{11}$ on a Ga-terminated GaAs, where **a** is the lattice constant. In the former case, ΔE_V is - 0.12eV (reduced by 0.62 eV), while in the latter it is 1.67 eV (increased by 1.17 eV).

1. INTRODUCTION

A possibility to artificially control the band discontinuity at a hetero-interface by inserting group-IV element layers has been a hot issue from both scientific and application points of view [1-6]. Although the theoretical predictions [1,2] and the experiment [3] have shown that the band discontinuity is successfully controlled at the (100) GaAs/AlAs interface, Hashimoto *et al.* [4,5] have shown that the inserted Si atoms mainly act as donors and do not serve to control the band discontinuity because no interface dipole is formed. It is due to an experimental difficulty to control the occupation sites of Si atoms at the (100) interface, which is crucial in forming an interface dipole to control the band discontinuity [4,5].

On the other hand, it is known that on a (311)A GaAs substrate, Si can be both donor and acceptor depending on the growth condition [7,8] and therefore we have a higher possibility to successfully form an interface dipole and to control the band discontinuity. However, no theoretical calculation of the band discontinuity and on a possibility to control it is available on the (311)A GaAs/AlAs interface.

The purpose of this paper is to theoretically clarify, (1) how much the valence-band discontinuity (ΔE_V) is at the (311)A GaAs/AlAs interface, and (2) how much ΔE_V can be controlled by insertion of Si double-layers at the interface. The result of the former is compared with our experimental ΔE_V measured by the X-ray photoemission spectroscopy (XPS). This study is the extension of our previous calculations by the self-consistent tight-binding method [5,6].

2. METHOD OF CALCULATION

The calculation is performed on the basis of the sp^3s^* semi-empirical tight-binding Hamiltonian [9]. The parameters are taken from the values of Vogl *et al.* [9]. Spin-orbit coupling is not included. The procedure for achieving an electrostatic self-consistency is essentially the same as that used by Muñoz *et al.* [10]. In this method, the atomic orbital energies are modified with the induced electro-

static potential at the interface [10]. In the present study, we apply this method to a GaAs/AlAs (311) superlattice and deduce ΔE_v. The similar studies on (100) and (110) superlattices were presented in our previous works [5,6].

We use a $(GaAs)_6/(AlAs)_5$ (311) superlattice. The period of this superlattice along the [311] direction is $a\sqrt{11}$, where a is the lattice constant of GaAs. Each GaAs well starts at a (311)*B* face and ends at a (311)*A* face. This means that both (311)*A* and (311)*B* GaAs/AlAs interfaces are included in the superlattice. Here *A* and *B* always refer to faces *for As or Ga, not for AlAs*. We focus mainly on the (311)*A* interface because it simulates the interface formed by AlAs growth on a (311)*A* GaAs substrate.

3. BAND DISCONTINUITY AT (311) *A* GaAs/AlAs INTERFACE

Figure 1 shows the atomic arrangement (a) and the potential profile (b) at the (311)*A* GaAs/AlAs interface. The potential sawtooth-likely oscillates due to the negative and positive net charges at the anion and cation sites [10]. The dipole potential ΔV, which is defined as the difference between average potentials in AlAs and GaAs, is 0.26eV. ΔV is modified by Si-insertion layers and consequently ΔE_v can be changed as shown in Section 4.

ΔE_v at the (311)*A* (and *B*) interface is calculated to be 0.50 eV (and 0.52eV). At the (100) and (110) interfaces, it is 0.51 eV by our calculations [5, 6]. The result indicates that ΔE_v is almost constant for various interface orientations, even for high-index planes.

The apparent orientation dependence of ΔE_v was experimentally shown by Hirakawa *et al.* [11] for major low-index planes; (100), (110), and (111)*B*. The measurement was done by XPS. In the present paper, we measured ΔE_v at the (311) *A* (and *B*) interface to confirm the theoretical result. The sample structures are ; AlAs(30Å)/GaAs(1μm)/[(311)*A* n⁺-GaAs(substrate)] for the (311)*A* interface, and GaAs(30Å)/AlAs(100Å)/GaAs(1μm)/[(311)*A* n⁺-GaAs (substrate)] for the (311)*B* interface. In the latter, the (311)*B* face of the top GaAs layer forms an interface with the underlying AlAs layer. The measurement technique is the same as reported in Ref.[11]. The values of ΔE_v measured in the present study and Ref.[11] are summarized in Table 1 together with our theoretical ΔE_v's. In the experiment, ΔE_v is found to be independent of the interface orientation even in the (311)*A* (and *B*) interface, which confirms our calculation.

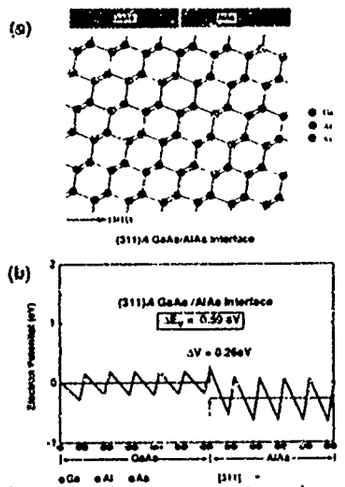

Fig.1. Atomic arrangement (a) and potential profile (b) at the (311)*A* GaAs/AlAs interface.

Table 1. Valence-band discontinuities ΔE_v (in eV) at GaAs/AlAs interfaces.

Interface	Experiment	Theory
(100)	0.44±0.05[a,b] *	0.51
(110)	0.44±0.05[a,b] *	0.51
(311)*A*	0.42,[b] 0.44[b]	0.50
(311)*B*	0.45[a]	0.52

[a](GaAs on AlAs), [b](AlAs on GaAs)
*Ref. 11)

4. EFFECTS OF Si-INSERTION LAYER ON BAND DISCONTINUITY

Si double-layers inserted at the (311)*A* interface can have the two configurations as shown in Fig 2(a) and Fig 3(a): the former is formed on an As-terminated GaAs where the first Si layer occupies Ga sites and the second does As sites with the layer spacing of $a/4\sqrt{11}$. The latter is formed on a Ga-terminated GaAs, where the occupation sites are reversed and the layer spacing is $3a/4\sqrt{11}$. An extra interface-dipole [1] is expected to be formed by these Si double-layers. In the present calculation, a lattice distortion due to the Si-insertion layer is not included.

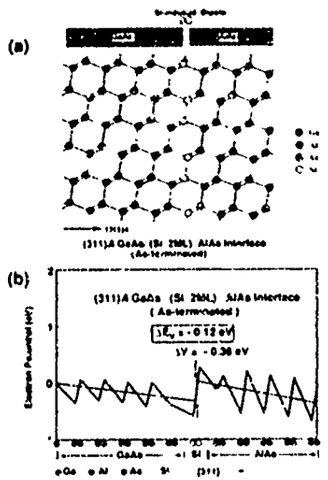

Fig.2. Atomic arrangement (a) and potential profile (b) at the (311)*A* GaAs/AlAs interface inserted with the Si double layers. GaAs is terminated at an As plane.

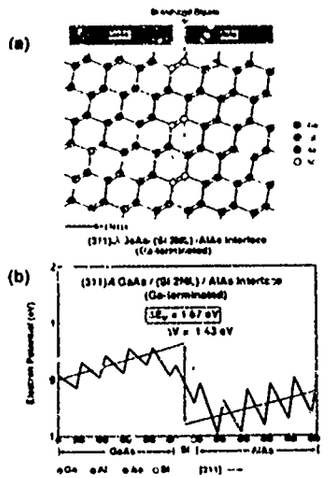

Fig.3. Atomic arrangement (a) and potential profile (b) at the (311)*A* GaAs/AlAs interface inserted with the Si double layers. GaAs is terminated at a Ga plane.

Figures 2(b) and 3(b) show the potential profiles at the (311)A GaAs/AlAs interface with the Si double-layers on an As-terminated and a Ga terminated GaAs, respectively. ΔV is -0.36 eV in the former and 1.43 eV in the latter. The change of ΔV from the original value is - 0.62 eV and + 1.17 eV, respectively. Therefore, ΔE_v with the Si double-layers is deduced as; ΔE_v = -0.12 eV on an As-terminated GaAs, and ΔE_v = 1.67 eV on a Ga-terminated GaAs. The sign of ΔE_v change depends on the polarity of the terminated plane and the magnitude mainly on the layer spacing. The gradient of the average potentials in GaAs and AlAs in Figs. 2(b) and 3(b) is an artifact caused by the periodic boundary condition of the superlattice as shown in Ref.[1,6]. This does not influence ΔE_v.

In the previous work [5], we studied the effects of Si-insertion layers at the (100) and (110) interfaces. With Si-double layers, ΔE_v is calculated to be - 1.36 eV and 2.1 eV at the As- and Ga-terminated (100) interfaces, respectively, and 0.35 eV at the (110) interface. It should be noted that an effect of Si-insertion layers on ΔE_v has a strong orientation dependence, although ΔE_v with no Si layers is almost independent of the interface orientation.

5. CONCLUSIONS

We analysed ΔE_v at the (311)A GaAs/AlAs interface and a possibility of ΔE_v control by insertion of the Si double-layers by using the self-consistent tight-binding method. The results are summarized as follows.

(i) ΔE_v at the (311)A (and *B*) interface is 0.50 eV (and 0.52 eV), while it is 0.51 eV at the (100) and (110) interfaces. The orientation independence of ΔE_v holds for the (311)A (and *B*) interface, being consistent with our experimental observation by XPS.

(ii) With insertion of Si double-layers, ΔE_v at the (311)A interface is calculated to be - 0.12 eV (reduced by 0.62 eV) and 1.67 eV (increased by 1.17 eV) on an As-terminated and a Ga-terminated GaAs, respectively. The result predicts a possibility to control ΔE_v at the (311)A GaAs/AlAs interface, on which Si can be either an acceptor or donor depending on growth conditions.

Acknowledgements- We thank Dr. K. Hirakawa for valuable discussions. This work is partly supported by the Grant-in-Aid from the Ministry of Education, Science and Culture, Japan and also by the Industry-University Joint Research Program "Mesoscopic Electronics."

REFERENCES

1. A.Muñoz, N Chetty, and R.M Martin, Phys.Rev **B41**, 2976 (1990)
2. M Peressi, S Baroni, R Resta, and A Baldereschi, Phys Rev **B43**, 7347 (1991)
3. L.Sorba, G.Bratina, G Ceccone, A Antonini, J.F Walker, M.Micovic, and A.Franciosi, Phys Rev **B43**, 2450 (1991)
4. Y.Hashimoto, G Tanaka, K Hirakawa and T Ikoma, in Proc. of *the 21st Int Conf on the Physics of Semiconductors*, p 725 (Beijing, China, 1992).
5. Y Hashimoto, T Saito, K Hirakawa, and T Ikoma, in Proc of *19th Int Symp GaAs and Related Compounds* , Karuizawa, Japan, 1992, (Inst Phys Conf Ser , No 129, p 259)

6. T Saito and T.Ikoma, Superlattices and Microstructures **12**, 81 (1992)
7. W Q Li, P.K.Bhattacharya, S H Kwok, and R Merlin, J.Appl Phys.**72**, 3129 (1992)
8. K Agawa, Y.Hashimoto, T Ikoma, T.Okumura, and S.-Q Shao, submitted to Proc.of *20th Int.Symp. GaAs and Related Compounds* , Freiburg, Germany, 1993.
9. P.Vogl, H.P Hjalmarson, and J.D.Dow, J.Phys Chem.Solids **44**, 365 (1983)
10. A.Muñoz, J Sánchez-Dehesa and F.Flores, Europhys Lett. **2**, 385 (1985), G.Platero, J Sanchez Dehesa, C.Tejedor and F.Flores, Surface Science **168**, 553 (1986)
11. K. Hirakawa, Y Hashimoto, and T Ikoma, Appl Phys Lett **57**, 2555 (1990).

MoC5

X-Ray Diffraction Analysis of GaAs/AlAs Multilayer Structures grown by Molecular Beam Epitaxy on (311) and (210) GaAs surfaces

M. A. Tagliente[a], L. De Caro[a], L. Tapfer[a], R. Nuzzi[b], A. Fischer[b], and K. Ploog[b,c]

a) Centro Nazionale Ricerche e Sviluppo dei Materiali
SS 7 per Mesagne Km 7,3 I-72021 Mesagne (Br), Italy

b) Max-Planck-Institut für Festkörperforschung
Heisenbergstrasse 1, D-7000 Stuttgart 80, Germany

c) present address: Paul-Drude Institut für Festkörperelektronik,
Hausvogteiplatz 5-7, D-10117 Berlin, Germany

Abstract

In this work, we investigate the structural properties of single and multiple AlAs/GaAs heterostructures grown on (311) and (210) GaAs surfaces by molecular beam epitaxy. The strain state and lattice deformation of epitaxial layers grown on high index surfaces is determined. The components of the strain tensor are calculated by minimizing the strain - energy density and are implemented in the normalized strain function of the Takagi-Taupin equations of the dynamical x-ray diffraction theory for distorted crystals in order to simulate the experimental x-ray diffraction patterns. Experimental results on AlGaAs single heterostructures and AlAs/GaAs multilayer structures reveal that the epitaxial layers are pseudomorphic and show a shear strain component different form zero in contrast to structures grown on (001) substrates surfaces. The measured data are in excellent agreement with the calculated strain fields.

I. Introduction

Semiconductor heterostructures grown on non singular surfaces have recently attracted much attention for fundamental reasons as well as for their potential device applications. The growth, the optical, electronic, and morphological properties of semiconductor multilayer structures grown on crystal substrates with high index crystallographic orientations have been studied extensively [1-8]. These studies show that the surface reconstruction during the growth, the surface morphology, the incorporation of impurity atoms (dopants), the bond configuration and the sticking coefficient of atoms depend strongly on the surface orientation. However, few investigations were devoted to the analysis of the structural properties of heterostructures grown on low-symmetry surfaces [9,10].

The strain state of epitaxial layers grown on high index surfaces with less than two fold symmetry has been recently determined by minimizing the strain energy density of the epitaxial structure and using the appropriate boundary conditions at the film/substrate interface [11]. These expressions have revealed the presence of a non-tetragonal type lattice deformation in epitaxial layers with low-symmetry orientations. In fact the shear strain is found to be different from zero for all surface directions except for the high symmetry (001), (110), (111) surfaces. Furthermore the shear displacement occurs normal to the direction of the highest symmetry of the interface plane. An exact knowledge of the lattice deformation is of high interest since strain fields generate electric fields in the heterostructures and affect both microscopic properties, such as the band gap and the macroscopic properties of crystals such as piezoelectric and photoelastic effects [8].

In this work, we report on a structural and strain analysis of AlAs/GaAs heterostructures grown on (311) and (210)-oriented GaAs substrates by using high resolution x-ray diffractometry (HRXRD). The components of the strain tensor are included in the normalized strain function of the Takagi-Taupin equations of the dynamical x-ray diffraction theory for distorted crystals in order to simulate the experimental x-ray diffraction patterns. A comparison between experimental and simulated diffraction patterns permit us to determine the lattice deformation and strain fields in epitaxial films [12].

II. Experimental

The HRXRD study of epitaxial layers and superlattices was performed by means of a computer-controlled high resolution double crystal x-ray diffractometer [12]. A rotating anode was used as x-ray source (λ=1.4056 nm) and an asymmetrically cut dislocation free germanium crystal was used as monochromator and collimator of the incident beam. The angular divergence of the x-ray beam incident on the specimen crystal is about 11 μrad. Sample rotation is achieved by a stepping motor and/or a piezoelectric crystal (elementary step is variable between $7*10^{-6}$ and $3.5*10^{-5}$ rads). The intensity of the diffracted x-ray beam is measured with a "wide open" NaI scintillation counter.

The GaAs/AlAs quantum wells and superlattices studied were grown by MBE simultaneously on (311) and (100), or (210) and (100) surfaces of GaAs. The growth rate for both AlAs and GaAs layers, as well as the shutter operation, were calibrated by monitoring the intensity oscillations of the reflection high-energy electron diffraction (RHEED) pattern on the (100) growth face [9].

III. Lattice Deformation

Here, we consider a coherent heterointerface between an epitaxial layer and a substrate crystal both of them of cubic symmetry. If we assume that the film thickness is much smaller than the substrate crystal, then the whole strain will occurs in the epitaxial layer and the elastic strain tensor is given by:

$$\varepsilon_{ij}(el) = S_{ij} - B_{ij} \qquad (1)$$

where $i, j = (x,y,z)$, S_{ij} is the total strain tensor and B_{ij} is the misfit tensor of the lattice parameters of the two materials. For cubic materials, the misfit tensor B_{ij} is defined as follows:

$$B_{ij} = \delta_{ij}(d_L - d_S)/d_L = -\varepsilon^*\delta_{ij}, \qquad (2)$$

where d_L and d_S is the lattice constant of the layer (L) and substrate (S), respectively, δ_{ij} is the Kronecker delta tensor, and

$$\varepsilon^* = (d_S - d_L)/d_L \qquad (3)$$

By minimizing the strain energy density starting from the commensurability constraint for coherent interface hypothesis), the elastic strain tensor components, with reference to the coordinate system of the epitaxial film, can be obtained [11]:

$$\begin{aligned}
&\varepsilon_{xx}(el) = \varepsilon_{yy}(el) = 0,\\
&\varepsilon_{yz}(el) = \{(C_{11}+2C_{12})C\varepsilon^*[C_{44}R_{14} + C(R_{11}R_{14} - R_{15}R_{16})]\}/2\Delta,\\
&\varepsilon_{xz}(el) = \{(C_{11}+2C_{12})C\varepsilon^*[C_{44}R_{15} + C(R_{12}R_{15} - R_{14}R_{16})]\}/2\Delta,\\
&\Delta\varepsilon = \varepsilon^*\varepsilon_{zz}(el) = \{(C_{11}+2C_{12})\varepsilon^*[C^2_{44} + CC_{44}(1-R_{33}) + 3C^2(T_{31}T_{32}T_{33})^2]\}/\Delta.
\end{aligned} \qquad (4)$$

where $\Delta\varepsilon$ is the tetragonal distortion, $\varepsilon_{yz}(el)$ and $\varepsilon_{xz}(el)$ are the shear strain elements, and Δ and C are given by:

$$\Delta = C_{11}(C_{44})^2 + (CC_{44}/2)(C_{11}+C_{12})(1-R_{33}) + C^2(C_{11}+2C_{12}+C_{44})(T_{31}T_{32}T_{33})^2 \qquad (5)$$

and

$$C = C_{11} - C_{12} - 2C_{44}$$

C_{11}, C_{12} and C_{44} in eqs (4) and (5) are the elastic stiffness tensor elements for crystals with cubic symmetry in the crystallographic reference system. The coefficients $R_{\alpha\beta}$ describe the transformation of the stiffness tensor elements from the crystallographic reference system to the epitaxial layer reference system, and are given by

$$R_{\alpha\beta} = T_{i1}\,T_{j1}\,T_{k1}\,T_{l1} + T_{i2}\,T_{j2}\,T_{k2}\,T_{l2} + T_{i3}\,T_{j3}\,T_{k3}\,T_{l3} \qquad (6)$$

where T_{ik} is the matrix of the transformation. Here, α and β = {1, ..,6} indicate the symmetric pairs of the indices ij and kl = {1,2,3}, respectively.

According to these relations, the unit cell of a epitaxial layer grown on high-symmetry surfaces, i.e. (100), (110) and (111), is tetragonally distorted. This means that the strain tensor ε_{ij} has only diagonal elements different from zero. On the other hand, if the film is grown on low-symmetry surfaces, the strain tensor has also shear strain components, which are different from zero. It should be noted that the axes x, y, z can be always chosen in such a way that only one component of shear strain is different from zero (either x or y should coincide with a principal axis of the strain tensor). These findings are valid for all material systems with cubic symmetry and are independent from the magnitude of lattice mismatch between the epitaxial layer and the substrate crystal. In Table I are reported the elastic shear strain component ε_{xz}(el) and the tetragonal distortion $\Delta\varepsilon$ for an epitaxial layer of AlAs grown on GaAs substrates for the crystallographic orientations under consideration. Here, the axes x and y of the epitaxial-layer reference system are chosen to obtain only one of the shear strain components different from zero [11]. It should be noted, that not only the tetragonal distortion but also the shear strain depends strongly on the lattice mismatch between epitaxial layer and substrate.

IV. X-Ray Diffraction Analysis

Double crystal x-ray Bragg diffraction experiments enables us to measure all the components of the strain tensor [12]. The position $\Delta\psi$ of the diffraction peak maximum of the film relative to the peak maximum of the substrate is given by

$$\Delta\psi(\pm,-) = \tan\theta_B\lambda\cos^2(\phi)\varepsilon_{zz}+\tan\theta_B\lambda\sin^2(\phi)\varepsilon_{xx}-2\sin^2(\phi)\varepsilon_{xz}+(\varepsilon_{yy}-\varepsilon_{xx})/2\mp\sin(2\phi)\cos(\theta_B)\varepsilon_{xz} \qquad (7)$$

where the plus sign corresponds to the glancing incidence geometry and the minus sign to the glancing exit geometry. Here ϕ is the angle between the reflection planes and crystal surface, θ_B is the *symmetrical Bragg* angle of the substrate crystal for the observed reflection and ε_{zz} is the zz component of the total distortion tensor, which contains also the relations of the structure. In the case of pseudomorphic growth, by substituting eqs. (7) for the eq. (4) we have

$$\Delta\psi(\pm,-) = \tan\theta_B\lambda\cos^2(\phi)\varepsilon_{zz}-2\sin^2(\phi)\varepsilon_{xz} = \sin(2\phi)\varepsilon_{zz}/2 \mp \sin(2\phi)\tan\theta_B\varepsilon_{xz} \qquad (8)$$

If we consider a symmetrical reflection, eq. (8) is reduced to the following

$$\Delta\psi = \tan\theta_B\varepsilon_{zz} \qquad (9)$$

Therefore, for a two-layer system film-substrate with a coherent interface we can determine both the normal strain ε_{zz} and shear strain ε_{xz} tensor components in the epitaxial layer by measuring the diffraction patterns in a symmetrical and asymmetrical reflection geometry (eqs. (8) and (9)). By this method, we can determine all the components of the strain tensor, if the principal axes are known, while in the case of a superlattice, eqs. (8) and (9) enable us to determine the average strain components of a superlattice period. Equation (7) is used for solving the Takagi-Taupin equation of the x-ray dynamical diffraction [14].

Furthermore, the angular distance $\Delta\omega$ between the satellite peaks gives the superlattice period length D

$$D \approx \lambda\,|\gamma_H| / (\Delta\omega \sin(2\theta_B)) \qquad (10)$$

where λ is the x-ray wavelength and $|\gamma_H|$ is the direction cosine of the diffracted wave. The values of the strain components and thickness of the individual epitaxial layers, which constitute the SL period, can be obtained by

the simulation of the experimental diffraction curves. The position as well as the peak hight of the satellites depends on the thickness and strain fields (strain modulation) of the individual layers. Since the strain in epitaxial structures is measured with respect to the substrate crystal, the calculated and measured strain components are related by the following expressions:

$$\varepsilon_{zz}(\text{exp}) = -\,d_L/d_S\,\Delta\varepsilon, \qquad (11)$$
$$\varepsilon_{xz}(\text{exp}) = d_L/d_S\,\varepsilon_{xz}(\text{el}).$$

However, it should be noted that for AlAs/GaAs structures the factor $d_L/d_S = 1.0014$ can be neglected due to the small lattice mismatch between the two material systems.

V. Results and Discussion

Figure 1 shows the experimental (dotted lines) and calculated (solid lines) rocking curves recorded in the vicinity of the (111) and (400) GaAs Bragg reflection for an AlAs layer, capped with GaAs, grown onto a (311) GaAs substrate. The dynamical theory in the recursive formalism has been used for the simulations. From the diffraction patterns we obtain by using eqs. (8) and (9) the lattice strain along the growth direction ε_{zz} (exp) = (2.49 ± 0.07) $*10^{-3}$ and the shear strain component ε_{xz} (exp) = (-5.6 ± 1.7) $*10^{-4}$. The considered errors in the determination of strain components are due to an error of $3.5*10^{-5}$ rad in the $\Delta\psi$ measurement. The comparison between the measured and calculated strain component values (see Tab. I) shows an excellent agreement. According to this finding we may conclude that the growth of AlAs on (311) GaAs surfaces is pseudomorphic (coherent interface), i.e. there is no in plane strain. The thickness of the AlAs epilayer and GaAs cap layer are found to be 313 nm and 7 nm, respectively, from the simulated patterns.

The lattice deformation in superlattices has been also investigated. In Fig. 2 is shown the experimental (a) and the calculated (b) rocking curves in the vicinity of the (400) reflection for an AlAs/GaAs superlattice constituted of 80 periods, grown on a (211)-oriented GaAs substrate. The SL period length determined by the angular distance between the satellite peaks is 11.6 nm. The best fit patterns have been obtained by considering an AlAs layer, 5.4 nm thick, in which the perpendicular strain is ε_{zz}(exp) = $2.51*10^{-3}$, while the GaAs layer is 6.2 nm thick and strain free. The shear strain of the AlAs layer is ε_{xz}(exp) = $-4.11*10^{-4}$ as determined from the (400) reflection measurement.

The maximum intensities of the first order satellite peaks S_{-1} and S_{+1} (see Fig. 3) are smaller than the calculated values for a perfect superlattice with ideal interfaces. Moreover, the tails of the experimental satellite peaks are much more pronounced than the calculated ones. However, the full-width at half-maximum (FWHM) of the satellite peaks is not affected and no line broadening is observed experimentally. These findings may be explained by considering an ordered interface corrugation as observed by RHEED and TEM analyses. In fact, the presence of GaAs (or AlAs) wires, whose formation is due to the interface corrugation [6,9], gives rise to a diffuse x-ray scattering observed as an increase of the tail intensities of the satellite peaks.

Figure 4 shows the experimental (dotted line) and calculated (solid line) rocking curves for the asymmetric (400) reflection of a two layer system composed of an AlAs layer and a GaAs cap layer grown onto a (210)-oriented GaAs substrate. The best fit reveals that the AlAs layer is 470 nm thick and the lattice mismatch along the growth axis is ε_{zz}(exp) = (2.38 ± 0.07)*10^{-3} and the shear strain is ε_{xz}(exp) = (3.2 ± 1.5)*10^{-4} while the GaAs cap layer is 10 nm thick and strain free. The difference between the theoretical ($2.48*10^{-3}$) and the experimental ($2.38*10^{-3}$) value of the normal strain ε_{zz} can be explained by assuming a non perfect sample surface orientation, which leads to a small descrepancy for the $\Delta\psi$ value.

Figure 5 shows the (400) experimental (a) and calculated (b) diffraction patterns recorded in the grazing incidence geometry for a (210)-oriented GaAs/AlAs superlattice constituted of 100 periods. The angular separation between the satellite peaks gives the superlattice period length of 5.74 nm. The thickness of the individual GaAs and AlAs layers were determined from the simulation and are 2.62 nm and 3.12 nm, respectively. The strain values ε_{zz}(exp) and ε_{xz}(exp) of the AlAs layers of the superlattice are found to be (2.48 ± 0.07)*10^{-3} and (-3.1 ± 1.5)*10^{-4} respectively. Comparing the experimental and calculated strain components (Tab. I) we may conclude that the epitaxial growth of AlAs on GaAs is pseudomorphic also for the (210) surface orientation. The descrepancy between the experimentally measured satellite peak intensities and

FWHM and the calculated values is due to the heterointerface roughness, which is caused by the formation pyramids on the (210) surfaces [6].

A comparison between the data obtained from AlAs/GaAs heterostructures grown simultaneously on (311) or (210) and (100) surfaces reveals that the thickness ration (in monolayers) $t_{[311]}/t_{[100]}$ and $t_{[210]}/t_{[100]}$ are 3.5 and 2.9, respectively which can be explained by the fact that the (100) surface is much more densely packed

In summary we have used high resolution x ray diffraction technique in order to measure all strain components of AlAs/GaAs quantum wells and superlattices grown on (210) and (311) surfaces The diffraction data obtained from rocking curves recorded in symmetrical and asymmetrical reflection geometries provide a detailed and complete description of the strain fields in heterostructures The measured values of the lattice strain along the growth axis and of the shear strain for both [210] and [311] orientation are in excellent agreement with the theoretical prediction for a coherent film-substrate interface Therefore, we may conclude that the analyzed AlAs/GaAs heterostructures and superlattices are pseudomorphic and there is no in plane strain at the heterointerfaces Furthermore, the deformation of the unit cells contains also a shear strain component if the epitaxial layer is grown on low-symmetry surfaces

References

[1] S Subbanna, H Kroemer and J L Merz *J Appl Phys* **59**, 488 (1986)
[2] W I Wang, R F Marks, and L. Vina, *J Appl Phys* **59**, 937 (1986)
[3] T Fukunaga, T Takamori and H Nakashima, *J of Crystal Growth* **81**, 85 (1987)
[4] Z V Popovic, M. Cardona E. Richter, D Strauch, L Tapfer, and K. Ploog, *Phys Rev* **B40** 1207 (1989)
[5] B Gil, Y El Khalil, H Mathieu, D de Paris J Massies, G Neu, T Fukunaga, and H Nakashima *Phys Rev* **B41**, 2685 (1990)
[6] R Nötzel, L. Däweritz, and K Ploog, *Phys Rev* **B46** 4736 (1992)
[7] T.F Kuech, R T Collins, D L. Smith, and C Mailhiot, *J Appl Phys* 67, 2650 (1990)
[8] C Mailhiot and D L. *Smith Rev Mod Phys* **62**, 173 (1990)
[9] R Nötzel, N N Ledentsov L Däweritz, K Ploog, and M Hohenstein, *Phys Rev* **B45** 3507 (1992)
[10] W J Bartels and W. Nijman, *J Cryst Growth* **44** 518 (1978)
[11] L. De Caro and L Tapfer *Phys Rev* **B48** (1993), in press
[12] Y P Khapachev and F N Chukhovskii *Sov Phys Crystallogr* 34, 465 (1989)
[13] L Tapfer and K. Ploog, *Phys Rev* **B40**, 9802 (1989)
[14] W.J Bartels J Hornstra, and D J W Landbek *Acta Crystallogr* **A32** 539 (1986)
[15] R Nötzel and K Ploog, *J Vac Sci and Technol* A 10, 617 (1992)

Table 1 The calculated tetragonal distortion and elastic shear strain of AlAs grown on GaAs for the [100], [210] and [311] substrate orientations

SUBSTRATE ORIENTATION	REFERENCE AXES		AlAs	
	x	y	$\Delta\varepsilon$	ε_{xy} (el)
[100]	[010]	[001]	$2.82\ 10^{-3}$	0
[210]	$[\bar{1}20]$	[001]	$2.48\ 10^{-3}$	$3.93\ 10^{-4}$
[311]	$[\bar{3}33]$	[011]	$2.51\ 10^{-3}$	$-4.11\ 10^{-4}$

Figure Captions

Figure 1 Double crystal x-ray diffraction patterns recorded in the vicinity of the (311) and (400) GaAs reflection of an AlAs epitaxial layer grown on (311) oriented GaAs substrate

Figure 2 Experimental (a) and simulated (b) diffraction patterns of an AlAs/GaAs superlattice grown on GaAs (311)

Figure 3 first order (311) satellite peaks of the AlAs/GaAs superlattice shown in Fig 2.

Figure 4 experimental (dotted line) and simulated (solid line) double-crystal x ray diffraction patterns ((408) reflection) of an AlAs layer grown on (210) GaAs.

Figure 5 Experimental (a) and simulated (b) diffraction patterns in the vicinity of the (400) reflection of an AlAs/GaAs superlattice grown on (210) GaAs

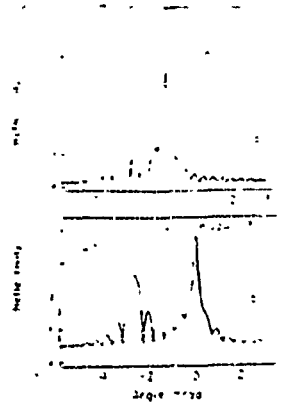

Figure 1

Double-crystal x-ray diffraction patterns recorded in the vicinity of the (111) and (311) GaAs reflection of an AlAs epitaxial layer grown on (311)-oriented GaAs substrate

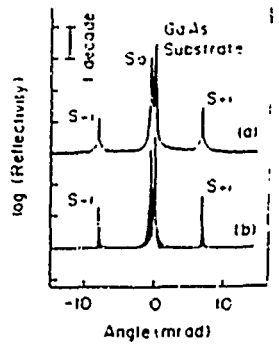

Figure 2

Experimental (a) and simulated (b) diffraction patterns of an AlAs/GaAs superlattice grown on GaAs(311)

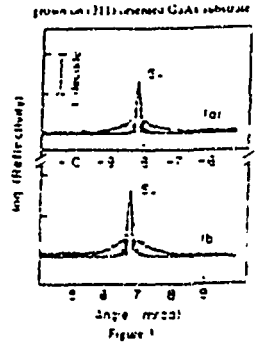

Figure 3

Experimental (a) and simulated (b) diffraction patterns of the (311) reflection of an AlAs/GaAs superlattice grown on (211) GaAs

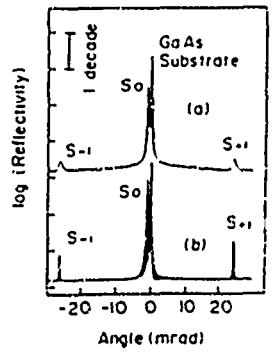

Figure 5

Experimental (a) and simulated (b) diffraction patterns of the (400) reflection of an AlAs/GaAs superlattice grown on (210)

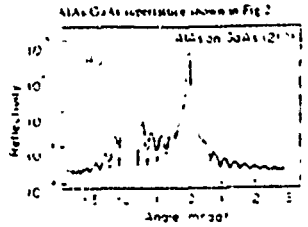

Figure 4

Experimental (dotted lines) and simulated (solid lines) double-crystal x-ray diffraction patterns of the (400) reflection of an AlAs/GaAs superlattice grown on (210) GaAs

MoC6

Folded Acoustic Phonons in GaAs/AlAs Superlattices Grown on Non-(100)-Oriented Surfaces

J. Spitzer, Z.V. Popović, T. Ruf, M. Cardona, R. Nötzel, and K. Ploog
Max-Planck-Institut für Festkörperforschung, Heisenbergstraße 1, Postfach 80 05 65, 70506 Stuttgart, Federal Republic of Germany

We present Raman spectra for folded acoustic phonons in GaAs/AlAs superlattices grown along the [111], [211] and [311] direction. The symmetry of these directions offer the possibility of observing transverse and longitudinal polarized folded acoustic phonons. The observed doublets of folded acoustic phonons are in accordance with the predicted selection rules, their frequencies and strengths are in agreement with calculations based on the continuum model. In the case of the (311)-oriented sample, folded-phonon to Brillouin ratios are calculated using elasto-optic constants of GaP in lieu of AlAs.

1 INTRODUCTION

Quantum wells and superlattices grown in directions other than [001] have generated increasing interest in the last few years [1-5]. It has been recently reported that high-quality superlattices can be grown by molecular-beam epitaxy (MBE) practically on any low-index crystallographic plane : (hkl), for h, k, l = 0, 1, 2, 3. The resulting GaAs/AlAs multilayer structures form asymmetric and symmetric quantum-dot structures on (311) and (211) GaAs, and quantum wire structures on (311) GaAs substrates [6,7]. The resulting lateral confinement of the carriers manifests itself in features such as increased exciton continuum energies or strong enhancement of the luminescence intensity compared to (100) reference superlattices [7]. Hence, this kind of structures is quite interesting for optical and electrical device applications. However, from the viewpoint of Raman spectroscopy high quality SL's grown in other directions than [001] are mainly interesting due to their symmetry properties. In contrast to superlattices grown along [001], in which only the longitudinal acoustic (LA) branch is Raman active in backscattering, samples grown along e.g. [111], [211] and [311] allow the observation of transverse and longitudinal acoustic modes.

In this paper we focus on the folded acoustic phonons of a series of GaAs/AlAs SL's grown along the directions mentioned above. The frequencies and intensities of the folded phonons are in good agreement with continuum model calculations. In the case of the [311] sample, folded phonon to Brillouin scattering ratios compare favorably with those predicted by using the elasto-optic constants of the electronically similar GaP, instead of those of AlAs which are not known.

2 EXPERIMENT

We studied GaAs/AlAs superlattices grown along the [111], [211], and [311] direction with a period between d=38 Å and d=127 Å. Details of the growth by MBE and the characterization with X-ray diffraction have been given earlier [6,7].

The Raman spectra were recorded in quasi-backscattering geometry, using a Spex Industries 1-m double-monochromator with 1800 grooves/mm holographic gratings and conventional photon counting techniques. For the [311] samples we used a SOPRA 2.12-m double-monochromator. The lines of an Ar^+-ion laser with an average power of 100 mW focused to a line were employed as excitation sources with the samples kept in vacuum at room temperature.

3 RESULTS AND DISCUSSION

The propagation properties of acoustic waves in a superlattice can be obtained from the propagation of acoustic waves in the parent material [8]. For cubic solids (e.g. GaAs), there are three directions of propagation ({100}, {110}, and {111}) along which the long-wavelength acoustic waves are purely longitudinal and transverse in character (in the {110} case only for small q, i.e. within the elastic approximation). This results for the samples grown along [111] in a purely transverse and a purely longitudinal mode, whereas the [211] and [311] samples exhibit besides pure transverse polarized modes also modes with mixed longitudinal and transverse character. The latter ones will be denoted in the following as quasitransverse (QT) and quasilongitudinal (QL). The Raman selection rules for the folded acoustic phonons of superlattices in the elastic approximation can be extracted from the Brillouin tensors of the corresponding bulk crystals [8]. The details of this procedure have been described earlier [1-5], the selection rules for all growth directions considered in this work are compiled in Table I [5,9]. The linear combinations of elasto-optic constants which contribute to the scattering in the different polarization geometries of Table I are

$$
\begin{aligned}
a &= (p_{11} - p_{12} - 2p_{44})c_0^2/3\sqrt{2} \\
b &= (p_{11} + 2p_{12} - 2p_{44})c_0^2/3 \\
c &= (p_{11} - p_{12} - 2p_{44})c_0^2/3\sqrt{2} \\
d &= (p_{11} + 3p_{12} - 2p_{44})c_0^2/3\sqrt{2} \\
e &= (p_{11} + 2p_{12} - 3p_{44})2c_0^2/9 \\
f &= (2p_{11} - 2p_{12} - 4p_{44})c_0^2/11\sqrt{2} \\
g &= (p_{11} + 10p_{12} - 2p_{44})c_0^2/11 \\
h &= (p_{11} - p_{12} - 2p_{44})3c_0^2/11\sqrt{2} \\
i &= 5c_0^2p_{12}/11\sqrt{2} \\
j &= (27p_{11} + 94p_{12} - 54p_{44})c_0^2/121.
\end{aligned}
\tag{1}
$$

Table 1: The polarization selection rules in backscattering geometry for the folded acoustic phonons of GaAs/AlAs superlattices grown along the [111], [211] and [311] direction as carried over from those of the bulk crystal. a-j are elasto-optic tensor components as described in the text.

		Polarization		Scattering cross section		
[hkl]	Configuration	Incident	Scattering	$TA_{x'}$	$TA_{y'}$	LA
[111]	$z(x'x')\bar{z}$	[110]	[110]	0	d^2	b^2
	$z(x'y')\bar{z}$	[110]	[112]	a^2	0	0
	$z(y'y')\bar{z}$	[112]	[112]	0	a^2	b^2
[hkl]	Configuration	Incident	Scattering	$T^{[011]}$	$QT^{[111]}$	$QL^{[211]}$
[211]	$z(x'x')\bar{z}$	[011]	[011]	0	c^2	d^2
	$z(x'y')\bar{z}$	[011]	[111]	c^2	0	0
	$z(y'y')\bar{z}$	[111]	[111]	0	0	e^2
[hkl]	Configuration	Incident	Scattering	$T^{[011]}$	$QT^{[233]}$	$QL^{[311]}$
[311]	$z(x'x')\bar{z}$	[011]	[011]	0	f^2	g^2
	$z(x'y')\bar{z}$	[011]	[233]	h^2	0	0
	$z(y'y')\bar{z}$	[233]	[233]	0	i^2	j^2

Figure 1 shows the Raman spectra of a (111) oriented (17,20) Å sample for all three polarizations. In agreement with the selection rules of Table I one can observe both, doublets of transverse ($TA_{x'}$) and longitudinal (LA) modes in parallel polarizations, whereas in crossed polarizations only the transverse ($TA_{y'}$) doublet is allowed. Due to the symmetry of this growth direction the transverse modes are degenerate. The upper part of Fig. 1 shows good agreement between the measured frequencies and a continuum model calculation. Comparable agreement can be achieved for the samples grown along [211], as demonstrated for a (28, 26) Å sample in Fig. 2. In contrast to the [111] sample, here the degeneracy of the transverse modes is lifted and, in accordance with the selection rules of Table I, doublets from all three acoustic branches can be observed in the various polarizations.

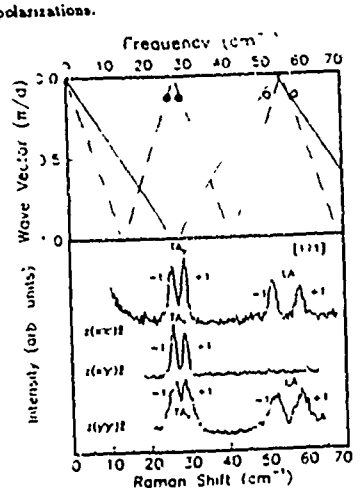

Fig.1 Raman spectra of a (111)-oriented (17 20) Å superlattice, measured at T=300 K with an excitation wavelength of 4579 Å in three different polarizations. The upper part shows the comparison of measured phonon frequencies with the continuum model ○ $z(x\,x)\bar{z}$, ● $z(x'y')\bar{z}$

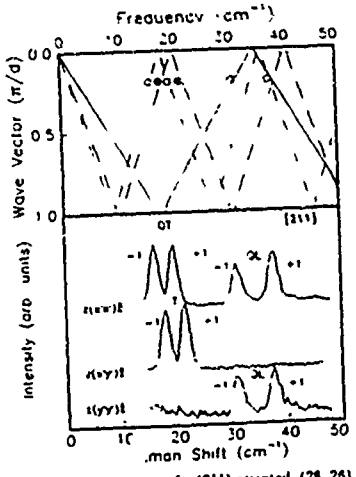

Fig.2 Raman spectra of a (211)-oriented (28, 26) Å superlattice, measured at T=300 K with an excitation wavelength of 4579 Å in three different polarizations. QL denotes the quasitransverse, QL the quasilongitudinal, and T the pure transverse mode. The upper part shows the comparison of measured phonon frequencies with the continuum model ○ $z(x'x')\bar{z}$, ● $z(x'y')\bar{z}$

We analyze next in some more detail the (311) oriented, (66,61) Å sample as typical example of the differently oriented samples we deal with in this work. Figure 3 shows the spectra of this superlattice, measured with a SOPRA 2 12 m monochromator to achieve better resolution and stronger suppression of elastically scattered light. Besides first order doublets, two weak features can be observed at 22.5 cm^{-1} and 25 6 cm^{-1}. We assign them to the third order QT doublet because of the agreement with the calculated frequencies (upper part of Fig. 3). In addition, also the QT-, QL- and T-Brillouin modes (labeled B_{QT}, B_{QL}, and B_T) are observed. The relative intensities of the folded phonons with respect to the Brillouin mode can be used, in principle, to determine the ratio of the elasto optic constants of GaAs and AlAs [10-13], using the expression

given in [10] or the more exact one in [11]. In our case, this yields the linear combinations of the elasto- optic constants contributing to the scattering intensities in the different polarization geometries, as given in Eqs (1). The accuracy obtained by applying this procedure is, however, very poor because of the small values of the elasto optic constants of AlAs in our frequency range. Whereas these constants (real and imaginary part) have been measured recently vs. frequency for GaAs [14], those of AlAs are unknown. Therefore we calculated the relative intensities of the folded phonons with respect to the Brillouin modes using the elasto-optic constants of GaP [15,16] which should be very similiar to those of AlAs in view of the fact that the band structures of both materials are nearly the same. The p_{ij} of GaAs and GaP for 4579 Å and 5145 Å are compiled in Table II. In Table III we give the experimental and calculated values for the relative intensities as the average of the m=−1 and the m=+1 modes. To account for the difference between GaP and AlAs we assume that their elasto-optic constants may differ by less than 10% (as corresponds to the differences in the relevant direct gaps). This yields an error of ≈ 1% for the calculated relative intensities. The measured and calculated values of all three intensity ratios agree then within the experimental uncertainty.

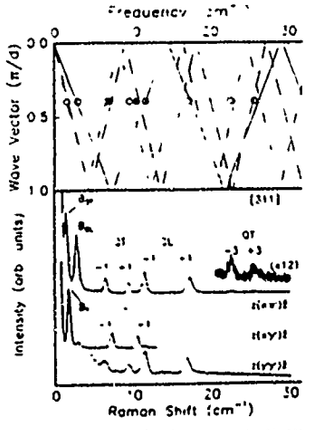

Fig.3 Raman spectra of a (311) oriented (GaAs)$_{41}$(AlAs)$_{41}$ superlattice measured with a SOPRA DILOR double-monochromator. In this case the Brillouin lines of all three branches B_T, B_{QT}, B_{QL}, as well as QT doublets up to the third order can be observed.

Table 2: Elasto-optic constants of GaAs [14] and GaP [15,16] defined as derivatives of the dielectric function (not its inverse) vs. strain.

Material	λ_L [Å]	Elasto-optic constants		
		p_{11}	p_{12}	p_{44}
GaAs	4579	115.7 − i 35.6	10.7 + i 199.1	199.7 + i 27.4
	5145	67.2 − i 28.7	11.7 + i 105.0	155.9 − i 10.7
GaP	4579	30.4	28.3	−5.8
	5145	13.9	19.9	−11.1

Table 3 Ratio of the intensities of the folded acoustic phonons to those of the corresponding Brillouin modes. The theoretical values were calculated using Eq (60) of Ref. [11] and the elasto-optic constants of GaAs [14] and GaP [15,16] (in lieu of AlAs). Both measured and calculated values represent the average of the m=−1 and m=+1 modes.

	I_m/I_B	
Acoustic mode	Experiment	Theory
Γ	0.325±0.050	0.361±0.004
QT	0.360±0.054	0.381±0.003
QL	0.360±0.054	0.380±0.001

This confirms that the elasto optic constants of GaP can be used instead of those of AlAs in the region below the direct gap E_0. The experimental values of Table III are taken from the spectra with z(x'x')z and z(x'y')z polarizations. In z(y'y')z polarizations Rayleigh scattering is stronger and the Brillouin mode could not be observed. This different behavior for both polarizations is presumably caused by the different orientation of the sample corrugation [6] with respect to the plane of incidence. However, this was the only hint of a possible influence of the corrugation on acoustic phonon spectra. A comparison of the linewidths of the folded acoustic phonons of this sample with a sample with the same thickness, but grown along [100] exhibited no differences. This is due to the fact that the acoustic waves are only sensitive to the average period of the superlattice.

4 CONCLUSIONS

We have measured folded acoustic phonons from GaAs/AlAs superlattices grown along [111], [211], and [311], respectively. In the case of the [111] samples purely transverse and longitudinal acoustic phonon modes could be observed. The [211] and [311] samples exhibit transverse (T), quasitransverse (QT) and quasilongitudinal (QL) folded acoustic phonon modes. The measured frequencies of all modes compare well with calculations based on the elastic continuum model. In the [311] sample we have also measured the Brillouin modes of all three acoustic branches and have shown that the relative intensities of the folded phonons to the corresponding Brillouin modes can be described by the elasto optic constants of GaAs and GaP.

References

† Permanent address: Paul Drude Institut für Festkörperelektronik, Hausvogteiplatz 5-7, 10117 Berlin, Germany

[1] Z.V. Popovic, J. Trodhal, M. Cardona, F. Richter, D. Strauch, L. Tapfer and K. Ploog, Phys. Rev. B 40, 1202 (1989).

[2] Z.V. Popovic, M. Cardona, E. Richter, D. Strauch, L. Tapfer and K. Ploog, Phys. Rev. B 40, 3040 (1989).

[3] Z.V. Popovic, M. Cardona, E. Richter, D. Strauch, L. Tapfer and K. Ploog, Phys. Rev. B 41, 5904 (1990).

[4] Z.V. Popovic, M. Cardona, E. Richter, D. Strauch, L. Tapfer and K. Ploog, Phys. Rev. B 43, 4926 (1991).

[5] Z.V. Popovic, J. Spitzer, F. Ruf, M. Cardona, R. Notzel and K. Ploog, Phys. Rev. B 48, 15 July 1993.

[6] R. Notzel, N.N. Ledentsov, L. Daweritz, K. Ploog, and M. Hohenstein, Phys. Rev. B 45, 3507 (1992).

[7] R. Notzel and K. Ploog, J. Vac. Sci. Technol. B 10, 2034 (1992).

[8] B. Jusserand and M. Cardona, in *Light Scattering in Solids V*, eds. G. Guntherodt and M. Cardona (Springer, Heidelberg 1989), p. 49.

[9] Z.V. Popovic, Univ. Beograd, Publ. Elektrotechn. Fak. Ser. Tek. fiz. 1, 5 (1992).

[10] C. Colvard, T.A. Gant, M.V. Klein, R. Merlin, R. Fisher, H. Morkoc, and A.C. Gossard, Phys. Rev. B 31, 2080 (1985).

[11] J. He, B. Djafari-Rouhani, and J. Sapriel, Phys. Rev. B 37, 4086 (1988).

[12] J. Sapriel, J. He, B. Djafari-Rouhani, R. Azoulay, and F. Mollot, Phys. Rev. B 37, 1099 (1988).

[13] J. He, J. Sapriel, and H. Brugger, Phys. Rev. B 39, 5919 (1989).

[14] P. Etchegoin, J. Kircher, M. Cardona, C. Grein, and E. Bustarret, Phys. Rev. B 46, 15139 (1992).

[15] F. Canal, M. Grimsditch, and M. Cardona, Solid State Commun. 29, 523 (1979).

[16] K. Strossner, S. Ves, and M. Cardona, Phys. Rev. B 32, 6611 (1985).

MoC7

Vibrational Properties of Si/Ge Superlattices: Theory and In-plane Raman Scattering Experiments

R.Schorer[1], G.Abstreiter[1], S.de Gironcoli[2], E.Molinari[2], H.Kibbel[3], and E.Kasper[4]

[1]Walter Schottky Institut, Techn. Universität München, D-8046 Garching, Germany
[2]INFM-Institute of Condensed Matter Theory (FORUM), Scuola Normale Superiore, Piazza dei Cavalieri 7, I-56100 Pisa, Italy
[3]Dipartimento di Fisica, Università di Modena, Via Campi 213/a, I-41100 Modena, Italy
[4]Daimler-Benz AG, Research Center Ulm, Wilhelm-Runge-Str.11, D-7800 Ulm, Germany

Abstract

Phonons in short-period (001)-Si_nGe_n Superlattices (SL's) have been studied both theoretically, by a first principles approach including strain and interface intermixing, and experimentally by micro-Raman spectroscopy where in-plane scattering geometries allow the observation of both longitudinal (L) and transverse (T) modes. Experimental data are found to deviate considerably from theoretical predictions for SLs with ideally sharp interfaces, both in frequency of higher-order confined Si-like modes and in the polarization dependence of the SiGe-like "interface" peak (lineshape and L-T splitting). Supercell calculations representing interface intermixing within a simple model by 2-3 monolayers of SiGe alloy at the interfaces are found to reproduce these major experimental findings. Measurements of Raman resonance profiles of various SL phonon modes strongly confirm their calculated different spatial localization.

The recent improvement of the growth technique of strained layers by introducing the graded buffer concept [1] has significantly rised the interest in short-period Si/Ge superlattices (SL's). Such structures now show a band gap related luminescence which is enhanced by two orders of magnitude as compared to the corresponding alloy [2]. However, for structures with single layer thicknesses of only a few monolayers (ML) the interfaces play a crucial role, i.e. interface roughness due to Ge segregation and interdiffusion during growth has to be taken into account both for vibrational and electronic properties. Raman spectroscopy is a useful tool for characterizing short-period SL's, since their vibrational properties depend strongly on the microscopic structure.

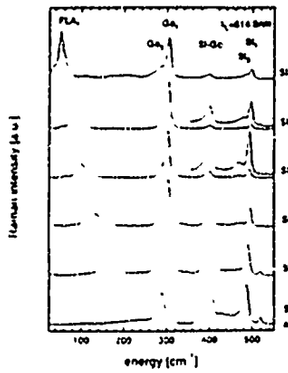

Fig.1 Raman spectra of various $(Si)_n/(Ge)_n$ SL's and the corresponding alloy, normalized to the intensity of the Ge-like phonon mode.

The conventional backscattering geometry from the (001) growth surface is limited to the observation of longitudinal phonon modes. However, for establishing a full picture of the vibrational modes of SL's, their symmetry and their coupling to light, it is necessary to perform Raman scattering along each primitive axis of the SL crystal. These studies are enabled by a recently developed microprobe technique, where the probe laser is focussed to a sub-μm spot by a microscope objective, thus allowing additional scattering geometries, such as from polished and cleaved sample edges [3-5]. According to the modified selection rules for SL's, polarization of the light parallel to the (001)-growth direction allows the observation of transverse phonon modes [5]. We studied $(Si)_n/(Ge)_n$ SL's with n = 4,5,6,8,12 grown at 310°C on strain-symmetrizing, partially relaxed $Si_{1-x}Ge_x$ alloy buffers on Si (001) substrate [6,7]. The measurements were performed at room temperature.

Additionally a theoretical study on strain-symmetrized $(Si)_n/(Ge)_n$ SL's was performed, taking into account both strain and interface intermixing. The calculations are based on interatomic force constants derived from first principles. Details on the method are given in Refs. 8,9. First we calculate the phonon frequencies for the SL's with ideally sharp interfaces (an example is given for the $(Si)_8/(Ge)_8$ SL in Fig. 2(c),(d)).

A first feature of the calculated spectra is the existence of optical modes well confined within the Si layers. Their frequencies can be decribed within a simple "standing wave" model with an effective wave-vector of

$$q_{eff} = 2m \cdot 2\pi / [a_0 \cdot (n+\gamma)] \qquad (1)$$

where m = 1,2....., n is the number of Si monolayers, a_0 is the cubic lattice parameter and γ describes the extent to which the modes penetrate into adjacent layers [10]. The mode frequencies are almost perfectly mapped onto the calculated, strain-shifted bulk dispersion branch, if γ is chosen as follows: γ=1 for L polarization (n even or odd) and T1 polarization (n even), γ=2 for T1 and T2 (n odd) and γ=3 for T2 polarization (n even). The different values of γ are due to the dependence of the mode confinement on the mode symmetry. For L polarization the displacement pattern is similar for any choice of n, leading to γ=1. For T vibrations we have to consider that the interplanar forces connecting atomic planes are of two different types, one much stronger than the other. The two types are alternating along the growth direction. If n is even, for a given T polarization (T1), both interfaces are strongly coupled, while for T2 the interface bonds are light. Hence there are two interface modes for T1 and no interface modes for T2. Interface planes involved in interface modes do not participate in Si-like vibrations, since the modes must orthogonalize to each other. Thus we obtain γ=1 for T1 and γ=3 for T2, which is consistent with the displacement patterns. For n odd, one of the two interfaces in the SL unit cell has a strong bond, while the other one is weak, giving rise to one single interface mode. As a result, in this case γ=2. Thus for ideal structures, the frequencies of Si-like confined optical modes can be described by a simple unfolding rule. The description of the Ge-like modes in terms of confinement, however, is less accurate due to their coupling to the acoustic Si dispersion branch [10]. Therefore they are only "quasi-confined".

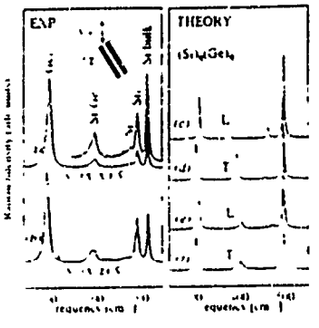

Fig.2 Experimental ((a) (b)) and theoretical ((c)-(f)) results for L and T Raman spectra of $(Si)_8/(Ge)_8$ SL. (c) and (d) refer to ideal SL's (no interface intermixing), while (e) and (f) are for a SL with two intermixed $Si_{0.5}Ge_{0.5}$ atomic layers at the interfaces. The vertical dotted lines are at the same frequencies in all panels

Fig.1 shows experimental Raman spectra of the L phonon modes, taken from the growth surface for all samples. The most pronounced feature of the SL spectra are the so-called folded-longitudinal acoustic modes (FLA) below 250cm⁻¹, which gain in intensity and are shifting linearly to lower frequencies with increasing period. Their appearance is due to folding of the averaged longitudinal acoustic dispersion branch of the bulk materials into the reduced Brillouin zone of the SL. The mode frequencies are well described within an elastic continuum model [11], at least below 150cm⁻¹, where the bulk dispersions are linear. For the quasi-confined Ge-like modes, the m=3 mode is resolved only for the $(Si)_{12}/(Ge)_{12}$ SL, while m=3 is

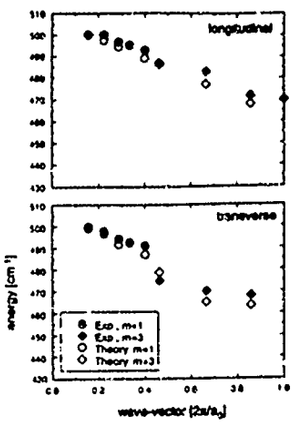

Fig.3 Experimental (full symbols) and calculated (hollow symbols) frequencies of L Si-like (a) and T Si-like (b) modes of strain-symmetrized $(Si)_n/(Ge)_n$ SL's, unfolded onto the corresponding bulk dispersion according to Eq.(1) with $\gamma = 1$. The calculations are for intermixed SLs with 3 monolayers Si_xGe_{1-x} with x=0.25, 0.50, 0.75 at the interfaces. Circles and diamonds correspond to m=1 and m=3 modes, respectively. Calculated T values are an average over T1 and T2.

resolved for the confined Si-like modes even for the $(Si)_3/(Ge)_3$ SL. Modes with even m are not observed, since they are Raman forbidden, to first order approximation. The appearance of a pronounced peak at 400cm^{-1} is contradictory to the calculation, where no interface mode is present for L polarization (see Fig.2(c)). Therefore, in earlier work this was assigned to alloy-like vibrations of Si-Ge bonds due to the presence of alloy layers at the interfaces [12-14]. The T-spectra were experimentally obtained from measurements in backscattering geometry from a (110)-edge of the samples, which is shown as an example in Fig.2(a),(b) for the $(Si)_8/(Ge)_8$ SL. Also in the T-spectrum a Si-Ge-like peak is present, but the frequency is shifted downwards and the lineshape is considerably changed. This gives clear evidence that the origin of this mode is different from that of the corresponding $Si_{0.5}Ge_{0.5}$ alloy, where no difference between L and T polarizations is observed. Fig.2(c),(d) presents calculated Raman spectra for a perfect $(Si)_8/(Ge)_8$ SL. No interface mode is present for L polarization, while in T polarization the well known "ideal" interface mode exists. However, its lineshape is in sharp contrast with the experiment. Fig.2(e),(f) show the result of the calculation, when interface roughness is modelled by two homogeneous $Si_{0.5}Ge_{0.5}$ alloy monolayers at each interface. It is evident that even this simple intermixing model reproduces the major experimental findings for the Si-Ge mode peak in the two polarizations. The basic features are independent of the exact interface composition profile. The broader and more symmetric lineshape of the T mode is due to the less sharp localization compared to the L mode which can be seen from the calculated local density of states in Fig.4. These effect are discussed in detail in Ref. 8. From the above discussion we conclude that interface roughness can not be neglected for our SL samples.

Now we come back to the confined Si-like modes. As could be expected, the experimental mode frequencies are found to deviate pronouncedly from the calculations for the *ideal* SL's both for L and T polarization, especially for modes associated with a large q_{eff}. In Fig.3 we present the results of a calculation where the interfaces were represented by three homogeneous alloy monolayers with x=0.25, 0.50 and 0.75. We note that, similar to the findings for the Si-Ge mode, the basic features are only weakly dependent on the exact profile. For simplicity, all values are plotted for γ=1, since we do not expect the unfolding rules derived for the ideal structures to be valid any longer for the intermixed SLs. Now the agreement between theoretical and experimental results both for L and T polarization is much closer, with the frequencies being considerably above the bulk dispersion for large q_{eff}.

These results can be interpreted as follows. The modes whose frequency falls above the alloy bands of the interface alloy layers are confined to the pure Si layer.

This is the case for modes with small q_{eff} which map close to the bulk dispersion for γ=1. For modes with large q_{eff} their frequency falls within the alloy bands. Thus they extend further into the alloy layers, which explains their deviation from the bulk dispersion. An effective confinement length n_{eff} can be extracted from the local density of states for a given intermixing configuration. This leads to γ=0 for LO_1 modes, while for higher order modes γ=2 to 2.5. Using this values, the SL mode frequencies are mapped closely onto the bulk dispersion. For T polarization, a splitting between T1 and T2 still remains for n even, although it is much smaller than for the ideal SLs. Thus n_{eff} still depends slightly on the SL symmetry. We believe the splitting is very difficult to be observed experimentally, since every monoatomic step on the substrate would rotate the SL unit cell by 90°, thus disturbing the orthorhombic symmetry expected for n even. The scattering volume contains many defects of that kind so that the effective symmetry is always tetragonal. Therefore it is resonable to average T1 and T2 before comparing with experiment.

Finally, we determined the Raman cross section of the observed SL phonon modes as a function of the excitation energy. This was done by normalizing the measured mode intensities to Si as a reference material for which the absolute Raman cross section is known. The Raman scattering cross section in a semiconductor material is enhanced, if the energy of the incoming or outgoing light equals a direct band-gap [15]. In a SL, the different phonon modes will thus display resonant behaviour at energies corresponding to electronic transitions which involve states extending to the same spatial region where they have their maximum vibrational amplitude. Resonance Raman experiments can thus be used to probe the actual localization of phonon modes, to be compared with the calculated local density of states.

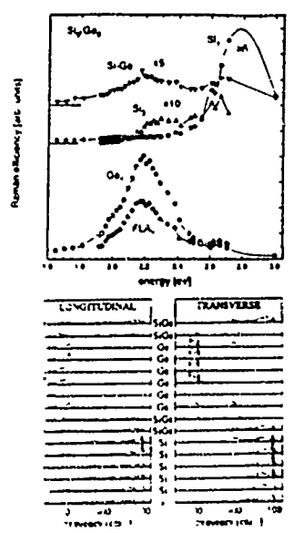

Fig 4 (top) Measured Raman resonance curves for various phonon modes of a $(Si)_8/(Ge)_8$ SL. (bottom) Local density of states for L and T1 polarizations on the (001) atomic planes of a $(Si)_8/(Ge)_8$ SL with two intermixed $Si_{0.5}Ge_{0.5}$ atomic layers at the interfaces (the composition of each plane is indicated)

We measured all samples in the visible range between 1.65eV and 3.0eV, thus covering the range of the E_1-like resonances of the bulk materials. These Raman resonance measurements will be discussed in detail elsewhere [16]. As an example, the result for the $(Si)_8/(Ge)_8$ SL for L polarized modes is shown in Fig.4. The most pronounced feature is a strong resonance peak at 2.20eV for the Ge_1 mode, which may be attributed to transitions between electronic states localized in the Ge layers. For the Si_1 mode no structure is observed below 2.5eV. This complete decoupling from the Ge_1 mode resonance is strong evidence for the almost perfect confinement of the Si_1 mode to the Si layers. The latter is consistent with the theoretical predictions of Fig.4, where the calculated vibrational density of states is shown for a $(Si)_8/(Ge)_8$ with two $Si_{0.5}Ge_{0.5}$ alloy layers at the interfaces. In contrast, for the Si_1 mode a pronounced structure is observed close to the Ge_1 resonance. From the local density of states it is obvious that the Si-like modes for m>1 have

considerable amplitudes at the border Si layers and even in the SiGe layers. This penetration enables a coupling to states confined to the Ge layers. The same holds for the Si-Ge mode which is mainly localized in the SiGe monolayers and the first Ge monolayer. Thus the coupling to Ge-like states is expected to be even stronger which is confirmed by the experimental resonance curve. The resonance behaviour of the FLA_1 mode is nearly identical to that of the Ge_1 mode, which is due to the completely propagating character of the acoustic modes. Around ~65eV a common resonance for all modes is observed, which is likely to be related to alloy-like transitions in the intermixed interface region.

In summary, we have shown that a simple model of interface mixing accounts for the experimentally observed anomalous behaviour of the lineshape and the L-T splitting of the alloy-like interface modes as well as for the deviation between unfolded Si-like SL mode frequencies and the bulk dispersion. Resonant Raman scattering is a helpful tool for probing locally electronic states in SL's and enables, on the other hand, to verify the calculated spatial localization of SL phonon modes.

Acknowledgements

We are greatful to A. Fasolino for a helpful discussion. The calculations were supported in part by CNR under grant 92.01598.PS69; the experiments were supported by ESPRIT Basic Research Project No 7128

References

[1] F.K. LeGoues, B.S. Meyerson, and F. J. Morar, Phys. Rev. Lett. 66, 2903 (1991)
[2] U. Menczigar, G. Abstreiter, J. Olajos, H. Grimmeis, H. Kibbel, and H. Presting, Phys. Rev. B 47, 4099 (1993)
[3] R. Heßmer, A. Huber, T. Egeler, M. Haines, G. Tränkle, G. Weimann, and G. Abstreiter, Phys. Rev. B 46, 4071 (1992)
[4] G. Scamarcio, M. Haines, G. Abstreiter, E. Molinari, S. Baroni, A. Fischer, and K. Ploog, Phys. Rev. B 47, 1483 (1993)
[5] R. Schorer, W. Wegscheider, K. Eberl, E. Kasper, H. Kibbel, and G. Abstreiter, Thin Solid Films 222, 269 (1992); R. Schorer, S. de Gironcoli, E. Molinari, H. Kibbel, E. Kasper, and G. Abstreiter, submitted to Phys. Rev. B
[6] K. Eberl, E. Friess, W. Wegscheider, U Menczigar, and G. Abstreiter, Thin Solid Films 183, 95 (1989)
[7] E. Kasper in *Physics and Application of Quantum Wells and Superlattices* ed. by E. E. Mendez and K. von Klitzing, NATO ASI Series B. Physics Vol 170 (Plenum, New York, 1987), p. 10
[8] S. de Gironcoli, E. Molinari, R. Schorer, and G Abstreiter, accepted for publication in Phys. Rev. B
[9] S. de Gironcoli, Phys Rev. B 46, 2412 (1992)
[10] A. Fasolino, E. Molinari, and A. Qteish, in *Condensed Systems of Low Dimensionality* ed. by J.L. Beeby *et al* (Plenum, New York, 1991), p. 495
[11] S. M Rytov, Sov. Phys. Acoust. 2, 68 (1956)
[12] H. Brugger, E. Friess, G. Abstreiter, E. Kasper, and H Kibbel, Semicond. Sci. Technol. 3, 1166 (1988)
[13] M.I. Alonso, F. Cerdeira, D Niles, M Cardona, E. Kasper, and H. Kibbel, J. Appl. Phys 66, 5645 (1989)
[14] A. Fasolino and E. Molinari, Journal de Physique C5, 569 (1987); Appl. Phys. Lett. 54, 1220 (1989)
[15] M. Cardona, *Resonance phenomena* in *Light Scattering in Solids II*, ed. by M. Cardona and G. Günterodt (Springer, Berlin, 1982)
[16] R. Schorer *et al.*, to be published

MoC8

Phonons and electron-phonon interaction in GaAs quantum wires

F Rossi[1,2] C Bungaro F Rota[1] P Lugli[3] and E Molinari[4]

[1] Dipart di Fisica, Universita di Modena, Via Campi 213/a, I 41100 Modena Italy
[2] Fachbereich Physik und Zentrum for Materialwissenschaften Philipps Universität Marburg Renthof 5 D 3550 Marburg, Germany
[3] Internat School of Advanced Studies (SISSA) Via Beirut 4, I 34100 Trieste Italy
[4] Department of Physics Clarendon Laboratory, Oxford University Oxford OX1 3PU England
[5] Dipart di Ingegneria Elettronica, II Universita di Roma Tor Vergata Via della Ricerca Scientifica 1 I 00133 Roma Italy

Abstract

Phonon dispersions and potential profiles for thin rectangular GaAs wires embedded in AlAs are calculated by means of a microscopic approach based on ab initio microscopic force constants. Besides non dispersive vibrations, well confined in GaAs, we find phonons with interface character along one or both of the in plane directions, the latter including modes with maxima at the edges of the wire. While confined phonon potentials are well described within the dielectric continuum (DC) model, interface mode profiles turn out to be more complex. Not only macroscopic models do not give analytic results in this case, but also numerical implementations of the DC model reproduce only partially the microscopic results in the thin wire regime.

1 Introduction

Polar optical phonons in semiconductor nanostructures are receiving increasing interest in recent years due to their relevant coupling with carriers. In particular they play an important role in determining the relaxation time of photoexcited carriers on the picosecond time scale as well as transport properties at high temperature. In order to reach a better understanding of the electron optical phonon (el ph) interaction a detailed description of both phonon and electron properties in these low dimensional materials is needed. The important quantity characterizing this interaction is the electrostatic potential associated with the polar optical phonons.

The dynamical properties of two dimensional (2D) semiconductor systems have been widely analyzed both from the theoretical and from the experimental point of view. Accurate three dimensional microscopic calculations have allowed a detailed understanding of the main features of the optical phonon modes involved in the scattering with confined electrons and of the corresponding electrostatic potential [1]

In particular the results of these microscopic studies, also supported by experimental evidence [2], have clarified that a good approximation to the electrostatic phonon potentials in 2D structures can be obtained by *one* of the simplified macroscopic models previously proposed: the dielectric continuum model in its original [3] or improved Huang Zhu [4] versions.

An increasing interest is currently devoted to one dimensional (1D) structures: a clear picture of the dynamical properties is therefore required also for these systems. The only available microscopic studies [5,6] focus on the frequency dispersions, and a systematic description of spatial mode profiles is still needed. Along the same line followed for 2D systems [1] we have performed a microscopic calculation based on ab initio interatomic force constants of phonon dispersions and displacement patterns for thin rectangular GaAs wires embedded in AlAs. In this scheme the electrostatic potentials for the calculation of electron optical phonon interaction are also obtained. In previous reports we have presented results for confined phonons, here we discuss in greater detail microscopic potentials for non confined modes and compare them with phonon potentials derived by simplified macroscopic models which may be of practical use in simulations.

2. Microscopic analysis

Phonon frequencies and displacements are obtained by direct diagonalization of the dynamical matrix of the three dimensional crystal, which is in turn constructed from ab initio interatomic force constants [7]. The electrostatic phonon potential associated to each optical mode at a given wave vector $\mathbf{q} = (0, 0, q_z)$ is then calculated from the microscopic displacements [7]. The results presented in this paper are obtained for a periodic array of infinite (002) oriented GaAs quantum wires (QWR) of rectangular section embedded in AlAs. The dimensions of the GaAs QWR are 4 and 5 monolayers along x and y respectively ($\approx 5.5 \times 11$ Å) and the width of the AlAs barriers is of 11 monolayers in both directions. The dispersion of the topmost optical GaAs like modes for small wave vectors parallel to the wire direction is displayed in Fig. 1(a). Their angular dispersion at $q_z = 0$ is displayed in Figs. 1(b) and 1(c). Here θ and ϕ are the angles between the phonon wave vector and the z direction in the yz and xz planes respectively. As in 2D systems, some of the modes have a non negligible angular dispersion: this is due to the long range Coulomb interaction, which is anisotropic at Γ.

In analogy with the 2D case, one might expect that the angular dispersion of modes will be a fingerprint of their interface (IF) character, and that angle independent modes will be confined in the wire. The classification of the actual calculated modes is however more complex. We can distinguish (*i*) modes which are not dispersive with θ nor with ϕ, (*ii*) modes which are dispersive either with θ or with ϕ, (*iii*) modes which are dispersive both with θ and ϕ.

As already shown in a partial account of the present calculations [8], a good understanding of the nondispersive modes (class (*i*)) has been reached: they are usually well confined in the wire, and their potential profiles are separable functions of x and y. For example, the profile of Fig. 2(a) may be obtained as a product of two confined profiles along x and y, both even with respect to the mirror planes through the centre of the wire; the profile of Fig. 2(b) from two confined profiles of odd parity [8].

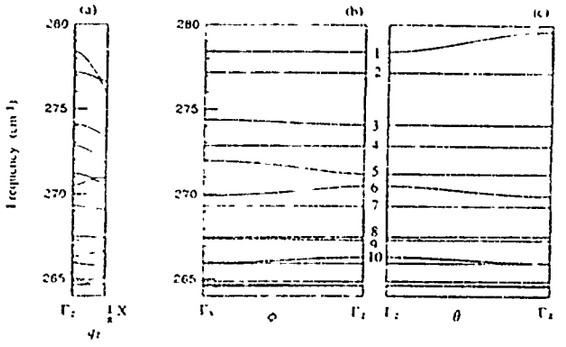

Fig. 1. Dispersion of the topmost GaAs like optical modes for the rectangular quantum wire array as obtained from the microscopic calculation. *(a)* Dispersion along the wire direction for $0 < q_z < 0.125\ 2\pi/a$. *(b)* and *(c)* Angular dispersion of zone center phonons in the yz and xz planes respectively.

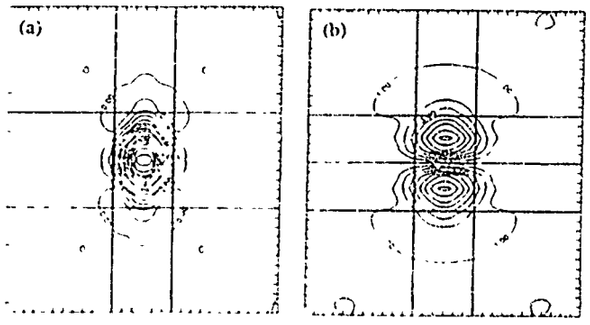

Fig. 2. Contour plot of the phonon potential (arbitrary units) in the xy plane for two non dispersive modes (modes 2 and 3 of Fig. 1) confined in the GaAs QWR. Here $q_z = 0.0.0.0125\ 2\pi/a$. The straight lines indicate the interface planes.

The potentials of two modes belonging to class *(iii)* are shown in Figs. 8(a) and 8(b). They clearly have an H character along one of the in-plane directions and a confined shape in the other direction. Indeed the potential in Fig. 8(a) (8(b)) is extended both in GaAs and AlAs along x (y) direction with a maximum on the interface perpendicular to this direction along y (x); the potential is instead confined in the GaAs wire. Potentials of this type can still be written in separable form (*H + confined*).

Modes which are dispersive both with θ and φ are not confined in both directions and have a well defined interface character which produces maxima at the edges of the wire (see for example Fig. 1). Contrary to the previous classes, clearly these mode profiles cannot be written as separable functions of x and y (*H + H*).

The above classification describes the main features of the calculated spectra, but not all the modes can be associated with one of these classes. In particular we have found some modes with very small or no angular dispersion (for example modes 4 and 5 of Fig. 1) whose potential is however extended both in GaAs and AlAs with some H-like character. We tentatively interpret this anomaly as due to coupling between states of different nature, although a more extensive study for different wire thicknesses would be needed for a conclusive assignment.

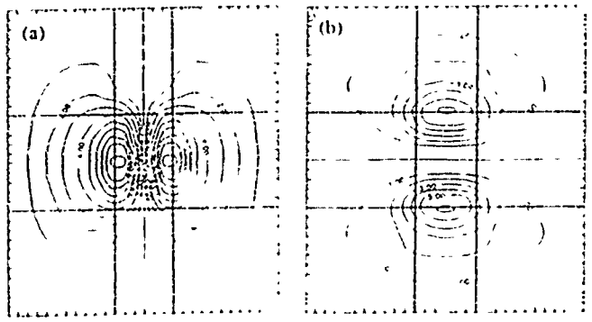

Fig. 3. Contour plot of the phonon potential (arbitrary units) in the xy plane for two QWR modes of class *(ii)* (modes 3 and 5 of Fig. 1) whose angular dispersion is significant only vs. θ or φ, respectively. Notations as in Fig. 2.

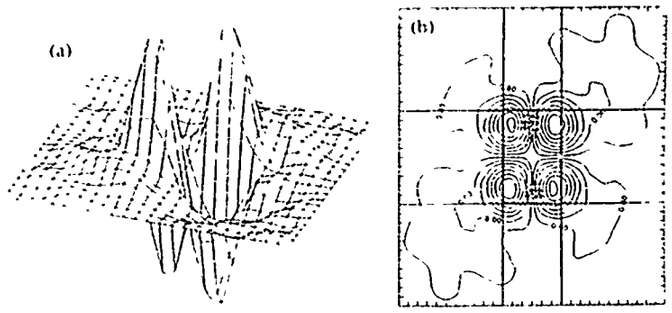

Fig. 4. *(a)* Three-dimensional and *(b)* two-dimensional contour plot of the phonon potential (arbitrary units) in the xy plane for a QWR mode of class *(iii)* (mode 10 of Fig. 1) whose angular dispersion is significant both vs. θ and vs. φ. Notations as in Fig. 2.

3. Comparison with simplified macroscopic models

Macroscopic descriptions such as the one of the previous section are certainly rigorous but are not of very practical and flexible use. Given its successful description of the e-ph interaction in 2D systems, it is therefore interesting to explore the possibility of extending the use of the macroscopic dielectric continuum model to the wire geometry.

In view of our microscopic results there are two major aspects of simplified macroscopic models to be discussed. The first is related to the fact that, within the DC model, interface and confined modes belong to two distinct sets of solutions of Laplace equations, i.e. a given mode can have *either* confined *or* non confined character [7]. Therefore modes belonging to class *(iii)* of Sect. 2 seem to have no counterpart in the DC scheme. This intrinsic limitation of the DC model has never been discussed explicitly so far; however our calculated potentials show that the contribution of these modes to e-ph rates should *not* be negligible unless for very large wires.

The second aspect concerns the accuracy of the separable approximation, which has been used extensively in connection with the DC model because of its simplicity [10]. There is no *a priori* justification for such approximation, except for very special wire geometries [11]. In wires of rectangular section it turns out to be quite acceptable for confined modes [8], as apparent from the above discussion of modes of class *(i)*. However our results demonstrate that such assumption is not justified for modes of class *(iii)*. For phonons with purely interface character, Kumpf and Ramecke [12,13] have shown that the problem can be overcome in wires of arbitrary geometries by means of a fully numerical treatment. From their calculated scattering rates[13], it is

clear that the separable approximation is too crude especially for small wire widths Indeed the order of magnitude of the errors introduced by such approximation is not much smaller than the error introduced by simply using bulk phonons rather than quantum wire phonons

In summary our detailed microscopic study of phonon potentials in thin rectangular GaAs QWRs shows that a significant contribution to el-ph rates is expected to come as in 2D systems [4] from modes with interface character Their description in terms of simplified models is however more difficult in this case Not only the macroscopic DC scheme cannot be reduced to two separable 1D problems and solved analytically in most cases but also numerical implementations of the DC scheme seem to reproduce only partially the microscopic results For a description of scattering rates associated to individual phonons in small QWRs further work on possible simplified schemes is needed

Acknowledgments We are grateful to Tom Reinecke for useful correspondence and for sending us results prior to publication We acknowledge partial financial support by the EEC Commission under the ESPRIT Basic Science Project NANOPT and by CNR under grant 92.03.38.PF69

References

[1] H Rucker E Molinari and P Lugli Phys Rev B 44 3463 (1991) *ibid* 45 6747 (1992) and references therein
[2] G Scamarcio M Haines G Abstreiter E Molinari S Baroni and K Ploog Phys Rev B 47 1485 (1993)
[3] B Sundaram J Menendez J Tsuchiya 41 2837 (1989)
[4] K Huang and B F Zhu Phys Rev B 38 2484 (1988) *ibid* 38 13377 (1988)
[5] Bang Fen Zhu Phys Rev B 44 1926 (1991)
[6] Shang Lou Ren and Yia Chung Chang Phys Rev B 43 14537 (1991)
[7] C Bungaro P Lugli F Rossi L Rota E Molinari in *SPIE Proceedings* SPIE Vol 1677 55 (1992)
[8] F Rossi E Rota C Bungaro P Lugli and E Molinari Phys Rev B 47 6955 (1993)
[9] E Molinari S Baroni P Giannozzi and S de Gironcoli Phys Rev B 45 4280 (1992)
[10] K W Kuo M A Stroscio V Bhatt R Mickevicius and V V Mitin Journ Appl Phys 70 3709 (1991) R Mickevicius et al Superlatt Microstruct 11 257 (1992)
[11] See e g P J Stiles and R Enderlein Superlatt Microstruct 12 219 (1992) and references therein
[12] P V Kupp and T L Reinecke Phys Rev B 45 9091 (1992)
[13] P V Kupp and T L Reinecke this conference and to be published

Tuesday, August 24

TuA	Quantum Wells - Electrical Properties
TuB	Vertical Transport - Resonant Tunneling
TuC	Quantum Wells, Superlattices - Optical Properties
TuP	Transport, Optics

TuA1

STRAINED SI/SIGE HETEROSTRUCTURES FOR DEVICE APPLICATIONS

E. Schäffler

Daimler-Benz AG, Research Center Ulm, P.O. Box 2360, D-89013 Ulm, Germany

Abstract

A review is given of the most recent development in the field of modulation doped Si/SiGe heterostructures. Main topics are the successful implementation of high-quality, strain-relaxed SiGe buffers, the realization of n-type and p type quantum well structures with unprecedentedly high electron mobilities, magnetotransport investigations of such structures, and their exploitation for devices with very high transconductance values

Proper exploitation of the strain-dependent band alignment in the lattice mismatched Si/SiGe heterosystem allows the realization of enhanced electron and hole mobilities by means of modulation (or remote) doping (MOD).[1,2] Since a finite conduction band offset is only achieved, if the Si channel is put under a tensile in-plane strain[3,4], a partly or completely strain-relaxed SiGe buffer layer is required as a virtual substrate for n-type structures[5]. p type quantum wells (QW), on the other hand, can be implemented using pseudomorphic SiGe channels, however, the low hole mobilities resulting from alloy scattering in such layers suggest the use of pure Ge QWs, which again require a relaxed SiGe buffer layer to maintain the mandatory compatibility with Si substrates.

Initially, $Si_{1-x}Ge_x$ buffer layers with constant x were grown to a thickness somewhat above the critical thickness for strain relaxation by the formation of misfit dislocations. These were sufficient to demonstrate the strain-induced Type II band ordering and the electron-mobility enhancement by modulation doping in a subsequently deposited Si/SiGe heterostructure with a Si quantum well (QW).[3] Also, the first n-type modulation-doped field effect transistors (MODFET) in this material system were based on this buffer type [6] Despite gradual improvements[7], however, the low temperature mobilities remained behind expectations. One of the main reasons was seen in the strain-adjusting SiGe buffer layers then used, which were known to contain a high density ($> 10^9$ cm^{-2}) of unwanted threading dislocations that end at the surface, thus penetrating through the active layers A major breakthrough with threading dislocation densities reduced by several orders of magnitude was achieved by introducing a linearly or step-wise increasing Ge content concomitant with relatively high growth

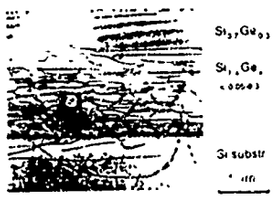

Figure 1 TEM cross sectional view of a $Si_{1-x}Ge_x$ buffer layer with linear grading of the Ge content from 5% ≤ x ≤ 30% Note the distribution of the misfit dislocation network over the thickness of the grading and the virtual dislocation free upper part of the buffer grown at a constant x

temperatures[8,9,10] Because of the gradual increase of the lattice mismatch in such a buffer, the misfit dislocation network is distributed over the range of compositional grading rather than being concentrated at the interface to the Si substrate, which would be the case if a constant Ge content is used throughout (Fig. 1) The reduced interactions between intersecting misfit dislocations promotes, in connection with close-to-equilibrium growth temperatures, long misfit dislocation segments, and thus low threading dislocation densities.

The greatly improved buffer quality soon led to low-temperature electron-mobilities in excess of 100000 cm^2/Vs[13], with the best value reported to date being 173000 cm^2/Vs at 1.5 K (Fig 2).[10] This is the highest known mobility of a two dimensional electron gas (2DEG) in Si, which is almost a

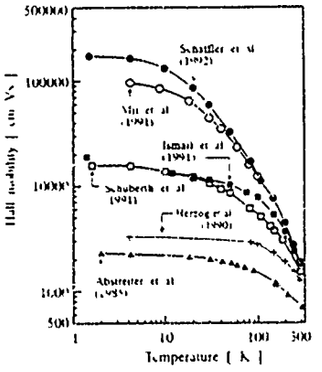

Figure 2 Development of the electron Hall mobilities in modulation doped Si/SiGe heterostructures in recent years The upper two curves were measured on samples with linearly graded SiGe buffer Data from References 10, 13, 11, 7, 12, 3 (from top to bottom)

factor of five higher than the best values found in Si MOSFETs.[14] Moreover, room temperature Hall-mobilities close to 2000 cm^2/Vs were found in the MODFET samples, which not only exceeds the values of commercial MOSFETs by a factor of two, but also is higher than the bulk mobility in intrinsic Si. This is due to the fact that the strain dependent band-ordering in the (001)-oriented Si/SiGe heterosystems allows only a population of the two-fold degenerate electron valleys corresponding to the conduction band ellipsoids in the direction perpendicular to the (100) heterointerface. Thus 2D transport within the channel plane is associated with the transversal effective mass m_t=0.19m_0, whereas the quantization (or subband) energies are determined by the much larger longitudinal effective mass parameter m_l=0.92m_0. In terms of carrier mobility this is the optimum combination of mass parameters, which not only provides the lowest possible transport mass, but also the minimum penetration depth of the electron wavefunction into the heterobarrier due to the large quantization mass. In contrast, the inferior mobility behavior of the MOSFET is mainly due to the inverse assignment of effective masses resulting from the fact that mainly the four-fold degenerate electron valleys are occupied at room temperature.

The success of n-MODQW structures grown on graded SiGe buffers with an effective composition of up to x=30% suggested an extension to higher Ge contents (up to 100%), to allow p-type QW structures with channels consisting of pure Ge. However, with increasing x_{eff} (and thus lattice mismatch), growth becomes more demanding. It requires a careful selection of growth parameters to maintain a low threading dislocation density without running into a three-dimensional growth mode which would spoil the surface morphology. A combination of Ge grading and down-ramping of the growth temperature at higher

x values appears as a possible solution to overcome such problems. Based on this concept, p-MODQW structures with Ge channels grown on Si substrates became available recently[15,16]. They show outstanding hole Hall-mobilities at room temperature (up to 1300 cm^2/Vs) and 77K (up to 14000 cm^2/Vs), but a premature mobility saturation observed below about 40K is indicative of relatively high defect or background doping concentrations within the Ge channel. Obviously, further refinements of the growth and doping conditions are required. Nonetheless, the basic superiority of a Ge channel and the compatibility with Si substrates has clearly been demonstrated, and, moreover, the quality of the QW structures presently available allows a variety of basic investigations and device applications that were not possible with conventional p-channel structures.

The very high electron and hole mobilities achieved in Si/SiGe and Si/SiGe/Ge MODQW structures led to detailed studies of the magnetotransport properties and of cyclotron resonance absorption. As an example, very narrow cyclotron resonance absorption lines have been observed, which allow a precise determination of the cyclotron effective masses of 2D electrons and holes as a function of the filling factor (Fig 3).[17,18] Magnetotransport studies, on the other hand, provide information on the single particle relaxation time τ_s, which is derived from the magnetic-field-dependence of the low-field amplitude of the Shubnikov-deHaas oscillations[19]. Comparison with the transport time τ_t gives insight into the dominant scattering mechanism. We find τ_t/τ_s ratios between 6 (best Ge-channels) and 26 (best Si channels) which are indicative of long-range scattering (mainly at remote impurities) rather than short-range scattering (e.g. at interface roughnesses) being the dominating mechanism that restricts the low temperature mobility in our MODQW structures. The lower ratios found in the Ge-channel samples are attributed to the not yet optimized growth conditions, which became also obvious in the low-temperature Hall measurements. Nevertheless even these first Ge-channel samples are still much better than Si MOSFETs, which are known to be limited by interface roughness scattering at the Si/SiO_2 interface, and hence show τ_t/τ_s ratios close to 1.

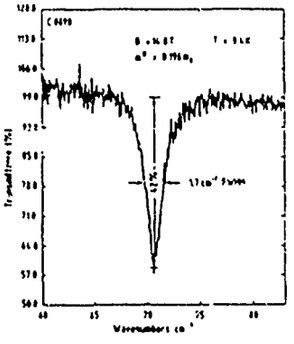

Figure 3 Cyclotron resonance absorption of the sample in Figure 2 with the highest mobility. Note the sharpness of the absorption line corresponding to the high electron mobility

One of the main attractions of the high-mobility Si/SiGe and Si/SiGe/Ge MODQW-structures is their potential in terms of high-speed device applications. Consequently, the availability of such samples almost immediately led to n type MODFETs with impressive transconductances.[20,21] The highest values reported so far are g_m=340 and 670 mS/mm at 300 and 77 K, respectively (Fig 4). Very recently, also p type MODFETs with Ge-channels grown on Si substrates were fabricated successfully[15]. Although their performance has not entirely reached the level of their n type conterparts as yet, transconductances of 125 and 290 mS/mm at 300K and 77K, respectively, are very promising for future developments.

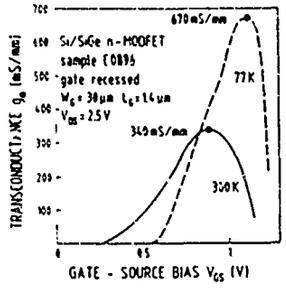

Figure 4 Output characteristics at room temperature and at 77K of a gate recessed n type (Si channel) MODFET device utilizing a high mobility Si/SiGe heterostructure grown on Si substrates (from Refs. 20)

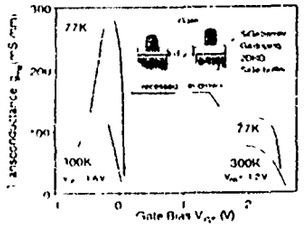

Figure 5 Output characteristics of Ge channel (p type) MODFETs with and without gate recessing at room temperature and at 77K (from Ref. 15)

The implementation of superior n- and p-MODFETs is a prerequisite for complementary transistors (CMODFETs) with matched characteristics, which can not be realized in any of the established material systems because of the far inferior properties of the respective p-type devices. With almost identical mobilities of electrons in Si and holes in Ge, the Si/SiGe/Ge heterosystem could for the first time provide such matched transistor pairs, and moreover, remain widely compatible with Si very large scale integration (VLSI) technologies. Initial steps to implement such CMODFETs are already under way. This is demonstrated in Fig 6, which shows a simplified double-mesa CMODFET with a layer sequence consisting of a n-MODFET structure grown on top of a p-MODFET without growth interruption. This development, which will certainly require more refined integration concepts and process steps, could once open the field of high-speed applications for the ubiquitous complementary logic, which is in its contemporary CMOSFET implementation the single-most important technology in microelectronics.

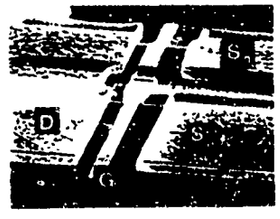

Figure 6 First test vehicle of a CMODFET with stacked p- and n-FETs. The common Drain metallization is on the left, the separate Source contacts at the right. The common T-shaped gate connects the p-FET in the foreground with the stacked n-FET in the background

The contributions and helpful comments of D Többen, C M Engelhardt, M.Sasson, G.Abstreiter, F Gornik, U.König, H-J.Herzog, and E.Kasper are gratefully

acknowledged. This work was financially supported by the Bundesministerium für Forschung und Technolog (Bonn, Germany)

[1] R People, J C Bean, D.V.Lang, A M Sergent, H L Störmer, K W Wecht, R T Lynch, and K Baldwin, Appl Phys Lett 45, 1231 (1984)

[2] H Jorke and H.-J Herzog, J Electrochem Soc 133, 998 (1986)

[3] G.Abstreiter H Brugger, T Wolf, H Jorke, and H -J.Herzog, Phys. Rev Lett 54, 2441 (1985)

[4] C G Van de Walle and R M Martin Phys Rev B34, 5621 (1986)

[5] E Kasper, Surf Sci 174, 630 (1986)

[6] H Daembkes, H.-J Herzog, H Jorke, H Kibbel, and E Kasper, IEDM Technical Digest, IEEE New York 1985, p 768

[7] G.Schuberth, F Schäffler, M Besson, G Abstreiter, and E Gornik, Appl Phys Lett 59, 3318 (1991)

[8] E.A Fitzgerald, Y H Xie, M L Green, D Brasen, A R.Kortan, J Michel, Y J Mii, and B E.Weir, Appl Phys Lett 59, 811 (1991)

[9] F K LeGoues, B S Meyerson, and J F.Morar, Phys Rev Lett 66 2903 (1991)

[10] F Schäffler, D Többen, H -J Herzog, G Abstreiter, and B Ho'ander, Semicond Sci Technol 7, 260 (1992)

[11] K Ismail B S Meyerson, and P J Wang, Appl Phys. Lett. 58, 2117 (1991)

[12] H -J.Herzog, H.Jorke, and F.Schäffler, Thin Solid Films 184, 237 (1990)

[13] Y J Mii, Y.H.Xie, E A Fitzgerald, D.Monroe, F A Thiel, B E.Weir, and L.C.Feldman, Appl. Phys Lett. 59, 1611 (1991)

[14] I V Kukushkin and V B.Timofeev, Sov Phys. JETP 67, 594 (1991)

[15] U Konig and F Schäffler, IEEE Electron Device Lett 14, 205 (1993)

[16] D Monroe, Y.-H Xie, E.A.Fitzgerald, P J Silverman, and G.Watson, J Vac Sci. Technol. (to be published 1993)

[17] M.Besson, C M.Engelhardt, F.Schäffler, and E Gornik, to be published

[18] see also the contribution of C.M Engelhardt et al. at this conference

[19] D Többen, F Schäffler, A.Zrenner, and G Abstreiter, Phys. Rev B15 (1992), to be published

[20] U König, A J Boers, F.Schäffler, and E Kasper, Electronic Lett 28, 160 (1992)

[21] K Ismail, B.S Meyerson, S P.shton, J Chu, S Nelson, and J Nocera, IEEE Electron Device Lett 13, 229 (1992)

TuA2

CAPTURE AND EMISSION OF ELECTRONS IN QUANTUM WELLS UNDER APPLIED ELECTRIC FIELD

B. VINTER, F. LUC, P. BOIS, E. THIBAUDEAU, and E. ROSENCHER
Laboratoire Central de Recherches
THOMSON - CSF
Domaine de Corbeville
91404 - ORSAY (France)

Important characteristics of Quantum Well Infrared Photodetectors are determined almost entirely by the photoionization rate of electrons out of the Quantum Well (QW) and the recapture into the QWs To elucidate these processes microscopically we have made structures in which the QWs are isolated from one contact by a completely blocking barrier, so that the steady state current vanishes The transient current induced by photoionization out of the QWs gives a direct measurement of the photoionization cross section and the escape probability of a photoexcited electron We have found that the variation of the latter with the electric field may be described by a simple barrier lowering model combined with statistical fluctuation of the QW width.

The capture process has been studied by impedance spectroscopy in samples containing only one well The capture velocity thus measured is found to decrease with increasing applied electric field but within experimental uncertainties it does not depend on the width of the well for well widths between 3 nm and 7.5 nm Theoretical results on optical phonon mediated transitions in the applied field from barrier to well states show a generally good agreement with experiment at low fields but less dependence on the field.

INTRODUCTION

The performances of Quantum Well Infrared Photodetectors (QWIP)[1] are determined by the rate at which electrons are ionized out of the Quantum Well (QW) either by photoionization or by thermal emission; and by the rate at which the excited electrons are recaptured into the QWs The photoionization determines the response and background limited noise; the thermal emission determines the thermal or dark-current noise, and the capture probability determines the responsivity through the photoconductive gain[2,3] In order to understand the microscopic physics of these mechanisms we have performed experiments on specially designed samples which give access to each mechanism in situations very close to that of the QWIP, *i.e.* unipolar conduction near a stationary state under an applied bias field

PHOTOIONIZATION CROSS-SECTION

In order to measure the rate at which electrons will be ionized out of the QW without the complications due to photoconductive gain and dark current, we have made measurements of the transient photocurrent from a multiquantum well structure in a Schottky diode. This technique is very similar to the Deep Level Optical Spectroscopy method developed to study the optical cross section of deep levels in semiconductors

The sample (see Fig.1), grown by molecular beam epitaxy, consists in ten periods of a 6 nm GaAs 5×10^{11} cm^{-2} δ-doped quantum well sandwiched between 35 nm $Ga_{0.25}Al_{0.75}As$ barriers on the top of a 500 nm 10^{18} cm^{-3} Si-doped GaAs contact layer.The sample has been designed so that there are two bound levels in the well (E_1 and E_2) with $E_{21} = E_2 - E_1 = 138$ meV and that the second energy level E_2 is a few meV below the $Ga_{0.25}Al_{0.75}As$ barrier E_B ($E_{B2} = E_B - E_2 \approx 8$ meV). The depth of the potential well as well as the barrier thickness have been chosen sufficiently high to suppress tunnel emission[4] as well as thermal emission for temperatures up to 60 K Mesa structures 200 µm x 100 µm were processed using standard lithography techniques An evaporated AuGeNi layer provides an ohmic contact at the bottom of the structure while Cr was evaporated to provide a semi-transparent Shottky diode on the top. *The Shottky diode insures that*

no refilling current flows through the structure for reverse biases down to -1 Volt in the considered temperature range (up to 60 K). Finally, only 10 QWs have been used since, as only a few 10^{12} electrons per cm^2 may be extracted from a depletion layer[5], a larger number of wells would just have increased the series resistance without providing any additional transient photosignal.

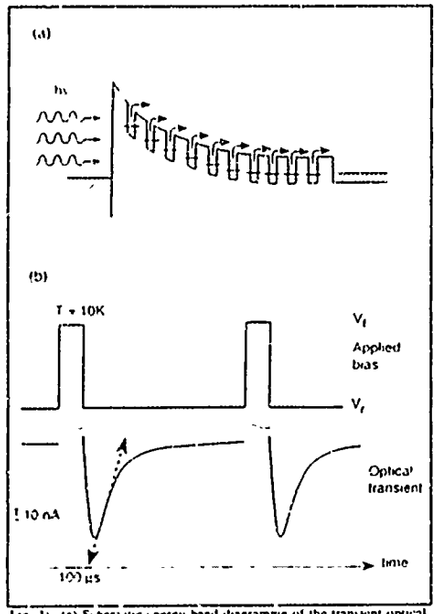

Fig. 1: (a) Schematic energy band diagramme of the transient optical spectroscopy sample. Note that the Schottky barrier blocks the refilling current. (b) Polarization cycle applied to the device and experimental transient current due to the photoionization of the QWs. The photoionization cross section is measured as the initial slope of the transients.

The experiment follows the usual voltage cycle of transient optical spectroscopy[6]. Under unfocused illumination, the structure is first forward biased so that electrons from the GaAs contact are injected in the $Ga_{0.75}Al_{0.25}As$ barrier and captured in the wells. The diode is then reverse biased and the trapped electrons are emitted from the well to the lower contact. The density of electrons N_i as a function of time in each well is determined by

$$\frac{\partial N_i}{\partial t} = -\sigma_p(i)\,\Phi\left(N_i - N_i^{eq}\right) \qquad (1)$$

where i stands for the well index, *eq* stands for equilibrium, Φ is the photon flux and $\sigma_p(i)$ is the photoionization cross section which may depend on the electric field at the i^{th} QW. Recent studies[3,7,8] have shown that the photoionization cross section can be phenomenologically written $\sigma_p = p_e\,\sigma_0$, where p_e and σ_0 are the escape probability and the optical capture cross section respectively. σ_0 is the quantity measured by absorption spectroscopy which is well accounted for by quantum mechanics[9]; for this sample, $\sigma_0 = 2.10^{-15}$ cm^2 at resonance. p_e is the probability for a photoexcited electron to be scattered into a diffusive energy state (instead of being scattered back to the fundamental state of the well). The internal quantum efficiency is equal to the product of the escape probability and the sample absorption.

Summing over the 10 wells and assuming a cross section $\sigma_p(i)$ independent of i, we find that integration of Eq (1) leads to a current exponentially decreasing with time. Note that, since the current has a transient behavior, the current is the *sum of the contribution of all the wells*. This is markedly different from steady state photoconduction where the current is constant through the structure. Figure 1 shows a typical transient signal obtained at Brewster angle for a 1.4 Volt V_f filling pulse (120 µs duration) and a reverse bias V_r of -1 Volt with a polarized tunable CO_2 laser source at $\lambda = 9.47$ µm (130 meV) for an incident power of 100 mW/cm^2. As a matter of fact, since the escape probability is dependent on the local electric field at each quantum well, this signal is not purely exponential since the electric field changes as a function of time. Nevertheless, when the reverse bias V_r has just been applied (t=0) the electric field F is homogeneous in the structure: $F=(V_r+V_0)/L$, where V_0 is the Schottky offset (V_0 = 750 meV) and L is the total structure length. $\sigma_p\Phi$ can therefore be measured directly as the initial slope of the transient current. For the case of Fig. 1 the experimental photoionization cross section is found to be $\sigma_p = 1.3 \times 10^{-15}$ cm^2 at 9.47 µm.

We then measure the variation of the photoionization cross section with the photon energy hν. The sample is illuminated by the light of a glowbar dispersed by a two-prism spectrometer. In order to get rid of the transient due to the background flux, we have used a boxcar technique. The experiment is performed at 10 K with a filling pulse of 1.8 V during 80 µs, a reverse bias of -1 V (i.e. an initial electric field of 40 kV/cm) and a chopping frequency of 200 Hz. Fig. 2 shows the resulting σ_p versus hν curve. It exhibits the usual resonance feature, with a maximum peak value of 2.2×10^{-15} cm^2 in total agreement with the quantum mechanical calculation[9] (hν *assuming an escape probability* p_e *close to 100%* (independent of hν).

We are now in position to study the electric field dependence of the escape probability. Indeed, since the QWs are symmetric, the variation of the optical cross section with the electric field F is negligible[9] so that the variation of σ_p directly reflects the influence of F on the probability p_e. The experimental results for a laser beam at 9.47 µm (130 meV), indicate a smooth variation of p_e from 100% down to 30% when the electric field is decreased from 40 kV/cm down to 4 kV/cm.

The escape probability is usually related to the electron escape time τ_e and the recombination time τ_r through the relation[10] $p_e = (1 + \tau_e / \tau_r)^{-1}$. When the electric field is enhanced, τ_r should not be significantly affected by orders of magnitude (see below) while τ_e should vary with the tunnel barrier transparency. However, the theoretical variation of the transparency with the electric field is very steep, from practically 0 to 1 for electric field values close to F_1 given by $qF_1L_w/2 = E_B - E_2$ where L_w is the quantum well width. *The variation of* p_e *should then be described by a Heaviside function at* $F = F_1$, which is clearly not in agreement with

the experimental results. We therefore believe that the smooth variation of ρ_e has a statistical origin i.e. the energy E_2 fluctuates in each QW with a Gaussian distribution, so that the ρ_e vs F curve is the convolution of the Heaviside function with this Gaussian distribution. The best fit of the experimental results[11], taking into account this distribution, is obtained by a deviation of $\Delta E = 3.5$ meV around a mean value 4 meV below the barrier. The former value can be reasonably accounted for by a *one monolayer fluctuation* in the QWs on both sides.

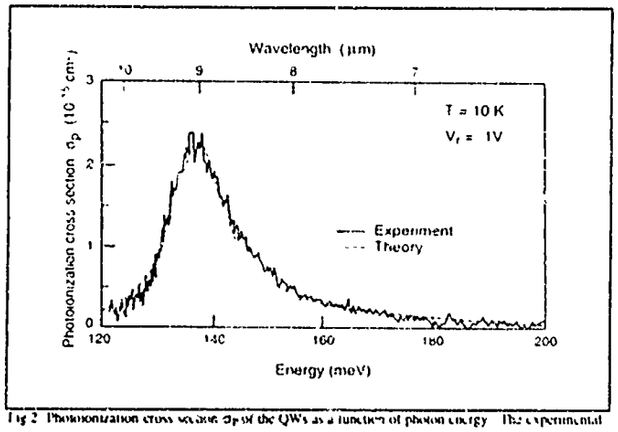

Fig 2 Photoionization cross section σ_p of the QWs as a function of photon energy. The experimental curve (full line) is fitted by the simple quantum mechanical model for intersubband absorption with a linewidth of 5 meV (dotted line).

CAPTURE INTO A QUANTUM WELL

The second set of experiments determine the capture of electrons from the continuum in the barrier layers into a QW. The method used is that of impedance spectroscopy on a sample containing only one QW in a semiconductor-insulator-semiconductor structure.

The samples (see Fig 3) consist of a sandwich of a 94 nm $Al_{0.4}Ga_{0.6}As$, 50 nm $Al_{0.22}Ga_{0.78}As$, a GaAs (undoped) QW of width L_w, 50 nm $Al_{0.22}Ga_{0.78}As$ structure. It is clad between two 500 nm 10^{18} cm^{-3} Si doped GaAs contacts. The well parameters (length, barrier height) have been chosen so that for L_w = 6 nm the first energy level E_1 is bound (59 meV above the GaAs conduction band) and the second level E_2 is quasi resonant with the $Al_{0.22}Ga_{0.78}As$ conduction band (E_2-E_1=117 meV). Moreover, on the one hand, the Al concentration of the $Al_{0.4}Ga_{0.6}As$ layer has been chosen sufficiently large so that this barrier is totally insulating at temperatures below 120 K, which has been experimentally verified. On the other hand, the Al concentration of the $Al_{0.22}Ga_{0.78}As$ intermediate barrier is low enough so that in the temperature range of our experiments (80 - 120 K), the QW is not far from the thermodynamical equilibrium with the electron reservoir of the lower contact. Consequently, *the Fermi level in the well is set by the lower contact*. This condition is the basis of the equivalent circuit analysis of interface traps in MOS structures so that we can extend this analysis to our SIS system[12]. Mesa structures

(265 μm × 265 μm) were fabricated using standard photolithography techniques and AuGeNi alloy contacts. The sample capacitance is independent of the applied bias in the +1,-1 V range at the temperature of 10 K and the value of 33 pF is in perfect agreement with the nominal total thickness of 200 nm. Admittance measurements are performed, using a lock-in technique, as a function of the frequency for different temperatures between 85 K and 115 K and for different applied biases.

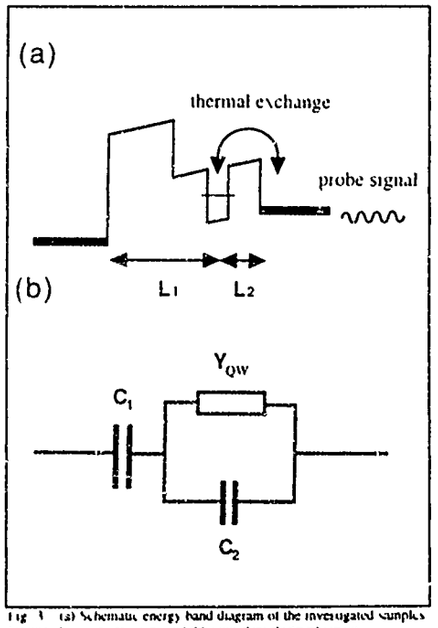

Fig 3 (a) Schematic energy band diagram of the investigated samples for impedance spectroscopy and (b) equivalent electrical circuit.

From a *direct analogy* with MOS devices, the electrical equivalent circuit of the structure for a sinusoidal signal can be immediately deduced (see Fig 3) by introducing the "quantum well admittance" Y_{QW} as[12]

$$Y_{QW} = \frac{\partial I_{QW}}{\partial V_{QW}} = G_{QW} + j\omega C_{QW} \quad . \qquad (2)$$

where V_{QW} is the potential drop between the well and the lower contact, ω is the signal radial frequency and I_{QW} is the current flowing into the well ($I_{QW} = -qA\,\partial N_{QW}/\partial t$, q is the elementary charge, N_{QW} is the electron density in the well and A is the sample area. The value of G_{QW} is deduced from the measured sample admittance and the known values of the geometrical capacitances C_1 and C_2. In our case the values of C_1 and C_2 are respectively 44 pF and 132 pF.

Considering the whole well as a single 2D trap, one can write the emission-recombination equation as:

$$A\frac{\partial N_{QW}}{\partial t} = c_n n - e_n N_{QW} \quad . \qquad (3)$$

where n is the 3D distribution of carriers above the well, e_n (s^{-1}) is the thermal emission rate from the QW while c_n (cm^3/s) is the classical capture coefficient in the QW. A classical treatment for small sinusoidal perturbations leads then to the expression of the equivalent impedance for such a mechanism[12].

$$\frac{G_{QW}(\omega)}{\omega} = C_T \frac{\omega\tau}{1+\omega^2\tau^2} \qquad (4)$$

with

$$C_T = \frac{q^2 A\, m^*}{\pi \hbar^2} \exp\left(\frac{E_1 + q V_{QW} - E_f}{kT}\right) \quad . \qquad (5)$$

where $\tau = AN_{eq}/c_n n_{eq}$. N_{eq} (resp. n_{eq}) is the 2D carrier density in the well (resp. 3D density above the well) in steady state. Since the well is undoped, N_{eq} is given by $N_{eq} = (m^*/\pi\hbar^2)\,kT \exp((E_F + qV_{QW} - E_1)/kT)$ where m^* is the effective mass of the electron in GaAs.

The experimental curves[13] $G_{QW}(\omega)/\omega$ vs ω can be well fitted by one time-constant τ in Eq. (4). This is the signature of an emission-recombination process occuring between *a single trap* and the $Al_{0.22}Ga_{0.78}As$ conduction band. In our case of a 2D trap, the capture coefficient c_n is proportional to the sample area so that the significant capture parameter is the recombination velocity v_{QW} defined as $v_{QW} = c_n / A$ [14]. This quantum well recombination velocity is related to the time constant τ through the relation $v_{QW} = N_{eq}/\tau n_{eq}$. If we make the assumption that the 3D equilibrium density of states is not affected by the presence of the quantum well, so that n_{eq} is given by the classical expression[5] $n_{eq} = N_c(T)\exp((E_f + qV_{QW} - E_2)/kT)$ we find

$$\tau = \frac{1}{v_{QW}}\left[\frac{2\pi\hbar^2}{m^* kT}\right]^{1/2} \exp\left(\frac{E_2 - E_1}{kT}\right) \qquad (6)$$

In Fig. 4a the corresponding Arrhenius plot is shown for a 6 nm wide quantum well. For the activation energy $E_2 - E_1$ a value of 113 meV is found independent of the field. This supports our assumption that the observed emission-recombination process occurs between the bound state of the well and the $Al_{0.22}Ga_{0.78}As$ conduction band. We also find $v_{QW} = 8\times10^3$ cm/s for an

electric field of 3 kV/cm. Moreover, in Fig. 4b we show that the experiments indicate a strong decrease of the recombination velocity for an increasing applied electric field. This can be seen to be the case for the samples of different well width, too. In contrast to what has been reported from time-dependent photoluminescence measurements[15], we find no clear dependence of the capture velocity on well width.

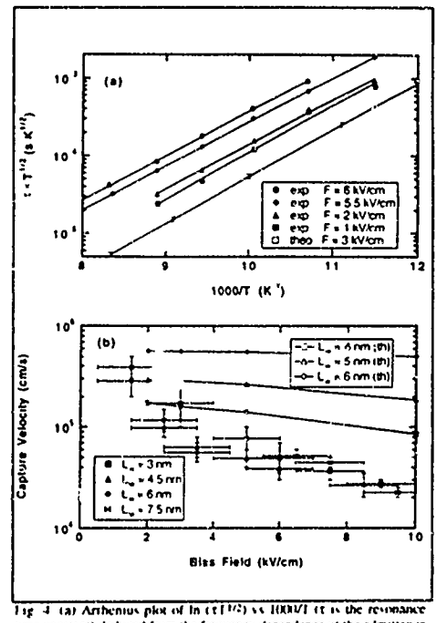

Fig. 4 (a) Arrhenius plot of $\ln(\tau T^{1/2})$ vs $1000/T$ (τ is the resonance time constant) deduced from the frequency dependence of the admittance for a 6 nm QW. The corresponding theoretical results are also shown for one field. The intersection of the extrapolation lines with the abscissa yields the recombination velocity in the QW. This velocity is shown in (b) as a function of the applied electric field and for several different QWs. (error bars indicate the experimental uncertainties).

The capture coefficient may be connected to the capture probability p only if a velocity v is introduced, i.e. $c_n = A\,p\,v$. If we take a usual drift velocity of a QWIP $v = 1 - 5\times10^6$ cm/s[2] with a minimum value of $v_{QW} = 3\times10^4$ cm/s, we find a capture probability $p = v_{QW}/v \approx 0.03 - 0.006$. This is in good agreement with the values obtained by photoconductive gain in QW infrared detectors[10].

THEORY OF THE QW IMPEDANCE

We have performed calculations of the net capture rate into a QW in a constant electric bias field. The hypotheses of the calculation are that the polar optical phonon scattering processes from levels of the continuum to the fundamental bound state subband of the QW control the capture time, the continuum states are assumed to be in thermal equilibrium with the Fermi energy of the contact, and the electrons in the QW are in thermal equilibrium in the ground state QW subband. In the electric field the wavefunctions can be written as linear combinations of Airy functions in the barriers and in the QW. Using Fermi's golden rule to calculate the scattering rates $S(\varepsilon_z,K \rightarrow \varepsilon_0,K_0)$ between states of the continuum (denoted ε_z,K) and states in the QW (denoted ε_0,K_0) we have:

$$\frac{\partial N_{QW}}{\partial t} = \sum_{\varepsilon_z,K,K} S^{emi}_{abs}(\varepsilon_z,K \rightarrow \varepsilon_0,K_0)\, f(\varepsilon_z,K)\,(1-f(\varepsilon_0,K_0)) - \sum_{\varepsilon_z,K,K} S^{abs}_{emi}(\varepsilon_0,K_0 \rightarrow \varepsilon_z,K)\, f(\varepsilon_0,K_0)\,(1-f(\varepsilon_z,K)) \quad . \tag{7}$$

which by using detailed balance between phonon emission processes in one direction and phonon absorption processes in the opposite direction can be reduced to $\partial N_{QW} / \partial t = -(N_{QW}-N_{eq}) / \tau$, where N_{eq} is the number of electrons in the quantum well when no ac voltage is applied, and

$$\frac{1}{\tau} = \frac{\pi \hbar^2}{m^* kT} \sum_{\varepsilon_z,K,K} S^{emi}_{abs}(\varepsilon_z,K \rightarrow \varepsilon_0,K_0) \exp\left(\frac{\varepsilon_0 - (\varepsilon_z + \hbar^2K^2/2\,m^*)}{kT}\right) \quad . \tag{8}$$

Results of this calculation are also shown for a 6 nm wide QW in Fig. 4a. It can be seen that time constants in the 100 µs to 10 ms range are indeed reproduced by the theory and that the activation energy is the same as experimentally observed. However, the dependence on bias field is much smaller than observed. This can be seen in the theoretical recombination velocity (derived by making the same fitting procedure as for the experiment) which is also plotted in Fig. 4b for different QW widths. In addition, one can also see a stronger QW width dependence. It remains an interesting question which transport processes create competing time constants in the experiment in order to explain these less important discrepancies.

CONCLUSION

The picture of the QWIP which emerges from several independent experiments is very close to that of an extrinsic photoconductor in which the quantum wells simply act as giant traps from which electrons are ionized and retrapped. We have measured the important parameters of these processes in specifically designed experiments and have found that they can be consistently explained by microscopic theory, and that they explain very satisfactorily the responsivity and detectivity performance of QWIPs.

REFERENCES

1. For recent developments, see e.g. E. Rosencher, B. Vinter, and B. Levine, Eds., *Intersubband Transitions in Quantum Wells*, Plenum, New York (1992).
2. B. F. Levine, in *Intersubband Transitions in Quantum Wells*, E. Rosencher, B. Vinter, and B. Levine, Eds., p. 43, Plenum, New York (1992).
3. H. C. Liu, A. G. Steele, M. Buchanan, and Z. R. Wasilewski, in *Intersubband Transitions in Quantum Wells*, E. Rosencher, B. Vinter, and B. Levine, Eds., p. 57, Plenum, New York (1992).
4. E. Martinet, E. Rosencher, F. Chevoir, J. Nagle, and P. Bois, Phys. Rev. B 44, 3157 (1991).
5. S. M. Sze, *Physics of Semiconductor Devices*, Wiley Interscience, New York (1981).
6. A. Chantre, G. Vincent, and D. Bois, Phys. Rev. B 23, 5335 (1981).
7. B. F. Levine, A. Zussmann, S. D. Gunapala, M. T. Asom, J. M. Kuo, and W. S. Hobson, J. Appl. Phys. 72, 4429 (1992).
8. E. Martinet, F. Luc, E. Rosencher, P. Bois, E. Costard, S. Delaitre, and E. Böckenhoff, in *Intersubband Transitions in Quantum Wells*, E. Rosencher, B. Vinter, and B. Levine, Eds., p. 299, Plenum, New York (1992).
9. E. Rosencher, E. Martinet, F. Luc, P. Bois, and E. Böckenhoff, Appl. Phys. Lett. 59, 3255 (1991).
10. H. C. Liu, Appl. Phys. Lett. 60, 1507 (1992).
11. F. Luc, E. Rosencher, and P. Bois, Appl. Phys. Lett. 62, 2542 (1993).
12. E. H. Nicollian and A. Götzberger, Bell Syst. Tech. J. 46, 1055 (1967).
13. F. Luc, E. Rosencher, and B. Vinter, Appl. Phys. Lett. 62, 1143 (1993).
14. W. Shockley and W. T. Read, Phys. Rev. 87, 835 (1952).
15. P. W. M. Blom, C. Smit, J. E. M. Haverkort, and J. H. Wolter, Phys. Rev. B 47, 2072 (1993).

TuA3

Observation by Spin-Resolved Resonant Magnetotunneling of Oscillatory Landé Factor in Two-Dimensional Electron Systems

E. E. Mendez and E. Nocera
IBM Research Division, T. J. Watson Research Center
Yorktown Heights, N.Y. 10598, USA
and
W. I. Wang
Department of Electrical Engineering, Columbia University
New York, N.Y. 10027, USA

We have shown by magnetotunneling spectroscopy that at certain magnetic fields the Landé factor g of two-dimensional electrons is significantly enhanced relative to its three dimensional value. The experiments were done using GaSb-AlSb-InAs-AlSb-GaSb heterostructures, in which a two dimensional electron gas in the InAs layer is probed by holes from the GaSb electrodes tunneling in and out of it. The field dependence of the g factor is accounted for by the exchange interaction between electrons of the same spin.

When a strong magnetic field H is applied perpendicular to the plane of a two-dimensional (2D) gas, the density of states of the latter becomes discrete, with sharp peaks at energies corresponding to Landau levels E_N, defined by the well-known relation $E_N = \hbar\omega_c(N + 1/2)$, where ω_c is the cyclotron frequency ($\omega_c = eH/m^*c$, and m^* is the effective mass). At very high fields each Landau level is split into its two spin components, the energy separation between which is the Zeeman energy $g\mu_B H$, where μ_B is the Bohr magneton and g is a proportionality constant called the Lande factor.

If the exchange interaction between 2D electrons is taken into account, that simple expression for the Zeeman energy may no longer be valid since the magnetic energies are affected by exchange terms between electrons of the same spin. The energy difference depends on the relative population of the various spin states, as illustrated by Fig. 1. When the number of spin-up (up) and spin-down (down) electrons is equal, the exchange energy is the same for both types of magnetic states and their energy separation is not altered by the exchange correction. On the other hand, when the populations of the up and down states are not equal the different exchange terms result in an enhanced energy separation between those states. We can then define an effective g factor, g^*, which is larger than the single-particle Landé factor.

This many-body effect has explained the g-factor values measured in Si-SiO_2 devices [1],[2] and it has been used in fitting magnetoresistance data of GaAs-GaAlAs heterostructures in the quantum Hall regime [3]. More recently, it has been manifested in angular-dependence measurements of Shubnikov-de Haas oscillations, which, with certain limitations, yielded enhanced g-factor values of 2D electrons in GaAs-GaAlAs structures [4].

Here we show that a tunneling current perpendicular to a 2D electron gas can provide a more direct way of determining the g factor, not only for states at the Fermi level but for any occupation number. This is demonstrated in GaSb-AlSb-InAs-AlSb-GaSb heterostructures, whose unique properties make it possible the observation of features in the tunneling current-voltage (I-V) characteristics associated with magnetic states.

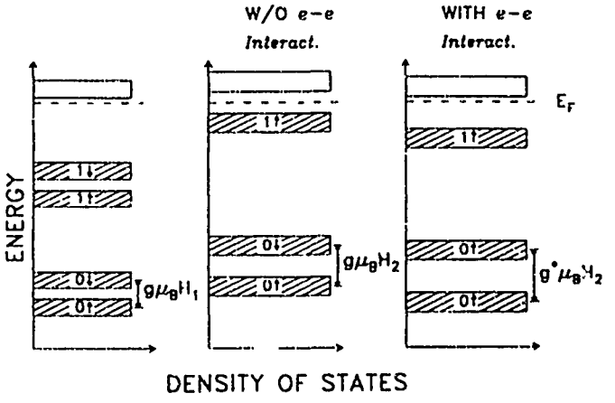

Fig. 1 - Sketch of the density of states for Landau levels, at two magnetic fields. On the left, the field H_1 is such that two spin resolved Landau levels (N = 0,1) are fully occupied. The Zeeman energy is independent of whether the electron-electron exchange interaction is taken into account. On the center and right panels the field H_2 is higher, and the N = 1 level is half occupied (1↑). The separation between the two spin states of the fully occupied N = 0 state is larger when the e-e interaction is included.

The top of the valence band of GaSb lies above the bottom of the conduction band of InAs, so that in a heterostructure made out of GaSb-AlSb-InAs-AlSb-GaSb electrons flow from the GaSb thick regions to the InAs quantum well, leaving holes behind. The amount of charge transferred is controlled by the thicknesses of the InAs and AlSb layers, which for the structure discussed here are 150Å and 40Å, respectively. The 2D electron density in InAs is 1.2×10^{12}cm^{-2}. (Although ideally the number of electrons balances the total number of holes accumulated on both GaSb interfaces, in real structures additional electrons from residual impurities or interface states brake that balance.) By applying hydrostatic pressure up to 13kbar, that density was reduced to 5.2×10^{11}cm^{-2}, as a result of the pressure-induced reduction of the overlap energy between the GaSb valence band and the InAs conduction band. When a voltage is applied between the two GaSb end layers acting as electrodes, current flows between them via resonant interband tunneling through the 2D quantum state, E_1, in the InAs well. (See

Fig. 2) The current is abruptly interrupted when the energy of the holes at the emitter is lower than E_f since then there no longer are states available for tunneling.

Because of the light effective mass of electrons in InAs, in the presence of a perpendicular magnetic field their cyclotron energy ($\simeq$ 5meV/T), even at moderate fields, is much larger than the Fermi energy of the heavy holes at the GaSb emitter ($\simeq$ 4meV). When, at a fixed field, an external voltage between the GaSb electrodes aligns the hole distribution with an electron Landau level, resonant tunneling occurs and the current increases sharply. With a further increase of the voltage the holes are aligned with a gap between two Landau levels, tunneling is then inhibited and the current drops abruptly. The same process is repeated for subsequent Landau levels and, thus, the I-V characteristic shows a sawtooth behavior, with each current peak corresponding to a Landau level of InAs [5]. As the number of occupied levels decreases with increasing field so does the number of peaks; at a given field this number is determined by the electronic density under equilibrium conditions. At very high fields, even the Zeeman spin splitting becomes large compared to the hole Fermi energy (see Fig. 2) and it is possible to resolve in the I-V characteristics features associated with individual spin states [6].

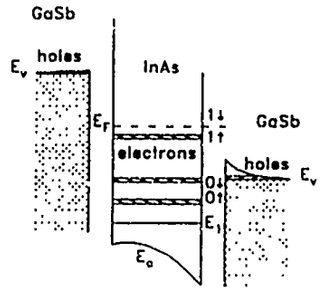

Fig. 2 - Energy band diagram of a GaSb-AlSb-InAs-AlSb-GaSb heterostructure under a magnetic field perpendicular to the interfaces, when a bias is applied between the two GaSb electrodes. The field is large enough to resolve the spin splitting of the Landau levels of the electrons in the InAs quantum well. The small Landau level quantization of the heavy holes has been ignored.

The experimental I-V characteristics exhibit at low temperature ($T \simeq 1.4K$) the negative-differential-resistance and sawtooth behavior anticipated above, as illustrated on Fig. 3 for fields ranging from 0 up to 28.5T. At $H = 0$ the peak voltage (voltage for maximum current) occurs when the quantum state E_1 is aligned in energy with the ground state of the accumulation layer of the GaSb emitter, and therefore that voltage is twice (assuming uniform distribution of the potential) the energy difference between electron and hole states. At moderate fields, e.g., several current peaks are observable, each corresponding to the alignment of an electron Landau level with the GaSb heavy-hole state. With increasing field each peak moves to lower voltage, until it eventually disappears when it is above the quasi Fermi level for electrons - in other words, when it becomes depopulated. The quantum limit (only N = 0 occupied) is reached at $\simeq$24T, but, even before, the N = 0 peak develops a shoulder (at H$\geq$15T) that gradually becomes a well-defined additional peak. A similar behavior is observed when the heterostructure is under hydrostatic pressure, the only difference being that the quantum limit is reached at lower fields, down to 11T at the maximum pressure of 13kbar, when the 2D density is 5.2×10^{11}cm^{-2}.

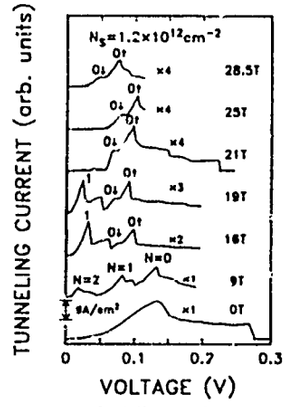

Fig. 3 - Low-temperature ($T \simeq 1.4K$) tunneling current-voltage characteristics at representative magnetic fields for a heterostructure like the one shown in Fig. 2. The thicknesses for the InAs and AlSb layers are 150Å and 40Å, respectively. The field was parallel to the current.

The Landau indices, as well as the 2D electron density, are readily deduced from a plot of the zero-bias tunneling conductance versus field, shown on Fig. 4 for both extreme pressures. The conductance exhibits Shubnikov-de Haas oscillations periodic with the inverse of the field, from which the 2D electron densities mentioned above are obtained. At high fields the deep minima approach zero, resembling the vanishing resistance of the quantum Hall effect of in-plane magnetotransport. This behavior is closely related to that well-known effect. At zero bias, the tunneling conductance vanishes whenever the

Fermi level lies between two well-separated Landau levels and becomes maximum when it is in the center of a level. Then, the Landau-level indices can be derived from the relation between the 2D density, the magnetic field, and the spin-resolved filling factor ν.

We explain the doublet observed in the I-V characteristics at high fields in terms of spin-polarized tunneling, based on the fact that in the $p = 13$kbar case the low-voltage peak ($0\downarrow$) passes through $V = 0$ precisely at the field (20T) at which the conductance shows the minimum corresponding to the emptying of the $0\downarrow$ state ($\nu = 1$). Although at lower pressure the extreme quantum limit ($\nu < 1$) was not reached even at 30T, based on a similar behavior with field, we ascribe the same origin to their respective $N = 0$ doublets.

After converting the voltage separation of the two $N = 0$ structures into energy, the g factor is derived simply by dividing that energy by the magnetic field and the Bohr magneton. The dependence of g with field for the configurations of extreme density is superimposed on Fig. 4. For the lowest density, g increases monotonically with field from a minimum value of 1 to a maximum of 9.

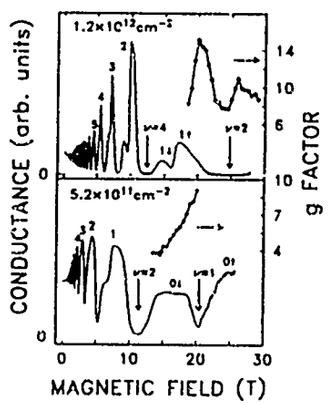

Fig. 4. Zero-bias magnetoconductance (continuous curves, left hand scale) and Lande g factor (black dots connected by lines, right hand scale) for two different carrier densities. The values of the g factors are averages for both voltage polarities in the I-V characteristics.

This enhancement of g with field can be understood from the nature of the exchange interaction, as explained in the introduction. At 11T, the minimum in the zero-voltage conductance for the low-density case indicates that both the $0\downarrow$ and the $0\uparrow$ states are below the Fermi level ($\nu = 2$). As the field increases the $0\downarrow$ state becomes depopulated and the population difference between $0\uparrow$ and $0\downarrow$ increases, reaching a maximum at 20T when $0\downarrow$ is very close to the Fermi level. The exchange-induced enhancement of the g factor follows precisely the increase in population difference.

Those experimental g values, especially g_{max}, may at first sight seem too small for InAs. However, it is important to note that they correspond to measurements done under hydrostatic pressure, which increases the band gap of a semiconductor, thus increasing effective masses and decreasing g factors. In fact, a theoretical calculation of g that includes the effect of pressure on the relevant band parameters of bulk InAs yields for g_{max} a value of 4.5, which compares favorably with the experimental value of 4.

As for the enhancement of g from 4 to 9, it is qualitatively explained by a Hartree-Fock calculation, which predicts an enhancement more than three times larger. In that approximation, the maximum increase of the energy difference between the $0\downarrow$ and $0\uparrow$, when the $N = 0$ level is partially occupied, is

$$\Sigma_{0\downarrow} - \Sigma_{0\uparrow} = \frac{e^2}{\epsilon\ell} \sqrt{\frac{\pi}{2}}\, X_{00} \qquad [1]$$

where ϵ is the dielectric constant of InAs, ℓ is the magnetic length ($\ell^2 = ch/eH$), and $X_{00} = 1$ [7].

At 20T, this difference translates into a Δg of 18. This value, derived under the assumption of an ideal system with no impurities or defects, is larger than the experimental observation, which should not be too surprising, except maybe for the magnitude of the discrepancy.

For the highest density case, the splitting of $N = 0$ is observable even when $N = 1$ is partially occupied, as Fig. 3 illustrates. The g factor has a value of 8 at 18.5T, a field at which, in equilibrium, $1\uparrow$ is still below the Fermi level. When the field increases so does g, reaching a maximum value of 15 at 20T. From then on, g decreases to 8 at 23T and finally it recovers to values between 9 and 10 beyond 26T. This oscillatory behavior is in qualitative agreement with the results obtained for the low-density configuration: g is minimum when the Fermi level is between two different Landau levels ($N = 1$ and $N = 0$) and is maximum when one of them is partially empty ($N = 1$).

A closer look, however, reveals a more complicated picture. The maximum g, g_{max}, should occur for a field at which the Fermi level is midway between two spin states within the same Landau level (or, equivalently, when the filling factor is odd), and g should be minimum when the Fermi level is between spin states of different Landau levels (that is, for even filling factors). Then, assuming that the plot of the conductance versus field reflects the 2D density of states, g_{max} should happen at 15T, not at 20T. Equally surprising is the observed enhancement of g at fields above 23T, where the broad zero-conductance region suggests a Fermi level between Landau levels.

Although we have no answer to this anomaly, the explanation may lie on the details of the density of states, especially in view of the presence of residual donor impurities in InAs that contribute to the imbalance between electrons and holes. It is known that impurities can lead to asymmetric density of states that shift the resistance minima of the QHE away from the expected magnetic fields [8]. For example, for a donor-induced attractive potential, an asymmetric density of states is predicted with an impurity band on the low energy side of the Landau levels. Such an asymmetry would be consistent with the observed shift of g_{max} to higher fields.

Calculations of the extreme g values agree well with the experiment. Thus, g_{max} is predicted to be 9, in comparison with an experimental $g_{max} = 8$. A Hartree-Fock expression for $\Sigma_\uparrow - \Sigma_\downarrow$ when the $N = 1$ Landau level is half-occupied reads the same as Eq. [1] re-

placing X_m with $X_m = 1/2$. At 23 T this difference translates into $\Delta\varepsilon = 9$, which is about twice the experimental enhancement. The fact that the difference is much smaller than in the case of low density may suggests that, in the latter, ε_{max} is not reached even at the highest fields at which the spin splitting is observable – a likely possibility especially when an asymmetric density of states is considered.

In summary, we have shown how magnetotunneling provides a good tool to obtain directly the Landé factor of two-dimensional systems. By probing the energy gaps in the density of states, the technique could in principle serve to detect anomalies in the density of states associated with fractional Landau level occupation responsible for the fractional quantum Hall effect. However, such an experiment would require a heavy-hole Fermi energy even smaller than that of the structure used in this work and possibly a 2D electron mobility superior to the one shown here. These are hard tasks – but hopefully not impossible.

The high-field measurements were done at the Francis Bitter National Magnet Laboratory, MIT, Cambridge, whose staff we thank for their help. This work has been sponsored in part by the Army Research Office (F. E. M.) and by the Office of Naval Research (W. I. W.).

References

1. I. F. Lanak, Phys. Rev. 178, 1416 (1969).
2. F. F. Fang and P. J. Stiles, Phys. Rev. 174, 823 (1968).
3. Th. Englert, D. C. Tsui, A. C. Gossard, and Ch. Uihlein, Surf. Sci. 113, 295 (1982).
4. R. J. Nicholas, R. J. Haug, K. v. Klitzing, and G. Weimann, Phys. Rev. B 37, 1294 (1988).
5. E. E. Mendez, H. Ohno, L. Esaki, and W. I. Wang, Phys. Rev. B 43, 5196 (1991).
6. E. E. Mendez, J. Nocera, and W. I. Wang, Phys. Rev. B 47, 13937 (1993).
7. A. H. MacDonald, H. C. A. Oji, and K. L. Liu, Phys. Rev. B 34, 2681 (1986).
8. R. J. Haug, R. R. Gerhardts, K. v. Klitzing, and K. Ploog, Phys. Rev. Lett. 59, 1349 (1987).

TuA4

WIRE-LIKE INCORPORATION OF DOPANT ATOMS DURING MBE GROWTH ON VICINAL GaAs(001) SURFACES

L. Däweritz, C. Muggelberg, R. Hey, H. Kostial and M. Höricke
Paul Drude-Institut für Festkörperelektronik
Hausvogteiplatz 5 - 7, D-10117 Berlin, Germany

ABSTRACT

The ordered incorporation of dopant atoms by combining lattice step growth on vicinal GaAs(001) surfaces and Si delta(δ)-doping has been studied by real time reflection high-energy electron diffraction (RHEED) measurements. For Si deposition on 2° toward the (111)Ga plane misoriented surfaces and 0.4° toward the (1$\bar{1}$1)As plane misoriented surfaces it is shown that the Si atoms arrange themselves preferentially along the step edges in a (3x2) structure consisting of an ordered array of Si dimers. For Si concentrations not exceeding substantially the amount expected to be attached at the step edges the GaAs growth can be continued at reduced substrate temperature without adverse effects on the growth front. By pulsed δ-doping an unusual high concentration of Si atoms can be incorporated as donors on Ga sites.

1. INTRODUCTION

Delta-doping of GaAs with Si by molecular beam epitaxy (MBE) is now a well established method to incorporate an electrical active impurity in a sheet of at most a few atomic layers in thickness [1,2]. The usually applied procedure consisting of a suspension of GaAs growth, evaporation of dopant atoms on the nongrowing surface while an arsenic flux is incident, and the growth of subsequent GaAs layers is assumed to result in a statistical in-plane distribution of the dopant atoms.

The introduction of an in-plane order of the dopant atoms would allow to study the intriguing electronic properties expected for such ordered structures. In particular it has been proposed to combine the lattice step growth on vicinal surfaces with planar doping to create a one-dimensional system of so-called doping quantum wires [3]. First studies on the deposition of Si atoms on vicinal GaAs(001) surfaces by reflection high-energy electron diffraction (RHEED) [4,5] suggest that a preferential attachment at the edges of misorientation steps occurs provided the vicinal surface is well ordered and the Si migration is strong enough. At present, however, neither the underlying surface processes nor the structure and ordering of the "wire-like" incorporated dopant atoms are well understood. In this work, we use real-time RHEED measurements for a systematic study of the incorporation of Si atoms on various vicinal GaAs(001) surfaces. Additional information on the site occupancy of the incorporated dopant atoms is derived from Hall effect measurements.

2. EXPERIMENTAL

The undoped semiinsulating GaAs(001) substrates misoriented 2° and 0.4° toward the (111)Ga or (1$\bar{1}$1)As plane were prepared in the usual way. A buffer layer of 0.5 μm thickness was grown and annealed at 580 °C. The GaAs growth rate was 0.7 ML (monolayers) s^{-1}, and an As_4 : Ga beam equivalent pressure (BEP) ratio of 15 was used. At substrate temperatures ranging between 550 °C and 610 °C a clear (2x4) reconstruction was found. Before Si deposition, growth interruptions in the order of 1 h duration and the successive deposition of several monolayers GaAs with growth interruptions of 2 min were used to smooth the initial GaAs surface. Si was deposited with a continuous or interrupted flux of 1.08×10^{11} cm^{-2} s^{-1} (1.7×10^{-4} ML s^{-1}). The subsequent GaAs layers on the Si modified surface were grown at a reduced substrate temperature of 540 °C. The Si flux was calibrated by capacitance-voltage (CV) depth profiling of a dopant staircase structure. To assess the site occupancy of the Si atoms at high concentrations 300 K low field Hall effect measurements were performed by using chemical etching and a van der Pauw configuration.

For real-time RHEED measurements a 15 keV electron beam with an incidence angle close to

the first out-of-phase condition for the diffraction at the stepped surface was used. The specular beam intensity was recorded by using an arrangement consisting of a collimator, optical fibre and photomultiplier. The incident beam was parallel to the step edges. With this geometry the specular beam intensity is sensitive to changes in step edge roughness and strain induced effects, adatom density and nucleation processes on the terraces [6,7]. In this azimuth the terraces are not shadowed by the steps. Therefore, Si induced changes in surface reconstruction near the step edges on the lower terrace can be detected from the very beginning. To determine the full symmetry of the Si induced structures complementary measurements with the RHEED beam incident in the orthogonal ⟨110⟩ azimuths have been performed.

3. RESULTS AND DISCUSSION

3.1. Structure of the vicinal GaAs(001) surfaces

The first step in the synthesis of doping quantum wires is the preparation of a regularly stepped vicinal surface with smooth terraces. Using the transition from an oscillating to a constant RHEED intensity as a function of the GaAs growth temperature [8] the critical temperature T_{cm} for a change from two-dimensional nucleation and step propagation mechanism to the desired step flow mechanism has been estimated [5]. For the given growth parameters and the 2° and 0.4° misorientation toward the (111)Ga plane it amounts to about 560 °C and 640 °C, respectively. For the corresponding misorientations toward the $(1\bar{1}1)$As plane these values are lower by about 20 degrees. This is consistent with a recent first-principle calculation on microscopic processes of Ga adatom diffusion on the (2x4) reconstructed surface according to that the Ga adatoms diffuse on the surface by passing through the missing dimer rows [9]. As can be seen in Figs. 1 and 2, this preferential diffusion path is normal to the As-terminated steps for the misorientation toward the $(1\bar{1}1)$As plane but parallel to the Ga-terminated steps for the misorientation toward the (111)Ga plane. Figs. 1 and 2 show also schematically the different behaviour of the two different step types. From scanning tunneling microscopy (STM) studies it is known that Ga-terminated steps are relatively straight whereas As-terminated steps are very ragged [10].

As a consequence of the growth mechanism the terraces of the vicinal surfaces grown above T_{cm} are expected to be smooth whereas on those grown below T_{cm} a certain concentration of holes and islands will exist even after annealing.

3.2. Si attachment

Fig. 3 shows the time evolution of the RHEED intensity during Si deposition on the 2° toward (111)Ga misoriented surface for different substrate temperatures that were kept constant during GaAs growth and Si deposition. The intensity change during the deposition of only 0.04 ML Si is in the same order as that during the deposition of 1 ML GaAs. The intensity behaviour observed for substrate temperatures below and above T_{cm} is quite different. In a first approximation, it can be understood by considering the two extreme cases, namely a random attachment of Si atoms on the terraces with statistically distributed defects and a preferential attachment of Si atoms at the edges of ordered steps.

At 550 °C the intensity decreases linearly with the Si coverage. This suggests that the Si adatoms form a lattice gas of increasing density. The change of the slope of the intensity curve at a coverage of about 0.1 ML can be explained by the formation of islands with a (3x2) structure evidenced by the appearance of half-order spots in the $[\bar{1}10]$ azimuth and of third-order spots in the [110] azimuth. At a coverage of about 0.24 ML asymmetric third-order spots are observed in the $[\bar{1}10]$ azimuth due to the formation of a distorted (1x3) structure.

The intensity behaviour at 580 °C and 590 °C with a nonlinear intensity decrease, a minimum at a Si coverage of about 0.05 ML and the appearance of half-order spots at about the same coverage is considered to be typical for a wire-like attachment of the Si atoms at the step edges as will be discussed below in detail for the interrupted Si deposition. It should be noticed that compared to the case considered before the (3x2) structure develops at a lower coverage whereas the distorted (1x3) structure is formed at higher coverages.

Fig. 4a shows the RHEED intensity recorded during Si deposition on the 2° toward (111)Ga misoriented surface in intervals of 90 s growth and 180 s growth interruption. The intensity decreases nonlinearly with the Si coverage and shows a slight recovery when the Si flux is interrupted. After reaching a coverage of 0.041 ML the intensity rises rapidly. At approximately the same coverage the (3x2) structure develops. These observations are consistent with the incorporation model schematically represented in Fig. 4b (cf. also Fig. 1). The nonlinear change in "kink" density and strain accompanying the attachment of migrating Si atoms as dimers at the step edges is reflected in a nonlinear intensity decrease. The recovery behaviour of the intensity suggests that this process including the ordering of the dimers can be completed by periodic interruptions of the Si flux. From symmetry and coverage arguments it is concluded that the Si dimers arrange themselves in units with two dimers and one missing dimer (model 1) or with one dimer and two missing dimers per unit mesh (model 2). The completion of (3x2) units along the step edge (to such extent that they can be detected by electron diffraction) and the attachment of a second row finally leads to the three-fold and two-fold periodicity in the $[\bar{1}10]$ and [110] direction, respectively. The final intensity rise is attributed to changes in strain and reconstruction accompanying the Si attachment. For an ideal wire-like attachment of Si dimers the first strip of (3x2) units will be completed at a coverage of 4/3 θ_{cm} (0.066 ML) and 2/3 θ_{cm} (0.033 ML), respectively, for model 1 and model 2, respectively, where the critical coverage θ_{cm} is given by the number of Ga sites at the step edges. The value of 0.041 ML found in the experiment discussed lies in between. The data compiled in Table 1 for a series of experiments suggest, however, that the dimer arrangement according to model 1 dominates. The scatter in the data can be explained by taking into account that in the real experiment a second row of (3x2) units will start to grow before the first one is completed and that the step edges are kinked. The latter effect that would shift the critical coverage to higher values will be, however, not very important since Ga-terminated steps are relatively straight. The considered deviations from the idealized case can also explain why the half-order spots belonging to the (3x2) structure do not necessarily appear exactly at the coverage corresponding to the RHEED intensity minimum but often at slightly lower or higher coverages.

Similar as for the 2° misorientation toward (111)Ga also for the 0.4° misorientation toward $(1\bar{1}1)$As a clear RHEED intensity minimum and at approximately the same coverage the development of a (3x2) structure was observed. A comparison with the Ga step-site density (cf. Table 1) reveals that the coverage of 0.021 ML Si corresponds nearly exactly to 2 θ_{cm}. The data reported by Wood [4] for a 0.2° misorientation toward $(1\bar{1}1)$As satisfy the same relation. This is consistent with the model for the Si attachment presented in Fig. 2. The intensity rise and the appearance of the superstructure reflections coincide with the beginning of the formation of a second strip of (3x2) units with two filled and one missing dimer rows that are now parallel to the step edge. A slight shift of the intensity minimum from the expected coverage to higher values can be attributed to the pronounced meandering of As terminated steps.

The conclusions on a wire-like incorporation of dopant atoms drawn above from the intensity behaviour are supported by the quite different intensity versus Si coverage plots found for Si deposition on the 0.4° toward (111)Ga misoriented surface. As a consequence of the competition between step-edge incorporation of dopant atoms and their clustering on the larger terraces, the coverage given by the RHEED intensity minimum deviates now strongly from the value expected for a preferential attachment at step edges, even at a substrate temperature of 610 °C [5]. This is explained by the limited migration across the terraces due to the large activation energy for diffusion along the [110] direction [9].

3.3. GaAs overgrowth

To study the effect of a high local Si concentration at the step edges on the subsequent GaAs growth, for the 2° toward (111)Ga misoriented surface RHEED intensity recordings for GaAs growth at 540 °C after Si deposition of 2×10^{13} atoms cm^{-2} and without the preceding Si deposition have been compared. The similar intensity behaviour shows that the Si modified surface can be overgrown by GaAs without adverse effects on the growth front morphology, although the reduced intensity indicates a reduced surface order.

To confirm the results of the RHEED measurements on the ordered Si incorporation Raman scattering by plasmon excitation was used. Difference spectra for light polarized parallel to the $[\bar{1}10]$ and

10] direction, respectively, showed a much stronger asymmetry for misoriented samples grown at onditions favourable for a wire-like Si incorporation than for reference samples grown on the perfectly riented GaAs(001) substrate [11]

The well-ordered (3x2) structure observed during interrupted Si deposition on the appropriately misoriented GaAs(001) surface has been explained by the ordered incorporation of Si atoms on Ga sites The Hall effect measurements of samples overgrown by GaAs confirmed that by pulsed δ doping Si can be incorporated in an unusual high concentration as donor. A sheet carrier concentration as high as 8 x 10^{13} cm^{-2} has been realized for the deposition of 0 61 ML Si on a 2° toward (111)Ga misoriented GaAs(001) surface at 590 °C. Using these data it can be concluded that the distorted (1x3) structure observed at very high Si coverages is due to the incorporation of Si atoms in the As plane For continuous δ doping this is observed at much lower Si coverages

4. CONCLUSION

In conclusion we have shown that at appropriate conditions, in particular for interrupted deposition, Si atoms arrange themselves on vicinal GaAs(001) surfaces in a (3x2) structure along the step edges This structure arises from an ordered array of filled and missing Si dimer rows parallel to the [110] direction The critical terrace width for that a preferential attachment of the Si atoms at the step edges can be realized is much larger for a misorientation toward (1$\bar{1}$1)As than for a misorientation toward (111)Ga. This shows that as for Ga adatoms also for Si adatoms the preferential diffusion path is along the [1$\bar{1}$0] direction From Hall effect measurements it is evident that nearly all Si atoms despite their high local concentration at the step edges are incorporated as donors on Ga sites This Si modified surface can be overgrown by GaAs without adverse effects on the growth fr ot morphology

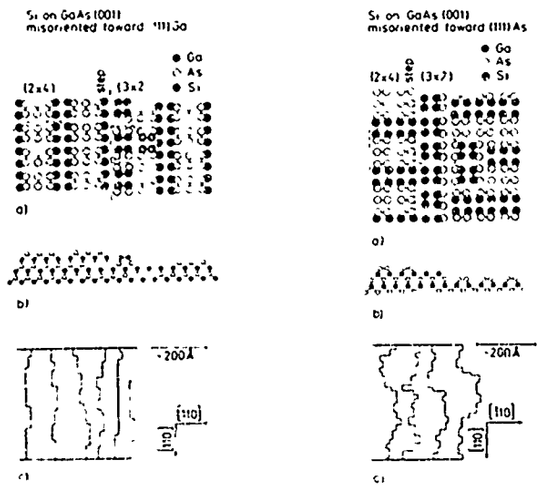

Figs 1 2 Schematic models of the (2x4) reconstructed vicinal GaAs(001) surface misoriented toward (111)Ga and (1$\bar{1}$1)As,respectively, with Si atoms attached in a (3x2) symmetry along the step edge in top (a) and side view (b) (c) is a schematic representation of the step edge roughness derived from STM studies [10]

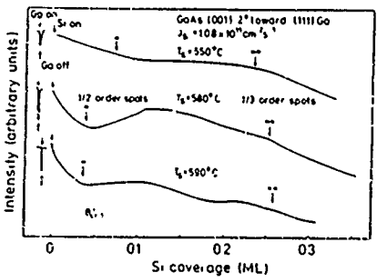

Fig 3 RHEED intensity recorded in the [1$\bar{1}$0] azimuth during continuous Si deposition at various substrate temperatures on GaAs(001) 2° misoriented toward (111)Ga The crosses mark the appearance of half order and asymmetric third order spots, respectively θ_{ML} is equivalent to the density of Ga step-edge sites

Table 1 Si coverages θ^{Si}_{min} corresponding to the minimum in the RHEED intensity recording. Model 1 refers to a (3x2) unit mesh with two Si dimers, model 2 to a (3x2) unit mesh with one Si dimer θ_{ML} is equivalent to the density of Ga step edge sites

misorientation	θ_{ML} (ML)	θ^{Si}_{min}			
		model 1	model 2	experiment	
				(ML)	(atoms cm^{-2})
2° toward (111)Ga	0 049	4/3 θ_{ML} = 0 066 ML	2/3 θ_{ML} = 0 033 ML	0 041-0 075	(2 6 - 4 7) x 10^{13}
0 4° toward (1$\bar{1}$1)As	0 010	2 θ_{ML} = 0 020 ML	1 θ_{ML} = 0 010 ML	0 021	1.3 x 10^{13}
0 2° toward (1$\bar{1}$1)As	0 005	2 θ_{ML} = 0 010 ML	1 θ_{ML} = 0 005 ML	0 010 - 0 014	(6-9) x 10^{12} ref [4]

Size effects in the transport properties of thin $Sc_{1-x}Er_xAs$ epitaxial layers buried in GaAs

R Bogaerts[a] A De Keyser[a] F Herlach[a] F M Peeters[a] J DeBoeck[a] C J Palmstrom[b] D Brehmer[c] and S J Allen Jr[c]

[a] Katholieke Universiteit Leuven, Departement Natuurkunde, B 3001 Leuven
[b] Universitaire Instelling Antwerpen, Departement Natuurkunde, B 2610 Antwerpen
[c] Bellcore, Red Bank, N J 07701-7040, USA
[d] University of California, Department of Physics, Santa Barbara, CA 93106

Size effects have been studied in the transport properties of $Sc_{1-x}Er_xAs$ layers with thicknesses ranging from 20 nm to 0.8 nm. Shubnikov-de Haas (SdH) measurements in tilted magnetic fields confirm the confinement of charge carriers in the $Sc_{1-x}Er_xAs$ quantum wells. For the layers with thickness less than 3.7 nm, the magnetoresistance is increasingly negative for decreasing thickness. Different size mechanisms which may be responsible for the observed behaviour are discussed.

1 Introduction

The progress in epitaxial growth methods, in particular Molecular Beam Epitaxy, has recently led to the fabrication of novel heterostructures consisting of semimetallic $Sc_{1-x}Er_xAs$ layers buried in GaAs [1]. With a view to the potential technological applications of these high carrier density systems, it is important to achieve a thorough understanding of the mechanisms dominating their transport properties. In earlier publications [2-4] the Fermi surface of $Sc_{1-x}Er_xAs$ layers with thicknesses of 71 monolayers (ML) (20 nm) and 20 ML (5.7 nm) was successfully described with a 3D model consisting of three electron ellipsoids at the X-points of the first Brillouin zone [2-4] and two hole spheres at the zone center [3,4]. SdH measurements in tilted magnetic fields on a 20 nm $Sc_{.33}Er_{.52}As$ sample however revealed that size quantization has to be taken into account: i) SdH oscillations were observed below the classical 3D cutoff condition [2], and ii) the SdH frequency attributed to one of the hole spheres clearly scaled with the *cosine of the angle* θ between the surface normal and the magnetic field [4].

In this paper we study the angular dependence of the SdH oscillations at 1.2 K in strong pulsed magnetic fields for six samples with Er concentrations ranging from $x=0.54$ to $x=1$, and thicknesses *ranging from* 71 ML to 20 ML. A detailed analysis is made of the quantum size effect characteristics present in the frequency spectra of the oscillations.

For $Sc_{1-x}Er_xAs$ layers with thickness $\leq$ 10 ML, interface scattering is so strong that no quantum structure can be detected. Instead, a complex behaviour of the magnetoresistance is observed, with an increase of negative magnetoresistance for decreasing thickness. We discuss different mechanisms governing the magnetoresistance in this region of layer thicknesses: i) indirect size effects due to the suppression of the antiferromagnetic order which is established below 5 K for bulk layers, ii) the decrease of the spin disorder resistivity when the 4f Er spins are lined up in an increasing magnetic field, iii) weak localization effects.

2 Quantum confinement

The samples were grown by MBE and consist of a 500 nm GaAs buffer layer on a semi-insulating substrate, followed by a $Sc_{1-x}Er_xAs$ layer and a 50 nm capping layer of insulating GaAs [1]. The mobility of the charge carriers in these structures is quite low ($\leq$ 1500 cm^2/Vs) and strong pulsed

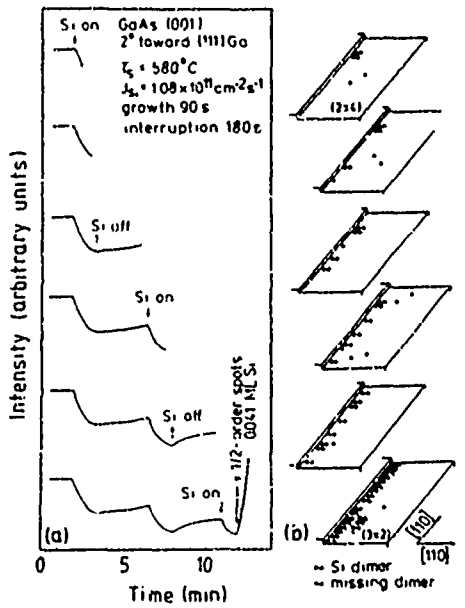

Fig 4 RHEED intensity recorded in the [110] azimuth during interrupted Si deposition at 580 °C on a vicinal GaAs(001) surface 2° misoriented toward (111)Ga (a) and the related incorporation model (b). The cross marks the appearance of half-order spots.

REFERENCES

[1] K. Ploog, M. Hauser and A. Fischer, Appl. Phys. A 45, 233 (1988)
[2] E. F. Schubert, J. Vac. Sci. Technol. A 8, 2980 (1990)
[3] G. E. W. Bauer and A. A. van Gorkum, Science and Engineering of One- and Zero-Dimensional Semiconductors, (S. P. Beaumont and C. M. Sotomayor Torres, Eds.), p. 133, Plenum, New York (1990)
[4] C. E. C. Wood, J. Appl. Phys. 71, 1760 (1992)
[5] L. Däweritz, K. Hagenstein and P. Schützendübe, J. Crystal Growth 127, 1051 (1993).
[6] M. G. Lagally, D. E. Savage and M. C. Tringides, Reflection High Energy Electron Diffraction and Reflection Electron Imaging of Surfaces (P. K. Larsen and P. J. Dobson, Eds.), p. 427, Plenum, New York (1988)
[7] L. Däweritz, J. Crystal Growth 127, 949 (1993).
[8] H. Neave, P. J. Dobson, B. A. Joyce and J. Zhang, Appl. Phys. Letters 47, 100 (1985)
[9] K. Shiraishi, Appl. Phys. Letters 60, 1363 (1992).
[10] M. D. Pashley, K. Haberern and J. M. Gaines, Appl. Phys. Letters 58, 406 (1991)
[11] M. Ramsteiner, J. Wagner, G. Jungk, D. Behr, L. Däweritz and R. Hey, this conference

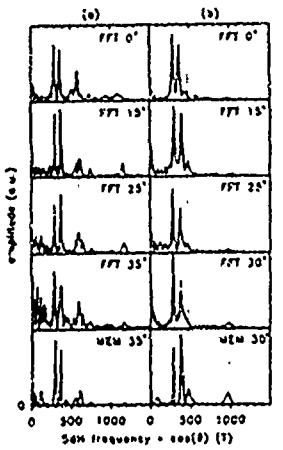

Fig 1 Angular dependence of the SdH spectra for (a) 40 ML $Sc_{.61}Er_{.39}As$, and (b) 20 ML $Sc_{.56}Er_{.44}As$ The frequency axes are rescaled with $\cos(\theta)$ The dotted lines indicate the hole frequencies For $\theta = 35°$ in (a) and $\theta = 30°$ in (b), the FFT spectrum is compared to the MEM spectrum

magnetic fields are required to observe the SdH oscillations generated by the hole spheres [3] The experiments in tilted magnetic fields were performed at 4 2 K on $Sc_{1-x}Er_xAs$ samples of 71 ML with $x=0.53$ and $x=0.68$, a sample of 40 ML with $x=0.56$, and samples of 20 ML with $x=0.54$ $x=0.70$ and $x=1$

The frequency spectra of the oscillations were determined by Fast Fourier Transform (FFT) and the Maximum Entropy Method (MEM) [5] The background in the MEM spectra is strongly reduced, and the peaks are more pronounced (Fig 1) The latter method is thus well suited to identify the frequencies corresponding to different

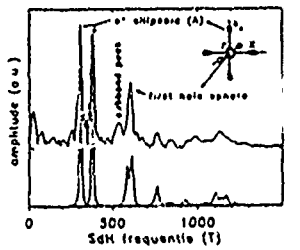

Fig 2 Comparison between the experimental FFT spectrum for 40 ML $Sc_{.61}Er_{.39}As$ (upper curve), and the spectrum simulated with the 3D Fermi surface model, which is shown in the inset The peak labeled with "subband peak" corresponds to the $N = 2$ subband of the holes in the first hole sphere

ent portions of the Fermi surface Unfortunately, this method may generate spurious peaks, which can be eliminated by comparison with the FFT spectra

The frequency axes of the spectra in Fig 1 which are representative of the spectra of all investigated samples are rescaled with $\cos(\theta)$ In this way the angular dependence of the entire spectrum can easily be interpreted For the frequencies generated by the hole spheres the $\cos(\theta)$ behaviour strongly deviates from three-dimensional behaviour and is indicative of magnetotransport in 2D subbands

This observation leads us to assume that the dominant frequencies in the SdH spectra are generated by the $N = 1$ subbands which are likely to have the highest mobilities A further question is whether oscillations generated by the other subbands are experimentally observed Reproducible peaks appear in the spectra of some of the samples on the left side of the frequencies associated with the $N = 1$ subbands in particular for the frequency of the hole sphere with the lowest carrier concentration (the "first hole sphere" in Figs 1a and 2) In order to evaluate the possibility that

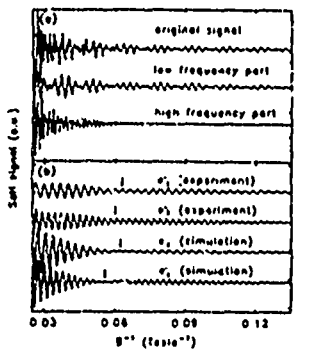

Fig 3 (a) Decomposition of the SdH signal of 40 ML $Sc_{.61}Er_{.39}As$ by means of inverse FFT The low frequency part, which is dominated by the e^- and e^- frequencies attributed to electron ellipsoid (A) [2], contains all frequencies below the $N = 1$ subband frequency of the first hole sphere The high frequency part is used to determine the effective mass of the holes
(b) Further decomposition of the low frequency part The two upper curves show the inverse FFT signals of the two dominant e^- frequencies The accompanying structure on the left side of the peaks is included for the inverse FFT The lowest curves show a simulation of the 2D signal arising from the $N = 1$ and $N = 2$ subbands for e^- and e^- The arrows indicate the nodes of the resulting beat pattern

these peaks are generated by 2D subbands, the subband energies and thus the effective masses of the charge carriers must be determined

For this purpose temperature dependent SdH measurements were performed on the 40 ML $Sc_{.61}Er_{.39}As$ sample The effective mass of the electron ellipsoids in the direction perpendicular to the long axis has already been obtained from SdH measurements in DC magnetic fields ($m^*_A = 0.17\ m_e$) [2] Here we attempt to measure the effective mass of the holes The SdH oscillations were decomposed into two parts by means of inverse FFT (Fig 3a): one part containing the frequencies below the $N = 1$ subband frequency of the first hole sphere, and another part containing all higher frequencies. The low frequency part mainly consists of two dominant frequencies, corresponding to one of the electron Fermi surfaces (surface (A) in Fig 2), which is split due to the exchange interaction with the 4f Er spins [2] The other part is dominated by the frequency of the first hole sphere, at least for magnetic fields up to 24 Tesla An analysis of the temperature dependence of the SdH amplitude in this magnetic field region leads to an effective mass of $m^*_h = (0.52 \pm 0.17)\ m_e$ for the holes of the first hole sphere The relatively large error is due to the small temperature region in which the experiments were carried out (1.4 K - 4.2 K). Also, we did not take into account the modulation of the amplitude by the exchange splitting of the hole Fermi energy, which is very small ($\Delta E_F / E_F \approx 4.5\%$) though observable [4].

The 2D hole subband energies $E_N = N^2\hbar^2\pi^2/2.m^*_h t^2$, as well as the subband frequencies $f_{SN} = m^*_h(E_F - E_N)/he$ have been determined using the value $m^*_h = 0.52\ m_e$. In these equations, t is the layer thickness and E_F is the Fermi energy calculated from the position of the hole peak in the FFT spectrum $f_A = m^*_h(E_F - E_0)/he \approx 613$ Tesla. In this calculation, the exchange splitting of the bands is neglected For the situation of Fig 2, with $t \approx 11.4$ nm and $E_F \approx 142$ meV, we obtain $E_F - E_0 \approx 136$ meV and $E_F - E_1 \approx 119$ meV, which leads to a SdH frequency for the $N = 2$ subband of 535 Tesla This is in good agreement with the observed additional peak at ≈ 558 Tesla in Fig 2

For the electron ellipsoid (A), m^*_e is estimated using the expressions $f_e = (f_{eb} + f_{ea})/2 = \hbar k_F^2/2e$, $n = k_{eB}^2 k_{eA}/3\pi^2$ and $\hbar^2 k_{eB}^2/2m_{eB} = \hbar^2 k_{eA}^2/2m_{eA}$, and inserting the values $m^*_{eA} = 0.17\ m_0$, $f_e = 152$ Tesla for the mean electron frequency, and $n = 3.1\ 10^{20}\ cm^{-3}$ for the total electron concentration The latter is obtained from an analysis of the SdH spectrum with the 3D Fermi surface model [3] From the values of the electron effective masses, we obtain for the SdH frequencies of

spin-down and spin up electrons in ellipsoid (A) the values (316, 308) Tesla and (388, 378) Tesla for the two lowest subbands Using these frequencies, we have simulated the 2D SdH signals for the spin-down and the spin-up electrons and compared these to the experimentally observed signals (Fig 3b). Although the different subband frequencies are not unmistakably visible in the experimental SdH spectrum, it is demonstrated here that the observed beating of the SdH amplitude for the electrons is due to the presence of at least two subband frequencies

3 Negative magnetoresistance

For [illegible]rs with thicknesses $\leq$ 10 ML size related [illegible]anisms dominate the transport properties at low temperatures The inset in Fig 1 shows the resistivity of a 20 ML and a 4 ML ErAs sample as a function of the temperature The almost linear decrease of the resistivity of the 20 ML sample at high temperatures is followed by a leveling-off at lower temperatures, and a drop in the resistivity at about 5 K, which is due to antiferromagnetic ordering of the magnetic spins [3] For the 4 ML sample deviations from this behaviour are observed in the low temperature region, i) below 40 K the resistivity shows a logarithmic increase with decreasing temperature ii) at the ordering temperature a rapid increase of the resistivity is observed In Ref [7], the latter is attributed to a suppression of the antiferromagnetic order in the thin layers, which leads to localisation of the charge carriers The effect is most pronou[illegible]ly present in the resistivity of the thinnest sample (3 ML) The logarithmic decrease which is clearly observed for ErAs samples of 3 4 and 5 ML extends over a larger temperature region for decreasing sample thickness

To gain insight into the mechanisms that cause the enhancement of the resistivity at low temperatures we have carried out transverse and longitudinal magnetoresistance (MR) measurements on ErAs samples of 3, 4 5 and 20 ML at 4 2 K 77 K and 150 K We discuss here the results obtained for the thinnest samples at 4 2 K, which are shown in Fig 4 The mobilities of the charge carriers in the layers are lower than the mobilities in the thicker $Sc_{1-x}Er_xAs$ layers. As a consequence, no quantum structure can be detected, and the classical orbital transverse MR component for a system with different types of carriers is strongly reduced Both the transverse and the longitudinal measurements show an increase of negative MR with decreasing thickness

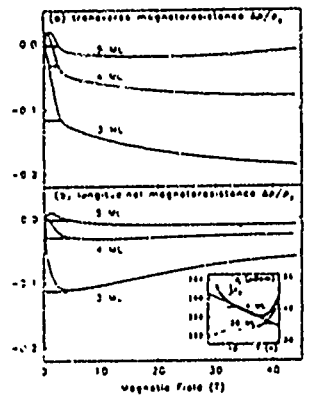

Fig 4 (a) transverse and (b) longitudinal MR for ErAs samples of 3 4 and 5 ML The inset shows the temperature dependence of the resistivity for the 4 ML sample and for a 20 ML ErAs sample The horizontal arrows in (a) and (b), which define new baselines for the high field MR, correspond to the negative MR contributions ρ_S/ρ_0, with ρ_S the resistivity due to suppression of the antiferromagnetic order below 4 K, which is indicated in the inset

At 4 2 K the behaviour of the MR in magnetic fields below 3 Tesla is closely related to the antiferromagnetic paramagnetic order transition The initial increase of the resistance, which characterizes the transition in bulk-like layers [6] is shifted to lower magnetic fields for the 4 ML sample and has disappeared for the 3 ML sample supporting the assumption of carrier localization due to suppression of the antiferromagnetic order

The logarithmic decrease of the resistivity above 5 K is extrapolated to 4 2 K as shown for the 4 ML sample in the inset in Fig 4 The difference between this extrapolated value and the measured value is attributed to the localization effect and corresponds to a negative MR contribution caused by quenching of the localization due to the alignment of the Er spins in a magnetic field Taking this negative contribution into account we define new baselines for the MR which are indicated by arrows in Fig 4 Remarkably a dominant negative high field component is observed for the transverse MR and a dominant positive component for the longitudinal MR Both are enhanced as the sample thickness decreases A negative contribution due to a decrease of the classical spin disorder scattering still has to be taken into account At 4 2 K this is however a constant contribution over a large part of the magnetic field range which does not change the general tendencies observed in the MR

The logarithmic temperature dependence of the resistivity between approximately 60 K (for the 4 ML sample) and 5 K suggests the presence of weak localization effects as an explanation for the observed MR Indeed, this mechanism can give rise to negative as well as positive MR contributions [8] the latter behaviour is observed in our samples A careful analysis of the measurements including a fit of these quantitative data to the combined expressions for weak localization and spin disorder scattering will be carried out in future work

4 Summary

SdH measurements on $Sc_{1-x}Er_xAs$ samples with thicknesses ranging from 20 nm to 5 7 nm have revealed clear evidence for 2D subband quantization in the entire frequency spectrum of the oscillations scales with the cosine of the angle between the surface normal and the magnetic field in 2D subband frequencies are present in the SdH spectrum at $\theta = 0°$ In order to determine the subband frequencies theoretically we have extracted the value of the effective mass of one of the hole splines from temperature dependent SdH measurements

For $Sc_{1-x}Er_xAs$ samples with thicknesses $\leq$ 5 7 nm size-related mechanisms, which are observed to be present in the temperature dependence of the resistivity lead to both negative and positive contributions in the magnetoresistance A detailed quantitative analysis of the measurements is in progress in order to investigate the exact origin of these contributions

Acknowledgements

R H is a Research Assistant and P M P a Senior Research Associate of the Belgian National Fonds voor Wetenschappelijk Onderzoek, which also provided funding for the experiments We acknowledge helpful discussions with Prof G Kido who drew our attention to the MEM method

References

[1] C J Palmstrom S Mounier T G Finstad and P J Wilkins Appl Phys Lett 56 362 (1990)

[2] S J Allen Jr J P Hellman C J Palmstrom and A Zrenner Phys Rev B 43 9959 (1991)

[3] R Rogaeva I Van Rechenberg I Herlach J M Perters J Hellman C J Palmstrom and S J Allen Jr Physica B 183 343 (1993)

[4] P Rogaeva A Van Esch I Van Rechenberg I Herlach G M Perters P Hellman C J Palmstrom and S J Allen Jr Physica B 183 340 (1993)

[5] W J Ventelon S A Ivankhikhin W H Press and B P Flannery Numerical Recipes p 681 edited by Cambridge University Press

[6] S J Allen Jr N Tabatabaie C J Palmstrom G W Hull T Sands F Hellman H L Gilchrist and R D Gunnison Phys Rev Lett 62 2309 (1989)

[7] S J Allen Jr N Tabatabaie C J Palmstrom G W Hull T Sands F Hellman H L Gilchrist and R D Gunnison Surf Sci 228 13 (1990)

[8] H Bruhl A Isihara and V Schmid Physica B 99 3999 (1980)

TuB1

SINGLE-ELECTRON TUNNELING AND COULOMB CHARGING EFFECTS IN ULTRASMALL DOUBLE-BARRIER HETEROSTRUCTURES

M. Tewordt,[a] V.J. Law, J.T. Nicholls, L. Martín-Moreno,[b] D.A. Ritchie, M.J. Kelly,[c] M.Pepper,[d] J.E.F. Frost, R. Newbury, G.A.C. Jones

Cavendish Laboratory, University of Cambridge, Cambridge CB3 0HE, United Kingdom

An extensive study of charge transport through submicron-diameter double barrier heterostructure diodes is reported. The occupation of the quantum well with single electrons, starting from zero, is observed in the form of sharp steps in the tunneling current. The magnitude of current steps can be controlled by changing the barrier thicknesses and thus their transparency for tunneling electrons. The plateau width of the current steps is related to the energies of the electron states in the quantum well which are affected by the combined vertical and lateral quantum confinement and by Coulomb charging effects. Diameter dependent studies of the tunneling current suggest that the lateral quantum confinement can result from the surface depletion potential, potential fluctuations, or single impurities. High magnetic field studies confirm this conclusion. The contribution of the Coulomb charging energy is investigated by using an asymmetric double barrier profile. It is shown that tunneling through submicron-diameter double barrier heterostructures provides valuable insight into the electronic properties of quantum boxes with very few electrons.

1. INTRODUCTION

Advanced technology now makes it possible to fabricate semiconductor nanostructures in which electrons are confined in small boxes with only a few hundred angstroms in size [1]. These tiny, artificially crafted electron systems are often referred to as "quantum dots" or "Coulomb islands". The interest in semiconductor quantum dots lies in their characteristic electronic properties. Firstly, when the size of the quantum dot is smaller than the Fermi wavelength and the electron mean free path, three-dimensional quantum confinement of the electronic states can be observed in vertical [2] and lateral [3] tunneling spectroscopy and in the optical spectra [4]. Secondly, the small size of the quantum dots implies that their electrostatic charging energy is quite significant. In analogy to classical electrostatics of a capacitor C, the Coulomb charging energy of a quantum dot is $E_C(N)=N^2e^2/2C$, where N is the number of electrons in the dot, and e is the electron charge.

Coulomb charging effects were first observed in small metal grains [5], but quantum confinement energies are much smaller and were never reported in these devices. However, in semiconductors, where both the electron effective mass and the Fermi energy are small, the confinement energies and the Coulomb charging energies [6] are comparable and can both be observed simultaneously [7]. This was first demonstrated in conductance studies of quantum dots formed in a high mobility two-dimensional electron gas (2DEG) [8].

A particularly interesting case occurs when the quantum dot is occupied by only a few electrons. This is difficult to achieve in microstructured 2DEG heterostructures, where Coulomb islands with typically 100 electrons can be isolated. The lowest number of electrons ever reported in such structures is 7 [9]. Recently, several groups have successfully observed the incremental charging of a quantum dot with single electrons, starting from *zero* [2,10-16]. They studied transport through ultrasmall diameter resonant tunneling diodes (RTDs) in which the GaAs quantum dot is formed between the two AlGaAs barriers. If the vertical confinement is strong enough the lowest dot states lie above the Fermi energy in the emitter at zero bias, and no electron occupies the dot. At low temperatures, incremental charging of the dot can be observed in form of sharp current steps in the tunneling current. This experiment is very sensitive (low noise level) and it is easy to perform. However, the electrons are stored dynamically in the quantum dot, i.e. the system is not in equilibrium. In recent theoretical models for transport through sub-micron scale RTDs lateral quantum confinement [17], Coulomb charging effects [6], and both contributions at the same time [7, 18] were considered.

Ashoori *et al.* [19] measured the capacitance signal of a quantum dot as it is charged up with single electrons, again starting from zero. In their device, no electrons tunnel through the dot, and therefore the discrete electron states can be probed under conditions closer to equilibrium.

In this paper, we present an extensive study of tunneling through nanometer scale AlGaAs-GaAs double-barrier quantum dots. The observation of single-electron charging is described under various experimental conditions that affect the electron transmission and the energetics of the quantum dot. Parameters studied include diameter, barrier thickness and asymmetry, magnetic field, and temperature. It will be shown that this system is a powerful experimental laboratory suited for the study of quantum dots in the limit of very few electrons.

2. SAMPLES AND EXPERIMENT

The diodes studied here were processed from 4 AlGaAs-GaAs double barrier heterostructures grown by molecular beam epitaxy on an n^+-type (100) GaAs substrate. The undoped active layers of structure 1 comprise a GaAs quantum well (thickness w=14nm) sandwiched between two $Al_{0.33}Ga_{0.67}As$ barriers (top barrier thickness b_1=10nm, substrate side barrier thickness b_2=7nm), and GaAs spacer layers (b_0=7nm). The top and bottom GaAs contacts, starting from the spacers, comprise a 350nm layer, Si-doped to $2\times10^{16}cm^{-3}$, a 28nm thick layer, with the doping graded from $2\times10^{16}cm^{-3}$ to $1.4\times10^{18}cm^{-3}$, and a 350nm thick layer, Si-doped to $1.4\times10^{18}cm^{-3}$. The other three heterostructures 2-4 are symmetric and have no graded doping profile in the contacts. The main design parameters of heterostructures 1-4 are summarized in table 1.

Free standing single RTDs with diameters between 0.1μm and 10μm were fabricated from the heterostructures by employing electron-beam lithography and CH_4-H_2 metallorganic reactive ion etching [10].

All samples were measured at T=4.2K or in a dilution refrigerator operating at base temperature of the mixing chamber (T=20mK). The diodes have to be measured under low temperatures, because the discrete electronic states can only be observed when the energy spacin

of the quantum dot states is smaller than the thermal broadening k_BT of the Fermi energy in the contacts. This condition is typically fulfilled at temperatures around T=1K (see section V).

Figure 1 shows the current-voltage (I(V)) characteristics of an asymmetric double barrier diode (structure 1) with *large* diameter d=10μm. Resonance peaks from tunneling through the first 2D subband are observed in both bias polarities. The asymmetry of the I(V) results from considerable charging of the quantum well only in forward bias. In forward bias, the rate of tunneling into the well is higher than that of tunneling out, leading to much higher electron charging of the quantum well than in reverse bias [20]. Therefore, the current peak in forward bias is larger than in reverse bias. Charging also leads to more inefficient biasing of the quantum well, resulting in a higher peak voltage in forward bias as compared to reverse bias [20].

3. TUNNELING IN SMALL DIAMETER DIODES

The charging of the well increases with bias and it is proportional to the area of the diode. If the diode diameter is made very small, the incremental charging with single electrons can be resolved. Every electron that occupies the well contributes to the current by a discrete amount $\Delta I=e/\tau$, where e is the electron charge and τ is the transit time. The width of the resulting current plateaus in bias depends on the spacing in energy of the electronic states in the well. Main contributions to the spacing are the confinement energy and the electrostatic charging energy.

In Fig. 2 (a), a typical small diameter RTD is depicted schematically. Electrons tunnel from the contact regions through the AlGaAs barrier into the quantum well. The electron motion is laterally confined between the diode sidewalls in both contacts and in the quantum well. Thus, one-dimensional subbands are formed in the contacts and discrete zero-dimensional (0D) states are obtained in the well ("quantum dot"). The 0D states can be probed by measuring the tunnel current upon applying a bias between the contacts.

The discrete confinement energy in the well is $E_z+E_{n,m}$, where E_z is the energy from the vertical quantum confinement between the barriers. We tentatively assume that discrete states $E_{n,m}$ result from the lateral surface depletion potential. It is usually modeled using a two-dimensional, circular symmetric parabolic potential with quantum energies $E_{n,m}=(2n+|m|+1)\hbar\omega_0$ with the radial n=0,1,... and the azimuthal m=0,±1,±2,... quantum numbers. The lateral confinement energies can also be modeled using the hard-wall potential $E_{n,m}=(n^2+m^2)\pi^2\hbar^2/2md^2$, where d is the wall separation. The lateral confinement potential is not necessarily from the surface depletion potential. Particularly in systems with only very few electrons it can result from potential fluctuations [16] and from single impurities [13].

The Coulomb charging energy can be modeled using a single effective capacitance C. This is the usual approach in studies of resonant tunneling in quantum dots [6,7], although recently, it has been noted that electron-electron interactions within the dot can be important [23]. The resonant energies of the quantum dot states can be written as

$$E(n,m,N)_{tot} = (e^2/C)(N-1/2) + E_z + E_{n,m} \quad (1).$$

The Coulomb charging energy of the quantum dot filled with N electrons gives the term $(e^2/C)(N-1/2)$ [7]. It can be estimated from the effective dot capacitance C by

$$C=(\varepsilon\varepsilon_0\pi d^2/4)(b_1^{-1}+b_2^{-1}). \quad (2)$$

The tunnel current for a single electron through the quantum well is given by [10,12]

$$\Delta I=e(\Gamma_1\Gamma_2/\Gamma_1+\Gamma_2) \quad (3),$$

where Γ_1, Γ_2 are the tunnel rates through the first and second barrier, respectively. Every time a discrete dot state falls below the Fermi energy in the emitter, a new current step ΔI will occur, leading to a current-voltage staircase. The tunnel rates Γ_1,Γ_2 depend exponentially on the barrier transparency and can be estimated in the WKB approximation by

$$\Gamma\sim(E_z/\hbar)T(E_t)=(E_z/\hbar)\exp[-(2b/\hbar)\sqrt{(2m^*(V_0-E_t)}] \quad (4)$$

where b is the barrier thickness, V_0 the barrier height, and E_t the electron energy. Other models are more suitable when considering the influence of temperature and dimensionality of emitter contacts on the shape of the I(V) steps [1, 6,7,8,10, 17].

Figure 2(b,c) shows a schematic band diagram to illustrate tunneling in a laterally confined *asymmetric* RTD from structure 1. Under reverse bias (Fig. 2(b)), there are 0D states in the accumulation layer at the interface of the thick barrier (box 1) and in the well (box 2). When in resonance, the energies of the 0D states in box 1 and box 2 line up and electrons can tunnel between the 0D states, leading to spikes in the I-V characteristics [21,22]. The tunneling rate Γ_1 through the thick (emitter) barrier is much lower than the tunneling rate Γ_2 through the thin (collector) barrier (i.e. $\Gamma_1<<\Gamma_2$), and therefore, at low biases, there is at most one electron at a time in box 2. The spacing of adjacent single particle states $\Delta E_n=\hbar\omega_0$ is related to the measured spike spacing in bias ΔV_S through the relation $\Delta V_S=\eta_{rev}\Delta E_n/e$, where $\eta_{rev}=(b_1+0.5w)/(b_1+w+b_2+b_0)$ is the fraction of the bias voltage dropped between the emitter and the well. Thus the resonance spacings in bias are related to the 0D single electron spectrum E_n in box 2.

The forward bias situation for tunneling is depicted in Fig. 2 (c). When the 0D states in the well fall below the electrochemical potential in the emitter contact, electrons can tunnel from the 1D subbands in the emitter through the thin barrier (with tunneling rate Γ_2), which is too transparent to form an accumulation layer. If a state below the Fermi energy is empty, an electron can tunnel from the emitter into the well after the time τ_1. Every electron that occupies the well will tunnel out

of it after a time τ_e and thus contribute to the current with a current step ΔI given in eqn (3) ($\Gamma_{1,2}=1/\tau_{1,2}$). Increasing the bias will lead to incremental charging and thus to a current-voltage staircase. If the quantum dot contains N electrons, a current step will occur when an additional electron tunnels into the quantum dot, and the energy of the dot will increase by $\Delta E(N, N+1)=\Delta E_n+\Delta E_C$. Thus, the plateau widths in bias, $\Delta V_P=\Delta E(N, N+1)/e\eta_{for}$, may be larger than the spike-spacing ΔV_S in reverse bias, where only the single electron spectrum E_n is probed.

4. RESULTS AND DISCUSSION

4.1. Fine structure at the current threshold

Figure 3(a) shows the I(V) of a diode from heterostructure 1, with conducting diameter d=150nm. The conducting diameter was estimated by extrapolating the 2D resonance peak current from a larger diameter diode. Since the asymmetry of the I(V) curve is retained compared to Fig.1, we can assume that the quantum well is charged considerably in forward bias. The interesting feature of this data is the appearance of fine structure at low biases.

In Fig. 3(b), the I(V) curve of a diode from structure 1 with diameter d=300nm is shown at low biases. At T=4.2K (see inset), a smooth bump is observed at the current threshold in each current direction. At T=20mK, fine-structure in forward bias has developed into a sharp current-voltage staircase, whereas in reverse bias, a complicated sequence of current spikes has appeared. The steps in forward bias have a magnitude between 5pA and 14pA and the plateau widths range in bias between 1mV and 5mV. Spacings of the spikes in reverse bias are ΔV_S=0.5-1mV, i.e., they are an order of magnitude smaller than the plateau widths.

The current steps in forward bias are related to the incremental charging of the well with single electrons. The first current step corresponds to one electron tunneling through the well, the second to two electrons and so on. The magnitude of the current steps depends on τ_i and τ_e, which can be calculated using the WKB approximation (see section 3).

The fine structure under low reverse bias seems to indicate that the well is not occupied with electrons between the spikes. The most reasonable explanation for this observation is that the first electron tunnels from discrete states in the accumulation layer at the emitter-barrier interface (box 1 in Fig. 2(b)). This is in accord with experimental data obtained from double quantum dot structures [21]. The current step at -35mV may result from a second electron tunneling through box 2. It is not clear, however, why the magnitude of current spikes in reverse bias is larger than in forward bias, because the transit time should be smaller.

The smaller spacing of spikes as compared to the plateau widths is in qualitative agreement with the assumption that in reverse bias charging effects do not contribute, because only one electron occupies the well at a time. The fine-structure in reverse bias contains information on the single-electron spectrum in box 2.

4.2. Diameter dependence

It was discussed in section 3 that both confinement energy and charging energy decrease with increasing quantum box size. We want to investigate if we can control this confinement by changing the diode diameter d. This control should be possible if the lateral confinement is dominated by the surface depletion potential of the diode sidewalls [2].

Figure 4 shows the I(V) of four diodes from structure 1 with different conducting diameters 150nm, 300nm, and 10μm as a function of applied bias. In forward bias (Fig. 4 (a)), the current displays sharp steps above the threshold voltage for all four diodes. Magnitudes of current steps are about 10pA for the 150nm and 300nm diameter diodes, and about 5pA for the 10μm device, i.e., there is only a very weak dependence on diode diameter. It is remarkable that nearly the same current steps are observed for diodes that differ in area by more than three orders of magnitude. This result shows that current steps are dependent on the heterostructure profile and clearly supports our model of single electron tunneling eqn (3) in which the magnitude of current steps is independent of the area of the diode. The value of the first current-step calculated using the WKB approximation (section 3) is ΔI=15pA. We have used equ. (3), the values for b_1, b_2, w, b_0, (from Table 1 for structure 1), V_0=256meV (for x=0.3), and assumed linear voltage drop over the double-barrier profile. The calculation is in good agreement with the experimental current steps ΔI.

The most remarkable result of this data is the observation of current steps even in a diode with d=10μm. In the Coulomb blockade model a plateau width of a few mV (see Fig. 4(a)) implies a capacitance of the order 10^{-16}F and thus according to eqn (2) a diameter d=160nm. Similar considerations hold when the plateau width is interpreted as related to lateral quantization. This result clearly favours an explanation in terms of localized states within the well (maybe due to potential fluctuations) and will have to be subject to further investigations. It can also be seen in Fig. 4 that the current threshold decreases with diode diameter, and at d=10μm it is just above zero bias. This latter observation will lead us below to argue in favour of a model of lateral confinement from potential fluctuations.

In reverse bias, the spike-like I(V) fine structure is retained for all diode diameters. This observation supports our model, that electrons tunnel from fully quantized emitter-states into the well-quantum dot. The fine-structure is difficult to quantify, but we cannot see any clear diameter dependence of the magnitude or spacing of spikes. Again we observe the decrease of the current threshold with increasing diode diameter.

4.3. Dependence on barrier thickness and symmetry

The tunnel current for a single electron through the quantum well is given by eqn (3). Therefore, we can use the experimental dependency of current step magnitudes on barrier thickness to test our model of single electron tunneling (eqn (3)) even further.

We have studied the dependence of current step magnitudes of four diodes with barrier thicknesses b=4.3nm, 5.2nm, and 7.1nm (nearly symmetric) and b=10nm (thicker barrier of the

asymmetric structure 1). All diodes have different diameters d, because the lateral confinement is difficult to control by processing. In Fig. 5, the first current step is plotted for four diodes with different barrier thicknesses b. The offset in bias has been changed for clarity. The temperature is T=20mK.

The magnitude of current steps decreases exponentially with barrier thickness. This is in agreement with eqn (3) for ΔL and eqn (4) for the tunnel rates. The experimental current steps are 5-10pA, 0.5nA, 12nA, and 50nA for barrier thicknesses 10nm, 7.1nm, 5nm, and 4.3nm, respectively (compare with table 1). The corresponding values calculated using the WKB approximation and parameters from table 1 are 15pA, 2nA, 18nA, and 50nA. While there is good agreement between experiment and theory, we can say that the dependency on barrier thickness supports the model of single-electron tunneling (eqn (3)). Other numerical calculations [9] show that in most cases, quantitative agreement is obtained between theory and model.

It is noteworthy that the structures 3 and 4 with thin barriers exhibit current-steps in both bias polarities. This is to be expected, since barrier transparency is too high to allow an accumulation layer to be formed at the emitter-barrier interface.

4.4. Tunneling in high magnetic fields

The quantum dot resonance spectrum exhibits a very characteristic dispersion as a function of the magnetic field which is suited for modeling the energetics of the 0D states. Alternatively, the 0D states can be studied by tuning the lateral confinement using side gates, but this approach is much more problematic [13,14]. Firstly, it is very difficult to process devices in which the electric field only squeezes the quantum dot and not the contact regions. Secondly, the complicated electrostatics makes a clean calibration between gate-voltage and confinement energy very difficult. All these problems can be circumvented by using magnetic fields to tune the 0D states.

We have studied a large number of quantum dot diodes with various diameters, barrier and well thicknesses and doping profiles in high magnetic fields. The fine structure often exhibits different phenomena for each sample which are difficult to interpret. Here, we will discuss one interesting sample to describe typical problems we had to deal with during our investigations.

The data was obtained from an 83nm diameter R1) from structure 3 [16]. The current-voltage characteristics in a magnetic field parallel to the current direction are shown in Fig. 6 (a). Figure 6(b) shows resonance positions in forward bias as a function of magnetic field B applied parallel to the current direction. With increasing magnetic field, all steps shift to higher bias following a parabolic shape. This is in contrast to single electron theories for two-dimensionally and three-dimensionally confined, nearly cylindrical quantum boxes in magnetic fields [24] where some states increase in energy with B, while others decrease. In high magnetic field, the experimental traces run parallel to $V=(1/e\eta)\hbar\omega_c/2)$, with $(\hbar\omega_c/2)$ being the cyclotron frequency. The cross-over to the linear increase occurs at around B=6T. The lateral quantum confinement can thus be estimated to be in the order of the magnetic length $l_0=\sqrt{(\hbar/eB)}=10nm$. This strong

confinement implies quantum energies in the order of ≈30meV, which is much greater than the energies $\Delta E=e\eta\Delta V=e(0.3855)5\text{-}12mV=2\text{-}5meV$ obtained from the plateau widths. We therefore propose that electrons tunnel into laterally separated minima of a disorder potential in the quantum dot [16, 19].

In the circular symmetric, two-dimensional harmonic oscillator model, the eigenenergies are [21]

$$E(B)_{n,m} = (2n+|m|+1)[(\hbar\omega_c/2)^2 + (\hbar\omega_0)^2]^{1/2} + m(\hbar\omega_c/2) \qquad (5)$$

We can fit the data in Fig. 6(b), using the formulas for the energy eqns (1), (2) and (5). Assuming that electrons occupy the lowest states with n=m=0 in the minima, we can fit several curves and obtain confinement energies between 9-35meV (for η=0.3855-0.5). The minima might arise from potential fluctuations in the central region which result from single impurities sitting in the well or from randomly distributed donors in the contacts (i.e., beyond the spacer layers, in a similar way as has been described for high mobility heterojunctions [25]). The parallel shift of the resonances with magnetic field suggests that the lateral extension of the wavefunctions of d≈10nm in all the states are about the same.

The model corroborates with the data obtained from the diameter dependence of the I(V) fine-structure in Fig. 4. With increased diode diameter, the probability for lower energy minima to occur in the disorder potential increases, resulting in lower bias current-thresholds. For tunneling through such a low lying state the effective barrier height is increased and current steps are decreased according to eqn (3).

We note that in other data, many new and interesting phenomena can be observed which still have to be investigated in detail. It is therefore quite conceivable that a device can be processed that clearly exhibits all the electronic properties that are expected in a model of lateral confinement from surface depletion, as was observed in [2]. We can thus identify lateral quantum confinement from surface depletion, potential fluctuations from randomly distributed donors, and single impurities.

4.5. Temperature Dependence

The temperature dependence of the shape of the fine-structure resonances is still controversial. In Fig. 7, a typical plot of the resonances arising in the low bias differential conductance-voltage (G(V)) characteristics is plotted for temperatures between T=4.2K and T=20mK. The diode was processed from structure 3 and has a conducting diameter of 83nm. The two plots at T=4.2K and T=1.25K were taken in a conventional He^4 cryostat, whereas the other data was taken in a dilution refrigerator (T is the temperature of the mixing chamber).

The linewidth of the G(V) resonances is broadened as T increases. Raising the temperature causes a broadening of the Fermi energy in the emitter contact. Therefore, thermally excited electrons will contribute to the tunnel current and broaden the observed resonance structure. If the

thermal broadening k_BT exceeds the spacing of the discrete electronic states in the quantum dot $\Delta E_{n,m}$ and ΔE_C, resonance structures cannot be resolved anymore.

At T=20mK, the linewidth of the lower bias resonances is ΔV=3mV. This corresponds to an energy broadening of ≈1.5meV which is more than one order of magnitude larger than the electron-state lifetime and the broadening of the Fermi energy in the contacts (k_BT=0.086meV at 1K). The electron state lifetime of the 0D states of this diode are in the order of 0.1meV (which is consistent with the current step-height). It has been suggested by the authors that inelastic scattering may cause this broadening [9] But it has not been possible to present a convincing model to explain the detailed broadening mechanism so far. Su *et al.* [12] suggested that the broadening may be due to electrical noise pick-up. However, it is difficult to understand how electrical noise pick-up leads to a linewidth broadening of 1.5meV (k_BT=1.5meV corresponds to T=17K). The problem of the linewidth broadening will have to be addressed in future investigations.

5. CONCLUSIONS

A single electron that tunnels through a double-barrier potential has a well defined transit time τ and therefore it contributes to the tunneling current by a discrete amount $\Delta I = e/\tau$. We have observed the incremental charging of the double-barrier diode with single electrons by measuring the tunneling current increasing from zero in current steps with magnitude ΔI. Increasing the transmission by decreasing the barrier thicknesses leads to correspondingly smaller current steps, in good accord with simple model calculations. The step-like I(V) is therefore a clear demonstration of single-electron tunneling.

Much more problematic is our understanding of the energetics involved. We have shown that the plateau-widths in bias of the current steps can explain the lateral confinement energies and electrostatic charging energies for submicron diameter quantum dot diodes. However, fine-structure was also observed in much larger diameter diodes. The plateau widths in that data was an order of magnitude too big to explain confinement or charging effects. High magnetic field data suggested that electrons in the lowest states are laterally confined to only d≈10nm. From this, we have concluded that lateral confinement is due to a disorder potential. The drawback is that presently we cannot control this disorder potential. Therefore, our target is to find a way to control lateral confinement as well as we can control vertical confinement. Possible improvements could be obtained by decreasing the impurity concentration by growing smoother barrier interfaces, and by reducing the surface damage during reactive ion etch.

In conclusion, we have shown that submicron diameter RTDs are very promising devices to study the electronic properties of quantum boxes containing only very few electrons. However, we have to improve the experiment with respect to the purity of the heterostructures in order to eliminate potential fluctuations and impurities from the dot. This could be achieved by reducing the impurity concentration in the well, surface roughness and sidewall damage.

Tunneling in small RTDs allows us to study the energetics in the limit of very few electron systems [23]. They allow also the observation of excited states [8]. Furthermore, the coupling of two or more dots (molecules or 1D crystals) can be investigated. For all these interesting experiments, this system continues to be a very promising candidate.

This work has been supported by the Science & Engineering Research Council (SERC). M.T. acknowledges support from the Commission of the European Communities and a Charles and Katherine Darwin Fellowship of Darwin College, Cambridge. L.M.M. acknowledges the Spanish Ministerio de Educación y Ciencia for support. J.T.N. is supported by the Leverhulme Trust and the I. Newton Trust.

REFERENCES

(a) Present address: Max-Planck-Institut für Festkörperforschung, Heisenbergstr. 1, W-7000 Stuttgart 80, Germany.
(b) Present address: Instituto de Ciencia de Materiales, Consejo Superior de Investigaciones Cientificas, Universidad Autonoma de Madrid, 28049 Madrid, Spain.
(c) Present address: Department of Physics, University of Surrey, Guildford, Surrey GU2 5XH, England.
(d) Also at the Toshiba Cambridge Research Centre, 260 Cambridge Science Park, Cambridge CB4 4WE, England.

1. Marc A. Kastner, *Physics Today*, Jan 1993, 25.
2. M.A. Reed *et al.*, *Phys Rev Lett* 60, 535 (1988); *Festkörperprobleme, Advances in Solid State Physics* 29, p 267 (1989).
3. C.G. Smith *et al.*, *J Phys C Solid State Phys* 21, L893 (1988).
4. Ch. Sikorski and U. Merkt, *Phys Rev Lett* 62, 2164 (1989); T. Demel *et al.*, *Phys Rev Lett* 64, 788 (1990); A. Lorke, J.P. Kotthaus, and K. Ploog, *Phys Rev Lett* 64, 2559 (1990).
5. T.A. Fulton and G.J. Dolan, *Phys Rev Lett* 59, 109 (1987); J.B. Barner and S.T. Ruggiero, *Phys Rev Lett*, 59, 807 (1987); I. Giaver and H.R. Zeller, *Phys Rev Lett* 20, 1504 (1968); I. Larkine and R.C. Jaklevic, *Phys Rev Lett* 22, 1371 (1969); reviewed by D.V. Averin and K.K. Likharev, *Mesoscopic Phenomena in Solids*, edited by B. Altshuler, P.A. Lee, and R.B. Webb (Elsevier, Amsterdam, 1991), p. 169.
6. H. van Houten and C.W.J. Beenakker, *Phys Rev Lett* 63, 1893 (1989); L.I. Glazman and R.I. Shekhter, *J. Phys Condens Matter* 1, 5811 (1989).
7. Atanas Groshev, *Phys Rev* B 42, 5895 (1990); C.W.J. Beenakker, *Phys. Rev* B 44, 1646 (1991).
8. P.L. McEuen et al., *Phys Rev Lett* 66, 1926 (1991); A.T. Johnson *et al.*, *Phys. Rev. Lett.* 68, pp (1992); see also in this context: U. Meirav, M. Kastner, and S.J. Wind, *Phys. Rev Lett.* 65, 771 (1990); L.P. Kouwenhoven *et al.*, *Z. Phys* B 85, 367 (1991).
9. J. Weis, R.J. Haug, K. von Klitzing, K. Ploog, Phys Rev. B 46, 12837 (1992).
10. M. Tewordt *et al.*, *J Phys Condens Matter* 2, 8969 (1990); *Appl. Phys Lett* 59, 1966 (1991); *Phys Rev* B 45, 14407 (1992).
11. S. Tarucha and Y. Hirayama, *Phys Rev* B 43, 9373 (1991).
12. B. Su, V.J. Goldman, M. Santos, M. Shayegan, *Appl. Phys Lett* 58, 747 (1991); B. Su, V.J. Goldman, J.E. Cunningham, *Science* 255, 313 (1992); *Phys Rev* B 46, 7644 (1992).
13. M.W. Dellow *et al.*, *Phys Rev Lett* 68, 1754 (1992).
14. P. Gueret, N. Blanc, R. Germann, H. Rothuizen, *Phys Rev Lett* 68, 1896 (1992).
15. A. Ramdane, G. Faini, and H. Launois, *Z Phys* B 85, 389 (1991); M. Van Hove *et al.*, *J appl. Phys* 72, 158 (1992).
16. M. Tewordt *et al.*, *Phys Rev* B 46, 3948 (1992).
17. Garnett W. Bryant, *Phys Rev* B 39, 3145 (1989), B 44, 12837 (1991).
18. D.V. Averin, A.N. Korotkov, and K.K. Likharev, *Phys Rev* B 44, 6199 (1991)
19. R.C. Ashoori *et al.*, *Phys Rev Lett* 68, 3088 (1992); see also W. Hansen *et al.*, *Phys Rev. Lett* 62, 2168 (1989); R.H. Silsbee and R.C. Ashoori, *Phys Rev Lett* 64, 1991 (1990).
20. A. Zaslavsky *et al.*, *Appl Phys Lett* 53, 1408 (1988)
21. M. Tewordt *et al.*, *Appl Phys Lett* 60, 595 (1992)
22. Garnett W. Bryant, *Phys Rev* B 44, 3054 (1991)
23. Garnett W. Bryant, *Phys Rev Lett* 59, 1140 (1987); N.F. Johnson and M.C. Payne, *Phys Rev Lett* 67, 1157 (1991), U. Merkt, J. Huser and M. Wagner, *Phys Rev* B 43, 7320 (1991)
24. C.G. Darwin, *Proc Cambridge Philos Soc* 27, 86 (1930), V. Fock, *Z Phys* 47, 446 (1928)
25. J.A. Nixon and J.H. Davies, *Phys Rev* B 41, 7929 (1990)

Structure	Barrier width (nm)[a]	Well width (nm)	Spacer (nm)	Doping ($10^{18}cm^{-3}$)[b]
(1)	10(7)	14	7	0.02
(2)	7.1(7.1)	5.5	5	~1.5
(3)	5.1(5.2)	5.5	5	~1.5
(4)	4.3(4.3)	6.1	5	~1.5

[a] Top (bottom) barrier.

[b] Doping of contacts close to the spacer layers.

TABLE 1.Summary of the double-barrier heterostructures.

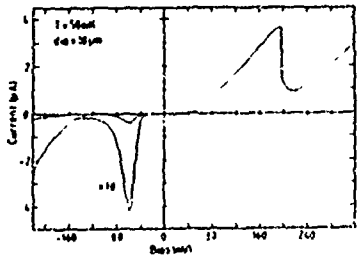

FIG. 1. I(V) characteristics of a *large* diameter asymmetric double-barrier diode from structure I.

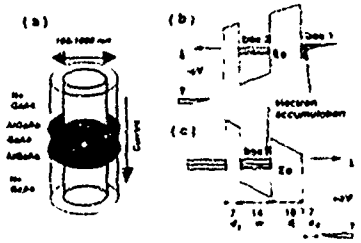

FIG. 2. (a) Schematic sketch of a submicron-diameter double-barrier diode. (b) Band diagram of structure I under reverse and (c) under forward bias.

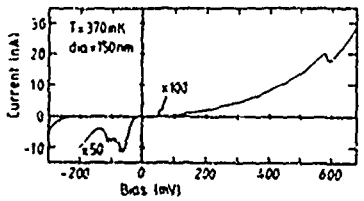

FIG. 3. (a) I(V) characteristics of a 150nm *diameter* asymmetric RTD from structure I at T=350mK.

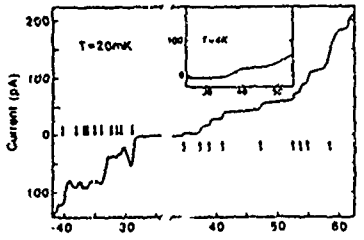

FIG.3. (b) I(V) at T=20mK of a 300nm diameter RTD from structure I at *low current levels, showing in forward bias the incremental charging of the quantum dot with single electrons, starting from zero.* The inset shows that the steps are washed out at T=4.2K. In reverse bias, tunneling between two quantum dots in series is observed.

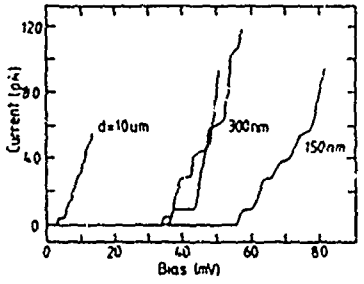

FIG. 4. (a) I(V) of four diodes from structure 1 *with conducting* diameters 10μm, 300nm, 300nm, and 150nm, in forward bias.

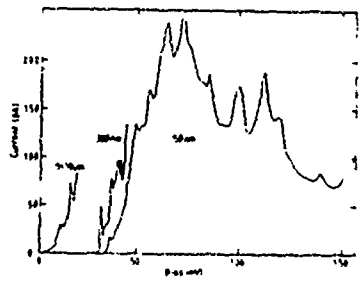

FIG 4 (b), as (a), but in reverse bias.

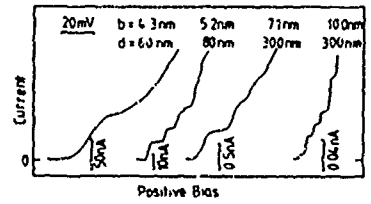

FIG. 5. I(V) of four diodes structure 1-4 with increasing barrier thickness b (and various electronic diameters d). The current steps ΔI decrease with increasing barrier thickness.

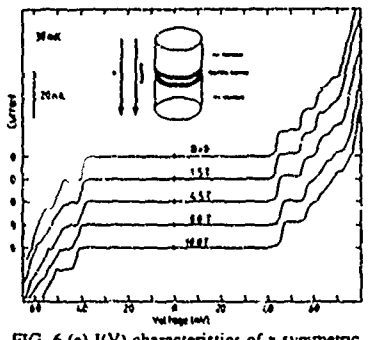

FIG. 6.(a) I(V) characteristics of a symmetric RTD from structure 3 with a conducting diameter of 83nm, as a function of magnetic field applied parallel to the current direction

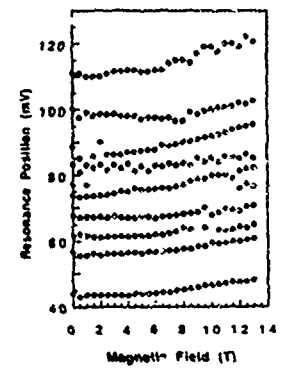

FIG.6. ,b) Positions of the resonance peaks in bias vs. magnetic field according to (a).

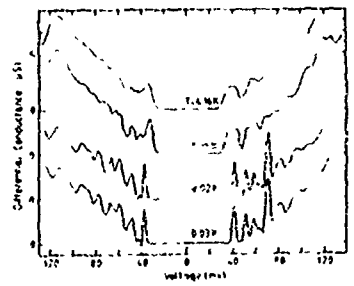

FIG. 7. Temperature dependence of the dI(V)/dV characteristics of a *symmetric* RTD structure 3 with d=83nm.

TuB2

Hydrostatic Pressure Sensors Based on Solid State Tunneling Devices

H. Brugger and U. Meiners
Daimler-Benz AG, Forschungszentrum Ulm, D-89081 Ulm, Germany
R. Diniz, T. Suski*), and E. Gornik
Walter-Schottky-Institut, TU München, D-85748 Garching, Germany
A. Förster and H. Lüth
Institut für Schicht- und Ionentechnik D 52425 Jülich, Germany

Abstract:

A new type of a hydrostatic pressure sensing device based on a thin AlAs/GaAs/AlAs double-barrier resonant tunneling (DBRT) structure is reported, which operates at room temperature. The current swing (ΔI) in the negative-differential resistance region depends linearly on the applied pressure (p). Diodes with an operating range of $\Delta p = 6000$ bar (12 000 bar) and a high sensitivity of 170×10^{-3} kbar^{-1} (85×10^{-3} kbar^{-1}) are realized with an AlAs barrier layer thickness of 2.8 nm (2.3 nm). Pressure sensing at 300 K is enabled by an elastic electronic tunneling process through the Γ-DBRT conduction band profile in combination with a sensitive pressure-dependent inelastic tunneling process through the transversal X-valleys in the AlAs barriers. The applied pressure decreases the GaAs/AlAs Γ-X discontinuity and yields to a significant enhancement of the valley current. The pressure coefficient ($\Delta I/\Delta p$) and operating range (Δp) can be adjusted by a variation of the AlAs barrier thickness.

1. Introduction

Double barrier resonant tunneling (DBRT) structures have been investigated intensively both for studying physical processes and for the development of novel device applications, mainly driven in direction of extremely high-speed electronic operations [1, 2, 3]. In the AlGaAs/GaAs material system the maximum achievable peak-to-valley current ratio (PVCR) values are limited by significant tunneling contributions through the indirect band-gap X-states in the $Al_xGa_{1-x}As$ barrier material ($x > 0.4$) in addition to the resonant current, which is determined by the Γ-conduction band profile. Hydrostatic pressure [4, 5, 6] and uniaxial stress [7] experiments have been performed by different groups to study the influence of the different conduction band minima on the tunneling characteristics of AlAs/GaAs/AlAs DBRT structures at helium and liquid nitrogen temperatures.

In this paper a room temperature operating AlAs/GaAs/AlAs DBRT-diode pressure sensing device is reported which takes advantage of the two tunneling channels through AlAs barriers, elastic (through Γ-Γ band profile) and inelastic (through Γ-X band profile). DBRT structures with a GaAs quantum well (QW) of 5 nm thickness and with AlAs barriers of thickness (L_B) in the range between 6 monolayers (6 ML, 1.7 nm) and 10 ML (2.8 nm) are realized. There is strong evidence of a significant inelastic Γ-X tunneling contribution through the X-valley states in AlAs, which influences the I/V characteristics. Applied hydrostatic pressure (p) yields to a decrease of the GaAs/AlAs Γ-X band offset and leaves the DBRT Γ–Γ profile almost unchanged. The dominant effect is an increase of the valley current density (j_v) and consequently a decrease of the PVCR. When the diodes are biased close to the negative-differential-resistance (NDR) region a linear behavior between the NDR current swing (ΔI) and the applied hydrostatic pressure (p) is observed. Sensing diodes with constant room temperature pressure sensitivities $S = \Delta I/\Delta p = 170 \times 10^{-3}$ kbar^{-1} and $S = 85 \times 10^{-3}$ kbar^{-1} over an operating range of $\Delta p \approx 6\,000$ bar and $\Delta p = 12\,000$ bar, respectively, are realized.

Figure 1. DBRT conduction band alignment for the direct Γ- (solid line) and indirect X- (broken line) valley minima. $E_0(\Gamma)$ and $E_0(X_t)$ are the first quasi-bond energy levels in the GaAs and AlAs QWs, respectively.

2. Layered Structure and Device Fabrication

The vertical layer sequence of the DBRT structure consists of two thin AlAs barriers with thickness L_B and a 5 nm thick GaAs quantum well (QW) grown by MBE in a VARIAN Mod-Gen II system on (100) oriented n$^+$-doped (2×10^{18}cm^{-3}) GaAs substrates. This is schematically shown in Figure 1 together with the conduction band profile. On both sides next to the DBRT structure 5 nm thick spacer layers and 10 nm thick dopant grading layers are used between the undoped DBRT layers and the 0.5 µm thick highly doped (6×10^{18}cm^{-3}) electrode regions.

The samples were grown at a fixed substrate temperature of $T_g = 600$°C (pyrometer measurement). The growth was interrupted at the normal interface (AlAs on GaAs) for 60 sec before the deposition of the AlAs layers in order to improve the morphological quality at the interfaces. From cross-sectional high-resolution TEM micrographs a roughness of only a one-monolayer-fluctuation at these interfaces with large area terraces is observed. Highest PVCR values of 5 at 300 K are achieved on this type of samples with $L_B = 6$ ML [8]. Layer thicknesses were accurately established by measuring RHEED oscillations on reference samples prior to the DBRT growth.

Device structures were fabricated by a standard lift-off process. Top side (cathode) circular contacts with a diameter between 12 µm and 20 µm and a large area backside (anode) contact were fabricated by alloyed GeNiAu, followed by a Ti/Au metallization for the bonding pads. The diodes are isolated by wet chemical mesa etching. The wafers were mechanically thinned below 100 µm thickness and diced in small squares. The chips were mounted on a gold plated ceramic carrier by a highly conducting and ductile two-component silver filled epoxy resin. The diodes were bonded by 10 µm thick gold wires. Reliable ohmic contacts were realized and the diode chips are carefully fixed to avoid any stress in the semiconductor material for operating temperatures between 2 K and 400 K and for pressure values up to 13 000 bar.

Device performance was investigated at room temperature with the diodes inside a UNIPRESS pressure-cell. Hydrostatic pressures up to 13 kbar were applied with light-petroleum as a pressure-transmitting fluid. The pressure values were monitored by a calibrated highly Te-doped InSb sensor. The current/voltage (I/V) behavior was measured in a pulsed mode to avoid thermal effects.

3. Experimental Results

In Figure 2 a series of room temperature I/V-curves at different applied hydrostatic pressure values between $p = 0$ (atmospheric pressure) and $p = 7$ kbar is shown for a diode with an AlAs barrier thickness of $L_B = 10$ ML. The electron flow direction was from the emitter top contact towards the collector substrate side. A monotonic enhancement of the peak current (j_P) and an exponential increase of the valley current is observed with increasing ambient pressure. This yields to a non-linear decrease of the PVCR which disappears completely for $p = 6$ kbar. The

*) on leave from UNIPRESS Warsaw (Poland)

peak-voltage V_P shows no significant change as a function of p. A similar behavior was observed for the opposite current direction.

The conduction band profile of the AlAs/GaAs/AlAs DBRT structure is shown schematically in Figure 1. From a transfer matrix calculation the first electron subband in the GaAs QW is expected at $E_0(\Gamma) = 105$ meV above the bottom of the conduction band. There is only a minor influence of $E_0(\Gamma)$ on barrier thickness for L_B in the range between 6 ML and 10 ML. The AlAs Γ-band minimum and the X-valley minimum are assumed to be 1.05 eV and 160 meV above the GaAs Γ-conduction band, respectively, and the indirect X-band minimum in GaAs to be 450 meV above the Γ-conduction band. For the X-valley electrons the AlAs layers are a QW rather than a barrier. From a simple square-well box model calculation the first allowed subband is expected at an energy of $E_0(X_t) = 90$meV for the four-fold degenerate transversal valley (X_t) and of $E_0(X_l) = 27$meV for the two-fold degenerate longitudinal valley (X_l). Due to size quantization the effective Γ-X offset at the GaAs/AlAs interface is accepted to be dependent on the AlAs barrier thickness.

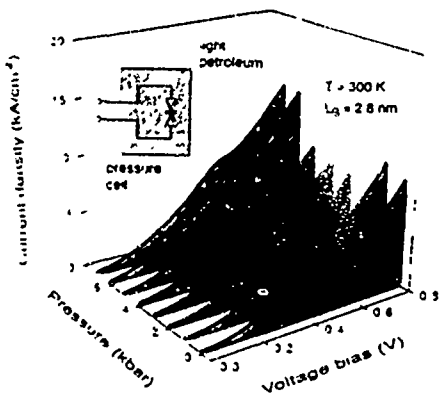

Figure 2. Room temperature I/V-curves for different applied hydrostatic pressures of a DBRT sensing diode with L_B = 10 ML (contact size diameter 16 µm).

The applied hydrostatic pressure leaves the DBRT Γ-profile almost unchanged but the Γ-X offset energy decreases linearly with p with a rate between -11 meV/kbar [9] and -12 meV/kbar [10, 11]. This enhances the non-resonant tunneling current through the AlAs X-valleys which pushes mainly the valley current in the DBRT structures to higher values. Diniz et al. [12] have shown that tunneling through the four-fold X_t-valleys predominates at room temperature while at helium temperature tunneling through the two-fold X_l-valleys dominate the non-resonant current contribution.

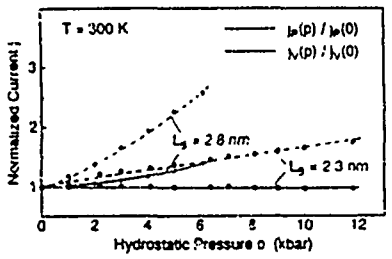

Figure 3. Normalized peak (solid line) and valley (broken line) currents as a function of applied pressure for two different devices.

Resonant tunneling is predominantly determined by the DBRT Γ-potential profile. However, Mendez et al. [4] have shown that a significant non-resonant tunneling contribution can take place through the Γ-X barriers in AlAs/GaAs/AlAs structures and that a reduction of the AlAs barrier thickness leads to a decrease of the Γ-X current contribution.

Table I Room temperature DBRT diode pressure sensor data. The devices are defined by mesa isolation, bonded by gold wires and mounted on a gold-plated ceramic carrier (1 ML = 0.2825 nm).

L_B (ML)	j_P (kA/cm²)	V_P (V)	PVCR	S (kbar⁻¹)	Δp (kbar)
10	5	0.3	1.9	0.17	6
8	20	0.4	3.1	0.09	12
6	60	0.4	5.0	0.06 *)	> 13 *)

*) pressure range limited by the experimental setup, non-linear Δj (p) behavior for p > 10 kbar.

In Figure 3 the normalized room temperature current densities as a function of applied pressure are shown for two different sensor devices consisting of a DBRT diode with L_B = 10 ML (data from Figure 2) and L_B = 8 ML. For the thinner barrier device the current vary with significantly lower rates as a function of p. This is attributed to the lower non-resonant X-tunneling contribution in thinner AlAs layers. This allows the L_B = 8 ML device to operate over a larger pressure range up to 12 kbar. In Tab. I the diode parameters of investigated samples are summarized. The highest operating pressure range of more than 13 kbar (limited by our experimental setup) was observed for a L_B = 6 ML (1.7 nm) diode. On this thin-barrier sample the influence of the X-tunneling contribution is rather small and the peak current already decreases slightly with applied pressure [12]. A decrease of the tunneling currents is expected from a pressure-induced increase of the tunneling electron mass. On the sample with L_B = 8 ML (see Figure 3) there was no resultant variation of j_P (p) found. This is advantageous for device applications, because a change of j_P can be used to monitor any additional extrinsic parameter, e.g. the ambient temperature.

The influence of electron-mass-induced and the Γ-X barrier-height-induced change of the current densities as a function of p was estimated quantitatively on the basis of a resonant tunneling model, neglecting any thermionic effects [12]:

$$j_P\,V(p)/j_{P,V}(0) \approx \exp(-\alpha(0)[m^*(0)^{-1}dm^*/dp + V(0)^{-1}dV/dp]p) \qquad (1)$$

with j(0) as the zero pressure current density, $\alpha(0) = L_B\sqrt{8\pi^2 m^* V(0)/h^2}$ as the transmission coefficient, V(0) as the effective Γ-X barrier height at p = 0 bar, and dV/dP = -11 meV/kbar. Equation (1) was obtained under the assumption, that at resonant bias the emitter-barrier-side transmission coefficient (α_E) dominates the tunneling characteristics over the collector-barrier-side one ($\alpha_E >> \alpha_C$).

The dominating effect in Equation (1) is the second term. For the L_B = 10 ML sample one obtains for the valley current component $j_V(p)/j_V(0) \approx \exp(ap/\text{kbar})$ with a = 0.15 kbar⁻¹ by using the transversal X-valley mass of $m^*(X_t) = 0.2m_0$. This is in excellent agreement with a fit to the experimental data which yields a = 0.16 kbar⁻¹. For comparison, a significantly higher pressure sensitivity (a = 0.39 kbar⁻¹) would be expected from equation (1) for the 10 ML sample if tunneling through the longitudinal X-valleys is considered ($m^*(X_l) = 1.1m_0$).

For thinner barrier samples α(0)/V(0) is reduced and yields to a lower contribution of the inelastic tunneling component in agreement with the observed behavior on samples with thinner barriers and otherwise identical material properties. As a consequence, we conclude that the dominant pressure sensing mechanism at room temperature is the pressure-induced non-resonant tunneling through the low-mass transversal valleys (X_t) in the AlAs barriers.

The peak current is mainly dominated by resonant tunneling contributions. The role of X-tunneling is more complicated. The experimental results indicate an influence with applied pressure but with a less pronounced rate (see Figure 3). This suggests that both Γ-X and Γ-Γ related mechanism contribute to j_P. Continuously improved PVCR values were observed by reducing the barrier thickness up to maximum values of 5 (12) at 300K (77K), respectively, for L_B=6ML. These are the highest observed values in standard AlAs/GaAs/AlAs DBRT structures. However, for $L_B \leq 6$ ML the PVCR decreases again due to the broadening of the resonance level $E_0(\Gamma)$ inside the GaAs QW [13].

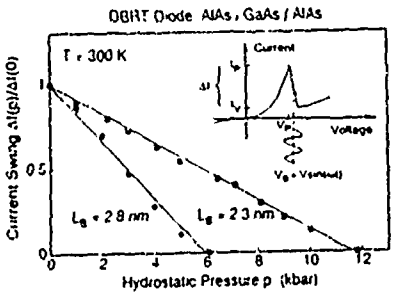

Figure 4. Hydrostatic pressure sensor characteristics for two different devices operating at room temperature.

Figure 4 shows the measured normalized current swing $\Delta I = j_P - j_V = j_P(1 - 1/PVCR)$ as a function of applied pressure. A linear dependence of ΔI vs p is observed. A constant pressure sensitivity over the whole operating pressure range is useful for device applications. The sensor diode with a 10 ML thick barrier exhibits a maximum operating range of $\Delta p = 0$ kbar with a sensitivity of $S = 170 \times 10^{-3}$ kbar^{-1}. The 8 ML diode has a 12 kbar operating range with $S = 85 \times 10^{-3}$ kbar^{-1}. The inset shows schematically the I/V-curve of a DBRT sensing diode. The device is biased close to the NDR region. Oscillations are avoided by a stabilizing network. With an amplitude-modulated ac-signal a convenient and accurate measurement of the current swing ΔI is achieved. There is no need of an absolute current or voltage measurement.

4. Conclusion

The use of DBRT structures as hydrostatic pressure sensing elements operating at room temperature has been demonstrated. There is strong evidence for a non-resonant tunneling through the transversal X-valleys in thin-barrier AlAs layers which enables pressure sensing. A constant pressure sensitivity is observed over a pressure range of more than 10 kbar. The NDR current swing shows a linear dependence on the applied pressure.

Presently used electrical high-pressure gauges are coils of fine ceranin (a) and manganin (b) wires and InSb (c) manometer. The electrical resistance varies with applied pressure. Room temperature sensitivity values are in the range between 1.5×10^{-3} kbar^{-1} (a) and 34×10^{-3} kbar^{-1} (c) [14]. The DBRT diode achieves $S = 170 \times 10^{-3}$ kbar^{-1} over a 6 kbar range. This is more than a factor of 5 more sensitive in comparison with commercially available electrical sensors.

Acknowledgement

The work was partially supported by the Bundesminister für Forschung und Technologie (Bonn, Germany) under contract numbers NT 2754 2 and TK 0368/7. One of us (R.D.) thanks CNPq (Brazil).

References

1. F. Capasso, *Physics of Quantum Electron Devices*, Springer Series in Electronics and Photonics, vol. 28, Berlin (1990)
2. L.L. Chang, E.E. Mendez, and C. Tejedor, *Resonant Tunneling in Semiconductors Physics and Applications*, Plenum, NewYork (1991)
3. E.R. Brown, *High Speed Resonant Tunneling Diodes*, in Heterostructure and Quantum Devices, ed. by N.G. Einspruch and W.R. Frensley, Series VLSI Electronics: Microstructure Science (1993), in press
4. E.E. Mendez, E. Calleja, and W.I. Wang, Appl. Phys. Lett. 53, 977 (1988)
5. R. Pritchard, D.G. Austing, P.C. Klipptein, J.S. Roberts, A.W. Higgs, and G.W. Smith, J. Appl. Phys. 68, 205 (1990)
6. Z. Othaman, A.J. Peck, S.J. Bending, G.A. Saunders, M. Roßmanith, K. Ploog, and K.von Klitzing, J. Appl. Phys. 70, 1548 (1993).
7. S.S. Lu, C.C. Meng, F. Williamson, and M.I. Nathan, J. Appl. Phys. 69, 8241 (1991)
8. H. Brugger, U. Meiners, C. Wölk, R. Deufel, J. Schroth, A. Förster, and H. Lüth, Proc. 13th Int. IEEE/Cornell Conf. on Advanced Concepts in High Speed Semiconductor Devices and Circuits, pp. 39-48 (1991)
9. S. Adachi, J. Appl. Phys. 58, R1 (1985)
10. A.R. Goni, K. Strössner, K. Syassen, and M. Cardona, Phys. Rev. B36, 1581 (1987)
11. K. Reimann, M. Holtz, K. Syassen, Y.C. Lu, and E. Bauser, Phys. Rev. B44, 2985 (1991)
12. R. Dimitz, J. Smoliner, E. Gornik, U. Meiners, H. Brugger, P. Wisniewski, and T. Cuski, Semiconductor Science and Technology 8 (1993), in press
13. H. Brugger, U. Meiners, A. Förster, and H. Lüth (to be published)
14. W.F. Sherman and A.A. Stadtmüller, *Experimental Techniques in High Pressure Research*, John Wiley, Chichester (1987)

TuB3

REALIZATION OF A NOVEL RESONANT TUNNELING HOT ELECTRON TRANSISTOR: COMPETITION OF ULTRAFAST RESONANT TUNNELING AND ENERGY RELAXATION

C. H. Yang and R. A. Wilson
Department of Electrical Engineering, Joint program of advanced electronic materials, Laboratory for physical sciences, University of Maryland, College Park, MD 20742, U.S.A.

ABSTRACT: We report a novel three-terminal hot electron transistor, where at 77K the transistor output characteristics can display novel features, including the negative differential resistance, extremely large peak-to-valley ratio, and a dc current gain. The operation of this novel transistor is based on quantum tunneling. The emitter injects hot electrons to the second lowest subband of a thin (100 Å) quantum well, and these non-thermalized hot electrons will then either resonantly tunnel to the collector or relax to the lowest subband and contribute to the base current. The resonant-tunneling probability of hot electrons between the emitter and the collector can be switched almost completely on and off, when either the base or the collector bias is swept. The new characteristics are shown to have application in dense logic circuits.

Hot electron transistors (HET) are expected to have applications in ultrafast electronics [1], since the non-thermalized hot electrons can traverse at high speed in semiconductors for a relatively long distance. Because of the many advantages, recent experimental works [2-5] have been primarily focused in semiconductor heterojunctions grown by MBE (molecular beam-epitaxy). For enlarging the current gain, ideally, hot electrons injected by the emitter should ballistically travel through the base region without scattering, and they only relax their excess kinetic energy in the collector.

Thus far, the most difficult step in fabricating an HET is to electrically contact the "base". Typically, the mesa is etched down until the base layer is revealed. Subsequently, the base metal will be deposited. However, the Fermi level pinning [6] at the GaAs surface will deplete the exposed surface region by $\sim\sqrt{2\epsilon V_{pinning}/qN_{doping}}$ in thickness, where ϵ is the GaAs static dielectric constant, $V_{pinning}$ (≈ 0.8 V) is the surface Fermi level pinning voltage, and N_{doping} is the doping level. For a doping level of $1\times10^{18}/cm^3$, the depletion width is about 400 Å. So, the base could be no thinner than 800 Å for a GaAs base [5]. When InGaAs is used as the base material [7], the quantum well thickness has been reduced to 250 Å, which still limited by the Fermi level pinning at the surface.

On the other hand, a base should be no thicker than about 1000 Å. The mean free path (MFP) of a ballistic non-thermalized hot electron can be estimated by taking a lifetime of 0.1 ps [8-12], a velocity of 10^8 cm/sec, and MFP is found to be only 1000 Å. Therefore, the current gain (I_c/I_B) would diminish, if the base is much thicker than about 1000 Å.

In view of the difficulties, we have designed and fabricated an HET that is based on resonant tunneling (RT). The emitter injects hot electrons to the second lowest subband of a thin (100 Å) quantum well, and these non-thermalized hot electrons will then either resonantly tunnel to the collector (and form the collector current I_c) or relax to the lowest subband and contribute to the base current (I_B). The RT probability of hot electrons between the emitter and the collector can be switched almost completely on and off, when either the base or the collector bias is swept.

Figure 1(a) shows a schematic energy band diagram of the new HET, and the expected output characteristic. The hot electrons tunnel through the second lowest state in the quantum well, while the electrons at the lowest subband are used as a third terminal. A double barrier (DB) RT structure is used to inject hot-electrons with a narrow energy spread. The energy width of injecting electrons can be experimentally obtained by using magnetotunneling spectroscopy. For example, 40 meV is measured for a DB diode with 30 Å barriers and a 100 Å quantum well. A narrow, peaked distribution can enhance the quantum selection rules. Given a full width of about 50 meV, when the energy of the second lowest quantum well state (E_2 in Fig. 1(a)) is shifted relative to the energy of injected hot-electrons (E_{inj}) by 70 meV, the RT current to the collector would be turned almost completely on and off. Fig. 1(b) illustrates such a three terminal transistor operation. Experimentally, this energy alignment (E_2 and E_{inj}) can be controlled by biasing the electrons in the QW base or by sweeping the collector voltage. Furthermore, when the E_2 and E_{inj} are off by an LO phonon energy, a phonon assisted RT process can also occur. The sufficient condition for observing the phonon-assisted RT tunneling is that the energy spread of non-thermalized hot-electrons at E_2 be less than both the LO phonon energy and $E_2 - E_1$.

Compared with conventional HETs, our HET has the following distinctive changes: (A) The base is now a quantum well, in which there are only a few quantum states. The hot electron transport perpendicular to the quantum well will therefore only involve a few states. (B) The hot electron energy spread is now reduced to be less than the GaAs LO phonon energy (36 meV). In conjunction with the fact that there are only a few quantum states involved in the tunneling process, the new HET will therefore be able to experimentally probe the energy distribution of injected hot-electrons with enough energy resolution to distinguish the true ballistic hot electrons from those that have emitted one LO phonon. (C) The "collector barrier" can now be higher than the kinetic energy of injecting hot-electrons. The collector current therefore comes from a RT process.

A new "tunneling in and tunneling out" approach is employed for contacting a thin quantum well. Standard fabrication processes are shown in Fig. 2. Starting from an as-grown wafer, the transistor mesa is first defined by wet-etching. The emitter and base contacts are then made by photolithography and metal evaporation. The region between the emitter and the base is etched, until there is barely any conduction between the emitter and the base at zero V_{CE}. Although the doped GaAs near the surface is not totally removed, the Fermi level pinning at GaAs surface can deplete the doped GaAs region at the surface, the DB RT structure and the doped QW. A schematic cross section of finished HET is shown in Fig. 3.

For an accurate structure design, numerical calculation for solving self-consistently the one-dimensional Poisson equation and Schrödinger equation is performed [13]. The positions of several important energy levels and their dependence on bias can be quantitatively predicted.

Grown on n^+ (001) GaAs substrates by MBE, the model structure reported here consists of an n^+ GaAs buffer layer as collector (Si-doped, $10^{18}/cm^3$, 5000 Å) followed by an undoped $Al_{0.3}Ga_{0.7}As$ collector barrier (3000 Å) and an n^+ GaAs QW (10^{18} cm^3, 100 Å), an undoped DB RT structure (30 Å $Al_{0.3}Ga_{0.7}As$ / 100 Å GaAs / 30 Å $Al_{0.3}Ga_{0.7}As$) as an energy filter, an n^+ GaAs cap layer ($10^{18}/cm^3$, 2000 Å), and finally a 500 Å graded $In_xGa_{1-x}As$ layer for non-alloying ohmic contacts.

Figure 4 shows the common emitter characteristics of an HET at 77K, where the collector current I_C is plotted against a sweeping V_{CE}, at several different base currents (I_B). No significant temperature dependence of the transistor characteristics was observed between 4.2K and approximately 77K. The double-peak feature as a result of the elastic and the phonon-assisted RT processes is clearly observed in I_C. When I_B is increased, the peaks in I_C shifts to higher V_{CE}, owing to that the band bending will adjust itself self-consistently. The smooth, rising background probably comes from a single-barrier tunneling current through the collector barrier, since there is no observable temperature dependence from 77K to 4.2K.

The observation of current gain of three (I_C/I_B) near resonance also verifies that at steady state 75% (= $I_C/[I_C+I_B]$) of the injected electrons can resonantly tunnel to the collector, while the rest 25% (= $I_B/[I_C+I_B]$) will relax to the lowest subband. This specific example demonstrates that the tunneling process can be faster than intersubband energy relaxation. In our particular case, the intersubband energy relaxation is known to be of the order of 0.1 ps, since the intersubband energy spacing is nearly 100 meV when the transistor is biased near resonance.

In summary, we have briefly reported our recent finding on a new HET, including the operating principles, the fabrication procedures, and the transistor output characteristics. The transistor has applications in dense static memory [11]. The lateral area of a static memory cell can be much reduced from current practices, because of the new output characteristics and that the electrical terminals can be stacked up. This new HET can also be applied in hot electron spectroscopy, and the resolution is improved to be able to distinguish a single LO phonon emission.

REFERENCES:

1. M. Heiblum, Solid-State Elec. **24**, 343 (1981), and references therein.
2. J.R. Hayes, A.F.J. Levi, and W. Wiegmann, Phys. Rev. Lett. **54**, 1570 (1985).
3. N. Yokoyama, K. Imamura, T. Ohnishi, H. Nishi, S. Muto, K. Kondo, and S. Hiyamizu, International Electron Devices Meeting Technical Digest (1984), p. 532.
4. M. Heiblum, M.I. Nathan, D.C. Thomas, and C.M. Knoedler, Phys. Rev. Lett. **55**, 2200 (1985).
5. K.K. Choi, P.G. Newman, and G.J. Iafrate, Phys. Rev. B **41**, 10250 (1990).
6. S.M. Sze, *Physics of Semiconductor Devices*, 2nd Edn., p. 77, eq. 156a, Wiley, New York, (1981).
7. K. Imamura, T. Adachihara, Y. Mori, S. Muto, and N. Yokoyama, IEEE Trans. Electron Devices **ED-30**, 479 (1983).
8. In three-dimensions, see, e.g., E.M. Conwell, *High Field Transport in Solids*, B.K. Ridley, Pergamon, New York (1967).
9. In two-dimensions, see, e.g., S. Das Sarma, D.K. Jain, and R. Jalabert, Phys. Rev. B **43**, 4561 (1990).

10. D.N. Mirlin, I.P. Nikitin, I.I. Reshina, and V.I. Sapega, JETP Lett. **30**, 193 (1979); D.N. Mirlin, I.Ya. Karlik, I.P. Nikitin, I.I. Reshina, and V.F. Sapega, JETP Lett. **32**, 11 (1980), and D.N. Mirlin, I.Ya. Karlik, I.P. Nikitin, I.I. Reshina, and V.F. Sapega, *Solid State Commun.* **37**, 757 (1980).
11. D.R. Auston, S. McAfee, C.V. Shank, E.P. Ippen, and O. Teschke, *Solid State Electronics* **21**, 147 (1978).
12. M. Heiblum, D. Galbi, and M. Weckwerth, Phys. Rev. Lett. **62**, 1057 (1989).
13. J. Chen, J.G. Chen, C.H. Yang, and R.A. Wilson, J. Appl. Phys. **70**, 6181 (1991).
14. For an example of using novel transistor characteristics in a memory cell, see J. Chen, C.H. Yang, and R.A. Wilson, Appl. Phys. Lett. **62**, 96 (1993).

FIGURE CAPTIONS:

1. (a) Schematic energy band diagram of the new HET, with the assumption that independent ohmic contacts can be made to the Emitter, the QW Base and the Collector. (b) Expected output/input characteristic of the new HET, where the collector current would peak when E_2 and E_{DB} are brought to resonance.
2. The fabrication procedure of a TITOHET. The transistor structure is not drawn to scale.
3. A schematic cross section of the new HET. The electrical components for characterization in the common-emitter configuration are also shown.
4. The common-emitter characteristics of an HET at 77K, where I_C is plotted against V_{CE}, and I_B is stepped from 5 μA to 10 μA.

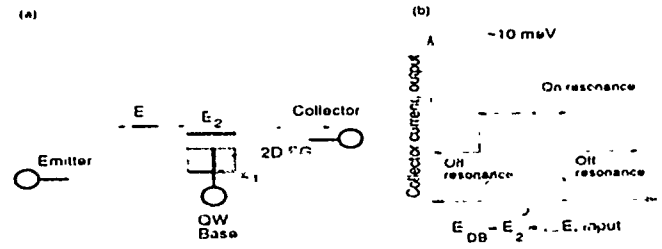

Fig. 1

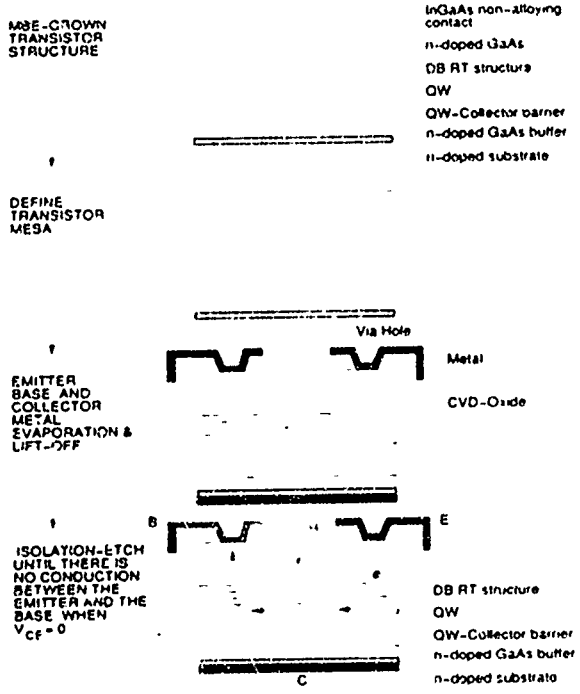

Fig. 2

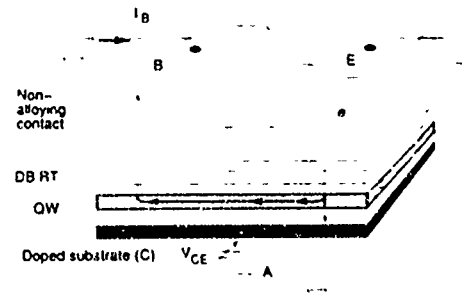

Fig. 3

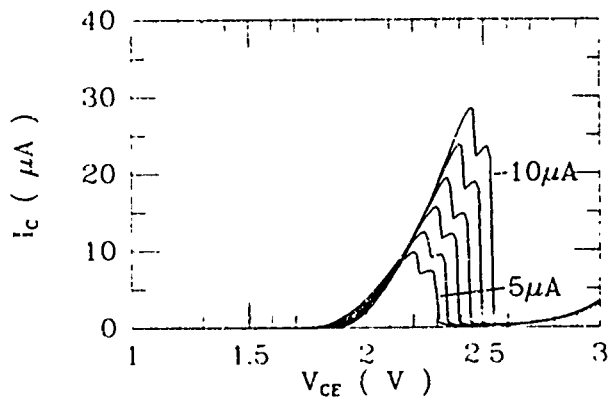

Fig. 4

TuB4

Γ-X Electron Transfer in Type II Tunneling Bi-Quantum Wells

Atsushi Tackeuchi*, Uwe Strauß, and Wolfgang W. Rühle,
Max-Planck-Institut für Festkörperforschung, Heisenbergstr.1, 70506 Stuttgart, Germany
Tsuguo Inata and Shunichi Muto
Fujitsu Laboratories Ltd., 10-1 Morinosato-Wakamiya, Atsugi 243-01, Japan
*On leave from Fujitsu Laboratories Ltd.

Abstract

We have studied the energy band structure and the Γ-X carrier transfer mechanism for type II tunneling bi-quantum wells consisting of GaAs wells, AlGaAs barriers of different thicknesses, and AlAs layers by cw and time-resolved photoluminescence measurements. The cw photoluminescence spectra of the indirect recombination of X electrons in the 7.1 nm thick AlAs layers with Γ holes in the 2.8 nm thick GaAs wells show weak zero-phonon lines indicating that the AlAs confined states at X_{xy} are lower than those at X_z. Time-resolved photoluminescence reveals that the carrier transfer time depends stronger on temperature for thicker AlGaAs barriers. Two scattering mechanisms, temperature-dependent phonon scattering and the temperature-independent interface scattering, are probably involved in the carrier transfer, the latter becoming smaller with increasing AlGaAs barrier thickness. Our results are compared with those obtained for similar type II GaAs/AlAs superlattices.

1. Introduction

Excitonic optical nonlinearity in quantum wells is useful for optical switching. Nonlinear absorption and refraction changes occur in MQWs with a time constant shorter than 1 ps due to photoexcitation of the exciton peak [1]. However, slow recovery of optical properties is often a severe restriction of these optical devices. The typical recovery time from excitonic absorption bleaching in a GaAs/AlGaAs MQW is 30 ns at 300 K [2]. Tackeuchi et al. [3] proposed the type II tunneling bi-quantum well (TBQ) structure to reduce and control the recovery time. The type II TBQ consists of a series of GaAs wells, AlGaAs barriers, and AlAs layers, as shown in Fig. 1. The structure uses optical nonlinearity at the exciton level in the GaAs well. The recovery time from excitonic absorption bleaching in the GaAs wells is governed by tunneling of electrons out of the well through an AlGaAs barriers into the X states in the AlAs layers. The recovery time can be made faster using thinner AlGaAs barriers without broadening the excitonic absorption peak of the GaAs wells. In type II TBQ, no significant optical absorption occurs in the AlAs layers during the excitation of e1-hh1 excitons in the GaAs wells since the lowest direct transition energy in AlAs layers is larger than that of the GaAs wells. Therefore this structure can be used, in contrast to type I TBQ [4,5], also in cavity devices. An all-optical gate operation of 17 ps has been already demonstrated with this structure in an etalon [6].

However energy band structure of this type II system and the carrier transfer mechanism are not clear, in contrast to the well-known type II superlattices (SLs) [7-10]. We investigate these features for different AlGaAs barrier thicknesses using cw and time-resolved photoluminescence measurements and compare our results with those which were obtained with similar type II SLs.

2. Energy band structure

The sample structures consist of 50 periods of 10 MLs (monolayers)-thick GaAs quantum wells, $Al_{0.51}Ga_{0.49}As$ barriers, and 25 MLs-thick AlAs wells. Four samples with different AlGaAs barrier thicknesses (from 4 MLs to 14 MLs) are studied. All structures were grown on a semi-insulating (100) GaAs substrate by molecular beam epitaxy.

Figure 2 shows the cw photoluminescence spectra at 4.2 K excited by a Kr^+ ion laser at 530.9 nm. We observe the direct e1-hh1 recombination in the GaAs wells at 704 to 711 nm. The e1-hh1 peak shifts to higher energy with decreasing AlGaAs barrier thickness since quantization energy is enlarged if the high AlAs Γ potential is closer to the GaAs wells providing a stronger carrier confinement [3].

The indirect type II emission between the X state in AlAs and the lowest Γ heavy-hole level in the GaAs wells at wavelengths longer than 720 nm comprises mainly four peaks which are labeled a, b, c, and d starting at the high-energy side. Table 1 compiles the energy differences between the various peaks. The energy differences between a-c (28-31 meV), and a-d (47-48 meV) are close to the LA and LO phonon energies at the AlAs X point which are 28 and 50 meV, respectively [11]. These energy differences are also close to the data obtained for type II SLs by Dawson et al. [7], who identified these peaks as AlAs phonon replicas. However, we can not exclude the contribution of AlAs like phonons in the AlGaAs barriers since they have similar energies. In summary, the a, b, c, and d peaks correspond to the zero-phonon, AlAs-like TA, LA and LO phonon replicas, respectively. Recombination involving GaAs like phonons is obviously not important.

The energy differences between the direct e1-hh1 recombination in the GaAs well and the zero-phonon lines of the indirect transition between the 10 MLs thick GaAs and the 25 MLs thick AlAs are only 42 meV, 25 meV, and 28 meV for 4 MLs, 8 MLs, and 12 MLs barriers, respectively. For comparison, in type II SLs with no AlGaAs barrier, this energy difference is 98 meV for a structure with 11 MLs thick GaAs and 24 MLs thick AlAs [9]. Obviously, energy crossover between X and Γ occurs at around 11 MLs thick GaAs wells in our type II TBQs, a value which is 1 to 2 MLs smaller than in type II SLs. This is a consequence of the reduced quantization energies due to the presence

of the AlGaAs intermediate layers in our TBQ structure.

One interesting feature of the present PL spectra is that the zero-phonon lines are relatively weak. In contrast, Dawson et al. [7] observed in type II SLs strong zero-phonon lines for 2.8 nm thick AlAs layers and weak zero-phonon lines for 6.8 nm thick and thicker AlAs layers. They interpret this phenomenon as the energy crossover between X_z and X_{xy} states in the AlAs layers: PL shows the strong zero-phonon line due to band mixing between Γ and X_z when the X_z states are lower. This interpretation is supported by optically detected magnetic resonance experiments which show that X_{xy} is lower than X_z when the AlAs layer is thicker than 5.5 nm in spite of the much larger effective mass of 1.1 m_0 at X_z state (0.19 m_0 at X_{xy}) [12]. Since the AlAs layers have a finite lattice mismatch to the GaAs substrates, the layers are under biaxial compression, and the resulting uniaxial stress lowers the X_{xy} states with respect to the X_z states. Therefore, the weak zero-phonon lines in our TBQ structures indicate that the X_{xy} states are lower than X_z states for the type II TBQs with 7.1 nm thick AlAs layers.

3. Γ-X carrier transfer

Previously, the carrier transfer time from Γ states in the GaAs wells to X states in the AlAs layers were measured at room temperature using time-resolved absorption measurement [3], and carrier transfer time depended exponentially on barrier thickness demonstrating that the transfer is governed by tunneling. However, the scattering mechanism which is involved in the tunneling process has not been clarified. In type II SLs with GaAs wells thinner than 12 MLs, Feldmann et al. showed that the Γ-X transfer is governed by interface scattering which does not depend on temperature [9].

We measure the time-resolved photoluminescence of e1-hh1 emission of GaAs wells using a synchroscan streak camera system and a synchronously pumped Rhodamin 6C dye laser with 82 MHz repetition rate. The time resolution, the full width at half maximum of the laser pulse on the streak camera, is about 12 ps.

The time evolutions of e1-hh1 photoluminescence peak at different temperatures are shown in Fig. 3 for the sample with 14 MLs AlGaAs barriers. The decay time becomes slower with lowering the temperature. This temperature dependence indicates that transfer in the type II TBQ does not exclusively occur via interface scattering. At high temperatures, a long-lived tail appears, its magnitude becoming larger with increasing temperature. A similar long-lived tail was observed previously at room temperature by time-resolved absorption measurements [3]. We believe the long-lived tail in luminescence and part of the long tail in absorption are due to thermally induced back-transfer of carriers.

Figure 4 shows the dependence of decay time on temperature: with increasing temperature, the decay times become close to the value measured at room temperature by time-resolved absorption measurement. The increase of the decay time at low temperature (<150 K) for the 12 MLs and 14 MLs barriers is due to the increase of radiative recombination time with increasing temperature. Except for these samples in this temperature range, decay time is dominated by the tunneling transfer. In the latter regime, the decay times decrease with increasing temperature, and the change in the decay time is larger for thicker barriers. The ratio of the decay times between low and high temperature are 2.2 and 3.0 for the structures with 4 MLs and 8 MLs barriers, respectively. This result differs from the data obtained by Feldman et al. [9] on type II SLs. They observed no temperature dependence for GaAs wells thinner than 12 MLs, whereas we observe the dependence of decay time on temperature for type II TBQ with even 10 MLs thin GaAs wells. They claim that interface scattering is the dominant temperature-independent scattering mechanism for thinner wells and that phonon scattering is the main scattering process for the thicker wells (>35 MLs).

This apparent contradiction is however well understood if we take into account that the AlGaAs barriers in our TBQ structures reduce the overlap of wavefunctions between Γ and X states at the interfaces. In type II SLs, the interface scattering due to the interface mixing potential and/or due to potential fluctuations caused by interface roughness at AlAs/GaAs interface are considered to be the dominant temperature-independent scattering mechanism [9]. In type II TBQs, AlAs/AlGaAs and/or GaAs/AlGaAs interface seems to mix similarly Γ and X states. We calculate the penetration probability of e1 electrons of the GaAs wells into the AlGaAs/AlAs interface (± 1ML) using envelope function approximation. The penetration probability for the TBQ with 4 MLs thick AlGaAs barriers is 1.1 % and 0.17 % for 8 MLs thick barriers as shown in Table 2. These values are clearly smaller than the penetration probability of 8.3 % for 10.3 MLs thick GaAs/17.1 MLs thick AlAs type II SLs which do not show any dependence of decay time on temperature. The values for the type II TBQs are close to the value of 0.45 % which is obtained for a 39.0 MLs thick $Al_{0.36}Ga_{0.64}As$/ 33.5 MLs thick AlAs type-II SL. Additionally, the ratios of the decay times at low and high temperatures, τ_{low} / τ_{high}, are also very similar for these three structures, namely 2.2 for 4 MLs thick barriers TBQ, 3.0 for 8 MLs thick barriers TBQ, and 2.3 for 39.0 MLs thick $Al_{0.36}Ga_{0.64}As$/33.5 MLs thick AlAs type II SLs. Obviously the penetration of electron wave functions at the AlAs/AlGaAs interface in our case are much more similar to those in type II 39.0 MLs thick AlGaAs/33.5 MLs thick AlAs SL, where phonon scattering is dominant, than to those in type II 10.3 MLs thick GaAs/17.1 MLs thick AlAs SL. Therefore we interpret the observed dependence of the decay times on temperature in our TBQ structures to be due to a combination of two scattering mechanisms: temperature-independent interface scattering and temperature-dependent scattering. The larger difference of decay times between low and high

temperatures with increasing AlGaAs barrier thickness is due to the decrease of interface scattering by less overlap of the wavefunctions at the interfaces which results in the relatively stronger contribution of temperature-dependent scattering. As for the temperature-dependent scattering, calculations show that phonon assisted scattering is the fastest scattering process [13,14]. Therefore phonon assisted tunneling seems to be the process which leads to the temperature dependence of the carrier transfer time in our TBQ structures.

4. Summary

We have studied the energy band structure and Γ-X carrier transfer of type II tunneling bi-quantum wells using cw and time-resolved photoluminescence measurements. Type II TBQ consists of GaAs wells, AlGaAs barriers, and AlAs layers. The cw photoluminescence spectra between X electrons in the 7.1 nm thick AlAs layers and Γ holes in the 2.8 nm GaAs wells exhibit weak zero-phonon lines indicating that the X_{xy} confined states are lower than the X_z confined states. The time-resolved photoluminescence shows a stronger temperature dependence of the carrier transfer time for thicker AlGaAs barriers. This dependence on temperature and barrier thickness is explained by taking into account two scattering mechanisms: temperature-dependent phonon scattering and temperature-independent interface scattering, the latter becoming less efficient for thicker AlGaAs barriers.

Acknowledgments

We would like to thank K. Rother and H. Klann for expert technical assistance. We also thank Professor H. J. Queisser for his hospitality during the course of this work. We acknowledge the work of Yoshiaki Nakata, Satoshi Nakamura, and Masaomi Yamaguchi with the sample growth.

References

[1] W.H. Knox, R. L. Fork, M. C. Downer, D. A. B. Miller, D. S. Chemla, C. V. Shank, A. C. Gossard and W. Wiegmann: Phys. Rev. Lett. **54**, 1306 (1985).
[2] D. S. Chemla, D. A. B. Miller, P. W. Smith, A. C. Gossard and W. Wiegmann, IEEE J. Quantum Electron. **QE-20**, 265 (1984).
[3] A. Tackeuchi, T. Inata, Y. Sugiyama, Y. Nakata, S. Nakamura and S. Muto, Jap. J. Appl. Phys. **31**, L660 (1992).
[4] A. Tackeuchi, S. Muto, T. Inata, and T. Fujii, Jpn. J. Appl. Phys. **28**, L1098 (1989).
[5] A. Tackeuchi, S. Muto, T. Inata, and T. Fujii, Appl. Phys. Lett. **58**, 1670 (1991).
[6] A. Tackeuchi, T. Inata, Y. Nakata, S. Nakamura, Y. Sugiyama, and S. Muto, Appl. Phys. Lett. **61**, 1892 (1992).

[7] P. Dawson, C. T. Foxon and H. W. van Kesteren, Semicond. Sci. Technol. **5**, 54 (1990).
[8] P. Sacta, J.F. Federici, R.J. Fisher, B.I. Greene, L. Pfeiffer, R.C. Spitzer and B.A. Wilson, Appl. Phys. Lett. **54**, 1681 (1989).
[9] J. Feldmann, R. Sattmann, E.O. Göbel, J. Kuhl, J. Hebling, K. Ploog, R. Muraliharan, P. Dawson and C.T. Foxon: Phys. Rev. **B42**, 5809 (1990).
[10] Y. Masumoto, T. Mishina, F. Sasaki and M. Adachi: Phys. Rev. **B40**, 8581 (1989).
[11] B. Monemar, Phys. Rev. **B8**, 5711 (1973)
[12] H. W. van Kesteren, E. C. Cosman, P. Dawson, K. J. Moore, and C. T. Foxon, Phys. Rev. **B39**, 13426 (1989).
[13] R. Ferreira, and G. Bastard, Phys. Rev. **B40**, 1074 (1989).
[14] S. Muto, T. Inata, A. Tackeuchi, Y. Sugiyama and T. Fujii, Appl. Phys. Lett. **58**, 2393 (1991).

L_B	e1-hh1 - a (meV)	a - b (meV)	a - c (meV)	a - d (meV)
4 MLs	42	12	31	48
8 MLs	25	13	28	48
12 MLs	28	11	30	47

Table. 1 Energy differences between photoluminescence peaks.

	Penetration probability	τ low / τ high
Type II TBQ		
GaAs/AlGaAs/AlAs		τ 5K / τ 300K
10 MLs / 4 MLs / 25 MLs	1.1 %	2.2
10 MLs / 8 MLs / 25 MLs	0.17 %	3.0
Type II SLs		τ 10K / τ 295K [9]
GaAs 10.3 MLs / AlAs 17.1 MLs	8.3 %	1.0
AlGaAs 39.0 MLs / AlAs 33.5 MLs	0.45 %	2.3

Table. 2 Penetration probabilities and the ratios of decay times between 5 K (10 K) and 300 K (295 K).

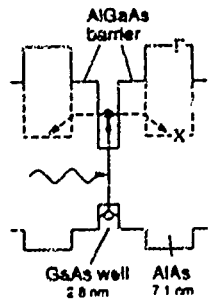

Fig.1. Schematic energy band diagram of a type-II TBQ structure.

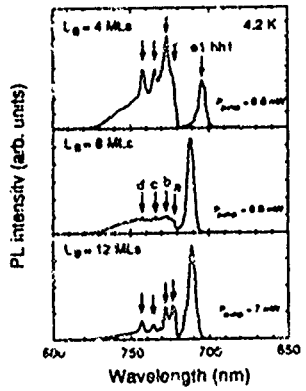

Fig. 2. CW photoluminescence spectra at 4.2 K.

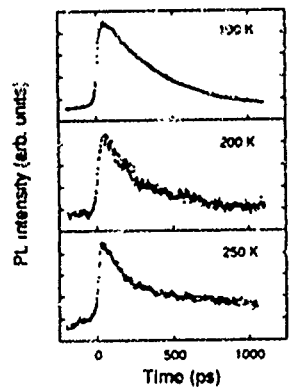

Fig. 3. Time resolved e1-hh1 photoluminescence for the TBQ structure with 14 MLs thick AlGaAs barriers at different lattice temperature

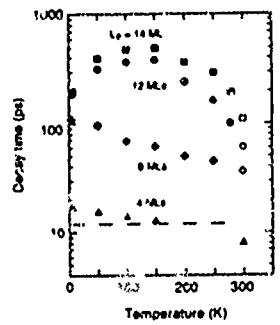

Fig. 4 Dependence of decay time on temperature. Also shown are the data (open symbols) obtained by time resolved absorption measurement at room temperature [3].

TuB5

Valley mixing effects on electron tunneling transmission in GaAs/AlAs heterostructures

E. L. Ivchenko and A. A. Kiselev
A. F. Ioffe Physico-Technical Institute, Russian Academy of Sciences, 194021 St Petersburg, Russia

Y. Fu and M. Willander
Department of Physics and Measurement Technology, Linköping University, S-581 83 Linköping, Sweden

We propose a set of boundary conditions for electron envelope functions at GaAs/AlAs (001) heterointerfaces so as to take into account Γ-X mixing in the effective mass method. The proposed conditions enable one to obtain the dependence of the mixing effect upon the parity of monomolecular layer numbers in $(GaAs)_N(AlAs)_M$ superlattices. The electron transmission spectra of $GaAs(AlAs)_MGaAs$ single barrier structures are calculated in the generalized effective-mass approximation. It is shown that the spectral fine structure depends essentially upon the parity of M. The low-temperature dc current-voltage characteristics of the single-barrier structure is derived taking into account the camel-back X-band structure in bulk AlAs and GaAs.

1. Introduction

Since mid 80s different pseudopotential and tight-binding models have been used for calculation of GaAs/AlAs (001) superlattice (SL) minibands and for the theoretical analysis of mixing between the Γ conduction band and (001) X valley (see the review [1]). The most striking common feature of the results is a qualitative sensitivity of the Γ-X mixing effects on the parity of monolayer numbers in AlAs and GaAs layers. Ando and Akera [2] (see also [3]) presented a formulation of the effective-mass method in which Γ-X mixing at interfaces is included by boundary conditions but in their formulation the parity of monolayer numbers has no influence on the miniband spectrum in contrast with the results of the empirical model calculations.

In the present paper it is shown that the boundary conditions of Ando and Akera are relevant to a single heteroboundary but they should be corrected in cases of double or multiple-interface structures. If a dimensionless Γ-X mixing coefficient is supposed to change its sign from one monolayer to another then the effective-mass approximation leads as well to the dependence of Γ-X mixing in a $(GaAs)_N(AlAs)_M$ superlattice on the parity of M. We also present a theoretical study of resonant tunneling through a $GaAs(AlAs)_MGaAs$ structure where the attention is focused on analytical properties of the transmission spectra and analytical description of the current vs. voltage dependence making allowance for a self-consistent electrostatic potential induced by the buildup X-electrons. It should be noted that there have been published numerous calculations of electron tunneling probabilities across a GaAs/AlAs single- or double-barrier heterostructures taking into account Γ-X mixing effects [2-9]. However only recently it has been realized [10, 11] that the transmission spectra depend on whether the AlAs layer contains an even or odd number of monomolecular layers.

2. Γ-X mixing in SLs in the effective mass approximation

Following Ando and Akera [2] we consider the three-band model taking into account mixing of Γ_1 states with those from two close-lying bands X_1 and X_3. The electron wave function is written then as

$$\Psi_e(r) = u(r)|\Gamma_1\rangle + v(r)|X_3\rangle + w(r)|X_1\rangle \quad , \qquad (1)$$

where $|\Gamma_1>, |X_3>, |X_1>$ are the corresponding Bloch functions and w, v, u are envelopes in the effective mass method. We assume w, v, u and $\partial u/\partial z$ to be continuous at heterointerfaces and use the boundary conditions for derivatives $\partial w/\partial z$ and $\partial v/\partial z$ in the form [2, 12]

$$\nabla_\Gamma^A w_A = \nabla_\Gamma^B w_B + t(z_f)\, v_B \quad , \quad \nabla_X v_A = \nabla_X v_B + t^*(z_f)\, w_B \quad . \tag{2}$$

Here z_f is the heteroboundary coordinate,

$$\nabla_\Gamma^t = a_0 \frac{m_0}{m_t} \frac{\partial}{\partial z} \quad , \quad \nabla_X = a_0 \frac{m_0}{m_X^{\perp\perp}} \frac{\partial}{\partial z} \quad .$$

a_0 is the lattice constant, m_0 is the free electron mass, m_t is the Γ-electron effective mass in bulk GaAs ($=A$) and AlAs (B), $m_X^{\perp\perp}$ is the effective mass describing parabolic term $\hbar^2 k_z^2/2m_X^{\perp\perp}$ in the two-band Hamiltonian of X-point electrons. The coefficient t was considered in [2, 3, 7] to be independent on the interface coordinate z_f. However, due to different translational properties of Γ- and X-point Bloch functions this coefficient changes its sign as a GaAs/AlAs interface is shifted by one monolayer along the principal axis z. Thus,

$$t(z_f) = t_{\Gamma X}\eta(z_f) \quad , \quad \eta(z_f) = \exp(2\pi z_f/a_0) \quad . \tag{3}$$

where $t_{\Gamma X}$ is a real dimensionless constant. Note that for a single heteroboundary the phase of η can be chosen arbitrarily since the corresponding phase change can be introduced into the envelope w or into the envelopes v, u, but this choice unambiguously fixes the phase $\Phi = 2\pi z_f/a_0$ at any other heteroboundary of the same structure.

In order to demonstrate the role of the phase factor $\eta(z_f)$ we consider the energy dispersion for the two lowest electron minibands in $(GaAs)_M(AlAs)_M$ SLs near the transition from type I to type II. In this case one can first calculate the lowest minibands $e1\Gamma$ and $e1X$ for $t_{\Gamma X}=0$ and then include the Γ-X mixing between them. The details have been published elsewhere [10, 12] and here we present the final result for the electron dispersion curves obtained in the tight-binding approximation of the effective mass method

$$E_\pm(\mathbf{k}) = \frac{1}{2}\left\{ E_\Gamma(\mathbf{k}) + E_X(\mathbf{k}) \pm \sqrt{|E_\Gamma(\mathbf{k}) - E_X(\mathbf{k})|^2 + 16\, V^2 \chi} \right\} \quad . \tag{4}$$

Here $\mathbf{k}$ is the $3D$ electron wave vector in the SL, $E_\Gamma(\mathbf{k})$, $E_X(\mathbf{k})$ are the energies of the unmixed $e1\Gamma$ and $e1X$ states,

$$V = \frac{\hbar^2 t_{\Gamma X}}{2a_0 m_0} w_{e1\Gamma}(BA) v_{e1X}(BA) \quad , \quad \chi = \cos^2[(k_z d + M\pi)/2] \quad . \tag{5}$$

$w_{e1\Gamma}(BA)$ is the electron envelope function in the state $e1\Gamma$ in a GaAs single quantum well of the width $a=Na_0/2$, $v_{e1X}(BA)$ and $u_{e1X}(BA)$ are the envelopes in the $e1X$ state in an AlAs single quantum well of the width $b=Ma_0/2$, $d=a+b$ is the SL period, the symbol BA means a coordinate of the heteroboundary AlAs/GaAs. The parity of AlAs monolayer number M is explicitly present in Eq (5) and, hence, in the dispersion (4). Note that the electron dispersion (4) is independent on the parity of N. The latter is due to a large value of the X-electron longitudinal effective mass which permits one to consider the GaAs/AlAs SL for X-electrons as a regular chain of isolated quantum wells and neglect the k_z-dependence of the curve $E_X(\mathbf{k})$.

3. Transmission through a GaAs$(AlAs)_M$GaAs structure

Fig. 1 shows normal-incidence electron transmission coefficients for single-barrier heterostructures with the monolayer number M ranging from 8 to 12. Solid curves are calculated in the generalized effective mass approximation [10] for $t_{\Gamma X}=1$, dotted curves present the recent results of Ting and McGill [11] obtained by using an eight-band second-neighbor sp^3 tight-binding model. In Fig. 1 the incident electron energies lie below the conduction X-edge in GaAs and, therefore, the transmission probability is contributed by Γ-Γ-Γ, Γ-X-Γ but not by Γ-X-X processes. One can see a close agreement in the parity dependence of the fine structure in the spectra calculated by different methods [10] and [11]. The difference in the peak positions can be evidently removed by fitting band offsets and X-band parameters. In the tunneling experiments [9,13] the sharp structures are smeared out due to contributions to the current from electronic states with different energies. However the analysis of these structures can be used for making comparison between various computation methods.

In order to understand the fine structure of the spectra we apply here the perturbation theory to derive a formula for transmission coefficient for incident electron energies E close to the energy E_ν of a quasibound X-state n in the AlAs layer.

It can be shown that the additional terms in the right-hand side of Eqs. (2) are equivalent to inclusion into the electron effective Hamiltonian of the operator

$$V_{\Gamma X} = \frac{\hbar^2 t_{\Gamma X}}{2a_0 m_0} \left| \delta(z-z_r) - (-1)^M \delta(z-z_l) \right| \quad . \tag{6}$$

where $z_{l,r}$ is the coordinate of the left- or right-hand interface and we set $\eta(z_r)=1$.

Using Fermi's golden rule and the resonance scattering theory one can present the transmission probability in the form

$$\Gamma_k = \frac{1}{\hbar v_z} \int_0^\infty dk'\, \delta(E_{k'} - E_k) |V_{r\,l}|^2 \quad , \tag{7}$$

$$V_{r\,l} = V_k^\Gamma + \frac{V_{r,\nu} V_{\nu,l}}{E_k - E_\nu + i\hbar\Gamma_\nu} \quad . \tag{8}$$

Here k is the incident electron wave vector ($k \| z$), $v_z = \hbar k/m_A$, Γ_ν is the escape rate from the E_ν level into the leads, $V_{r,\nu}$ and $V_{\nu,l}$ are the coupling constants connecting the bound state ν to free G-states in the right and left leads, V_k^Γ is the coupling constant due to nonresonant tunneling via Γ-states of the AlAs layer.

Integrating Eq. (7) over k' and taking into account that $|V_{r,\nu}| = |V_{\nu,l}|$ and $\Gamma_\nu =$

$|V_{r,v}|^2/\hbar^2 v_z$ we finally obtain

$$T_k = \left| \frac{4\sqrt{\kappa}}{1+\kappa_v^2} e^{-\kappa_v b} \pm \frac{\hbar\Gamma_1(-1)^M}{E_k - E_v + i\hbar\Gamma_v} \right|^2 \quad (9)$$

Here the sign + or - corresponds to even or odd envelope $v_v(z)$.

$$\kappa_v = \frac{m_A}{m_B}\frac{\kappa_v}{k_v}, \quad k_v = (2m_A E_v/\hbar^2)^{1/2},$$
$$\kappa_v = [2m_B^2 E_\Gamma(\mathrm{AlAs}) - E_v]/\hbar^2]^{1/2}.$$

$E_\Gamma(\mathrm{AlAs})$ is the energy position of the Γ_1 minimum in AlAs, $b=Ma_0/2$ is the AlAs layer thickness. Eq. (9) is valid provided the Γ-Γ Γ tunneling probability is small, i.e. $\exp(-\kappa_v b) \ll 1$. In this case the transmission peak position practically coincides with E_v. One can see that the parity dependence of the Γ-X mixing operator (6) is repeated in Eq. (9) because the product $V_{r,v}V_{v,l}$ is proportional to $(-1)^M v_v(z_l)v_v(z_r)$. For the lowest state $v=1$ (e1X) the envelope $v_1(z)$ is even and $v_l(z)$ is odd and we should take the negative sign in Eq. (9). Thus, the energy position $E_1^{(d)}$ of the E_1-related dip is given by

$$E_1^{(d)} = E_1 + (-1)^M \frac{1+\kappa_1^2}{4\kappa_1} e^{-\kappa_1 b} \hbar\Gamma_1 \quad (10)$$

the peak-dip distance being much larger than $\hbar\Gamma_1$. It follows then that for M odd the transmission zero is followed by the peak in agreement with the spectra in Fig. 1 for $M=9, 11$. On the other hand, if M is even the transmission zero occurs above the energy E_1 (Fig. 1, $M=8$). For thick enough $(\mathrm{AlAs})_M$ layers, the resonant contributions to T_k due to the E_1 and E_2 peaks exceed the nonresonant contribution in the whole region between E_1 and E_2 and, for M even, the peak E_1 is not followed by a zero (Fig. 1, $M=12$).

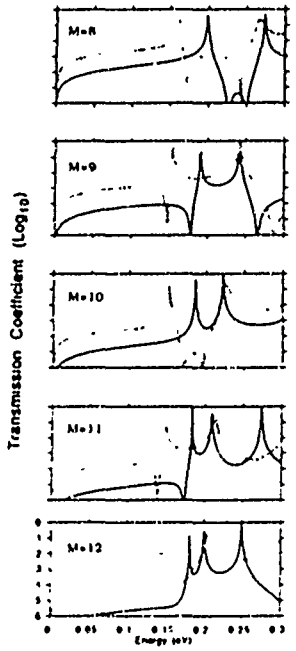

Fig. 1. Comparison between theoretical transmission spectra calculated for GaAs $(\mathrm{AlAs})_M$GaAs structures with M=8-12 by using the generalized effective mass approximation (10) (solid curves) and the eight-band second-neighbor sp^3 tight-binding model of Ting and McGill (from [11], dotted).

4. Resonant tunneling current in a single-barrier structure

The tunneling current density can be written as

$$J = \frac{1}{2\pi^2}\frac{em_A}{\hbar^3}\int dE_{\parallel} dE_{\perp}\, T(E_{\parallel}, E_{\perp})(F_l - F_r) \quad . \quad (11)$$

where $E_{\parallel} = \hbar^2 k_z^2/2m_A$, $E_{\perp} = \hbar^2 k_{\perp}^2/2m_A$, $k_{\perp}^2 = k_x^2 + k_y^2$, $T(E_{\parallel}, E_{\perp})$ is the transmission probability under oblique incidence, $F_{l,r}$ are the electron distribution functions in the left and right leads described at low temperatures by the step functions $F_l = \Theta(E_F - E)$, $F_r = \Theta(E_F + eV - E)$, E_F being the Fermi energy and V being the bias between the leads. We take $V>0$ so that the product eV is negative. We consider the region of electric fields where the level $E_{1e\mathrm{V}}$ is tuned to resonance with the left-lead states occupied by the degenerate electron gas and F_r in Eq. (11) can be put to zero. The current is calculated self-consistently taking into account an electrostatic field induced by the electrons temporarily confined inside the AlAs layer. The whole electrostatic potential, $\phi(z)$, is determined from the Poisson equation

$$\frac{d^2\phi}{dz^2} = -\frac{4\pi e N_1}{\epsilon}\left[u_1^2(z) + v_1^2(z)\right] \quad . \quad (12)$$

where N_1 is the 2D density of the confined electrons. The structure is assumed to contain GaAs spacers of effective thicknesses L_l and L_r on both sides of the $(\mathrm{AlAs})_M$ layer. Neglecting the field-dependence of $L_{l,r}$ in the E_1-resonance region, we take for the potential the boundary conditions $\phi(-L_l - b/2)=0$, $\phi(L_r + b/2)=V$, the origin $z=0$ being chosen at the center of the AlAs layer.

Note that in the narrow resonant regions, $|E-E_v| < \hbar\Gamma_v$, the nonresonant contribution in Eq. (9) is negligible while in off-resonant regions V_k^r can dominate if the AlAs layer is not very thick. Thus, the resonant and nonresonant contributions to the tunneling current can be calculated separately. In the following for simplicity we take into consideration only the resonant contribution to $T(E_{\parallel}, E_{\perp})$.

Neglecting the reflection of electron waves from spacer areas we can approximately present this coefficient in the form

$$T(E_{\parallel}, E_{\perp}) = \frac{(\hbar\Gamma_1)^2}{[E_{\parallel} + E_{\perp}(1 - m_A/m_X^t) - E_1 - e\phi_0]^2 + (\hbar\Gamma_1)^2} \quad . \quad (13)$$

where

$$\phi_0 = \int dz\, \phi(z)\left[u_1^2(z) + v_1^2(z)\right] \quad .$$

m_X^t is the in-plane effective mass of an X electron. For normal incidence $T(E_{\parallel}, 0)$ reduces to the resonant contribution to the transmission probability given by Eq. (9). Neglecting variation of $\Gamma_1(E_{\perp})$ within the energy interval of the width E_F we can connect J and N_1 by a simple relation

$$J = \frac{1}{2} e N_1 \Gamma_1 \quad . \tag{14}$$

Substituting Eq (13) into Eq (11), integrating Eq. (11) over $E_{1\parallel}$ and $E_\perp$ and taking into account Eq. (14) we obtain a final I-V characteristics

$$J(V) = J_0 \begin{cases} 0 \ , & \text{if } V<V_{min} \text{ either } V>V_{max} \ , \\ (V - V_{min})/(V' - V_{min}) \ , & \text{if } V_{min}<V<V' \ , \\ (V_{max} - V)/(V_{max} - V') \ , & \text{if } V'<V<V_{max} \end{cases} \tag{15}$$

Here

$$J_0 = \frac{1}{2\pi} \frac{e m_A}{\hbar^2} \Gamma_1 E_F \ , \ V_{min} = \frac{E_1 - E_F}{|e|\xi} \ , \ V_{max} = \frac{E_1}{|e|\xi} \ ,$$

$$|e|\xi V' = E_1 - E_F \left\{ 1 - \frac{m_A}{m_X^*} \cdot \frac{e^2 m_A}{\pi\hbar^2} \left[\frac{2\pi\xi}{\varepsilon} (L_c - L_l) + \phi_0 \right] \right\} \ , \ \xi = \frac{L_l + b/2}{L_l + L_r + b} \quad \text{For}$$

convenience we introduced the function $\dot{\phi}(z)$ so as $eN_1\dot{\phi}(z)$ is an even solution of Eq (12) with the boundary condition $\dot{\phi}(-L_l - b/2)=0$.

$$\dot{\phi}_0 = \int dz\, \dot{\phi}(z) \left| u_1^2(z) + v_1^2(z) \right| \ .$$

It is clear that $\dot{\phi}(z)$ is independent on the applied bias.

Fig 2 shows a shape of the resonant $J(V)$ curve neglecting (dashed) and including the self-consistent potential influence (solid line) We use the notation

$$|e|\xi V_0 = E_1 - E_F (1 - m_A/m_X^*) \ .$$

In general the parameters of a heterostructure can be such as V' exceeds V_{max} in which case the current-voltage dependence exhibits an intrinsic bistability.

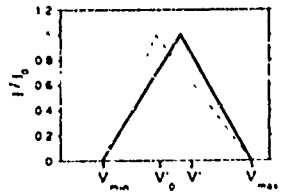

Fig 9. Shape of the resonant current-voltage characteristics of GaAs(AlAs) GaAs structure (dashed curve) and including (solid) the self-consistent potential influence

5. Conclusion

The version of the effective mass approximation used in this work can be readily extended to treat valley-mixing in heterostructures grown along other crystallographic axes Really, in general two Bloch states with the wave vectors $\boldsymbol{K}_1$ and $\boldsymbol{K}_2$ can be mixed by heteroboundary with the normal $\boldsymbol{N}$ if there exists a $3D$ reciprocal lattice vector, $\boldsymbol{b}$, that satisfies the condition $(\boldsymbol{K}_1 - \boldsymbol{K}_2 - \boldsymbol{b})_\perp = 0$, where $\boldsymbol{K}_\perp$ means the in-plane component of the vector $\boldsymbol{K}$. The envelope functions corresponding to the $\boldsymbol{K}_1$ and $\boldsymbol{K}_2$ valleys can be mixed by boundary conditions similar to those given by Eq (2) It is evident that in such generalized boundary conditions the phases of $\boldsymbol{K}_1$ - $\boldsymbol{K}_2$ mixing coefficients should depend on the interface position as $t_{mix} = \exp[i(\boldsymbol{K}_1 - \boldsymbol{K}_2 - \boldsymbol{b})_{\parallel} z_f]$, where the symbol $\parallel$ means the component of a $3D$ vector parallel to the structure principal axis $\boldsymbol{N}$ and z_f is a linear combination of $\boldsymbol{a}_{j\parallel}$ with integer coefficients, $\boldsymbol{a}_j$ (j=1,2,3) being the basic translation vectors of the bulk lattice These simple considerations can be modified to be valid for strained SLs.

References

1 L J Sham and Y -T. Lu, J Lumin. 44, 207 (1989)
2 T Ando and H Akera, Phys. Rev. B40, 11619 (1989)
3 H C Liu, Appl. Phys Lett. 51, 1019 (1987).
4 A. C Marsh, Semicond Sci. Technol 1, 320 (1986)
5 D Y K Ko and J. C Inkson, Semicond Sci Technol 3, 791 (1988)
6 K.V Rousseau, K L Wang and J. N. Schulman, Appl Phys. Lett. 54, 1341 (1989).
7 J. -B Xia, Phys. Rev. B41, 3117 (1990)
8 T. B. Boykin and J S Harris, Jr , J. Appl. Phys. 72, 988 (1992).
9 Y. Carbonneau, J. Beerens, L. A Cury, H. C. Liu and M. Buchanan, Appl. Phys. Lett 62, 1955 (1993).
10 Y Fu, M Willander, E L Ivchenko and A A Kiselev, Phys. Rev. B47, 13498 (1993)
11 D Z -Y Ting and T C. McGill, Phys Rev B47, 7281 (1995).
12 I L Aleiner and E L Ivchenko, Fiz. Tekhn Poluprov. 27, 594 (1993) (Sov. Phys Semicond 27, (1993))
13 E E Mendez, W I Wang, E Calleja and C E T. Goncalves da Silva, Appl. Phys Lett. 50, 1263 (1987), R. Beresford, L. F. Luo, W I. Wang and E E. Mendez, Appl Phys Lett 55, 1555 (1989)

TuC1

Luminescence Investigation on Strained $Si_{1-x}Ge_x/Si$ Modulated Quantum Wells

S.Fukatsu
Research Center for Advanced Science and Technology (RCAST), The University of Tokyo, 4-6-1 Komaba Meguro-ku, Tokyo 153 Japan

Luminescence characterization is presented on *potential-modulated* strained $Si_{1-x}Ge_x/Si(100)$ quantum wells. Interwell coupling was studied in a series of coupled quantum wells (CQW) with a intervening Si barrier for symmetric and asymmetric configurations. Systematic red shift of photoluminescence peak energy was observed in symmetric CQWs with decreasing Si barrier width centered at CQW. Interwell coupling was further evidenced in asymmetric CQWs luminescence as spectral dominance switch between the narrower and the wider wells, reflecting the tunneling-controlled carrier *transfer*. Evolution of Kronig-Penney superlattice state was observed as consistent luminescence peak shift with change in the structural parameters. Diffusion induced blue-shift of luminescence peak amounting to 22meV was observed.

I. Introduction

Recent progress in epitaxial growth technology has enabled to control materials growth to an atomic dimension, leading us to discovery of novel quantum effects in a variety of detailed structures. Potential profile modulation opens a way to a new research domain where interesting quantum physics is expected to manifest itself. Coupled quantum well (CQW) represents a new class of QWs[1-4] with such a potential modulation that can be introduced by growth alone and has been a major focus of interest. Within these structures, interwell coupling plays an essential role determining energy spectrum and resultant electronic as well as optical properties. Interwell coupling also dictates the evolution of a superlattice state[4] which is a repeated extension of CQW. To date, luminescence investigation on the interwell coupling in semiconducting materials has been limited to compound semiconductors whereas group-IV materials have been scarcely explored due primarily to the lack of emission efficiency. Owing to recent progress of vapor phase epitaxy technology, however, photon emissivity in strained $Si_{1-x}Ge_x/Si$ systems has reached a point viable for realistic optical study using photoluminescence[5-18]. On the other hand, atomic diffusion at heterointerfaces is expected to induce a potential modulation in a different way due to profile extension driven by concentration gradient.

In this paper, we present a systematic photoluminescence (PL) study on strained $Si_{1-x}Ge_x/Si$ CQWs and interdiffusion-driven potential profile modulation in QWs.

Introduction of Potential Modulation

Potential modulation can be introduced either by growth, i.e., appropriate design of a heterostructure, or by post-growth manipulation. In this paper, CQW and diffusion induced modulation are demonstrated for the former and the latter, respectively. Shown in Fig.1 are schematic diagrams of potential-modulated strained $Si_{1-x}Ge_x/Si$ QWs and the associated energy spectrum. In the remainder of the text, these specific structures are referred to as symmetric CQW(SCQW) (a), asymmetric CQW (ACQW) (b), and superlattice (c). Fig.1(d) illustrates a diffusion-driven potential modulation as a consequence of Ge redistribution (solid line) deviating from its original rectangular profile (broken line).

In SCQW, ground states (n=1) both in the conduction and heavy hole (hh) bands split up into symmetric (S) and antisymmetric (A) states due to interwell coupling[1]. S state is lower in energy compared to n=1 state of SQW. This energy difference increases with decrease of Si barrier width due to increased overlap of wavefunctions. For a very thick Si barrier, the two wells are isolated, while SCQW system is reduced to a SQW of double width in the limit of vanishing Si barrier.

Superlattice can be regarded as a repeated sequence of SCQW[4] as shown in Fig.1(c) where miniband formation is expected to occur according to Kronig-Penney calculation due to extension of carriers over the entire structure. Evolution of a superlattice state is observed as steady downward shift of luminescence peak energy with increasing number of wells coupled to each other.

On the other hand, in ACQW system, where two wells of different widths are separated by a Si thin tunnel barrier (Fig.1(b)), energy level splitting is not so pronounced as in SCQW. Nevertheless,

ACQW offers us an interesting aspect of interwell coupling in the form of tunnel transfer of carriers[2,3] through the Si barrier, from the narrower well (right well) to the wider (left well), as schematically shown in Fig 1(b). This can be visualized as relative intensity variation of PL with changing Si barrier width, and is interpreted in terms of tunneling time, or in the context of carrier flow kinetics controlled by tunneling rate and recombination lifetime.

Interdiffusion at heterointerface significantly modifies Ge profile, resulting in effective well width narrowing with concomitant uprise of confining potential minimum as indicated by the arrow. Resultant Ge profile is expressed as an error function provided that Ge concentration dependence can be neglected. Similar to the case of Ge surface segregation-induced potential modulation, which has already been addressed previously by the *author*s[11] and Brunner *et al* [12], PL peak shift is likely to be brought in the same sense, viz. blue shift.

II. Experimental

All samples were grown in a purpose-built gas source Si MBE system (Daido Hoxan, VCE-S2020) with a base pressure of 4×10^{-10}Torr pumped by uhv diffusion pumps. Si_2H_6 and GeH_4 were used as source gases. Further details of sample preparation are found elsewhere[19]. After standard degreasing, wafers were dipped for 1min in 2.5-w.t.% diluted hydrofluoric acid to demude the surface oxide and to hydrogen terminate the surface. Following thermal clean at 800°C for 20min in uhv, nominally undoped QWs of Ge composition, x=0.127 and 0.16, were grown on on-axis p-type Si(100) substrates at temperatures of 620-740°C. Ge composition and layer width was calibrated using x-ray diffraction and transmission electron microscopy for fully strained alloy layers and multiple QWs grown under the same conditions. Taking advantage of excellent controllability and reproducibility of gas source MBE, a series of single QWs (SQWs) and CQWs with a centered thin Si barrier were grown.

Steady state PL was collected in standard lock-in configuration using a defocused Ar^+ ion laser beam operating at an optical excitation power density of 0.1 0.01W/cm^{-2} over the sample surface. Luminescence was dispersed through a 1-m grating monochromator blazed at 1.5μm, and detected using a liquid-nitrogen-cooled Ge detector (North Coast EO-817L). Time-resolved luminescence spectroscopy was performed using a synchronously pumped pyridine-2 dye laser operating at a wavelength of 693nm being excited by a mode-locked Ar ion laser. An ultra low dark-current S-1 type photomultiplier (Hamamatsu R3236) was operated in single photon counting mode with time resolution better than 1nsec[20]. Signals were processed through a time-to-amplitude converter and accumulated on a multichannel analyzer. Sample temperature was controlled by a closed-cycle refrigerator, a helium vapor stream variterap cryostat, or immersion in pumped liquid helium.

Post-growth annealing was performed in vacuum, $\sim10^{-9}$Torr, to prevent surface oxidation during annealing since a thermal oxide thicker than natural oxide was found to exert significant surface stress, leading to drastic band-gap shrinkage of QWs[21,22].

III. Results and discussion

Symmetric coupled quantum wells (SCQW)

19-K PL spectra of SCQWs of Lz=34Å with Si barrier width (Lb) of 9.6, 19.2, 28.8, 38.4, 76.8, 96Å are shown in Fig.2. PL spectra of single QWs of Lz=34Å and Lz=68Å are also shown for comparison. NP, TA, and TO refer to no-phonon and transverse-phonon-involving lines (A-acoustic, O-optical), respectively. Luminescence of Si substrate is seen on the higher energy side of QW luminescence around 1094-1097meV.

PL peaks are seen to shift downward as Lb is decreased as shown in Fig.2, demonstrating the interwell coupling between two symmetrically aligned wells due to wavefunction penetration across the Si barrier[1,4,23]. Accordingly, n=1 states in both the conduction and heavy hole (hh) bands split up into symmetric (S) and antisymmetric (A) states as shown in the inset. For Lz=34Å, n=1 bound state is established in the valence band for all SCQWs and SQW, and n=2 bound state almost lines up with band-edge of the Si barrier. In contrast, n=2 state is not a real bound state in the conduction band. On the other hand, A-hh state is established only in the valence band and it is above the Si barrier band-edge in the conduction band. Thus the observed luminescence is plausibly attributed to the optical transition associated with the lower-lying S states of electron (e1) and heavy hole (hh1)[23]. Note here that the light hole (lh) state is expected to be split in a similar manner, but the S state is located still higher than symmetric hh1 state. Meanwhile, for a much thicker barrier, two wells are effectively isolated and NP peak is expected to exactly fall on the counterpart of a SQW with the same width, 1050.8meV. This is what we observe in our samples for Lb>80Å where NP peak energies are centered at 1050.8meV. For Lb=0, CQW system with Lz=34Å reduces to a SQW with a doubled width, Lz=68Å.

NP peak energy, E_{NP}, extrapolated to vanishing excitation is shown in Fig.3 as a function of Lb. Solid line represents the theoretical peak energy assuming a rectangular QW potential profile. Standard envelope function approach within the effective mass approximation was used in the calculation[19].

The effective masses of electron (m_e) and heavy hole(m_{hh}) used were m_e=0.19m_0, and m_{hh}=0.2656m_0, respectively, where m_0 is the free electron mass. m_{hh} was obtained by linearly interpolating the values for Si and Ge. Excitonic NP peak energy was obtained by the relationship E_{NP}=1155-(ΔE_c-$\Delta E_c'$)-(ΔE_v-$\Delta E_v'$)(meV), where $\Delta E_c'$, and $\Delta E_v'$ represent the confinement energies calculated in the conduction and the valence bands, respectively. The exciton binding energy was assumed to be independent of the well width and fixed at 15meV[19]. Recently, Gail et al. reported the well width dependence of exciton binding energy, showing that the binding energy varies ±2meV over L_z=30-70Å for x=0.19[24]. Therefore, the assumption of fixing the binding energy at 15meV is expected to allow for an uncertainty of ±2meV in the present calculation. The E_{NP} of a 1500Å-alloy was measured to be 999meV at 19K, where no quantum size effect manifest itself and therefore the sum of the band discontinuities should be 156meV. As ΔE_v is systematically increased, with a constraint that ΔE_c+ΔE_v=156meV, the theoretical curve shifts toward higher energies. To an accuracy of ±1meV, the data fall on the curve with ΔE_v=149meV shown by the solid line. This value was then used to fit the experimental NP peak energy of SQWs as a function of L_z. An excellent match was obtained between the calculation and the data, consistent with the result reported previously by the authors that the potential profile should be rectangular when a QW is grown by gas source MBE[18,19].

It is interesting to check here the well-established formula, ΔE_v=0.84x(eV) (0<x<1)[25] obtained by Van de Walle and Martin for strained $Si_{1-x}Ge_x$/Si(100) on the basis of the deformation potential theory. Using this formula, we obtain ΔE_v=149meV for x=0.177, which is in close agreement with the experiment. Hence one can say that the 0.84x law holds so *far* as we are concerned with strained $Si_{1-x}Ge_x$/Si(100). *With reference to this*, the band alignment of strained $Si_{1-x}Ge_x$/Si (100) should be of type-I as shown in Fig.4. This can be justified by the fact that no successful fit was obtained when the conduction band offset was neglected (broken line in Fig.2) or a negative offset (staggered) was assumed in the calculation. This seems to conflict with previous reports[13,16] claiming the absence of conduction band discontinuity or type-II band lineup (staggered).

Indirect-gap Kronig-Penney superlattice

Figure 5 illustrates the evolution of a superlattice state with increasing number of coupled wells. The upper panel shows PL spectra and the lower panel shows E_{NP} variation. E_{NP} shifts to lower energies with increasing number of coupled wells and the peak shift is in good agreement with a Kronig-Penney type calculation.

Figure 6 shows 18-K PL spectra taken for 99-period strained $Si_{1-x}Ge_x$/Si superlattices of various periodicity with a fixed L_z:L_b ratio of 5.7 : 6. Spectral features are almost identical with those for SQWs, but NP to TO line intensity ratio was reduced presumably due to dilution of Ge composition averaged over a single period. Note the total absence of deep level features like D lines, as shown in the inset (sample a). The NP peak moves systematically with changing the periodicity, and is fairly explained by a simple Kronig-Penney type calculation for the optical transition between n=1 electron and hole states as shown in Fig.7 using the parameters cited in the preceding section. It is interesting to recall that the effective mass approximation well reproduced E_{NP} in the case of SQWs and SCQWs, whereas in the superlattices shown in Fig.7 a discrepancy amounting to 5meV is recognized between the data points and the calculated curve, except the sample e where gas switching lag is likely to be responsible for further increased downward shift. Temperature dependence of different specimens with SQW sandwiched between superlattice barriers revealed that exciton localization sets in below 30K due to the presence of potential fluctuation within the superlattices, ~5meV in depth, and are delocalized at increased temperatures. Figure 8 shows PL spectra of a strained $Si_{0.76}Ge_{0.24}$/Si SQW with L_z=53Å between $Si_{0.823}Ge_{0.177}$/Si superlattices with L_z:L_b=40Å:42Å. As the cold bath temperature is raised, dominance of PL intensity between the superlattice and the SQW switches around 30-39K with the net intensity almost being unaltered. The QW peaks develop with increasing temperature as the excitons are delocalized and being captured by the QW, which is apparently in the opposite sense to what is usually observed in thermal activation in the two level systems. A finite offset is recognized on the superlattice NP peaks between 39K and 16K. Therefore, 5meV shift seems to be accounted for by this exciton localization energy.

Asymmetric coupled quantum wells (ACQW)

19K PL spectra of ACQWs with two different wells, L_z=46Å (QW1) and L_z=34Å (QW2), are shown in Fig.9 for L_b=96, 86, 96, 115, 192Å. Note, QW2 was grown first and therefore is on the substrate side. In this arrangement, photocarriers are created mostly in the Si substrate and diffuse toward the first-grown QW[26]. Thus the apparent dominance of PL due to the narrower well (QW2) for decoupled case, say L_b>100Å, is due to increased carrier flow into QW2. In contrast, spectral dominance is gradually switched to QW1 with decreasing L_b. Although the spectral separation seems to

be rather poor at 18K, the two peaks are well resolved in 2K spectra as shown in the inset. This indicates that QW2 is progressively depleted of carriers due to tunnel transfer from QW2 to QW1 across the Si barrier with steady decrease of L_b[2,3]. Alternatively, PL dominance is controlled by interwell tunneling. According to a preliminary calculation, electron transfer time is much faster than hole transfer time since the electron mass is smaller than the hole mass and electron confinement barrier is relatively smaller, ΔE_c=7meV. The wavefunction of electron is therefore extended over the two wells and the hole tunneling becomes a rate-controlling process.

To check that the hole tunneling controls the PL profile variation with L_b, relative PL intensity of QW1 and QW2, I_2/I_1, as shown in Fig.10 was compared with theoretical calculation. Data points could not be obtained for L_b<70Å, since I_2 quickly rolled off due to faster tunneling. An expression for particle transmission through a potential barrier and a kinetic equation of carrier recombination were combined to obtain the expression for the fitting curve of the form[27],

$$I_2/I_1 = \frac{(\tau_1/\tau_2)}{(\frac{\tau_1}{\tau_2})(\frac{g_2}{g_1}) + \tau_2\{(\frac{h}{\sqrt{4\pi m_{hh}Lz^2}})(\frac{4kE(V-E)}{4kE(V-E)+(V+(k-1)E)^2\sinh^2(Lb/\lambda)})\}\{1+(\frac{g_2}{g_1})\}} \quad (1)$$

where h is Planck's constant, L_z(QW2)=34Å, τ_1 (τ_2) and τ_1 (τ_2) are intrinsic and experimental radiative decay times in QW1(QW2), respectively, g_1(g_2) is carrier generation rate in QW1(QW2), k (=1.04) is hole mass ratio in the Si and in the QW, E (=16meV) is confinement energy in QW2, V is confinement barrier height (=149±5meV), and λ is the penetration depth, 11.8Å, obtained as reciprocal of decay constant in the Si barrier. τ_1/τ_2 was estimated in a quantum mechanical calculation to be on the order of unity. The intrawell (experimental) radiative decay time, τ_1 and τ_2, includes the influence of nonradiative carrier waste, and was separately obtained by time-resolved PL spectroscopy to be 0.8μsec and 0.5μsec[20], respectively. The inset shows such a temporal decay profile of PL for L_z=46Å[10]. Eq.(1) well reproduces the data points in Fig.10 by putting the only unknown parameter to the most plausible value, g_2/g_1 ~1. Close agreement between the data and Eq.(1) indicates that the PL intensity variation shown in Fig.9 is essentially dictated by the hole tunneling. There it turns out that holes should be localized on either of the wells similar to effective mass filtering[2]. However, there was no marked evidence for space charge buildup[3] in terms of E_{NP} shift. This may be related with total absence of Stark shift for strained $Si_{1-x}Ge_x$/Si(100) system of type-I band lineup[28,29].

The L_b dependence entered Eq.(1) as tunneling rate given by the rectangular bracket[27]. The tunneling time is then obtained as inverse of the tunneling rate to be ~0.5μsec for L_b=86-96Å comparable with radiative decay time of the narrower well. This value seems to be intuitively reasonable since the interwell tunneling time competes with the radiative decay time. Otherwise, carrier redistribution will be such that it is concentrated on QW1 or tunnel escape to QW2 is dominant. These have been eventually observed for much thicker and thinner Si barriers, respectively.

It is worth mentioning here that interwell tunneling could be identified for rather wider Si tunnel barriers compared to direct-gap materials systems like AlAs/GaAs[27]. This seems to reflect an intrinsic aspect of SiGe luminescence, and is primarily because the competing process, i.e., radiative lifetime, is two to three orders of magnitude longer in SiGe than the typical radiative lifetime of GaAs, ~1nsec[27]. Such a long-lived carrier in SiGe find more chance of encountering the tunnel barrier, leading to an apparent increase of classical period of motion[30]represented by the first parenthesis in the rectangular bracket, and thereby increasing the upper limit of L_b below which interwell tunneling can happen.

Ge/Si interdiffusion

Post-growth annealing in SQW samples were performed to assess both structural stability of QWs and diffusion-induced potential modulation. Shown in Fig.11(a) is 18-K free excitonic PL spectra of a SQW with x=0.16 and L_z=73Å after post-growth isochronal (30min) annealing at Ta=800-900°C. As Ta increases, NP peak progressively shifts upward and the peak shift amounts to 22meV at Ta=900°C. For QWs with L_z>73Å, we could obtain much larger peak shift after 900°C annealing amounting to well over 50meV[21]. However, the peak shift was smaller for thinner wells. These observations support a view that diffusion-induced peak shift is pronounced at intermediate well width similar to the case of segregation-induced peak shift[21]. This is because the potential bottom upshift brings significant NP peak blue-shift for wider wells while the interface gradation exercise negligible influence on the NP peak energy. To the contrary, the situation is reversed for thinner wells where potential bottom upshift is upper-bounded by Si barrier band-edge. Such characteristics seem to hold promise for wavelength control using diffusion-induced potential modulation.

NP peak shift in Fig.11 was found to be fitted with a single interdiffusivity of the form, D=D_0exp(-E_a/kT), by solving standard 1-dimensional (1-D) diffusion equation. D was assumed to be

independent of Ge concentration. Recently, Gail *et al.* have reported *in situ* interdiffusion occurring at heterointerfaces during high temperature MBE[24]. They showed that Ge concentration dependence is necessary to fully account for NP peak shift over a wider range of Ge composition of SQWs in apparent contradiction with our result. In the calculation, first the diffusion profile was obtained for a trial D and the NP peak was subsequently obtained by solving 1-D Schrödinger equation. This sequence was repeated until reasonable match was obtained with the data as shown in Fig.11(b). By plotting the interdiffusivity against temperature, the activation energy and preexponential factor were obtained to be Ea=3.47±0.3eV, and $D_0=10^{-6}cm^2/sec$, respectively, as shown in Fig.11(c).

Ea seems to be rather smaller compared to what have been reported in a previous work reported by Van de Walle *et al.*[31] Nevertheless, Ea value of Ea was largest in recent x-ray characterization of interdiffusivity in strained-layer superlattices by Baribeau *et al.*[32] and Hollander *et al.*[33] It is very likely that superlattices samples are unstable because they were allegedly grown by low temperature kinetic MBE growth[22,23]and strain enhancement of diffusivity would have brought a smaller Ea, compared to unstrained samples. Hence, we believe that the intermediate values obtained here reflects improved stability in gas source grown samples which were grown in *equilibrium* conditions. It seems worthwhile to mention here that solid source MBE grown samples exhibited a drastic NP peak shift for Ta closer to Ts unlike gas source growth samples. This seems to be in agreement with a finding that solid source grown QW is not of a high structural stability compared to gas source grown QWs[6,8].

Another point observed in the figure is that the absolute PL intensity increases with Ta, although the spectra have not been scaled. This can also be understood in the context of crystal quality improvement as a consequence of reduction of nonradiative pathways after annealing[8,24].

IV. Conclusions

In conclusion, we have demonstrated the luminescence investigation on the potential modulated quantum wells, ranging from coupled quantum wells, Kronig-Penney superlattices and diffusion-modulated quantum wells. Interwell coupling was studied in strained SiGe/Si SCQWs and ACQWs where systematic energy variation was found in SDQW in close agreement with theoretical calculation and tunneling-controlled spectral change was clearly observed in ACQWs. Superlattice evolution was witnessed by changing structural parameters and the exciton localization was observed in superlattice-barrier single quantum wells. Diffusion induced potential modulation was observed to bring large blue-shift of luminescence peak energy.

The author wishes to acknowledge Y.Kato, N.Usami, H.Sunamura, K.Murakl, Y.Takahashi, and S Ohtake for their expert technical assistance. The author wishes to gratefully acknowledge Y.Shiraki, and R.Ito for encouragement throughout the work. The author was supported financially by Ikutani Foundation, Japan.

References

1 C.Delalande, U O.Ziemelis, G.Bastard, M Voos, A.C.Gossard, and W.Wiegmann, Surf. Sci.142, 498(1984).
2 R.Sauer, K.Thonke, and W.T.Tsang, Phys Rev.Lett. 61, 609(1988).
3 R.Sauer, T.D.Harris, and W.T.Tsang, Phys.Rev.B39, 12929(1989).
4 R.Dingle, A.C.Gossard, and W.Wiegmann, Phys.Rev.Lett. 34,1327(1975).
5 J. C. Sturm, H. Manoharan, L. C. Lenchyshyn, M. L. Thewalt, N. L. Rowell, J.-P. Noël and D. C. Houghton, Phys. Rev. Lett. 66, 1362 (1991).
6 D. J. Robbins, P. Calcott, and W. Y. Leong, Appl. Phys. Lett. 59, 1350 (1991).
7 D.Dentre, G.Brémond, ASouifi, and T.Benyattou, Phys.Rev. B44,11525(1991)
8 T.D.Steiner, R.L.Hengehold, Y.K.Yeo, D.J.Godbey, E.Thompson, and G.S.Pomrenke, J.Vac.Sci. Technol. B10,924(1992).J Crystal Growth 127, 473(1993).
9 J.Spitzer, K.Thonke, R.Sauer, H.Kibbel, H.-J. Herzog, and E.Kasper Appl. Phys. Lett. 60, 1720 (1992).
10 L.Vescan, A.Hartman, K.Schmit, Ch. Dieker, and H.Lüth, Appl.Phys.Lett. 60,2183(1992).
11 J.Brunner, U.Menczigar, M.Gail, E.Friess, and G.Abstreiter, Thin Solid Films 222,27(1992);J.Crystal Growth 124,443(1993): J.Brunner, J.Nützel, M.Gail, U.Menczigar, and G.Abstreiter, J.Vac.Sci.Techno.B (to be published).
12 S.Fukatsu, H.Yoshida, N.Usami, A.Fujiwara, Y.Takahashi, Y. Shiraki and R. Ito, Thin Solid Films 222,1(1992); J Crystal Growth 127,489(1992), Jpn.J.Appl.Phys.31,L1393(1992): N.Usami, S Fukatsu, and Y.Shiraki, Appl.Phys.Lett. 61,1706(1992): S.Fukatsu, N.Usami, Y.Shiraki, T.Chiarei, A.Nishida, and K.Nakagawa, Jpn.J.Appl.Phys. 31,L1015(1992): S.Fukatsu, N.Usami, and Y.Shiraki, Jpn.J.Appl Phys 31,L1015(1992): S.Fukatsu, N.Usami, Y.Shiraki, A.Nishida, and K.Nakagawa, J.Crystal Growth 127, 1083(1993). Appl.Phys.Lett. 63 (to be published): N Usami, S.Fukatsu, and Y.Shiraki, Appl.Phys.Lett. 63 (to be published).
13 M.Wachter, K.Thonke, R.Sauer, FSchäffler, H.-J.Herzog, and E.Kasper, Thin Solid Films 222,10(1992).
14 J.Hulse, N.Rowell, J.-P.Noël, and S.Rolfe, Thin Solid Films 222,59(1992).
15 D.W.Greve, R.Mirra, T.E.Schlesinger, C.McLaughlin, and M.A.Capasso, *Thin Solid Films* 222, 47(1992).
16 F.Schäffler, M.Wachter, J.-J.Herzog, K.Thonke, and R.Sauer, J.Crystal Growth 127, 411(1993).
17 V.Arbet-Engels, J.M.G.Tijero, A.Manisadjian, and K.L.Wang, J Crystal Growth 127, 406(1993).
18 S.Fukatsu, N.Usami, and Y.Shiraki, Jpn.J.Appl.Phys.Lett. 32,1502(1993).
19 S.Fukatsu, H.Yoshida, A.Fujiwara, Y.Takahashi,Y. Shiraki and R. Ito, Appl.Phys Lett.61,804(1992).
20 S Fukatsu, K.Murakl, Y. Takahashi, and Y.Shiraki, (unpublished)
21 H.Sunamura, S.Fukatsu, N.Usami, and Y.Shiraki, Appl.Phys.Lett. (to be published)
22 K.Takeuchi, and M.Aoki, Appl.Phys.Lett. 61,2566(1992).
23 S.Fukatsu, and Y.Shiraki, Appl.Phys.Lett. (to be published).
24 M Gail, J.Brunner, U.Menczigar, A.Zrenner, and G Abstreiter, Mat Res.Soc.Proc.(to be published).
25 C.G.Van de Walle, and R.M.Martin, Phys.Rev. B34,5621(1986).
26 S Fukatsu, N.Usami, and Y.Shiraki, Jpn.J.Appl.Phys. 31,L1525(1992)
27 T.Tada, A.Yamaguchi, T.Ninomiya, H.Uchiki, T.Kobayashi, and T.Yao, J.Appl.Phys. 63,5491(1988).
28 H.Temkin, T.P.Pearsall, J.C.Bean, R.A.Logan, and S.Luryi, Appl.Phys.Lett. 48,963(1986).
29 J.S.Park, R.P.G Karunasiri, and K.L.Wang, J.Vac.Sci. Technol. B 8,217(1990).
30 A.Messiah, Quantum Mechanics (North-Holland, Amsterdam, 1970), Vol.1, p.96
31 G.F.A.Van de Walle, L.J Van Ijzendoorn, A.A.Van Gorkum, R.A.Van den Heuvel, A.M.L.Thomissen, and D.J Gravesteijn, Thin Solid Films 183,183(1989).
32 J.-M.Baribeau, R.Pascual, and S.Saimoto, Appl.Phys.Lett. 57,1502(1990)
33 B.Hollander, R.Butz, and S.Mantl, Phys.Rev.B46,6975(1990).
34 S Fukatsu, N.Usami, and Y.Shiraki, J.Vac.Sci.Technol.B 11,895(1993)

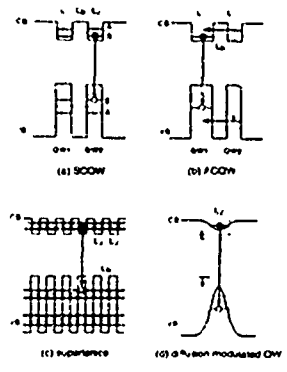

FIG 1 Schematic diagram of potential modulated QWs (a)symmetric coupled quantum well (SCQW) (b)symmetric coupled quantum well (ACQW) (c)superlattice (d) diffusion modulated QW

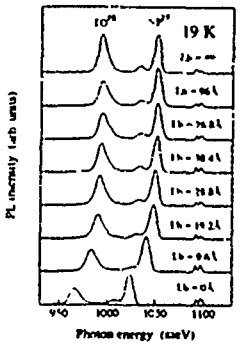

FIG 2 19 K PL spectra of strained $Si_{0.823}Ge_{0.177}/Si$ SCQWs with Lz=34Å with Si barriers of different thickness, Lb and SQWs with Lz=34Å and Lz=68Å

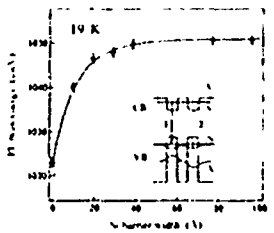

FIG. 3 E_{NP} vs Lb for strained $Si_{0.823}Ge_{0.177}$ Si SCDQWs with Lz=34Å. Solid line is the theoretical curve calculated by effective mass approximation. Broken line represents theoretical curve in the absence of conduction band offset. Inset shows the schematic of the coupled well with split energy levels

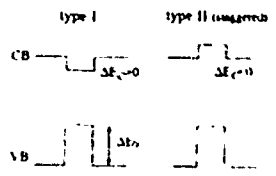

FIG. 4 Schematic potential line up for type I and type II configurations

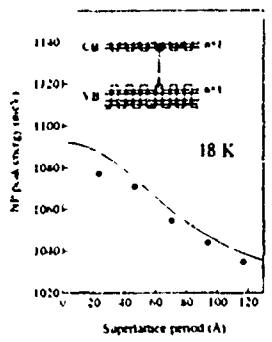

FIG. 7 NP peak energy shift with superlattice period in 99 period strained $Si_{0.823}Ge_{0.177}$ Si superlattices

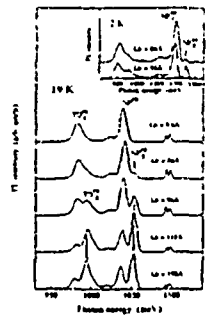

FIG 8 PL spectra of strained $Si_{0.76}Ge_{0.24}$/Si SQW with strained $Si_{0.823}Ge_{0.177}$/Si superlattice buffer layers of Lz Lb=40Å 42Å

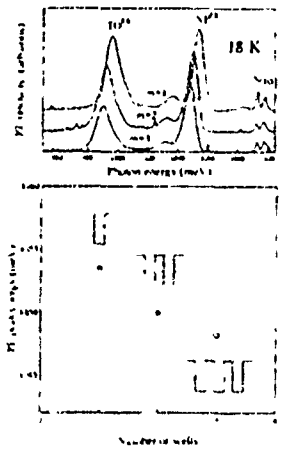

FIG 5 Evolution of a Krong Penney type superlattice Upper and lower panels show PL spectra and PL peak energy with number of coupled wells The schematic inset shows the associated energy spectrum

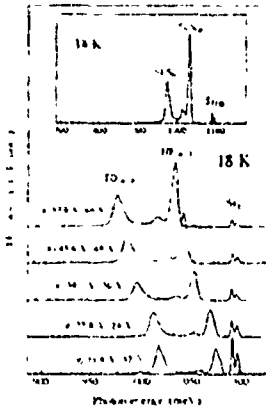

FIG 6 18 K PL spectra of 99 period strained $Si_{0.823}Ge_{0.177}$ Si superlattices with a fixed Lz Lb ratio of 3 7 3 0 The inset shows the lower energy spectrum of sample a

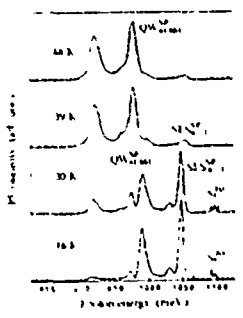

FIG 9 19 K PL spectra of strained $Si_{0.823}Ge_{0.177}$/Si ACQWs of Lz=34A (QW2) and Lz=46A (QW1) with different Si barrier thickness. Lb=9 6, 36 96 115 192A The inset shows 2K spectra for Lb=86 and 96A

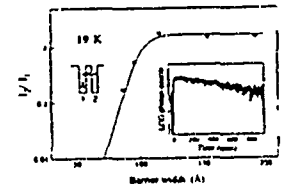

FIG 10 Peak intensity ratio, I2/I1, vs S, barrier width Lb The inset schematically shows the tunneling transfer of hole from QW2 to QW1 The inset figure shows a typical temporal PL decay profile for Lz=46A

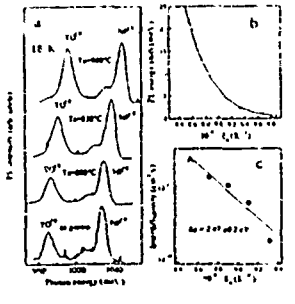

FIG 11 (a) PL spectra of a strained $Si_{0.84}Ge_{0.16}$/Si SQW with Lz=73Å after annealing at various Ta (b)PL peak shift vs Ta. Solid line is the calculated curve and open circles are data points (c) Calculated diffusivity vs Ta Solid line is a linear fit to the data (closed circles)

TuC2

Fermi Sea Shake-up in Quantum Well Luminescence Spectra

M S Skolnick[a], K J Nash[a] D J Mowbray[a] M K Saker[a] T A Fisher[a], D M Whittaker[a] D W Pegg[a]
N Miura[a], S Sasaki[a] R S Smith[a], and S J Bass[a]

[a]Department of Physics, University of Sheffield Sheffield S3 7RH, UK
[b]DRA, St Andrews Road, Malvern, Worcs, WR14 3PS UK

[a]Institute for Solid State Physics, University of Tokyo, Roppongi, Minato-ku, Tokyo 106 Japan
[b]GEC Marconi Materials Technology Ltd Caswell Towcester, Northants NN23 6EQ, UK

Abstract
Evidence for many body shake up in the magneto-luminescence spectra of quantum wells is presented Results for both lattice matched InGaAs-InP and strained layer AlGaAs-InGaAs GaAs structures covering a wide range of carrier densities are presented In all the structures coupling between shake up and LO phonon excitations is observed Strong enhancement of the shake up satellite of the $N_e = 1$ Landau level (LL) recombination due to resonant coupling with the $N_e = 0$ LL is presented

Fermi sea shake-up is a fundamental many body effect in which excitations of the Fermi sea arise during the recombination between a photocreated hole and a high density electron system [1-3] Shake up corresponds to the creation of an electron hole quasi particle pair on either side of the Fermi energy during recombination The energy of the photon which is emitted in the presence of shake up is lower than in its absence, the difference in the energies corresponds to the energy of the electron hole quasi-particle pair created during shake up Such pair excitations across the Fermi level have a continuous range of energies and thus give rise to a broad low energy tail to recombination spectra For this reason, until very recently [4] the only evidence for shake up processes in semiconductor spectra was obtained from lineshape analyses [5] or from the observation of anomalously strong photoluminescence (PL) in the forbidden $k_z z$ geometry in GaAs AlGaAs quantum well (QW) spectra [6,7] However, we have shown within the last few months that definitive observations of shake up can be obtained from the study of the PL spectra of QWs in magnetic field [4] In magnetic field the electron states are quantised into Landau levels, with the consequence that the only possible shake up excitations are to unfilled Landau levels (LLs) above the Fermi level As a result the broad low energy tail in the PL spectra is transformed into a series of discrete shake up satellites Comparison of the zero and finite magnetic field spectra then shows that the B = 0 tail is also due to shake up

The work of ref 4 was carried out from 0 to 10T on a lattice matched InGaAs InP QW containing 1 15 x 10^{11}cm^{-2} electrons In the present paper these results are extended up to 20T Interaction between the shake-up satellites and LO phonon lattice excitations is observed of very similar form to that reported recently for an $Al_xGa_{1-x}As$-$In_xGa_{1-x}As$ GaAs strained layer QW containing a relatively high density ($\sim 2 \times 10^{11}$ cm^{-2}) of carriers[8,9] New results for the strained layer QW up to higher field are also reported Strong evidence for the enhancement of the satellites due to resonant inter LL coupling will be presented Finally the satellite behaviour for the strained layer QW will be shown to be of very similar form to that observed in an InGaAs InP QW also containing a high density of carriers (9.2×10^{11}cm^{-2})

Details of the InGaAs-InP and AlGaAs-InGaAs GaAs samples are given in refs 4 8 and 10 The PL experiments were carried out at 4.2 or 2K in either a 14T superconducting or 20T Bitter magnet PL was excited with ~ 25mW/cm^2 of 633nm radiation from a He Ne laser dispersed by a grating spectrometer and detected using a cooled Ge photodiode

The PL spectra for the lattice matched $In_{0.53}Ga_{0.47}As$ InP 150Å wide QW ($n_e = 1.15 \times 10^{11}$cm^{-2}) were presented in ref 4 and will not be repeated here At B = 0, the spectrum consists of a zero phonon line (ZPL) at 847.4 meV and LO phonon satellite structure in the 800 to 820 meV region to lower energy Above 2.0T the phonon satellites are resolved into contributions from the GaAs and InAs-like LO modes of the InGaAs QW material and from the InP modes of the barrier

This behaviour is summarised in the fan diagram of transition energies against magnetic field shown in Fig 1 Splitting of the ZPL into n = 0 and n = 1 LLs is seen with the n = 1 LL depopulating at 2 4T at a filling factor $\nu = 2$, corresponding to $n_e = 1.15 \times 10^{11}$ cm^{-2} The ZPL variation with B is replicated at 27 33 and 43 meV to lower energy by the 'InAs' GaAs and InP LO modes mentioned above In addition, lower energy Γ_1, Γ_2 and Γ_3 shake-up satellites are visible The Γ_n satellites correspond to inter Landau level Fermi sea excitations in which an additional electron is promoted from the $N_e \neq 0$ state to $N_e = 1$ 2 or 3 higher LLs The spacing of the Γ_n satellites below the ZPL is close to integral multiples of $\hbar\omega_c$ the inter LL separation Closer inspection of Fig 1 shows that the ZPL-Γ_1 separation is greater than the Γ_1 - Γ_2 Γ_2 - Γ_3 splittings, and that the

Γ_1 energy varies in a non linear fashion with B The ZPL - Γ_1 spacing (ΔE) can be expressed in terms of an apparent effective mass m_T^*, using the expression $\Delta E = \hbar eB/m_T^*$ The variation of m_T^* with B is shown in the inset to Fig 1 m_T^* varies from 0.037 m_0 at 2.3T to 0.047 m_0 at 9.6T, close to the QW band edge effective mass m_e^* of 0.05m_0 in these InGaAs InP QWs[5] This behaviour was explained in ref 4 by noting that the shake up excitations correspond to inter LL magneto plasmon excitations of the Fermi sea The energy of the magneto plasmon excitations is only equal to $\hbar\omega_c$ for in-plane wave-vector $q \ll 0^{[11-13]}$ At $\nu = 1$, the departure from $\hbar\omega_c$ of the maximum in the magneto plasmon density of states is given by $E_1 = 0.17e^2/\varepsilon l_0$ where $l_0 = (\hbar/eB)^{1/2}$ is the magnetic length The factor e^2/l_0 in E_1 varies as $B^{1/2}$, and as a result the apparent effective mass m_T^* is expected to tend towards m_e^* with increasing B as observed in the inset to Fig 1

The Γ_1 satellite intensities decrease with increasing B in the low field range (0 to 10T) As shown in Fig 2 Γ_1 decreases in intensity by a factor of ~ 5 from 8.5 to 10T, where it is only barely visible with ~ 0.01% of the intensity of the ZPL From 10.5 to 17.5T Γ_1 is not observed but it then re appears in the 18 to 19.5T range as shown in Fig 2c For B > 17T, Γ_1 is at lower energy than the LO phonon satellites (see Figs 1,2) Its re appearance in the high field range arises from resonant mixing between Γ_1 and the much stronger LO phonon satellites of the ZPL Very similar resonant interactions are discussed below for the high density AlGaAs-InGaAs GaAs and InGaAs-InP QWs In those cases the resonant interactions are observed at much lower field since higher LLs are populated to relatively higher fields As a result the LO phonon satellites of $n \geq 1$ LLs interact with the Γ_n satellites at lower magnetic field

The B = 0 PL spectrum of the strained layer $Al_yGa_{1-y}As$-$In_xGa_{1-x}As$-GaAs ($y = 0.23$, $x = 0.10$) 150Å wide QW with $n_e = 7.2 \times 10^{11}$cm^{-2} ($E_F = 25.4$ meV) is shown in Fig 3a It consists of a peak at 1.117 eV corresponding to recombination of electrons at q = 0 at the bottom of the QW conduction band, together with a broad high energy tail extending to the electron Fermi energy at E_F The q ≠ 0 transitions up to the Fermi wave-vector (2×10^6cm^{-1}) are made allowed by the weak disorder in the system In magnetic field the spectrum breaks up into LL transitions (N_e, N_h) At 10T ($\nu = 3$) only the $N_e = 0$ and 1 LLs are populated Recombination of $N_e = 1$ electrons with holes in both the $N_h = 0$ 1 LLs is observed due to the non-thermal distribution of the photo-created holes The intensity of the $N_e = 1$ transitions decreases with increasing field from 10 to 14T (Figs 3b to 3e), as the $N_e = 1$ LL depopulates towards $\nu = 2$ (14.9T) To lower energy below the (0 0) principal recombination line Γ_n shake up satellites and N_L LO phonon satellites of the N_eth LL are observed These results are summarised in the fan diagram of Fig 4 Spectra below 10T were presented in ref 8, together with a discussion of oscillations of intensity of the N_L satellites with B which occur at crossing points with the Γ_n satellites

In the present paper we will concentrate on the new results above 10T in particular the resonant anti-crossing between 1_L and T_1 in the 9 to 13T region and the behaviour of the T_1^* feature with B As for the InGaAs-InP sample of Figs 1,2 the (0 0) - Γ_1 separation is greater than $\hbar\omega_c$ The dashed line representing the variation of the Γ_1 energy with B is drawn for an energy of 1.25 $\hbar\omega_c$, with the corresponding Γ_2 and Γ_3 energies at 2.25 $\hbar\omega_c$ and 3.25 $\hbar\omega_c$ below (0 0) as expected from the magneto-plasmon theory of Kallin and Halperin[11,13] For this sample the variation of the Γ_1 energy with B is strongly perturbed by resonant anti-crossings with the N_L satellites thus precluding any determination of the variation of the departure of the Γ_1 - (0 0) energy from a linear variation with B equivalent to the variation of m_T^* with B in the inset to Fig 1)

The resonant interaction between 1_L and T_1 is clearly seen in the fan diagram of Fig 4, where anti-crossing is observed in the 9 to 14T region Away from resonance the 1_L satellite is dominant, as seen in the spectra of Figs 3b c at 10 and 14T respectively In the intermediate region Γ_1 gains intensity due to resonant mixing with 1_L with the two satellites having equal intensity at 11.5T The variation of intensities between the two sides of the resonance is shown in the 11 and 12T spectra of Figs 3c, d respectively

The variation of the intensity of T_1^* the low energy shoulder ~ 5 meV below (0 0) at 10T is particularly interesting In ref 8, this feature was tentatively ascribed to a shake up satellite of (1,0) enhanced in intensity by resonant mixing with (0 0) This attribution is given strong support by the higher field data presented in the inset to Fig 4 where the intensity of T_1^* relative to that of the (1 0) transition is presented If T_1^* is a satellite of (1 0) the ratio of the two intensities is expected to be a constant, independent of magnetic field This is exactly the behaviour observed in the inset to Fig 4 where the intensity ratio of ~ 7.5 is seen to vary by less than 15%

from 9 to 14 T (ν = 2.3 to 2.1). This observation provides strong support to the attribution of the Γ_1^* feature to a shake-up satellite of (1,0). The shake up excitation corresponds to the promotion of an additional electron from $N_e = 0$ to $N_e = 1$. Γ_1^* occurs ~ 1.3 $\hbar\omega_c$ below (1,0) consistent with the separation observed between (0,0) and Γ_1, as required since both Γ_1 and Γ_1^* arise from $\Delta N_e = 1$ inter-LL excitations.

The high intensity of Γ_1^* relative to (1,0) is also noteworthy. (1,0) is relatively weak compared to (0,0) even when $N_e = 1$ is filled at 7.4 T (ν = 4), since (1,0) is a $\Delta N_e = 1$ transition observed only due to the presence of weak disorder in the system[14]. Γ_1^* is ~ 7.5 times stronger than its parent line (1,0) since it is nearly degenerate with the dominant recombination transition (0,0), and is strongly enhanced in intensity by resonant mixing with (0,0).

Finally we describe briefly magneto-PL results for an InGaAs-InP QW with high n_s of 9.2×10^{11} cm^{-2}, which shows very similar LO phonon and shake up satellites to those described above for the AlGaAs-InGaAs-GaAs structure. This sample exhibits a strong Fermi energy edge singularity[15] in its PL spectrum due to the strong localization of photo-created holes in alloy fluctuations in the InGaAs QW. This contrasts with the behaviour for the more perfect AlGaAs-InGaAs-GaAs QW of Figs. 3, 4 where only a weak feature at E_F is observed in Fig. 3a. In this paper we present only the variation of the transition energies against magnetic field, a discussion of the spectra in the satellite region being reserved for a separate publication. PL spectra for the principal LL transitions up to 10 T can be found in ref. 10.

The transition energies against magnetic field are shown in Fig. 5. $\Delta n = 0$ LL transitions (N_e,0) are observed for N_e from 0 to 8. The straight lines through the experimental points correspond to $(N_e + \frac{1}{2})\,\hbar\omega_c$ variations with $m_e^* = 0.05\, m_0$[10]. Two points in particular should be noted concerning the (N_e,0) transitions. Firstly the main transitions exhibit oscillations around the linear $(N_e + \frac{1}{2})\,\hbar\omega_c$ variation as a function of filling factor. These oscillations have been attributed to oscillations of exchange and correlation energies due to variations in the self-consistent potential with filling factor[16-18]. Secondly, the (3,0), (2,0) and (1,0) transition energies deviate to lower energy below the linear fits as soon as the respective LL begins to empty with increasing B (e.g. (1,0) above ν = 4 where $N_e = 1$ begins to empty)[19]. This deviation probably arises due to the finite width of the distribution of LL energies. As the filling factor is reduced, recombination from the tail of the broadened distribution dominates the PL spectrum to a progressively greater extent, with the result that the observed LL transition energies decrease increasingly below $(N_e + \frac{1}{2})\,\hbar\omega_c$.

To lower energy, N_L LO phonon satellites and T_0 shake up satellites are observed in a very similar manner to that reported in Figs. 3, 4. The dominant LO phonon satellites 2_L, 1_L and 0_L arise from the 33 meV GaAs like LO phonon modes of the InGaAs QW, as seen for the low density InGaAs-InP QW in Figs. 1, 2. The satellite labelled 1_A arises 43meV below the (2,0) transition and is due to emission of an InP barrier LO phonon (the InP LO phonon energy is 43meV). The attribution of 1_A to an LO phonon satellite of (1,0) is supported by the very similar intensity variation of 1_A and (1,0) with field as $N_e = 1$ depopulates towards ν = 2.

The straight lines representing the Γ_1 and T_2 transitions which give the best fits to the experimental points are drawn $\hbar\omega_c$ and $2\hbar\omega_c$ below the (0,0) energies. The difference between these splittings and the 1.25$\hbar\omega_c$ - 2.5$\hbar\omega_c$ splittings of Fig. 4 may arise from the greater distribution of Landau level energies in this case, as shown already by the departure below $(N_e + \frac{1}{2})\,\hbar\omega_c$ of the (N_e,0) transitions for partially filled LLs. The results for the principal (N_e,0) transitions show that tail states dominant the recombination for small LL filling, such a distribution of LL energies may also perturb the observed shake up energies and thus lead to the ~ $\hbar\omega_c$ and ~ 2$\hbar\omega_c$ energies observed. As discussed for the strained layer QW of Fig. 4, anti-crossing between the LO phonon and shake up satellites is observed in Fig. 5 between the 0_L and Γ_1 satellites from 12 to 19 T. The splitting of the two branches at resonance is 10 meV fairly close to that observed for the Γ_1 1_L anti-crossing of Figs. 3, 4.

In conclusion, shake-up and LO phonon satellites in the magneto-PL spectra of lattice matched and strained QW structures covering a wide range of carrier density have been presented. Interaction between the Fermi-sea and lattice excitations has been observed in all the samples investigated. Enhancement of the shake up satellite intensity by resonant coupling with the dominant $N_e = 0$ LL recombination line has been demonstrated.

Acknowledgement. We thank J. C. Maan for collaboration at the Max Planck Institut, Grenoble where the experiments up to 20T were performed.

References

1. See e.g. G. D. Mahan, *Many Particle Physics* (Plenum, New York, 1990) Chap. 8.
2. Y. A. Bychkov and E. I. Rashba, Zh. Eksp. Teor. Fiz. 96, 757, 1989 (Sov. Phys. JETP 69, 430, 1989).
3. T. Uenoyama and L. J. Sham, Phys. Rev. Lett. 65, 1048, 1990.
4. K. J. Nash, M. S. Skolnick, M. K. Saker and S. J. Bass, Phys. Rev. Lett. 20, 3115, 1993.
5. See, for example, J. H. Collet, W. W. Ruhle, M. Pugnet, K. Leo and A. Million, Phys. Rev. B40, 12296, 1989 and references therein.
6. R. Sooryakumar, A. Pinczuk, A. C. Gossard, D. S. Chemla and L. J. Sham, Phys. Rev. Lett. 58, 1150, 1987.
7. G. D. Sanders and Y. C. Chang, Phys. Rev. B32, 5521, 1985.
8. M. S. Skolnick, D. J. Mowbray, D. M. Whittaker and R. S. Smith, Phys. Rev. B47, 6823, 1993.
9. Similar interaction phenomena between LC phonon and shake-up satellites has also been reported by L. V. Butov, V. I. Grinev, V. D. Kulakovskii and T. G. Andersson, Phys. Rev. B46, 13627, 1992.
10. M. S. Skolnick, K. J. Nash, S. J. Bass, P. E. Simmonds and M. J. Kane, Solid State Commun. 67, 637, 1988.
11. C. Kallin and B. Halperin, Phys. Rev. B31, 3635, 1985.
12. A. H. Macdonald, J. Phys. C18, 1003, 1985.
13. A. Pinczuk, J. Valladares, D. Heiman, A. C. Gossard, J. H. English, C. W. Tu, L. Pfeiffer and K. West, Phys. Rev. Lett. 61, 2701, 1988.
14. At 10T, the ratio of the (1,0) to (0,0) intensity is 1:20.
15. M. S. Skolnick, J. M. Rorrison, K. J. Nash, D. J. Mowbray, P. R. Tapster, S. J. Bass and A. D. Pitt, Phys. Rev. Lett. 58, 2130, 1987.
16. S. Katayama and T. Ando, Solid State Commun. 70, 97, 1989.
17. T. Uenoyama and L. J. Sham, Phys. Rev. B39, 11044, 1989.
18. R. Stepniewski, W. Knap, A. Raymond, G. Martinez, T. Rotger, J. C. Maan and J. P. Andre, in High Magnetic Fields in Semiconductor Physics, edited by G. Landwehr (Springer-Verlag, Berlin), p. 62.
19. Similar but smaller deviations of the (1,0) and (2,0) transitions from linearity when the N_e = 1 and 2 LLs are partially filled are visible in Fig. 3.

Figure Captions

1. Transition energies against magnetic field for InGaAs-InP quantum well of 150Å width containing 1.15 x 10^{11} cm^{-2} electrons. Splitting of the zero phonon line (ZPL) into n = 0,1 Landau levels is observed at low magnetic field. To lower energy LO phonon satellites and shake up satellites (Γ_1, T_2, T_3) of the n = 0 LL recombination are observed. The inset shows the variation of m_T^* with B, where m_T^* is deduced from the n = 0 LL - Γ_1 separation ΔE, where $\Delta E = \frac{eB}{m_T^*}$.
2. LO phonon and Γ_1 satellite spectra for InGaAs-InP sample at 8.5, 10 and 19T. Γ_1 is observed at 19T due to resonant interaction with the strong LO phonon satellites.
3. PL spectra at B = 9, 10, 11, 12 and 13T in Figs. 3a-e for AlGaAs-InGaAs-GaAs 150Å wide, modulation doped strained layer quantum well. Landau level transitions (N_e, N_f) are observed in Figs. 3b-e with Γ_1 shake up and 1_L, 0_L LO phonon satellite lines to lower energy. The resonant exchange of intensities between 1_L and Γ_1 in the 11-12T region is seen in Figs. 3c, d. Away from resonance the LO phonon 1_L line is the dominant satellite. The inset shows the variation of the intensity of Γ_1^*, the shake up satellite of (1,0) relative to that of (1,0). The near constant intensity ratio of $\Gamma_1^*/(1,0)$ shows that Γ_1^* is a satellite of (1,0) resonantly enhanced by interaction with (0,0).
4. Transition energies against magnetic field for AlGaAs-InGaAs-GaAs quantum well. LL filling factors (ν) are indicated. The dashed lines to indicate the shake up transitions (Γ_1, T_2, T_3) are drawn at energies 1.25 $\hbar\omega_c$, 2.25 $\hbar\omega_c$, 3.25 $\hbar\omega_c$ below (0,0). The fields indicated by the indices in the lower part of the figure correspond to the crossing points of T_0 with the N_f satellites, at fields corresponding to the resonance condition $(m + \frac{1}{4})\hbar\omega_c = \hbar\omega_{LO}$ as discussed in ref. 7.
5. Transition energies against magnetic field for InGaAs-InP quantum well with $n_s = 9.2 \times 10^{11}$ cm^{-2}. (N_e,0) LL transitions are observed, with N_e = 0 to 8. GaAs-like and 1_A (1_{InP}) LO phonon satellites and Γ_1 and T_2 shake up satellites are observed to lower energy, with clear resonant anti-crossing between 0_L and Γ_1 from 12 to 19T. LL filling factors (ν) are indicated at the bottom of the figure.

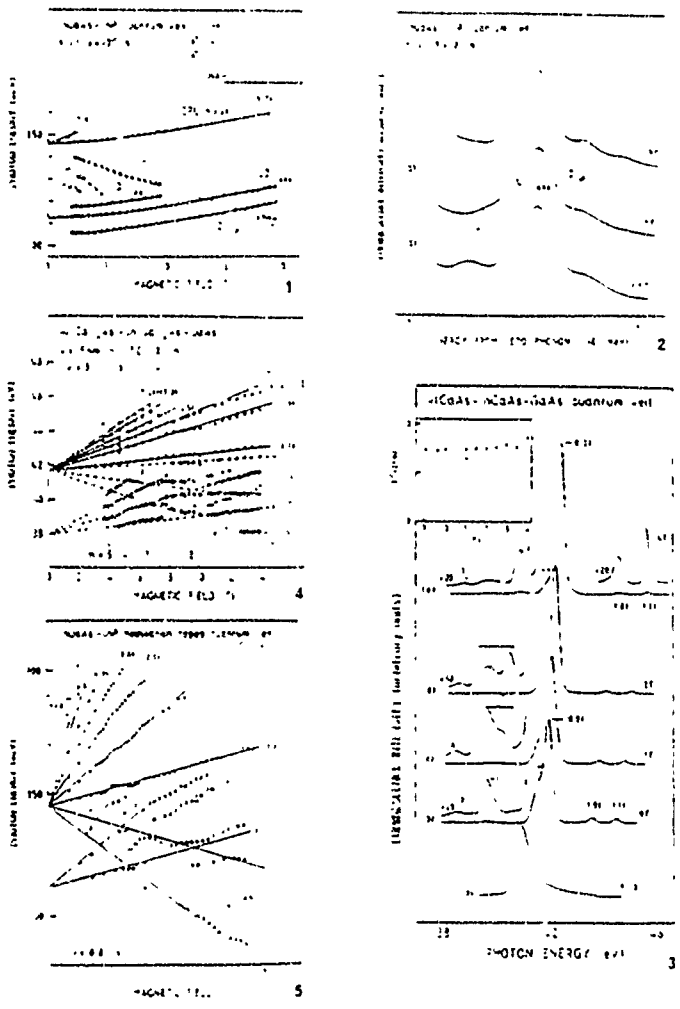

TuC3

Optical investigation of superlattice orbits and impurity states in InGaAs/GaAs

R. J. Warburton,[1] J. G. Michels,[1] P. Peyla,[1] R. J. Nicholas,[1] and K. Woodbridge[2]

[1] *Clarendon Laboratory, Parks Road, Oxford, OX1 3PU, U.K.*

[2] *University College London, Department of Electronic and Electrical Engineering, Torrington Place, London, WC1E 7JE, U.K.*

Abstract

We have measured optically-detected-cyclotron resonance on $In_{0.05}Ga_{0.95}As/GaAs$ superlattices with large magnetic fields applied both parallel (Faraday) and perpendicular (Voigt) to the growth direction. Cyclotron resonance in the Voigt geometry reveals a band structure in the growth direction. A semi-classical quantization of the Kronig-Penney dispersion gives good agreement with the data, providing that the cyclotron radius is larger than the superlattice period. We observe $1s - 2p_+$ transitions from residual impurities which lie predominantly in the barrier regions. The impurity transition has a remarkable behaviour in the Voigt geometry, moving from the bulk $1s - 2p_+$ field to close to the bulk free electron field as the barrier thickness increases, and is exactly mid-way between these two limits when the cyclotron radius equals the barrier thickness.

1 Introduction

A superlattice consists of quantum wells sufficiently close together such that inter-well coupling occurs. If a magnetic field is applied perpendicular to the growth direction, the electrons are forced to tunnel through the barriers. This can be pictured semi classically because of the band dispersion in the growth direction. However, once the cyclotron diameter, $2r_c$ ($r_c = \sqrt{\hbar/eB}$), is smaller than, or comparable to, the superlattice period, L, then the effective mass picture breaks down. For a one-dimensional superlattice potential, the electron energy becomes dependent on the orbit centre [1], for a two-dimensional potential, a rich and fascinating energy level scheme emerges [2].

This transition when $2r_c \sim L$, from a semi classical to a strongly quantum mechanical behaviour, has received only limited experimental coverage. Belle and co workers [observed a weakening of PLE features when a Landau level's energy exceeded the top of the miniband. Calculations showed that it is at this point that the electron energy becomes strongly dependent on the orbit centre. There is great advantage in probing the modes directly with f ar red (FIR) radiation, as has been reported by Duffield *et al* [3, 4] for GaAs/AlGaAs superlattices. These authors made cyclotron resonance experiments for $2r_c > L$, modelled successfully within

a semi-classical picture, but for $2r_c < L$ a new mode, corresponding to a state bound to the barriers, was observed.

The binding energy of impurities within a superlattice geometry is also of interest, as the impurity binding energy can depend strongly on the position of the impurity in the superlattice, which is in some ways analogous to the dependence of the Landau energy on orbit centre for $2r_c \leq L$. The impurity binding energy is a minimum when the impurity lies in the middle of the barrier, and a maximum when the impurity lies in the middle of the well [5]. If the impurities are spread evenly throughout the superlattice then there are two peaks in the density of states, leading to characteristic absorption edges [6]. Experimental work has in general concentrated on well bound impurities [7 - 9].

In this paper we present measurements on a series of $In_{0.05}Ga_{0.95}As/GaAs$ superlattices with the field **B** either **B** ∥ z (Faraday) or **B** ⊥ z (Voigt), where z lies along the growth direction. There are a number of differences to previous work. Most importantly, the electron band offset in $In_{0.05}Ga_{0.95}As/GaAs$ is only ~ 40 meV giving sizeable miniband widths for relatively large barrier widths, L_b. This should be compared to the more familiar GaAs/AlGaAs system in which superlattice behaviour is only apparent for very thin barrier widths, $L_b \leq 20$ Å. With $In_{0.05}Ga_{0.95}As/GaAs$ we are able to achieve not only $2r_c < L$, but also $2r_c < L_b$. Secondly, we have employed an optically-detected technique in which the electrons are excited optically into the conduction band, allowing us to make cyclotron resonance experiments at low temperature, without the constraints of impurity freeze-out. Finally, we report measurements of *barrier* centred $1s - 2p_+$ impurity transitions, also in both field orientations.

2 Experiments

The samples were grown at Philips, Redhill, and consist of twenty periods of nominally undoped $In_{0.05}Ga_{0.95}As/GaAs$, with nominal well/barrier thicknesses (L_w/L_b) 50/50, 50/100, 50/150 and 50/200 Å. The actual sample dimensions, as measured by x-ray diffraction [10], differ slightly, although we refer throughout to the samples by their nominal thicknesses. Measurements on these samples confirming their high quality, have already been published, notably a PL and PLE study [10] to determine the miniband widths and exciton binding energies.

The PL from each sample excited with a 3 mW HeNe or solid state diode laser, consisted of a single line. Our optically detected cyclotron resonance (ODCR) technique involves monitoring the change in PL intensity induced by far infra-red radiation. We found that the sign of the ODCR signal did not depend on the exact detection wavelength, and so the data were collected with poor resolution, to give as large a PL signal as possible. The sample was cooled to 2 K, and fields up to 15 T were applied. At resonance, we could reduce the PL by up to 20% with our conventional optically pumped FIR gas laser. It should be borne in mind that the ODCR signal may not have a straightforward relation to the absorption of FIR.

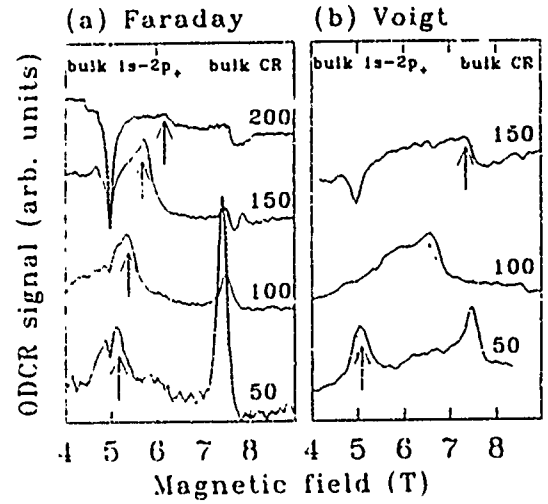

Figure 1. ODCR traces taken with the 96 μm laser line for the four samples, labelled with the nominal barrier widths. The arrows mark the superlattice impurity transitions. The dashed lines show the fields of the bulk GaAs $1s - 2p_+$ and cyclotron resonance transitions.

3 Results

3.1 Faraday orientation

Typical ODCR traces, taken with the 96 μm FIR laser line, are shown in Fig. 1a. Each sample gives two main features, the one at lower field due to a $1s - 2p_+$ impurity resonance, and the one at higher field due to a cyclotron resonance. The impurity transitions are thought to be related to a low density of residual donors distributed throughout the superlattice. There are also, particularly for the 50/150 and 50/200 samples, *sharp* features of opposite sign. The field values of these sharp features, and their independence from sample to sample, suggest that they arise from $1s - 2p_+$ and CR transitions in bulk GaAs, most probably from the GaAs capping layer, where any FIR absorption could affect the transfer of electrons into the superlattice, so contributing to an ODCR signal from the superlattice itself.

The CR field for the 50/50 sample occurs at a lower field than for bulk GaAs, but the field increases as the barrier width increases. This means that the cyclotron mass, $m^* = eB/E$, increases for increasing L_b, and this is a consequence of a reduction in inter-well coupling. As the wells couple to form a superlattice, the confinement energy of the first electron level (E_1) decreases, so causing a reduction in the non-parabolicity enhancement to the band edge mass.

L_b	Δ	m_f^{exp}	m_f^{th}	$1s-2p$	$1s-2s$	$r_c = L_b$
55.0	16.7	0.0665	0.06680	4.3	5.3	21.8 T
101.1	12.7	0.0671	0.06699	4.2	4.7	9.1 T
146.0	5.9	0.0677	0.06711	4.6	4.1	3.8 T
202.7	2.5	-	0.06725	4.0	3.5	1.6 T

Table 1 A summary of sample details and some results. L_b is the barrier width in Å, Δ is the electron miniband width in meV, m_f^{exp} (m_f^{th}) is the measured (calculated) effective mass at energy 10.17 meV in the Faraday orientation, $1s-2p$ ($1s-2s$) is the $B=0$ impurity energy estimated experimentally (theoretically), and $r_c = L_b$ defines the magnetic field at which the cyclotron radius r_c is equal to the barrier thickness.

We have taken non parabolicity into account with an eight band k.p calculation [11]. The agreement with the data is good at cyclotron energies above ~ 8 meV (see Table 1), but at low energy the measured masses fall to anomalously low values. This behaviour is reminiscent of CR from conventional GaAs quantum wells where anomalously low effective masses have been observed at low field [12], attributed to shallow localizing potentials from well width fluctuations.

Fig. 1a shows two effects concerning the impurity transition: with increasing barrier width the field increases, implying that the binding energy reduces, and the line shape becomes asymmetric, with the signal falling rapidly on the high field side. Both imply that the impurities are predominantly in the barriers, although the broadness of the impurity resonance compared to the cyclotron resonance does mean that there is a distribution of impurities throughout the superlattice. The high field (low energy) absorption edge comes from the peak in the density of states from impurities in the middle of the barrier. As the barrier width increases, the superlattice potential draws the wave function further away from the impurity centre, so lowering the binding energy, as observed. Our calculations of the shallow donor $1s-2s$ energy reproduce this trend, and give reasonable agreement with the $B=0$ transition energy estimated experimentally (see Table 1).

3.2 Voigt orientation

ODCR traces in the Voigt geometry are plotted in Fig. 1b, again for the 96 μm FIR laser line. In this case, we have a clear CR only from the 50/50 sample, which occurs at higher field than in the Faraday geometry of Fig. 1a. We emphasise that the Voigt geometry enables us to sample the new band structure in the superlattice direction, and a semi-classical interpretation of cyclotron resonance consists of the electrons spiralling along the direction of the magnetic field, tunnelling through the barriers in the course of their cyclotron orbits. For the 50/50 sample, the cyclotron diameter is always larger than the superlattice period for the fields used here, so we use a semi-classical quantization of the miniband dispersion to model the data. The superlattice dispersion $E(q)$, where q is the wave vector along the superlattice direction, implies a cyclotron mass according to

$$m^* = \frac{\epsilon\hbar B}{E(q_1) - E(q_0)}, \quad q_0^2 = \frac{\epsilon B}{\hbar}, \quad q_1^2 = \frac{3\epsilon B}{\hbar} \qquad (1)$$

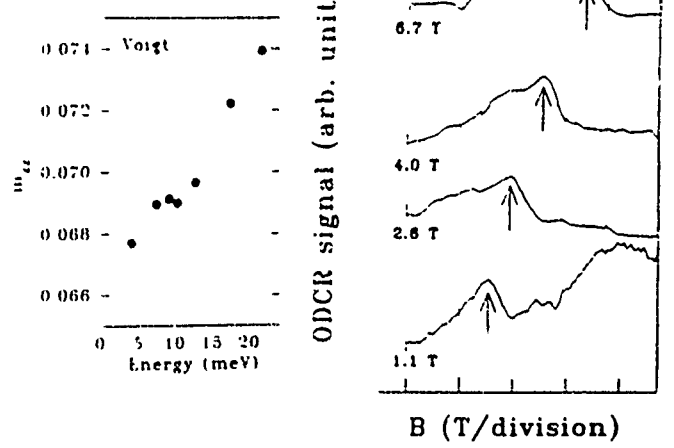

Figure 2 A comparison between the measured and calculated masses along the superlattice direction for the 50/50 sample. Figure 3 ODCR traces for the 50/100 sample, for four different laser wavelengths, 163, 118, 96 and 70 μm. The field has been offset such that the bulk $1s-2p_+$ fields (2.1, 3.6, 5.0 and 7.7 T respectively) are coincident. The arrows mark the superlattice impurity transitions.

We calculated $E(q)$ with the eight band program, although the result is not significantly different from the straightforward Kronig Penney model. The measured mass m^* is actually a geometric average of m_{xx} and m_{yy}, where m_{xx} is the mass for in-plane motion. Fig. 2 is a plot of $(m^*)^2/m_{xx}$, using the m_{xx} measured in the Faraday orientation for the same FIR energy, and shows how this semi classical model gives good agreement with the data.

The semi classical approach breaks down when q_1 approaches π/L, the minizone edge. In real space, this corresponds to $2r_c \sim L$. $2r_c = L$ at 21.9 T for the 50/50 sample, but at 10.1 T for the 50/100. However, we do not see any clear CR in the semi classical regime for the 50/100 sample ($B < 6$ T), possibly because the field is too low. Furthermore, we do not see any of the new modes corresponding to well bound, barrier bound or skipping orbits, which might be expected for the 50/100, 50/150 and 50/200 samples once $2r_c < L$.

Instead, Fig. 1b shows that the impurity resonance shifts remarkably with increasing barrier width, moving from close to the bulk GaAs $1s-2p_+$ field for $L_b = 50$ Å, to close to the bulk GaAs

CR for $L_z = 150$ Å. Fig. 1 contains data for the 50/100 sample for different FIR wavelengths illustrating how the impurity transition moves towards the bulk CR for increasing field. In fact we can collect the Voigt data, for all samples and FIR wavelengths, in the unified curve of Fig. 4, a plot of

$$100 \times \left(\frac{B(\lambda) - B_{1s-2p}(\lambda)}{B_{fc}(\lambda) - B_{1s-2p}(\lambda)} \right) \quad \text{vs} \quad \frac{L_b}{r_c} \tag{2}$$

where $B(\lambda)$ is the measured field, and $B_{1s-2p}(\lambda)$, $B_{fc}(\lambda)$ the fields for bulk GaAs $1s \rightarrow 2p_+$ and free electron CR respectively, all for the same FIR wavelength λ. Fig. 4 shows how for $L_b/r_c \ll 1$ the resonance is close to the bulk $1s \rightarrow 2p_+$ field, but for $L_b/r_c > 1$ the resonance moves to the free electron CR field, being exactly midway between the two when $L_b = r_c$. We propose that the origin of this effect is a concentration of the wave function into the well closest to the impurity as the field is increased.

We have calculated the E_1 and 1s energies in the Voigt geometry by adapting the exciton calculation of Leavitt and Little [13], formally equivalent to a Born-Oppenheimer separation of the Schrodinger equation. The impurity is taken to lie in the middle of a barrier within the superlattice. The important effect of the magnetic field is to add a term

$$\frac{e^2B^2}{2m}(z - z_0)^2 \tag{3}$$

to the superlattice and impurity potentials in the effective Hamiltonian, where z_0 is the centre of the orbit. Fig. 5 shows the results for the 50/100 sample, with the orbit centre either at the middle of the well or at the middle of the barrier: it can be seen in Fig. 5a that for $B < 6$ T, the 1s well- and barrier-centred states are almost degenerate, but the energies diverge at higher field. The divergence occurs at precisely the field when $r_c = L_b$ (6 T), the critical point observed experimentally in Fig. 4. An examination of the impurity wave function, Fig. 5b, reveals that there are appreciable nodes in at least four wells at low field, but at high field these nodes disappear and the wave function is Gaussian like, centred close to the middle of the well adjacent to the impurity.

The critical field, defined by $r_c = L_b$, can be understood semi-classically as the coupling from one well to the next is much reduced once the cyclotron orbit centred on one well does not extend into the neighbouring well. This gives $r_c = L_b + \frac{1}{2}L_w$, or, assuming that all the curvature of the orbit lies in the barrier, $r_c = L_b$. The important point is that the field concentrates the wave function into the well, not the barrier. In the latter case the critical field would be $r_c = L_b/2$ which is not observed experimentally.

Our model cannot easily include the $2p$ levels, and hence the exact transition energies are difficult to calculate. However, it appears likely that the divergence of the well- and barrier-centred 1s energies at $r_c = L_b$, and the associated concentration of the ground state wave function, is the cause of the experimental behaviour as it successfully reproduces the critical point at $r_c = L_b$. In fact the well-centred 1s wave function is very similar to the first Landau eigenfunction (a Gaussian), suggesting that the transition energy for $r_c \ll L_b$ may well be that of a harmonic potential, i.e. the bulk cyclotron resonance energy.

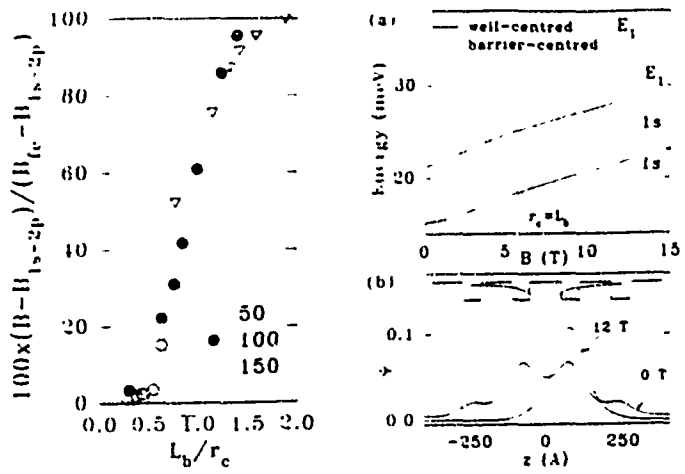

Figure 4: A summary plot of the experimental impurity resonances taken in the Voigt orientation. The dashed line is a guide to the eye (based on an error function). Figure 5: (a) The calculated 1s and E_1 energies for the 50/100 superlattice, in the Voigt orientation. The orbit centre lies either at the *centre of the well* or at the centre of the barrier. (b) The calculated wave functions, at 0 T and 12 T, for the *well* centred 1s state. The impurity lies at $z = 0$, and the superlattice and impurity potentials are sketched.

4 Conclusions

We report a series of ODCR experiments on $In_{0.05}Ga_{0.95}As/GaAs$ superlattices, with magnetic fields applied both parallel and perpendicular to the growth direction. We prove that we have a well defined superlattice band structure by observing cyclotron resonance with the field perpendicular to the growth direction. The in-plane mass is also found to be sensitive to inter-well coupling. Mid-barrier impurities are investigated, and found to have a binding energy that reduces with increasing barrier width. In the perpendicular field case, the transition energy of the mid-barrier impurity decreases rapidly when the cyclotron radius equals the barrier width. This is explained as a concentration of the wave function into the quantum well adjacent to the impurity.

Acknowledgements This work was funded by the S E R C of the U K R J W would like to thank Christ Church Oxford for the provision of a Junior Research Fellowship and P P would like to thank the Ministere Français des Affaires Etrangères for financial support

References

[1] G Belle, J C Maan, and G Weimann Solid State Commun 56, 65 (1985)

[2] D R Hofstadter, Phys Rev B 14, 2239 (1976) F H Claro and G H Wannier Phys Rev B 19, 6068 (1979)

[3] T Duffield, R Bhat, M Koza, F DeRosa, D M Hwang, P Grabbe, and S J Allen, Jr., Phys Rev Lett 56, 2724 (1986)

[4] T Duffield, R Bhat, M Koza, F DeRosa, K M Rush, and S J Allen, Jr., Phys Rev Lett 59, 2693 (1987)

[5] P Lane and R L Greene, Phys Rev B 33 5871 (1986)

[6] T. Duffield, R Bhat, M Koza, M C Tamargo, J P Harbison, F DeRosa, D M Hwang, P GraSbe, and S J Allen, Jr Solid State Commun 60 537 (1986)

[7] N C Jarosik, B D McCombe, B V Shanabrook, J Comas, J Ralston, and G Wicks, Phys Rev Lett 54, 1283 (1985)

[8] G Brozak, B D McCombe, and D M Larsen, Phys Rev B 40, 1265 (1989)

[9] M Helm, F M Peeters F DeRosa, E Colas, J. P Harbison, and L. T Florez, Phys Rev B 43, 13983 (1991)

[10] K. J. Moore G Duggan, A Raukema, and K Woodbridge, Phys Rev B 42, 1326 (1990)

[11] R J Warburton R J Nicholas L K Howard, and M T Emeny, Phys Rev B 43 11921 (1991).

[12] R J Warburton, I G Michels, R J Nicholas J J Harris and C T Foxon, Phys Rev B 46 13491 (1992)

[13] R P Leavitt and J W Little, Phys Rev B 42, 11774 (1990)

TuC4

Miniband Formation in Graded-Gap Superlattices

H.T. Grahn[1], F. Agulló-Rueda[2], A. D'Intino[2], K.H. Schmidt[1], G H. Döhler[3], and K. Ploog[1]

[1]Paul-Drude-Institut für Festkörperelektronik,
Hausvogteiplatz 5-7, D-10117 Berlin, Germany

[2]Instituto de Ciencia de Materiales de Madrid (CSIC),
Universidad Autónoma, C-IV Cantoblanco, E-28049 Madrid, Spain.

[3]Institut für Technische Physik, Universität Erlangen Nürnberg,
Erwin-Rommel-Str. 1, D-91058 Erlangen, Germany.

ABSTRACT

A graded gap superlattice has been investigated to study the formation of miniband states at finite electric fields. In contrast to conventional superlattices only one type of states, either the conduction band or the valence band states, form a miniband. The transition from extended miniband states at finite electric fields back to localized states is clearly observed with increasing electric field. Calculations of the miniband structure using different methods support the formation of a miniband in the conduction band at finite electric fields

I. INTRODUCTION

Artificial superlattices made from III-V semiconductors represent a model system for the investigation of quantum phenomena, e.g. resonant tunneling [1]. The study of semiconductor superlattices with strong coupling, i.e. wide minibands, has led to the observation of Wannier-Stark localization [2] and Franz-Keldysh oscillations from the lower and upper miniband edge [3]. Both Both effects have not been observed in bulk semiconductors. In conventional superlattices the conduction and valence minibands appear together at zero electric field. Due to the much heavier mass of the valence band ground state the conduction miniband is much wider than the lowest valence miniband. With increasing electric field the conduction and valence miniband states transform into Stark ladders. Eventually at large enough electric fields the system exhibits two-dimensional subbands as in a multi quantum well system These effects have a promising potential for applications in electro-optic devices

We have designed a novel compositionally graded superlattice which is quasiperiodic. The distance between wells, i.e. the spatial period, and the well width are constant but the composition is changed from well to well in order to monotonically increase the band gap keeping the same barrier height relative to the bottom of each well. A schematic diagram of the structure is shown in Fig. 1 for several applied electric fields. At zero electric field (cp Fig. 1(a)) the superlattice is completely decoupled due to the graded gap. This system exhibits for a critical field different from zero a strong coupling between the conduction band levels leading to the formation of miniband states (cp. Fig. 1(b)). The valence band states are completely localized at this field strength.

II. EXPERIMENTAL

The superlattice consisted of 15 'periods' of 4 nm $Al_xGa_{1-x}As$ alternating with 2 nm of $Al_yGa_{1-y}As$ with a constant increase in the Al mole fraction from one period to the next. The nominal values of the Al mole fraction are $x = 0.03(n-1)$ and $y = x + 0.3$, where $n = 1, \ldots, 15$ is the well number. The sample was grown by molecular beam epitaxy on a (100) n^+ GaAs substrate. The growth was interrupted for 50 sec at each interface to adjust the fluxes and to reduce the interface roughness. Two Al effusion cells were used. One of them was open only during the barrier growth and its flux was kept constant to produce the constant barrier height. The other one together with the Ga cell was open during well and barrier growth and their fluxes were compensated to produce the desired composition profile. A 25 nm GaAs layer on the low concentration side and a 25 nm $Al_{0.4}Ga_{0.6}As$ layer on the high concentration side of the superlattice together with the superlattice itself were forming the intrinsic region of a p^+-i-n^+ diode. The n^+-region consisted, in this order, of the substrate, a 100 nm GaAs buffer layer, and a 540 nm $Al_xGa_{1-x}As$ window layer with $x = 0.6$ in the central 300 nm, all with a Si doping of 1×10^{18} cm^{-3}. The p^+-region contained a 370 nm $Al_xGa_{1-x}As$ window layer with $x = 0.6$ in the last 300 nm and a 8.5 nm GaAs cap layer both with a C doping of 3×10^{19} cm^{-3}. The high Al concentration side of the superlattice (well $n = 15$) was closer to the n^+-region.

Individual devices were prepared by evaporating AuGe/Ni and Cr/Au contacts on the substrate and top side of the sample, respectively, and etching mesas of 120 μm in diameter down to the substrate. The mesa is bonded via a contact pad of 70 μm in diameter. We used photocurrent-voltage characteristics, photocurrent spectroscopy (PCS) and differential photocurrent spectroscopy (DPCS) illuminating through the p^+-layer to investigate the field dependent optical properties of the superlattice. For the first two methods the white light from a Xe lamp was dispersed through a 0.6 m double monochromator with an excitation density smaller than 1 μW cm^{-2}. The incident light intensity was modulated by a chopper and the photocurrent was recorded using a lock-in amplifier. The DPCS method, which is based on a wavelength modulation, was developed recently [4]. In DPCS only a small range of wavelengths of a halogen lamp passes through a monochromator and is guided with a mirror onto a slit. By moving the mirror different wavelengths of the transmitted spectrum pass through the slit. The periodic modulation of the wavelength results in a modulated photocurrent. Keeping the change in the wavelength small the modulated part of the photocurrent, which is detected with a lock-in amplifier, is proportional to the first derivative of the DC component of the photocurrent [4]. For a two-dimensional (2D) system the absorption spectra display step-like features when excitonic effects are neglected. The derivative of the absorption spectra of a 2D-system will therefore exhibit strong peaks. In PC spectroscopy the observed transitions always ride on a smoothly increasing background. Because DPCS is a first derivative technique this background will be strongly suppressed and a much better signal-to-noise ratio compared to the numerical derivative of the PC spectrum (cp. Ref. 5) can be achieved.

III. TRANSPORT PROPERTIES

Under a bias voltage V_{ap}, the electric field in the superlattice is homogeneously distributed and given by $F_{ap} = (V_{bi} - V_{ap})/W$, where $V_{bi} \approx 1.63$ V is the built-in voltage (determined as the voltage for which the photocurrent (PC) crosses the zero value) and $W = 141$ nm is the intrinsic-region width. Due to the design of the sample an alignment of the conduction band levels of all quantum wells can only be achieved at a bias voltage $V_{ap} < V_{bi}$, i.e. at a finite electric field. Furthermore no carriers are injected from the contacts in this configuration. Fig. 1 shows schematically the potential profile (including the electrostatic contribution) of the conduction and the valence band in a graded-gap superlattice for three representative values of the applied electric field.

When the applied voltage is equal to the built-in voltage the effective electric field vanishes (Fig. 1(a)) and the conduction band states are decoupled. Note that the valence band states are always decoupled for a bias voltage $V_{ap} < V_{bi}$. The bandgap of the quantum wells increases between two adjacent wells by approximately 43 meV (cp. Ref. 5). The photocurrent spectrum should therefore consist of 15 transitions with an average separation of 43 meV starting at 1.66 eV ($n = 1$) and reaching 2.26 eV for the last well ($n = 15$). No electron current is flowing at this field strength, since the photoexcited electrons cannot reach the n^+-contact, which is located on the large Al mole fraction side of the superlattice. In Fig. 1(b) the electric field for the alignment of the conduction band levels is shown. The field strength for the coupling condition can be estimated from the spacing of the levels in the conduction band. For the nominal Al mole fraction this field strength is expected to be 46 kV cm^{-1}, which corresponds to an applied voltage of approximately 0.98 V. No photoexcited electrons can flow through the whole superlattice region and contribute to the current until the critical field strength is reached. In Fig. 1(c) the high field condition is shown, when all wells in the conduction band are decoupled again.

In Fig. 2 photocurrent-voltage traces for different excitation energies are shown. There is a clear onset behavior at 1.1 V for energies above 1.7 eV in reasonable agreement with the discussion of Fig. 1 above. This onset is caused by the blocking of electron transport at low fields, because the grading of the Al mole fraction forms a barrier for the electrons in this field range. When the applied field reaches the critical field strength all electrons excited in the superlattice region can reach the n^+-contact. Below 1.7 eV only the first well close to the p^+-contact is excited, while at 2.0 eV almost all wells are excited and therefore contribute to the current. This clearly demonstrates that the transport properties of this system are governed by the electrons. The system exhibits a strongly field dependent photocurrent edge, which is not an absorption edge, but originates from the graded gap in conjunction with the applied field [5].

In Fig. 3 photocurrent spectra are shown for several applied voltages. The wide spectrum displays a lot of fine structure which can be assigned to the transitions of the individual wells. The average spacing between two small peaks is about 34 meV, which is only 80% of the expected one. It can be explained by a reduced Al mole fraction in each well so that the average composition follows approximately $x = 0.024(n-1)$. This observation agrees with the fact that the threshold for transport through the superlattice occurs at 1.1 V. Due to the reduction in Al mole fraction the critical electric field should have a value of 37 kV cm^{-1} resulting in an applied voltage of 1.11 V. It is also consistent with a reduction of the spectral width of the graded-gap superlattice. All observed transitions correspond to the heavy-hole-to-electron intrawell transitions. The light-hole transitions have not been observed, their expected oscillator strength being a factor of three smaller.

It is apparent from Fig. 3 that it is impossible to observe the resonant coupling phenomenon, i.e. miniband formation at finite electric fields, discussed in Fig. 1 directly in the photocurrent spectra. We tried to take the numerical derivative of the PC spectra [5], but

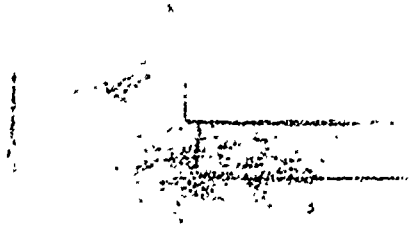

the signal-to-noise ratio was not large enough. Only with the help of a modulation technique such as differential photocurrent or electroreflectance spectroscopy it becomes possible to observe the small modulation in the photocurrent spectra directly.

IV. MINIBAND FORMATION

Fig. 4 shows a series of differential photocurrent spectra of the graded-gap superlattice taken at 77 K for different bias voltages. Although complex in structure, they are very reproducible. Due to the first derivative of the photocurrent spectra the peak energies in the DPC spectra correspond directly to the transition energies. In contrast to standard superlattices where only one peak from all the wells is observed for each type of transition (e.g. heavy and light hole) each well of the graded-gap superlattice contributes a unique peak to the spectrum. It is therefore very difficult to observe the Wannier-Stark ladder transitions. Nevertheless, the formation and destruction of a miniband should be observable through a red-shift and blue-shift, respectively, of each quantum well transition (cp. Fig. 1), when the electric field is increased.

One can distinguish several regions of voltages in Fig. 4, which can be interpreted by the effect of the electric field on the conduction band. At higher voltages close to the built-in voltage the photogenerated electrons cannot surmount the increasing potential due to the increasing Al concentration (Fig 1a), which separates them from the n^+-contact (the substrate), and consequently they cannot be collected at the contact. Therefore, no photocurrent can be measured in this voltage range. For slightly smaller voltages the transport of electrons is still very slow and only the wells closer to the substrate contribute to the photocurrent. At 1.1 V the conduction band levels are approximately aligned (Fig. 1b) because this voltage corresponds to the critical field. Below 0.9 V all the wells contribute. Here we are mostly interested in the region between 1.2 V and 0.5 V where the change from coupled to uncoupled conduction band levels takes place.

The red-shift, which should occur at small electric fields when the miniband is formed, is difficult to detect with photocurrent spectroscopy, but we are currently investigating this regime with electroreflectance spectroscopy. The blue-shift at larger electric fields, when the transition from extended back to localized states occurs, can be clearly seen in Fig. 4 going from 0.9 to 0.6 V. It appears as a change in sign of the amplitude of the DPCS-signal, but it is actually a blue-shift. Between 0.9 and 0.6 V the DPCS spectra become very flat in the high energy transition region due to the Wannier-Stark localization. It is apparent from Fig. 4 that only wells 9 to 15 form a miniband in this field range. The blue-shift is about 15 meV, corresponding to a miniband width Δ of 30 meV. A simple Kronig-Penney model for a conventional 4 nm GaAs and 2 nm $Al_{0.3}Ga_{0.7}As$ superlattice leads to an upper bound for the actual miniband width of our system. Using the parameter cited in Ref. 5, we obtain 82 meV. However, due to the variation in the Al mole fraction only a subset of the wells is expected to couple simultaneously. Therefore, we have also solved the Schrödinger equation as a function of the applied electric field numerically for a portion of the graded-gap superlattice consisting of only wells 8 and 9, surrounded by outer barriers of 10 nm. The x values were taken equal to the nominal ones. The coupling between the two wells produces an anticrossing resonance with a minimum splitting of 25 meV. Consequently, the real miniband width of the graded gap SL should fall between 25 and 82 meV. This result is in good agreement with the observed blue-shift

We have also estimated the Stark shift as described in Ref. 6 for a 4 nm GaAs well, resulting in a decrease of the heavy-hole-to-electron transition energy of less than 5 meV when increasing the electric field from 0 to 200 kV/cm (≈ -1.2 V). Consequently, the spectra do not show a significant red-shift between 0.5 and -0.2 V, which corresponds to the maximum displayed electric field.

One should note that similar effects should occur for the valence band states, but for opposite electric fields, i.e. for applied voltages above 1.63 V in this particular structure. Therefore, graded-gap superlattices offer the possibility of miniband formation at finite electric fields occurring separately for the conduction band and valence band. Due to the electrical injection of electrons and holes in the forward bias regime the measurement of PC and DPC spectroscopy is not suitable in this regime. To study the formation of a hole miniband the graded-gap superlattice should be grown in the reverse order, the low Al mole fraction wells near the n^+-contact and the high Al mole fraction wells near the p^+-contact.

V. SUMMARY

In summary, we have observed strong resonance effects between the conduction band states of a novel graded-gap superlattice leading to miniband formation at finite electric fields. The transition from miniband states to Wannier-Stark states is observed through a blue shift of the optical transitions from the individual wells. We are currently investigating the red-shift at low electric fields, which originates from the transition from localized to miniband states, with electroreflectance spectroscopy. Since the resonance in the conduction band can be achieved independently from that of the valence band, this kind of structure allows an independent control of the transport of electrons and holes.

VI. ACKNOWLEGDMENTS

We would like to thank A. Fischer for sample growth and U. Behn, K. von Klitzing and N. Linder for many fruitful discussions. One of us (F. A.-R.) thanks the Spanish CICyT for partial support under the project MAT91-0419. The work was supported in part by the Bundesminister für Forschung und Technologie.

VII. REFERENCES

[1] See, e.g., H.T. Grahn, Physica Scripta T48, in press (1993) and references therein.

[2] See, e.g., E.E. Mendez and F. Agulló-Rueda, J. Lumin. 44, 223 (1989) and references therein.

[3] K.H. Schmidt, N. Linder, G.H. Döhler, H.T. Grahn, K. Ploog, and H. Schneider, submitted to Phys. Rev. Lett. (1993).

[4] K.H. Schmidt, A. D'Intino, N. Linder, M. Tuna, G.H. Döhler, H.T. Grahn, K. Kawashima, and K. Fujiwara, Superlattices Microstruct. 12, 181 (1992)

[5] F. Agulló-Rueda, H.T. Grahn, A. Fischer, and K. Ploog, Phys. Rev. B45, 8818 (1992).

[6] G. Bastard, E.E. Mendez, L.L. Chang, and L. Esaki, Phys. Rev. B28, 3241 (1983).

VIII. FIGURES

Fig. 1: Schematic conduction band (Γ-edge) and valence band potential profiles in a compositionally graded superlattice like the one considered here for different values of the applied electric field: (a) flat band, (b) at the critical field, showing miniband formation in the conduction band, and (c) at high electric field. The z-axis corresponds to the superlattice direction with the substrate and the n^+-contact on the right hand side, while the p^+-contact is on the left hand side. A typical optical transition is marked by a vertical arrow

Fig. 2: Photocurrent (PC) vs. applied voltage for different photon energies at 6 K. The maximum value of the PC was of the order of 100 pA. The data have been corrected for the light source spectral dependence.

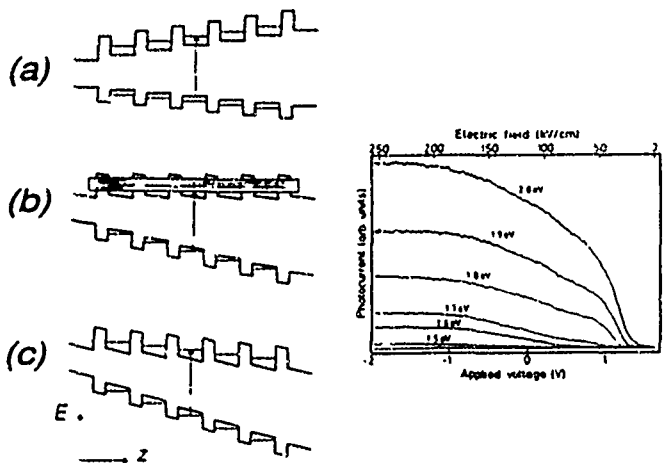

Fig. 3: Photocurrent (PC) spectra near the absorption edge at 6 K for different applied voltages. The electric field is given by $F_{sp}[\mathrm{kV\ cm^{-1}}]=70.9(1.63\cdot V_{sp}[\mathrm{V}])$. The data have been corrected for the light source spectral dependence and shifted vertically for clarity. The maximum PC was of the order of 100 pA.

Fig. 4. Differential photocurrent spectra at 77 K for different values of the applied bias voltage The spectra have been shifted vertically for clarity.

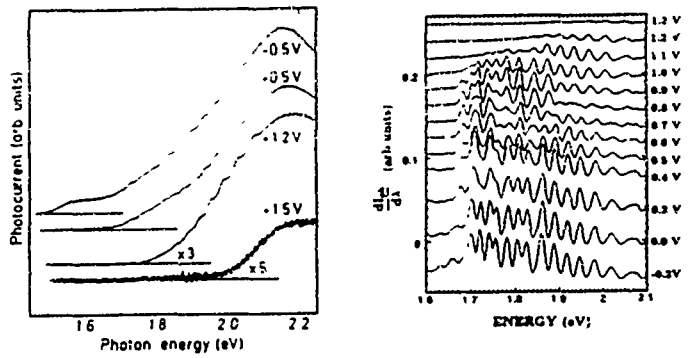

TuC5

Stark-Ladder Transitions in GaAs/AlGaAs Superlattices

M Yamaguchi M Morifuji H Kubo K Taniguchi and C Hamaguchi
Department of Electronic Engineering, Faculty of Engineering,
Osaka University, Suita City, Osaka 565, Japan

G Gnoeni
Walter Schottky Institut, Technische Universitat Munchen
Am Coulombwall, D-8046 Garching, Germany

P Gornik
Institut fur Festkoperelektronik, Technische Universitat Wien
Gusshausstraße 25-29/362, A-1040 Wien, Austria

ABSTRACT

Electroreflectance measurements have been carried out in order to investigate Stark ladder transitions in a GaAs(40 Å)/AlGaAs(20 Å) superlattice under various uniform electric fields, and compared with the transition energies calculated on the basis of a microscopic tight-binding description. The observed electroreflectance spectra in a wide range of energies (1.5eV-2.2eV) shift in proportion to an applied electric field. The signals in the higher photon energy region (1.9eV-2.2eV) indicate an existence of the transition from the spin-orbit split-off band in the valence band to the Wannier-Stark localization states in the conduction band. The assignment is supported by the tight-binding calculation. The resonant couplings of the localized states are also observed.

1. INTRODUCTION

Wannier-Stark (WS) localization in superlattices (SLs) has attracted a great interest recently [1]-[6]. In SLs consisting of a periodic repetition of quantum wells separated by narrow potential barriers, the discrete energy levels of the quantum well are broadened to form a miniband. Under this condition, the optical transition occurs from the miniband of the valence band states to this miniband of the conduction band states. When a uniform electric field is applied to the SL, the energy degeneracy between the wells is broken, resulting in discrete levels. Therefore it is possible to observe new transitions which are called Stark ladder transitions.

The WS localization is studied experimentally by using electroreflectance (ER) and photocurrent methods [2]-[5], and analyzed theoretically by the theories of effective mass approximation [5] and tight-binding (TB) approximation [6]. We have to note that many experiments and analyses are made in the low photon energy region related to the Stark ladder transitions from heavy-hole and light hole states to the conduction band states. As far as we know, there has been no report in relation to the spin-orbit split off (SO) band in valence band. In order to investigate the Stark ladder transition from the SO band, we study here the WS localization in a GaAs/AlGaAs SL under various uniform electric fields not only in lower photon energy region but also in higher photon energy region. We report the first observation of the Stark-ladder transition associated with the SO band. The experimental results are compared with the transition energies calculated by the theory based on the microscopic TB description, where we take account of the applied electric field in the matrix.

2. EXPERIMENTS

We have carried out ER measurement for a GaAs(40 Å)/$Al_{0.3}Ga_{0.7}As$(20 Å) SL. The uniform electric field is achieved by applying DC voltage to a *p-i-n* structure and the ER measurement is carried out by using modulation voltage of amplitude 100mV and frequency 8kHz. The sample of GaAs(40 Å)/$Al_{0.3}Ga_{0.7}As$(20 Å) SL used in the present work was grown on an n^+ GaAs (001) substrate by molecular beam epitaxy. The SL has 50 periods and is clad by undoped GaAs (60 Å) and undoped $Al_{0.3}Ga_{0.7}As$ (60 Å) spacers. These layers are sandwiched by a 0.6μm thick $1 \times 10^{18}cm^{-3}$ *n*-GaAs layer first grown on an n^+ GaAs substrate and *p*-$Al_{0.3}Ga_{0.7}As$ top layers (p^- and p^+-$Al_{0.3}Ga_{0.7}As$ layers with 0.2 μm (5×10^{17} cm^{-3}) and 0.2 μm (2×10^{18} cm^{-3}) thickness, respectively) to form *p-i-n* structures.

Figure 1 shows the observed ER spectra of the GaAs/AlGaAs SL under various applied voltage (from +0.6V to −3.0V) at 77K. The ER signals in lower photon energy region shown in Fig. 1 exhibit peak shifts in proportion to the applied voltage toward both lower and higher energy sides. The shifts of transition energies indicate a progress of the WS localization. These peaks in the photon energy region 1.5-1.8eV are assigned as the transitions of H_hE_ν and L_hE_ν for $\nu = 0, \pm 1$, and ± 2, where the labels $H_mE_n\nu$ ($L_mE_n\nu$) indicate the transitions with the Stark-ladder index ν between the m-th heavy hole (light hole) subband H_m (L_m) and n-th electron subband E_n. The ER signals in the photon energy region 1.8-2.2eV are also shown in Fig. 1, which will be discussed later. We find all the transition energies E_ν are well expressed by the following relation

$$E_\nu = E_0 + \nu eFd \qquad (\nu = 0, \pm 1, \pm 2, \ldots) \tag{1}$$

where E_0 is an interband transition energy, ν is a Stark-ladder index, F is the uniform electric field, e is the electronic charge, and d is the SL period.

3. ENERGY BAND CALCULATION

In order to analyze the ER experimental spectra, especially in higher photon energy region, we employ the empirical TB theory for the energy band calculation [6]-[8]. We employ a real-space representation for the basis function along the direction of the electric field (*z* direction), since the translational symmetry is lost in this direction. Thus the basis functions are specified by the atomic position l along the *z*-axis and a two-dimensional wave vector $k_\parallel$ as

$$\zeta^{k_\parallel\mu}_{l,j}(r) = \frac{1}{\sqrt{N}} \sum_{l,j} e^{ik_\parallel \cdot r_{l,j}} \phi^{k_\parallel\mu}_{l,j}(r) \tag{2}$$

where $\phi^{k_\parallel\mu}_{l,j}(r)$ is an atomic orbital located at the site of the crystal (l, j). k and μ denote the kind of atoms (k = cation (c) or anion (a)) and the type of atomic orbitals ($\mu = s$, p_x, p_y or p_z), respectively. Considering that the optical properties are mainly governed by the band structure at the Γ point, we set $k_\parallel = 0$.

We calculate energies and wave functions of WS localization states by solving the secular equation

$$\det|H_{m,n;\mu,\mu'} - \delta_{l,l'}\delta_{k,k'}\varepsilon_{m,\mu}| = 0 \tag{3}$$

where

$$H_{m,n;\mu,\mu'} = < \zeta^{k\mu}_l(r)|H|\zeta^{k'\mu'}_{l'}(r) > \tag{4}$$

The effect of the electric field is included in the diagonal elements of the Hamiltonian matrix, and the Hamiltonian contains the intra-atomic spin-orbit interaction.

In order to solve the secular equation Eq. (3), we consider a finite domain in the *z* direction because the number of the SL periods of a real system is finite and no translational symmetry exhists along the *z* direction. In the present study, we calculate the energy band structure for 10 periods of $(GaAs)_{14}/(Al_{0.3}Ga_{0.7}As)_7$. The valence band offset was set to be 0.11eV.

4. DISCUSSION

From the TB calculation, we find that the heavy-hole states are well localized in each GaAs layer at 80kV/cm and that the conduction band states are not completely localized at the electric field reflecting their lighter effective mass. However, the TB calculation shows that the conduction band states are localized in a higher electric field.

Calculated charge densities of an SO state under several uniform electric fields are presented in Fig. 2, where the squared amplitude of the eigenstates is plotted at each atomic site for several electric fields. The calculated results show that the SO states are gradually confined in a GaAs layer as the electric field increases. Thus an existence of the Stark ladder of the SO states are expected. In Fig. 2 the delocalization of the charge density at $F = 40$ kV/cm is due to a mixing between a localized SO state and an extended state of miniband which was folded into the 1st Brillouin zone.

Figure 3 shows the calculated transition energy between the valence band states and the conduction band states as a function of the electric field, where the observed peaks of the ER spectra are also plotted by open circles. Electric fields in the sample are estimated from the built-in voltage of 1.50V. The solid curves (a) in the lower energy region correspond to the transitions $H_1E_1 0$, $H_1E_1 \pm 1$, and $H_1E_1 \pm 2$, while the solid curve (c) extrapolated to 1.71eV is $H_2E_2 + 1$, and the solid curves (e) at the higher energy region correspond to the transitions $H_2E_2 0$ and $H_2E_2 \pm 1$. The dashed curves (b) in the lower energy region correspond to the transitions $L_1E_1 0$, $L_1E_1 \pm 1$, and $L_1E_1 + 2$. The dashed curve (d) at 1.82eV is the transition corresponding

to $L_2L_1,0$ and the dashed curve (f) extrapolated to 2.0eV is L_2E_2-1. The good agreement between the observation and the calculation indicates that the Stark ladder is well described within the TB theory. In particular, the signals in the lower photon energy region (1.7-1.8eV) are well explained as the Stark ladder transitions between the valence band states and the conduction band states. The calculated transition energy between localized SO states and the localized conduction band states are shown in this figure by dotted curves (g). Although there exists a slight deviation the calculated curves fit to the observed ER signals in the photon energy region 1.9-2.2eV. This agreement indicates that the observed ER spectra in the higher photon energy region are attributed to the Stark-ladder transitions between the SO states and the conduction band states. We also found that calculated optical transition probabilities between SO states and conduction band states have a magnitude large enough to be observed.

Next we will discuss a resonant coupling of the Stark ladder states. Figure 4 gives a full detail of the ER spectra around the photon energy 1.84eV at the applied voltages from −1.2V to −1.675 by a step 25mV. This figure indicates that $H_1E_1,0$ transition energy and H_2L_2-2 transition energy do not cross each other indicating an apparent existence of an resonant coupling. A resonant coupling between neighboring localized states is expected to occur at a crossing point of their transition energies. In Fig. 4 we plotted the calculated transition energies by neglecting the splitting induced by the resonant coupling. However, the ER spectra in the lower photon energy region in Figs. 3 and 4 indicate an existence of the resonant coupling between neighboring localized states. As we can see in the figures, there exists a considerable change in the spectra near photon energy 1.61eV when the applied bias is changed from −1.2V to −1.6V. This change is caused by the resonant coupling at the applied voltage around −1.4V. Although the experimental results plotted in Fig. 3 show that the applied voltage −1.4V (97kV/cm) is the crossing point between $H_1E_1,0$ and L_1L_2-1, TB calculation indicates that the resonant coupling between $H_1E_1,0$ and L_1E_1-1 is very weak and that the crossing occurs at about 50kV/cm. Therefore the distortion of the ER spectra near −1.4V is not due to the resonant coupling between $H_1E_1,0$ and L_1E_1-1. TB calculation also indicates an existence of a resonant coupling between $H_1E_1,0$ and H_2E_1-2 at 70kV/cm, and this resonant coupling is stronger. In addition to the resonant coupling at 97kV/cm we find in Fig. 1 that distortion of the ER signal occurs at photon energy 1.61eV at 120kV/cm and 147kV/cm which may be interpreted in terms of resonant couplings between $H_1L_1,0$ and H_1E_2-2, and between $H_1E_1,0$ and H_2E_2-1, respectively.

In conclusion we summarize the present results as follows. We carried out ER measurement of a GaAs (10Å)/AlGaAs(20Å) SL. The observed peaks in the ER spectra shift with increasing the electric field applied along the growth axis of the SL, and they clearly indicate the existence of the Stark ladder electric field induced localization states. In addition, we also observed ER signals in the higher photon energy region which suggests the existence of Stark-ladder of the SO states. In order to analyze the ER spectra we carried out an energy band calculation based on the TB theory including the intra atomic spin orbit interaction. By comparing the calculated results with the observed data we found that the ER spectra in the lower photon energy region agree well with the calculated results and thus that the Stark-ladder is well described by the TB theory. Furthermore we found that the SO states are localized in an electric field as well as the states at the band edge. The calculated transition energies from the localized SO states to the localized conduction band states agree well with the ER spectra in the energy region 1.9-2.2eV. Thus these ER signals are attributed to the Stark ladder transitions from the SO states to the conduction band states. We also observed the three resonant couplings between $H_1L_1,0$ and H_2E_1-2, between $H_1L_1,0$ and H_1L_1-2, between $H_1L_1,0$ and H_2E_2-1. The anti-crossing between $H_1L_1,0$ transition and H_1L_1-2 transition is clearly seen in ER measurement (Fig. 1), but the others are seen only as the distortion of the ER spectra.

5. REFERENCES

[1] J. Bleuse, G. Bastard and P. Voisin, Phys. Rev. Lett. 60, 220 (1988).

[2] E. E. Mendez, F. Agulló-Rueda and J. M. Hong, Phys. Rev. Lett. 60, 2426 (1988).

[3] P. Voisin, J. Bleuse, C. Bouche, S. Gaillard, C. Alibert and A. Regreny, Phys. Rev. Lett. 61, 1639 (1988).

[4] K. Fujiwara, Jpn. J. Appl. Phys. 28, L1718 (1989).

[5] M. Nakayama, I. Tanaka, H. Nishimura, K. Kawashima and K. Fujiwara, Phys. Rev. B 44, 5675 (1991).

[6] M. Morifuji, Y. Nishikawa, C. Hamaguchi and T. Fujii, Semicond. Sci. and Technol. 7, 1017 (1992).

[7] D. J. Chadi, Phys. Rev. B 16, 790 (1977).

[8] P. Vogl and P. Hyldmarson and J. D. Dow, J. Phys. Chem. Solids 44, 365 (1983).

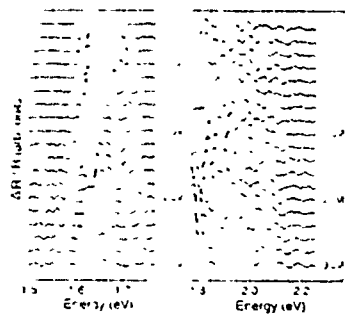

Fig. 1 Electroreflectance spectra for the superlattice at applied voltages from +0.6V to −1.0V by a step 0.2V as indicated in the figure at 77K.

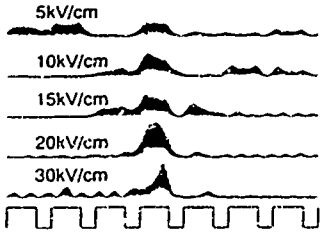

Fig. 2 Charge density distribution of the SO state calculated by the TB method.

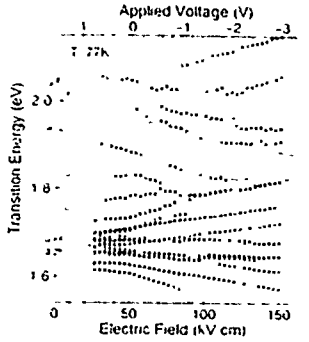

Fig. 3 Calculated transition energies from valence band states to conduction band states. The solid curves (a) in the lower energy region correspond to the transitions $H_1E_1,0$, $H_1E_1\pm1$ and $H_1E_1\pm2$. The solid curve (e) extrapolated to 1.7eV is H_1L_1+1 and the solid curves (c) at the higher energy region correspond to the transitions $H_2L_2,0$ and $H_2L_2\pm1$. The dashed curves (b) in the lower energy region correspond to the transitions $L_1L_1,0$, $L_1E_1\pm1$ and L_1E_1+2. The dashed curve (d) at 1.82eV is the transition correspond to $L_2L_1,0$ and the dashed curve (f) extrapolated to 2.0eV is L_2L_2-1. The dotted curves (g) show the transition energies from the localized SO states to the conduction band states. Observed peaks of ER spectra are shown by open circles.

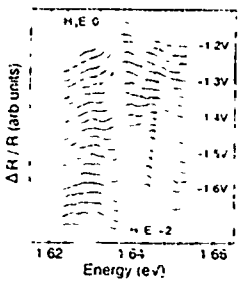

Fig. 4 Electroreflectance spectra around the photon energy 1.6eV for the superlattice at applied voltages from −1.2V to −1.675V by a step 25mV as indicated in the figure at 77K.

TuC6

Modulated Blue Shift of the Quantum Well Electroluminescence in a GaAs/AlAs Superlattice Resonant Tunnelling Device

O. Kuhn, D.K. Maude and J.C. Portal
CNRS-SNCI, B.P.166 X, 38042 Grenoble CEDEX 9,
and CNRS-INSA, 31077 Toulouse, France

M. Henini and L. Eaves
Dept. of Physics, University of Nottingham, NG7 2RD, U.K.

G. Hill and M. Pate
Dept. of Electronic and Electrical Engineering,
University of Sheffield, S1 4DU, U.K.

Abstract

Electrical transport and electroluminescence measurements have been performed on a p-i-n superlattice resonant tunnelling device with a narrow 3.1 nm quantum well in the centre. The electroluminescence observed from the centre quantum well blue shifts with increasing electric field. The application of a magnetic field perpendicular to the layers modulates the blue shift of the quantum well recombination. Possible physical origins for the blue shift are discussed.

The behaviour of electrons and holes confined in GaAs/(AlGa)As heterostructures in the presence of external electrical and magnetic fields has been the subject of numerous optical experiments [1-4]. Recently double and triple barrier structures have been incorporated into p-i-n diode devices, and electroluminescence (EL) as well as magnetotransport studies have been performed [5-7]. In such a structure electrons and holes are electrically injected into the quantum well (QW) by resonant and nonresonant tunnelling processes. We have extended this work using a novel superlattice resonant tunnelling device (SLRTD) to study the simultaneous injection of electrons and holes into the centre QW and their subsequent radiative recombination.

In this paper, we report electrical transport and electroluminescence measurements on a p-i-n double barrier resonant tunnelling structure which incorporates superlattices in the emitter and collector region. The superlattices are designed to increase charge build-up in the QW and hence increase the electroluminescence efficiency. In contrast to previous work [1,2,5-7], for the extremely narrow (3.1 nm) QW in our structure, we observe a blue shift of the QW recombination with increasing applied voltage. The application of a magnetic field perpendicular to the layers modulates the blue shift of the QW recombination. In order to explain the data, we propose a simple model in which the magnetic field modulates the electric field distribution across the device and thus modulates the blue shift of the QW recombination.

The structure used in the study was grown by Molecular Beam Epitaxy. It consists of an undoped region with a 3.1 nm GaAs-QW layer sandwiched between two 5 nm AlAs-barrier layers. Electrons and holes are injected into this centre QW via two superlattices. Each superlattice is formed by three coupled 6 nm wide GaAs-QWs, respectively n- and p-doped in the centre over a region of 2 nm with a nominal dopant concentration of 5×10^{17} cm^{-3}. The AlAs-barrier layers in the superlattices have a thickness of 2 nm. As each superlattice only has three periods it would be technically more correct to speak of coupled quantum wells and hybridized quantum well states. However, for the sake of simplicity, in this paper we will refer to superlattices and minibands [8]. The active region is contacted with heavily doped (2×10^{18} cm^{-3}) n-type and p-type regions. A 25 nm thick $Al_{0.33}Ga_{0.67}As$ window layer is incorporated in the n^+ contact, to increase the efficiency of EL collection. Standard photolithographic and etching techniques were used to define mesas of between 25 and 800 μm. A transparent top contact was made by evaporating gold in the form of an annular ring. The device used for the measurements reported here was a circular mesa of 800 μm diameter.

The superlattices are intended to serve as energy filters. Each superlattice acts simultaneously as an emitter for majority carriers and as a collector for minority carriers which have tunnelled through to the opposite contact. The superlattices enhance the charge build-up in the centre QW, since under an applied bias carriers injected from the miniband in the emitter do not have a corresponding miniband in the collector to resonantly tunnel into. This situation is illustrated schematically in Figure 1 which shows the conduction and valence band of the device under an applied voltage of 1.8 V. Escape from the centre QW is thus limited to nonresonant tunnelling processes involving scattering or phonon emission. The structure is such that the electron (E1) and light hole (LH1) resonances occur at approximately the same bias, allowing the simultaneous resonant injection of electrons and holes into the QW. Therefore, in such a structure radiative recombination of electrons and holes should be greatly enhanced.

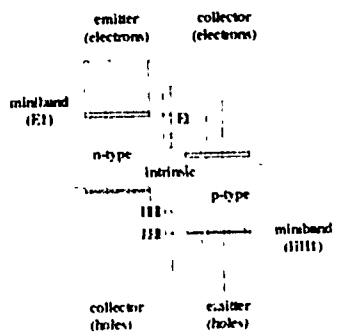

Figure 1: Schematic of the superlattice resonant tunneling device under an applied bias of about 1.8 V.

The experiments were performed using a superconducting magnet with the magnetic field parallel to the sample growth axis The set-up allows for optical and transport measurements to be performed simultaneously in the temperature range 1.5 - 300 K The EL from the sample was collected with an optical fibre, analysed with a single monochromator and detected using a standard multi-alkali photomultipher tube and lock-in amplification

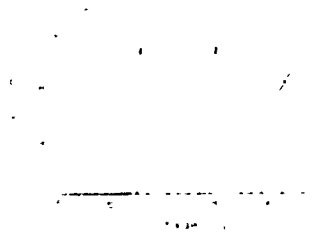

Figure 2: Current-Voltage characteristics measured at T = 4.2 K The heavy hole (HH1), electron (E1) and light hole (LH1) resonances are indicated. The dashed line shows the second differential

Under forward bias, the device presents a diode-like current voltage characteristic (Figure 2). Most of the turn on voltage of around 1.6 V is required to overcome the built-in voltage of the p-i-n diode structure. At least two resonances appear clearly in the current-voltage characteristic which are identified with the HH1 and the combined E1/LH1 resonances. These are seen more clearly in the d^2I/dV^2 plots also shown in Figure 2. At 77 K and under an applied bias of ≈2 V red light emission from the QW is clearly visible with the naked eye.

A typical EL-spectrum, taken with an applied bias of 2.0 V and at 4.2 K, is shown in Figure 3(a). EL is observed in three spectral regions of interest corresponding to recombination in the contacts, superlattice and centre QW. At low energies peaks originating from the GaAs-bulk contact regions are observed. The strongest at an energy of about 1.491 eV, 28 meV below the bandgap energy of undoped GaAs, is either the fundamental recombination from the band gap being renormalized due to the heavy doping or else corresponds to an electron-neutral acceptor transition The two small peaks found at 1.525 eV and at 1.549 eV have yet to be identified The energy of the lowest peak is close to the band to band recombination energy in bulk GaAs The second spectral region is marked by the EL originating in the superlattices. The corresponding luminescence energy is 1.612 eV. The EL from the central 3.1 nm QW has an energy of 1.779 eV and shows a very narrow line width of less than 4 meV (FWHM) indicating the extremely high quality of the interfaces. The superlattice and QW recombinations are almost certainly excitonic in origin due to the increased overlap of the electron and hole wave functions caused by the confinement. It is interesting to note that no hot luminescence (E1-LH1) is observed even though at this bias voltage (2.0 V) there is significant hole injection into the LH1 state. This is because the relaxation between the LH1 and HH1 states is much faster than the radiative recombination time which is of the order of nanoseconds

The energy of the QW recombination blue-shifts slightly with increasing applied bias as shown in Figure 3(b) This is in contrast to the red shift reported for

wider QW's and triple barrier p-i-n's in which the major effect of the longitudinal electric field is to spatially separate the quantum confined electrons and holes lowering the ground state energy levels [1,5]. Since the electric field induced Stark shift varies as the fourth power of the well width [9], for the narrow (3.1 nm) QW in our structure the Stark shift is negligible. The blue shift may be due to an electric field induced decrease in the exciton binding energy [10,11]. Here it is important to note that our structure is close to the infinite well case, because of the large band offsets at the Γ-point of 1 eV and 0.55 eV in the conduction and valence band respectively. The penetration of the electron and hole wavefunctions into the AlAs-barriers is negligible and the excitons retain a highly two-dimensional nature. In the extreme two-dimensional limit, the exciton binding energy is four times the effective three-dimensional exciton Rydberg. In a deep and narrow QW, even though the electric field induced polarisation of the exciton is small, it reduces the two-dimensional nature of the exciton and thus lowers its binding energy. However, there is some doubt as to whether or not, in the extremely narrow QW of our device, the electric field induced decrease of the exciton binding energy is sufficient to account for the magnitude of the observed blue shift. It is also possible that the blue shift is associated with screening and many bodied effects [12]

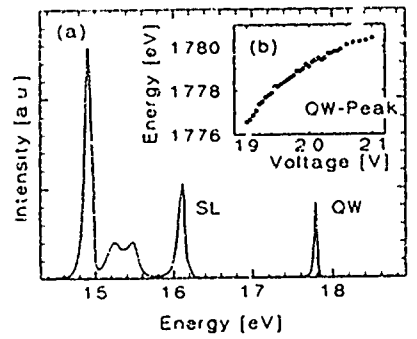

Figure 3: (a) Electroluminescence spectrum for an applied bias of V = 2.0 V measured at B = 0 T and T = 4.2 K. The peaks originating in the centre quantum well (QW) and in the superlattices (SL) are marked respectively. (b) Energy of the quantum well electroluminescence as function of applied bias.

The energies found for both the superlattice and QW recombination coincide within a few meV with those calculated within the effective mass envelope function approximation using a transfer matrix method which takes into account only the Γ-conduction band profile. For the 3.1 nm QW the calculated energy levels are E1 = 205 meV and HH1 = 58 meV which, using a bandgap of 1.52 eV for GaAs at 4.2 K, gives a total energy of 1.783 eV. From this it is necessary to subtract the exciton binding energy in a 3.1 nm QW. From reference [13] we estimate the exciton binding energy to be ≈ 12 meV when no electric field is applied. This gives a calculated recombination energy of 1.771 eV under flat band conditions and is in good agreement with the value obtained by extrapolating the experimental data taken between 1.9 - 2.1 V (Figure 3(b)) down to flat band conditions at about 1.6 V. The good agreement between theory and experiment clearly demonstrates that the

X-minima in the indirect gap AlAs-barriers play no role in determining the energy of the bound states in the quantum well. This result is also in agreement with previous electrical transport measurements on GaAs/ AlGaAs unipolar double barrier structures by Mendez and co-workers [14] and the calculations of Ko and Inkson [15]

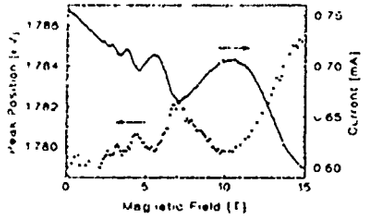

Figure 4: Oscillations in the current and in the peak electroluminescence energy of the centre quantum well as a function of magnetic field (B || J) measured at T = 4.2 K and V = 2.0 V. The dashed line indicates the quadratic correction to the exciton binding energy in a magnetic field as given in reference [16].

For a bias voltage of 2.0 V, a magnetic field was applied perpendicular to the layers and EL spectra taken every 0.1 T up to 15 T. The energy of the QW recombination plotted in Figure 4 is an oscillatory function of the magnetic field and periodic in 1/B Similar oscillations, but in antiphase, also appear in the current versus magnetic field characteristic and also as an extremely weak variation in the intensity of the QW recombination When the magnetic field is rotated, the fundamental period $\Delta(1/B)$ of the oscillations in the current follows a $\cos(\theta)$ law confirming the two dimensional origin of the oscillations. In addition to the oscillations, a small quadratic blue shift of the QW recombination energy with increasing magnetic field is seen as a background in Figure 4. It can be explained by a magnetic correction to the exciton binding energy [11,16].

Similar oscillations in the current versus magnetic field characteristic have been reported in unipolar double barrier resonant tunnelling devices [17] The origin of the oscillations in such a case stems from the quantization into Landau levels of the two dimensional accumulation layer in the emitter which periodically modulates the density of states for tunnelling. A similar model, in which electron charge build-up occurs in the emitter superlattice QW directly adjacent to the double barrier can also explain the origin of the oscillations in our device. The magnetic field quantizes the electrons in the emitter into Landau levels. With increasing magnetic field the Landau level separation increases and to a first approximation $2eB/h$ electrons are ejected every time a Landau level passes through the Fermi energy The modulation of the charge density in the emitter QW modulates the electric field across the double barrier and hence modulates the blue shift of the centre QW recombination. The current modulation also arises from the modulation of both the electric field across the double barrier and the charge in the emitter QW which changes the transmission coefficient of the barriers and the supply function for tunnelling respectively.

From the period of the oscillations in 1/B space, $\Delta(1/B) = 11$ T at a voltage of 2.0 V, the charge in the emitter QW is 5×10^{11} cm^{-2}. Using Gauss's law it is possible to estimate the electric field variation across the emitter barrier and centre QW We estimate that at 5.5 T, when the n = 2 Landau level passes through the Fermi energy, the electric field across the emitter barrier and centre QW is decreased by 4×10^4 Vcm^{-1}. In reality this model is too simple and it is necessary to perform a self consistent calculation which takes into account the potential redistribution across the various regions of the device.

In conclusion, we have observed a blue shift with applied electric field of the excitonic recombination in a narrow (3.1 nm) QW This is in contrast to the red shift normally observed in wider QW's due to the quantum confined Stark effect which dominates over the electric field induced decrease in the exciton binding energy. For narrow QW's the Stark shift is negligible and screening and many bodied effects, together with the electric field dependence of the exciton binding energy may be important. Further theoretical work, including a detailed calculation of the electric field dependence of the exciton binding energy in narrow QW's is necessary to determine the origin of the blue shift.

Acknowledgements

O.K. and D.K.M. gratefully acknowledge the financial support of the EEC (ESPRIT). We acknowledge useful discussions with E.L.Ivenchenko and A A Toropov. Part of this work was supported under ESPRIT project 7193.

References

1. E. E. Mendez, G. Bastard, L. L. Chang, L. Esaki, H. Morcoc, R. Fischer; Phys. Rev. B 26, 7101 (1982). For a review see E. E. Mendez, F. Agullo-Rueda; Journal of Luminescence 44, 223 (1989).
2. D. A. B. Miller, D. S. Chemla, T. C. Damen, A. C. Gossard, W. Wiegmann, T. H. Wood, C. A. Burrus; Phys. Rev. Lett. 53, 2173 (1984).
3. D. C. Rogers, J. Singleton, R. J. Nicholas, C. T. Foxon, K. Woodbridge; Phys. Rev. B 34, 4002 (1986).
4. M. S. Skolnick, P. E. Simmonds, D. G. Hayes, C. R. H. White, L. Eaves, A. W. Higgs, M. Henini, O. H. Hughes, G. W. Smith, C. R. Whitehouse, Semicond. Sci. Technol. 7, B401 (1992).
5. C. R. H. White, H. B. Evans, L. Eaves, P. M. Martin, M. Henini, G. Hill, M. A. Pate; Phys. Rev. B 45, 9513 (1992). See also H.B.Evans, L. Eaves, C. R. H. White and M.Henini; NATO ARW on Frontiers of Optical Phenomena in Semiconductor Structures of Reduced Dimensions, Napa Valley, California, 1992 (to be published).
6. P.M.Martin, R.K.Hayden, C.R.H.White, M.Henini, L.Eaves, D.K. Maude, J. C. Portal, G. Hill, M. A. Pate, Semicond Sci. Technol. 7, B456 (1992)
7. P.A.Harrison, H.B.Evans, P.M Martin, T.S.Turner, L.Eaves, M.Henini and G.Hill; Proc. Int. Conf. on Electronic Properties of Two Dimensional Systems, Newport, Rhode Island, 1993; To be published in Surface Science.
8. R.A.Davies, M.J.Kelly and T M.Kerr; Phys. Rev. Lett. 55, 1114 (1985).

9. G.Bastard, E.E.Mendez, L.L.Chang, L.Esaki, Phys. Rev. B 28, 3241 (1983)
10. G. A. Brum, G. Bastard; Phys. Rev. B 31, 3893 (1985).
11. X.-L. Zheng, D. Heiman, B. Lax, F. A. Chambers, K. A. Starr, Appl. Phys. Lett. 52, 984 (1988).
12. H.Sakaki, H.Yoshimura and T.Matsusue; Japn. J.Appl. Phys. 26, L1104 (1987)
13. R. L. Greene, K. K. Bajaj, D. E. Phelps, Phys. Rev. B 29, 1807 (1984).
14. E. E. Mendez, E. Calleja, W. I. Wang, Phys. Rev. B 34, 6026 (1986).
15. David Yuk Kei Ko, J. C. Inkson; Semicond. Sci. and Technol. 3, 791 (1988).
16. D. Heiman, Semiconductors and Semimetals 36, 1 (1992).
17. C. A. Payling, E. Alves, L. Eaves, T. J. Foster, M. Henini, O. H. Hughes, P. E. Simmonds, J. C. Portal, G. Hill, M. A. Pate; Proc. 3rd Int. Conf. on Modulated Semiconductor Structures, Montpellier (1987)

TuP1

A metastable state in self-electro-optic effect devices using Stark ladder transitions

M. Hosoda, K. Kawashima*, and K. Tominaga
ATR Optical and Radio Communications Research Laboratories, Hikaridai, Seika-cho, Soraku-gun Kyoto, 619-02 JAPAN

K. Fujiwara
Department of Electrical Engineering, Kyushu Institute of Technology, Tobata-ku, Kitakyushu city, 804 JAPAN

Abstract: A self-electro-optic effect device (SEED) based on Wannier-Stark localization in GaAs/AlAs superlattices, can show multiple negative differential resistance (NDR) regions in the photocurrent versus reverse bias voltage curve. This phenomenon comes from the multiple Stark ladder transitions, which successively come into resonance with the optical input to the SEED, when the external electric field intensity is varied. Using these multiple NDR regions in a symmetric SEED configuration, we have found, for the first time, a metastable point isolated inside the bistable hysteresis curve of the optical switching characteristics, in the sense that it can not be reached by conventional CW light quasistatic intensity variations. Optical on-state switching via this intermediate state has been observed in transmission by an optical pulse excitation method, and can be explained clearly with a novel global stability analysis of differential equations for photocurrents in the symmetric SEED system.

1 INTRODUCTION

Self-electro-optic effect devices (SEEDs) are potential elemental devices for signal switchers of optical interconnections or optical networks and for logic gates and logical latches of optical digital signal processing systems, because of their low switching power, high sensitivity and integratability [1]-[3]. There are many reports on optical bistability in symmetric SEEDs (S-SEEDs) [4]. Achieving multistability in an optical processing element is a subject that has attracted a great deal of interest due to the potential applications to multivalued logics or threshold devices. To this purpose, S-SEEDs using the Wannier-Stark localization effect (WSL-S-SEEDs) have been able to easily demonstrate the multistability because their photocurrent versus reverse bias voltage characteristics (I-V curves) contain multiple peaks and multiple negative differential resistance (NDR) regions, resulting from the resonant peak shift of the Stark ladder transitions with an external electric field [5], [6]. This phenomenon comes from the multiple Stark ladder transitions which successively come into resonance with the optical input wavelength when the external electric field is varied [6], [7], [8].

By using these WSL S-SEEDs, various types of stabilities, for example tri-stability as well as bistability were obtained [8],[9],[10]. Recently, we have found a novel stable state, called a metastable state, isolated in the bistable hysteresis curve of a WSL-S-SEED system [11]. When an appropriate optical pulse excitation was used, this system showed an additional new stable point, metastable point. In this paper, we report this new-type of stability of WSL-S-SEED systems with an analysis based on global stability analysis of differential equations for photocurrent balance in S-SEED circuit systems.

2 WSL-SEED having thin barriers

One class of SEEDs has been realized using the quantum confined Stark effect (QCSE) in multiple quantum wells [12]. The electro-absorption mechanism of the WSL effect is much different from that of the QCSE. When a strong resonant coupling between energy states in QW's is present, the eigenstates of the periodic system form minibands of width $\Delta E1$ and $\Delta H1$ for conduction and valence band states, respectively. These eigenstates are distributed in the minibands and the electrons and holes do not localize in one well. When an electric field applied along the growth axis is greater than the miniband width, $\Delta E1$ or $\Delta H1$, the eigenstates tend to localize over a few adjacent QW's due to the drastically reduced resonant coupling. This localization, called Wannier Stark localization, raises up the band gap energy of the superlattice by $0.5(\Delta E1+\Delta H1)$, which means a blue shift of the absorption band edge [13]. If the input wave

* Present address: Semiconductor Research Center, SANYO Electric Co. Ltd., 18-13 Hashiridani, Hirakata City, Osaka 573, Japan

length is tuned to near this band edge region, these types of thin barrier superlattices can have an NDR region in their i-V curves. By using this NDR region, the WSL-SEED can be operated as a bistable optical switching device.

When the Wannier Stark localization occurrs, a certain degree of the electronic wave function extends over a few periods of the superlattice due to the tunneling of the thin barrier. The overlap integrals of this "seeped" wave function of the electron from the adjacent wells, with that of the localized heavy hole in a well make possible spatially indirect transitions, called Stark ladder states, with evenly spaced energies, Eg+neFd (n=±1, ±2 ...); where Eg is the band gap energy of an isolated QW [6],[13]. Because the Stark ladder transition energy of each index number "n" varies with the applied electric field F, if the input wavelength were properly tuned, the Stark ladder transitions can successively come into resonance with the optical input to the WSL-SEED by varying the applied voltage. The i-V curves of the WSL-SEED can have additional NDR regions.

Figure 1 shows these NDR regions resulting from the Stark ladder transitions. We used a sample which has a short period superlattice with very thin barriers. The superlattice p-i-n structured sample was grown on a (100)-oriented n⁺-GaAs substrate by molecular beam epitaxy. The nominally undoped superlattice layer consisted of 100 periods of GaAs/AlAs with GaAs QW widths of 31.3-Å and 5.7-Å-thick AlAs barriers. The sample was fabricated into p-i-n diode mesas of approximately 800 μm² with a 200 μm circular window, and about a 400 μm² area of the GaAs substrate underneath the optical window was etched off by selective wet chemical etching to fabricate a transmission device.

3 STABILITY ANALYSIS

These multiple NDR regions make it easy to realize multistability in SEED operations [10]. Usually, a load line graphical analysis has been used to find the stable point in the SEED operation, but this method becomes less convenient when the i-V curve become more complex. Moreover, with the load-line analysis, it is very difficult to trace the temporal track of voltage movement when the optical input temporally varies. For this reason, we propose a novel analytical method based on the global stability analysis of differential equations for photocurrent balance in SEED circuits. This method can

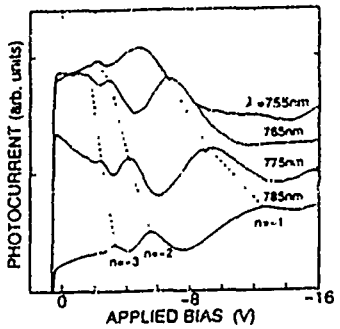

Fig. 1 Photocurrent versus applied reverse bias voltage curves for several illumination wavelengths from a p-i-n structured short period superlattice. Each peak indexed by n corresponds to the resonance of a Stark ladder state, to an incident optical wavelength.

clearly describe the transitions between stable points, even when the system is in intermediate unstable state and even if the i-V curve is very complex.

Figure 2 shows a S-SEED circuit. The electrical current balance in the S-SEED system is denoted by

$$Pc1(V_0 - V) + \frac{dQ_1}{dt} = Pc2(V) + \frac{dQ_2}{dt}, \quad (1)$$

where $Pc1$ and $Pc2$ represent the photocurrent of SEED p-i-n diodes D1 and D2, respectively, and are functions of the applied voltage and the input optical intensity; $Q1$ and $Q2$ denote the charge in the device capacitance $C1$ and $C2$ of each SEED diode, V_0 is the voltage of the constant voltage source, and V is the voltage between diodes D1 and D2 (Fig. 2). Suppose that both SEED diodes have the same capacitance, then the varying velocity of voltage V is derived from Eq. (1)

$$\frac{dV}{dt} = \frac{1}{C}\left\{Pc1(V_0 - V) - Pc2(V)\right\} = \frac{1}{C}\Delta Pc(V) \quad (2)$$

In this analysis, for conciseness, the capacitance $C(V)/2$ of each diode is assumed to be constant for all voltage changes. Assuming the existence of a potential-like function $U(V)$, the equation of motion for the voltage changes is ascribed as

$$\frac{dV}{dt} = -\frac{\partial U}{\partial V} = -\frac{1}{C}\left\{Pc2(V) - Pc1(V_0 - V)\right\} \quad (3)$$

This potential function represents the global stability of the differential equation (2) [14]. Explicitly, the potential function U is written as

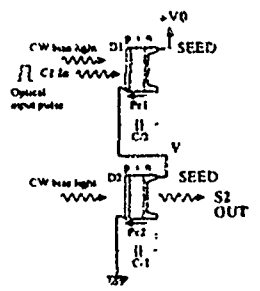

Fig. 2 Schematic diagram of a S-SEED circuit.

$$U(V) = \frac{1}{C}\int_0^V \left\{Pc2(V') - Pc1(V_0' - V')\right\}dV' \quad (4)$$

Equation (4) can be numerically integrated explicitly because the functional form of the photocurrents, $Pc1(V)$ and $Pc2(V)$, is already known as a numerical function of the data. This potential function specifies the stability points as well as the motion of the voltage. The local minima of the potential are stable points where the voltage V can no longer move. Using this potential function, the global stability analysis of the differential equations for the photocurrent and the analysis of temporal variations in voltage V are reduced to an analysis of the curve profile of the potential function $U(V)$. Compared to the ordinary method of load-line graphical analysis, the merit of this potential function method is that, even far from the stable point, we can understand intuitively the dynamical behavior of the system, like the method of the potential function in classical mechanics.

4 METASTABLE STATE AND EXPERIMENT

Now, we introduce a metastable state. Figure 3 shows the i-V curves of the above sample at 770 nm wavelength. In this figure, the load lines of this WSL-S-SEED and their corresponding potential function curves for various intensities of optical input to diode 1 of the S-SEED are shown in addition to the dependence of the optical transmission rate of the SEED diode D2 on the applied reverse bias voltage. This S-SEED showed optical bistability clearly with CW (continuous wave) light irradiation.

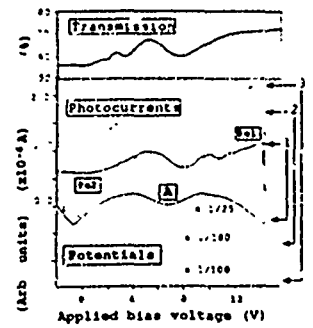

Fig. 3 Load-line graphs for a WSL-S-SEED with V0=13.5V at 770 nm illumination wavelength, and the corresponding potential curves. The index numbers 1 to 3 on the right hand side of the figure indicate the increase in the optical incident intensities into SEED diode 1. These potential curves are scaled down vertically for view with the factors indicated in the figure. The top curve shows the transmission versus voltage characteristics of SEED diode D2.

However, as shown in Fig. 3, the potential function, indexed by number 1, has three local minima when both optical inputs to the SEEDs are nearly the same. Starting from the left most stable point, the potential function varies with increasing optical input power for diode 1 (as indicated by the numbers 1 to 3 in Fig. 3), and this unstabilized system falls to a new local minimum, i.e., the most right-hand stable point. Because the center stable point "A" also concurrently vanishes, the movement cannot stop at the center point and reaches the most right-hand end. Consequently, with an ordinary CW light input, this system shows optical bistability. This implies that the stable point "A" cannot be reached with a quasistatic process like DC incident light variation. So, we call it a *metastable* point.

However, because the transition requires a finite time, just when the voltage is passing near the point "A", if the optical input intensity were reduced suddenly, it is possible to force the potential to return to the condition having three stable minima, i.e., an excitation with an optical pulse. This procedure makes it possible to reach the new metastable point hidden isolatedly inside the bistable hysteresis, and the voltage once settled in the point "A" can stay there until the potential shape changes. We may consider

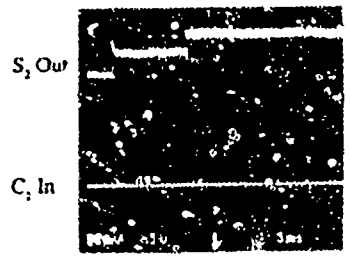

Fig 4 Oscilloscope traces of a metastable transition The upper trace shows the transition of optical output S2 shown in Fig 2. The lower trace is optical excitation pulse C1 The middle plateau of the upper trace represents the metastable state

this metastable point as a sort of temporally stable state because when the shape of the potential function curve is changed with varying optical input intensity, it falls into the rightmost or left-most bistable points.

Considering the above discussion, confirmation of the metastable state can be made by the following experimental setups By irradiating both SEED diodes with equivalent CW bias lights, and making the potential function have three stable points as shown Fig 3, the observation of the metastable state can be made with an over-ridden optical pulse excitation Figure 2 shows the optical input, and output signals for this experiment A 770 nm CW light from a Ti-Sapphire tunable wavelength laser is divided to generate the CW bias lights in Fig 2 and an optical excitation pulse C1 which passes through an acousto optical modulator. The output light S2 from diode 2 is detected by a silicon avalanche photodiode and is displayed by an oscilloscope Figure 4 shows experimental results of optical switching between the triple-stable states using approx 200 μsec optical pulses Although this S-SEED shows only bistability in ordinary measurements with CW light excitation, this photograph shows the transition to the intermediate metastable state with an optical pulse input and the transition to the next final bistable point by an additional optical pulse. These three transmission states exactly coincide with those expected from the transmission versus voltage curve in Fig 3

5 SUMMARY

The operational mode of the WSL S SEED using short optical pulse s has some advantages The switching properties, bistability or triple-stability, can be selected by adjusting the optical pulse width condition. Namely, a tri-state device can be obtained by using the same simple device configuration as that used for bistable devices, having considerable flexibility for designing functional photonic devices

In summary, we have observed a metastable state in a WSL-S-SEED system with optical pulse excitation. Through this metastable point, optical tri-state switching is demonstrated. Our results show the great advantages of the S-SEED based on the Wannier Stark localization mechanism for applications to functional photonic devices

References:

1 A L Lentine, H S Hinton, D A B Miller, J E Henry, J E Cunningham and L M F Chirovsky, *IEEE J Quantum Electron* QE-25, 1928 (1989)

2 A L Lentine, H S Hinton, D A B Miller, J E Henry, J E Cunningham and L M F Chirovsky, *Appl Phys Lett* 52 1419 (1988).

3 D A B Miller, *Optical Quantum Electronics* 22 S61 (1990)

4 D A B Miller, D S Chemla, T C Damen, T H Wood, C A Burrus Jr, A C Gossard and W Wiegmann *IEEE J Quantum Electron* QE-21, 1462 (1985)

5 K Kawashima, K Fujiwara, T Yamamoto M Segata and K Kobayashi, *Jpn J Appl Phys* 30, L793 (1991)

6 H Schneider, K Fujiwara H T Grahn, K v Klitzing and K Ploog, *Appl Phys Lett* 56, 605 (1990)

7 E E Mendez, F Agullo Rueda and J M Hong, *Phys Rev Lett* 60, 2426 (1988)

8 K Fujiwara, *Optical Quantum Electronics* 22 S61 (1990)

9 J Bar Joseph K W Goossen J M Kuo, R F Kopf D A B Miller and D S Chemla, *Appl Phys Lett* 55 340 (1989)

10 K Kawashima, K Fujiwara T Yamamoto M Segata and K Kobayashi *Jpn J Appl Phys* 30 L1532 (1991)

11 K Kawashima, M Hosoda and K Fujiwara *Appl Phys Lett* 62, 133 (1993)

12 D A B Miller, D S Chemla, T C Damen A C Gossard, W Wiegmann T H Wood and C A Burrus *Phys Rev B* 32, 1043 (1985)

13 J Bleuse G Bastard and P Voisin *Phys Rev Lett* 60 220 (1988)

14 H Haken *Synergetics* 2nd ed Chap 5 Springer Verlag New York (1978)

TuP2

"Spin"-flip of holes in asymmetric quantum wells

R. Ferreira and G. Bastard

Laboratoire de Physique de la Matière Condensée de l'Ecole Normale Supérieure

24 rue Lhomond - 75005 - Paris

We consider theoretically "spin" flip and "spin"-conserving processes for holes in single quantum wells. The presence of a spatial asymmetry in the hole envelope function hamiltonian or the small linear-in-*k* perturbation lifts the parity degeneracy of the Luttinger dispersions of the symmetric quantum well. We show that in this case a D'Yakonov and Perel' like mechanism holds for the relaxation of the holes "spin".

Semiconductor quantum wells (QW) present quasi-bidimensional confined states resulting from the quantum well like potential profile along the growth axis [1]. To each bound state are associated two (due to the spin) bidimensional dispersion branches associated with the free in-plane motion of the carriers. In general the free in-plane motion of an electron or of a hole depends upon its confined motion along the growth axis, i.e., the quasi-bidimensional confinement in one direction affects the free motion in the layer plane. Let us consider initially (and briefly) the D'Yakonov and Perel' spin-flip mechanism for conduction electrons

For structures based on wide gap III-V or II-VI materials we can in a first approximation consider a parabolic (bulk-like) conduction dispersion. In that case the electron spin projection along the growth axis is a good quantum number and each state is doubly degenerate. Thus, any non magnetic scattering center in the QW region can induce only spin-conserving scatterings for conduction electrons To study spin-flip processes for electrons in zincblende semiconductors we need to consider the small non-parabolic corrections to the hosts' conduction dispersions [2]. That non-parabolic correction mixes the two spin states and lifts the double degeneracy. Then spin-flip scatterings for electrons induced by a scalar potential become possible (Elliot-Yafet mechanism [3]). In addition, a broadening Γ_c of the energy levels is present in real structures, due to the various possible scattering mechanisms. Let $\mathbf{k}_\perp=(k_x,k_y)$ be the in-plane wavevector. Let the $\mathbf{k}_\perp$ dependent band-structure energy splitting $\hbar\omega_B$ be such that $\hbar\omega_B(\mathbf{k}_\perp)<<\Gamma_c(\mathbf{k}_\perp)$ or $\omega_B\tau_c<<1$, where $\Gamma_c=\hbar/(2\tau_c)$ for a given scattering mechanism and τ_c the spin-conserving scattering time for the parabolic states Then, as shown by D'Yakonov and Perel for bulk semiconductors [2], the non-parabolic part of the conduction hamiltonian is responsible for spin-flip processes, but its effects are greatly reduced in the strong scattering limit (motional narrowing [4]). Their work has been extended to quantum wells by D'Yakonov and Kachorovskii[5], who showed that the non-parabolic part of the conduction effective hamiltonian in a QW can be put in the form $(\hbar/2)\boldsymbol{\sigma}_\perp\cdot\boldsymbol{\Omega}_\perp$, where $\boldsymbol{\Omega}_\perp$ is a $\mathbf{k}_\perp$ dependent vector, with $|\boldsymbol{\Omega}_\perp|=\omega_B$, $\boldsymbol{\sigma}_\perp=(\sigma_x,\sigma_y)$ and σ_x, σ_y are the 2x2 Pauli matrices The "physical" meaning follows directly The "up" and "down" parabolic states are no more eigenstates of the full hamiltonian and so the electron spin should precess between these two pure states in presence of an in-plane effective magnetic field proportional to $\boldsymbol{\Omega}_\perp$. Scattering events change the electron in-plane

wavevector continuously and thus the precession axis. For decreasing $\omega_B \tau_c << 1$ the electron spin loosely follows the rapid variation of $\Omega_{\perp}$, and the spin relaxation becomes inhibited.

Contrarily to the conduction case the in-plane valence states of the QW are strongly non-parabolic [1,6]. The valence band hamiltonian in heterostructures is given by the 4x4 Luttinger matrix for the four uppermost hosts levels $|J=3/2, J_z=\pm 3/2, \pm 1/2>$ [1], where J is quantized along the growth axis (hereafter assumed to be the 001 direction). The diagonal part corresponds to a parabolic description of the hole states. The off-diagonal terms vanish at $k_{\perp}=0$ and the eigenstates are decoupled into heavy ($J_z=\pm 3/2$) and light ($J_z=\pm 1/2$) hole states. At $k_{\perp}\neq 0$ the off-diagonal terms mix these $k_{\perp}=0$ heavy and light hole states and give rise to the non-parabolic dispersions. In addition, for symmetric heterostructures each state is doubly degenerate for a given in-plane wavevector $k_{\perp}$ (parity degeneracy), and the mean values of the projection of the total angular momentum along the growth axis for the two degenerate states have opposite sign : $\pm|<J_z(k_{\perp})>|$ at $k_{\perp}=0$ $<J_z>=\pm 3/2$ ($\pm 1/2$) for heavy (light) states]. Hence, it is convenient to label these two degenerate levels as two "spin" sublevels. Spin-orbit interactions are important for the valence states, and a non magnetic scattering center can induce hole scatterings where a change in the "spin" state is concomitant with the change in the "orbital" state ($\Delta k_{\perp}\neq 0$). Such "spin"-flip processes are possible for holes in symmetric quantum wells in addition to the "spin"-conserving scatterings [7,8]. Let τ_{sc} and τ_{sf} be respectively the $k_{\perp}$-dependent "spin"-conserving and "spin"-flip assisted elastic scattering times for holes in the Luttinger description. We have shown in ref.[8] that for various scattering mechanism of interest $1/\tau_{sf}$ in unbiased wells vanishes at $k_{\perp}=0$ and rapidly increases with increasing $k_{\perp}$, whereas the "spin"-conserving processes are much more probable at small wavevectors and present a very weak dependence upon $k_{\perp}$.

In this work we consider two different mechanisms leading to a breaking of the parity degeneracy and investigate its influence on the relaxation of the hole "spin".

The first one recalls D'Yakonov and Perel's model for electrons, i.e., it has also a band structure origin and is due to a small correction to the hole hamiltonian in a perfect heterostructure. In fact, the valence hamiltonian for bulk materials with zincblende-like structure displays small linear-in-$|k|$ terms which account for the lack of centro-symmetry of the bulk unit cell [9]. They are generally neglected and vanish exactly for a diamond like structure. Let $|\Psi_{k_{\perp}\uparrow}>$ and $|\Psi_{k_{\perp}\downarrow}>$ be the $k_{\perp}$-dependent 4x1 wavevectors defined in ref.[8] for the twofold degenerate ground valence dispersion of the symmetric QW. We diagonalize the linear hamiltonian $H_{lin}(k)$ within these two states. For the sake of generality we write the resulting eigenvalue hamiltonian as $H(k_{\perp})-\varepsilon =$

$$\begin{array}{c} \\ <\Psi_{k_{\perp}\uparrow}| \\ <\Psi_{k_{\perp}\downarrow}| \end{array} \begin{array}{c} \begin{array}{cc} |\Psi_{k_{\perp}\uparrow}> & |\Psi_{k_{\perp}\downarrow}> \end{array} \\ \begin{pmatrix} H_{\uparrow\uparrow}-\varepsilon & H_{\uparrow\downarrow} \\ H_{\downarrow\uparrow} & H_{\downarrow\downarrow}-\varepsilon \end{pmatrix} \end{array} \cdot \begin{pmatrix} \varepsilon_{\uparrow}(k_{\perp})-\varepsilon & \delta e^{iV(\theta)} \\ \delta e^{iV(\theta)} & \varepsilon_{\downarrow}(k_{\perp})-\varepsilon \end{pmatrix} \qquad (1)$$

where $\delta=\delta(k_{\perp})$, $V(\theta)=c_1\theta+c_2$ with $c_{1,2}$ real constants, $\varepsilon_{\uparrow}(k_{\perp})=\varepsilon_{\downarrow}(k_{\perp})$ are the twofold degenerate Luttinger dispersions of the symmetric QW given in ref.[8], and 1 is the 2x2 unity matrix. For H_{lin} the predominant perturbative term at small in-plane wavevectors reads, $\delta=-\sqrt{3}\,C_k\,k_{\perp}/2$; $V(\theta)=-3\theta$ with C_k being the Kane constant in ref.[9]. The linear hamiltonian lifts the "up"-"down" degeneracy (parity degeneracy) of the Luttinger dispersion and the energy splitting is given by $2|\delta| = \sqrt{3}\,C_k\,k_{\perp}$.

The second mechanism we consider arises from an asymmetry in the total confining potential for the envelope function. We write for the total confining potential along the growth axis : $V(z)=V_S(z)+V_A(z)$ where $V_{S(A)}(-z) = +(-)V_{S(A)}(z)$, V_S defines the symmetric square well and V_A corresponds to a small asymmetry to be considered as a perturbation on the states generated by V_S. For instance, $V_A(z)=eFz$ by application of a weak external electric field $F//z$, or $V_A(z)=-\Delta V$ ($+\Delta V$) if $z<-L/2$ ($z>L/2$) when the two barriers have different energy heights (L is the well width and the z origin is taken at the center of the square well). For small wavevector and asymmetry we diagonalize $V_A(z)$ within $|\Psi_{k_{\perp}\uparrow}>$ and $|\Psi_{k_{\perp}\downarrow}>$. The resulting 2x2 hamiltonian is also given by eq (1) with $\delta = 2a\eta|I_A|/(1+a^2+\eta^2)$ $V(\theta)=\theta-\pi/2$, where a and η are normalisation coefficients given in ref.[8]. $I_A=<\chi_1(z)|V_A(z)|\chi_2(z)>$, with $\chi_{1,2}(z)$ being the symmetric (χ_1) and antisymmetric (χ_2) quantum-well envelope functions for the two lowest bound heavy hole states at $k_{\perp}=0$ (energies HH_1 and HH_2 respectively). The asymmetry term $V_A(z)$ lifts the parity degeneracy of the Luttinger dispersion [1,6], with an energy splitting given by $2|\delta| \propto (k_{\perp})^3\,|I_A|$, since $a \propto 1/(k_{\perp})^2$ and $\eta \propto k_{\perp}$ when $k_{\perp}\to 0$. Note that $2|\delta|$ is proportional to the strength of V_A (i.e. to F or ΔV). This energy splitting is understood as follows. For a given $k_{\perp}=0$ hole state only one component of the 4x1 spinor does not vanish, and it is either even or odd with respect to z (for instance for the ground +3/2 heavy hole state we have $\xi^{(3/2)}(z) = \chi_1(z)$ and $\xi^{(J_z=\pm 1/2,\,-3/2)} = 0$, where $\xi^{(J_z)}$ are the four z-dependent components of the valence spinor). At $k_{\perp}\neq 0$ various components of the spinor do not vanish, but again each component is either a even or a odd function of z. Also, for a given spinor component (say the $J_z=+3/2$), the parities for the "up" and "down" energy degenerate states must be opposite to comply with the orthogonality condition. Thus, for each "spin" component the two degenerate states can in principle be coupled by an asymmetric external perturbation $V_A(z)$ (We can show also that for a given spinor the parities for the $+J_z$ and $-J_z$ components are opposite). The coupling interactions for all the "spin" components add. Finally, this dipole-like coupling can be viewed as an effective "spin"-orbit coupling (and vice-versa), which vanishes for vanishing in-plane wavevector. Note that $V_A(z)$ couples also the $k_{\perp}\neq 0$ hole states of different parities (and same heavy or light nature). I_A corresponds to an asymmetry induced dipole, which is responsible for a red shift of the ground QW state (quantum confined Stark shift for $V_A(z)=eFz$, also present for the conduction parabolic levels [1]). But this asymmetry induced shift of the $k_{\perp}\neq 0$ levels is neglected in this work, since (i) it is quadratic in V_A and (ii) we are

interested here mostly on the $k_{\perp} \neq 0$ states and suppose that $V_A(z)$ can be considered as a small perturbation.

Since $H_{\uparrow\uparrow} = H_{\downarrow\downarrow}$ and $H_{\uparrow\downarrow} = H_{\downarrow\uparrow}^*$ we can rewrite H in the more transparent form :

$$H = H_{\uparrow\uparrow} I + (\hbar/2)\sigma_{\perp} \Omega_{\perp} \qquad (2)$$

where $(\hbar/2) \cdot \Omega_{\perp}(k_{\perp}) = (\lambda/2)\,(\Omega_x, \Omega_y) = [\mathrm{Re}(H_{\uparrow\downarrow}), -\mathrm{Im}(H_{\uparrow\downarrow})] = \delta\ \kappa_{\perp}$, where $\kappa_{\perp} = \cos(V(\theta))x - \sin(V(\theta))y$ is an in plane unity vector ($\kappa_{\perp} // k_{\perp}$ if $V(\theta) = -\theta$). Thus, as expected, we recover a 2x2 pseudo spin 1/2 hamiltonian when folding the Luttinger matrix onto the "up" and "down" states of the degenerate ground heavy hole dispersion. If the off-diagonal term is sufficiently small ($2|\delta| = |\hbar|\Omega_{\perp}| << |\hbar|(2\tau_{sc})|$) we can follow the D'Yakonov and Perel's treatment for electrons. We focus on the two HH_1 dispersions and write a general 2x2 density matrix $\rho = (\rho_0)^{-} I + (\Delta\rho)\sigma_z + \mathrm{Re}(\rho_{\uparrow\downarrow})\sigma_x - \mathrm{Im}(\rho_{\uparrow\downarrow})\sigma_y$, where $\rho_0 = (\rho_{\uparrow\uparrow} + \rho_{\downarrow\downarrow})/2$, $\Delta\rho = (\rho_{\uparrow\uparrow} - \rho_{\downarrow\downarrow})/2$ and we take $\rho_{\downarrow\uparrow} = \rho_{\uparrow\downarrow}^*$. According to ref [3] the D'Yakonov and Perel contribution to the time evolution of the density matrix is given in our case (eqs (1-2) with $c_1 = 1$ or -3) by

$$\partial[(\rho_{\uparrow\downarrow})_{\Delta V}]/\partial t = -(\rho_{\uparrow\downarrow})_{\Delta V} / \tau_{DP}(k_{\perp})$$
$$\partial[(\Delta\rho)_{\Delta V}]/\partial t = -(\Delta\rho)_{\Delta V}\ (2/\tau_{DP}(k_{\perp}))$$
$$\partial[(\rho_0)_{\Delta V}]/\partial t = 0,$$
$$1/\tau_{DP}(k_{\perp}) = (1/2)\,\tau^*_{sc}\,\delta\Omega_{\perp}|^2 \qquad (3)$$

where τ^*_{sc} is the $(k_{\perp})$-dependent velocity relaxation time for the "spin"-conserving scatterings and $\langle \ldots \rangle_{\Delta V}$ means average over the in-plane direction of $k_{\perp}$.

We obtain the "spin" relaxation rate $\langle 1/\tau_{DP} \rangle$ of a non-degenerate hole gas by averaging $1/\tau_{DP}(k_{\perp})$ over a Boltzmann distribution. For the scattering mechanisms we consider in this work (see below) $\tau^*_{sc}(k_{\perp}) = (\tau^*_{sc})_0$ is practically $(k_{\perp})$-independent for small wavevectors. Also, for $k_{\perp} \to 0$ we have $\varepsilon_{\uparrow}(k_{\perp}) = E_1 - \hbar^2 k_{\perp}^2 / 2(m_{h\perp})^*$, where $(m_0/\mu_{h\perp})^* = (m_0/(m_{h\perp})^* - 4(\gamma_2)^2\ [\hbar^2 k_{\perp}^2/2m_0] / [HH_1\text{-}LH_1]$, where $(m_{h\perp})^*$ is the parabolic in-plane heavy hole effective mass , m_0 the free electron mass , γ_2 a mean Luttinger parameter and LH_1 the $k_{\perp} = 0$ ground light hole energy for the symmetric QW. On account of these approximations, we can show that for $|\Omega_{\perp}(k_{\perp})|$ proportional to $(k_{\perp})^n$ we have

$$\langle 2/\tau_{DP} \rangle \approx n!\ (\tau^*_{sc})_0\ \Omega_{\perp}(k_T)^2\ \{\ 1 + \Delta\ [(n+1)(n+2)\ \ 2]\ \} \qquad (4)$$

where $\Delta = 3\ [\gamma_2\ (m_{h\perp})^* / m_0]^2\ K_B T / [HH_1\ LH_1]$ is the first order correction associated with the non-quadratic hole dispersion , n=1 (n=3) for the linear-in-(k) hamiltonian (for $V_A(z)$) contribution, and k_T is defined by $\hbar^2 k_T^2/2(m_{h1})^* = K_B T$ (the thermal energy). $\Delta << 1$ at low temperature (T<20K) and for thin wells (L≤100Å). Then for the $V_A(z)$ asymmetry $\langle 1/\tau_{DP} \rangle \propto [\Delta_A]^2 T^3$, whereas $\langle 1/\tau_{DP} \rangle \propto T$ for $H_{lin}(k)$. These trends are well reproduced in fig (1), where we show the calculated temperature dependence of the decimal logarithm of

$\langle 2/\tau_{DP} \rangle$ for a L=80Å $Ga_{0.47}In_{0.53}As$-InP quantum well for three different cases : external electric field F=5kV/cm ; $\Delta V/V_S$=3%, where V_S = 365 meV is the average hole barrier height, and linear-in-(k) hamiltonian with C_k=-7.5 meVÅ (see [9] for an estimate). We consider in fig (1) "spin"-conserving scattering induced by alloy fluctuations in the ternary well region, which represents an important scattering mechanism in $Ga_{0.47}In_{0.53}As$ based structures. For these delta-like scatterers [8] $\tau^*_{sc} = \tau_{sc}$, and we calculate $(\tau^*_{sc})_0$ = 1 ps for L=80Å.

Acoustical phonons should dominate the "spin"-conserving scattering of low energy holes in very "clean" GaAs based quantum wells. However, in this case τ^*_{sc} depends upon the temperature : the acoustic phonon emission rate $1/\tau^*_{sc}(T)$ increases for increasing T, as shown in fig.(2) for a 75Å GaAs-$Ga_{0.7}Al_{0.3}As$ QW. We evaluate $\langle 2/\tau_{DP} \rangle^{-1}$ ≈ 30ps, ≈17ps and ≈12ps at T=4K, 10K and 20K respectively, with C_k = - 3.4 meVÅ [9]. We note that these values are close from Damen et al's findings in a high quality GaAs-Ga(Al)As QW [10].

We consider finally the "spin"-relaxation of minority (non-degenerate) holes in presence of an (eventually degenerate) electron gas (as for n-doped structures [11]). For scatterings by residual ionised impurities the screening by the electron gas of the scattering potential must be accounted for. In order to obtain a rough estimate of this effect the "spin"-conserving velocity relaxation time has been approximated by

$$1/\tau^*(k_{\perp}, N_s, T) = \alpha_o\, N_{imp}\ \{\ k_{\perp}\delta\partial\varepsilon_{\uparrow}/\partial k_{\perp}\ |\}\ \int d\theta\ (1-\cos(\theta))\ |V(q_{\perp}, z_{imp})|^2 / (q_{\perp} + q_s)^2 \qquad (5)$$

where $\alpha_o = (2\pi/\hbar)\,(e^2/\kappa)^2$ (κ is the relative dielectric constant), N_s is the electron density (we consider only one electron level occupied) , the ionised impurities (areal density N_{imp}) sit at the plane $z = z_{imp}$, $q_{\perp} = 2\ k_{\perp}\ \sin(\theta/2)$, $V(q_{\perp}, z_{imp}) = \sum_{J,} \langle \xi^{(J)}_{\lambda}(z)\, e^{-(q_{\perp}|z - z_{imp}|)}\, \xi^{(J)}_{\lambda}(z) \rangle$ is the impurity form factor , $q_s(q_{\perp}, N_s, T)$ the RPA like screening of the electrons [1]. Finally, we neglect screening of the holes and direct hole/electron gas interactions. Note that eq (5) becomes exact for parabolic holes confined between hard walls. We present in fig.(3) the temperature dependence of $\langle 1/\tau_{DP} \rangle$ for three electron densities (lower axis) and the N_s dependence of $\langle 1/\tau_{DP} \rangle$ at T=4K (upper axis). The structure is the same as in fig (2) , $H_{lin}(k)$, and for a degenerate gas. Decreasing N_s weakens the static screening and rises the scattering rate and thus τ_{sf} increases with decreasing N_s.

"Spin"-flip assisted scatterings between the "up" ($|\Psi_{k\perp\uparrow}\rangle$) and "down" ($|\Psi_{k\perp\downarrow}\rangle$) states add their contribution to $1/\tau_{DP}(k_{\perp})$. The total "spin"-flip probability will be (for a given wavevector or for a thermal average) $1/\tau_s = 1/\tau_{sf} + 1/\tau_{DP}$. We remark that at low enough temperature $\langle 1/\tau_{DP} \rangle$ is greater or much greater than $\langle 1/\tau_{sf} \rangle$, unless τ^*_{sc} is extremely short (i.e. "dirty" samples). Thus, the D'Yakonov Perel' mechanism for holes should be dominant in the generic case.

The D'Yakonov and Perel' mechanism correlates the sample "quality" (via the velocity relaxation time) and the spin depolarisation time. Holes in bulk materials lose their spin almost

instantaneously, and the D'Yakonov and Perel' mechanism can be tested for electrons in p-doped samples by measuring the temperature dependence of both the electron mobility and the spin decay time [2,3]. In quantum wells both the electron and the hole spins at [illegible] contribute to the measured c.w. polarisation or depolarisation time [illegible] effects which correlate tightly the electron and hole motions complicate [illegible] of each species significantly. To circumvent these difficulties n-doped or p-doped wells are used : the sample polarisation is given by the minority photocreated carriers which are in the presence of a sea of majority carriers of opposite charge which can reasonably (for weak laser intensities [10,11]) be taken as unpolarised. However, to our knowledge, no systematic study has been performed (in particular the temperature dependence of τ_{DP}) to test as in the bulk case the D'Yakonov-Perel' mechanism.

Only a few c.w. and/or time-resolved spin-orientation experiments have been done on quantum wells [10-13]. Also, from work to work the sample "quality" is quite different. Generally speaking, real structures always present small asymmetries and deviations from the nominal square well shape, as (a) electrostatic fluctuations in the well region associated to a residual doping near a preferential interface or to different charge distributions in the two interfaces ; (b) different doping contents in the two barriers, and (c) interface roughness. In addition, random fluctuations scatter elastically the carriers (e.g. alloy and roughness scatterings) and render the polarisation study in quantum wells strongly sample dependent. In fact, very different c.w. polarisation results and/or depolarisation times have been reported in the literature, even in the best known GaAs-Ga(Al)As QW systems. However, the observed inverse correlation between sample quality and the hole spin depolarization time [10-13] is we believe a strong indication that a D'Yakonov-Perel' mechanism holds for holes.

We would like to thank Drs. C. Delalande, G. Lampel, G. C. La Rocca, P. Rolland and Ph. Roussignol for very fruitful discussions. The LPMC is a "Unité de Recherche Associée au Centre National de la Recherche Scientifique (URA 1437)".

REFERENCES :

[1] Bastard G., Wave Mechanics Applied to Semiconductor Heterostructures (Les Editions de Physique, Les Ulis) 1988

[2] D'Yakonov M. I. and Perel' V.I., Sov. Phys. JETP 33 (1971) 1053 ; Sov. Phys. Solid State 13 (1972) 3023

[3] Pikus G. E. and Titkov A. N., in Optical Orientation (ed. by F. Meier and B. P. Zakharchenya), North-Holland, Amsterdam (1984) p. 73 [Modern Problems in Condensed Matter Sciences, Vol. 8.7]

[4] Slichter, C. P., Principles of Magnetic Resonance (Springer Series in Solid-State Sciences, Edt. P. Fulde, Spring-Verlag - 1978)

[5] D'Yakonov M. I., Kachorovskii V. Yu., Sov. Phys. Semicond. 20 (1) (1986) 110

[6] See also Ekenberg U. and Altarelli M., Phys. Rev. B 30 (1984) 3569 for the hole levels in asymmetrically p-doped structures and Ferreira R., Thesis (Paris 6 - 1992, unpublished) and Goldoni G. and Fasolino A., Phys. Rev. Lett. 69 (1992) 2567 for the hole states in asymmetric double quantum wells

[7] Uenoyama T. and Sham L. J., Phys. Rev. B 42 (1990) 7114

[8] Ferreira R. and Bastard G., Phys. Rev. B 43 (1991) 9687

[9] Kane E. O., J. Phys. Chem. Solids 1 (1957) 249 ; also in : "Handbook of Semiconductors", vol. 1, eds. T. S. Moss and W. Paul (North-Holland, 1982) pg. 193 ; see also Cardona M., Christensen N. E. and Fasol G., Phys. Rev. Lett. 56 (1986) 2831

[10] Damen T. C., Viña L., Cunningham J. E., Shah J. and Sham L. J., Phys. Rev. Lett. 67 (1991) 3432

[11] Roussignol Ph., Rolland P., Ferreira R., Delalande C., Bastard G., Vinattieri A., Martinez-Pastor J., Carraresi L., Colocci M., Palmier J-F. and Etienne B., Phys. Rev. B 46 (1992) 7292

[12] Bar-Ad S. and Bar Joseph I., Phys. Rev. Lett. 68 (1992) 349

[13] Quivy da Silva E. C. F., Chitta V., Toet D., Potemski M., Maan J. C. and Ploog K., Semicond. Sci. Technol. 7 (1992) 1359

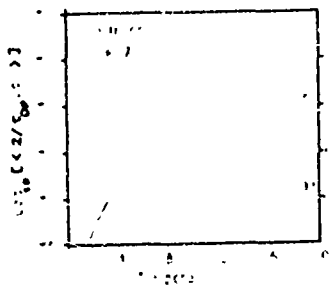

Fig (1) The calculated decimal logarithm of $<2/\tau_{DP}>$ is plotted versus temperature for a L=80Å $Ga_{0.47}In_{0.}$ ..As-InP quantum well. The scattering mechanism is the alloy scattering Three inversion asymmetry terms are taken into account (a) asymmetry barrier height ($\Delta V/V_S$=3%) , (b) a weak electric field (5kV/cm) and (c) the linear-in-(k) hamiltonian (C_k = -7.5 meVÅ)

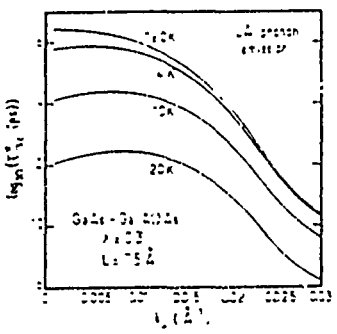

Fig (2) Dependence with $k_{_}$: the "spin"-conserving velocity relaxation time $\tau^{D}_{e_}$ for a 75Å GaAs - $Ga_{0.7}Al_{0.3}As$ QW at various temperatures : T=0K, 4K, 1 K and 20K Emission of acoustic phonons deformation potential approximation)

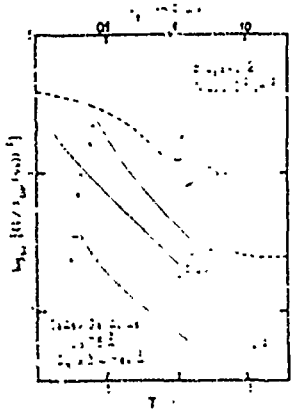

Fig (3) Theoretical dependence of $<1/\tau_{DP}>$ with (1) the temperature for various electron densities (lower horizontal axis) , (2) the electron density at T=4K (upper horizontal axis) L=75Å GaAs-$Ga_{0.7}Al_{0.3}As$ QW , scattering by residual ionised impurities z_{imp}=-L/2 and $N_{imp}=10^{10}cm^{-2}$

TuP3

Interactions between Wannier - Stark states
R. Ferreira, P. Voisin and G. Bastard
Laboratoire de Physique de la Matière Condensée
Ecole Normale Superieure, 24 rue Lhomond F75005 Paris (France)

We examine the interaction between the Wannier Stark ladders derived from two minibands in a semiconductor superlattice We show that it leads to anticrossings whose magnitude and electric field position can be modelled in a simple way. The eigenenergies depart from a linear dependence upon the electric field. In the time domain, the wavepackets show spatial oscillations between the main locations of the particle in the two interacting states The frequency of the absorbed and emitted photons between such unevenly spaced ladders become different. In contrast to the one band case, a net absorption or emission becomes possible, although not at the Bloch frequency

The destruction of the quasi continuous electron spectrum of a crystalline material by a constant electric field and its replacement by ladders of evenly spaced levels, the Wannier - Stark ladders (energy separation: $\hbar\omega_B$ = eFd, where d is the spatial period) has been predicted by Wannier in the late fifties [1] and since then considerably debated on the theoretical side [2,3]. The existence of such ladders has been established by steady state optical experiments performed on semiconductor superlattices [4,5]. These are high quality materials characterized by large periods along the growth axis (= 60 Å) and therefore small bandwidths (= 60 meV) which become comparable to the electric field effects over a period (eFd = 60 meV if F = 100 kV/cm and d = 60 Å). Wannier's approach, a one band analysis, leads to discrete Wannier - Stark states and to a linear dependence of their energies upon F The status of the interband couplings induced by the field, or equivalently the field induced couplings between the Wannier - Stark ladders belonging to different bands, is still a matter of debates [5], in particular because there is an infinite number of bands and hence an infinite number of field induced anticrossings between the ladders belonging to different bands in a finite energy range. This may transform the discrete levels of the one band approximation into resonant levels, eventually long lived. Early treatments of the interband couplings have relied on Kane's analysis [6] who first calculated the tunnel current associated with these interband transitions in a semi - classical approach Formal treatments of Wannier - Stark ladders with two or a finite number of bands have been undertaken (see e.g. [7,8]) but no attention has been paid to the specific case of semiconductor superlattices, in particular to the fact that in these materials one may tailor situations in which one well defined discrete (or quasi discrete) Wannier - Stark level of one band is made to anticross another level belonging to another band, as demonstrated and analyzed by Schneider et al [9] Recent time - resolved experiments on Wannier - Stark levels [10,11] have been analyzed in terms of an oscillatory motion of carriers at the Bloch frequency ω_B

In this paper, we wish to address the questions of i) a simple, yet accurate enough, modelling of the anticrossings between two discrete Wannier - Stark levels belonging to two different bands and ii) the consequences that such anticrossings may have on the frequency of the motion of wavepackets of interacting Wannier - Stark levels as well as on the frequency of the absorbed or emitted light between the levels of such interlaced ladders.

In the envelope function approximation, the stationnary conduction (Γ_6 related) eigenstates of a semiconductor superlattice in the presence of a longitudinal electric field are the solutions of

$$\{ T + V_{SL}(z) + eFz \} \psi(z) = \varepsilon \psi(z) \qquad (1)$$

where $V_{SL}(z)$ is the piecewise constant superlattice potential with period d and T the longitudinal kinetic energy (equal to $-\hbar^2 \partial/\partial z[1/2m^*(z)]\partial/\partial z$) Without electric field the superlattice eigenstates are for a wide class of materials well described by nearest neighbour tight binding models as witnessed by the excellent fit of the exact dispersion relations to a single cosine law We restrict our considerations to the two lower minibands We call

Δ_1 and Δ_2 their widths and $w_1(z - nd)$, $w_2(z - md)$ the Wannier functions of these two bands, where n and m are relative integers. The electric field term admits diagonal and off diagonal matrix elements in the Wannier basis. For the intra - band terms there is

$$< w_{1,2}(z - nd)| z |w_{1,2}(z - n'd)> = nd\delta_{n,n'} \qquad (2)$$

As for the interband terms we have found that the approximation

$$< w_1(z - nd)| z |w_2(z - n'd)> = Z_0\delta_{n,n'} + Z_1\delta_{n,n'\pm1} \qquad (3)$$

works well for a variety of superlattices. Note that the Z_0 contribution is essentially an intra-well term. It represents for a single quantum well the polarisation of the isolated wells wavefunctions by the field (the one which gives rise to the Stark effect). We show in fig (1) the d_0 dependence of the matrix element $<o_{kc}^{(1)}(z)| . |o_{kc}^{(2)}(z - d_0)>$ where the o_{kc}'s are the isolated well eigenfunctions at zero field. This matrix element should provide a fair approximation of $< w_1(z - nd)| z |w_2(z - n'd)>$. Note that the values calculated for $0 < d_0 < 80$ Å do not correspond to physical situations. The calculation at $d_0 = 0$ is meaningful : it is the intra - well contribution. As shown in fig (1), the intra - well (i.e. Z_0) term ($d_0 = 0$) is *dominant*. For periods $d \approx 12$ *nm*, Z_1 is ≈ 7 times smaller than Z_0. It remains however important to keep it in the analysis in order to get an accurate description of the splitting at the anticrossings for the following reason. Without interband coupling each miniband gives rise to an evenly spaced (by eFd) ladder [1] with energies

$$E_{1\nu} = <\varepsilon_1(q)> + \nu eFd; \qquad E_{2\mu} = <\varepsilon_2(q)> + \mu eFd \qquad (4)$$

where μ and ν are relative integers and where $<\varepsilon_1(q)>$ and $<\varepsilon_2(q)>$ are the average energies of the E_1 and E_2 subbands respectively. $<\varepsilon_1(q)>$ and $<\varepsilon_2(q)>$ are close in energy from the isolated quantum bound states. The corresponding wavefunctions are

$$\psi_{1\nu} = \sum_n J_{\nu-n}(-\Delta_1/2eFd)\, w_1(z - nd); \qquad (5)$$

$$\psi_{2\mu} = \sum_m J_{\mu-m}(\Delta_2/2eFd)\, w_2(z - md) \qquad (6)$$

where J_n is the Bessel function of integer order n. The uncoupled ladders intersect at fields $F_{\mu\nu}$ equal to $|<\varepsilon_1(q)> - <\varepsilon_2(q)>| /(\mu-\nu)ed$. The interband couplings transform these crossings into anticrossings. The anticrossing between $|1,\nu>$ and $|2, \mu = \nu - p>$ gives rise to the energies $\varepsilon_\pm(\nu, p)$. For $F = F_{\mu\nu}$ the $\varepsilon_\pm(\nu, p)$ are the solutions of

$$\begin{pmatrix} E_{1\nu} - \varepsilon_\pm(\nu, p) & \delta_p \\ \delta_p & E_{2\mu} - \varepsilon_\pm(\nu,p) \end{pmatrix} \begin{pmatrix} c_1^\pm(p) \\ c_2^\pm(p) \end{pmatrix} = 0 \qquad (7)$$

where we have only retained the two resonant contributions in the analysis and

$$\delta_p = eF\{Z_0 J_{-p}[(\Delta_1 + \Delta_2)/2eFd] + Z_1 \textstyle\sum_\pm J_{-p\pm1}[(\Delta_1 + \Delta_2)/2eFd]\} \qquad (8)$$

Thus, the difference between Z_1 and Z_1 can be offset by the magnitude of the J's appearing in δ_p, e.g. in strong fields when the arguments of the Bessel functions become small and if $p = 1$ the magnitude of $Z_1 J_0$ becomes comparable or even larger than that of $Z_0 J_{-1}$ and both terms have the same sign. At resonance the anticrossing gap is $2|\delta_p| F_{\mu\nu}$. Note also that

$\varepsilon_\pm(\nu+1, p) = \varepsilon_\pm(\nu, p) + eFd$ and that the coefficients c_1 and c_2 are ν independent. This complies with James' theorem [12] which states that the translation by d of the argument of one eigenfunction of eq (1) with energy ε produces another eigenfunction of eq (1) with energy ε + eFd.

The non resonant contributions can be inserted into eq (7) up to the second order. This amounts to adding diagonal contributions of the form $e^2F^2\Sigma_{\mu'\neq\mu} |<\psi_{2\mu'}|z|\psi_{1\nu}>|^2 [\varepsilon_\pm - E_{2\mu'}]^{-1}$ to $E_{1\nu}$ and a similar term to $E_{2\mu}$ where $1, \mu$ and μ' are interchanged with $1, \nu$ and ν' respectively. We have checked that the inclusion of those terms are not essential : they hardly affect the magnitude of the anticrossing gaps and merely amounts to shifting the $F_{\mu\nu}$'s towards *high fields*. We summarize in fig (2) our modelling of the two band anticrossing for a 8nm - 8nm GaAs - GaAlAs superlattice. Since we do not know the w_1 and w_2 functions explicitly [13], we have replaced them by the o_{kc}'s defined previously in the evaluation of Z_0 and Z_1. We note a fair description of the $\varepsilon_\pm(\nu, p)$ versus F curves by eq (7) when compared with an "exact" (i.e. numerical) calculation of the central eigenstates (to avoid edge effects) of a 15 periods superlattice.

The oscillator strength of the optical transitions between the levels $|-,\nu, p>$ and $|\pm,\nu' p>$ of such an hybrid ladder is proportionnal to $|<-,\nu,p)| z |\pm,\nu ,p)>|^2$ (see fig (3)). The energies of such transitions are $\varepsilon_\pm(\nu', p) - \varepsilon_-(\nu, p)$. Clearly, all the transitions $|-,\nu, p> \rightarrow |-,\nu',$ $p>$ occur at the energy $(\nu'-\nu)eFd$, i.e. at the fundamental and harmonics of the Bloch energy. However, like in the one band case [14], the oscillator strengths of the absorption is exactly equal to that of the induced emission. Thus, there is no net absorption of the electromagnetic wave in an infinite superlattice due to $|-,\nu, p> \rightarrow |-,\nu p>$ transitions. Clearly, the same conclusion is reached if $|-,\nu, p> \rightarrow |+,\nu', p>$ transitions are involved. In actual, i.e. finite materials, absorption or emission may take place due to edge effects [14]. Their signature would be their independence upon the superlattice thickness. Possible stimulated emission or absorption are associated with $|-,\nu, p> \rightarrow |+,\nu', p>$ transitions. There is an absorption *corresponding* to $\nu = \nu'$, at the energy $\varepsilon_+(\nu, p) - \varepsilon_-(\nu, p)$, which is not compensated by an emission at the same energy and with the same initial state. This solitary line is accompanied by an absorption sideband shifted in energy by eFd and by an emission sideband at the energy eFd $- |\varepsilon_+(\nu, p) - \varepsilon_-(\nu, p)|$. Note that all these uncompensated (because the energies are different) absorption / emission processes are of the inter - subband type (like $E_1 \rightarrow E_2$ in a single quantum well) rather than of the Wannier - Stark type. They should produce net absorption or emission of an electromagnetic wave depending of the steady state (or transient) occupancy of the $|\nu, \pm>$ hybrid levels.

Recent time resolved optical experiments have been used to study the dynamical behaviour of electrons in superlattices under an electric field [10,11,15]. In particular, the time varying polarization that accompanies the tunnelling back and forth of an electron between the two wells of a double quantum well has been detected in the form of a 1.5 THz emission [11].

The time dependent counterpart of the anticrossings studied in eq (7) is a Rabi precession between the two interacting states if the system is prepared in an initial state which is not an eigenstate of eq (7). This is realized if a short light pulse (characteristic width $\delta T \leq \hbar/\Delta\varepsilon_p$) is shined onto the crystal. Assume for simplicity that $|\psi(t = 0)> = |1, \nu>$. Then, the probability P(t) to find the system in the state $|2, \mu = \nu - p>$ is equal to

$$P(t) = |< 2, \mu = \nu - p| \exp(-i\Omega t/\hbar) | 1, \nu >|^2 \qquad (9)$$

Working with the same approximation as in eq (7) and since

$$< \pm, \nu, p | 2, \mu > = c_2^{\pm}(p)\delta_{\nu\nu'} \qquad (10)$$

$$< \pm, \nu, p | 1, \nu > = c_1^{\pm}(p)\delta_{\nu\nu'} \qquad (11)$$

we find easily that

$$P(t) = |c_1^{+}c_2^{-}|^2 + |c_1^{-}c_2^{-}|^2 +$$
$$2c_1^{+}c_1^{-}c_2^{+}c_2^{-}\cos[(\varepsilon_+(\nu, p) - \varepsilon_-(\nu, p))t/\hbar] \qquad (12)$$

This Rabi precession is accompanied by an oscillatory displacement of the electron between the ν^{th} and the μ^{th} period of the superlattice. We calculate the average position of the electron at time t, $z(t) = < \psi(t) | z | \psi(t) >$ with the same assumptions as previously ($|\psi(0)> = |1, \nu>$) and find

$$z(t) = (c_1^{+})^2 < +, \nu, p | z | +, \nu p > + (c_1^{-})^2 < -, \nu\ p | z | -, \nu, p >$$
$$+ 2\, c_1^{+}c_1^{-} < +, \nu, p | z | -, \nu, p > \cos[(\varepsilon_+(\nu, p) - \varepsilon_-(\nu, p))t/\hbar] \qquad (13)$$

In addition, there is

$$< \pm, \nu, p | z | \pm, \nu, p > = (c_1^{\pm})^2 < 1, \nu | z | 1, \nu > +$$
$$(c_2^{\pm})^2 < 2, \mu | z | 2, \mu > + 2c_1^{\pm}c_2^{\pm} < 1, \nu | z | 2, \mu >$$
$$= (c_1^{\pm})^2 \nu d + (c_2^{\pm})^2(\nu - p)d + 2c_1^{\pm}c_2^{\pm}\delta_p/eF \qquad (14)$$

$$< +, \nu, p | z | -, \nu, p > = c_1^{+}c_1^{-}\nu d + c_2^{+}c_2^{-}(\nu - p)d +$$
$$(c_1^{+}c_2^{-} + c_1^{-}c_2^{+})\delta_p/eF \qquad (15)$$

We show in fig (4) the calculated time dependence of z(t) for a 8nm / 4nm GaAs/Ga(Al)As superlattice. The anticrossing between the |1, 0> and |2, -1> levels takes place at F_c = 96.8 kV/cm. The different curves correspond to different field detuning $\Delta F = F - F_p$ from ΔF = -20kV/cm to +20kV/cm from the resonance field. The (F dependent) time scale is the period of the Rabi precession, $\tau = h/|\varepsilon_+(\nu, p) - \varepsilon_-(\nu, p)|$. It is only at exact resonance that the particle excursion extends over one period. Off resonance there is an increasing spatial localization with increasing detuning. There exists a slight asymmetry between the +ΔF and -ΔF curves. It is due to the fact that δ_p in eq (7) is field dependent. Note that the z(t) curves which correspond to the |1, 0> and |2, -p>, p>1 anticrossings would qualitatively be the same as those shown in fig (4) with, however, much sharper resonance like profiles and, of course, at the resonance field an excursion down to the -p period. As has been shown by Schneider et al [9] these resonant delocalizations of the eigenstates provide an efficient way for the vertical transport of the carrier.

Another kind of wavepacket can be studied. It corresponds to the creation of an electron around the n^{th} site at t = 0 and to its detection at the m^{th} site at time t with a change in the "atomic" eigenstate. We model this situation by calculating

$$P_{nm}(t) = |< w_1(z - nd)| \exp(-i\Omega t/\hbar) | w_2(z - md)>|^2 \qquad (16)$$

which is equal to

$$P_{nm}(t) = J^2_{p+m-n}[(\Delta_1^2 + \Delta_2^2 + 2\Delta_1\Delta_2\cos(\omega_B t))^{1/2}/(2eFd)]\times$$
$$\left\{ \Sigma_{\pm} c_1^{\pm 2}c_2^{\pm 2} + 2c_1^{+}c_2^{+}c_1^{-}c_2^{-}\cos[(\varepsilon_+(\nu, p) - \varepsilon_-(\nu, p))t/\hbar] \right\} \qquad (17)$$

This probability depends, as expected, on two periodic functions of time. The first one corresponds to the intraband motions (period $2\pi/\omega_B$) in either bands while the second is related to the interband coupling as expressed by the energy difference $(\varepsilon_+(\nu, p) - \varepsilon_-(\nu, p))$. Note that P_{nm} is only a function of n - m, a characteristic feature of perfect, infinite superlattices. In addition we find that $P_{n-m} \neq P_{m-n}$: low energy transitions are favored, while in a one band analysis the quantity equivalent to P_{nm} is an even function of (n - m). Eq. (17) is the discrete (in site and Wannier - Stark indices) version of the interband tunnelling probability. As pointed out by Kane [6], the latter is calculated in bulk materials under the assumption that the discrete Wannier - Stark levels in either bands are not resolved (because of the unfavorable ω_B / broadening ratio). In semiconductor superlattices, where the Wannier - Stark levels are well resolved, we believe that the use of the bulk - like formula is unwarranted. The total interband probability $P = \Sigma_m P_{nm}$ is obtained from eq (17) by summing over all the final sites m. This procedure erases the Bessel function in eq (17). Hence P becomes n independent. At the resonance fields ($F_{\mu\nu}$) P is simply equal to $\sin^2[(\varepsilon_+(\nu, p) - \varepsilon_-(\nu, p))t/2\hbar]$, irrespective of p.

Therefore, the total interband probability can become equal to unity. It has however to be stressed that the narrowness of the anticrossings increases with p, which implies that unless one deals with low index resonances (p = 1,2) the interband transition probability will for almost all field remain modest. Finally, it is worth pointing out that the existence of the other bands of the superlattice at zero field should modify the Rabi precession between the two well defined Wannier levels. The actual situation is that of two interacting levels which are each coupled to a quasi continuum, the one provided by all the Wannier - Stark levels belonging to the other bands of the superlattice and which are in the energy range of the anticrossing. These quasi - continuum will provide the source of an irreversible escape of the carrier (while in the two levels model the carrier oscillates between the two eigenstates forever). Whether the escape time is shorter or longer than the Rabi frequency remains to be studied in actual superlattices. The fact that anticrossings have been optically detected is in favor of a negligible escape.

References

[1] G. H. Wannier, "Elements of Solid State Theory", Cambridge Univ. Press, Cambridge, U.K. 1959

[2] J. Callaway, "Quantum Theory of the Solid State", Academic Press, Boston, U.S. 1991

[3] For a recent review see G. Nenciu, Rev. Mod. Phys 63, 91 (1991) and references therein

[4] E. E. Mendez, F. Agullo - Rueda and J. M. Hong, Phys. Rev. Lett. 60, 2426 (1988)

[5] P. Voisin, J. Bleuse, C. Bouche, S. Gaillard, C. Alibert and A. Regrény, Phys. Rev. Lett. 61, 1639 (1988)

[6] E. O. Kane, J. Phys. Chem. Solids, 12, 181 (1959)

[7] J. E. Avron and J. Zak, J. Math. Phys. 18, 918 (1977)

[8] X. G. Zhao, J. Phys. Condens. Matter, 4, L383 (1992)

[9] H. Schneider, H. T. Grahn, K. von Klitzing and K. Ploog, Phys. Rev. Lett. 65, 2720 (1990)

[10] K. Leo, P. H. Bolivar, F. Brüggemann and R. Schwedler, Solid State Commun. 84, 943 (1992)

[11] H. G. Roskos, M. C. Nuss, J. Shah, K. Leo, D. A. B. Miller, A. M. Fox, S. Schmitt - Rink and K. Kohler, Phys. Rev. Lett. 68, 2216 (1992)

[12] H. M. James, Phys. Rev. 76, 1611 (1949)

[13] for a recent discussion of the Wannier functions for the Kronig - Penney model see F. B. Pedersen, G. T. Einevoll and P. C. Hemmer, Phys. Rev. B44, 5470 (1991)

[14] G. Bastard and R. Ferreira, C. R. Acad. Sci. Paris, t.32, Série II, 971 (1991)

[15] G. von Plessen and P. Thomas, Phys. Rev. B 45, 9185 (1992)

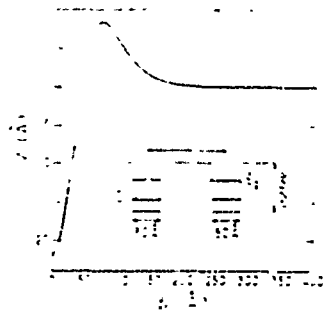

Fig (1) $Z = \langle \phi_{kx}^{(1)}(z) \, z \, \phi_{kx}^{(2)}(z - d_0) \rangle$ is plotted versus d_0 for a 80Å - 40Å GaAs/GaAlAs superlattice. Five conduction band discontinuity is taken equal to 0.21eV

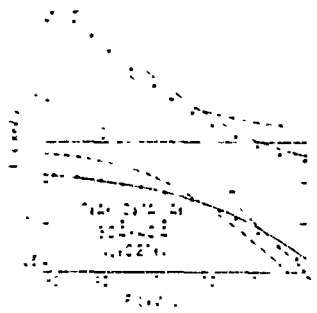

Fig (2) Calculated field dependences of the Wannier - Stark levels $\nu = 0$ and $\mu = -1$ belonging to two different subbands (ground and first excited) of a 80Å - 40Å GaAs/GaAlAs superlattice under various approximations. Straight lines: uncoupled ladders. Dashed lines: interacting ladders without diagonal corrections (eq (7)). Solid lines: interacting ladders with diagonal corrections as discussed in the text. Large dots: numerical computation of the central energy levels of 15 periods superlattice.

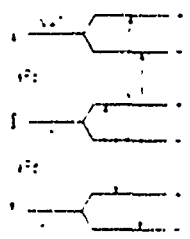

Fig (3) Level scheme of a two bands Wannier - Stark ladder with possible optical transitions (straight and curly vertical lines).

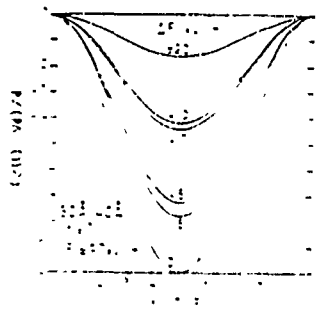

Fig (4) Calculated time dependence of the position of the center of the wavepacket in a 80Å - 40Å GaAs - GaAlAs superlattice for several field detunings $M = F - F_0$ with respect to the resonance field F_0. Here $F_0 = 97$ kV/cm corresponds to the crossing of the unperturbed $|\nu = 0\rangle$ and $|\nu = -1\rangle$ Wannier - Stark levels.

TuP4

Resonant coupling between buried single-quantum-well and Wannier-Stark-localization states in a GaAs/AlAs superlattice

I. Tanaka, M. Nakayama, and H. Nishimura
Department of Applied Physics, Faculty of Engineering, Osaka City University, Sugimoto, Sumiyoshi-ku, Osaka 558, Japan

K. Kawashima
Optoelectronic Device Laboratory, Semiconductor Research Center, Sanyo Electric Corporation, Hashiridani, Hirakata, Osaka 573, Japan

K. Fujiwara
Department of Electrical Engineering, Faculty of Engineering, Kyushu Institute of Technology, Tobata-ku, Kitakyushu, Fukuoka 804, Japan

We have investigated the resonant coupling between the quantized state in a GaAs single quantum well (6.4 nm) buried in the center of a GaAs(3.2 nm)/AlAs(0.9 nm) superlattice and the Wannier-Stark-localization state in the superlattice by using electroreflectance spectroscopy. It is found that the electroreflectance-line shapes of the heavy-hole and light-hole exciton transitions associated with the first (n=1) subbands in the buried single quantum well drastically change under the resonant-coupling condition: the splitting feature of the line shapes due to the formation of the bonding and antibonding states and the intensity reduction due to the wave-function delocalization over the coupling space. We have detected the various resonant couplings of electrons and holes. The experimental results are discussed from a transfer-matrix analysis with Airy functions.

I. INTRODUCTION

Recently there has been a growing interest in electric-field effects on electronic and optical properties of semiconductor quantum wells (QWs) and superlattices (SLs) for various applications to optoelectronic devices. Much of interest has centered around the properties of Wannier-Stark (WS) localization corresponding to the wave-function localization induced by breakdown of the resonant condition of miniband states in a SL due to an applied electric field[1-15]. The WS localization leads to Stark-ladder transitions $E_w + \nu eFD$ ($\nu = 0, \pm 1, \pm 2, \ldots$), where E_w is an interband-transition energy in an isolated QW, D is a SL period, and ν is a Stark-ladder index indicating an oblique transition in real space. Under the condition of $meFD = \Delta\Gamma_{12}$ ($m = 1, 2, 3, \ldots$), where ΔE_{12} is the energy spacing between the n=1 and n=2 electron (hole) subbands, the WS-localization state of the n=1 subband in a QW resonantly couples with that of the n=2 subband in the mth-nearest-neighbor QW on the lower (higher) electrostatic potential side[6,7,11-13]. In our previous works[12,14], we have indicated that the resonant coupling between the WS-localization states in a SL appears as the splitting feature of the electroreflectance (ER)-line shapes due to the formation of the bonding and antibonding states and as the ER intensity reduction of the related Stark-ladder transitions due to the wave function delocalization over the coupling space.

In the present work, we have investigated the resonant coupling between the quantized state in a GaAs single QW (SQW) with 6.4 nm buried in the center of a

GaAs(3.2 nm)/AlAs(0.9 nm) SL and the WS-localization state in the SL by using LR spectroscopy. In the present case, the distance between the center of the buried SQW and that of the mth-nearest-neighbor QW in the SL is given by $d_{sqw}/2+md+d_{qw(s)}/2$, where d_{sqw} and $d_{qw(s)}$ are the layer thicknesses of the SQW and the QW in the SL, respectively. Therefore, the mth-nearest-neighbor resonant coupling between the SQW state and the WS-localization state takes place under the condition of $eF(d_{sqw}/2+md-d_{qw(s)}/2)=\Delta E$, where ΔE is the energy spacing between the SQW state and the WS-localization state in the SL. Although Agullo-Rueda et al.[6] studied the similar resonant coupling by using photocurrent (PC) spectroscopy, they could not observe the resonant coupling between the hole states. From the LR profiles of the n=1 heavy-hole and light-hole exciton transitions [HH1(SQW) and LH1(SQW)] in the buried SQW as a function of electric field, we have detected the various resonant couplings of electrons and holes. We analyze the LR results of the resonant coupling by using a transfer-matrix (TM) method with Airy functions.

2. EXPERIMENTAL

The sample used in this work was grown on an n-type (Si-doped) (001)-GaAs substrate by molecular-beam epitaxy. The GaAs SQW with 6.4-nm thickness is buried in the center of the GaAs(3.2 nm)/AlAs(0.9 nm) SL with 80 periods. The whole system is placed in the center of a p-i-n diode structure, where the n and p layers are Si-doped ($\sim 1\times10^{18}$ cm^{-3}) and Be-doped ($\sim 1\times10^{18}$ cm^{-3}) $Al_xGa_{1-x}As$ layers with $\sim$0.40 μm and $\sim$0.18 μm, respectively. The method for making an ohmic contact is described in Ref.[5]. The LR measurements were performed at 77 K. The probe light was produced by combination of a halogen lamp (50 W) and a monochromator with 0.5-nm resolution. The reflected light was detected with a Si photodiode. The electric field was modulated with the amplitude of 50 mV and the frequency of the 210 Hz around a given dc bias. The LR signals were obtained by a conventional lock-in technique.

3. RESULTS and DISCUSSION

We have calculated the electric-field dependence of the eigenenergies in the SL:SQW:SI system by using the TM method proposed by Hutchings[16], which was already applied in our previous works[12-14]. Figures 1(a) and 1(b) show the calculated eigenenergies of the electron and light-hole states as a function of electric field, respectively. In the TM calculations, the

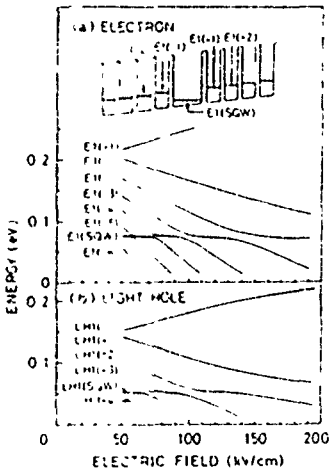

FIG.1 Calculated eigenenergies of (a) the electron states and (b) the light-hole ones in the SL:GaAs(6.4 nm)-SQW/SI system where the SL consists of six periods of 3.2-nm GaAs and 0.9-nm AlAs layers. The notations of E1(SQW), E1(-m), HH1(SQW) and HH1(-m) are explained in the text. The inset shows the potential profile of the SL:SQW/SI system.

GaAs(3.2 nm)/AlAs(0.9 nm) SL's on both sides of the central GaAs SQW are approximated by a system of six QW's, and the whole system is sandwiched by semi-infinite AlAs layers. In the present calculation, we used the following parameters: the conduction-band-offset ratio is 0.66, and the effective masses of electrons, heavy holes, and light holes in units of m_0 are m_e=0.063, m_{hh}=0.34, and m_{lh}=0.082 for GaAs, m_e=0.15, m_{hh}=0.4, and m_{lh}=0.153 for AlAs. All the values except for m_e for GaAs are the standard values taken from Ref.[17], and the value of m_e for GaAs is a little smaller than standard value of 0.0665 owing to fitting the calculated results to the experimental ones. Since the base line of the SL potential is proportional to the growth coordinate under the electric field, eF, the energies are measured respect to the center of the SQW which corresponds to the center of the system. As shown in the inset of Fig.1(a), the notation of E1(SQW) indicates the n=1 electron state in the central SQW, that of E1(±m) indicates the WS-localization state of the n=1 electron subband in the mth-nearest-neighbor QW from the SQW, and the + (-) sign means the QW in the higher (lower) electrostatic potential side. It is the same with the light-hole states. In Figs.1(a) and 1(b), we find various anticrossing behaviors due to the resonant couplings between the SQW and WS-localization states. We note that the SQW-electron state couples with the WS-localization one on the lower potential side, while the SQW-hole state couples with the WS-localization one on the higher potential side.

Noticing the electric-field range of 130-150 kV/cm in Fig.1(a), we find the anticrossing of E1(SQW)-E1(-2), which originates from the resonant coupling between the SQW state and the WS-localization state of the n=1 electron subband in the second-nearest-neighbor QW. Figure 2 shows the LR spectra at 77 K in the energy range of the HH1(SQW) and LH1(SQW) transitions in the electric-field range of the E1(SQW)-E1(-2) resonant coupling. The value of the electric field is estimated from the built-in voltage of 1.77 V corresponding to the applied voltage at which the Stark-ladder transitions in the GaAs(3.2 nm)/AlAs(0.9 nm) SL converge. The LR spectra are not normalized by reflectance (R) because the surface ohmic electrode prevents us from obtaining the real R signal from the SL. Noticing the LR spectra at F=137 kV/cm and 141 kV/cm, both the LR signal of the HH1(SQW) transition and that of the LH1(SQW) transition drastically change the signals clearly exhibit the splitting line shapes resulting from the formation of the bonding and antibonding states, which is due to the E1(SQW)-E1(-2) resonant coupling predicted by the TM analysis in Fig.1(a). The anticrossing behavior will be shown together with other couplings in Fig.4(c). In our previous works[12-14], we have

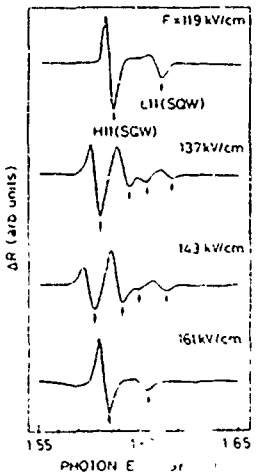

FIG.2 LR spectra at 77 K in the energy range of the HH1(SQW) and LH1(SQW) transitions in the electric-field range of the E1(SQW)-E1(-2) resonant coupling.

demonstrated that ER spectroscopy is much more sensitive for detecting the resonant coupling than PC spectroscopy. In the present work, we could not obtain the clear information of the resonant coupling from the PC spectra.

Figure 3 shows the ER spectra at 77 K in the energy range of the HH1(SQW) and LH1(SQW) transitions in the electric-field range of the E1(SQW)-E1(-3) and E1(SQW)-E1(-4) resonant couplings, which correspond to ~100 kV/cm and ~75 kV/cm as shown in Fig 1(a), respectively. Noticing the ER spectra at F=75, 77, 96, and 99 kV/cm, both the ER signal of the HH1(SQW) transition and that of the LH1(SQW) transition clearly exhibit splitting line shapes. Furthermore, the ER intensities under the resonant-coupling conditions are remarkably reduced, which is induced by the wave-function delocalization over the coupling space[12,13]. Focusing on the ER spectra at F=~100 kV/cm, the split of the LH1(SQW) transition, ~13 meV, is larger than that of the HH1(SQW) transition, ~10 meV. The calculated results shown in Figs 1(a) and 1(b) indicate that the E1(SQW)-E1(-3) and LH1(SQW)-LH1(+2) resonant couplings simultaneously occur at F=~100 kV/cm, therefore, the large split of the LH1(SQW) transition is due to the overlap of the two resonant couplings.

Finally, we focus on the electric-field dependence of the ER intensities and energies of the HH1(SQW) and LH1(SQW) transitions. We assume that the transition intensity corresponds to the amplitude from the peak to the dip of the ER signals and that the transition energies correspond to the dip-position energies of the ER signals as indicated

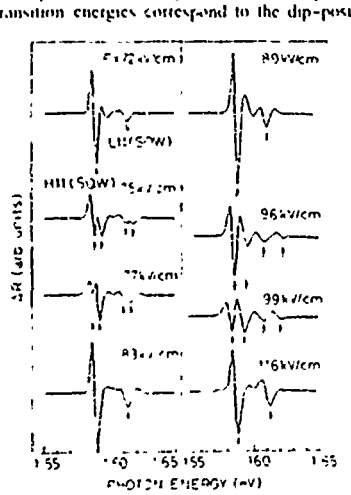

FIG 3 ER spectra at 77 K in the energy range of the HH1(SQW) and LH1(SQW) transitions in the electric-field range of the E1(SQW)-E1(-3) and E1(SQW)-E1(-4) resonant couplings.

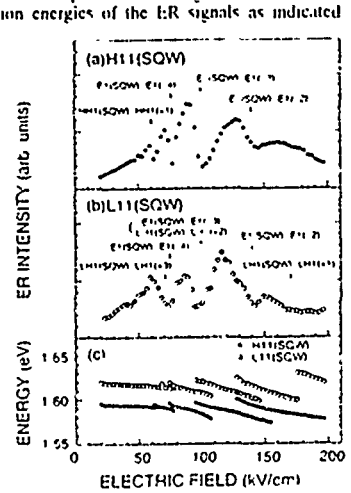

FIG 4 ER intensities of the (a) HH1(SQW) and (b) LH1(SQW) transitions as a function of electric field where the arrows indicates the calculated electric fields for the various resonant couplings by using the TM method. (c) Observed energies of the ER signals for the HH1(SQW) and LH1(SQW) transitions.

by the arrows in Figs 2 and 3. Figures 4(a) and 4(b) show the ER intensities of the (a) HH1(SQW) and (b) LH1(SQW) transitions as a function of electric field, respectively. The arrows in Figs 1(a) and 1(b) indicate the calculated electric fields for the various resonant couplings by using the TM method. For the electron states, both the reduction of the ER intensity of the HH1(SQW) transition and that of the LH1(SQW) transition at F=140, 110, and 75 kV/cm result from the E1(SQW)-E1(-2), E1(SQW)-E1(-3), and E1(SQW)-E1(-4) resonant couplings, respectively. The electric fields for the second-, third-, and fourth-nearest-neighbor resonant couplings between the SQW and WS-localization states should be in the ratio of 1.98:1.439:1.180=1.8:1.3:1 because the resonant condition is proportional to the inverse of the distance between the center of the SQW and that of the nth-nearest-neighbor QW in the SL: $eF(d_{n/2}/2+mD-d_{n/2-1}/2)=\Delta E$. The experimental ratio, 140:100:75=1.9:1.3:1, is consistent with the expected one. In Fig 4(a), only the ER intensity of the LH1(SQW) transition is reduced at F=60 kV/cm, resulting from the HH1(SQW)-HH1(-1) resonant coupling, which means the first-nearest-neighbor resonant coupling of the n=1 heavy-hole subbands. In Fig 4(b), only the ER intensity of the LH1(SQW) transition is reduced around F=170 kV/cm owing to the LH1(SQW)-LH1(+1) resonant coupling. The TM analysis predicts that the LH1(SQW)-LH1(+2), LH1(SQW)-LH1(+3) resonant couplings occur at F=~100 kV/cm and F=~70 kV/cm, respectively; however, the resonant conditions overlap with those of E1(SQW)-E1(-3) and E1(SQW)-E1(-4). Figure 4(c) shows the observed energies of the HH1(SQW) and LH1(SQW) transitions indicated by the closed and open circles, respectively. We clearly find the anticrossing behaviors of the various resonant couplings. Thus, the above indicates that the quantized state in the SQW can be modulated by the resonant coupling between the SQW and WS-localization states.

4 SUMMARY

We have systematically measured the ER spectra of the GaAs SQW (6.4 nm) buried in the center of the GaAs(3.2 nm)/AlAs(0.9 nm) SL at 77 K. It is found that the resonant coupling between the SQW state and the WS-localization state in the SL results in the change of the ER-line shapes of the HH1(SQW) and LH1(SQW) transitions: the splitting feature of the line shapes due to the bonding and antibonding states, and the intensity reduction due to the wave-function delocalization over the coupling space. We have detected the various resonant couplings: the second-, third-, and fourth-nearest-neighbor resonant couplings of the n=1 electron subbands, the first-nearest-neighbor resonant coupling of the n=1 heavy-hole subbands, and the first-, second-, and third-nearest-neighbor resonant couplings of the n=1 light-hole subbands. The resonant coupling can be applied to modulate the buried SQW states.

ACKNOWLEDGMENT

This work was supported in part by Grant-in-Aid for Joint Research, No.05044109, from the Ministry of Education, Science and Culture of Japan. One of the authors (I.T.) acknowledges the financial support of the Japan Society for the Promotion of Science for Japanese Junior Scientists.

REFERENCES

1 J Bleuse, G Bastard, and P Voisin, *Phys Rev Lett* **60**, 220 (1988)
2 E E Mendez, F Agullo-Rueda, and J M Hong, *Phys Rev Lett* **60**, 2426 (1988)
3 P Voisin, J Bleuse, C Bouche, S Gaillard, C Alibert, and A Regreny, *Phys Rev Lett* **61**, 1639 (1988)
4 F Agullo-Rueda, E E Mendez, and J M Hong, *Phys Rev* **B40**, 1357 (1989)
5 K Fujiwara, *Jpn J Appl Phys* **28**, L1718 (1989)
6 F Agullo-Rueda, E E Mendez, H Ohno, and J M Hong, *Phys Rev* **B42**, 1470 (1990)
7 H Schneider, H T Grahn, K v Klitzing, and K Ploog, *Phys Rev Lett* **65**, 2720 (1990)
8 A J Shields, P C Klipstein, M S Skolnick, G W Smith, and C R Whitehouse, *Phys Rev* **B42**, 5879 (1990)
9 M Nakayama, I Tanaka, T Doguchi, H Nishimura, K Kawashima, and K Fujiwara, *Solid State Commun* **77**, 303 (1991)
10 M M Dignam and J E Sipe, *Phys Rev* **B43**, 4097 (1991)
11 Y Tokuda, K Kanamoto, Y Abe, and N Tsukada, *Phys Rev* **B43**, 7130 (1991)
12 M Nakayama, I Tanaka, H Nishimura, K Kawashima, and K Fujiwara, *Phys Rev* **B44**, 5935 (1991)
13 A M Fox, D A B Miller, G Livescu, J E Cunningham, and W Y Jan, *Phys Rev* **B44**, 6231 (1991)
14 I Tanaka, M Nakayama, H Nishimura, K Kawashima, and K Fujiwara, *Phys Rev* **B46**, 7656 (1992)
15 I Tanaka, M Nakayama, H Nishimura, K Kawashima, and K Fujiwara, *Phys Rev* **B48** (1993) in press
16 D C Hutchings, *Appl Phys Lett* **55**, 1082 (1989)
17 *Physics of Group IV Elements and III-V Compounds*, edited by O Madelung, M Schultz, and H Weiss, Landolt-Bornstein Numerical Data and Relationships New Series Group III, Vol.17a (Springer, Berlin, 1982)

TuP5

Fermi Edge Singularities in doped quantum wires and quantum wells

F J Rodríguez and C Tejedor
Departamento de Física de la Materia Condensada,
Universidad Autonoma de Madrid,
Cantoblanco 28049, Madrid Spain

Abstract

The optical properties of quantum wires and quantum wells are investigated We are concerned with the effects produced by the localization of electrons and holes either in the same (direct transitions) or different (indirect transitions) spatial regions The emission and absorption spectra are obtained by solving an effective Bethe Salpeter equation including a static screened Coulomb interaction Fermi Edge Singularities (FES) are obtained and their dependence on temperature and density of carriers are analyzed In order to obtain strong FES it is necessary that two special points are fulfilled (i) the hole mass goes to infinity and (ii) a spatial symmetry breaking of the system (spatially indirect transitions) When the latter condition is satisfied and the bottom of the second conduction subband approaches the first one a new channel of scattering is favoured and the spectra show a large enhancement at the Fermi level We compare our results with the experimental situations

Available experiments[1] [2] [3] [4] [5] on the optical properties of modulation doped quantum wires (Q1D) and quantum wells (Q2D) show the possibility of observing many-body effects such as the Fermi edge singularities (FES) For Q1D systems some optical absorption and emission measurements[2] performed in the extreme quantum limit clearly show a strong peak at the Fermi energy In contrast, some other experiments[3] [4] [5] performed in quite similar conditions, in which electrons and holes are spatially separated, do not seem to detect such FES in the optical spectra The theoretical models describing the optical properties of quantum wires[6] [7] [8] [9] [10] do not show a clear explanation for such apparent discrepancy All of them always present a bottom singularity (typical of the one dimensional density of states) accompanying the FES which lacks in some experiments[2] The aim of this paper is to consider a model of two conduction bands and one hole band for spatially indirect quantum wires and consequently to allow the coupling between spatially symmetric and antisymmetric wavefunctions[10] For the Q1D and the Q2D case we consider that both electrons and holes are completely confined in the xy plane The electrons are free to move as a plane wave along the wire direction while they are confined by parabolic potentials in the transversal direction In order to obtain a clear FES [12] [13] extended holes with zero mobility due to random fluctuations of the potential are considered in the Q1D and Q2D cases

The emission spectra are calculated using the relation between the linear optical susceptibility $\chi(\omega)$ and the interacting electron-hole Green function $G_{\ldots}(k,k',\omega)$ by

$$\chi(\omega) \propto |M|^2 \sum_{kk'} G_{\ldots}(k,k',\omega) \qquad (1)$$

where $n=0$ and $n=0,1$ are valence and conduction states respectively k,k' are the hole and electron wavevectors and $M(k,k')$ is the single particle dipole element which we take as a constant As discussed in Ref [10] $G_{\ldots}(k,k',\omega)$ can be obtained from the noninteracting

electron-hole Green's function $G^{e,h}_{n,n'}(k,k',\omega)$ and from the static electron-hole interaction potential $V_{n,n',n'',n'''}(k,k')$ by solving a Bethe-Salpeter equation. Singularities are described by a spectral function for the hole in order to give the adequate power-law shape of the singularity[10].

The interacting electron-hole Green function is given by

$$G_{n,n',n'',n'''}(k,k',\omega) = G^{e}_{n,n''}(k,-\omega)\,G^{h}_{n',n'''}(k',\omega)\,\delta(k-k') + \frac{1}{\Omega}\sum_{q}\sum_{n_1,n_2} G^{e}_{n,n_1}(k+q,\omega)\,G^{h}_{n',n_2}(k'-q,\omega)\,V^{q}_{n_1,n_2,n'',n'''}(k+q,k') \qquad (2)$$

From the wave functions of electrons and holes, it is straightforward to get the bare Coulomb interaction between them, all the necessary components of the one-exciton electron-hole interaction that we need are $V^{q}_{0000}(k)$, $V^{q}_{0101}(k)$, $V^{q}_{0001}(k)$ and $V^{q}_{0100}(k)$[9]. The screening of the Coulomb interaction is only due to electrons, it is exactly the same than in the direct wire where we used a RPA approximation[10]. The RPA polarizability for the two dimensional case is taken from[11]. In contrast from the direct case the coupling between electrons belonging to the first and second subband $V^{q}_{0101}(k)$ is different from zero allowing the coupling between the 1 and even electronic bands which brings to a strong enhancement of the FES when the Fermi level lies just below the bottom of one of the bands as we will show below.

Experiments in which FES have been detected[2] are performed with wires having a Fermi energy in the range 3.5 to to 4.5meV and an intersubband spacing Δ roughly 0.5meV higher than E_F. Therefore we work in the extreme quantum limit in which the Fermi level lies below the bottom of the second subband for QWD and QWD systems. We perform our calculations with $E_F = 0.6E_0$ and $\Delta = 0.7E_0$ where E_0 is the binding exciton energy. Also to cover the experimental range, we take the temperature $0.02E_0/k_B \sim 1K \le T \le 0.1E_0/k_B \simeq 7K$. The electron effective mass is that of GaAs while for the holes we take infinite mass in order to get a significant FES[10]. Experiments[2] with $a = 100nm$ show FES while others[3] with $a = 250nm$ do not. Therefore, we will cover the range $80nm \le a \le 250nm$.

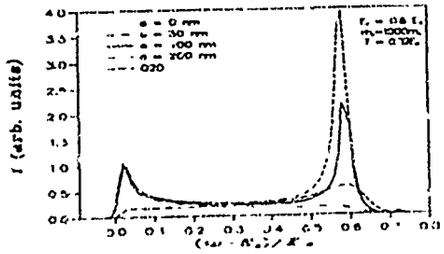

Figure 1. Emission spectra for direct QWD system and indirect wires with different electron-hole separation a. E_0 is the single particle band gap.

As we discuss in a recent work[10] we obtain a very strong enhancement of the FES when the difference between the Fermi level and the subband separation is of the order of the eV. If the difference is greater than this separation the FES becomes unappreciated.

Due to the asymmetry of the potential, V_{0001} couples G_{0000} with G_{0101}. This gives a very strong contribution to the total emission. In a direct wire the off-diagonal term is zero and no strong singularity appears even when the intersubband separation is slightly larger than the Fermi energy[7],[10].

Once the importance of the proximity of E_F and Δ is established, let us analyze the importance of the electron-hole spatial separation as the key to understand differences between experiments. Figure 1 shows the emission spectra for several values of a. Both for small and large values of a the FES is rather weak. Only in the range between 50 and 100nm, the singularity becomes strong. Our results show a maximum of $V_{0,0}$, in these range while the two diagonal terms V_{0000} and V_{0101} decrease monotonously with increasing a. For $a = 0$ the symmetry tends to decouple the first and the second electron subbands and the singularity weakens. For very large a, the interaction between the electron and the hole is so small that the second term of equation (2) goes to zero and the Green's function tends to be G_0 which does not present singularity at all. Our results are in agreement both with experiments[2] which present FES in wires, having $a = 100nm$ and with those[3] which do not have singularity at $a = 250nm$. Moreover, the FES is so strong that the bottom singularity becomes negligible in the whole emission spectrum as experimentally observed[2].

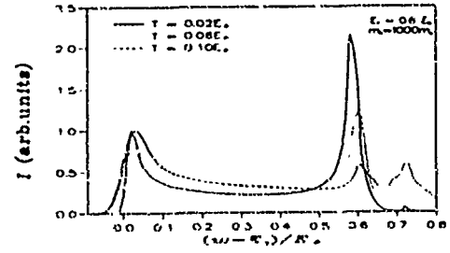

Figure 2. Emission spectrum of an indirect wire with electron-hole separation $a = 100nm$, $\Delta = 0.7E_0$ and $E_F = 0.6E_0$, for different temperatures. E_0 is the single particle band gap.

Another property comparable with the experiment is presented in figure 2. There the emission spectrum for a wire with $E_F = 0.6E_0$, $\Delta = 0.7E_0$ and $a = 100nm$ is given for several temperatures. For a temperature of 2K much smaller than E_F, the FES has weakened so much that it is comparable to the bottom singularities of the first ($\omega - E_0 \simeq 0$) and the second ($\omega - E_0 \simeq 0.7E_0$) subband to something undetectable in the experiment. This again agrees with the experimental temperature dependence.

A very important point must be stressed. Our calculation has been performed in a single indirect wire while the experiments are done with multiple wires. In actual samples the hole does not move along the z direction most probably due to fluctuations of the wire potential. The position z of such a localization is completely random for different wires of the array and the system is not symmetric any more.

In other words, the symmetry is not restored by the existence of a multiple array and all the results presented here for a single indirect wire are perfectly comparable with actual experiments.

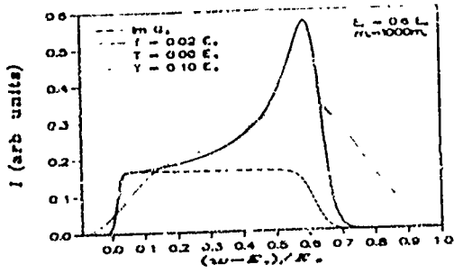

Figure 3 Emission spectrum of an Q2D electron gas with $E_F = 0.6E_0$ for different temperatures E_0 is the single particle band gap

We calculate the two dimensional case with the same Fermi energy In these systems there are not singularities for mobile holes due to peak broadenings produced by indirect transitions from the top of the valence band to the fermi level accompanied by very low energy excitations of the Fermi sea to ensure momentum conservation The singularities just appear if the holes has and infinite mass

In figure 3 we show the emission spectra for the two dimensional case From the figure the FES is clearly observed if it is compared with the backgrounds Due to the low density of electrons the FES is weakened when the temperature is around 15 K The FES survives longer than in Qld case

This work has been supported in part by the PRECAM grant No 170 92 and the European Community under contract ESPRIT BRA 6719 (NANOPT) One of us (J R) acknowledges COLCIENCIAS of Colombia for financial support.

References

1 M Erdze, V S Nurmikko P Hawrylack, EP2DS-10 Newport (1993)

2 J M Calleja, A R Goni, B S Dennis, J S Weiner A Pinczuk, S Schmitt Rink J A Pfeiffe K W West, J F Mueller and V E Rockenstein Solid St Commun 79, 911 (1991)

3 J Hirler R Buchler, R Strenz, G Abstreiter, G Bohm J Smoliner G Trankle and G Weimann Surf Sc 263 536 (1992)

4 J S Skolnick J M Rorison K J Nash, D J Mowbray P R Tapster S J Bass and A D Pitt Phys Rev Lett 58 2130 (1987)

5 J S Weiner J M Calleja A Pinczuk, A Schmitter B S Dennis A R Goni J Pfeiffer and K W West Proc of

6 J F Mueller, Phys Rev B 42 11389 (1990)

7 P Hawrylak, Solid St Commun 81, 525 (1992)

8 J F Mueller V E Rockenstein and S Schmitt Revs Phys Re B 45 8902 (1992)

9 T Ogawa, A Furusaki and N Nagaosa, Phys. Rev Lett 68, 3638 (1992)

10 J Rodriguez and C Tejedor, Phys Rev B, 47, 4536 (1993).

11 P Hawrylak, Phys Rev B 45 6262 (1991)

12 C Tejedor and J J Rodriguez in "Frontiers on optical phenomena in semiconductor structures of reduced dimensions" ed by D J Lockwood and A Pinczuk (Kluwer Academic Publishers) to be published

13 J J Rodriguez and C Tejedor, Phys Rev B, 47, 13015 (1993).

14 T Ando A B Fowler and F Stern Rev Mod Phys 54 437 (1982).

TuP6

Excitonic enhancement of the Fermi edge singularity and recombination kinetics of photogenerated electrons in p-type δ-doped GaAs:Be/$Al_xGa_{1-x}As$ double-heterostructures

J. Wagner [a], *D. Richards* [b], *H. Schneider* [c], *A. Fischer* [c], *and K. Ploog* [d]

[a] *Fraunhofer-Institut für Angewandte Festkörperphysik, Tullastrasse 72, D-79108 Freiburg, Federal Republic of Germany*

[b] *Cavendish Laboratory, Madingley Road, Cambridge CB3 0HE, UK*

[c] *Max-Planck-Institut für Festkörperforschung, Heisenbergstrasse 1, D-70506 Stuttgart, Federal Republic of Germany*

[d] *Paul-Drude-Institut für Festkörperelektronik, Hausvogteiplatz 5-7, D-10117 Berlin, Federal Republic of Germany*

Abstract

We have studied the photoluminescence (PL) spectrum, and the strength of the Fermi edge singularity (FES) in that spectrum, of the two-dimensional hole gas (2DHG) formed in GaAs/$Al_xGa_{1-x}As$ double-heterostructures as a function of the width of the GaAs layer, the centre of which is p-type δ-doped. A variation of that layer width allows us to tune, for a fixed doping concentration, the energetic spacings between the hole subbands. From these experiments, we conclude that the observation of a FES in the PL spectrum of a 2DHG is brought about by a resonant hybridisation between occupied states close to the hole Fermi energy and exciton levels involving nearby lying unoccupied hole subbands. The recombination and spin-flip scattering times of the photogenerated electrons are found to decrease drastically with decreasing GaAs layer width which reflects the increase in the electron-hole wavefunction overlap.

1. Introduction

$Al_xGa_{1-x}As$/GaAs/$Al_xGa_{1-x}As$ double-heterostructures, p-type δ-doped in the centre of the GaAs layer, have proven to be very useful for the photoluminescence (PL) study of a two-dimensional hole gas (2DHG) [1-3]. The GaAs/$Al_xGa_{1-x}As$ heterojunction barriers confine the photogenerated minority carriers (electrons), which are repelled by the space-charge induced potential well confining the holes, sufficiently close to the 2DHG to enhance the electron-hole wavefunction overlap for efficient radiative recombination [1,2]. A schematic energy-band diagram of such a double-heterostructure is shown in Fig. 1.

In the optical spectra of two-dimensional electron gases (2DEG) an enhancement of the emission intensity or the absorption strength at the Fermi edge has been observed [4,5]. This so-called Fermi edge singularity (FES) is a consequence of many-body interactions between the 2DEG and photogenerated holes [6,7]. To observe a Fermi edge enhancement in emission, electrons with energies close to the Fermi energy E_F, and consequently a wavevector close to the Fermi wavevector k_F, have to recombine with photogenerated holes with a wavevector of essentially zero. If only momentum conserving transitions are allowed, this recombination would be forbidden and therefore, the FES would be strongly suppressed. Thus one possibility to observe a strong FES in emission is a localization, and thus a spread in k-space, of the holes [4]. Another possible mechanism for the observation of a FES in luminescence, suggested by Chen et al. [8,9], is the resonant hybridisation of occupied states at the Fermi edge with virtual excitons involving unoccupied electron subbands [10,11].

Recently, a FES has also been observed in the PL spectrum of a high-density 2DHG formed in a δ-doped $Al_xGa_{1-x}As$/GaAs:Be/$Al_xGa_{1-x}As$ double-heterostructure [1,2]. In thise case, the photogenerated electrons are unlikely to be localized because of their much smaller mass. Instead, it has been suggested that the observation of a FES in the PL spectrum of a 2DHG is due to a resonant hybridisation between states at E_F and an unoccupied hole subband [2]. In the present paper we present experimental evidence in support of this suggestion. This evidence is based on the measured dependence of the 2DHG PL spectrum in $Al_xGa_{1-x}As$/GaAs:Be/$Al_xGa_{1-x}As$ double-heterostructures on the width of the GaAs layer, the centre of which is p-type δ-doped. Further, we report on the variation of the recombination and spin-flip scattering times with increasing electron-hole wavefunction overlap upon reduction of that layer width.

2. Results and Discussion

A. Fermi Edge Singularity

Fig. 2 shows a sequence of low-temperature (6 K) PL spectra of δ-doped GaAs:Be/$Al_xGa_{1-x}As$ double-heterostructures where the width d of the GaAs layer was varied between 20 and 60 nm. The two-dimensional hole concentration was kept fixed at 4×10^{12} cm^{-2}. For this doping concentration and a layer width of d=60 nm three or four hole subbands, namely the first (hh1) and the second heavy-hole (hh2) and the first (lh1) and possibly the second light-hole band (lh2), are expected to be occupied [2]. Thus the emission peak lowest in energy arises from recombination of holes in the first heavy-hole and light-hole subbands whereas emission at higher energies is due to transitions involving holes in the hh2 and possibly the lh2 subbands. The overall luminescence intensity is found to decrease by almost one order of magnitude upon reduction of the GaAs layer width from d=60 to 20 nm. For the narrowest layer width of d=20 nm the whole luminescence spectrum is shifted to higher energies primarily due to the reduction in electron-hole separation. This reduction leads, for a constant electric field above and below the doping spike (see Fig. 1), to a blue-shift of the 2DHG emission.

For d=60 nm there is a well resolved Fermi edge enhancement at the high-energy side of the emission spectrum. When the GaAs layer width is decreased to d=40 nm the strength of the FES is considerably reduced and for d=20 nm there is no detectable enhancement left. Temperature-dependent PL spectra of the sample with the widest GaAs layer (d=60 nm) are shown in Fig. 3. There is a monotonic

decrease in intensity of the Fermi edge enhancement with increasing temperature, which is a characteristic finger-print of a FES [4,6]. For temperatures ≥ 40 K the intensity of the hh2/lh2 recombination band remains constant which indicates a complete disappearance of the FES due to the thermal spread of the holes. From the temperature dependence of the FES intensity the binding energy of the Mahan exciton can be deduced to be about 1.5 meV. This value is about twice as large as the binding energy of 0.6 meV found for the FES in a 2DEG in δ-modulation doped $GaAs/In_yGa_{1-y}As/Al_xGa_{1-x}As$ quantum wells [12].

With increasing temperature an additional emission peak appears at the high energy side of the spectrum arising from recombination of holes which are thermally excited into the hh3 and/or lh2 hole subbands [2]. Thus the present temperature-dependent PL measurements allow us to determine the energetic spacing between E_F and the nearest hole subband not occupied at low temperature. In Fig. 4 PL spectra are plotted recorded at 6 and 50 K from the samples with GaAs layer widths of d=60 and 40 nm. The apparent energetic spacing, as determined from the half maximum points of the leading edges in the spectra, are 12 and 17 meV for d=60 and 40 nm, respectively. Taking into account the temperature shift of the GaAs band gap energy, the actual energetic spacings turn out to be $\approx$15 and $\approx$20 meV for the two different layer widths. For the sample with the narrowest GaAs layer of d=20 nm no emission from thermally populated hole subbands could be detected indicating an even larger energetic spacing between E_F and the nearest hole subband not occupied at low temperatures. This increase in subband spacing with decreasing GaAs layer width directly reflects the effect of the $Al_xGa_{1-x}As$ barrier separation on the energy spectrum of higher lying hole subbands.

Combining the above results on the GaAs layer width dependence of the strength of the FES and of the hole subband spectrum, we can conclude that the FES decreases in strength with increasing energy separation between E_F and the nearest unoccupied hole subband. This finding gives full support to the view that the observation of a FES in the luminescence spectrum of a 2DHG is due to a resonant hybridisation between occupied states at the Fermi edge and exciton levels involving nearby unoccupied hole subbands [2]. For this hybridisation mechanism the strength of the Fermi edge enhancement is indeed expected to depend strongly on the energy separation [8-12]. It has been pointed out by Rodriguez and Tejedor [13] that a hybridisation between states from adjacent subbands is not possible for carriers confined in a symmetric potential. The present δ-doped GaAs:Be/$Al_xGa_{1-x}As$ double-heterostructures are indeed symmetric by design. However, there are a number of possible reasons for the introduction of an asymmetry, such as the effect of the position of the Fermi level at the nearby surface on the electron-confining potential [2,14,15] and a segregation of the dopant atoms not detectable within the depth resolution of secondary ion mass spectroscopy [2].

Alternatively, one may think of an enhanced scattering of the photogenerated electrons by the ionized acceptor impurities upon reduction of the GaAs layer width

as a possible reason for the decrease in the strength of the FES. However, if this scattering had a strong effect on the FES intensity one would expect also a reduction in that intensity when, for a given GaAs layer width, the acceptor impurities are spread over a larger distance along the growth direction. An increase of the two-dimensional (δ) acceptor concentration results in a larger spread of the acceptors along the growth direction [4] because of diffusion and segregation of the dopant impurities. But in this case even an increase in the strength of the Fermi edge enhancement is observed with increasing 2D acceptor concentration, most likely because of a change in the hole subband structure [2]. For that reason we discard the idea of enhanced impurity scattering as a likely explanation for the observed decrease in FES strength with decreasing GaAs layer width, at least for widths $d \geq 40$ nm.

B. Recombination Kinetics

The recombination kinetics of photogenerated electrons are expected to depend strongly on the electron-hole wavefunction overlap and thus, for the present double-heterostructures, on the GaAs layer width. Therefore we have studied the recombination kinetics of the photogenerated electrons by time-resolved photoluminescence spectroscopy. The recombination time of 300 ps measured for the present hole concentration of 4×10^{13} cm^{-2} and d=60 nm is consistent with a recombination time of 400 ps reported previously for a hole concentration of 3×10^{13} cm^{-2} and the same GaAs layer width [2]. On the other hand, these time constants are much shorter than that of 2 ns reported for d=60 nm and a hole concentration of 8×10^{12} cm^{-2} [3]. Upon reduction of the GaAs layer width the recombination time is found to decrease, for a hole concentration of 4×10^{13} cm^{-2}, to 130 and 35 ps for d=40 and 20 nm, respectively, as compared to 300 ps for d=60 nm. The above described dependence of the minority carrier recombination time on both the hole concentration and the GaAs layer width indicates a pronounced enhancement of the recombination rate with increasing electron-hole wavefunction overlap. As the decrease in recombination time with decreasing layer width goes along with a reduction of the cw luminescence intensity (see Fig. 2), we can conclude that with increasing wavefunction overlap the nonradiative recombination rate increases faster than the radiative one. As we deal with a highly p-type doped system Auger recombination is the most likely non-radiative process.

The short recombination time constants in the present samples prevented us from a direct measurement of the spin-flip scattering time of the photogenerated electrons as a function of the GaAs layer width [3]. However, using optical excitation with circularly polarised light and detecting the degree of circular polarisation of the emitted recombination radiation we could measure the average degree of circular polarisation P_{av} from cw PL measurements and the initial degree of polarisation P_0 immediately after the exciting laser pulse in a time-resolved PL experiment. P_0 was found to be of the order of 20 % independent of the GaAs layer width whereas P_{av} decreased from $\approx$20 % for d=60 nm to $\approx$12 % for d=40 and 20 nm, respectively.

Using the relation $P_{av} = P_0 \cdot \{\tau_{sp}/(\tau_{rec} + \tau_{sp})\}$ [16], where τ_{rec} and τ_{sp} are the recombination and spin-flip scattering time constants, respectively, we can obtain a rough estimate for τ_{sp} from the measured values for P_{av}, P_0, and τ_{rec}. For $d = 60$ nm τ_{sp} turns out to be much larger than the recombination time of 300 ps, whereas for $d = 40$ and 20 nm spin-flip scattering times of ≈ 200 and ≈ 50 ps are obtained.

The above results clearly indicate a strong increase of the spin-flip scattering rate for electrons upon increasing electron-hole wavefunction overlap, as is expected from previous experiments on a less heavily p-type δ-doped GaAs:Be/$Al_xGa_{1-x}As$ double-heterostructure with a GaAs layer width of 60 nm, for which a spin-flip scattering time of ≈ 20 ns has been reported [3]. The spin-flip scattering times of ≤ 200 ps observed for the two narrowest GaAs layers are comparable to those, which are of the order of 100 ps, reported for electrons in homogeneously p-type doped GaAs with dopant concentrations in the mid 10^{19} cm^{-3} range [17].

3. Conclusions

We have studied the strength of the Fermi edge singularity in the emission spectrum, and the recombination kinetics, of photogenerated minority carriers in GaAs:Be/$Al_xGa_{1-x}As$ double-heterostructures as a function of the width of the GaAs layer, the centre of which is p-type δ-doped. With decreasing layer width the energetic spacing between the Fermi edge and the nearest unoccupied hole subband increases and the strength of the FES is found to decrease. These finding lead us to the conclusion that the observation of a FES in the luminescence spectrum of a 2DHG is due to resonant hybridisation between occupied states at the Fermi energy and exciton levels involving nearby unoccupied hole subbands. The recombination and spin-flip scattering times of photogenerated electrons are found both to depend strongly on the GaAs layer width and to decrease with increasing electron-hole wavefunction overlap.

Acknowledgements

We would like to thank F. Koidl and H.S. Rupprecht for stimulating discussions and for continuous support of the work at the Fraunhofer-Institut. Part of the work at the Max-Planck-Institut was sponsored by the Bundesministerium für Forschung und Technologie.

References:

1. J. Wagner, A. Ruiz, and K. Ploog, Phys Rev. B 43, 12 154 (1991).
2. D. Richards, J. Wagner, H. Schneider, G. Hendorfer, M. Maier, A. Fischer, and K Ploog, Phys. Rev. B 47, 9629 (1993).
3. J. Wagner, H Schneider, D. Richards, A. Fischer, and K. Ploog, Phys. Rev. B 47, 4786 (1993).
4. M.S. Skolnick, J.M. Rorison, K.J. Nash, D.J. Mowbray, P.R. Tapster, S.J. Bass, and A.D. Pitt, Phys. Rev. Lett. 58, 2130 (1987).
5. G. Livescu, D.A.B. Miller, D.S. Chemla, M. Ramaswamy, T.Y. Chang, N. Sauer, A.C. Gossard, and J.H. English, IEEE J. Quantum Electron. QE-24, 1677 (1988).
6. S. Schmitt-Rink, C. Ell, and H. Haug, Phys. Rev. B 33, 1183 (1986).
7. A.E. Ruckenstein and S. Schmitt-Rink, Phys. Rev. B 35, 7551 (1987).
8. W. Chen, M. Fritze, A.V. Nurmikko, D. Ackley, C. Colvard, and H. Lee, Phys. Rev. Lett. 64, 2434 (1990).
9. W. Chen, M. Fritze, A.V. Nurmikko, M. Hong, and L.L. Chang, Phys. Rev. B 43, 14 738 (1991).
10. J.F. Mueller, Phys. Rev. B 42, 11 189 (1990).
11. P. Hawrylak, Phys. Rev. B 44, 6262 (1991).
12. W. Chen, M. Fritze, W. Walecki, A.V. Nurmikko, D. Ackley, J.M. Hong, and L.L. Chang, Phys. Rev. B 45, 8464 (1992).
13. F.J. Rodriguez and C. Tejedor, Phys. Rev. B 47, 13 015 (1993).
14. D. Richards, J. Wagner, K. Ploog, and A. Fischer, Mat. Res. Soc. Symp. Proc. Vol. 261, 63 (1992).
15. D. Richards, J. Wagner, A. Fischer, and K. Ploog, Appl. Phys. Lett. 61, 2685 (1992).
16. R R. Parsons, Phys. Rev. Lett. 23, 1152 (1969).
17. K. Zerrouati, F. Fabre, G. Bacquet, J. Bandet, J. Frandon, G. Lampel, and D. Paget, Phys. Rev. B 37, 1334 (1988).

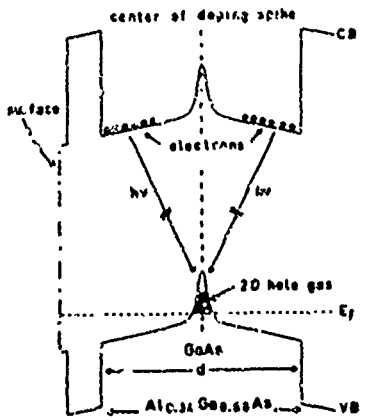

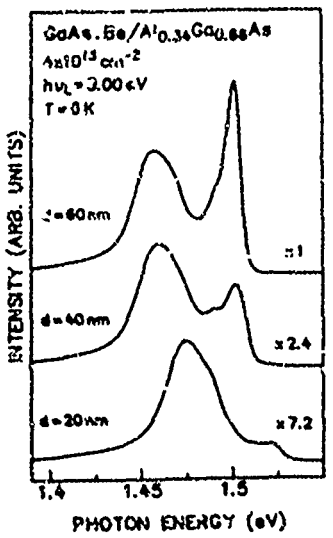

Fig. 1 (left) Schematic energy-band diagram of the Be δ-doped $Al_xGa_{1-x}As$/GaAs/$Al_xGa_{1-x}As$ double-heterostructures used in the present study.

Fig. 2 (right) Low-temperature PL spectrum of p-type δ-doped GaAs:Be/$Al_{0.34}Ga_{0.66}As$ double heterostructures as a function of the width d of the GaAs layer in the centre of which the doping spike is placed. The spectra were excited at 3.00 eV. Vertical lines mark the enhancement in luminescence intensity at the Fermi edge.

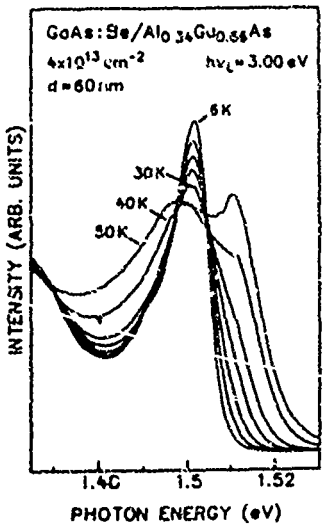

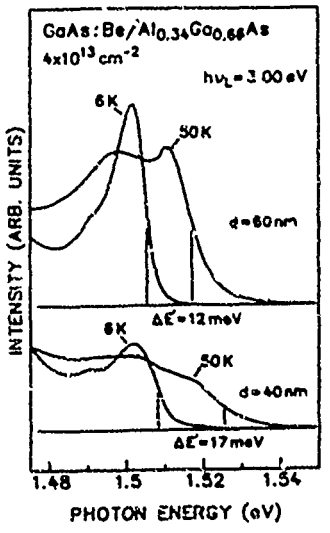

Fig. 3 (left) Temperature-dependent PL spectra showing the Fermi edge enhancement at the high-energy side of the emission spectrum of the sample with the widest GaAs layer width of d = 60 nm. The temperature, at which each spectrum was taken, is given in the figure except for those spectra between 6 and 30 K which were recorded at 15, 20, and 25 K, respectively.

Fig. 4 (right) PL spectra recorded at 6 and 50 K for GaAs layer widths of d = 60 and 40 nm, respectively. Apparent energy spacings ΔE' between the Fermi edge and the nearest hole subband unoccupied at low temperatures, determined from the half maximum points of the leading edge in the spectra, are marked in the figure.

TuP7

Free to Bound Exciton Relaxation in [001] and [111] GaAs/GaAlAs Quantum Wells

L. Muñoz,[1,2] L. Viña,[1,2] N. Mestres[3] and W.I. Wang[3]

[1]*Instituto de Ciencia de Materiales de Madrid, C.S.I.C., Cantoblanco, 28049 Madrid Spain.*
[2]*Departamento de Física de Materiales C-IV, Universidad Autónoma, 28049 Madrid, Spain.*
[3]*Elect. Eng. Department and Center for Telecomm. Research, Columbia University, New York, NY 10027, U.S.A.*

Abstract

We have investigated the relaxation from free to bound excitons in [001] and [111] $GaAs/Ga_{0.7}Al_{0.3}As$ quantum wells by analyzing the photoluminescence polarization in the presence of a magnetic field applied in the Faraday configuration. The Stokes shifts of our samples, which amount to ~ 3 meV, indicate that the photoluminescence is due to excitons bound to some kind of defects in the quantum wells. We have obtained a systematic decrease of the degree of polarization with increasing magnetic field for resonant excitation of heavy-hole excitons. We interpret this fact as a manifestation of the decrease of correlation between momenta and spins of the excitons as they decay from free to bound excitons. We obtain an effective out-scattering time due to the processes of energy relaxation from free to bound excitons of the order of 50 fs, which is independent of the crystallographic orientation.

1. Introduction.

The optical properties of excitons in quantum wells (QW's) have been the subject of intense research in recent years for fundamental and applied reasons. A large body of experimental work deals with absorption, or pseudo-absorption, via photoluminescence excitation (PLE), and photoluminescence (PL) spectroscopy, in which excitons play a fundamental role. A usual finding is the shift of the peak of the PL below those of the absorption or PLE spectra. This is the so called "Stokes shift", which is widely used as a negative indicator of sample quality. Bastard et al. explained the Stokes shift in terms of exciton trapping at random interfaces defects [1], and obtained that Stokes shifts smaller than ~10 meV could be due to "intrinsic" interface defects of the order of 200 Å. In a more recent work, a linear relation between the line-width of the PLE excitonic peak and the Stokes shift has been found [2]. This behavior can be explained assuming the existence of randomly distributed interface defects and that the well width fluctuations extend over a length scale which is large compared with the size of the excitons [2].

Nowadays, it is generally accepted that good samples can exhibit Stokes shifts of a few meV, and that they are due to the difference in the binding energy between free and bound excitons. As the samples studied here present Stokes shifts of ~ 3 meV, we believe that their PL is due to bound excitons. In order to study the free to bound exciton relaxation we have used optical orientation methods.

Optical orientation, which allows the excitation of states with a preferential spin orientation, using selective optical excitation with circularly polarized light, is very powerful for investigating electronic properties of semiconductors [3]. The optical orientation manifests itself in a polarization of the PL, which is a consequence of the excitation of states with a preferential spin orientation, and it depends on the ratio between the lifetime and the spin relaxation time of excited states [4]. Usually, the polarization excited by circularly polarized light is quantified by means of the degree of circular polarization, $\mathcal{P}$. For one of the exciting helicities, $\mathcal{P}$ is defined as the fractional difference of the PL intensities of two circular polarizations, σ^+ and σ^-, at a given energy, i.e., for σ^+ excitation $\mathcal{P}=(I^+ - I^-)/(I^+ + I^-)$.

In this work, we investigate the relaxation between free and bound excitons by studying the dependence of $\mathcal{P}$ on magnetic field, under resonant excitation of the heavy-hole exciton and detection at the maximum of the Stokes-shifted PL.

2. Experimental details.

The samples studied here were grown by MBE on [111]B semi-insulating GaAs substrates, with crystal orientation tilted 3° to improve their optical quality, and have been described previously [5]. Four different $GaAs/Ga_{0.7}Al_{0.3}As$ samples with well thicknesses of 60, 75, 100, and 130 Å were investigated. We have also studied a [001]-oriented $GaAs/Ga_{0.7}Al_{0.3}As$ QW of 100 Å for comparison purposes. PL and PLE spectra were obtained, at 2 K, with magnetic fields applied in the Faraday configuration up to 13.5 T. The samples were excited with the light from a LD700 dye laser, a Rhodamine 6G dye laser or a Ti-Zf laser, pumped by ion lasers. The incident light was circularly polarized by means of an achromatic λ/4 plate. The emitted light was analyzed into its σ^+ and σ^- components, and it was detected with photon counting techniques.

3. Results and discussion.

Figure 1 depicts PLE spectra of a 75-Å [111]-oriented QW at two different magnetic fields: the sample was excited with σ^+ light, and the emission, that was detected at the maximum of the PL, was analyzed into its σ^+ (solid PLE spectra) and σ^- (dashed PLE spectra) components. The upper traces of Fig. 1(a) and 1(b) correspond to the degree of polarization of the luminescence as a function of the exciting energy.

At zero magnetic field, Fig. 1(a), the pseudo-absorption spectra show two clear peaks, at 1.555 eV and 1.575 eV, which correspond to the ground state of the heavy-hole ($h_1(1s)$) and light-hole ($l_1(1s)$) excitons. The structure near 1.67 eV is due to the h_2 transition between the second confined electron and hole states. We have assigned the small peak at 1.562 eV in the σ^+-PLE spectrum to a forbidden transition between the second heavy-hole and the first electron subband levels, h_{12}. The degree of polarization as a function of the exciting energy, Fig. 1(a) upper trace, presents three clear structures: two peaks, corresponding to the $h_1(1s)$ and h_{12} excitons, where $\mathcal{P}$ exceeds 50%, and a deep at the $l_1(1s)$ exciton, where $\mathcal{P}$ is slightly negative. These values of $\mathcal{P}$ can be explained in terms of the spin of electrons and holes involved in the different excitonic transitions, considering that the spin-relaxation time of holes is much shorter than that of the electrons, and that the relaxation of holes occurs preferentially with conservation of hole parity [6]. In the case of the h_{12}, the positive value of $\mathcal{P}$ can be understood taking into account valence band-mixing effects.

Let us consider now the effects of a magnetic field. The PLE spectra recorded at our maximum field (Fig. 1(b)) are much richer than those obtained at zero field. The new structures are due to excited states of excitons, whose observation is favored by the reduction of exciton radii and the increase in binding energies [7]. Conversely, the degree of polarization of the PL at 13.5 T (Fig. 1(b), upper trace) is almost zero for all the exciting energies. This result is in contrast with recent PLE experiments under high magnetic fields, which have shown that the relaxation time of the magnetic moment of electrons is much longer than the recombination time, and that the magnetic moment is conserved in the recombination as well as during the thermalization process from the excited states [8]. Moreover, calculations of the spin relaxation time of QW electrons in a magnetic field have obtained an enhancement of this time, in the $n=0$ Landau level, amounting to 1.6 when the field is increased from 6 to 15 T [9]. However, our results present a systematic decrease of the degree of polarization with increasing field for the different samples, as it is clearly seen in Fig. 1(b) for the 75 Å QW. Due to the fact that the decrease in $\mathcal{P}$ is observed in the whole

spectral range, i.e. for the ground- and excited-excitonic states, we believe that it does not arise during the excited- to ground-state excitonic relaxation, but during the relaxation from free to bound excitons. In order to study this latter relaxation, we will concentrate in the case of resonant excitation of the $h_1(1s)$ exciton state.

Figure 2 shows the degree of polarization of the PL, exciting at the energies of the $h_1(1s)$ excitons observed in PLE, for the 60-Å (solid points) and the 100-Å (open points) [111]-oriented QW's as a function of the magnetic field. The exciting light was σ^+ polarized; the values of $\mathcal{P}$ were obtained at the maximum of the PL spectra. We also show in the inset of Fig. 2 the magnetic field dependence (up to 9 T) of $\mathcal{P}$ for the 100-Å [001]-oriented QW.

In some cases, it is possible to observe a Zeeman splitting between the σ^+ and σ^- components of the emission at high magnetic fields. For the [111]-oriented QW's, the Zeeman splitting of the PL is negligible, therefore, $\mathcal{P}$ was obtained with the spectrometer set at the same energy for both polarizations. However, in the case of the [001] QW, the presence of a Zeeman splitting for fields higher than 9 T originates a situation in which $\mathcal{P}$ depends markedly on the detection energy. Thus, we have limited our analysis for this sample up to 9 T, since for higher fields it is not possible to observe a clear trend in the behavior of $\mathcal{P}$.

In the situation considered here of resonant creation of excitons, all the intermediate states during the absorption, energy and spin relaxation and emission processes are correlated electron-hole pairs [10]. However, one must consider that the initial and final states are not the same, since we are pumping free excitons, while the PL is due to excitons bound to some genre of defect in the QW. We have obtained that the zero-field degree of polarization, $\mathcal{P}(0)$, is 45±10% for all the samples, including the [001]-oriented QW, while the drop between 0 and 13.5 T varies from 10% (130-Å QW) to 40% (75-Å QW). The $\mathcal{P}(0)$ value indicates that the spin scattering time is not very short on the scale of the total excitonic lifetime, and the dependence of $\mathcal{P}$ on field denotes that the spin-flip rate of the free exciton during its energy relaxation to bound exciton increases with magnetic field.

An analogous decrease of $\mathcal{P}$ has been reported for the hot luminescence of GaAs when the magnetic field, applied in the Faraday configuration, is increased [11]. This decrease is interpreted as a manifestation of the correlation between momenta and spins of the photoexcited carriers and it is found to follow the Lorentzian expression

$$\mathcal{P}(H) = \frac{\mathcal{P}(0)}{1 + (\omega_c')^2 \tau_1^2} \qquad (1)$$

where ω_c' is the reduced cyclotron frequency and τ_1 represents an effective out-scattering time due to any processes of energy relaxation. For two-dimensional systems, Zakharchenya et al [12] have not observed any decrease of circular polarization up to 7 T and therefore they claim that the correlation between momenta and spins is absent in 2D systems. However, our results show a systematic decrease of the excitonic polarization for resonant excitation with increasing magnetic field, and we believe that this is due to the destroying of the aforementioned correlation during the free to bound excitonic relaxation. Assuming that Eq (1) is valid to describe this process for excitons, with the knowledged of ω_c' ($\omega_c'=eH/m_r^*$, where m_r^* is the in-plane reduced effective mass of the exciton) it is possible to obtain an indication of the relaxation time from free to bound excitons.

The cyclotron frequency can be easily obtained from an analysis of the magnetooptical data. Figure 3 shows the fan chart of the PLE peaks, exciting with σ^- polarized light, for a [111]-oriented 100-Å QW. Two sets of transitions can be clearly distinguished: the ground

and excited states of the heavy-hole exciton, $h_1(ns)$, n=1 to 3 (solid circles), and the corresponding light-hole excitons, $l_1(ns)$ (open circles). Fitting the experimental results with a 2D hydrogenic-like excitonic model [13], it is possible to obtain the in-plane effective masses of the excitons. The result of fitting simultaneously the ground and excited states of the heavy- (light-) hole excitons are shown in Fig. 3 as solid (dashed) lines.

We have fitted $\mathcal{P}$ as a function of magnetic field with Eq.(1), using the values of m_r^* which have been reported recently for the same samples [5]. The result of the fits, with $\mathcal{P}(0)$ and τ_1 as adjustable parameters, are shown in Fig. 2 as solid lines for the 60-Å [111]-QW (τ_1 = 20±15 fs) and for the 100-Å [001]-QW (τ_1 = 35±15 fs), and as a dashed line for the 100-Å [111]-QW (τ_1 = 30±15 fs). For the two other samples this effective scattering time is of the same order. The uncertainties in τ_1 are rather large since ω_c' is also obtained through a fitting procedure. The fact that the scattering times do not show any systematic dependence on QW width is not surprising since the defects to which the excitons bound may randomly fluctuate from sample to sample. Similarly, it seems that the process of relaxation from free to bound excitons does not depend strongly on crystallographic orientation.

Figure 4 depicts the spectral dependence of $\mathcal{P}$ for the 130-Å [111]-oriented QW exciting at $h_1(1s)$, for three different fields. The PL spectra, also shown in Fig. 4, were recorded exciting at 1.7 eV with σ^+ light. For this sample, the Stokes shift is negligible. We attribute the high- (low-) energy component of the PL spectra to free- (bound-) exciton recombination. It can be easily seen in Fig. 4 that the blue shift of the PL with increasing field is larger for the bound-exciton component of the PL than for the free-exciton one; in fact, at 13.5 T it is not possible to resolve both components. We believe that this is due to the different effective masses of the free and bound excitons.

The results shown in Fig. 4 yield further evidence of our claim that the decrease of $\mathcal{P}$ with magnetic field is related to the process of free to bound exciton relaxation. Although it is not possible to investigate $\mathcal{P}$ under resonant conditions at the free excitonic peak, we have indications that it does not decrease so markedly with increasing field as it does at the bound exciton emission. Actually, the stronger decrease of $\mathcal{P}$ with increasing field as the detection energy is scanned towards the low energy tail of the PL, where the bound exciton emission dominates the spectra, is apparent in Fig. 4. However, there are two peculiarities in this figure which indicate that further investigations are need in order to understand the relaxation of excitons in QW's: first, the higher polarization of the bound-exciton component of the PL as compared with that of free excitons at zero magnetic field, and, secondly, the negative degree of polarization in the low energy tail of the PL at high fields.

4. Summary.

We have investigated the relaxation from free to bound excitons using optical orientation methods in [111]- and [001]-oriented QW's. A systematic decrease of the degree of polarization of the photoluminescence has been found with increasing magnetic field, applied in the Faraday configuration. This behavior has been interpreted as a manifestation of the decrease of correlation between momenta and spins of the excitons as they decay from free to bound excitons. An analysis of the results have obtained an effective out-scattering time due to the processes of energy relaxation from free to bound excitons of the order of 50 fs independently of well width and crystal orientation.

Acknowledgments.

This work was sponsored by CICYT and PRI-CAM Grants MAT-91-0201 and 170-92. The work at Columbia University was supported by the US Office of Naval Research.

References

1.- G. Bastard, C. Delalande, M.H. Meynadier, P.M. Frijlink, and M. Voos, Phys. Rev. B 29, 7042 (1984).
2.- F. Yang, M. Wilkinson, E.J. Austin, and K.P. O'Donnell, Phys. Rev. Let. 70, 323 (1993).
3.- See, for example, F. Meier and B.P. Zakharchenya, in *Optical Orientation, Modern Problems in Condensed Matter Sciences*, edited by V.M. Agranovich and A.A. Maradudin (North Holland, Amsterdam, 1984), Vol. 8, p. 1.
4.- L. Viña, T.C. Damen, J.E. Cunnigham, J. Shah, and L.J. Sham, Superl. and Microst. 12, 377 (1992).
5.- L. Viña, L. Muñoz, F. Calle, N. Mestres, J.M. Calleja, and W.I. Wang, Phys. Rev. B 46, 12234 (1992).
6.- T. Uenoyama and L.J. Sham, Phys. Rev. B 42, 7114 (1990).
7.- G. Bauer and T. Ando, Phys. Rev. B 38, 6015 (1988).
8.- M. Potemski, J.C. Maan, A. Fasolino, K. Ploog, and G. Weimann, Phys. Rev. Let. 63, 2409 (1989).
9.- G. Bastard, preprint.
10.- R. Planel and C. Benoit a la Guillaume, *ibid* Ref. 3, p. 355
11.- D.N. Mirlin, *ibid* Ref. 3, p. 133; I. Ya Karlik, D.N. Mirlin, L.P. Nikitin, D.G. Polyakov, and V.F. Sapega, JETP Lett. 36, 192 (1982).
12.- B.P. Zakharchenya, P.S. Kop'ev, D.N. Mirlin, D.G. Polakov, I.I. Reshina, V.F. Sapega, and A.A. Sirenko, Solid State Commun. 69, 203 (1989).
13.- A.H. MacDonald and D.D. Ritchie, Phys. Rev. B 33, 8336 (1986); M. Potemski, L. Viña, G.E.W. Bauer, J.C. Maan, K. Ploog, and G. Weimann, Phys. Rev. B 43, 14704 (1991)

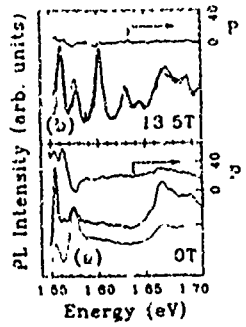

Fig. 1: Intensity (left axis) and degree of polarization (right axis) of the maximum of the photoluminescence as a function of the exciting energy at two different magnetic fields, for a 75 Å [111]-QW: (a) 0 T and (b) 13.5 T. The solid (dashed) PLE spectra were recorded in the $\sigma^+\sigma^+$ ($\sigma^+\sigma^-$) configuration

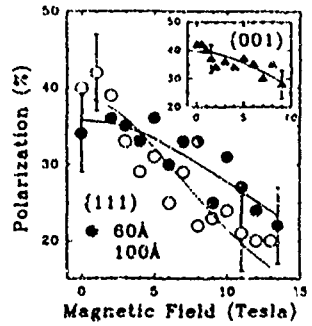

Fig. 2: Degree of polarization versus magnetic field for resonant excitation of the heavy-hole exciton in a 60-Å [111]-oriented QW (solid points) and in a 100-Å [111]-oriented QW (open points). The lines represent the best fit with Eq. 1. The inset shows the degree of polarization and the best fit for a 100-Å [001]-oriented QW

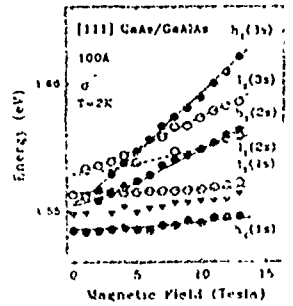

Fig. 3: Energies vs. magnetic field for σ^- excitation of the ground and excited state heavy-hole (solid: points) and light-hole (open points) excitons for a 100-Å [111]-oriented QW. The triangles depict the forbidden h_{1s} exciton. The full (dashed) lines show the result of the fits with a two dimensional excitonic model for the heavy-hole (light-hole) excitons.

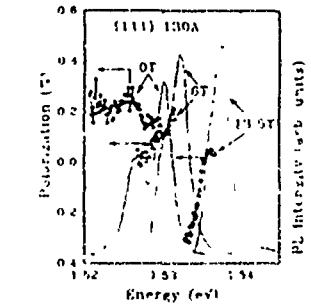

Fig. 4: Degree of polarization of the luminescence, as a function of the detection energy, for resonant excitation of the heavy hole excitonic-ground state, $h_1(1s)$ (left axis), and photoluminescence spectra exciting at 1.7 eV (right axis) for three different magnetic fields. The sample was grown in the [111] direction with a QW width of 130 Å

TuP8

Resonant Quenching of Exciton Photoluminescence in Coupled GaAs/AlAs Quantum Wells: Effect of Exciton Binding Energy

RARALD SCHNEIDER,[a] JOACHIM WAGNER,[a] AND KLAUS PLOOG[b]

[a] *Fraunhofer-Institut für Angewandte Festkörperphysik, Tullastr. 72, D-79108 Freiburg, Federal Republic of Germany*

[b] *Paul-Drude-Institut für Festkörperelektronik, Hausvogteiplatz 5-7, D-10117 Berlin, Federal Republic of Germany*

Abstract

We have studied the electric field dependence of the photocurrent and of the excitonic photoluminescence (PL) from the first and second conduction subband in weakly coupled GaAs/AlAs quantum wells. Resonant subband alignment between adjacent QW's results in a quenching of the PL intensity from the first subband, an enhancement of the PL from the second subband, and a maximum of the photocurrent. These resonant extrema are observed at slightly different electric fields. We show that this behavior arises from the different binding energies of intra- and inter well excitons.

Introduction

Sequential resonant tunneling processes between biased multiple quantum wells (MQW) have been studied by a variety of methods, including measurements of the steady state photocurrent (PC) [1-3], time dependent PC [3-5], steady state photoluminescence (PL) [2,3], time-dependent PL [6], and by optical pump/probe experiments [7]. What one usually observes is a resonance induced decrease of the PL intensity and decay time and a corresponding resonant increase of the PC and of the transport rates. In addition, this transport effect induces a non thermal carrier population of the final state, thus giving rise to additional PL emission lines involving higher subbands [8,9].

Relating these detection methods to each other, the conceptual question arises, which is the precise nature of resonant alignment that is probed using a specific detection method. Sequential resonant tunneling in a MQW of period d in an electric field F usually results from a resonant alignment of the *subband energies* E_1 and E_2, Fig. 1(a), giving rise to the resonance condition

$$eFd = E_2 - E_1 \tag{1}$$

However, if the transport behavior is probed by optical spectroscopy, the apparent resonance field may actually correspond to a different condition involving *exciton energies*. Two possible resonance configurations including exciton effects are indicated in Figs. 1(b) and 1(c).

Here E^d_{11}, E^i_{21}, E^d_{22}, and E^i_{12} are the binding energies of the spatially direct and spatially indirect e1-h1 and e2-h1 excitons, respectively. h1 denotes the first heavy hole subband.

As these binding energies are generally different, the resonance field for the situation of Fig. 1(b) is given by

$$|eFd| = E_{e2} - E_{e1} + E^d_{11} - E^i_{21}, \tag{2}$$

whereas the resonance in Fig. 1(c) corresponds to

$$|eFd| = E_{e2} - E_{e1} + E^d_{11} - E^d_{22}. \tag{3}$$

Since the binding energies E^d_{11} and E^d_{22} of the intra well excitons are expected to be larger than those of the inter well excitons E^i_{21} and E^i_{12}, the resonance in Fig. 1(b) occurs at a larger field than the resonance in Fig. 1(c), with the difference given by

$$\Delta F = \frac{1}{ed}(E^d_{22} - E^i_{21} + E^i_{21} - E^i_{12}). \tag{4}$$

We show in the following that each of the resonance conditions in Fig. 1 can be probed separately by appropriate detection methods, thus giving rise to different resonance fields.

Results and Discussion

For our experiments we use an undoped MQW structure with 50 periods of 12.3 nm GaAs wells and 2.1nm AlAs barriers. The MQW forms the intrinsic region of a p-i-n diode structure. The sample is illuminated by 647.1 nm radiation from a cw Kr-ion laser with a spot size of about 100 μm on the sample. The PL is measured using a triple monochromator and an intensified linear Si diode array detector.

The electric field F is calculated from the applied voltage V by using the equation $F = \alpha(V - V_{bi})/L$, with the MQW thickness $L = 0.78$ μm and the built-in voltage $V_{bi} = 1.35$ V. The field-screening parameter α was determined from the intensity dependence of the resonance field. We obtained $\alpha = 0.93$ and 0.76 at excitation powers of 0.06 mW and 0.3 mW, respectively. These values also give satisfactory agreement between the field dependences of the e1-h1 PL wavelength at different excitation powers.

PL spectra at different electric fields in the spectral region of the e1-h1 and e2-h1 transitions are shown in Figs. 2(a) and 2(b), respectively. The e1-h1 transition is observed at 1.539 eV at low fields and is Stark shifted with increasing field (1.508 eV at 116kV/cm). We note that the thermally populated light hole exciton forms a PL line at about 11 meV above the e1-h1 exciton. The e2-h1 transition is observed at 1.617 eV (66 kV/cm). A strong reduction of the e1-h1 PL intensity and a pronounced enhancement of the e2-h1 emission is observed at around 60 kV/cm where the tunneling resonance is expected.

In Fig. 3, we have plotted the field dependence of the e1-h1 and e2-h1 PL intensities, as obtained from a numerical integration of a similar series of PL spectra as shown above, but for 0.06 mW excitation power. The resonance maximum of the e2-h1 luminescence is observed to occur at clearly smaller fields than the resonance minimum of the e1-h1 luminescence. As indicated by the dashed lines, the difference between these resonance fields in Fig. 3 is about 7 ± 1 kV/cm. The data shown in Fig. 2 recorded with an a higher optical power of 0.3mW, indicate a similar difference (5 kV/cm) in the e1-h1 and e2-h1 resonance fields.

The field dependence of the PC, measured under identical experimental conditions as those of Fig. 3, is shown in Fig. 4. Under steady state conditions and at low intensity, the PC increases with increasing ratio between the transport and recombination rates. Therefore, the field value of 60 kV/cm, where the relevant maximum of the PC is observed, is associated with the tunneling resonance. This field value lies in between the resonance fields as obtained from the e1-hh1 PL and from the e2-hh1 PL, which are also indicated in Fig. 4. We note that the resonance maximum of the PC is less pronounced than the extrema of Figs. 2 and 3 since the PC saturates if the transit time becomes much smaller than the recombination time.

In Fig. 4, there are some additional structures which can also be observed in PL experiments [10]. The step-like structure in Fig. 4 at 5 kV/cm is related to miniband conduction. The step at around 32 kV/cm corresponds to phonon assisted tunneling. The increase of the PC above 160 kV/cm is partly due to enhanced non-resonant tunneling rates and to the e1-e3 resonance. It is not associated with avalanche multiplication processes which can only be observed above 220 kV/cm [5]. Previously, time-resolved measurements of the PC under pulsed optical excitation have been carried out [13] in order to determine directly the resonance field for photocarrier transport. Although essentially the same resonance fields have been obtained, the results are not directly transferrable to the present situation since the precise influence of the space-charges in both experiments is probably not identical. Space-charge effects are also expected to play a somewhat different role [10] in previous higher subband luminescence studies [8] performed under pulsed excitation.

We now develop a physical picture to relate the different experimental approaches to the alignment conditions of Fig. 1. In a photoconduction experiment, the resonance condition corresponds to the alignment of the conduction subbands (Fig. 1(a) and Eq. 1). This is due to the fact that most of the drifting carriers are located in free carrier states and not in exciton states. In addition, *only the free carriers induce a PC*, whereas the electrically neutral excitons cannot contribute to the PC.

Conversely, as the PL is excitonic in nature, *only the carriers located in the respective exciton states give rise to PL*. Now, for the intra-well e1-hh1 PL, the quenching is expected to be strongest when the respective exciton energy coincides with the energy of the spatially indirect e2-hh1 exciton. Therefore we expect that the situation outlined in Fig. 1(b) and Eq. (2) is relevant for the resonance minimum of the e1-hh1 PL intensity. Similarly, the enhancement of the e2-hh1 PL should occur if the energies of the intra-well e2-hh1 exciton and of the inter-well e1-hh1 excitons are in resonance, as shown in Fig. 1(c) (see also Eq. (3)). Indeed, the situation of Fig. 1(c) gives rise to an efficient population of the intra-well e2-hh1 exciton states by carriers that have formed spatially indirect e1-hh1 excitons. Carrier relaxation into inter-well e1-hh1 exciton states is important because of the relatively strong Coulomb-interaction [11], in spite of the small oscillator strength of these excitons.

The binding energies of inter-well excitons have been calculated by Fox et al. [11] for similar sample parameters (9.5 nm GaAs wells, 1.5 / 5.5 nm $Al_{0.3}Ga_{0.7}As$ barriers) with the result $E^{e}_{b1} \approx E^{hh}_{b1} \approx 3.6 \pm 1.7$ meV and $E^{e}_{b1+1} \approx E^{hh}_{b1+1} \approx 7.7 \pm 1$ meV. This gives rise to a difference in binding energy of [13] $(E^{e}_{b1+1} - E^{e}_{b1}) \approx (E^{hh}_{b1+1} - E^{hh}_{b1}) = 4.25 \pm 0.25$ meV. Adopting these values for the present situation, the theoretically expected field difference between the resonances shown in Figs. 1(c) and 1(b) (see Eq. (1)) is $\Delta F = 5.90 \pm 0.35$ kV/cm. This value is in quantitative agreement with the experimental value of 5.7 kV/cm.

In principle, resonant alignment between different subbands of adjacent wells induces a line splitting, which has been observed in MQW's with a stronger inter-well coupling [11-13] than in the present case. In those *strongly coupled* MQW structures, the resonance field where this line splitting is most pronounced, depends on the particular excitonic transition under study. The reason for this effect also arises from differences between the binding energies of the participating excitons [11,13]. Such a splitting cannot be observed in the present case since the spectral width of the transitions involved exceeds the expected line splitting. However, in these *weakly coupled* MQW's, the coupling between adjacent wells still has a strong influence on carrier transport. Therefore, the resonance splitting of the strongly coupled system translates into characteristic transport effects. Analogous signatures of different exciton binding energies are thus observed when the respective exciton states are probed in PL measurements.

Conclusion

We have presented a detailed study of the electric field dependence of the photocurrent of the e1-hh1 PL, and of the e2-hh1 PL in a weakly coupled GaAs/AlAs MQW. Resonantly enhanced tunneling rates give rise to a maximum of the photocurrent, to a minimum of the e1-hh1 PL intensity, and to a maximum of the e2-hh1 PL intensity. These resonance effects are observed at different fields. This difference in the resonance fields has been shown to be a consequence of the different binding energies of intra- and inter-well excitons. Consequently, the measured resonance field does not only depend on the subband spacing and on the MQW period, *but also on the experimental detection method*.

Acknowledgements

The authors are grateful to P. Kordl (Freiburg) for the encouragement of this work. We also acknowledge partial support by the Bundesministerium für Forschung und Technologie.

References

[1] F. Capasso, K. Mohammed, and A. Y. Cho, Appl. Phys. Lett. **48**, 478 (1986).

[2] S. Tarucha, K. Ploog, and K. v. Klitzing, Phys. Rev. B **36**, 4558 (1987).

[3] S. Tarucha and K. Ploog, Phys. Rev. B **38**, 1998 (1988).

[4] H. Schneider, K. v. Klitzing, and K. Ploog, Superlatt. Microstruct. **5**, 481 (1989).

[5] H. Schneider, K. v. Klitzing, and K. Ploog, Europhys. Lett. **8**, 575 (1989).

[6] *H. Schneider, W. W. Rühle, K. v. Klitzing, and K. Ploog, Appl. Phys. Lett. 54, 2656* (1989).

[7] G. Livescu, A. M. Fox, D. A. B. Miller, T. Sizer, W. H. Knox, A. C. Gossard, and J. H. English, Phys. Rev. Lett. **63**, 438 (1989).

[8] H. T. Grahn, H. Schneider, W. W. Rühle, K. v. Klitzing, and K. Ploog, Phys. Rev. Lett. **64**, 2126 (1990).

[9] H. T. Grahn, W. W. Rühle, and K. Ploog, SPIE Vol. 1675 Quantum Well and Superlattice Physics IV, edited by G. H. Döhler and E. S. Koteles *36 (1992)*

[10] H. Schneider, J. Wagner, and K. Ploog, Phys. Rev. B, to appear.

[11] A. M. Fox, D. A. B. Miller, G. Livescu, J. E. Cunningham, and W. Y. Jan, Phys. Rev. B **44**, 6231 (1991); A. M. Fox, D. A. B. Miller, J. E. Cunningham, W. Y. Jan, C. Y. P. Chao, and S. L. Chuang, Phys. Rev. B **46**, 15365 (1992).

[12] H. Schneider, H. T. Grahn, K. v. Klitzing, and K. Ploog, Phys. Rev. Lett. **65**, 2720 (1990).

[13] A. M. Fox, D. A. B. Miller, G. Livescu, J. E. Cunningham, J. E. Henry, and W. Y. Jan, Phys. Rev. B **42**, 1841 (1990).

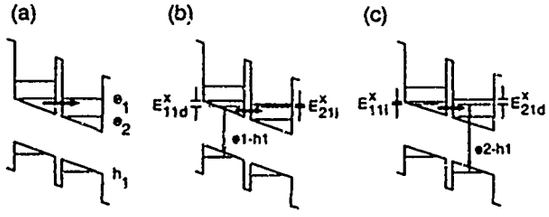

Figure 1: Schematics of resonant alignment of (a) the e1 and e2 subbands, (b) the intra-well e1-h1 and the inter-well e2-h1 excitons, and (c) the intra-well e2-h1 and the inter-well e1-h1 excitons in weakly coupled quantum wells. Dashed lines mark the energies of the excitons involving the h1 subband located in (b) the left quantum well and (c) the right quantum well, as counted from the respective valence subband energy. E_{11}^{x}, E_{11}^{x}, E_{21}^{x}, and E_{21}^{x} are the binding energies of the spatially direct and spatially indirect e1-h1 and e2-h1 excitons, respectively (not to scale). Vertical arrows indicate the e1-h1 and e2-h1 PL.

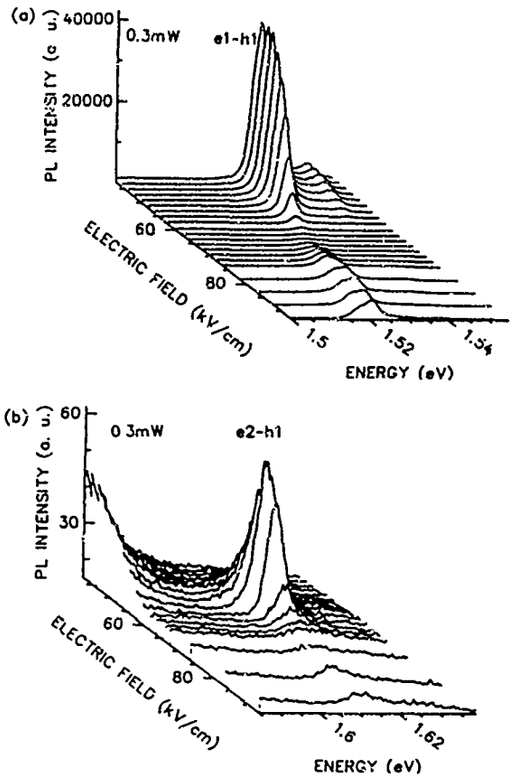

Figure 2: Quasi-3D plot of PL spectra showing the spectral regions of the (a) e1-h1 and (b) e2-h1 transitions as a function of electric field at 77 K and an excitation power of 0.3mW.

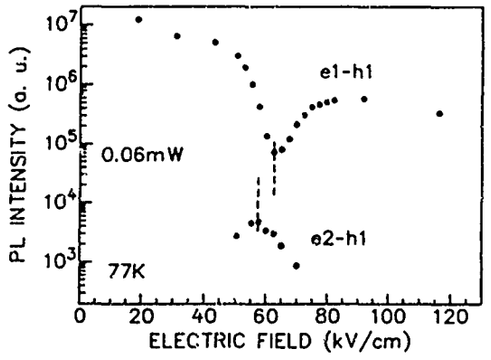

Figure 3: PL intensities of the e1-h1 and e2-h1 transitions at 0.06 mW excitation power versus electric field. The dashed lines indicate the resonance extrema.

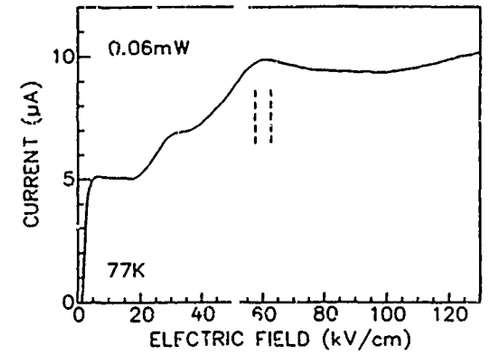

Figure 4: PC versus electric field at 0.06 mW excitation power. The dashed lines indicate the observed resonance extrema of the e2-h1 and e1-h1 PL intensities.

TuP9

PRESSURE DEPENDENCE OF PHOTOLUMINESCENCE IN $In_xGa_{1-x}As/Al_yGa_{1-y}As$ STRAINED QUANTUM WELLS WITH DIFFERENT WIDTHS

Zhen-Xian Liu, Guo-Hua Li, He-Xiang Han and Zhao-Ping Wang

National Laboratory for Superlattices and Microstructures
Institute of Semiconductors, Chinese Academy of Sciences
P. O. Box 912, Beijing 100083, P. R. China

Abstract

A systematic investigation on the photoluminescence (PL) properties of $In_xGa_{1-x}As/Al_yGa_{1-y}As$ ($x=0.15$, $y=0$, 0.33) strained quantum wells (SQWs) with well widths from 1.7 to 11.0 nm has been performed at 77K under high pressure up to 40 kbar. The experimental results show that the pressure coefficients of the exciton peaks corresponding to transitions from the first conduction subband to the heavy-hole subband increase from 10.05 meV/kbar of 11.0 nm well to 10.62 meV/kbar of 1.8 nm well for $In_{0.15}Ga_{0.85}As/GaAs$ SQWs. However, the corresponding pressure coefficients slightly decrease from 9.93 meV/kbar of 9.0 nm well to 9.73 meV/kbar of 1.7 nm well for $In_{0.15}Ga_{0.85}As/Al_{0.3}Ga_{0.7}As$ SQWs. Calculations based on the Kronig-Penney model reveal that the increased or decreased barrier heights and the increased effective masses with pressure are the main reasons of the change in the pressure coefficients.

Introduction

There is currently much interest in strained quantum wells (SQWs) and superlattices, in which the lattice mismatch between layers is accommodated by the coherent elastic strain.[1] This leads to a change in the band gap and a splitting of the valance band at the Γ point. Therefore the properties of SQWs are different from those of lattice-matched quantum wells, such as GaAs/AlGaAs QWs. The study of PL under high pressure at 77K[2,3] showed that the pressure coefficients of the exciton peaks corresponding to transitions from the first conduction subband to the heavy-hole subband for $In_xGa_{1-x}As/GaAs$ SQWs decreased with increased well width, which is contrary to that of $GaAs/Al_yGa_{1-y}As$ QWs.[4] Therefore, it will be interesting that what is happened for $In_xGa_{1-x}As/Al_yGa_{1-y}As$ SQWs?

In this paper, we report systematic investigations of PL measurements on $In_{0.15}Ga_{0.85}As/Al_yGa_{1-y}As$ SQWs with different well widths at 77K under high pressure up to 40 kbar. We found a slight increase in the pressure coefficient of the exciton peak with increased well width for $In_{0.15}Ga_{0.85}As/Al_{0.33}Ga_{0.67}As$ SQWs, which is in contrast to the case of $In_{0.15}Ga_{0.85}As/GaAs$ QWs. Calculations based on the Kronig-Penney model reveal that the increased or decreased barrier heights and the increased effective masses with pressure are the main reasons of the change in the pressure coefficients. The calculated results are in good agreement with the experimental data.

Experimental

The samples used in this study were prepared by molecular-beam-epitaxy (MBE). A 0.5-μm-thick buffer layer of GaAs was first grown on (001)-oriented GaAs substrate, then followed by five $In_{0.15}Ga_{0.85}As/Al_yGa_{1-y}As$ SQWs with the well-width sequences of 11.0, 7.0, 4.6, 2.6, and 1.8 nm for $y=0$ and 9.0, 6.0, 4.0, 2.4, and 1.7 nm for $y=0.33$ along the growth direction, respectively, where the thicknesses of barrier layers are always 30 nm to prevent coupling between wells. Finally a 30-nm GaAs layer capped the structure.
The samples were mechanically thinned from the backside to approximately 20μm and cleaved into 100×100 μm^2 square. The samples were loaded into a gasketed diamond-anvil cell, together with a piece of ruby to act as pressure gauge.[5] Pressure calibration was also done by the shift of the GaAs substrate band gap.[6] This gives a high accuracy in the pressure determination and reliable coefficients can thus be obtained. Argon was used as a pressure medium in order to ensure hydrostatic conditions. The PL measurements were performed at 77K on a micro-optical system. PL was excited by the 488.0 nm line of an Ar^+ laser, and dispersed by double monochromator, and detected by a photomultiplier and a photon counting system.

Results and Discussion

The PL spectra of $In_{0.15}Ga_{0.85}As/GaAs$ and $In_{0.15}Ga_{0.85}As/Al_{0.33}Ga_{0.67}As$ SQWs at 77K and different pressures are shown in Figures 1(a) and 1(b). The value of the pressure is indicated at the corresponding spectrum and the PL intensities are normalized according to the strongest peak. In the spectra, the transitions between the first conduction subband and heavy-hole subband are labelled with E_i ($i=1$-5) for five SQWs, respectively. The peak, E_s, is attributed to emission from the GaAs substrate. With increasing pressure, the relative intensities of the peaks in Fig. 1(a) change dramatically but the absolute intensities of the narrow wells does not decrease obviously. On the other hand, the relative intensities of the

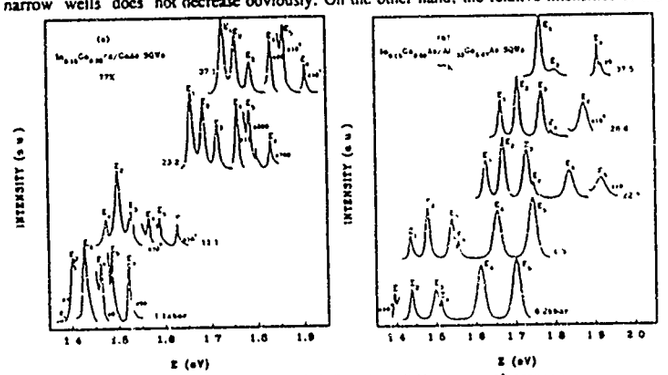

Fig. 1. 77K PL spectra for $In_{0.15}Ga_{0.85}As/Al_yGa_{1-y}As$ SQWs at several pressures.
(a) $In_{0.15}Ga_{0.85}As/GaAs$ (b) $In_{0.15}Ga_{0.85}As/Al_{0.33}Ga_{0.67}As$

peaks in Fig. 1(b) change drastically with increasing pressure and the intensities of the narrow wells become too weak to be observed under higher pressure. This rapid decrease attributes to the Γ-X subband crossover in the quantum-well structures.
Figures 2(a) and 2(b) show the dependence of the transition energy on pressure for each QW for $In_{0.15}Ga_{0.85}As/GaAs$ and $In_{0.15}Ga_{0.85}As/Al_{0.33}Ga_{0.67}As$ SQWs, respectively. The solid lines are least-squares fits to the experimental data giving a linear function:

$$E_i(P)=E_i(0)+\alpha_i P, \tag{1}$$

where the energies are in eV and the pressure P is in kbar and the factor α_i is the linear pressure coefficient. Figure 3 shows the linear pressure coefficients (solid symbols) obtained from the SQWs data in Figs. 2(a) and 2(b) as a function of the well width. It can be seen that the well-width dependencies of these two kinds of SQWs have clearly different trends. For $In_{0.15}Ga_{0.85}As/GaAs$ SQWs the pressure coefficients decrease with increased well width, while those of $In_{0.15}Ga_{0.85}As/Al_{0.33}Ga_{0.67}As$ SQWs slightly increase. The transition energy of a SQW can be expressed as

$$E_{PL}=E_g+E_{1e}+E_{1h}-E_{ex}, \tag{2}$$

where E_g is the band gap of the well material, E_{1e} and E_{1h} are the confined energies of electrons and heavy holes, respectively, and E_{ex} is the exciton binding energy. Thus the pressure dependencies of these parameters determine to the change of the pressure coefficient with well width. We have used the Kronig-Penney model[7] to calculate the well-width dependence of the pressure coefficients for the two studied samples, in which several main effects have to be considered. Firstly, the well width diminishes with the pressure and the pressure dependence of the well width L_z can be obtained from the elasticity theory:

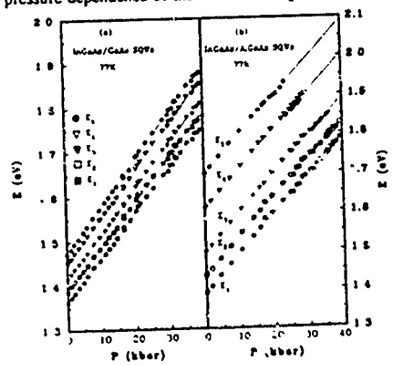

Fig. 2 Pressure dependence of the peak energies for $In_{0.15}Ga_{0.85}As/Al_yGa_{1-y}As$ SQWs.
(a) $In_{0.15}Ga_{0.85}As/GaAs$ SQWs
(b) $In_{0.15}Ga_{0.85}As/Al_{0.33}Ga_{0.67}As$ SQWs

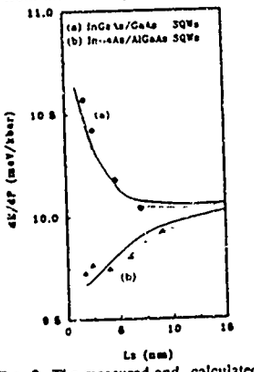

Fig. 3. The measured and calculated pressure coefficients in SQWs as a function of well width. The solid and dashed lines are the calculated results

$$L_z(P) = L_z(0)[1-(S_{11}+2S_{12})P], \quad (3)$$

where S_{11} and S_{12} are the elastic constants of the well material. Secondly, the well and barrier materials have different pressure coefficients. In the calculations, we take the pressure coefficients for GaAs and $Al_{0.33}Ga_{0.67}As$ as 10.73 meV/kbar[4] and 9.8 meV/kbar,[4] respectively. The experimental pressure coefficients for $In_{0.15}Ga_{0.85}As$ have not been reported to date. Here we take the value as 10.1 meV/kbar. If we suppose the valance-band offset does not change with pressure, the pressure-induced change of the barrier height can be expressed as

$$V(P) = V(0)+(\alpha_B-\alpha_W)P, \quad (4)$$

where α_B and α_W are the pressure coefficients of the barrier and well materials, respectively. In the case of $In_{0.15}Ga_{0.85}As/GaAs$ SQWs, the barrier height will increase with pressure since $\alpha_B > \alpha_W$, while those of the $In_{0.15}Ga_{0.85}As/Al_{0.33}Ga_{0.67}As$ SQWs will decrease with pressure. Finally, the size quantization and the change of the gaps with pressure lead to an increase of the effective masses in the well and in the barriers. This change can be expressed by Kane's three bands model:[8]

$$\frac{m_i(P)}{m_i(0)} = \frac{E_{gi}+\alpha_i P}{E_{gi}} \cdot \frac{E_{gi}+\Delta_i+\alpha_i P}{E_{gi}+\Delta_i} \cdot \frac{2\Delta_i+3E_{gi}}{2\Delta_i+3(E_{gi}+\alpha_i P)} \quad (5)$$

where E_{gi} is the band gap, Δ_i the spin-orbit energy splitting, and i stands for B and W in barrier and well, respectively. As the pressure-induced change of E_{gi} is very small, it can be neglected. After numerical calculation of the confined energy for electrons and heavy hole at $P_i = 4i$ kbar (i=0-10), we obtained the pressure coefficients of the PL-peaks energies according to the least-squares fits to the calculated data. The calculated coefficients for $In_{0.15}Ga_{0.85}As/Al_xGa_{1-x}As$ SQWs are also indicated in Fig. 4 by the solid curves. It can be seen that the results are in good agreement with the experimental data. The dashed lines in Fig. 4 represent the calculated results in which the compression of well width does not considered. These lines are very close to the corresponding solid lines, respectively. It implies that the influence of the well-width compression on the pressure coefficients can be neglected.

[1] G. C. Osbourn, P. L. Gourley, I. J. Fritz, R. M. Biefeld, L. R. Dawson, and T. E. Zipperian, Semicond. Semimet. 24, 459(1987).
[2] H. Q. Hou, L. J. Wang, R. M. Tang, and J. M. Zhou, Phys. Rev. B42, 2926(1990).
[3] G. H. Li, B. Z. Zheng, H. X. Han, Z. P. Wang, T. G. Andersson, and Z. G. Zhen, Phys. Rev. B45, 3489(1992).
[4] U. Venkateswaran, M. Chandrasekhar, and H. R. Chandrasekhar, Phys Rev. B33, 8416(19286).
[5] H. K. Mao, J. Xu, and P. M. Bell, J. Geophys Res. 91, 4673(1986).
[6] D. J. Wolford and J. A. Bradley, Solid State Commun. 53, 1069(1985).
[7] H. S. Cho and P. R. Prucnal, Phys. Rev. B36, 3237(1987).
[8] E. O. Kane, Semiconductors and Semimetals, Academic, New York, Vol. 1. (1966).

TuP10

Optical Transitions in GaAs/AlAs Superlattices with Different Miniband Widths

K. Fujiwara, K. Kawashima,* T. Yamamoto* and K. Ploog°
Kyushu Institute of Technology, Tobata, Kitakyushu 804, Japan
*ATR Optical and Radio Communi Res Lab., Sorakugun, Kyoto 619-02
°Paul-Drude-Institut für Festkörperelektronik, O-1086 Berlin

Abstract

Band edge optical transitions and their external - ectric field effects are systematically studied in GaAs/AlAs superlattices with different miniband widths (2Δ) by low temperature photocurrent spectroscopy. Distinct H excitons related with saddle-type M_1 critical points at the miniband top are clearly observed both for heavy-hole and light-hole excitons. Under the applied field strength F, discrete transitions due to Wannier-Stark localization are observed and it is found their intensities of n^{th} order stark ladder transitions with negative indices show F^{2n} and Δ^n dependences in agreement with the field theory.

Introduction

Optical transitions involved with excitons in semiconductor superlattices (SL) and quantum wells (QW) have been attracted great attention[1]. One of the interesting properties of SL compared to QW is the tunability of miniband widths (2Δ) by designing the layered structures and, as a result, controlling quantum mechanical tunnelling. From the previous studies of optical absorption in $GaAs/Al_xGa_{1-x}As$ SL, it is known that there are various types of fine structures originating from miniband dispersions [2-5], stark ladders [6-9], and Franz-Keldysh oscillations [10]. However, attribution of such fine structures observed by one author is not always consistent with others' data, possibly because of non-uniform sample qualities and different experimental conditions. Therefore, basic studies of optical transitions in SL and especially their relevance to miniband widths are important for understanding of the origins of the absorption spectral features. In this paper, optical absorption spectra are investigated in a series of GaAs/AlAs SL with different well and barrier parameters, thus varying the miniband width systematically, by means of low temperature photocurrent (PC) spectroscopy. Direct spectroscopic evidences are provided for the miniband dispersion effects which show excitonic effects originating from the miniband bottom (M_0) and miniband top (M_1) critical points. We have also studied the external field effects as a function of both field strength F and miniband width Δ. It is shown that

the observed energies and oscillator strengths of the Stark ladder transitions are in good agreement with those predicted by the exact binding theory.

Experimental

High-quality GaAs-AlAs SL samples were grown on n-type GaAs (001) substrates by molecular beam epitaxy (MBE) in a fully computer-controlled system. The nominally undoped SL layer is contained in the intrinsic layer of p-i-n diodes[9]. Two series of seven SL samples are studied in this work. A first series consisted of AlAs barriers with a thickness of 5.6 Å and GaAs wells whose width was ranged from L_z=62.6 Å (#1) 39.2 Å(#2), 31.3 Å(#3) to 25.1 Å(#4). Another series consisted of GaAs wells with a width L_z=3.3 Å and AlAs barriers ranged from L_B=5.7 Å(#5) 3.5 Å(#3), 11.4 Å(#6) to 7.3 Å(#7). The sample #3 is common in the two series. The SL period was measured by small-angle X-ray diffraction experiments which were used to estimate nominal values of well and barrier parameters. The 100-period SL layers were confined between $Al_{0.4}Ga_{0.6}As$ cladding layers in the Schottky structure. PC experiments were performed around ~ 6 K in the closed-loop-helium cryostat using a combination of tungsten-halogen lamp and monochromator for excitation and a standard electrometer for dc detection.

Results and discussion

Figure 1 shows PC spectra of the SL diode samples #1(a), #2(b), #3(c) and #4(d) for L_z variations. Solid curves correspond to the spectra measured near the flat-band conditions (forward bias conditions), while dashed ones under a reverse bias voltage (VB) of 10 V. In the solid PC spectra sharp absorption thresholds are observed. The threshold wavelength (energy) decreases (increases) from the spectra (a) to (d) as the GaAs well width L_z decreases. At the absorption edge a sharp peak (indicated by left upwards arrows) is observed in the spectra (a)-(d) indicating excitonic effects for the optical transitions. Beside the leading absorption peak, several peaks and/or shoulders are also seen in the solid spectra of Fig. 1. A secondly sharper peak (indicated by left downwards arrows) is observed next to the leading peak. Relatively broader peaks or shoulders (indicated by right arrows) are located at shorter wavelengths (higher energies). On the other hand, when the external electric field is applied along the growth z-axis, a number of new fine structures appear as shown in the dashed spectra. First we note that in the dashed curves a main steep edge appears at shorter wavelength sides of the threshold peak in the corresponding solid spectra and that the energy separation between them increases with decreasing L_z. Secondly, weaker edges are also seen in the dashed spectra of (b) to (d) at the longer wavelength. Their intensity increases with decreasing L_z.

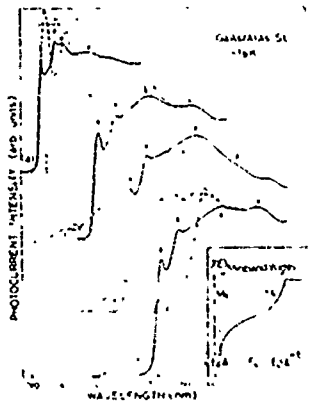

Fig. 1 Photocurrent spectra of GaAs/AlAs SL samples at ~16 K (a) #1, (b) #2, (c) #3 and (d) #4. Solid spectra are corresponding to those near the flat-band conditions (forward bias of +1 V except for #1 (+1.5 V)), while dashed ones under the reverse bias voltage of -10 V. Spectra are vertically shifted for clarity. Solid (dashed) horizontal bars are calculated wavelength ranges of valence-to-conduction subband transitions associated with heavy-holes (light-holes). An inset figure shows Van Hove singularities in the joint-density of states (JDS) (M_0 singularity at E_0-Δ and M_1 saddle-type at E_0-Δ).

The experimental results observed in Fig. 1 can rigorously be explained by the miniband dispersion effects as discussed below. In the SL structure, we have a slightly different energy scheme for the optical transitions from the QW as schematically illustrated in the inset of Fig. 1. When the barrier thickness is thin enough so that the inter QW layer coupling is enhanced, we have more three dimensional characters for the subbands. That is, the miniband is formed along the growth direction whose bandwidth 2Δ is basically determined by the SL structural parameters, L_z and L_B. In this case we have Van Hove singularities of M_0 type at the miniband bottom and of M_1 type at the upper edge. In order to more quantitatively show the effects of inter-well-coupling on the transition energies, the theoretical energies of the interband transitions are calculated using the Krönig-Penney model within the effective mass approximation[5]. The expected wavelength range for the transitions are indicated in Fig. 1 by horizontal solid (dashed) bars for the heavy-hole (light-hole) related transitions. Good relationship is observed between experimental and calculated values in spite of neglecting exciton effects. The sharper two leading peaks near the threshold in the solid spectra are therefore assigned to heavy-hole (HH) and light-hole (LH) Γ excitons associated with the miniband bottoms. On the other hand, the high energy structures observed in the solid curves of Fig. 1 are attributed to the Π excitons which are associated with the M_1 Van Hove singularity[3]. Peaked nature of the optical absorption indicates excitonic effects for their origins of the HH-related as well as LH-related transitions. We would like to stress that

the peaks of high energy Γ excitons and low energy Γ excitons show excellent correlation with the calculated miniband width. At the best of our knowledge, the peaked structures in optical absorption spectra are the first observed for the saddle point Γ exciton. Although not shown, we have also studied SL samples for L_b variations. It is found that the transition energies and their barrier thickness dependence are in excellent agreement with those predicted by the simple theory for both Γ and Γ excitons [11].

The external field effect on the PC spectra is rigorously explained by Wannier-Stark localization [6-8]. We have measured PC spectra as a function of F for each SL samples and evaluated the transition energies and their intensities in details. The observed transition energies are found to evolve as $E(n)=E_n+neFD$ as expected for the Stark ladder transitions. Here E_n is the eigenenergy of an isolated QW, n is a Stark ladder index (n=0, ±1, ±2 ---), and D is L_w+L_b. This confirms our attribution of the observed optical transitions under the applied field to Stark ladder transitions. In the dashed spectra of Fig. 1, the threshold peaks at longer wavelengths are attributed to the -1st and 0th order Stark ladder exciton transitions, as indicated by dashed vertical bars. From the energy difference between the localized QW (n=0) and the SL Γ exciton transitions, we estimate half of the experimental miniband width, Δ_{exp}, to be 15 (5 Å), 35 (8 Å), 68 (6 Å), and 73 (8 Å) meV. We neglected the difference of the exciton binding energy between the two cases [5]. We note that this Δ_{exp} value gives a lower limit for Δ because of the smaller binding energy for the SL exciton.

In order to show field-induced variations of the oscillator strength of the Stark ladder transition, the relative intensity (I_{-1}/I_0) of the -1st order Stark ladder transition normalized by the 0th order transition is plotted in Fig. 2 for L_b series of SL samples (L_b=5.7 Å (#5), 5.6 Å (#3), 11.4 Å (#6) and 17.3 Å (#7)) as an example. In Fig. 2(a), a plot is given as a function of eFD. The field strength F is calculated by $(V_b-V_0)/L$ where V_0 is the built-in voltage and L is the width of the intrinsic layers. For SL samples with thicker L_b, the intensity of the -1st order transition decreases more rapidly with F because of the weaker tunnelling probability. According to the tight-binding theory by Bleuse, Bastard, and Voisin [7], the oscillator strength of the nth order transition with negative indices is approximated by $I_{-n}/I_0 \propto [J_n(-\Delta/(eFD))]^2 \propto [(\Delta/(2eFD))^n/(n!)]^2$ in the high field limit where J_n is the Bessel function of integer index n and Δ is a sum of conduction and valence miniband half widths. Solid curves in (a) are the expected theoretical dependences assuming the Δ_{exp} values. In spite that we neglect theoretical exciton effects, good correlation is obtained between the two dependences. It is worth to mention that the observed Δ dependence of the ratios I_{-1}/I_0 is correctly accounted

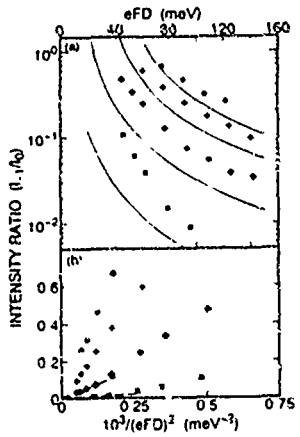

Fig. 2 Relative oscillator strength of the -1st order Stark ladder transition normalized by the 0th order transition I_{-1}/I_0 vs (a) eFD and (b) $10^3/(eFD)^2$ for SL samples #5(●, Δ_{exp}=15 meV), #3(◇, 68 meV), #6(◆, 35 meV) and #7(×, 73 meV). Solid curves in (a) indicate the theoretical ones calculated by the exact Bessel function. Dotted and dashed lines in (b) indicate least-squares fitting for the majority of closed symbols and a few points at the highest field regimes, respectively.

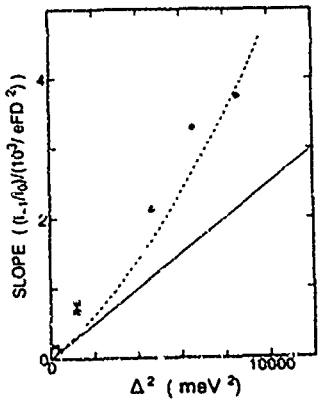

Fig. 3 Slope of the field-induced variations of the transition intensity ratio I_{-1}/I_0 vs square half of the miniband width, Δ^2. The theoretical slopes calculated by the asymptotic and exact Bessel functions are indicated by a solid line and a dashed curve, respectively at the experimental mean fields. Data points are for #1(×), #2(✱), #3(▲), #4(○), #7(▼), #6(□) and #5(●).

for by the theory. We expect in the extreme high field limits, inverse quadratic dependence of I_{-1}/I_0 on eFD so that another plot is also given in (b) as a function of $10^3/(eFD)^2$. It is clearly shown in Fig. 2(b) that the oscillator strength ratios I_{-1}/I_0 exhibit the expected F^{-2} dependence being quite consistent with the theory. Furthermore, we also evaluated the ratios I_{-n}/I_0 for higher nth order Stark ladder transitions and confirmed the theoretical F^{-n} dependences in general [12]. The slope of $10^3/(eFD)^2$ dependence in Fig. 2(b) which should be a function of Δ is consistent with the theory and in fact found to be steeper for larger Δ values. In Fig. 3, the experimental slope in the high field limit is plotted as a function of Δ^2 to test the theoretically expected dependence for all the SL samples investigated. A solid curve indicates the theoretical quadratic dependence on Δ given by $\Delta^2/4$. This quadratic dependence is in good

agreement with the observed for the narrow Δ samples. If we use the exact Bessel function for the slope (indicated by a dashed curve) better agreement is obtained for the absolute values when the slope is evaluated at the experimental mean fields. The results given above show that the relative oscillator strength of the Stark ladder transitions basically depends on Δ, being consistent with the theory. Moreover, the F^{-n} dependence of the relative transition intensity is valid over the wide range of the SL miniband widths studied.

In summary, miniband edge optical transitions and their variations with the external field are investigated in photocurrent spectra of GaAs/AlAs p-i-n diode superlattices with different miniband widths. Distinct spectral features of the Π excitons due to the saddle-type M_1 singularity are directly observed in absorption spectra. Excellent correlation with the miniband width is obtained between the experimental and theoretical transition energies both for heavy-hole and light-hole excitons under the applied field. Stark ladder transitions are clearly observed over a wide range of well and barrier parameters, and F^{2n} and Δ^2 dependences of their relative oscillator strengths are observed and explained with the tight binding theory.

Acknowledgments

This work was supported in part by Scientific Research Grant-in-Aid No 63604109 from the Ministry of Education, Science and Culture of Japan.

References

1 See for example, the special issue of Optical and Quantum Electronics, eds. A. M. Glass and F. K. Schubert (Chapman & Hall, London, 1990) Vol. 22, p. s1-268.
2 H. Shen, S. H. Pan, F. H. Pollak, M. Dutta and F. P. DeCola, Phys. Rev. B38, 3351 (1988).
3 J. I. Song, P. S. Yoon, H. Cho and Y.-W. Choe, Phys. Rev. B38, 5562 (1988).
4 B. Deveaud, A. Chomette, F. Clerot, A. Regreny, J. C. Maan, K. Rodes, and G. Bastard, H. Cho and Y.-C. Chang, Phys. Rev. B40, 5802 (1989).
5 K. Fujiwara, N. Tsukada and K. Ploog, Solid State Commun. 72, 383 (1989).
6 E. E. Mendez, F. Agullo-Rueda and J. M. Hong, Phys. Rev. Lett. 60, 2426 (1988).
7 J. Bleuse, G. Bastard and P. Voisin, Phys. Rev. Lett. 60, 220 (1988).
8 H. Schneider, K. Fujiwara, H. T. Grahn, K. v. Klitzing and K. Ploog, Appl. Phys. Lett. 56, 605 (1990).
9 K. Kawashima, K. Fujiwara, T. Yamamoto, M. Sweeny and K. Kobayashi, Surf. Sci. 267, 643 (1992).
10 H. Schneider, A. Fischer and K. Ploog, Phys. Rev. B45, 6329 (1992).
11 K. Fujiwara, K. Kawashima and T. Yamamoto, Japan. J. Appl. Phys. 32, 1321 (1993).
12 K. Kawashima, T. Yamamoto, K. Kobayashi and K. Fujiwara, Phys. Rev. B47, 9925 (1993).

TuP11

Electromodulation Spectroscopy Study of a GaAs/GaAlAs Asymmetric Triangular Quantum Well Structure

Y-S. Huang and W.S. Chi
Department of Electronic Engineering, National Taiwan Institute of Technology
Taipei, Taiwan, Republic of China
and
H. Qiang* and Fred H. Pollak*
Department of Physics, Brooklyn College of the City University of New York
Brooklyn, NY 11210, USA
and
D.L. Mathine and G.N. Maracas
Department of Electrical Engineering, Arizona State University
Tempe, AZ 85287, USA

ABSTRACT

Using the contactless electromodulation methods of photoreflectance and contactless electroreflectance we have studied the intersubband transitions from a (001) GaAs/GaAlAs asymmetric triangular quantum well (ATQW) structure at 300K and 80K. The sample was fabricated by molecular beam epitaxy using a digital alloy composition grading (DACG) method. Comparison of the observed intersubband resonances with a theoretical calculation (envelope function method) provided a self-consistent verification that the DACG produced the intended result, i.e., an effective linearly graded profile. An external uniaxial stress along [100] was used to confirm the the heavy-or light-hole nature of some of the spectral features. Furthermore, the temperature dependence of both the energy and broadening parameter {Γ(T)} of the fundamental conduction to heavy-hole exciton feature were investigated in the wide temperature range 10K < T < 450K. These observations, particularly the anomalous behaviour of Γ(T), will be compared to recent results for GaAs/GaAlAs symmetric rectangular quantum wells of comparable dimensions.

I. INTRODUCTION

Graded bandgap materials are of great importance in band-gap engineering and are being widely used in photodetectors, lasers, heterojunction bipolar transitors, etc. For example, although rectangular quantum wells have been extensively employed as active regions of opto-electronic devices, they have certain limitations. These symmetrical rectangular quantum wells (SRQW) have an overlap integral betwen the fundamental conduction and heavy-hole wavefunctions that are very close to unity when no electric field is applied. However, in most opto-electronic devices the quantum well is subjected to internal and external fields from the device that decrease this overlap because of the separation of the particles. This reduction in the ovelap integral creates a correponding reduction in the emission or absorption process. In novel quantum well designs, such a those containing compositional gradients, there exist the potential for increasing this overlap. Therefore, such novel quantum well structures should increase the absorption or emission process in opto-electronic devices. Recently, arbitrary shaped quantum wells have been implemented by molecular beam epitaxy (MBE) in such devices with an emphasis in asymmetric triangular quantum wells (ATQW) [1-6].

In this paper we report a study of the intersubband transitions from a (001) GaAs/GaAlAs ATQW structure at 300K and 80K using photoreflectance (PR)[7-8] and contactless electroreflectance (CER)[9]. These modulation methods have proven to be extremely useful in the investigation and characterization of semiconductor microstructures. The sample was fabricated by molecular beam epitaxy (MBE) using a digital alloy composition grading (DACG) method. A number of *mn*H(L) intersubband features were observed in the spectra, where *mn*H(L) denotes a transition from the m^{th} conduction to n^{th} valence subband of heavy(H)- or light(L)-hole character. The envelope function approximation[10] was used to calculate the bound energy states using the DACG profile determined from the growth conditions. Comparison of the observed ATQW resonances with the theoretical calculation provided a self-consistent check of the ATQW composition profile. A comparison of the energy levels with the properties of a linearly graded

well (LGW)[11] also will be presented. The heavy- or light-hole nature of various transitions was verified by a uniaxial stress ($\vec{S}$) experiment for $\vec{S}\|[100]$. Furthermore, the temperature dependence of both the energy position and broadening parameter [$\Gamma(T)$] of the 11H exciton feature were investigated in the wide temperature range 10K<T<450K. These observations, particularly the anomalous behaviour of $\Gamma(T)$, will be compared to results for III-V and II-VI SRQWs of comparable dimensions[12-16]. We found no evidence for Franz-Keldysh oscillations due to the quasielectric field in the ATQW, as recently reported on DACG structures[5]. Our spectra were due to intersubband transitions, similar to the electron beam electroreflectance experiment on a LGW.[11]

II. EXPERIMENTAL DETAILS

The ATQW used in this study was fabricated by the DACG method, which approximates the alloy composition profile by using alternating layers of $Ga_{1-x}Al_xAs$ and GaAs where the ratio of layer thicknesses produces an average alloy composition. The average Al composition in an alloy cell (typically 25-30Å) is approximated by shuttering the Al effusion cell such that the thickness of a layer of GaAlAs centered in the alloy cell provides enough Al to equal the required Al composition. The average Al composition in such a cell is given by:

$$\langle x_i \rangle = (d_i/t)x \tag{1a}$$

where x is the composition of the Al present in the GaAlAs layer and d_i is the width of the $Ga_{1-x}Al_xAs$ layer centered in the i^{th} cell of width t. The width of the GaAlAs layer is expressed as

$$d_i = t^2(i-0.5)/L_w \tag{1b}$$

where i ranges from unity to L_w/t and L_w is the width of the ATQW.

The ATQW was grown on a three inch semi-insulating (001) GaAs substrate using a solid source molecular beam epitaxy system. The resulting structure consisted of a 2000Å buffer layer of GaAs, followed by a 500Å cladding layer of GaAlAs. Next, a nominal 200Å ATQW was grown with the digital alloy approximation using a nominal 25Å alloy cell width. The structure was finished with a 500Å cladding layer of GaAlAs, followed by a 20Å cap layer.

The PR[7,8] and CER[9] methods have been reported in the literature. The pump beam of the PR experiment was the 6328Å line of a 3mW He-Ne laser chopped at 200 Hz. The procedure for going to elevated temperatures is discussed in Ref. 14.

III. EXPERIMENTAL RESULTS AND ANALYSIS

A. Intersubband Transitions

Shown by the solid lines in Figs. 1 and 2 are the PR spectra of the sample at 300K and 80K, respectively. The CER data were quite similar. The first feature in the spectra corresponds to the direct band gap of GaAs, denoted E_0(GaAs), and originates in the GaAs buffer/substrate of the structure. The peaks at 1.753 eV (200K) and 1.842 eV (80K) are E_0(GaAlAs). The energy of this feature enables us to determine an Al composition[6] of 23%.

The rich spectra between E_0(GaAs) and E_0(GaAlAs) are due to various *mn*H(L) quantum transitions transitions of the ATQW. In order to accurately determine the energies of these resonances we have fit the experimental data with a first-derivative

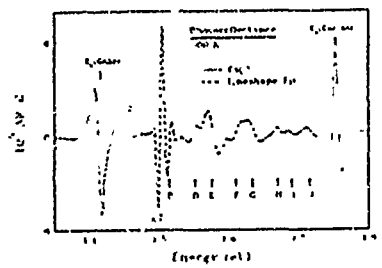

Fig. 1 Photoreflectance spectrum (solid line) at 300K from a GaAs/GaAlAs asymmetric quantum well. The dashed line is a least-squares fit to a FDGL function. The obtained energy values are denoted by arrows.

Gaussian lineshape (FDGL) function[17], as shown by the dashed lines. The obtained energies of the features denoted *A-J* are indicated by arrows and are listed in Table I. The ATQW spectra in Figs. 1 and 2 are due to intersubband transitions, similar to Ref. 11, and are not Franz-Keldysh oscillations, as claimed in the PR study of Ref. 5.

In order to identify the nature of the large number of intersubband transitions observed from the ATQW we have performed a theoretical calculation based on the envelope function approximation[18] using the intended DACG profile from the growth conditions. Non-parabolic effects were not included. The only adjustable parameter was L_w. We used a conduction band offset, $Q_c = 0.65$[19], conduction[17]/valence[18] band masses for GaAs and $Ga_{0.7}Al_{0.3}As$ listed in the literature and E_0(GaAs)/E_0(GaAlAs) taken from this experiment (see Figs. 1 and 2). Listed in Table I are the results of the calculation for 300K and 80K with L_w=260Å. There is very good agreement if we identify the feature *A* with 11H, *B* with 11L, *C* with 12H, etc. For the sake of comparison we also have performed a similar calculation for a LGW profile with the same L_w as displayed in the parentheses in Table I. There also is very good agreement between experiment and theory for this potential profile. This correspondence is verification that the DACG method has produced the desire result, i.e., an effective linearly graded potential profile.

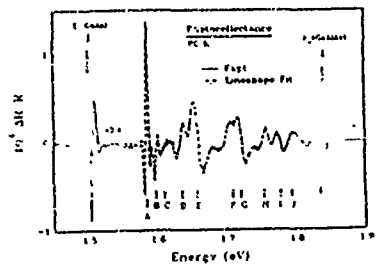

Fig. 2 Photoreflectance spectrum (solid line) at 80K from a GaAs/GaAlAs asymmetric quantum well. The dashed line is a least-squares fit to a FDGL function. The obtained energy values are denoted by arrows.

B. Effects of $\vec{S}\|[100]$

In order to verify the heavy- or light-hole nature of the observed *mn*H(L) transitions from the ATQW we have performed a PR experiment at 80K for $\vec{S}\|[100]$ with the electric field vector $\vec{E}$ of the incident light polarized parallel ($\|$) or perpendicular ($\perp$) to $\vec{S}$. For such a stress it is well known that heavy(light)-hole resonances have small(large) stress-dependence because of the cancellation (addition) of the hydrostatic and shear components of the strain. Furthermore, when the stress-induced splittings/shifts become larger than the quantum confinement effects, *mn*H features are allowed for both $\vec{E}\|\vec{S}$ and $\vec{E}\perp\vec{S}$, *mn*L resonances are seen only for $\vec{E}\perp\vec{S}$ and the intensity ratio $I^{\|}_{nH}/I^{\perp}_{nH}=1/3$.[19]

Displayed by the solid lines in Fig. 3 are the PR spectra at 80K for $S=0$ and $S=2.1$ kbars with $\vec{E}\|\vec{S}$ and $\vec{E}\perp\vec{S}$ in the region of the 11H-22H features. For $S=0$ the intensity ratio $I_{nH}/I_{nL}\approx 3$ because of matrix

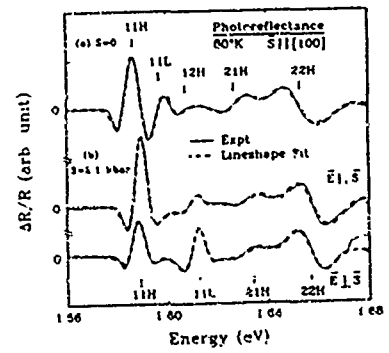

Fig. 3 Photoreflectance spectra (solid lines) at 80K for $S=0$ and $S=2.1$ kbars for $S\|[100]$ with $E\|S$ and $E\perp S$. The dashed lines are least-squares fits to a FDGL function.

element effects Again the dashed lines are a FDGL fit to the experimental data. The obtained energies are indicated by arrows. For the *nnH* resonances there is very little change in energy with the applied stress while for 11L there is a distinct blue shift. At S=2.1 kbars the 11L peak becomes degenerate with the weak "symmetry-forbidden" 12H feature and hence the latter is not resolved. Also, for the parallel configuration the intensity of 11L is weak while for the perpendicular case $I^{\perp}_{11H}/I^{\perp}_{11L} \approx 1$. The ratio is not yet 1/3 since 2.1 kbars is not the high stress limit

C. Temperature Dependence of E_{11H} and Γ_{11H}

We also have studied the temperature dependence of the energy and broadening parameter of the fundamental 11H excitonic transition in the temperature range $10K < T < 450K$ using both PR and CER

The temperature dependence of $E_{11H}(T)$ can be fit to either the Varshni semi-empirical relationship [20]

$$E_{11H}(T) = E_{11H}(0) - \alpha T^2/(\beta + T) \tag{2a}$$

where $E_{11H}(0)$ is the energy at T=0 and α and β are the Varshi coefficients or a Bose-Einstein expression [21,22]

$$E_{11H}(T) = E_{11H}(0) - 2a_B\,[\exp(E_\varphi/kT)-1] \tag{2b}$$

In Eq (2b) a_B represents the strength of the electron-average phonon interaction and E_φ corresponds to an average phonon energy

Shown by the open circles in Fig 4 are the experimental values of $E_{11H}(T)$ in the range $10K < T < 450K$ obtained from PR/CER The solid line is a least-squares fit to Eq (2a) The obtained values of $E_{11H}(0)$, α and β are listed in Table I We also have fit the experimental data to Eq (2b) and have recorded the obtained values of a_B and E_φ in Table II For comparison purposes corresponding numbers for the relevant parameters for bulk GaAs also are displayed

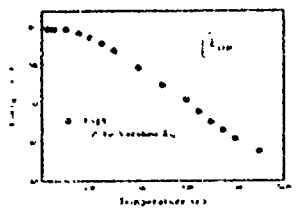

Fig 4 Experimental values (circles) of $E_{11H}(T)$ The solid line is a least-squares fit to Eq (2a)

The values for the parameters of the temperature dependence of E_{11H} are essentially the same as the constituent bulk material of the quantum wells This can also be seen in Figs 1 and 2 where the difference between E_{11H} and E_g(GaAs) is independent of temperature This observation is consistent with studies of GaAs/GaAlAs[23] and InGaAs/GaAs[24] SRQW systems

The variation of the linewidth with temperature also can be expressed by a Bose Einstein type expression[21,22]

$$\Gamma_{11H}(T) = \Gamma_{11H}(0) + \Gamma_\varphi\,[\exp E_{LO}/kT)-1] \tag{3}$$

The first term of Eq (3) corresponds to broadening mechanisms due to both intrinsic (lifetime, electron-electron interaction) and extrinsic (well width fluctuations) effects The parameter Γ_φ is an electron(exciton)-phonon coupling coefficient and E_{LO} is the zone center longitudinal optic (LO) phonon energy (36 meV for GaAs)

Displayed in Fig 5 by the squares are the experimental PR/CER values of $\Gamma_{11H}(T)-\Gamma_{11H}(0)$ as a function of $[\exp(E_{LO}/kT)-1]^{-1}$ (with $E_{LO}=36$ meV) The value of $\Gamma_{11H}(0) = 1.8$ meV Clearly the data

do not lie on a straight line This is in contrast to measurements on a large number of III-V and II-VI SRQW systems in which a linear relation is obeyed[12-14], the slope yielding Γ_φ The exception is a recent work on a GaAs/GaAlAs SRQW in which a deviation from linearity was observed due to an internal electric field.[23] Our result could be due to the quasielectric field of the ATQW structure Another possible reason for the anomalous behaviour of our sample may be due to the contribution of interface modes [24] Prior SRQW studies were performed on samples with well widths greater than 60Å Our ATQW, although it has L_w=260Å, consists of many heterointerfaces spaced closer than 20Å apart and thus is in a regime were interface modes may become important. These points are under further investigation

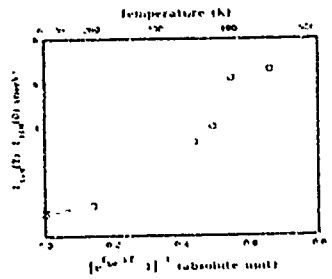

Fig 5 Experimental values of $\Gamma_{11H}(T)-\Gamma_{11H}(0)$ vs $[\exp(E_{LO}/kT)-1]^{-1}$ with E_{LO}=36 meV and $\Gamma_{11H}(0)$=1.8meV. The temperature scale is at the top of the figure.

IV SUMMARY

We have studied the intersubband transitions from a (001) GaAs/GaAlAs ATQW structure, grown by the DACG method, at 300K and 80K using PR and CER Comparison of the observed ATQW resonances with a theoretical calculation, based on the DACG growth conditions, provided a self-consistent check of the ATQW composition profile in addition to the band offset parameter There also is very good agreement between experiment and theory for a LGW potential profile This correspondence is verification that the DACG method has produced the desired result, i.e., an effective linearly graded potential profile The heavy- or light-hole nature of various transitions was verified by a uniaxial stress ($\vec{S}$) experiment for $\vec{S}\parallel[100]$. While the temperature dependence of $E_{11H}(T)$ was in agreement with results on SRQW microstructures an anomalous behaviour for $\Gamma_{11H}(T)$ was observed We found no evidence for Franz-Keldysh oscillations due to the quasielectric field in the ATQW

V ACKNOWLEDGEMENTS

The authors HQ and FHP acknowledge the support of US Army Research Office contract #DAAL03-92-G-0189 and the Olympus Corporation The work of DLM and GNM was supported by US Air Force University Initiative contract AFOSR-90-0118

REFERENCES

a) Also at the Graduate School and University Center of the City University of New York, New York, NY 10036
1 D Holm and H Taylor, IEEE J Quant Electron 25, 2266(1989)
2 D Gerber, R Droopad and G N Maracas, Appl Phys Lett. 62, 525 (1993)
3 T Ishikawa and K Tada Jap J Appl Phys 28, L1982 (1989).
4 K-K Law, P H Yan, A C Gossard and J L Merz, J Appl Phys 67, 6461 (1990)
5 H Xu X Zhou, G Xu, Q Du, E Wang, L Zhang and C Chen, Appl Phys Lett 61, 2193 (1992)
6 D L Mathine, G N Maracas, D S Gerber, R Droopad, R J Graham and M R McCartney, submitted to J Appl Phys
7 F H Pollak and O J Glembocki, Proc Soc Photo-Optical Instrum Engineers (SPIE, Bellingham, 1988) 946,2(1988)
8 O J Glembocki and B V Shanabrook, Semiconductors and Semimetals, Vol 67, ed D G Seiler and C L Littler (Academic, New York, 1992) p 222
9 Y Yin and F H Pollak, Appl Phys Lett 59, 2305 (1991)
10 G Bastard, Phys Rev B24, 5693(1981), also, Phys Rev B25, 7584(1982)
11 R F Kopf, M H Herman M L Schnoes, A P Perley, G Livescu and M Ohring, J Appl Phys 71 5004 (1992)

12. H Qiang, F H Pollak, C M Sotomayor Torres, W Leitch, A.H Kean, M A Stroscio, G J Iafrate and K W Kim, Appl Phys Lett 61, 141(1992)
13. F H Pollak in Phonons in Semiconductor Nanostructures, ed J-P LeBurton, J Pasqual and C Sotomayor Torres (Kluwer, Dordrecht, 1993) p. 341
14 Y S Huang, H Qiang, F H Pollak, G.D Pettit, P D. Kirchner, J M Woodall, H Stragier and L B. Sorensen, J Appl Phys. 70, 7537 (1991)
15 F H Pollak in Properties of Aluminum Gallium Arsenide, ed by S Adachi (INSPEC, London, 1993) p 53
16 M Missous in Properties of Aluminum Gallium Arsenide, ed S Adachi (INSPEC, London, 1993) p 73
17. S Adachi in Properties of Aluminum Gallium Arsenide, ed by S Adachi (INSPEC, London, 1993) p 58
18 S Adachi in Properties of Aluminum Gallium Arsenide, ed by S Adachi (INSPEC, London, 1993) p 66
19 F H Pollak, in Semiconductors and Semimetals, Vol. 32, ed by T P Pearsall (Academic, New York, 1990) p 17
20 F H. Pollak, in Properties of Aluminum Gallium Arsenide, ed by S Adachi (INSPEC, London, 1993) p 79
21 P Lautenschlager, M Garriga and M Cardona, Phys. Rev B35, 9174 (1987), also, Phys Rev B36, 4813 (1987)
22. A Kangarlu, H R Chandrasekhar, M Chandrasekhar, Y M Kapoor, F A Chambers, B A Vojak and J. M. Meese, Phys Rev B37, 1035 (1988).
23 J Filipowicz, C. Ghezzi and L Tarricone, Solid State Comm 74, 533 (1990)
24 M A. Stroscio, G J Iafrate, K.W Kim, M A Littlejohn, H Goronkin and G N Maracas, Appl Phys. Lett. 59, 1093 (1991).

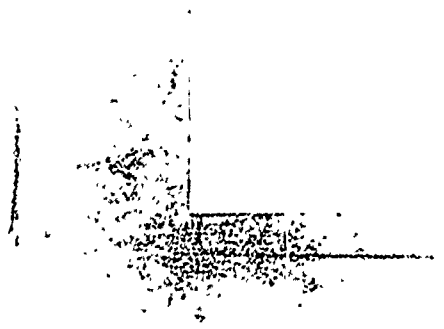

TABLE I Comparison of the experimental and theoretical (DACG) values for the *mn*H(L) transitions of the ATQW with $L_w = 260$Å. The numbers in parentheses are for a similar calculation *for a* LGW profile using the same L_w

Spectral Feature	300K		80K		*mn*H(L)
	Expt (eV)	Theory (eV)	Expt (eV)	Theory (eV)	
A	1 503	1 502(1 505)	1 585	1 587(1 590)	11H
B	1 516	1 515(1 516)	1 598	1 600(1 601)	11L
C		1 523(1 527)	1 611	1 608(1 612)	12H
D	1 553	1 558(1 562)	1 636	1 643(1 647)	21H
E	1 577	1 579(1 584)	1 658	1 664(1 669)	22H
F	1 611	1 623(1 629)	1 709	1 708(1 714)	32H
G	1 635	1 640(1 648)	1.721	1 725(1.733)	33H
H	1 671	1 671(1 678)	1 754	1 756(1 763)	35H
I	1 691	1 694(1 702)	1 778	1 779(1.787)	44H
J	1 717	1 710(1 716)	1 794	1.795(1 801)	45H

TABLE II Values of the parameters α, β, a_B and E_{ep} which describe the temperature dependence of the energy of the 11H transition in the GaAs/GaAlAs ATQW

Material	α (10-4 eV K)	β (K)	a_B (meV)	E_{ep} (meV)
ATQW	5 7±0 3	228±40	57±3	21±4
Bulk GaAs	5 5(1 3)[a] 5 1(5)[a]	225(174)[a] 190(82)[a]	57(29)[a]	21(10)[a]

a Ref 20 The numbers in parentheses indicate error margins in units of the last significant digit

TuP12

Spectroscopic studies of ultra-thin quantum-wells of GaAs and GaInAs in InP grown by MOVPE

D. Hessman, X. Liu, M-E. Pistol, L. Samuelson and W. Seifert
Department of Solid State Physics, Lund University, Box 118, S-221 00 LUND, Sweden

Abstract

Quantum-well (QW) structures comprised of nominally 1, 2, and 3 monolayers of *either GaAs or GaInAs, embedded in InP have been grown by low pressure metal* organic vapour phase epitaxy (LP-MOVPE). Such QW structures are known to be strongly affected by interface layers due to As replacing P on the bottom interface and due to As carry-over from the QW into the top InP barrier. Theoretically one expects GaInAs/InP to form a type I QW while a "clean" GaAs layer embedded in InP is assumed to be of type II. However, the inclusion of the InAs-like interface layers has a strong effect on the type-I versus type-II conditions. Based on a systematic study of growth and interface interrupt conditions we have been able to find conditions which yield the best QW interfaces, as judged from photoluminescence (PL) combined with modeling of the electronic structures. PL peak half widths of 7-10 meV are obtained. First, conditions are described for the formation of such very thin, high quality QWs. We then report good qualitative agreement between the spectroscopic data and the results of the modeling of the QWs, which includes contributions from the growth-dependent interface layers

I. Introduction

$Ga_xIn_{1-x}As/InP$ is a material system of great technological importance, offering a wide variability for fabrication of heterostructures for optical and high-speed applications. By varying the composition of the well material, this material system ranges from compressively strained InAs/InP, to lattice matched $Ga_{0.47}In_{0.53}As/InP$, and on to tensilely strained GaAs/InP. The band line-up of GaAs/InP is believed to be of type II [1, 2], meaning that the GaAs layer acts as a well for holes but a barrier for electrons, suggesting poor optical properties. For thin enough GaAs layers, however, the electron tunneling through the barrier is considerable, giving a non-negligible matrix element for electron-hole recombination. With the epitaxial techniques available today, quantum well (QW) structures can be grown with $Ga_xIn_{1-x}As$ thicknesses in the monolayer range. Clearly, for such thin QWs, the exact composition of the atomic layers close to the interfaces separating the well material from the barrier material becomes very important. An indication of the importance of these interfaces, is the spread in photoluminescence (PL) energy, measured for nominally 1 monolayer thick $Ga_{0.47}In_{0.53}As/InP$ QWs, where values between 1.1 and 1.38 eV have been reported [3,4]. Theoretical calculations, neglecting interface contributions, predict values around 1.38 eV. The process responsible for these discrepancies is the unintended incorporation of As into the barrier material, at both the first and the second interface.

In this work, we have investigated the interface properties by measuring the PL of $Ga_{0.47}In_{0.53}As$ and GaAs QWs, grown under different growth conditions. The PL peak energies are found to shift continuously with some conditions such as growth temperature, in contrast to the discrete set of PL peaks obtained when changing the growth time. This discreteness is understood as monolayer changes of the QW thickness, while the continuous shifting is an alloying effect at the interfaces. We also include the As incorporation at the interfaces in a theoretical calculation, giving qualitative agreement with the experimental results.

In section II, we describe the experimental conditions for the LP-MOVPE growth. In section III we give a brief theoretical background to the use of the effective mass theory on monolayer thin QWs, including a proposal of a simple method for defining the potential structure on the atomic scale. The experimental and theoretical results are presented in section IV, together with some discussion about the mechanisms of the As incorporation. The conclusions are given in section V.

II. Experimental

The samples used for this investigation were grown in a RF-heated LP-MOVPE apparatus (EPIQUIP RP-50) equipped with a vent/run switching and a pressure balance system. The total flow was 6.5 l/min H_2 and the total pressure was 50 mbar. 100 % PH_3 and AsH_3 and the metalorganics TMG (with a special dilution line) and TMI were used. Each switched component was compensated by a corresponding counterflow so that the pressure difference between vent- and run-lines during the switching process could be regulated to be <±0.2 mbar. All samples consisted of an exactly oriented (100) InP substrate, a 500 nm InP buffer, a 500 Å GaInAs reference layer, and a stack of QWs. Two different types of QWs were grown: lattice matched $Ga_{0.47}In_{0.53}As$ /InP and strained GaAs/InP. The QWs were grown using a 2s growth interruption when going from InP to the well material: 1 s after the TMI had been switched off, the PH_3 was switched off and the AsH_3 was switched on. 1s later the TMG (and TMI) was switched on. The reverse procedure, 1s of only AsH_3 flow followed by 1s of only PH_3 flow, was used when going back to InP at the top interface. The QWs were grown under varying growth conditions, such as deposition temperature (typically 520-620°C) and molar fraction of AsH_3 (typically 0.5-2x10-3).

The samples were characterized by low-temperature (5 K) photoluminescence measurements. The excitation source was the 514 nm line of an Ar^+-ion laser, giving an excitation power of about 10 W/cm^2. The emitted light was dispersed by a double monochromator and detected by a liquid nitrogen cooled Ge detector.

III. Theory

Since the mid-seventies, the effective-mass theory [5] (EMT) using an ideal square-well potential has been very successful in modeling the electronic energy levels of semiconductor quantum wells (QW). Despite its simplicity, this model gives good agreement with experiment also as the QWs become very thin, although some problems do arise. For example, the increased confinement energy, necessitates the inclusion of band non-parabolicity. This can be solved for instance by using an energy dependent effecive mass or by generalizing the EMT to a multi band problem, allowing for explicit band mixing. Moreover, the uncertainty of parameters such as the band offset becomes more important as the confined states approach the top of the QW. The parameters of the barrier material also increase in importance, since the wave function of a carrier confined by a single monolayer will have a large penetration into the barrier material. Even including these refinements, it is still questionable that the EMT should be applicable to the ultra-thin QWs of this work, having thicknesses of only a few monolayers. The failure in modeling the experimental results on QWs intended to be one monolayer thick has previously been attributed to a possible break down of the EMT. However, as we report in this paper, additional interface layers, arising from different surface processes during growth, are incorporated in the structure. These interface layers have a large influence on the potential and on the resulting electronic states, and it is therefore crucial that they are included in the model. Two approximations in the (generalized) EMT that could be invalid in the case of monolayer sized QWs are the assumptions that (i) the potential is slowly varying compared to the atomic spacing and that (ii) the wave function of a confined state can be expanded in Bloch functions close to some critical point in the Brillouin zone. The first approximation can not be valid for the steps in the potential at the interfaces. However, this approximation would be fatal also in QWs with thicknesses of 10 monolayers or more, and is therefore not an issue specific for monolayer thin QWs. Why the EMT can be used in spite of the abrupt potential drop in a QW is a problem that still lacks a satisfactory explanation, though some progress has been made [6,7]. The second approximation is equivalent to a requirement that also the envelope function is slowly varying on the atomic scale. This is actually not a severe restriction, since the relatively small masses of electrons and holes in semiconductors cause the wave functions to penetrate far into the barrier material in ultra-thin QWs, with a corresponding localization in k-space.

Another problem that has to be addressed here is what potential structure to use. This is illustrated in figure 1a, which shows one monolayer of GaAs embedded in InP. Curve (i) shows the corresponding conduction band line-up, as usually used for thicker QWs. However, by pairing the atoms differently, this structure can equally well be described as one monolayer GaP and one monolayer InAs embedded in InP, as indicated by conduction band line-up (ii)

Comparing the two potentials, potential (i) might seem to be a more natural choice, however, at a closer look, it does not contain the symmetry of the atomic structure, as does potential (ii). In order to overcome this ambiguity, we propose a procedure that gives a unique potential for a specific atomic structure. In addition to that, the potential thus obtained will have the symmetry of the grown structure. The basic idea of this simple method, is to assign the band edge energy to the bonds connecting two planes of atoms. In this way we divide the structure into half-monolayer units, i. e. a/4, where a is the length of the fcc unit cell. Using this concept, conduction band (iii) in figure 1a is obtained.

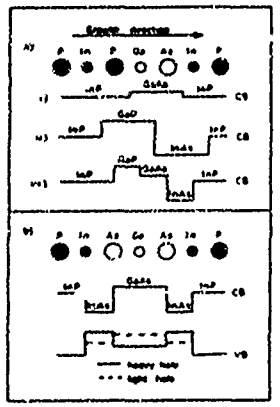

Figure 1. In a), the atomic structure of a nominally one monolayer GaAs/InP QW is shown together with three different conduction band edge line-ups. Potential i) is the one normally used. Potential ii) is obtained by considering the Ga atom to belong to a layer of GaP instead of GaAs as in case i). Potential iii) is constructed according to the model proposed in this work, which assigns the band edge energies to the bonds connecting the atoms. Note that only ii) and iii) have the same symmetry as the atomic structure. In b), the P atoms at the lower interface have been replaced by As atoms. The corresponding conduction and valence band structure is obtained using our model. With a partial P to As replacement the potential structure becomes that shown in figure 2b).

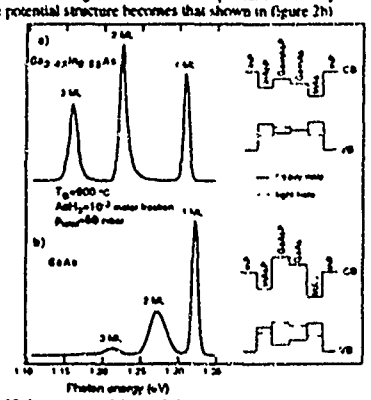

Figure 2. PL spectra of two QW samples, each of them containing three QWs with 1, 2, and 3 monolayer nominal thickness. a) is $Ga_{0.47}In_{0.53}As/InP$ and b) is GaAs/InP. To the right are shown the corresponding potential structures for electrons, light holes and heavy holes, as used in the calculations. The only free parameter is the As/P-ratio at the lower (left) interface.

If the grown structure is not perfect, e. g. if the composition of the atomic layers close to an interface differs from the intended one, the model potential has of course to be modified. As discussed in this paper, when starting to grow the GaAs layer the phosphorous atoms of the InP surface will almost instantaneously be replaced by As atoms. Assuming a complete P to As replacement, the atomic structure is that shown in figure 1b, where also the corresponding conduction and valence band line-up, obtained according to our proposal, is indicated. Note that both the atomic structure and the potential are symmetric with respect to the Ga atom, while the structure in figure 1a is not. With band line-up (i) in figure 1a, the pure GaAs/InP QW is of type II, with unbound electrons and bound holes. With band line-up $(iii)_a$ however, the electrons become bound, though with a binding energy (≈1 meV) much smaller than a typical exciton binding energy, since this is an extremely thin well of only half a monolayer. Including the P/As replacement at the lower interface, a double-well structure is formed for the electrons, thereby slightly increasing their binding energy (< 5 meV), provided that the GaAs barrier is thin enough.

For all QWs in this study, the calculated PL recombination energies are for electron-heavy hole transitions, though for a thicker GaAs QW (> 3 monolayers), where the confinement energy is smaller, the electron-light hole transition has a lower energy. This is because the

tensile strain in the case of GaAs, lifts the light hole band above the heavy hole band. Including strain to first order, the band edge energies of the conduction and valence bands are [1]

$$\begin{cases} V_{CB} = E_g + V_{offset} + a_c\left(\epsilon_{xx} + \epsilon_{yy} + \epsilon_{zz}\right) \\ V_{VB} = V_{offset} \pm b\left(\epsilon_{zz} - \frac{1}{2}\left(\epsilon_{xx} + \epsilon_{yy}\right)\right) \end{cases} \qquad (1)$$

where the - (+) sign gives the heavy (light) hole valence band. E_g is the bandgap, V_{offset} the valence band offset relative to InP, a_c is the hydrostatic deformation potential of the conduction band and b is the sheer deformation potential of the valence band (the hydrostatic deformation potential of the valence band is small and therefore taken to be zero). The strain tensor elements are $\epsilon_{xx} = \epsilon_{yy} = \left(a_{InP} - a_{AB}\right)/a_{AB}$ and $\epsilon_{zz} = -\left(c_{11}/c_{11}\right)\epsilon_{xx}$ where a_{InP} and a_{AB} are the lattice constants of InP and the unstrained material respectively and c_{ij} are the components of the elastic moduli tensor. The parameters used in the calculations are taken from reference [1], where the parameters (apart from the bandgap) of ternary compounds are linearly interpolated from the parameters of the corresponding binary compounds.

Solving the Schrödinger equation for a piece-wise constant potential is just a question of fitting plane waves at each interface so that the envelope function, $F(z)$, fulfills

$$\begin{cases} F\left(d^-\right) = F\left(d^+\right) \\ \frac{1}{m_d^*} F'\left(d^-\right) = \frac{1}{m_{d'}^*} F'\left(d^+\right) \end{cases} \qquad (2)$$

where $d^{-(+)}$ indicates the interface approached from the left (right) side. With multiple interfaces, this may be solved using a transfer matrix technique [8].

The single band calculations described above have also been compared to the results of a more involved multi-band calculation, taking into account the electron, light hole and spin-orbit hole mixing due to strain and confinement. Both methods yield, however, approximately the same result for the electron heavy hole transitions. The multi-band model is based on the variational method of Ref. [6] with an eight-band $k \cdot p$-Hamiltonian, including the strain [9].

When comparing the theoretical results with experiment, there are still many unknown parameters, e. g. the exact extent of the As incorporation into the lower and the upper barrier material. By varying the growth conditions, however, we have found conditions where such effects could be reduced. The agreement between the calculations and our experimental data, give no indication that the effective mass theory should be invalid for monolayer thick QWs.

IV. Results and discussion.

The highest quality $Ga_xIn_{1-x}As$ QWs, having the sharpest PL peaks, were grown at i) low growth rates (typically 0.5 ML/s for the QW and 0.25 ML/s for the barriers), ii) low hydride molar fractions (typically 1x10-3 for AsH_3 and 1x10-2 for PH_3) and iii) deposition temperatures at about 580 -600 °C. With these growth conditions, we obtain PL peak half-widths of 7-10 meV. Figure 2a shows a typical PL spectrum of a $Ga_{0.47}In_{0.53}As$ sample. The different peaks correspond to $Ga_{0.47}In_{0.53}As$ layers with nominal thicknesses of 0.5, 1.5, 2.5 and 5 monolayers. An increase of the growth time to yield nominal thicknesses of 1, 2 and 3 monolayers for the thinnest wells does not change the spectrum, indicating that, apart from any interface contributions, the QWs grow in monolayer steps. Changing the growth temperature or the AsH_3 pressure, however, shifts the PL peak position continuously. The reason for this continuous shift, which will be discussed in more detail later on, is mainly the incorporation of As at the second interface, i. e. at the interface between the $Ga_{0.47}In_{0.53}As$ and the top InP. There is, however, an important As incorporation also at the first (bottom) interface, a process which is much less sensitive to the growth conditions. Previous studies, under UHV-conditions[11,12], have shown that, in the temperature interval used here, the surface P layer of InP is completely replaced by As atoms within less than a second, when exposed to AsH_3, while As replacement in deeper lying P layers is a considerably slower process [12]. This means that as soon as the PH_3 flow in the reactor has been changed into an AsH_3 flow, the P atoms sitting on the surface of the InP, are expected to be replaced by As atoms and that almost no As goes into the depth of the InP during the short growth interruption.

If the growth temperature is decreased or if the AsH_3 partial pressure is increased, the PL peak position is shifted towards lower energy. Assuming, as discussed above, that the replacement of P atoms by As atoms at the first interface is instantaneous and, for the growth parameters used in this work, independent of growth conditions, this red shift of the PL must be indicating an increased As incorporation at the second interface. As we discuss below, the mechanism is that one or more layers of excess As are accumulated on the surface during the $Ga_{0.47}In_{0.53}As$ growth, containing more As for lower temperatures and higher AsH_3 pressures. Most of this excess As will then remain on the surface, and as the TMI is switched on, the As is incorporated into the InP grown immediately after the upper interface, giving a graded InAsP interface layer.

The PL energies of $Ga_{0.47}In_{0.53}As$ QWs grown at 600°C are plotted versus the AsH_3 molar fraction in figure 3. For low AsH_3 molar fraction, the PL energies seem to approach a constant value, suggesting that under these growth conditions, no excess As is incorporated at the second interface. Also included in the figure are the results of a calculation of the transition energies, assuming that no As is incorporated at the second interface but with different amounts of P replaced by As at the first interface. Including interface layers in the calculations, the experimental values are easily reproduced. Comparing experiment and calculation, the P layer does not appear to be completely replaced by As, in contrast to what was assumed above. Transients in the gas switching, e. g. the delay before the AsH_3 pressure at the sample position reaches its maximum value, are possible explanations for the reduced P to As replacement compared to reference [11]. For the thicker QWs, the P to As replacement at the first interface appear to be enhanced. Most probably, however, this is a non-negligible As incorporation at the second interface, due to the increased As accumulation induced by the longer growth times. This explanation is supported by figure 3, where the thicker QWs clearly need lower AsH_3 pressures to reach a region of constant PL energy, i. e. the region of zero excess As at the second interface.

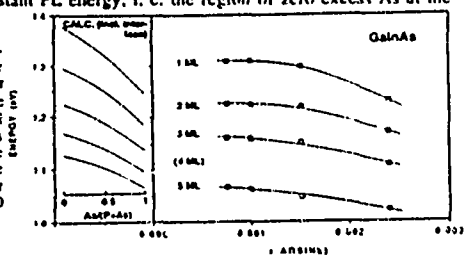

Figure 3. To the right is plotted the low-temperature (5 K) PL peak positions for $Ga_{0.47}In_{0.53}As/InP$ QWs versus molar fraction of AsH_3. The growth temperature was 600 °C. ML denotes the nominal thickness in monolayers. To the left is shown the results of a calculation using the potential structure shown in figure 2a, where the P to As replacement at the lower interface, As/(P+As), has been varied from 0 to 1.

Figure 4 shows the PL energies of intentionally 1 monolayer thick GaAs QWs, grown at different temperatures and AsH_3 molar fractions. There is no tendency to approach a constant value at low AsH_3 molar fraction, as was the case for $Ga_{0.47}In_{0.53}As$ (figure 3). Even at our highest temperature and lowest AsH_3 molar fraction, we therefore have a substantial As carry over at the second interface. Assuming that most of the incorporated As is coming from excess As sitting on the growing surface (and not from e. g. the reactor cell), the amount of incorporated As should be determined by the GaAs reconstruction. A phase diagram of GaAs reconstructions versus AsH_3 partial pressure, $p(AsH_3)$, and inverse temperature [13], is shown schematically as an insert in figure 4. There is a boundary separating a region with a "2x4"-like reconstruction at low $p(AsH_3)/T$-ratio from a region with a "4x4"-like reconstruction, at high $p(AsH_3)/T$-ratio. The "4x4"-like reconstruction has double layers of As, which can act as a source for As carry over into the upper InP, while the "2x4"-like reconstruction has a single layer of As, giving no As carry over. All of our GaAs QWs were grown in the "4x4"-like region and consequently they show As transients at the second interface. The corresponding phase diagram for $Ga_{0.47}In_{0.53}As$ is not known. Our results, however, suggest that a corresponding boundary exists also for $Ga_{0.47}In_{0.53}As$, however shifted to higher p/T ratios so that the boundary intersects the region in $p(AsH_3)$-T-space covered in this work. In this way, we can find growth conditions where As carry-over into the upper InP barrier is drastically reduced.

Figure 4. To the right is the low-temperature (5 K) PL peak positions for GaAs/InP QWs versus molar fraction of AsH_3. To the left is shown the calculated energies using the potential structure shown in figure 2a, where the P to As replacement at the lower interface, As/(P+As), has been varied from 0 to 1. The insert shows schematically a phase diagram of GaAs reconstructions versus AsH_3 pressure and inverse temperature. The growth parameters of this work are indicated by the shaded area.

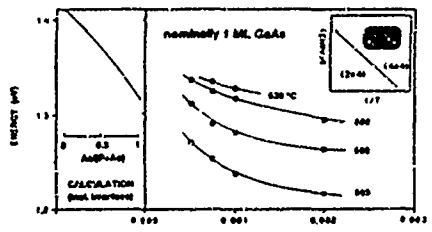

V. Conclusions

We have optimized the growth of monolayer thick QWs of GaInAs and GaAs in InP, thus obtaining PL peak half-width of 7-10 meV. In addition to this, we have studied the As incorporation at the interfaces as a function of the growth conditions, using PL measurements as a probe. Theoretical calculations have been used as an important tool for understanding the spectroscopic results. The main conclusions are the following:

a) When the InP at the bottom interface is exposed to AsH_3 as the growth of the well material is about to begin, a substantial fraction of the surface P atoms are replaced by As. This process is rapid and occurs, at all the studied temperatures and AsH_3 pressures, during a growth interruption of 1s.

b) During the growth of the well material, the growing surface is covered by one or more As layers. The amount of As is determined by the surface reconstruction, and is therefore strongly dependent on the growth conditions. With the growth conditions used in this work, a growing GaAs surface is always covered by more than one layer of As, as supported by studies of GaAs reconstructions under AsH_3 exposure. In the case of GaInAs, however, we have indications that we are able to decrease the amount of As to a single layer by choosing high temperature and low AsH_3 molar fraction. This suggests that the boundary between "2x4"-like and "4x4"-like reconstructions on GaInAs is moved towards higher AsH_3 pressures and lower temperatures compared to on GaAs.

c) Terminating the growth of the well material, most of the excess As will remain on the surface. Then as the TMI is switched on to start growing the upper InP barrier, this As will be incorporated, giving a graded $InAs_xP_{1-x}$ interface layer. The extent of this As carry-over effect is therefore mainly determined by the reconstruction of the growing $Ga_xIn_{1-x}As$ surface.

d) Using the knowledge about the As incorporation at the two interfaces in the modeling, the spectroscopic data are reproduced by calculations using the effective mass theory. There are no indications of a break-down of the EMT. A consistent description on the atomic scale of the energy potential is obtained by assigning the band edge energy to the bonds connecting the atoms. In this way the symmetry of the atomic structure will also be maintained in the potential structure.

References

1 D Gershoni and H Temkin, J Luminescence 44, 281 (1989)
2 M -E Pistol, M. Gerling, D Hessman, and L. Samuelson, Phys Rev B 45, 3628 (1992) (1989)
3 T Y Wang and G B Stringfellow, J Appl Phys 67, 344 (1990)
4 H. M Cox, P C Morais, D M Hwang, P Basion, T J Gmitter, L. Nazar, J M Worlock, E. Yablonovich and S G Hummel, Inst Phys Conf Ser No 96, Int Symp GaAs and Related Compounds, Atlanta Georgia, 1988
5 J M Luttinger and W Kohn, Phys Rev 97, 869 (1955)
6 G A Baraff and D Gershoni, Phys Rev B 43, 4011 (1991)
7 M G Burt, J Phys C 4, 6651 (1992)
8 E Merzbacher, Quantum Mechanics, 2nd Edn, p 93, John Wiley and Sons, New York (1970)
9 T. B Bahder, Phys Rev B 41, 11992 (1990)
10 W Seifert, X Liu and L. Samuelson, Appl Phys Lett 62,949 (1993)
11 N Kobayashi and Y Kobayashi, Jap J Appl Phys 30, L1699 (1991)
12 A. Watanabe, T. Isu, M Hata and Y Katayama, J Crystal Growth 115 371 (1991)
13 I Kamiya, H. Tanaka, D E. Aspnes, L. T Florez, E. Colas, J P Harbison and R. Bhat, Appl Phys Lett 60 1238 (1992)

TuP13

Optical Properties of Symmetrically Strained (GaIn)As/Ga(PAs) Superlattices Grown by Metalorganic Vapour Phase Epitaxy

S. Lutgen, T.F. Albrecht, T. Marschner, W. Stolz, E.O. Göbel
Wiss. Zentrum für Materialwissenschaften (WZMW) und Fachbereich Physik,
Philipps-Universität, D-35032 Marburg, Germany

Abstract

Symmetrically strained (GaIn)As/Ga(PAs) superlattice structures (symm. SLS) have been realized by metalorganic vapour phase epitaxy (MOVPE). The high structural as well as optical quality of these symm. SLS has been established by detailed high-resolution X-ray diffraction (XRD) and in particular photoluminescence (PL) and excitation spectroscopy (PLE) investigations. The optical recombination at low temperatures is due to excitons localized in statistical potential fluctuations in the (GaIn)As well layer. The exciton binding energy is determined in these symm. SLS to (5.5+-1) meV according to a theoretical description of the PLE spectra using a two-dimensional (2D) absorption model. Therefore, the exciton binding energy is a significantly reduced as compared to unstrained GaAs quantum wells, caused by a considerably smaller in-plane hole mass for the top most valence subband. An estimate of this mass based on the determined exciton binding energy yields a value of about 0.05 m_o.

Introduction

Strained III/V-semiconductor heterostructures are becoming increasingly important with respect to both fundamental physics [1] as well as applications in particular for optoelectronic devices [2]. This is due to the unique possibility of designing the effective band gap and the valence subband structure as a function of strain. For strained layer systems, however, two critical layer thicknesses with respect to strain relaxation by formation of misfit dislocations exist. These are the critical layer thickness of the individual strained layers and in case of SLS that of the total SLS structure. This leads to a severe restriction in the strain level and/or the number of SLS periods, which can be deposited before strain relaxation by misfit dislocation formation occurs. This becomes in particular true for one-side strained material systems like (GaIn)As/GaAs, which have been studied almost exclusively in the literature up to now. In order to overcome the limitations with respect to the critical layer thickness of the total SLS, the concept of symmetrically (symm.) or strain-balanced SLS, i.e. alternating layers with built-in compressive and tensile strain, has been introduced. Symm. SLS structures have been realized using gas source molecular beam epitaxy (GSMBE) [3,4] and metal organic vapour phase epitaxy (MOVPE) [5] in the (GaIn)As/Ga(PAs) material system on GaAs substrate as well as in the (GaIn)(PAs) on InP system [6,7].

In this work, we present a study of the optical properties of (GaIn)As/Ga(PAs) symm. SLS, which have improved structural properties as compared to those in the literature. The low-temperature photoluminescence (PL) and photoluminescence excitation spectroscopy (PLE) investigations reveal the achieved high-crystalline perfection of these structures. From the PLE studies the exciton binding energy in these symm. SLS is determined as a function of incorporated strain. These data are compared to the case of unstrained as well as one-side strained quantum well structures reported in the literature. From the exciton binding energy the in-plane hole mass is estimated in these symm. SLS as a function of strain, leading to values, which are comparable to the effective electron mass in these symm. SLS.

Experimental

The epitaxial growth of the (GaIn)As/Ga(PAs) symm. SLS has been performed by MOVPE in a commercial equipment (Aix 200, Aixtron Corp.) at a reactor pressure of 100 mbar and a substrate temperature of 650°C. The nominal layer sequence for the series of samples consists of 50 periods of a 9.5 nm (GaIn)As / 1.7 nm GaAs / 9.5 nm Ga(PAs) / 1.7 nm GaAs layer structure. Lattice mismatches of up to +-2.4*10^{-2} in the individual (GaIn)As and Ga(PAs) layers have been realized (x_{In} < 0.17, y_P < 0.35). The thin GaAs intermediate layers in between the ternary (GaIn)As and Ga(PAs) layers have been deposited in order to avoid the possible formation of strained quaternary (GaIn)(PAs) interface layers. Details of the optimization of these symm. SLS structures have been published elsewhere [5].

The optical investigation have been performed in a standard luminescence set-up, using an Ar ion laser or a Ti:Sapphire laser as excitation source. The samples were mounted in a liquid He continuous flow cryostat. The luminescence singal was dispersed by a 1 m monochromator and detected by a GaAs photomultiplier using standard lock-in technique.

Results and Discussions

The structural properties of the symm. SLS have been evaluated by means of high-resolution X-ray diffraction (XRD) in combination with a theoretical description of the experimental XRD pattern using dynamical diffraction theory [5,8]. The average lattice mismatch in the samples in the present study is below +-5*10^{-4}, proving the almost perfect strain balancing in these structures. The linewidth of the symm. SLS XRD satellite pattern is constant in the range of 20" to 30" (FWHM) irrespective of the value of the incorporated strain. These values of XRD linewidth are significantly narrower as compared to those reported so far for the (GaIn)As/Ga(PAs) material system [3,4], approaching the theoretical value of 18" (FWHM) for the above chosen layer structure. These results indicate the high structural perfection of the realized symm. SLS. The structural parameters (compositions, layer thicknesses and strain values) of the samples chosen for the present optical investigations are summarized in Table 1., as obtained from a detailed XRD study [8].

Table 1. Structural parameters of the (GaIn)As/Ga(PAs) symm. SLS as determined by X-ray diffraction analysis

#	x_{In}	$d_{(GaIn)As}$ (nm)	d_{GaAs} (nm)	y_P	$d_{Ga(PAs)}$ (nm)	D_{SLS} (nm)
1	0.031	9.35	1.35	0.042	9.35	21.4
2	0.043	9.25	1.35	0.084	9.25	21.2
3	0 052	9.40	1.35	0.102	9.40	21.5
4	0.070	8.90	1.35	0.158	8.90	20.5
5	0 081	8.80	1.35	0.203	8.80	20.3
6	0.095	8.65	1.35	0.220	8.65	20 0
7	0.114	8.60	1.35	0.240	8.60	19.9
8	0.126	8.40	1.35	0.271	8.40	19.5
9	0.141	8.20	1.35	0.292	8.20	19.0
10	0 158	7.70	1.35	0.335	7.70	18.1
11	0.171	7.65	1.35	0.350	7.65	18.0

The low temperature (5 K) luminescence spectra of three samples out of this series, excited with a Ti:Sapphire laser, are shown in Fig. 1 for different In-concentrations x_{In} in the ternary (GaIn)As quantum well layer as indicated. With increasing x_{In} a red shift in energy is observed for both the PL spectra (dotted line) as well as the PLE spectra (full line), reaching a value of 165 meV with respect to the GaAs band gap for the PL line for x_{In} = 0.171 and a well width of 7.7 nm. Excitonic resonances also for higher subband transitions are observed in the PLE spectra of the different samples. A description of the subband structure of this novel symm. SLS material system is not attempted in the present study, because of the uncertainties in the values of the carrier effective masses, of the deformation potentials and in particular in the values of the band offsets (see for example the discussion in [9] and references therein for the (GaIn)As/GaAs strained material system).

For the lowest E_{1h} transitions these excitonic resonances are resolved from the respective subband transitions, which allows to determine the exciton binding energy as described below. The luminescence spectra for the sample having an In-concentration x_{In} = 0.114 are shown in Fig. 2 in more detail around the lowest E_{1h} subband transition. The luminescence line (dashed line), having a linewidth of 3.0 meV (FWHM), is "Stokes"-shifted by 2.0

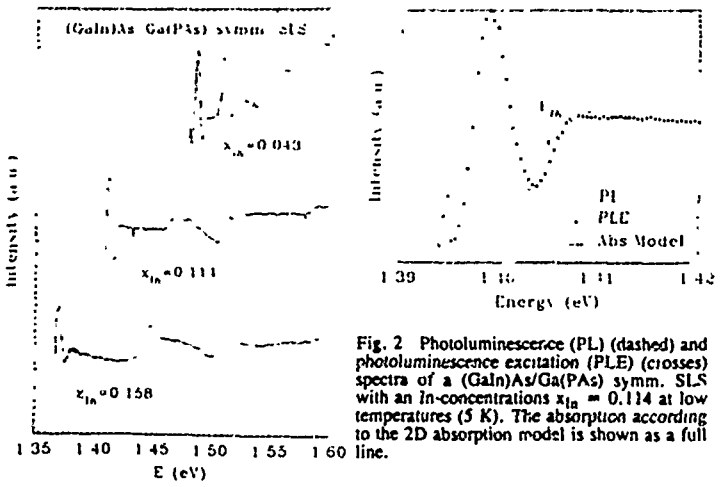

Fig. 2 Photoluminescence (PL) (dashed) and photoluminescence excitation (PLE) (crosses) spectra of a (GaIn)As/Ga(PAs) symm. SLS with an In-concentrations x_{In} = 0.114 at low temperatures (5 K). The absorption according to the 2D absorption model is shown as a full line.

Fig. 1 Photoluminescence (PL) and photoluminescence excitation (PLE) spectra of (GaIn)As/Ga(PAs) symm. SLS samples with different In-concentrations x_{In} at low temperatures (5 K).

meV with respect to the excitonic resonance in the PLE spectrum (crosses). The resonance in the PLE spectrum has a linewidth of 4.3 meV (FWHM). It is characteristic for the symm. SLS in the present study that the PL linewidth is always narrower as compared to the excitonic resonance in the PLE spectra. For excitation densities in the range of 3 mW/cm^2 to 3 W/cm^2 using the Ar ion laser (2.41 eV) the energetic position and the linewidth of the luminescence line remain constant. For higher excitation densities (> 3 W/cm^2) a broadening of the luminescence line to the high energy side is observed.
These findings can be understood in the model of excitons relaxing energetically in a statistically fluctuating potential after resonant optical excitation. For the symm. SLS studied here, these potential fluctuations are caused by the intrinsic statistical alloy fluctuations of the ternary (GaIn)As well material and eventually by fluctuations in well width. For the absorption process the total bandwidth of the potential fluctuations contributes to the linewidth of the excitonic resonance. After excitation, the excitons relax to the local minima of the fluctuating potential before radiative recombination. This leads to a red shift as well as to a narrowing of the excitonic luminescence line with respect to the resonance in the absorption process. A quantitative theoretical description of this behaviour has been given recently using a topographical theory of exciton spectra in terms of statistical properties of a Gaussian random function [10]. According to this description a direct proportionality exists between the Stokes-shift and the linewidth of the excitonic resonance in absorption. The coefficient of proportionality is found to be $\gamma \approx 0.553$ [9]. This correlation for the studied (GaIn)As/(Ga(PAs) symm. SLS is summarized in Fig. 3, where the Stokes-shift of the luminescence line is depicted as a function of the linewidth of the excitonic resonance in the PLE spectrum. A good aggreement betweeen the experimental values and the theoretical description, as given by the straight line in Fig. 3, is observed. This behaviour as well as the observation, that the excitonic luminescence line does not show a shift in energy with increased excitation density, prove that the observed

luminescence in these (GaIn)As/Ga(PAs) symm. SLS is due to the recombination of excitons, which are localized in statistical potential fluctuations. No additional localization processes due to extended interface defects and/or charged impurities are observed. This points to the high crystalline perfection also with respect to the optical properties of the studied (GaIn)As/Ga(PAs) symm. SLS.
In the following, the exciton binding energy in these structures as a function of strain is determined and compared to unstrained quantum well structures. The exciton binding energy is evaluated from a theoretical description of the PLE spectra using the 2D absorption model [11]. This absorption model has been successfully applied to the determination of exciton binding energies for unstrained (AlGa)As/GaAs as well as (GaIn)As/(AlIn)As multiple quantum well heterostructures [12,13]. In the case of the (GaIn)As/Ga(PAs) symm. SLS the absorption model can be simplified as compared to the case of the unstrained quantum well systems. In the strained material system only one subband transition and the corresponding excitonic resonance has to be taken into account. This is due to the strain-induced energy splitting between heavy and light hole subbands, leading to a simplier structure of the top most valence subbands.
For all samples the PLE spectra have been described around the lowest subband transition by using this 2D absorption model, as already included in Fig. 2, with the E_{1h} subband transition energy as indicated by the arrow. A good agreement between the experimental PLE spectra and the 2D absorption model is found also for the other samples studied in this work. The exciton binding energy, as determined by the energy separation of the exciton resonance with respect to the E_{1h} subband transition, is shown in Fig. 4 as a function of the In-concentration in the (GaIn)As well material. An almost constant value for the exciton binding energy of the (GaIn)As/Ga(PAs) symm. SLS of (5.5+-1) meV is determined. These values are considerably smaller as compared to the case of unstrained (AlGa)As/GaAs quantum well structures having a similar well width of about 9 nm, where heavy hole exciton binding energies of (13+-1) meV were reported [12,14]. For small values of the In-concentration around x_{In} < 0.07, the (GaIn)As/Ga(PAs) symm. SLS form a shallow quantum well systems, because of the small band edge difference between (GaIn)As and Ga(PAs) for these concentrations. As we would like to point out, however,

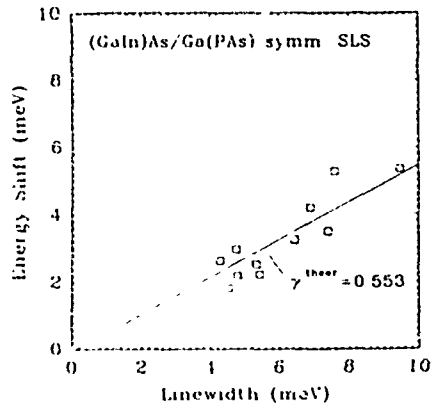

Fig. 3 "Stokes-shift" of the luminescence line of (GaIn)As/Ga(PAs) symm. SLS (squares) as a function of the linewidth (FWHM) of the exciton resonance in the PLE spectrum. The full line represents the theoretical values according to Ref. [9]

for In-concentrations above $x_{In} > 0.10$ the band edge differences in the (GaIn)As/Ga(PAs) material system are comparable or even larger than in the (AlGa)As/GaAs system for Al-concentrations of about $z_{Al} = 0.3$. Therefore, the quantum well depths are expected to be comparable for the two material systems. In this way, the change in exciton binding energy in the two material systems can be directly correlated to the amount of strain incorporated in the (GaIn)As/Ga(PAs) material system. The values reported here for the (GaIn)As/Ga(PAs) symm. SLS system with well widths of about 8 nm seem to be smaller than those in the one-side strained (GaIn)As/GaAs material system. In the latter material system exciton binding energies of 9 meV have been reported for quantum well structures with well widths in the range of 3 to 5 nm for In-concentrations $x_{In} = 0.15$ [15]. However, in the case of the (GaIn)As/GaAs material system, the E_{1h} subband transition is assumed at the top of the edge in the PLE spectrum [15], which does not agree with the theoretical 2D absorption model used in the present study. This difference in the determination of the subband transition energy might be the reason for the apparent discrepancy in exciton binding energies between the (GaIn)As/GaAs system [15] and the (GaIn)As/Ga(PAs) system, studied here.

The significant reduction in exciton binding energy in the strained (GaIn)As/Ga(PAs) material system as compared to the unstrained GaAs/(AlGa)As system leads to the conclusion, that the in-plane hole mass of the top most valence subband is reduced significantly for the strained material system as compared to the unstrained quantum well case. An estimate of the in-plane hole mass from the determined exciton binding energy can be obtained using the analytical description of excitons in a fractional dimension space [16,17]. Because the respective band offsets are unknown for the (GaIn)As/Ga(PAs) material system, we use the infinite well model for the description of the excitonic properties in our structures. This aproximation should give a valid description of the experimental results for structures with In-concentrations $x_{In} > 0.10$, having deep enough quantum wells. All parameters entering the calculations (effective electron mass, Luttinger parameters) for the (GaIn)As well layer have been linearly interpolated betweeen the values of the binary GaAs and InAs materials. The fractional dimension parameter σ is defined by [17]

$$\sigma = 3 - \exp(- L_z/a_0^*) \qquad (1)$$

where L_z is the well width and a_0^* the effective Bohr radius in three dimensions (3D). For these structures, this parameter is eugal to $\sigma = 2.2$, justifying the application of the theoretical 2D absorption model for the description of the PLE spectra. According to this model the exciton binding energy in the quantum well E_b is given by the following expression [17]

$$E_b \; / \; E_o^* = (\; 1 \; + \; (\sigma-3)/2 \;)^{-2} \qquad (2)$$

with E_o^* being the exciton binding energy in 3D. With the experimentally determined value of E_b and the parameter σ the value of E_o^* is obtained. From this value the reduced effective mass μ^* and, thus, the in-plane hole mass can be estimated using the known effective electron mass in the symm. SLS. Using this procedure for the (GaIn)As/Ga(PAs) symm SLS with In-concentrations $x_{In} > 0.10$, estimates for the in-plane hole mass of the top most valence subband of $m_{hh}^* = 0.05\ m_o$ are obtained. These estimated values are a lower bound of the in-plane masses due to the used infinite potential well model. However, this estimate shows the possibility to design SLS with in-plane hole masses, which are comparable to the effective electron mass of $m_e^* = 0.06\ m_o$ in these structures. This behaviour is of great importance in the design of optoelectronic device structures, in particular for semiconductor lasers with improved gain properties.

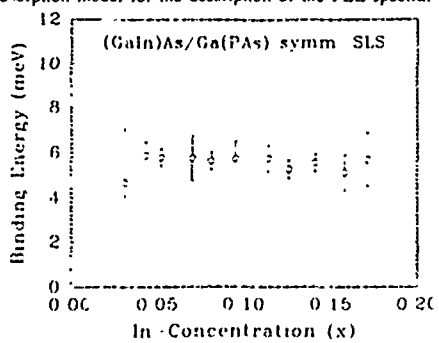

Fig. 4. Exciton binding energy of (GaIn)As/Ga(PAs) symm SLS as a function of In-concentration.

Summary

In conclusion, (GaIn)As/Ga(PAs) symm. SLS have been realized by MOVPE with lattice mismatches of up to $+-2.4 * 10^{-2}$ in the individual constituent ternary layers. The high crystalline perfection is established by sharp XRD pattern with linewidths of 20-30" (FWHM) [5,8]. The almost perfect strain balancing in these structures with an average lattice mismatch of below $+- 5 * 10^{-4}$ for these symm. SLS results in a significant increase in the critical layer thickness of the total SLS in this highly strained system beyond values of 1 μm. With increasing In-concentration in the compressively-strained (GaIn)As well layer the luminenescence peaks show a red shift of up to 165 meV ($x_{In} = 0.171$, $L_z = 7.7$ nm) with respect to the GaAs band gap. No shift of the PL line with increased excitation density in the low excitation density limit is found. Luminescence linewidths are about 3 meV (FWHM), while the Stokes-shift is about 2 meV with respect to the excitonic resonance in the PLE spectrum in optimized structures. The excitonic resonance is clearly resolved from the lowest E_{1h} subband transition with a linewidth typically of 5 meV (FWHM). These findings prove that the luminescence is caused by the recombination of excitons, which are localized in statistical potential fluctuations, caused by the ternary alloy disorder and eventually by well width fluctuations. No additional localization processes due to extended interface defects and/or chraged impurities are observed, indicating the high crystalline perfection of these symm. SLS. The exciton binding energy is determined as a function of strain by use of a 2D absorption modelling of the PLE spectra. Values of the exciton binding energy of (5.5+-1) meV are determined for these structures, which are considerably smaller as compared to unstrained (AlGa)As/GaAs quantum wells of similar well width, where excitons binding energies of (13+-1) meV were reported in the literature. This considerable reduction in exciton binding energy indicates that the in-plane hole mass of the top most valence subband is significantly smaller in these symm. SLS. The in-plane hole mass has been estimated based on the analytical description of exciton properties in a fractional dimensional space in the infinite well approximation. This approximation has been applied due to the at present unknown values for the band offsets in the (GaIn)As/Ga(PAs) material system. This estimate leads to values of the in-plane hole mass, which are comparable to the effective electron mass of 0.06 m_o in these symm. SLS.

Acknowledgments

The authors are indebted to T. Ochs for expert technical support. This work has been supported by the Deutsche Forschungsgemeinschaft (DFG, Bonn).

References
[1] e.g. J. Singh, in "Condensed Systems of Low Dimensionality", Ed. J.L. Beeby, NATO ASI Series B. Physics Vol 253, Plenum Press (New York) (1991), p. 653
[2] e.g. Proc. 13th Int. Conf. Semiconductor Lasers, Takamatsu (1992), J. Quantum Electronics (1993), to be published.
[3] J.E. Cunningham, K.W. Goossen, M. Williams, W.Y. Jan, Appl. Phys Lett. 60, 727 (1992)
[4] T.H. Chiu, J.E. Cunningham, T.K Woodward, T. Sizer II, Appl. Phys. Lett. 62, 340 (1993)
[5] S. Lutgen, T. Marschner, T.F. Albrecht, W Stolz, E.O. Göbel, L. Tapfer, Mater. Sci. Engineering B, to be published
[6] A. Mircea, A. Ougazzaden, G Prinot, C. Kazmierski, J. Crystal Growth 124, 737 (1992)
[7] J.Y. Emery, C. Starck, L. Goldstein, A. Ponchet, A. Rocher, J Crystal Growth, to be published
[8] S. Lutgen, T. Marschner, W.Stolz, E.O. Göbel, L. Tapfer, unpublished.
[9] V D. Kulakovskii, T.G. Anderson, L.V. Butov, Semicond. Sci. Technol. 8, 477 (1993)
[10] F. Yang, M. Wilkinson, E.J. Austin, K.P. O'Donnell, Phys. Rev. Lett. 70, 323 (1993)
[11] M. Shinada, S. Sugano, J. Phys. Soc. Japan 21, 1936 (1966)
[12] H. Iwamura, H. Kobayashi, H. Okamoto, Jap. J. Appl. Phys. 23, L795 (1984)
[13] W. Stolz, J.C. Maan, M Altarelli, L. Tapfer, K. Ploog, Phys. Rev B36, 4301 (1987)
[14] J.C. Maan, G. Belle, A. Fasolino, M. Altarelli, K. Ploog, Phys. Rev. B30, 2253 (1984)
[15] K.J. Moore, G. Duggan, K. Woodbridge, C. Roberts, Phys. Rev B41, 1090 (1990)
[16] X.-F. He, Phys Rev B43, 2063 (1991)
[17] H. Mathieu, P. Lefebvre, P. Christol, J. Appl. Phys. 72, 300 (1992)

TuP14

Impurity-Bound Excitons in Selectively Doped Strained-Layer Quantum Wells in High Magnetic Fields

A B Dzyubenko[a,b] and A.Yu.Sivachenko[a]

[a] *General Physics Institute, RAS, Moscow 117942, Vavilov St.38, Russia*
[b] *Delft University of Technology, Dept. of Theoretical Physics, Lorentzweg 1, 2628 CJ Delft, The Netherlands*[1]

We report on the theoretical study of quasi two-dimensional (Q2D) excitons bound to the ionized and neutral shallow donor, (D^+,X) and (D^0,X), in high magnetic fields $B > 10$T in strained layer InGaAs/GaAs quantum wells (QWs) with simple valence band; our results are also semiquantitatively applicable to heavy-hole impurity bound excitons in GaAlAs/GaAs QWs In a quantizing field B, due to the absence of kinetic energy (i) the effective mass ratio is not strongly coupled to the problem (so there always exist stable (D^+,X) states), and (ii) both interparticle interactions and that with the Coulomb impurity are strongly enhanced We expand wavefunctions of an N-particle impurity bound complex with the total angular momentum projection M_z in terms of the non interacting wavefunctions of Q2D electrons (e) and holes (h) in B, the wavefunctions from the constructed complete orthonormal set are localized in different parts of r space, thus providing a systematic and rapidly convergent scheme for studying bound states [1]

We obtain the energies and wavefunctions of the (D^+,X) and (D^0,X) exciton complexes by direct diagonalization of the interaction Hamiltonian and derive the energies and oscillator strengths of interband magneto optical transitions; we study their dependencies on the magnetic field strength B, on a QW width and on the position of the impurity in a QW

Strictly-2D consideration predicts in the high magnetic field approximation the effect of *unbinding* of the optically active impurity-bound s excitons (D^+,X), (D^0,X) when B is increased [1] In our consideration we examine (i) Q2D effects, taking into account, in particular, the difference in the wavefunctions of transverse motion of e and h $\zeta^{(e)}(z) \neq \zeta^{(h)}(z)$, and (ii) mixing between Landau levels (which give rise to *different corrections* to the *in*-plane wavefunctions of e and h when $\hbar\omega_c^{(e)} \neq \hbar\omega_c^{(h)}$) We found, that the binding energies of the optically active s-excitons (in contrast to higher momentum states) reveal rather weak dependence on B, which is in a qualitative agreement with the experiments [2] The possibility to observe unbinding of optically active impurity bound excitons in available magnetic fields B in strained-layer Q2D QWs is discussed

[1] contact address, Tel +31-15-781719 Fax +31-15 612536

1 A B Dzyubenko, *Phys Lett* A173 (1993) 311
2 H B Ambmann, R Stepniewski, G Martinez and B Etienne, *Helv Phys Acta* 65 (1992) 323

TuP15

OPTICALLY DETECTED MAGNETIC RESONANCE STUDY OF THE TRANSITION FROM PSEUDODIRECT TYPE II TO TYPE I GaAs/AlAs SUPERLATTICES

N.G.Romanov, P.G.Baranov, I V Mashkov,
A F.Ioffe Physical-Technical Institute, Russian Academy of Sciences,
194021 St.Petersburg, Russia

P.Lavallard
Groupe de Physique des Solides - CNRS - Universités Paris 6 et 7
Tour 23 - Place Jussieu - F75251 Paris Cédex 05, France

R.Planel
Laboratoire de Microstructures et Microélectronique - CNRS UP20
196, avenue Henri Rivera - F92220 Bagneux, France

Abstract

Optically detected magnetic resonance and level anticrossing spectroscopy have been applied for the first time for a study of GaAs/AlAs superlattices (SL) in the transition region type-II SL (Γ hole in the GaAs layer and X electron in the AlAs layer) - type I SL (Γ hole and Γ electron both in the GaAs layer). Three kinds of heavy-hole excitons which are typical for type-II SL, for the transition type-II/type-I and for type-I SL with the lifetime down to 300 ps have been evidenced in the transition region and their g-factors and exchange splitting parameters have been measured.

Introduction

High sensitivity, spatial selectivity and very high resolution of optically detected magnetic resonance (ODMR) [1,2] and cyclotron resonance [3] make it possible to apply these powerful techniques for a study of excitons and unbound carriers in low-dimensional systems such as type-II GaAs/AlAs superlattices (SL) [4-7]. In these SL the lowest X-confined state of the conduction band in the AlAs barrier has a lower energy than the lowest Γ-confined state in the GaAs well. The lowest-energy recombination occurs therefore between the electrons in the AlAs and the holes in GaAs layers. The excitons in type-II SL have rather long radiative lifetime (in the us range) and small exchange energy splitting (in the ueV range).

In [6,7] the exchange energy splitting parameters and g-factors of heavy-hole excitons in type-II GaAs/AlAs SLs have been studied by ODMR as a function of the SL composition and the emission wavelength. An importance of the measurements of level anticrossings (LAC) for the analysis of the exciton energy levels has been emphasized.

In this paper we report on the first study of GaAs/AlAs superlattices in the transition region between type II SL (Γ hole in the GaAs layer and X electron in the AlAs layer) and type I SL (Γ hole and Γ electron both in the GaAs layer) using ODMR and LAC spectroscopy.

Experimental results and discussion

The GaAs/AlAs SLs were grown by molecular-beam epitaxy. The sample B223 was a typical type-II SL. The GaAs/AlAs composition (in Å) was 17.4/26 and the emission decay time τ=1 us. the sample E219 '18/12 Å, τ=10 ns) was a pseudodirect SL close to type-II/type-I transition. The sample E913 was grown with the spatial gradient of the GaAs/AlAs composition in the SL plane along the sample length: from 20.8/12.2 Å at x=0 to 22.8/11.2 Å at x=23.4 mm. A smooth transition from type-II SL (x=0) to type-I SL (x=22 mm) has been evidenced in this sample at x= 13 to 20 mm by the luminescence measurements [8]. Luminescence decay time decreases in this region down to 300 ps.

ODMR and LAC were recorded at 1.6 K by monitoring the circular polarization of photoluminescence or the intensity of one of its circularly polarized components. The excitation light of the argon-ion laser and the emission light were directed along the magnetic field while the sample could be rotated around an axis which was perpendicular to the field. The ODMR spectrometer is described in [2].

Fig.1 shows LAC spectra in type-II SL B223 and E913 (x=0). Two broad resonance signals marked as AC1 and AC2 have different signs and belong to LAC of a non radiative exciton level 1 with two radiative levels (2 and 3) as shown in the simplified energy level scheme (see Fig.1a). The levels 1 to 4 correspond to the exciton spin states |mJ,mS> (high field approximation) |3/2,1/2>, |3/2,-1/2>, |-3/2,1/2>, and |-3/2,-1/2>, respectively. LAC signals have also been detected as changes of the intensity of one of circularly polarized components of the emission and amounted up to 0.1 of this intensity. Depending on the excitation light intensity and the emission wavelength LAC signals change their value and shape. This seems to be due to a complicated interplay of the pumping, emission and relaxation rates and will be a subject of future studies.

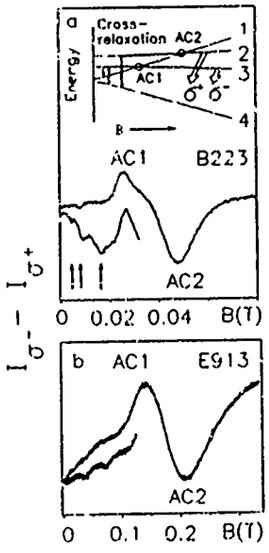

Fig 1.
Level anticrossing and cross-relaxation signals of excitons in type-II GaAs/AlAs SL: a) B223 b) E913 (x=0) at T=1.6 K and excitation light 488 nm 1 mW (upper records) and 20mW (lower records).

New resonance signals corresponding to cross-relaxation (CR) between the excitons levels have been found in type-II SLs. These signals are more pronounced on the records made at higher intensity of the exciting light (lower curves in Fig 1a and 1b). Since cross-relaxation implies an interaction between excitons it should be larger at higher light intensity. Some of cross-relaxation resonances are shown in Fig 1a. Observation of LAC and cross-relaxation resonances in addition to ODMR in type-II SL allow to determine the complete set of the exciton exchange splitting parameters. Using the notations of Ref.6 for the exchange interaction term of the spin-Hamiltonian J c S we obtain for the sample B223 (composition 17.4/26 Å): g_e= 1.d86, g_h = 2.75, c_e= 4.97 ueV,

c_x= 2.77 μeV, c_y= 0.85 μeV and for the sample E913 (type-II side, composition 20.8/22 Å) : g_x=1.90, g_y= 2.6 μeV, c_z=40 μeV, c_{xy}=6 μeV. It is to be noted that the exchange parameters vary by ca. 10 percent within the emission line.

Variations of ODMR and LAC with the shift of the excitation spot from type-II side (x=0) to type-I side (x=23.4 mm) of the sample E913 are shown in Fig.2. Although the emission decay time decreases down to 500 ps we could detect ODMR. This implies the existence of excitons with a longer lifetime.

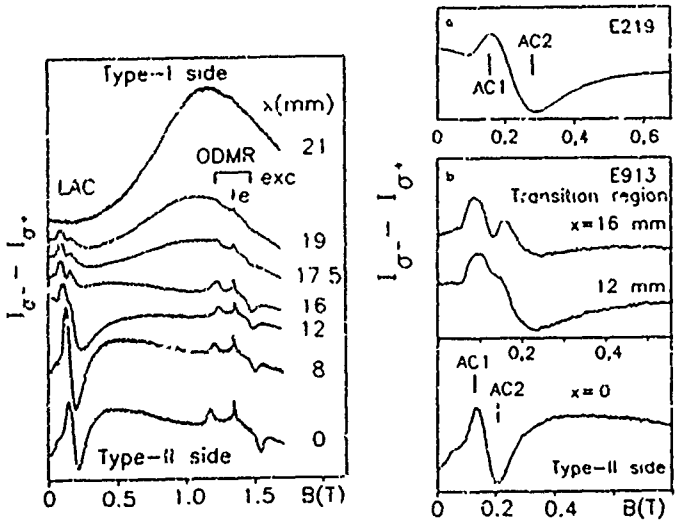

Fig 2.
Circular polarization of the emission under the action of 35 GHz microwaves in the sample E913 recorded with the shift of the excitation spot from type-II to type-I side. B // z.

Fig 3.
Level anticrossing signals in the samples E219 (a) and in the type-II and the transition regions of E913. The x-axis scale is normalized to the splitting of the exciton ODMR lines.

The splitting of the exciton ODMR lines which is proportional to c_x decreases showing a decrease of the isotropic splitting of the exciton levels. This should result in the shift of LAC signals to lower fields. Such LAC signals are really seen in the transition region but they are superimposed on another set of LAC signals corresponding to larger exchange. The LAC signals in type-II SL (E913, x=0) and in the transition region (E913, x=12, 16 mm and E219) are plotted in Fig.3 where the x-axis scale is normalized to c_x. With this scale additional LAC in E913 is similar to LAC in E219. The splitting between the radiative exciton levels has been measured in these samples with the quantum beats techniques [8] and was found to be 8.3 μeV and 6.3 μeV, respectively. The exciton radiative lifetime was about 20 ns what is too short for ODMR. The limitation arises from the condition $\gamma_{HF} \ll \gamma_{MW}$ where B_1 is the amplitude of the microwave field. Normally this prevent from the observation of ODMR for τ<100 ns. LAC effect is due to nonvanishing microscopic interaction (e.g. hyperfine interaction) coupling the approaching states. This interaction may be much stronger than the interaction with the microwave field and allow the observation of LAC for shortly lived states.

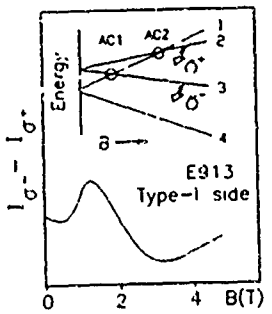

Fig.4. Exciton levels and LAC in type-I SL (E913).

One can see in Fig.2 that a very broad LAC-like signal appears in the sample E913 at the expense of the ODMR and low-field LACs with the shift of the excitation spot to type I side. This signal is shown in Fig.4. It seems to belong to excitons in type-I SL. We have observed similar signals in other type-I SL. No splitting between the exciton radiative levels is expected in type-I SL. The hole g-factor can be estimated from the general dependence on the GaAs width [7]. Thus, one can calculate the isotropic exchange splitting and electron g-factor. The positions and angular variations LAC in E913 (type-I side) can be in type-I SL explained with g_h=2.6, g_e=0.9 and c_{xy}=320 μeV.

Conclusions

The measurements of ODMR, LAC and CR allowed us distinguish between three kinds of excitons in GaAs/AlAs SLs. "Excitons II" with the lifetime ca 5-10 μs are formed in type-II SLs by the electrons and the holes localized in different layers. They can be detected with both ODMR and LAC techniques. "Excitons I"-I" with shorter lifetime (down to 1 ns) and larger exchange are appear in the transition region type-II/type-I where the energy difference between the X_z minimum of the conduction band in AlAs the Γ-minimum in GaAs decreases and tunneling of the electrons between the layers is expected. In type-I SL in which both the electron and the hole are in the same GaAs layer we have detected LAC of "excitons I" and estimated the exchange energy splitting and the electron g-factor. Since LAC can be detected even for very short exciton lifetimes the LAC spectroscopy seems to be very promising for a study of type-I SL and the transition type-II/type I.

References

1. B.C.Cavenett. *Adv.Phys.* 30. 475 (1981).
2. P.G.Baranov and N.G.Romanov. *Applied Magnetic Resonance* 2, 381 (1992).
3. P.G.Baranov, Yu.P.Veshchunov, R.A.Zhitnikov, N.G.Romanov and Yu.G.Shreter. *JETP Lett.* 26, 249 (1977).
4. H.W. van Kesteren, E.C.Cosman, W.A.J.A. van der Poel, and C.T.Foxon. *Phys.Rev. B* 41, 5283 (1990).
5. J.M.Trombetta, T.A.Kennedy, D.Gammon, B.V.Shanabrook, and S.M.Prokes. *Material Science Forum* 83-87, 1361 (1991).
6. P.G.Baranov, P.Lavallard, R.Planel and N.G.Romanov. *Superlattices and Microstructures* 12, 327 (1992).
7. P.G.Baranov, I.V.Mashkov, N.G.Romanov, P.Lavallard, and R.Planel. *Solid State Commun.* (1993), in press.
8. C.Gourdon and P.Lavallard. *Phys.Rev. B* 46, 4644 (1992).

TuP16

Valence-Subband Level Crossing in GaAs/GaAsP Strained-Barrier Quantum Well Structures Observed by Circularly Polarized Photoluminescence Excitation Spectroscopy

Hiroaki Yaguchi, Kazuyoshi Ota, Kentaro Onabe,
Yasuhiro Shiraki* and Ryoichi Ito

Department of Applied Physics, The University of Tokyo,
7-3-1 Hongo, Bunkyo-ku, Tokyo 113, Japan

*Research Center for Advanced Science and Technology (RCAST),
The University of Tokyo,
4-6-1 Komaba, Meguro-ku, Tokyo 153, Japan

Abstract

We have investigated the level configuration of the valence subbands in GaAs/GaAs$_{1-z}$P$_z$ ($z \approx 0.23$) strained-barrier quantum well structures as a function of the well width. Circularly polarized photoluminescence excitation (CPPLE) spectroscopy was used to identify the heavy- or light-hole character of the optical transitions. Distinct polarization properties were observed in the strain-split heavy- and light-hole bands in the GaAsP barriers, which indicates the photoexcited electrons in the barriers retain spin orientation well even after the capture into the quantum well relaxation process. Utilizing this polarization tendency of the transitions in the barriers, we could distinguish unequivocally the heavy- and light-hole character of the quantum well-related transitions. By varying the well width systematically, we observed the level crossing between $n \approx 1$ heavy- and light-hole transitions around the well width of 4 nm. This is in good agreement with the calculation based on the effective mass approximation.

1. Introduction

Recently, there has been considerable interest in strained-layer quantum wells and superlattices. Since the introduction of the strain modifies significantly the electronic and optical properties of semiconductor materials, it is expected to extend the possibility of the band gap engineering. In particular, strained-layer quantum wells are promising for the improvement of the semiconductor laser performances.[1-4] Among a number of strained-layer heterostructures, GaAs/GaAsP heterostructures have been widely studied.[5-8]

When GaAs/GaAsP quantum well structures are grown on GaAs substrates, GaAsP barrier layers are strained to accommodate the lattice mismatch. In the GaAsP strained barriers, heavy- and light-hole bands, which are degenerate at the Γ point in the absence of strain, split into two bands owing to the tetragonal symmetry caused by the strain. Since the GaAsP barrier layers are under tensile strain, the heavy-hole band edge is located lower in energy than the light-hole one.

It is well known that the heavy and light holes in the quantum well are confined by the heavy- and light-hole barriers, respectively, ignoring the spin-orbit coupling effects. If

cited by a σ^+ polarized light made from the linearly polarized light of the Ti:sapphire laser each barrier height is the same, the $n = 1$ heavy hole subband is located higher in energy than the $n = 1$ light-hole one because of the difference in the effective masses. In the GaAs/GaAsP strained-barrier quantum well structures, however, since the barrier height for heavy hole is larger than for light hole, the level crossing of the $n = 1$ heavy- and light-hole subbands should be observed by varying the well width.

In the present study, we report on the observation of the valence-subband level crossing in the GaAs/GaAsP strained-barrier quantum well structures using circularly polarized photoluminescence excitation (CPPLE) spectroscopy.[9] For the excitation using the right circularly (σ^+) polarized light, the absorption by the transition associated with the heavy hole creates an electron with $m_j = -1/2$ and a heavy hole with $m_j = -3/2$ according to the selection rule of the transition by circularly polarized light.[9] The circular polarization of photoluminescence defined as $P = (I_+ - I_-)/(I_+ + I_-)$ depends on the character of the valence subband states related to the emission because the spin orientation of the photoexcited electrons is hardly changed in the relaxation process of energy and momentum while the hole spin is almost relaxed.[10] Here I_+ (or I_-) is the photoluminescence intensity with σ^+ (or σ^-) polarization.

In our CPPLE measurements, the detection of the luminescence was fixed at the lowest-energy transition in the quantum well. If the lowest-energy transition is associated with the heavy-hole state, since a down-spin electron ($m_j = -1/2$) recombines a heavy-hole state with $m_j = -3/2$, σ^+ polarized luminescence should be observed. On the other hand, if the lowest-energy transition is associated with the light hole, the luminescence with the σ^- polarization should be observed in the case of the recombination of a down-spin electron ($m_j = -1/2$) and a light-hole state with $m_j = 1/2$. Thus, we can extract the information about the valence band character from the polarization tendency. However, the CPPLE measurement is valid only when there is a reference to judge the valence band character because the lowest-energy level in the CPPLE always shows the σ^+ polarization. In our experiment, the reference is the electron-heavy hole (e-hh) interband transition in the GaAsP strained barriers. We succeeded in clearly observing the polarization tendency associated with the heavy- and light-hole transitions in the barriers for the first time. From this polarization tendency of the e-hh transition in GaAsP strained-barrier layers, we could unequivocally determine the character of the transitions and observe the valence-subband level crossing by varying the well width.

2. Experimental

GaAs/GaAsP strained-barrier quantum well structures were grown on GaAs(100) substrates by metalorganic vapor phase epitaxy (MOVPE). They consisted of an undoped GaAs/GaAs$_{1-z}$P$_z$ ($z \approx 0.23$) single quantum well structure with the well width ranging from 21 to 158 Å. Strained-barrier layers were about 500 Å thick. The layer thickness and the phosphorus composition were determined by double-crystal x-ray diffraction.[7] Although the barrier layer thickness exceeds the critical thickness,[11] the barrier layers were found to be almost fully strained from the asymmetric x-ray diffraction measurements.

CPPLE spectra were obtained using a Ti:sapphire laser pumped by an Ar$^+$ laser. The CPPLE measurements were carried out at 7 K in a closed-cycle cryostat. Samples were excited by a σ^+ polarized light made from the linearly polarized light of the Ti:sapphire laser by using a Babinet-Soleil compensator. We fixed the detection wavelength at the lower energy side of the lowest-energy photoluminescence peak of the spectrum. The luminescence light containing both the σ^+ and σ^- polarized components was made into linearly polarized light by a $\lambda/4$-plate. We could selectively detect the σ^+ or σ^- polarized luminescence light

by rotating the $\lambda/4$-plate by 90°.

3. Results and Discussion

Figures 1 (a), (b) and (c) are the PLE and circular polarization spectra of GaAs/GaAsP quantum wells with the well width of 21, 82 and 39 Å, respectively. PLE spectra were obtained by the summation of the σ^+ and σ^- polarized luminescence. The label mnH (or L) shown in these figures denotes the transition between the m-th conduction subband and the n-th valence subband of heavy-hole (or light-hole) character, which could be assigned as discussed later. As seen in these figures, the peaks associated with the intersubband transitions are distinctly observed as well as the transitions corresponding to the band gap of the strained GaAsP barrier layers.

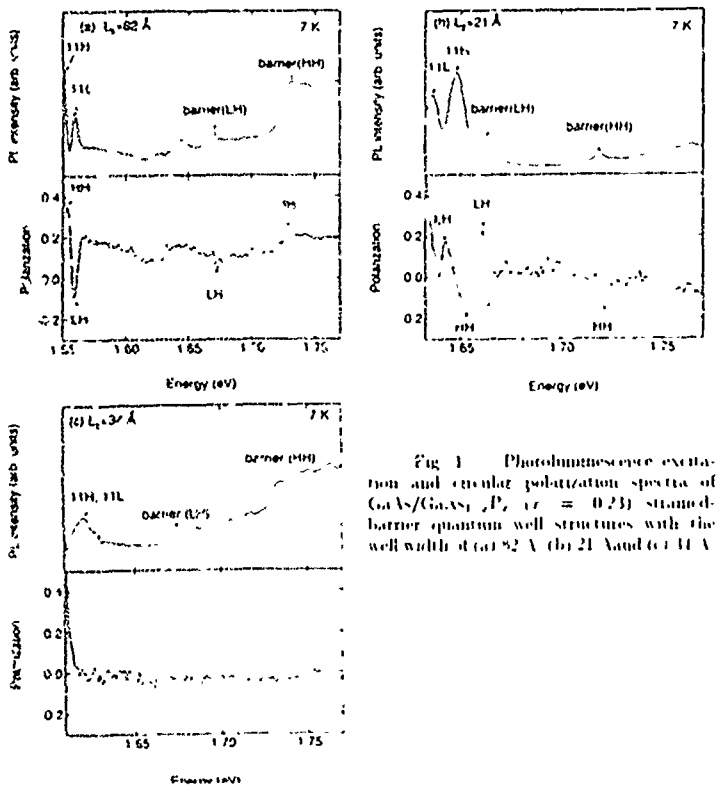

Fig. 1 Photoluminescence excitation and circular polarization spectra of GaAs/GaAs$_{1-y}$P$_y$ (y = 0.23) strained-barrier quantum well structures with the well width of (a) 82 Å, (b) 21 Å and (c) 41 Å.

In Fig. 1(a), the polarization spectrum of the e–hh (or lh) transition in the barriers shows clearly the σ^+ (or σ^-) polarization tendency. This indicates the photoexcited electrons in the barrier layers retain the spin orientation even after the capture into the well layer and the relaxation process. The lowest-energy transition has the same polarization tendency as the e–hh transition in the barriers. Therefore, we can assign this transition as the 1H transition. On the other hand, since the second lowest-energy transition has the opposite tendency, it is found to be due to the 1L transition. On the contrary, in Fig. 1(b), the e–hh transition in the barriers exhibits the σ^- polarization. The lowest-energy transition has the opposite tendency to the e–hh transition in the barriers. This indicates that the lowest-energy peak derives from 1L transition and that the second lowest-energy peak is associated with the 1H transition. In Fig. 1(c), only one peak associated with the quantum well level could be observed since the difference between the 1H and 1L transition energies was very small compared with their linewidths. Moreover, distinct polarization tendency could not be observed all over the spectrum because both the 1H and 1L transitions were detected simultaneously in this PLE measurement.

It should be noted that the integrated intensity of the lowest-energy peak is larger than the second lowest-energy peak as shown in Fig. 1(a) and that vice versa in Fig. 1(b). This fact reflects that the oscillator strength of the e–hh transition is larger than that of the e–lh transition. This is in good agreement with the theoretical calculation where the oscillator strength ratio of the e–hh transition to the e–lh one is predicted to be 3 : 1.[12] Therefore, also from the difference in the integrated luminescence intensity, it is confirmed that the 1H transition energy is lower than the 1L in the wider well, as shown in Fig. 1(a). On the contrary, the integrated luminescence intensity shows that the 1H transition energy is higher than the 1L in the narrower well shown in Fig. 1(b). In this way, we can also distinguish the characters of the band on the basis of the luminescence intensity of the transitions.

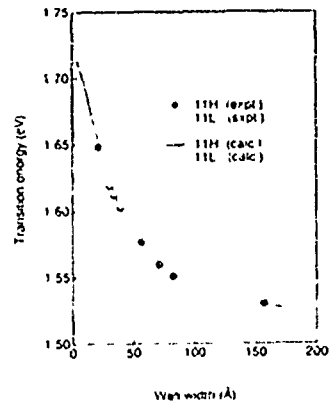

Fig. 2 Well-width dependence of transition energies in GaAs/GaAsP strained barrier quantum well structures. The solid and open circles represent 1H and 1L transitions obtained by the CPPLE measurements respectively. The solid and dashed lines show the 1H and the 1L transition energies respectively, calculated by the effective mass approximation using the band offset ratio Q_c = 0.57.

In Fig. 2, the well-width dependence of the 11H and 11L transition energies is shown. The solid and open circles represent 11L and 11H transition energies obtained by the CPPLE measurement, respectively. The solid and dashed lines are the calculated 11H and 11L transition energies, respectively. The calculation was based on the effective mass approximation assuming the square well potential. The result of the calculation can explain well the experimental data. In this study, we could obtain directly the exact barrier height from the spectra. Thus, we do not have to use the literature values, e.g. the band gap energy of the barrier layer and deformation potentials, which may cause errors in the quantum well level calculation. In the calculation, we used band offset ratio $Q_c \approx 0.57$, where $Q_c = \Delta E_c/(\Delta E_c + \Delta E_v)$, for the GaAs/GaAsP heterojunction obtained from our previous study using photoreflectance and photoluminescence measurements.[6, 7] This value is rather larger than that obtained by Van de Walle's model-solid theory ($Q_c \approx 0.39$).[13] The calculation using $Q_c \approx 0.39$ does not agree with the experiment. Therefore this CPPLE result supports our previous studies.

4. Conclusions

We have studied the valence-subband level crossing in the GaAs/GaAsP strained-barrier quantum well structures using CPPLE spectroscopy. Since we succeeded in clearly observing the polarization tendency of the transitions in barriers, we could distinguish unambiguously the heavy- and light-hole related transitions in the quantum well. The valence-subband crossover behavior we observed is in excellent agreement with the calculation based on the effective mass approximation using the band offset ratio $Q_c \approx 0.57$, which was obtained from our previous studies.

Acknowledgements

We would like to thank S. Miyoshi for his cooperation in the crystal growth and T. Machida for his assistance in measuring CPPLE spectra. We are very grateful to S. Ohtake for his technical assistance. We are also pleased to thank Dr. S. Fukatsu for his valuable suggestion and advice.

References

[1] E. Yablonovitch and E. O. Kane, IEEE J. Lightwave Technol. LT-4, 504 (1986).

[2] I. Suemune, L. A. Coldren, M. Yamanishi and Y. Kan, Appl. Phys. Lett. 53, 1378 (1988).

[3] T. Ohtoshi and N. Chinone, IEEE Photon. Technol. Lett. 1, 117 (1989).

[4] L. F. Tiemeijer, P. J. A. Thijs, P. J. de Waard, J. J. Binsma and T. van Dongen, Appl. Phys. Lett. 58, 2738 (1991).

[5] M. E. Pistol and N. Liu, Phys. Rev. B 45, 4312 (1992).

[6] X. Zhang, F. Onabe, Y. Nitta, B. Zhang, S. Fukatsu, Y. Shiraki and R. Ito, Jpn. J. Appl. Phys. 30, L1631 (1991).

[7] H. Yaguchi, X. Zhang, K. Ota, M. Nagahara, K. Onabe, Y. Shiraki and R. Ito, Jpn. J. Appl. Phys. 32, 544 (1993).

[8] X. Zhang, K. Onabe, H. Yaguchi, Y. Shiraki and R. Ito, Jpn. J. Appl. Phys. 32, L375 (1993).

[9] R. C. Miller and D. A. Kleinman, J. Lumin. 30, 520 (1986).

[10] T. Ogawa and K. J. Shan, Phys. Rev. B 42, 7111 (1990).

[11] J. W. Matthews and A. E. Blakeslee, J. Cryst. Growth 27, 118 (1974).

[12] M. Yamanishi and I. Suemune, Jpn. J. Appl. Phys. 23, L35 (1984).

[13] C. G. Van de Walle, Phys. Rev. B 39, 1871 (1989).

TuP17

Magneto-optics of dense electron plasmas in modulation-doped GaInAs/AlInAs single quantum wells

Yong-Hang Zhang[1], James L. Merz[1], M. Potemski[2], J. C. Maan[2], K. Ploog[3,§]

[1]QUEST, University of California, Santa Barbara, CA 93106, U. S. A.
[2]Max-Planck-Institut für Festkörperforchung, Hochfeldmagnetlabor, Grenoble, France
[3]Max-Planck-Institut für Festkörperforchung, Stuttgart, Germany

Abstract

Dense electron plasmas in modulation-doped GaInAs/AlInAs single quantum well structures have been studied with magnetoluminescence at 2 K. An electron-sheet-concentration (n_s)-dependent band-gap renormalization is measured in the magnetic field. The data agree well with that measured at zero magnetic field. This finding indicates that the inter- and intra-Landau-level many-body interactions are comparable at high filling factor for the electron plasma. A rigid effective-mass increase for electrons with different *k*-states in the conduction band is observed as the n_s decreases, which is contrary to the results obtained for an electron-hole plasma in GaInAs/InP quantum well.

I. Introduction

Recently, the study of the two-dimensional dense electron-hole two-component plasma and electron one-component plasma in semiconductor quantum structures subjected to high magnetic fields has attracted considerable attention.[1-4] There are usually two ways to generate these plasmas, either by using intense photoexcitation or by modulation doping the barrier regions near the well. In the former case, the carriers usually have a much higher temperature than that of the host lattice. Both the photoluminescence and the magnetoluminescence spectra are consequently complicated due to at least two facts: i) the complicity of the valence band structure; and ii) the spatially inhomogeneous distribution of the photogenerated carriers due to lateral diffusion, lateral reabsorption of wave-guided light.[5] In high magnetic fields the density of states of these structures forms discrete Landau levels due to the quantization of carrier movement. The energy splitting ($\hbar eB/\mu$) of the Landau-level peaks in magnetoluminescence is inversely proportional to the reduced mass ($1/\mu=1/m_e^*+1/m_h^*$). A recent magnetoluminescence study of the dense electron-hole plasma in GaAs/AlGaAs quantum wells has revealed a large reduction of the reduced mass for magnetoluminescence transitions with increase of the carrier concentration.[1] In addition, a gradient of this reduction of reduced mass as a function of Landau-level index has been observed for the dense electron-hole plasma in GaInAs/InP quantum well structures.[6] However, due to the involvement of the photogenerated holes in the valence band for the magnetoluminescence transitions, it is not possible to unambiguously separate the contributions from different types of carriers to the observed effect.

In the present paper, we report on a detailed magnetoluminescence study of dense electron plasmas in modulation-doped (MD) n-GaInAs/AlInAs single-quantum-well (SQW) structures grown on InP substrates. The special design of these samples allows the observation of a collective recombination of the two-dimensional electron plasma with localized photogenerated holes. In this manner, we are able to study the density-dependent properties of the electron one-component plasma in a magnetic field without including the contribution of dense holes in the valence band. It is therefore possible to determine whether the origin of the reduction of the reduced mass results mainly from the conduction-band electron-electron interactions or from the complicity of the valence band. Furthermore, there are several additional advantages provided by this technique. First, since the experiments are performed under very low photoexcitation (0.7 W/cm^2 to 200 W/cm^2), the electron temperature in the samples investigated should be close to that of the lattice. Thermal effects are therefore avoided. Second, the lateral electron distribution is expected to be homogeneous because the light spot size is of the order of 200 microns, two orders of magnitude larger than the photogenerated carrier diffusion length.

II. Experiments

The samples used for the present study are n-type MD GaInAs/AlInAs SQW grown lattice-matched on InP substrates by solid-source molecular-beam epitaxy. The well widths are 90 Å and 110 Å for Sample 1 and 2, respectively. In the center of the GaInAs well a region of 63 Å is lightly doped with Be acceptors to ~ 3×10^{16} cm^{-3}. The unintentionally-doped AlInAs barrier layers (spacers) adjacent to the well region are 200 Å. Conventional low-temperature (4.2 K) Hall-effect measurements and

§ Present Address: Paul-Drude-Institut für Festkorperelektronik, Hausvogteiplatz 5-7, Berlin, Germany.

magnetoresistance measurements (2 K) are performed to determine the electron sheet concentration (n_s) in the well. A summary of the sample structural and electrical properties is given in Table 1.

The magnetoluminescence spectra are taken in a split-coil superconducting magnet with a Faraday configuration at 2 K. The excitation energy, 7800 Å from a dye laser pumped by a Kr^+ laser, is slightly above the band-gap (1.5 eV) of the AlInAs barriers in order to minimize the heating of the electron gas in the well. The luminescence from the sample is dispersed with a double-grating monochromator and then detected with a cooled (77 K) Ge detector.

III. Results and Discussion

Fig 1 gives the magnetoluminescence spectra of Sample 1 in different magnetic fields. The photoexcitation density is about 1 W/cm^2. At zero magnetic field, a rectangular spectrum is observed, which results from the collective recombination of electrons with different k-states and the photogenerated holes localized by the intentionally introduced acceptors. The step-like line shape of the spectrum at 0-field represents clearly the unique feature of the two-dimensional density of states. A detailed discussion of the optical properties of these samples at zero magnetic filed can be found in Ref. 7. In high magnetic fields, the luminescence spectrum splits into distinct Landau levels due to the quantization of the electron movement. For instance, at 10 Tesla there are 6 Landau levels fully occupied. The degeneracy of each Landau level is $2eB/h = 4.83\times10^{10}$ B(T) cm^{-2}. Therefore, the estimated electron sheet concentration is 2.9×10^{12} cm^{-2}, which is in very good agreement with the value of 2.8×10^{12} cm^{-2} determined from the Shubnikov-de Haas oscillations of the magnetoresistance. This finding shows that under low photoexcitation the electron concentration *does not* change, providing a direct way to determine the electron concentration in the illuminated part of the sample. In the next section we use this result to obtain the electron sheet concentration under different excitations. This technique is essential to obtain the electron sheet concentration without fitting the experimental line shape. Since the Landau-level degeneracy is only a linear function of the strength of the magnetic field and is independent of the material parameters, we believe that this can more accurately determine the electron sheet concentration than line shape fitting, because the latter depends strongly on the theoretical model and the accuracy of used parameters used, which is not always guaranteed. For instance, due to many-body effects as well as the fact that the momentum (k) is not a good quantum

number in the crystal, the k-selection rule can be partially relaxed. If one uses a k-conserving model, the electron concentration may be over-estimated. In addition, another uncertainty arises from the conduction-band electron effective mass, which is found strongly electron-sheet-concentration dependent in the present study, as well as by other authors [1,6]. Therefore, any line-shape-fitting model that does not take this effect into account introduces errors in the estimated electron concentration.

As having been discussed in Ref. 8, above a certain photoexcitation threshold the electron sheet concentration decreases with increase of the photoexcitation density due to a charge transfer effect. Since the photo-excitation energy used in these experiments is higher than the band-gap of the AlInAs barrier material, the electron-hole pairs are mainly generated in the barrier layer. The strong electric field in the barrier layer near the well then drives the photogenerated electrons away from the well into deeper barrier, while the holes are driven into the well. These holes then recombine with the electrons in the well, causing the reduction of the electron sheet concentration in the well. Our previous study has shown that this effect can be used to simultaneously monitor the band-gap energy and the electron sheet concentration.[7] In the following we are going to discuss the evolution of the magnetoluminescence spectra as the photoexcitation density changes.

Fig. 2 shows the magnetoluminescence spectra of Sample 2 under different photoexcitation at 7 Tesla. Under low photoexcitation (< 0.7 W/cm^2) there are 6 Landau levels fully occupied, giving an electron sheet concentration of 2.0×10^{12} cm^{-2}, identical to to the value determined by the Shubnikov-de Haas oscillations of the magnetoresistance. When the photoexcitation is increased to 20 W/cm^2 and 200 W/cm^2, there are only 5 and 3 Landau levels fully occupied, respectively, corresponding to an $n_s = 1.67\times10^{12}$ cm^{-2} and 1.0×10^{12} cm^{-2}. The peak positions of different Landau levels are plotted in Fig. 3 as function of electron sheet concentration. Careful inspection of Fig. 3 reveals two major findings. First, the peak energies of the Landau levels move to higher energy monotonically as n_s decreases. The lowest Landau-level peak blue shifts about 11 meV to higher energy when the n_s reaches 1.0×10^{12} cm^{-2} from 2.0×10^{12} cm^{-2}. Second, the energy splitting of the Landau levels also decreases monotonically as n_s decreases, from 15.2 meV to 12.5 meV within the n_s range mentioned above. In the next paragraph we address these two findings in more detail.

The lowest Landau level represents the band-gap. When the electron concentration decreases, the band-gap renormalization becomes smaller, which results mainly from the many-body interactions between electrons as well as between electrons and photogenerated holes in our case. This effect causes the blue shift of the lowest Landau level to higher energy. This 11 meV shift agrees well with the theoretical value (11 meV) drawn from the calculation by Jalabert et. al. (Ref. 9) for an electron one-component plasma at zero magnetic field, which is confirmed by experimental results[8]. This excellent agreement implies that the density dependent band-gap renormalization is not perturbed by the magnetic field within the electron concentration range used for the present study. This behavior is actually understandable because our experiments satisfy the limit of large filling factor (the cyclotron energy, $\hbar\omega$ << the Fermi energy, E_F). In that case the exchange interaction energy of the two-dimensional electron gas scales according to the total density of carriers, irrespective of their principle Landau level quantum number.[10] It is worth mentioning that the electron-hole two-component plasma generated by intense photoexcitation in some GaAs/AlGaAs QW samples has shown a saturation of the BGR under applied magnetic field,[1] while the photogenerated electron-hole plasma in GaInAs/GaAs as well as GaInAs/InP QWs does not show this saturation up to a very high carrier concentration (5.0×10^{12} cm^{-2}).[3] This discrepancy in experimental results is not well understood to date. Present data are consistent with those reported in Ref. 3.

The reduction of the Landau-level splitting with decrease of n_S results from the increase of the reduced mass. The splittings (12.5 meV and 15.2 meV) of the lowest Landau level at different electron sheet concentration give reduced masses of 0.0652 and 0.0534, respectively. It is important to emphasize that in the samples investigated here the photogenerated holes are localized. It is thus reasonable to assume that the reduced mass is identical to the effective mass (m_e^*) of electrons. Our results then clearly reveal that the effective mass has a rigid 22% increase for all electrons in the conduction band, when n_S changes from 2.0×10^{12} cm^{-2} to 1.0×10^{12} cm^{-2}. This tendency of the experimental data agrees qualitatively with the theoretical calculation.[11] The theory predicts a change of only about 2%, an order of magnitude smaller for the corresponding electron concentration range of interest. It is also worth noting that similar effects have been observed in other III/V QWs under intense photoexcitation.[1,6] In those cases the splitting of the Landau-level peaks decreases with increase of the Landau-level index. Since the contribution from the renormalization of the hole effective mass is included, in view of our new data we believe that the gradient of the Landau-level splitting in those cases is probably due to the contribution of free holes.

IV. Conclusions:

In summary, the electron transfer effect induced by the photoexcitation of a MD SQW has been confirmed by the magnetoluminescence. An electron density-dependent band-gap renormalization for a cold electron plasma has been clearly observed in high magnetic fields. The measured value is very similar to that obtained at zero magnetic field, implying that for the electron system the inter- and intra-Landau-level many-body interactions are comparable at high filling factor. A large increase (22%) of the electron effective mass has been observed for electrons with different k-states.

References:

1) M. Potemski, J.C. Maan, K. Ploog, and G. Weimann, *Proceedings of the 19th Int. Conf. on Phys. of Semicond.*, p. 119; J.C. Maan, M. Potemski, K. Ploog, and G. Weimann: *Spectroscopy of Semiconductor Microstructures*, edited by G. Fasol, A. Fasolino, P. Lugli, p. 425, Plenum Press, 1989.
2. R. Cingolani, G. C. La Rocca, H. Kalt, K. Ploog, M. Potemski, and J.C. Maan, *Phys. Rev.* B43, 9662 (1991).
3. L.V. Butov, V.D. Egorov, V.D. Kulakovskii, and T. G. Andersson, *Phys. Rev.* B46, 15156 (1992).
4. M. Potemski, Y.H. Zhang, M. Hausenblas, J.C. Maan, G. Martinez, and K. Ploog, *Surface Science* 263, 591 (1992).
5. H. Hillmer, S. Hansmann, and A. Forchel, *Phys. Rev.* B45, 8782 (1992) and the references therein.
6. L.V. Butov, V.D. Kulakovskii, A. Forchel, and D. Grutzmacher, *JETP Lett.* 52, 121 (1990).
7. Y.H. Zhang and K. Ploog, *Phys. Rev.* B45, 14069 (1992)
8. Y.H. Zhang, R. Cingolani, and K. Ploog, *Phys. Rev.* B44, 5958 (1991)
9. R. Jalabert, S. Das Sarma and S. -R. Eric Yang, *Phys. Rev.* B41, 8288 (1990).
10. see the appendix of Ref. 2.
11. R. Jalabert and S. Das Sarma, *Phys. Rev.* B40, 9723 (1989).

Table 1: A list of the well widths, the electron sheet concentration determined by both conventional Hall-effect (n_s^{Hall}) and the Shubnikov-de Haas (SdH) oscillations of the magnetoresistance (n_s^{SdH}), as well as the Hall mobilities (μ_H) for the studied samples.

Sample	Well width (Å)	n_s^{Hall} (cm^{-2})	n_s^{SdH} (cm^{-2})	μ_H (cm^2/Vs)
1 (#51066)	90	3.8×10^{12}	2.8×10^{12}	36,000
2 (#51068)	110	2.2×10^{12}	2.0×10^{12}	54,000

Figure Captions:

Fig. 1 Low temperature magnetoluminescence spectra taken in different magnetic fields for Sample 1. The electron sheet concentration in the sample is 2.8×10^{12} cm^{-2}, while the photoexcitation density is about 1 W/cm^2.

Fig. 2 Low temperature magnetoluminescence spectra taken under different photoexcitation conditions in a magnetic field of 7 Tesla for Sample 2. The highest Landau level is depopulated as the photoexcitation *increases*. At a photoexcitation density of 200 W/cm^2, there are only 3 Landau levels fully occupied, while there are 6 under low photoexcitations.

Fig. 3 Peak position of the optical transition of different Landau levels as a function of electron sheet concentration for Sample 2. The peak position of the Landau levels as well as their splittings decreases with the decrease of electron concentration.

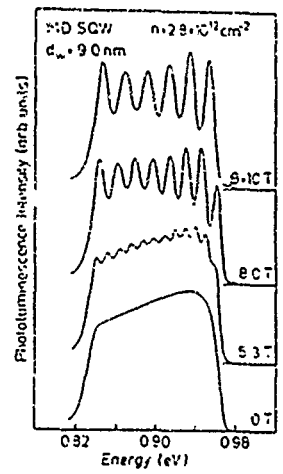

Fig 1

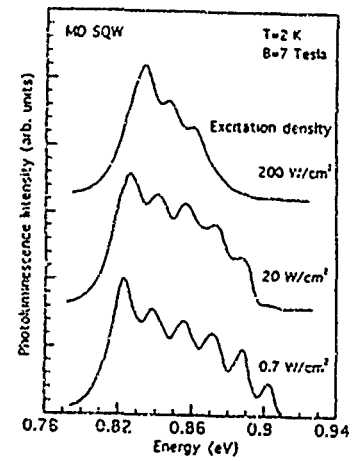

Fig 2

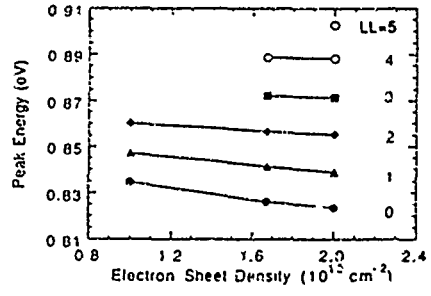

Fig 3

TuP18

High Magnetic Field Effects on the Dynamics of Excitons in a GaAs Quantum Well

S. Haacke[1], A P Heberle[2], M Potemski[1], J C. Maan[3], W W Ruhle[2], and G Weimann[4]
[1]Grenoble High Magnetic Field Laboratory, MPI-FKF/CNRS, B P 166, F-38042 Grenoble, France
[2]Max-Planck-Institut f Festkorperforschung, Heisenbergstr 1, D-70706 Suttgart, F R.G
[3]High Field Magnet Laboratory, University of Nijmegen, NL-6525 ED Nijmegen, Netherlands
[4]Walter-Schottky-Institut, Techn Universitat München, D-85748 Garching, F R.G

Abstract

The time-resolved photoluminescence of excitons in a 9 nm GaAs/(Al,Ga)As quantum well structure under high magnetic fields (B≤ 21 T) applied along the growth direction is reported. Magnetoexcitons related to the lowest light-hole subband with a well defined orientation of the magnetic moment are selectively excited. The thermalisation between the two Zeeman split 1s heavy-hole exciton ground states is found to be accelerated by the magnetic field. Moreover, a decrease of the PL rise-time is observed with respect to the zero field case where light-hole excitons and the electron heavy-hole continuum states are simultaneously excited.

Introduction

The energy diagram of quantum well (QW) excitons under high magnetic fields has been intensively studied in recent years by steady-state photoluminescence (PL) but far fewer experiments have focused on the dynamics of magnetoexcitons Absorption spectra taken with the magnetic field parallel to the growth direction show discrete peaks associated with magneto-excitons and a disappearance of any free-carrier continuum Such a modified energy spectrum is thought to change the dynamics of magneto-excitons when, for instance, thermalization processes are important Moreover, magneto-excitons are spin-split by the Zeeman effect according to their different orientation of magnetic moment (M_S= ±1) Steady-state PL experiments have suggested that the conservation of M_S during the relaxation from the excited states to the 1s ground state is favoured with increasing magnetic field and that the M_S-relaxation time between the two 1s heavy-hole magneto-excitons with opposite M_S is comparable to the excitonic radiative lifetime [1]
At zero magnetic field the dynamics of QW excitons have attracted great interest [2][3], especially concerning the presumed enhanced radiative recombination due to the size confinement of excitons in QW's [4] Magnetic moment relaxation times of 50-150 ps depending on the excitation density have recently been found for excitons at zero field [5]
High magnetic fields allow to excite excitonic states of a well-defined magnetic moment selectively by adjusting the laser energy and polarization to a given magneto-excitonic resonance, and to study the carrier dynamics in such a situation Assuming a time-independent radiative lifetime at any moment, the photoluminescence (PL) intensity is proportional to the population of the magneto-excitons The aim of the present paper is to investigate the relaxation processes between the two lowest Zeeman-split heavy-hole magnetoexcitons implying a reversal of the magnetic moment by recording their PL decay The PL rise gives information about the relaxation processes between the excited and the luminescent exciton state

Experimental Aspects

The sample investigated consists of three GaAs QW's of 90 Å thickness sandwiched between $Al_{0.26}Ga_{0.74}As$ barriers grown on an undoped (100) GaAs substrate A large barrier thickness (1000 Å) allows us to consider the GaAs layers as decoupled single QW's
The cw experiments have been carried out with a conventional PL set-up using a Ti sapphire laser (λ=720-840 nm) pumped by an Ar-ion laser A spectral resolution of 1 Å (0 2 meV) is provided by a 1 5m-monochromator
For the time-resolved studies a Styryl 8 dye laser (λ=730-820 nm, autocorrelation pulse width 7-8 ps) synchronously pumped by a mode-locked Nd YAG laser (ν=76 MHz) was used A two-dimensional synchroscan streak camera in conjunction with a 0 32m-monochromator was used in order to obtain a simultaneous recording of time- and energy-resolved PL spectra The spectral and temporal resolutions are of 0 5 meV and 15-25 meV, respectively Deviations of the electron beam in the streak camera by the stray magnetic field in the wavelength axis were were corrected by recalibration for each magnetic field The effect on the time-axis was negigible The sample was placed in a He bath cryostat (T≤ 2 K) mounted in the centre of a 21 T resistive magnet with the magnetic field and the exciting laser beam parallel to the QW growth direction (Faraday configuration) Achromatic λ/4 plates and polarizers were used to generate and to detect light of circular polarisation

Steady-state results

For zero magnetic field the luminescence spectra at T= 2 K show two transitions related to the 9 nm QW's at 1 550-1 555 eV separated by 1 meV and with a narrow line width of 1-1 5 meV (excitation density ≈50 W/cm², inset fig 1a) The excitation spectra reveal a quite small Stokes shift of 1 3 meV with respect to the high energy PL peak The dependence of the relative intensities of both transitions on the excitation density enables us to identify the high energy transition as the free (e_1,hh_1)-exciton, the low energy transition being attributed to localized exciton states saturated by high excitation densities For magnetic fields $B_{//} \geq 10$ T four transitions - two pairs of two transitions with opposite polarisation - can be resolved (fig 1a) Both high energy transitions can be identified as the Zeeman split excitonic transitions (labelled excitons A and B) with opposite magnetic moment M_S= |-1> for the σ^+ and M_S= |+1> for the σ^- polarised transition following a diamagnetic shift with increasing $B_{//}$ The two localized transitions are labelled A' (σ^+) and B' (σ^-), respectively

Excited magnetoexciton states have been probed by PL excitation (PLE) spectroscopy [1] At 10 meV above the 1s state of the (e_1,hh_1)-exciton one can distinguish the 1s state of the light-hole (e_1,lh_1)-exciton showing a diamagnetic shift For magnetic fields $B_{//}$ >5 T the excited states of the heavy-hole exciton (2s, 3s,) appear at higher energies than the 1s light-hole exciton with a more or less linear field dependence It should be stressed that for $B_{//}$ >12 T and due to the narrow PLE linewidths (≈1 meV), magnetoexcitons of well defined magnetic moment can be selectively excited by tuning the laser energy resonant to the corresponding transition As an example, fig 1a displays the σ^+ and σ^- polarized PL spectra at B=14 T for an excitation of the M_S= |+1> component of the 1s light-hole state (E_2 in fig 1b) The most striking feature of fig 1a is the fact that the excitonic high energy peak B is roughly twice as big as peak A With the reasonable assumption that A and B have the same probability for radiative recombination, it follows that A and B are not thermalized, i e their respective populations n_A, n_B do not follow a Boltzmann law $\frac{n_B}{n_A} \propto \exp(-\frac{\Delta E}{kT_L})$, with ΔE the energy separation (1 2 meV), and the lattice temperature T_L (2 K)

The preferential population of exciton B is due to the fact that is has the same electronic spin direction as the excited (e_1,lh_1) exciton component The observation of a non-thermal population of excitons A and B under cw excitation has indicated that the magnetic moment reversal time between the exciton B and A is of the same order of magnitude than the radiative lifetime [1] In a similar way, exciton A can be made dominant with an excitation energy resonant to the M_S= |-1> low energy component of the 1s (e_1,lh_1) exciton (labelled E_1)

Increasing the magnetic field leads to an increase of the intensity ratio B/A (excitation of E_2) This intensity ratio will be followed in the time-resolved experiments as a function of the magnetic field

Picosecond PL

Before we discuss the results of the time-resolved luminescence we will summarise the relaxation processes that govern the exciton dynamics (see fig 1b)

1 Relaxation from the excited light-hole state (either E_1 or E_2) down to the heavy-hole excitons A and B Due to an energy difference of 10-11 meV, emission of acoustical phonons is expected to be the relevant relaxation process When exciting in E_2 relaxation to A with the lifetime τ_{RA} requires reversal of the electron spin (see fig 1b) Relaxation down to B conserves the spin (lifetime τ_{RB})

2 Relaxation from exciton B to A implying reversal of the spin of both electron and heavy-hole is characterized by a lifetime τ_S The energy separation between both excitons can amount to 2 meV at $B_{//}$= 21 T The relaxation therefore requires emission of acoustical phonons

3 Relaxation from the B or A exciton to the corresponding localized state B' and A', respectively with a lifetime τ_{therm}

The PL decay rate of exciton B is a sum of $1/\tau_S + 1/\tau_{therm} + 1/\tau_{rad}$ (τ_{rad} being the radiative exciton lifetime) whereas process 1 determines the PL rise-time

A decay behaviour with two characteristic decay times is observed for the B exciton when the excitation energy coincides with the E_2 light-hole exciton state In this excitation condition the B exciton is twice as intense as the A exciton in the cw spectra The time-resolved data have been obtained under excitation conditions such that the time-integrated spectra are equivalent to the cw results The mean exciton density is estimated to be 10^{10} cm^{-2} The time evolution of the four PL transitions B, A, B', and A' at $B_{//}$= 21 T is displayed in fig 2a Note the dominance (by a factor of 10) of the B exciton during the first 120 ps After a rapid decay with a lifetime τ_1, the B exciton shows the same decay than the A,A' and B' levels with a longer lifetime τ_2= 180-200 ps The two slopes show a different dependence on the magnetic field For $B_{//} \geq 12$ T a clear decrease of the τ_1 time can be observed In fact, from the zero field value of $\tau_1(B=0) = 180 \pm 5$ ps the decay time decreases down to $\tau_1 = 44 \pm 2$ ps at $B_{//}$=21 T Thus two-component decay behaviour can be understood by looking at the other transitions represented in fig 2a The localized states (A' and B') show a monoexponential decay with a slope τ of the same value than τ_2 Apparently, for longer times (t> 300 ps) the exciton B and the localized states A' and B' are in thermal equilibrium, which means, for A' as an example, that the ratio of the populations (n_B,$n_{A'}$) is determined by a carrier temperature T_c following $\frac{n_B}{n_{A'}} = \exp(-\frac{\Delta E_{B,A'}}{kT_c})$ The shorter decay τ_1 can thus be interpreted as a relaxation time from the exciton B to all low-energy states, i e exciton A (with the lifetime τ_2) and the localized states A' and B' (lifetime τ_{therm})

In the opposite excitation condition when the light-hole E1 levels is excited selectively, the exciton A is preferentially populated and the high energy exciton B is roughly one order of magnitude smaller than the A luminescence The temporal behaviour of the four PL lines is depicted in fig 2b for $B_{//}$= 21 T The A exciton shows two decay times (τ_1,τ_2) much like the B exciton in the excitation condition discussed above It is interesting to note that the τ_1 decay time of exciton A is the same (95 ps) here than under excitation of the E_2 level confirming the interpretation of this time as a thermalization time with the localized states

In fig 3a the ratio B/A of the PL transients is depicted on a logarithmic scale for different magnetic field values With the reasonable assumption that both excitons have the same recombination probability, the intensity ratio is a direct measure of the ratio of exciton population $I(t) = \frac{n_B}{n_A}(t)$

Fig 3a shows a dominance of B excitons with respect to A by a factor I_0=10-20 immediately after the laser pulse (t=0) confirming the interpretation of the cw spectra that $\tau_{RB}<\tau_{RA}$ when the E_2 level is excited The following thermalization process between the populations of B and A is characterized by an exponential decay with an inverse slope of τ= 52 ± 3 ps at $B_{//}$= 21 T For t ≥ 250 ps an equilibrium situation is reached with a temperature of T_C= 18K The dominance of the B exciton in the cw spectra can now be explained by the preferential population of B at short times For lower values of the magnetic field the excess population ratio I_0 at t=0 decreases with respect to the equilibrium value I_e at long times (see fig 3b) That is the reason for the decrease of the B/A intensity ratio in the cw spectra with decreasing $B_{//}$ The dependence of τ on the magnetic field is displayed in fig 3b A decrease of τ with increasing $B_{//}$ is observed It is not possible to conclusively identify the relaxation time τ with the M_S reversal time τ_S for two reasons It is not clear for the moment if the equilibrium between all radiative states is not rather determined by the low-energy localized states and it is also possible that the relaxation from B to A occurs through optically inactive intermediate states

An effect of the magnetic field on the PL rise time can be found for low magnetic fields $B_{//} \leq 8$ T In fig 4 the PL transients of exciton B under excitation of the light-hole level E_2 at $B_{//}$= 0 and 8 T demonstrate a displacement of t_0, the time of maximum PL intensity, by roughly 100 ps towards shorter times The same behaviour is observed for the A exciton under excitation of the light-hole level E_1. Since the PL decay time is roughly the same for magnetic fields $B_{//} \leq 8$ T, the shift of t_0 must be the result of a shortening of the rise-time. On the other hand, for higher fields ($B_{//}$= 12 T) the displacement of t_0 (not shown here) is a consequence of the decrease of the decay time τ_1

Following Ref 2 and 3 the slow rise-time at $B_{//}$=0T is always observed for laser excitation with excess energies of several meV above the heavy-hole exciton The rise time reflects the slow exciton cooling through emission of acoustical phonons and it is decreased by reducing the excitation energy [3] In our case, we kept the laser energy resonant with the high hole exciton that is 11 meV above the heavy-hole exciton. The effect of the magnetic field is to shift the (e_1,hh_1) continuum to higher energies than the K≈0 states of the light-hole exciton for $B_{//} > 5$ T and at $B_{//} = 8$ T only K≈0 light-hole excitons are excited The faster PL rise time that we observe is consistent with rise-times found in Ref 3 under similar exciton densities (10^{10} cm^{-2}) and for a larger QW sample where light-hole excitons could be excited selectively In our case, the magnetic field allows to modify the energy spectrum and thus to shorten the PL rise time

Summary, Conclusion

In summary, the time-resolved magneto-optical experiments show that relaxation between the light and heavy-hole magnetoexcitons occur preferentially with conservation of the electron spin

As a consequence, under excitation conditions which favour the higher Zeeman split component, a highly non-thermal population of the 1s heavy-hole excitons is created and can be observed during the first 100 ps after the excitation pulse Increasing the magnetic field leads to a higher degree of spin conservation during the relaxation from the light to the heavy-hole excitons and also to a faster thermalization between the two Zeeman split components The net result of these two effects explains the cw spectra and the first effect is in agreement with previous interpretations The faster thermalization, hardly accessible with cw experiments, gives new insight into spin dynamics of magnetic-excitons. Further experiments clarifying the role of the localized excitons are needed to identify the thermalization time within the 1s heavy-hole exciton components with the magnetic moment reversal time

In addition, in the range of lower magnetic fields a field-induced decrease of the PL rise-time is observed which can be related to the selective excitation of light-hole excitons for $B_{//}>5$ T in our particular sample In order to clarify such an effect of the density of states modified by the magnetic field , the low field region should be studied more carefully

Acknowledgements. We would like to thank H Krath for technical assistance S H is grateful for a scholarship from the Deutscher Akademischer Austauschdienst (HSPII/AUFE)

References:

[1] M Potemski, J C Maan, A Fasolino, K Ploog, and G Weimann, Phys Rev Lett 63, 2409 (1989)
[2] T C Damen, J Shah, D Y Oberli, D S Chemla, J E Cunningham, J M Kuo, Phys Rev B 42, 7434 (1990)
[3] R Eccleston, R Strobel, W W Ruhle, J Kuhl, B F Feuerbacher, and K Ploog, Phys Rev B 44, 1395 (1991)
[4] B Deveaud, F Clerot, N Roy, K Satzke, B Sermage, and D S Katzer, Phys Rev Lett 67, 2355 (1991)
[5] T C Damen, L Viña, J E Cunningham, J Shah, and L J Sham, Phys. Rev Lett 67, 3432 (1991)

Figures

(a)

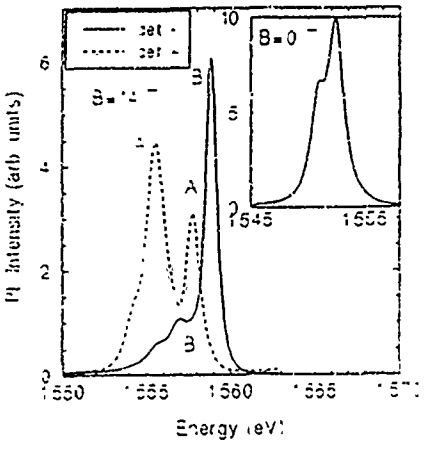

Figure 1. (a) Steady-state PL spectra at $B_{//}$= 14 T under excitation of the light-hole level E_2 showing the four main transitions B, A, B', and A' Inset Steady-state PL spectrum at $B_{//}$= 0 T (b) Representation of the excited 1s light-hole levels E_1 and E_2, the heavy-hole 1s ground states A and B and the respective localized states A' and B' The different relaxtion channels with the corresponding lifetimes are indicated (see text)

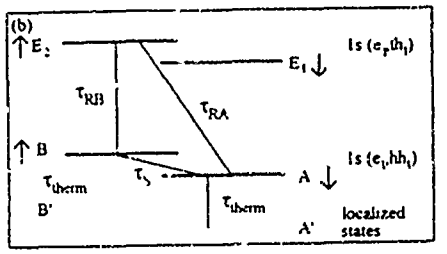

Figure 2. (a) Transients of the PL transitions B, A, B', and A' at 21 Tesla under excitation of E_2 (semi-log scale) Note the fast decay slopes τ_1 of exciton A and B (b) The same transients at 21 Tesla under excitation of E_1 Exciton A shows the same decay behaviour as in (a)

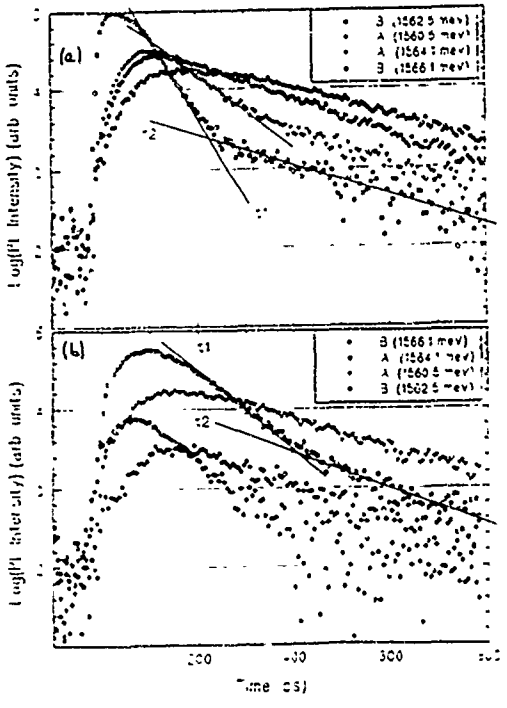

Figure 3 (a) Temporal behaviour of the intensity ratio B/A on a semi-log scale showing an exponential decay with a lifetime τ (= 52 ps at 21 T) for the relaxation of the exciton populations at different values of the magnetic field. Note the decrease of τ but the increase of the amplitude I_0 with increasing magnetic field. The curves for 14 and 18 T are vertically shifted for clarity. (b) Dependence of the thermalization time τ and of the excess population $I_0/I(t=\infty)$ upon magnetic field. The dashed and solid lines are guides to the eye.

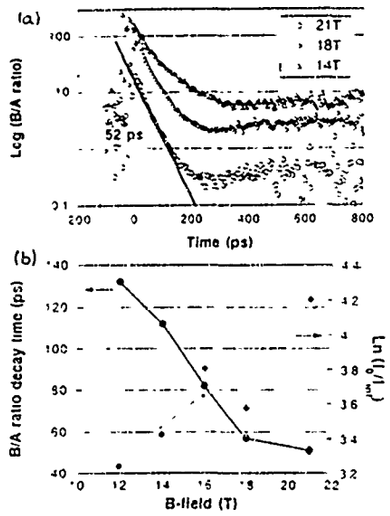

Figure 4 Normalized PL transients of exciton B under excitation of E_2 for 0 and 8 Tesla. The time of maximum PL intensity t_0 is displaced by 100 ps to shorter times at 8T revealing a decrease of the PL rise-time.

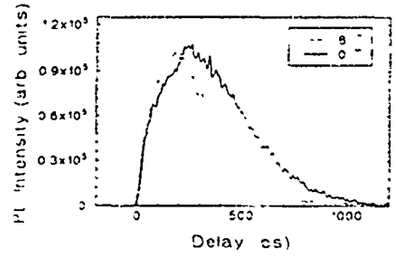

TuP19

Optical Properties of Pseudomorphic $(Si)_n/(Ge)_{10-n}$ superlattices

C. Tserbak and G. Theodorou
Department of Physics
Aristotle University of Thessaloniki
54006 Thessaloniki, GREECE

Abstract

Calculations of linear optical properties of short-period pseudomorphic strain-symmetrized $(Si)_n/(Ge)_{10-n}$ superlattices, with $n = 3, \ldots, 7$, are presented. The calculations are based on an empirical tight-binding model in the three-center representation, which includes third-neighbor and spin-orbit interactions. These strain-layer superlattices (SLS) exhibit a direct gap and their band structure is calculated. Their dielectric function, ε_2, is also calculated and the behavior of E_1 and E_2 structures of ε_2 is investigated. In addition the absorption coefficient, α close to the band gap is evaluated, taking into account only direct transitions. It is found that for some cases α has a linear dependence on energy, while for others a more rapid increase. Finally their static dielectric constant is calculated.

Progress in the various methods of crystal growth and in particular the Molecular Beam Epitaxy has provided us with the capability of constructing pseudomorphic strained-layer superlattices (SLS)[1]. This can lead to a greater flexibility in the tailoring of electronic and optical properties in the field of semiconductor microstructures and in turn to the development of technologically advanced devices[2]. The possibility of creating a direct gap semiconductor, out of constituent materials that have indirect gaps, is what makes this class of SLS particularly interested[3]. Among them the SLS Si/Ge is the most prominent one, because Si is a material with a highly advanced technology based on it, which can not be used directly in optical devices since it is an indirect gap semiconductor. Consequently the formation of a direct gap material based on Si will be of great technological importance.

Various studies have made the prediction that the $(Si)_n/(Ge)_m$ SLS with $n+m=10$ are the most promising candidates for the creation of direct gap materials, since the resulting folding brings the minimum of the Si conduction band along the growth axis at the center of the Superlattice Brillouin Zone (SBZ)[4-7]. In addition, a tensile lateral strain of the Si layers reduces the energy of the Si-like conduction band minima along the growth axis thus enhancing the possibility of obtaining direct gap materials. This tensile lateral strain can be accomplished by the growth of the SLS on a buffer alloy $Si_{1-x}Ge_x$ (001) rich in Ge.

Furthermore, experimental results support the prediction for the formation of (quasi) direct band gap materials. Zachai et al.[8] performed optical measurements on the strain symmetrized $(Si)_n/(Ge)_4$ SLS. They found an intense photoluminescence peak close to 0.84 eV, attributing it to a fundamental quasi-direct band-gap transition with an enhanced dipole-allowed transition rate. Menczigar et al.[9] in photoluminescence measurements on the strain-symmetrized $(Si)_6/(Ge)_4$ SLS, reported a peak at 0.76 eV, also attributing it to a direct transition. Olajos et al.[10] have performed detailed spectroscopic measurements on a series of strain symmetrized $(Si)_n/(Ge)_n$ SLS (n=4, 5, 6). They have fitted the experimental results for the absorption coefficient close to the absorption edge by the expression $\alpha(\omega) = A^* (\hbar\omega - E_g)^2$. Recently dielectric function spectra have also been reported for some Si/Ge SLS[11]. Many structures appear in these measured optical spectra, and therefore detailed theoretical calculations are needed in order to determine which of these structures are due to superlattice effects.

It is the purpose of this paper to study the optical properties of the strain symmetrized $(Si)_n/(Ge)_m$ SLS with $m+n=10$. More specifically we will investigate the in

fluence of the SLS composition, n/m, on the previously mentioned properties The method used is the empirical tight-binding (ETB) in the three center representation with interactions up to third neighbor[7] The spin-orbit interaction is also included in the calculations The imaginary part ε_2 of the dielectric function was calculated in the range between 0 and 10 eV using the tetrahedral method[11,12] and a uniform mesh of k-points for the integration procedure It should be noted that only direct transitions are taken into account while phonon-assisted transitions and extonic effects are ignored The real part of the dielectric function was obtained by the Kramers-Kronig relation, with the contribution from energies larger than 10 eV taken into account by the tail formula $\beta\omega/(\omega^2+\gamma^2)^2$, where γ is taken equal to 4 5 eV and β is determined by the continuity condition[13]

Fig 1 shows the band structure of the strain symmetrized SLS $(Si)_4/(Ge)_6$ along some symmetry lines of the SBZ Notice that this SLS has a direct gap, its value being $E_g^d = 0.73$ eV while the indirect gap in the Δ direction parallel to the growth plane has the value $E_g^i(\Delta_{\parallel}) = 0.94$ eV The two lowest conduction bands parallel to the growth direction ΓZ, exhibit small dispersion which indicates the confined character of these states As far as

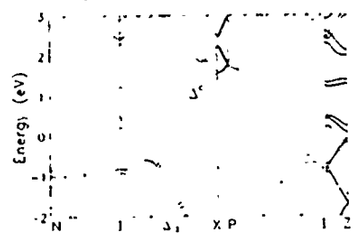

Figure 1 The band structure of the strain symmetrized SLS $(Si)_4/(Ge)_6$

the energy dispersion of the rest of the SLS under consideration, strain-symmetrized $(Si)_4/(Ge)_6$, $(Si)_6/(Ge)_6$, $(Si)_4/(Ge)_4$ and $(Si)_2/(Ge)_2$ our calculations show that close to the fundamental gap the bands exhibit behavior similar to that of $(Si)_4/(Ge)_6$ This is justified by the same folding of the bands for these SLS

Fig 2 shows the dependence of the direct and indirect gaps E_g^d and $E_g^i(\Delta_{\parallel})$ respectively, on the composition All these SLS exhibit a direct gap that depends strongly on

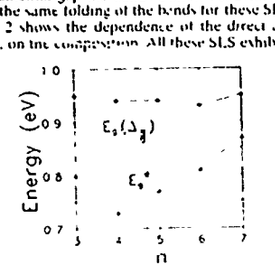

Figure 2 Direct (E_g^d) and indirect ($E_g^i(\Delta_{\parallel})$) gaps for different values of n for the strain symmetrized $(Si)_n/(Ge)_{10-n}$ SLS

the composition and increases with the exception of n = 3, with n The indirect gap $E_g^i(\Delta_{\parallel})$ remains approximately constant, independent of the composition. For SLS $(Si)_3/(Ge)_7$, $(Si)_5/(Ge)_5$, $(Si)_6/(Ge)_4$ and $(Si)_7/(Ge)_3$ the lowest transition, V_1-C_1, is allowed, is polarized in the interface plane and has significant transition probability In SLS $(Si)_4/(Ge)_6$ this transition is prohibited by symmetry In last case, the lowest allowed transition is V_1 - C_2, with energy 0 83 eV and relatively strong probability amplitude

In order to investigate the optical behavior of the Si/Ge SLS we have calculated the imaginary part of the dielectric function $\varepsilon_2(\omega)$ In fig 3(a,b) are shown the spectra of $\varepsilon_2(\omega)$ for SLS $(Si)_n/(Ge)_{10-n}$ with n = 3 4, 5, 6 and 7, and for two polarizations $\varepsilon_2^{\perp}$ denotes the average value $(\varepsilon_2^x + \varepsilon_2^y)/2$ parallel to the interface while $\varepsilon_2^{\parallel} = \varepsilon_2^z$ is the component along the growth direction At this point we should mention that SLS $(Si)_4/(Ge)_6$ and $(Si)_6/(Ge)_4$ have orthorombic symmetry and as a result they exhibit in addition an anisotropy in to the interface plane This anisotropy is relatively small The anisotropy between the components $\varepsilon_2^{\parallel}$ and $\varepsilon_2^{\perp}$ has its larger value in the region 2-4 eV For energies larger than 4 eV this anisotropy becomes smaller

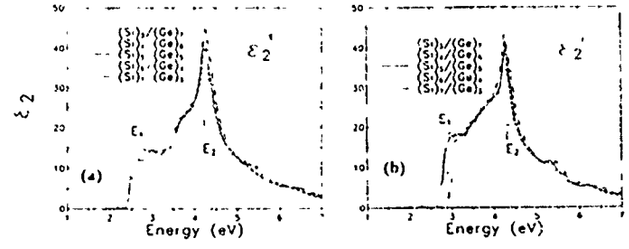

Figure 3 Imaginary part of $\varepsilon(\omega)$ for the strain symmetrized SLS $(Si)_n/(Ge)_{10-n}$ with n = 3, ,7 and polarization (a) parallel and (b) perpendicular to the interface

In the dielectric function spectra we observe mainly two structures The first is in the region 2 5-3 5 eV, is relatively extended , and comes from the corresponding E_1-structures of the constituent materials, Si and Ge The E_1-transitions of Si and Ge differ significantly (~1 2 eV) A consequence of this is the E_1-type structure in the SLS spectrum to be relatively extended and significantly influenced by the composition of the SLS As the number of Si layers increases the E_1 structure is shifted to greater energies and becomes more Si-like The second and more intense structure around the 4 3 eV has its origin in the E_2-structures of the constituent materials The E_2-structures of Si and Ge appear in similar energies and consequently the E_2 peak in the SLS will be sharp and its position will not be affected by the composition of the superlattice The amplitude of the E_2-peak increases and the one of E_1 decreases with an increase of the Si content of the SLS, resulting in a conservation of oscillator strength In the scale used in fig 3 the behavior of ε_2 close to the absorption edge is not visible The contribution to ε_2 in this region comes mainly from the quasi-direct transitions that are characterized by transition probabilities 2-3 orders of magnitude smaller than the corresponding ones of the average crystal

The absorption coefficient of strain-symmetrized $(Si)_n/(Ge)_{10-n}$ SLS with n = 3 4 7, close to the absorption edge and for polarization parallel and perpendicular to the growth plane is shown in Fig 4 For both polarizations the absorption coefficients for SLS $(Si)_4/(Ge)_6$ has stronger variation because of the larger values of the transition probabilities For SLS $(Si)_2/(Ge)_2$ and $(Si)_3/(Ge)_5$ and polarization along the [100] direction.

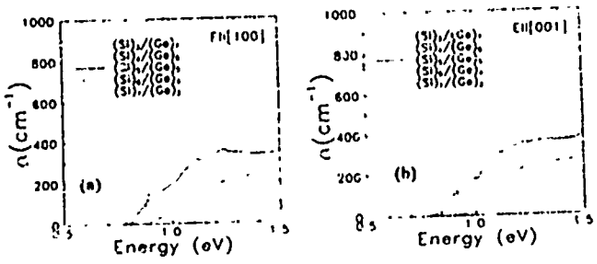

Figure 4 Absorption coefficient for the strain symmetrized SLS $(Si)_n/(Ge)_{10-n}$ with n = 3, 7 and polarization (a) parallel and (b) perpendicular to the interface

the absorption coefficient close to the gap exhibits more or less a linear behavior with respect to the energy. For the rest of the SLS as well as for polarization along the [001] direction α exhibits a more rapid increase. Consequently, in a sample where the number of layers, as well as the polarization, are not sharply defined the absorption coefficient may exhibit behavior different than the linear one.

The real part of the dielectric function is obtained from ε_2 using the Kramers-Kronig relations. The static dielectric constant of the superlattice is then obtained. The results for stain-symmetrized $(Si)_n/(Ge)_{10-n}$ and for polarization parallel ($\varepsilon_0^{//}$) and perpendicular ($\varepsilon_0^{\perp}$) to the growth plane are shown in table I. The value of ε_0 decreases

Table I Static dielectric constant for the strain symmetrized SLS $(Si)_n/(Ge)_{10-n}$ and n = 3, 7 and polarization parallel and perpendicular to the interface

n	3	4	5	6	7
$\varepsilon_0^{\perp}$	12.3	12.0	11.6	11.4	11.1
$\varepsilon_0^{//}$	12.2	11.9	11.4	11.2	11.0

with the increase of n. This can be understood from the fact that the dielectric constant of bulk Si (equal to 11.7) is smaller than the corresponding one of Ge (equal to 15.8)[15]

ACKNOWLEDGMENTS. This work has been supported in part by the ESPRIT Basic Research Action N° 7128

REFERENCES

1. E Kasper, H J Herzog, H Dambkes, and G Abstreiter in Layered Structures and Epitaxy edited by J M Gibson, G C Osbourn and R M.Tromp Materials Research Society Symposium Proceedings, vol.56 (Materials Research Society, Pittsburg, PA, 1986)
2. H Presting, H Kibbel, M.Jaros, R M Turton, U Menczigar, G Abstreiter and H G Grimmeiss, Semicond Sci. Technol 7, 1127 (1992)
3. U Gnutzman and K Clausecker, Appl Phys 3, 9 (1974).
4. S Satpathy, R M.Martin and C G Van de Walle, Phys Rev. B38, 13237 (1988).
5. R J Turton and M.Jaros, Mat. Sci. Engineering B1, 37 (1990).
6. U.Schmid, N.E.Christensen, M.Alouani and M.Cardona, Phys. Rev. B43, 14597 (1991).
7. C.Tserbak, H.M.Polatoglou and G.Theodorou, Phys. Rev B47, 7104 (1993).
8. R Zachai, K.Eberl, G.Abstreiter, E Kasper and H.Kibbel, Phys. Rev. Lett. 64, 1055 (1990)
9. U.Menczigar, J.Brunner, E.Friess, M.Gail, G Abstreiter, H Kibbel, H.Presting and E Kasper, Thin Solid Films 222, 227 (1992).
10. J Olajos, J Engvall, H G.Grimmeiss, H.Kibbel, E.Kasper and H.Presting, Thin Solid Films 222, 243 (1992)
11. U Schmid, J Humlicek, F Lukes, M.Cardona, H.Presting, H.Kibbel, E Kasper, K.Eberl, W Weyschetder and G Abstretter, Phys. Rev. B45, 6793 (1992).
12. O Jepsen and O K.Andersen Solid State Commun. 9, 1763 (1971)
13. G Lehmann and M.Taue, Physica Status Solidi b54, 469 (1972)
14. Y Petroff, M.Balkanski, J P Walter and M.L.Cohen, Solid State Commun. 7, 459 (1968)
15. C Kittel, Introduction to Solid State Physics (John Wiley, New York 1976)

TuP20

Band-edge Photoluminescence of SiGe/strained-Si/SiGe Type-II Quantum Wells on Si(100)

D. K. Nayak, N. Usami, H. Sunamura, S. Fukatsu, and Y. Shiraki
Research Center for Advanced Science and Technology (RCAST)
The University of Tokyo, 4-6-1 Komaba, Meguro-ku, Tokyo 153, Japan.

ABSTRACT

High-quality completely relaxed SiGe buffer layer is grown on Si(100) by gas source molecular beam epitaxy. Pseudomorphic Si layer is grown on this relaxed SiGe buffer to form SiGe/strained-Si/SiGe type-II (staggered) quantum wells. Intense band-edge photoluminescence is observed from these quantum wells for the first time. Quantum confinement effect in SiGe/strained-Si/SiGe type-II quantum wells is demonstrated from the systematic shift of photoluminescence energy peaks with the width of the quantum well. Transitions from the strained-Si quantum well are identified as radiative recombination of excitons, which are confined into the quantum well.

Epitaxial $Si_{1-x}Ge_x$ layers on Si are being studied extensively for potential use in Si-based optoelectronic device technology. In particular, strained-layer $(Si)_m/(Ge)_n$ superlattices (SLS) are important for possible efficient light emitting applications in the near-infrared region. $(Si)_m/(Ge)_n$ SLS show enhanced photoluminescence (PL) properties compared to indirect bandgap Ge and Si. Also, the possibility of artificially producing quasidirect bandgap in SLS has generated much interest in $(Si)_m/(Ge)_n$ SLS [1-12]. In such SLS, Si layer must be under lateral tensile strain, which is produced by growing alternating layers of pure Si and pure Ge on a relaxed SiGe buffer layer. In this case, Si and Ge layers are strained, and radiative interband recombination occurs between minibands of conduction and valence bands.

Earlier report on the photoluminescence study of $(Si)_m/(Ge)_n$ SLS was controversial because of the poor quality of SiGe buffer [9,10]. With the recent development in SiGe buffer layer technology, however, enhanced luminescence from $(Si)_m/(Ge)_n$ SLS grown on graded SiGe buffer has been obtained [12]. The luminescence is described in terms of recombination of excitons localized at random potential fluctuations in SLS. However, no study on the properties of relaxed-SiGe/strained-Si/relaxed-SiGe quantum well, which forms type-II (staggered) heterostructure and acts as the basic block for many optical devices, has been reported. In this letter, we report for the first time a systematic study of band edge photoluminescence characteristics of SiGe/strained-Si/SiGe quantum wells, which are grown on a thick relaxed $Si_{0.82}Ge_{0.18}$ buffer layer on Si(100). Quantum confinement effects and photoluminescence properties of excitons in this quantum well are presented.

Basic requirement for the growth of strained-Si layer is to obtain a good quality relaxed SiGe buffer layer on Si substrates. Recently, it has been shown that a high quality buffer layer can be grown by grading Ge concentration in the buffer layer [5]. In this study, we use step-graded buffer layer which is grown by gas source MBE (Daido Sanso VCE-S2020) at 800°C [10]. The starting material consists of 4" p-type, 5-10 Ω-cm, Si(100) wafer, 3000 Å Si buffer, 3.8 μm step graded SiGe buffer (0 to 18% Ge in 9 steps), and 2.5 μm $Si_{0.82}Ge_{0.18}$ buffer cap layer. Five quantum wells with equal well width were grown on this buffer layer at 700°C. The barrier between adjacent wells was 350 Å $Si_{0.82}Ge_{0.18}$, which eliminates any coupling between the quantum wells. All epitaxial layers were undoped.

PL spectra were recorded using a standard lock-in technique. A multi-line argon laser was used for excitation. Signal was monochromatized using a 1 m dispersive monochromator, and was detected by a liquid-nitrogen cooled Ge photodetector. Temperature control was achieved by a closed-cycle refrigerator.

Figure. 1(a) shows PL spectra from a thick (6.3 μm) step-graded relaxed $Ge_{0.18}Si_{0.82}$ buffer layer at 4.2K. A peak at 1.093 eV, denoted as SUB[TO], is due to TO assisted excitonic recombination in Si substrate. A sharp peak at 1.072 eV corresponds to NP transition from the relaxed buffer layer. Transitions from buffer (barrier) layer are denoted by "B". Full-width at half-maximum of this peak is 4 meV at 4.2K, which shows that the top region of the buffer is of good quality. Phonon-assisted momentum-conserving transverse-acoustical (TA) and transverse-optical (TO) replicas are found at lower energies, TA at 16 meV, TO(Ge-Ge) at 36 meV, TO(Ge-Si) at 51 meV, and TO(Si-Si) at 58 meV. Locations of these energy peaks agree well with PL measurement results on SiGe buffer layers by others [17]. Complete relaxation of the buffer layer was confirmed by x-ray diffraction measurements. Broad peaks at 0.880, 0.906 and 0.923 eV are identified as dislocation- and point defect-related transitions D2, D3 and D4 [18,19]. Dislocation-related transition at 0.81 eV, D1, appears only for thin buffer layers, but it disappears as the buffer layer thickness exceeds 3 μm. These dislocation-related PL, D1-D4, have been also reported for fully relaxed SiGe buffer layers grown by solid source MBE [15,19].

Five quantum wells with equal well width were grown on the above buffer layer at a lower temperature (700°C) in order to avoid thermal relaxation of strain and Ge/Si interdiffusion in the quantum well. PL spectra from the multiple quantum wells are shown in Figure. 1(b). All transitions from the strained-Si quantum well are denoted by "X". Well and barrier widths were 10Å and 350Å, respectively. Figure. 1(b) looks identical to Figure. 1(a) except that two new peaks (as a pair) appear at 0.985 and 1.043 eV in Figure. 1(b). We assign the peak at 0.985 eV to be TO phonon-assisted band-edge transition of confined excitons in strained-Si quantum well. As shown in Figure. 2, type-II band alignment results at the strained-Si/relaxed-SiGe-buffer heterointerface [20]. Therefore, TO-assisted excitonic transition occurs between the confined conduction band state (lowest lying in energy) of strained-Si quantum well and the top of valence band of SiGe buffer layer (Figure. 2). The peak at 1.043 eV in Figure. 1(b) can be assigned to NP transition from the quantum wells, and always appears as a pair with the TO-assisted transition. These two peaks were separated by 56 meV, which corresponds to TO phonon energy of Si-Si bond. In case of this narrow strained-Si quantum well, the excitonic wave function penetrates considerably into SiGe barriers, where NP transition is allowed due to the randomness of alloying, resulting in NP transition from the confined conduction band state of strained-Si layer (Figure. 2).

In order to demonstrate quantum confinement effect in the SiGe/strained-Si/SiGe quantum well, samples with different quantum well width were prepared. In these samples, the buffer layer structure was kept exactly the same. Well width dependent PL peak energy shifts for excitonic phonon-assisted as well as NP transitions are shown in Figure. 3. Figure. 3(f) is PL spectrum from the buffer layer without any quantum well. As before, transitions from strained-Si quantum well are marked by "X". For a given well width, the high-energy peak ("X") is NP free excitonic transition from the quantum wells, whereas the low-energy peak is its TO replica. Both these peaks move to lower energy as the quantum well width is increased, Figures. 3(a) and (b). As the well width is increased further, the relative intensity of NP peak becomes weaker with respect to its TO replica, Figures. 3(c), (d) and (e). This is because the penetration of excitonic wave function into SiGe barriers diminishes with increasing well width, and therefore the NP transition probability becomes smaller. TO-assisted transition for the 10Å-well appears at 0.986 eV, and moves down to 0.947 eV for the 22Å-well. This shift of 39 meV can be used to estimate the conduction band discontinuity at the relaxed-$Si_{0.82}Ge_{0.18}$/strained-Si heterointerface. Using an envelope function calculation, this is found to be about 86 meV.

Temperature dependence of excitonic transitions from strained-Si quantum wells was found to be different from that of SiGe buffer (Figure. 3). With increasing temperature, the NP transition intensity from the buffer layer, B^{NP}, diminishes rapidly. At 29K, the NP peak almost disseppear, while the transition from the quantum well, X^{TO}, remains unchang compared to its 16K value. X^{TO} can be observed until 49K. This shows that free e s are effectively confined into the quantum well and that strained-Si layer may ve less nonradiative pathway for carrier recombination compared to its SiGe buffer counterpart.

In summary, intense band-edge photoluminescence for SiGe/strained-Si/SiGe type-II (staggered) quantum wells is reported for the first time. Quantum confinement effect in this quantum well is clearly demonstrated from the systematic shift of PL energy peaks with the width of the quantum well. Transitions from the strained-Si quantum well are identified as radiative recombination of excitons, which are confined in the quantum well.

Acknowledgement . We would like to thank H. Oku, Y. Ohmori, T. Ohnishi and K. Okumura of Daido-Hoxan for their technical help in using gas source MBE. We also like to thank S. Ohtake of RCAST for technical assistance.

References

1. R. People and S. A. Jackson, *Phys. Rev. B* **36**, 1310 (1987).
2. M. S. Hybertsen and M. Schluter, *Phys. Rev. B* **36**, 9683 (1587).
3. T. P. Pearsall, J. Bevk, L. C. Feldman, J. M. Bonar, J. P. Mannaerts, and A. Ourmazd, *Phys. Rev. Lett.* **58**, 729 (1987).
4. S. Froyen, D. M. Wood, and A. Zunger, *Phys. Rev. B* **37**, 6893 (1988).
5. S. Satpathy, R. M. Martin, and C. G. Van de Walle, *Phys. Rev. B* **38**, 13237 (1988).
6. E. A. Montie, G. F. A. van de Walle, D. J. Gravesteijn, A. A. van Gorkum, and C. W. T. Bulle-Lieuwma, *Appl. Phys. Lett.* **56**, 340 (1990).
7. H. Okumura, K. Miki, S. Misawa, K. Sakamoto, T. Sakamoto, and S. Yoshida, *Jpn. J. Appl. Phys.* **28**, L1893 (1989).
8. R. Zachai, K. Eberl, G. Abstreiter, E. Kasper, and H. Kibbel, *Phys. Rev. Lett.* **64**, 1055 (1990).
9. U. Schmid, N. E. Christensen, and M. Cardona, *Phys. Rev. Lett.* **65** 2610 (1990).
10. R. Zachai, K. Eberl, G. Abstreiter, E. Kasper, and H. Kibbel, *Phys. Rev. Lett.* **65**, 2611 (1990).
11. J. Olajos, J. Engvall, H. G. Grimmeiss, U. Menczigar, G. Abstreiter, H. Kibbel, E. Kasper, and H. Presting, *Phys. Rev. B* **46**, 12857 (1992).
12. U. Menczigar, G. Abstreiter, J. Olajos, H. Grimmeiss, H. Kibbel, H. Presting, and E. Kasper, *Phys. Rev. B* **47**, 4099 (1993).
13. K. H. Jung, Y. M. Kim, and D. L. Kwong, *Appl. Phys. Lett.* **56**, 1775 (1990).
14. F. K. LeGoues, B. S. Meyerson, and J. F. Morar, *Phys. Rev. Lett.* **66**, 2903 (1991).
15. E. A. Fitzgerald, Y. H. Xie, M. L. Green, D. Brasen, A. R. Kortan, J. Michel, Y. -J. Mii, and B. E. Weir, *Appl. Phys. Lett.* **59**, 811 (1991).
16. S. Fukatsu, H. Yoshida, A. Fujiwara, Y. Takahashi, Y. Shiraki, and R. Ito *Appl. Phys. Lett.* **61**, 804 (1992).
17. J. Weber and M. I. Alonso, *Phys. Rev. B* **40**, 5683 (1989).
18. R. Sauer, J. Weber, J. Stolz, E. R. Weber, K. -H. Kusters, and H. Alexander, *Appl. Phys. A* **36**, 1 (1985).
19. V. Higgs, E. C. Lightowlers, E. A. Fitzgerald, Y. H. Xie, and P. J. Silverman, *J. Appl. Phys.* **73**, 1952 (1993).
20. R. People, *IEEE J. Quantum Electronics* **22**, 1696 (1986).

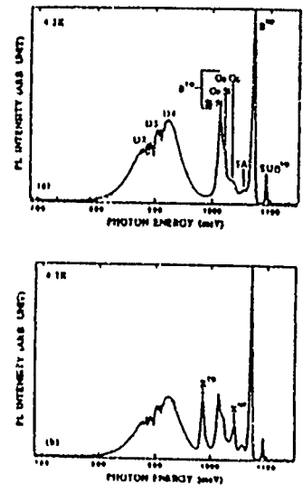

Figure 1 (a) PL spectra at 4.2K from a fully relaxed thick (6.3 μm) step-graded SiGe buffer layer. (b) PL spectra at 4.2K from 10Å strained-Si quantum wells grown on this buffer layer at 700°C.

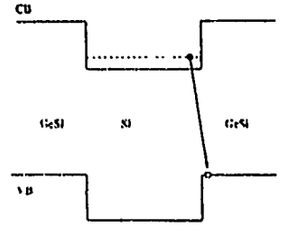

Figure 2 Schematic type-II band alignment at relaxed-SiGe/strained-Si/relaxed SiGe heterointerfaces.

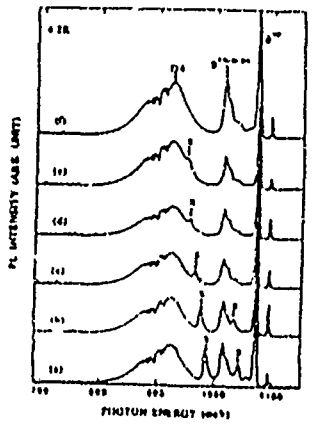

Figure 3 : PL spectra at 4.2K from five quantum well structures, which were grown on the buffer layer described in Figure. 1. (a) 10Å, (b) 13Å, (c) 16Å, (d) 19Å, (e) 21Å and (f) no quantum well.

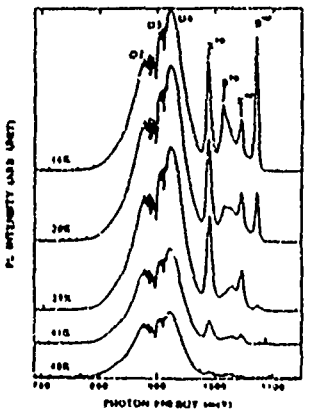

Figure 4. Temperature dependence of PL spectra at 16K, 20K, 29K, 41K, and 48K.

TuP21

On the two dimensional character of absorption spectra of Si/Ge superlattices

H.M. Polatoglou

Physics Department
Aristotle University of Thessaloniki Thessaloniki, GR-54006, GREECE
e-mail: cacz02@grtheun1.bitnet
(fax ++ (30) 31 206148

The optical properties of strained $(Si)_n/(Ge)_m$ superlattices grown on the [001] surface of $Si_{1-x}Ge_x$ have attracted recently great interest. Such modulated semiconductor structures are by now the main ingredients of many integrated optoelectronic devices developed on Si. Although much progress has been achieved in the past, it is the idea of strained-symmetrized superlattices which enabled absorption measurements on well characterized samples[1,2]. These absorption spectra indicate the existence of an absorption edge which can be related to the superlattice. The energy dependance of the absorption coefficient is found to be the one which for the case of the bulk semiconductors is connected to an indirect absorption edge. Theoretical work on the absorption spectra of these superlattices indicated that a large portion of the experimentally observed absorption spectral can be related to direct band-to band transitions[3]. Concerning the energy of the absorption edge a good agreement is found between theory and experiment. Theory predicts an almost linear energy dependance for the absorption coefficient, in disagreement with the experimental findings. Whichever is true, the energy dependance is not the one expected for such two-dimensional structures. The aim of the present work is to investigate the contribution of each direct transition to the absorption spectra and analyze their three- or two-dimensional character. To achieve these we decompose each contribution into the density of available superlattice states and the polarizability. It is found that polarizability is as important in determining the absorption spectra as the density of available states. Furthermore, the signature of direct transitions from the Σ point of the superlattice Brillouin zone is predicted to be presented by a structure in the absorption spectra about 1 eV above the absorption onset. Therefore, if experimental results are available at the above energy range, there would be a good chance to observe direct superlattice transitions away from the Brillouin zone center.

[1] J. Olajos, J. Engvall, H.G. Grimmeiss, J. Kibbel, E. Kasper, and H. Presting, International Conference on Electronic Materials, E-MRS 1992 Spring meeting, Strasbourg France (Thin Solid Films, in press)
[2] C. Menczigar, J. Brunner, E. Kasper, M. Gail, G. Abstreiter, H. Kibbel, H. Presting, and E. Kasper, International Conference on Electronic Materials, E-MRS 1992 Spring meeting, Strasbourg France (Thin Solid Films, in press).
[3] H.M. Polatoglou, submitted.

The author has been partially supported by the EEC Esprit Basic Research Action program N° 7125

TuP22

SYSTEMATIC STUDY OF INTERSUBBAND ABSORPTION IN MODULATION-DOPED p-TYPE $Si/Si_{1-x}Ge_x$ QUANTUM WELLS

T. Fromherz, E. Koppensteiner, M. Helm, G. Bauer
Institut für Halbleiterphysik, Universität Linz, A-4040 Linz, Austria

J. F. Nützel, G. Abstreiter
Walter Schottky Institut, TU München, W-8046 Garching, Germany

ABSTRACT

A study of intersubband absorption in modulation-doped p-type Si/SiGe quantum wells is presented for a variety of SiGe well widths and Ge-contents. Narrow absorption lines (20 meV) between 470 cm^{-1} and 1035 cm^{-1} are observed. If the well width is 30Å, the first excited heavy-hole subband is located close to the top of the quantum well, which results in a strong mixing between well- and barrier bound states. The latter arise from the hole transfer from the barrier into the well. A self-consistent calculation is used to fit the measured absorption spectra

I. INTRODUCTION

The absorption of infrared radiation through intersubband transitions in quantum wells has been studied extensively in the past few years, because of its possible application for infrared detectors [1]. Besides the GaAs/AlGaAs system, the Si/SiGe system has attracted a lot of attention recently. From the technological point of view, it is preferable to employ valence-band transitions in SiGe quantum wells, since the latter can be grown directly on a silicon substrate in a pseudomorphically strained fashion. Even though a number of results on this system have already been reported, [2, 3] there is no detailed knowledge yet about the optimum sample parameters (e.g., layer thicknesses, Ge-content) for infrared detection. In this paper we present a study of the hole-intersubband absorption in SiGe quantum wells for a variety of well thicknesses and depths, the latter being determined by the Ge-content of the alloy material.

II. EXPERIMENT

The samples investigated in this work were grown by molecular beam epitaxy on semi insulating [100] Si wafers. The samples consist of 10 SiGe alloy quantum wells with a Ge-content of 20%-30%, separated by 180 Å Si barriers, the center 60Å of which are boron doped to a level of 2.2×10^{18} cm^{-3}. Three groups of samples with different well widths (approximately 30 Å, 50 Å, 70 Å) were grown. During growth, the wafer was not rotated but rather kept fixed. This results in a controlled variation of the Ge-content and well- and barrier-width within one wafer. The exact structural parameters were determined by high-resolution triple axis x-ray diffraction and are listed in Tab.1. The x-ray data show that the SiGe quantum wells are pseudomorphically strained with the in-plane lattice constant of the Si substrate. Infrared absorption measurements were performed in a Bruker IFS 113 Fourier transform spectrometer at a temperature of 5 K. The samples were prepared in multipass waveguide geometry [4] as indicated in Fig. 1. The radiation is coupled into the sample at one facet which is wedged at an angle of 36°, and then undergoes approximately 8 (depending on the ratio of the thickness to the length of the sample) total internal reflections at a reflection angle of 52° . On top of the multiquantum well structure a layer of gold (300 nm) was deposited in order to enhance the electric field of the infrared radiation polarized parallel to the growth direction [5]. The transmission spectra were measured both in p-polarization (electric field parallel to the growth direction) and in the s-polarization (electric field perpendicular to the growth direction). The ratio of the transmitted intensity of p- and s- polarized radiation was normalized to the respective ratio measured at a reference Si substrate prepared in the same way as the multiquantum well samples.

III. RESULTS AND DISCUSSION

The solid lines in Fig. 1 show the absorption spectra of the 70 Å and 50 Å quantum wells, respectively. The broken lines in Fig. 1 are the result of a fit to a model describing the sample consisting of substrate, quantum wells and gold layer as a multilayer dielectric stack. The transmission through this dielectric stack was calculated using a standard matrix method [6]. According to the experimental geometry (Fig.1), the sample transmission is determined by calculating the reflection coefficient R at the sample surface. Then, if n reflections occur, the transmission will be R^n. The optical properties of quantum wells (growth direction z) can be described by an anisotropic dielectric function given by [5]

$$\varepsilon_{zz} = \varepsilon_\infty - \frac{\varepsilon_\infty f \omega_p^2}{\omega^2 - \omega_{21}^2 + i\omega\Gamma} \qquad (1)$$

$$\varepsilon_{xx} = \varepsilon_{yy} = \varepsilon_\infty - \frac{\varepsilon_\infty \omega_p^2}{\omega^2 + i\omega/\tau} \qquad (2)$$

Here ω_p is the plasma frequency defined by $\omega_p=(n_s e^2/\varepsilon_\infty \varepsilon_0 m^* a)^{1/2}$, where a is the well width, n_s is the two-dimensional carrier density, ε_∞ is the dielectric constant of the well, f is the intersubband transition oscillator strength, Γ ist the intersubband linewidth and τ ist the relaxation time for the in-plane transport. The frequency ω_{21} is defined by $\omega_{21}=E_{21}/\hbar$, where E_{21} is the transition energy between ground- and excited states of the quantum wells. As discussed in Ref. [7] for layers with thicknesses small compared to the wavelength of the incident radiation, the absorption for p-polarized light is determined only by ε_{zz}, which is a consequence of the gold overlayer. Therefore, the calculated transmission spectra shown in Fig. 1 do not depend on the value of τ.

In the calculation, E_{21}, Γ and f were treated as fitting parameters. The results for f range between 0.6 and 1 for both well widths and are in reasonable agreement with theory (f=0.96 for infinite quantum well). For E_{21} we get the results listed in Tab.1 and indicated in Fig 1. As the calculations show, the maximum absorption does not occur at the transition energy E_{21}, but at energies shifted by approximately 40 cm^{-1} to higher values. This again is a consequence of the gold layer, which shifts the absorption peak from the maximum of $Im(\varepsilon_{zz})$ to the maximum of $Im(-1/\varepsilon_{zz})$ [7]. For the intersubband linewidth Γ we get 150 cm^{-1} for both well widths. To our knowledge, this is the smallest linewidth so far observed in p-type $Si/Si_{1-x}Ge_x$ quantum wells and it is only twice as large as in comparable GaAs quantum wells.

In the lower part of Fig. 2 the absorption spectra of the 30 Å quantum wells are shown. Here, the absorption maxima shift from 725 cm^{-1} to 1035 cm^{-1} with increasing Ge-content (19% to 29%) and decreasing well width (36 Å to 26 Å). Furthermore the absorption linewidth is significantly larger than for the other samples. To understand the shape of the absorption lines, one has to calculate the energy levels of the multiquantum wells taking into account the electrostatic potential arising from the charge transfer from the doped region of the barrier to the quantum wells. If we take the z-direction parallel to the growth direction and restrict ourselves to the case of zero in-plane wavevector, the heavy-hole band is decoupled from the light-hole and split-off band [8]. Therefore, the energy levels are the eigenvalues of the one-band Schrödinger equation of the form

$$\left[\frac{1}{2}p_z\frac{1}{m_{llll}(z)}p_z + V_{llll}(z) + e\Phi_{s.c.}(z)\right]\chi(z) = E\chi(z) \qquad (3)$$

and $\Phi_{s.c}$ is the solution of Poisson's equation

$$\Delta\Phi_{s.c.} = -\frac{en_A^-}{\varepsilon\varepsilon_0}\left[\chi^*(z)\chi(z) - \vartheta(z)\right] \qquad (4)$$

Here n_A^- is the sheet concentration of occupied acceptors per well, $\Theta(z)$ is their normalized spatial distribution function, e is positive. The mass of the heavy holes along [100] direction in the SiGe is calculated from the well established values for Si (m_{llll}=0.28 m_0) and Ge (m_{llll}=0.21 m_0) [9] by linear interpolation. The band offset of the heavy-hole band in Si and SiGe was treated as a fitting parameter. For convenience, the energy of the hole states is counted positive in Eq. (3)

As an example, the results of the calculation for a quantum well with a germanium content of 24% and a well width of 30 Å are shown in Fig. 3. Due to band bending, bound states exist in the barrier. The transitions from the well bound ground state (labeled 1 in Fig 3b) to these states (labeled 2, 3 in Fig. 3b) are indirect in real space and therefore have small oscillator strengths. The levels labeled 4 and 5 in Fig. 3b are mixtures between well- and barrier-bound states. The transitions from the ground state to these states have the highest oscillator strengths (see Fig. 3a) and therefore dominate the absorption spectra. The final states of these transitions are delocalized with a significant dispersion in k_z direction, which results in a rather broad absorption. The calculations show, that the transitions in the 30Å quantum wells are most sensitive to the valence band offset, since the excited states with the highest oscillator strength have energies close to the top of the quantum well. Consequently, the absorption spectra of these samples were used to determine the valence band offset. Using a heavy-hole valence band offset of 740 meV between Si and pseudomorphically strained Ge (and linear interpolated values for the alloy) [10], the solution of Eqs. (3,4) yields the transmission spectra plotted in the upper part of Fig. 2. The results of the calculation not only reproduce the positions of the measured absorption maxima, but also the structures observed in the high energy shoulder of the absorption band (especially for the quantum well with 25% Ge content). We point out that it is crucial to take into account transitions to several excited states, which all contain considerable oscillator strength. Therefore, dielectric simulation as above does not appear sensible due to the large number of fit parameters. For the 50 Å and 70 Å samples, however, the results of the calculation do not coincide well with the experimental results (see Tab.1). The reason for this discrepancy is not yet clear, but could be caused by intersubband transitions at finite in-plane wavevector values which are not taken into account in the present calculation.

To summarize, we have performed a systematic experimental study of the infrared absorption of modulation doped p-type Si/SiGe quantum wells with various Ge-content and well widths. As long as the wavefunctions of the excited states do not couple to continuum states, the linewidth of the absorption is only 20 meV, showing the high quality of the present samples. For the 30 Å samples, the results of a model calculation agree very well with the experimental results, if a band offset of 740 meV between Si and pseudomorphically strained Ge is assumed.

ACKNOWLEDGEMENTS

This work is supported in part by ESPRIT Basic Research Action 7128 by the FWF under Proj. Nr. 9119, and by the "Jubiläumsfonds der Österreichischen Nationalbank"

REFERENCES:

[1] B. F. Levine, Semicond. Sci. Technol. 8, S404 (1993).
[2] R. P. G. Karunasiri, J. S. Park, Y. J. Mii, K. L.Wang, Appl. Phys. Lett. 57, 2585 (1990), R. P. G Karunasiri, J. S. Park, K. L. Wang, Appl. Phys. Lett. 59, 2588 (1991).
[3] R. People, J. C. Bean, C. G. Bethea, S. K. Sputz, L. J. Peticolas, Appl. Phys. Lett. 61, 1122 (1992).
[4] H. Hertle, G. Schuberth, E. Gornik, G. Abstreiter, F. Schäffler, Appl. Phys. Lett. 59, 2997 (1991), H. Hertle, F. Schäffler, A. Zrenner, G. Abstreiter, E. Gornik, Thin Solid Films 222, 20 (1992).
[5] M. J. Kane, M. T. Emeny, N. Apsley, C. R. Whitehouse, D. Lee, Semicond. Sci. Technol. 3, 722 (1988).
[6] B. Harbecke, Appl. Phys. B39, 165 (1986)
[7] T. Fromherz, M. Helm, G. Bauer, H. Kibbel, E. Kasper, Thin Solid Films 222, 251 (1992)
[8] G. Bastard, Wave Mechanics Applied to Semiconductor Heterostructures, Les Éditions de Physique 1988.
[9] Landolt-Börnstein, New Series, III/17a, Springer Verlag Berlin, Heidelberg, New York 1982
[10] L. Colombo, R. Resta, S. Baroni, Phys. Rev. B44, 5572 (1991)

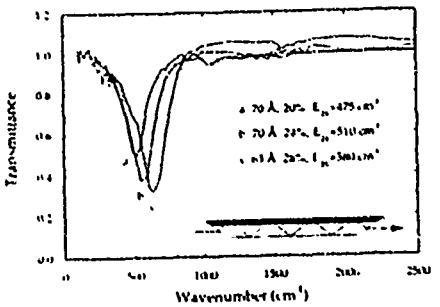

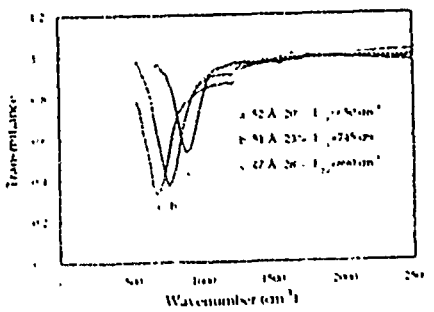

Figure 1: Transmission spectra of three modulation doped p-type Si/SiGe multi- quantum wells measured at 5 K (solid line). The respective Ge content and width of the quantum wells are indicated in the plot. The broken lines and the values of E_{21} are the result of the fitting procedure described in the text. Note, that the peak absorbance occurs at energies greater than E_{21}

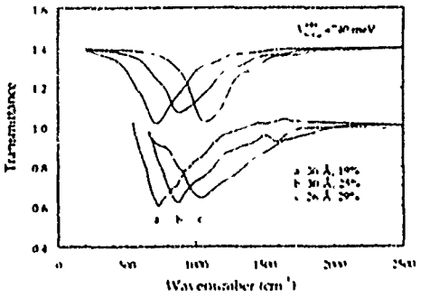

Figure 2: Calculated (upper curves) and at 5 K measured (lower curves) transmission spectra of 3 modulation doped p-type Si/SiGe multiquantum wells. The well width and Ge content of the various quantum wells are indicated in the plot. For the calculation, a band offset of 740 meV between the heavy hole bands of Si and pseudomorphically strained Ge was assumed. For clarity, the calculated transmission spectra are shifted vertically by 0.4

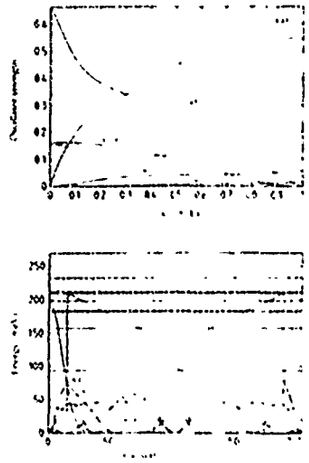

Figure 3: Results of the calculation described in the text for a modulation doped multiquantum system with 30 Å $Si_{0.76}Ge_{0.24}$ quantum wells and 177 Å Si barriers. In (a) the oscillator strength for transitions from the ground state to the first 6 excited states is plotted versus the reduced wavevector along the growth direction (L denotes the period in growth direction). The selfconsistent potential and the energy bands are plotted in (b). For convenience, the energy of the holes is counted positive. Also shown in (b) are the wavefunctions of the miniband edge states. The first digit of the labels of the wavefunctions indicates bandindex, the second the value of the reduced wave vector (in units of π/L).

Table 1: Sample parameters determined by high resolution triple axis x-ray diffraction and FIR transmission measurement. For the 30Å quantum wells, the values marked with (*) represent the measured peak position, as for reasons explained in the text no dielectric simulation was performed for these samples. The values in the parentheses were used to obtain the best fit of the peak positions to the results of a self-consistently solved Schrödinger equation.

Ge content (%)	well width (Å)	barrier width (Å)	Transition energy (cm^{-1}) measured	calculated
20	70	193	475	350
24	70	178	510	390
28	63	160	580	480
20	52	193	650	520
23	51	176	745	610
28	47	162	890	750
19 (20)	36 (35)	180	725*	720
25 (24)	30 (30)	177	865*	880
29 (29)	26 (30)	160	1035*	1060

TuP23

Characterization of the valence band offset in p-Si/Si$_{1-x}$Ge$_x$/Si by space charge spectroscopy

K. Schmalz, H. Rücker, I. N. Yassievich*), H. G. Grimmeiss,
B. Dietrich, H. Frankenfeld, W. Mehr, H. J. Osten, P. Schley
Institute of Semiconductor Physics, Frankfurt (Oder), Germany
*) Physico-Technical Institute, St. Petersburg, Russia

Abstract
Results are presented concerning direct comparison of admittance spectroscopy and DLTS on p-Si/Si$_{1-x}$Ge$_x$/Si quantum well (QW) structures with x = 0.17 using n$^+$p mesa diodes with buried QW layer. The experimental results are analysed taking into account the external electric field as well as internal electric fields induced by holes confined in the QW. The temperature dependence of potential barriers at the QW and of the Fermi level determine the activation energy E_a of the conductance across the QW. From E_a a band offset of ΔE_V = 0.16 eV was esumated. DLTS data suggest that hole emission from QW was observed with activation energy in correspondence with ΔE_V.

1. Introduction

The admittance spectroscopy [1] and the DLTS [1] can be considered as very similar dynamic techniques for the investigation of carrier capture and emission in quantum wells (QW). The admittance spectroscopy measures the charge carrier transport over the QW, and by DLTS the carrier emission from the QW can be detected. In both cases there exists a thermally activated current limited by potential barriers closely related to the band offset ΔE.
Although several DLTS-investigations [1-4] and admittance spectroscopy measurements [1, 5] were published for semiconductor heterostructures, there was not performed a direct comparison of these methods on the same device structure. This may be related to the fact that the specifications needed for the device structures are quite different. Recently, there is great technological interest in Si/Si$_{1-x}$Ge$_x$ heterostructure layers due to possible applications in silicon based device technology. Admittance spectroscopy measurements of the valence band offset ΔE_V were performed on p-type Si/Si$_{1-x}$Ge$_x$/Si QW structures for Ge-concentrations up to 30 at.% [5]. The present work is focused on an experimental and theoretical study of carrier capture and emission processes in p-type Si/Si$_{1-x}$Ge$_x$/Si QW structures for conditions of admittance- and DLTS-investigations. For our investigations we have used specially designed n$^+$p-diode structures allowing DLTS- and admittance spectroscopy on the same QW.

2. Theoretical study of carrier capture and emission processes

To obtain the valence band offset from experimental results of space charge spectroscopy measurements, it is necessary to examine carefully the capture and emission processes of holes in QWs for equilibrium and nonequilibrium conditions taking into account external electric fields as well as the local electric fields induced by confined carriers. The density of the emission current from a QW is given by $j_e = e_1 n_w$, where e_1 is the thermal emission rate and n_w the hole surface concentration in the QW. In the framework of the thermionic theory, the capture flux density is given by $j_c = 2 n_b \langle v \rangle$, where n_b is the free carrier concentration in the barrier layer and $\langle v \rangle$ is the average thermal velocity of carriers. For the condition of thermal equilibrium $j_c = j_e$ one gets for the emission rate

$$e_1 = 2 \langle v \rangle / \lambda_T \exp(-(\Delta E_V - E_1)/kT)\, g^{-1} \qquad (1)$$

where $\lambda_T = (2\pi\hbar^2/m\,kT)^{1/2}$ is the thermal length of carriers with the mass m and E_1 is the confinement energy of the first level in the well. For Boltzmann statistics the occupation factor g reduces in the limit of small wells ($E_1 \gg kT$) to g = 1 and in the opposite limit ($E_1 \ll kT$) we have $g = a/\lambda_T$ with a being the width of the well. The main peculiarities of a QW compared to a classical well consist in the existence of bound states in the QW and quasistationary levels in the continuous spectrum induced by reflection of carriers at the QW boundaries. The basic result is to replace the thermal average velocity $\langle v \rangle$ by the effective capture velocity v_c, which accounts for optical phonon emission and is calculated in the framework of quantum theory [6]. In the nonpolar Si/Si$_{1-x}$Ge$_x$/Si QW structures, where the deformation potential controls the carrier-optical phonon interaction, the capture velocity v_c for wells with ΔE_V = 140 meV and widths a of about 30 nm oscillates between $0.5 \cdot 10^6$ cm/s (broad minimum at a = 29... 30.5 nm) and $4 \cdot 10^6$ cm/s (sharp maxima at 28.5 and 31 nm), and is practically temperature independent in the region from 100 K to 200 K [7]. For p-type Si/Si$_{1-x}$Ge$_x$/Si QW structures with large carrier layers which determine the position of Fermi level, the confined holes in the QW produces a depletion region in the vicinity of QW due to the charge neutrality condition. As a result the bottom of the QW moves down, and an electric potential barrier U_0 appears. For the calculation of the energy levels in the QW and the charge density, we have solved Schrödinger and Poisson equations selfconsistently. The charge transfer between well and barriers aligns the barriers Fermi level close to the energy of the first heavy hole level in the well where the density of states is high. The calculated temperature dependence of the potential barrier eU_0 relative to the Fermi level E_F is given in Fig. 1 for different band offsets ΔE_V and acceptor concentrations N_A.

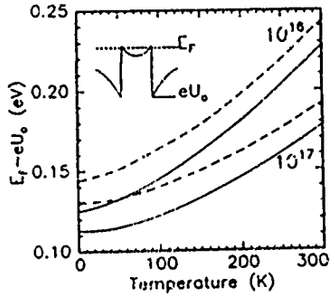

Fig. 1. Potential barrier eU_0 relative to E_F versus temperature for a 30 nm QW with valence band offsets ΔE_V = 0.14 eV (solid lines) and ΔE_V = 0.16 eV (dashed lines) for acceptor concentrations $N_A = 10^{16}$ cm^{-3} and $N_A = 10^{17}$ cm^{-3}, respectively. The valence band edge in the vicinity of the QW is indicated in the inset.

The potential barrier eU_0 induced by confined charge in the QW changes essentially the rates of carrier capture. For capture processes an effective velocity v_c^{eff} can be introduced by

$$j_c = 2\, v_c^{eff}\, n_b \qquad (2) \qquad \text{with} \qquad v_c^{eff} = v_c \exp(-eU_0/kT) \qquad (3),$$

where n_b is the concentration in the neutral region of barrier layer. Now, we consider the time

dependence of the density of capture flux in the QW. The initial condition should correspond to the absence of carriers in the QW, i. e. $n_w = 0$. The change of the carrier concentration in the well is given by $dn_w / dt = (j_c (t) - j_e (t))$. For the capture flux density given by Eqs. (2, 3) U_0 should be replaced by $U_{tt} = U_0 (t)$, the potential barrier induced by carriers captured in the time interval t . As a characteristic time for capture processes we obtain $\tau_0 = (\varepsilon_r \varepsilon_0 N_A kT / 2 e^2 v_c^2 n_h^2)^{1/2}$, where $\varepsilon_r \varepsilon_0$ is the dielectric constant. For times $t \leq \tau_0$ the population of the QW increases linearly with time. An estimation of τ_0 for $N_A = 10^{17} cm^{-3}$, $n_h = N_A$ and $T = 100$ K gives $\tau_0 \sim 10^{-12}$s. In DLTS measurements the scale for pulse duration is usually $t > 10^{-7}$ s. That means, that one can only observe an increase of the carrier concentration in QW in the vicinity of equilibrium concentration of the QW.

3. Experimental

In difference to the mesa-diode structures used in previous DLTS studies, a mesa diode geometry was developed for which the $Si_{1-x}Ge_x$ QW -layer exists as a buried layer.The three - chamber MBE equipment used in this work has been described elsewhere [8] . P-type Si (100)- substrates were prepared by an appropriate ex situ and in situ cleaning procedure, resulting in atomically clean and (2x1) reconstructed silicon surfaces as verified with RHEED First, a Si buffer layer was deposited at a growth temperature of 600 °C with an e-beam evaporator. Elemental boron was evaporated from a high -temperature effusion cell with graphite crucible (EPI), Ge and Sb were evaporated from conventional water-cooled PBN Knudsen cells. The SiGe layers were grown at a substrate temperature of 500 °C.
The following layer sequence was deposited : / 60 nm n*-Si cap layer , Sb doped with about $10^{18} cm^{-3}$ /, /150 nm p-Si cap layer, B doped with about $10^{17} cm^{-3}$/, /50 nm Si cap layer, undoped/, /30 nm $Si_{1-x}Ge_x$ layer, undoped/, /50 nm Si buffer layer, undoped /, / p-Si substrate, (100)-orientated, B doped with $10^{15} cm^{-3}$/. The undoped layers were of p-type due to the background boron contamination The concentration at the interface buffer/substrate reaches up to few $10^{17} cm^{-3}$. Employing mesa technology we have prepared n*p-photodiodes on the MBE samples. The depth of the mesa etching was 80 nm to realize buried $Si_{1-x}Ge_x$ layer. The area of the n*-contact was $A = 1.2 * 10^{-3} cm^2$. From the current voltage characteristics , an ideality factor of 1.4..2.0 was observed for the diodes. The reverse current I_R at $U_R = 2$ V was about 10^{-6} A.. For the diodes the Ge-concentration of $Si_{1-x}Ge_x$-layer was controlled by means of Raman spectroscopy. The values obtained for the investigated diodes of samples DOT25 and DOT26 are x= 0.17 and 0.25, respectively.

4. Admittance spectroscopy investigations

The temperature dependence of the sample capacitance C = C(T) at f = 1 MHz for DOT25 and DOT26 shows a qualitatively different behaviour for $Si_{1-x}Ge_x$-QW layers located in the neutral region or in the space charge region of the n*p-diode. In the second case, realized for DOT25 at reverse bias $U_R = 4$ V, the capacitance decreases only weakly with lower temperature (s. Fig. 2). On the other hand, if the $Si_{1-x}Ge_x$-layer is in the neutral region (for $U_R = 0$), as checked by our CV measurements, the C_p (T)-curve shows a characteristic decrease ΔC_p at lower temperatures From the equivalent circuit for the space charge region of the n*p diode and the QW situated in the neutral region we get C_p and G_p (C and G measured in parallel equivalent circuit) as a function of C_1, C_2, G and $\omega = 2\pi f$, where C_1 is the capacitance of the space charge region, C_2 the capacitance of QW and G the conductance across QW [5]. At higher temperatures leading to high conductivity, we get $C_p^h = C_1$ For low G we have $C_p^l = C_1 C_2 / (C_1 + C_2)$ A maximum in $G_p(T)$ is achieved at $G_p^* = 2\pi f (C_1 + C_2)$

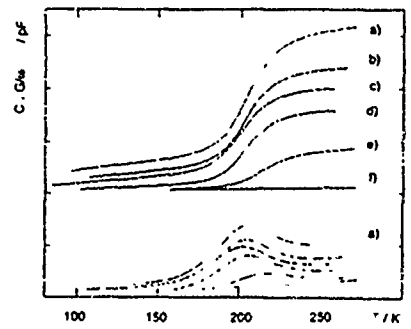

Fig. 2 . Temperature dependence of capacitance C and normalized conductance G / ω for measurement frequency f = 1 MHz for different reverse bias U_R : (a) - U_R = 0 V, (b) - 0.5 V, (c) - 1.0 V, (d) - 2.0 V, (e) - 3.0 V, (f) - 4.0 V

From the experimental results presented in Fig .2 we obtain the QW capacitance $C_2 = 80$ pF at about 100 K. The step ΔC_p decreases for larger reverse bias and diminishes for $U_R > U_R^*$. The value U_R^* corresponds to the U_R, for which the QW becomes depleted from confined carriers, i.e. $C_2 = 0$. For the sample DOT25 we obtained $U_R^* = 4$ V, and for DOT26 $U_R^* = 2$ V. The width W of the depletion region for U_R^*, which is obtained from our CV results, lies between the depth of the QW and the interface buffer/substrate, suggesting that the step in the C(T)-curves is directly related to the $Si_{1-x}Ge_x$ layer. The temperature of the conductance peak does not change with increasing reverse bias up to 2 V (s. Fig. 2), suggesting that the QW is yet in the neutral region. For the step in C_p(T) and the corresponding peak in G_p(T) we have observed a shift to lower temperatures for lower measurement frequencies f. According to Eqs. (2, 3) the temperature dependence of conductance G of the QW is given by $G(T) \sim T^{1/2} \exp (-eU_0 - E_f) / kT)$. The activation energy E_a was obtained from the resonance condition $G_p^* = 2\pi f (C_1 + C_2)$ drawing the Arrheninus plot $\ln (\alpha f / T^{1/2}) = -E_a / kT$ (α -constant), giving for the sample DOT25 $E_a = (0.14 \pm 0.01)$ eV . To obtain from E_a the band offset ΔE_V , we have to compare E_a with $(eU_0 - E_f)$ averaged over the temperature range of measurement (100..200 K) The calculated temperature dependence of $(eU_0 - E_f)$ is given for $\Delta E_V = 0.14$ and 0.16 eV in Fig. 1 . For $\Delta E_V = 0.16$ eV and $N_A = 10^{17} cm^{-3}$ we get $(eU_0 - E_f) = 0.14 .. 0.16$ eV in correspondence with $E_a = 0.14$ eV. The calculated potential barrier $U_0 = 0.10$ eV at 100 K corresponds to a equilibrium hole concentration in the QW of $n_w^{eq} = 7 * 10^{11} cm^{-2}$. From the measured capacitance of the QW a depletion width $L_0 = 80$ nm can be estimated. In order to obtain this L_0 we have to assume an acceptor concentration of a few $10^{16} cm^{-3}$ in the vicinity of the QW in agreement with our CV measurements.

5. DLTS-investigations

The values U_R^* of reverse bias , for which the QW becomes depleted, determine the optimal U_R for DLTS investigations of carrier emission from the QW, because in this case the influence of the electric field on carrier emission is minimal In the DLTS spectra measured for

$U_R = U_R'$, we have detected peaks which could be attributed by DDLTS depth profiling to a region close to the depth of the $Si_{1-x}Ge_x$ layer . For the two levels observed for sample DOT25 (s. Fig. 3), the Arrhenius plot gives the activation energies E_A = 0.17 eV (A) and 0.42 eV (B) (s. Fig. 4).

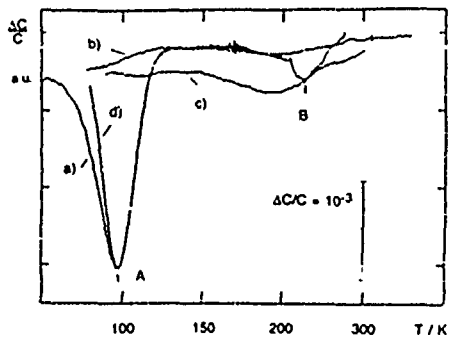

Fig. 3 DDLTS spectra measured for rate window e_n = 220 s^{-1}, pulse duration t_p = 50µs , reverse bias U_R = 4 V, and different pulse biases U_1 and U_2 (a) - U_1 = 1.5 V, U_2 = 2 V, (b) - U_1 = 0 V, U_2 = 0.5 V , (c) - U_1 = 3.0 V, U_2 = 3.5 V. Peak simulation for parameters from the Arrhenius plot : (d) - activation energy E_a = 0.17 eV, Gauss distribution of E_a is assumed with ΔE_a = 15 meV

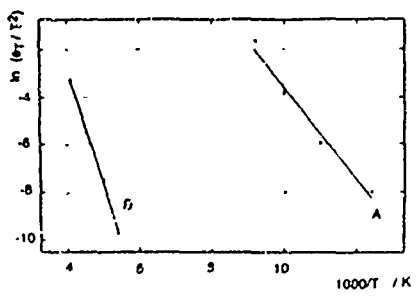

Fig. 4 . Arrhenius plot of the normalized emission rate e_T/T^2 versus 1/T for the DLTS peaks A and B for measurements with reverse bias U_R = 4 V, pulse bias U_1 = 0 V , and pulse duration t_p = 50 µs

The concentration of the deep levels B was found to vary essentially for the different diodes of DOT25 and DOT26. The relative concentration ΔC/C was for DOT25 and DOT26 in the

range (0.5 4)*10^{-3} and (0.5 3)*10^{-2}, respectively, that means considerably larger for the higher Ge-concentration. It is important that peak A with ΔC/C up to few 10^{-3} could be observed only, if the relative concentration of deep levels B was ΔC/C ≤ 10^{-3}. For diodes with higher ΔC/C of about 10^{-2}, a strong broadening of the peak shape was observed suggesting process-induced structural defects. The DLTS spectra of DOT25 measured down to 50 K do not show any other peaks in the spectrum besides the peaks A and B, but a slowly increasing signal for temperatures below 100 K, which originates presumably from states at the interface buffer/substrate. The peak corresponding to E_A = 0.17 eV may be due to direct emission of holes from the QW, because the activation energy is nearly the same one as measured by admittance spectroscopy at the same diode. To get further evidence we have investigated the following points in more detail, (a) estimation of the pre exponential factor of emission rate, (b) dependence of the emission rate on the electric field, and (c) capture of holes. For the conditions of DLTS investigation of carrier emission , the emission rate e_T is given by Eq (1) . The activation energy $E_a = \Delta E_V - E_1$ obtained from this Arrhenius plot is E_a = (0.18 ± 0.02) eV , and the pre exponential factor is equal to $(2\nu_c/\lambda_T\, g)$ = 5*10^{11} s^{-1} . For the parameters of our QW we have calculated g = 1 .Using the relation for λ_T , we have estimated a capture velocity ν_c of about ν_c = 6*10^5 cm/s close to the theoretical value of ν_c. This supports the assumption that we have really observed hole emission from the QW. The shape of the DLTS peak simulated with parameters taken from the Arrhenius plot is narrower than the peak shape measured. But, assuming Gauss distribution of the activation energy E_a with ΔE_a = 15 meV, the peak shape can be fitted (s. Fig. 3). The broadening to lower temperatures should be related to the influence of states from the interface buffer /substrate. To obtain the valence band offset ΔE_V from the activation energy E_a, we have to consider the shift of the lowest confined level E_1 in dependence on the electric field F. The energy E_1 for the QW in the presence of external electric field can be calculated using the formula for energy levels in a triangular well, i. e. $E_1 = (\hbar^2/2m)^{1/3}(9\pi/8\ eF)^{2/3}$ [9] . For U_R = 4 V, we have estimated from our CV data at 300 K that F is about 2*10^4 V/cm at the $Si_{1-x}Ge_x$/Si interface of the QW , leading to E_1 = 0.01 eV. Therefore, we obtain for the valence band offset $\Delta E_V = E_a + E_1$ a value of ΔE_V = 0.19 eV. In the case of DLTS measurement with given rate window e_n (e. g. e_n = 22 s^{-1}) for the emission rate e_T we have detected that the peak temperature T_p of the DLTS peak decreases for larger reverse bias U_R . For U_R = 6 V, corresponding to F of about 10^5 V/cm at the $Si_{1-x}Ge_x$/Si interface, we have found a decrease of the activation energy ΔE_a = 20 meV compared to E_a at U_R = 4 V. The theoretical value ΔE_a = 40 meV is somewhat larger. The hole surface concentration n_w captured in the QW can be obtained from the relation $\Delta C/C = n_w L / (2 N_A W^2)$, where L is the depth of QW layer, W the width of space charge region, and N_A the acceptor concentration. Taking N_A = 1*10^{17} cm^{-3}, we get for t_p = 50 µs that n_w = 2*10^{10} cm^{-2}. The capture of holes into the QW was investigated by the dependence of the DLTS peak ΔC/C on the filling pulse t_p. The relative signal ΔC/C of the DLTS peak depends approximately logarithmic on t_p. The characteristic time t_0 obtained from the experimental dependence $\Delta C/C \sim \ln (t_p/t_0)$ by extrapolation to ΔC = 0 is t_0 = 10^{-6} s. This dependence of the hole concentration n_w in the QW on the pulse duration t_p cannot be described satisfactory, because for $t_p > 10^{-6}$ s it is expected from the theoretical estimations for the capture process that n_w is nearly equal to the equilibrium concentration n_w^{eq} = 7*10^{11} cm^{-2}. Maybe this discrepancy is due to donor like defect states at the QW interfaces, which cause a lower effective capture velocity. Beside this, it can not be excluded that defect states at the interface buffer /substrate have also some influence due to the proximity to the QW

6. Conclusions

For the investigation of capture and emission processes of holes in p type $Si/Si_{1-x}Ge_x/Si$ QW structures by means of admittance spectroscopy and DLTS we have used n⁺p mesa diodes with a buried $Si_{1-x}Ge_x$ layer to prevent leakage current across the QW layer. To analyse the experimental results, it is essential to take into account the external electric field as well as the internal electric field induced by charge carriers confined in the QW. The potential barriers at the QW which are formed due to carrier confinement were calculated by solving self-consistently the Schrödinger and Poisson equations. The temperature dependence of these potential barriers and of the Fermi level determines the activation energy E_a of conductance across the QW. Therefore, the E_a depends sensitively on the acceptor concentration in the surrounding barrier layers. The DLTS data suggest that we have observed direct hole emission from the QW, but only for low defect concentration in the $Si/Si_{1-x}Ge_x/Si$ structure. The ΔE_V= 0.19 eV obtained by DLTS is in correspondence with the value ΔE_V = 0.16 eV estimated from admittance spectroscopy. These values are somewhat larger than the calculated values [10] and the photoemission measurements [11] of the band offset giving ΔE_V = 0.14 eV for x= 0.17.

References

1. D. V. Lang, *Physics and Device Applications*, p.377, Ed. by F. Capasso and G. Margaritondo, Elsevier Science Publisher, Amsterdam (1987)
2. N. Debbar, Dipankar Biswas, and Pallab Bhattacharya, *Phys. Rev.* B40, 1058 (1989)
3. X. Letartre, D. Stievenard, and E. Barbier, *Appl. Phys. Lett.* 58, 1047 (1991)
4. L. Vescan, R. Apetz, and H. Lüth, *J. Appl. Phys.* (1993), in press
5. K. Nauka, T. I. Kamins, J. E. Turner, C. A. King, J. L. Hoyt, and J. F. Gibbons, *Appl. Phys. Lett.* 60 (2), 195 (1992)
6. I. N. Yassievich, K. Schmalz, and M. Beer, Semicond. Sci. Techn. (1993) to be published
7. I. N. Yassievich, K. Schmalz, and M. Beer, *Proc. internat. Conf. on the Formation of Semiconductor Interfaces*, June 1993, Jülich, in press
8. H. J. Osten, G. Lippert, and J. Klatt, *J. Vac.Sci. Techn.* B 10, 1151 (1992)
9. C. Weisbuch and B. Vinter, *Quantum Semicond. Structures*, p 20, Academic Press, (1991)
10. C. G. van de Walle and R. M. Martin, *Phys. Rev.* B 34, 5621 (1986)
11. W. X. Ni and G. V. Hansson, *Phys. Rev.* B 42, 3030 (1990)

TuP24

High mobility 2D hole gases in strained Ge channels on Si substrates studied by magnetotransport and cyclotron resonance

C. M. Engelhardt, D. Többen, M. Aschauer, F. Schäffler[1], G. Abstreiter, and E. Gornik*
Walter Schottky Institut, TU München, Am Coulombwall, D-85748 Garching, Germany, FAX# +49 89 320 66 20
[1] Daimler-Benz AG, Research Center Ulm, Wilhelm-Runge-Str. 11, D-89081 Ulm-Eselsberg, Germany
* Institut für Festkörperelektronik, TU Wien, Gusshausstraße 25-29, A-1040 Wien, Austria

Abstract

High mobility two-dimensional hole gases have been achieved in p-type modulation doped Ge/SiGe heterostructures grown by MBE on a relaxed graded SiGe buffer. Hall mobilities of up to 15 500 cm² V/s at carrier densities of 1.0x10¹² cm⁻² are observed at 0.4 K in magnetotransport. The cyclotron resonance (CR) shows a narrow (FWHM 15 cm⁻¹) and strong absorption of up to 15 %. Quantum transitions are resolved. A splitting of the CR is observed, attributed to the lifting of the spin degeneracy of the ν=1 2 states at B = 0 due to the asymmetric confinement potential. Mean CR masses of 0.14 m_0 up to 0.20 m_0 are found depending on well width and carrier density.

Introduction

Conventional Si-MOSFETs (metal-oxide-semiconductor field effect transistors) are intrinsically limited by the poor quality of the oxide-semiconductor interface [1]. The electron mobilities achieved in n-type modulation-doped Si/SiGe heterostructures, however, have exceeded those of Si-MOSFETs both at low and at room temperatures within recent years [2-4]. This success is mainly due to the use of relaxed SiGe buffers with graded Ge contents which serve as a pseudo-substrate to exert the required tensile stress on the Si layer containing the two-dimensional electron gas. Low-temperature mobilities of 170 000 cm²/Vs and above have been observed.

Two-dimensional hole gases (2DHGs) in the Si/Ge system have so far been realized either in pseudomorphic SiGe/Si quantum wells [5-7] or in Ge/SiGe structures grown on Ge wafers [8]. In the first case the 2DHGs are confined in the strained SiGe layers and their mobility is limited by alloy scattering. The second approach is not compatible with standard Si technologie. Recently, however, high-mobility 2DHGs have been realized by depositing Ge channels on top of relaxed graded SiGe buffers grown by MBE on Si substrates [9-11]. These heterostructures displayed high hole mobilities and p-type MODFETs (modulation doped field effect transistors) were realized.

In this work we report on Shubnikov-de Haas (SdH) Hall, and cyclotron resonance (CR) investigations of such p type modulation-doped Ge/SiGe heterostructures.

Sample structure and experimental technique

The samples investigated were grown at Daimler-Benz and have been described in detail in ref. 9. The nominal parameters are listed in Table I. A rather thick relaxed SiGe buffer with linearly increasing Ge content was grown on an n-Si substrate. The active structure consists of a Ge channel and a modulation-doped SiGe barrier. The Ga δ-doping layer has an integral concentration of $5x10^{12}$ cm^{-2}. A thin Si cap layer was finally deposited to protect the structure against oxidation. TEM (transmission electron microscopy) micrographs of sample 1 have yielded an actual width of the Ge channel of 168 Å rather than the nominal 125 Å. Similar values are expected for samples 2 and 3. Because of the in-plane compressive strain the degeneracy of light- (lh) and heavy-hole (hh) bands at k = 0 is lifted. Therefore the hh-bands should be occupied and should exhibit a reduced effective mass.

For the CR measurements the sample substrates were wedged to avoid interferences. Ohmic contacts were alloyed into the corners to determine the sheet density via two-point magnetoresistance measurements. The experiments were performed using a Fourier transform spectrometer at magnetic fields up to 17 T. Evaluation of the spectra is done by a Drude formalism to determine the resonance positions ω_c, from which the CR masses m_c=eB/ω_c can be deduced. The scattering rates 1/τ and carrier densities n_s as described in ref. 12.

The samples used for the magnetotransport meas-

sample	1	2	3
Si cap [Å]	30	30	20
spacer thickness [Å]	100	100	75
Ge content of barrier	0.6	0.6	0.5
channel width [Å]	125	125	75
final Ge content of buffer	0.7	0.7	0.7
graded buffer thickness [µm]	6	3	3

Table I: Nominal sample parameters

surements had been processed into standard Hall bars by using optical lithography and wet chemical etching.

Magnetotransport

Fig. 1 displays Hall mobility and density of sample 1 as a function of temperature. A specimen in Hall geometry was used for the measurements up to about 60K while van-der-Pauw geometries were employed at higher temperatures. Good agreement is found in the data obtained from both geometries. The superior mobility of the Ge channel becomes obvious in the temperature range down to about 77 K. At this temperature 12 000 cm^2/Vs are reached. However, the saturation behaviour at lower temperatures to a value of 15 500 cm^2/Vs is indicative of a relatively high defect density or background doping concentration within the Ge channel. Further optimization of the growth and doping parameters is certainly required to match the high standards reached with n-type heterostructures on relaxed SiGe buffers [2]. Very recent reports claiming Hall mobilities as high as 55 000 cm^2/Vs are very promising [11]). Nevertheless, the mobilities reached in these samples are high enough for a variety of magnetotransport and CR studies, which were formerly not possible.

The SdH and Hall traces of sample 1 at T = 370 mK are shown in Fig. 2. The Hall curve exhibits very precise quantum Hall plateaus accompanied by vanishing longitudinal resistivity ρ_{xx} at higher magnetic fields. At a magnetic field of about 6 T the spin splitting begins to be resolved corresponding to a filling factor $\nu = 2$. The early onset of the oscillations, with regard to the mobility of 15 500 cm^2/Vs, is a first evidence of a rather low transport mass. It is noteworthy that – contrary to magnetotransport work conducted on hole gases confined in strained SiGe layers – we observe SdH oscillations linked to even filling factors at small fields.

By evaluating the damping of the purely oscillatory part of ρ_{xx} as a function of the inverse magnetic field as described in ref. 13 with an effective mass $m^* = 0.14\ m_0$ obtained from the CR measurements (see

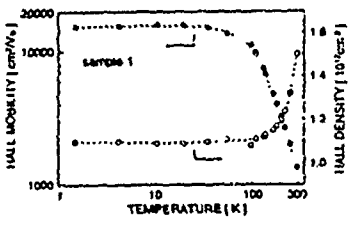

Fig. 1: Temperature-dependent Hall mobility and Hall density of sample 1

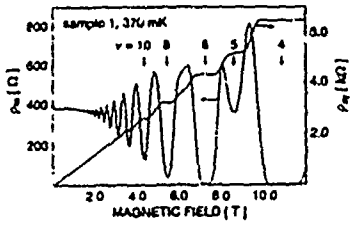

Fig. 2: Shubnikov-Haas and Hall-traces of sample 1 at 370 mK, measured in Hall-geometry

below) one finds that the transport relaxation time τ_t is about 3.9 times larger than the single-particle relaxation time τ_s. The value of this ratio was found to lie in between 10 and 26 for high-mobility electron gases in Si/SiGe heterostructures [13]. We therefore conclude that the dominant scattering mechanism in the p-type structures investigated in this work is of long-range nature, but that there is still a significant short-range contribution as well. This would also account for the premature saturation of the mobility below T = 40 K described above.

Table II summarizes the low-temperature carrier densities of all three samples as determined by magnetotransport and CR, the Hall mobilities, and the CR masses in the low-magnetic field limit. Excellent agreement was found for the carrier densities obtained from the Hall, SdH, and CR data. The SdH experiments yielded the existence of a bypass in sample 2. The hole mobility is therefore overestimated in this sample. At higher temperatures sample 2 always exhibits mobilities little below that of sample 1 [9].

Cyclotron resonance

Direct information on effective masses of holes is obtained from CR. In ref. 14 the CR of holes in a $Si_{0.63}Ge_{0.37}$ channel on top of a Si substrate was reported. Due to the lower mobilities only a single broad

sample	1	2	3
magnetotransport, 0 T			
n_s [$10^{12}cm^{-2}$]	1.04	1.07	1.79
μ_{Hall} [cm^2/Vs]	15 500	21 700*	9 800
cyclotron resonance, 1.5 K			
n_s [$10^{12}cm^{-2}$]	1.06	1.10	1.78
m_c [m_0]	0.142	0.151	0.200

*Table II: Low-temperature characteristics obtained by magnetotransport and cyclotron resonance in the low-magnetic field limit. *) this mobility value appears to be distorted by a bypass*

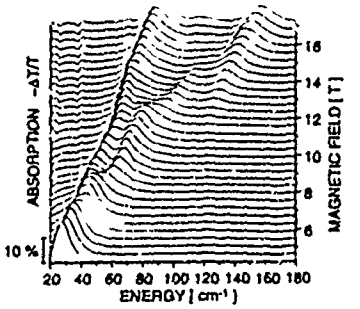

Fig. 3: Sample 1 at 1.5 K. Series of cyclotron resonance spectra for magnetic fields of 4.2 T up to 17 T. The CR absorption -ΔT/T = (T(B) - T(0)) / T(0) is plotted in the vertical scale, the spectra for different magnetic fields are shifted vertically for convenience.

and shallow resonance was observed, allowing the determination of an effective mass. In contrast the CR of the Ge p-channels investigated in this work reveals a rich structure due to the much higher mobility.

A series of CR spectra of sample 1 for magnetic fields from 4.2 T up to 17 T measured at 1.5 K is displayed in Fig. 3. At low magnetic fields the resonance exhibits up to 15 % absorption and a FWHM of 15 cm^{-1}.

Fig. 4 gives the evaluation of the spectra in Fig. 3 for sample 1. At low fields a CR mass of 0.142 m_0 is determined by fitting the resonance with a single line. The sharp resonances and the rather low CR masses allow quantum transitions to be resolved at higher magnetic fields in all samples. At fields above B = 6 T two resonances are clearly resolved. Below 6 T the fit with two lines is stable and independent of starting values, therefore also in this regime two CR masses are plotted. Typical scattering rates are $1.0\times10^{12}\ s^{-1}$ for samples 1 and 2, and about $1.5\times10^{12}\ s^{-1}$ for sample 3.

In Table II the carrier densities and CR masses of the three samples are given as determined by fitting the resonance with a single line at low magnetic fields. The absolute values confirm the expectation that the in-plane mass is light. For the mean CR masses a strong variation is found for the three samples. Since all three Ge channels are subjected to the same amount of strain, variations in CR mass are attributed to the different well widths and carrier densities. The increased subband energy and higher carrier density in sample 3 leads to a higher Fermi energy. The increased CR mass reflects the strong nonparabolicity of the valence band.

In all three samples two different CR masses are found at low fields. Note, that due to the strain only hh-bands with axial quantum number $\pm3/2$ are occupied. The splitting is found to be 13-18 % of the total CR energy. It is attributed to the lifting of the spin degeneracy of the +3/2 and -3/2 bands at B = 0 and k = 0 by the asymmetric confinement potential [15]. Such a splitting has been observed in GaAs p-type heterostructures [16]. This effect was often confused with the Kramers degeneracy in the literature. The inconsistency has recently been clarified [17].

The two CR masses oscillate with the magnetic field. The lower trace splits at about 12 T. The branch with the higher CR mass is observed as an asymmetry in the high energy tail of the lowest energy resonance. Also, at 12 T a high energy resonance appears, corresponding to the lowest CR masses in Fig. 4. It gains intensity just as much as the resonance at lower energy loses it. The periodicity of the mass oscillations

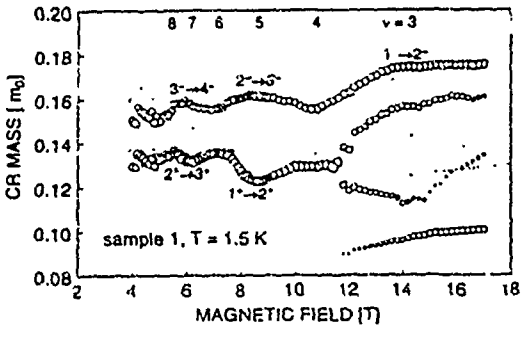

Fig. 4: Combined plot of CR masses and carrier densities (circles) of the circles) for sample 1 at 1.5 K as evaluated from the spectra shown in Fig. 3. The filling factors ν = n_s eB corresponding to a carrier density of $n_s = 1.06\times10^{12}\ cm^{-2}$ are given by the dotted lines. Also shown by the dashed lines is the result of a model calculation giving the expected CR masses for the different possible transitions at a given filling factor which may serve as a guide to the eye.

appears to be linked to the filling factor which is calculated from the carrier density determined at low magnetic fields.

In the following we shall use the notation introduced in ref 18, which is the basic work on the CR of holes in strained bulk Ge. The dashed lines in Fig 4 represent a calculation of the CR masses for the different possible transitions according to the filling factor of the system. The model assumes different, energy-dependent densities of states for the ±3/2 bands. It has been fitted to the data in the range between 5 T and 9 T. In this model the transitions are identified as labeled in Fig. 4. The decrease of the CR masses with magnetic field occurs because the splitting between $n-1 \rightarrow n$ and $n \rightarrow n+1$ transitions is not resolved when the n-th Landau level passes the Fermi energy. This interpretation is supported by the observation of increased scattering rates, i.e. linewidths of the resonances in this region.

However, this model fails to describe the high field data. Above 12 T additional transitions are resolved. With respect to the filling factor of the system the highest energy resonance has to be attributed to an excitation from the lowest Landau level. The apparent splitting within the $1^- \rightarrow 2^-$ transition above 12 T comes as a surprise. The observation of more than three transitions implies either a crossing of two levels at the Fermi energy or the observation of previously forbidden transitions. The latter has been suspected in the case of GaAs 2DHGs [19, 20]. Furthermore, in this high field region the evaluated total carrier density appears to increase with magnetic field. Understanding of the CR in the limit of few filled Landau levels therefore has to await detailed bandstructure calculations including z-quantization, strain and magnetic field.

Conclusion

High mobility Ge p-channels have been achieved on Si substrates using the graded buffer technique. The good quality of the samples has been demonstrated by magnetotransport and CR. A dominance of remote ionized impurity scattering over short range scattering is found. The determined CR masses confirm the expectations that the hh-bands have a light in-plane effective mass when the hh-lh-degeneracy is lifted by strain. The lifting of the spin degeneracy at B = 0 in the asymmetric confinement potential provides a qualitative understanding of the low field CR. Further theoretical work is required for a more quantitative understanding.

Acknowledgements

The authors would like to thank U Rößler and J F Nützel for valuable discussions and V Roßkopf for experimental help.

References

[1] T Ando, A B Fowler, F Stern, Rev. Mod. Phys. 54, 437 (1982)
[2] F Schäffler, D Többen, H -J Herzog, G Abstreiter, B Hollander, Semicond. Sci. Technol. 7, 260 (1992)
[3] E A Fitzgerald, Y -H Xie, D Monroe, P J Silverman, J M Kuo, A R Kortan, F A Thiel, B E Weir, J. Vac. Sci. Technol. B 10, 1807 (1992)
[4] S F Nelson, K. Ismail, J. J Nocera, F F Fang, E E Mendez, J O Chu, B. S. Meyerson, Appl. Phys. Lett. 61, 64 (1992)
[5] R People, J C Bean, D V Lang, A M Sergent, H L Störmer, K W Wecht, R. T Lynch, K Baldwin, Appl. Phys. Lett. 45, 1231 (1984)
[6] J F Nützel, F Meier, E Friess, G Abstreiter, Thin Solid Films 222, 150 (1992)
[7] L Vescan, R. Loo, A. Hartmann, U. Zastrow, A. Leuther, T. Schäpers, T. Stoica, H. Lüth, to be published in Proc. of ICFSI-4 (1993).
[8] M Miyao, E Muraki, H. Etoh, K. Nakagawa, A. Nishida, J Cryst. Growth 111, 912 (1991)
[9] U König, F Schäffler, IEEE Electron. Dev. Lett. 14, 205 (1993)
[10] Don Monroe, Y -H Xie, E. A. Fitzgerald, P. J. Silverman, G. Watson, to be published in Proc. of PCSI-20, J. Vac. Sci. Technol. (1993)
[11] Don Monroe, Y -H Xie, E. A. Fitzgerald, P J Silverman, G. Watson, to be published in Proc. of EP2DS-10, Surf. Sci. (1993)
[12] C M Engelhardt, E. Gornik, M Besson, G Böhm, G Weimann, to be published in Proc. of EP2DS-10, Surf. Sci. (1993)
[13] D Többen, F Schäffler, A Zrenner, G Abstreiter, Phys. Rev. B 46, 4344 (1992)
[14] J -P Cheng, V P Kesan, D A. Grützmacher, T O Sedgwick, J A Ott, Appl. Phys. Lett. 62, 1522 (1993)
[15] T Ando, J Phys. Soc. Jpn. 54, 1528 (1985)
[16] H L Störmer, Z Schlesinger, A Chang, D C Tsui, A C Gossard, W Wiegmann, Phys. Rev. Lett. 51, 126 (1983)
[17] G Goldoni, A Fasolino, Phys. Rev. Lett. 69, 2567 (1992) G Goldoni, A Fasolino Phys. Rev. Lett. 70, 2051 (1993)
[18] K Suzuki, J C Hensel, Phys. Rev. B 9, 4184 (1974), J C Hensel, K. Suzuki, ibid. p 4219
[19] W Erhardt, W Staghuhn, P Bruzewski, M von Ortenberg, G Landwehr, G Weimann, L van Bockstal, P Janssen, F. Herlach, J Witters, Surf. Sci. 170, 581 (1986)
[20] Y Iwasa, N Miura, S Tarucha, H Okamoto, T Ando, Surf. Sci. 170, 587 (1986)

TuP25

Magnetotransport and microwave photoresistivity of two-dimensional hole gases in $Si-Si_{1-x}Ge_x$ heterostructures.

Y Guldner, J.M. Berroir, J.P. Vieren, M. Voos
Laboratoire de Physique de la Matière Condensée, Ecole Normale Supérieure, 24 rue Lhomond, 75005 Paris, France

I. Sagnes, P.A. Badoz, P. Warren and D. Dutartre
France Télécom-CNET, BP 98, 38243 Meylan, France

Abstract

Shubnikov-de Haas and quantum Hall effect measurements in p-type modulation doped Si-SiGe-Si double heterostructures with both symmetric and asymmetric doping grown by rapid thermal chemical vapor deposition, show that the two interfaces are highly equivalent and that the charge (hole) transfer can be quantitatively explained by a simple model. The two-dimensional hole gas effective mass parallel to the interfaces is determined by microwave photoresistivity experiments. Furthermore, the limitation of the hole mobility is discussed in terms of alloy scattering.

Introduction

In recent years, two-dimensionnal (2D) hole gases in $Si-Si_{1-x}Ge_x$ heterostructures have received a great deal of attention, which is due, in particular, to their potential interest in microelectronics, and it is clearly important to investigate and understand in detail the transport properties of this quantum well system. Transport experiments have been performed on high-quality p-type modulation-doped Si-SiGe heterostructures [1- 7] fabricated by different growth techniques. We describe here transport, magneto-transport and microwave photoresistivity experiments on such structures grown by rapid thermal chemical vapor deposition (RTCVD) with a single or a symmetric double hole gas. Shubnikov-de Haas oscillations and integral quantum Hall plateaus were observed at 1.6 K and the 2D hole mass parallel to the interfaces is obtained from microwave photoresistivity data. Our results show unambiguously that these structures present equivalent Si-SiGe and SiGe-Si interfaces and that the charge transfer is governed by the undoped spacer layer thickness. We discuss also the hole mobility limitation in these heterostructures.

Experimental Results and Discussion

Our samples are listed in table 1 and are constituted by a $Si-Si_{0.8}Ge_{0.2}-Si$ double heterostructure deposited on a (100) Si substrate using the RTCVD technique. The 40 nm thick SiGe layer is unintentionally doped. For the symmetrically doped samples (S1 - S3), the two Si barriers contain a 16 nm boron-doped region with an acceptor density $\approx 2\times10^{18}cm^{-3}$. In the single-side doped samples, only the last (S4) or the first (S5) grown barrier contains a similar doped region. Undoped Si spacer layers of thickness d are inserted between the doped regions and the SiGe layer. A cap layer (undoped 40 nm Si layer followed by a p-type 20 nm Si layer) was grown on top of all samples.

The valence band diagram is determined (figure 1) by requiring that the Fermi level E_f remains constant throughout the structure. The heavy-hole valence band discontinuity is $\Delta E_v \approx 160 mev$ for x=0.2 [2]. The ground hole subband HH_1 is in the cusp of the selfconsistent potential and, as a result, two parallel hole gases occur in the symmetric samples. Due to the large 2D hole density of states, the separation $E_f - HH_1$ is a few meV's for hole densities $p<10^{12}cm^{-2}$ and

only HH_1 is populated at low temperature. Carrier densities obtained at 1.6 K from quantum Hall (p_{QHE}) and Shubnikov-de Haas effects (p_{SdH}) are given in table 1. In the symmetric situations (S1- S3), $p_{SdH} \sim 0.5\ p_{QHE}$. This has been observed previously by other groups [4,7] and suggests that the two interfaces are equivalent and that the wavefunctions of the two 2D hole gases are nearly independent. For example in sample S1, a wavefunction extension of ≈ 3 nm is calculated from a simple triangular potential model, yielding a 34 nm distance between the two symmetric hole gases. Due to the SiGe band bending a potential barrier of a few tens of meV's separates the two gases, so that tunneling between the two channels is negligible and no splitting of the HH_1 ground subband is evidenced. For S4 and S5, similar p_{SdH} values are obtained, which shows that the charge transfer is equivalent at Si-SiGe and SiGe-Si interfaces. Sample S4 corresponds to a "normal" modulation-doped Si-SiGe heterojunction, and $p_{SdH} \approx p_{QHE}$ as expected if there is no parallel conduction. Sample S5 corresponds to an "inverted" modulated-doped SiGe-Si heterojunction, and there is a difference of $\sim 1.4 \times 10^{11}$cm^{-2} between p_{SdH} and p_{QHE} which can be explained by an additional charge transfer from the boron doped cap layer to the SiGe layer, leading to another 2D hole gas with a lower density at the upper Si-SiGe interface.

The analysis of the charge transfer can be achieved from a simple electrostatic calculation. The Fermi level E_f is constant throughout the structure and the following expression is obtained at low temperature :

$$\Delta E_v = HH_1 + \pi\hbar^2 (p_{SdH})/m_{//} + e^2 d\ p_{SdH}/\varepsilon + e^2(p_{SdH})^2/2\varepsilon N_a$$

Here $m_{//} \approx 0.4 m_0$ is the 2D hole mass parallel to the interfaces, and $\varepsilon = 12\varepsilon_0$ is the SiGe dielectric constant. Using a triangular potential approximation to calculate HH_1 and the data shown in table 1, one obtains $\Delta E_v = 165 \pm 10$meV for all samples (S1 - S5). This result, which is consistent with previous determinations of ΔE_v [2], shows that the charge transfer is essentially governed by the thickness d of the undoped spacer layer and is not too dependent on the nature of the interfaces.

The Hall resistance as a function of the magnetic field B at 1.6 K is given in figure 2 for samples S1 and S2, and it has been observed that these curves depend on the angle θ between B and the surface normal as $(\cos\theta)^{-1}$. Quantized plateaus of resistance h/ie^2 with filling factor i up to i = 32 can be seen (fig. 2a). $B \geq 1.5$ T (fig 2b), which evidences the high quality of the 2D hole gases. For $B < 4$ T, the Landau level spin splitting is not detected due to level broadening, and plateaus are observed only for i = 4n, where n is an integer (i = 12, 16, 20, 24, 28, 32 in sample S1 and i = 8, 12, 16, 20 in sample S2). However, plateaus at i = 2n are observed in the asymmetric samples : the inset in figure 2b presents the Hall resistance at low B in sample S4 where plateaus occur at i = 8, 10, 12...18, and similar plateaus at i = 2n are also observed in sample S5. These results demonstrate that two parallel highly equivalent channels contribute to the Hall effect in the symmetrically-doped structures. Indeed, between two successive plateaus, four Landau levels are crossing the Fermi level instead of two in a single 2D hole gas. Similarly, for higher B where the spin splitting is resolved, plateaus are observed only for even filling factors in samples S1 to S3, while plateaus at both odd and even i can be seen in the asymmetric samples. As previously reported [6], the plateaus and magneto-resistance minima at odd filling factors in the single-side doped samples are likely to be due to the large spin splitting of the Landau levels which can be comparable or larger than the cyclotron energy in the studied 2D hole gases.

Hall measurements in S1, S2 and S3 show that the 2D hole mobility μ is enhanced when the temperature T is decreased as a result of the spatial separation between the ionized impurities and the holes. One obtains $\mu \approx 4000$ cm^2/Vs at low T for d = 10 - 20 nm. As can be seen in figure 2 and in figure 3 which will be described later, the onset of oscillations or Hall plateaus occurs at $B \sim 1.5$ T, which corresponds to $\mu \sim 6000$ cm^2/Vs. An important mobility limitation could result from alloy scattering since the 2D hole gas is essentially confined in the SiGe alloy. If one uses a simple model (one-band approximation, Fang and Howard wavefunction for the 2D hole ground state [8], short range scatterers, same spatial average of the fluctuating alloy potential as in III-V ternary compounds [9]), one can obtain the alloy-limited mobility, namely $\mu_{all} \approx 5000$ cm^2/Vs. This is in good agreement with our values and those of other groups [3,4,7]. As a result, alloy scattering is likely to be a limiting factor for the mobility

at low temperature, even if other factors should also be considered like the background impurity concentration in the SiGe layer or the interface quality.

We have also measured the 2D hole mass parallel to the interfaces $m_{//}$ from photoresistivity measurements under microwave illumination which is a more accurate method than direct transmission measurements to obtain the cyclotron mass. With a DC bias current I = 1 μA, changes Δρ in the magneto resistivity ρ due to the chopped microwave radiation were detected using a lock-in amplifier. Figure 3 gives typical data obtained for ρ and Δρ in S4 at 1.6 K. Magneto-oscillations in Δρ correspond to the Shubnikov-de Haas effect and arise from 2D carrier heating. An important enhancement can be seen around $B_0 \approx 4$ T at 270 GHz and 4.5 T at 333 GHz, which corresponds to the 2D hole cyclotron resonance (CR) when the hole absorption of the microwave radiation is maximum. The CR absorption correlates with the envelope of Δρ as shown in figure 3 by the dashed line. The half width at half amplitude ($\Delta B = 2$T) at 333GHz yields $\mu \approx 5000$ cm^2/Vs at low T in a classical CR model, and $\mu = 4700$ cm^2/Vs from $\Delta B = 0.65\ B_0^{1/2}\mu^{-1/2}$ which has been used in the case of 2D electron gases [10,11]. These values are in agreement with those obtained from transport experiments and the onset of the Shubnikov-de Haas oscillations in S4. The maximum of the dashed line gives $m_{//} = (0.42 \pm 0.02)m_0$ in S4, and similar experiments in S1 and S2 yield $m_{//} = (0.45 \pm 0.02)m_0$ and $m_{//} = (0.42 \pm 0.02)m_0$, respectively. These values are comparable or larger than results obtained previously from Shubnikov-de Haas measurements on analogous structures [1,4], but we think that the microwave photoresistivity method is actually more reliable.

Conclusion

The electronic properties of 2D hole gases have been investigated in p-type modulation-doped Si-SiGe heterostructures fabricated by RTCV. We have evidenced that the charge transfer is equivalent at each interface and depends only on the undoped spacer thickness. The hole mass in the plane of the layers has been determined, showing that it does not vary appreciably with the hole concentration. We have finally shown that alloy scattering is certainly an important limiting mechanism at low T for the carrier mobility.

Acknowledgements

This work has been partly supported by the Direction des Recherches, Etudes et Techniques (DRET). The Laboratoire de Physique de la Matière Condensée de l'ENS is associated to CNRS and to University Paris VI.

References :

1 R. People, J.C. Dean and D.V. Lang, J. Vac. Sci. Technol. A(3), 846 (1985)
2 R. People, IEEE J. Quantum Electron. QE22, 1696 (1986).
3 T. Mishima, C.W. Fredriksz, G.F.A. van de Walle, D.J. Gravesteijn, R.A. van den Heuvel and A.A. van Gorkum, Appl. Phys. Lett. 57, 2567 (1990).
4 P.J. Wang, F.F. Fang, B.S. Meyerson, J. Nocera and B. Parker, Appl. Phys. Lett. 54, 2333 (1989).
5 P.J. Wang, B.S. Meyerson, F.F. Fang, J. Nocera and B. Parker, Appl. Phys. Lett. 55, 2701 (1989).
6 F.F. Fang, P.J. Wang, B.S. Meyerson, J. Nocera and K.E. Ismail, Surface Science 263, 175 (1992).
7 V. Venkataraman, P.V. Schwartz, C.J.C. Sturm, Appl. Phys. Lett. 59, 2871 (1991).
8 F.F. Fang and W.E. Howard, Phys. Rev. Lett. 16, 797 (1966).
9 G. Bastard, Wave mechanics applied to semiconductor heterostructures, Les Editions de Physique, Paris, p. 219 (1988).
10 C. Absteiter, J.P. Kotthaus, J.F. Koch and G. Dorda, Phys. Rev. B14, 2480 (1976).
11 P. Voisin, Y. Guldner, J.P. Vieren, M. Voos, P. Delescluse and N.T. Linh, Appl. Phys. Lett. 39, 982 (1981).

Sample	Spacer d(nm)	p_{SdH} ($10^{11}cm^{-2}$)	p_{QHE} ($10^{11}cm^{-2}$)
Symmetrically doped structures			
S1	10	6.2	12.4
S2	20	4.0	7.8
S3	40	2.25	4.3
Single side doped structures			
S4	10	6.8	6.8
S5	10	6.7	8.1

Table 1 Parameters of the symmetrically and asymmetrically doped Si-Ge structures used here

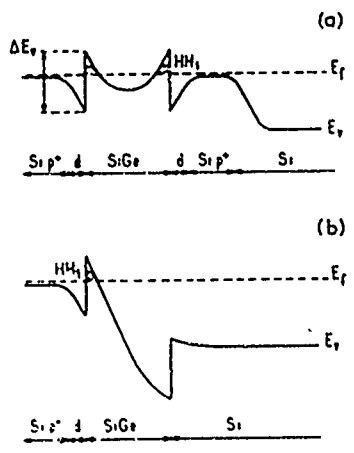

Figure 1 Valence band diagram for (a) a symmetrically doped structure and (b) a single side doped structure as S4 The cap layer is not shown

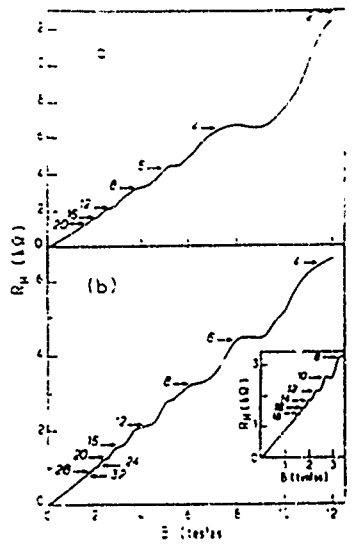

Figure 2 : Hall resistance versus B at T=1.6K for (a) S2 and (b) S1. The arrows give the position of the quantized plateaus with the corresponding filling factors. The unset represents the Hall resistance at low B in S4.

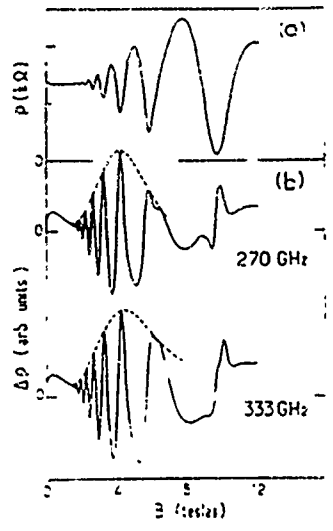

Figure 3 : (a) ρ and (b) Δρ versus B at 1.6K in S4

TuP26

Photoluminescence and magnetotransport of 2D hole gases in Si/SiGe/Si heterostructures

R. Loo, R. Apetz, L. Vescan, A. Hartmann, U. Zastrow, A. Leuther, T. Schäpers and H. Lüth

Institut für Schicht- und Ionentechnik (ISI), Forschungszentrum Jülich GmbH, D-52425 Jülich, Germany

Abstract

p-type modulation-doped $Si/Si_{1-x}Ge_x/Si$ strained layer double heterostructures with $x \sim 0.2$ have been epitaxially grown on (100) Si substrates using low pressure chemical vapor deposition (LPCVD). The modulation doping effect has been obtained by two remote boron-doped Si layers $\sim 10\,nm$ thick. Hole mobilities as high as $3900\,cm^2/Vs$ have been obtained at 4.2 K comparable to the best reported values, so far. The temperature dependence of the 2D hole concentration and mobility shows characteristic remote ion-dominated scattering. Clear quantum Hall plateaus and Shubnikov-de Haas oscillations were observed. The photoluminescence (PL) from the SiGe quantum well (QW) shows excitonic behaviour in its variation with excitation power. A general trend of increasing PL intensity with the mobility of the 2D hole gas was observed. The high hole mobility and strong PL reflect the good interfacial quality of the LPCVD Si/SiGe/Si heterointerfaces.

1 Introduction

In recent years the SiGe/Si system has attracted much interest because of its potential applications in silicon-based circuits. In particular, 2D hole gases play the key role in the p channel modulation doped field effect transistor (MODFET). There is also some hope that SiGe/Si structures could be used for optoelectronic devices like detectors as well as light emitting diodes. In this paper, we present optical and electrical investigations of modulation doped Si/SiGe/Si QW structures grown by LPCVD. It results that LPCVD is a suitable method for the fabrication of structures containing 2D hole gases with mobilities comparable to the best published values. We report the observation of strong PL from modulation doped Si/SiGe/Si structures and explain the origin of the different peaks, first presented by us in [1]. A very interesting property is a considerable enhancement of the PL intensity from the modulation doped SiGe QW relative to undoped QW structures.

2 Experiment

The Si/SiGe/Si heterostructures were epitaxially grown by LPCVD on n-type Si (100) $1000\,\Omega cm$. The samples consist mainly of an undoped $Si_{0.8}Ge_{0.2}$ layer ($\sim 15\,nm$) between two remote p^+Si layers ($\sim 10\,nm$, boron doped $\sim 3 \times 10^{18}\,cm^{-3}$) separated by undoped Si spacers (10-40 nm). The characterisation details are given in [2]. A self-consistent calculation of the band edges of this samples is shown in Fig. 1. The Hall effect was measured on samples patterned with van der Pauw geometry, while for Shubnikov-de Haas measurements the Hall bar geometry was used. Ohmic contacts were Al/Ti/Au/Cr alloyed at 380°C for 2 min. Photoluminescence was carried out with a Fourier transform spectrometer equipped with a cooled Ge-detector. The samples were mounted in a continuous flow He-cryostat and excited by an Ar ion laser (488 nm).

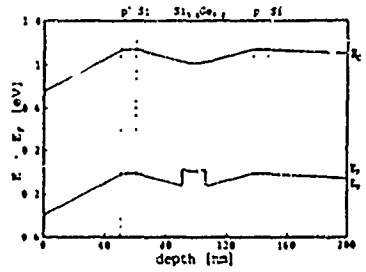

Fig. 1. Self-consistent calculated band edges of a modulation doped $Si/Si_{0.8}Ge_{0.2}/Si$ structure at 20 K without illumination. The hole density in the QW was computed to $5.3 \times 10^{11}cm^{-2}$.

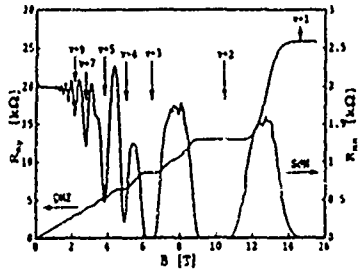

Fig. 2. QHE and SdH measurements at 50 mK of the modulation doped sample with the highest mobility.

3 Magnetotransport

In low field Hall effect measurements we observed a weak temperature dependence of hole mobility and concentration below 30 K and a clear dependence on spacer thickness in our samples. This demonstrates clearly the presence of a 2D hole gas where remote ion scattering is dominating. Fig 2 shows well defined Shubnikov-de Haas (SdH) oscillations and clear quantum Hall (QHE) plateaus of the sample with the largest Hall mobility, exhibiting $\mu = 5900\,cm^2/Vs$ at 4.2 K and $\mu = 6870\,cm^2/Vs$ at 50 mK. These values are comparable with the best published results so far [3, 4]. The onset of SdH oscillations is already observable at fields as low as B=0.5 T. Apart from filling factor $\nu = 2$ and 4 only odd filling factors were observed. This is possibly due to the overlap of Landau levels due to spin splitting at lower fields [3, 4]. The low field Hall effect hole density was $p_H = 4.5 \times 10^{11}cm^{-2}$ while the density determined from SdH was $p_{SdH} = 4.8 \times 10^{11}cm^{-2}$. This indicates that only one 2D conducting channel is present in the SiGe layer in agreement with self-consistent calculations (Fig. 1). From the calculations we obtained the value $p_{calc} = 5.3 \times 10^{11}cm^{-2}$ using the characterisation data for doping and layer sequence and effective masses obtained by solving the 6x6 Luttinger-Kohn Hamiltonian. There are no harmonic components in the SdH oscillations showing that only one subband is occupied which is also in agreement with the calculations. Furthermore there are no parallel conducting channels in the sample at low temperatures demonstrated by the vanishing longitudinal magnetoresistance R_{xx} at the QHE plateaus.

4 Photoluminescence

PL spectra of a modulation doped sample containing a 15 nm SiGe layer are presented in Fig 3. They show no-phonon transitions and their TO-phonon replicas arising from

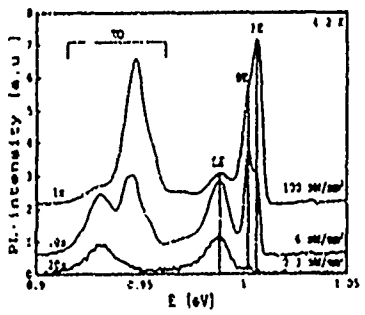

Fig. 3. PL spectra of a modulation doped sample at different excitation power densities at 4.2 K.

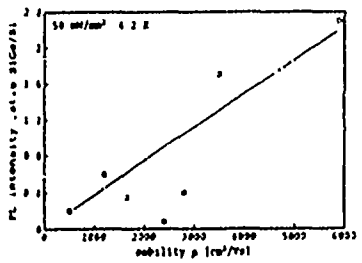

Fig 4. Correlation between PL intensity and mobility of the modulation doped samples. The PL intensity ratio is given by the ratio of the FE peak heights of SiGe and Si at 4.2 K.

the SiGe quantum well similar to that observed by many other authors in undoped structures [5, 6]. By temperature and excitation power density dependent measurements the different no-phonon peaks were assigned to localized excitons (LE), bound excitons (BE) and free excitons (FE). In Fig. 3 spectra with three different excitation power densities P are shown. The intensity $I \sim P^m$ of the FE peak exhibits linear to supralinear behavior with m=1-1.3 while the BE peak varies sublinearly with m=0.79-0.94. The LE peak shows saturation behavior typical for localized excitons [6]. The FE and BE peaks are very sharp with half widths of 4-6 meV. With increasing temperature only the FE peak remains. The energy difference between the FE and the BE peak ($\sim$ 5 meV) is the typical binding energy for excitons at shallow impurities, very probably residual boron ($\sim 1 \times 10^{15}$ cm^{-3}) in our samples. The energy shift with excitation power density of the FE peak is small being of the order of 2 meV. So there is no marked difference to undoped samples except that the PL intensity is enhanced more than one order of magnitude. This is in contrast to measurements on modulation doped InGaAs, for instance, where a strong broadening ($\sim$ 50 meV) of the FE peak is observed due to band filling by the doping [7]. The difference could be explained by the higher 2D density of states in SiGe due to the nearly one order of magnitude greater effective mass. An explanation of the strong enhancement of PL intensity can be the existence of an attractive potential in the conduction band (Fig. 1). This well is a result of modulation doping and will lead to an confinement of the photoexcited electrons in the region of the SiGe layer. Fig 4 demonstrates a correlation of PL and mobility from our modulation doped samples. The general trend could probably be explained by the fact that the PL efficiency just as the mobility decreases with increasing concentration of defects and impurities in the QW or at the interfaces. Furthermore it is obvious that a thicker spacer causing a higher mobility in our samples will give rise to a lower boron concentration in the region of the QW. This will also lead to a reduction of the nonradiative recombinations. The large scattering of the data could have several reasons. At first we compare samples where different parameters (spacer thickness, doping concentration etc.) are changed. Furthermore, some kinds of impurities not easily controlable in the epitaxy process may have a much greater influence on PL than on mobility. Possibly they determine in some samples the PL efficiency.

5 Conclusions

In conclusion, we observed high mobility and strong PL of LPCVD grown modulation doped Si/SiGe/Si structures. This demonstrates the high quality of the Si/SiGe heterointerfaces and the low concentration of impurities and defects. It was shown that p-type modulation doping leads to a strong enhancement of luminescence compared to undoped samples. This was explained by the additional confinement of the photoexcited electrons by an attractive potential caused by the modulation doping.

6 Acknowledgments

The authors are grateful to G. Abstreiter for interesting discussions. The authors also wish to thank P. Gartner for the effective mass calculations, T. Stoica for the Hall bar samples and K. Wambach for technical assistance.

References

[1] L. Vescan, R. Loo, A. Hartmann, U. Zastrow, A. Leuther, T. Schäpers, T. Stoica and H. Lüth, *to be published in Proc. Int. Conf. on the Formation of Semiconductor Interfaces 4*, Jülich, Germany, eds. H. Lüth, W. Mönch, J. Pollmann, World Scientific (1993)

[2] L. Vescan, K. Schmidt, C. Dieker, H.P. Tang, T. Vescan and H. Lüth, *Thin Solid Films* **222**, 5 (1992)

[3] F.F. Fang, P.J. Wang, B.S. Meyerson, J.J. Nocera and K.E. Ismail, *Surface Science* **236**, 175 (1992)

[4] J.F. Nützel, F. Meier, E. Friess and G. Abstreiter, *Thin Solid Films* **222**, 150 (1992)

[5] J.C. Sturm, H. Manoharan, L.C. Lenchyshyn, M.L.W. Thewalt, N.L. Rowell, J.-P. Noël and D.C. Houghton, *Phys. Rev. Lett.* **66**, 1362 (1991)

[6] L.C. Lenchyshyn, M.L.W. Thewalt, J.C. Sturm, P.V. Schwartz, E.J. Prinz, N.L. Rowell, J.-P. [illegible] and D.C. Houghton, *Appl. Phys. Lett.* **60**, 3174 (1992)

[7] M.S. Skolnick, J.M. Rorison, K.J. Nash, D.J. Mowbray, P.R. Tapster, S.J. Bass and A.D. Pitt, *Phys. Rev. Lett* **58**, 2130 (1987)

TuP27

A NEW TECHNIQUE FOR DIRECTLY PROBING THE INTRINSIC TRISTABILITY AND ITS TEMPERATURE DEPENDENCE IN A RESONANT TUNNELING DIODE

M. L. F. Lerch, A. D. Martin and P. E. Simmonds
Department of Physics, University of Wollongong, Wollongong, NSW 2522, Australia.

L. Eaves and M. L. Leadbeater
Department of Physics, University of Nottingham, Nottingham NG7 2RD, England.

ABSTRACT

A new measurement technique employing a positively sloping load line has been used to probe the region of apparent bistability near a tunneling resonance in the electrical characteristic of a resonant tunneling diode. This technique is equivalent to using a voltage source and negative series resistance. The appearance of bistability is an artifact of the conventional measuring technique which uses a load line with negative slope. The complete characteristic is found to be a continuous Z shaped curve between 20 K and 150 K, corresponding to tristability and in accordance with theoretical models based on the effects of charge accumulation in the central quantum well of the diode. The width of the tristable region passes through a maximum at 40 K and, at 150 K, disappears as the resonance broadens. Above this temperature the resonance develops a region of negative differential resistance (NDR). As the device is cooled below 20 K additional structure develops in the central arm of the Z, with some portions of the characteristic exhibiting five stable current states at temperatures below 15 K. At 1.2 K, the effect of an in plane magnetic field mimics that of increasing temperature.

INTRODUCTION

The occurrence of intrinsic bistability in the electrical characteristics (I(V) curves) of semiconductor double-barrier structures (DBSs) has attracted considerable recent attention, both experimentally and theoretically. When a DBS device is biased, electron tunneling through the barriers and enclosed quantum well can show large resonances which occur when incoming electrons coincide in energy and transverse momentum with quantum states quasi-localized in the well. The characteristics in the vicinity of these resonances have regions of either negative differential resistance (NDR) [1] or apparent bistability [2-5] and devices which display both types of curve have been subject to detailed experimental study. In the bistable case there has been some initial debate as to the cause, since circuit oscillations in a region of NDR, or NDR together with a series resistance, can simulate this effect [6-8]. It is now clear that bistability which is intrinsic to the device has been realized experimentally in appropriately designed structures [3-5] and is caused by electrostatic feedback due to charge buildup in the well [2,5,9-11]. This effect is particularly pronounced in devices with asymmetric barriers. The asymmetry facilitates the accumulation of free charge in the well when the device is biased so that the probability of tunneling into unoccupied well states through the emitter barrier greatly exceeds that of tunneling out through the thicker collector barrier [3-5]. The conventional technique for measuring the device characteristic uses a voltage source in series with the device together with some positive resistance. Although the resistance can be made arbitrarily small, *the interior of the bistability* remains inaccessible to this technique. The appearance of bistability may therefore be an artifact of the conventional measuring technique and could conceal an important portion of the static characteristic which would indicate tristability or, possibly, more complex behaviour. Theoretical models, which include effects of charge accumulation in the well [9-11], predict a characteristic in the form of a continuous Z shaped curve provided that the tunneling resonance is sufficiently sharp. Such a characteristic should more correctly be called tristable [10]. The form of the characteristic in this region could yield useful information on the details of the tunneling process, particularly where there is substantial charge density in the well. In this paper we show that the interior of the bistability in one such device is indeed accessible to a measurement technique which employs a load line with positive slope, corresponding to a voltage source and a negative series resistance. The characteristic near the first tunneling resonance of the device under study is a continuous Z shaped curve between 150 K and 20 K and develops additional structure as the device is cooled further. At 4.2 K, the effect of a small in plane magnetic (B < 1 T) field mimics that of increasing temperature.

DEVICE STRUCTURE AND CHARACTERISTICS

The active region of the asymmetric device studied consists of a 5.8 nm GaAs quantum well, sandwiched between $Al_{0.4}Ga_{0.6}As$ barriers of different widths, 8.3 nm and 11.1 nm. Lightly doped GaAs spacer layers separate this region from the heavily doped n^+ contact regions. An applied bias voltage causes an accumulation layer and associated two dimensional electron gas (2DEG) to form adjacent to the emitter barrier. Resonant tunneling occurs when this voltage brings one of the two quasi-bound states in the well into energy coincidence with the quasi-bound state in the emitter. Full details of the layer structure are given in Refs. 4 and 5 and a schematic diagram of the conduction band edge under forward bias is shown in the inset to Fig. 1(a). The electrical characteristics have already been reported in detail and show two resonances in each bias direction [5]. Under reverse bias (electrons tunneling into the well through the thicker barrier) the resonances are sharp and exhibit NDR. Under forward bias the respective peak resonant currents are more than an order of magnitude larger, much broader and show apparent bistability. The characteristic due to the first resonance measured conventionally at 2 K is shown in Fig. 1(a). The region of apparent bistability near a bias of 0.7 V is studied in the present work. The charge buildup in the well which causes the extended voltage range of the first forward bias resonance (0.3 V to 0.7 V) has been confirmed by detailed magneto-capacitance and luminescence studies [5,14]. The fact that the device exhibits NDR under reverse bias (where no charge build up is detected) is in itself strong evidence in support of the intrinsic nature of this bistability.

MEASUREMENT TECHNIQUE AND CIRCUIT STABILITY

The measurements reported here (Fig's 3 and 4) were taken using a voltage supply designed to have a negative output resistance (NOR), corresponding to a load line with positive slope. This enables the portion of the characteristic inside the region of apparent bistability to be probed (see Fig. 2(a)). An active circuit designed to meet the NOR requirement is shown in Fig. 2(b). Additional details of this circuit will be reported elsewhere. Provided that the device characteristic is continuous, the load line can be made to intersect any part of it inside the bistability at a point Q if $|R_L| > R_d$. Here R_d is the dynamic resistance dV/dI of the device at Q and $-1/R_L$ is the slope of the load line. Under these conditions the the total circuit resistance $R_L+R_d < 0$ and circuit oscillations can occur due to the exponential growth of any initial perturbation. Circuit analysis, based on dynamic circuit models of the NOR measuring circuit [15] and device [5,12,13], predicts a narrow range of values of R_L and C_L for which stability should occur. (C_L is a capacitance which appears in parallel with R_L in the NOR equivalent circuit. Both parameters are adjustable). These values form an "island of stability" in R_L-C_L space. Stable measurements, for which no oscillations up to 400 MHz were observed, could be made with values of R_L and C_L close to those predicted, giving some confidence in the circuit models used. Varying R_L or C_L outside this range caused large amplitude oscillations at frequencies up to a few hundred kHz.

MEASUREMENTS USING THE NOR CIRCUIT AND DISCUSSION

Measurements made with the NOR circuit on the device characteristic outside the bistable region gave the same results as those obtained using conventional techniques and, for measurements obtained at 4.2 K, correspond closely to published data for an essentially identical device [4]. Adjusting the position of the load line by varying V_{in} and R_1 (see Fig. 2 (b)) gave a smooth, continuous and reversible transition into the interior of the bistability. The results of these measurements are shown in Fig. 3, where the complete characteristics of the device near the peak of the first tunnelling resonance close to a bias of 0.7 V are plotted for a number of temperatures between 160 K and 4.2 K. For temperatures between about 150 K and 20 K these results clearly demonstrate the continuous and tristable nature of the intrinsic device characteristic inside the region of apparent bistability as measured conventionally. The re-entrant form of the the I(V) curve (resonance overhang) predicted in Ref. 10 (3DEG in the emitter) and Ref. 11 (2DEG in the emitter, corresponding to the present device) is reproduced qualitatively in the experimental data. As the temperature is reduced below 20 K the overhang region of the characteristic develops more complex behaviour. Between 20 K and 4.2 K the resonance exhibits marked narrowing close to the current peak and an additional broader shoulder develops between the peak and foot. This coincides with a decrease both in the overall voltage width ΔV of the overhang and in the peak current. Very similar behaviour is observed for three different devices on two separate chips and is insensitive to (necessarily) small variations in the slope of the load line.

Plots of the voltage width ΔV, together with bias at the current peak V_p, against T are shown in the inset to Fig. 3. As expected, very similar data are obtained from conventional bistability width measurements [12] although switching between high and low current states in conventionally measured data occurs at bias voltages near the peak and foot of the resonance overhang. As the temperature is increased above 4.2 K, both ΔV and V_p initially increase, with ΔV reaching its maximum value near 40 K. At still higher temperatures, broadening of the resonance causes a decrease in ΔV and the tristability vanishes near 150 K. Above this temperature the resonance exhibits NDR, an observation consistent with previous measurements [12].

The detailed origin of the low temperature structure in the overhang region is unclear. The sharp corresponding reverse bias resonance displays no such satellite structure and quite separate LO phonon satellites lie at higher biases. The broad shoulder is possibly caused by an inelastic process due some form of electron-electron interaction, for example electron shake-up or emission of a plasmon at k near k_f in the emitter 2DEG. Either of these processes would be expected to give satellite structure separated by a few mV from the main emitter to well resonance voltage. Further experiments on different device structures would be required to establish that the complex characteristic observed here is an intrinsic feature of the tunneling process in devices displaying bistability. In the present asymmetric structure which exhibits strong charge build-up in the well at the first resonance, the peak-to-valley current ratio is significantly degraded relative to the sharp reverse bias resonance, and weak off-resonance and satellite tunnelling processes appear relatively enhanced. This is because the peak forward bias current is limited by the maximum carrier density, $n_{w,max}$ which can accumulate in the well at resonance ($E_0=E_f$) together with the low transmission probability of the wide collector barrier. This value of $n_{w,max}$ (2.2×10^{11} cm^{-2}) occurs when the Fermi energies of the 2D emitter and the well (and hence the sheet densities n_e, $n_{w,max}$ respectively) are approximately equal, as has been confirmed experimentally [4,5].

Another feature of interest in Fig.3 is the initial increase in ΔV and V_p with temperature despite the obvious broadening of the re-entrant resonance curve (made evident by the new technique which exposes the full lineshape). This observation suggests that $n_{w,max}$ can be enhanced by thermal effects beyond its 'resonance' value so that $n_{w,max} > n_e$. It has been previously demonstrated that strong enhancement in the value of $n_{w\,max}$ at resonance can be achieved by application of a quantising magnetic field (BIJ) with consequent large increase in peak current and ΔV [14]. Alternatively, a smaller increase in $n_{w,max}$ and ΔV is obtainable by

application of a small in - plane field ($\mathbf{B} \perp \mathbf{J}$). Results taken at $B(\perp) = 0.5$ and 1 T, at 4.2 K are shown in Fig. 4. The effect of the field is strikingly similiar to that caused by an increase in temperature. This observation suggests a possible explanation for the temperature induced increase in V_p and overhang ΔV shown plotted in the inset to Fig 3. The in - plane B field generally causes spreading and a shift in the resonance cut off to slightly higher emitter to well voltage [16]. At the new resonance cut off the levels E_1(well) and E_0(emitter) are misaligned with E_1 lying at energy δE *below* E_0. This allows the stored charge density for $B > 0$ to exceed its *maximum zero field value* (*i.e.* $n_{w,max} > n_e$) since, as mentioned above, $n_{w,max}$ corresponds to alignment of emitter and well Fermi levels. Field induced enhancement of the resonance overhang and increased V_p and peak current are expected, and observed (see Fig. 4), since all three depend on $n_{w,max}$ (peak current is approximately $\propto n_{w,max}$). From the discussion in Ref. 16 we estimate a B field induced spreading $\delta E \approx \hbar^2 k_F \Delta k/m$ where $\Delta k = eBL_{ew}/\hbar$, k_F is the emitter Fermi wavevector and $L_{ew} = 18$ nm, the effective emitter to well separation [4]. For $B = 1$ T, this yields $\delta E \sim 1$ meV corresponding to $\sim 15\%$ increase in $n_{w\,max}$, from which an increase in ΔV of ~ 65 meV is estimated, in good agreement with ~ 70 mV obtained experimentally. Since elevated temperature and applied magnetic field have similiar effects on the characteristic there may be an underlying common mechanism in which thermal broadening of the resonance plays a role analogous to the field induced spreading.

ACKNOWLEDGEMENTS

The expert technical assistance of Dale Hughes is gratefully acknowledged. This work was partially supported by the Australian Research Council and the U.K. Science and Engineering Research Council

REFERENCES

1 See, e.g, E. E. Mendez, *'Physics of resonant tunneling in semiconductors'*, in *Physics and Applications of Quantum Wells and Superlattices*, edited by E. E. Mendez and K. von Klitzing, NATO ASI, Series B Physics , Vol 170, p. 159 (Plenum, New York, 1988)

2 V. J. Goldman, D. C. Tsui and J. E. Cunningham, *Phys. Rev. Lett.* **58**, 1256 (1987).

3 A. Zaslavsky, V. J. Goldman, D. C. Tsui and J. E. Cunningham, *Appl. Phys Lett* **53**, 1408 (1988).

4 M. L. Leadbeater, E. S. Alves, L. Eaves, M. Henini, O. H. Hughes, F. W. Sheard and G. A. Toombs, *Semicond. Sci. Technol.* **3**, 1060 (1988).

5 M. L. Leadbeater, E. S. Alves, F. W. Sheard, L. Eaves, M. Henini, O. H. Hughes and G. A. Toombs, *J. Phys.: Condens Matter* **1**, 10605 (1989)

6 T. C. L. G. Sollner, *Phys. Rev. Lett.* **59**, 1622 (1987); V. J. Goldman, *Phys. Rev. Lett.* **59**, 1623 (1987).

7 T. J. Foster, M. L. Leadbeater, L. Eaves, M. Henini, O. H. Hughes, C. A. Payling, F. W. Sheard, P. E. Simmonds and G. A. Toombs, *Phys. Rev.* **B39**, 6205 (1989).

8 W. D. Goodhue, T. C. L. G. Sollner, H. Q. Le, E. R. Brown and B. A. Vojac, *Appl. Phys. Lett.* **49**, 1086 (1986); M. Tsuchiya and H. Sakaki, *Appl. Phys. Lett.* **49**, 88 (1986).

9 F. W. Sheard and G. A. Toombs, *Appl. Phys. Lett.* **52**, 1228 (1988).

10 D. D. Coon, K. M. S. V. Bandara and H. Zhao, *Appl. Phys. Lett.*, **54**, 2115 (1989)

11 F. W. Sheard and G. A. Toombs, *Semicond. Sci. Technol.* **7**, B460 (1992)

12 M. L. Leadbeater, Ph.D. Thesis, University of Nottingham (1990)

13 F. W. Sheard and G. A. Toombs, *Solid - State Electron.* **32**, 1443 (1989)

14 L. Eaves, M. L. Leadbeater, D. G. Hayes, E. S. Alves, F. W. Sheard, G. A Toombs, P. E. Simmonds, M. S. Skolnick, M. Henini and O. H. Hughes, *Solid - State Electron.* **32**, 1101 (1989).

15 A. D. Martin, M. L. F. Lerch, P. E. Simmonds, L. Eaves and M. L. Leadbeater *Eighth International Conference on Hot Carriers in Semiconductors* (Oxford, U.K. 1993)

16 M. L. Leadbeater, L. Eaves, P. E. Simmonds, G. A. Toombs, F. W. Sheard, P. A Claxton, G. Hill and M. A. Pate, *Solid - State Electron.* **31**, 707 (1988)

FIGURE CAPTIONS

Figure 1
(a) I(V) characteristics at 2K of the asymmetric double barrier structure, measured using a conventional (near vertical) load line. Only the first resonance is shown in each bias direction. In forward bias the current switching directions observed using this measurement technique are indicated by arrows and delineate the region of apparent bistability. The broad peak near 0.9 V is associated with LO phonon assisted tunneling.
Inset: Schematic conduction band energy diagram for the device under forward bias.

Figure 2.
(a) Schematic region of apparent bistability shown on an expanded voltage scale. The conventional load line corresponds to a voltage source V_{in} and a (small) positive series resistance R_L. The gradient of the load line is $-1/R_L$. Switching occurs at A and B as the load line is swept through the device characteristic by varying V_{in} and any part of the characteristic between A and B is inaccessible for any positive value of R_L. The load line for a voltage source and a negative series resistance (an NOR supply) has a positive slope and can be used to probe the region between A and B provided that the slope of the load line is less than the slope of the device characteristic at Q ($1/R_d$). This is equivalent to the requirement that $R_L+R_d < 0$.
(b) Circuit diagram for a NOR voltage supply. The output voltage is given by $V_D = V_{in} + (R_1.R_3/R_2).I$ (i.e. V_D **increases** as more current I is drawn from the supply) This is the equation of the NOR load line shown in Fig. 2(a). The circuit is equivalent to a voltage source V_{in} in series with a negative resistance $R_L = -R_1 R_3/R_2$.

Figure 3.
Temperature dependence of the device characteristics measured near the peak of the resonance using the NOR supply. The onset of tristability and the development of more complex structure is shown as the temperature is lowered
Inset: Variation with temperature of the width, ΔV, of the voltage overhang and V_p, the voltage at the resonance peak.

Figure 4.
Effect of an in plane ($B \perp J$) magnetic field on the device characteristic at 4.2K. The field extends the range of the voltage overhang and has a similiar effect to that caused by increasing the temperature between 4.2 K and 50 K, as shown in Fig. 3

Figure 1

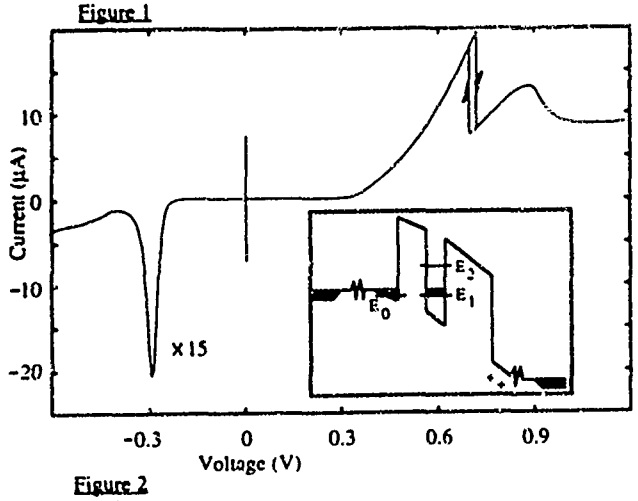

Figure 2

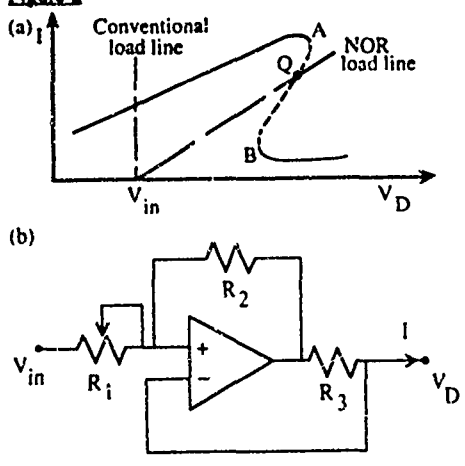

Figure 3

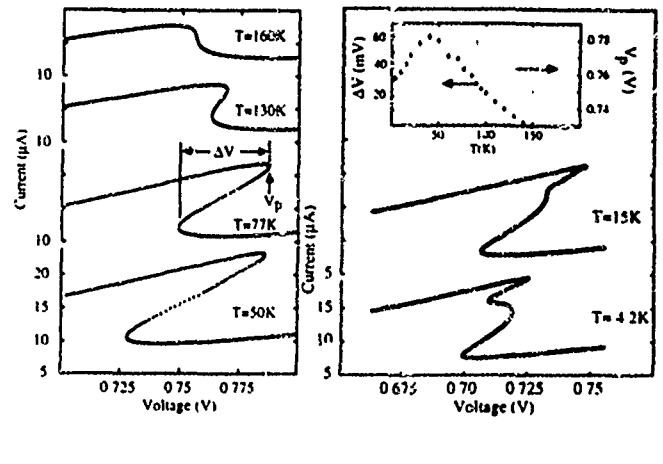

Figure 4

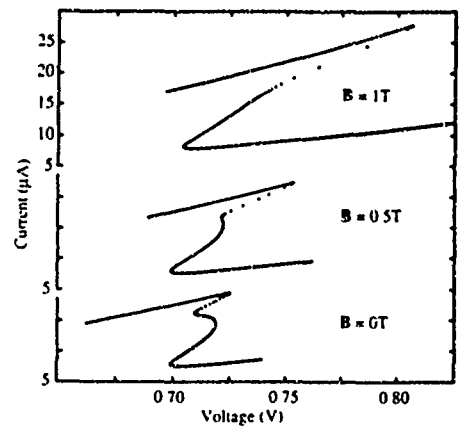

TuP28

Mesoscopic Effects in Resonant Tunnelling Diodes

J W Sakai[a], N La Scala Jr[a], P C Main[a], P H Beton[a], T J Foster[a], A K Geim[a], *L. Eaves[a], M Henini[a], G Hill[b] and M A Pate[b].*

[a] Department of Physics, University of Nottingham, Nottingham, NG7 2RD, UK.
[b] Department of Electrical Engineering, University of Sheffield, Sheffield, UK.

Abstract

We have investigated resonant tunnelling in GaAs/(AlGa)As heterostructures which have been fabricated into mesas of cross section 6μm x 6μm. A δ-layer of donors ($n \sim 2 \times 10^9$ cm^{-2}) has been incorporated at the centre of the quantum well which is 9 nm wide. The I(V) characteristics show a feature at −70 mV, which is below the threshold for the main resonance and is due to resonant tunnelling through single donor states in the well. This feature is also present in large mesas. At lower biases and at low temperatures we see a new set of resonances which, although they occur in all small area mesas, differ in detail between devices with regard to their strength and bias position. The form of the low-bias structure is strongly dependent on temperature, T, below 4 K where several very sharp steps appear, becoming sharper as T is decreased. We have also investigated the dependence of the new structure on magnetic field, B, parallel to the current direction. The features become sharper with increasing B in forward bias while, in reverse bias, the structure breaks up into a set of smaller peaks and we are able to see spin-splitting effects. We attribute the new features to tunnelling through potential fluctuations on the mesoscopic scale due to donor clustering. Although our devices are not small enough to observe 0D quantisation or size-related Coulomb blockade, the effects we observe are qualitatively and quantitatively similar to those seen in sub-micron mesas by other authors and attributed to these effects.

There has been a great deal of recent interest in the electronic transport properties of systems in which there is confinement of the electrons in all three dimensions. One method of attempting to achieve this confinement is to fabricate a resonant tunnelling diode (RTD) with lateral dimensions less than 1 μm [1- 6]. An RTD involves electron tunnelling through levels in the quantum well formed between two barriers and for wells a few nm wide, quantum effects can be observed even at room temperature. However, the quantum effects due to the lateral confinement have proved more elusive to identify unambiguously. Although a number of extra features in the current-voltage characteristics, I(V), have been observed in small area diodes at low temperatures, they have been variously attributed to quantum confinement [1,2,4], single electron charging effects [2,4,6] and impurities [3]. In earlier work [3] we have demonstrated that, whatever other effects may be important in a given device, it is vital to consider impurities which may segregate or diffuse into the quantum well.

In this paper, we investigate the effects of impurities by studying devices in which we have incorporated a δ-layer of impurities into the quantum well. Furthermore, the devices are intermediate in lateral dimension (~ 6 μm) between the sub-micron and the large area (~ 100μm) diodes. These devices are not small enough to show lateral quantum effects but are *mesoscopic* in the sense that they show sample-specific features, qualitatively similar over a range of different devices but differing in quantitative detail.

0.6 μm	GaAs	$n = 2 \times 10^{24}$ m^{-3}
80.6 nm	GaAs	$n = 2 \times 10^{23}$ m^{-3}
50.9 nm	GaAs	$n = 2 \times 10^{22}$ m^{-3}
10.2 nm	GaAs	undoped spacer
5.7 nm	$Al_{0.4}Ga_{0.6}As$	barrier
4 nm	GaAs	undoped 1/2 well
1 nm	GaAs	$n = 2 \times 10^{22}$ m^{-3}
4 nm	GaAs	undoped 1/2 well
5.7 nm	$Al_{0.4}Ga_{0.6}As$	barrier
10.2 nm	GaAs	undoped spacer
50.9 nm	GaAs	$n = 2 \times 10^{22}$ m^{-3}
80.6 nm	GaAs	$n = 2 \times 10^{23}$ m^{-3}
2 μm	GaAs	$n = 2 \times 10^{24}$ m^{-3}
-	GaAs	n^+ substrate.

Table 1

The double barrier RTD's were grown by molecular beam epitaxy on n^+GaAs substrates. The centre plane of the 9 nm wide quantum well is doped with a narrow layer (~ 1 nm) of 2 x 10^{22} m^{-3} Si donors such that the mean separation of the donors is much greater than the Bohr radius in GaAs, 9.9 nm. The barrier thickness is 5.7 nm and there is a 10 nm spacer layer between each barrier and the doped contact regions. The detailed structure is shown in Table 1. We also grew control samples in which the δ-layer of impurities had been omitted. In addition, devices were grown at different substrate temperatures to control the segregation of dopants during growth. Mesas ~ 6μm square were fabricated using photolithography and dry etching. Electrical measurements were made using standard dc techniques at temperatures down to 280 mK.

In Figure 1 we show I(V) at T = 4.2 K in both forward and reverse bias for a 6 μm square mesa incorporating a δ-layer of impurities and grown with a substrate temperature of 630 °C. We define forward bias as the top contact positive so that the electrons are travelling up from the substrate. The curve is essentially identical to that of a large area mesa, suitably scaled. There is a small shoulder at ~ 70 mV, visible in the x 50 expanded curve, which we have shown previously is due to tunnelling via states bound to single donors in the quantum well [7]. Devices which are grown at 550°C, where there is far less segregation of dopants, show this feature far more clearly. When the scale is expanded x 25000 some additional structure with I < 100 pA appears at low bias (|V| < 50 mV). Unlike the principal resonant peak at approximately ± 150 mV this structure is strongly asymmetric between forward and reverse bias. In addition, although we see similar features in all devices incorporating donors in the well, the detailed peaks are different, characteristic of a mesoscopic system. Generally, for higher concentration of impurities or higher substrate temperature during growth, the structure occurs at biases closer to zero. For consistency, all curves shown in this paper will be for the same device but we shall emphasize which features of the data are universal and which are device specific. In the control samples, where we have taken considerable trouble to reduce the number of stray donors by incorporating larger spacer layers and growth at low temperatures, there is still some additional structure but it occurs very close to the threshold for the main resonance. In one or two control devices we have observed single, isolated peaks at V ~ 60 mV.

The sub-threshold structure in the doped devices is strongly temperature-dependent below T = 4.2 K. This is illustrated in Figure 2 where we plot ln(I) versus V to emphasize the low bias structure. Curves for the five temperatures are offset for clarity and the current scale refers to the lowest curve. The dotted lines represent our noise threshold. The curve at T = 4.2K is the

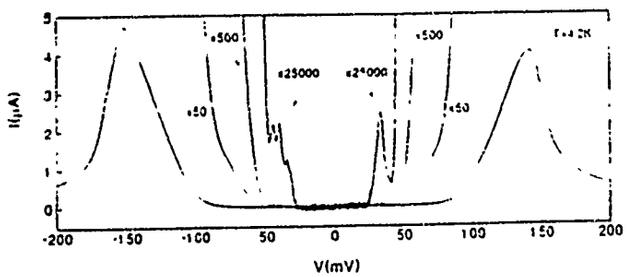

Figure 1.
I(V) characteristics at 4.2 K of a device of lateral dimension 6 μm in forward and reverse bias.

same as is shown in Figure 1. As temperature is decreased, although the curve at high bias is unchanged, two notable features emerge. First, the structure becomes more pronounced at low temperatures although it is more or less unchanged below 1K. Secondly, the onset of the structure, defined as the point at which the current is measurable above the noise, becomes very sharp indeed and at slightly higher bias there is a series of further sharp steps in both forward and in reverse bias. The sharpness of these curves is illustrated by the fact that the slopes of the onset and the next step (at -48 mV and +45 mV) in both bias directions are limited only by the bath temperature. This is shown in Figure 3 where we plot the slope of the onsets of the structure of Figure 2 versus temperature. The solid line represents the equation

$$I = I_0 \exp\{-\alpha e\Delta V/k_B T\} \quad : \quad I_0 = 50 \pm 10 \text{ pA and } \alpha = 0.32 \qquad (1)$$

where ΔV is the measured voltage relative to the onset at T = 0. The constant α represents the relationship between energy difference and applied voltage near the onset of the structure. Equation 1 implies that the sharpness of the current onset is limited only by the thermal activation of electrons from the emitter chemical potential, implying that the emitter electrons are in thermal equilibrium with the main heat bath. Despite the peak structure being quantitatively different in different devices the sharpness of the onset appears to be universal, appearing in all devices studied, including the controls. This activated behaviour is discussed in more detail below but we note the similarity between our data and that seen elsewhere in smaller, sub-micron, devices and attributed to quantisation effects and Coulomb blockade [2].

Figure 4 illustrates the pronounced effect of a magnetic field on the sub-threshold features in I(V). The graph plots ln I versus V at T = 1.24 K for magnetic fields, B, of 0 to 16 T applied parallel to the current direction. Successive curves are offset for clarity and the current scale refers to the B = 0 curve. The dotted lines represent the noise level. Below about 4 T, the magnetic field has very little effect in both forward and reverse bias. At higher fields in forward bias, there is a general sharpening of the features and a shift of the onset to lower voltage with

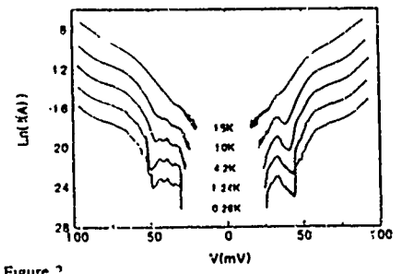

Figure 2.
ln (I) versus V near the current threshold for 5 temperatures. The dotted lines represent the noise level. Curves are offset for clarity and the current axis refers to the lowest curve.

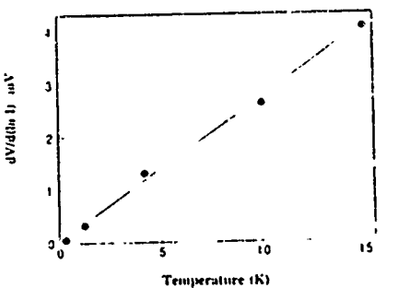

Figure 3.
dV/d(ln(I)) near the current threshold plotted against temperature. The straight line is the best fit.

increasing B. The features decrease in amplitude at the highest fields and there is also some evidence for additional structure appearing at intermediate values of B. The effect of the field is much more pronounced in reverse bias. The same general observations apply as in forward bias but, in addition, for 7 T < B < 11 T we see the emergence of a set of sharp peaks, more or less evenly spaced in V. Furthermore, although the structure beyond onset at B = 0 is independent of temperature below 2 K (see Figure 2), the features around B = 10 T become sharper as T is reduced below 1 K. This is shown in detail in Figure 5 in which we plot actual I(V) in reverse bias at T = 280 mK for 7 T < B < 13 T. Successive curves are offset by 100 pA. At B = 10 T the sharp, T-limited onset to the structure remains but there are now also six well-defined and evenly spaced peaks, four of which are split. We believe that this splitting, which has not previously been observed in sub-micron RTD's, is due to spin (see below). The spin-split peaks have a linewidth which is limited by temperature, even at 280 mK.

The presence of the six well-defined peaks at B = 10 T is not a universal property of the devices. However, it is quite generally the case that, with increasing B, (a) the structure is always sharper in reverse bias than in forward bias, (b) peaks develop and become sharper as B increases but eventually disappear for sufficiently large B, (c) the structure moves to lower bias, ie closer to zero and (d) spin splittings occur.

All the results displayed refer to a device ~6 μm square. On this length scale there is no possibility of lateral quantum confinement causing the structure. Equally, the Coulomb charging energy for a single electron, $e^2/2C$, where C is the capacitance of a 6 μm planar diode, is ~100

neV, which is far too small to explain the observed effects. Considering the thermally activated onset of the structure, equation 1 implies that, in the vicinity of the onset, we can relate applied voltage, V, to an energy scale, E, by E ≈ 0.32V eV. An energy of 100 neV is entirely negligible compared with the ~10 meV (ie V ~ 30 mV) which is required for onset of the structure. Nevertheless, our observations are very similar both qualitatively and quantitatively to those reported by other authors in sub-micron diodes which have been ascribed to Coulomb blockade.

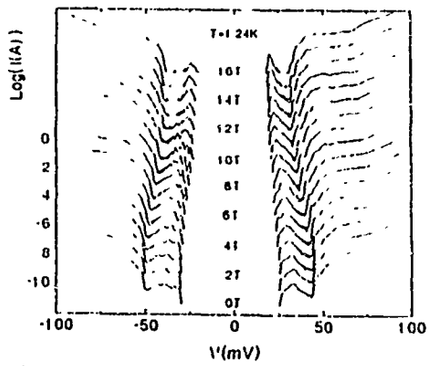

Figure 4.
I(V) versus V at 1.24 K for various magnetic fields. The dotted lines are the noise level and curves are offset for clarity with the current axis referring to the lowest curve.

On the principal resonance of a RTD of this type, in which a spacer layer separates the barriers from the electrical contacts, it is well established that tunnelling takes place from a two-dimensional electron gas (2DEG) in an accumulation layer next to the emitter barrier into two-dimensional bound states in the well [8]. Our observed structure occurs at voltages well below the threshold for this process and lower even than that for tunnelling into shallow states in the well which are bound to single donor atoms [7]. Therefore, we are led to the conclusion that the structure must be due to tunnelling into deep localised states, possibly associated with clusters of donors in the well. Deeper energy levels allow tunnelling at biases closer to zero as seen in the experiment. We estimate that there are ~ 700 donors in the quantum well which, if we assume a random distribution, implies that there is a very high probability (~ 95%) of two donors lying within an effective Bohr radius of each other and a reasonable probability of three (~25%). The localised nature of the states has been confirmed by measurements made with B perpendicular to the current direction which will be reported elsewhere [9]. However, at such low biases in a disordered material we consider it unlikely that there is a uniform and continuous 2DEG from which to tunnel. Rather, it is likely that the electrons accumulate next to the emitter barrier as localised puddles in regions of low potential. At the relevant biases the mean sheet density is a few times 10^{14} m^{-2}. Some of these puddles may be associated with the same clusters of donors which give rise to the localised states in the well. Our model is that the structure at B = 0 at least, is due to tunnelling between an emitter state, possibly only containing a few electrons, and a more strongly localised state in the well. The shift of the onset of the structure to lower bias with increasing B is also consistent with the emitter state being more weakly confined. The sharpness of the onset is limited by thermal activation from the quasi-Fermi level in the emitter accumulation layer into the localised state in

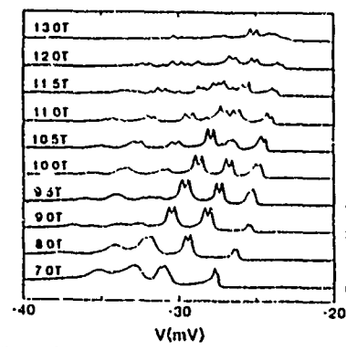

Figure 5.
I(V) on a linear scale at T ≈ 280 mK and various magnetic fields. Successive curves are offset by 100 pA.

the well, which is consistent with the observed experimental results. The natural linewidth of the state in the well may be very small if it is limited by the dwell time in the well, which we estimate to be about 3 ns. The sharp onset indicates that the electrons in the emitter are in thermal equilibrium with the main thermal reservoir even though we are in the régime where $eV >> k_BT$. Note that there is no need to invoke Coulomb blockade as the origin of the steplike structure although it is likely that electron charging energies may be important in the localised states. Steps in I(V) which occur at higher values of bias may then be due to a succession of localised states in the well.

An important feature of our data is that the structure appears in I(V) and not in the differential conductance. In an RTD, the current is essentially a measure of the charge in the well. The initial current step, therefore is probably a signature of a single electron in the well. The current of 50 pA would correspond to a lifetime ~ 3 ns for the state in the well, consistent with the barrier height and thickness. The structure we observe at higher magnetic field, as shown in Figure 5, is different in that it comprises a set of well defined *peaks* whose width is limited only by temperature. This is very important because it means that in between the peaks there is no charge in the well, which is good evidence for the structure being due to tunnelling from one localised state to another. There are however two important points to be made with regard to the peaks. First, at 10 T for example, the voltage spacing of the peaks is only ~ 2 mV. Even if we associate this directly with an energy difference, it is much smaller than the Landau level spacing at 10 T (~ 17 meV) which should represent the minimum energy separation of single particle states. Secondly, assuming that spin is conserved in the tunnelling process, the observation of peaks split by the magnetic field indicates that there must be a different spin splitting for the two states. Furthermore, the splitting itself is voltage dependent at a given magnetic field although at a given bias the splitting is reasonably linear in B. At 10 T it varies from ~ 280 μV at V = -26 mV to ~ 420 μV at V = -28 mV indicating a strong dependence on energy. These splittings can be related to a *difference* in the effective Landé g-factor, Δg^*, between the two states using $\Delta E = \Delta g^* \mu_B m_s B$ where ΔE is the splitting in energy, μ_B is the Bohr magneton and $m_s = 1/2$. Assuming the energy is related to voltage by $E = \alpha eV$ with $\alpha = 0.32$, this gives values of Δg^* ~ 0.3 - 0.5 to be compared with the value $g^* = -0.44$ for electrons in bulk GaAs.

The above observations are consistent with the model of tunnelling from a weakly localised state near the emitter barrier into a more strongly localised state in the well. The different values of

g^* are consistent with the difference in localisation [10]. However, the presence of peaks with equal spacing in energy much less than the Landau level spacing indicates that the structure is probably due to the addition of electrons to the electron puddle localised near the emitter barrier. The observed spacing of ~ 1 meV is reminiscent of the charging energies observed by Ashoori et al [11] but in a device more than an order of magnitude smaller in lateral dimension than our mesas.

In summary, we have observed strong sub-threshold structure in the I(V) characteristics of RTD with lateral dimensions ~ 6μm. At all magnetic fields, there is a very sharp onset to the structure which is limited by temperature even at T = 280 mK. For B > 7 T a series of peaks appears in I(V) whose width is also limited by k_BT and which show spin splitting at the lowest temperatures. We interpret these results tentatively in terms of tunnelling between two localised states, one which is considerably more localised than the other. Further, we are able to see structure which we can only attribute to Coulombic effects. There are two important features to emerge from our work. First, it is possible to observe quantum box effects in devices which themselves are far too large to cause the quantisation directly. This means that the interpretations of results in all devices must be carried out very carefully to distinguish between effects due to impurities and effects due to confinement provided either by the device geometry or by a gate potential. Secondly, we have been able to observe spin-splitting effects which are due to a different value of g^* in the two localised states. We find that Δg^* is dependent on bias, and hence energy, and this may prove to be a new technique for studying the variation of g^* with increasing localisation.

Acknowledgements

This work is supported by the SERC (UK). JWS and NLaS wish to thank CNPq (Brasil) and PHB the Royal Society (UK) for financial support.

References

[1] M A Reed, J N Randall, R J Aggarwal, R J Matyi, T M Moore and A E Wetsel, Phys. Rev Lett 60, 535 (1988)

[2] B Su, V J Goldman and J E Cunningham, Science 255 313 (1992).

[3] M W Dellow, P H Beton, C J G M Langerak, T J Foster, P C Main, L Eaves, M Henini, S P Beaumont and C D W Wilkinson, Phys Rev Lett. 68, 1754 (1992)

[4] M Tewordt, L Martín-Moreno, J T Nicholls, M Pepper, M J Kelly, V J Law, D A Ritchie, J E F Frost and G A C Jones, Phys. Rev B45, 14407 (1992)

[5] P Guéret, N Blanc, R Germann and H Rothuisen, Phys Rev Lett. 68, 1986 (1992).

[6] S Tarucha, T Honda, T Saku and Y Tokura to be published in Surf. Sci. (Proceedings of EP2DS10, Newport, USA, 1993)

[7] J W Sakai, T M Fromhold, P H Beton, M Henini, L Eaves, P C Main, F W Sheard and G Hill Physica B184 241 (1993).

[8] M L Leadbeater, E S Alves, F W Sheard, L Eaves, M Henini, O H Hughes and G A Toombs, J. Phys Condens Matter 1 10605 (1989)

[9] For an explanation of the technique see J W Sakai, T M Fromhold, P H Beton, L Eaves, M Henini, P C Main, F W Sheard and G Hill, to be published in Phys Rev (1993).

[10] M J Snelling, G P Flinn, A S Plaut, R T Harley, A C Tropper, R Eccleston and C C Phillips, Phys. Rev B44 11345 (1991)

[11] R C Ashoori, H L Stormer, J S Weiner, L N Pfeiffer, S J Pearton, K W Baldwin and K W West, Phys. Rev Lett 68 3088 (1992) and to be published in Surf Sci (Proceedings of EP2DS10 Newport, USA, 1993)

TuP29

SCHOTTKY-BARRIER TUNNELING SPECTROSCOPY OF A 2D ELECTRON SYSTEM IN DELTA-DOPED Si(100) LAYERS

J LINDNER, B KLEIN, and U KUNZE,
Institut für Technische Physik, Universität Erlangen-Nürnberg, D-91051 Erlangen, Germany
and
W KRUNKE and I EISELE,
Fakultät für Elektrotechnik, Universität der Bundeswehr München, D-85577 Neubiberg, Germany

Abstract—Schottky-barrier tunneling junctions have been prepared on Si (100) layers with the sequence p-type buffer Sb δ-doping layer, and an intrinsic layer ranging from zero to 10 nm thickness. The tunneling characteristics show structures arising from subband edges, from the bulk conduction band edge, and from the tunneling of holes into the metal. Exact layer thickness and doping parameters are gained from a self-consistent calculation of the subband structure.

In a number of experiments quantized two-dimensional (2D) electron systems have been investigated by electron tunneling spectroscopy, where the bias position of subband-edge-induced features in the second derivative d^2I/dV^2 of the current(I)-voltage(V) characteristic directly reflects the subband energies. The electron layer has been induced by native interface donor states in InAs [1], by the work-function difference of the electrodes in PbTe [2], Si [3], and InGaAs [4] metal-oxide-semiconductor (MOS) structures, by barrier doping in GaAs-AlGaAs heterostructures [5], and by planar-delta(δ)-doping layers in GaAs-[6,7] and Si [8-10]. In particular for the tunneling experiments on Si the Schottky barrier junctions on δ-doped layers [8-10] showed considerably poorer quality than MOS-junctions with electron inversion layers [3]. In the latter samples subband levels could be detected up to energies of more than 500meV above the Fermi level, subbands of the lower (unprimed) and higher (primed) series could be clearly distinguished, and the occurrence of large and reproducible subband-edge-induced structures in d^2I/dV^2 prevented one from misidentifying additional structures that arise from impurity-assisted tunneling. In the present work we demonstrate a substantial progress in fabricating Schottky-barrier tunneling junctions on Si(100) resulting in a new insight into the tunneling mechanisms in these quantum layer devices.

The preparation started from high-resistive Si(100) wafers. A several μm thick p-type layer was diffused from a spun-on boron dopant source. Then the δ-doping layer was grown by molecular beam epitaxy (MBE). The layer growth started with a 100 nm (wafer A) or 300 nm (wafer B) undoped buffer. Annealing for 15 min at 1000 °C flooded the buffer layer with boron, resulting in a surface concentration of about 10^{18} cm^{-3}. Subsequently an Sb δ doping layer of about 2×10^{13} cm^{-2} covered with 2-3 nm Si was grown by solid-phase epitaxy followed by about 10 nm nominally undoped Si grown at 700 °C [8]. From these wafers samples with different intrinsic layer thicknesses were prepared by anodic oxidation and subsequent etching with hydrofluoric acid. Details of this controlled removal of Si up to 30 nm with an accuracy of better than 1 nm will be described elsewhere. Finally, 25 nm Ti and 200 nm Au were evaporated and 35,

50, and 70 μm square contacts lithographically defined The counterelectrode was formed by another Schottky contact of several mm² separated from the tunneling contact by a 5 μm gap

Figure 1 illustrates the band structure of the Schottky-barrier tunneling junction as calculated self-consistently for an intrinsic layer thickness d_i 5 nm, a δ-doping density n_D=1 8×10¹³ cm⁻² with a uniform distribution of width d_δ=1 nm, a bulk doping level N_I 1 8×10¹⁸ cm⁻³ and a Ti Schottky barrier height of Φ_b=0 5 eV The parameters d_i, n_D, d_δ, and N_I have been gained from a fit to the experimental data as described below

The sheet electron density n_s in the δ-layer is given by

$$n_s = n_D - n_m - n_{depl} \qquad (1)$$

Here the surface charge density at the metal electrode n_m corresponds to an electric field in the intrinsic layer $F_s = e n_m/\varepsilon_0\varepsilon_{Si}$ For a δ-layer with populated electron subband the surface potential drops across the intrinsic layer, which results in $F_s = (\Phi_b - eV)/d_i$ The depletion charge density in the p-type buffer is given by $en_{depl} = (2\varepsilon_0\varepsilon_{Si}N_I E_G)^{1/2}$, where we assume that the acceptor concentration is uniform and the bulk Fermi level coincides with the valence band edge It is obvious from eqn (1) that at low d_i and high reverse bias V n_m increases and the electron layer becomes depopulated In the limiting case of n_s=0 the surface potential drops across the total depletion layer, consisting of d_i and the bulk depletion zone $d_{depl} = n_{depl}/N_I$ This leads to a weaker increase of F_s as bias is increased than for the case of populated electron layer

The measurements were performed at a sample temperature of 80 and 4 K taking the I-V, dI/dV and d^2I/dV^2 characteristics Figure 2 shows a typical set of characteristics taken at T 4 K from a junction on wafer B with 2 nm removed layer Distinct kinks in I-V corresponding to maxima in the conductance and to oscillations in d^2I/dV^2, arise from the subband levels of the quantized 2D electron layer Maxima in the tunneling conductance close to the subband edges rather than a step-like increase as in MOS tunneling [4] probably result from the crystalline barrier, which leads to a wave-vector dependent tunneling probability [11] The stretching of the oscillation period at reverse biases in excess of 500 mV cannot be explained by an increase of the subband separation in the triangular potential well as F_s increases with bias The origin is the gradual depletion of the electron layer, which leads to the distribution of the voltage drop across the *total* depletion zone As a result, the potential well is raised in energy as illustrated in Fig 3 Some additional bias shift may arise from the series resistance of the electron layer, in particular at biases V<-500 mV, where the current increases Around zero bias tunneling into subband states is effectively suppressed due to the energy-dependent thickness of the triangular barrier The large dip structure at V=-1 15±0 01 V reflects the onset of tunneling into the extended conduction band states of the bulk As can be seen from Fig 3, its bias position is independent of the population of the potential well

The structures mentioned above are reproducible from different junctions, in contrast to the series of narrow peaked structures at forward and large reverse biases However, this random pattern is not due to noise but is reproducible from consecutive bias runs We attribute these structures to tunneling via localized impurity levels in the barrier

At elevated temperatures the impurity-induced fine structure is not resolved If now the intrinsic layer is sufficiently thin tunneling spectroscopy of the very weak subband-induced structures around zero bias becomes possible Figure 4 shows an example of a junction prepared on wafer A with 6 nm removed layer At T 80 K the enlarged recording reveals small dips at low forward and reverse bias that arise from the lowest three subbands E_0, $E_{0'}$, and E_1. Another three large dip structures occur at about the same bias position as in the T=4 K characteristic According to the result of the self-consistent calculation indicated in Fig 4 we assume that these structures reflect the primed subbands as in MOS tunneling junctions [4] due to their larger density of states and lower effective mass in the tunneling direction

The junction modelling, details of which are discussed below, indicates a beginning of the electron layer depopulation at V=-460 mV, which is close to the value V=-470 mV obtained from eqn (1) These results are confirmed in Fig 4 by the fading of the oscillatory component at larger negative bias When the electron layer becomes depopulated the Fermi level in the potential well is no longer pinned by the high density of states in the subband and large potential fluctuations lead to an averaging of the subband-edge induced structures It should be noted that the large structure at V=-1 15 V arising from the conduction band edge is still present at T=80 K At reverse bias V<-1 3 V a strong current rise leads to the steep slope in d^2I/dV^2 which probably reflects the onset of hole tunneling As indicated in Fig 3 a substantial lowering of the hole barrier occurs at small d_i and at high reverse bias where the electron layer is depopulated, which facilitates tunneling of holes At forward bias V=250 mV the bell-shaped maximum indicates the transition from the exponential Schottky diode I-V characteristic to the saturation of the conductance dI/dV due to the series resistance

Figure 5 summarizes the results from samples on wafer B with the removed layer thickness as parameter It is obvious that the subband structure is extremely sensitive to the intrinsic layer thickness At 6 nm removed Si the electron layer is nearly depleted, at 9 nm the only current component is hole tunneling A removal of more than 9 nm Si will not lead to further changes in the tunneling characteristics A numerical calculation shows that at d_i<1 nm the δ-doping layer has only a weak influence on the hole barrier height Therefore we estimate the initial thickness of the undoped layer at 10±1nm

We have used the estimate of the remaining intrinsic layer thickness d_i as a parameter for the model calculation, where in the fit to the experimentally determined subband energies under bias the variation of d_i is limited to the uncertainty of 2 nm Further fit parameters are the δ-doping density n_D, the δ-doping spread d_δ and the buffer doping concentration N_I For the Ti Schottky barrier height a value Φ_b=0 5 eV has been assumed In spite of the large number of four different fit parameters the determination of a conclusive set of d_i, n_D, d_δ, and N_I is feasible because each of the parameters efficiently influences only some part of the subband spectrum The δ-doping n_D strongly influences the energy position of the lowest subbands E_0, $E_{0'}$, E_1, E_2, and $E_{1'}$ relative to the Fermi level, whereas the spread d_δ determines their separation Higher subband energies mainly depend on d_i and N_I Reducing both d_i and N_I while keeping a given E_n constant leads to a stronger decrease of the subband separation with increasing energy A critical test of the parameters is possible because the changes of the subband structure due to the Si removal has to be modeled only by the known variation of d_i

The resulting parameters of wafer A are an initial d_i 11 nm, n_D=1 8×10¹³ cm⁻², d_δ 1 nm, and N_I 1 8×10¹⁸ cm⁻³ and of wafer B d_i 9 5 nm, n_D=1 6×10¹³ cm⁻², d_δ=1 nm, and N_I 2 2×10¹⁸ cm⁻³, where the average deviation from the experimental E_n-k_0 is about 5% It should be noted that the calculation is based on an idealized model, e g the true donor distribution, image-force corrections, and the imaginary k dispersion in the band gap have been

neglected The systematic deviation of the calculated E_1 level towards lower energies is probably the result of neglecting the 0-population due to band tailing However, also the experimentally determined subband energies are inaccurate because of the voltage drop across the series resistance

In conclusion, we have observed three different tunneling channels in Schottky-barrier contacts to i-δn-p structures on Si(100) with intrinsic layer thickness $d_i \leq 10$ nm Around zero bias and at reverse biases up to several 100 mV the d^2I/dV^2 curves exhibit subband edge induced dips and at a fixed bias $V = -1$ 15 V a large structure arising from the bulk conduction band edge The onset of hole tunneling from the bulk valence band edge to the metal is observed at high reverse bias and small thickness d_i, where the potential well is depopulated The results of a model calculation agree reasonably with the experimentally determined bias and thickness d_i dependent subband structure

Acknowledgement—This work was supported by the Deutsche Forschungsgemeinschaft

REFERENCES

1 D C Tsui, *Phys. Rev. B* 4, 4438 (1971)
2 D C Tsui, G Kaminski, and P H Schmidt, *Phys. Rev. B* 9, 3524 (1974)
3 P -F Lu, D C Tsui, and H M Cox, *Appl. Phys. Lett.* 45, 772 (1984)
4 U Kunze, *J. Phys. C* 17, 5677 (1984)
5 J Smoliner, M Hauser, and E Gornik, *Appl. Phys. Lett.* 52, 33 (1988)
6 M Zachau, F Koch, K Ploog, P Roentgen, and H Beneking, *Solid State Commun.* 59, 591 (1986)
7 F Basmaji, A C Notari, B Schrappe, M H Degani, L Ioriatti, and O Hipolito, *Surf. Sci.* 263, 231 (1992)
8 H P Zeindl, T Wegehaupt, I Eisele, H Oppolzer, H Reisinger, G Tempel, and F Koch, *Appl. Phys. Lett.* 50, 1164 (1987)
9 I Eisele, *Superlatt. Microstruct.* 6, 123 (1989)
10 H -M Lin, K -F Berggren, W -X Ni, B E Sernelius, M Willander, and G V Hansson, *J. Appl. Phys.* 67, 1962 (1990)
11 C B Duke, *Tunneling in Solids*, Academic, New York 1969

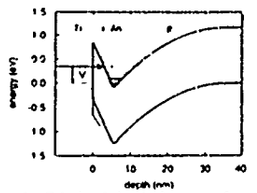

Fig 1 Calculated band diagram of a tunneling junction with 5 nm intrinsic layer under reverse bias $V = -0.34$ V Solid and dashed horizontal lines represent the energies of the lowest subbands E_0 and E_1 respectively The arrow indicates the tunneling channel that detects the E_1 subband level Thin lines represent the band diagram at zero bias

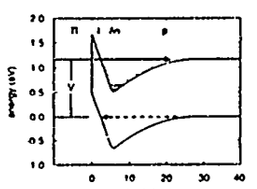

Fig 3 As Fig 1, with electron layer depopulated by the large reverse bias $V = -1.16$ V Tunneling into the conduction band states of the p-type layer and hole tunneling from the valence band into the metal is indicated by arrows

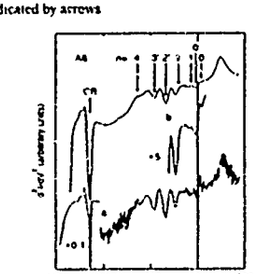

Fig 4 Tunneling characteristics of a junction on wafer A with 6 nm removed layer measured at (a) $T = 4$ K and (b) $T = 80$ K Calculated subband levels are indicated

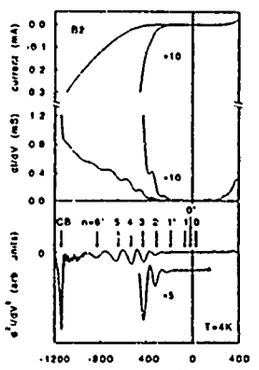

Fig 2 I-V, dI/dV and d^2I/dV^2 tunneling characteristics of a junction on wafer B with 2 nm removed layer The assignment of dip structures with calculated subband levels and the conduction band edge (CB) is indicated

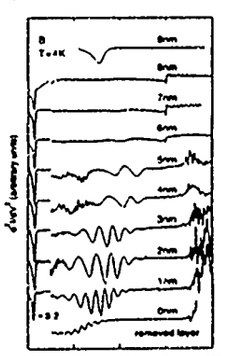

Fig 5 d^2I/dV^2 characteristics of samples on wafer B with different removed layer thickness as given

TuP30

PHOTOHOLE-INDUCED RESONANT TUNNELING OF ELECTRONS IN SELECTIVELY ETCHED SMALL AREA GaAs/AlAs DOUBLE BARRIER DIODES

H. Buhmann, J.Wang, L. Mansouri, P.H. Beton, L. Eaves, M. Heath and M. Henini

Department of Physics, University of Nottingham, Nottingham, NG7 2RD, U.K.

Abstract

The influence of light of wavelength 670 *nm* on the low temperature $I(V)$ characteristics of selectively etched small area resonant tunneling diodes (RTD) has been investigated. These diodes have with physical dimensions down to 0.5 μm and their design allows easy optical access. Under illumination new sub-threshold peaks appear in $I(V)$. The sub-threshold peaks are also observed in large area diodes, and are found to be strongly influenced by the presence of a magnetic field applied either parallel or perpendicular to the plane of the barriers. We show that our results cannot be explained in terms of resonant tunneling of photo-excited holes and propose an explanation based on the Coulombic electron-hole interaction.

Resonant tunneling diodes (RTDs) are an attractive system for the study of quantum transport since the strong non-linearities observed in their current voltage characteristics, $I(V)$, are a direct consequence of the quantum confinement of carriers within a quantum well [1]. The incorporation of donors within the quantum well of an RTD leads to the formation of laterally bound hydrogenic-like states which are localized within the plane of the quantum well. These bound states are lower in energy than the quantum well continuum and provide an additional channel for resonant tunneling, which in turn leads to additional non-linearities in $I(V)$ [2, 3]. Resonant tunneling therefore provides a means of detecting the presence of any low energy states which are formed within the quantum well.

In this paper we describe a series of experiments in which we investigate the possibility of using RTDs to probe the presence of holes in the quantum well. The holes are introduced by means of photo-excitation and they give rise to sub-threshold peaks in $I(V)$. We argue that these peaks are a close analogue of the peaks generated by the presence of donors.

Our experiments are conducted on both large (100 − 400 μm square) mesas (which are suitable for optical access) and also a range of small area diodes with dimensions down to 0.5 μm. An important element of our work is the development of a fabrication process for a sub-micron RTD which is suitable for optical access. This process, based on optical lithography and wet etching and as described below, does not require the use of either dry etching (a possible source of damage) or dielectric layers (which might impair the optical access of the devices) for isolation of bonding pads and metallic tracks.

The devices were fabricated from a GaAs/AlAs double-barrier heterostructure grown on a semi-insulating (100) GaAs substrate, using molecular beam epitaxy (MBE). The layer composition of the heterostructure is given in Table 1.

100.0 *nm*	GaAs	$n = 2 \times 10^{18}$	top contact
80.6 *nm*	GaAs	$n = 2 \times 10^{17}$	
50.9 *nm*	GaAs	$n = 2 \times 10^{18}$	
20.4 *nm*	GaAs		spacer
5.9 *nm*	AlAs		barrier
9.1 *nm*	GaAs		well
5.9 *nm*	AlAs		barrier
20.4 *nm*	GaAs		spacer
50.9 *nm*	GaAs	$n = 2 \times 10^{18}$	bottom contact
80.6 *nm*	GaAs	$n = 2 \times 10^{17}$	
200.0 *nm*	GaAs	$n = 2 \times 10^{18}$	
7.6 *nm*	AlAs		etch stop
1000.0 *nm*	GaAs		
		semi-insulating	Substrate

Table 1: *Sample structure. Growth-direction from bottom to top. The donor is Si and the MBE growth temperature was 550°C*

To fabricate the small area diodes the GaAs (top contact) layer is selectively etched using NH_4OH/H_2O_2 (5:95), to form a narrow lines with a width in the range of 0.5 to 3 μm. The lines are formed between large ohmic contacts ($\sim 100\ \mu m \times \sim 100\ \mu m$). Note that optical lithography is used for pattern definition, so that significant undercut etching is required to achieve sub-micron dimensions. A second (non selective) etch was used to penetrate the AlAs barriers and reveal the lower GaAs doped (bottom contact) layer. Finally, this buried n type GaAs layer was also selectively etched to form a freestanding GaAs bridge in the emitter layer. Au/Ge/Ni ohmic contacts were then deposited on the top and bottom contact doped layers. A schematic representation of the final device is shown in Figure 1. Note that the metallised region on the top contact is connected to the active region of the device by the freestanding GaAs bridge. This serves to isolate the bottom contact from the doped region beneath the top contact eliminating any possible parallel conduction path. This novel fabrication route produces small area diodes with low contact resistance which can be easily illuminated. The dimensions of the small area devices discussed below are: I $\sim 0.5\ \mu m \times 60\ \mu m$, II $\sim 1.0\ \mu m \times 60\ \mu m$ and III $\sim 3.0\ \mu m \times 60\ \mu m$. We have also investigated large area control devices with metal contacts which are sufficiently small for light to penetrate the device.

The low temperature current-voltage characteristics ($T = 4.2\ K$), $I(V)$, for device I, II and III are shown in Figure 2 a). For all measurements the convention of positive bias implies a positive potential applied to the top contact. Comparing the $I(V)$ of the small area and large area devices (inset Fig. 2a), no significant difference is observed, except for the smallest device (I). The main electron peak positions remain approximately the same, and a small asymmetry in the bias region beyond the main resonance is common to all devices.

The $I(V)$ for the smallest diode, device I, shows a broadening of the main electron resonance together with a shift to higher voltage in forward bias, while in negative bias it

exhibits no obvious changes. A similar asymmetry has been observed in gated resonant tunneling devices [4], where the active tunnel area is progressively decreased with increased gate voltage. This has been explained in terms of the shape of the equipotential close to the tunnel barriers.

We may estimate the side wall depletion, d_s, in the small area diodes from the value of the peak current, I_{peak}, of the main resonance from the relation: $I_{peak} = j_{peak}(l_l - d_s)l_b$, where j_{peak} is the peak current density and l_l and l_b are defined in Figure 1. From the values of I_{peak} for devices I, II and III we find $j_{peak} = 0.17\ nA\ \mu m^{-2}$ and $d_s = 0.4\ \mu m$. Note that this means the conducting width for device I is 0.1 μm. Our experimental value for j_{peak} is in good agreement with the peak current density measured for the corresponding large area devices, $j_{peak\,large} = 0.18\ nA\ \mu m^{-2}$.

The devices were illuminated in a flow cryostat via an optical fibre. Under constant illumination ($P_L \leq 100\ \mu W\ cm^{-2}$) with 670 nm wavelength laser light, changes in $I(V)$ are observed. In Figure 2 b) $I(V)$ for device II is plotted for various levels of illumination. The features which are observed for device II are typical of all devices. The main electron resonance peak position and threshold value shift to lower voltage and new resonances occur in the sub-threshold region just below the threshold voltage for the main resonance. These new features are indicated by arrows in Fig. 2 b). The strength of these additional resonances increases with excitation power. In addition to the appearance of these features we also observe an increase in the peak and valley currents of the main resonance with increased illumination. The valley current is greatly enhanced in forward bias.

To understand the effects of illumination we refer to the band profiles of the device shown in Figure 3. The incident light creates electron-hole pairs in the depletion region beyond the collector barrier. The photo-created electrons (majority carriers) are swept into the doped collector region, but the photo-created holes (minority carriers) drift up towards the collector barrier where they form an accumulation layer. This process has been discussed previously in the context of photoluminescence experiments on resonant tunneling diodes [5, 6, 7]. The presence of the photo-created holes close to the collector barrier modifies the band bending in the device and accounts for the shift of the threshold and peak of the main resonance to lower voltage.

Similar effects have previously been observed in the $I(V)$ of large area resonant tunneling diodes under illumination [6, 7] which were attributed to resonant tunneling of photo-created holes. In the remainder of this paper we discuss the dependence of the photo-induced peaks on magnetic field. This data indicates that the additional peaks we observe cannot be described solely in terms the conventional model involving independent resonant tunneling of photo created holes. Instead we suggest that they may arise from resonant tunneling of electrons through excitonic bound states formed due to the presence of photo-created holes in the quantum well of the device. Note that this Coulomb-assisted tunneling process is analogous to the tunneling of electrons via donor states in the quantum well as discussed in Refs. 1 and 2.

Our discussion of the magnetic field dependence refers to $I(V)$ for large area diodes, since for these devices we have a more complete set of data, and can make a direct comparison with previous work [6, 7]. Figure 4 a) shows $I(V)$ up to the threshold voltage for the main resonance for a 466 nm square device illuminated with an excitation power $P_L \leq 10\ mW/cm^2$ in the presence of a magnetic field B between 0 and 10 T oriented perpendicular to the plane of the barriers. For $B = 0$ (lowest curve) we observe a sub-threshold resonance in each bias direction at V$\sim$ -110 mV and V$\sim$ 120 mV (peaks marked D in Fig. 4 a). For $B < 4\ T$ this peak remains unaffected by magnetic field, however as B is progressively increased it shifts to larger voltage and its amplitude is reduced. For $B > 3\ T$ several more peaks appear which occur at even lower voltage. These are labelled A, B and C on Fig. 4 a). The peaks show a fair degree of symmetry between bias directions, although their amplitude is higher in forward bias (because of an effective difference in the light intensity incident on the depletion region in forward and reverse due to absorption effects). The voltage positions of peaks A, B and C are only weakly dependent on magnetic field, however their amplitude is a strong function of field. At the highest magnetic fields peaks A and B split into two peaks. This can be seen more clearly for peak B, for which the split peak is stronger. The separation of the split peaks in voltage is $\sim 5\ mV$.

$I(V)$ for the same diode under illumination in the presence of a magnetic field oriented parallel to the barrier is shown in Figure 4 b). Note that for our experimental arrangement illumination of a sample oriented parallel to the field is more difficult. The maximum level of illumination is lower than for the perpendicular case and the corresponding photo-induced peaks have smaller amplitude than the data in Fig. 4 a). For $B = 0\ T$ we observe two sub-threshold peaks as in Fig. 4 a) (peaks marked D), however as B is increased beyond 3 T another more peak appears (peak B). As the magnetic field is increased peak D moves to higher voltage, and a weak splitting is observed.

The behaviour of the peak in $I(V)$ corresponding to the main resonance displays quite different behaviour for parallel and perpendicular oriented fields. For a perpendicular field its voltage position and amplitude are only weakly dependent on field, however for a parallel field the threshold moves to higher voltage. Note that peak D in the parallel field moves to a higher voltage at a similar rate to the threshold for the main electron resonance.

Thus our data shows a series of photo-induced peaks whose amplitude and voltage position are extremely sensitive to magnetic field. We first consider whether the dependence of their amplitude and voltage position on magnetic field is consistent with conventional resonant tunneling of photo-created holes. We focus on peak D since this peak is observed even for $B = 0T$. Previous work on p-i-p resonant tunneling diodes [8] shows that the voltage position of the lowest two hole resonances referred to as hh1 and lh1 (corresponding to resonant tunneling via the lowest heavy and light hole subbands respectively) is almost independent of magnetic field for $B < 11\ T$, the range shown in Fig. 4 b). Clearly peak D cannot be due to hole resonant tunneling via the hh1 or lh1 subbands since its voltage position is shifted by a parallel field. Hayden et.al. found that the lowest hole subband resonance which has a strong parallel field dependence of its voltage position is hh2, the first excited state heavy hole state. However, firm identification of peak D as the hh2 resonance is not possible, since in that case we would expect to observe a peak in $I(V)$ of comparable amplitude at lower voltage corresponding to the lh1 resonance as observed by Hayden et.al. In addition we have calculated the expected peak positions for electron and hole resonances using a simple model for the band bending of the device which uses the Fang-Howard wavefunction to model the state in the electron accumulation layer and treats the state in the hole accumulation layer as an Airy function. This model predicts

that the hh2 resonance should occur at a higher voltage than the electron resonance. We also note that in similar p-i-n resonant tunneling diodes the hh2 peak always occurs at higher voltage than the lowest electron resonance [9].

Another result established in the study of p-i-p resonant tunneling diodes is that the amplitude and voltage position of the peaks in $I(V)$ due to hole resonances are insensitive to the presence of perpendicular magnetic fields for $B < 10\ T$. Certainly nothing comparable with the dramatic magnetic field enhancement of peaks A, B and C in Fig. 4 a) has been observed for p-i-p devices. We are thus unable to account either qualitatively or quantitatively for our data in terms of conventional resonant tunneling of photo-excited holes.

We have also investigated these effects in several other wafers which differ from the heterostructure shown in Table 1 only in the thickness of the AlAs tunnel barriers. For barrier widths of 4.5 and 3.0 nm we do not observe such clear additional peaks under illumination, but see a step like behaviour at lower voltage which is highly reminiscent of the data shown in Ref. [7]. For barrier widths 5.9 and 7.5 nm we observe structure similar to that in Fig. 4. Note that the peak current density for our devices, j_{peak}, is two orders of magnitude smaller than that for the material used by Vodjdani et.al. [7]. This dependence of the peaks on barrier width clearly complicates the comparison of our data with that previously reported.

We have stressed above that our data cannot be explained solely in terms of resonant tunneling of photo-excited holes. Our alternative explanation is that the presence of a hole in the quantum well gives rise to an alternative resonant conduction path which is lower in energy than the quantum well continuum due to the Coulomb interaction of the electron and hole, i.e. tunneling of electrons via an excitonic state. Similar peaks have been observed in $I(V)$ for devices in which ionized donors are introduced into the quantum well. The threshold for peak D is approximately 30mV below that of the main resonance. According to our band bending calculations this corresponds to an energy below the continuum of of $\sim 5.5\ meV$. This should be compared with the binding energy of $\sim 7\ meV$ for a light hole exciton and $\sim 9\ meV$ for a heavy hole exciton. Although these numbers are not in exact agreement they are close, however we are not able to determine the type of exciton from our present data set. Note, however, that associating peak D with an excitonic transition is at least consistent with its shift to higher voltage in parallel field. However our model is so far unable to explain the appearance of the lower voltage peaks A, B and C with increasing magnetic field.

In conclusion we have observed a series of peaks which appear when a resonant tunneling diode is illuminated. The dependence of these peaks on magnetic field is no consistent with resonant tunneling of holes. We have proposed an alternative explanation based on resonant tunneling via hole-induced excitonic states in the well. Further work, in particular photoluminescence studies, are required to clarify the detailed origin of these peaks.

References

[1] L.L. Chang, L. Esaki and R. Tsu, Appl. Phys. Lett. 24, 593 (1974).

[2] M.W. Dellow, P.H. Beton, C.J.G.M. Langerak, T.J. Foster, P.C. Main, L.Eaves, M. Henini, S.P. Beaumont and C.D. Wilkinson, Phys. Rev. Lett. 64, 1754 (1992).
[3] J.W. Sakai, T.M. Fromhold, P.H. Beton, M. Henini, L. Eaves, P.C. Main, F.W. Sheard and G. Hill, to be published in Phys. Rev. B.
[4] P.H. Beton, M.W. Dellow, P.C. Main, T.J. Foster, L. Eaves, A.F. Jezierski and M. Henini, Appl. Phys. Lett. 60, 2508 (1992).
[5] J.F. Young, B.M. Wood, G.C. Aers, R.L.S. Devine, H.C.Liu, D. Landheer, M. Buchanan, A.J. SpringThorpe and P. Mandeville, Phys. Rev. Lett. 60, 2085 (1988).
[6] C.R.H. White, M.S. Skolnick, L. Eaves, M.L. Leadbeater, M. Henini, O.H. Hughes, G. Hill and M.A. Pate, Phys. Rev. B 45, 6721 (1992).
[7] N. Vodjdani, D. Côte, D. Thomas, B. Sermenge, P. Bois, E. Costard and J. Nagle, Appl. Phys. Lett. 56 (1), 33 (1989).
[8] R.K. Hayden, D.K. Maude, L. Eaves, E.C. Valadares, M. Henini, F.W. Sheard, O.H. Hughes, J.C. Portal and L. Cury, Phys. Rev. Lett. 66, 1749 (1991).
R.K. Hayden, Thesis, University of Nottingham, 1992.
[9] P.M. Martin, R.K. Hayden, C.R.H. White, M. Henini, L. Eaves, D.K. Maude, J.C. Portal, G. Hill and M.A. Pate, Semicond. Sci. Technol. 7, 456 (1992).

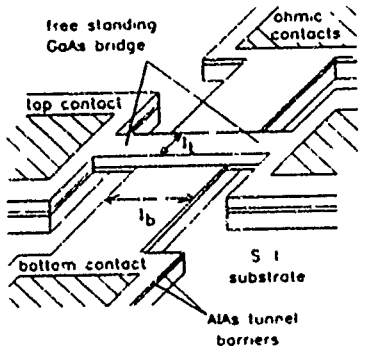

Figure 1. *Schematic picture of the small area device*

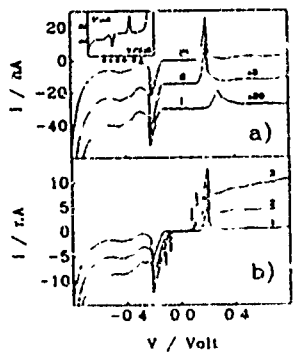

Figure 2: *a) I(V) characteristics of device I, II and III in darkness. Inset: I(V) of a large area device, 100 µm × 100 µm. b) I(V) characteristic of device II under illumination. 1: 0 µW/cm², 2: 1 µW/cm² and 3: 3 µW/cm²*

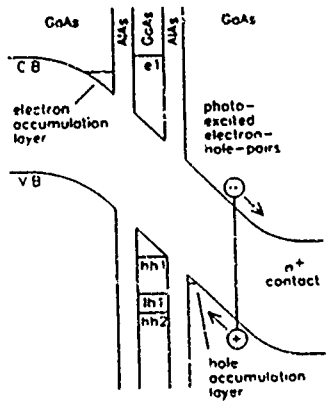

Figure 3. *Schematic band profile of the device.*

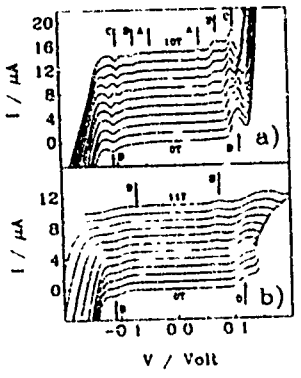

Figure 4. *I(V) characteristics for a 400 µm square mesa in a) perpendicular and b) in parallel magnetic field configuration*

TuP31

INTERFACE EFFECTS, BAND OVERLAP AND THE SEMIMETAL TO SEMICONDUCTOR TRANSITION IN InAs/GaSb INTERBAND RESONANT TUNNELING DIODES

U M Khan-Cheema* P C Klipstein* D G Austing**, J M Smith*, N J Mason*, P J Walker* and G Hill

* Department of Physics, Clarendon Laboratory, University of Oxford, Parks Road, Oxford, OX1 3PU, UK
** Department of Electrical and Electronic Engineering, The University, Mappin Street, Sheffield, S1 3JD, UK
• Present Address: N T T Research Laboratories, 3-9-11 Midori-cho, Musashino-shi, Tokyo 180, Japan

We report some of the highest 77K peak to valley ratios (PVRs) for single heterojunction InAs/n)/GaSb(p) resonant conduction diodes. The devices were grown with low background doping ($n = p \approx 10^{16}$ cm^{-3}) on (100) oriented substrates by atmospheric pressure MOVPE, and were prepared by switching the precursors in a predetermined order, to have "InSb" or "GaAs" like interfaces. We observe a stronger resonance with a weaker temperature dependence when the interface is "GaAs" like. In all samples, the voltage of the resonance and the peak current both decrease with hydrostatic pressure, due to the pressure induced decrease of band overlap. Our results are consistent with a shift of -10meV/kbar, and overlaps of 120±20 meV and 250±50 meV respectively for "InSb" like and "GaAs" like interfaces, and are in agreement with high pressure parallel transport results in superlattices with "InSb" like interfaces.

InAs/GaSb structures, particularly when combined with AlSb, offer the possibility of interband tunneling devices exhibiting Negative Differential Resistance (NDR), with a very high Peak to Valley Ratio (PVR), and a large peak current density, two qualities which are desirable for high frequency applications [1-3]. The GaSb/InAs material system is distinguished from the more conventional GaAs/AlAs by a novel band alignment where the InAs conduction band edge lies approximately 145meV below the GaSb valence band edge [1], and by the existence of two types of interface, with either "GaAs" or "InSb" character [4]. In this paper we examine the role of the interface on interband tunneling in single heterojunction structures.

Five structures were grown by atmospheric pressure Metal Organic Vapour Phase Epitaxy (MOVPE), and each comprised a GaSb p+ substrate, 0.3μm u-GaSb, 100Å u-InAs, and 0.5μm n-InAs ($n \approx 4 \times 10^{18}$ cm^{-3}). For both materials, the background carrier concentration at room temperature was 1-2 x 10^{16} cm^{-3}. For samples A, B and C the interface was biased to "InSb", by switching the flow of precursors in the following order: Ga off, In on, Sb off, As on with a 1s pause between each event. Sample D was biased to "GaAs" (Sb off, As on, Ga off, In on), while sample E was unbiased (all four switching events occurring simultaneously) *. The structures were processed into 16μm diameter mesa structures prior to contacting.

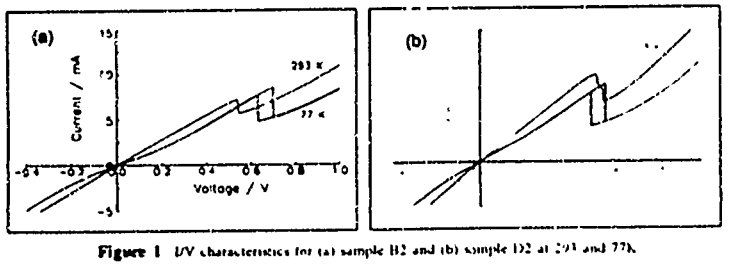

Figure 1 I/V characteristics for (a) sample B2 and (b) sample D2 at 293 and 77K.

In figure 1, the forward bias characteristics (InAs negative with respect to GaSb) are shown for (a) an "InSb" interface and (b) a "GaAs" interface. In this bias direction a resonance is observed, in which the peak occurs when the bottom of the subband from the first confined electron state in the approximately triangular potential well of the conduction band aligns close to the top of the first light hole subband in the equivalent valence band potential well [5]. For different mesas from the same wafer, the voltage of the peak can be variable (typically lying between 0.2 and 0.6 V in all cases) due to a significant contact resistance, but the peak and valley current densities are generally more reproducible, showing a scatter within about ± 5% (which we attribute to a parasitic parallel conductance, perhaps due to the state of the etched surface of the mesa). It is apparent from figure 1 that with increasing temperature the resonance shifts down in bias, consistent with previous reports [6], although the PVR shows a larger decrease, particularly for the InSb interface. This downshift can be explained by the shift of the Fermi level at zero bias towards midgap in both materials (a simple calculation gives a shift of 0.19V), which may be offset slightly by an increase in the band overlap due to thermal expansion (equivalent to a negative pressure of a few kbar). The stronger resonance and weaker suppression with temperature in the "GaAs" case is indicative of a larger band offset compared to the "InSb" case, which would tend to suppress the thermionic emission of both electrons and holes at high temperatures. Further evidence that this is the case is obtained by considering the effect of high pressure.

In figure 2, the forward bias characteristics of sample C are plotted at different pressures. For the mesa shown, the resonance occurs at a very low bias suggesting that for this mesa contact resistance effects are negligible. It is apparent from figure 2 that the resonance is almost totally suppressed by 11.6 kbar. The suppression is explained by a reduction of the band overlap with increasing pressure. Results for all the samples are summarised in figures 3(a) and (b) respectively, where the PVR and the resonance voltage, normalised to its 1 bar value, are plotted as a function of pressure. With the exception of the "unbiased" interface, a clear pattern seems to emerge, where the "GaAs" interface exhibits a higher PVR at 1bar and is not suppressed by pressure as quickly as the "InSb" interface. Unfortunately, it is not so straightforward to estimate from the data the exact pressure, P_c, at which the band overlap goes to zero. One might expect that because the alignment of confined electron and hole subbands is no longer possible above P_c, resonant behaviour should clearly vanish at this pressure. However, although the confinement energies go to zero at this pressure, so do the electron and hole concentrations in the subbands, so the strength of the resonance will also go to zero at P_c, making it hard to observe. Furthermore, above P_c the device may start to exhibit tunnel diode behaviour at low bias, when electrons near the bulk conduction band edge of InAs tunnel into hole states near the bulk valence band edge of GaSb. Since the concentration of both types of carrier is quite small, any resonance of this type should be fairly weak. Nevertheless, a weak resonance may persist beyond P_c, making a clear identification of P_c difficult. Such an effect may explain why the resonance voltages for the "InSb" samples in figures 2 and 3(b), do not appear to go to zero at high pressure, but instead saturate at about 10% of the initial 1 bar values. Therefore, in figure 3(b), it is probably more reliable to extrapolate data taken below about 8 kbar to the point at

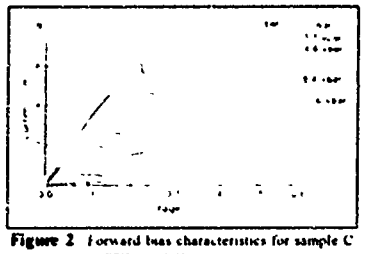

Figure 2 Forward bias characteristics for sample C at 77K for different pressures.

which it intercepts the x-axis, to obtain an estimate for P_r. This is the procedure which we follow below. Even though the contact resistances (assumed pressure independent) influence the resonance voltages in figure 3(b), as discussed above, it is clear from figure 2 that the intrinsic

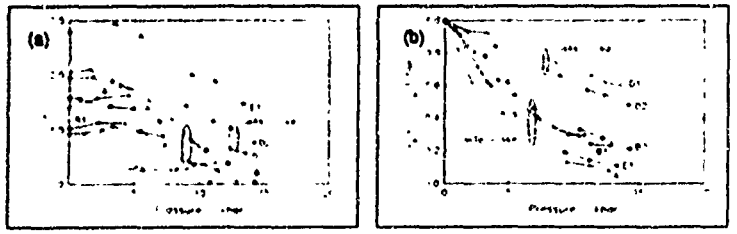

Figure 3 Sample PVRs and (b) their corresponding normalised resonance voltages vs pressure at 77K

device resistance is not a strong function of pressure, increasing by no more than a factor of 2 in about 10 kbar. Therefore even if in some cases the contact resistance at 1 bar is comparable to the intrinsic device resistance, the *normalised* bias voltage as plotted in figure 3(b) will still be within about 70% of the true intrinsic value at 10 kbar. Thus, contact effects may account for the small variation between different samples or mesas of the same interface type in figure 3(b), but they cannot account for the larger variation between samples with "InSb" or "GaAs" interfaces, which is therefore taken to be a genuine effect.

Extrapolation of the data in figure 3(b) as discussed above suggests that for the "GaAs" samples P_r = 25±5 kbar, while for the "InSb" samples, P_r = 12±2 kbar. A slightly lower value, but within the stated error limits, is predicted from figure 3(a) for the "GaAs" samples. Notwithstanding the difficulties in obtaining a precise value for P_r, it is clear that its value for "GaAs" is approximately 13±7 kbar larger than for "InSb". Symons et al [7] have performed Quantum Hall measurements on superlattice samples from the same MOVPE reactor as the present samples, where "InSb" interfaces were used to achieve the high carrier mobilities necessary for the measurements. They derived values for the band overlap and pressure shift of 145±5 meV, and -9.9±1.0 meV/kbar. These values are in good agreement with our value of P_r for the "InSb" samples. Assuming that the pressure shift, which is close in magnitude to the pressure shift of the bandgaps of InAs and GaSb (10 and 14 meV/kbar respectively [8]), is not strongly dependent on the interface type, our results predict an increase in band overlap of about 130±70 meV on going from an "InSb" interface to a "GaAs" one. This increase has been predicted in recent calculations by Foulon and Priester [9], and by Hemstreet et al [10], who report values of 31 and about 50 meV respectively. Our result is therefore not surprising, although the value of about 130±70 meV for the increase in the overlap is somewhat larger than expected.

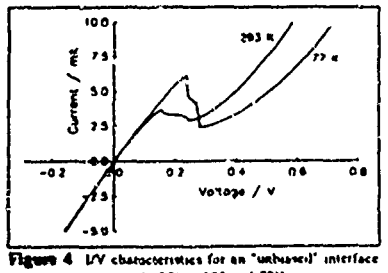

Figure 4 I/V characteristics for an "unbiased" interface (sample F2) at 293 and 77K

Finally, we note that the sample with the "unbiased" interface gave a PVR at 77K and 1 bar of 2.6, which to our knowledge is the largest PVR reported for a single heterojunction device of this type. The large PVR is due to a particularly low valley current compared to other samples. This may reflect the fact that the interface was grown without pauses. To decide the nature of the interface is a little problematic, since the data in figure 3(a) appears to extrapolate to an intercept on the x-axis close to that for the "GaAs" samples, whereas in figure 3(b) the behaviour is clearly "InSb" like. The low valley current may simply reveal a tunnel diode resonance once the resonance due to band overlap at the interface has been suppressed, so the PVR data in figure 3(a) may be misleading, whereas the bias data in figure 3(b) is more directly related to the offset. Therefore, we suspect that the "unbiased" interface has essentially "InSb" character. This attribution is confirmed by the strong temperature dependence of the NDR in the "unbiased" sample, plotted in figure 4, which is clearly characteristic of an "InSb" interface as discussed above.

In conclusion, we have presented electrical data on a number of similar single heterojunction InAs/GaSb interband tunneling devices, in which the only difference has been to vary the character of the interface between "InSb" or "GaAs". The "GaAs" interface appears to give a stronger resonance, with a weaker temperature dependence, than the "InSb" interface. The resonance is suppressed by pressure in all cases, with a threshold, P_r, which is approximately 13±7 kbar higher on going from an "InSb" to a "GaAs" interface. Our results are consistent with overlaps of 120±20 and 250±50 meV respectively for the two interfaces. Further measurements are in progress, looking at more "GaAs" interface samples up to higher pressures, which should yield a more precise value for the difference in band overlap for the two interface types. Finally, measurements on an "unbiased" interface indicate that the interface may have adopted an "InSb" like character.

References

1 D H Chow, J R Soderstrom, D A Collins, D Z-Y Ting, E T Yu and T C McGill, *SPIE Quantum Well and Superlattice Physics III*, 1283 2 (1990)
2 J R Soderstrom, D H Chow and T C McGill, *IEEE Electron Device Lett* 11, 27 (1990)
3 K F Longenbach, L F Luo and W I Wang, *Appl Phys Lett* 57, 1554 (1990)
4 C Lopes, R J Springett, R J Nicholas, P J Walker, N J Mason and W Hayes, *Surf Sci* 267, 176 (1992)
5 D H Collins, E T Yu, Y Rajakarunanayake, J R Soderstrom, D Z-Y Tung, D H Chow and T C McGill, *Appl Phys Lett* 57, 683 (1990), L F Luo, R Beresford, K F Longenbach and W I Wang, *J Appl Phys* 68, 2854 (1990)
6 E E Mendez, *Surf Sci* 267, 170 (1992)
7 D M Symons, M Lakrimi, R J Warburton, R J Nicholas, N J Mason, P J Walker and M J Lycett, *to be published* (1993)
8 Landolt-Bornstein New Data Series, vol 17a, *Physics of Group II elements and III-I compounds*, ed O Madelung, Springer, Berlin (1982)
9 Y Foulon and C Priester, *Phys Rev B* 45, 6259 (1992)
10 L A Hemstreet, C Y Fong and J S Nelson, *Bull Am Phys Soc* 38, 183 (1993)

* Oxford sample numbers: A 928, B 1189, C 1192, D 1191, F 1190

TuP32

InAs/Antimonide-Based Resonant Tunneling Structures with Ternary Alloy Layers

J.N. Schulman, D.H. Chow, and T.C. Hasenberg
Hughes Research Laboratories
3011 Malibu Canyon Road
Malibu, California 90265 USA

Abstract

We have studied two modifications of mixed arsenide/antimonide resonant tunneling structures, in which one of the binary components is replaced by a ternary alloy. The first structure is based on an InAs/AlSb/GaSb resonant interband tunneling structure with the GaSb quantum well layer replaced by a $GaAs_xSb_{1-x}$ alloy layer. The added As decreases the lattice constant in the well, and the resulting strain can shift the heavy hole subbands below the incoming electron energy. We find that the negative resistance effect can be enhanced by properly adjusting the splitting via the As concentration. A maximum enhancement in the peak-to-valley ratio was obtained with a 10% As concentration in the diodes we fabricated.

The second structure is a modification of a conventional InAs/AlSb double barrier structure, in which the AlSb barriers are replaced by $Al_xGa_{1-x}Sb$ with x=0.5. In these structures, the pronounced type II band alignment results in an entirely new type of current versus voltage characteristic exhibiting intrinsic current bistability (double-valued currents for a given voltage) instead of the conventional voltage bistability. Peak-to-valley voltage ratios as high as 1.5 have been observed with current densities in the 10^5 A/cm^2 range.

Introduction

Resonant tunneling structures based on the InAs/AlSb/GaSb material system have produced diodes with unique characteristics and enhanced performance. Two systems have been studied in detail in recent years. First is the interband tunneling structure, which utilizes the broken-gap band line-up of InAs and GaSb, usually in combination with AlSb barrier layers[1-3]. In these structures band gap blocking for bias voltages above the tunneling resonance results in extremely high peak-to-valley current ratios. The second structure of current interest is the relatively conventional InAs/AlSb double barrier structure. This structure has demonstrated the highest oscillation (700 GHz) and switching speeds (1.7 ps) to date for resonant tunneling devices [4,5]. The individual layers in both of these devices are usually made from binary compounds, i.e., InAs, GaSb, and AlSb. Here we investigate the effects of replacing one or more of these layers with ternary alloys, $GaAs_xSb_{1-x}$ for GaSb in the case of interband structures, and $Al_xGa_{1-x}Sb$ for AlSb in the case of conventional double barrier structures. We demonstrate dramatic variations in both cases, including an improved peak-to-valley ratio in the first case, and a novel bistable current feature in the second.

InAs/AlSb/$GaAs_xSb_{1-x}$ Interband Tunneling Structure

Figure 1(a) is a band edge diagram of a typical InAs/AlSb/GaSb structure. In these devices, electrons are emitted from the InAs conduction band, tunnel through the AlSb barrier into the GaSb valence band resonances, and then out the other side. Other variations which have been studied include reversing the roles of the InAs and GaSb as the cladding and well layers, and making various asymmetric structures [6-8].

Here we are only concerned with cases in which the quantum well portion is in the valence band, as in Fig. 1(a). Shown schematically is the band edge diagram of the structure and two of the valence band resonances, the first heavy hole (HH1) and first light hole (LH1) levels. The HH1 level lies above the LH1 level, as is always the case for unstrained materials. The close proximity of HH1 above LH1 produces a degradation in the negative differential resistance effect, however, which can be understood as follows. The LH1 state is the dominant channel for tunneling due to the large coupling between the InAs conduction states and the GaSb light hole state [9]. The coupling to the heavy hole state is small due to the differing orbital composition of the heavy hole states near the Brillouin zone center. As bias is applied to the diode, the incoming electrons will encounter the HH1 resonance at higher biases than the LH1 resonance. Thus, depending on the precise widths of the layers and other structural parameters, tunneling through the HH1 level contributes to the valley current and tends to degrade the peak-to-valley current ratio of the device. In addition, if the well layer is thick enough, there may be one or two additional heavy hole levels above the LH1 level contributing to the valley current.

The valley current can be divided into two contributions, that due to scattered and due to unscattered electrons. Theoretical calculations usually include only the unscattered portion [9,10]. This calculated heavy hole current contribution to the valley current is small and is probably undetectable, especially at higher temperatures. The main contribution, however, is probably the more difficult to account for contribution due to scattering. This is certainly the case for conventional structures such as n-type GaAs/GaAlAs double barrier diodes. In this case, experimental values for the valley currents are usually much larger than the theoretical predictions. The major missing theoretical ingredient is generally agreed to be the scattering through the indirect conduction band valleys, via phonons, impurities, defects, or other mechanisms. It would be reasonable to expect that similar mechanisms involving scattering through the heavy hole band are significant in the InAs/AlSb/GaSb system.

We have attempted to eliminate the heavy hole channel by adding As to the central GaSb well layers. Since GaAs has a smaller lattice constant than GaSb, the introduced As creates a lattice mismatch which splits the heavy hole band to lower energy than the light hole band. Figure 1(b) shows a schematic diagram of such a structure. If the mismatch is sufficient, this splitting can dominate over the quantum confinement induced splitting and actually push the heavy hole band below both the light hole level and the InAs conduction band minimum energy. It is then entirely inaccessible for tunneling at any applied bias.

We have grown by MBE and fabricated InAs/AlSb/GaAsSb structures with As concentrations of 0, 10, 15, and 30%. The arsenic concentration in the $GaAs_xSb_{1-x}$ layer was controlled by utilizing a valved arsenic cracking effusion cell. The well and barrier thicknesses were 51Å and 12Å, respectively, with the InAs electrodes doped to $2x10^{18}$ cm^{-3}, separated from the AlSb barriers on either side by lightly doped 600Å InAs spacer layers. Figure 2 shows the room temperature current-voltage curve for one such device, with x=0.1 in the $GaAs_xSb_{1-x}$.

Table I summarizes the average peak-to-valley ratios and the peak currents in the four structures. Due to variations in device area produced by the processing procedure, the differences among the values of the peak currents for the 0%, 10%, and 15% As samples are not large enough to be significant, and should be considered as roughly similar. The peak-to-valley ratios do not depend on area, and it can be seen that the 10% As sample has the maximum peak-to-valley ratio among the set. We believe that this enhanced peak-to-valley ratio is due to the lowering of the heavy hole resonance energy below the light hole resonance energy for this alloy concentration.

Calculations of the energy levels in these structures were done using a twenty-band tight-binding model, to include the heavy hole-light hole coupling [10]. The standard offset of 150 meV was used for the offset between the InAs conduction band and the GaSb valence band. A valence band discontinuity of 43% of the band gap difference was used between AlSb and GaSb to set the AlSb band edges [3]. These values are relatively well determined in the literature. A much more uncertain parameter is the dependence of the band offsets on the As concentration in the GaAsSb layers. In lieu of any better technique to determine this value, a constant 43% discontinuity rule for the unstrained GaAsSb valence band offset was used. This is somewhat arbitrary, since the accuracy of this procedure is unknown, and therefore the theoretical results should be taken as qualitative only.

The calculation for the 0% As case gives a HH1 energy about 60 meV above the LH1 energy. Adding 10% As brings the LH1 energy to within 15 meV of HH1, but still above it. An additional 10% As, to 20% total, shifts HH1 to 35 meV below LH1, which is about 10 meV above the InAs conduction band edge. The experimental result of an enhanced peak-to-valley ratio for 10% As implies that that the HH1 energy should have already passed to below the LH1 level for this concentration, but given the aforementioned uncertainties, this level of agreement is all that can be expected. We believe that the abrupt decrease in the measured peak-to-valley ratio for 15% and 30% As is due to the composition induced shift of the light hole resonance itself towards the InAs conduction band edge. As LH1 decreases in energy, the overlap of its density of states with the

incoming InAs density of states eventually decreases, resulting in smaller currents and degraded peak-to-valley ratios. Thus, we have shown that adding As to the central GaSb layers has a significant effect on the current-voltage characteristic. Similar effects should be found in related structures, e.g., InAs/AlSb/GaSb/AlSb/GaSb and other structures.

InAs/$Al_xGa_{1-x}Sb$ Current Controlled Negative Differential Resistance Structure

The starting point for the second system to be discussed, InAs/AlSb double barrier heterostructures, utilize relatively conventional conduction band resonant tunneling. Their main advantages arise from the use of high mobility InAs in the cladding layers, which provides low contact resistance. The AlSb barriers have large conduction band offsets with InAs and are nearly lattice matched. These structures have been used to make oscillators with frequencies up to 712 GHz [4] and switches with 10%-90% rise times as short as 1.7 ps [5].

As in the previously described InAs/AlSb/GaSb structures, the devices reported here are also based on a type II resonant tunneling structure. However, in this case the staggered lineup involves the barrier layers, instead of the wells. The operating principle of the device is that, under certain conditions, two different steady state charge distributions are obtainable for a single bias voltage. These conditions arise due to the presence of hole states in the quantum barrier layers, providing regions for positive charge to be trapped. As device current is strongly affected (via band bending) by changes in the steady state charge distribution, a pronounced bistability in device current is observed.

In all of the structures studied here, the active device region consists of an InAs(n)/$Al_xGa_{1-x}Sb$/InAs/$Al_xGa_{1-x}Sb$/InAs(n) stack in which the middle three layers form a double barrier structure for electrons tunneling from one InAs(n) electrode to the other. Figure 3(a) shows a schematic band edge diagram of this structure at zero bias. The cladding layers consist of ~1μm n^+ InAs. Lightly doped (500Å, $n=1x10^{17}cm^{-3}$) and undoped (100Å) InAs spacer layers are used to bracket the active double barrier region. The InAs quantum well layer is 75Å thick in all samples, while barrier layer compositions and thicknesses are intentionally varied from sample to sample. Each structure is completed by a 2000Å InAs(n^+) cap layer.

The I-V curves are taken on an HP4145A Semiconductor Parameter Analyzer configured either to input a current sweep while measuring voltage, or to input a voltage sweep while measuring current. Due to the nominally symmetric layer sequence used for the structures investigated here, we observe nearly symmetric I-V curves in all of the devices studied.

Figure 4(a) is an I-V curve displayed by a structure with symmetric, 18 Å thick (AlSb)1ML/(GaSb)1ML ordered alloy barriers, taken by sweeping the voltage from 0 mV up to 750 mV and then back down to 0 mV, while measuring the current through the device. A pronounced hysteresis is displayed in the figure, with the lower current line corresponding to the sweep from low to high bias. The observation of hysteresis in the DC I-V curve is indicative of a bistability in device current for a given applied bias. In contrast, no hysteresis is observed in the I-V curve obtained from a structure with symmetric, 18 A thick AlSb barriers (a "conventional" InAs/AlSb resonant tunneling diode), taken using the same measurement configuration.

Figure 4(b) is the current-voltage curve obtained from the device used for Fig.4(a) taken by sweeping the *current* while the *voltage* is measured. The curve displays a current-controlled ("S"-shaped) negative differential resistance region, in contrast to the voltage-controlled ("N"-shaped) curves displayed by conventional resonant tunneling diodes. We note that in this measurement configuration there is no voltage bistability (the voltage as a function of current is a single valued function), and that conventional resonant tunneling diodes will normally display hysteresis when tested under this measurement configuration. We have also observed the I-V behavior displayed in Figs. 4(a) and (b) in samples with symmetric: (*i*) 21 Å thick $Al_{0.4}Ga_{0.6}Sb$ barriers, (ii) 15 Å thick $Al_{0.6}Ga_{0.4}Sb$ barriers, and (*iii*) 18 Å thick $Al_{0.5}Ga_{0.5}Sb$ barriers.

At 400 mV applied bias, the current ratio between the high and low states of the I-V curve displayed in Fig.4 is greater than 2. This figure of merit might be expected to have implications for state separation in digital circuit applications. A potentially more significant figure of merit is the current density obtained from the device, which is greater than $2x10^5 A/cm^2$ in the current-controlled negative differential resistance region of the curve. Large current densities in these devices generally indicate potential for high speed operation due to short RC time constants [11]. The current densities observed here are only a factor of 1.5 smaller than the peak current density of an InAs/AlSb resonant tunneling diode that has demonstrated 1.7 ps switching times [5]. Therefore, we anticipate that the class of devices reported here will be suitable for future high speed circuits.

The special characteristics of this double barrier structure that produce the unique double-valued current behavior can be understood by considering the band edge diagrams shown in Figure 3. Figure 3(a) shows the bands with no applied bias. The conduction band edges are similar to those of a conventional double barrier structure. However, the $Al_xGa_{1-x}Sb$ layers are barriers for electrons only; they form wells for the holes, with the InAs layers acting as barriers. These hole wells can trap positive charge, depending on the applied bias and the Fermi level in the positively biased side, and significantly alter the potential distribution in the structure.

For small bias the current can still be described by conventional conduction band double barrier resonant tunneling. A key point here is that the voltage drop in the space charge region adjacent to the barriers on the positively biased side can be substantial, depending on the doping concentration, and is a large contribution to the total measured voltage. For sufficiently large applied bias the Fermi level on the right approaches the allowed hole energy levels in the right $Al_xGa_{1-x}Sb$ well. At some point, depending on bias and tunneling rates, the hole population in the $Al_xGa_{1-x}Sb$ layers will increase to the extent that the holes substantially screen out the electric field in the space charge region. This occurs near 0.6 volts in Fig. 4. The potential drop will then become greater across the double barriers themselves and smaller in the space charge region. Since the tunneling current follows the voltage across the barriers, this causes the sudden jump in current at that voltage. Figure 3(b) and (c) show band diagrams for the two possible potential distributions for a given total bias. The current is relatively small in (b) due to the smaller voltage drop across the double barriers, while the current is larger in (c) due to the larger voltage drop there. Measurements at low temperature reveal that the conventional negative differential resistance effect due to tunneling through the conduction band resonance also occurs, but at higher bias.

In summary, we have designed and demonstrated a novel resonant tunneling device based on type-II, InAs/$Al_xGa_{1-x}Sb$ heterostructures. Due to hole accumulation in the active device layers, these structures are capable of possessing multi-state charge distributions at a given applied bias, resulting in bistable device currents. The demonstrated devices display hysteretic I-V behavior under voltage-controlled measurement conditions, and "S"-shaped negative differential resistance under current-controlled conditions. Device operating currents are in excess of $1.5x10^5 A/cm^2$, suggesting the potential for good high speed performance due to low RC time constants.

The authors wish to acknowledge helpful technical discussions with A.T. Hunter, E.T. Croke, and R.H. Miles and the technical assistance of L.D. Warren.

References

1. M. Sweeny and J. Xu, Appl. Phys. Lett. 54, 546 (1989).
2. J.R. Söderström, D.H. Chow, and T.C. McGill, Appl. Phys. Lett. 55, 1094 (1989).
3. L.F. Luo, R. Beresford, and W.I. Wang, Appl. Phys. Lett. 55, 2023 (1989).
4. E.R. Brown, J.R. Söderström, C.D. Parker, L.J. Mahoney, K.M. Molvar, and T.C. McGill, Appl. Phys. Lett. 58, 2291 (1991).
5. E. Özbay, D.M. Bloom, D.H. Chow, and J.N. Schulman, to appear in Elec. Dev. Lett.
6. R. Beresford, L.F. Luo, K.F. Longenbach, and W.I. Wang, Appl. Phys. Lett. 56, 952 (1990).
7. D.Z.-Y. Ting, D.A. Collins, E.T. Yu, D.H. Chow, and T.C. McGill, Appl. Phys. Lett. 57, 1257 (1990).
8. M.P. Houng, Y.H. Wang, C.L. Shen, J.F. Chen, and A.Y. Cho, Appl. Phys. Lett. 60, 713 (1992).
9. D.Z.-Y. Ting, E.T. Yu, and T.C. McGill, J. Vac. Sci. Technol. B9, 2405 (1991).
10. M.S. Kiledjian, J.N. Schulman, K.L. Wang, and K.V. Rousseau, Phys. Rev. B46, 16012 (1992).
11. S.K. Diamond, E. Özbay, M.J.W. Rodwell, D.M. Bloom, Y.C. Pao, and J.S. Harris, Appl. Phys. Lett. 54, 153 (1989).

Table 1. Room temperature peak-to-valley ratios (P/V) and approximate current densities for InAs/AlSb/GaAsSb double barrier structures with 0, 10, 15, and 30% As concentrations.

x	P/V	Peak Current Density (Amps/cm^2)
0	8	2.5×10^{4}
0.1	11	1.5×10^{4}
0.15	3	1.3×10^{4}
0.30	3	0.5×10^{4}

Figures

Figure 1. Band edge diagram of (a) InAs/AlSb/GaSb and (b) InAs/AlSb/GaAsSb double barrier resonant tunneling structures.

Figure 2. Room temperature current versus voltage curve for InAs/AlSb/GaAsSb double barrier structure with 10% As in the GaAsSb.

Figure 3. Schematic band edge diagram of the InAs/Al$_x$Ga$_{1-x}$Sb structure with three potential distributions. (a) has no applied bias, and (b) and (c) have the same applied bias. Holes may accumulate in the Al$_x$Ga$_{1-x}$Sb barriers for sufficient bias.

Figure 4. (a) I-V curve, taken by sweeping the voltage in both directions while measuring current, for an InAs/Al$_{0.5}$Ga$_{0.5}$Sb double barrier structure with 18Å thick barrier layers. (b) I-V curve taken by sweeping the current in both directions while measuring voltage. Room temperature

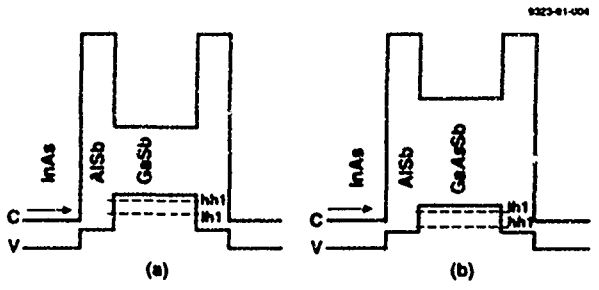

Figure 1

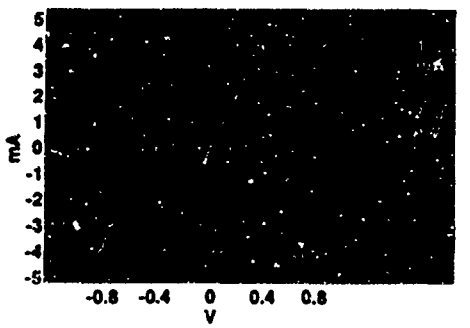

Figure 2

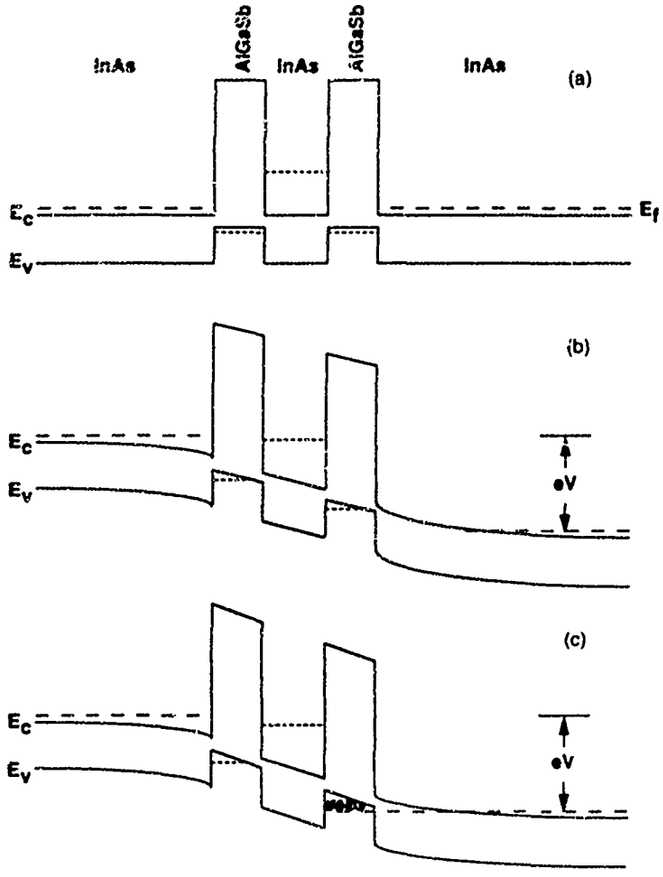

Figure 3

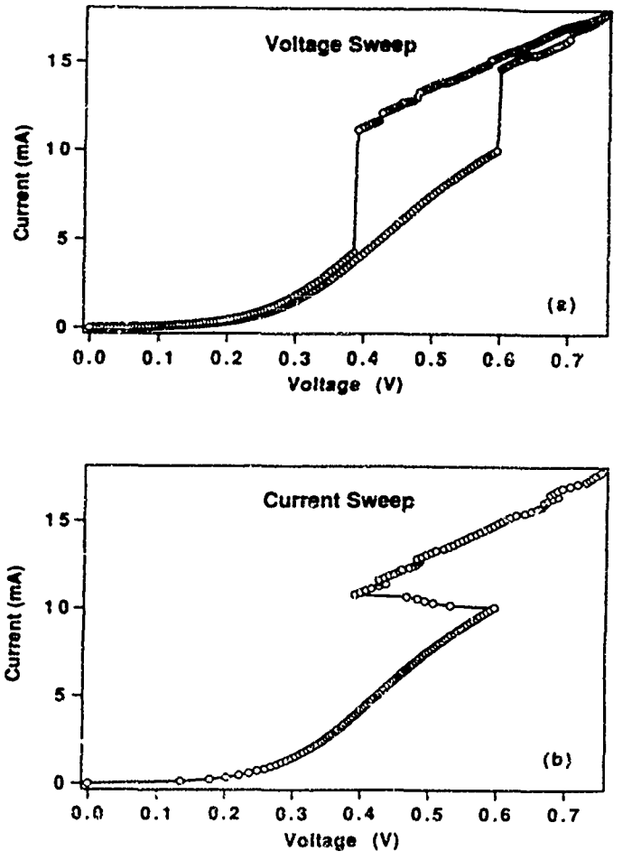

Figure 4

TuP33

Thermally desactivated resonant current in high peak to valley current ratio (69:1) GaAs/GaAlAs resonant tunneling structures : a spectroscopic view of the emitter density of state.

F. Laruelle and G. Faini

Laboratoire de Microstructures et de Microélectronique, C.N.R.S.
B.P. 107, 92225 Bagneux Cedex, France

Abstract

We describe the realization of very high peak to valley current ratio double barrier resonant tunneling structures by molecular beam epitaxy. We find that the resonant current through the ground state resonance decreases as the temperature is raised. This unique behavior is explained within the Esaki-Tsu formalism and originates in the Fermi-Dirac statistics.

I- Introduction

Since the first observation of resonant tunneling by Chang, Esaki and Tsu [1] the peak to valley current ratio (PVR), known as the figure of merit of double barrier resonant tunneling structures (DBRTS), keeps increasing with time due to technological efforts. However the best PVR's are well below values predicted by coherent tunneling theories that ignores relevant scattering mechanisms in these systems [2-3]. As first shown by Muto et al. [4], undoped spacer layers, inserted between heavily doped electrodes and tunneling barriers, prevent the incorporation of segregated impurities into the active part of the structure during epitaxial growth. It is now well established that ionized impurities are very efficient scatterers in these systems which strongly degrade the PVR [5]. It has been recently suggested that, provided impurity segregation is minimized, extremely high PVR can be obtained [6]. We will confirm this idea and further show that these high quality structures help to gain insights into the thermal and bias dependence of resonant tunneling.

II- Experiments

The DBRTS has been grown by molecular beam epitaxy (MBE). The sample is grown on a n$^+$ type, Si doped substrate and consists of : 5000 Å GaAs:Si 1×10^{18} cm^{-3}, 5000 Å GaAs:Si 2×10^{17} cm^{-3}, 3000 Å GaAs undoped, 170 Å $Ga_{0.79}Al_{0.21}As$, 96 Å of GaAs, 170 Å $Ga_{0.79}Al_{0.21}As$, 120 Å GaAs undoped, 5000 Å GaAs:Si 2×10^{17} cm^{-3}, 5000 Å GaAs:Si 1×10^{18} cm^{-3}. Growth rates are precisely measured in situ with the help of reflection high energy electron diffraction : 2.09 Å.s^{-1} for Ga and 0.545 Å.s^{-1} for Al. The growth temperature is 640 °C and the As$_4$ flux is minimized to ensure the As rich growth front in the 3x4 surface reconstruction. 100x100 µm square mesas are defined by photolithography and $SiCl_4$ reactive ion etching. Ohmic contacts are made of alloyed AuGeNi multilayers. The back contact is made on the backside of the n$^+$ wafer. J-V curves are measured in a variable temperature cryostat from T= 1.8 K up to 150 K. Forward bias refers to electrons propagating from the substrate toward the surface : the large spacer layer lies then on the emitter side of the DBRTS. The current density is simply obtained by dividing the measured current by the DBRTS nominal etched area, measured during scanning electron microscope inspection.

III- Results and discussion

We will first concentrate on the low temperature J-V characteristics. As can be seen in figure 1, the first resonance under forward bias consists of a very narrow peak at 78 mV followed first by a pronounced valley at 136 mV and then by a shoulder at 175 mV. To convert external voltages into energies relative to the emitter Fermi energy, we solve Poisson's equation in the Thomas-Fermi approximation. We use nominal thicknesses and alloy composition. Doping densities are extracted from the best fit with the experimental J-V curve : they are found slightly lower than what was expected from doping calibrations. The multiplying coefficient to get energy from voltage is 0.315 for forward bias and 0.063 for reverse bias. It is worth pointing out that these coefficients are smaller (down to 20%) than if we assume a constant electric field across the DBRTS. This potential profile is then used to solve Schrodinger's equation in the effective mass approximation to get the energy dependent transmission coefficient T(E,V) for each external voltage.

We determine the threshold voltage and the total width of the resonance by extrapolating the linear part of the peak on both side. We find 69 mV and 32 mV respectively. The width of the resonance is related to the Fermi energy of the emitter i.e. 10.1 meV which corresponds to a three dimensional Fermi sea of 7.8×10^{16} cm^{-3} , a value close to the density of the doping level in the contact layer. The threshold voltage is related to the energy difference between the emitter Fermi level and the quantum well (QW) ground state : 18.9 meV. This gives a ground state energy of 29.0 meV, in good agreement with envelope function calculation done with the nominal thickness and Al composition : 31.8 meV. The peak current is measured for a voltage of 78 mV and the peak current density is 450 µA cm^{-2}. The peak current arises when the QW ground state lies 4.4 meV above the bottom of the emitter conduction band.

The valley current density around 136 mV is only 6.5 µA cm^{-2} setting the PVR to 69:1 which is a typical value measured for several diodes across this wafer. The shoulder around 175 mV is offset by +15 mV or 36.3 meV with respect to the first resonance threshold. We attribute it to a first resonance replica with emission of a GaAs LO phonon. The valley current is dominated by the emergence of inelastic optical phonon scattering : it is of intrinsic origin.

The reverse bias J-V curve looks very similar except that the bias scale is expanded roughly 5 times since the thick undoped spacer layer lies now on the collector side. We find a Fermi energy of 13.7 meV (Fermi sea density of 1.2×10^{17} cm^{-3}) and a ground state energy of 33.8 meV in agreement with the forward bias determination. We notice that the PVR is much smaller (26:1) compared to the other polarity whereas the peak current density is quite similar (600 µA.cm^{-2}). We find that the shoulder after the valley current appears at 807 mV and is offset only by 30.7 meV. This is smaller than the GaAs LO phonon energy. This suggests that for the reverse polarity, the valley current is not dominated by phonon diffusion. The phonon contribution (36.3 meV) can be faintly seen around -900 mV (note that the slope of the J-V curve is changing at this value).

In another DBRTS, identical to this one except a thinner QW (70 Å instead of 96 Å), we measure a current density of 10 mA cm^{-2} and a PVR of 61:1 under forward bias at T= 1.8 K, showing that this structure is well suited for high PVR structures provided the required current density is not too large.

Cunningham et al. reported similar measurements on DBRTS grown by gas source MBE and claim higher PVR's up to 130:1 at 1.1K [6]. However there are some discrepancies with our results : for positive bias their resonance appears at 400 mV with a current density around 350 µA cm^{-2}. We use the same polarity convention as Goldmann et al. [7]. With such peak voltage and current density, we are tempted to say that the polarity is not correct. Otherwise, they observe the second resonance that we also observe at 400 mV for positive bias, with a current density of 150 mA.cm^{-2} in our sample. In that case, their current density is much too low. The resonance in ref. [6] exhibits a hysteresis loop that we do not observe around our first resonance which has a very smooth shape. Other electrical data obtained on comparable structures published by the same group [7] with resonance line shape similar to ours present PVR of 54:1 for forward bias with current densities around 1 A.cm^{-2} : the PVR in such samples is also limited by polar optical phonon scattering.

Figure 2 shows the J-V characteristics for several temperatures up to 100 K. The thermal activation of the valley current is well known. The first resonance disappears above 150 K : it is entirely dominated by the current flowing through the second resonance. We also note the thermal activation of the current on the low voltage side of the first resonance due to the electronic state population above the Fermi level. More surprising is the pronounced drop of both peak current and peak voltage which is present for both polarities although this effect is stronger for direct bias.

To elucidate the origin of this phenomenon, we have calculated the J-V characteristics using the Tsu-Esaki formula [8] :

$$J(V) = \frac{em^* k_B T}{2\pi^2\hbar^3}\int_0^\infty T(E,V)\,\ln\left(\frac{1+\exp(\frac{E_f-E}{k_B T})}{1+\exp(\frac{E_f-E-eV}{k_B T})}\right) dE \quad . \qquad (1)$$

where T(E,V) is the transmission probability coefficient for an incident electron of energy E upon the double barrier biased with potential V. Equation (1) can be simplified since T(E,V) is sharply peaked around E_r with a maximum value T_{max} and a width γ, these three values depending on V implicitly :

$$J(V) = \frac{em^* k_B T}{2\pi^2\hbar^3}\ln\left(\frac{1+\exp(\frac{E_f-E_r}{k_B T})}{1+\exp(\frac{E_f-E_r-eV}{k_B T})}\right) T_{max}\,\gamma \quad . \qquad (2)$$

In our calculation, the Fermi energy (and the related doping level) is determined as the best parameter to fit the J-V curve at low temperature following the above described procedure to measure the width of the resonance.

From equation (2) we deduce that all J/T curves cross for the polarization such that E_r equals E_f provided that eV is large compared to $k_B T$ and that E_f does not depend on temperature. In principle this allows to determine with a good precision the threshold voltage for which the Fermi level is in resonance with the QW ground state. Inspection of figure 3 on which J/T curves are displayed shows that this is not the case neither for reverse nor for direct bias. Computing equation (2) with a constant Fermi energy leads to an increasing current density with temperature : the hypothesis that the Fermi energy does not depends on temperature implies that the emitter electron density increases with temperature because the three dimensional density of states is a growing function of energy. To compute equation (2) correctly, we have to calculate the Fermi energy for each temperature in order to keep the electron density constant. We then get a good agreement with our experimental results. The Fermi energy variation is very large in our experiments : the inset of figure 4 shows the calculated relative Fermi energy variation between 0 K and 100 K for two electronic densities : 8×10^{16} and 1×10^{18} cm^{-3}. It is clear that, when the Fermi energy gets larger and larger, the 3D density of states varies more and more slowly.

To understand the decrease of both peak current and peak voltage we have to keep in mind the consequences of the elastic tunneling selection rules, namely electron energy and in-plane momentum (k_x,k_y components) conservation. For each bias, tunneling electrons are located on a disk intersecting the emitter Fermi sphere at energy E_f [9]. The emitter electron

density participating to the elastic tunneling current resonance is given by :

$$n(E_z) = \int_0^{\infty} \frac{1}{1 + \exp\left(\frac{E - E_F + E_z}{k_B T}\right)} \, dE \, . \qquad (3)$$

From equation (3) it is clear that smaller E_z implies larger $n(E_z)$ whereas decreasing E_z has the opposite consequence. For higher voltages, there are more tunneling electrons (the disk area is larger) but each state carries less current : the momentum component along the z direction gets smaller and smaller. In other words : as voltage increases, tunneling electrons have a larger and larger incident angle respective to the plane of the barriers.

When the temperature is raised, the Fermi energy decreases. If the resonant level lies well below (above) the Fermi energy, the current decreases (increases). This implies that i) the peak voltage shifts toward lower bias and ii) the peak current drops.

Figure 4 presents calculated J-V curves for different temperatures. They reproduce qualitatively the thermal behavior of the measured DBRTS. It is not clear why the measured current variation with temperature is larger than the calculated one. One possibility is the build-up of a two-dimensional accumulation layer which would change the density of state used in the calculation. The larger emitter Fermi energy for reverse bias explains the smaller temperature sensitivity for this polarity. Another striking difference is the pronounced current rise at high temperature and low bias in the theoretical calculation. This discrepancy with experimental results is puzzling. We finally note that the onset of the J-V curves gets sharper and sharper when the temperature is lowered in contrast with the experimental behavior where the onset sharpness saturates at 15 K. Spectroscopy around this onset should allow to determine the width of the resonance which is probably inhomogeneously broadened by interface roughness scattering.

Chen et al. report a similar temperature study concerning the second resonance of a similar DBRTS and find the same overall behavior [10]. They attribute temperature changes to the modification of the accumulation layer electron density in the emitter rather than to a statistics effect. If the accumulation layer is strongly affected by the temperature, this can be checked easily with magneto-tunneling experiments [11].

IV- Summary

In conclusion we have demonstrated that in high quality DBRTS the PVR is dominated by optical phonon scattering at low temperature and can reach 69:1. The J-V characteristics dependence on temperature is simply explained by first considering the electron statistics with a constant electron density and a variable Fermi energy and then by taking into account elastic tunneling selection rules. The resonance occurs from a subtle compromise : as bias increases, the tunneling electron density increases but each state brings a smaller contribution to the total current. We evidence that the resonance occurs when the QW ground state lies several meV above the bottom of the emitter conduction band, in contrast with the usual idea that the current drops sharply when the ground state lies below the emitter conduction band edge. When the resonant level is aligned with the emitter conduction band edge, electron are allowed to tunnel only parallel to the plane of the DBRTS and no current is flowing from one side of the DBRTS to another.

Acknowledgements

We wish to thank V. Thierry-Mieg for providing help during the growth of the samples, F. R. Ladan and C. Mayeux for their valuable support during the process of the DBRTS. We gratefully acknowledge fruitful discussions with B. Etienne, A. Sibille and J. F. Palmier.

References

1. L.L. Chang, L. Esaki, and R. Tsu, Appl. Phys. Lett., 24, 393 (1974).
2. F. Chevoir, and B. Vinter, Phys. Rev. B, 47, 7260 (1993).
3. P. Roblin, and W.R. Liou, Phys. Rev. B, 47, 2146 (1993).
4. S. Muto, T. Inata, H. Ohnishi, N. Yokoyama, and S. Hiyamizu, Jpn. J. Appl. Phys., 25, 577 (1986).
5. F. Laruelle, A. Ramdane, and G. Faini, Surf. Sci., 267, 396 (1992).
6. J.E. Cunningham, V.J. Goldman, B. Su, and W.Y. Jan, J. Cryst. Growth, 127, 695, (1993).
7. V.J. Goldman, B. Su, and J.E. Cunningham, Phys. Rev. B, 46, 7644 (1993).
8. R. Tsu, and L. Esaki, Appl. Phys. Lett., 22, 562, (1973).
9. S. Luryi, Appl. Phys. Lett., 45, 490 (1985).
10. J. Chen, J.G. Chen, C.H. Yang, and R.A. Wilson, J. Appl. Phys, 70, 3131 (1991).
11. Y. Galvao Gobato, F. Chevoir, J.M. Berroir, P. Bois, Y. Guldner, J. Nagle, J.P. Vieren, and B. Vinter, Phys. Rev. B, 43, 4843 (1991).

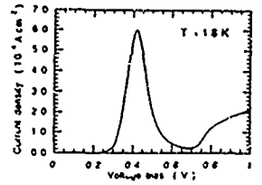

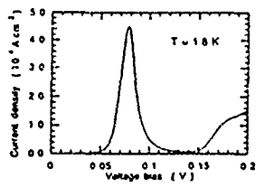

Figure 1 : Low temperature J-V characteristics of DBRTS described in the text at T=18 K. Bottom : forward bias, top : reverse bias. The plot is made with absolute values.

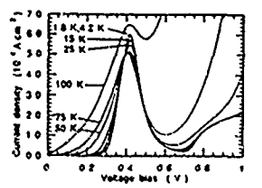

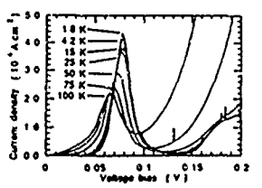

Figure 2 : J-V curves of the same device as in fig. 1 for different temperatures. Bottom : forward bias; top : reverse bias. The plot is made with absolute values.

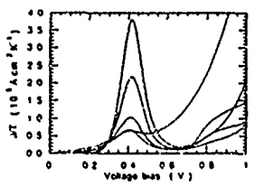

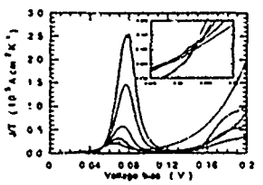

Figure 3 : dJ/dV characteristics of the same device as in fig. 2. Bottom : forward bias, top : reverse bias. The plot is made with absolute values. Temperatures are 15 K, 25 K, 50 K, 75K, and 100 K from the top of the peak to the bottom. Inset shows the detailed dJ/dV curves around 54 mV where dJ/dV curves nearly cross each other. In the top right hand side corner of the inset, temperatures from left to right are 15 K, 25K, 50K, 75K, and 100 K.

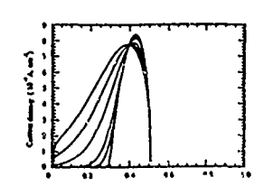

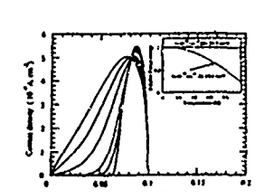

Figure 4 : Theoretical J-V curve for the DBRTS described in the text. Bottom : forward bias; top : reverse bias. The plot is made with absolute values. Temperatures are 4 K (the sharpest), 15 K, 25 K, 50K, 75 K, 100K (the smoothest). Inset shows the calculated relative Fermi energy variations between 0 K and 100 K.

TuP34

Theoretical Analysis of Resonant Magnetotunneling Spectroscopy of Holes

G. Goldoni[1] and A. Fasolino[2]

[1]*Scuola Internazionale Superiore di Studi Avanzati, via Beirut 2-4, 34014 Trieste, Italy*

[2]*Università degli Studi di Modena, Dipartimento di Fisica, via Campi 213/A, 41100 Modena, Italy*

We calculate the hole energy band structure in GaAs-AlAs Quantum Wells (QW's) in high in plane magnetic fields and simulate Resonant Magnetotunneling Spectroscopy (RMS) experiments, recently proposed as a probe of the hole energy dispersion. We find that the high magnetic fields used in RMS result in small modifications of the QW hole subbands in thin QW's. However for wide QW's or very large magnetic fields, the field strength affects the hole dispersion by changing the heavy hole light hole mixing. We give a simple expression to evaluate to which extent the mixing is modified as a function of the QW width and field strength.

Resonant Magnetotunneling Spectroscopy (RMS) of *p*-doped GaAs-AlAs double barrier structures [1] has recently been proposed as a probe of the complicated hole subband dispersion in Quantum Wells (QW's) [2]. RMS has also been reported in Single QW's [3]. In RMS holes are injected from an accumulation layer into an adjacent QW through a barrier. The quantized levels of the QW are brought in resonance with the emitter Fermi level by an electric field perpendicular to the interfaces. The carriers when tunnel into the QW moving under the influence of a magnetic field B parallel to the interfaces acquire an in plane wavevector $k_\parallel$. The acquired $k_\parallel$ has to match that of the quasi-bound QW hole levels for resonant tunneling to take place therefore the magnetic field is in one to one correspondence with $k_\parallel$.

In GaAs-AlAs double barrier structures the shifts of the resonance peaks with magnetic field maps very well onto the theoretical QW hole dispersion vs $k_\parallel$ calculated at zero field [4]. The agreement is rather surprising in view of the high in-plane magnetic fields used in the experiments, since high fields are expected to shift the energy, modify the heavy hole (HH)-light hole (LH) mixing and yield a spin splitting of the hole subbands.

In order to analyze the interplay between the QW potential and the magnetic field in determining the HH-LH mixing as a function of the field strength and of the QW width L we calculate exactly, in the k·p framework, the hole subbands including high electric and magnetic fields, and simulate the magnetotunneling experiment for a 42 Å GaAs-AlAs QW as in Ref. [1], and a much larger one (120 Å GaAs-AlAs QW).

The in plane momentum acquired by holes tunneling through the double barrier structure amounts in a perturbative picture to [5]

$$k_\parallel = \frac{eB}{\hbar} \Delta z \qquad (1)$$

where Δz is the average distance travelled by holes in going from the accumulation layer to the QW. We model the HH-LH mixing by use of the 4×4 Luttinger Hamiltonian [6] with the substitution $k_z \to k_z - A$. The Hamiltonian can be separated in 2 blocks since given the energy dispersion vs $k_\parallel$ [6,7]. The magnetic field removes the degeneracy between the two blocks (spin splitting) that would apply to symmetric QW's at zero field.

In order to simulate the RMS experiment, we calculate, from the Luttinger hamiltonian, the hole energies at $k_\parallel$ given by (1) in a wide range of magnetic fields by using a recently developed real space approach [8]. Results are reported with solid lines in Fig. 1 as a function of the new (equivalent) of $k_\parallel$ through (1) for a 42 Å QW and a 120 Å QW. As in Ref. [1] we assume Δz to be the sum of the experimental average standoff distance of the accumulation layer charge from the barrier interface (50 Å), the barrier width itself (51 Å) and half of the QW width. Consider first the 42 Å QW. An average electric field (in the range 9 - 30kV/cm) has to be included in the calculation of each subband, to approximate the resonance condition (applications performed with no bias (dashed lines) demonstrate the small effect of the electric field). Appreciable spin splitting appear at $\sim 20T$ in the HH_1 and LH_1 subbands, but at lower fields ($\sim 10T$) for the higher subbands. It is remarkable that no evidence for such spin splitting is found in experiments even if our calculations indicate that they are of the same order of magnitude as the anisotropies observed by changing the field orientation in the QW plane [4]. However apart from the spin splitting, small deviations of the subband dispersion are found with respect to the zero field case (dotted lines in Fig. 1). In this respect, our calculation gives support to the interpretation of RMS as a probe of the unperturbed hole subbands given in Ref. [4].

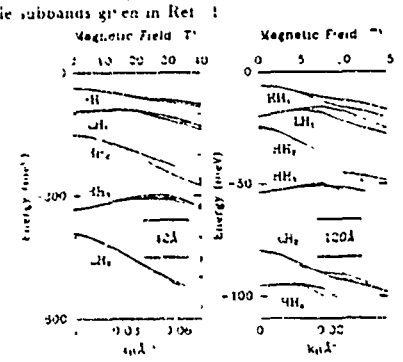

FIG. Simulated RHS with hole energies calculated at $k_\parallel$ given by Eq. (1) as a function of the magnetic field for a 42 Å (left) and a 120 Å (right) GaAs-AlAs QW. Solid lines: magnetic levels calculated including an applied bias in the growth direction. Dashed lines: magnetic levels calculated at zero electric field. Dotted lines: hole subbands with zero electric and magnetic field, as a function of $k_\parallel$ (using Eq.). The HH and LH labeling refers to the hole character at $k_\parallel = 0$.

We also simulate the results for the 42 Å QW with those for the 120 Å GaAs-AlAs QW. No electric field was applied in the latter case in view of the negligible effects found above since even smaller electric fields would be necessary for this larger well. The magnetic length $l_B = \sqrt{\hbar/eB}$ at 37 T (55 Å approximately) half of the width of this larger QW. Notice that larger fields are necessary in this case to sample the relevant range of $k_\parallel l_B$ where HH-LH anticrossings occur. Confinement energies scale approximately as $1/L^2$ since the

terms introduced in the Hamiltonian by the field depend mainly on the field strength, the larger the QW, the more effective is the field in modifying the HH-LH mixing.

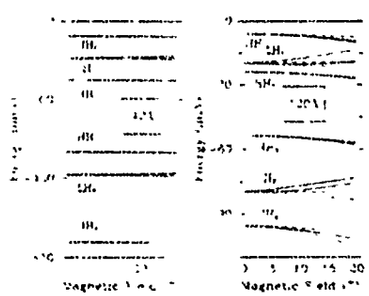

FIG. 2. Shift of the subband edges as a function of the magnetic field. Solid lines: hole magnetic levels at $k_{\parallel} = 0$. Dashed lines: expected diamagnetic shift for exactly decoupled HH's and LH's. The HH and LH labelling refers to the hole character at $B = 0$.

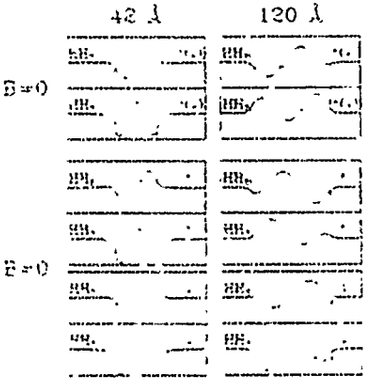

FIG. 3. Wavefunctions of the subbands labelled HH and HH in Fig. 1 at $k_{\parallel} = 0.075$ Å^{-1} at $B = 30$ T for the 42 Å and 120 Å QW. Solid lines: HH component. Dashed lines: LH component. Vertical lines: position of the QW barriers. The arrows show the spin state and the $B = 0$ value the bands degenerate.

As it can be seen, by comparing the simulated RMS spectra for the two QW's, in fact, while the spin splitting is of the same order of magnitude for the two QW's (note the different energy scales), in the larger QW the HH-LH mixing is strongly modified with respect to the zero-field subbands. This is evident by comparing anticrossings between different subbands (HH$_1$-LH$_1$, HH$_2$-HH$_3$, LH$_2$-HH$_3$): note in particular how the LH$_2$-HH$_3$ anticrossing is strongly affected by the field. Note also that anticrossings shift differently both in $k_{\parallel}$ and in energy for the two spin split subbands.

For carriers with parabolic energy dispersion, as, e.g., conduction band electrons, the in-plane magnetic field forms a parabolic effective potential in the growth direction, with curvature determined by the effective mass. This effective potential rigidly shifts upwards the subbands as soon as the magnetic length becomes comparable to the QW width. The situation for holes is far more complicated since holes have a mixed HH-LH character. The field moreover modifies the HH-LH coupling. In Fig. 2 we plot the shift of the subband edges ($k_{\parallel} = 0$) of holes as a function of the magnetic field for the 42 Å and the 120 Å QW's considered. The dashed lines represent the diamagnetic shift that would be expected for pure HH and LH's. A Zeeman splitting has been added in this case for LH's subbands. At $B = 0$ LH's and HH's are exactly decoupled in the Luttinger hamiltonian so that solid and dashed lines coincide. In the 42 Å QW the HH's and LH's remain nearly decoupled up to high fields. For the 120 Å QW, however, the shift of the subband edges deviates from the uncoupled case. The field significantly mixes LH's with HH's even at $k_{\parallel} = 0$: the acquired heavy component produces a positive, electron-like diamagnetic shift of LH's. The opposite is true for HH's. Note that positive diamagnetic shifts appear when HH and LH edges with same parity happen to be near in energy, since the field-related terms at $k_{\parallel} = 0$ can be shown to mix only HH's and LH's with same parity. HH$_1$ and HH$_3$ edges, instead, shift according to the uncoupled case.

The magnetic field can also affect the HH-LH mixing at finite in-plane wavevector $k_{\parallel} \neq 0$. In Fig. 3 we plot the wavefunctions in proximity of the anticrossings of the subbands labelled HH$_1$ and HH$_3$ in Fig. 1 for both QW's: we compare the wavefunctions at $B = 0$ and $B \neq 0$. It is evident from the figure that in the 42 Å QW the wavefunctions are only slightly modified by the field so that, apart from spin splitting, small deviations of the RMS spectra are expected with respect to the unperturbed subbands. For the 120 Å QW, however, the $B \neq 0$ wavefunctions are significantly different from the $B = 0$ ones.

To identify the relevant couplings introduced by the field, we use a simple representation of the Luttinger hamiltonian in the truncated basis formed by the three topmost states at $k_{\parallel} = 0$: HH$_1$, LH$_1$ and HH$_2$; the relative wavefunctions are taken to be those of the infinite well. It turns out that the largest off-diagonal term couples the LH$_1$ and HH$_2$ edges:

$$\text{LH}_1\text{-HH}_2 \text{ coupling} \quad \frac{1}{2}\left(\frac{l}{L_z} - 1\right)\frac{\hbar^2}{2m_0 l}$$

where the numerical constant $\frac{1}{2}\left(\frac{l}{L_z} - 1\right) \approx -0.27$ and the $\pm$ sign applies to the two spin states. The second term in 2×2 matrix present at $B = 0$ and is responsible, in our simple representation, for the positive effective mass of the LH subband. The first term instead is introduced by the field which consequently mixes the HH-LH coupling. By comparing the two terms of the previous QW, one can evaluate to which extent the field affects the couplings in a RMS experiment. As an example, for the QW's examined above, the field-related term $\frac{\hbar^2}{2m_0 l}$ amounts to ≈ 0.7 of the zero-field LH$_1$-HH$_2$ coupling for the 42 Å QW at $B \approx 30$ T, while for the 120 Å QW at the same field it amounts to $\approx 30\%$ of the zero-field coupling.

In conclusion we have calculated the hole magnetic levels in a QW with strong in-plane magnetic field and we simulated RMS spectra for two different regimes of the the QW width. For a 42 Å QW our calculations give support to the interpretation of RMS in *p* doped QW as a probe of the hole dispersion. For a 120 Å QW instead our calculations show that the HH-LH mixing and the subband dispersion are significantly modified by the field. In particular the field position of the anticrossings between the zero field subbands shifts in a different fashion for the two spin split partners as a function of the field.

This work has been partially carried out within the European Program *Human Capital & Mobility* project MagNET n. ERB4050PL921454

1 R. K. Hayden, D. K. Maude, L. Eaves, E. C. Valadares, M. Henini, F. W. Sheard, O. H. Hughes, J. C. Portal and L. Cury, Phys. Rev. Lett. 66, 1749 (1991).
2 M. Asmerilli, J. Ekemoerz and A. Fasolino, Phys. Rev. B 32, 5139 (1985).
3 U. Ekenberg, A. P. Kesan, D. A. Sippers, F. F. Smith III, S. S. Iyer and E. S. Yang, Phys. Rev. Lett. 67, 3828 (1991).
4 R. K. Hayden, T. Takamasu, D. K. Maude, L. Valadares, L. Eaves, U. Ekemberg, N. Miura, M. Henini, J. C. Portal, O. Hill and M. A. Pate, Semicond. Sci. Technol. 7, B413 (1992).
5 J. M. Luttinger, Phys. Rev. 102, 1030 (1956).
6 G. Goldoni and A. Fasolino, Phys. Rev. Lett. 69, 2567 (1992); E 70, 2051 (1993).
7 G. Goldoni and A. Fasolino, submitted for publication.
8 A. Fasolino, G. Platero, M. Potemski, J. Maan, K. Ploog and G. Weimann, Surf. Sci. 267, 509, (1992).

TuP35

Control of Electron Populations in the Quantum Well Levels of GaAs-AlGaAs Double Barrier Resonant Tunnelling Structures.

P. D. Buckle, J. W. Cockburn, M. S. Skolnick and D. M. Whittaker
Department of Physics, University of Sheffield, Sheffield S3 7RH, United Kingdom

R. Grey, G. Hill, and M. A. Pate
Science and Engineering Research Council Central Facility for III-V Materials, Department of Electronic and Electrical Engineering, University of Sheffield, Sheffield S1 3JD, United Kingdom

G. W. Smith
Defence Research Agency, St. Andrew's Road, Malvern, Worcestershire WR14 3PS, United Kingdom

In double barrier resonant tunnelling structures (DBRTS), the potential exists to control independently the populations of individual quantum well (QW) confined levels. For example, when biased on the second electron tunnelling resonance the ratio of the electron populations of the ground (E1) and first excited (E2) state of the QW (n_2/n_1) within the DBRTS is controlled by the ratio of the inter-sub-band scattering time (τ_i) to the ground state tunnelling out time (τ_1)[1]. In this work both electroluminescence (EL) and photoluminescence (PL) techniques are employed to provide spectroscopic information on the level populations as a function of bias. From these results we demonstrate the control of the population ratio n_2/n_1 by independent variation of *both* τ_1 and τ_i in different structures.

The tunnelling-out time (τ_1) from the E1 level is expected to be a very sensitive function of collector barrier width. We demonstrate a 40 times enhancement of n_2/n_1 by reducing the collector barrier width from 80Å to 50Å in a structure with 80Å QW, in good agreement with the decrease in τ_1 predicted from a tunnelling resonance calculation. Furthermore, by application of a magnetic field perpendicular to the plane of the QW, a strong oscillatory variation of the EL intensity from E2 electrons, periodic in 1/B, is observed. These oscillations in EL intensity, proportional to the changes in E2 population, are shown to arise from modulation of the inter-sub-band scattering time τ_i as Landau levels from the E1 sub-band are swept through the E2 level. As a result, the control of the n_2/n_1 ratio by variation of the inter-sub-band scattering time (τ_i) is demonstrated in a very clear manner.

Finally, the observation of a population inversion between highly excited states of a wide well (200Å) DBRTS is reported. In this case the population ratios are shown to be controlled by the differences in longitudinal optic phonon inter-sub-band scattering times between the highly excited states of the QW. The experimentally determined values of the inverted population ratios are found to be in good agreement with a rate analysis.

TuP36

Single-Electron Transistors Realized in In-Plane-Gate and Top-Gate Technology

R J Haug, H Pothier, F Wern, K v Klitzing, and K Ploog*
Max-Planck-Institut für Festkörperforschung, D-70569 Stuttgart, Federal Republic of Germany
(1 July 1991)

Using the two-dimensional electron gas (2DEG) in an AlGaAs/GaAs heterostructure the zero-dimensional system necessary for the observation of charging effects (single electron effects) can either be realized by etching trenches and using the in plane-gate technology or by depleting the 2DEG with the help of gate structures evaporated on top of the heterostructure. In such structure single electron effects are studied in dependence of the applied gate voltages, the source-drain voltage and the magnetic field. The advantages and disadvantages of the different structures are discussed.

1. Introduction

In recent years a great interest arose into single-electron effects in nanostructures [1]. In the experiments studying tunneling through quasi-isolated systems the discreteness of the electron charge manifests itself in the conductance as a result of the Coulomb repulsion of individual electrons. The observability of these charging effects can be described by two conditions employing classical parameters. First, the elementary charging energy $E_c = e^2/2C$ with C the total capacitance of the quasi-isolated system has to be larger than the energy $E_{th} = k_B T$ (with T the temperature and k_B the Boltzmann constant) of the thermal fluctuations. This condition implies that the system has to be small enough to result in a small capacitance and that the temperature has to be correspondingly low. The second condition involves the tunneling resistance characterizing the coupling between the quasi-isolated system and the leads. These tunneling resistances have to be at least on the order of h/e^2 (with h Planck's quantum) to avoid smearing by quantum fluctuations. Due to the technological achievements in electron-beam lithography small enough systems can be produced nowadays in a sufficiently well defined way to study these charging effects at readily available temperatures (of about a tenth of a kelvin). Therefore, extensive studies have been performed in metal based systems and since few years also in semiconductors based systems using AlGaAs/GaAs heterostructures.

Single-electron transistors have been realized by using three charging effects. Here, an additional gate electrode capacitively coupled to the quasi-isolated system allows to change the electrostatic potential of the quasi-isolated system. The tunneling current is then modulated depending on the gate voltage and the charge on the quasi-isolated system. Single-electron transistors can be produced in different material systems and in different ways [2]. In semiconductors single-electron effects are studied in vertical [3] (perpendicular to the surface of the sample) and lateral transport (parallel to the surface). Here, we will concentrate on lateral transport and we will discuss two approaches for the realization of single-electron transistors. The emphasis will be on a comparison between these two approaches. The first method uses the in-plane gate technology, i.e. the full structure is fabricated in the semiconductor. In the second approach the nanostructure is defined by metallic gates on top of the semiconductor.

The in-plane gate technology has first been applied by using a focused-ion beam for the isolation of narrow regions which can serve as gates by having separate ohmic contacts to them. A full transistor operation has been shown for such structures [4]. Using these in-plane gates not only the conductance through a narrow channel can be varied but also the steepness and the form of the edge potential of a wide structure can be influenced [5]. Instead of bombarding the sample with ions narrow trenches can be etched to isolate narrow regions. Transistor operation [6] and quantum interference effects [7] have been studied in such systems. Figure 1a shows schematically a cross-section of such a device fabricated in an AlGaAs/GaAs heterostructure with a two-dimensional electron gas (2DEG) at the interface. Two gate regions are isolated from the conducting channel by the etched trenches. By having separate ohmic contacts to the conducting channel and to the gate regions a voltage can be applied between the conducting channel and the gates. By changing the gate voltage the conductance through the channel is varied. Charging effects have been observed in such in-plane gate devices already in simple point contacts due to unwanted related potential fluctuations in the conducting channel [8]. But, only recently the successful operation of a full single-electron transistor in in-plane gate technology has been demonstrated [9].

The second, more widely used approach is shown schematically in Fig. 1b. Top gates are produced by evaporating metallic layers on the surface of the AlGaAs/GaAs heterostructures. By application of negative gate voltages relative to the 2DEG the electronic system beneath the metallic regions can be depleted. A gap in the middle between the two gates causes the formation of a narrow conducting channel by the application of negative enough gate voltages to the two gate parts. The width and the carrier concentration of this conducting channel can be varied by applying more negative gate voltages to the gates. This method has been applied to study transport through narrow, long wires and ballistic one-dimensional transport through point-contact geometries. In recent years it was widely used for the study of single-electron effects in lateral transport through quantum dots [10] - [22].

In the following two examples of single-electron transistors will be shown to discuss the advantages and disadvantages of the different methods.

2. The experiments

In the experiments the two-dimensional electron gas (2DEG) in an AlGaAs/GaAs heterostructure with a carrier density of $n_s = 3.4 \cdot 10^{15} m^{-2}$ and a mobility of $\mu = 60 m^2/Vs$ is used as the basis of the structures. The distance between the 2DEG and the surface of the heterostructure is 80nm. The measurements have been performed in a top-loading dilution refrigerator with a base temperature of T=22mK. The conductance through the devices has been measured using standard lock-in technique at 13.4Hz with excitation voltages down to 5μV.

2.1 In-plane-gate single-electron transistor

Figure 2 shows schematically the geometry used for the realization of an in-plane gate single electron transistor (see also [9]). The etched regions are shown as shaded areas. The six gates used for the formation of the single-electron transistor are consecutively numbered. In the conducting channel going from source (S) to drain (D) a barrier can be formed by application of a negative gate voltage to at least one of the gates 1 & 6 and 3 & 4. By having two barriers an quasi-isolated system is located in the middle of the structure schematically shown by a dashed circle (with a diameter on the order of 1μm). The device has been fabricated in the following way. A Hall bar mesa has been defined by optical lithography and wet chemical etching, followed by the evaporation of the metallization necessary for the ohmic contacts (AuGeNi). Then, electron-beam lithography has been performed in writing the structure shown schematically in Fig. 2 into PMMA covering the sample. The shaded regions shown in Fig. 2 were then etched by reactive ion etching. The etch depth being about 75nm (as obtained from a test sample). By a subsequent annealing process the etched walls have been passivated and at the same time, the ohmic contacts have been formed. Typical measurements of the conductance through such a device in the regime of single-electron tunneling are shown in Fig. 3. The oscillation of the conductivity shows the Coulomb oscillations. The main result of such measurements is the understanding that in contrast to metallic gates the semiconducting in plane gate can also be depleted [9]. This effect is clearly shown in Fig. 3 as a drastic change in periodicity of the Coulomb blockade oscillations (marked by the arrows in Fig. 3). At these gate voltages gate 5 is depleted due to the influence of the electrostatic potential of gates 6 and 4 and due to the corners in the geometrical design of gates 6 and 4 (marked by arrows in Fig. 2). At this jump in the periodicity a drastic change in the effective capacitance (on the order of 30 percents) between the gate and the quasi-isolated system occurs due to the decoupling of the finger of the gate. But, also at smaller gate voltages a gradual change of the periodicity occurs corresponding to a slight decrease in the effective capacitance due to the depletion of the tip of the gate finger. So, the in-plane-gate technology allows for a successful realization of a single-electron transistor. But, at the same time it shows effects of the depletion of the gates themselves.

2.2 Single-electron transistor using top-gate technology

Quasi isolated systems or quantum dots (if they are small enough to show quantum confinement effects) can also be defined in semiconductors by electron beam lithography and evaporation of metallic gate structures onto the surface. Here, we will concentrate on a structure with 6 gates enclosing an area of about 350nm diameter as schematically shown in the inset of Fig. 4 (see also [10]). By application of negative gate voltages (on the order of -0.7V) to the six gates a quantum dot is isolated in the middle between the gates. The electrostatic potential of the quantum dot can be changed by application of a gate voltage to a metallization on the backside of the device.

Figure 3 shows the measured conductance versus backgate voltage for a vanishing bias voltage. Clearly, sharp conductance resonances due to single electron tunneling through the dot are observed. The gate-voltage ranges of vanishing conductance in between the resonances mark the Coulomb-blockade regime.

The variation in the peak values of the conductance resonances hints towards the quantum nature of the states in the quantum dot (on the order of 20 electrons are expected to be enclosed in the dot)

To investigate the different quantum states of the dot in more detail finite source-drain voltages allowing for tunneling in a finite energy range can be applied By measuring the differential conductance for different source-drain voltages spectroscopy of the electronic states in the dots can be performed [16,22] Excited states of the dot system are observed and can be classified from the measurements Application of a magnetic field can further help to identify the different states observed [22] and can clarify the role of spin and correlation effects [23]

3. Discussion

In recent years single-electron effects have been studied in metals and in semiconductors [1] Whereas in metals the typical number of electrons enclosed in a metallic island is on the order of 10^6 electrons, in semiconductor-based systems the number of electrons can be much smaller (on the order of 10 or even less) due to the lower density [18] Such small devices have, up to now, only be realized in top-gate technology In contrast to metallic systems quantum confinement effects are playing an important role in these semiconductor structures (quantum dots) Transport through such quantum dots can be described in simplified pictures by a combination of charging and quantum confinement effects, but for small numbers of electrons a full treatment of the interaction and correlation effects has to be used In the small quantum dots formed by the top-gate technology spectroscopy of the different quantum states in the dot can experimentally be performed by varying the source-drain voltage [16,19-21] and by varying the magnetic field [11,22]. So, single electron transistors formed with top-gate technology allow due to their flexibility (barriers can be tuned number of electrons can be tuned, form of the enclosed system can be tuned) detailed studies of quantum effects connected with single-electron transport. However, many groups seem to have problems with the stability of the devices leading to the effect that only a very small number of devices can be studied

The in-plane-gate technology allows in the moment not for very small devices But it is much simpler in the device preparation Here, originally some doubts existed whether a successful demonstration would be possible due to the surface states and impurities produced by the etching of the trenches But from the experiments it appeared that the stability of this devices is not worse than of devices produced in top-gate technology The most interesting observation in these devices was the depletion of the gates themselves [9] Especially the influence of the gate geometry and of the electrostatic potential of all the neighboring gates makes this effect interesting and at the same time it complicates the design of all the transistors using in-plane gates This effect could be exploited by making devices where the response depends on the status of neighboring devices There has been some hope, that making devices in in-plane gate technology reduces the effective capacitances and therefore allows for faster switching or for operation at higher temperatures in the case of single-electron transistors The experiments presented do not really strengthen this expectation, but they show that one has to be extremely careful in these devices with the effective capacitances included in simulations

4. Conclusions

For realizing single-electron transistors in lateral transport through semiconducting heterostructures the top-gate technology as well as the in plane gate technology can be used. In the present status of technology the top-gate technology allows to form quantum dots down to sizes in the range of 100nm and with less than 20 electrons Here very nicely the interplay between quantum confinement effects and charging effects can be studied But the technology is complicated and many groups have problems with the stability of the devices In contrast, the in plane gate technology is simpler But, with the present day etching technology and the heterostructures available it seems to be difficult to produce extremely small, defined devices Interesting effects are observed in the in-plane gate geometries due to the depletion of the gates themselves This effect limits to some extend the possibility for designing arbitrary gate-geometries and has to be taken into account in all devices using in-plane-gate technology (transistors etc)

Part of the work has been supported by the Bundesministerium für Forschung und Technologie H P is under contract SC 915165 of the European Community

* present address Paul-Drude-Institut für Festkörperelektronik, O-1086 Berlin, Germany

[1] e.g. *Single-Electron Tunneling and Mesoscopic Devices*, edited by H Koch and H Lübbig, Springer Series in Electronics and Photonics, Vol. 31 (Springer, Berlin, 1992)

[2] e.g. *Single Charge Tunneling* edited by H. Grabert and M H Devoret (Plenum, New York, 1992)

[3] e.g. N. Teweldt, V.J Law, J.T Nicholls, L. Martin-Moreno, D A. Ritchie, M J. Kelly, M Pepper, J E.F Frost, R. Newbury, G A C. Jones, Solid State Electron. (this volume) and references therein

[4] A.D. Wieck and K. Ploog, Appl. Phys. Lett. 56, 928 (1990).

[5] R J Haug, A.D Wieck, K v Klitzing, and K. Ploog, Physica B 184, 192 (1993)

[6] J Nieder, A D. Wieck, P Grambow, H Lage, D. Heitmann, K v. Klitzing, and K. Ploog, Appl. Phys. Lett 57, 2695 (1990).

[7] Y Feng, T . Thornton, J J Harris, and D Williams, Appl. Phys Lett. 60, 94 (1992)

[8] K Nakazato, T J Thornton, J White, and H. Ahmed, Appl Phys Lett. 61, 3145 (1992).

[9] H Pothier, J Weis, R J Haug, K v. Klitzing, and Ploog, Appl. Phys. Lett. 62, 3174 (1993).

[10] U Meirav, M A. Kastner, and S J Wind, Phys Rev Lett. 65, 771 (1990)

[11] P L. McEuen, E B Foxman, U Meirav, M A Kastner, Y Meir, N S Wingreen, and S J. Wind, Phys. Rev Lett. 66, 1926 (1991)

[12] L P Kouwenhoven, N C van der Vaart, A T Johnson, K Wees, C P J Harmans, J. G. Williamson, as A.A. M Staring, Z Phys. B 85, 367 (1991)

[13] R J Haug, J.M. Hong, and E Y Lee, Surf Sci 263, 415 (1992)

[14] A A M Staring, B W Alphenaar, H van Houten, L W Molenkamp, H A A Mabesoone, and O J A. Buyk, Phys Rev. b 46, 7236 (1992,

[15] R P Taylor, A S Sachrajda P Zawadzki, R.T. Coleridge, and T A. Adams, Phys Rev. Lett. 69, 1989 (1992)

[16] J Weis, R.J Haug, K v Klitzing, and K Ploog, Phys Rev B 46, 12837 (1992)

[17] C Pasquier, U. Meirav, F I B Williams D C Glattli, Y Jin, and B Etienne, Phys. Rev Lett. 70, 69 (1993)

[18] R J Haug, K Y Lee, and J.M Hong in Ref [1], J Weis, R.J Haug, K v. Klitzing, and K. Ploog, Physica B (1993)

[19] J Weis, R. Haug, K v Klitzing, and K Ploog, Proceedings of EP2DS-10, to be published in Surf Sci.

[20] A T. Johnson, L P Kouwenhoven, W de Jong, N C. van der Vaart, C.J P M Harmans, and C.T. Foxon, Phys Rev Lett 69, 1592 (1992)

[21] E.B Foxman, P L McEuen, U Meirav, N S Wingreen, Y Meir, P A Belk, N R Belk, M A Kastner, and S J Wind, Phys Rev. B 47, 10020 (1993)

[22] J Weis, R J. Haug, K v Klitzing, and K Ploog, (to be published)

[23] W Pfaff, D Weissmann, W Hansler, B. Kramer, and U Weiss (preprint)

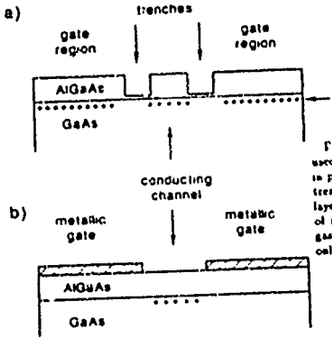

FIG 1 Schematical pictures of the different approaches used for the realizations of single-electron transistors (a) in plane gate technology for the isolation of the gate regions treaches are etched, (b) for the top-gate technology metallic layers are evaporated onto the sample surface, by application of negative gate voltages relative to the 2DEG the electron gas beneath the gates is depleted leaving a conducting channel only in the gap region

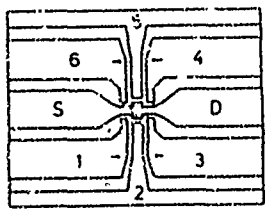

FIG 2. Schematical picture of a single-electron transistor. The geometry was used for the realization of the in-plane gate single-electron transistor. The different gates are numbered, whereas source and drain of the conducting channel are characterized by S and D. The shaded areas show the etched regions.

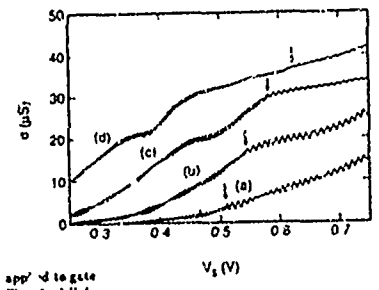

FIG 3. Conductance versus gate voltage V_3 applied to gate 3 of the in-plane gate geometry as shown in Fig. 2. While for the different curves the voltages $V_1 = -0.8$V, $V_2 = -0.6$V and $V_4 = 0$ are kept constant, the gate voltages $V_5 = V_6$ are varied: (a) -40mV, (b) 0mV, (c) 40mV, (d) 80mV. The arrows indicate the position of the abrupt changes in the periodicity of the conductance oscillations.

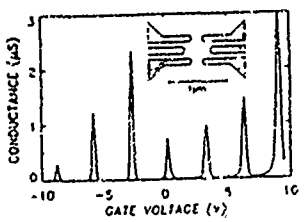

FIG 4. Conductance versus back gate voltage measured for a quantum dot defined by the top-gate geometry as shown schematically in the inset. The voltages applied to the top gates had been kept constant (at values of about 0.7V).

TuP37

Quasi One-Dimensional In-Plane-Gate Field-Effect-Transistor

U. Meiners, H. Brugger, B. E. Maile, and C. Wölk
Daimler-Benz AG, Forschungszentrum Ulm, D-89081 Ulm, Germany
F. Koch
Physik-Department, TU München, D-85748 Garching, Germany

Abstract:

A new type of a quasi one-dimensional planar field-effect-transistor (FET) with two lateral and symmetric in-plane-gate electrodes (IPG) is realized. The vertical layer sequence consists of a GaAs/AlGaAs heterostructure and a δ-doped pseudomorphic InGaAs quantum well with a high-density two-dimensional electron gas. The device configuration results in a strong lateral concentration of the confining electric field in the 2DEG plane. The fabricated devices operate excellently at room temperature with maximum currents (I_{DS}) above 0.3 mA and transconductance (g_m) values of 0.2 mS. Perfect pinch-off is achieved by a negative gate-voltage. Devices with planar arrays of quasi one-dimensional channels exhibit $I_{DS} > 6$ mA and $g_m = 5$ mS. A PMMA electron beam lithography process followed by a selective isolation implantation is used for the fabrication of IPG-FET devices.

1. Introduction

Low dimensional transport properties are intensively investigated for future electronic and optoelectronic device applications. In a one-dimensional electron-gas (1DEG) system a drastic suppression of the scattering rate was predicted theoretically by H. Sakaki [1]. The expected mobilities should be well beyond the values of a corresponding *two-dimensional* electron-gas (2DEG) system. One of the many novel device structures being investigated today is a quasi-1DEG field-effect-transistor (FET) with a lateral in-plane-gate (IPG) electrode configuration which was first proposed and demonstrated by A. B. Wieck and K. Ploog [2]. The expected reduced scattering rate in one-dimensional channels and the inherent low gate/channel-capacitance of the IPG structure makes this type of device very promising for high speed operation. The fully planar device configuration and the simple fabrication process offers the possibility of in-situ epitaxial regrowth for multi-functional three-dimensional integration. IPG-FETs have already been realized by trench etching isolation with reactive ion etching [3] and resistive p-type barrier isolation by focused-ion-beam (FIB) implantation of Ga ions [4, 5, 6].

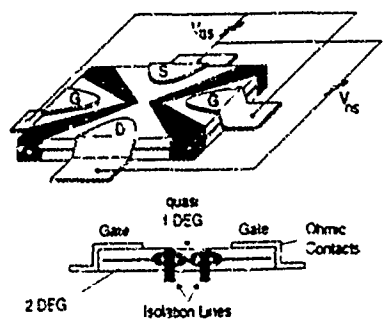

Figure 1. Schematics of the IPG-FET device. The quasi one-dimensional channel conductance is controlled by a lateral electric field via two symmetric gate electrodes.

In this paper we report about a novel IPG-FET and a selective isolation implantation technique for fabricating planar device structures. Starting from an MBE-grown AlGaAs/GaAs heterostructure with a pseudomorphic InGaAs

2DEG-layer quasi-1DEG channels are formed by two closely spaced isolation barriers. The fabricated devices operate excellently at room temperature. Current levels of more than 0.3 mA and transconductance values of 0.2 mS are realized on single-channel devices. These are to our knowledge the highest ever reported values on one-dimensional FETs. Perfect pinch-off is achieved at a gate voltage of V_{GS} = -2 V. On IPG-FETs with multiple quasi 1-DEG channels device source-drain currents above 6 mA and maximum transconductance values of 5 mS are realized. The electrical isolation of the gate-electrodes from the channel region is realized by a selective dual energy implantation with single charged boron ions. The achieved resistance of > 10^9 Ω/sq. is higher than the corresponding value of the used semiinsulating substrate and yields to a very low gate leakage current density and to a high break-down voltage.

2. Layered Structure and Device Fabrication

A schematic illustration of the device layout is shown in Figure 1 together with a cross-sectional view of the intrinsic part of the device. The vertical layer sequence consists of an MBE-grown pseudomorphic GaAs/InGaAs/AlGaAs heterostructure with a high-density 2DEG. Details about the epitaxial layers are summarized in Table 1.

Table 1. MBE Layer sequence used for the fabrication of IPG-FET devices. The substrate temperature was 620 °C up to the growth of the buffer layer and was reduced to a value of 530 °C for the growth of the final heterostructure layers.

layer	material	thickness	Si-doping
cap	GaAs	10 nm	5×10^{18} cm^{-3}
barrier	$Al_{0.25}Ga_{0.75}As$	10 nm	5×10^{17} cm^{-3}
quantum well	$In_{0.2}Ga_{0.8}As$	12 nm	2×10^{12} cm^{-2}
buffer	GaAs	750 nm	undoped
superlattice	AlAs/GaAs	2 nm / 2 nm	undoped

To improve carrier confinement and to enhance the 2DEG electron density in the quantum well (QW) a pseudomorphic InGaAs layer was used as a channel material. The InGaAs QW is δ-doped with a nominal Si concentration of 2×10^{12} cm^{-2}. A thin top-side and moderately doped AlGaAs barrier region is incorporated for a strong 2DEG confinement. A final, thin and highly doped GaAs cap-layer is used for the fabrication of low-resistance ohmic contacts. In order to avoid any parallel conductance through the cap layers the doping concentrations and layer thicknesses of the AlGaAs/GaAs heterostructure layers are completely surface-depleted. The 2DEG carrier density (n_s) and mobility (μ_H) were measured by Hall. Typical values are $n_s = 1.7 \times 10^{12}$ cm^{-2} and $\mu_H = 2050$ cm^2/Vs at 300 K.

As shown in Figure 1 the IPG-FET devices are defined by wet chemically etched mesa squares (12 µm x 12 µm) which contain source (S), drain (D) and two symmetric gate (G) electrodes. The ohmic contacts are fabricated by photolithography and standard alloyed NiGeAu metallization. The quasi one-dimensional current channel is realized in the center of the mesa by a small spacing between two thin V-shaped isolation lines along the mesa diagonal. The isolation regions are fabricated in the following way: The wafers are covered with a 0.6 µm thick polymethyl methacrylate (PMMA) resist layer. E-beam lithography is used for patterning the PMMA layer without a spatial dose variation to correct proximity effects. The resist pattern acts as a mask for the following implantation process. A dual implantation by boron ions is used with two different energies of 25 keV and 80 keV and dose values of 5×10^{12} cm^{-2} and 5×10^{13} cm^{-2}, respectively, for the isolation. A high resistance behaviour is achieved by damage-induced carrier trapping in the implanted regions. The measured sheet resistance on test structures is beyond 10^9 Ω sq. which is higher than the corresponding resistance of the used semi-insulating GaAs-substrate. The ion energies and dose values are optimized with the help of a Monte-Carlo simulation [7] to achieve extremely high resistances.

Realized isolation line widths (w_I) are in the range between 100 nm and 1.1 µm. The quasi one-dimensional channel width (w_{ch}) is varied between 200 nm and 2.0 µm. Outside the channel region wider isolation lines are used to minimize the capacitance and to reduce the leakage current as can be seen in Figure 1. The effective isolation line width is expected to be larger than the geometrical width w_I due to lateral straggling effects during the implantation and due to lateral depletion zones between the implanted regions and the channel. The 0.6 µm thick PMMA resist absorbs completely the high energy boron ions and protects the underlying semiconductor material to be damaged. For the fabrication of multi-channel devices a series of single-channels are connected in parallel by use of an airbridge technology. Details about the process technology are published elsewhere [8].

3. Experimental Results

A typical transistor room temperature current/voltage (I/V) curve is shown in Figure 2. The IPG FET device consists of only one single IPG-FET with a nominal width of w_{ch} = 2.0 µm and an isolation line width of w_I = 0.4 µm. The channel is totally pinched-off by a gate voltage of V_{GS} = -2 V. A very low gate leakage current of less than 70 nA is measured even for V_{DS} = 6 V and V_{GS} = -2.5 V. This is attributed to the excellent resistivity of the gate isolation region. The DC I/V performance was measured by a HP 4145B parameter analyzer with the device in the dark. The IPG-FET exhibits a maximum measured source/drain current (I_{DS}) of above 0.3 mA in the saturation range and a maximum transconductance (g_m) of 200 µS at a gate voltage of V_{GS} = 0 V. These are to our knowledge the highest ever reported values for an IPG-FET device.

The devices realized by the reported selective isolation implantation technique operate in a depletion mode. The transistor can be slightly enhanced by a positive gate voltage. The excellent controllability of the channel conductance is attributed to the QW-doped 2DEG structure. By applying a negative gate voltage the electric field is directed in the plane of the 2DEG towards the quasi one-dimensional channel as can be seen schematically in the lower part of Figure 1. In the proposed surface-depleted vertical layer sequence there exist no free charges in the AlGaAs and GaAs layers and therefore the conductance is strictly limited to the thin 2DEG QW layer. This yields to a nearly perfect lateral field-effect.

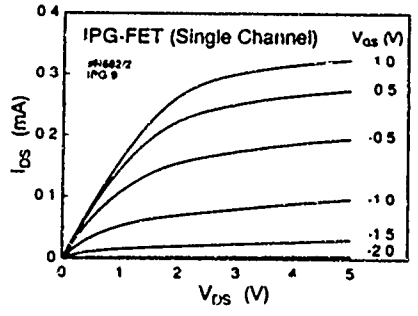

Figure 2 Room temperature I/V characteristics of a single channel IPG-FET in the dark

Experiments on conventional modulation-doped 2DEG samples have shown significantly lower transconductance values and reduced maximum current levels of the IPG-FET device. Only for $w_{ch} \leq 1$ µm a complete depletion is achieved by a negative gate voltage. For $w_{ch} > 1$ µm a gate/drain break-through occurs before pinch-off. Therefore a more effective lateral field-effect is expected in QW-doped structures in comparison with modulation-doped heterostructures.

The maximum channel current and the device transconductance are directly influenced by the spacing of the insulating barriers which determines the width of the channel

region. In Figure 3 the measured functional dependence of I_{DS} (V_{DS} = 4 V, V_{GS} = 0V) and g_m on the nominal channel width (w_{ch}) is shown. The curves are obtained from devices with a constant isolation line width of w_i = 0.4 µm and the measurement performed in the dark. With increasing number of carriers in the channel also the transconductance increases steadily with wider w_{ch}. At a nominal width of w_{ch} = 350 nm the channel is completely depleted even for V_{GS} = 0V. Therefore the effective electrical width of the channel is expected to be 350 nm smaller than the nominal one. This is attributed to the lateral straggling of the boron ions during the implantation process and due to lateral depletion zones between the isolated regions and the conductive channel. Additional experiments on the dependence of I_{DS} and g_m on the isolation width have shown that w_i has only a minor influence on the device performance. An IPG-FET device with w_{ch} = 0.6 µm and w_i = 0.6 µm exhibits an enhancement of g_m by about 20 % if the isolation width is reduced to w_i = 100 nm.

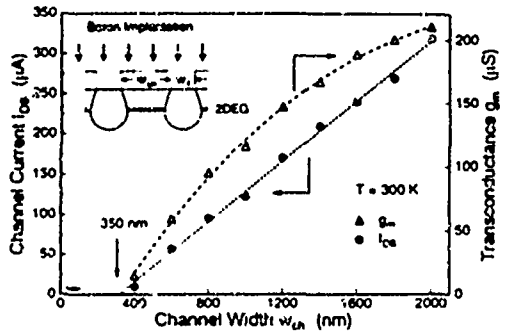

Figure 3. Measured source/drain-currents at V_{DS} = 4 V and V_{GS} = 0 V and maximum transconductance values of single-channel IPG-FETs as a function of the channel width in the dark. The isolation barriers are w_i = 0.4 µm.

In the saturation range of the operating transistor the observed linear dependence of I_{DS} on w_{ch} can simply be described by the following formula:

$$I_{DS} = e \times n_s \times w^*_{ch} \times v_{sat} \qquad (1)$$

with the electronic charge e, the 2DEG carrier density n_s, $w^*_{ch} = (w_{ch} - 350\ nm)$ as the effective electronic channel width and the saturation velocity v_{sat}. From the experimental data in Figure 3 and the measured two dimensional carrier density $n_s = 1.7 \times 10^{12}\ cm^{-2}$ a saturation velocity of $v_{sat} = 0.9 \times 10^7$ cm/s is obtained from equation (1). This value is close to the expected saturation velocity in GaAs material at high electric fields (= 10^7 cm/s).

In Figure 4 the I/V performance of a multi-channel device with 48 single channels in parallel is demonstrated. Maximum current levels above 6 mA are observed. The electrical connection of individual quasi one-dimensional channels is realized by micro-airbridges in a coplanar design. The maximum observed transconductance is 5 mS. Perfect pinch-off is achieved for gate voltages V_{GS} = -2.5 V. The individual channels are fabricated with w_{ch} = 0.8 µm and w_i = 0.6 µm. The current level and the transconductance value of the multi-channel device directly scales with the number of the quasi-1DEG channels connected in parallel. This demonstrates the high performance of the used technology in fabricating this new type of FET device. Also the gate leakage current of the multi-channel device is less than 1 µA at an applied gate voltage of V_{GS} = -2 V and V_{DS} = 5 V. A maximum source drain voltage of V_{DS} = 9 V at V_{GS} = -3 V can be applied before gate-drain break-through occurs. Due to the intrinsic current limitations of 1DEG FETs a parallel conducting matrix-array arrangement is necessary to push the current level in the mA-range for real device applications.

The maximum available speed of the IPG-FET device is expected to be limited by extrinsic parasitic components and internal capacitances (C_{GD}). Therefore the overall dimensions of IPG-FET devices (esp. the multi-channel configuration) should be kept as small as possible and a low loss connecting transmission line network is necessary to minimize extrinsic capacitances and resistors. Otherwise the inherent advantage of this novel quasi-1DEG FET (a very small gate capacitance) is dominated and limited by extrinsic effects. A detailed analysis on speed limiting effects in IPG-FET devices is performed by high frequency characterization experiments and will be published elsewhere.

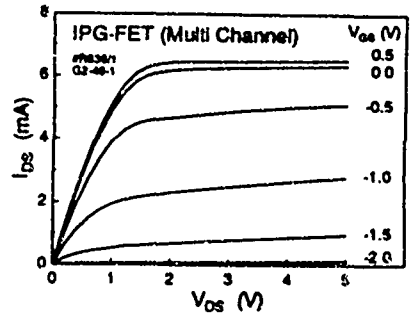

Figure 4. Room temperature I/V characteristics of a multi-channel IPG-FET (planar array of 48 channels).

4. Conclusion

A selective isolation implantation technique is used for a successful fabrication of a fully planar quasi one-dimensional field-effect-transistor with in-plane gates. A strong lateral electric field concentration is achieved by a QW-doped 2DEG layer sequence. Highest room temperature transconductance values of 0.2 mS and maximum channel currents of more than 0.3 mA are realized on single-channel devices. The high performance of the used technology is demonstrated on devices with a planar array of parallel conducting channels yielding I_{DS} > 6 mA and g_m = 5 mS.

Acknowledgement

The work was partially supported by the Bundesministerium für Forschung und Technologie (Bonn, Germany) under contract number (FKZ) BMFT 120/7.

References

[1] H. Sakaki, Jap. J. Appl. Phys. 19, L735 (1980)

[2] A. D. Wieck and K. Ploog, Appl. Phys. Lett. 56, 928 (1990)

[3] J. Nieder, A. D. Wieck, P. Grambow, H. Lage, D. Heitmann, K. v. Klitzing, and K. Ploog, Appl. Phys. Lett. 57, 2695 (1990)

[4] A. D. Wieck and K. Ploog, Appl. Phys. Lett. 61, 1048 (1992)

[5] Y. Hirayama, Appl. Phys. Lett. 61, 1667 (1992)

[6] J. A. Adams, L. M. Templeton, E. V. Kornelsen, and S. P. McAllister, Proc. of the Int. Semiconductor Device Research Symposium, Charlottesville (U. S. A.), Dec. 4 - 6 (1991)

[7] J. Ziegler, J. Biersack, and V. Littmark, *Doping and Range of Solids*, Pergamon Press, New York (1985)

[8] U. Meiners, B. E. Maile, and H. Brugger (to be published)

TuP38

Reflection of Ballistic Electrons by Diffusive 2D Contacts

A K.Geim, P C Main, R Taboryski*, H Carmona, C V Brown, T J Foster, P. B S Oakeshott+, and E Veje*

Department of Physics, University of Nottingham NG7 2RD, England

*Niels Bohr Institute, The Oersted Laboratory, DK-2100 Copenhagen, Denmark

+Department of Physics, Imperial College, Prince Consort Road, London SW7 2BT

We report quenching of high-magnetic-field Shubnikov-de Haas oscillations and shrinking of the Hall plateaux with *decreasing* temperature in a quantum Hall effect conductor with low-mobility contact leads. Selective He-ion bombardment has been employed to reduce the mobility of a two-dimensional electron gas (2DEG) in the contacts. We explain the results in terms of the Milne reflection of electrons from these disordered regions. At sufficiently low temperatures, inelastic scattering is suppressed and electrons are scattered back by elastic collisions before thermalisation can occur.

The Landauer-Buttiker formalism provides a method of characterising conduction processes in a quantum conductor. Usually, the conductor is conceptually divided between regions of non-dissipative transport in the bulk of the conductor and contact regions ("thermal reservoirs") where electrons are completely thermalised [1]. The boundary between these two regions is not clearly defined in real experiments and may depend on external parameters such as temperature and magnetic field. In quantum Hall effect (QHE) experiments, low-mobility alloyed AuGe contacts are usually considered as "ideal" contacts which totally absorb and thermalise incident electrons. This simplistic model that AuGe contacts act as ideal thermal reservoirs has appeared to explain experimental results well [2]. This is a surprising fact since it is known from astrophysics and neutron physics that ballistic particles penetrating into a strongly scattering medium are mainly reflected back if the inelastic scattering length l_i is much longer than the elastic length l_e (the Milne problem [3]). The condition, $l_i >> l_e$, is always valid for alloyed metal contacts at helium temperatures. It is probably the mismatch in electron concentration and dimensionality at the metal-2DEG interface which is responsible for the suppression of the expected backscattering from alloyed contacts in the range of temperatures usually employed [4].

To investigate the role of the Milne reflection and contact dissipation in quantum resistance measurements we have fabricated 2DEG devices with long and narrow diffusive leads where the mobility was reduced with respect to the rest of the conductor by He-ion bombardment. Unlike conventional QHE devices, our samples have no distinct boundary between the quantum conductor and the contact regions since electrons thermalise in the low-mobility contact leads. Changes in the inelastic scattering rate with temperature cause changes in the effective position of the contacts relative to the quantum conductor which dramatically influences resistance measurements. The devices with disordered 2D leads exhibit a rapid quenching of the high field Shubnikov-de Haas (SdH) oscillations and a significant decrease of the width of the quantum Hall plateaux at the temperature decreases, in contrast to the behaviour of unimplanted devices and larger conventional QHE devices.

We explain the observed behaviour by considering the thermalisation of electrons in the disordered regions. At high temperatures, electrons entering the disordered region from the edge states in the high-mobility region are able to thermalise rapidly and the implanted areas act as conventional contacts. At low temperatures the electrons are backscattered by elastic collisions in the disordered regions before thermalisation can occur. We present a model which shows that the longitudinal resistance goes to zero and the quantum Hall plateaux shrink as the inelastic scattering rate decreases with decreasing temperature. The model assumes that the innermost edge state is mostly influenced by the disorder and elastically scattered back when $l_i >> l_e$ (the analogy of the Milne problem for the edge state regime).

Three types of devices have been used in our experiment. Hall bar structures with several voltage probes were fabricated using electron beam- and photo-lithography from a modulation-doped GaAlAs heterostructure with 2D electron concentration $n \approx 4.5 \times 10^{15}$ m^{-2} and mobility $\mu \approx 20$ m^2/Vs. The devices differ in their configurations of the contact leads as shown schematically in the insets to Figure 1. The first two types of Hall bar (Fig 1a,b) have a conducting width $w \approx 1\mu$m of all 2DEG sections and l distance between adjacent voltage probes l between 10 and 20 μm. The measurement leads have a relatively long length of $\approx 50\mu$m terminated by conventional AuGe contact pads. Type-A devices (see Fig 1a) were exposed to bombardment by 50keV alpha-particles of a total dose 3×10^{16} m^{-2} with the central part of the device, including 5μm sections of the contact leads, protected by a thick metal mask. The bombardment dramatically reduced the mobility of the exposed 2DEG (the measured 2DEG mobility of an unmasked device is $\mu_{im} \approx 2$ m^2/Vs) while the mobility in the central part is found to be unchanged. Details of the He-ion implantation procedure and characteristics of implanted 2DEGs can be found elsewhere [5]. We refer to unimplanted Hall bars of the same geometry as type-B devices. For completeness, we have also fabricated control samples (type C) from the same heterostructure with the contact lead geometry as shown in Fig 1c. The width of the leads rapidly increases from $\approx 1\mu$m to 10μm where they are terminated by the alloyed contact pads (see Fig 1c).

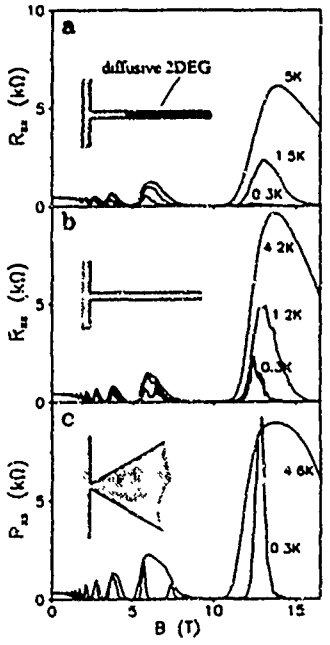

Figure 1. Longitudinal magnetoresistance at different temperatures in QHE devices with various configurations of the contact leads shown in the insets.

A central qualitative result is presented in Figure 1a where the longitudinal magnetoresistance R_{xx} of a type-A device is shown for three different temperatures It is clearly seen that, as temperature decreases from 4K down to 0 3K, the amplitude of SdH oscillations above 3T decreases considerably and the last peak in R_{xx} at about 14T (ν=1 5) virtually disappears. A detailed temperature dependence in the range 0 3-3K for this peak is shown in Figure 2. Note the strong resistance fluctuations at low temperatures in Fig.2 which have been attributed to resonant tunnelling between opposite edge states in these mesoscopic devices [6] The quenching of R_{xx} at low temperatures is in stark contrast to the usual behaviour of QHE devices [7] and to theory (see e.g. [8]) which both give nearly constant amplitude of Shubnikov-de Haas peaks as temperature decreases Figure 1c shows the behaviour of R_{xx} in the control device The high-field SdH peaks become narrower at low temperatures but their amplitudes remain nearly constant as temperature decreases. Type-B devices exhibit an intermediate behaviour as shown in Fig 1b and the peak at ν=1 5 decreases by a factor of 4 with decreasing temperature from 4 2K to 0 3K The amplitude of this peak is found to saturate below 0 6K Note that two other peaks at about 3T and 7T in the samples A and B (Figs 1a,b) are also suppressed as temperature decreases although the effect is not as pronounced as for the peak at 14T In addition, different degrees of spin-splitting of the peak at about 7T (see Fig 1) make it rather difficult to compare the temperature dependences of P_{xx} for this magnetic field

Figure 3 shows the Hall resistance R_{xy} in a type-A device at different temperatures The width of the quantum Hall plateau at ν=2 decreases at both high and low temperatures and the plateau is widest at about 5K The lower plateau at ν=4 also has some tendency to shrink at low temperatures (not visible in the figure) This behaviour is in contrast to the behaviour of conventional QHE devices [7,8] and our control samples where the plateaus are *always* wider at lower temperatures Note that there is an interval of magnetic fields, for example from 10 to 11T, where the longitudinal resistance goes to zero as temperature decreases while the Hall resistance goes up and away from its quantised value (compare Fig 2 and 3) We conclude that zeros of the longitudinal resistance in type-A devices do not necessarily imply quantised values of the Hall resistance as is normally the case in QHE devices

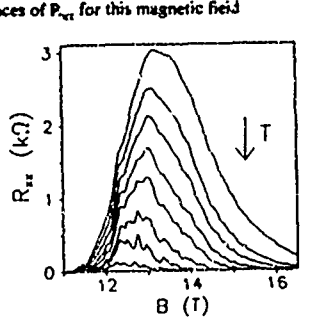

Figure 2 Detailed temperature dependence for the high-field peak of Fig 1a in the range 0 3-3K

Considering the quantitative behaviour of R_{xx} with temperature we first address the temperature dependence in magnetic fields far away from the field of magnetoresistance maxima The changes in this regime are exponential and can be described for all the devices by the functional form $R_{xx} \propto \exp(-\alpha T^{-\beta})$ [7,9] where α is a field dependent constant We find β≅0 5 for both B and C devices and on both sides of the high-field magnetoresistance peak Examples of this behaviour are shown in Fig 4a where R_{xx} is plotted versus $T^{-1/2}$ for a type-B device at 13 5 and 15T The solid lines in Fig 4 show the case of β=1/2 The same temperature dependence can also describe $R_{xx}(T)$ in type-A devices far away from the resistance maximum

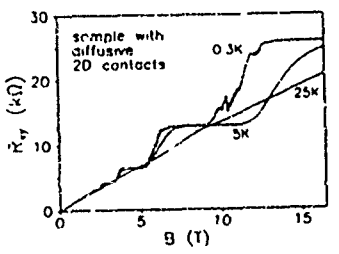

Figure 3 The Hall resistance in a type-A device (see Fig 1a) for three different temperatures

(see Fig 4b, the filled circles are for B=15T) However, due to the strong mesoscopic fluctuations at low temperatures the accuracy of the measurements of β is much lower and only implies β=0 7±0 4 for this device The observed exponential dependence with β=1/2 is in agreement with theory, which attributes this behaviour to a variable-range-hopping conductance modified by the Coulomb gap in the density of states [9] (see also [7]) The temperature dependences in the immediate vicinity of the SdH maximum are different and vary between the different devices For C devices the magnetoresistance changes are weak, corresponding to a nearly constant height of the R_{xx} peak In contrast, for type-A devices the changes at the maximum near 13T are exponential and are decribed by a stronger function of temperature than in the case well away from the maximum Fig 4b shows the temperature dependence for the magnetic fields of 13T and 13 2T in a type-A sample (open symbols) The best fit to the experimental dependence over the whole temperature interval in Fig 4b yields $R_{xx} \propto \exp(-c/T)$ as shown by the dashed line

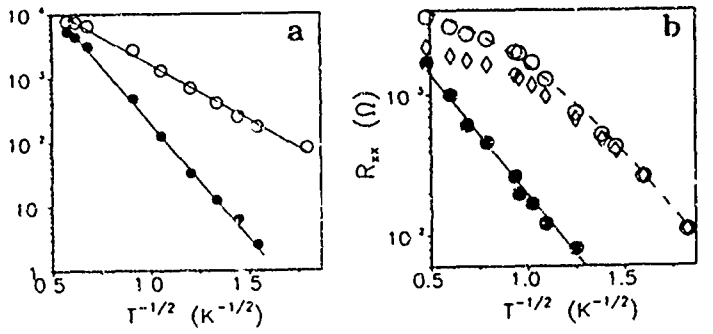

Figure 4 Changes of the longitudinal magnetoresistance with temperature for different magnetic field (a) - type-B sample at B=13 5T (open circles) and 15T (closed circles) (b) - type-A device at B=15T (closed circles), 13 2T (open circles) and 13T (diamonds) The latter two values are at the position of the peak maximum The solid line show the best fits to the dependence $R_{xx} \propto \exp(-\alpha T^{-1/2})$ The dashed line corresponds to $R_{xx} \propto \exp(-\alpha T^{-1})$

To explain the results we assume that it is the innermost occupied edge state which is mostly influenced by the disorder [1] and strongly scattered back by the low-mobility contact leads An electron entering the diffusive region can be either scattered back elastically or thermalised in the lead which then is effectively a contact As the temperature decreases, the inelastic scattering rate also decreases so that the electrons can spend more time in the lead before undergoing an inelastic event This increases the probability of back-scattering by involving a longer section of the lead in the process and effectively moving the position of the boundary between the quantum conductor and the contact further inside the contact leads For an infinitely long lead and no inelastic scattering there would be 100% probability of back-scattering. We expect that this result, obtained for zero magnetic field [3,4], is also valid for the case of the edge-state transport

For a quantitative analysis we consider a model of the type-A device shown schematically in Fig 5 [10] Only two occupied Landau levels are taken into account, corresponding to the experimental situation for the high-field peak at 13T Note that the edge states of the central part of the device remain well defined in the disordered 2DEG regions where $\mu_{tm}B>>1$ at these magnetic fields The backscattering in the central part is neglected since $\mu>>\mu_{tm}$ and this section is relatively short We model the back-scattering in the implanted leads assuming that there is some characteristic length of the edge state thermalisation $L_{th}(T)$ Referring to the qualitative considerations of the previous paragraph and to avoid an involved analysis for the distributed QHE networks [11], we assume that the thermalisation of the edge states occurs at a distance of L_{th} inside the disordered regions Following ref [12], we express the transmission probability T of the inner edge state into the thermal reservoir placed at the distance L_{th} as

$$T = \frac{1}{1+\sigma_{xx}^{L}(h/e^2)(L_{th}/w)} \qquad (1)$$

where σ_{xx}^{L} is a parameter which can be interpreted as the electron conductivity of the uppermost Landau level [12] The temperature dependence of σ_{xx}^{L} is metallic near half-integer filling factors when the electron states are extended [8] For other magnetic fields, it is expected that $\sigma_{xx}^{L} \propto \exp(-\alpha T^{-1/2})$ due to variable-range hopping [9]

In Fig 5 the transmission probabilities T and t through the current and voltage leads, respectively, are chosen to be different This corresponds to our experimental geometry but also reflects the fact that the voltage probes are noninvasive, whereas passing a current could influence the properties of the current leads in the real experiment Following the standard procedure for QHE networks [1,12], we obtain for the geometry in Fig 5

$$R_{xx} = h/e^2 \frac{tT(1-t)(1-T)}{2(t+T)(1+tT)} \qquad (2)$$

A similar analysis for the Hall geometry gives

$$R_{xy} = h/e^2\left(1 - \frac{t+T}{2(1+tT)}\right) \qquad (3)$$

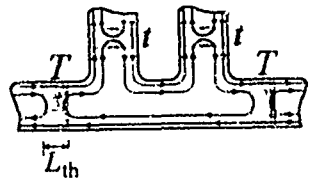

Figure 5 Model of the edge state reflection from the disordered regions in type-A devices

If T or t goes to either zero or unity, R_{xx} vanishes When either t or T equals unity, R_{xy} corresponds to its normal quantised value $h/2e^2$ and if $t=T=0$, $R_{xy}=h/e^2$

To explain the observed behaviour of R_{xx} and R_{xy} in type-A devices, we consider the magnetic field interval 10-11T where the anomalies are most pronounced In this regime we have observed near-zero values of R_{xx} while R_{xy} goes away from $h/2e^2$ up to near h/e^2 Referring to Equations 2 and 3, this behaviour unambiguously implies a rapid decrease of both t and T toward zero as the temperature decreases

The temperature dependence of the transmission coefficients is determined by both σ_{xx}^{L} and L_{th} (see Eq 1) which have *opposite* temperature dependences, i.e. L_{th} increases with decreasing temperature while σ_{xx}^{L} decreases or remains constant. Near the R_{xx} maxima, the changes in the conductivity σ_{xx}^{L} are slow and $L_{th}(T)$ dominates in the temperature dependence of T and t From the observed exponential decay of R_{xx} near $\nu=1/2$ in Fig.4b, we infer that the thermalisation length can be described by an activated behaviour, i.e. $L_{th} \propto \exp(c/T)$ This dependence is in agreement with experiment, where the inter-edge scattering rate has been found to depend exponentially on temperature, [13] and also with theory which predicts exponential dependences for both inter- and intra-edge scattering [13-15] Far away from the resistance maxima, the temperature dependence of R_{xx} is determined by the competition between σ_{xx}^{L} and $L_{th}(T)$ This competition can explain other features in the behaviour of type-A samples and, in particular, the shift in the position of the maximum seen in Fig 2.

Finally, we discuss the observed difference in the behaviour of R_{xx} and R_{xy} for the different devices The reason is presumably due to the different relationship between L_{th} and the length of the 2DEG contact leads for the different devices. When the contact leads are shorter than L_{th}, their length should be substituted into Eq (1) instead of L_{th} since the edge state electrons are rapidly thermalised in the alloyed contacts [4] This situation is expected to be valid for type-C devices at helium temperatures In the type-B sample, the increase of L_{th} can describe the initial decay of the SdH peak with decreasing temperature while at 0.6K L_{th} probably becomes comparable with the length of the leads and the amplitude of the peak saturates at lower temperatures In type-A devices, the thermalisation length in the leads is suppressed with respect to the B-devices by the He-ion bombardment [13,14] and we can expect that it is always shorter than the length of the leads for the employed temperature interval

In conclusion, we have studied reflection of edge state electrons at the boundary between high and low mobility 2DEGs The quenching of the longitudinal resistance and the narrowing of the Hall plateaux with decreasing temperature are explained in terms of the temperature dependent position of the Landauer thermal reservoirs The experiment emphasises the important role of dissipation in quantum resistance measurements We note that the proposed model of the effect can also explain nonlocal magnetoresistance oscillations which have been observed at elevated temperatures in n$^+$GaAs quantum wires [16]

This work was supported by SERC We want to thank Y B Levinson and L Eaves for helpful discussions

References

1 For a review, see H van Houten and C W J Beenakker, in *Solid State Physics*, edited by H Ehrenreich and D Turnbull (Academic, New York, 1991), vol 44

2. Note that in several papers the non-ideal behaviour of the alloyed contacts has been reported [S Komiyama, H Hirai, S Sasa, and T Fujii, Solid State Commun 73, 91 (1990), H van Houten, C W J Beenakker, and B J van Wees, in *Semiconductors and Semimetals*, edited by M A Reed (Academic, New York, 1991)]

3. P M Morse and H Feshbach, Methods of Theoretical Physics, McGraw-Hill, 1953

4 Y B Levinson, in *Proceedings of EP2DS-10*, Newport 1993 (to appear in Sur Sci)

5 R.Taboryski and P E Lindelof, Semicond Sci Technol 5, 933 (1990)

6 A K Geim, P C Main, C.V Brown, R Taboryski, H Carmona, T Foster, P E Lindelof, and L Eaves, in *Proceedings of EP2DS-10*, Newport 1993. (to appear in Sur Sci)

7 H P Wei, D C Tsui, M A Paalenen, and A M M Pruisken, Phys Rev Lett 61, 1294 (1988) S Koch, R J.Haug, K.v Klitzing and K Ploog, Phys Rev B 43, 6828 (1991) Note that QHE devices [e g. H P.Wei, S.Y.Lin, D C.Tsui, and A M M Pruisken, Phys Rev B 45, 3926 (1992)] can also exhibit a decreasing amplitude of SdHO with decreasing temperature somewhat similar to the behaviour found in our type-B devices This behaviour has not been explained but can be understood in terms of the present paper

8 J Kucera and P.Streda, J Phys C 21, 4357 (1988)

9 D G Polyakov and B I.Shklovskii, Phys Rev Lett 70, 3796 (1993) and references therein

10 To avoid confusion we note that the ion bombardment also slightly decreases the electron concentration in the contact leads [5] We have measured change of ≅10% in an unmasked device after bombardment The different electron concentration in the contact leads makes type-A devices somewhat similar to QHE devices with gated contacts [1] We have proved directly that this difference does not influence the observed temperature effects In our experiment, we have illuminated type-A devices and discretely increased the electron concentration in the leads leaving the concentration in the masked central part unchanged For all illumination doses we observe the quenching of SdH oscillations and the shrinking of the Hall plateaus There is no concentration difference in type-B devices

11. The analysis will be given elsewhere

12. P L McEuen, A.Szafer, C.A Richter, B W Alphenaar, J K Jain, A D Stone, R G Wheeler and R N Sacks, Phys Rev.Lett 64, 2062 (1990)

13. S Komiyama, H Hirai, M Ohsawa, Y Matsuda, S Sasa, and T Fujii, Phys Rev B 45, 11085 (1992) and references therein

14 D L Maslov, Y B Levinson, and S M Badalian, Phys Rev B 46, 7002 (1992)

15 Note that impurity scattering is mainly responsible for the inter-edge scattering [13,14] However, this is not sufficient to reach the true equilibrium and some inelastic process has to be involved in the thermalisation On the other hand, the elastic process may be the one which determines the observed temperature dependences as in the case of impurity scattering in normal metals

16 A K Geim, P C Main, P H Beton, P Streda, L Eaves, C D W Wilkinson, and S P Beaumont, Phys Rev Lett 67, 3014 (1991)

TuP39

Giant Temperature Resonances of Noise in Submicron Quantum Well Structures

A.K Geim[a], S T.Stoddart, S J.Bending
School of Physics, University of Bath, Claverton Down, Bath BA2 7AY, UK
J J Harris
Interdisciplinary Research Centre, Imperial College, Prince Consort Road, London SW7 2BT
A J Peck
Max-Planck-Institute fuer Festkoerperforschung, Heisenbergstr.1, D-70569 Stuttgart, Germany
K Ploog
Paul-Drude-Institute fuer Festkoerperelectronik, Hausvogteiplatz 5-7, O-1086 Berlin, Germany

We show that excess noise in micron-sized samples fabricated from Si-doped GaAs/GaAlAs quantum wells and heterostructures is a strong non-monotonic function of temperature with several sharp peaks below room temperature The noise power at the peaks exceeds the background noise by several orders of magnitude The observed behaviour represents a classical noise source where only a *single* type of switching defect with a well-defined activation energy is present We attribute the resonances to deep metastable donors and provisionally identify one of the donors as the known DX-center in GaAs and GaAlAs

Low-frequency noise in solids has received considerable attention in recent years It has been shown that almost any resistor demonstrates excess noise with an approximately 1/f-shaped power spectrum and it is well established that this noise can be described as arising from the thermally activated switching of defect states [1,2] Each defect gives rise to a Lorentzian power spectrum whose superposition leads to 1/f-noise if the distribution of relaxation rates is fairly flat Recently, using sufficiently small-length-scale devices random telegraph noise due to single defect switchings has been observed [3-5] If the sample size is increased, the number of the elementary noise sources increases and it is possible to follow the transformation of the telegraph noise into 1/f-noise [2-4] New noise sources can also be activated by raising the temperature which changes the spectrum into 1/f-form and leads to a monotonic increase of the noise power

In this paper we report noise with a resonant-like temperature dependence Sharp peaks in the noise have been seen against a negligibly small background in micron and submicron devices fabricated from δ-doped GaAs quantum wells and GaAlAs/GaAs heterostructures containing a high-mobility two-dimensional electron gas (2DEG) The temperature resonances in the noise are in striking contrast with one's common experience that noise is a monotonic or, at least, smooth function of temperature (see reviews [1],[2]) Despite the fact that this type of noise behaviour has never been observed before, we show that it corresponds to the simplest model of random telegraph noise [1,2,6] The observed noise arises when the switching defects are *exactly the same* and differences in their thermally activated relaxation times τ are minimal This condition appears to be fulfilled in Si-doped GaAs and GaAlAs where the dominant defect (Si) becomes metastable at high concentrations [7] A Si atom can only occupy a few strictly determined sites in the crystal lattice of GaAs and its energy is not affected by lattice imperfections as in the case of polycrystalline and amorphous materials which have previously been studied We show that the dominant contribution to the observed noise arises from the thermally activated switching of DX-like centres [7] The noise can be persistently quenched by

infra-red illumination which also leads to persistent photoconductivity (PPC) in our structures The switching defects influence the electrical conduction due to the sensitivity of the resistance of a small sample to the state of every single impurity within it

Two types of structures have been investigated in our experiment The δ-doped GaAs quantum wells were grown by molecular-beam epitaxy on semi-insulating GaAs substrates and consisted of 500nm of undoped $Ga_xAl_{1-x}As$ followed by a GaAs quantum well of the width in the range 10-20nm and terminated with 250nm of undoped $Ga_xAl_{1-x}As$ and 20nm GaAs capping layer A Si delta-doped plane of nominal concentration in the range (2 5-5)x10^{12}cm^{-2} was placed in the centre of the quantum well. The quantum confinement of the Si doping layer increases the separation between the two-dimensional (2D) electron subbands and allows one to work in the simplest situation when only one 2D subband is occupied Further information about the structures and their characterisation can be found elsewhere [8] The second type of structure we have studied is the standard modulation-doped GaAlAs heterostructure with 2D electron concentration ≅2.7x10^{11}cm^{-2} and mobility ≅750 000cm^2/Vs at 4 2K

Hall bar structures with several voltage probes were fabricated using photolithography and wet chemical etching. Samples with different conducting widths b between 0 5 and 8μm have been investigated and the separation between the centres of adjacent voltage probes is twice the characteristic sample width DC currents between 1 and 100 μA/μm are passed through the sample and signal fluctuations at the voltage probes ($\sqrt{\langle \Delta I^2 \rangle}$) are measured using the noise option of a EG&G 5210 Lock-in amplifier at a chosen frequency f in the range 1-104Hz Bandwidths Δf in the range 0 1-1Hz around the centre frequency were selected Figure 1 shows typical examples of the temperature dependence of the noise at f=30Hz for both types of structure studied Three peaks near 50, 80 and 170K are clearly seen for the case of the 10nm wide delta-doped quantum well (n_{2D}=5x10^{11}cm^{-2}) and only one peak near 180K has been observed for the modulation doped sample

We find that the noise signal changes linearly with the current ($\sqrt{\langle \Delta I^2 \rangle} \propto I$) indicating that these are fluctuations in the resistance R Consequently, experimental data are presented using the normalized noise power $S(f) = \langle \Delta I^2 \rangle / I^2 = \langle \Delta R^2 \rangle / R^2$ The power S is found to be inversely proportional to the distance between voltage probes and the sample width b (i e $S \propto 1/A$ where A is the sample area) In the plots, S is multiplied accordingly by the active area ($S_n = SxA$) and is given in units m^{2}Hz^{-1}

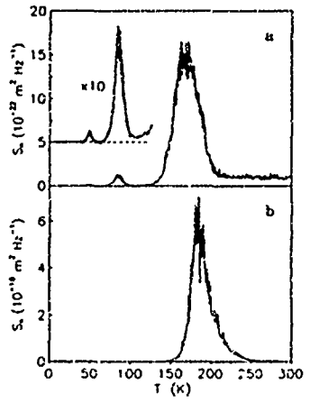

Figure 1 (a) Noise power as a function of temperature in a 2μm wide sample fabricated from a 10nm wide δ-doped GaAs quantum well and (b) in a 0 5μm modulation-doped heterostructure sample The low temperature section of Fig 1a is magnified by a factor of 10 and shifted for clarity

The positions and the amplitudes of the noise peaks as a function of temperature depend on the measurement frequency f Figure 2 shows an example of this dependence for the top trace in Fig 1 In Fig 3a,b the positions, T_{max}, and heights, S_n^{max}, of two of the noise maxima observed in the quantum well sample are plotted as a function of frequency We note that S_n^{max} decreases with frequency as $1/f$ and $1/T_{max}$ decreases as $\ln(f)$ At a fixed temperature, $S_n(f)$ has exactly the Lorentzian form $S_n(f) \propto [1+\alpha f^2]^{-1}$ as also shown in Fig 3a for the peak near 170K

All our results follow directly from the standard theory of excess noise [1,2] A switching defect can be characterised by its relaxation time τ and the magnitude δr of changes in the sample resistance $\Delta R(t) \equiv \delta r \exp(-t/\tau)$ The noise power spectrum due to N identical but uncorrelated defects is given then by

$$S(f) = N(\delta r/R)^2 \tau / [1+(2\pi f \tau)^2] \qquad (1)$$

At moderate temperatures the switches are usually thermally activated and can generally be described by $\tau = \tau_0 \exp(-E_A/kT)$ If there are many defects present with a wide spread in their activation energies E_A , the integration of Eq (1) leads to a 1/f dependence and the noise is a smooth function of temperature [1,2]

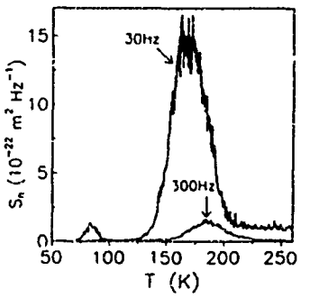

Figure 2. Noise peaks in the δ-doped GaAs quantum well of Fig 1 at two different measurement frequencies

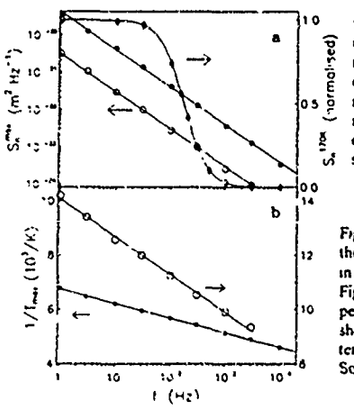

However, in the case where E_A and τ_0 have well-defined values, a noise peak will occur A characteristic frequency of the random resistance switches ($\nu \equiv \tau^{-1}$) changes exponentially rapidly with temperature, resulting in a resonance when ν matches the measurement frequency Due to this exponential behaviour the resonance can survive over a very wide frequency band

Figure 3 (a),(b)-Frequency dependence of the magnitude and position of noise maxima in the δ-doped quantum well structure of Fig 1 Open and closed circles are for the peaks near 80K and 170K respectively Also shown is the noise power spectrum for a fixed temperature of 170K (rhombic symbols) Solid lines are the best fits to Eq (1)

and for the maximum bandwidth $\Delta f = 10^5$Hz available in our experimental set-up (the integral noise power in the range f=1-10^{5}Hz) the peak widths in Fig 1 would only increase by a factor of three We note that more detailed models of two-state random telegraph noise [9,10] which take into account the balance between generation and recombination processes can not explain resonances in the noise The appearance of peaks requires that the recombination process is a background process and its relaxation rate not be coupled to the generation frequency via a balance equation

Equation (1) implies that $S_n^{max} \propto 1/f$ and $E_A/T_{max} = -\ln(2\pi f\tau_0)$ Solid lines in Fig 3 show the best fits to the experimental dependencies for the quantum well structure We obtain $E_A^1 \cong 0$ 1eV, $E_A^1 = 0$ 145eV, $E_A^3 = 0$ 37eV, where the upper index denotes different switching defects in the order of appearance with increasing temperature, and τ_0 is found to lie in the range 10^{-11}-10^{-13} sec When the values of E_A and τ_0 are known, Eq (1) allows us to compare directly the experimental temperature dependences of S_n with theory without using any fitting parameters An example of such a comparison is shown in Fig.4 where the theoretical curve follows the observed temperature dependence perfectly The agreement is excellent for peaks 1 and 2 although peak 3 is 30% wider than expected from Eq (1) probably indicating that there is some small spread in the value of the activation energy for this type of defect The same analysis for GaAlAs/GaAs heterostructure samples gives $E_A = 0.42(\pm 0.02)$eV and $\tau_0 \cong 10^{-13}$ sec

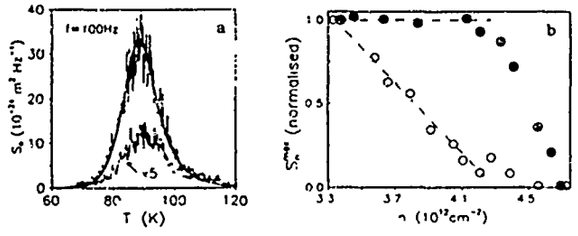

Figure 4 Persistent suppression of the noise peak by infra-red illumination in the δ-doped quantum well structure of Fig 1 (a) Noise in the dark (upper curve, n=3 3x10^{11}cm^{-2}) and after partial illumination (lower curve, $n\cong$3 8x10^{11}cm^{-2}) Solid line in Fig 4a shows temperature dependence of noise calculated directly from Eq (1) (b) Variation of the height of the noise peaks with total electron concentration

Both studied types of structure demonstrate strong low temperature persistent photoconductivity (PPC) indicating that deep metastable donors are present in a concentration comparable with the Si doping level Figure 4 shows a direct connection between the noise and PPC in the quantum well structure As the electron concentration increases upon infra-red illumination the noise decreases rapidly indicating that deep donors (probably DX-like centres whose concentration decreases under illumination) are responsible for the observed noise All the peaks are significantly suppressed by illumination Note that neither the position nor the shape of the peaks alters while the Fermi energ of the 2DEG increases substantially. This implies that conduction electrons at the Fermi level do not directly participate in the noise and we observe switches between the deep-donor state and some intermediate state rather than the shallow-donor state It is very probable that the dominant peaks near 170K in the noise spectra of both our structures are due to the known DX-center. The activation energy for this peak in the GaAlAs/GaAs heterostructure is in good agreement with the known value of 0 43eV for the DX-center in GaAlAs [7] However, the dominant peak in the quantum well has $E_A^3 = 0$ 37eV which is only in fair agreement with ≅0 33 eV measured by DLTS for the DX-center in n^+-GaAs [7] This is probably due to considerable changes in the band structure arising from δ-doping in a quantum well [8] Another deep donor in the quantum well device with an activation energy of 0 145eV can possibly be attributed to a donor which was found in $Al_xGa_{1-x}As$ for x<0 15 and has a thermal emission energy in the range 0 13-0 16eV [10] The donor responsible for the small peak near 50K remains unidentified

Note that different types of donor are present in the δ-doped GaAs quantum well rather than a single donor with different energy levels This is evident from Fig.4b which shows the dependences of S_n^{max} on electron concentration after illumination for the two major peaks in the quantum well sample The very different behaviour of the peaks under illumination implies that different defects are responsible for these resonances It is clear from Fig.4b that illumination removes the captured electrons much easier from defects of type 2 and only then starts to depopulate type-3 deep donors This difference in sensitivity to illumination for the two states has been directly confirmed by measuring the time variation of the total concentration under continuous illumination which shows two distinct levels of saturation, one with a short and another with a long time constant

Finally, we discuss the scaling of the noise and its absolute magnitude A switching DX-like center changes the scattering cross-section for conduction electrons (σ) by a value $\delta\sigma$ First order corrections to the Boltzman equation due to the switching of a single impurity lead to resistance changes $\delta r/R = (1/N)\delta\sigma/\sigma$ where N_i is the total number of impurities in a sample which differs from the number of switching defects N [11] The noise power in the peak (see Eq 1) is given $N(\delta r/R)^2 \propto N/N_i^2 \propto 1/A$ as observed in the experiment Assuming that the impurity concentration N/A is equal to the doping level, data in Figures 3a and 4b can be used to show that $\delta\sigma/\sigma \cong 0.1$ and 0 3 for peaks 2 and 3 in the quantum well structure, respectively The fact that the inferred values of $\delta\sigma/\sigma$ are of the order of unity confirms that coupling between the switching defects and the conductance occurs via a change in the scattering cross-section of the DX-like centres This simple consideration is not directly applicable to the modulation-doped heterostructure since donors are remote from the carriers, phonon scattering is dominant for the 2DEG at these temperatures and a parallel conductance in the Si-doped GaAlAs layer is probably present

In conclusion, micron-sized samples of δ-doped GaAs quantum wells and modulation-doped heterostructures show giant peaks in the temperature dependence of the excess noise power This noise is caused by the temperature activated switching of many Si donors with a single well-defined relaxation rate The defect leading to the strongest resonance near 170K is tentatively identified as the known DX-center Noise measurements of the type described here represent a powerful tool for the identification and characterisation of deep metastable defects and have clear implications for practical limits on the operation of submicron quantum well devices

This work was supported by SERC grant No GR/H23573

LIST OF REFERENCES

[a]Current address Physics Department, University of Nottingham, Nottingham NG7 2RD, England

1 P Dutta and P M Horn, Rev Mod Phys 53, 497 (1981)
2 M B Weissman, Rev Mod Phys 60, 537 (1988)
3 K S Ralls, W J Skocpol, L D Jackel, R E Howard, L A Fetter, R W Epworth, D M Tennent, Phys Rev Lett 52, 228 (1984)
4 C.T Rogers and R A Buhrman, Phys Rev Lett 55, 859 (1985) C T Rogers, R A Buhrman, H Kroger, L N Smith, Appl Phys Lett 49, 1107 (1986)
5 C E Parman, N E Israeloff, K Kakalios Phys Rev B 44, 8389 (1991) and Phys Rev Lett 69, 1097 (1992)
6 A L McWhorter, in *Semiconductor Surface Physics* edited by R H Kingston (University of Pennsylvania, Philadelphia, 1957)
7 P M Mooney, J Appl Phys 67, R1 (1990)
8 J J Harris, R Murray and C T Foxon, Semicond Sci Technol (to appear)
9 S Machlup, J Appl Phys 25, 341 (1954)
10 J R Kirtley, T N Theis, P M Mooney, S L Wright, J Appl Phys 63, 1541 (1988)
11 R S Sorbello, G S Chu, IBM J Res Develop 32, 58 (1988)

TuP40

NON-LINEAR TRANSPORT PROPERTIES OF MINIBAND CONDUCTION IN THE PRESENCE OF CROSSED ELECTRIC AND MAGNETIC FIELDS: A SEMI-CLASSICAL APPROACH

F Aristone[†‡], J F Palmier[§], A Sibille[¤], D K Maude[†], J C Portal[†‡] and F Mollot[¢]

† CNRS-SNCI, B P 166-X, 38042 Grenoble Cedex - France
‡ CNRS-LPS-INSA, Complexe Scientifique de Rangueil, 31077 Toulouse Cedex - France
§ CNET, 196 Av Henri Ravera, 92220 Bagneux Cedex - France
¤ ENSTA - Dept d'Electronique, 32 Boulevard Victor, 75015 - Paris - France
¢ IEMN - DHS / UMR - USTL, 59655 - Villeneuve d'Ascq - France

ABSTRACT *In this paper we compare a series of perpendicular transport measurements for short period GaAs-AlAs superlattices in presence of a magnetic field applied parallel to the layers with the semi-classical calculations of the miniband conduction properties. The theoretical approach takes into account the local solution of the Boltzmman equation in the presence of scattering mechanisms such as phonons and interface fluctuations. The Poisson and drift-diffusion equations have been self-consistently solved to obtain the current density versus the applied electrical field characteristics, which is directly compared with the experimental measurements. A good agreement is found at 300K for all values of the electric and magnetic fields. At low temperatures a pronounced disagreement is observed when the electric field F is greater than the critical value F_c that determines the negative differential resistance regime in the current-voltage characteristics. We discuss the physical origin of this difference.*

The concept of superlattices (SL's) was introduced some years ago by L Esaki and R Tsu[1] as a new class of semiconductor material SL's are formed by the alternate growth of electronically different materials (typically two) along one direction, with individual widths small enough to give significant quantum effects, i e , of the order of 100Å This new one-dimensional man-made crystal presents a Brillouin zone smaller than that of the bulk materials due to the larger period of the artificial lattice The energy spectrum along the growth direction is composed of minibands and minigaps The first miniband width for conduction electrons is typically of the order of a few meV up to 200meV in comparison to the usual 1eV for the conduction band in pure materials These minibands occur because of the non-zero tunnelling probability between two consecutive wells The energy-momentum dispersion of these minibands should allow the observation of the negative differential velocity (NDV) regime for electrons moving in the presence of a sufficiently large applied electrical field The NDV regime is a direct consequence of the negative effective mass experienced by the carriers

This new type of material with a miniband width controllable only by external (growth) parameters has attracted much interest due to the potential applications for the elaboration of devices such as ultra-high frequency (≥10GHz) oscillators Very recently Hadjazi et al [2] have obtained a 60GHz oscillator with a GaAs-AlAs SL structure SL's have been studied either by electrical transport measurements, such as thermal-saturation of miniband transport[3], tunnelling between two-coupled SL's[4], under hydrostatic pressure[5] and also using optical techniques such as photo-luminescence[6] and electro-reflectance[7]

The existence of the NDV regime in SL's as a bulk material effect has been demonstrated by Sibille et al [8] in undoped samples Studying n-type doped samples they also demonstrated the existence of the negative differential resistance (NDR) in

short period SL's[9] Palmier and co-workers[10] have calculated in detail the effects of a crossed electric and magnetic fields in the velocity versus the electrical field relation -V(F)- by solving the Boltzmman transport equation in the presence of a limited number of scattering mechanisms

As a starting point we take the local V(F) relation and calculate the current density as a function of the applied bias voltage solving a self-consistent system of the Poisson and drift-diffusion equations taking into account the conservation of the carriers These results are directly compared to the experimental curves, obtained for different values of the applied magnetic field and over a range of temperature

The samples studied consist of a series of periodic SL's of GaAs-AlAs hetero-layers grown my molecular-beam-epitaxy They are lightly Si-doped i.e., $n \approx 2\times10^{16}cm^{-3}$ and were grown on a highly doped substrate ($\approx 2\times10^{18}cm^{-3}$)

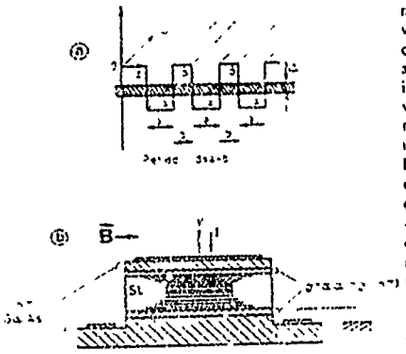

Figure 1 *Schematic SL device and the experimental set-up* (a) *Potential profile for a periodic SL of materials A and B. Δ is the miniband width of accessible energy for electrons.* (b) *SL device in presence of the applied electric and magnetic fields*

The doping concentration was graded on either side of the active region to avoid abrupt hetero-junctions between the SL and the contacts Standard contact techniques with typical mesa's areas of $2800\mu m^2$ were used

In this work we present results obtained for 3 samples of miniband widths equal to 4, 9 and 16 meV These samples are nominally of 22/8, 19/5 and 22/5 monolayers of GaAs/AlAs respectively The active region is about $1\mu m$, which means typically a total of 125 periods in each sample The miniband widths have been calculated using a K P model, taking into account a constant averaged mass of GaAs and AlAs Identical results have also been obtained using a transfer matrix approach

In Fig 1 a schematic representation of the sample structure is shown The miniband width, the applied electric field and the orientation of the magnetic field are represented Only the Γ conduction band for the GaAs and for the AlAs is shown

Transport properties of electrons moving along the growth direction of a SL were first investigated by Shik[11] He also considered the presence of a magnetic field applied perpendicular to current However, in his approach only low values of B for which the energy quantisation by the magnetic field was negligible have been take into account Recently Palmier et al[10] have presented a detailed numerical solution of the Boltzmman equation under the same conditions and they obtained the local V(F) -velocity versus the applied electrical field- characteristics for different values of the magnetic field intensity In their work the temperature T and the interface fluctuation Δ that describes the interface roughness, are additional parameters in the formulation of the problem

We have considered the solution of the Boltzmann equation in presence of polar optical and transversal phonons together with the interface roughness scattering mechanisms, as described in ref[10] To calculate the J(V) -current density versus the applied bias voltage- curve in order to compare it with experimental results we have used the Poisson equation

$$\frac{\partial F}{\partial z} = -\frac{q}{\varepsilon_r}(n - N_d) \qquad (1)$$

and the drift-diffusion equation

$$J_n = q\left\{ n\, V_D(F) - D_n(F)\frac{\partial n}{\partial z}\right\} \qquad (2)$$

where n is the density of negative carriers, N_d is the doping concentration of donors, ε_r is the static dielectric constant and D_n is the diffusion constant The carriers conservation equation in the absence of any generation and recombination mechanism (dark conditions of measurements) and in steady-state condition is given by

$$\frac{1}{q}\frac{\partial J}{\partial z} = 0 \qquad (3)$$

In order to apply suitable boundary conditions we simply write Eq (1) in terms of the electrostatic potential φ, given by $F = \frac{\partial \varphi}{\partial z}$, and from Eqs (2) and (3) we obtain

$$\frac{\partial}{\partial z}\left\{q\, n\, V_D(F) - q\, D_n(F)\frac{\partial n}{\partial z}\right\} = 0 \qquad (4)$$

Assuming a starting known expression for the n(z) distribution and the F(z) in Eqs (1) and (4) respectively we rewrite (1) and (4) in terms of difference equations using the finite-element method (FEM)[12] The non-linear decoupled system is solved by the Newton-Raphson algorithm The iterative procedure is repeated until a stable and convergent solution for n(z) and F(z) is simultaneously obtained We note that the present model may not be applied when $\frac{\partial V_D}{\partial F} < 0$ nor when $N_d L$ exceeds a certain critical value[13], where L is the length of the (active) SL region This procedure has been validated for pure GaAs samples, whose $V_D(F)$ law is well known

In our experiments we have measured the current-voltage characteristics for a series of samples in presence of a magnetic field applied parallel to the SL's interfaces, i.e., perpendicular to the current direction In Table I we present the most important parameters of our samples

Typical J(V) characteristics for each sample are shown in Fig (2) for different temperatures The current increases with applied bias for applied electric fields less than the critical value F_c At room temperature we observe that the current intensity does not really decreases but remains almost constant when the applied electric field is higher than F_c

When the temperature decreases the current intensity decreases abruptly for electric fields such that $F > F_c$, i.e., the NDR is more pronounced and the peak in the J(V) curves is clear The increase of the current when the temperature decreases is essentially due to the decrease of the scattering relaxation time τ, which occurs because phonons scattering is less important at lower temperatures At very low temperatures (T≈50K) the current decreases with the decreasing temperature A more detailed discussion of these effects will included in a future publication

Sample	Δ(meV)	widths (Å)	# of periods
S1	4	62/22	118
S2	9	54/20	135
S3	16	62/14	131

Table I *Main parameters of the 3 samples studied in this paper The minibands widths have been calculated with a Kronig-Penney model using a constant averaged mass and also using the transfer matrix technique The period of these SL's have been obtained from X-ray diffraction The electrical contacts were formed using standard Lithographic techniques and had an areas of $2800\mu m^2$ The active region of the samples were doped at $2\times10^{16}cm^{-3}$*

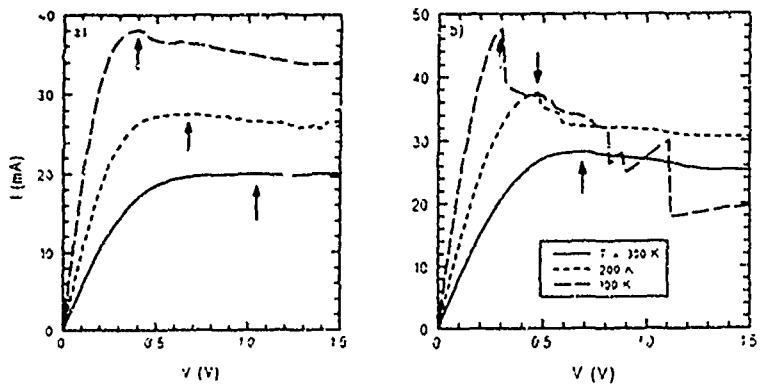

Figure 2 *Experimental I(V) characteristics for samples S2* (a) *and S3* (b) *-see Table 1- for B=0T. The variation of temperature is shown in the insert. The critical electric field F_c is indicated by the arrows and shifts to high values when the temperature increses. We note that the NDR is more pronounced for low temperatures*

For all temperatures and nunband widths we have observed that with increasing magnetic field F_c shifts to higher values. This effect occurs mainly because of the distortion of the electronic orbits . . . e presence of the magnetic field, which tends to localize the electronic movement. A small effect due to the nature of scattering mechanisms is present although it is only a second order correction.

In Fig (3) we have plotted both experimental and calculated J(V) curves. In spite of the fact that our model can not be applied for electric fields higher than F_c we do not observe a strong disagreement between theory and experiment at high temperature for electric fields in the NDR region. However, in the low temperatures regime the experimental results in the NDR region diverge from the calculated values. A satisfactory agreement is achieved in the non-linear but positive domain of the differential resistance. We do not obtain from our analysis a decrease in the current density, i.e., the NDR because the the assumptions on which our model is based are no longer valid in this region. The shift of the critical field F_c to higher values due to the presence of the applied magnetic field is understood in terms of a competition between electric localisation, i.e., the Bragg reflection at the Brillouin zone and the magnetic localisation.

From our analysis we have observed that a relatively simple classical description of the transport properties in a Si lead to a satisfactory agreement in all of the positive domain of the differential resistance. However a better quantitative agreement between the theoretical and experimental results of the NDR region remains to be obtained.

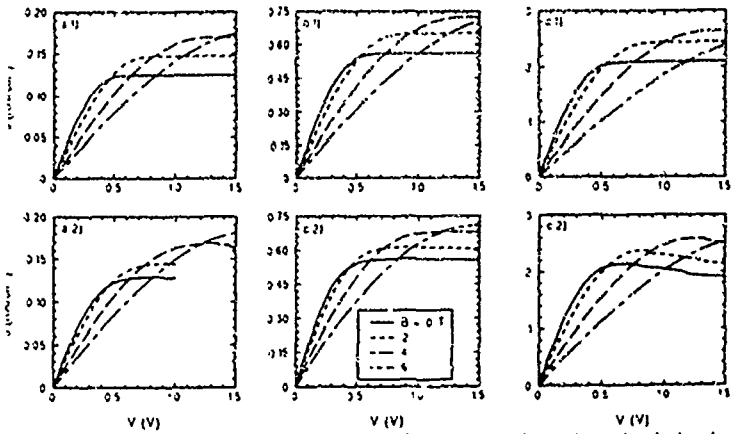

Figure 3 *Direct comparison between experimental results (a 2, b 2, c 2) and calculated curves (a 1, b 1, c 1) for samples S1* (a), *S2* (b) *and S3* (c) *-see Table 1- for T=300K. Very good agreement is obtained for all curves below the critical electric field F_c. Fairly agreement is obtained in the NDR region. We note that the disagreement in the NDR region increases with decreasing temperature*

ACKNOWLEDGEMENTS

We thank S Vuye and J C Esnault for sample mounting and M Rabary for technical support. F A is grateful to CAPES-Brazil for a grant. We acknowledges CNET, EEC and Conseil Regional des Midi-Pyrenees for financial support.

REFERENCES

[1]L Esaki and R Tsu, *IBM J Res Develop* 14(1970)61

[2]M Hadjazi, J F Palmier, A Sibille, H Wang, E Pans and F Mollot, *Electr Lett*, 29 (1993) 648

[3]G Brozak, M Helm, F de Rosa, C H Perry, M Koza, R Bhat and S J Allen Jr, *Phys Rev Lett* 64 (1990) 3163

[4]R A Davies, M J Kelly and T M Kerr, *Phys Rev Lett* 55 (1985) 1114

[5]F Aristone, A Sibille, J F Palmier, B Gonthier, J C Portal and F Mollot, *Jpn J Appl Phys.* 32 (1993) 144

[6]B J Skromme, R Bhat, M A Koza, S A Schatz, T S Ravi and D M Huang, *Phys Rev Lett* 65 (1990) 2050

[7]P Voisin, J Bleuse, C Bouche, S Gaillard, C Alibert and A Legreny, *Phys Rev Lett* 61 (1988) 1639

[8]A Sibille, J F Palmier, H Wang and F Mollot, *Phys Rev Lett.* 64 (1990) 52

[9]A Sibille, J F Palmier, H Wang, J C Esnault and F Mollot, *Appl Phys Lett* 53 (1990) 256

[10]J F Palmier, G Etemadi, A Sibille, M Hadjazi, F Mollot and R Planel, *Surface Science* 267 (1992) 574

[11]A Ya Shik, *Soviet Phys Semicond* 7 (1973) 187

[12]J F Palmier, *Resonant Tunneling in Semiconductors*, Edited by L L Chang et al, Plenum Press, New York, 1991 p 361

[13]Hakki, B W *J. Appl. Phys* 32 (1967) 808

Wednesday, August 25

WeA Metal/Semiconductor and Type II Interfaces

WeB Atomic Scale Characterization

WeA1

Electronic Interactions at Superconductor-Semiconductor Interfaces

Herbert Kroemer, Chanh Nguyen, and Evelyn L. Hu
Department of Electrical and Computer Engineering
University of California, Santa Barbara, CA 93106

Abstract

Two current flow mechanisms across a superconductor-semiconductor-superconductor double heterostructure are discussed: The conventional proximity effect, and Andreev reflections. The emphasis is on Nb-InAs-Nb structures, with the InAs being in the form of a quantum well with AlSb barriers, for which current flow by multiple Andreev reflections can lead to an enhancement of the zero bias conductance by a large factor. For sufficiently short inter-electrode spacings, the multiple Andreev reflections can lead to a true supercurrent flow.

Introduction

When a superconductor and a semiconductor are brought together into atomically intimate contact, with an interface that is free from intervening oxides and /or contaminants, and which does not form an electron-blocking Schottky barrier, the electrons in the two materials can interact with each other in ways that can drastically alter the current flow through what may be called "super-semi-super double heterostructures." An example of a particularly suitable structure for the observation of such interaction effects is shown in Fig. 1 [1-3]. It consists of a thin layer of InAs, in which the electrons are confined at top and bottom by AlSb barriers, forming a 2D electron gas. This gas is then contacted by superconducting Nb electrodes

One of the reasons for the use of InAs is that the Fermi level at Metal-InAs contacts tends to be pinned inside the InAs conduction band, thus leading to an absence of Schottky barriers impeding the flow of electrons. As a result, such structures behave like pure resistors above the critical temperature of the Nb electrodes (9.2 K), and any new effects due to super-semi interactions are especially pronounced, unencumbered by non-superconducting complications. The reason for singling out a quantum well over a bulk structure is to achieve high electron concentrations by modulation doping while retaining high mobilities [4], and to suppress mobility reductions due to surface scattering, a problem especially severe with InAs, because of the absence of surface band bending. Typical sample parameters are: Well width of 15nm, a channel length ranging from sub-μm dimensions to several μm, and an electron sheet concentration of several-times $10^{12}cm^{-2}$.

The super-semi interaction effects in such structures are pronounced. Fig. 2 shows the 4.2K differential conductance of a structure as in Fig. 1, as a function of bias voltage [3]. The device shows a very narrow conductance spike around zero bias, inside which the conductance is enhanced by a factor 7 relative to the conductance just above the critical temperature of Nb (9.2K). With increasing bias the conductance decreases, but shows a rich structure up to bias voltages equivalent to the superconducting gap of Nb (≈3.2 mV). These phenomena disappear when the Nb electrodes "go normal."

The structure and the behavior shown are by no means the only manifestation of super-semi interactions, nor are advanced quantum well structures necessary for all such observations. A variety of interaction phenomena have been observed in a variety of structures, employing a variety of semiconductors, including GaAs [5], (Ga,In)As [6], and Si [7]. Complete references can be found in the papers cited.

Proximity Effect, Weak Links and Josephson FETs

There are two distinct basic forms of super-semi interactions: The well-known *Proximity Effect*, and the less-well-known, but perhaps more important *Andreev Reflections*.

In the conventional proximity effect, the Cooper pairs that are the carriers of supercurrent inside the superconductor, can tunnel into the a normal conductor, causing induced superconductivity there, falling off exponentially with distance, with a characteristic length called the *coherence length*. If the separation between the superconducting electrodes is sufficiently small — typically of sub-μm dimensions — this can lead to what is called a *weak link*, a structure capable of carrying a true resistance-less supercurrent through the semiconductor.

In 1980, Clark et al. [8] drew attention to the promise of semiconductors rather than conventional metals as the non-superconductor in proximity effect studies. They proposed a Hybrid Josephson FET (= JOFET), basically a weak link the critical current of which can be modulated, leading to a current-voltage characteristic resembling that of a field effect transistor, except for a very different voltage scale, in the low-millivolt range, and of course a very different physics. The central idea was that the critical current that can be passed through a weak link employing the proximity effect depends strongly on the superconductive coherence length inside the semiconductor, which in turn depends on the electron

concentration in the semiconductor, which can be modulated with a gate electrode. The overall result would be a current-voltage characteristic as *shown* schematically in Fig. 3.

What distinguishes JOFETs from conventional FETs are not only the much lower voltage (and current) scales, but the existence of a *true* zero-resistance on-state. This makes a JOFET a device of potential interest as a current routing switch in superconducting networks. There is some doubt as to whether such JOFETs would ultimately be useful as amplifiers or logic gates: The gate voltage swings required for current modulation tend to be larger than the drain voltage swings obtainable from the current modulation.

Clark et al. pointed out that InAs appeared to be the ideal semiconductor for such studies, not only because of the absence of Schottky barriers at metal-to-InAs interfaces, but also because of its unusually high *electron mobilities*, which in turn reflect the low effective mass of electrons in InAs. Because of this low effective mass, heavily n-type doped InAs has a Fermi velocity approaching that of many true metals, and as a result, InAs in contact with a superconductor behaves more like a high-mobility metal than like a semiconductor. In particular, large coherence lengths should be achievable.

Weak links and JOFETs employing a Nb-InAs-Nb structure were subsequently demonstrated, by Takayanagi et al. [2, 3], followed by others. However, the current-voltage characteristics of those early structures were relatively poor, and JOFETs with much better characteristics were obtained in GaAs and even Si [7], despite the theoretical superiority of InAs. Perhaps the most interesting of those early JOFET structures was that of Ivanov et al [5], which appears to have been the first to employ a quantum well channel [GaAs-(Al,Ga)As] in a weak link or JOFET, demonstrating the superiority of such a design.

Following the development of a technology for high-quality InAs-AlSb quantum wells during the '80s, we ourselves turned to the problem of InAs weak links, and the balance of this paper deals with that work. In 1990 were able to demonstrate weak links showing unprecedentedly high critical current densities above 2×10^5 A/cm^2 for a remarkable large n^+-electrode spacings of 0.6μm [1]. We were naturally interpreting these results as caused by the conventional proximity effect. More recent observations challenge this interpretation, and suggest a different superconductivity mechanism in terms of multiple Andreev Reflections, our next topic.

Andreev Reflections

Consider a semi-super interface between a degenerately doped semiconductor and a superconductor, with a band diagram as shown in Fig. 4. On the superconductor side, a superconducting energy gap has opened up. If now a small bias voltage V is applied, as shown, the existence of the gap then prevents a *single* electrons at the Fermi level of the semiconductor from entering the superconductor. This argument suggests that, in the absence of the proximity effect, the onset of superconductivity in the metal thus actually *increases* the electrical resistance to current flow across the interface, due to this gap formation. However, even a single electron may pair up with a second electron at the bias energy qV *below* the Fermi level, forming a Cooper pair, which *can* enter the superconductor, causing a doubling of the current compared to that in the absence of superconductivity, rather than the reduction that would occur in the absence of this pair formation. As the electron below the Fermi level is removed from the semiconductor, it leaves behind a hole below the surface of the Fermi sea. The generally accepted jargon associated with this phenomenon is to say that the incident electron is *reflected as a hole*, a kind of reflection process called an *Andreev reflection*, honoring the originator of the concept [11]. The *Andreev hole* left behind, being a "bubble" under the surface of the Fermi sea in the conduction band, must not be confused with a valence band hole.

In a semiconductor with a large mean free path for the electrons (≈3μm in our structures), the Andreev hole left behind at the interface has a large mean free path itself, roughly equal to that of the electrons, and theory shows that the hole travels back into the semiconductor along a trajectory that is essentially the time reversal of the trajectory of the original incident electron. If its mean free path is sufficiently large, the hole will eventually reach the negative superconducting electrode. If the bias across the structure is sufficiently small, the energy of the hole is still within the superconducting gap on that side. Such a hole cannot enter the superconductor, but it can be annihilated by breaking up a Cooper pair inside the adjacent superconductor: One of the electrons of the pair annihilates the hole, the other electron takes up the annihilation energy, and is injected into the semiconductor as a ballistic electron above the Fermi level, at an energy above that of the initial electron. This process, illustrated in Fig. 5, can evidently be repeated, until either an electron or a hole has been "pumped up" to an energy outside the superconducting gap, on one of the two sides of the structure. If all reflections of electrons and holes were Andreev reflections rather than "ordinary" reflections, the result would be an enhancement of the conductivity by a factor equal to the number of ballistic round trips before escape or before collision events randomize either the electron or the hole flow in this chain reaction. As a rule, the conductance enhancement in past structures has been much smaller, presumably due to a low AR probability, itself caused by strong normal reflections due to residual potential barriers at the interfaces.

One of the "fingerprints" of multiple ARs is a rich "sub-harmonic gap structure" in the conductance-vs.-voltage characteristic, with steps occurring at voltages equal to the integer fractions of the superconducting gap voltage [12-14]. A discussion of this structure lies outside the scope of the present paper, but the occurrence of such a structure is evident in the characteristics of Fig. 2, thus clearly indicating the multiple-AR origin of the conductance peak. What is new compared to earlier data reported in the literature is the huge enhancement in the differential conductance, by a factor of seven in the example of Fig. 2. The behavior appear superficially as if the proximity effect were present. However, we will show below that contact resistance measurents rule out such an explanation.

Andreev-Reflection-Induced Superconductivity?

The large conductance enhancement suggests that it might be instructive to carry the above multiple-AR argument to its extreme limit, the case of zero applied bias, and assuming that *all* reflection events at the Sp-Sm interfaces are AR events, and that *no* scattering of any kind *inside* the semiconductor randomizes the electron and hole velocities. In this case, a given AR "chain" would go on forever. During each electron-hole round trip, one Cooper pair is annihilated at one of the electrodes, and re-constituted at the other electrode on the opposite side, leading to the net transfer of one Cooper pair per round trip. Given an initial net current, this current would persist, just as in the proximity effect, but by an altogether different mechanism.

These are extreme assumptions, especially the assumption of a 100% AR probability, yet the final conclusion appears to be correct. The quantum mechanics of this hypothetical multiple-AR mechanism has recently been analyzed in detail by Schlüssler and Kümmel (SK) [15], using a model assuming the existence of a *definite fixed phase difference* between the pair potentials in the two superconducting electrodes, and neglecting scattering in the semiconductor channel, but not assuming a 100% AR probability. The authors showed that under their conditions the multiple Andreev Reflections of phase-conjugate ballistic quasi-particles (i. e., electrons and Andreev holes) form indeed a very effective mechanism for Cooper pair transfer between the electrodes, capable of carrying a much higher zero-resistance current densities than the conventional proximity effect.

We believe that the narrow central conductance spike shown in Fig. 2, with the up-to-sevenfold enhancement of the differential conductance, is a *precursor* of the true Andreev-caused supercurrent postulated above, and analyzed by SK. We have to call it a precursor, because our data indicate a still-finite conductance, occurring over a narrow but nonzero voltage range (≈ 5μV). Presumably, the finite height and width of the central conductance

spike is the result of residual scattering events present in the relatively long (1 µm) InAs-AlSb QW channel, eventually randomizing the quasiparticle velocities. Furthermore, we believe that the true superconducting limit can indeed be achieved in Nb-InAs-Nb quantum well structures with a shorter inter-electrode spacing.

In their work, SK *assume* that there is a fixed phase relation between the pair wave functions in the two superconducting electrodes, and analyze the consequences. They do not address the question of how such a phase relation, and with it any supercurrent, might be maintained in the presence of scattering in the semiconductor channel. In the absence of such scattering, the assumption of a fixed phase relation between the pair wave functions in the two superconducting electrodes is entirely self-consistent. On the other hand, in the presence of sufficiently strong scattering, as in the case of a sufficiently wide inter-electrode spacing, any current not driven by an external voltage must eventually decay. This raises the question as to the nature of the transition to the SK superconducting limit, as the scattering in the semiconductor channel is reduced, by reducing the temperature and/or the inter-electrode spacing: Will the zero-bias resistance of the overall structure drop towards zero continuously, without ever reaching the true superconducting limit? Or will collective effects cause a "condensation" of the Andreev pairs into a new correlated many-body state, in which the de-phasing effects of scattering are quenched, similar to the way the BCS transition quenches the ordinary resistivity in a BCS superconductor?

We believe that the latter is indeed the case, and that our earlier observation of very large weak link current densities in structures with 0.6µm electrode spacing was indeed an manifestation of such a mechanism. To pursue this idea further, we have utilized laser holography to prepare what is essentially a grating of ≈300 parallel Nb lines making periodic contact to an InAs quantum well with AlSb barriers, with a 1µm period and a ≈0.4µm spacing between the Nb lines. The rest of the technology was basically the same as in the structure whose data were shown in Fig. 2. In the direction perpendicular to the grating lines, the structure acts basically as a series-connection of 300 diodes of the type shown in F.g. 1. At 4.2K, this structure showed a characteristic qualitatively similar to that of Fig. 2, with the "Andreev fingerprint" of sub-gap harmonics, but with a ≈300-fold enhanced voltage scale. More importantly, the conductance enhancement was by a factor 75, presumably as a result of the shorter inter-electrode spacing. With decreasing temperature, the zero-bias resistance dropped further, reaching an immeasurably low value between 3.9 and 3.8K.

This grating structure was still being evaluated at the time of the deadline for this manuscript; up-to-date results will be presented at the conference.

The Contact Resistance Problem

Our interpretation of the conductance enhancement in terms of multiple ARs rather than as a precursor of the ordinary proximity effect is supported by measurements of the specific contact resistance at the Nb-InAs interface, using the conventional *transmission line method* widely used in semiconductor technology [16]. The latter consists of measuring the set of voltage drops across a monolithic array of metal contacts to a thin semiconductor layer, with various lithographic inter-contact spacings L, and fitting the measured voltages and their current derivatives to an expression of the form

$$\frac{dV}{dI} = 2\frac{dV_c}{dI} + \rho_s \cdot \frac{L}{w}. \qquad (1)$$

Here I is the current through the array, w is the width of the array, and ρ_s is the ordinary sheet resistance of the semiconductor layer in the limit that L and w are large compared to the electron mean free path. In (1), the length-proportional term represents the "ordinary" path resistance of a semiconductor path of length L, and $2dV_c/dI$ represents the effects of whatever additional voltage drops are present at or near the two contacts. The latter include the true contact resistances at the two interfaces, plus any deviations from *bulk* behavior inside the semiconductor near the electrodes, for example due any proximity effect. If the latter is present, a DC current across the SpSm interface would be carried entirely by Cooper pairs. We would then expect the true contact resistance associated with the Nb-InAs interface to be zero, and the resistive portion of the semiconductor path to be shortened below the lithographic length, leading to a *negative* value of the intercept voltage $2V_c$ and to a negative *apparent* contact resistance, represented by the leading term in (1). Our measurements, shown in Fig. 6, indicate that the apparent contact resistance remains positive, thus ruling out the proximity effect as an explanation of the zero-bias conductance spike.

Acknowledgments

This work was supported in part by the Office of Naval Research and in part by the National Science Foundation, the latter through the NSF Science and Technology Center for Quantized Electronic Stuctures, Grant #DMR 91-20007, as well as through the NSF Materials Research Laboratory Program, Award #DMR 912-3048. One of us (C.N.) wishes to acknowledge the financial support from the UCSB Vice Chancellor's Fellowship for Advanced Research on Quantized Structures

References

[1] C. Nguyen, J. Werking, H. Kroemer, and E. L. Hu, Appl. Phys. Lett. **57**, 87 (1990).

[2] C. Nguyen, H. Kroemer, and E. L. Hu, Phys. Rev. Lett. **69**, 2847 (1992).

[3] C. Nguyen, H. Kroemer, and E. L. Hu, to be published (1993).

[4] C. Nguyen, B. Brar, C. B. Bolognesi, J. J. Pekarik, H. Kroemer, and J. H. English, J. Electron. Mater. **22**, 255 (1993).

[5] Z. Ivanov, T. Claeson, and T. Andersson, Jpn. J. Appl. Phys. **26 Supplement 3**, DP31 (1987). (Proc. 18th Internat. Conf. on Low Temperature Physics, Kyoto, 1987).

[6] A. Kastalsky, A. W. Kleinsasser, L. H. Greene, R. Bhat, F. P. Milliken, and J. P. Harbison, Phys. Rev. Lett. **67**, 1326 (1991).

[7] T. Nishino, M. Hatano, H. Hasegawa, F. Murai, T. Kure, A. Hiraiwa, K. Yagi, and Y. Kawabe, IEEE Elect. Dev. Let. **10**, 61 (1989).

[8] T. D. Clark, R. J. Prance, and A. D. C. Grassie, J. Appl. Phys. **51**, 2736 (1980).

[9] H. Takayanagi and T. Kawakami, Phys. Rev. Lett. **54**, 2449 (1985).

[10] H. Takayanagi and T. Kawakami, Proc. of Internat. Electron Devices Meeting, 1985, p. 98.

[11] A. F. Andreev, Sov. Phys. JETP **19**, 1228 (1964).

[12] T. M. Klapwijk, G. E. Blonder, and M. Tinkham, Physica B+C **109&110**, 1657 (1982).

[13] M. Octavio, M. Tinkham, G. E. Blonder, and T. M. Klapwijk, Phys. Rev. B **27**, 6739 (1983).

[14] K. Flensberg, J. B. Hansen, and M. Octavio, Phys. Rev. B **38**, 8707 (1988).

[15] U. Schussler and R. Kümmel, Phys. Rev. B **47**, 2754 (1993).

[16] R. E. Williams, *Gallium Arsenide Processing Techniques* (Artech House, Inc., 1984).

Figure Captions

Fig. 1. Schematic InAs-AlSb quantum well structure with superconducting Nb electrodes, for the investigation of electron-electron interaction effects across a super-semi interface

Fig. 2. Very strong enhancement at zero bias of the differential conductance of a recent InAs-AlSb quantum well structure with Nb electrodes [3], of the type shown in Fig. 1, with a 1μm electrode separation. The rich structure shown on the flanks of the central identifies the conductance peak as due to multiple Andreev reflections (see text)

Fig. 3. Schematic JOFET structure and its *I-V* characteristics.

Fig. 4. Andreev reflection (AR) of an electron at a biased super-semi interface.

Fig. 5. Multiple Andreev reflections (AR) alternating between the super-semi interfaces at opposite ends of the semiconductor region

Fig. 6. Zero-bias differential resistance $R = dV/dI$ at 4.2K of a set of Nb-InAs(QW)-Nb structures with different inter-electrode spacings, plotted as function of spacing. The straight line is a linear fit through the data, including a point at $L = 200\mu m$, not shown on the plot. The intercept value, representing twice the line contact resistance, is positive.

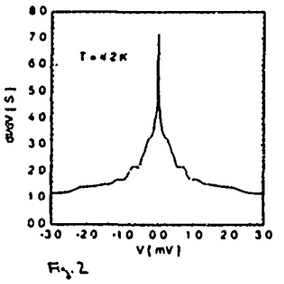

Fig. 2

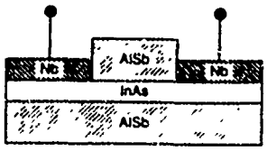

Fig. 1

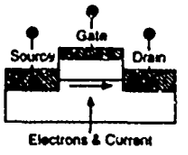

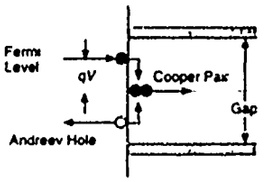

Fig. 4

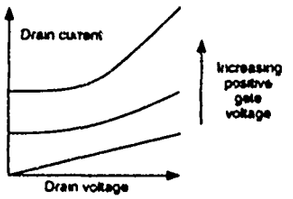

Fig. 3

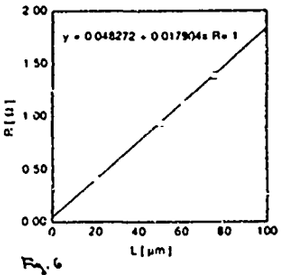

Fig. 6

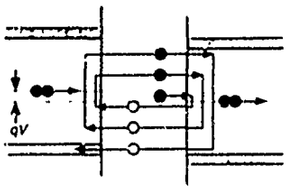

Fig. 5

WeA2

Direct Observation of the Semimetal to Semiconductor Transition in Crossed Band Gap Superlattices at Magnetic Fields of up to 150T

D.J. Barnes[a,*], R.J. Nicholas[b,a], R.J. Warburton[b], N.J. Mason[b], P.J. Walker[b] and N.Miura[a]

[a] ISSP, Tokyo University, Roppongi 7-22-1, Tokyo 106, Japan
[b] Physics Dept., Clarendon Lab., Parks Rd., Oxford OX1 3PU, U.K.

Abstract

Ultra-high magnetic field (>150T) cyclotron resonance has been performed on type II InAs/Ga(In)Sb superlattices. The electron density data reveals a dramatic depopulation at a critical magnetic field corresponding to the uncrossing of the lowest electron and hole Landau levels. The magnitude of this critical field decreases with decreasing superlattice period.

The type II heterostructure InAs/GaSb has an extreme band gap line-up such that the valence band of the GaSb lies at a higher energy than the conduction band of the InAs, resulting in charge transfer across the interface until the band bending equalises the Fermi energy across the two materials. Thus, electron and hole gases are intrinsically generated on either side of the interface [1]. When a superlattice is constructed from these materials the subband confinement energy can strongly modify this behaviour. The relatively light mass of the electron in the quantum wells of InAs (m^*=0.023) makes the subband energy extremely sensitive to the well width and so the electron energy can be pushed up through the valence band energy within feasible layer thicknesses, of order 85Å InAs [2]. Once this has been achieved, the band lineup is essentially semiconductor-like and the structure shows a rapid depopulation of the carriers.

The semimetal to semiconductor transition can also be generated magnetically [3], in a completely reversible manner for a single structure. As the hole Landau levels fan downwards in energy with increasing magnetic field and the electron levels upwards, at a sufficiently high magnetic field the lowest hole and electron Landau levels uncross, leading once again to depopulation. The threshold magnetic field depends on the magnitude of the original band gap overlap, determined by the period. For a typical superlattice with a band gap overlap of 70meV, the uncrossing has been calculated to occur in the region of 40T [4] and for long period structures with overlaps of order 100meV or more, the transition is expected to occur at still higher fields up to the megagauss region.

There have been many transport and FIR studies performed on both semimetallic and semiconducting InAs/GaSb superlattices. Simple Hall measurements [5] and later two-carrier-fits to Hall measurements [6,7] have demonstrated the semimetal to semiconductor transition due to subband confinement, while cyclotron resonance (CR) data has exploited the strong non-parabolicity of InAs to confirm the presence of well developed superlattice subbands which raise the electron mass well above the band edge mass value [8]. Moreover, low magnetic field CR studies have observed complex data in multiply populated subbands, which have been interpreted as due to both interband (ie electron to hole) resonances as well as the expected intralevel electron cyclotron resonance[9-11].

We present a comprehensive study of the magnetically induced semimetal to semiconductor transition examined as a function of superlattice period over the range 30 to 150T. We have studied the superlattices using electron CR which allows simultaneous access to the effective mass and carrier density through the resonance position and the integrated absorption of the resonance. (The heavy mass of the hole, around 0.1m_e, puts the resonance field well beyond the maximum magnetic field accessible.) The experiments were performed at the Institute of Solid State Physics, Tokyo University where up to 150T for 5μsec can be generated by the fast discharge of a 100kJ, 40kV capacitor bank across a copper, single turn coil. The IR wavelengths used were provided by CO_2 and CO lasers and the transmitted radiation measured by a fast action, N_2 cooled HgCdTe detector. The samples, unwedged, were held in place by a phenol cryostat and cooled to about 30K by the continuous flow of liquid Helium. Embedded in the cryostat was a pickup coil able to measure the magnetic field to better than 2%. Further details of the technique of CR at 150T are available in ref.s 12 and 13.

A series of InAs/GaSb and InAs/$Ga_{1-x}In_xSb$ superlattices have been grown by MOVPE at Oxford University. The superlattices were grown onto semi-insulating GaAs substrates with a 2μm thick buffer layer of GaSb to accommodate the strain from the first substrate GaSb interface. During the growth, the gas switching at the interface between the InAs and GaSb layers is timed to favour the formation of an InSb monolayer interface[14], whose presence has been detected by Raman scattering [15], in order to reduce the presence of interface defects [16]. Thus, these superlattices possess a much higher intrinsic carrier density than their MBE grown predecessors which were only in the order of 25% intrinsic. The high quality of these superlattices and the high density of the hole gas has been proven recently by the measurement of hole CR [17]. As short period superlattices are known to have low carrier concentrations, a larger number of layers were grown to enhance the absorption.

The superlattices were grown simultaneously onto two substrate orientations (001) and (111)A. As the (111)A direction is piezoelectrically active, the small strain inherent in InAs/GaSb, 0.6..., induces a strong electric field which acts to further increase the band overlap, and thus also increase the carrier concentration in long period structures [18]. More significantly, Symons *et al* [19] have shown that the band structure is strongly orientation dependent due to the presence of an interface dipole, which leads to an additional overlap of order 65meV for (111)A samples. The InAs/GaSb superlattices were grown with a thickness ratio 5:3 and the InAs/GaInSb superlattices with the ratio 5:1. The addition of 10% In into the GaSb layer has the effect of shifting the valence band and thus increasing the band gap overlap by ~30meV [20]. The addition of In also affects the lattice mismatch causing the strain to increase to, of order, 1%, which is expected to be significant for the (111)A superlattices.

Cyclotron resonance was performed for a wide range of InAs/GaSb superlattices with periods in the range 60Å to 600Å at wavelengths of 10.6μm and 9.2μm. In contrast with the complex CR structure seen in low field measurements, the striking aspect of all the data is its simplicity: all the superlattices produced single resonances corresponding to electron CR, with the resonances shifted to higher magnetic fields due to the strong non-parabolicity of InAs. The long period superlattices exhibit narrow and strong resonances which become weaker and broader and move up in magnetic field as the periodicity decreases, until at very short periods the resonances disappear almost entirely. Due to the presence of a small proportion of extrinsic carriers the depopulation is not total, and the remaining CR allows the extrinsic carrier density to be measured and the effective mass to be determined even beyond the depopulation point. The decreased mobility associated with short periods is attributed to the increased importance of scattering at the interfaces, which are thought to be significant sources of charged defect states, and the increasing influence of layer width fluctuation which are found by TEM in the smaller structures. Three of the best superlattices - 1249, 1252 and 1253 - were then chosen as representative of semimetallic, zero band gap and semiconducting superlattices and studied further at 5.7μm and 5.3μm in order to gauge the magnetic field dependence of the depopulation effects.

To illustrate these trends, a set of CR data is shown for InAs/GaSb superlattice 1252(001) (InAs layer thickness 106Å). At low magnetic fields, around 40T, the resonance is strong corresponding to a high carrier density. By 50T, as the transition field is approached for this superlattice and the carrier density reduced, the resonance is considerably weaker, and by 110T, the hole and electron Landau levels have completely uncrossed and the sample depopulated.

As the integrated absorption area of a resonance is directly related to the total carrier concentration, the collapse of the cyclotron resonance due to the semimetal to semiconductor transition can be quantified. The electron density deduced from the CR for a selection of superlattices has been used in Fig. 2 to show the general trends in behaviour. This figure clearly demonstrates the link between a high, low-field carrier concentration and depopulation occurring at high magnetic fields. In long period superlattices the large band gap overlap generates high density 2D electron gases essentially isolated by the resultant strong band bending. The large band overlaps of these superlattices are only overcome, and the sample depopulated, with the large Landau level energy caused by large magnetic fields. As the superlattice period is decreased

and the confinement energies increased however, the effective band gap is reduced, thus lowering the carrier concentration and reducing the magnetic field required to depopulate the superlattice.

The structures grown on the (111)A substrate show essentially the same behaviour as their (001) counterparts (Fig. 1), except that their carrier densities are significantly higher (typically doubled) and that the transition magnetic field moves to an appropriately higher value (Fig. 2). This is attributed to the effects of the piezoelectric field and the larger band gap as reported recently by Symons *et al* [19].

The InAs/GaInSb superlattices were studied at 10.6μm, 9.2μm and 5.5μm and showed similar behaviour to the InAs/GaSb superlattice1249 (Fig. 2), though the resonances show less distortion. The higher carrier densities are due to the larger band gap caused by the wider InAs layer and due to the shift of the GaInSb valence band [20]. A comparison of the CR before and after depopulation shows that about 95% of the carriers are intrinsic, which agrees with low field Hall data that the ratio of electrons to holes in these superlattices is close to 1:1.

The dependence of the effective mass on both energy and superlattice period has been examined. Even at such high energies, both the InAs/GaSb and InAs/GaInSb superlattices on both (001) and (111)A substrate directions, can be described by the simple linear dependence, $m^* = m_0^*(1 + 2.6\hbar\omega_c/E_{g(InAs)})$ which is the functional form expected for a simple two band non-parabolic approximation for the effective mass, using the InAs band gap and an increased value of the energy prefactor. As an example, the (001) and (111)A data for a InAs/GaSb and InAs/GaInSb superlattice are shown in Fig. 3. Also plotted is the effective mass taken from the magnetic field dependence of the lowest two Landau levels which was calculated using a full eight band k.p perturbation theory for both a net band gap of 0meV and -70meV. The effective mass from the calculation fits the data and the observed linear dependence well. The effective mass values for the InAs/GaInSb superlattices are slightly lower than the InAs/GaSb superlattices due to the larger InAs thicknesses which lead to lower confinement energies and so, by non-parabolicity, to a lower mass. In contrast, the (111)A structures have a slightly higher mass due to the larger confinement energies which result from the stronger self-consistent confinement potential caused by the higher carrier densities which result from the increased band overlap for this orientation.

The effective mass has also been studied as a function of InAs layer thickness for a fixed laser wavelengths of 10.6μm and 9.2μm for both (001) and (111)A InAs/GaSb superlattices in Fig. 4. The InAs thickness is more significant than the superlattice period as the electron resonance is dominated by the contribution from the InAs conduction band. A systematic increase in mass can be seen as the thickness is decreased due to the corresponding increase in the quantum well confinement energy increasing the mass through the non-parabolicity. This effect can be modelled with the expression:

$$m^* = m^*_{InAs} \left((E_g + 2.6\hbar\omega_c)/E_g \right) \left((E_g + 2.6\hbar\omega_c + E_c) / (E_g + 2.6\hbar\omega_c) \right) \quad \text{(Eqn 1)}$$

where m^*_{InAs} and E_g are the band edge InAs mass and band gap, and E_c the confinement energy, again calculated by k.p theory. The first term accounts for the InAs non-parabolicity at the cyclotron frequency, as discussed above for the energy dependence, and the second term is the non-parabolicity from the superlattice confinement. There is a smooth change in effective mass across the semimetal to semiconductor transition (which occurs, e.g., for (001) superlattices at 10.61μm at about 100Å), which implies relatively little mixing between the lowest conduction and valence bands due to the large difference in quantum number for these two states.

In conclusion, we can state that we have shown clear evidence for the existence of a magnetic field induced semimetal to semiconductor transition in a wide range of structures, which is particularly dramatic due to their low extrinsic doping levels.

1. L.L. Chang, *J. Phys. Soc. Jpn* 49 997 Supp A (1990)
2. L. Esaki and L.L. Chang *J. Magn. Magn. Mater* 11 208 (1979)
   L. L. Chang and L. Esaki *Sur. Sci.* 98 70 (1980)
3. N.J. Kawai, L.L. Chang, G.A. Sai-Halasz, C. A. Chang and L. Esaki
   Appl. Phys. Lett. 36 369 (1992)
4. D.J. Barnes, R.J. Nicholas, N.J. Mason, P.J. Walker, R.J. Warburton and N. Miura
   Physica B 184 168 (1993)
5. L.L. Chang, N. Kawai, G.A. Sai-Halasz, R. Ludeke and L. Esaki
   Appl. Phys. Lett. 35 939 (1979)
6. E.E. Mendez, L. Esaki and L.L. Chang *Phys. Rev. Lett.* 55 2216 (1985)
7. H. Munekata, E.E. Mendez, Y. Iye and L. Esaki *Sur. Sci.* 174 449 (1986)
8. H. Bluyssen, J.C. Maan, P. Wyder, L.L. Chang and L. Esaki
   Solid State Comm. 31 35 (1979)
9. Y. Guldner, J.P. Vieren, P. Voisin, M. Voos, L.L. Chang and L. Esaki
   Phys. Rev. Lett. 45 1719 (1980)
10. J.C. Maan, Y. Guldner, J.P.Vieren, P. Voisin, M. Voos, L.L. Chang and L. Esaki
    Solid State Comm. 39 683 (1981)
11. J.C. Maan, Ch. Uihlein, L.L. Chang and L. Esaki *Solid State Comm.* 41 755 (1982)
12. K. Nakao, F. Herlach, T. Goto, S. Takeyama, T. Sakakibara and N. Miura
    J. Phys. E: Sci. Instr. 18 1018 (1985)
13. S.P. Najda, S. Takeyama, N Miura, P. Pfeffer and W. Zawadzki
    Phys. Rev. B40 6189 (1989)
14. M. Lakrimi, R.W. Martin, N.J. Mason, R.J. Nicholas and P.J. Walker
    J. Cryst. Growth 110 677 (1991)
15. C. Lopez, R.J. Springett, R.J. Nicholas, P.J. Walker, N.J. Mason and W. Hayes
    Surf. Sci. 267 176 (1992)
16. J. Luo, H. Munekata, F.F. Fang and P.J. Stiles Phys. Rev. B38 10142 (1988)
17. G.M. Sundaram, R.J. Warburton, R.J. Nicholas, G.M. Summers, N.J. Mason and P.J. Walker *Semi. Sci. Techn.* 7 985 (1992)
18. M. Lakrimi, C. Lopez, R.W. Martin, G.M. Sunimers, G.M. Sundaram, K.S.H. Dalton, N.J. Mason, R.J. Nicholas and P.J. Walker *Surf. Sci.* 263 575 (1992)
19. D.M. Symons, M. Lakrimi, R.J. Warburton, R.J. Nicholas, N.J. Mason, P.J. Walker and M.I. Eremets *To be published* (1993)
20. S.K. Haywood, E.T.R. Chidley, R.E. Mallard, N.J. Mason, R.J. Nicholas, P.J. Walker and R.J. Warburton *Appl. Phys. Lett.* 54 922 (1989)
21. D.J. Barnes, R.J. Nicholas, N.J. Mason, P.J. Walker, R.J. Warburton and N. Miura to be published

• D.J. Barnes now at: Sektion Physik, Universität München, Geschwister-Scholl-Platz 1, 8000 Munchen 22, Germany

	Number of Periods	InAs(Å)	GaSb(Å)	GaInSb(Å)
1265(100)	20	500		100 •
1265(111)A	20	500	-	100 •
1252(100)	100	106	53	-
1252(111)A	100	155	77	-
1253(100)	100	64	32	-
1253(111)A	100	66	33	-
1249(100)	20	228	112	-
1249(111)A	20	202	100	-

Table 1: Superlattice details. Thickness measured by TEM except • calculated by time of growth.

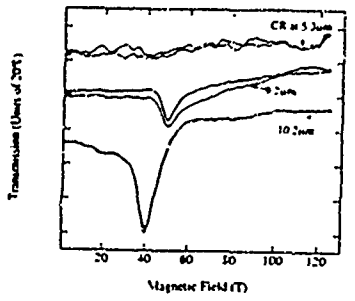

Figure 1: Cyclotron resonance data for InAs/GaSb superlattice 1252(001)

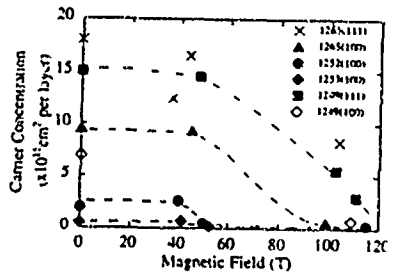

Figure 2: The electron concentration per layer of InAs/GaSb and InAs/GaInSb (1265) superlattices deduced from cyclotron resonance measurements. The dotted lines are *guides for the eye* only.

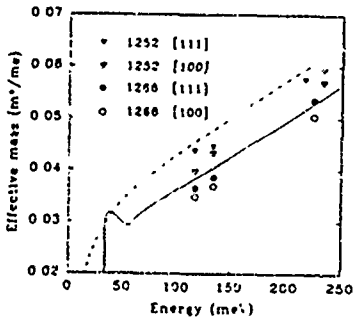

Figure 3: Effective mass (m^*) deduced from CR measurements as a function of energy for InAs/GaSb superlattice 1252 and InAs/GaInSb superlattice 1265, both on the (001) and (111)A substrate directions. The m^* expected from 8 band k.p theory calculations are shown for ~70meV (solid line) and 0meV (dotted line) band gaps.

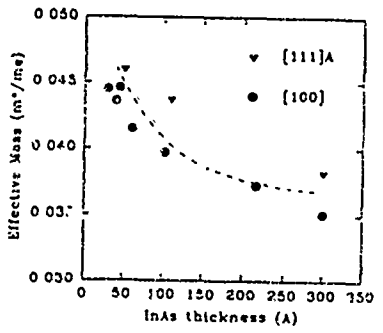

Figure 4: Effective mass of InAs/GaSb superlattices deduced from CR measurements as a function of *InAs layer thickness* for both (001) and (111)A substrate directions at 10.6μm. The fit to the data is from eqn 1 (in text) using $m^*=0.021$ and the confinement energy E_c calculated from 8 band k.p theory

WeA3

Magnetotransport Properties of MBE-Grown Magnetic Superlattices of Mn-Based Intermetallics on GaAs Heterostructures

M Tanaka*, J P Harbison, T Sands, J DeBoeck**, T.L. Cheeks and V G. Keramidas
Bellcore, 331 Newman Springs Road, Red Bank, NJ 07701-7040, U.S.A.
**On leave from Dept. of Electrical Engineering, The University of Tokyo, Japan.*
***Present Address, Interuniversity Microelectronics Center (IMEC), Belgium.*

We have studied magnetic and magnetotransport properties of two kinds of new epitaxial magnetic superlattices, MnGa/NiGa and MnAl/NiAl, consisting of ferromagnetic tetragonal MnGa (MnAl) and nonmagnetic CsCl-type NiGa (NiAl), grown by molecular beam epitaxy (MBE) on (001) GaAs substrates. Strong perpendicular magnetization is evidenced in both types of superlattices, with the values of remanent magnetization higher than those of MBE-grown MnGa and MnAl thin films reported previously. At room temperature, the hysteresis loops in the extraordinary Hall effect (EHE) measurements on the MnGa/NiGa superlattices exhibit evenly-spaced multiple steps, while the MnAl/NiAl superlattices show rectangular single-stepped EHE hysteresis loops with nearly perfect squareness. The capability of growing these kinds of new epitaxial magnetic superlattices gives a new degree of materials design of the magnetic thin films on GaAs substrates, offering the possibility of integrating magnetic devices with III-V semiconductor electronics and photonics.

Introduction

The progress in heteroepitaxial growth techniques such as molecular beam epitaxy (MBE) has made it possible to prepare a variety of heterostructures consisting of materials that are dissimilar in terms of crystal structure, chemical bonding, electronic and magnetic properties [1]. One of the most unique and attractive future directions, both for materials science and device applications, is the integration of magnetic materials and compound semiconductors [2]. Epitaxial ferromagnetic films grown directly on III-V semiconductors offer a wide range of possibilities for the fabrication of new devices including non-volatile memory coupled with underlying high speed optical/electronic III-V circuitry.

We have recently demonstrated successful MBE growth of metastable ferromagnetic τMnAl thin films [3][4], and thermodynamically stable ferromagnetic δMnGa [5] thin films on GaAs substrates. In both these MnAl and MnGa thin films, we have used MBE heteroepitaxy to align the c-axis of the tetragonal unit cell of the MnAl and MnGa, which is the easy magnetization axis, perpendicular to the substrate. This perpendicular magnetization is desired for many applications of magnetic thin films, since it allows high storage density in nonvolatile magnetic memory applications, and allows the use of the extraordinary Hall effect (EHE) and the magneto-optic Kerr effect (MOKE). Furthermore, we have also explored MBE growth of (MnNi)Al [6] and (MnNi)Ga [7] alloy thin films with perpendicular magnetization, and have found that the structural and magnetic properties can be controllably changed by Ni additions.

In order to derive more functionality and to increase the freedom in materials design by utilizing the atomic-scale controllability of the film thickness in MBE, we have created two kinds of *new ultrathin epitaxial magnetic superlattice (SL) structures of metallic compounds*, MnGa/NiGa superlattices and MnAl/NiAl superlattices, on (001) GaAs substrates. These superlattices consist of *ferromagnetic* tetragonal MnGa (MnAl) and *nonmagnetic* cubic CsCl-type NiGa (NiAl). In this report, we present the magnetic and magnetotransport properties of both the MnGa/NiGa and MnAl/NiAl SLs, with emphasis on their extraordinary Hall effect (EHE) characteristics.

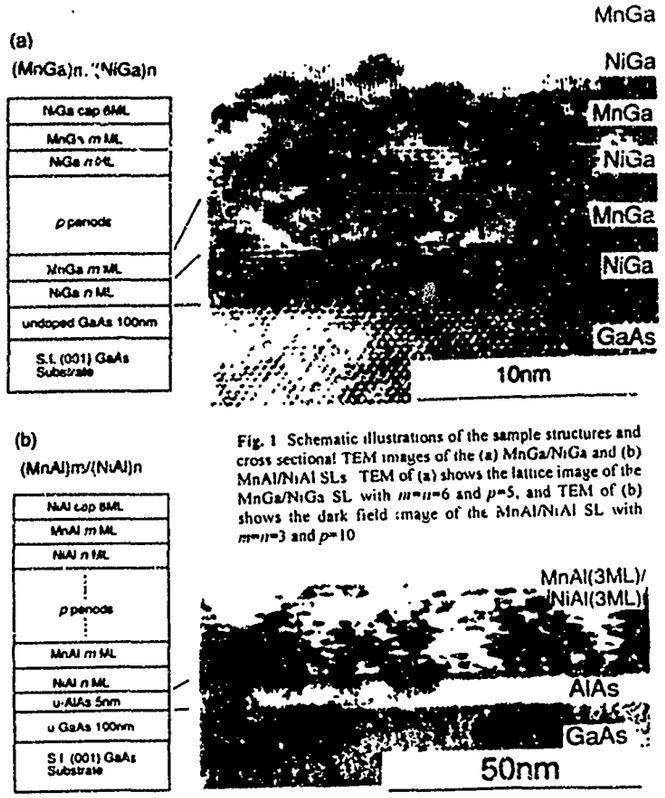

Fig. 1 Schematic illustrations of the sample structures and cross sectional TEM images of the (a) MnGa/NiGa and (b) MnAl/NiAl SLs. TEM of (a) shows the lattice image of the MnGa/NiGa SL with m=n=6 and p=5, and TEM of (b) shows the dark field image of the MnAl/NiAl SL with m=n=3 and p=10.

Formation of $Mn_xGa/NiGa$ and MnAl/NiAl Magnetic Superlattices on GaAs

In the bulk, both Mn_xGa_{1-x} and Mn_xAl_{1-x} with the Mn content x around 0.6 have ferromagnetic phase with tetragonal crystal structure. The tetragonal MnGa is a thermodynamically stable phase, while the tetragonal MnAl is a metastable phase. The easy magnetization axis is the c-axis in both materials. The lattice constants a_0 in the basal plane of the tetragonal unit cell of the MnGa and MnAl are 0.272 nm and 0.277 nm, respectively, and c_0 along the c-axis are 0.369 nm and 0.354 nm, respectively. On the other hand, both NiGa and NiAl with stoichiometric composition are nonmagnetic intermetallics, with cubic CsCl-type crystal structures having the lattice constant a_0 of 0.289 nm. Since the a_0 values of these transition metal (TM) - group III intermetallics are close to half (0.283 nm) the lattice constant of GaAs, one can expect that both MnGa/NiGa and MnAl/NiAl heterostructures should be compatible in heteroepitaxy with GaAs and related III-V semiconductors, with the desired "cube-on-cube" crystal orientations of [110](001) TM-III // [110](001) GaAs.

The growth of MnGa/NiGa and MnAl/NiAl SLs on GaAs (001) substrates was performed with a conventional III-V MBE machine (Riber-2300) equipped with Mn and Ni effusion cells. Schematic sample structures are shown in Fig. 1. Since the details of the MBE growth and characterizations are described in recent publications [8][9], we briefly summarize the growth procedure here. After growing a 100 nm-thick undoped GaAs buffer layer at 580°C on the semi-insulating GaAs substrate, the substrate temperature T_s was cooled to 200°C - 220°C while completely eliminating the As flux in the growth chamber. The Ni shutter was opened to deposit one monolayer (ML) of Ni on c(4x4) GaAs surface, and then Ni and Ga were codeposited to grow n MLs of NiGa, followed by the codeposition of Mn and Ga to grow m MLs of MnGa. The Ni/Ga and Mn/Ga ratio were set to 50/50 and 60/40, respectively. After growing the MnGa/NiGa SLs with p periods at 200 - 220°C, a postgrowth annealing was done at 300°C for 1 - 2 minutes to improve the structural and magnetic properties of the MnGa/NiGa SLs [8]. The sample structure and the growth process of the MnAl/NiAl SLs are similar to that of the MnGa/NiGa but the metallic layers of aluminides were grown on a 5 nm-thick AlAs layer and the growth temperature and postgrowth annealing temperature were higher, 250°C and 350°C, respectively [9]. Throughout the growth, the reflection high energy electron diffraction (RHEED) patterns were very streaky and sharp, indicating that epitaxial monocrystalline metallic layers with good quality are successfully grown. Figures 1 (a) and (b) also show cross sectional transmission electron microscopy (TEM) images of the MnGa/NiGa SL with m=n=6 and p=5 and the MnAl/NiAl SL with m=n=3 and p=10, respectively, giving the direct evidence of the successful formation of the compositional SLs with atomically abrupt and smooth interfaces. We have confirmed the "cube on cube" epitaxial relationship as expected, where the c-axis of the tetragonal MnGa and MnAl is aligned perpendicular to the film plane, by these RHEED and TEM analyses. From the TEM diffractions, both the MnGa and the MnAl in the SLs are found to have reduced tetragonality, with the c_0 of 0.35 nm (MnGa) and 0.33-0.34 nm (MnAl), the values smaller than those of bulk. *This reduced tetragonality influences on the* magnetic properties, particularly on the coercive field of the ferromagnetic films.

MnGa/NiGa Superlattices on GaAs: Magnetic and Magnetotransport Properties

To investigate the magnetic properties, we have performed magnetization measurements at room temperature by using vibrating sample magnetometry (VSM). The M-H curves of the MnGa/NiGa SLs measured by VSM show square-like hysteresis loops for the magnetic field applied perpendicular to the film plane, indicating the perpendicular magnetization of the SL samples. This perpendicular magnetization is desired for many interesting device applications, including high density non-volatile memory coupled with underlying high speed III-V electronics and photonics. Table I shows the magnetic properties of the $(MnGa)_m/(NiGa)_n$ SLs with p periods, in comparison with those of a single 10nm-thick $Mn_{60}Ga_{40}$ film [6] and a single 10nm-thick $Mn_{30}Ni_{30}Ga_{40}$ *alloy* film [7], grown on

m (MLs)	10	6	6	$Mn_{40}Ga_{60}$	$Mn_{30}Ni_{10}Ga_{60}$
n (MLs)	10	6	1	10nm	10nm
p	3	5	5		
M_r (emu/cm^3)	267	302	286	113 - 225	14
H_c (kOe)	2 60	2 29	5 35	1 30 - 3 15	1 27

Table I Magnetic properties of the $(MnGa)_m/(NiGa)_n$ SLs with p periods, in comparison with those of a single 10nm-thick $Mn_{40}Ga_{60}$ film and a single 10nm-thick $Mn_{30}Ni_{10}Ga_{60}$ *alloy* film, grown on (001) GaAs by MBE The values of remanent magnetization M_r and coercive field H_c measured at room temperature are shown

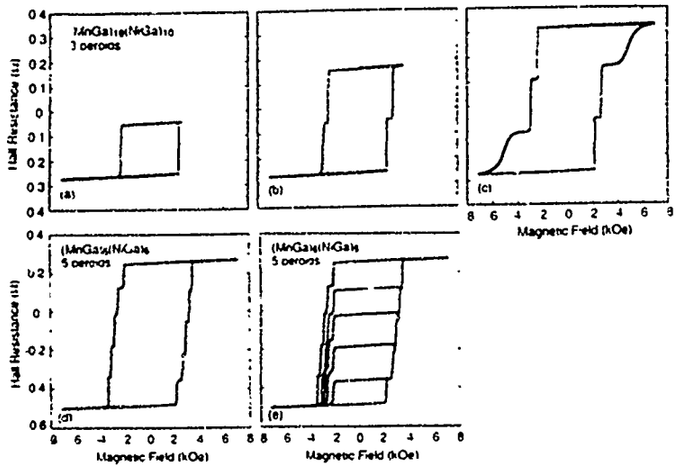

Fig. 2 EHE hysteresis loops of the MnGa/NiGa SLs with (a)-(c) $m=n=10$ and $p=3$ and with (d)(e) $m=n=6$ and $p=5$, measured at room temperature with differing the maximum values H_{max} of the applied magnetic field perpendicular to the substrate plane The H_{max} value was set to (a) 2 7 kOe, (b) 4 0 kOe and (c) 7 0 kOe for the $(MnGa)_{10}/(NiGa)_{10}$ SL with 3 periods, and (d) 7 0 KOe and (e) 2 6 - 7 0 kOe for the $(MnGa)_6/(NiGa)_6$ SL with 5 periods

(001) GaAs by MBE All these SLs and thin films showed square-like M-H curves with perpendicular magnetization The values of remanent magnetization M_r of the present MnGa/NiGa SLs are 267 - 302 emu/cm^3 when normalized by the total volume of the ferromagnetic MnGa layers, the values which are higher than those of the MBE-grown 10nm-thick MnGa thin film and 10nm-thick MnNiGa alloy thin film This is probably because the crystal quality of the epitaxial layers of the SLs is better than that of the MnGa and MnNiGa films, as indicated by the RHEED studies [6]-[8]

It is known that the Hall effect measured in a ferromagnetic film has an "extraordinary" component resulting from the asymmetric s-d scattering of carriers with magnetic atoms This extraordinary Hall effect (EHE) is a very powerful probe to characterize the properties of perpendicularly magnetized thin films, because the Hall resistivity measured in a patterned Hall bar is proportional to the magnetic moment perpendicular to the film plane [10] We have found that EHE is more sensitive, and therefore, more suitable than VSM for clearly detecting the detailed magnetic structures in such SLs with periods of only several monolayers

Figures 2 show the EHE hysteresis loops of the MnGa/NiGa SLs with (a)-(c) $m=n=10$ and $p=3$, and with (d)(e) $m=n=6$ and $p=5$, measured at room temperature with differing the maximum values H_{max} of the applied magnetic field perpendicular to the substrate plane The H_{max} value was set to (a) 2.7 kOe, (b) 4 0 kOe and (c) 7 0 kOe for the $(MnGa)_{10}/(NiGa)_{10}$ SL with 3 periods, and (d) 7 0 kOe and (e) 2 6 - 7 0 kOe for the $(MnGa)_6/(NiGa)_6$ SL with 5 periods When the applied field is as high as 7 0 kOe, the entire magnetic structure is saturated for both SLs Note that the EHE hysteresis loops have evenly-spaced multiple steps when H_{max} is 7 0 kOe, as shown in Fig 2 (c) and (d), where three steps and five steps are clearly seen in the EHE loops of MnGa/NiGa SLs with 3 periods and 5 periods, respectively Since the number of steps in the loops are the same as the number of ferromagnetic MnGa layers, each step is formed by the reversal of magnetization in one of the MnGa layers. This is because the MnGa layers have different coercive forces H_c from one to another In principle, these phenomena can be applied to multi-level signal recording, which can lead to much higher storage density The capability of reading and writing multi-level signals is demonstrated for the MnGa/NiGa SL with 3 periods in Fig 2 (a) - (c), where four different static values of Hall resistance are realized with varying the value of H_{max} Likewise, in Fig 2 (e), six different values of Hall resistance are shown for the MnGa/NiGa SL with 5 periods

The possible origin of the different H_c values in the MnGa layers of the SLs is the difference in lattice strain Since the bulk a/c values of tetragonal MnGa and CsCl-type NiGa have the lattice mismatch of -3 8% and +2 1% respectively, the c/a ratio in the lattice of the epitaxial MnGa layers of the SLs can be slightly different due to the difference in strain, leading to the difference in H_c. Another possible reason for the different H_c may be the difference in the interface roughness or defect density The full understanding of the mechanisms and the artificial "design" of the EHE hysteresis will be interesting future issues

MnAl/NiAl Superlattices on AlAs/GaAs: Magnetic and Magnetotransport Properties

To investigate the magnetic properties of another type of magnetic superlattices, MnAl/NiAl SLs, we have performed VSM measurements at room temperature Table II shows the the values of remanent magnetization M_r and coercive field H_c for various $(MnAl)_m/(NiAl)_n$ SLs with p periods, in comparison with those of a single 10nm-thick $Mn_{60}Al_{40}$ film and a single 10nm-thick $Mn_{30}Ni_{10}Al_{60}$ *alloy* film, grown on AlAs/GaAs by MBE For the magnetic field applied perpendicular to the substrate, all these SLs and thin films showed M-H curves with almost perfect squareness indicating strong perpendicular magnetization The M_r values of the present MnAl/NiAl SLs (when normalized by the total thickness of the MnAl) are higher than those of the MnAl and the MnNiAl thin films and even higher than those of MnGa/NiGa SLs (see table I and II) On the other hand, the H_c values of the MnAl/NiAl SLs are relatively low The lower coercivity of the SLs is due to the reduced tetragonality, as evidenced by the TEM analysis, of the MnAl layers in the SLs, which is caused by the strain

m (MLs)	3	3	3	6	$Mn_{50}Al_{50}$	$Mn_{50}Ni_{25}Al_{25}$
n (MLs)	1	3	6	6	10nm	10nm
p	10	10	10	5		
M_r (emu/cm^3)	211	314	251	342	170 - 215	56
H_c (kOe)	2.84	0.95	1.96	0.85	1.6 - 5.0	3.22

Table II Magnetic properties of the $(MnAl)_m(NiAl)_n$ SLs with p periods in comparison with those of a single 10nm-thick $Mn_{50}Al_{50}$ film and a single 10nm-thick $Mn_{50}Ni_{25}Al_{25}$ *alloy* film, grown on AlAs/GaAs by MBE. The values of remanent magnetization M_r and coercive field H_c measured at room temperature are shown.

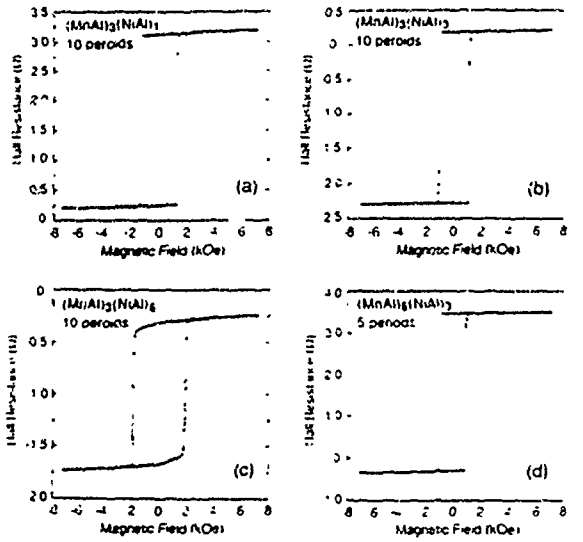

Fig. 3 EHE hysteresis loops of the MnAl/NiAl SLs with (a) m=3, n=1 and p=10, (b) m=n=3 and p=10, (c) m=3, n=6 and p=10, and (d) m=n=6 and p=5, measured at room temperature. The maximum value H_{max} of the applied magnetic field perpendicular to the substrate plane was 7.0 kOe in all the measurements.

Fig. 3 shows EHE hysteresis loops of the MnAl/NiAl SLs with (a) m=3, n=1 and p=10, (b) m=n=3 and p=10, (c) m=3, n=6 and p=10, and (d) m=n=6 and p=5, measured at room temperature. Here the maximum value H_{max} of the applied magnetic field perpendicular to the substrate plane was 7.0 kOe in all the measurements. Unlike the multi-stepped EHE characteristics of the MnGa/NiGa SLs, the MnAl/NiAl SLs have shown rectangular EHE hysteresis loops with a single step. Most of the MnAl/NiAl SLs show perfect squareness in the hysteresis loops with 100 % remanence, as shown in Fig. 3. In some of the MnAl/NiAl SLs, the coercive field H_c was found to depend on the maximum value of the previously applied magnetic field H_{pre} of the opposite direction, keeping the nearly perfect squareness of the EHE hysteresis loops [9]. For example, for the $(MnAl)_3/(NiAl)_3$ SL with 10 periods, the H_c can be lowered to ~2.0-5 kOe when the H_{pre} was 0.6 kOe. This lower value of H_c is practically important for the application to non-volatile magnetic memory, since it may enable the on-chip writing with locally generated fields in combination with high current pulses.

This set of magnetic properties of the present SLs, strong perpendicular anisotropy, perfect squareness of the hysteresis loops, high remanent magnetization, relatively low coercive field, EHE signal at room temperature, good compatibility with GaAs/AlAs, is very attractive for the application to semiconductor-based non-volatile digital memory.

Conclusions

We have studied room-temperature magnetic properties and EHE characteristics of two kinds of MBE-grown magnetic SLs of metallic compounds, MnGa/NiGa and MnAl/NiAl. Strong perpendicular magnetization have been evidenced for both types of SLs, with M_r higher than those of MBE-grown MnGa, MnAl and related alloy thin films. The EHE hysteresis loops of the MnGa/NiGa SLs are found to have multiple steps, while the MnAl/NiAl SLs show rectangular EHE hysteresis loops with perfect squareness. These new epitaxial magnetic SLs, having appealing magnetic properties as well as good compatibility with existing III-V semiconductor technology, offer a wide range of possibilities for device applications such as non-volatile memory coupled with III-V electronics/photonics.

Acknowledgments

The authors wish to thank B. Philips, D.M. Hwang, and L.T. Florez for their valuable cooperations. One of the authors (M. T.) acknowledges financial support by the Japan Society for the Promotion of Science (JSPS).

References

[1] For example, Materials Research Society Symp. Proc. Vol. 221 "Heteroepitaxy of Dissimilar Materials", edited by R. Farrow, J. Harbison, P. Peercy and A. Zangwill, Materials Research Society, 1991.
[2] G.A. Prinz, Science 250, 1092 (1990).
[3] T. Sands, J.P. Harbison, M.L. Leadbeater, S.J. Allen, Jr., G.W. Hull, R. Ramesh, and V.G. Keramidas, Appl. Phys. Lett. 57, 2609 (1990).
[4] J.P. Harbison, T. Sands, R. Ramesh, L.T. Florez, B.J. Wilkens, and V.G. Keramidas, J. Crystal Growth 111, 978 (1991).
[5] J.P. Harbison, T. Sands, J. DeBoeck, T.L. Cheeks, P. Miceli, M. Tanaka, L.T. Florez, B.J. Wilkens, H.L. Gilchrist and V.G. Keramidas, J. Crystal Growth 127, 650 (1993).
[6] M. Tanaka, J.P. Harbison, J. DeBoeck, T. Sands, B. Philips, T.L. Cheeks and V.G. Keramidas, Appl. Phys. Lett. 62, 1565 (1993).
[7] M. Tanaka, J.P. Harbison, T. Sands, B. Philips, T.L. Cheeks, J. DeBoeck, L.T. Florez and V.G. Keramidas, to be published in Materials Research Society Symp. Proc. 313, (1993).
[8] M. Tanaka, J.P. Harbison, T. Sands, B. Philips, T.L. Cheeks, J. DeBoeck, L.T. Florez and V.G. Keramidas, to be published in Appl. Phys. Lett. (1993).
[9] M. Tanaka, J.P. Harbison, T. Sands, T.L. Cheeks, J. DeBoeck, D.M. Hwang, L.T. Florez and V.G. Keramidas, to be published in Appl. Phys. Lett. (1993).
[10] E.D. Dahlberg, K. Riggs and G.A. Prinz, J. Appl. Phys. 63, 4270 (1988).

WeA4

Studies of GaSb-capped InAs/AlSb quantum wells by resonant Raman scattering

J. Wagner, J. Schmitz, M. Maier, J.D. Ralston, and P. Koidl
Fraunhofer-Institut für Angewandte Festkörperphysik,
Tullastrasse 72, D-79108 Freiburg, Federal Republic of Germany

Abstract

We have used resonant Raman scattering to study GaSb-capped AlSb/InAs/AlSb quantum wells grown by molecular-beam epitaxy. The shutter sequence for the growth of the InAs/AlSb heterointerfaces was such as to promote the formation of an InSb-like interface. Scattering by an InSb-like mode at $\approx$190 cm^{-1} is found to resonate at approximately the InAs $E_1/E_1+\Delta_1$ gap energy, supporting its assignment to an interface mode. Resonance effects in scattering by longitudinal optical (LO) phonons enabled us also to distinguish between scattering by the almost degenerate LO phonon modes in the InAs quantum well and in the GaSb cap layer. The GaSb and the AlSb one-LO phonon spectra indicate the unintentional incorporation of As at concentrations up to 18-19 % in the GaSb and AlSb layers for As background pressures in the growth chamber exceeding 10^{-9} Torr. The incorporation of As was confirmed independently by secondary ion mass spectroscopy.

1. Introduction

Nearly lattice matched InAs/AlSb quantum wells are interesting semiconductor heterostructures for the study of two-dimensional electron systems because of the large conduction band offset of 1.35 eV and the small electron effective mass in the InAs well [1]. Potential applications for such heterostructures include high-speed field-effect transistors [2]. Across the InAs/AlSb heterointerface there is no common anion or cation, resulting in two different types of interfaces, either InSb- or AlAs-like. It has been shown that the in-plane transport properties of the two-dimensional electron gas (2DEG) formed in the InAs quantum well depend critically on the type of heterointerface [3].

Raman spectroscopy has proven to be a valuable experimental technique for the analysis of the InAs/AlSb heterointerface via inelastic light scattering by interface modes [4-6]. However, all these studies published so far are based on Raman spectra recorded with optical excitation at a fixed photon energy. On the other hand, it is known from numerous studies on GaAs/Al_xGa_{1-x}As quantum wells that, when the optical excitation is tuned into resonance with an electronic interband transition, resonance effects in the Raman scattering cross-section can enhance the Raman signal considerably, and thus facilitate a more detailed study of vibrational modes in such heterostructures [7].

In the present study we have used resonant Raman scattering by longitudinal optical (LO) phonons and by interface modes to analyse GaSb-capped InAs/AlSb quantum wells grown by molecular-beam epitaxy (MBE). We show that tuning the incident photon energy into resonance with an appropriate band-gap energy of one of the constituents allows the vibrational properties of that particular layer to be probed with a high degree of selectivity. Exploiting such resonance effects, a splitting of the GaSb LO phonon mode and a high-frequency shift of the AlSb LO phonon is resolved for As background pressures in the growth chamber exceeding 10^{-9} Torr, indicating the unintentional incorporation of As at concentrations up to 18-19 % in the AlSb and GaSb layers.

2. Results and Discussion

Sample growth was performed by solid-source MBE on (100) GaAs substrates. InAs/AlSb single quantum wells with a width of 15 nm were grown on a buffer layer consisting of 1 µm of AlSb and a 10-period 2.5nm GaSb/2.5nm AlSb superlattice. The InAs quantum well was sandwiched between a 40 nm wide AlSb barrier on the substrate side and a 10 nm wide AlSb barrier on the surface side. The top barrier was capped with 10 nm of GaSb to prevent the oxidation of the underlying AlSb. The shutter sequence for the growth of the InAs/AlSb heterointerfaces was chosen such as to promote the formation of InSb-like interfaces [3]. Growth of the quantum well structure was performed at a substrate temperature of 500 °C. Three different samples were investigated, differing only in the As background pressure during the deposition of the AlSb and GaSb layers. Sample A was grown using a conventional As effusion cell producing an As_4 molecular beam and an As background pressure of 2×10^{-8} Torr with the shutter closed. For the growth of sample B and C a valved cracker cell was used as the source of an As_2 molecular beam. Sample B was grown with the valve open resulting in an As background pressure of 4×10^{-9} Torr. During the deposition of the AlSb and GaSb layers of sample C both the shutter and the valve were closed, leading to an As background pressure of 5×10^{-10} Torr.

In Fig. 1, low-temperature (77 K) Raman spectra of sample A are plotted. The spectra were excited at 2.71 eV, close to the E_1 band-gap resonance of InAs [8], and recorded in backscattering from the (100) growth surface. Spectra were recorded with the polarizations of the incident and scattered light selected to be either parallel to the same (100) crystallographic direction [x(z,z)$\bar{x}$] or perpendicular to each other [x(y,z)$\bar{x}$]. In polarized spectra [x(z,z)$\bar{x}$], intrinsic two-LO phonon scattering is allowed, whereas one-LO phonon scattering by the deformation potential mechanism is symmetry-forbidden. For resonant excitation, however, intrinsic one-LO phonon scattering via the Fröhlich mechanism, as well as defect-induced one-LO phonon scattering, contribute to the Raman spectrum [9]. The present spectra show one-LO phonon scattering by the InAs quantum well and by the AlSb barriers, as well as two-LO phonon scattering from InAs. The presence of an InAs two-LO phonon signal, and the observation that InAs one-LO phonon scattering is stronger for parallel than for crossed polarizations, show clearly the resonant enhancement of LO phonon scattering from the InAs quantum well [8]. The non-resonantly excited AlSb one-LO phonon signal, in contrast, is, as expected [9], most intense for crossed polarizations. For this scattering configuration [x(y,z)$\bar{x}$], the spectrum shows also a

peak at 190 cm^{-1} which is assigned to scattering by a longitudinal InSb interface mode [IF(InSb)] [4,5].

The photon energy dependence of scattering by the InSb-like interface mode is shown in Fig. 2, which presents three room-temperature Raman spectra excited at photon energies varying from 2.41 to 2.71 eV. The InSb-like interface mode is strongest in intensity for excitation at 2.71 eV, matching the InAs $E_1/E_1+\Delta_1$ band gap resonance, and is only weakly resolved for 2.41 eV excitation. This resonance behaviour is consistent with the assignment to an interface mode, since scattering by such modes is expected to be strongest for excitation in resonance with interband transitions of the quantum well [7]. From studies on ultrathin Ge layers embedded in crystalline Si it is known that for layer thicknesses exceeding three to four monolayers, Raman scattering from the embedded layer shows a resonance behaviour similar to that of the corresponding bulk material [10]. For the present case of InSb a bulk-like resonance behaviour would lead to an enhancement of the InSb-like mode for excitation in resonance with the $E_1+\Delta_1$ band gap at $\simeq$2.4 eV [11], contrary to the experimental observations. Thus, the measured resonance behaviour of the InSb-like interface mode places an upper limit of three to four monolayers on the thickness of the interfacial layer producing this mode.

Fig. 3 shows a series of depolarized Raman spectra $\{x(y,z)\bar{x}\}$ recorded from samples A, B, and C for excitation in resonance with the GaSb $E_1+\Delta_1$ band gap [11]. There are pronounced resonance effects in the Raman spectra of sample A as seen from the comparison of the spectrum recorded for excitation at 2.41 eV (Fig. 3 a), which is well below the InAs E_1 gap resonance, and that recorded with 2.71 eV excitation (Fig. 1, lower curve) in resonance with that band gap [8]. For 2.41 eV excitation the relative strength of the InAs one-LO phonon line is drastically reduced, as compared to excitation at 2.71 eV, and two peaks appear above and below the InAs one-LO phonon line. These new peaks arise from one-LO phonon scattering in the GaSb cap layer. In the spectrum excited at 2.71 eV these two GaSb-related phonon peaks are only just resolved as weak shoulders on either side of the InAs one-LO phonon peak. Two GaSb one-LO phonon modes, namely a GaSb-like ("GaSb") and a GaAs-like ("GaAs") mode [12], are observed because of the formation of $GaSb_{1-x}As_x$, rather than binary GaSb. The formation of a pseudo-ternary alloy is due to the unintentional incorporation of As caused by the relatively high As background pressure. The AlSb one-LO phonon line shows no splitting but is shifted to higher frequencies, as compared to binary AlSb, indicating the formation of $AlSb_{1-x}As_x$ [13]. The difference in mode behaviour is consistent with the reported single-mode behavior for $AlSb_{1-x}As_x$ [13], which is in contrast to the partial two-mode behaviour found in $GaSb_{1-x}As_x$ [12].

Upon reduction of the As background pressure (sample B), the splitting of the two $GaSb_{1-x}As_x$ LO phonon modes is reduced (Fig. 3 b), and for the structure grown at the lowest background pressure (sample C) just one GaSb one-LO phonon line is resolved (Fig. 3 c). From the splitting between the GaSb-like and the GaAs-like

phonon modes As concentrations of 19 and 7 % are deduced for samples A and B, respectively [12]. The AlSb one-LO phonon line shifts to lower frequencies with decreasing As background pressure. From the measured shift of the AlSb one-LO phonon line (Fig. 3), As concentrations of 18 and 8 % are inferred for samples A and B, respectively, in good agreement with the values extracted above from the $GaSb_{1-x}As_x$ mode splitting. The AlSb LO phonon frequency observed in sample C, in contrast, is that of binary AlSb [13].

For an independent confirmation of the above findings, secondary ion mass spectroscopy (SIMS) has been used for a semi-quantitative analysis of the As incorporation in the AlSb layers of the present samples. The measurements were carried out using a Cs^+ primary ion beam at an energy of 3 keV impinging on the sample surface at an angle of 45 degrees. CsX^+ molecular ions were detected since for these ions the SIMS matrix effect is small. Fig. 4 shows SIMS depth profiles of $CsAs^+$ and, for reference purposes, of $CsAl^+$. For all three samples, there is a maximum in the $CsAs^+$ signal at the expected depth of the InAs quantum well, accompanied by a minimum in the $CsAl^+$ signal intensity. However, the $CsAs^+$ signal observed in the regions above and below the InAs layer, which consist of nominally binary AlSb, increases strongly with increasing As background pressure. There is a difference of almost three orders of magnitude in the As background concentration between the structure grown at the highest As background pressure (sample A) to that grown at the lowest pressure (sample C). In the latter case the As signal drops below the detection limit of the SIMS apparatus. The $CsAs^+$ signal intensity for sample B is only about one third of that measured for sample A (Fig. 4 a and b), which compares favourably with As concentrations of 8 and 18 %, respectively, measured by Raman spectroscopy.

The present finding of a significant As incorporation in the GaSb or AlSb layers of MBE grown InAs/AlSb or InAs/GaSb heterostructures, for As background pressures in the growth chamber exceeding 10^{-9} Torr, is consistent with recent Raman spectroscopic [6] and SIMS data [14] reported by other groups. On the other hand, the present results clearly demonstrate that, using a valved cracker As effusion cell, the As background pressure can be reduced significantly, facilitating the growth of truly binary/binary InAs/AlSb and InAs/GaSb heterostructures

3. Conclusions

We have shown how resonant Raman scattering by LO phonons and by interface modes can be used to analyse GaSb-capped InAs/AlSb quantum well structures. Tuning the incident photon energy into resonance with an appropriate band-gap energy of one of the constituents allows the vibrational properties of that particular layer to be probed with a high degree of selectivity. The LO phonon spectra of GaSb and AlSb are found to depend critically on the As background pressure during layer growth, which indicates the unintentional incorporation of As at concentrations up to 18-19 % for background pressures exceeding 10^{-9} Torr.

Acknowledgements

We would like to thank G. Bihlmann for valuable technical assistance in the MBE growth, F. Pohl for expert technical support of the Raman measurements, and F. Fuchs for helpful discussions and comments.

References:

1. See, e.g., A. Nakagawa, H. Kroemer, and J.H. English, Appl. Phys. Lett. 54, 1893 (1989); S. Ideshita, A. Furukawa, Y. Mochizuki, and M. Mizuta, Appl. Phys. Lett. 60, 2549 (1992); Ch. Gauer, J. Scriba, A. Wixforth, J.P. Kotthaus, C. Nguyen, G. Tuttle, J.H. English, and H. Kroemer, Semicond. Sci. Technol. 8, S137 (1993); M.J. Yang, P.J. Lin-Chung, R.J. Wagner, J.R. Waterman, W.J. Moore, and B.V. Shanabrook, Semicond. Sci. Technol. 8, S129 (1993).
2. G. Tuttle and H. Kroemer, IEEE Trans. Electron Devices ED-34, 2358 (1987); J.D. Werking, C.R. Bolognesi, L.D. Chang, C. Nguyen, E.L. Hu, and H. Kroemer, IEEE Electron. Device Lett. 13, 164 (1992).
3. G. Tuttle, H. Kroemer, and J.H. English, J. Appl. Phys. 67, 3032 (1990).
4. I. Sela, C.R. Bolognesi, L.A. Samoska, and H. Kroemer, Appl. Phys. Lett. 60, 3283 (1992).
5. M. Inoue, M. Yano, H. Furuse, N. Nasu, and Y. Iwai, Semicond. Sci. Technol. 8, S121 (1993).
6. J. Spitzer, H.D. Furhs, P. Etchegoin, M. Cardona, B. Brar, and H. Kroemer, Appl. Phys. Lett. 62, 2274 (1993).
7. See, e.g., B. Jusserand and M. Cardona, in *Light Scattering in Solids V*, eds. M. Cardona and G. Güntherodt (Springer, Berlin, 1989), p. 49.
8. R. Carles, N. Saint-Cricq, J.B. Renucci, A. Zwick, and M.A. Renucci, Phys. Rev. B 22, 6129 (1980).
9. See, e.g., M. Cardona in *Light Scattering in Solids II*, eds. M. Cardona and G. Güntherodt (Springer, Berlin, 1982), p. 19.
10. J.C. Tsang, S.S. Iyer, J.A. Calise, and B.A. Ek, Phys. Rev. B 40, 5886 (1989)
11. See, e.g., W. Richter in *Springer Tracts in Moderne Physics*, Vol. 78, ed G. Höhler (Springer, Heidelberg, 1976), p. 121.
12. T.C. McGlinn T.N. Krabach, M.V. Klein, G. Bajor, J.E. Greene, B. Kramer, S.A. Barnett, A. Lastras, and S. Gorbatkin, Phys Rev. B 33, 8396 (1986).
13. I. Sela, C.R. Bolognese, and H. Kroemer, Phys. Rev. B 46, 16 142 (1992).
14. J.T. Zborowski, W.C. Fan, T.D. Golding, A. Vigliante, P.C. Chow, H.D. Shih, and J.M. Anthony, J. Appl. Phys. 71, 5908 (1992).

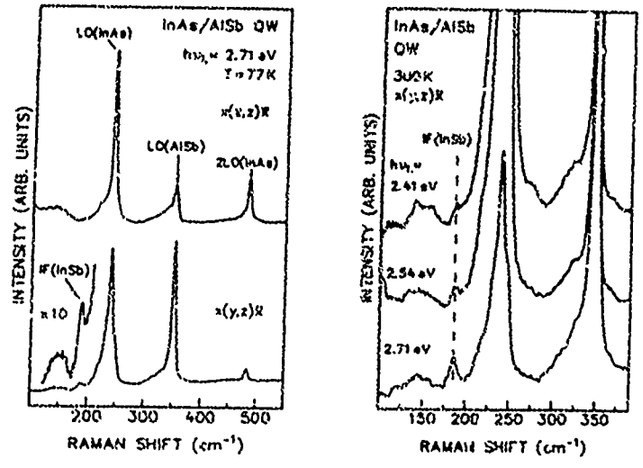

Fig. 1 (left) Low-temperature (77 K) Raman spectra of an InAs/AlSb single quantum well (sample A). The spectra, excited in resonance with the InAs E_1 band gap, were recorded with the polarization of the scattered light either parallel $\{x(z,z)\bar{x}\}$ (α-p) or perpendicular to that of the incident light $\{x(y,z)\bar{x}\}$ (bottom). Here x, y, and z denote (100) crystallographic directions.

Fig. 2 (right) Room-temperature Raman spectra of an InAs/AlSb single quantum well (sample A) recorded for different incident photon energies $\hbar\omega_L$ indicated in the figure. The spectra were recorded with the polarization of the scattered light perpendicular to that of the incident light $\{x(y,z)\bar{x}\}$.

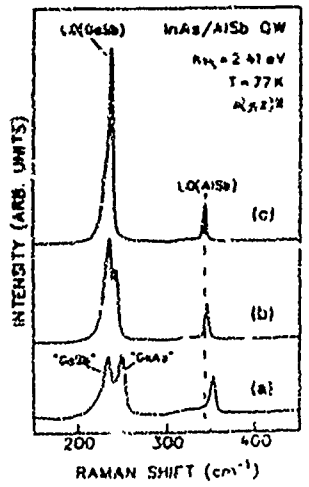

Fig. 3 (left) Depolarized $\{x(y,z)\bar{x}\}$ low-temperature (77 K) Raman spectra of an InAs/AlSb single quantum well excited at 2.41 eV. The spectra were recorded (a) from sample A, (b) from sample B, and (c) from sample C with the As background pressure in the growth chamber decreasing from sample A to C.

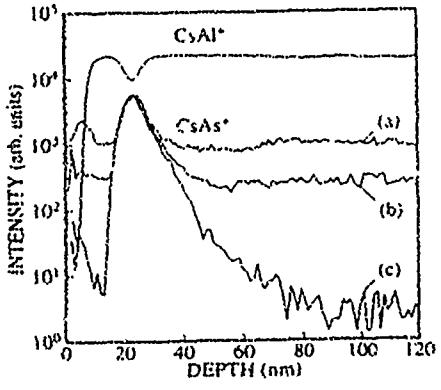

Fig. 4 (right) SIMS depth profiles of Al ($CsAl^+$) and of As ($CsAs^+$) for (a) sample A, (b) sample B, and (c) for sample C. The As background pressure in the growth chamber decreases from sample A to C.

WeA5 Luminescence up-conversion by Auger process at InP-AlInAs type II interfaces

A. Filkov*,**, W. Seidel*, J.P. Andre**, P. Voisin* and M. Voos*

*Laboratoire de Physique de la Matière Condensée de l'Ecole Normale Supérieure
24 rue Lhomond, F75005 Paris, France

**Laboratoire d'Electronique Philips
22 av. Descartes, F94453 Limeil-Brevannes, France

Abstract

Luminescence of bulk InP at 1.42 eV is observed when exciting a type II InP-AlInAs single heterojunction above the heterojunction bandgap at 1.23 eV. We show that this energy up-conversion results from Auger process producing high energy holes which redistribute over the heterostructure and recombine with native electrons in the InP layer.

Auger processes in semiconductors have both a fundamental interest as three-particle recombination mechanisms and a practical importance as the main limitation to radiative efficiency under high injection, for instance in semiconductor light-emitting devices [1]. Auger constants are usually determined somewhat indirectly from the saturation of photo-luminescence intensity when increasing the pump intensity [2-4]. The nature of the main process (one electron-two holes, two electrons-one hole ..) can also be determined by comparing the situation of p-type and n-type materials. Calculations [5] of Auger recombination rates are uneasy because they involve high-energy states in the conduction or valence band, which cannot be described by simplified k.p models. Auger effects in bulk materials like GaAs [2,3], GaSb [2,4] and InGaAs [6] have been carefully studied, but the case of semiconductor heterostructures, in spite of the technological importance of heterostructure lasers, is not completely clarified. It seems, however, that in the case of InGaAs-based quantum wells Auger coefficients are close to the bulk value [6]. Type II heterostructures offer a completely new situation with respect to radiative as well as Auger recombination processes, since electrons and holes are spatially separated and recombination is allowed only by the weak overlap of the wavefunction tails outside the wells where they are localized. Recently, we observed low threshold laser emission in InP-AlInAs superlattices [7], which are certainly the most "regular" type II systems, with Γ-electrons (holes) localized in InP (AlInAs) [8]. This intriguing observation, which seems to contradict the standard expectation as well as a theoretical prediction of enhanced Auger rates [9] due to the increased accessible phase-space, is a strong motivation to study Auger effects in these materials. In addition, we anticipated that the type II configuration offers a unique opportunity to detect directly Auger hot carriers through a luminescence up-conversion effect: hot carriers produced by Auger events can indeed redistribute over the heterostructure and recombine with the other particles, which are confined in the "barrier". Hence, Auger carriers will induce barrier luminescence, possibly at a higher energy than the pump itself. Here, we report first results of the investigation of the "Auger fountain" effect in a InP-AlInAs single type II heterojunction.

Our sample was grown by Metal-Organic Chemical Vapor Deposition (MOCVD). This heterostructure, as shown schematically in Fig.1a, simply consists of a 1000 Å thick InP buffer layer (undoped, with a n-type residual doping in the 10^{14} cm^{-3} range) deposited on a n$^+$ InP substrate, and followed by a 1000 Å AlInAs layer, non-intentionally doped (n-type residual doping in the 10^{16} cm^{-3} range). The free surface is protected by a 50 Å InGaAs cap. Calculation [10] of the charge transfer at the heterojunction for a conduction band offset ΔE_c = 470 meV [8] and a doping level N_D= 2 10^{16} cm^{-3} in the AlInAs layer yields a two-dimensional electron gas with an

areal density $n_S = 3\ 10^{11}$ cm^{-2}, and corresponding to an electron Fermi level of 10 meV. The electric field at the interface is 30 kV / cm. Electron and heavy hole confinement energies in their respective quasi-triangular quantum wells are 30 meV and 20 meV respectively.

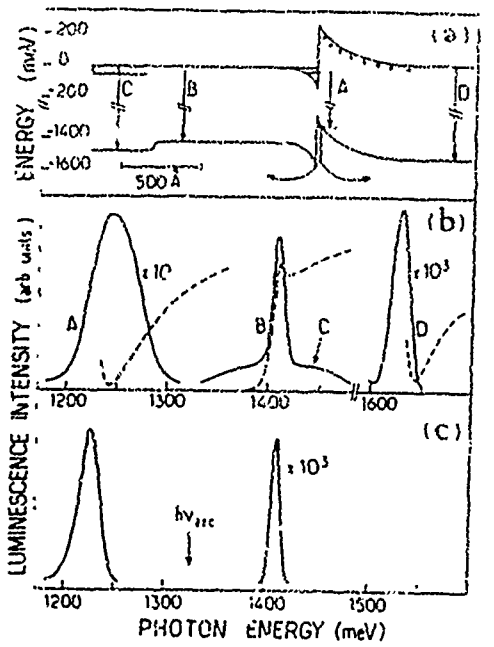

Fig.1 : (a) Sketch of the band structure of the InP-AlInAs heterojunction.
(b) Luminescence spectrum (solid lines) under low power excitation with an He-Ne laser, and excitation spectra (dashed lines) of the various lines [8].
(c) Luminescence spectrum with a 20 mW excitation power at $h\nu_2 = 1.325$ eV, showing the up-converted InP luminescence.

The low temperature (2K) luminescence spectrum under low power excitation by a He-Ne laser is shown in Fig. 1b. A strong line "A", corresponding to recombination through the type II interface, is observed at 1.23 eV. The luminescence from the InP buffer layer is seen as a sharp peak "B" at 1.41 eV, emerging from a broad background "C" due to the substrate luminescence. In addition, a weak luminescence line "D" from the $Al_{0.53}In_{0.47}As$ layer (which is 5% Al-rich with respect to the lattice matched composition x_0=0.48) is observed at 1.63 eV. Excitation spectra [11] of these different lines (dashed lines in Fig. 1b) exhibit the absorption gaps associated with the InP and AlInAs layers. More surprisingly, the gap associated with the interface can also be measured directly from the excitation spectrum of the 1.23 eV luminescence line, in spite of the very small absorption coefficient associated with the type II single heterojunction. From the calculation of the ground-state wavefunction overlap, the threshold absorption should indeed be as small as $3\ 10^{-5}$, to be compared with $\approx 10^{-2}$ in the case of a type I quantum well.

In the following, we discuss results obtained using a Ti:Saphir tunable laser with a power of a few tens of mW and loosely focused on the sample using a long focal (0.8 m) lens. The diameter of the exciting spot, determined as the product of the nominal divergence of the laser beam ($1.2\ 10^{-4}$ rd) by the focal length, is 1 mm. For an excitation energy above the InP bandgap ($h\nu_1$ = 1.51 eV), the luminescence spectrum shows very little dependence on the excitation power. In particular, as shown in Fig. 2a, the integrated intensities of the InP ("B") and interface ("A") lines vary linearly with the pump power over several decades. This proves that the radiative efficiency is nearly constant. It is also noteworthy that the lineshapes do not change in this range of excitation powers. However, when the sample is excited at $h\nu_2$ = 1.32 eV (ie between the InP and the interface bandgaps), a very unusual feature can be observed: as shown in Fig. 1c, the luminescence from the InP buffer layer can still be observed, although much weaker than before. We now observe a quadratic dependence of the "B" line on the laser intensity while the dominating interface line "A" still shows the linear dependence (Fig. 2b). As great care has been taken to ensure perfect spectral filtering of the laser beam, this InP luminescence clearly corresponds to an up-conversion of the exciting photon energy, and the laser intensity dependence proves that this is due to a non-linear effect. Various mechanisms can be envisaged, like two-photon absorption, intra-band absorption by photo-carriers, or, more likely, Auger processes.

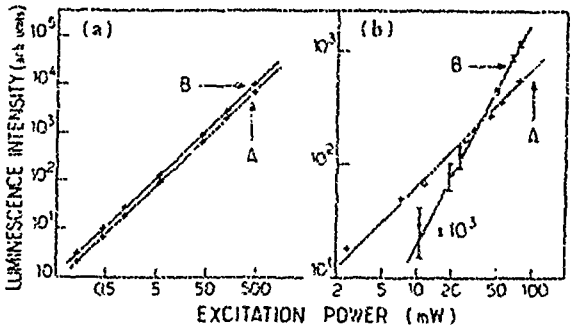

Fig. 2 : Integrated intensities of the interface "A" and InP "B" luminescence lines versus the pump intensity (a) for an excitation energy $h\nu_1$ = 1.51 eV and (b) for an excitation at $h\nu_2$ = 1.325 eV

To discriminate between these possible explanations, we have examined the excitation wavelength dependence of the InP luminescence, at a fixed pump intensity. We find that the signal varies like the square of the interface absorption coefficient α^A deduced from the PLE spectrum of Fig. 1b. Considering that in the range of excitation power density used in our experiment (< 1 W/mm^2) the areal density of photo-carriers is by far lower than the density of native electrons in the two-dimensional electron gas, this result proves that the up-converted luminescence signal is directly proportional to the square of the photo-hole density p, which rules out intra-band absorption (which would depend linearly on p, hence on α^A) and two-photon absorption, which would not depend on p or α^A. Clearly, the only mechanism which explains the I_{ex}^2 and $\alpha^{A\,2}$ dependences is a one electron-two hole Auger recombination process. The way we interpret the up-conversion is illustrated in Fig. 1a: Auger recombination processes involving a native electron and two photo-holes provide high energy holes which, during thermalization, are redistributed in the heterostructure. Those falling into the InP side are finally pushed away from the interface by the

electric field, and they thermalize at the top of the InP valence band and recombine there with native electrons (or, possibly, with excess electrons provided by an other Auger process): this is the "Auger fountain" effect.

In order to discuss these results more quantitatively, we use simplified rate equations governing the ratio of the luminescence signals. Under cw excitation, a luminescence signal L can always be written as:

$$L = g \eta G \qquad (1)$$

where g is an external coupling constant (which is the same for the A and B luminescence lines), η the radiative efficiency and G the carrier generation rate. For photo-carriers, G is given by:

$$G = \alpha I (1-R) / h\nu \qquad (2)$$

where α is the absorption, R ≈ 0.3 the sample reflecuvity, I the pump power and $h\nu$ the energy of the exciting photons. For Auger holes, we assume that the generation rate can be written, in formal analogy with the bulk situation, as:

$$G = 0.5\, S\, C_p\, n\, p^2 \qquad (3)$$

where S is the surface of the excited region. As already mentioned, n is essentially constant and equal to the areal density of native electrons in the two-dimensional electron gas. The 0.5 factor accounts for the fact that a maximum of only one half of the Auger holes will be fed to the InP buffer layer.

η is clearly different for the interface and the InP luminescences, since the huge difference in absorptions (≈10-4 and ≈0.1, respectively) results in nearly equal integrated intensities. With the superscripts A, B referring to the interface and InP luminescence lines and the subscripts 1, 2 refering to the excitation energies 1.51 eV and 1.32 eV respectively, we thus write four equations:

$$L^{A,B}_{1,2} = g\, \eta^{A,B}\, G^{A,B}_{1,2} \qquad (4)$$

where $G^A_{1,2}$ and G^B_1 are given by Eq. 2 and G^B_2 by Eq. 3. Finally, we assume that the interface recombination follows an exponential law with a time constant τ^A. Hence, the steady state density of photo-holes is simply:

$$p_{1,2} = G^A_{1,2}\, \tau^A / S \qquad (5)$$

This system of equations immediately gives the Auger coefficient as:

$$C_p = 2\, \frac{L^B_2}{L^A_2}\, \frac{L^A_1}{L^B_1}\, \frac{\alpha^B_1}{\alpha^A_1}\, \frac{1}{(\tau^A)^2}\, \frac{1}{\alpha^A_2}\, \frac{S\, h\nu_2}{(1-R)\, I_2}\, \frac{i}{n} \qquad (6)$$

From the interface PLE spectrum, we know that $\alpha^A_1 / \alpha^A_2 = 3$. Besides, the absorption coefficient of bulk InP at 1.51 eV is 10^4 cm^{-1}, hence the absorption by the 1000 Å thick layer is $\alpha^B_1 \approx 0.1$. Equation 6 unfortunately still contains two unknown quantities, α^A_2 and τ^A. In order to determine τ^A we have measured the time decay of the interface luminescence,

using a cavity-dumped Ar^+-laser delivering ≈15 ns pulses. The decay curves of the InP (which essentially reflects the exciting pulse) and the interface luminescences are shown in Fig. 3. Although a deconvolution of the two responses is needed for better accuracy, it is clear that the interface luminescence involves a characteristic time constant of ≈15 ns, which is indeed significantly longer than the decay times usually observed at low temperature in type I heterostructures or bulk materials (< 1ns).

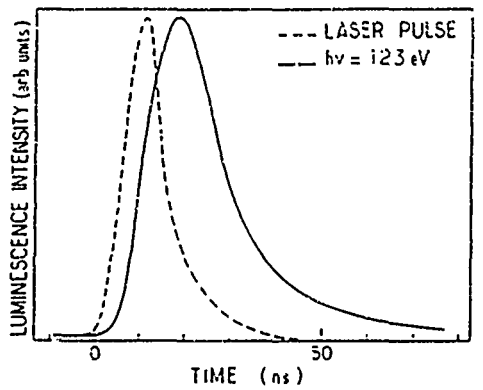

Fig. 3 : Time decay of the interface (solid line) and InP luminescences (dashed line). The dashed line essentially represents the shape of the exciting pulse of the cavity dumped Ar^+ laser, convoluted with the response of our detection. The broadening of the interface response indicates a lifetime τ^A ≈15 ns.

Unfortunately, the absolute value of the absorption by the interface cannot be measured directly, and our evaluation of C_p has to rely on the theoretical estimate of α^A_2. As already mentioned, the numerical calculation of the overlap of the ground-state wavefunctions indicates a threshold absorption equal to $3.\ 10^{-5}$. The absorption at $h\nu_2$ = 1.325 eV, about 75 meV above the interface bandgap, may be significantly larger because other two-dimensional subbands can contribute to the absorption, which, incidentally, do not obey any parity selection rule. The number of hole subbands is probably restricted because the corresponding quantum well is rather deep (see Fig. 1a), but the situation of electron subbands is more difficult to handle because we deal with an accumulation rather than with an inversion situation. However, from the smooth lineshape of the PLE spectrum, and its comparison with various numerical simulations, we believe that $\alpha^A_2 = 10^{-4}$ is a representative figure, and should not be wrong by more than a factor of 2. Using this value, and the experimental data $L^B_2 / L^A_2 \approx 10^{-3}$ for a pump intensity I_2=20 mW at 1.325 eV, focused on a 0.8 mm^2 spot, we get $p = 10^7$ cm^{-2} (hence $p \ll n$) and:

$$C_p = 1.2\ 10^{-11}\ \text{cm}^4\,\text{s}^{-1} \qquad (7)$$

The main uncertainties in this determination certainly lies in the evaluation of the interface absorption α^A_2 , and, as usual with investigations of Auger effects, in the estimation of the size of the excited region. All together, we estimate that these uncertainties should not exceed a factor of 10. More questionable might be the assumption, implicit up to now, that all the Auger holes falling into the InP layer actually thermalize and recombine in InP instead of tunneling back to the AlInAs side of the interface. This assumption is in fact supported by the examination of the extended interface PLE spectrum [8,10]: the absorption by InP manifests itself by a moderate raise (merely a factor of two) in the interface luminescence, which proves that only a very small fraction

of the holes photo-created in InP actually tunnel and feed the interface luminescence.

Finally, it is certainly desirable to attempt a comparison between our new two-dimensional Auger recombination process and the situation of bulk materials (InP, GaAs) where Auger coefficients are in the range:

$$C_p^{3D} \approx 10^{-28} \cdot 10^{-30}\ cm^6\ s^{-1} \qquad (8)$$

It is not clear whether this procedure is fully justified, but, in analogy with what was done in the case of type I quantum wells [6], a simple way to derive an "equivalent 3-dimensional Auger coefficient" consists in writing:

$$eq.\ C_p^{3D} = C_p^{2D}\ L_c L_p^2 / (L_c + L_p) \qquad (9)$$

where $L_{c,p}$ are characteristic lengths for the electron and hole wavefunctions along the z-direction. Taking the extension of the classical motions, L_c= 100 Å and L_p = 70 Å, we get :

$$eq.\ C_p^{3D} = 3.\ 10^{-24}\ cm^6\ s^{-1} \qquad (10)$$

This value is several orders of magnitude larger than the reported values for bulk materials with small spin-orbit splitting, like GaAs or InP. This result supports the idea that phase-space and matrix-elements considerations make Auger processes more "efficient" at type II interfaces [9]. This conclusion seems at odd with the observation of laser emission in InP-AlInAs superlattices [7]. The solution of this apparent paradoxe is probably the fact that our investigations also indicate that the type II interface has a much better radiative efficiency than the bulk material ($\eta^A \approx 30\ \eta^B$), which favors lasing at low carrier density.

In conclusion, we have evidenced a novel energy up-conversion mechanism, the Auger hot-carrier fountain effect in type II InP-AlInAs heterojunctions. This effect, which may become quite efficien, at unusually low pump power, might have potential applications. On a more fundamental ground, it allows a new experimental approach to Auger recombination in semiconductor heterostructures. Extension of this first study to the case of InP-AlInAs superlattices will help the elucidation of the apparent contradiction between high Auger recombination rate and fair laser effect in these materials.

Acknowledgements: we thank T. Lebihen and C. Delalande for their help and the use of their Ti:Saphir laser, and P. Roussignol for fruitful discussions. LPMC-ENS is Unité Associée N° 1437 at CNRS

references:

+ permanent adress: Ioffe Phys. Tech. Inst. RAS, St Petersburg, Russia
1 H.C. Casey and M.B. Panish, Heterostructure Lasers, Academic Press, New York (1978)
2 G. Benz and R. Conradt, Phys. Rev. B16, 843 (1977)
3 U. Strauss, W.W. Rühle and K. Köhler, Appl. Phys. Lett. 62, 55 (1993)
4 A.N. Titkov, G. N. Iluridze, I.F. Mironov and V.A. Cheban, Sov. Phys. Semicond. 20, 14 (1986)
5 A. Haug, J. Phys. C16, 4159 (1983)
6 B. Sermage, D.S. Chemla, D. Sivco and A.Y. Cho, IEEE J. Quantum Electronics, QE 22, 774 (1986) and references therein.
7 E. Lugagne-Delpon, P. Voisin, M. Voos and J.P. André, Appl. Phys. Lett. 60, 3087 (1992)
8 E. Lugagne-Delpon, J.P. André and P. Voisin, this conference, and Solid State Comm. 86, 1 (1993)
9 The Unknown Russian Theoretician, private communication
10 E. Lugagne-Delpon, Doctorat Thesis, Université Paris VI (1993) (unpublished)
11 These excitation spectra are obtained using an extremely low power excitation set-up using an halogen lamp followed by a monochromator as the excitation source

WeB1

High-Resolution Transmission Electron Microscopy of Heterostructures

H. Cerva
Siemens AG, Research Laboratories, Otto Hahn Ring 6,
D-81730 München, Germany

Abstract

Chemical information on a near-atomic scale may be obtained from high-resolution transmission electron microscope (HREM) images. This requires first a distinct contrast difference in the adjacent semiconductor materials in a particular projection direction for a wide range of objective lens defoci and specimen thicknesses for the given microscope parameters (acceleration voltage, spherical aberration constants). Second this contrast difference must behave almost linear with layer composition. The contrast formation in the sytems Al/GaAs and Si/Ge, where such conditions may be found and which are representatives for amplitude and phase contrast respectively, is discussed. The method of chemical lattice imaging is applied to $Al_xGa_{1-x}As$ structures and reveals differences in the abruptness of GaAs on $Al_xGa_{1-x}As$ and $Al_xGa_{1-x}As$ on GaAs interfaces. Selected area diffraction is shown to yield the period length of short period superlattices in unstrained Al/GaAs and strained Si/Ge systems with high accuracy.

Introduction

Semiconductor heterostructure layer systems with their geometric structures and compositional variations in near-atomic dimensions are suitably characterized by transmission electron microscopy (TEM) because of its high spatial resolution. Dark-field imaging with the (200) reflection and bright-field imaging of conventionally ion-beam-milled thin cross sections or cleaved 90° wedge-shaped specimens are nowadays routinely used to characterize layer growth and processing [1]. High-resolution electron microscopy (HREM) provides not only structural but also quantitative chemical information of interfaces at atomic or near-atomic scale. This requires to relate the image intensities observed with appropriate imaging conditions in the specifically different HREM contrast patterns at the interface and on both sides of the interface to the chemical variation across the interface, and develop an algorithm to extract the chemical signal quantitatively [2]. Over the last years this algorithm [2,3], applied to images projected in <100>, has been extensively used for various systems such as Al/GaAs and Hg/CdTe to study structural and chemical interface properties and point defects [4,5,6]. A theoretical treatment of the image contrast in <100> projection based on the non-linear imaging theory was described for the Al/GaAs and Si/Ge system [7,8] and was experimentally demonstrated for the Al/GaAs system by using a different algorithm for quantitative analysis[7,9]. This algorithm was used to verify the different abruptness of the AlAs/GaAs and the GaAs/AlAs interfaces [10]. Successful quantitative analysis of strained Si/Ge superlattices in <100> and <110> projection has been reported recently by using a similar approach as in [7,8,9] but by taking also into account in the

algorithm the lattice distortions at the interface [11,12]. First, the important issues of the imaging process as well as the algorithm for extracting the quantitative information will be discussed and reviewed. Then, the applications to an Al/GaAs resonant tunneling structure and a short period superlattice (SPS) are presented. Finally, it is shown that selected area electron diffraction (SAD) yields additional information of strained and unstrained SPS structures.

Quantitative Chemical HREM Analysis

(a)General and Al/GaAs <100> Images

The main task is to find the appropriate imaging conditions (ranges of defocus Δf, and specimen thickness t) for a given TEM to distinguish between two adjacent materials with identical lattice but different elemental constituents by their HREM contrast which should be quantifiable. The HREM image in fig. 1 shows a cleaved 90° wedge-shaped specimen of an AlAs/GaAs superlattice in <100> projection recorded with 400 kV at optimum imaging conditions for this system. At the defocus Δf=-25nm±5nm and for the thickness range 7<t<13nm, the AlAs layer is characterized by a strong (200)-pattern contrast with the white dots corresponding to Al-atom columns and black dots to As-atom columns, whereas in GaAs a (220)-pattern contrast prevails where white dots represent positions of Ga- or Al-atom columns and black dots are tunnels in the structure. When crossing the interface these contrasts change gradually. At the given imaging conditions this change in contrast going along with a change of the Al-content can be described by those Fourier components of the image intensity which contain the linear beam interactions between the transmitted and the (200) beams as well as the non-linear interactions between (200) and (220) beams [7,9]. This behaviour stems from the fact that in the <100> projection the amplitudes of the (200) beams in $Al_xGa_{1-x}As$ increase with the Al-content x whereas those of the (220) beams remain almost constant for the chosen imaging conditions.

In the contrast patterns the smallest unit cell is chosen which contains all the chemical information for the quantification procedure. In the case of $Al_xGa_{1-x}As$ in <100> projection this is a 0.28 nm^2 square shaped cell [2,3]. This is due to the fact that the (200) beams with their 0.28 nm spacing contain the chemical information. The reference cells for AlAs and GaAs are shown by the white small frames in fig.1. The resolution of this method, however, is not only determined by the size of the unit cell. Assuming perfect coherent illumination, the imaging conditions are periodic with defocus. Then, however, the Fourier-transformed contrast transfer function, which is a function of the TEM parameters, is broadend at higher defoci. At larger defoci this results in larger deviations in the quantitatively determined compositions of individual columns from the actual values because of the influence from neighbouring columns with different compositions [9]. In the Al/GaAs system quantifiable images may be obtained with a Jeol 4000EX microscope at Δf=-20, and -70nm [9,13] but spreading starts at -120nm [9]. In material systems where a much smaller unit cell can be chosen because of the smaller spacings of the reflections which contain the chemical information, a TEM with improved resolution would have to be used.

There exist various pattern-recognition approaches to extract the compositional information from the intensity distribution [2,3,9,14]. In our approach only those Fourier components are derived from the intensity distribution which contain the chemically sensitive linear and non-linear contributions of the (200) beams [9]. The sum of these chemically sensitive Fourier components yield a chemical signal which is normalized with help of the reference cells in the, e.g., AlAs and GaAs layers and is almost linear with the Al-content. This chemical signal becomes 0 for GaAs and 1 for AlAs. Testing this algorithm on simulated images of sharp and graded interfaces at the optimum imaging conditions showed that the composition profiles across the interfaces deviate from the given profiles by only $\Delta x \leq 0.03$ for each unit cell [9]. In comparison to the cross-correlation method of Ourmazd et al. [2,3] which is a real-space method including all Fourier components almost exactly, the same results for Al/GaAs interfaces were obtained [9]. Since in HREM imaging we are dealing with projected images the accuracy of about $\Delta x \approx 0.03$ within each unit cell allows to detect a vacancy of one Al-atom (or a replacement by one Ga-atom) in a cation column of a 11nm thick specimen [3,9]. Experimentally beam and crystal tilts can be controlled to be ≤ 1.4 and 2.8mrad by checking fine contrast details in the image at other defoci, and the systematic error becomes $\Delta x \leq 0.05$ [9].

Electron irradiation at 400kV leads to knock on damage in AlAs and GaAs but does not affect the contrast as long as images are taken within 15 minutes irradiating the same area [3,9]. In order to reduce the random error caused by quantum noise (amplified by the photographic process) and surface roughnesses of the specimen, the chemical signal for the reference unit cells is obtained by averaging over several cells in the reference layers. This reduces the noise for a cell with unknown composition. For chemically etched cross sections of Al/GaAs specimens the best signal to noise ratio reported is S/N=20 [3] whereas it is about 10 for cleaved wedge specimens [9] and 5 for ion-beam thinned samples [3,9]. The accuracy is then given by the sum of the systematic and random error and in the best case is $\Delta x \leq 0.1$. The accuracy of compositional profiles may, however, be improved by averaging over several cells along the interface. Cleaved 90° wedge-shaped specimens of Al/GaAs structures have the advantage that they are quickly prepared and that the specimen thickness is easily controlled (fig.1). Moreover, from the change of the contrast with thickness, the width of an interfacial transition layer may qualitatively be estimated [9,10].

(b) Si/Ge images

In the case of Si or Ge there exist no so called chemically sensitive reflections, such as the (200) beams in the compound semiconductors, owing to their diamond structure. Taking the <100> projection as example mainly the transmitted and the four (220) beams contribute to the HREM image. In contrast to the Al/GaAs case where the difference in the amplitudes of the (200) beams yields information on the Al-content, the amplitudes of the (220) reflections do not differ significantly in Si and Ge for thicknesses <18nm. However, there is a distinct difference in the phases of the (220) beams in Si and Ge. Considering the linear beam interaction between transmitted and (220) beams, an image contrast difference between Si and Ge will be obtained at imaging conditions where the generalized transfer functions (GTF) $\cos(\Theta_{220} - \Theta_{000} + \chi_{220})$ for Si and Ge are different (Θ ..phase shift due to scattering, χ . phase shift by objective lens). Defocus and thickness may be chosen such that the difference is $\pi/2$ or π. In the first case one layer shows a strong (220)-pattern contrast ($|GTF|=1$) while in the other layer "half-spacing" contrast dominates ((400)-pattern), (GTF=0) which originates from non-linear beam interactions between the various (220) beams [8]. In the second case the GTF is +1 for the layer where the atom columns appear as white dots and the tunnels as black dots, while the GTF is -1 for the layer with reversed contrast. This situation is shown for 400kV in the simulated images of a Si_1Ge_1 superlattice (fig.2). Si-atom columns are dark, Ge-atom columns are bright. The sharp interfaces chosen in the model are marked by the arrows and lie between the pair of bright dots which are 0.14nm apart. In the upper left corner of fig.2 the Fourier component I(220) of the image intensity is plotted for Ge and Si as a function of t at Δf=-55nm. From this plot it can be

seen that a phase difference of π is obtained in the thickness range $13 \le t \le 18$nm. The image simulation reveals that this contrast is stable for $-60 \le \Delta f \le -50$nm [8]. The same results were reported by Stenkamp and Jäger [11,12]. Moreover, they showed that the contrast becomes linearly quantifiable for $Si_{1-x}Ge_x$ ($0 \le x \le 1$). In the <110> projection it is the phase of the (111) beams which has to be considered similarly to the (220) beams in the <100> case. Experimental <110> HREM images of Si_mGe_n SPS have been successfully quantified by applying a similar Fourier approach as described in [9] but implementing a new method taking into account the tetragonal lattice distortions [12]. They also report that the cross-correlation method fails in this case because it is not selective to those Fourier components which are chemically sensitive for the chosen imaging conditions but also includes Fourier components which behave non-linearly.

(c) AlAs/GaAs <110> images

When <100> and <110> HREM images recorded at 400kV of the same MOCVD (metal organic chemical vapour deposition) grown AlAs/GaAs superlattice were compared by visual inspection, different interface abruptnesses were observed (fig.3a and fig.4b) [1]. The interface was analyzed quantitatively from the <100> image in fig.3a which was taken at optimum imaging conditions. The Al-concentration profile is shown in fig.3b and reveals an interfacial transition zone being five cation layers broad. By averaging over 64 cells along the interface the statistical error for the Al-content x in the cation layers of the transition region was reduced to about 0.04. The error bar $\Delta x = \pm 0.01$ drawn in fig.3b gives an upper limit of the uncertainty for the composition determination resulting from both statistical and systematic errors.

Judging visually the <110> image of the same superlattice, the interface zone may be estimated to be only one to two cation layers broad. <110> HREM images of AlGaAs layer-structures are often imaged under conditions where one layer shows up with a strong (111)-pattern while in the other layer "half-spacing" contrast dominates (fig.4b) [15]. In such <110> images the (111)-pattern contrast comes mainly from the linear contributions of the (111) beams whereas the half-spacing contrast stems from non-linear contributions of the (111), (200), and (220) beams [16]. In contrast to the <100> projection this specific contrast difference comes only from a difference in the phase [16]. Half-spacing contrast and (111)-pattern contrast occur in one or the other layer for numerous imaging conditions. For, e.g., the imaging conditions $\Delta f \approx -35$nm, and $t = 20.8$nm the (111)-pattern dominates in the GaAs whereas a half-spacing contrast appears in the AlAs layer (fig.4b). Figure 4a shows the corresponding chemical signal as a function of Al-content x. Only for a narrow composition range $0.6 \le x \le 0.9$ a linear relationship exists. For lower x values the function is ambiguous. Hence, the interface appears to be much sharper in the <110> image. Such imaging conditions are not suitable for quantification and also a qualitative visual evaluation of the interface is unreliable or even erroneous. Moreover, the ranges of Δf, and t for imaging the layers with these contrasts are not very broad and alternate rapidly with thickness [16].

Applications

(a) $Al_xGa_{1-x}As$/GaAs double barrier quantum wells

The interface quality of double barrier quantum wells (DBQW) used in resonant tunneling structures determines their electrical properties and, therefore, the interface quality is of decisive importance. Figure 5a shows a <100> HREM image of a conventional thin cross section from a

$Al_{0.4}Ga_{0.6}As$/GaAs DBQW structure grown by molecular beam epitaxy (MBE) [10]. Specimen thickness and defocus are within optimum range. There is a clear difference in interface abruptness between normal ($Al_{0.4}Ga_{0.6}As$ on GaAs) and inverted interfaces (GaAs on $Al_{0.4}Ga_{0.6}As$): the normal interfaces appear abrupt and the inverted ones diffuse. To quantify this impression the Al-concentration profiles across the interfaces were determined using the algorithm described above (fig.5b). By averaging over 64 cells along the individual interfaces the statistical error for the Al-content x in the cation layers of the transition region was reduced to ≤ 0.04. The normal interface exhibits a transition region extending over one cation layer whereas the diffuse inverted interface extends over three cation layers. This difference between normal and inverted interface is also observed in AlAs/GaAs DBQWs and can be explained by the higher surface mobility of Ga atoms on the GaAs surface compared to that of the Al atoms on the $Al_xGa_{1-x}As$ surface during MBE growth. These results are in perfect agreement with asymmetries in electrical transport measurements [10].

(b) Short period superlattices

Short-period superlattices (SPS) of compound and elemental semiconductors deposited by MBE reveal interesting physical properties. Multiquantum well structures using $(GaAs)_m(AlAs)_n$ SPS instead of $Al_xGa_{1-x}As$ alloy layers as barriers reveal better optical properties. Strained-layer Si_mGe_n SPS have a modified electronic bandstructure compared to Si and Ge. Besides new electronic devices which become possible, they offer to realize a quasi-direct band gap semiconductor made from the indirect host materials. Characterization of period length, thickness and composition of individual layers, and layer thickness fluctuations is important to optimize growth conditions.

Superlattices of the type $(GaAs)_m(AlAs)_n$ grown on {100} substrates have an artificial tetragonal structure with reduced point group symmetry compared to the host materials. The spacegroup of the superlattice depends on whether the total number of monolayers in the unit cell is even or odd [17]. Each layer of GaAs or AlAs is a double-layer (DL) consisting of a cation layer and an arsenic layer with the DL thickness being that of the (200) lattice spacing d_{200}. Thus, for a given SPS the number (m+n) of DLs corresponds to the period $d_{SL} = (m+n)\, d_{200}$ of the SPS in <100> direction. The artificial superlattice structure causes superlattice spots (SLS) in the diffraction pattern lying on rows between the reflections of the bulk material having reciprocal lattice vectors $\{h00\}$ perpendicular to the {100} surface. The SLSs have a spacing of $1/d_{SL} = 1/(d_{200}\,(m+n))$ [18,19]. Only for (m+n) being an integer the $k\cdot(m+n)^{th}$ SLSs coincide with a reflection of the bulk material. Due to double diffraction in thick TEM specimen areas (typically 20-500nm thickness) the rows of SLSs appear centred on each bulk reflection. Hence, for non-integer periods (m+n) a SLS "splitting" occurs as the SLSs do not coincide [20,21]. Figure 6 shows a section of the <100> SAD pattern of a nominally $(GaAs)_3(AlAs)_3$ SPS, 1 µm thick, obtained from a cleaved 90° wedge-shaped specimen. The aperture diameter used for SAD which defines the area where the diffraction information comes from was typically 0.3 to 0.5 µm. The arrows in fig.6 indicate the SLSs which are centred on the (200) and (000) spots. The fact that these rows of spots do not coincide reveals that the periodicity is incommensurate. The reciprocal spacing of the spots is in both cases $d_{SL} = 10.76$ DLs. If the diameter of the SAD aperture is smaller than the total thickness of the SPS structure, then several SAD patterns may be recorded as a function of growth direction. This allows to search for growth irregularities such as areas with different superlattice periodicities. The individual layer thicknesses are difficult to measure in conventional bright- or dark-field images of conventional cross sections or cleaved specimens when the thickness approaches or is below 1nm [1]. Then HREM imaging

in <100> projection is useful to determine interface abruptness and average individual layer thickness. Both SAD and HREM imaging may rather quickly be carried out on cleaved 90° wedge-shaped specimens. Figure 7a shows the <100> lattice image recorded at optimum imaging conditions for 400kV together with the optical diffraction pattern (ODP) obtained from the negative with a small aperture corresponding in the image to a circular area with a diameter of about 25 nm. The ODP reveals also SLSs yielding a periodicity of 10.77 DLs. The Al-concentration profile was calculated for about 2.5 periods of the SPS by averaging over 12 cells parallel to the interface. The total error in determination of the Al-content is ±0.1. When averaging the Al-content x of all cation layers this SPS corresponds to an alloy with x =0.25 which is in good agreement with the results obtained from photoluminescence measurements. The profile in fig. 7b also shows that the period is not strictly 10 DLs but varies between 10 and 11 DLs. Both interfaces are not abrupt which for AlAs on GaAs is in contrast to the finding of the DBQW structure (see above). Both structures were grown with similar growth parameters, but probably because of the thinner GaAs layers in the SPS structure the GaAs surfaces do not become flat. The individual layers consist of: 7-8 GaAs layers (4-5 cation layers with x=0±0.1 and 2-4 cation layers with x=0.25±0.1) and 3-4 AlAs layers (1-2 cation layers with x=1±0.1 and 1-2 cation layers with x=0.7±0.1).

Another situation exists for SPSs of the type Si_mGe_n because they are strained due to the 4.2% lattice mismatch of the host materials, and in contrast to the compound semiconductors on {100} surfaces the thinnest individual layer that may be grown is either a monolayer (ML) of Si or Ge with the thickness d_{001}. This leads to various possible spacegroups for various combinations of *m/n* whether m and/or n are even or odd [17]. For the case (m+n) even the number (m+n) of MLs corresponds to the period $d_{SL}=(m+n)\cdot d_{001}$ of the SPS in <100> direction, whereas for (m+n) odd twice the number (m+n) of MLs corresponds to the period $d_{SL}=2(m+n)\cdot d_{001}$. This causes an interesting effect in the SAD patterns of <110> zone axes recorded parallel to the interfaces: for (m+n) odd there is a "doubling" of SLSs between (200) and (000). Thus, a SPS Si_mGe_n with (m+n) odd shows the same number of spots as a SPS $Si_{2m}Ge_{2n}$ [22]. This effect is due to Umweganregung of the kinematically forbidden (200) reflection via the {111} reflections. Figure 8 shows sections of <110> SAD patterns between two fundamental spots for a series of Si_mGe_n SPSs. From the left to the right in fig. 8 the measured period (m+n) decreases from 8.4 to 6.6. Arrows which are linked indicate positions of related SLSs emanating from the same fundamental spot. Comparing fig. 8b and 8d the number of SLS positions has doubled for the SPS with the odd period length. The SLSs emanating from one fundamental spot lie exactly in between those SLSs coming from the other fundamental spot. This causes a virtual doubling of the period length [23]. Experimentally this effect is only observed for very short SPSs when the rows of SLSs overlap [22]. Since the SPSs are strained the total thickness is small (typically 20-200nm) to avoid plastical relaxation. The selected area aperture (diameter typically 0.3-0.5µm), therefore, contains mainly diffraction information from the substrate. Hence, the superlattice spots are much weaker than in the case of the thick $(GaAs)_l(AlAs)_k$ SPS in fig. 6. Besides, the intensity of the SLSs is a criterium for the perfection of the layers and interfaces [24].

In $(GaAs)_m(AlAs)_n$ SPSs the effect of SLS doubling does not occur for odd (m+n) because the smallest individual layer possible is two MLs thick. However, due to the Umweganregung in <110> orientation a doubling of the number of SLSs may occur for half-integer periods. The doubling of the number of SLSs may also happen in <100> projection of Si/Ge SPSs at the period length is half-integer (2(m+n)+1)/2. Then, the number of SLSs between (000) and (400) spots is theoretically the same as for a Si/Ge SPS with the period 2(m+n)+1.

As noted before the Si_mGe_n SPSs are strained and, therefore, (100) spots with l=2n of the Si or Ge substrate do not coincide with SLSs. The separation may be well observed in the SAD pattern at the positions of higher orders of (100). Assuming a totally elastically strained SPS the lateral lattice constant of the SPS corresponds to that of the substrate. Then, the average perpendicular lattice constant of the SPS may be determined from the SLSs period d_{SL} while the substrate spots are used for calibration. Moreover, this allows to calculate the composition of the SPS with an accuracy of about 5% [23]. If it is assumed that the lattice parameter within the layer of that Si_mGe_n constituent is not changed which is identical with the substrate material, the perpendicular lattice parameter in the layers of the other constituent may be calculated: $d_{\perp}^{(100)}=d_{SL}\cdot d_{\perp}^{(000)}$ and $d_{\perp}^{(000)}=d^{(100)}$ [25]. If the SPS is plastically relaxed then the lateral lattice parameters of SPS and substrate are different and this may be observed in a "splitting" of the diffraction spots of the lateral planes [26].

Conclusion

Chemical information may be obtained from high-resolution lattice images with near-atomic resolution. For every material combination the electron beam specimen interaction has to be studied in order to find imaging conditions where the contrast depends almost linearly on the layer composition. The imaging conditions (defocus and thickness) have to be stable in a wide range for a given projection direction and a given TEM with its specific electron optical parameters and acceleration voltage. Contrast differences may either arise due to a monotonic behaviour of the amplitude of a specific - so called chemically sensitive - reflection with layer composition (this case applies to the Al/GaAs system) or is due to a phase difference for a particular reflection (this case applies to the Si/Ge system). The resolution for the quantification procedure depends on the lattice plane spacing of the reflection which shows the amplitude or phase variations, the size of the unit cell used in the quantification algorithm, and the electron microscope parameters. An accuracy of $\Delta x \leq 0.1$ can be achieved. Various applications, either in this paper or in the literature, have demonstrated the usefulness of this method. Selected area diffraction has been shown to be an important additional method available in the TEM to characterize the period lengths of short-period superlattices. Cleaved 90° wedge-shaped specimens of compound semiconductors were shown to allow rapid investigation by HREM imaging and electron diffraction.

Acknowledgements: The author thanks Drs. H. Riechert and L. Korte for supplying the Al/GaAs samples and for discussions.

References

[1] e.g. H. Cerva, H. Oppolzer, Prog. Crystal Growth and Charact. 20, 231 (1990), H. Cerva, Appl. Surf. Sci. 50, 19 (1991).

[2] A. Ourmazd, D.W.Taylor, J. Cunningham, C.W. Tu, Phys. Rev. Lett. 62, 933 (1989).

[3] A. Ourmazd, F.H. Baumann, M. Bode, Y. Kim, Ultramicroscopy 34, 237 (1990).

[4] M.H. Bode, A. Ourmazd, J.Vac.Sci.Technol. B10, 1787 (1992).

[5] Y. Kim, A. Ourmazd, R.D. Feldman, J.Vac.Sci.Technol. B8, 1116 (1990).

[6] A. Ourmazd, M. Scheffler, M. Heinemann, J-L. Rouvier, MRS Bulletin 12, 24 (1992)

[7] S. Thoma, H. Cerva, Ultramicroscopy 35, 77 (1991)

[8] S. Thoma, PhD Thesis, Technical University München, Germany (1992).

[9] S. Thoma, H. Cerva, Ultramicroscopy 38, 265 (1991).

[10] S. Thoma, H. Riechert, A. Mitwalsky, H. Oppolzer, J Cryst.Growth 123, 287 (1992).

[11] D. Stenkamp, W. Jäger, Proc. EUREM'92 1, 545 (1992).

[12] D. Stenkamp, W. Jäger, Inst. Phys. Conf. Ser. (1993) to be published

[13] F.H. Baumann, M. Bode, Y. Kim, A. Ourmazd, Ultramicroscopy 47, 167 (1992)

[14] A.F. De Jong, D. Van Dyck, Ultramicroscopy 33, 269 (1990)

[15] A. Poudoulec, B. Guenais, C. D'Anterroches, A. Regreny, J.Cryst.Growth 100, 529 (1990).

[16] S. Thoma, H. Cerva, submitted for publication

[17] M.I. Alonso, M. Cardona, G.Kanellis, Solid State Communications 69, 479 (1989), Corrigendum 70, 1 (1989)

[18] P.M. Petroff, A.C. Gossard, W. Wiegmann, A. Savage, J Cryst Growth 44, 5 (1978).

[19] P.M. Petroff, Inst.Phys.Conf.Ser. 74, 259 (1984)

[20] K. Kifune, S. Kaji, Y. Komura, N. Sano, H. Terauchi, Proc 11th Int.Cong. on Electron Microscopy, Kyoto, (1986), p1475

[21] B. Guenais, A. Poudoulec, P Auvray, M. Baudet, A. Regreny, B. Lambert, J.Cryst Growth 88, 125 (1988).

[22] K. Eberl, W. Wegscheider, G. Abstreiter, H. Cerva, H. Oppolzer, Superlattices and Microstructures 9, 31 (1991)

[23] G. Lütjering, Diploma Thesis, Technical University München, Germany (1992)

[24] T.S. Kuan, W.I. Wang, E.L. Wilkie, European Cong. on Electron Microscopy, Budapest, (1984), Vol 1, p. 535

[25] W. Wegscheider, K. Eberl, G. Abstreiter, H. Cerva, H. Oppolzer, Appl. Phys. Lett. 55, 448 (1989)

[26] W. Wegscheider, PhD Thesis, Technical University München, Germany (1991)

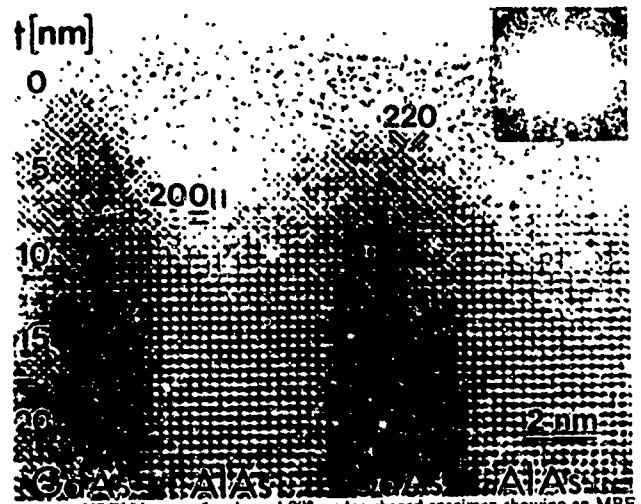

Fig. 1. <100> HREM image of a cleaved 90° wedge-shaped specimen showing an MBE grown AlAs/GaAs superlattice. Pronounced (200)- and (220)-pattern contrast in AlAs and GaAs, respectively, in the thickness range 5≤t≤15 nm for the conditions 400kV, Δf=-25nm. The white frames indicate the 0.28nm² square unit cell of the contrast pattern in AlAs and GaAs used for quantitative analysis. The insert shows an optical diffraction pattern.

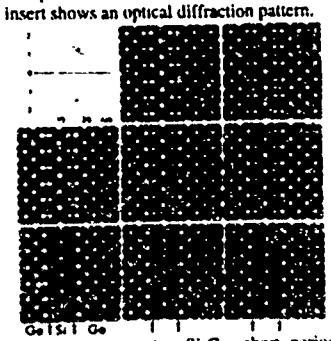

Fig. 2. Simulated <100> HREM images of a Si_1Ge_6 short period superlattice with abrupt interfaces (arrows indicate position of the interfaces). All simulated images show white spots at the positions of the Ge-atom columns and black spots at the positions of Si-atom columns for the thickness and defocus ranges given in the images (in nm). (400)kV, defocus spread 9nm, beam semi-convergence angle 0.7 mrad). The insert shows plots of the Fourier component I(220) of the image intensity for Si and Ge as a function of thickness.

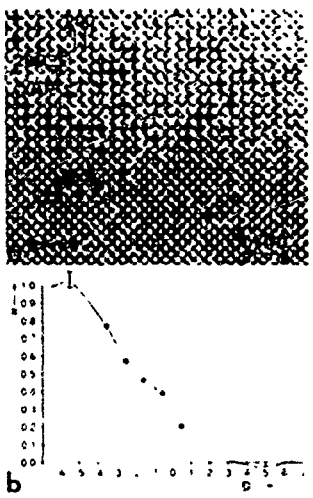

Fig. 3 (a) <100> HREM image of an MOCVD-grown GaAs/AlAs interface (400kV, Δf=-75nm, t≈10nm). (b) Corresponding Al-concentration profile obtained by quantitative contrast analysis and averaging over 64 cells parallel to the interface. There is a 5 cation layers broad interfacial transition zone (*). Conventionally ion beam thinned TEM cross section.

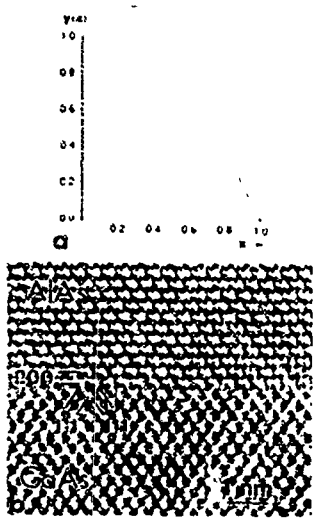

Fig. 4 <110> HREM imaging of a MOCVD-grown AlAs/GaAs interface at imaging conditions, 400kV, Δf=-35nm, t≥15nm (a) Chemical signal y as a function of Al-content x for the quantitative analysis of the <110> HREM image in (b). Conventionally ion beam thinned TEM cross section

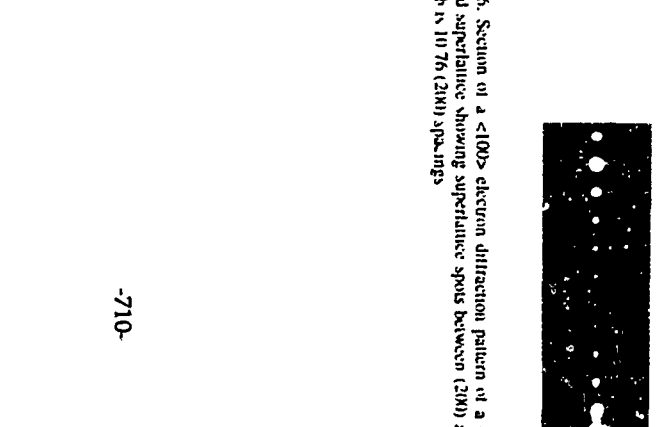

Fig. 5 (a) Experimental <100> HREM image of a cross-sectional specimen containing an MBE-grown GaAs/$Al_xGa_{1-x}As$ double-barrier quantum well structure recorded with Δf=-20nm. $Al_xGa_{1-x}As$ on GaAs interfaces are marked by arrows. (b) Al-concentration profiles determined for the $Al_{x_1}Ga_{1-x_1}As$ on GaAs interface (—) and the reverse interface (- - -) in (a). The profile of a perfectly abrupt interface is also plotted (· · ·)

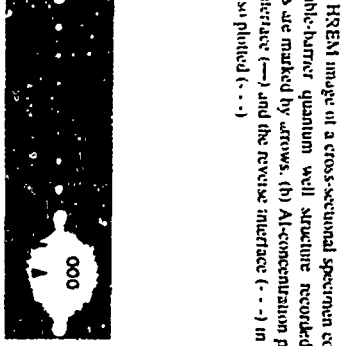

Fig. 6. Section of a <100> electron diffraction pattern of a nominally $(GaAs)_7(AlAs)_3$ short period superlattice showing superlattice spots between (200) and (000) spots. Measured period length is 10.76 (2NM) spacings

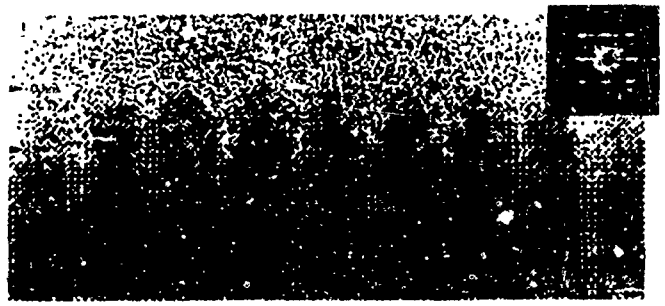

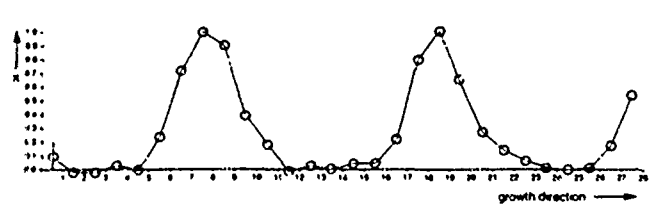

Fig 7 (a) <100> HREM image of an $(GaAs)_5(AlAs)_5$ short period superlattice (cleaved 90° wedge-shaped specimen, 400kV, Δf=-20nm). The optical diffraction pattern reveals additional superlattice spots. (b) Al-concentration profile obtained from 2.5 periods of the superlattice Averaged over 12 cells parallel to the interface.

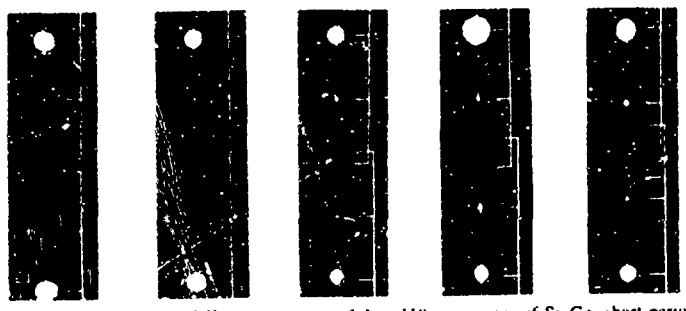

Fig. 8. Sections of electron diffraction patterns of the <110> zone axis of Si_mGe_n short period superlattices. The (200) reflection and the superlattice spots emenating from it are excited because of Umweganregung via the {111} reflections. Nominal m/n values: (a) 2/6, (b) 3/5, (c) 2.5/5, (d) 2/5, (e) 2/5. Measured periods (m+n) are given in the images

WeB2

Cross-Sectional STM on Superlattices and the Effect of Doping

H.W.M. Salemink, M.B. Johnson, O. Albrektsen* and P. Koenraad#

IBM Research Division, Zurich Research Laboratory, CH-8803 Rüschlikon, Switzerland
*Telecommunications Research Laboratory, DK-2970 Hørsholm, Denmark
#Physics Dept., Eindhoven University of Technology, NL-5600 MB Eindhoven, The Netherlands

Extended Abstract

The analysis of semiconductor multilayer structures by cross-sectional STM is discussed. The majority of the work reported is concerned with observations on the UHV cleaved (110) plane of epitaxially grown III-V compounds [1]. The group-III (empty state) or the group-V (filled state) sublattices are selectively imaged by tunneling into the conduction states or out of the valence states, respectively [2]. The heterostructure interfaces are quantified on both the group-III (Al-Ga) and group-V (As) sublattices with atomic resolution in direct space [3]. In particular we demonstrate the definition of the AlGaAs-GaAs interfaces at the atomic scale. Sublattice ordering is observed in domains with a dimension of a few nanometers, and we discuss the consequences of this "clustering" for the homogeneity of ultrathin ternary layers [4].

Fig. 1. (a) Filled-state image of GaAs (110) buffer layer, Be doping level 1×10^{19} cm^{-3}. Sample voltage is −2.1 V, dimensions are 31 × 29 nm. The individual As sites are visible. The hillocks are attributed to the signature of individual doping sites in the topmost layer(s). (b) Charge density corrugation traces across an assigned Be doping site in [001] and [1$\bar{1}$0].

The effect of the doping concentration is visible in two ways. First, we observe the electronic signature of the individual active dopant sites in the top several layers (Fig. 1). Such measurements have been made across modulation-doped GaAs multilayers, and the observed doping site density compares well with SIMS data (Be

dopant density is 10^{18}-10^{19} cm^{-3}) [5]. In addition, clear indicatuons are found for the incorporated delta layer.

The second effect of the doping density is observed via the band-bending inside the semiconductor surface, caused by the electric field strength of the tunneling potential (Fig. 2). The tunneling current (out of the valence band in Fig. 2) traverses two consecutive barriers, the subsurface band-bending zone, which is doping dependent, and the usual vacuum tunnel barrier. Using a numerical model for this tunneling process, we expect an attenuation of the valence band current (Fig. 3) when the doping density is lowered, in agreement with our experimental results. The important role of the doping concentration has been used to analyze the spectroscopic data across heterojunctions [5].

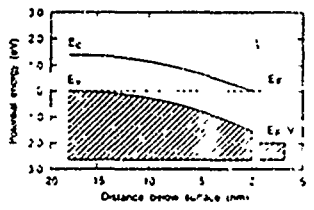

Fig. 2. Energy diagram for tunneling out of valence states; note subsurface band-bending.

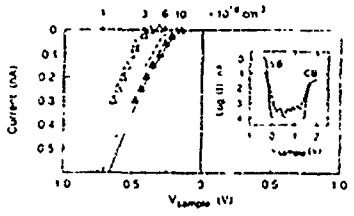

Fig. 3. Calculated valence band current for various dopant densities of Be in GaAs. The symbols are experimental data from current voltage spectroscopy for concentrations of nominally 5 (Δ) and 10×10^{18} cm^{-3} (▲).

[1] H.W.M. Salemink and O. Albrektsen, *J. Vac. Sci. Technol. B* 10, 1799 (1992).
[2] R. Feenstra et al., *Phys. Rev. Lett.* 58, 1192 (1987); O. Albrektsen et al., *Appl. Phys. Lett.* 57, 31 (1990).
[3] H.W.M Salemink et al., *Phys. Rev. B* 47, 16044 (1993).
[4] M.B. Johnson et al., *Appl. Phys. Lett.* 62 (1993) in press.
[5] M.B. Johnson et al., submitted to Appl. Phys. Lett.
[6] H.W M. Salemink et al., *Phys. Rev. B* 45, 6946 (1992).

WeB3

The Surface Evolution and Kinetic Roughening during Homoepitaxy of GaAs (001)

B G. Orr, J. Sudijono, M.D. Johnson, and A.W. Hunt
The Harrison M. Randall Laboratory
University of Michigan
Ann Arbor, MI 48109-1120

Scanning tunneling microscopy studies have been performed on GaAs homoepitaxial films grown by molecular-beam epitaxy. Images show that in the earliest stages of deposition the morphology oscillates between one with two-dimensional islands and flat terraces. After the initial transient regime, the system evolves to a dynamical steady state. This state is characterized by a constant step density and as such the growth mode can be termed step flow. Comparison with RHEED shows that there is a direct correspondence between the surface step density and the RHEED specular intensity. Thick films (up to 1450 monolayers) display a slowly-increasing surface roughness. Analysis of the scaling properties and comparison with theories of film growth will be made.

Thin film deposition has become a critical technology for the advancement of modern electronics. A large number of artificial heterostructures have been produced by using various growth techniques. Molecular Beam Epitaxy (MBE) is particularly important because it affords monoatomic layer thickness control over films growing from the vapor phase at relatively low temperatures under supersaturation conditions [1]. This means that thermodynamically unstable structures can be made by tuning the growth rate and temperature. In fact, with careful choice of the growth parameters to control the surface kinetics, one can create different multi-layered structures in which individual layers maintain their chemical integrity and form compositionally abrupt interfaces with one another.

To understand the growth kinetics, one needs to focus on the growth process at the atomic level. The importance is clear. Semiconductor heterostructures and superlattices possess novel electrical and optical properties. For optimum performance of devices based on these artificial materials, the morphological sharpness of the interfaces is required. Roughness leads to increased carrier scattering in active regions, lowering the carrier mobility. A detailed microscopic examination of the surface kinetic processes will therefore enhance our ability to produce higher quality device structures. In this paper we concentrate on three major processes during MBE growth of GaAs on GaAs (001), i.e. nucleation, growth, and coarsening. Nucleation occurs when adsorbed adatoms make a random walk on the surface until they meet another adatom and form islands. Growth follows when islands larger than a critical nucleus extend with further attachment of adatoms. Coarsening is considered as the transition stage when growth approaches steady-state. This occurs when the step density becomes so high that the growth mode evolves to step flow.

For many years Reflection high-energy electron-diffraction (RHEED) has been the standard *in situ* characterization tools for thin film MBE [2]. In addition to providing information on the evolution of surface structures, RHEED specular intensity oscillations are widely used to monitor growth from the transient (2D nucleation) regime to steady-state (Step-flow) mode. However, being a macroscopic averaging diffraction technique, RHEED fails to give local topographic information. Efforts aimed at modeling nonequilibrium film growth phenomena are thus hindered due to the lack of a real space picture of the growth front as it evolves. This provides motivation for using scanning tunneling microscope (STM) to obtain real space pictures of the surface evolution during growth.

The first part of these experimental studies is to examine the relationship between the RHEED oscillations and the surface evolution of GaAs during deposition. The second part has to do with the investigation of surface roughening during the steady-state growth, i.e. regime where RHEED specular beam no longer oscillates. The experiment consists of initiating growth from a recovered surface and then terminating deposition at a specific point during the growth process. This procedure is then repeated for various termination points. Because the samples are removed from the

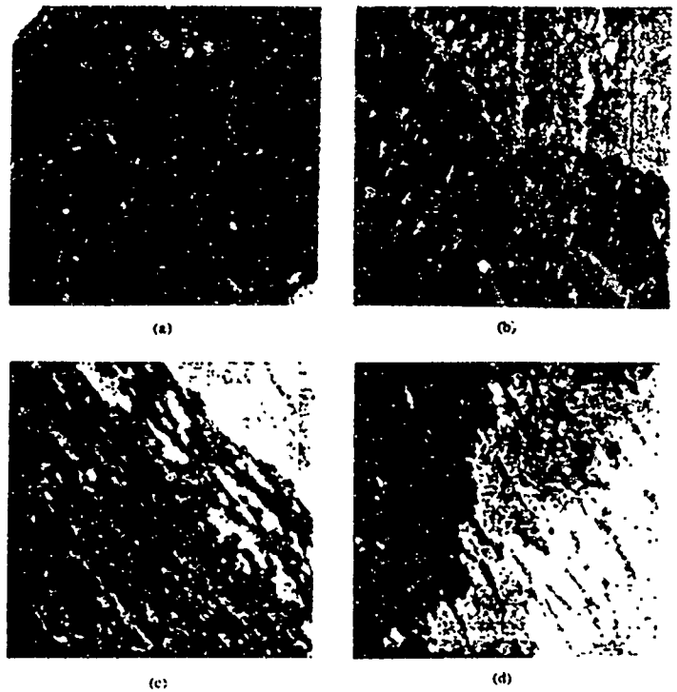

FIG 1 (a) STM image of a GaAs(001) buffer layer. The scan range is 200nm x 200nm. The tunneling voltage (V_t) was +2.8V, applied to the sample, and the tunneling current (I_t) was 80pA. (b) STM image of GaAs(001) surface after deposition of 0.25 monolayer of GaAs. (c) and (d) STM image of GaAs(001) surface after termination of growth at the fourth RHEED minimum and maximum. Notice the change in the local direction of the striations in the figures.

STM for regrowth, no direct comparison can be made between any specific feature in the progression of the images. We have imaged large areas at multiple sites on multiple samples. The images shown are thus representative of the surface.

Deposition was performed in a standard ultra-high vacuum system, base pressure 7×10^{-11}T. Effusion cells were used to produce both the Ga and As_4 fluxes. Commercial GaAs(001) substrates were first chemically cleaned then loaded in the vacuum system where the oxide was removed at 580°C under an As_4 flux. Prior to the experiments a 300 nm thick buffer layer was grown. The substrate temperature during deposition was 555° C. The As to Ga pressure ratio was 15 and the deposition rate was 0.18 micron/hr. The sample miscut as determined by STM was approximately 0.15 degree. The direction and magnitude of the local vicinality was found to vary appreciably. The incident angle of the RHEED beam was approximately 0.9° and corresponded closely to the "in-phase" Bragg condition. The diffraction condition was chosen to yield a reduction in specularly scattered electron intensity as growth commences.

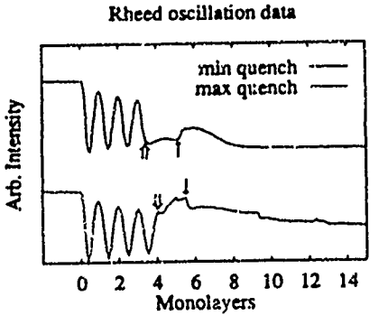

FIG 2 RHEED specular intensity oscillations for GaAs on GaAs(001). The incident angle was 0.9° and the azimuth was along [110]. The δ labels the point at which growth was terminated for each sample and the ‡ indicates an experimental artifact due to the quenching procedure. STM data presented in figures 2c and 2d were acquired from these samples.

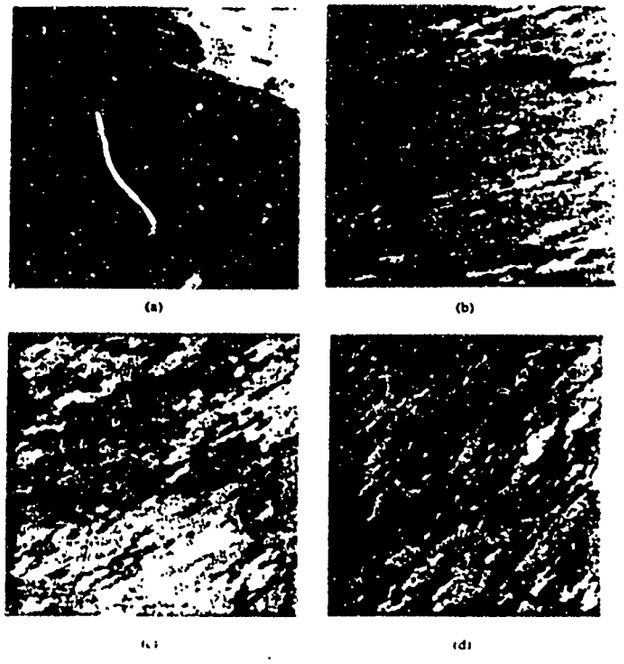

FIG 3 (a) STM image of GaAs(001) after termination of growth of 60 monolayers(ML). (b), (c), and (d) are STM images of GaAs(001) after deposition of 120 MLs, 540 MLs, 1350 ML, respectively. The size of all images is 200nm x 200nm.

The key feature of the experiment was the ability to quench the surface morphology as it appeared during growth. To accomplish this a resistively heated low thermal mass sample was used. The sample temperature could be reduced from that during growth (555°C) to below 430° C in 1.5 sec. A LN_2 cooled baffle with a cooled shutter shrouds the sample [3] The quench procedure has been described previously.[4] Upon the completion of quench, the sample was transferred *in situ to the analysis chamber* equipped with an STM. The RHEED intensity was recorded up to the time of the transfer We found that the RHEED intensity is quite steady during this period indicating that no significant surface evolution has occured.

Figure 1a, shows an STM image of a recovered surface. The terrace size is large and the step edges are smooth. This is the GaAs surface as it appears before growth. Figure 1b shows the surface after deposition of 0.25 *monolayer of GaAs. The typical size of islands* and the average separation between islands are 80 and 300 Å respectively. The coverage seems to be less than 25 percent because growth may have occured at some preexisting step-edges. Figures 1c and 1d are respectively, *images of the surface* as it appeared at the fourth RHEED intensity minimum, and the fourth maximum during the oscillatory regime. The quenched RHEED curves are reproduced in Fig. 2 for completeness.

There is clearly a morphological change in the sample surface profile as it evolves from a RHEED maximum to a RHEED minimum. The surface quenched at an intensity maximum shows few islands on terraces and an approximately equal number *of monolayer deep holes. In contrast*, the surface quenched at a RHEED minimum shows many two-dimensional islands on the terraces. There is a much lower density of monolayer deep holes. The terrace edges for both samples are relatively smooth.

To understand the observed morphological evolution in the context of temporal variation of the RHEED specular intensity, we briefly review various models on the interpretation of the diffraction process. One simple approach uses a kinematical approximation to determine the interaction of the scattered electrons with the surface.[5] In this picture the measured intensity is due to the interference of the electrons scattered from different terraces on the surface. At the correct incident angle (off-Bragg condition) this leads to an oscillation of the specularly reflected intensity due to a changing terrace occupation during deposition. As each growing layer proceeds from zero coverage through half filling and finally to a complete layer the specular intensity cycles through one period. A second, largely phenomenological, model which attempts to incorporate diffuse scattering has been proposed to explain RHEED oscillations. In this model the relevant quantity is not the terrace occupation but the step edge length per unit area, termed step density [6] Steps provide a mechanism for diffuse scattering of the electron beam. With an increase in step density the specularly reflected intensity decreases. As in the previous model, if the surface morphology cycles from islanded to flat then the RHEED intensity would vary accordingly. Monte-Carlo growth simulations have shown an excellent correspondence between the step density and experimental RHEED data taken on vicinal surfaces.[7] There has been criticism of these models due to the incomplete treatment of multiple scattering (MS). While it has been experimentally demonstrated that the behavior of the scattered electrons is a complicated function of both azimuthal and polar angles,[8] results from the dynamical approach[9] remain impractical due to stepped-surface structure idealization. However, much progress has been made in understanding *RHEED* through the MS approach. Mitura and Maksym[10] have recently used MS to successfully study the RHEED Azimuthal Plots, i.e. the specular beam intensity under rotation about the perpendicular axis of the surface. Furthermore, it has been shown that for the out-of-phase diffraction condition, the MS results for specular intensity behavior agree with that of the kinematical approach.[11]

Our STM data can be interpreted within the context of the step density model.[12] The diffraction conditions correspond to the "in phase" Bragg condition where electrons reflected from adjacent terraces constructively interfere. The specular intensity varies not because of interference but, because of diffuse scattering from step edges *There* is a correspondence between films with higher step density and lower RHEED specular intensity. On closer inspection, we find that, within a modified Born approximation, the Bragg scattering from holes less than 5 nm in diameter contribute much less to the diffuse scattering than do islands and terrace edges. As a first approximation, if the step density contribution from small holes is subtracted from the total then the agreement between this modified step density and RHEED intensity is quite strong, see Figure 4.

To further investigate the growth process, we have also examined the sample surface after the decay of RHEED oscillations. Figure 3a shows the surface after 60 *monolayers* have been deposited and the RHEED oscillation amplitude has decayed to less than 5% of its original value. The sample is quenched in the same manner as before. The typical feature size has increased and in contrast to the earlier data the *two-dimensional islands* and terraces edges are now quite ramified. Figure 3b displays the surface after deposition of 120 monolayers. The surface in figure 3a has coarsened so much that it starts to roughen and nucleate 2D islands on top of the terraces. This *may explain the increase* in step density between 60-monolayer deposited surface and that of 120 monolayers. Nevertheless, the overall morphology remains flat, with about four layers present. Surprisingly, further growth does not seem to increase the *surface roughness*, as evidenced by figure 3c and 3d. These STM images obtained after depositing 540 and 1450 monolayers (figs. 3c, 3d respectively) show essentially identical topography to that of the 120 monolayer film. The rms roughness of these *surfaces is* ~ 2.5 Å. *This points to a central feature* of the data, that is the decay of the oscillation amplitude has occurred *without* an increase in the interface roughness. As shown in Figure 4a, the interface width of the grown surface increases extremely *slowly*. Furthermore, the *surface* has achieved a steady state configuration, through a balance of island nucleation and step-edge attachment, which evolves with a constant step density. In short, the surface has reached the *step flow* growth mode.

During deposition an adatom can either diffuse to an existing upward step or kink

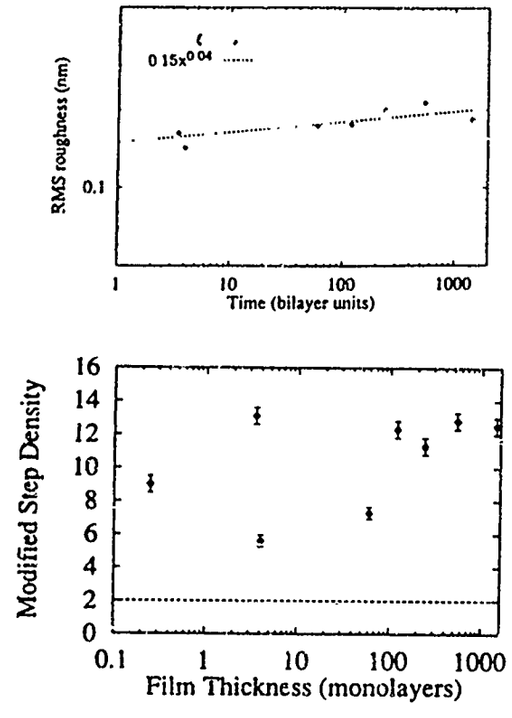

FIG. 4 (a) RMS roughness (in nm) of the surfaces as a function of deposition time (bilayer units) The rms roughness is defined as $\sqrt{\frac{1}{N}\sum_i (h_i - \bar{h})^2}$ where h_i is the height and the sum is over a 200nm x 200nm area. (b) Plot of the surface step densities (in units of 10^{-2} nm^{-1}) as a function of thicknesses (in monolayers) The modified step density is explained in the text The dashed line represent the starting growth substrate

on a terrace edge and be incorporated, diffuse to an existing downward step and be incorporated in the lower terrace, or collide with another adatom and form a new stable island. If the formation of new stable 2D nuclei is dominant then the growth is called layer-by-layer[13]; however, if diffusion to an existing step dominates then the growth is termed step flow. The relative probability of an adatom to follow one of these trajectories is a complicated function of the substrate temperature, growth rate, and surface morphology. The experimental results indicate that evolution of growth of GaAs can be characterized by a change in the relative probability to nucleate a new island versus attaching to an existing step edge. This evolution may be thought of as a *dynamical* transition to step flow growth. What is remarkable is that even though the substrate temperature and growth rate are constant, the surface morphology has been transformed to allow a new growth mode. This type of growth is not what is conventionally called step flow, i.e. a uniform progression of the steps across the surface. The classic step flow occurs when the substrate has a sufficient density of steps and very mobile adatoms. The new feature presented here is that deposition has dynamically generated a sufficient step density to allow for the change from layer-by-layer growth to step flow growth mode.

With this picture in mind, we will now perform the scaling analysis on the steady-state surface, i.e. during step-flow growth. Many theoretical models have been recently proposed to study kinetic roughening of surfaces grown with Molecular Beam Epitaxy (MBE) [14-22] The interest stems from the success at understanding such diverse growth phenomena as directed polymers in random media, evolution of bacterial colonies, UV Chemical Vapor Deposition (UVCVD), and sedimentation in lake beds. These systems, it turns out, share common universality classes and display interesting non-trivial scaling behavior in the dynamics of their interfaces However, there has not been agreement in how to apply these models to the case of MBE or in fact which universality class MBE growth falls under. This controversy is due in part to the lack of experimental evidence to decide which model and universality class is appropriate to describe MBE growth.

Despite the large amount of literature describing MBE growth, the only measurements of dynamic scaling in MBE growth roughening we know of are on films which were grown with low substrate temperatures and thus rough by MBE standards[23-25]. The diffusion length of an adatom on a terrace in these systems is relatively short and it is possible that these systems are governed by a different dynamics than that of typical MBE growth with rapid surface diffusion.

Dynamic renormalization group implies that in order to determine the asymptotic time evolution of a growing surface $h(\vec{r},t)$ one need only consider the contributions from long wavelength modes The higher order terms are irrelevant and will not affect the long-time behavior A universality class can be characterized by a simple equation for the growing interface involving only the relevant operators and from which the scaling properties can be determined. The primary quantities used to describe kinetic roughening are the asymptotic growth exponents α and β which are

expected to satisfy $\xi^2 \propto L^{2\alpha} f(t/L^{\alpha/\beta})$[26] where ξ is the rms roughness, L is the size of the system, and $f(x) \propto x^{2\beta}$ for short times eventually saturating to a constant at $x \sim \mathcal{O}(1)$

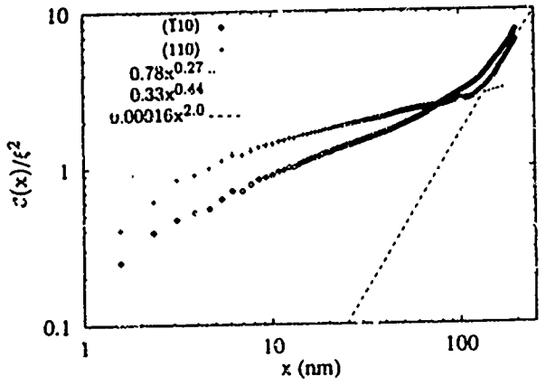

FIG 5 A Logarithmic plot, for two perpendicular crystallographic directions, of the normalized height height correlation function, $C(x) = 1/\xi^2 < (h(r) - h(r+x))^2 >_r$ where ξ is rms roughness. The plots were calculated by averaging the height-height correlation function of 10 independent 2x0nm x 2x0nm images which were plane subtracted so that terraces had no slope. The steep region of the function indicates the cutoff of scaling due to vicinality.

Although MBE growth appears to be conceptually quite simple, i.e. no reevaporation of deposited particles and no formation of voids,[27] an analytic description has not yet been determined to describe the scaling behavior. On the other hand, many numerical simulations of various growth models have been performed to determine the growth exponents α and β. In order for universality to be meaningful the details of the rules used in the simulations should not effect the asymptotic behavior of the interface. However, this does not appear to be the case for the numerical investigations. Despite various models, a conclusive statement has yet to be made regarding the MBE growth.[11-20]

Nevertheless, our experimental measurement of β=0.04 (see Fig. 4a) appears to agree with the prediction of the Edwards-Wilkinson (EW) model, i.e. β=0$^+$.[14] We should mention at this point a need for caution when interpreting the experimental results in terms of theoretical models. To determine the growth exponent $\beta < 0.1$ one needs to measure the roughness over a length scale L for which the interface width has not yet saturated. The time to saturation goes as L^z, where $z = \alpha/\beta$. For a real system this crossover time is very large, however we cannot be sure that for our measurement of β we are not still in an initial transient regime before scaling has set in. In order to be completely confident one would need to grow long enough to see the interface width saturate. Since this would involve growing to many more than 10^4 monolayers, this time will never be reached for typical device quality growth. While it is possible to grow with lower substrate temperaturer to reduce the time to saturation, most experimenters and device growers are trying to produce as smooth a surface as possible and may never reach long term growth.

In an attempt to further study the surface characteristics of these films we have examined the height-height correlation function defined as $C(x) = < (h(r) - h(r+x))^2 >_r$. Figure 5 shows $C(x)$ for a surface after deposition of 1450 monolayers. The correlation function is predicted to scale as $C(x) \sim x^{2\alpha}$.[28] In fig. 5 one can observe two distinct regimes in the correlation function. The small distance dependence indicates a maximum value for the growth exponent $\alpha \leq 0.2$. The extent over which this behavior is exhibited is approximately one decade in distance. For larger distances the behavior is dominated by the vicinality of the sample. For a miscut substrate (all physically realisable samples are miscut) asymptotically $C(x)$ approaches x^2. Our data shows this crossover at approximately x = 100nm. For our experiment the sample miscut was relatively small, $\sim$ 0.15°, producing a typical terrace width of 100 nm. The STM images show quite clearly that during growth there is the dynamic generation of steps and roughness with lengths smaller then the terrace spacing. However, as shown in the dependence of the height-height correlation function $C(x)$ the longest wavelength behavior is dominated by the terrace width for deposition thicknesses up to 1450 layers. The discrepancy between the measured α=0.2 and the EW values (α=0$^+$, β=0$^+$) is larger than that for measured β=0.04. This is most probably due to a greater effect which the vicinality has on surface correlations than on surface roughness.

In conclusion, we have studied the evolution of the GaAs surface during MBE growth. Starting from a recovered substrate, upon the initiation of growth the surface progresses through a transient regime, where cyclic changes in the step density are found, to a steady state. Using in-phase diffraction conditions, we have shown a clear connection between the surface morphology in terms of step density and RHEED intensity oscillations. A striking result is that the decay of the RHEED oscillations is *not* due to an increase in surface width, but the dynamical evolution of the surface to step flow growth, defined as a steady state with a constant step density. The measured surface roughness is consistent with the EW universality class.

The authors would like to thank Dr. D. Kessler and Professor L. Sander and Professor A. Zangwill for stimulating discussions. We also thank M. B. Elowitz and R. Sears for assistance with data analysis. This work has been supported by Grants No. N00014-89-J-1519 and No. NSF/DMR 8857828.

REFERENCES

[1] B.A. Joyce, Contemporary Physics, **32**, 21 (1991) and references therein.
[2] *Reflection High Energy Electron Diffraction and Reflection Electron Imaging of surfaces* NATO ASI series B vol. 188 edited by P.K. Larsen and P.J. Dobson (Plenum, New York, 1988).
[3] B.G. Orr, C.W. Snyder, and M.D. Johnson, Rev. Sci. Instrum, **6**, 1400 (1991).
[4] J. Sudijono, M.D. Johnson, C.W. Snyder, M.B. Elowitz, and B.G. Orr, Phys. Rev. Lett. 69, 2811 (1992).
[5] P.R. Pukite, C.S. Lent, and P.I. Cohen, Surf. Sci. **161**, 39 (1985).
[6] S. Clarke and D.D. Vvedensky, Phys. Rev. Lett. **58**, 2235 (1987).
[7] T. Shitara, D.D. Vvedensky, M.R. Wilby, J. Zhang, J.H. Neave, and B.A. Joyce, Appl. Phys. Lett. 60 (12), 1504 (1992).
[8] P.J. Dobson, B.A. Joyce, J.H. Neave, and J. Zhang, J. Crystal Growth, **81**, 1 (1987).
[9] T. Kawamura and P.A. Maksym, Surf. Sci. **161**, 12 (1985).
[10] Z. Mitura and P.A. Maksym, Phys. Rev. Lett. 70, 2904 (1993).
[11] M.G. Knibb, preprint.
[12] Our STM data are not meant to rule out other models. The experimentally chosen diffraction condition provides little information on the models.
[13] J.H. Neave, B.A. Joyce, P.J. Dobson, and N. Norton, Appl. Phys. A. **31**, 1 (1983).
[14] S.F. Edwards, and D.R. Wilkinson, Proc. R. Soc. Lond. A **381**, 17 (1982).
[15] M. Kardar, G. Parisi, and Y.C. Zhang, Phys. Rev. Lett. **56**, 889 (1986).
[16] D.E. Wolf and J. Villain, Europhys. Lett. **13**, 389 (1990).
[17] Z.-W. Lai and S. Das Sarma, Phys. Rev. Lett. **66**, 2348 (1991).
[18] S. Das Sarma and P. Tamborenea, Phys. Rev. Lett. **66**, 325 (1991).
[19] D.A. Kessler, H. Levine and L.M. Sander, Phys. Rev. Lett. **69**, 100 (1992).
[20] J. Villain J. Phys. I 1 19 (1991).
[21] H. Yang, Phys. Rev. Lett. **68**, 3048 (1992).
[22] M. Siegert and M. Plischke, Phys. Rev. Lett. **68**, 2035 (1992).
[23] J. Chevrier, V. Le Thanh, R. Buys, and J. Derrien, Europhys. Lett. **16**, 737 (1991).
[24] Y.L. He, H.-N. Yang, T.-M. Lu, and G.-C. Wang, Phys. Rev. Lett. **69**, 3770 (1992).
[25] R. Chiarello, V. Panella, J. Krim and C. Thompson, Phys. Rev. Lett. **67** 3408 (1991).
[26] F. Family, J. Phys. A: Math. Gen. **19** L441 (1986).
[27] The conservative nature of MBE growth, i.e. no voids, leads us to eliminate theories which do not conserve surface currents.
[28] B.B. Mandelbrot, *The Fractal Geometry of Nature* (Freeman, New York, 1982).

Thursday, August 26

ThA	**II-VI, IV-VI and Magnetic Structures**
ThB	**Dots and Wires - Optical Properties**
ThP	**Optics, Magnetic Structures, Infrared, Devices**
ThC	**Electronic Excitations - Superlattices**

ThA1

ZEEMAN TUNING OF II-VI-BASED DILUTED MAGNETIC SEMICONDUCTOR SUPERLATTICES

J. K. Furdyna
Department of Physics, University of Notre Dame, Notre Dame, IN 46556 U.S.A.

ABSTRACT

Electronic levels in II-VI-based diluted magnetic semiconductors (DMSs, e.g., $Zn_{1-x}Mn_xTe$) experience extremely large Zeeman shifts when a magnetic field is applied, reaching values of the order of 100 meV at low temperatures. Zeeman shifts of the conduction and the valence band can thus have profound consequences on the properties of DMS/non-DMS superlattices, since they provide the opportunity of tuning the band alignment in such structures simply by varying the applied field. We discuss the consequences of such Zeeman-tuning, with emphasis on the creation of spatial spin modulation and on mapping of wave function distribution in superlattices.

1. INTRODUCTION

Semiconductor superlattices owe most of their spectacular properties to our ability of depositing a sequence of alternating layers of different materials, so as to form one monolithic structure. The resulting energy gap discontinuities at the interfaces of the constituent layers then define the new band structure of the system, and thus its electronic and optical properties. Investigation of the effect of band alignment in such multilayer structures is clearly of fundamental importance to the understanding of those systems. To do so, however, in most cases (e.g., in the well-known GaAs/$Ga_{1-x}Al_xAs$ system) requires the preparation of a series of samples, each with a different alloy composition. It would of course be much more desirable to have the means of varying the band alignment continuously in a single sample during the experiment. Here II-VI-based diluted magnetic semiconductors offer a number of attractive possibilities, as discussed below.

Diluted magnetic semiconductors (DMSs) are semiconducting ternary or quaternary alloys whose lattice is made up in part of substitutional magnetic ions[1,2]. $Zn_{1-x}Mn_xSe$, $Cd_{1-x}Mn_xTe$, or $Pb_{1-x}Mn_xTe$ are examples of such systems. One of the most interesting and important properties of DMSs is the spin-spin exchange interaction between the band electrons and the magnetic ions localized in the lattice. This interaction -- often referred to as the sp-d interaction -- leads to an enormous amplification of Zeeman splittings of conduction and valence band edges, which at low temperatures can reach values of the order of 100 meV in moderate magnetic field (e.g., 5 Tesla). This in turn has exciting implications for quantum wells and superlattices consisting of combinations of non-magnetic and DMS layers, since it provides a handle for "tuning" the band alignment at the interfaces of constituent layers over a significant range (typically over several tens of meV) simply by varying an applied magnetic field.

2. SPIN-SPIN (sp-d) EXCHANGE INTERACTION

Before proceeding with specific structures, we first briefly describe the sp-d exchange interaction itself, since this mechanism is responsible for all effects presented in this paper. Let us, for specificity, consider $Zn_{1-x}Mn_xSe$, which will appear in several superlattices to be discussed below. In order to account for the effect of exchange interaction between the band electrons and the localized Mn spins in $Zn_{1-x}Mn_xSe$, one must include a new term into the band-structure Hamiltonian, as follows:

$$H_{ex} = x_{eff} N_0 J \sigma_z \langle S_z \rangle , \qquad (1)$$

where x_{eff} is the effective Mn concentration, N_0J is the exchange integral appropriate either for the conduction or for the valence band, σ_z is the electron spin, and $\langle S_z \rangle$ is the thermally averaged Mn spin, given by

$$\langle S_z \rangle = -\tfrac{5}{2} B_{5/2}[5\mu_B B/k_B(T + T_0)] . \qquad (2)$$

Here $B_{5/2}$ is the Brillouin function of the argument in square brackets, μ_B is the Bohr magneton, B is the applied magnetic field, k_B is the Boltzmann constant, T is the temperature, and T_0 is a parameter representing antiferromagnetic interactions between the Mn ions [3]. The consequences of Eq. (1) have been extensively discussed in the literature [2]. The resulting Zeeman splitting of the conduction and valence band edges is schematically depicted in Fig. 1. Spin-up and spin-down states are symbolized by arrows in the figure, and the light-hole-band splitting is shown by horizontal dashed lines. Allowed interband transitions are shown by vertical lines, with corresponding circular polarizations indicated by σ_L and σ_R.

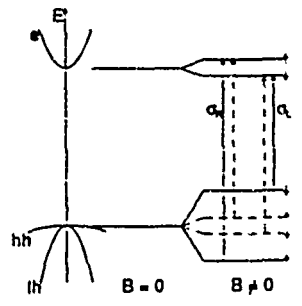

Fig. 1

As seen in the figure, the splitting of the heavy-hole band is considerably larger than for the conduction band, and is opposite in sign (i.e., the energy for spin-up electrons increases, and for spin-up heavy holes it decreases, when a magnetic field is applied). The behavior of light holes, on the other hand, is nearly identical to that of electrons, in sign and in magnitude. In the present paper we shall be interested in the dominant features observed in optical properties of DMS-based superlattices, which are determined by the spin-conserving transitions indicated by arrows in Fig 1. Since transitions involving light holes (broken lines in the figure) are generally much weaker than those associated with heavy holes, in this brief presentation we will restrict ourselves to effects associated only with the heavy holes.

The Zeeman splittings in Fig. 1 can be conveniently represented by an effective g-factor in the form

$$\Delta E = g_i^{eff} \mu_B B , \qquad (3)$$

where the subscript i refers to the conduction or the heavy-hole band, and g_i^{eff} is given by

$$g_e^{eff} = g_e^{\circ} - N_0\alpha\, x_{eff} \langle S_z \rangle / \mu_B B , \qquad (4)$$

$$g_{hh}^{eff} = g_{hh}^{\circ} - N_0\beta\, x_{eff} \langle S_z \rangle / \mu_B B . \qquad (5)$$

Here g_i° is the g-factor obtained from the band structure without the exchange contribution (typically of the order of unity), and $N_0\alpha$ and $N_0\beta$ are the traditional designations for the s-like conduction electron and p-like heavy hole exchange integrals [1]. The terms containing α and β are strongly temperature dependent because of the presence of $\langle S_z \rangle$ (see Eq. (2)), and can be as large as 100 or more at low temperatures.

As already pointed out, the sp-d exchange interaction has particularly important implications for DMS/non-DMS superlattices, since it can be used to vary the superlattice potential profile in a single sample. Below we will focus on two striking examples of such "Zeeman tuning" in DMS-based superlattices: spin segregation, and "mapping" of the spatial wave function distribution.

3. SPIN-SEPARATING STRUCTURES

A. Spin Superlattices

A "spin superlattice" (SSL) is a superlattice in which carriers with opposite spin states are confined in different layers. In order to achieve such spin-modulation, we look for a structure in which the energy gaps of the constituent layers are initially (i.e., in the absence of magnetic field) equal, and the band offsets at the interfaces are initially zero, as shown at the top of Fig 2 (where DMS regions are designated by shading). When a magnetic field is applied, the large Zeeman splitting of the band edges in the DMS layers results in induced band offsets and, consequently, in a spatial separation of the spin-up and spin-down states, as shown in Fig 2

(bottom). The SSL phenomenon has already been observed experimentally in several DMS/non-DMS multi-quantum well systems [4,5].

One particularly attractive DMS system for achieving the structure described above -- which will be used as an example in the present paper -- is the ZnSe/$Zn_{1-x}Mn_xSe$ superlattice. The energy gap of $Zn_{1-x}Mn_xSe$ exhibits a rather striking bowing with Mn concentration x at low temperatures, first decreasing with x, and then rapidly increasing[6]. It is thus possible to find a value of x at which $Zn_{1-x}Mn_xSe$ has the same energy gap as ZnSe (this occurs for x = 0.04 at 1.5 K). Furthermore, since the valence band offsets at ZnSe/$Zn_{1-x}Mn_xSe$ interfaces are close to zero by the common anion rule (which works reasonably well in wide gap II-VIs), the value of x which gives equal energy gaps in ZnSe and $Zn_{1-x}Mn_xSe$ automatically leads to zero (or, in practice, to very small) band offsets in the conduction and the valence bands, thus satisfying the properties stipulated in the preceding paragraph.

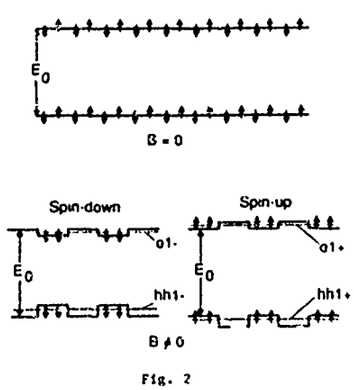

Fig. 2

Examining Fig. 1 we note that, when the magnetic field is applied, the band edge of $Zn_{1-x}Mn_xSe$ for spin-down electrons will move down, and it will move up in energy for spin-down holes. The $Zn_{1-x}Mn_xSe$ layers thus become wells for both carriers of the spin-down orientation. Similarly, for spin-up states the conduction band moves up in energy, and the heavy-hole band moves down, so that for this spin orientation the ZnSe layers become the wells. This magnetic-field-induced band offset has therefore the consequence of *spatially separating* electron and hole states of different spin orientation. It is particularly convenient to observe the formation of such spin separation in magnetoabsorption experiments with the magnetic field applied perpendicular to the SSL layers (the Faraday geometry), in which only spin-conserving transitions are allowed ($\Delta S = 0$). Using left- and right-handed circular polarizations (from here on designated by σ_L and σ_R), one can then observe separately transitions between spin-up valence and conduction band states (corresponding to σ_R), and those between spin-down states (σ_L).

Fig. 3

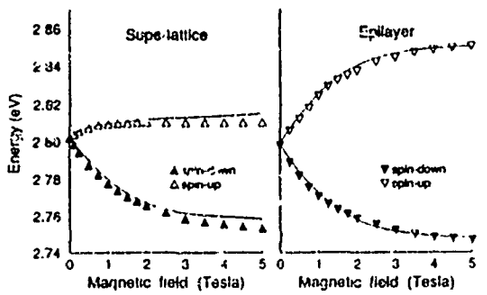

Figure 3 (left) shows the magnetic field dependence of excitonic transitions observed with the σ_L and σ_R polarization in a ZnSe/$Zn_{.96}Mn_{.04}Se$ SSL, with DMS and non-DMS layers 112Å wide. The figure illustrates very nicely the spatial separation of spins occurring in the SSL. Considering first the spin-down (σ_L) transitions, we see the rapid red shift of the σ_L absorption line, since the initial and final states of the transition are both in the DMS layers at finite magnetic field, and follow the field dependence of the valence and conduction band edges of the DMS material (see Fig. 1). In contrast, the spin-up transitions take place between states localized in the ZnSe layers, which become the wells for this spin orientation when the field is applied. This is responsible for the flatness of the transition energy at higher fields -- i.e., the offset becomes well defined. The small initial rise in energy seen in Fig. 3 at low fields (i.e., when the offset is just beginning to form) arises from the fact that in that region of extremely shallow wells the state in the ZnSe well is much more sensitive to the height of the (DMS) barrier, which increases with the field. As the barrier continues to increase, the energy of the state confined in the ZnSe well becomes less and less sensitive to the barrier height and eventually flattens out, approaching the behavior of the non-magnetic quantum well in which that state is confined [4,5].

For comparison, we show on the right of Fig. 3 the position of free exciton magnetoabsorption data observed for σ_L and σ_R polarizations in an *epilayer* grown with the same Mn concentration as the $Zn_{1-x}Mn_xSe$ layers of the SSL. Note that, in contrast with the SSL data, the σ_L and σ_R branches for the epilayer are quite symmetric. The asymmetry seen on the left-hand side is a characteristic signature of spin-separating structures.

B. Magnetic-Field-Induced Type-I → Type-II Transition

Systems closely related to the SSL are DMS-based superlattices which exhibit a transition between type-I and type-II band alignment. Consider as an example a DMS/non-DMS superlattice with a type-I band alignment at B = 0, consisting of deep conduction band wells and shallow wells in the valence band, both occurring in DMS layers, as shown in Fig. 4 (top). As before, DMS regions are indicated by shade. Consider now what happens when a magnetic field is applied. For one spin orientation (spin-down) this will only enhance the type-I nature of the band alignment (i.e., wells in both bands become deeper). For the other spin state, however, the enormous Zeeman splitting of the valence band will at some field exceed the initial offset of that band, transforming the original valence band well into a barrier, as shown in Fig. 4 for B ≠ 0.

Conversion from type-I to type-II superlattices is manifested by a dramatic change in optical properties, because in a type-II structure the carriers initially involved in the strongest optical transitions are now physically separated into different layers. The phenomenon of such band-alignment conversion has already been experimentally observed in several systems, e.g., in $Zn_{1-x}Fe_xSe$/ZnSe [7] and $Cd_{1-x}Mn_xTe$/CdTe [8].

It is important to note that this phenomenon is particularly important in II-VI-based DMS superlattices involving common-anion systems (e.g., ZnMnSe/ZnSe), since these are typically characterized by very small valence-band offsets. Such small offsets can be easily overcome by the large Zeeman shift of the valence band, thus changing the type of alignment even at moderate magnetic fields. When this is achieved, we automatically obtain spatial separation of spin states similar

Fig. 4

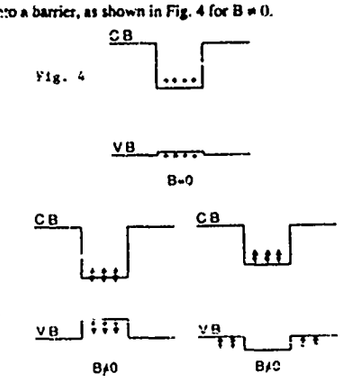

to the spin superlattice discussed earlier, but for one band only. As in the case of the SSL, such spin separation again leads to the characteristic asymmetry of transition energies already seen in Fig. 3 because of the difference in the values of α and β.

4. MAPPING OF WAVE FUNCTIONS IN SUPERLATTICES

One of the most important properties of semiconductor superlattices is their ability to localize electrons and holes in specific layers. Localization of carriers (as measured by their spatial wave-function distributions) is fairly obvious for low-lying states in deep quantum wells. It is an altogether different matter, however, for states at energies above the barriers: these may be confined in well layers, in barrier layers, or may not be localized at all. Furthermore, below-barrier states with energies close to the top of the barrier (i.e., states in very shallow wells, or high-lying excited states) exhibit significant leakage into the barrier regions. Determination of the degree of leakage in the latter case, and of the region of localization in the case of above-barrier subbands, presents a major challenge.

One can meet this challenge by exploiting the fact that, in superlattices consisting of DMS and non-DMS layers, the Zeeman splitting of a given state will reflect its weighted probability distribution over the two media. In other words, the Zeeman splitting will be determined effectively by how many localized magnetic moments does the electron "see". This has already been alluded to in the case of spin superlattices (the spin-up transitions in the left panel of Fig. 3), and in this section we emphasize the application of this idea further, specifically as a tool for mapping the wave function (or probability) distribution in superlattices and other heterostructures.

Consider first below-barrier states. Figure 5 shows photoluminescence (PL) spectra obtained at several magnetic fields on two superlattices consisting of non-DMS quantum wells ($Zn_{1-x}Cd_xSe$, $x = 0.12$) and DMS barriers ($Zn_{1-x}Mn_xSe$, $x = 0.20$) with different well widths (45Å and 135Å) [9]. States in the narrower wells, lying closer to the top of the barrier, should experience a greater degree of penetration into the DMS barrier layers -- and thus a greater Zeeman splitting -- than states in the wider wells. This is clearly seen in Fig. 5 by the amount of red shift exhibited by PL from the two superlattices when magnetic field is applied. We remark parenthetically that in the PL data in Fig. 5 only the red shift is observed (corresponding to spin down transitions i.e., to the σ_L polarization), since these lower energy transitions become energetically favored as the field increases. In fact there can also be observed a weak blue-shifted line corresponding to the σ_R polarization, but this decreases rapidly in intensity with field, and at fields shown in Fig. 5 is no longer seen on the scale of the figure. The rate of decay of the σ_R component can in fact be used to investigate spin lifetimes [10] -- another important topic in the area of Zeeman-tuning which, however, is outside the scope of the present paper.

Fig. 5

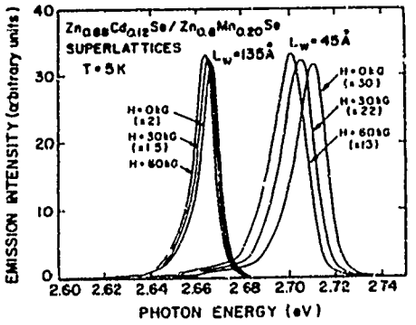

A more challenging -- and qualitatively different -- aspect of wave function mapping is the distribution of superlattice subbands with energies exceeding the top of the barriers. We will illustrate this by discussing the localization of above-barrier excitons in type-I ZnSe/ZnMnSe superlattices, and of type-I (spatially-direct) excitons in type-II ZnTe/CdMnSe and ZnMnTe/CdSe superlattices.

A. ZnCdSe/ZnMnSe Type-I Superlattice

The observations of transitions involving above-barrier states in superlattices were first reported several years ago [11,12]. Since then it has become clear that such high-lying subbands participate strongly in optical transitions due to the formation of *localized* states above the barriers. This has been clearly demonstrated experimentally for type-I ZnCdSe/ZnMnSe superlattices [13], and we will use such a superlattice ($Zn_{.88}Cd_{.12}Se/Zn_{.90}Mn_{.10}Se$, with well and barrier widths both equal to 75Å) as an example. The band structure of this system is depicted in the inset of Fig. 6. Since the energy gap of ZnCdSe is considerably smaller than that of ZnMnSe for the Cd and Mn concentrations used here, the wells correspond to the nonmagnetic layers, while the barriers are magnetic.

Fig. 6

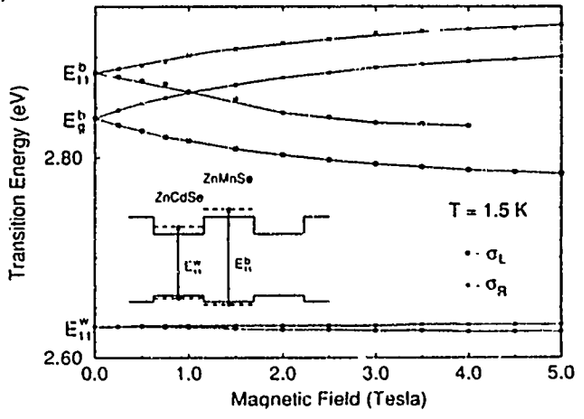

The structure exhibits several strong excitonic peaks at low temperatures. We concentrate on the lowest energy peak (labeled E^w_{11} in Fig. 6), which is identified as the free exciton transition between the first heavy-hole ground state and the conduction electron ground state of the superlattice; and peak E^b_{11} which is identified as the transition between the first above-barrier heavy-hole state and the first above-barrier electron state (the lowest-energy above-barrier transition). Note that E^b_{11} occurs at a higher energy than the energy gap of the barrier material, the latter determined on an epilayer of $Zn_{.90}Mn_{.10}Se$ grown under identical conditions as the barriers and labeled E^b_g in the figure.

When an external magnetic field is applied, the band edges of the ZnMnSe barriers will be Zeeman-split, leading in turn to the splitting of optical transitions in the superlattice. Figure 6 shows the energies of the E^w_{11} and E^b_{11} transitions as a function of the applied field. Also shown in the figure is the Zeeman splitting of the exciton line E^b_g. The solid lines in the figure are only to

guide the eye. It is significant that the spin splitting of the above-barrier transition E^b_{11} is clearly much larger than that of the below-barrier transition E^w_{11}, and almost (*but not quite*) as large as that in the ZnMnSe epilayer.

We recall that the structures investigated are type-I superlattices, consisting of nonmagnetic wells and magnetic barriers. The relatively small (but observable) Zeeman splitting of the ground-state exciton transition E^w_{11} (which originates and terminates in the nonmagnetic wells) thus arises from the partial penetration of the wave functions of the initial and final states into the magnetic barriers. By contrast, the much larger Zeeman splitting of E^b_{11} (almost the same as that for the bulk $Zn_{.90}Mn_{.10}Se$ material) indicates that the E^b_{11} transition originates and terminates on states localized predominantly in the DMS (i.e., the barrier) regions. The fact that the splitting of E^b_{11} is slightly (about 15%) below that observed for the $Zn_{0.9}Mn_{0.1}Se$ epilayer indicates that a part of the above-barrier wave functions which determine the transition extends into the non-DMS layers. The data shown in Fig. 6 thus provide direct evidence that above-barrier excitons in a type-I superlattice are localized in the barrier layers.

B. CdSe/ZnMnTe and CdMnSe/ZnTe Type-II Superlattices

Using the same techniques, it was also shown that there exist spatially direct type-I-like excitons in type-II superlattices [14,15]. The inset in Fig. 7 shows a schematic diagram of the type-II band alignment for a CdMnSe/ZnTe superlattice. Here the quantum wells for electrons and for holes exist in different (i.e., adjacent) layers. The conduction electrons at energies below the barriers are localized in the CdMnSe layer, while the below-barrier heavy holes are in the ZnTe layers. Excitonic transitions have been considered unimportant in such a system, because wave functions of the electrons and the holes are spatially separated, resulting in weak Coulomb attraction.

As seen in the inset, two types of excitonic transitions are possible in such type-II superlattices. One takes place between electron states localized in CdMnSe wells and hole states in ZnTe wells, as shown by the arrow marked "II" in Fig. 7. This is the well-studied type-II

ZnMnTe/CdSe ZnTe/CdMnSe

Fig. 7

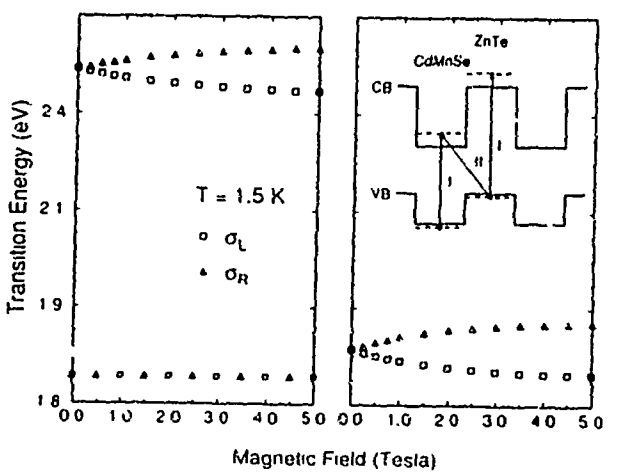

excitonic transition. The other occurs between electron (or hole) subbands confined in the wells, and hole (or electron) subbands at above-barrier energies, confined in the barriers. In that case both the initial and the final state involved in a given transition are localized *in the same layer*, as shown by the arrows marked "I" in Fig. 7. We shall refer to these spatially direct processes as *type-I excitonic transitions*.

To show the existence of type-I excitons in type-II superlattices, and to pin-point their localization, we studied two systems: $CdSe/Zn_{.94}Mn_{.06}Te$, where conduction electrons are localized in a nonmagnetic well; and $Cd_{.92}Mn_{.08}Se/ZnTe$, where electrons are localized in a magnetic well. In these two cases the type-I excitons confined in the nonmagnetic layer will exhibit very different magneto-optical properties from those confined in the DMS layer.

The magneto-absorption spectrum measured on CdSe/ZnMnTe superlattices revealed two clear excitonic absorption peaks, whose energies are shown on the left in Fig. 7. The lower energy peak was identified as the type-I (spatially direct) excitonic transition between the lowest electron state confined in the CdSe conduction-band wells and the first above-barrier hole state confined in the CdSe valence-band barrier layers. The higher-energy peak was attributed to a similar type-I transition, between the above-barrier electron state confined in the ZnMnTe barriers and the hole state confined in the ZnMnTe wells.

The difference in the magnetooptical behavior of both transitions is shown in Fig. 7, where energies observed for σ_L and σ_R circular polarizations are plotted as a function of magnetic field. It is quite striking that there is no observable splitting for the lower-energy transition, confirming that this transition indeed takes place between states strongly localized in the nonmagnetic CdSe layers. In contrast, there is a large Zeeman splitting for the higher-energy transition, which clearly indicates that it occurs between states localized in the DMS layer.

On the right of Fig. 7 we also show the Zeeman splitting of the lowest-energy absorption peak observed in the ZnTe/CdMnSe superlattice. This absorption line now exhibits a large Zeeman splitting, indicating that the transition occurs between electrons localized in CdMnSe wells and above-barrier holes localized in the same layers. (The higher-energy line, which now would correspond to states localized in the ZnTe layers, was obscured by the absorption due to the ZnTe buffer on which this structure was grown.) Both panels of Fig. 7 thus clearly establish the existence of type-I excitons in type-II superlattices, and identify their localization.

The unambiguous experimental demonstration of how above-barrier states are distributed in space was accomplished by exploiting the difference in Zeeman splitting in the DMS and the non-DMS regions comprising the superlattices. However, it should be emphasized that the effects discussed here are of course not limited to systems based on the DMSs, but represent *general properties* of type-I and type-II superlattices. The role of the DMS component is only used as a "marker," in order to bring out these general properties of wave function distribution.

5. CONCLUDING COMMENTS

In this relatively brief review we have described several important illustrations of Zeeman tuning effects in DMS/non-DMS superlattices, but the material covered should by no means be considered as exhaustive. We have thus not concerned ourselves with the application of Zeeman tuning as a tool for band offset determination in quantum wells [16], with its possible applications in narrow-gap semiconductors (where the consequences of Zeeman splitting are expected to be especially striking, since it can in those materials be comparable to the gap itself), with the interesting prospect of Zeeman-tunable coupling in double quantum wells separated by DMS barriers [17], with the already mentioned spin lifetime determination [10], or the yet unexplored territory of band-edge tuning relative to impurity levels in modulation-doped structures (magnetic freeze-out and boil-off) [18,19]. With further advances in the preparation of new DMS/non-DMS heterostructure configurations, the number and sophistication of these novel situations can only be expected to increase.

ACKNOWLEDGMENTS

The author wishes to acknowledge invaluable discussions and collaborations with his colleagues M. Dobrowolska, H. Luo, L. R. Ram-Mohan, N. Dai, and F. Zhang. The work was supported by the U.S. National Science Foundation Grant DMR-9208400.

REFERENCES

1. J. K. Furdyna and J. Kossut, eds., *Diluted Magnetic Semiconductors*, Vol 25 of *Semiconductors and Semimetals* (Academic, Boston, 1988)
2. J. K. Furdyna, J. Appl. Phys. 64, R29 (1988)
3. J. A. Gaj, R. Planel, and G. Fishman, Solid State Commun 29, 435 (1979).
4. W. C. Chou, A. Petrou, J. Warnock, and B. T. Jonker, Phys Rev. Lett. 67, 3820 (1991).
5. N. Dai, H. Luo, F. C. Zhang, N. Samarth, M. Dobrowolska, and J. K. Furdyna, Phys Rev Lett. 67, 3824 (1991).
6. A. Twardowski, T. Dietl, and M. Demianiuk, Solid State Commun 48, 845 (1983)
7. X. Liu, A. Petrou, J. Warnock, B. T. Jonker, G. A. Prinz, and J. J Krebs, Phys Rev Lett 63, 2280 (1989).
8. E. Deleporte, J. M. Berroir, G. Bastard, C Delalande, J. M. Hong, and L. L. Chang, Phys Rev. B 42, 5891 (1990).
9. R G. Alonso, Eunsoon Oh, A. K. Ramdas, H. Luo, N. Samarth, J K Furdyna, and L R Ram-Mohan, *Phys. Rev. B 44*, 8009 (1991).
10. B. T. Jonker, L. P. Fu, W. Y. Yu, W. C. Chou, A. Petrou, and J Warnock, J. Electronic Materials 22, 489 (1993).
11. J. E. Zucker, A Pinchuk, D. S. Chemla, A. Gossard, and W Weigman, Phys. Rev B 29, 7065 (1984).
12. J. J. Song, Y. S. Yoon, A. Fedotowsky, Y B. Kim, J. N. Schulman, C W Tu, D Huang, and H Morkoc, Phys. Rev. B 34, 8958 (1986)
13. F. C. Zhang, N. Dai, H. Luo, N. Samarth, M. Dobrowolska, J. K Furdyna, and L R Ram-Mohan, Phys. Rev. Lett. 68, 3220 (1992).
14. F C. Zhang, H. Luo, N Dai, N. Samarth, M. Dobrowolska, and J K. Furdyna, Phys. Rev B 47, 3806 (1993).
15. H. Luo, W. C. Chou, N. Samarth, A. Petrou, and J. K. Furdyna, Solid State Commun 85, 691 (1993).
16. W. J. Walecki, A. V. Nurmikko, N. Samarth, H. Luo, J. K. Furdyna, and N. Otsuka, Appl Phys. Lett. 57, 466 (1990).
17. J. F. Smyth, D. D. Awschalom, N. Samarth, H. Luo, and J. K Furdyna, Phys Rev B 46 (Rapid Comm.), 4340 (1992).
18. S. Datta, J. K. Furdyna, and R. L. Gunshor, Superlatt and Microstruct 1, 327 (1985)
19. J. Kossut and J. K. Furdyna, Acta Phys. Polon. A 73, 851 (1988)

ThA2

Novel Magnetic Phase Transition Behavior in Short Period EuTe/PbTe Superlattice

J J Chen, Z H Wang, M S Dresselhaus, G Dresselhaus
Massachusetts Institute of Technology
and
G Springholz and G Bauer
Johannes Kepler Universitat Linz

Abstract

{EuTe(ξ)/PbTe(η)}ₙ short period superlattices were grown by MBE along the [111] growth direction with ξ denoting the number of monolayers of EuTe separated by η monolayers of diamagnetic PbTe and 2 ≤ ξ ≤ 5 alternated with 6 ≤ η ≤ 15. We find that superlattices with even ξ numbers show antiferromagnetic phase transitions, those with odd ξ show ferromagnetic phase transitions, while bulk EuTe is a simple two-sublattice antiferromagnet. The transition temperatures T_c observed for these short period superlattices are all below or close to the bulk phase Neel temperature and T_c increases as ξ increases. An antiferromagnetic interlayer correlation along the direction ⊥ to the superlattice planes is found for superlattices with η ≤ 12. In the paramagnetic regime, the Curie-Weiss law fits well for all superlattices except ξ=2, which has its $M(T)$ proportional to 1/lnT instead of the usual 1/T dependence. Positive paramagnetic Curie-Weiss temperatures θ are obtained for superlattices with odd ξ numbers, while negative θ are obtained for even ξ.

In this work we show that Molecular Beam Epitaxial (MBE) growth technology allow us to prepare a ferromagnetic or antiferromagnetic superlattice (SL) using the same building blocks by growing magnetic layers of different numbers of monolayers in the superlattice. Naively, if the number ξ of magnetic layers is *an even number, then antiferromagnetism* should result but if ξ is odd then ferrimagnetism should result. Thus by selecting the number of layers different magnetic behavior is observed with no change in atomic structure or chemical species.

In our study we chose our magnetic material to be EuTe, a Heisenberg antiferromagnet (AFM type II with the MnO structure and a Neel temperature T_N = 9.6 K). Along with other europium chalcogenides (EuO, EuS, EuSe), the magnetic properties of bulk EuTe have been investigated *in detail [1]. Both* EuTe and PbTe crystallize in the rock salt structure. Their lattice mismatch is 2.1%. The (111) planes perpendicular to the growth direction contain either Eu(Pb) or Te ions. Within the (111) planes the Eu ions have ferromagnetic coupling denoted by J_1 and antiferromagnetic coupling between adjacent planes denoted by J_2, *and in the bulk* $J_2/J_1 \sim -3.5$. Recently the MBE growth of such (EuTe/PbTe)ₙ superlattices was *studied[2] and x ray* investigations have shown their high structural perfection.

We report here temperature-dependent magnetization results from 2 K to 100 K *for short period* EuTe/PbTe superlattices. The effects of the number of contiguous EuTe layers in the superlattice and of the spacing between these EuTe layers on the magnetic transition temperatures and on the magnetic correlation along the [111] axis (perpendicular to the superlattice plane), is discussed. The observed phase transitions *in the magnetization* results are analyzed by *mean field theory*. The Curie-Weiss law is used to *fit the magnetization* data in the high temperature regime and paramagnetic Curie-Weiss temperatures are obtained.

{EuTe(ξ)/PbTe(η)}ₙ short period SL's were grown by MBE along the [111] growth direction. These superlattices have EuTe thicknesses ξ ranging from 2 to 5 monolayers with intervening PbTe thickness η ranging from 6 to 15 monolayers. Typically 4000 Å of PbTe was first deposited to relieve the substrate film interface strain before the growth of alternating EuTe and PbTe layers[2]. These samples all have lateral dimensions of approximately 3 mm by 4 mm. In each of the superlattice samples, the ratio η/ξ is kept at 3, so that the biaxial in plane strains of $\varepsilon_{\parallel}^{EuTe} = -1.52\%$ and $\varepsilon_{\parallel}^{PbTe} = 0.55\%$, assuming a free standing SL stack, are the same for all measured samples.

The temperature dependent magnetization of these SL's was measured by SQUID magnetometry with the *H* field in the plane of the foil. The sample

Figure 1 Temperature dependent magnetization for a bulk EuTe thin film and a superlattice $[EuTe(4)/PbTe(12)]_{400}$ The applied field is in the plane of the film with strengths of 1,000 gauss for the EuTe sample and 75 gauss for the superla

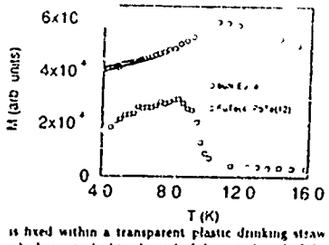

is fixed within a transparent plastic drinking straw which is attached to the end of the sample rod of the magnetometer (Quantum Design MPMS5 system) Magnetization measurements $M(T, H)$ are made after the sample is cooled in zero field to below the transition temperature, and the strengths of the applied field are varied from 10 to 50 gauss Since the applied field is quite small the remanent field H, is monitored by a palladium reference sample, and it is kept below 0 7 gauss by eliminating trapped flux

First, the temperature-dependent magnetization (Fig 1) of a MBE-grown EuTe film with a thickness of 3 μm was measured by SQUID magnetometry with H = 1000 gauss applied in the plane of the film A Neel temperature of T_N=9 6 K was thus found in agreement with that for bulk single crystal EuTe [1] The magnetization measured by applying an H field perpendicular to the film plane shows no interesting features because the spins are lying in the film plane, and pointing in equivalent {110} directions [3]

The same type of $M(T)$ measurements were then made on short period EuTe SLs with the low H fields applied in the film plane After the sample was cooled in the zero field Indeed a ferromagnetic transition (Fig 2) is observed for $[EuTe(3)/PbTe(9)]_{400}$ superlattices with three EuTe monolayers, which has a transition temperature of T_c =8 25 K (discussed below) this superlattice also shows clear hysteresis effects for magnetization measurements below T_c (in Fig 2) a manifestation of the formation of long range order In contrast, we found an antiferromagnetic transition (Fig 1) in the $[EuTe(4)/PbTe(12)]_{400}$ superlattice with four EuTe monolayers which has a magnetic ordering temperature of T_N ~9 4 K Furthermore, the $[EuTe(5)/PbTe(15)]_{400}$ superlattice with five EuTe

Figure 2 Temperature dependent magnetization measured with the external field B = 1 gauss applied parallel to the thin film plane of superlattice $[EuTe(3)/PbTe(9)]_{400}$ The solid line shows a fit to the data using a modified Brillouin function with T_0 = −0 2 K The inset shows the hysteresis loop of same sample taken at 4 7 K

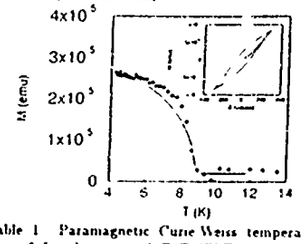

Table 1 Paramagnetic Curie Weiss temperatures θ for short period EuTe/PbTe superlattices

EuTe(ξ)/PbTe(η)	2/6	3/9	4/12	5/15
θ (K)		3 66	-3 32	0 44

monolayers again shows a ferromagnetic transition at 9 6 K while the $[EuTe(2)/PbTe(6)]_{400}$ superlattice with two EuTe monolayers shows antiferromagnetic behavior (Fig 4) The temperature dependence of the susceptibility above the transition temperatures were analyzed by the Curie Weiss law and in Table 1 we summarized various paramagnetic Curie Weiss temperatures for the short period SLs

We found positive paramagnetic Curie-Weiss θ_c temperatures for superlattices showing ferromagnetic transitions, negative θ_c for antiferromagnetic transitions Except for the ξ = 2 sample, where $M(T)$ is proportional to $1/\ln T$ instead of $1/T$ from 8 K to 200 K Thus no meaningful θ_c is obtained for the ξ = 2 sample

In addition, for superlattices with ξ = 3 and 5 when the samples were cooled to 1 7 K in the absence of a field and the magnetization was then measured as the sample was warmed up in a field it was observed that the moment is initially low as if the sample were antiferromagnetic For example as the temperature T of the ξ = 3 sample was increased the moment rose abruptly at about 4 5 K to a broad maximum and then started to decrease as T was further increased (Fig 3) When the same sample was cooled in the presence of a field no decreased moment

Figure 3 Parallel magnetization versus temperature (denoted by solid circles) measured after superlattice $[EuTe(3)/PbTe(9)]_{400}$ was cooled in zero field (i e , at 0.7 gauss) Open circles show the parallel $M_{||}(T)$ measured after the same superlattice was cooled in an external field of 50 gauss Both measurements were taken with an external field of 50 gauss

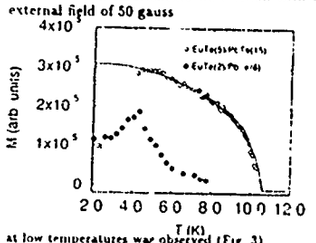

at low temperatures was observed (Fig 3)

In our analysis, T_c is determined by maximizing the range of $\log(1 - T/T_c)$ in a plot of $\log M$ versus $\log(1 - T/T_c)$ such that the data points that are retained form a straight line [4] Based on this criterion, T_c for ξ = 3 and ξ = 5 samples were found to be 8 25 K and 9 6 K respectively Once T_c is determined, the results for the critical exponent β can be readily obtained, where β is defined by

$$M(T_c) \sim \left(\frac{T - T_c}{T_c}\right)^{\beta} \qquad (1)$$

yielding β = 0 129 for the $[EuTe(3)/PbTe(9)]_{400}$ SL and β = 0 252 for $[EuTe(5)/PbTe(15)]_{400}$ These β values were found to fall in between β = 0 125 and β = 0 33 for the 2D and 3D universality classes, consistent with the observed magnetic phase transitions being of lower dimension than the phase transitions occurring in bulk samples

For the ξ = 2 and ξ = 4 samples antiferromagnetic transitions are observed Following the convention in determining T_N for bulk EuTe, we obtained T_N = 4 30 K for the ξ = 2 sample For the ξ = 4 superlattice it is seen that there is a ferromagnetic transition (at 9 4 K) followed by antiferromagnetic behavior at lower temperatures transition (see Fig 1) Thus the T_c (maximum intensity position of the steepest rise $M(T)$ is determined to be the ordering temperature at 5 4 K Notice that $M(T)$ is nearly symmetric about T_c for ξ = 2 superlattices (see Fig 1) whereas $M(T)$ is asymmetric about T_c for bulk EuTe This difference agrees with the prediction of $x(T)$ for 2D and 3D antiferromagnetic phase transition [5]

The dependence of the experimental magnetic or

Figure 4 Magnetization versus temperature for superlattices $[EuTe(2)/PbTe(6)]_{400}$ and $[EuTe(5)/PbTe(15)]_{400}$ The solid line shows a fit to the data using a modified Brillouin function with T_0 = −1.8 K.

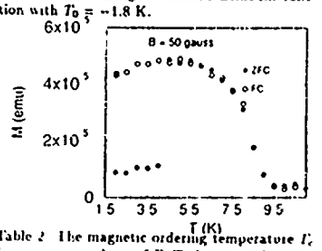

Table 2 The magnetic ordering temperature T_c for various numbers of EuTe layers ξ (for bulk EuTe, T_N = 9 6 K).

# of EuTe monolayers	2	3	4	5
T_c (K)	4 33	8 25	9 4	9 6

dering temperature T_c on the number of EuTe layers ξ is summarized in Table 2, showing an increase in T_c with an increase in ξ We note the rapid convergence in T_c to the bulk T_N value with increasing ξ

We studied the effect of the number of intervening PbTe monolayers η on the magnetic correlation along the [111] axis, the axis perpendicular to the film plane by measuring the temperature dependent magnetization $M(T)$ of a SL $[EuTe(5)/PbTe(93)]_{10}$ and comparing this $M(T)$ to that of $[EuTe(5)/PbTe(15)]_{400}$ The measurements for T_c show little difference between the two samples, thus suggesting the absence of magnetic correlation between two adjacent EuTe blocks separated by an intervening PbTe block of ≥15 monolayers, in agreement with elastic neutron scattering experiments on the $[EuTe(5)/PbTe(15)]_{400}$ superlattice which shows almost no magnetic correlation along the [111]-axis with $T \geq 1.8$ K [6] On the other hand, for the SL's $[EuTe(4)/PbTe(12)]_{400}$ and $[EuTe(3)/PbTe(9)]_{400}$ strong magnetic correlations along the [111] axis are observed by neutron scattering experiments at 4 2 K in zero external magnetic field [6] These results imply that an antiferromagnetic interlayer correlation exists along the [111] axis provided that the PbTe layer thickness is no more than 12 monolayers The interlayer correlation in the $[EuTe(3)/PbTe(9)]_{400}$ SL arises from dipole-dipole interaction between two EuTe trilayers across the intervening PbTe which reduces the net magne

tization of the sample. Our STM investigations have shown that local deviations of ±1 monolayer from the average EuTe layer thickness occur. Typical distances between monolayer steps on the EuTe surface are of the order of 100-200Å, in comparison to the step distances of the order of 1000Å for the PbTe surface. Such steps also are expected to reduce the net magnetization of short period SL's.

We postulate that instead of a strict NSNS magnetic structure, short period EuTe/PbTe SL's can be modeled by an antiferromagnetic spiral structure in the temperature range between 1.7 K to 9.6 K. In this approach the magnetic phase transition temperatures T_c are calculated by mean field theory. The Hamiltonian for the bulk EuTe magnetic interactions is written as

$$H = -J_1 \sum_{nn} S_i S_j - J_2 \sum_{nnn} S_i S_j \qquad (2)$$

where nn and nnn denote nearest neighbor and next nearest neighbor interactions. By a straightforward application of mean-field theory using the Hamiltonian of Eq. 2 we found T_c for the $[EuTe(2)/PbTe(6)]_{100}$ SL to be given by

$$T_c = \frac{2S(S+1)(-3J_2\cos\theta + 6J_1 + 3J_2\cos\theta)}{3k_B} \qquad (3)$$

where θ denotes the angle between the average magnetization of two adjacent EuTe layers. The coupling between sequential EuTe blocks is neglected. In the bulk EuTe crystal, θ is 180°, which in turn gives T_c = 5.89 K for the SL $[EuTe(2)/PbTe(6)]_{100}$ if the bulk J_1 = 0.03 k_B and J_2 = −0.15 k_B values are used [2]. However, the observed T_c value for this $[EuTe(2)/PbTe(6)]_{100}$ SL is 4.33 K. Agreement with the measured T_c value is achieved by taking θ = 120° in Eq. 3. Similarly for the $[EuTe(3)/PbTe(9)]_{100}$ superlattice mean field theory gives an expression

$$T_c = \frac{2S(S+1)(6J_2\cos\theta + 6J_1 + 6J_2\cos\theta)}{3k_B} \qquad (4)$$

Obviously for θ = 180° in Eq. 4 we recover the T_N expression for bulk EuTe crystal which is

$$T_N = \frac{2S(S+1)(-6J_2)}{3k_B} \qquad (5)$$

and for bulk T_N = 9.6 K. For the 3 layer EuTe superlattice the observed transition temperature is again lower than the bulk value at 8.25 K, requiring θ = 150° in Eq. 4 to yield agreement with experiment. This suggests that the antiferromagnetic spiral structure is suppressed as the number ξ of EuTe layers increases. For SL's with 4 monolayers of EuTe or more within each period we assume the bulk T_N expression to be valid which gives a 9.6 K transition temperature that is fairly close to the observed transition temperatures. Furthermore the zero field magnetizations of superlattices $[EuTe(5)/PbTe(15)]_{100}$ can be fitted reasonably well by a modified Brillouin function (see Fig. 4), showing that this sample behaves more like 3D magnets than 2D magnets.

In summary, short period EuTe/PbTe SL's show different magnetic behavior depending on the number of EuTe layers ξ in each period. The T_c values for superlattices with $\xi \geq 4$ EuTe layers in each period are very close to the bulk EuTe Neel temperature (9.6 K), thus suggesting they maybe behave more like 3D magnets than 2D magnets. Indeed a modified Brillouin function provides a good fit to the zero field magnetization data for $[EuTe(5)/PbTe(15)]_{100}$. However, $M(T)$ observed for the small period superlattices $[EuTe(3)/PbTe(9)]_{100}$ and $[EuTe(2)/PbTe(6)]_{100}$ indicate that they are more like 2D magnets. The critical exponent β for $[EuTe(3)/PbTe(9)]_{100}$ is 0.139 much closer to 0.125 for the 2D universality class than to 0.33 for the 3D class. Furthermore in the high temperature regime the magnetization of $[EuTe(2)/PbTe(6)]_{100}$ is proportional to $1/\ln(T$ instead of $1/T$ as a conspicuous signature of marginal dimension phenomenon. The specific effects that a small number of EuTe monolayers impose on the superexchange and indirect exchange mechanisms giving rise to J_1 and J_2, respectively, are to be worked out. Such studies are needed to provide a firm theoretical basis for the explanation of the magnetic phases of short period magnetic SL's.

The MIT authors acknowledge NSF grant #DMR-92 01578 for the financial support of this project. The Linz authors acknowledge support from #8446 FWF Vienna.

References

[1] P. Wachter, in *Handbook on the Physics and Chemistry of Rare Earths*, edited by K. A. Gschneidner Jr. and L. Eyring, North Holland Publishing Company, Amsterdam 1979.

[2] G. Springholz and G. Bauer, Appl. Phys. Lett. 62, 2399 (1993).

[3] R. P. Silberstein, *Raman scattering and magnetic symmetry in EuS and FeSe*, PhD thesis, Massachusetts Institute of Technology, February 1975.

[4] D. L. Connelly, J. S. Loomis and D. L. Mapother, Phys. Rev. B3, 924 (1971).

[5] Shang-keng Ma, *Modern Theory of Critical Phenomena, Frontiers in Physics*, Vol. 46, Addison-Wesley Publishing Co., New York, 1982.

[6] T. Gicbultowicz, (1993), private communication.

ThA3

Band Offsets and Electronic Structures of (ZnCdHg)(SSeTe) Strained Superlattices

Takashi Nakayama
Department of Physics, Faculty of Science, Chiba University, Yayoi-cho, Chiba 263, Japan

abstract

Band offsets and electronic structures of various II-VI strained superlattices are calculated by the first-principles pseudopotential method in the local density approximation. The differences of band structures under strain between wurtzite and zinc blende crystal structures are first analyzed. The deformation potentials are calculated for all II-VI compounds. However the strain in II-VI superlattices is so large that nonlinear variation of energy levels with changing the magnitude of strain appears. There is a chemical trend of offset that energy levels of the heavy hole and the electron states increase as the atomic number of anion and cation atoms increases, respectively. The calculated band offsets drastically vary with changing strain surroundings. The practical usage of the present results is illustrated.

1. Introduction

II-VI semiconductor compounds have a high potential to opto electronic usage, because their band gaps cover the spectral region of visible light. It has become possible by the developements of crystal growth techniques to synthesize II-VI strained superlattices (SLs) of good quality. Recent experiments [1-3] showed that II-VI widegap SLs such as $Zn_xCd_{1-x}S_ySe_{1-y}$/$Zn_xCd_{1-x}S_ySe_{1-y}$ are one of the leading candidates for blue-light emitting devices. However electronic structures of these systems, especially the band offsets under various strain environments, have not been understood well. In this view, in order to clarify these fundamental electronic quantities, we have calculated the band structures and band offsets of II-VI SLs made of all the combinations of II-VI compounds (from ZnS to HgTe) under various strain environments by the first-principles theoretical method. Among various characteristics seen in these systems, we concentrate on the difference of the strain effect on band-gap energy between bulks of zinc-blende and wurtzite structures, and the variation of band offsets with changing the substrate for the heavy-hole and the electron states of SLs in this paper. This work is the extension of previous works on zinc-compounds SLs [4,5] to all II-VI compounds. The present theoretical calculation will help the evaluation of the quality of grown crystals and encourage the challenge to produce new types of devices.

2. Calculational Method

Because of the difference of lattice constant and the presence of substrate, II-VI SLs become in general strained systems. In order to determine the crystal structures of SLs, the macroscopic elastic theory [6] is employed, the details of which are described elsewhere [4]. For the band structure calculation of SLs, we have adopted the plane-wave first-principles pseudopotential method within the local density approximation [4,7]. We use pseudopotentials constructed by Bachelet *et al.* [7], where 3d electrons are treated as core electrons.

and the spin-orbit interaction is not included [15]. The X_α potential with $\alpha=0.7$ is used for the exchange-correlation potential. From the calculated band structures, we evaluate the band offset, the method of which is a standard one in the first-principles scheme [15,8]. Table I shows the lattice constants under no strain and the elastic constants of various II-VI compounds, which are used in this work.

3. *Results and Discussion*

Before going to the calculated results of SLs, two points are discussed. At first, it should be noticed that CdS and CdSe are normally of wurtzite (WZ) structure in bulks, while they show the zinc-blende (ZB) structure when epitaxialized as SLs. *Therefore we have to take* into account the difference of electronic structure between WZ and ZB. Figures 1(a) and (b) show the calculated band-gap energy of ZB-CdSe and the difference of the band-gap energy between WZ and ZB, as a function of strains $\varepsilon_{\parallel(111)}$ and $\varepsilon_{\perp(111)}$, parallel and perpendicular to the (111) direction. Here the calculated band gap energy of CdSe is increased constantly by +0.17eV to correct the values in the local density theory. As seen in Fig 1(a), the band-gap energy increases as the strain becomes negatively large. This is because the more negative the strain is, the smaller the bond length becomes. As a result, the transfer energy between atoms increases and the band-gap energy increases. Comparing WZ and ZB structures, WZ has larger band-gap energy than ZB *in most strained region* in Fig 1(b). It is generally shown that the difference of band-gap energy originates from the difference of positions of the 3rd nearest neighbouring atoms between WZ and ZB structures [10] and that all direct-gap semiconductors have larger band-gap energies in WZ forms than in ZB forms [11]. When the lattice constant along (111) decreases; $|\varepsilon_{\perp(111)}|$ increases in a negative region, the distance to the 3rd nearest neighbouring atoms in WZ structure becomes so short that the band-gap energy of WZ sharply increases. This fact indicates that the variation of electronic structure of ZB with changing strain surroundings is more moderate than that of WZ.

However, *secondly*, the lattice constants of II-VI compounds scatter in such a wide region that the strain becomes considerably large ($\sim$ 0.1) when II-VI SLs are produced. Therefore, we have to examine the variation of the electronic structure under large strain. Most SLs are produced along (100) and the lattice constant perpendicular to (100) becomes equal to that of the substrate. In this case, only the diagonal components of strain tensor exist [1], which have the following relation in the linear elastic theory.

$$\varepsilon_{\parallel(100)} = -2\frac{C_{12}}{C_{11}}\varepsilon_{\perp(100)} \tag{1}$$

Establishing the strained structures of II-VI bulks based on this formula, the band-gap energies and the splitting energy between the light and the heavy-hole states are calculated from the first-principles, which are shown in Figs 2(a) and (b), respectively, as a function of the lattice constant of the substrate. Here the band gap corresponds to the transition from the heavy-hole state to the lowest conduction-band state at the center of the Brillouin zone. Though the band structure calculation in the local density theory *underestimates* the band-gap energy, the variation of energy levels with changing strain surroundings is well described by the calculation. Thus the calculated band-gap energies are constantly shifted in order to coincide with observed values [9] only for the unstrained cases, for example, +0.106 (ZnS), +0.691 (ZnSe) and +0.500 eV (ZnTe). Most striking feature seen in Fig 2(a) is that the band-gap energy of each material has the largest value and the slow variation with changing the substrate, in the region near the unstrained lattice constant. However far away from this region, though the strain of crystal is treated in the linear theory, the band-gap energy rapidly decreases in a non linear manner. Similar characteristics are observed in Fig 2(b) for the splitting energy between the light and the heavy-holes.

As seen in Figs 2(a) and (b), though the deformation potential seems to be a well-defined quantity only around the unstrained lattice constant, it becomes the measure of energy-level variation. Without the spin-orbit interaction, the band-gap energy between the heavy-hole and the lowest conduction-band electron states $E_x - E_{hh}$ and the splitting energy between the light and the heavy-holes $E_{lh} - E_{hh}$ are given as follows,

$$E_x - E_{hh} = a(2\varepsilon_{\perp(100)} + \varepsilon_{\parallel(100)}) - b(\varepsilon_{\perp(100)} - \varepsilon_{\parallel(100)}) \tag{2}$$

$$E_{lh} - E_{hh} = -\tfrac{1}{2}b(\varepsilon_{\perp(100)} - \varepsilon_{\parallel(100)}) \tag{3}$$

Fitting the calculated results to these formulas, we obtain the deformation potentials a and b in Table II.

Then we consider the calculated results of II-VI strained SLs. Most features of electronic structures of various II-VI SLs are similar to those in case of zinc-compounds SLs in previous calculations [5]. Thus, at first, we shortly comment on this. By examining the layer-thickness dependence of band gap energies of SLs and the manner of charge distribution of respective band-edge state of SLs in constituent layers, it is concluded that the quantum well picture is well applicable to the states around the fundamental gap in all II-VI strained SLs. This result allows us to define the band offset. Figures 3(a) and (b) show the calculated band offsets of (various II-VI semiconductors)/ZnS interface for the heavy-hole and the lowest conduction-band states, respectively, as a function of the lattice constant of the substrate. As seen in these figures, band offsets drastically vary with changing the substrate, i.e. changing strain strength. These changes are caused by the competition between the energy-level shift by strain and the charge transfer at the interface [5]. There appears a chemical trend that the offsets for the heavy-hole state of Te-compounds are large, while those of S-compounds are small. This is because the top of the valence-band states mainly consists of p-orbital of cation atom, and because the energy of cation p-orbital is higher for Te than for S.

On the other hand, as for the electron state, the energy position is high for Zn-compounds and low for Cd and Hg compounds. This is the reflection from the magnitude of band-gap energies of these materials, and is explained by the fact that the lowest conduction-band state is the center of the Brillouin zone is the anti-bonding state of cation s-orbitals. HgSe and HgTe are metals, which have negative band-gap energies as shown in Fig 2(a) even in the strained structures. This is probably the reason why their energy positions are extremely low. In order to clarify the relative position of the band-edge states among II-VI compounds, the band offsets on the ZnSe substrate are shown in Fig 4. From this figure, it is easily concluded, for example, that ZnS/ZnSe and ZnSe/CdSe SLs are of type II, which is in good agreement with experimental observations.

Then we compare the calculated offsets with experiments. The $ZnSe/Zn_{0.7}Cd_{0.3}Se$ superlattice coherently grown on ZnSe [12] is considered for example. Though the spin-orbit interaction is absent in the present first-principles calculation, such an effect can be included a posteriori [5] when we use the observed values of spin-orbit splitting energies Δ_0 in experiments [9]. 0.067, 0.12 and 0.42 eV for ZnS, ZnSe and CdSe, respectively. The calculated offset for the heavy-hole state of ZnSe/ZnS on ZnSe substrate is evaluated as follows.

$$\Delta E(ZnSe/ZnS) = 0.59 + \frac{1}{4}\times(0.12 - 0.067) = 0.609\text{eV} \tag{4}$$

Similarly, because the band offset linearly depends on the strain as shown in Fig 3(a), the offset of $Zn_{0.7}Cd_{0.3}Se/ZnS$ on ZnSe is estimated as

$$\begin{aligned}\Delta E(Zn_{0.7}Cd_{0.3}Se/ZnS) &= 0.77\times(0.69) + \frac{1}{4}\times(0.12 - 0.067)) \\ &+ 0.23\times(0.90) + \frac{1}{4}\times(0.12 - 0.0611) = 0.861\text{eV}\end{aligned} \tag{5}$$

Using both values, we obtain

$$\Delta E(Zn_{0.75}Cd_{0.25}Se/ZnSe) = 0.861 - 0.809 = 0.052eV \quad (b)$$

This value is in good agreement with estimated value (0.075eV) from experiments by Pelekanos *et al* [12]. It should be noticed here that, in the above evaluation, we used the fact that band offset is transitive for the combination of materials, $\Delta E(A/B) = \Delta E(A/C) + \Delta E(C/B)$, as long as SLs are grown on the substrate of the same lattice constant. This property is approximately satisfied in all the present II-VI SLs because the charge transfer across the interface is additive for each combination of II-VI compounds [5].

Finally, we make remarks on the effect of atomic configuration at the interface on the band offset. For multinary SLs such as ZnS/CdSe, there exist two kinds of clean interfaces S/Cd and Zn/Se. Table III shows the calculated band offsets for the heavy-hole states at cation/Se and anion/Zn interfaces. The calculated band offset differs by ±20meV between these interfaces, due to the difference of charge distribution at the interface. Though this variation is small, such difference will become important when the configuration of interface atoms is controlled, which is not clear in experiments in the present stage.

In summary, we have calculated electronic structures and band offsets of various II-VI strained superlattices by the first-principles pseudopotential method in the local density approximation. It is shown that the variation of the band-gap energy with changing strain surroundings is more moderate in zinc blende structure than in wurtzite one. The deformation potentials are calculated for all II-VI compounds. However, the variation of energy levels is not limitted to the linear variation due to the large strain in II-VI superlattices. The calculated band offsets for the heavy-hole states drastically vary with changing strain strength. There is a chemical trend that the energy position of the heavy-hole state is high for Te-compounds and low for S-ones, while that the energy position of the lowest conduction-band state is high for Zn-compounds and low for Hg-ones. For multinary superlattices such as ZnS/CdSe, the dependence of the band offset on the kind of atoms at the interface is small. We demonstrate the usage of the calculated band offsets and compared with experiments.

Acknowledgements

We are pleased to thank Miss Misao Murayama for preparing the manuscript. This work is supported by a Grand-in-Aid from the Ministry of Education, Science and Culture, Japan.

References

1. J.Ding, H.Jeon, T.Ishihara, M.Hagerott, A.V.Nurmikko, H.Luo, N.Samarth and J.Furdyna Phys. Rev. Lett. **69**, 1707 (1992)
2. Sh.Fujita, Y.Wu, Y.Kawakami and Sg.Fujita, J. Appl. Phys. **72**, 5251 (1992)
3. Y.Yamada, Y.Masumoto, J.F.Mullins and J.Taguchi, Appl. Phys. Lett. **61**, 2190 (1992)
4. T.Nakayama, J. Phys. Soc. Jpn. **59**, 1029 (1990)
5. T.Nakayama, J. Phys. Soc. Jpn. **61**, 2331 (1992)
6. L.D.Landau and E.M.Lifshitz, *Elastic Theory* (translated in Japanese), Sec.10, Tokyo-tosho Publisher (1972)
7. G.B.Bachelet, D.R.Hamann and M.Schluter, Phys. Rev. **B26**, 4199 (1982)
8. C.G.Walle and R.M.Martin, J. Vac. Sci. Tech. **B3**, 1256 (1985)
9. *Semiconductors, Physics of II-VI and I-VII Compounds, Semimagnetic Semiconductors* ed. O.Madelung, M.Schulz and H.Weiss, Landolt-Bornstein New series III/17b, Springer-Verlag, Berlin, Heidelberg, New York (1982)
10. M.Murayama and T.Nakayama, J. Phys. Soc. Jpn. **61**, 2119 (1992)
11. M.Murayama and T.Nakayama, Superlattices and Microstructures **12**, 215 (1992)
12. N.T.Pelekanos, J.Ding, M.Hagerott, A.V.Nurmikko, H.Luo, N.Samarth and J.K.Furdyna Phys. Rev. **B45**, 6037 (1992)

Table I. Lattice constants a and elastic constants C_{11} and C_{12} of various II-VI compounds used in this work. All values are taken after reference 9. Elastic constants are in $10^{10}N/m^2$ unit.

	a [Å]	C_{11}	C_{12}
ZnS	10.206	10.42	6.54
ZnSe	10.691	8.720	5.280
ZnTe	11.509	7.140	4.070
CdS	10.901	8.420	5.450
CdSe	11.420	7.490	4.620
CdTe	12.228	5.351	3.710
HgS	11.010	8.130	6.220
HgSe	11.470	6.980	5.190
HgTe	12.191	5.351	3.860

Table II. Calculated deformation potentials for various II-VI compounds in eV.

	a	b
ZnS	-6.93	-1.25
ZnSe	-4.73	-1.23
ZnTe	-5.53	-1.31
CdS	-4.77	-1.07
CdSe	-4.64	-1.11
CdTe	-4.13	-1.13
HgS	-4.91	-1.24
HgSe	-4.96	-1.16
HgTe	-4.72	-1.22

Table III. Calculated band offsets for the heavy-hole states at multinary (II-VI compounds)/ZnSe interfaces on the ZnSe substrate. C and A indicate the interfaces cation/Se and anion/Zn, respectively.

	C	A
CdS	0.513	0.193
HgS	0.459	0.239
CdTe	1.109	1.189
HgTe	1.551	1.322

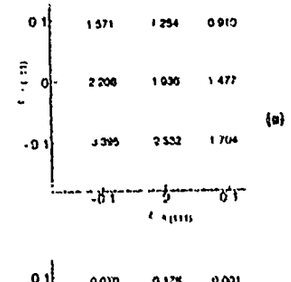

Fig.1. Contour map plots of calculated band-gap energy of zinc-blende CdSe and the difference of the band-gap energy between wurtzite and zinc-blende CdSe as a function of the strain $\varepsilon_{xx}(\%)$ and $\varepsilon_{yy}(\%)$.

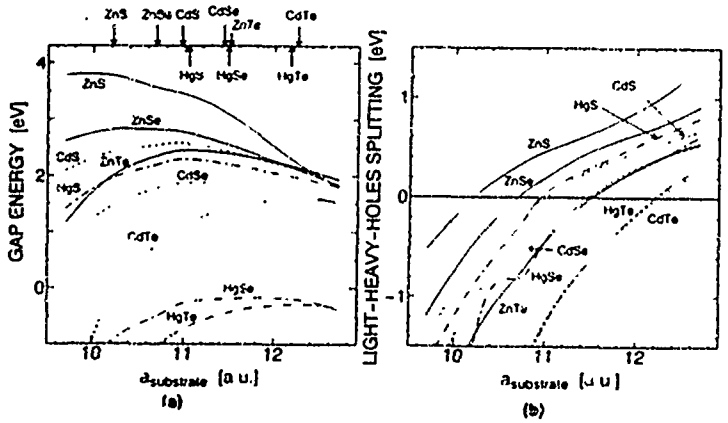

Fig.2 (a) Calculated band gap energies and (b) splitting energies between the light and the heavy-hole states of various II-VI compounds as a function of the lattice constant of the substrate. Points as of unstrained lattice constants are denoted by arrows around the upper line. (figure (a). Solid line corresponds to Zn compound, dotted line to Cd compound and dashed line to Hg compound.

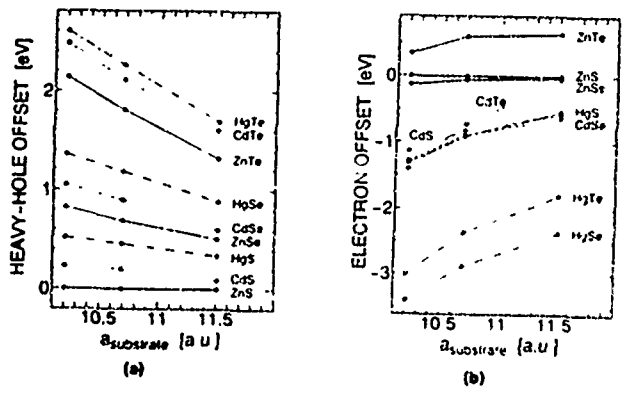

Fig.3 Calculated band [illegible] of various II-VI [illegible] grown on ZnS as a function of the lattice constant of the substrate. (a) [illegible] and (b) for the lowest [illegible] states. Solid line corresponds to Zn compound, dotted line to Cd compound and dashed line to Hg compound.

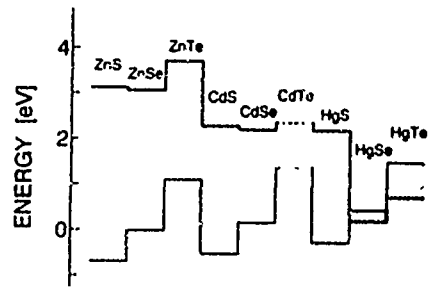

Fig.1 Calculated band alignment of the top of valence bands and the bottom of conduction bands for various II-VI compounds on the ZnSe substrate, in eV.

ThA4

LIGHT INDUCED INVERSION OF MAGNETIC HYSTERESIS IN CdTe/(Cd,Mn)Te SUPERLATTICES

V P Kochereshko, I A Merkulov, G R Pozina, and I N Uraltsev
A F Ioffe Physico-Technical Institute, Russian Academy of Sciences, 194021 St.Petersburg, Russia

D R Yakovlev*, W Ossau, A Waag, and G Landwehr
Physikalisches Institut der Universitat Wurzburg, 97074 Wurzburg, Federal Republic of Germany

Circular polarized photoluminescence induced by magnetic fields in Faraday geometry has been used for the study of spin relaxation processes in CdTe/$Cd_{1-x}Mn_xTe$ short-period superlattices The spin relaxation has been found to be effective for the free carriers with kinetic energy and to be suppressed for carriers localized at fluctuations of magnetization The effect of the inversion of sign of the magnetic hysteresis has been observed under excitation by nonpolarized light in the presence of magnetic field The effect is due to a nonequilibrium magnetization of the Mn-ions which is induced by spin orientation of carriers on Zeeman sublevels in magnetic fields This magnetization has a long relaxation time of about 10^3 s at temperatures of 1 6 K caused by the "frozen" magnetic moments of spin-glass clusters situated in barrier layers

1 Introduction

Due to the recent progress in the molecular-beam-epitaxy technology for II-VI semiconductors the growth of high quality quantum well structures and superlattices incorporating layers of semimagnetic semiconductors is feasible The model semiconductor system for such structures is CdTe/$Cd_{1-x}Mn_xTe$ The specific of semimagnetic semiconductors with strong exchange interaction of carrier spins with spins of magnetic ions has been incorporated into the physics of quantum-confined heterostructures That made possible the observation of novel effects such as the type I - type II transition of the band alignment induced by external magnetic fields [1,2], the two-dimensional magnetic polarons [3], the modification of magnetic properties of semimagnetic semiconductors in the quasi-two-dimensional layers [4] and at heterointerfaces [5] In this paper we report a study of the spin relaxation phenomena in semimagnetic superlattices CdTe/$Cd_{1-x}Mn_xTe$ The inversion of sigh of the magnetic hysteresis is found and explained in terms of the Overhauser effect

2 Experimentals

We have studied CdTe/$Cd_{0.9}Mn_{0.1}Te$ superlattices (SL) grown by molecular-beam epitaxy on (100)-oriented CdTe substrates after a 0 2-μm thick $Cd_{0.9}Mn_{0.1}Te$ buffer layer Structures have equal thickness of well and barrier layers and the periods varied from 40 to 120 Å (for details of growth conditions see [6])

In Fig 1 photoluminescence (PL) spectrum of a 40-Å-period superlattice taken at 1 6 K is shown by solid curve PL has been excited by the nonpolarized beam of a He-Ne laser (E_l = 1 96 eV) with low excitation density of 1 W/cm^2 The PL excitation (PLE) spectrum is represented by the dashed curve and exhibits a strong line with maximum at 1 679 eV and a full width at half maximum of 10 meV Analyzing the Zeeman pattern [7] we have identified the PLE maximum

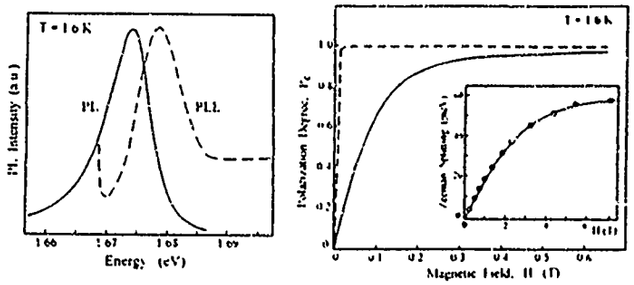

Fig 1 Photoluminescence (solid line) and PL excitation (dashed line) spectra of a 40-Å-period CdTe/$Cd_{0.9}Mn_{0.1}Te$ superlattice

Fig 2 Circular polarization degree of PL vs magnetic field for a 40-Å-period CdTe/$Cd_{0.9}Mn_{0.1}Te$ superlattice Nonpolarized excitation with energy 1 96 eV and density of 1 W/cm^2 has been used. Solid line - experiment, dashed line - results of calculation in the asumption $\tau_s << \tau$ The insert shows the Zeeman splitting of the heavy-hole exciton

due to the heavy-hole exciton absorption and have measured a splitting between light-hole and heavy-hole excitons of 4 meV The low temperature luminescence is dominated by a heavy-hole exciton recombination The Stokes shift of 4 5 meV between the maxima of PL and PLE spectra is due to a localization of excitons on fluctuations of SL periods and shows the high structural quality of samples under study No direct evidences for the exciton magnetic polaron formation have been found by use of the selective excitation technique [3]

3 Magnetic-field-induced polarization of photoluminescence

The circular polarization of photoluminescence induced by magnetic fields in Faraday geometry is due to the thermal population of the Zeeman sublevels [8] The degree of polarization is determined by $P_c = (I_+ - I_-)/(I_+ + I_-)$, where I_+ and I_- are the intensities of the luminescence with right- and left-handed circular polarization, respectively These intensities correspond to the population of the upper and lower Zeeman sublevels and depend on the temperature T, the value of the Zeeman splitting $\Delta(H)$ and on the ratio of lifetime τ to spin relaxation time τ_s In CdTe/$Cd_{1-x}Mn_xTe$ superlattices, where the light-hole states are split off by strain and quantum confinement, the polarization degree is

$$P_c(H) = \frac{\tau\left(1+\exp(-\Delta(H)\ kT)\right)}{\tau_s + \tau\left(1+\exp(-\Delta(H)\ kT)\right)} \tanh\frac{\Delta(H)}{2kT} \qquad (1),$$

where τ and τ_s could be functions of the magnetic field H In the case when $\tau_s << \tau$ the polarization degree reflects the thermoequilibrium population of the Zeeman sublevels At $\tau_s >> \tau$

the carriers recombine before the thermoequilibrium population could be achieved An analysis of the polarization degree gives an insight into spin relaxation processes

In Fig 2 the solid line shows the circular polarization degree of a 40-Å-period $CdTe/Cd_{0.9}Mn_{0.1}Te$ superlattice as a function of magnetic field at 1 6 K Magnetic fields have been applied parallel to the growth axis (Faraday geometry) An insert shows the Zeeman splitting of the heavy-hole exciton taken from reflectivity spectra (for details see [1]) The large value and the Brillouin function like behaviour of the Zeeman splitting is typical for semimagnetic semiconductors where the splitting of spin sublevels in magnetic fields is due to the strong exchange interaction of carrier spins with spins of magnetic ions, namely Mn-ions for $Cd_{1-x}Mn_xTe$ [9]

We have put experimental values of the Zeeman splitting in Eq 1 and calculated the polarization degree assuming thermoequilibrium conditions ($\tau_s << \tau$) The result of the calculation is shown by the dashed line in Fig 2 A strong disagreement between calculation and experiment in low magnetic fields ($\leq$ 0 3 T) let us conclude that the carrier system is far from the thermodynamic equilibrium with the lattice and the spin relaxation time exceeds the lifetime of the carriers, i e $\tau_s > \tau$

In order to have a detailed insight into the spin relaxation processes we have done an optical orientation experiment [10] PL in zero magnetic field has been excited by circular polarized light at a laser energy of 1 70 eV and the polarization degree of luminescence has been analyzed The circular polarized light generates carriers with spin orientation and luminescence will be circular polarized with the degree

$$P_\omega = \frac{\tau_s}{\tau + \tau_s} P_0 \qquad (2),$$

where P_0 is the maximal polarization degree which depends on the structure of electron and hole levels involved in the process In the considered case, when carriers are photoexcited from light- and heavy-hole subbands but recombination involves the heavy-hole subband only, P_0=0 5 [10] In the $CdTe/Cd_{0.9}Mn_{0.1}Te$ superlattice we have found $P_\omega \approx 0$ That means that $\tau_s << \tau$, i e that free carriers with kinetic energy effectively lose their spin orientation The considerable value of P_ω has been reported for the nonmagnetic QW structures $CdTe/Cd_{1-x}Zn_xTe$ [11] We conclude that very fast carrier spin relaxation in the semimagnetic SLs is due to the carrier scattering on the spins of Mn ions

Summarizing the data of optical orientation experiments, where $\tau_s << \tau$ has been found, and of magnetic-field-induced circular polarization of PL, where $\tau_s > \tau$ has been established, we conclude that the spin relaxation is effective for the free carriers with kinetic energy and is considerably suppressed for carriers localized at the extrema of conduction and valence bands Similar results have been reported for bulk (Cd,Mn)Se and have been explained in terms of a bottleneck in a spin diffusion process [12]

As the next step we have studied the magnetic-field-induced polarization in tilted magnetic fields Fig 3 shows by solid lines the PL polarization degree as a function of transverse magnetic field $H_\perp$ (field is perpendicular to the growth axis) taken at fixed longitudinal field components $H_\parallel$= 0 08, 0 2 and 1 4 T The polarization degree is completely suppressed by transverse magnetic fields when the longitudinal field is small (< 0 1 T) Contrary at the high longitudinal field of 1 4 T there is a very weak influence of the transverse field on the polarization degree Dashed lines in Fig 3 show the polarization dependences calculated according to the following equation with the assumption that carrier g-factors are isotropic

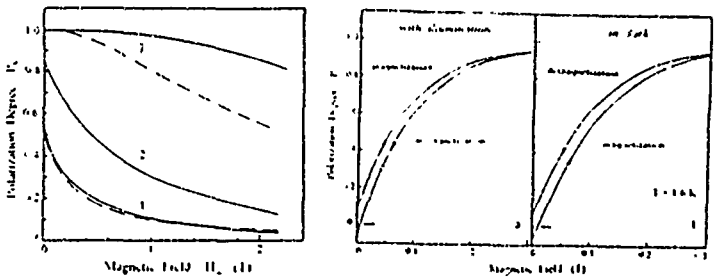

Fig 3 Polarization degree of PL as a function of transverse magnetic field $H_\perp$ (Voight geometry) taken at presence of longitudinal field component $H_\parallel$ = 0 08 T (1), 0 2 T (2) and 1 4 T (3) for a 40-Å-period $CdTe/Cd_{0.9}Mn_{0.1}Te$ superlattice T=1 6 K Solid lines - experiment, dashed lines - calculations with the isotropic g-factor

Fig 4 Hysteresis behaviour of the polarization degree of PL in the remagnetization cycle realized under light illumination (a) and in dark conditions (b) for a 40-Å-period $CdTe/Cd_{0.9}Mn_{0.1}Te$ superlattice

$$P_s(H) = \frac{\tau(1+\exp(-\Delta(H)\ kT))}{\tau_s + \tau(1+\exp(-\Delta(H)\ kT))} \frac{H_\parallel}{H} \tanh\frac{\Delta(H)}{2kT}$$

where $H = \sqrt{H_\parallel^2 + H_\perp^2}$ Experimental data fit well with the calculated dependences at $H_\parallel$ = 0 08 T and differ considerably at $H_\parallel$ = 1 4 T We consider that both electrons and holes are contributing to the polarization degree and the total polarization degree of luminescence is expressed by the equation

$$P_\Sigma = (P_e + P_h)/(1 + P_e P_h) \qquad (3),$$

where P_e and P_h are electron and hole polarization degrees, respectively The electron g-factor is isotropic, whereas the g-factor of heavy-hole in superlattice has a strong anisotropy due to the reduction of the symmetry from T_d in a bulk to D_{2d} in a superlattice Holes have larger exchange constant and effective mass than electrons and are better localized by the fluctuations of magnetization As a consequence at low fields the electron system is closer to the thermodynamic equilibrium and provides the dominating contribution to the circular polarization of the luminescence At stronger longitudinal fields the input of holes to the polarization increases and the polarization anisotropy caused by the anisotropical g-factor of holes became pronounced

4 Hysteresis phenomena

From the detailed study of the magnetic-field-induced circular polarization we found that the dependence $P(H)$ is affected by the history of the sample, i e dependent on illumination

and/or magnetic fields applied before the measurement We have found a magnetic hysteresis loop on $I_c(H)$ and an effect of the inversion of magnetic hysteresis under nonpolarized illumination of the sample at the interband transition energies

Fig 4a shows a hysteresis loop observed in a 40-Å-period $CdTe/Cd_{0.9}Mn_{0.1}Te$ superlattice at 1 6 K under the continuous nonpolarized illumination by the light of 1 96 eV photon-energy with excitation density of about 1 W/cm^2 In Fig 4b the hysteresis loop taken without illumination is presented In the latter case the magnetization procedure has been performed in the dark and the structure has been illuminated for a short time of about 10 seconds to registrate the polarization signal only We have checked that such short time of exposition gives a negligible contribution in comparison with the continuous illumination

In both figures (4a and 4b) magnetization and demagnetization branches do not coincide in magnetic fields below 0 3 T, where $I_c(H)$ is below the saturation value Without illumination the magnetization branch is below that for demagnetization which is typical for magnetization hysteresis effects [13] The inversion of the ordering of the branches is caused by the illumination The energy of the spin system of Mn-ions changes in the remagnetization cycle on the value $L = -\oint MdH$ (where M is the magnetization), which is the work performed by the external magnetic field and corresponds to the area under the hysteresis loop In the dark cycle the spin system lowers its energy but under illumination the energy is increased It is obvious that in the latter case the absorbed energy is taken from the photoexcited carriers We have found that the amplitude of the inverse hysteresis loop is a function of magnetic field and reaches the saturated value of 0 1 when the field strength exceeds 0 5 T

The nonequilibrium remanent magnetization of 0 05 in zero magnetic field (see Fig 4a) has a relaxation time of about 10^3 s at T=1 6 K Such long relaxation times are characteristic for systems with a large number of strongly correlated spins [14] At low temperature applied in the experiment (1 6 K) the correlation in spin clusters is due to the exchange interaction between the spins of Mn ions located as nearest- and next-nearest-neighbours in a Cd sublattice The constants of the exchange interaction in the Heisenberg Hamiltonian $\mathcal{H} = -2J(S_1S_2)$ are J_1= -0 526 meV and J_2= -0 095 meV for nearest and next-nearest neighbour interaction, respectively [15] Here S_1 and S_2 are spins of Mn-ions The total energy of the exchange interaction of a nearest-neighbour pair is 14 J = - 7 9 meV This energy exceeds significantly the thermal energies kT=0 1 meV at T=1 6 K and that provides such a long relaxation time of the spin orientation of large spin-glass clusters

We suggest the following model of the optically induced orientation of spin-glass clusters Electrons and holes photoexcited by the nonpolarized light relax in energy and populate all spin states with equal probabilities In magnetic fields the carrier system aims for the equilibrium population of the Zeeman sublevels which is accompanied by the orientation of carrier spins along the field direction The carriers pass their spin to the system of Mn-ions and turn the Mn spins opposit to the magnetic field direction If the energy passed by the carriers is large enough, not only paramagnetic spins but high-coercive clusters will be oriented also As a result of such specific Overhauser effect [16] the magnetic moments of clusters with long spin relaxation times will be oriented against the magnetic field This orientation will manifest itself in the long-living remanent magnetization and in the inverse hysteresis loop

The energy which carriers could transfer to Mn ions is equal to the value of the Zeeman splitting and depends strongly on the magnetic field (see insert of Fig 2) At low fields (< 0 1 T) this energy is not enough to change the orientation of large clusters and no remanent magnetization has been found At higher fields of about 0 5 T the energy of carriers of 10 meV gives us the characteristic energies which are required for the reorientation of clusters which are comparable with the energy of the exchange interaction of a nearest-neighbour pair. At these fields the long-living remanent magnetization oriented against the external field direction will be induced by the illumination This remanent magnetization exhibits the inverse sign of hysteresis loop

It is worth to note that the suggested model of the effect does not content any specific feature of SLs with thin layers of semimagnetic semiconductors However having investigated 2-μm thick epilayers of $Cd_{0.9}Mn_{0.1}Te$ we have not observed the effect of the photoinduced inversion of the hysteresis loop The usual hysteresis which is analogous to the dark hysteresis in SL has been found only In thin barriers of SL the spin-glass clusters of large sizes modify their structure because their extention in the growth axis direction is limited by the thickness of the barrier layers The appearence of the thermohysteresis phenomena in thin (≤20 Å) layers of $CdTe/Cd_{0.95}Mn_{0.15}Te$ has been demonstrated [4] A modification of the magnetic properties of clusters at the interfaces have been reported recently for $CdTe/Cd_{1-x}Mn_xTe$ quantum well structures [5]

5 Conclusions

The methods of polarized luminescence have been used for the study of the spin relaxation processes in $CdTe/Cd_{0.9}Mn_{0.1}Te$ semimagnetic superlattices Very efficient spin relaxation has been found for free carriers whereas localized carriers conserve their spin orientation due to the exchange interaction with the magnetic moments of the spin-glass clusters Two inputs from electrons and holes into the circular polarization degree of luminescence have been revealed by the application of longitudinal and transverse magnetic fields The effect of the inversion of sign of the magnetic hysteresis under nonpolarized illumination in magnetic fields has been found This effect is explained in terms of the Overhauser effect when the magnetic moments of clusters with long spin relaxation times are oriented against the magnetic field via their interaction with the carrier system thermalizing on the Zeeman sublevels

Acknowledgement The part of this work provided in the Ioffe Institute has been supported by the Soros Foundation Grant awarded by the American Physical Society I A M and V P K acknowledge support of their stay in the University of Wurzburg from NATO grant CRG 921121

* on leave from A F Ioffe Physico-Technical Institute, St Petersburg, Russia

1 E L Ivchenko, A V Kavokin, V P Kochereshko G R Posina I N Uraltsev, D R Yakovlev, R N Bicknell-Tassius, A Waag, and G Landwehr, Phys Rev B 46, 7713 (1992)
2 N Dai, H Luo, F C Zhang, N Samarth, M Dobrowolska and J K Furdyna, Phys Rev Lett 67, 3824 (1991)
3 D R Yakovlev, W Ossau, G Landwehr, R N Bicknell-Tassius A Waag, S Schmeusser, and I N Uraltsev Solid State Commun 82 29 (1992)
4 D D Awschalom, J M Hong, L L Chang, and G Grinstein Phys Rev Lett 59,1733 (1987)
5 W J Ossau and B Kuhn-Heinrich, Physica B 184, 422 (1993)
6 A Waag, S Schmeusser, R N Bicknell-Tassius, D R Yakovlev, W Ossau, G Landwehr and I N Uraltsev, Appl Phys Lett 59, 2995 (1991)
7 B Kuhn-Heinrich M Popp, W Ossau E Bangert, A Waag, and G Landwehr, Semicond Science and Technology, in press
8 M I Dyakonov and V I Perel Sov Phys Solid State14,1245 (1972)

9 J A Gaj, R Planel, and G Fishman, Solid State Commun 29, 435 (1979)
10 M I Dyakonov and V I Perel, in Optical Orientation, Eds F Meier and B P Zakharchenya (North-Holland, Amsterdam, 1984), p 40
11 Y Merle d'Aubigne, L S Dang, F Dalbo, G Lentz, N Magnea, and H Mariette, Superlattice and Microstructures 5, 367 (1989)
12 D Heiman, J Warnock, P A Wolff, R Kershaw, D Ridgley, K Dwight, and A Wold, Solid State Commun 52, 909 (1984)
13 K Binder and A P Young, Rev Mod Phys 58, 801 (1986)
14 S Oseroff and P H Keesom, in Semiconductors and Semimetals Vol 25, Eds J K Furdyna and J Kossut (Academic Press, London 1988), p 413
15 X Wang, D Heiman, S Foner, and P Becla, Phys Rev B 41, 1155 (1990)
16 A W Overhauser, Phys Rev 92, 411 (1958)

ThA5

Photomodulation Spectroscopy and Cyclotron Resonance of $Cd_{1-x}Mn_xTe/CdTe$ Semimagnetic and Strained Multi-Quantum Well Structures

S.C.Shan*, L.J.Zhang*, W.Lu* and R.N.Bicknell+

* Laboratory for Infrared Physics, Shanghai Institute of Technical Physics, Chinese Academy of Sciences, Shanghai 200083, China
+ Physikalisches Institut der Universität Würzburg Am Hubland, D-8700, Würzberg, F.R.Germany

Abstract

Photomodulation spectroscopy and cyclotron resonance of free carriers of $Cd_{1-x}Mn_xTe/CdTe$ multi-quantum wells are reported for the first time. 5 peaks have been observed in the energy region of 1.55 to 1.80eV by photoreflectance measurement at low temperature and assigned to excitonic transitions in quantum well. The bandedge alignment and the valence band structure are determined by comparison of experimental transitions to envelope function calculation including strain effect. The cyclotron resonance of electrons in $Cd_{1-x}Mn_xTe/CdTe$ MQW has been observed by use of a modulated cyclotron resonance technique combined with an extra and monochromatic light excitation. The cyclotron mass m_c^* and $\omega_c\tau_{res}$ are determined from fitting the experimental line-shape to the expressions of resonance and to be $0.096m_0$ and around 2 respectively.

I Introduction

$Cd_{1-x}Mn_xTe$ is a semimagnetic semiconductor or diluted magnetic semiconductor and has been best investigated among this kind of materials during last 20 years[1-8]. With a fraction x of Cd^{2+} ions replaced by magnetic ions Mn^{2+} in II-VI compound CdTe, the mixed crystal $Cd_{1-x}Mn_xTe$ has some novel properties and performances mainly originated from the magnetic exchange interaction between Mn^{2+} ions and movable charge carriers, such as giant Faraday rotations and Voigt effects, large Zeeman splittings of the excitons and g factors of electron, strongly circularly polarized band edge luminescence, large and minus pressure coefficient of interband transition for $Cd_{1-x}Mn_xTe$ with $x > 0.4$, as well as magneto-tunable band-gap and electronic states[1-9]. In addition the materials are also attractive for potential application in optoelectronic devices, such as Faraday rotators, optical isolators and magnetic field sensors.

It is believed that the quantum well structures and superlattices of $Cd_{1-x}Mn_xTe/CdTe$ which combines semimagnetic and usual semiconductor materials, should show a significant enhancement of the electro-optical coefficient with respect to

bulk $Cd_{1-x}Mn_xTe$ materials[10], and be attractive from both academic and practical points of view.Thus a great effort has been made in last few years for preparing the lattice mismatched $Cd_{1-x}Mn_xTe$/CdTe multi-quantum wells and superlattices as well as investigating their confined quantum states and related performances by use of photoluminescence excitation, photoluminescence, modulation spectroscopy and other methods[11-19]. R.L.Harper et al[17] have investigated excited confined quantum states in $Cd_{1-x}Mn_xTe$/CdTe MQW and superlattices by use of the piezomodulated reflectivity spectroscopy and the interband transitions up to quantum number 5 have been observed at 10 K for the MQW structure with x=0.13 and $L_w=L_z=180Å$. They also deduced from their data that the valence band offset for $Cd_{1-x}Mn_xTe$/CdTe heterostructures might be zero or only a very small part of the total band gap offset Eg. Alex Hartwit and his coworkers[15] have observed the formation of miniband in the CdTe/$Cd_{1-x}Mn_xTe$ quantum well system with the decrease of the width of the barriers layer $Cd_{1-x}Mn_xTe$ and the influence of the perpendicular electric field upon the miniband behavior.

But nevertheless there are still lack of impressive experimental results on the confined quantum states, carriers behavior in the wells and related properties, probably due to the difficulty for the preparation of the qualified structures of MQW and superlattice $Cd_{1-x}Mn_xTe$/CdTe and doping technology. We have fortunately observed the excitonic transitions up to 33H in this MQW structures by use of photomodulation spectroscopy and the cyclotron resonance of free electrons in the QW by use of the modulation technique of cyclotron resonance combined with an additional and monochromatic light excitation, and report the results here in this paper.

By photomudulation spectroscopy, 5 peaks have been observed in the energy region of 1.55 to 1.80eV at low temperature and attributed to 11H, 11L, 22H and 33H excitonic transitions for $Cd_{0.72}Mn_{0.28}Te$(15nm)/CdTe(15nm), in combination with a modified envelope function calculation. The different temperature dependenciss for the transition energies of different transitions have been understood in connection with the wavefunction compositions of the sublevels. It has been also demonstrated that the light holes in valence band and the electrons in the conduction band might form second kind of superlattice and exist in different layers for the structures investigated in this paper. The energy splitting for the light and heavy holes at the top of valence band of CdTe layer is determined to be 18meV.

A sharp peak and a broader band have been observed respectively for $Cd_{0.79}Mn_{0.21}Te$(15nm)/CdTe(15nm) MQW by the derivative measurement of the cyclotron resonance absorption caused by a chopped and additional monochromatic excitation light beam with photon energy larger than (especially resonant to) 11H exciton transition. The measurement with tilted magnetic field has shown that the broader resonant band is corresponding to the resonance of free electrons in QW's. The effective mass and relaxation parameters for the quasi 2D electrons in this semimagnetic and strained QW structures have been extracted from the observation of the cyclotron resonance in this way and with different FIR laser beam with different wavelengths.

II Experimental

The samples used in this investigation were grown by MBE technique. A buffer layer of $Cd_{1-x}Mn_xTe$ or CdTe with thickness of 0.9μm was grown at first on CdTe substrate oriented along <100> direction, 50 periods of $Cd_{1-x}Mn_xTe$ex/CdTe with thickness of 150Å for both wells and barriers were followed, and a cap layer of CdTe with thickness of 150-300Å were grown at last. The x value for the barrier layers of $Cd_{1-x}Mn_xTe$ were experimentally determined from photoluminescence and photomodulation reflectance measurement and to be 0.19 and 0.28 for two diffsrent samples used in this investigation.

The photomodulation spectra were measured by a home-made spectrometer. A chopped laser beam of 6328Å from He-Ne laser is used as pumping light beam while another swept monochromatic beam from a monochrometer is used as probe beam and the Si photodiode or cooled Ge photodiode are used for detectors. The sample is mounted on the cold finger of a He-recycle refrigerator and the sample temperature can be adjusted between 10 to 300K.

A new and modulated cyclotron resonance technique[20] was tried for the observation of cyclotron resonance of carriers in $Cd_{1-x}Mn_xTe$/CdTe MQW since the conventional FIR CR method has failed for a long time for the observation of CR in this system. By the new method, the derivative of the CR absorption induced by a chopped and monochromatic bandedge excitation light beam is recorded while FIR radiation is kept in constant and the samples are mounted in the inner cryostats(1.5K) of a Oxford superconducting magnet. The monochromatic, chopped and tunable bandedge or interband excitation light beam is come from a monochrometer or He-Ne laser and transmitted to the sample by use of a fibre. The power of excitation light beam has been measured at the end of the fibre and was around or below 0.1mW. Faraday configuration was used for this derivative CR measurement.

III Photomodulation Spectroscopy

We show in Fig.1 the typical photoreflectance spectra for $Cd_{0.72}Mn_{0.28}Te$(150Å)/CdTe(150Å) MQW at temperature of 300 and 100K. It is seen from the figure that 5 peaks or spectral

structures can be observed even at room temperature. The peaks and structures become very clear and definite at low temperature due to the big improvement of signal to noise ratio. As an example, 5 peaks located at 1.573, 1.600, 1.626, 1.782 and 1.982 eV respectively can be defined at 100K except two question marks at 1.648 and 1.750eV respectively.

The peak at 1.982eV can be attributed to interband transition in the barrier of $Cd_{1-x}Mn_xTe$ and x=0.28 can be deduced from this transition energy while other peaks and questions marks are come from interband transitions in the wells of CdTe. For the accurate determination of the transition energies, a fitting calculation of the experimental spectra to the Aspnes' line shape function has been performed. The transition energies listed above have been corrected via such fitting calculation instead of reading directly from the figures. An envelope function calculation including the effect of lattice mismatch of 0.64% between CdTe and $Cd_{0.72}Mn_{0.28}Te$ has been made for estimation of the sublevel positions in the wells and the transition energies between sublevels of conduction and valence bands. It is found by the calculation that the energy band discontinuity parameter Q_c=0.90 could result in the best agreement of the calculated transition energies to experimental ones. The strain-induced split of the heavy and light holes is calculated to be 18 meV, thus all the light holes are roughly in extended states while there are still confined heavy hole states up to n=2 even 3 in CdTe quantum wells. By comparison of the experimental results to calculation, the peaks observed in Fig.1 below 1.8eV can be assigned to transitions of 11H, 11L, 22H and 33H respectively, while the questions marks may be connected with some forbidden transitions.

We plot in Fig.2 the energies for above assigned transitions as a function of temperature, as measured from photomodulation spectroscopy. It is worthwhile to mention that the temperature coefficient of transition energy for 33H is -0.48meV/K, while the coefficients for transitions 11H, 11L and 22H are between -0.30 to -0.35meV/K, that is, similar to that of bulk CdTe. It is known that semimagnetic semiconductor $Cd_{1-x}Mn_xTe$ has much larger temperature coefficient of energy gap (-0.78meV/K as measured in this paper) due to the introduction of Mn^{2+}, the transition 33H in QW CdTe has temperature coefficient much larger than bulk material and QW transitions with low quantum numbers, which implies the stronger interaction and overlapping between the wavefunctions of well and barrier layers for 33H transition.

IV Cyclotron Resonance of Photoexcited Electrons in $Cd_{0.79}Mn_{0.21}Te$/CdTe MQW

We summarize in Fig.3 the CR transmission and its derivative induced by an interband and monochromatic excitation versus the magnetic field for the sample of $Cd_{0.79}Mn_{0.21}Te$(150Å)/CdTe(150Å) MQW. The vertical coordinate is CR transmission for the conventional FIR CR measurement and the derivative of the CR transmission for the modulated CR measurement. The curve a in Fig.3 is the CR transmission versus magnetic field B as measured with conventional FIR CR technique and without extra-excitation light, it is clear from the curve that one could not observe any trace of CR absorption, though we have tried many times to improve the quality of measurement and increase the signal to noise ratio. The curves b-d are CR derivative or modulation induced by the extra-excitation light beam of 6328Å line of a pocket type He-Ne laser with a power lower than 0.1mW. The wavelengths of FIR radiation used in the measurements of curve b-d are 96, 104 and 118.8μm respectively. It is seen from the curve that there are two resonant peaks or structures located in the magnetic field below 3 Tesla and around 10 Tesla respectively. The actual positions of the peaks are dependent on the wavelength of FIR radiation, as an example, they are located at about 3 and 10.7 Tesla respectively for FIR radiation of 96μm. The curves e and f are CR modulation under magnetic field tilted to the direction of the MQW growth with an angle of 15°, which demonstrate that the broad peak at the region of 10 Tesla is corresponding to CR absorption of carriers in QW since its position shifts to higher magnetic field according to the law of $B_{CR}(\text{tilt})=B_{CR}(\vec{B}\|\vec{n})/\cos\alpha$, while the peak at 3 Tesla is not influenced by the tilt of the magnetic field and thus demonstrated to be process in barrier layer or substrate material.

The experiment has been performed with monochromatic light excitation with different wavelengths ($\hbar\omega$=1-3eV) as well as with white light excitation directly from a tungsten halogenide lamp and with a much stronger power than monochromatic excitations. It is found that the monochromatic excitation matched with exciton transition in QW or interband transition in barrier layers will enhance the derivative structure of CR absorption resonantly while the white light excitation can hardly induce the derivative structure of CR absorption in investigated QW structure though the power is much stronger (more than 10^3 times) than that of monochromatic excitation. The 6328Å line of the He-Ne laser used in this experiment is nearly resonant with the interband transition of barrier layer $Cd_{0.79}Mn_{0.21}Te$ at the experimental temperature of 1.6K.

The cyclotron mass m_c can be determined from the positions of the broad peaks of the curves b to d, or determined together with ω_{res} from the fitting calculation of the lineshape of the resonance to the classical expression $p\propto(1+(\omega_c+\omega)^2\tau_{res}^2)/([1+(\omega_c^2-\omega^2)\tau_{res}^2]^2+4\omega^2\tau_{res}^2)$ since we measured actually the cyclotron

resonance of photo-excited electrons in QW. Thus we obtain a cyclotron mass $m_c^*=0.096m_0$ and $\omega_c\tau=2$, which means that the cyclotron mass determined from this experiment is in good agreement with the m_c^* values in QW of CdTe as calculated from theory or measured by using other technique, while the scattering time τ_{res} under magnetic field as well as τ_0 [$1/\tau_{res} = 0.65\times(1/\tau_0)$] in the absence of a magnetic field are in the order of 10^{-12} second.

References

[1] N.B.Brandt and V.V.Moshchalkov, Adv.Phys.,33, 193(1984)
[2] R.R.Galazka, Shoichi Nagata and P.H.Keesom, Phys.Rev., B22, 3344(1980)
[3] J.K.Furdyna and J.Kossut, in "Semiconductors and Semimetals", edited by R.K.Willardson and Albert C. Beer (Academic, Boston, 1988), vol.25
[4] Wei Shan, S.C.Shen and H.R.Znu, Sol.Sta.Commun., 55,473(1985)
[5] S.C.Shen and S.Jiang, Japan J. Appl. Phys., 32, suppl. 32-1, 264(1993)
[6] Z.J.Tian and S.C.Shen, J.Phys. (Cond. Matters), 2, 6295(1990)
[7] D.L.Peterson, A.Petrou, M.Datta, A.K.Ramdas and S.Rodriguez, Sol.Sta.Commun, 43, 667(1982)
[8] S.M.Ryabchenko,O.V.Terletskii,I.B.Mizetskaya and G.S. Olenik, Sov.Phys.-Semicond., 15, 1345(1981)
[9] J.A.Gaj, R.R.Galazka and M.Nawrocki, Sol.Sta.Commun., 25, 193(1978)
[10] K.Nakamura nd H.Nakano, Japan J. Phys. Soc., 59, 1154(1990)
[11] R.N.Bicknell, N.C.Giles-Taylor, D.K.Blanks, R.W.Yanka, E.L. Buckland and J.F.Schetzina, J.Vac.Sci.Technol., B1,709(1985)
[12] S.K.Chang, A.V.Nurmikko, L.A.Kolodziejski and R.L.Gunshor, Phys.Rev., B33, 2589(1986)
[13] G.M.Williams, A.G.Cullis, C.R.Whitehouse, D.E.Ashenford and B.Lunn, Appl. Phys.Lett., 55, 1303(1989)
[14] D.D.Awschalom, J.M.Hong, L.L.Chang and G.Grinstein, Phys. Rev.Lett., 59, 1733(1987)
[15] Alex Harwit, C.Hsu, F.Agullo Raeda and L.L.Chang, Appl.Phys. Lett., 57, 1769(1990)
[16] J.J.Dubowski, A.P.Rott, Z.R.Wasilewski and S.J.Rolfe, Appl.Phys.Lett., 59, 1591(1991)
[17] R.L.Harper, Jr.R.N.Bicknell, D.K.Blanks, N.C.Giles, J.F. Schetzina, Y.R.Lee and A.K.Ramdas, J.Appl Phys., 65, 624(1989)
[18] H.Ossau, S.Fischer and R.N.Bicknell, J.Cryst.Growth, 101, 905(1990)
[19] K.M.Yenice, W.Williamson, S.A.Lee and J.J.Dubowski, Bull. Amer. Phys. Soc., 38, 531(1993)
[20] S.C.Shen, W.Lu and H.Von Ortenberg, 16th Inter. Conf. on IR and MM Waves, Aug. 26-30, 1991, Lausanne, Switzerland

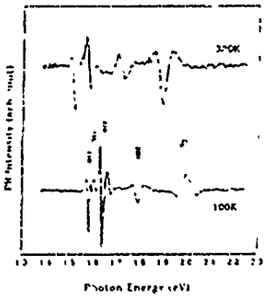

Fig.1 Photoreflectance spectra for $Cd_{0.72}Mn_{0.28}Te$(150Å)/CdTe (150Å) MQW at the temperatures of 300K and 100K.

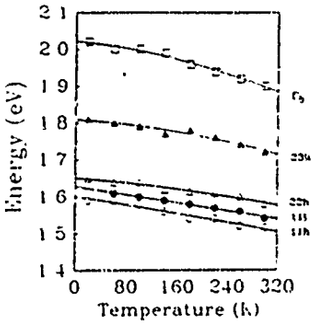

Fig.2 Transition energies of different transitions for $Cd_{0.72}Mn_{0.28}Te$(150Å)/CdTe(150Å) MQW measured by photoreflectance .The points are the experimental results while the curves are the fitting to formula $E(T)=E_0-\alpha T^2/(\beta+T)$.

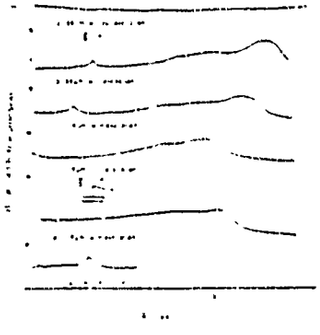

Fig.3 Cyclotron resonance transmission and its derivative to extra excitation power versus magnetic field for $Cd_{0.79}Mn_{0.21}Te$/CdTe MQW. The detailed elucidation of the curves is described in the text.

ThB1

Optical Properties of Etched GaAs/GaAlAs Quantum Wires and Dots

J Y Marzin, A Izrael and L Birotheau,
France Telecom, CNET PAB, Laboratoire de Bagneux,
F92220 Bagneux, France

Abstract
We show that very narrow wires and dots, exhibiting reduced dimensionality features, can be obtained through etching from a single quantum well structure. The importance of surface cleaning and passivation is emphasized The low temperature optical data obtained on arrays of wires and dots allow us to estimate quantitatively the size regularity The peculiar behaviour of the photoluminescence intensity is attributed to huge electrodynamic effects while the predicted intrinsic limitations imposed by slowed down energy relaxation are not evidenced We finally present experimental photoluminescence and photoluminescence excitation spectra obtained on single wires, as small as 6x25x135 nm^3

Introduction

The improvement of semiconductor optoelectronic devices obtained in the last two decades in quantum wells based structures, as well as theoretical predictions[1-4] on further potential gain through that of quantum wires and dots, stimulated an active research for fabricating these lower dimensionality objects Though spectacular effects have already been demonstrated in transport properties, the progress in the field of one and zero dimensional structures for optical applications is much slower The necessity of confining both electron and holes, together with that of large confinement energies for room temperature operating devices lead to stringent requirements on fabrication processes Up to now, numerous techniques are used to produce these wires and dots[5], i e. no ideal technique has been found so far. One may classify these techniques in two main groups, the techniques starting with a quantum well, providing confinement in one direction, and adding confinement in one or the two remaining directions, and those where a single growth step produces the wires or dots In the first family, a large number of effects have been put to work to obtain the additional confining potentials like etching [6-14], local interdiffusion (either laser induced [15,16], or assisted by ion implantation[17-21]), local strain (either with etched stressors[22,23] or on the lateral surface of a strained quantum well structure[24]) Similarly, the direct growth of wires or dots was obtained on vicinal surfaces (growth of vertical superlattices[25,26] or of inserted grids in quantum wells[27]), on supersteps [28], on high index surfaces with faceted growth [29], on patterned substrates (in V grooves [30-32], or using localised growth[33,34]).

For most of these techniques, the first demonstration has still to be followed by a careful study of their advantages and drawbacks In particular most of them are potentially able to produce very narrow structures (with lateral dimensions of the order or even smaller than 10 nm), so that the key issues concern now more the mastering of size fluctuations and the understanding of intrinsic limitations such as the slowed down energy relaxation in wires and dots [35,36] In this paper, we will focus on GaAs/GaAlAs structures fabricated with electron beam lithography reactive ion etching and overgrowth Low temperature optical data will be presented which underline several key properties of etched wires and dots

Fig 1: Typical SEM micrographs of etched GaAs/GaAlAs wires before (a) and after the anodic oxydation/desoxydation step.

Fig 2: Typical SEM micrographs of etched GaAs/GaAlAs dots before (a) and after (b) the GaAlAs overgrowth

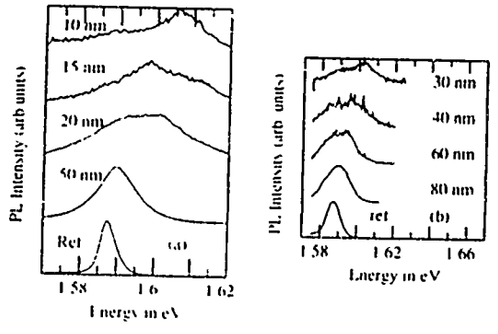

Fig 3: Typical 10 K PL spectra of gratings of wires (a) and arrays of dots (b) The spectra are normalized to their maxima and their zeros have been shifted for clarity

Fabrication

Typical samples on which the optical studies were performed were molecular beam epitaxy grown single GaAs quantum wells (6 nm thick), cladded between 50 to 80 nm $Ga_{0.7}Al_{0.3}As$ barriers, grown on a GaAs (100) substrate and 1500 nm GaAs buffer layer. The choice of the 6 nm thickness for the quantum well locates the low temperature photoluminescence (PL) far enough in energy from the GaAs band gap and avoids that the high energy tail of the buffer layer emission dominates the PL spectra for the narrowest structures. 40x40 μm^2 gratings of wires or arrays of dots with various pitch (typically 0.5 µm) and lateral dimensions (ranging from less than 20 to 2000 nm) as well as single wires are defined by electron beam lithography using a JEOL 5DIIU machine. A Ni mask is defined through standard lift-off, and used for a $SiCl_4$ Reactive Ion Etching (RIE) procedure (0.3µm). The following step is the key one for obtaining very narrow structures and consists in an anodic oxidation which enables to remove, by subsequent desoxidation, a surface layer of controlled thickness[37]. This peeling step allows: i) to remove the surface layer containing most of the RIE induced defects; ii) to reduce the width of the wires and sizes of the dots by a controlled amount (typically 60 to 70nm). It is indeed otherwise difficult to define usable metal masks with dimensions smaller than about 30 nm. The beauty of this technique is that it appears to be completely isotropic and that the thickness of the oxide formed during anodic oxidation can be easily controled with a 5nm precision. Figure 1 shows the scanning electron micrograph (SEM) of the same wire grating before (a) and after (b) the anodic oxidation and desoxidation steps (such SEM micrographs are used to estimate the quantum wires and dots sizes). Finally, a 0.2 to 0.3 µm $Ga_{0.7}Al_{0.3}As$ layer is overgrown by Metal Organic Chemical Vapour phase Deposition (MOCVD). Figure 2 shows the SEM micrograph of an array of dots, before (a), and after (b) the GaAlAs overgrowth. In the earliest stages of this work, the overgrowth morphology on wires was very dependent on the orientation of wires [14], whereas it seems to be much less sensitive when it is preceded by anodic oxidation, presumably because of a much cleaner surface. Thanks to that fact, dots could be fabricated recently with this process. This final step is essential to the observation of PL in the narrowest structures because it prevents non radiative recombination on the lateral surfaces [38], yielding an interface recombination velocity that can be lowered by two orders of magnitude as compared to the surface one. Unfortunately, it also appeared to be the limiting step as far as the lateral dimensions are concerned. Mass transport occurring during the 10 min 800°C annealing preceding the growth itself destroy the narrowest structures (<10nm).

As we will discuss in more details in the next section, the main drawbacks of this technique lay in the relatively poor homogeneity of sizes[38]. Size fluctuations of ±5nm are observed on the wires prior to the overgrowth final step. All our studies tend to attribute these fluctuations to the earliest lithography stages of the process, and it seems that the RIE and anodic oxidation just transfer the irregularities on the final object. Several attempts to reduce these fluctuations, among which the use of lower molecular weight PMMA resist failed to reduce these below ±3 nm. With this respect, the use of a chemical etch revealing crystallographic planes which was recently proposed[39], or that of inorganic resists seem very promising. The second severe problem is linked to the use of the overgrowth. The introduction of such a high temperature step in the process is quite delicate and overgrowing a layer with sufficient passivation properties without degrading the optical properties of the starting quantum well is difficult to obtain with a good reproducibility. One must bare in mind that the overgrowth takes place, on the lateral edges of the etched structures, on AlGaAs whose oxides are more stable thermally than those of GaAs. On the other hand, one would like to minimize the overgrowth temperature to prevent from unwanted intermixing and diffusion of defects created at the overgrown layer interface. This trade off leads to a two steps process: a high temperature annealing (around 800 °C) followed by a low temperature (around 700°C) growth. Let us emphasize that quantum wires and dots issued from a patterned quantum well structure will have anyway to go through overgrowth to obtain a real device. This constitutes perhaps the best argument in favour of the fabrication techniques where the wires or dots result from the growth itself. Up to now, we nevertheless lack data to assess precisely and thus compare meaningfully the different fabrication techniques, mainly as far as size and homogeneity control are concerned.

The following section is devoted to the low temperature optical data obtained on the wires and dots produced by the etching plus overgrowth technique.

Optical studies

photoluminescence

Figure 3 shows typical 10K photoluminescence spectra obtained on gratings of wires (a) and arrays of dots of various sizes (b). The PL is excited by the focused beam (power of the order of 50µW, spot diameter 2µm, corresponding to 5·10 wires and 100 dots) of a Sapphire·Ti laser pumped by an Ar^+ laser. The excitation energy is 1.75 eV, well below the GaAlAs band gap energy so that carriers are photocreated only in the wires or dots. Even with these low excitation conditions, the PL of the narrowest structures is observed with reasonable signal to noise ratio, showing the efficiency of the anodic oxidation and overgrowth procedures for removing the etching defects and passivating the lateral surfaces, respectively. The spectra of Fig. 3 are normalized and their respective intensities will be discussed in the following. We clearly see a high energy shift of the PL spectrum (up to 20 meV) when the size Lx is decreased, which is attributed to the additional confinement. For the smallest Lx, the peak broadens, mainly towards the high energy side. The origin of this broadening is attributed to two effects: part of it is due to the inhomogeneity in the width of the structure while defects migration occurring during the overgrowth step is likely to contribute significantly to the broadening of the PL spectrum for the narrowest wires and dots.

The integrated intensity per unit wire or dot area is the relevant quantity to compare the emission intensities as a function of Lx because the absorption scales as this area, at least when 1D subbands or 0D levels form a quasi continuum (sizes > 100 nm). This corrected integrated intensity (CII) is plotted in Fig. 4 for wires and dots. Electrodynamic effects [11,40] may play an important role in the observed increase of the CII for intermediate Lx (around 100 nm). Experimentally, the effects are more important in dots (or in single short wires) than in arrays of wires, but no quantitative analysis of the data could obtained up to now. Another important point is the reduction by only a factor of 2 of the CII between the reference 2D regions and the narrowest wires or dots. This is somewhat in contradiction with the recent theoretical prediction of a dramatic decrease of the radiative efficiency for small dots or wires[36]. The strong reduction of the carrier scattering rates by acoustic phonons, together with the impossibility for electrons in small boxes to emit LO phonons should quench by orders of magnitude the emission intensity of the smallest structures. Though there may be a certain compensation of the predicted decrease in intensity by a better coupling with the incoming laser light through electrodynamic effects, energy relaxation seems still pretty fast in the smallest (≈20 nm wide) wires or (≈30x30 nm^2) dots. Some recent experimental evidence pleades for the existence of additional efficient energy relaxation mechanisms. We have indeed observed short PL rise times through time-

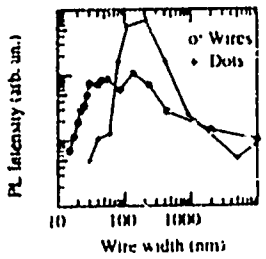

Fig 4: 10 K corrected integrated intensities observed in wires (o) and dots(+) Please note the logarithmic scales.

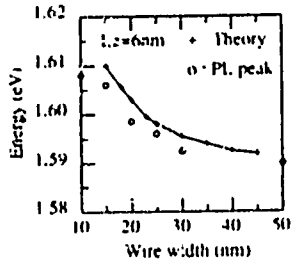

Fig 5: Experimental (o) and calculated (+) energies for the PL peak energy in quantum wires, as a function of their width Lx The calculation includes the excitonic effect

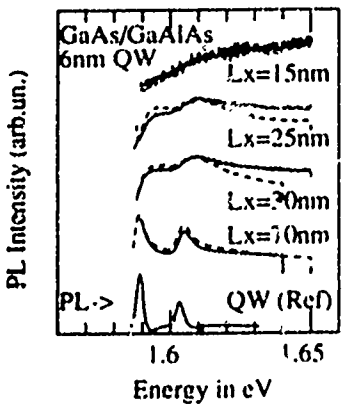

Fig 6: 10 K PLE spectra observed on the reference part of one sample, and on gratings of wires of various width Lx All the spectra were normalized to their maxima and correspond to E_{laser} parallel (broken line) and perpendicular (full line) to the wire axis.

resolved spectroscopy for the narrowest dots (less than 100 ps). A similar result was obtained in InAs dots embedded in GaAs[41], with shorter times (15 ps). The typical size of these latter dots is 30x30x2 nm^3 In both cases, the carriers were photocreated in the barrier material. These short times thus includes diffusion to the dots and energy relaxation inside them. In the particular case of InAs dots, the surface of the sample is flat and electrodynamics effects do not modify the apparent radiative efficiency. Though recent theoretical estimates show that Auger effects may provide the channels for a quick electron energy relaxation in these moderate sizes dots[42], additional experiments have still to be performed to deepen the understanding of carrier energy relaxation in these structures.

Finally, Fig.5 shows the good agreement between the experimental maximum energies of the PL spectra and theoretical estimates of the energy of the first excitonic transition, in the case of wires.

Photoluminescence Excitation

The expected signature of 1D effects in the PLE spectra are: i) a shift of the onset of the absorption; ii) polarization effects for E_{laser} polarized along or across the wire axis Y; iii) the appearance of transitions between excited 1D electron-hole states.

It should be emphasized that the differences in the TE (E along the wire axis) and TM (H along the wire axis) PLE spectra, obtained with an incoming laser perpendicular to the surface, do not constitute alone a proof of reduced dimensionality effects on the hole band structure. As evidenced in ref. 40 , in the TM configuration, due to the non-planarity of the surface, the electric field has a significant component along the growth axis z. This component may change the relative strengths of the transitions in the TE and TM absorption spectra. Fortunately, this effect should be moderate thanks to the parity of E_z which is odd in x (x being the direction transverse to the wire).

Figure 6 shows the 10K excitation spectra for gratings of wires for various Lx, and X and Y polarizations. Whereas the first two criteria are met in those spectra, no 1D excited transitions are observed. The two e_1hh_1 and e_1lh_1 excitons seen in the reference PLE spectrum broaden progressively instead, and are completely smeared out in the narrowest wires We attribute this broadening mainly to wire width inhomogeneities, as discussed in the previous section. We nevertheless observe a shift of the onset of the absorption together with clear polarization effects As far as the differences in the spectra obtained in the two polarizations, please note that all the spectra are normalized to their own maxima, because there is a difference in the collected intensity in the two polarizations due to the electrodynamic effects. Nevertheless, the first transition is always more polarized along the wire axis than that of the second one, in good agreement with the calculated absorption spectra displayed in Fig 7 These spectra were calculated assuming a finite potential in z, an infinite one in x It takes into account the full hole band structure and neglects the excitonic interaction[43]. We furthermore take into account the width fluctuations [38], by calculating the absorption coefficient for a collection of wires with a Gaussian distribution (mean width Lx, standard deviation ΔLx) Fig 7 (a) shows the evolution of the absorption spectrum for a Lx=30 nm wide wire with the width fluctuation ΔLx The spectra of Fig 7(b), calculated for various Lx and ΔLx=5nm, show a reasonable agreement with the experimental spectra. SEM top view micrographs of the etched wires, just before the overgrowth step, allow to extract a typical value of ±5 nm for the width fluctuations, confirming this analysis. Though a satisfactory agreement is found for the PLE experiments when these width inhomogeneities are taken into account, they are not sufficient to yield alone, as mentioned in the previous section, the broadenings that are observed in the PL spectra of Figure 3 The additional broadenings, beyond those due to the size

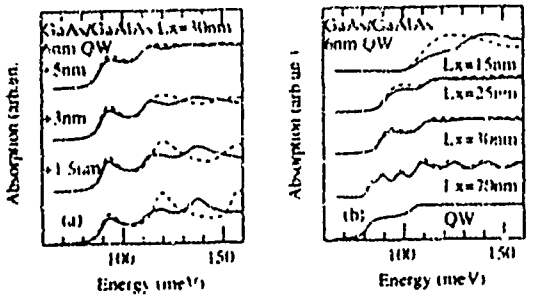

Fig 7: Calculated absorption spectra (neglecting excitonic effects) on collections of wires with a gaussian distribution of sizes, of average Lx, and standard deviation Δd. In a), Lx=30nm and Δd= 0, 1.5, 3 and 5 nm. In b) Δd=5nm and Lx=15,25,30,70 nm. In both cases, all transitions are broadened by 5 meV.

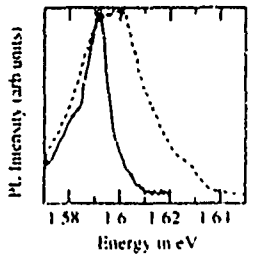

Fig 8: 10 K PL spectra of a single 6x20x145 nm^3 wire (full line), and of a grating of 6x20x60000 nm^3 wires (dashed line)

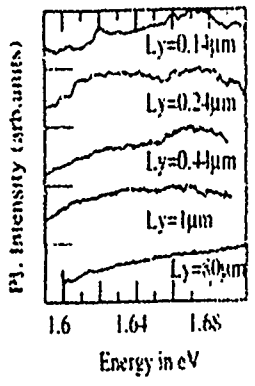

Fig 9: 10 K PLE spectra of a grating of 8x25x60000 nm^3 wires and of single 6x25xLy nm^3 wires with various length Ly

inhomogeneities, scale as the lateral surface to volume ratio for wires and boxes, and this suggests strongly that they may be due to defects migration (or intermixing) during the annealing and overgrowth step.

Though there are other possible ways to reduce the effects of inhomogeneities, the simplest one is to study single objects. The results of such studies are presented in the next section.

Single wires

Thanks to the high PL efficiency obtained in the narrowest wires, we could perform PL and PLE spectroscopy on isolated (and even short) wires. Figure 8 shows the 10K PL spectrum of a single 6x20x145 nm^3 wire as compared to that obtained on a grating of wires (5 to 10 wires), with the same excitation conditions. Let us emphasize again that the obtention of the PL spectrum of this single short wire (still excited below the GaAlAs band gap with a 100 μW, 2μm diameter spot) shows the efficiency of the process to give narrow quantum structures with a low density of non radiative defects and a good radiative efficiency. The Full Width at Half Maximum (FWHM) of the PL spectrum of the single wire is reduced by a factor of 2, as compared to that of the spectrum obtained on the grating. However, the reduction of the broadening is not symmetric. It is difficult to exclude that this particular single wire is somewhat wider than the average wire width in the grating.

Perhaps more convincing is the evolution of the PLE spectra for single wires with decreasing lengths displayed in Figure 9. Whereas it is featureless for the longest wires, some structures are progressively evidenced in shorter and shorter wires. The detail of the PLE spectrum for single short wires of varying width is shown in figure 10. Though the experiments are difficult on these objects, we could verify than the main features in the spectra are significative. We assign them to transitions between 1D excited electron and hole subbands. Unfortunately, the length of the shortest wires is still large as compared to the typical length where the width is uniform (20 to 50 nm); they are still rather disordered objects, for which a quantitative comparison with calculated transition energies is not satisfactory.

In our opinion, the spectroscopy of single shorter wires can be performed which will give us information on the intrinsic properties of 1D and 0D objects, and clarify the energy relaxation problems.

Conclusion

To summarize, we have shown that electron-beam lithography, associated with reactive ion etching, anodic oxidation and overgrowth, is a suitable tool for fabricating quantum wires and dots. The low temperature optical properties show that reasonable efficiencies can be restored even in the narrowest structures, which display reduced dimensionality features. However, the fluctuations of their sizes have still to be reduced (to typically better than 1.5 nm) to meet the drastic requirements needed to improve the characteristics of optoelectronic devices.

Acknowledgement
The authors wish to thank to J.M. Gerard, M. Voos and G. Bastard for many fruitful discussions. This work was partly funded by the ESPRIT Basic Research program of the European Community.

References
1. Y.Arakawa, K.Vahala and A Yariv, Appl Phys.Lett 45, 950 (1984)
2. M.Asada, Y.Miyamoto and Y Suematsu, Jap.J Appl Phys 24, L95 (1985)
3. C.Weisbuch, in "Applications of Multiquantum Wells, Selective Doping, and Superlattices", Semiconductors and semimetals Vol.24, R Dingle editor, Academic Press, Boston, 1 (1987)
4. T.Takahashi and Y.Arakawa, Optoelectron Dev. and Technol. 3, 155 (1988)
5. K.Kash, Journal of Luminescence 46, 69 (1990) and references therein.
6. D Gershoni, H.Temkin, J.Dolan, S N G Chu and M B Panish, Appl Phys Lett 53, 995 (1988)
7. M. Walt, C.M. Sotomayor-Torres,R. Cheung, C.D.W. Wilkinson,H.E.G. Arnot and S.P. Beaumont, Superlattices and Microstruct. 4, 2124 (1988)
8. W.E.Leitch, C.M.Sotomayor Torres, D.Lootens, S.Thoms, P.van Daele, C.R.Stanley, P.Demeester and S.P.Beaumont, Surf.Sci 263, 622 (1992)
9. A. Forchel, B E. Maile, H Lei and R. Germann, Springer Series in Solid States Sciences 83,"Physics and Technologies of submicron structures" (Springer, Berlin, 1988), p.28.
10. M.Kohl, D.Heitmann, P.Grambow and K Ploog, Phys.Rev.Lett. 63, 2124 (1989)
11. M.Kohl, D.Heitmann, W W Rühle, P.Grambow and K.Ploog, Phys.Rev.B 41, 12338 (1990)
12. R.Cingolani, H.Lage, L.Tapfer, H Kalt, D Heitmann and K Ploog, Phys.Rev.Lett 67, 891 (1991)
13. A. Izrael, B. Sermage, J-Y. Marzin, O. Ougazzaden,J. Etrillard, Appl Phys. Lett. 58, 830 (1990).
14. A.Izrael, J.Y.Marzin, B Sermage, R.Azoulay and V.Thierry-Mieg, Microelectron. Eng. 11, 39 (1990)
15. K. Brunner, G. Abstreiter, M. Walther, G Bohm and G. Trankle, Surf. Sci 267, 218 (1992)
16. K. Brunner, U. Bockelmann, G. Abstreiter, M Walther, G. Bohm, G. Trankle and G. Weimann, Phys. Rev. Lett 69, 3216 (1992)
17. J.Cibert, P.M.Petroff, G.J.Dolan, S.J.Pearton, A C.Gossard and J.H English, Appl.Phys.Lett. 49, 1275 (1986)
18. J. Cibert, P M. Petroff, G.J. Dolan, S J Pearton, A C Gossard and J H English Superlatt. and Microstruct 3, 35 (1987)
19. Y. Hirayama, S Tarucha, Y Suzuki and H Okamoto, Phys Rev B37, 2774 (1988)
20. C. Vieu, M. Schneider, D Mailly, R. Planel, H. Launois, J Y Marzin and B.Descouts, J. Appl. Phys. 70, 1444 (1991)
21. H. Leier, A Forchal, G Hörcher, J Hommel, S Bayer, H Rothfritz, G Weimann and W. Schlapp, J. Appl. Phys 67, 1805 (1990)
22. K. Kash, J.M. Worlock, M.D Sturge, P Grabbe, J P. Harbison, A Scherer and P S D Lin, Appl Phys. Lett 53, 782 (1988)
23. K.Kash, B.P Van der Gaag, Derek.D Mahoney, A S Gozdz, L T Florez and J.P Harbrson, Phys Rev Lett. 67, 1326 (1991)
24. D. Gershoni, J.S. Weiner, S N G Chu, G A Baraff, J M Vandenberg, L N. Pfeiffer, K. West, R A. logan and T.Tanbun-Ek, Phys. Rev Lett 65 (1990)
25. P.M Petroff, A.C. Gossard and W. Wiegmann, Appl Phys Lett 45, 620 (1984)
26. M.S Miller, C.E. Prior, H. Weman, L A Samuska, H Kroemer and P M Petroff, J. of Cryst. Growth 111, 323 (1991)
27. M. Tanaka and H. Sakaki, Appl. Phys Lett 54, 1326 (1989)
28. E. Colas, E. Kapon, S Simhony, H M Cox, R Bhat, K Kash and P S Lin, Appl Phys Lett 55, 867 (1989)
29. R Notzel, N N Ledentsov, L. Daweritz and K. Ploog, Phys. Rev B 45, 3507 (1992)
30. E. Kapon, J.P Harbison, C P Yun and N G. Stoffel, Appl Phys Lett. 52, 607 (1988)
31. E Kapon, D.W Hwang, M Walther, R Bhat and N G.Stoffel, Surf.Sci. 267, 593 (1992)
32. S. Tsukamoto, Y. Nagamune, M. Nishioka and Y. Arakawa, J. Appl. Phys. 71, 533 (1992)
33. H Asai, S. Yamada and T Fukui, Appl Phys Lett. 51, 1518 (1987)
34. Y Nakamune, S. Tsukamoto, M. Nishioka and Y. Arakawa, Proceedings of the international Conference on Solid States Devices and Materials 1991 (Yokohama, Japan) (1991)
35. U.Bockelmann and G Bastard, Phys. Rev B 42, 8947 (1990)
36. H Benisty, C.M Sotomayor-Torrès and C.Weisbuch, Phys.Rev B 44,10945 (1991)
37. A. Izrael, unpublished, patent pending
38. L. Birotheau, A. Izrael, J-Y Marzin, R Azoulay, V. Thierry Mieg and F R. Ladan, Appl. Phys. Lett 3023 (1992)
39. M Notomi, M Nakao and T Tamamura, Appl Phys. Lett 62, 2350 (1993)
40. U Bockelmann and G Bastard, Europhys Lett 16, 601 (1991)
41. J-M Gerard and B. Sermage, unpublished
42. U Bockelmann and T. Egeler, Phys. Rev B 46, 15574 (1992).
43. U Bockelmann and G Bastard, Europhys Lett 15, 215 (1991)

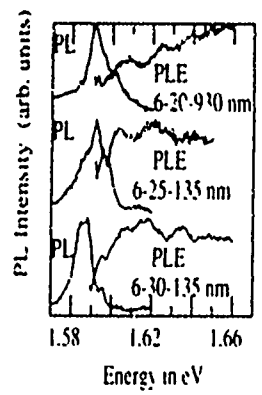

Fig 10: 10 K PLE spectra of single wires, whose characteristics are indicated in the figure (The first figure is the quantum well width, the second Lx and the third Ly)

ThB2

Radiative Recombination in Pseudomorphic InGaAs/GaAs Quantum Wires Grown on Nonplanar Substrates

M Grundmann[1,2] V Turck[2] J Christen[2] F Kapon[1] D M Hwang[1] C Caneau[1] R Bhat[1] D Bimberg[2]

[1] *Bellcore 331 Newman Springs Road Red Bank NJ 07701 USA*
[2] *Institut für Festkörperphysik Technische Universität Berlin Hardenbergstr 36 D 10623 Berlin Germany*

Abstract

The concept of fabricating quantum wires (QWRs) by growing quantum wells (QWL) over non planar substrates is extended to the pseudomorphic system InGaAs/GaAs. The InGaAs QWR is grown as the active region in a laser structure between graded $Al_yGa_{1-y}As$ (y=0 2 0 7) cladding layers on a V grooved GaAs substrate The different spectral components of the luminescence stemming from the AlGaAs barriers, the top quantum well on the ridge in between the grooves (L_x≈7nm which is about half the critical thickness), the sidewalls and the InGaAs wire itself can be unambiguously attributed to the respective regions using spatially resolved cathodoluminescence (CL) The wire emits at T=5K with a peak wavelength of λ=795nm (1 2985eV) with a full width at half maximum of 11meV From time resolved experiments (over all time resolution ≈350ps) we find a recombination time constant of 110 ps This value compares well with earlier findings for InGaAs quantum wells of similar thickness and shows that the recombination is dominated by radiative processes

Introduction

The improvement of properties of novel semiconductive electronic and photonic devices using charge carriers of reduced dimensionality is commonly expected However the nano-technological realization of such structures has to fulfill stringent requirements [1] such as small feature size with reproducible dimensions small lateral size fluctuations and for photonic devices lack of nonradiative interface defects With respect to these requirements the concept of fabricating quantum wires (QWRs) with dimensions in the nm regime by growing quantum wells on non planar substrates has been successfully implemented in the $Al_xGa_{1-x}As/GaAs$ system [2] Due to the in situ formation of the confining interfaces in the V groove during OMVPE (Organometallic Vapor Phase Epitaxy) these structures exhibit high luminescence efficiency and long carrier lifetime Lasers fabricated with this material exhibit sub-mA threshold currents at room temperature[3]

The incorporation of strain into the active region of the QWR laser is expected to improve the laser performance due to the modification of the band structure as in the case of conventional QWL structures [4] With biaxial compressive strain the light hole states are shifted from the bandedge and thus their thermal population is reduced yielding higher optical gain and a preference for TE polarization [4] The lower effective mass of the heavy holes also leads to a larger splitting of the heavy hole one dimensional (1D) subbands InGaAs/GaAs QWR lasers grown by OMVPE on sub µm pitch gratings have been studied and operated up to room temperature [6] Recently InGaAs/GaAs QWR lasers grown by molecular beam epitaxy (MBE) have also been demonstrated and operated at room temperature with record low threshold currents as low as 200 µA [7] Other authors reported on MBE growth of InGaAs/GaAs QWI s on patterned GaAs substrates although the luminescence from the wires was not identified unambiguously in that case [8]

In this paper we report about the fabrication and characterization of InyGa1-yAs/GaAs pseudomorphic quantum wires with emission at 795nm Cathodoluminescence images (CLI) directly visualize the origin of different peaks in the laterally averaged spectrum The wire luminescence exhibits a long recombination time constant of 1ns Time delayed CL spectra show thermalization of carriers into a second recombination channel with a much longer time constant which is attributed to an extrinsic process

Experimental

As a substrate we used a (100) water n GaAs with 1 5µm pitch wet chemically etched V grooves oriented in the [01T] Following the growth of an AlGaAs/GaAs superlattice buffer the QWR is formed in the bottom of the V grooves by growing a 7nm $In_{0.20}Ga_{0.80}As$ quantum well within a Graded Index Separate Confinement Heterostructure (GRINSCH) laser structure The cladding layers are made of undoped $Al_yGa_{1-y}As$ with linearly varying concentration between y=0 2 to y=0 2 The lower part of the structure is doped with Si the upper one with Zn and the InGaAs active layer and graded regions are undoped Fig 1 shows the schematic layer sequence The structure was grown by atmospheric pressure OMVPE at 150°C

The luminescence from this structure was analysed with spectrally, spatially and time resolved cathodoluminescence [9] As detector we used a Si avalanche photodiode with a sensitivity range up to λ≤1 1µm By using beam blanking we accomplished pulsed excitation with arbitrary pulse length (1 4ns) and repetition rate up to 100MHz The total time resolution of 25ps achieved with a fast photomultiplier was limited to 350ps by the speed of the Si diode [10]

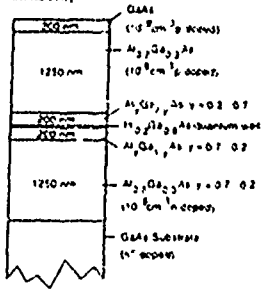

Fig 1 Schematic sample structure

Fig 2 TEM image of bottom of V-groove (marker indicates 50nm)

Results and Discussion

The cross sectional TEM (Transmission Electron Microscopy) image of the bottom of one V-groove (see Fig 2) shows the crescent-shaped InGaAs QWR in the center The InGaAs QWL layer grown on the side walls exhibit quasi periodic thickness modulation with a pitch of approx. 60nm, possibly due to strain accumulation which results in three dimensional growth similar periodic structures were reported also by Gratziouli et al [11]. The thickness of the QWR in the center is 22nm the lateral geometrical width 73nm. The critical thickness for a QWL of x=0 20 is L_x≈15nm, following the energy balance model of Matthews and Blakeslee [12] which has been confirmed by experimental results [13] Our QWI s are well below L_x whereas part of the QWR has a thickness above the critical thickness However in TEM we could not find any defects due to the lattice mismatch The strain energy stored in such a narrow QWR may not exceed the energy required to generate the misfit dislocation even though the thickest part is 50% thicker than L_x calculated for a planar structure The electric field in the undoped GRINSCH and QWR region is about 4 10^5V/cm A field of this magnitude is estimated to have a minor effect of a few meV shift in the energy levels [14]

The low temperature (T=5K) laterally averaged spectrum of the cross sectional view (see Fig 3) consists of several peaks attributed to different regions of the structure as visualized by monochromatic CL images (s Fig 4) The $Al_yGa_{1-y}As$ GRINSCH emits at wavelengths 790 800nm (see Fig 4a) at 820nm the GaAs substrate dominates the spectrum (see Fig 4b) The broad peak at 810nm consists of the emission from the sidewall QWL at the high energy side (s Fig 4c at 800nm) and the top QWL emitting on the lower energy side (see Fig 4d at 925nm) The distinct peak with a FWHM of 11meV at 795nm stems from the quantum wire (see Fig 4e)

The transient luminescence properties of the QWR were evaluated by using a reduced scan area of about 1µm² around the wire center (see inset in Fig 5) The luminescence pulse of the QWR measured under pulsed excitation with 30ps pulses and 1 6MHz repetition rate is shown in Fig 5 The transient has an initial time constant of 1ns over the first 1 5 decades This time constant is longer than 100ps measured for AlGaAs/GaAs QWRs [15] most probably due to the lateral size of the wire Its luminescence from the top QWL measured with reduced scan area on the top of the ridges) has an initial time constant of 1 1ns a value similar to what has been reported before for pseudomorphic InGaAs/GaAs quantum wells [10] The transient of the QWR has a tail with a much larger decay time constant of about 10ns

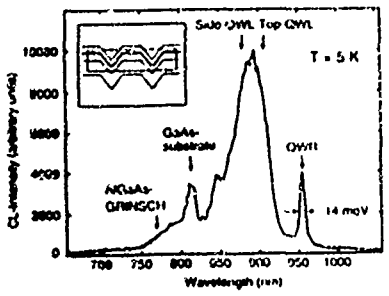

Fig 3 Laterally averaged CL spectrum

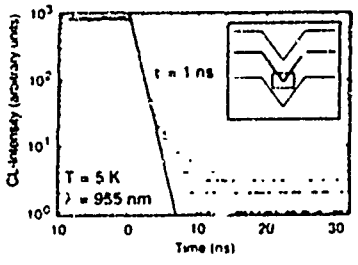

Fig 4 Transient of QWR luminescence

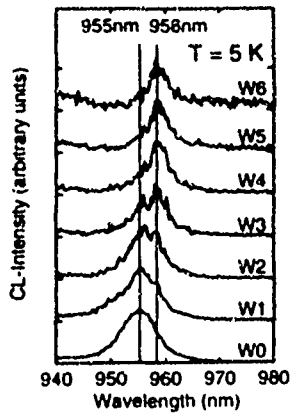

Time delayed (TD) spectra allow the identification of the corresponding recombination channel We have set seven time windows W0=-16 0ns, W1=0 1 6ns W2=1 6 3 2ns, W3=3 2 5 8ns W4=5 8 14 9ns W5=14 9-59 1ns W6=59 1-130 9ns in the transient of Fig 5

W0 is set at the end of the excitation pulse where the sample has reached quasi equilibrium, whereas W1-W6 are set within the luminescence decay The TD spectra are shown in Fig 6 After the decay of the QWR luminescence at 955nm within the first nanoseconds a peak at 958nm evolves which is present even after long delay times > 100ns We attribute this peak to an extrinsic process The small energy difference to the intrinsic peak indicates an impurity bound exciton A similar process is seen in TD spectra of the top QWL Additionally pairband emission is found for long delay time >70ns [16]

Fig 6 Time delayed spectra of QWR time windows W0-W6 are given in the text

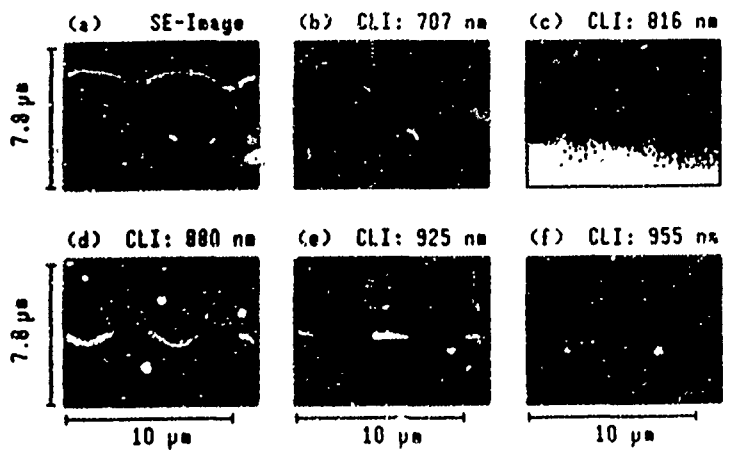

Fig 5 Secondary electron image of cross section and monochromatic CLIs at different wavelengths

Conclusion

In0.2Ga0.8As/GaAs quantum wires with high optical quality have been fabricated on V-grooved GaAs substrate The wires emit at T=5K at 955nm with a FWHM of 14meV Cathodoluminescence experiments performed on single wires yield a recombination time constant of the intrinsic excitonic component of 1ns In time delayed spectra an extrinsic process shows up below the bandgap with orders of magnitude slower decay rates

References

[1] E Kapon M Walther J Christen M Grundmann C Caneau D M Hwang L Colas R Bhat G H Song, D Bimberg Superlatt Microstruct 12 391 (1992)

[2] E Kapon D M Hwang R Bhat Phys Rev Lett 63 430 (1989)

[3] S Simhony E Kapon L Colas D M Hwang N G Stoffel P Worland Appl Phys Lett 59 225 (1989)

[4] J P O Reilly, Semicond Sci Technol 4 121 (1989)

[5] D Ahn T-K Yoo Appl Phys Lett 60 548 (1992)

[6] M Walther E Kapon C Caneau D M Hwang L M Schiavone Appl Phys Lett 62, 2170 (1993)

[7] S Tiwari G D Pettit K R Milkove R J Davis J M Woodall F Legoues Proc Int Conf Electr Dev Mat p859 (1992)

[8] R P Mirin J B Tang H Wenisch M Leonard T Yasuda J E Bowers E L Hu J Vac Sci Technol A 10 697 (1992)

[9] J Christen M Grundmann D Bimberg J Vac Sci and Technol B 9 2358 (1991)

[10] M Grundmann J Christen D Bimberg Superlatt and Microstr 9 65 (1991)
M Grundmann D Bimbere A Fischer Colbrie J N Miller Phys Rev B 41 10120 (1990)

[11] P Gorzinski Y Zou J S Osinski P D Dapkus J Crystal Growth 107 383 (1991)

[12] J W Matthews A E Blakeslee J Crystal Growth 27 (1974) 118

[13] M Grundmann U Lienert J Christen D Bimberg A Fischer Colbrie J S Miller J Vac Sci Technol B8 751 (1990)

[14] G Bastard E E Mendez L L Chang L Esaki Phys Rev B 28 3241 (1983)

[15] J Christen E Kapon M Grundmann D M Hwang M Joschko D Bimberg phys stat sol (b) 173 307 (1992) and
J Christen M Grundmann E Kapon L Colas D M Hwang D Bimberg Appl Phys Lett 61 67 (1992)

[16] M Grundmann V Tuerck E Kapon J Christen D M Hwang C Caneau R Bhat D Bimberg Appl Phys Lett (1993) unpublished

ThB3

Optical characterization of InGaAs/GaAs quantum dots defined by lateral top barrier modulation

A. Schmidt, A. Forchel, F. Faller, * I. Itskevich, A. Vasiliev

Technische Physik, Universität Würzburg, Am Hubland, D-97074 Würzburg, Germany
* on leave from Russian Academy of Science, Tchernogolovka, Russia

Abstract. We have produced effectively buried quantum well dots on the basis of InGaAs/GaAs single quantum wells using high resolution electron beam lithography and selective wet etching of the top barrier. The lateral barriers are realized by the difference in quantization energy in quantum wells with a semiconductor top barrier compared to quantum wells with a vacuum potential barrier. Dot structures with widths down to 20 nm have been generated. We observe that the structures maintain high luminescence efficiencies down to the smallest sizes. We also observe a blueshift of up to 12 meV for 30 nm quantum dots which are nonselectively etched. Furthermore we have studied the dependence of the quantization energies for well material with different Indium content.

1. Introduction

Recently, low dimensional semiconductor structures have been the subject of intense studies. Crystal growth techniques like molecular beam epitaxy (MBE) and metalorganic vapor phase epitaxy (MOVPE) allow to realize quantum well layers exhibiting quantum confinement in one direction. For structures exhibiting quantum confinement in two or even three dimensions like quantum wires or dots, several different approaches are used [1-8]. High resolution electron beam lithography and transfer of the pattern to the semiconductor quantum well substrate e.g. by dry or wet etching, impurity induced disordering processes or selective epitaxy on patterned or high-index substrates are the most commonly used patterning methods. Surface effects and defects due to e.g. etching processes limit the quantum efficiency in luminescence experiments.

In the presently used approach the selective removal of the top barrier layer in a wet etching step generates virtually no open sidewalls and leads to a laterally confining potential for electrons and holes in the unetched regions under the remaining cap layer [5]. By the selective wet etch step the GaAs/InGaAs conduction and valence band discontinuities (on the order of 1 eV) are replaced by the substantially higher energy difference of the InGaAs-vacuum transition (electron affinity of about 5 eV). If the quantum wells are appropriately thin, the barrier height controls the quantization energy of electron and hole states. In the etched region the increase of the confining energy pushes the wavefunctions of electrons and holes to the GaAs barrier layer below the quantum well. This leads to higher energies for the ground state in GaAs/InGaAs/vacuum quantum wells than in GaAs/InGaAs/GaAs quantum wells. The difference in the quantization energies leads to a lateral confinement potential and localizes the carriers beneath the GaAs cap layer in the InGaAs material.

The unetched InGaAs quantum well layer acts both as active quantum dot and barrier material. Virtually no defects are induced by the selective wet chemical etching process to the active regions. By this method effectively buried structures are generated with low surface recombination velocities.

2. Lithography and pattern transfer

The starting material for the patterning process were InGaAs/GaAs single quantum wells with different In content grown by molecular beam epitaxy on undoped < 100 > oriented GaAs substrates. The samples were spin coated with a positive tone high resolution electron beam resist. For the exposure a conventional scanning electron microscope equipped with an external pattern generator and scan controller was used. Quadratic dot grids of field size of 100µm × with an area filling factor of 1/16 and dot sizes down to 25 nm in diameter were exposed in the resist. After developing the exposed structures a 15 nm Al mask was thermally evaporated. By a lift off process in an ultrasonic bath Al dot etch masks were obtained. The Al pattern then was transferred to the quantum well using H_2O_2:NH_4OH buffered to pH 7 [9].

With this process we generate dots with structure sizes down to 20 nm in diameter with a dot pitch of 90 nm. The dot sizes were measured in an field emission scanning electron microscope. Fig. 1 shows the 45 nm features obtained after mask removal with 1% NaOH solution.

Fig. 1: 45 nm dot structures prepared by electron beam lithography and wet chemical etching after mask removal.

3. Experimental results and discussion

The samples were characterised by photoluminescence in an He immersion cryostat at 2 K An Argon laser was used as excitation source Spectral resolution was accomplished with a 250 mm focal length grating spectrometer with a 1200 line grating. For detection an optical multichannel analyzer with S25 photocathode was used

Fig 2 shows several luminescence spectra of quantum dots of different dot sizes All spectra are normalized to their maximum The filling factor corrected quantum efficiency was greater than ten percent for all dot sizes down to 20 nm From this we conclude that we have produced almost defect free quantum structures We see no abrupt drop in luminescence yield

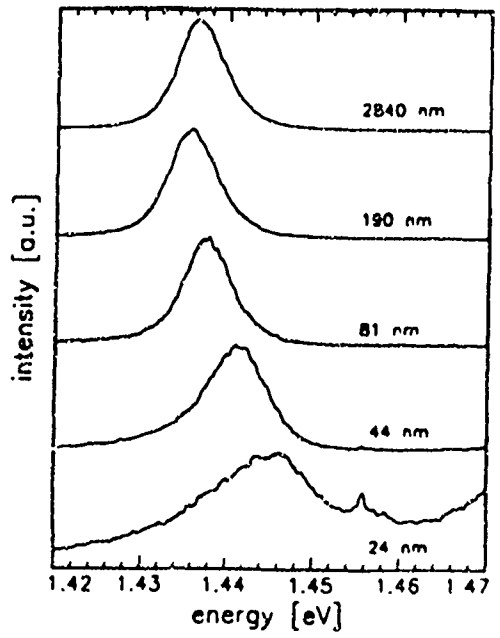

Fig 2 Photoluminescence spectra for several different dot sizes in a selectively etched quantum well structure Spectra are normalized to their maximum The excitation density was approximately 30 W cm²

as proposed by other authors for quantum dots[9] The normalized intensity even exceeds unity by almost a factor of eight We attribute this to effective carrier capture from the GaAs barrier beneath the InGaAs quantum well. The maximum capture efficiency is reached at dot distances of ≥600 nm This implies an ambipolar diffusion length on the order of 800 nm

For dot structures below 100 nm in size we observe in fig 2 an energetic blue shift This value is approximately two times the value of the onset of the blueshift in barrier modulated wires Simultaneously with the blueshift we observe that for small structures an increase of the linewidth up to a value of 14 meV for the smallest structures From the dependence of the blueshift on the dot size we can estimate the size fluctuations within a dot array to be on the order of ± 5 nm

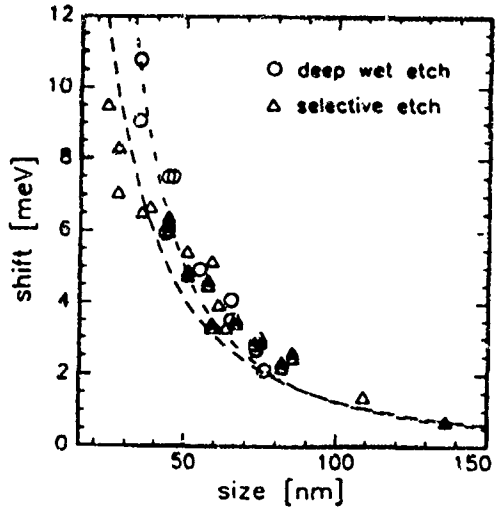

Fig 3 Energy shift plotted versus dot size for the sample of Fig. 2 (open triangles) and for a sample where the QW material was also etched laterally (open circles) The lines show results of simple model calculations for quantum dots with 25 meV (solid line) and 5 eV (dashed line) lateral potential

In fig 3 the blueshift of the luminescence maximum for two differently processed samples is plotted versus the dot diameter The triangles denote data taken from a sample from which the top barrier layer has been selectively removed The circles represent data of quantum dots which have been prepared by deep wet chemical etching In this case the lateral confinement energy is directly given by the electron work function The maximum energy shift is 10 meV

for barrier modulated dots with 23 nm diameter This is about half the value of the laterally confining potennal in the barrier modulated structures (25 meV)[10] The dashed line in the graph represents a model calculation for the shift of the lowest subband edge in a quantum dot The model does not account for the increasing excitonic correlation in a quantum dot structure This may influence the observed energy shift especially for dots below 40 nm in diameter as shown by Le Goff and Stébé [11]

The dash-dotted line in Fig 3 shows a model calculation for the deep etched dots based on a lateral vacuum barrier of five eV due to the semiconductor work function For dot sizes above 40 nm the lateral quantization induced energy shift of the luminescence in barrier modulated and deep etched structures is similar As expected, due to the larger confinement potential, we observed slightly stronger quantization effects in small deep etched structures than in barrier modulated dots of comparable size Fig 3 indicates that barrier modulated structures are well suited to observe lateral quantization effects in dots with diameters of about 20 nm

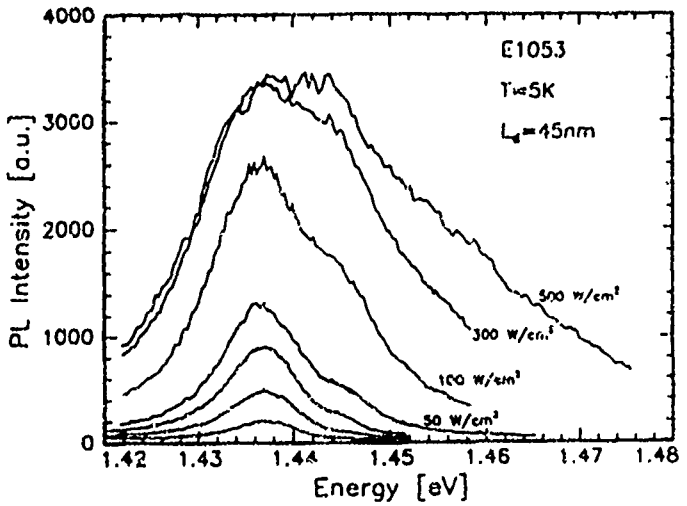

Fig 4: Low temperature (5K) cw-high excitation spectra of 45 nm dots taken under Ar laser excitation Two peaks separated by 8 meV can be clearly seen

Furthermore, we have investigated the behavior of small structures under cw-high excitation The result of this measurements is depicted in Fig 4 for a dot structure with an average dot diameter of 45 nm It can be seen that the lowest subband peak increases with increasing laser excitation and finally saturates at an intensity of 500 W/cm². Already at relatively low excitation powers a second luminescence band in the spectrum. It is located about 8 meV to higher energy from the first peak. Our model predicts a subband separation of about 10 meV which would suggest tha we see the second lateral subband luminescence. We may attribute the early onset of the second level luminescence signal peak to the slowed relaxation by reduced phonon scattering rates in quantum dots.

4. Conclusion

We have fabricated high-quality low damage quantum dots by selective wet chemical etching in the InGaAs/GaAs material system. The quantum structures exhibit high normalized luminescence ratios. Furthermore small structures show a strong energetic blueshift correlated with the structure size. From the relationship between blueshift and dotsize the broadening of luminescence linewidths can be explained by an inhomogeneous size distribution in the range of ±7 nm. High excitation measurements reveal the existence of a second lateral subband in smaller dot structures. The early onset of luminescence from the lateral subband is possibly due to reduced phonon scattering in quantum dots.

5. Acknowledgements

We thank M. Emmerling for the assistance in preparing the quantum well substrate for lithography. The financial support of this work by the Deutsche Forschungsgemeinschaft is gratefully acknowledged.

References

1 B.E. Maile, A Forchel, R. Germann, J. Straka, L. Korte, and C.Thanner, Appl Phys. Lett. 57, 807 (1990).

2 A. Israel, B. Sermage, J.Y. Marzin, A. Ougazzaden, R. Azoulay, J. Etrillard, V Thierry-Mieg, and L. Henry, Appl. Phys. Lett. 56, 850, (1990).

3 M. Notomi, M Naganuma, T. Nishida, T. Tamamura, H. Iwamura, S. Najima, and M. Okamoto, Appl. Phys. Lett. 58, 720 (1991).

4 Y. Nagamune, Y Arakawa, S. Tsukamoto, M. Nishioka, S. Sasaki, and N. Miura, Phys. Rev. Lett. 69, 2936 (1992)

5 Ch. Gréus, L. Butov, F. Dahminger, A Forchel, P.A Knipp, T.L. Reinecke, Phys Rev B 47, 7626 (1993)

6 H. Leier A. Forchel, B.E. Maile, G. Mayer, J. Hommel, G. Weimann, and W. Schlapp, Appl. Phys. Lett. 56, 48 (1990)

7 J.A. Lebens, C S. Tsai, K.J. Vahala, and T.F. Kuech Appl. Phys. Lett 56. 2642 (1990)

8 R. Nötzel, , N.N. Lebentsov, L. Däweritz, K Ploog, and M. Hohenstein, Phys. Rev. B 45, 3507 (1992)

9 H. Benisty, C M. Sotomayor-Torres, and C. Weisbuch, Phys. Rev. B 44, 10945 (1991)

10 A. Schmidt, A. Forchel, J. Straka, I. Gyuro, P Speser, and E Zielinski, J Vac Sci. Technol. B 10, 2896, (1992)

11 S. Le Goff and B. Stébé, Phys. Rev. B 47, 1383 (1993)

ThB4

Electron-Phonon Scattering Rates in Quantum Wires

P. A. Knipp
Department of Physics and Computer Science
Christopher Newport University
Newport News, VA 23606-2998
and
T. L. Reinecke
Naval Research Laboratory
Washington, D.C 20375

Electron-phonon scattering rates for quantum wires of arbitrary shapes are calculated rigorously within the dielectric continuum approach for the phonons. An integral equation approach is developed for the interface phonons, and the contribution to the scattering rates from the confined phonon modes are expressed in terms of the interface modes by a simple relation. Detailed results are given for the intrasubband and intersubband transition rates as functions of the electron energy and of the wire width for wires of rectangular cross section. The relative importance of the interface and confined phonons is discussed as a function of wire size. A quantitative appraisal is given of scattering rates obtained using simple separable approximations for the phonons.

Quantum wire systems composed of a wire of one compound semiconductor material within another have attracted considerable interest recently both because of their use in potential device applications as well as for the opportunity of studying novel physical phenomena in these quasi-one-dimensional systems. Electron-phonon interactions and scattering rates have been of particular interest in these systems. They control such phenomena as the cooling of excited carriers on the picosecond time scale and room temperature optical properties. They have been a focus of attention in studying the effects of phonon confinement on the optical and transport properties of semiconductor nanostructures.

To date, however, a rigorous, quantitative treatment of electron-phonon scattering rates for wires of the general shapes of interest experimentally has not been given. The principal difficulty in treating electron-phonon interactions in quantum wires is that the equations of motion and boundary conditions for the phonons do not separate in these geometries. Recent work has been reported for the simple case of a cylindrical quantum wire for which the treatments separate into one dimensional problems [1]. *Ad hoc* approximations [2] have been used to treat the phonons for rectangular cross sections. The results given here show that such approximations lead to significant errors in the scattering rates.

The scattering rate of an electron from a subband α with wavevector k_i to a subband β with wavevector k_f accompanied by the emission of a phonon of wavevector $q = k_i - k_f$ is given by

$$\Gamma_{\alpha k_i \to \beta k_f} = \frac{2e^2\pi}{\hbar}\sum_{\nu}\{N(\omega_{\nu}(\psi))+1\}\left|\int d^2r\,\Psi_{\alpha}(\vec{r})\Psi^{*}_{\beta}(\vec{r})\Phi_{\nu\psi}(\vec{r})\right|^2 \times \delta(E_{\beta k_f} - E_{\alpha k_i} + \hbar\omega_{\nu\psi}) \qquad (1)$$

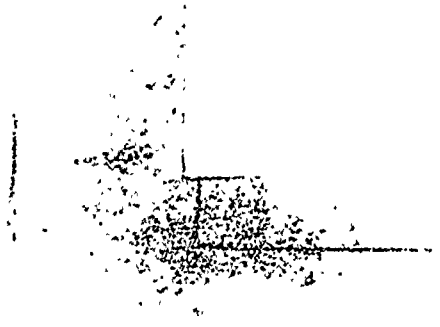

The rate for electron scattering due to phonon absorption is similar. Ψ_α are the electron wavefunctions, $\Phi_{\nu\psi}$ are the phonon potentials, and N is the Bose function. E_i and $\hbar\omega_{\nu\psi}$ are the electron and phonon energies respectively. The index ν indicates the optical phonon modes of the system including both "confined" or "interface" phonons. The confined modes are localized either in the wire region or in the exterior region.

The intrasubband and intersubband electron scattering rates calculated here due to phonon emission at room temperature are shown as functions of energy in Fig. 1 for a 100 A x 200 A wire of GaAs in AlAs. In these calculations a small imaginary part (= 0.25%) has been included in the phonon frequencies to represent their finite lifetimes due primarily to anharmonicity. The sharp features arise from the divergent density of electronic states at the bottom of the ground subband. For this wire width the energy difference between the first and second subbands is 34.2 meV. For smaller wires the intersubband spacing is larger than the phonon energies, and thus for them these sharp features are not present in the intersubband rates. The electron scattering rates due to phonon emission are shown as functions of wire width in Fig. 2. Results are also given here for models of bulk GaAs phonons and bulk AlAs phonons. For large wires the confined modes in the GaAs wires tend to dominate the scattering, and the intrasubband scattering rate approaches that for bulk GaAs phonons. For small wire sizes the AlAs-like interface modes make a large contribution, and the intrasubband scattering rate approaches that for bulk AlAs phonons.

We have used the macroscopic dielectric continuum approach [3] to treat the optical phonons of the quantum wires. This approach gives analytic results for the electron-phonon interactions, and it makes possible the treatment of wires of general size and shape. For quantum well systems this approach gives scattering rates in good agreement with those obtained using lattice dynamics results for the phonons [4]. The principal challenge in treating the phonons of quantum wires within macroscopic approaches is that the problem is not in general separable. For wires with general cross sections we have developed a treatment [5] in which Laplace's equation and the boundary conditions for the interface modes are transformed into an integral equation

$$\oint_c ds'\,\lambda(s,s')\sigma(s') = \lambda(\omega)\sigma(s) \qquad (2)$$

where c is the contour around the wire perimeter, and σ is the surface charge density associated with the interface phonon. $\lambda(\omega) = \{\epsilon_1(\omega) + \epsilon_2(\omega)\}/\{\epsilon_1(\omega) - \epsilon_2(\omega)\}$ where $\epsilon_1(\omega)$ and $\epsilon_2(\omega)$ are the dielectric functions for the wire and the exterior region respectively. Equation (2) can be solved by straightforward matrix diagonalization.

We have used this approach to study the interface phonons of wires with arbitrary cross sectional shapes. In this work one of the most interesting features that has arisen is that the interface phonons tend to be localized in regions of large curvature of the wire interfaces with a degree of localization that increases strongly with the degree of sharpness of the corners. An example of such a corner localized phonon is shown in Fig. 3. In order to study the effects on the electron scattering rates of this corner localization of the interface phonons we have calculated the scattering rates for rectangular wires with varying corner curvatures characterized by a/R where a is the radius of curvature of the corner, and R is the wire width. We find that the scattering rates vary by less than 1 % for variations in a/R between 0.2 and 10^{-4}. Thus although the interface modes are sensitive to the sharpness of the wire corners, the total scattering rates, which involve a sum over the modes, are not.

In the present work we have calculated the electron states within the effective mass approximation with finite potential barriers using the usual masses and potential offset [6]. The wavefunctions were calculated using a technique that we developed earlier [7] which involves discretizing Schrödinger's equation in the plane perpendicular to the wire and iteratively solving the resulting matrix equation. We have investigated the effects on the

scattering rates of using simple separable approximations for the electron wavefunctions and have found the effects of these approximations to be small for the wire widths studied here (on the order of a few per cent for wire widths of 100 Å).

In recent years there has been some controversy concerning the boundary conditions to be used in calculating the confined phonons in semiconductor nanostructures [8]. For quantum wells it has been found that scattering rates calculated using the simple dielectric continuum model agree quite well with those based on lattice dynamics for the phonons [4]. In the dielectric continuum model [3] the electrostatic potential of the confined phonons goes to zero at the interfaces, and the corresponding optic phonon displacements have a maximum there. On the other hand, lattice dynamics calculations indicate that the optic phonon displacements as well as the electrostatic potentials goes to zero at the interfaces. Recently we have investigated [9] the effects on the electron-phonon scattering rates of these boundary conditions on the confined phonons in a variety of nanostructures We have found that provided the confined phonons satisfy Maxwell's equations at the interfaces the additional constraint that the phonon displacement go to zero there has no effect on the scattering rates. We ascribe this result to the fact that the contribution of the confined phonons to the scattering rates involves a sum over a complete set of degenerate phonon states In general the contribution of the confined phonons to physically measurable quantities such as scattering rates is given by the structure factor

$$\rho(\vec{r},\vec{r}') = \sum_i \frac{\Phi_i(\vec{r})\Phi_i^*(\vec{r}')}{\int d^3r'' \left|\vec{\nabla}\Phi_i(\vec{r}'')\right|^2} \qquad (3)$$

where the sum over i is over the confined phonon states. Results for $\rho(\vec{r},\vec{r}')$ for a cylindrical wire are shown in Fig 4 From these results and those for other nanostructures given in Ref [9] we see that $\rho(\vec{r},\vec{r}')$ given by these two sets of boundary conditions are identical.

As a part of this study of the confined phonon modes we have derived a useful expression for the contribution of the confined phonon modes to the scattering rates in nanostructures. It is given by

$$\rho(\vec{r},\vec{r}') = \frac{1}{4\pi|\vec{r}''-\vec{r}|} - \sum_\lambda \frac{\Phi_{s,\lambda}(\vec{r})\Phi_{s,\lambda}^*(\vec{r}')}{\int d^3r'' \left|\vec{\nabla}\Phi_{s,\lambda}(\vec{r}'')\right|^2} \qquad (4)$$

for $\vec{r}$ and $\vec{r}'$ within the nanostructure Here $\Phi_{s,\lambda}$ are the potentials associated with the interface modes. Thus the contribution of the confined modes can be written in terms of the interface phonon potentials. This form is convenient for systems of low symmetry, and it has been used in the present calculations to obtain the contributions of the "confined" phonons in the AlAs material outside of the wires These modes are extended throughout the exterior region, and it is difficult to form a complete set of them as required for the scattering rate by other means

In order to discuss the electron scattering rates it is useful to look at their dependence on wavevector transfer This is given by the quantity

$$f_\nu(q) = \frac{\left|\int d^2r \Psi_\alpha(\vec{r})\Psi_\beta^*(\vec{r})\Phi_{\nu,q}(\vec{r})\right|^2}{\int d^2r \left|\nabla\Phi_{\nu,q}(\vec{r})\right|^2} \qquad (5)$$

$f_\nu(q)$ describes the contribution to the scattering rate of the ν^{th} phonon mode (interface or confined) evaluated at the wavevector q involved in the scattering process. The sums of the contributions $f_\nu(q)$ from all interface modes and from all confined modes for intrasubband and intersubband processes are shown in Fig. 5. For both interface and confined modes these quantities are decreasing functions of qR. The interface modes make the larger contribution to the scattering rates at small qR, and thus they dominate for small wire size. In addition, when the subband splitting is comparable to the phonon energies small wavevectors are dominant in the intersubband scattering processes This accounts for the broad maximum in the intersubband rate for $R = 100Å$ in Fig. 2b It is interesting to note that for small q the sum of the interface modes $f_IF(q)$ diverges as q^{-1} for quantum wells and only as -ln(qR) for quantum wires. Thus we expect that the approach of the intrasubband rate to that for bulk AlAs should be faster for quantum wells than for quantum wires of comparable size. This appears to be the case in comparing our results in Fig. 2 with those in Ref. 4 .

A widely used approximation [2] for the interface modes of rectangular quantum wires involves a separable approximation for the phonon potentials In Fig 5 we compare the sum of the interface modes $f_IF(q)$ from the present complete calculations with corresponding results obtained using this separable approximation The contribution of the interface phonons in this approximation goes to a constant for small qR rather than diverging This qualitative error is a result of its poor representation of the totally symmetric interface mode As a result this approximation gives poor results for the intrasubband scattering rates, especially for small wire sizes. In addition, this separable approximation gives no contribution at all from the interface modes to the intersubband scattering rate between the first excited electronic subband and the ground subband as a result of the absence of interface modes which are symmetric along one direction and asymmetric along the other.

This work was supported in part by contracts of the U S. Office of Naval Research (PAK and TLR).

FIGURES

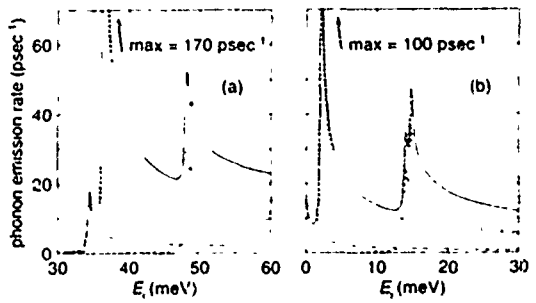

Fig 1 (a) Intrasubband and (b) intersubband electron scattering rates due to phonon emission as functions of the initial electron energy for quantum wires of size 100 Å x 200

A. The intersubband splitting for this wire size is 34 2 meV. Energies are measured from the respective subband bottoms, i.e. from the bottom of the lowest subband for the intrasubband rate and from the bottom of the next higher subband for the intersubband rate. The total scattering rates are given by the solid lines, the contributions of the confined phonons by the dotted lines, the contributions of the AlAs-like interface phonons by the short dashed lines, and the contributions of the GaAs-like interface phonons by the long dashed lines.

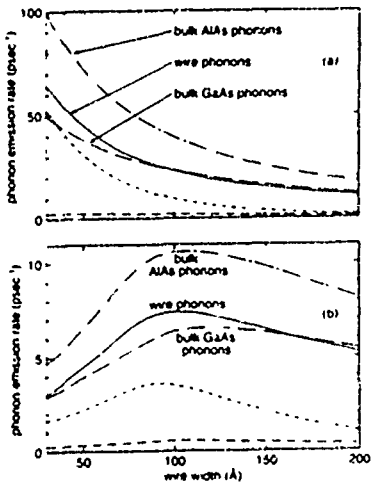

Fig 2 (a) Intrasubband and (b) intersubband electron scattering rates due to phonon emission as function of wire width R R is the smaller of the two sides of the cross sections of rectangular wires having aspect ratios of 2 1 The initial electron energy has been chosen to be 60 meV above the respective subband bottoms. The total rate is given by the solid line, and the rates from models of bulk GaAs and bulk AlAs phonons are given by the dot-dashed and long dashed-short dashed lines respectively The contributions from the confined phonons, the AlAs-like interface phonons and the GaAs-like interface phonons are given by the dotted, the short dashed, and the long dashed lines respectively

Fig 3 Interface phonon potential for a mode with wavevector kR = 2 and azimuthal quantum number m = 0 for a rectangular quantum wire with aspect ratio 1 2 and corner curvature a = R/20

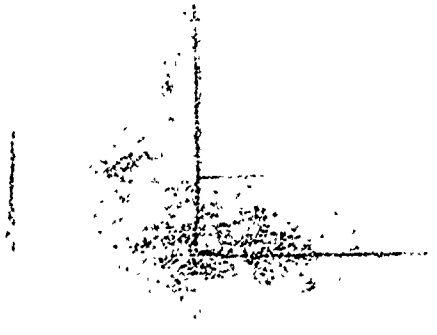

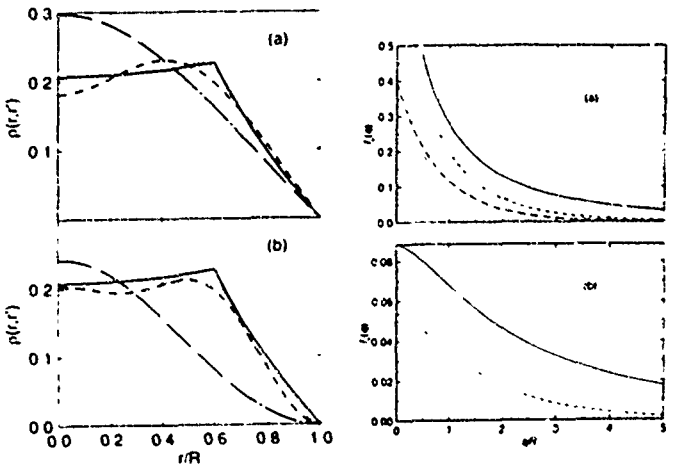

Fig 4 The contribution to the structure factor defined in Eq (3) for a cylindrical quantum wire from confined phonon modes which have azimuthal quantum number m = 0 and wavevector kR = 1 0 Here R is the cylinder radius, r is the radial distance, and r' = 0.6R. (a) is for confined phonons from the dielectric continuum model, and (b) is for phonons whose displacement also is required to go to zero at the interfaces. The dot-dashed, dashed, dotted and solid lines indicate truncation of the sum in Eq (3) after 1, 3, 10 and ∞ terms respectively

Fig 5 $f_\nu(q)$ from Eq (5) for (a) intrasubband and (b) intersubband scattering as functions of qR where R is the wire width The total contribution from the confined modes and total from the interface phonons are given by dotted line and the short dashed line respectively, and total from all modes is given by the solid line The long-dashed line in (a) gives the contribution of the interface phonons in the separable approximation of Ref. [2 1.

REFERENCES

1 P E Selbmann and R Enderlein, Superlattices and Microstructures 12, 219 (1993)
2 K W Kim *et al* , J Appl Physics 70, 319 (1991), R Mickevicius *et al* , Superlattices and Microstructures 11, 277 (1992)
3 See, e g M V Klein, IEEE J Quantum Electron QE-22, 1760 (1986)
4 H Rucker, E Molinari, and P Lugli, Phys Rev B 44, 3463 (1991), Phys Rev B 45, 6747 (1992)

5. P. A. Knipp and T. L. Reinecke, Phys B 45, 9091 (1992).
6. The effective masses for electrons in GaAs and AlAs were taken to be 0.0665 and 0.15 respectively, and the conduction band offset was 873 meV
7. Ch. Gréus, L. Butov, F. Daminger, A. Forchel, P. A. Knipp and T. L. Reinecke, Phys. Rev. B 47, 7626 (1993)
8. S. Rudin and T. L. Reinecke, Phys. Rev. B 41, 7713 (1990), Phys. Rev. B 43, 9298 (1991).
9. P. A. Knipp and T. L. Reinecke, Phys. Rev. B (to be published)

ThB5

Relaxation and radiative decay of excitons in GaAs quantum dots

U. Bockelmann, K. Brunner and G. Abstreiter
Walter Schottky Institut, Technische Universität München
Am Coulombwall, D-8574b Garching, Germany

Radiative and non-radiative exciton states of quantum dots with parabolic lateral potentials are calculated in an effective-mass approximation. Energy spectrum, radiative recombination rates and LA phonon scattering rates of the different excitons are discussed in their dependence on the lateral confinement potential. For sufficiently strong lateral potentials the relaxation of excitons by LA phonon emission becomes so weak that several excitonic levels should be observable in a photoluminescence experiment even at low excitation intensity. The theoretical results are compared to microscopic photoluminescence data collected from a series of single GaAs quantum dots fabricated by laser induced local interdiffusion.

In quantum dots or quasi-zero-dimensional (0D) systems the charge carriers are confined in all three spatial directions and therefore the energy spectrum consists of atomic-like, discrete levels. In principle, artifical 0D structures based on direct gap semiconductors (e.g. the GaAs/GaAlAs system) could be studied in great detail by interband optical spectroscopy, i. e. by photoluminescence (PL) and photoluminescence excitation (PLE) spectroscopy. The interband spectra should reflect the details of the confining potentials as well as exciton and many-body effects. Information on the exciton relaxation dynamics could be deduced from the intensity ratios of the different PL peaks and also from a comparison of PL and PLE spectra [1]. In practice, samples prepared for optical studies often contain a large number of quantum dots supposed to be equal. Differences in composition and size between the individual structures however lead to important inhomogeneous line broadening which usually covers the details of the interband spectra. This problem can be circumvented by local spectroscopy of a single quantum dot. This way, distinct narrow lines have been observed in microscopic PL and PLE spectroscopy on a series of single quantum dots fabricated by focused laser beam induced interdiffusion of GaAs/GaAlAs quantum wells [2].

In this contribution, we present theoretical results on energy states, relaxation and radiative decay of excitons in quantum dots based on GaAs/GaAlAs quantum wells. The theoretical description is well suited for a comparison with the quantum dot samples fabricated by laser induced interdiffusion. We present PL spectra measured at low excitation power from a series of dots of different lateral size and compare them to the theoretical results.

For quantum dots fabricated from quantum wells the confinement induced by the lateral potential is usually weak compared to the confinement along the quantum well growth axis z. We therefore build the near band gap exciton states of the quantum dot on the electron and heavy-hole ground subbands of the underlying quantum well (envelope functions $\chi_e(z)$ and $\chi_h(z)$, respectively), neglecting heavy-hole light-hole mixing and excited subbands. The envelope function of the quantum dot excitons are of the form.

$$\Psi_{ex}(\mathbf{r}_e,\mathbf{r}_h) = \phi(x_e,y_e,x_h,y_h)\,\chi_e(z_e)\,\chi_h(z_h) \qquad (1)$$

The functions ϕ depending on the lateral electron and hole coordinates are the eigensolutions of the Hamiltonian

$$H = H_0 + H_{eh}$$

$$H_0 = \sum_{\nu=e,h} \frac{-\hbar^2}{2m_\nu}\left(\frac{\partial^2}{\partial x_\nu^2} + \frac{\partial^2}{\partial y_\nu^2}\right) + \frac{1}{2} m_\nu \omega_{0\nu}^2 \left(x_\nu^2 + y_\nu^2\right)$$

$$H_{eh} = -\iint dz_e\, dz_h \left|\chi_e(z_e)\right|^2 \left|\chi_h(z_h)\right|^2 \frac{e^2}{\varepsilon_i |r_e - r_h|}$$

We describe the lateral confinement by rotational-symmetric, parabolic potentials with different angular frequency for electrons and holes (ω_e and ω_h). The Hamiltonian H is diagonalized numerically by expanding it on the set of analytical eigenfunctions of H_0. H_0 describes two-dimensional harmonic oscillators independent for the electrons and holes. The solutions, originally derived by Fock [3], are parametrized by the radial quantum numbers n_e, n_h (0,1,2,...) and the angular momentum quantum numbers l_e, l_h (0,1,2,. .). The total angular momentum $j=l_e+l_h$ is a good quantum number of the Hamiltonian H because of the rotational symmetry of the lateral potential. The expansion on a basis of independent electron hole states has been used in earlier theoretical studies of radiative excitons in quantum dots [4-6]. In an alternative approach, H is written as a function of the center-off-mass (CM) coordinate $R=(m_e r_e + m_h r_h)/(m_e+m_h)$ and the relative coordinate $r=r_e-r_h$ of the exciton. The expansion on a set of functions depending separately on R and r exhibits a faster convergency for weak lateral confinement but has the important disadvantage that the r-dependent basis functions are not analytical [5,6].

Excitons with a non-zero value of j are non-radiative. From the wavefunction of the j=0 excitons we determine the radiative lifetimes τ_0 in the dipol approximation:

$$\tau_0^{-1} \propto \left|\int d\mathbf{r} \psi_{ex}(\mathbf{r},\mathbf{r})\right|^2 \qquad (3)$$

Energies and radiative lifetimes of quantum dot excitons are presented in fig. 1. We consider dots fabricated from a 30Å wide $GaAs/Ga_{0.7}Al_{0.3}As$ quantum well with a constant ratio ω_h/ω_e to allow for a detailed comparison with our experimental results. Only radiative excitons are included in the figure where the length of the lines is chosen to be proportional to the rate of radiative recombination. At small $\hbar\omega_e$, the spectrum is dominated by a series of equidistant lines. In this limit, the CM coordinate R and the relative coordinate r of the exciton are only weakly coupled. The equidistant lines originate from the quantization of the CM coordinate by the parabolic potential. The additional, weakly radiative excitons appearing at higher energies involve excited states of the relative motion. With increasing $\hbar\omega_e$, the energy levels shift to higher values and the CM and the relative motion become increasingly coupled. The radiative lifetime of excitons originating from the ground state (excited states) of the relative coordinate increase (decrease) with increasing lateral confinement. The Coulomb attraction strongly influences the energy spectrum and radiative lifetimes of the quantum dot. The binding energy of the ground state exciton grows from 7.9 meV to 15.4 meV with $\hbar\omega_e$ increasing from 1 to 10meV which is in no case small compared to the lateral confinement energies. When the electron hole Coulomb interaction is neglected, the radiative lifetime of the ground state of the $\hbar\omega_e$=6meV dot is 0.3 ns, three times longer than the excitonic lifetime given in fig.1.

The relation between the electron and hole confinement parameters used in fig.1, is suggested by a simple model calculation of the process of laser induced thermal interdiffusion

[2]. Fig 2 demonstrates that the lowest exciton energies change only slightly when the ratio ω_e/ω_h is varied. All exciton states (radiative and non-radiative ones) are plotted for fixed $\omega_e+\omega_h$. The total angular momentum j of the exciton is indicated by the length of the plotted line. The exciton spectrum becomes increasingly dense with increasing energy separation from the ground-state.

Let us now discuss the relaxation properties of the exciton. At low temperature and carrier density, emission of longitudinal acoustic (LA) phonons represent the dominant relaxation mechanism of excited states of energy below the optical phonon branches. It has been shown theoretically, that in quantum dots the electron LA phonon scattering rates decrease by several orders of magnitude when the separation of the discrete energy levels increases above a threshold value [7]. How do the corresponding results look like for excitons? The rate of a transition from an initial exciton state i to a final state f accompanied by emission of a phonon at zero temperature is given by the Fermi golden rule

$$\tau_{i\to f}^{-1} = \frac{2\pi}{\hbar} \sum_{\mathbf{q}} \left|\left\langle \Psi_{ex}^{f} \middle| W \middle| \Psi_{ex}^{i} \right\rangle\right|^2 \delta\left(E_{ex}^{f} - E_{ex}^{i} + \hbar\omega_q\right) \qquad (4)$$

The sum extends over the wavevector q of the phonon of energy $\hbar\omega_q$. We consider bulk GaAs LA phonons neglecting confinement effects on the phonon spectrum. An isotropic dispersion relation $\omega_q = c_s q$ is assumed, with c_s=3700m/s. To derive the exciton-phonon interaction potential W we first determine the strain tensor associated with the phonon. The interaction potential is then given by the sum of the strain induced shift of the electron and hole part of the exciton. The latter is obtained from the diagonal part of the Γ_8 strain Hamiltonian, derived by Pikus and Bir [8]. For heavy holes W takes the form

$$W \propto q^{1/2}\left(De^{iqr_z} + \left[\frac{l+m}{2}\frac{\left(q_x^2+q_y^2\right)}{q^2} + m\frac{q_z^2}{q^2}\right]e^{iqr_z}\right) \qquad (5)$$

where D is the conduction band deformation potential and l, m are valence band deformation potentials.

Fig.3 shows the relaxation rate τ_r^{-1} of the first excited radiative exciton in comparison to its radiative decay rate τ_0^{-1}. The quantity τ_r^{-1} is defined as the sum over the LA phonon scattering rates to all exciton states below the initial state at zero temperature. We assume that the final states are unoccupied. Scattering between any pair of exciton states is possible. This also means that non-radiative excitons are important for the relaxation dynamics of radiative states. The contribution of a given transition depends strongly on the energy separation of the involved levels which is equal to the phonon energy (energy conservation expressed by the delta function in eq.4). For small q the exciton phonon matrix element increases with q due to the prefactor $q^{1/2}$ of eq.5. For q above about $2\pi/l_z$, the matrix element decreases strongly with increasing q (increasing energy). Roughly speaking, when the phonon wavelength becomes small compared to the smallest dimension of the quantum dot (usually the well width L_z) the exciton-phonon coupling becomes weak, in a similar way as in the case of the electron-phonon interaction [7].

The relaxation rate of the first excited j=0 state, plotted in fig1, is dominated by scattering into the j=±1 ground state. Typically, PL spectra of one, two and three dimensional semiconductor structures show only one peak corresponding to the exciton ground state. This is because the relaxation of excited states is more efficient than their radiative decay. From

fig.3 it appears clearly, that in 0D systems the relaxation rate of excited excitons can be comparable or even smaller than the rate of radiative recombination. From a detailed rate equation analysis based on calculated rates of exciton relaxation and radiative recombination follows that it should be possible to observe strong PL signals from excited quantum dot states even for very low excitation intensity [9].

For the experimental studies a series of single quantum dots of different lateral size has been fabricated by laser-induced thermal interdiffusion of a 30Å wide $GaAs/Ga_{0.65}Al_{0.35}As$ single quantum well [2]. A schematic cross section of the dot structures is given in the inset of fig.4. The lateral potential is defined by drawing a square frame of size w with a focused Ar^+ laser beam on the sample surface. Afterwards an area of 6μm x 6μm around the dot is interdiffused by scanning the beam continuously. This procedure gives rise to a lateral modulation of the band-gap as shown schematically in the lower part of the inset. The strongly nonlinear temperature dependence of the interdiffusion allows to realize steep potential barriers for electrons and holes. PL and PLE spectroscopy have been performed with a spatial resolution of about 1.5μm at liquid helium temperature. Only one quantum dot is measured at a time and consequently there should be no inhomogeneous broadening of the experimental spectra. Details of sample preparation and experimental setup are given in ref.2.

In fig.4 we present PL spectra of three quantum dots of different lateral size w. Excitation was performed with a HeNe laser of low power density. The PL linewidths have been found to increase with intensity [2]. The energy shift of the lowest PL peak with increasing structure size w is a combined effect of lateral confinement and alloying of the dot center. The effective size of the lateral confinement is given by the interdiffusion profile and not just by the geometrical size w. Decreasing w from large values, the laser induced barriers move closer together which leads to an increasing lateral quantization. Maximum confinement is obtained when the barriers are about to meet at the dot center. We expect this to be realized in the w=450nm dot where a maximum line splitting of about 10meV is observed. Further decreasing w, the increasing Al content near to the center of the dot leads to a strong blue shift of the PL ground state but the lateral barrier hight decreases. For w->0, we approach the case of a homogeneously alloyed 2D layer without lateral confinement. Near the dot center, a simple model of the local quantum well interdiffusion gives nearly isotropic and parabolic lateral potentials with a similar curvature for electrons and heavy holes. This means $m_e\omega_e^2=m_h\omega_h^2$ or equivalently $\omega_h=\omega_e(m_e/m_h)^{1/2}$, the relation used above in calculating figures 1 and 3. The PL spectra of the 400nm and 500nm dots are dominated by the lowest energy peak but display clear structures of almost equidistant spacing at higher photon energies. The position of the experimental lines compare quite well with fig.1 if we consider $\hbar\omega_e$ = 5meV (2meV) for w=400nm (500nm). For the 450nm dot the interdiffusion model gives $\hbar\omega_e$=8meV. The 10meV separation between the lowest two peaks agrees with fig.1 but the threefold splitting of the excited state is not born out by the calculation. Fig.2 shows that the fine structure cannot be explained either by varying the ratio ω_h/ω_e. However, the first excited radiative (j=0) state is almost degenerate with the j=±2 ground states (fig.2). A deviation of the lateral potential from the rotational symmetry could mix the three states i.e. the non-radiative excitons would gain oscillator strength. Such a deviation can be due to charged defects introduced by the laser processing in the surrounding area or simply by not perfectly constant interdiffusion conditions during writing the square frame which defines the dot. PLE spectra of the 450nm dot as shown for example in reference 2 display for detection at the lowest luminescence peak small peaks with roughly an equidistant energy separation of about 2meV between the luminescence ground state and first excited state. These weak structures cannot be understood from the calculated exciton energies, even if we assume a much weaker confinement for the holes than for the electrons (see fig2). The main features of the experimental PL lines (fig.4), especially the fact that the excited states are most prominant

in the dot with the largest level splitting are in agreement with a strong decrease of the exciton relaxation rate with increasing lateral confinement.

In conclusion, relaxation and radiative recombination of excitons in quantum dots have been studied theoretically. The calculations show that the radiative lifetimes of one part of the exciton states increase with increasing lateral confinement (in particular the lowest states) but there exist also exciton states that exhibit the opposite dependence. In quantum dots of sufficiently strong lateral confinement the relaxation of excited excitons by emission of LA phonons can be less efficient than their radiative decay. This suggest that excited excitons can be observed in PL, which is in agreement with recent microscopic PL experiments on single quantum dots. The variation of position and intensity of the PL peaks with lateral structure size qualitatively confirms the theoretical results.

This work has been supported in part by the "Deutsche Forschunggemeinschaft (SFB 348)" the "Bundesministerium für Forschung und Technologie (DFE Verbundprogramm TK363/2)" and by a "PROCOPE" contract.

[1] G. Bastard, "Wave Mechanics Applied to Semiconductor Heterostructures (Les Editions de Physique, les Ulis, 1988)
[2] K. Brunner, U. Bockelmann, G.Abstreiter, M. Walther, G. Böhm, G. Tränkle and G. Weimann, Phys. Rev. Lett. 69, 3216 (1992)
[3] V. Fock, Z. Phys. 47, 446 (1928)
[4] G. W. Bryant, Phys. Rev. B37, 8763 (1988)
[5] V. Halonen, T. Chakraborty and P. Pietiläinen, Phys. Rev. B45, 5980 (1992)
[6] W. Que, Phys. Rev B45, 11036 (1992)
[7] U. Bockelmann and G. Bastard, Phys. Rev. B 42, 8947 (1990)
[8] G. E. Pikus and G. L. Bir, Fiz. Tverd. Tela 1, 1502 (1959) [Sov. Phys. Solid State 1, 1502 (1960)]
[9] U. Bockelmann, submitted for publication

Fig.1 Energy and inverse radiative lifetime τ_0^{-1} of the radiative excitons as a function of the confinement parameter $\hbar\omega_e$. The value of τ_0^{-1} is given by the length of the lines, in comparison to the double-arrow on the right. Zero-energy corresponds to the bandgap of the underlying quantum well, namely the sum of the bandgap of bulk GaAs and the confinement energies associated with $\chi_e(z)$ and $\chi_h(z)$.

Fig.2
Exciton energy spectra for a ratio ω_e/ω_h varying from 0.5 to 5 but fixed sum $\omega_e+\omega_h$=10meV of the electron and hole lateral confinement potentials. The length of the lines indicate the quantum number j of the total angular momentum.

Fig.3
Relaxation rate τ_r^{-1} (solid line) and radiative recombination rate τ_0^{-1} (dashed line) of the first excited radiative exciton as a function of lateral confinement.

Fig.4
PL spectra of single dot structures for three lateral sizes w. Laser excitation was at 1.96eV with a power of 1μW (125nW for w=450nm) focused to a spot of 1.5μm diameter. The dot structure fabricated by focused laser beam interdiffusion of a single quantum well is presented schematically in the inset.

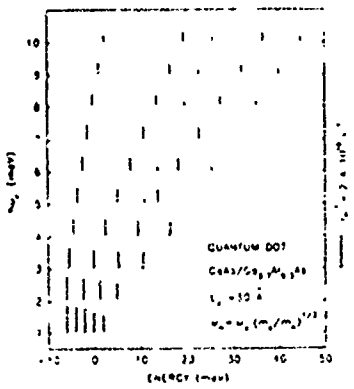

Fig. 1

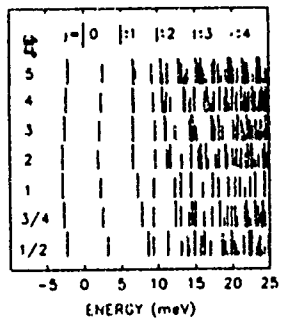

Fig. 2

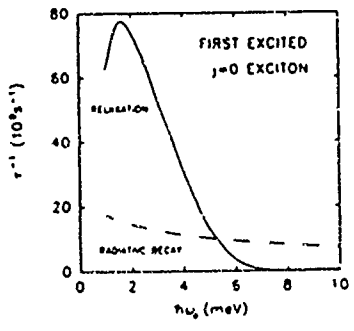

Fig. 3

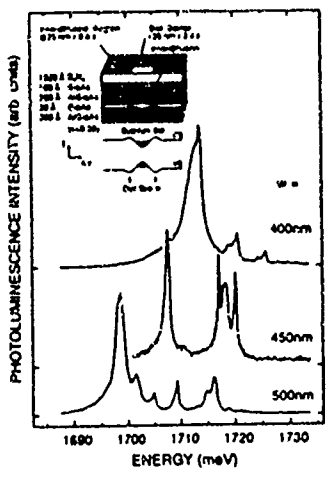

Fig. 4

ThP1

DETERMINATION OF BAND-EDGE OFFSET BY WEAK FIELD HALL MEASUREMENT ON MBE PbSe/PbEuSe MULTI-QUANTUM WELL STRUCTURES ON KCL

Z. Shi, A. Lambrecht and M. Tacke

Fraunhofer Institute of Physical Measurement Techniqes (IPM) Heidenhofstrasse 8, W-7800 Freiburg, Federal Republic of Germany

Weak field Hall effect measurements between 34 and 300K were applied to three PbSe/PbEuSe (Eg[PbEuSe]=440meV at 300K) MQW samples on KCL. By calculating the quasi-Fermi energy levels the temperature dependent band-edge offsets were determined. The valence band offset ΔEv was found to be 65meV at 34K with a positive temperature coefficient of 0.68 meV/K. ThusΔEv=43+0.68T (meV) is suggested.

IV-VI lead salt semiconductors are widely used for lasers and detectors in the wavelength of 3-32μm[1,2]. Heterojunctions (HJs) and quantum well structures are used in the devices to provide selective control over carrier transport by means of energy band discontinuity. Former investigations of IV-VI band-edge offset were mainly on PbSnTe/PbTe HJs by two groups[3,4] with different results, obtaining a type I alignment as well as type I'. By Hall measurement of multiquantum well (MQW) samples with different barrier thickness, a type I aligment was suggested by Shi et al[5]. Later, Pb-SrEuSeTe and PbSe/PbEuSe were also investigated by several methods. Photoluminescence (PL) gave an alternative result of ΔEc:ΔEg=0.9 or 0.1[6] for PbTe/PbEuSeTe and ΔEc:ΔEv=9:8 was used to interpret the PL result of PbSe/PbEuSe[7]. Problems of PL were also sumarised in [7]. By comparing the interband transition energies deduced from the infrared spectroscopy and the calculated energy shifts Ishida et al[8] and Yuan et al [9] found that the band offsets in the PbTe/$Pb_{1-x}Eu_xTe$ system (x<5%) is quite symmetric. Electron-Beam-Induced current measurements were also applied for the determination of band-edge offset of PbTe/PbEuSeTe and PbSe/PbEuSe heterostructure[10]. Such junction methods of IV-VI materials usually suffer from the following problems: (1) R_0A is low, about three magnitudes lower than that of HgCdTe; (2) There are probably relatively large number of interface states; (3) possible deep traps with high concentrations which are up to now not well investigated, (4) Fermi-energy levels are usually obtained on insulating (111) BaF_2 while the junction measurments are on (100) PbTe or PbSe substrats. This may cause estimated errors of several tens of meV.

In this paper a similar method as [5] but with quantitive analysis was applied to a series of p-P PbSe/PbEuSe MQW structures. The valence band, and thus the conduction band discontinuities between 34-180K were determined. Problems 2 to 4 of electrical analysis are expected to be relevant within the frame of this method.

The static dielectric constant in PbSe and $Pb_{1-x}Eu_xSe$ (with low x) is high(200) and a typical screening length is several thousands angstrom. In good approximation one can neglect the band bending effect in the MQW structure when both the well layer and the barrier are narrow enough. The calculated quasi-Fermi levels on both sides should then be

$F_1 = E_F + V_{b1}$ and $F_2 = E_F + V_{b2}$, where E_F is the equilibrium Fermi level measured from the respective band edge , V_{b1} is the built in PbSe potential of the interface and V_{b2} PbEuSe potential. Thus the energy band-edge offset can be obtained by adding quasi-Fermi levels F_1 and F_2. By doing so the following advantages are expected: (1) The carrier concentration is very sensitive to the quasi-Fermi level so that the quasi-Fermi level can be determined quite correctly even when there are certain errors in the concentration; (2) Since all deep traps are depleted within the PbEuSe band gap and fully occupied within PbSe band gap they will not affect the result; (3) Interface states add almost the same amount to the quasi-Fermi levels of both sides and compensate themself when calculating the band discontinuity so that the influence of the interface states can be neglected.

A series of p-P PbSe/PbEuSe MQW were thus grown for Hall measurements by molecular beam epitaxy (MBE) with alternating Eu growth chamber under Se rich condition. The background vaccum during growth is 3*10-8 Torr. The substrates are cleaved KCL (100) and the substrate temperature is 360 C. The growing rate is 30nm/min. Table 1 gives the related parameters of the samples.

sample number	buffer layer (PbEuSe)	PbSe-PbEuSe numbers	period	top layer (PbEuSe)	total thickness
1513-1	150nm	20-20nm	68	150nm	3.02μm
1514-3	150nm	20-40nm	48	150nm	3.18μm
1515-3	150nm	20-60nm	35	150nm	3.10μm

Table 1 Growth parameters of the PbSe/PbEuSe MQW structure.

The aim of the buffer and the top layer is to avoid any interface and surface potential effects on the Hall data. The use of KCL substrates has the advantage that the subbands from four valleys are equivalent for the (100) surface. The PbEuSe layers have a minimum thickness of 20nm to ensure a quantum well condition under the assumption that holes are confined to the PbSe layer and a maximum thickness of 60nm to make the neglect of band bending still a good approximation. The Hall measurements were performed by Van der Pauw method with gold wires soldered with Indium to edges of the specimen. The energy band gap of PbEuSe at room temperature was measured to be 440meV by infrared transmission spectroscopy. For optimium comparability of the above three samples, they were grown one after another under the same growth condition and substrate pieces were cut from the same block of KCL.

For two layer structures the Hall coefficient can be written as [11]:

$$R_H = (d_1 n_1 \mu_1^2 + d_2 n_2 \mu_2^2)(d_1 + d_2)/e(d_1 n_1 \mu_1 + d_2 n_2 \mu_2)^2 \qquad (1)$$

Measurements on single PbSe and PbEuSe (E_g=440meV at 100K) epitaxial layers showed that the mobility of PbSe on KCL is 10 to 20 times larger than that of PbEuSe between 180K and 34K. The hole concentration in the PbSe layers of a MQW structure is expected to be at least 10 times larger than that in the PbEuSe layers because of the carrier injection from PbEuSe barrier layers. For all samples in this experiments the PbEuSe layer thicknesses d is at most a factor of 3.1 larger than that of PbSe layer, hence we can approximate equation (1) by neglecting the terms for PbEuSe layers. Fig.1 shows the hole concentration ($1/eR_H$) of the samples. In this paper only the data between 34K and 180K

were used because above 180K the difference of mobility is not big enough for the one layer model approximation. For a QW structure the relation between E_F and the carrier concentration n is given as

$$n(E_F) = n_d \sum_{i=1}^{\infty} \int \rho_i(E) f(E) dE \qquad (2)$$

where

$$f(E_i) = \frac{1}{(1 + \exp[\frac{(E_i - E_f)}{KT}])}$$

$$\rho_i(E) = \frac{m_d}{\pi \hbar^2} \theta(E - E_i)$$

and[12]

$$E_i = \frac{1}{2}(-E_g + \sqrt{E_g^2 + \frac{2\hbar^2}{m_z}(\frac{i\pi}{d})^2 E_g}) \qquad (3)$$

$\rho_i(E)$ is the density-of-states, Ei is the subband energy level and E_F is measured from the band edge of the bulk crystal[13]; $m_d = m_t^*(2K+1)/3$, $m_z = m_t^*3K/(2K+1)$, m_t is the transverse effective mass at the band edge, Eg is the energy gap in bulk crystal, n_d=4 is the number of valleys, d is the width of well layer and i is the quantum number of subband. The temperature dependence of the PbSe-related parameters were obtained from[14]. The quasi-Fermi energy level and the subband energy level were thus calculated according to equation (2) and (3) under the assumption that equation (2) is also suitable for the quasi-Fermi level. The non-parabolicity of the two dimension density-of-states was not considered in this paper. The results were shown in Fig.2, where E_F^a, E_F^b and E_F^c represent the quasi-Fermi energy levels in the PbSe well layers of samples 1513-1, 1514-3 and 1515-3, respectively.

Equation (3) is based on the assumption that the height of the well potential is sufficiently larger than the Fermi level and that the two band model is applicable in each quantum well. It is noteworth that a small change of Ei turned out to change the calculated ΔE_V only slightly, so that the change of ΔE_V can be neglected. Therefore, we would not be in the dilemma that we should first know ΔE_V for the evaluation of Ei.

The increase of the hole concentration in the PbSe well layers of samples 1514-3 and 1515-3 compared with 1513-1 is due to the increased thickness of the PbEuSe barrier layer. Holes of the barrier layer will flow into the well layer as long as the increase of barrier width is within $2x_d$, where x_d is the depletion length. In the following expression for convenience the subscript 1 and 2 will be used to represent PbSe and PbEuSe respectively, the superscript a, b, and c stand for the 1513-1, 1514-3 and 1515-3 samples respectively, d represent the thickness of a single well or barrier layer and S the area, and p_0 represent the hole concentration in a PbEuSe single bulk epitaxy layer. With these definitions, the increase of hole concentrations in 1514-3 to 1513-1 can be expresed as following. a PbEuSe layer with a hole concentration of p_0 and a volume of $d_2^b * S$ injects its holes into the well layer so that its hole concentration become p_2^b and increases p_1^a to p_1^b. Because of the conservation of hole numbers, we can write with this reasoning:

$$S*(d_2^b - d_2^a)(p_0 - p_2^b) = S*d_1^b(p_1^b - p_1^a) + S*d_2^a(p_2^b - p_2^a) \qquad (4)$$

For the comparision of 1515-3 and 1513-1, we can get in the same way:

$$S^a(\delta_2{}^c \cdot d_2{}^a)(p_0 \cdot p_2{}^c) = S^a d_1{}^c(p_1{}^c \cdot p_1{}^a) + S^c d_2{}^a(p_2{}^c \cdot p_2{}^a) \qquad (5)$$

The left hand side gives the difference in the number of holes transferred from the barries of samples a and b into the wells. It neglects deep levels and assumes that the barrier doping is equivalent to the bulk concentration p_0. The first term on right hand gives the resulting increase of the well carrier concentration. It is corrected by the second term which takes into account the different barrier concentrations of samples a and b that result from the *different barrier thickness*.
By combining equation (4) and (5) one can get an equation without p_0.
The advantage of using another QW sample instead of a bulk sample as a reference sample is:
(1) If there are deep energy levels in PbEuSe layer, one can not use the p_0 data measured from a single PbEuSe epitaxial layer for equation (4) and (5). The reason is that the deep levels contribute differently to p_0 due to the difference of Fermi levels in PbEuSe barrier layers and a single epitaxial layer.
(2) Since deep levels are all depleted in PbEuSe barrier layer and the difference of Fermi levels in two different MQW samples are small, one can consider a consistent p_0 in all QW samples in this experiment. Thus the effect of deep levels can be neglected.
With the definition at thermal equibrium:

$$E_{F1}{}^b \cdot E_{F1}{}^a = E_{F2}{}^b \cdot E_{F2}{}^a = \delta E_{F1} \qquad (6)$$

$$E_{F1}{}^c \cdot E_{F1}{}^a = E_{F2}{}^c \cdot E_{F2}{}^a = \delta E_{F2} \qquad (7)$$

and the hole concentration for bulk narrow gap semiconductor is given by[15]:

$$p = \frac{2}{\sqrt{\pi}} N_v G^{\nu}(\eta)$$

where $\eta = EF/kT$ is the reduced Fermi energy and $G^{\nu}(\eta)$ is equal to the generalised Fermi integral $\frac{2}{3}\mathcal{L}_{\frac{3}{2}}^{0}(\eta,\beta)$

so

$$p_2{}^b/p_2{}^a = \exp(\delta E_{F1}/kT) \qquad (9)$$

$$p_2{}^c/p_2{}^a = \exp(\delta E_{F2}/kT) \qquad (10)$$

Since $p_1{}^a$, $p_1{}^b$, $p_1{}^c$, E_{F1} and E_{F2} can be obtained from Fig.2 $p_2{}^a$, $p_2{}^b$, $p_2{}^c$, and thus the quasi-Fermi energy level $E_{F2}{}^a$, $EF_2{}^b$, $E_{F2}{}^c$ can then be derived from the combination of equation (4)-(10) for these calculation. The effective mass of PbEuSe was assumed to increase proportionally to the increase of the energy band gap. The temperature dependence coefficient of the PbEuSe energy gap is assumed to change linearly from that of

PbSe to the Photoluminescence result of [7] and assumed that it can be extended to the situation that Eu composition is slightly larger. By adding the quasi-Fermi energy levels of the PbSe layers and PbEuSe layers of the same sample the valence band-edge offset was obtained and is shown together with the band gap difference in Fig.3.

As seen in Fig.3, the valence band discontinuity increases and thus the conduction band discontinuity decreases almost linearly with the incresing temperature. The temperature dependence coefficient for ΔEv was thus obtained from Fig.3 as 0.68meV/K and for this certain Eu composition $\Delta Ev = 43 + 0.68T$ (meV) is thus suggested. It seems quite possible that PbSe/PbEuSe (Eg=460meV) will change from type I at lower temperature to a staggered structure at 300K. This will influence the QW laser operation at high temperature, which is waiting to be approved.

There are two possible error sources in our measurements. one lies in the fact ,that a minimum of three samples have to be used , hence all three relative sample errors enter. The experiments were performed on two independent sets of three samples with the same results, hence we believe that this error can be neglected. Second, the KCL substrate material has a mismatch of the thermal expansion coefficients as compared to the MQW. Hence, our results may be influenced by resulting strains.
In summary, we evaluated the data of the PbSe/PbEuSe band-edge offset by calculating the quasi-Fermi energy levels of both barrier layer and well layer in a proper designed MQW structure. To accomplish this, Hall measurments were performed on a series of MBE PbSe/PbEuSe MQW structures on KCL. The temperature dependence ΔEv and ΔEc were obtained.

Acknowledgement- The authers acknowledge helpful discussion with their collagues B. Halford, H. Böttner, J. Xu,and K. Steiner. The work was supported in part by an exchange program of the Fraunhofer Geselischaft and the Chinese Academy of Scieaces.

REFERENCES

[1] D.L. Partin, IEEE J. Quantum Electron., 24, 1716(1988)
[2] M.Tacke, Jounal de Physique IV, C7-23 (1991)
[3] M. Kriechbaum, K.E. Amborosch, E.J. Fantner, H. Clemens, and G. Bauer, Physical Rev., B30, 3394(1984)
[4] K. Murase, S. Shimomura, S. Taksoka, A. Ishida, and H. Fujijasu, Supperlattices and Microstructures 1, 177(1985)
[5] Z. Shi, W. Chen, H, Song, H. Yang, Y. Fu, Y. Jin, Chines J. Infrared Millim. Waves, 9(4), 255(1990).
[6] W. Goltsos, J. Nakahara, A.V. Nurmikko, and D.L. Partin, Appl. Phys. Lett., 46, 1173(1985).
[7] M.V. Valeiko, I.I. Zasavitskii, A.V. Matveenko. B.N. Matsonashvili, and Z.A. Rukhadze, Supperlattices and Microstructures, 9(2), 195(1991).
[8] A. Ishida, S.Matsuura, M.Mizuno, and H. Fujiyasu, Appl. Phys. Lett. 51, 478(1987)
[9] S. Yuan, H.Krean, G.Springholz, and G. Bauer, Apll.Phys. Lett. 62, 885(1993)
[10] H. Heinrich, C. Panhuber, A. Eizenbeiss, H. Preier, and Z. Zeit:, Supperlattices and Microstructures, 5(2), 175(1989).
[11] F.F. Sizov and Darchuk, Phys. Stat. Sol. (a), 113, 107(1989).
[12] S. Takakr, T. Okumura and K. Murase, A. Ishida, and H. Fujiyasu, Solid State Communications, 58, 673(1986).
[13] F. Stern and W E. Howard, Phys. Rev., 163, 816(1967).
[14] H. Preier, Appl. Phys., 20, 189(1979).
[15] G. Nimtz and B. Schillicht, Narrow-Gap Lead Salt, Springer Tracts in Modern Physics, Vol.98, P.52, Eds. G. Höhler.

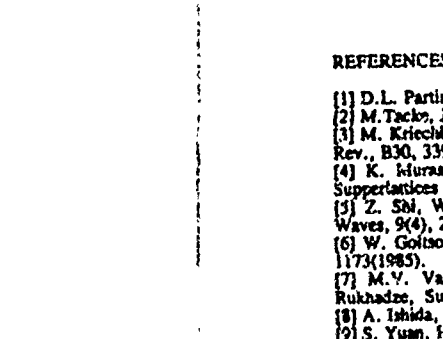

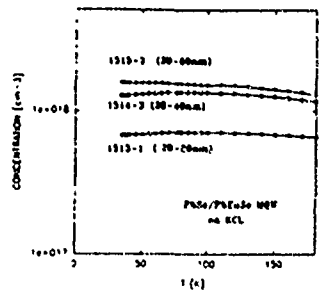

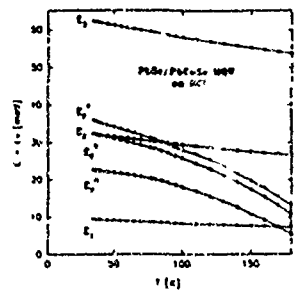

Fig 1 Temperature dependence of the
Fig 1 Temperature dependence of the Hall effect
carrier concentration of MQW structures

Fig 2 Subband energy levels and quasi-Fermi
energy levels in PbSe with layers of
different samples v.s. temperature

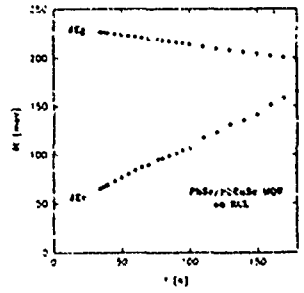

Fig 3 Temperature dependence of valence
band offset and the band gap differ-
ence of $Pb_{0.802}Eu_{0.198}Se$ and PbSe

ThP2

Static and dynamical properties of the bound magnetic polaron in CdTe/Cd$_{1-x}$Mn$_x$Te quantum wells

P BOUDINET and G BASTARD
Laboratoire de Physique de la Matière Condensée
Ecole Normale Supérieure, 24 rue Lhomond, F-75005 PARIS

We study the static and dynamical properties of the bound magnetic polaron in CdTe Cd$_{1-x}$Mn$_x$Te quantum wells
In the case of a heavy hole bound to an acceptor located in the barrier and for some parameters of the heterostructure, the calculations of the stationary states show the existence of a transition of the BMP between a magnetic and a non magnetic state
The relaxation of the BMP is calculated on the basis of a mechanism of spin exchange between the manganese ions involved in the BMP and the other ones which are randomly lined up We show that the BMP displays a two times dynamics It has two stable states of opposite polarisation and reaches one of these states in a short time In a longer time, a complete equilibrium takes place between the two states

The bound magnetic polaron (BMP) has been widely studied in the case of bulk materials and the theoretical calculations are in good agreement with the experimental results [1, 2, 3] However only a few calculations [4, 5, 6] have been carried out in the case of BMP occuring in heterostructures Except [5, 6] there is to our knowledge no work dealing with the dynamical properties of the BMP in quantum wells A model exists for the bulk case [9]
We will firstly present our theoretical results concerning the static properties of an acceptor bound magnetic polaron in a CdTe/Cd$_{1-x}$Mn$_x$Te quantum wells and show that qualitative differences with the bulk case can arise We will subsequently deal with the dynamical properties of the BMP in quantum wells
For the static properties, our model of BMP is the following In a CdTe/Cd$_{1-x}$Mn$_x$Te quantum well an acceptor lies in the barrier at a distance z_1 from the interface A heavy hole of effective mass m^* experiences the potential V created for one part by the quantum well and for another part by the coulombic attraction of the acceptor Let H_0 be its hamiltonian Since there are also the magnetic ions (spin S_i) in the barrier they interact with the hole (spin S) with the exchange hamiltonian

$$H_{ex} = -J\sum_i S_i \, s\,\delta(r - r_i) \qquad (1)$$

S_i denotes the spin of an ion located at r_i H_{ex} is responsible for the polaron effect A given S_i also interacts with its possible nearest neighbors with the antiferromagnetic hamiltonian

$$H_{ant} = \alpha\sum_{i,j} S_i S_j \qquad (2)$$

The summation is restricted to the nearest neighbors When x is strong enough to localise the hole the interaction between S and the S_i's leads to the formation of a BMP The localisation and the binding energy of the hole are determined by the exchange interaction In order to calculate them we have determined variationally, the ground state $H = H_0 + H_{ant} + H_{ex}$
We have assumed that the S_i are classical vectors The ideal procedure to treat H would be the following Firstly, given a configuration $(S_1, S_2, \ldots)$ of the S_i's one should determine the eigenstates of energy $E(S_1, S_2, \ldots)$ and eigenfunctions $\Psi_{S_1, S_2, \ldots}(r)$ of $H(S_1, S_2, \ldots)$ Secondly one should calculate the thermodynamically averaged energy $E_p(\beta)$ of the BMP by the Boltzmann formula

$$E_p = \beta^{-1}\{\Sigma_{S_1, \ldots} E(S_1, \ldots) \exp[-\beta E(S_1, \ldots)]\} / [\Sigma_{S_1, \ldots} \exp[-\beta E(S_1, \ldots)]] \qquad (3)$$

where β is the inverse temperature

In the same way one should calculate the localisation of the hole Since the number of configurations of the multiplet $(S_1, S_2, \ldots)$ rises very quickly with the number N of S_i's involved in the BMP, we used rather the following approximate procedure Firstly, given a fixed wave function $\Psi(r)$, we determined the value of $\langle\Psi|H_m|\Psi\rangle$ and the thermodynamically averaged value of $\langle\Psi|H_{ex}|\Psi\rangle$ Secondly, we minimised the sum of both the previous terms with respect to Ψ The minima are identified to $E(\beta)$ We have verified that, at the first order in perturbations, the two procedures are equivalent Differences arises at the second order We used the following form for $\Psi(r)$

$$\Psi(r) = \chi(z)\exp(-r/a) \qquad (4)$$

$\chi(z)$ is the wave function which corresponds to the ground state of the square well potential (growth axis Z), and $\exp(-r/a)$ is the wave function of the hole localised on the acceptor in a bulk problem The effective Bohr radius a has been our variational parameter We took Hanle in account in the following way Since it leads to the destabilisation of the BMP we assumed that for a given S_i if $|\Psi(r_i)|^2$ is greater than a certain Ψ_c^2, then the S_i participates to the BMP without antiferromagnetic interaction If this is not the case this S_i is not involved in the BMP Ψ_c is estimated following reference [1] We have averaged the positionnal disorder of the S_i's by calculating the sum of the energies related to each occupable site, and multiplying it by the occupation probability, x
When the ground state of the acceptor is deeper than the well, the hole will always be located on the acceptor The result is a polaron effect which is qualitatively the same as in the bulk Cd$_{1-x}$Mn$_x$Te When the depth of the well equals the ground state of the acceptor, qualitative differences arise Fig 1 shows the averaged magnetic energy for two different values of z_1 in the case of x=0.3 and L=86 Å When z_1 is large enough (which corresponds to two clearly separated attractive potentials), there exists a certain critical temperature T_c Below T_c, the hole is located near the acceptor and there is a polaron effect and above T_c, the hole is located in the well with no polaron effect When the acceptor is close to the well there is no such phenomena and the magnetic energy behaves qualitatively like in the bulk case A physical explanation is the following The hole localised near the acceptor interacts with the S_i's and forms a BMP like in the bulk case The energy E_1 of this system depends on T On the contrary the energy E_2 of the system formed by the hole in the square well is almost temperature independent to the extent that the hole wave function is exponentially small in the barrier T_c is qualitatively defined as $E_1(T_c) = E_2$ When $T < T_c$ $E_1 < E_2$ and there is a polaron effect (the hole prefers to be localised near the acceptor) When $T > T_c$, there is no polaron effect since the hole prefers to be localised in the well In chemical terms we have a polarised bond between the well and the acceptor whose polarisation is temperature dependent and driven by exchange interaction
Let us now turn to the dynamical properties of the BMP We retain a slightly different model for our BMP system The potential which localises the hole is assumed to be an interface defect rather than an acceptor This assumption ensures that Ψ is not strongly dependent on the temperature as above We firstly compute and classify the eigenstates of the BMP Secondly, we compute the transition probability between the states of the BMP (which leads to its relaxation) The evolution of the BMP can be solved numerically However we shall present a comparison between the numerical and approximate algebraical results It should be stressed that any relaxation mechanism must be able to transfer spin out of the BMP in order to allow its polarisation to vary We showed [7] that the hamiltonian H which must be used is the sum of the Luttinger hamiltonian of the hole and the exchange term H_{ex} The Luttinger hamiltonian is necessary to introduce a coupling between the heavy and light

hole states, and therefore to allow the hole spin-flip. Otherwise with unmixed $J=3/2$ heavy hole states there would be no possible relaxation. We no longer assumed that the S_i's are classical vectors.

Since we are interested by the heavy hole states, we reduce H into an effective hamiltonian h acting only on the $S_z=\pm 3/2$ states. We further reduce H into a simplified hamiltonian H_{eff} acting in the spin space of the heavy hole:

$$H_{eff} = \begin{pmatrix} B_+ & \sum_i b_i m_{iz} \\ \sum_i b_i m_{iz} & B_- \end{pmatrix} \otimes A \qquad (5)$$

where $b_i=(3/2)|\Psi(r_i)|^2$. The B_+, B_-, A are fixed by the shape of the wave function and the parameters of the Luttinger hamiltonian (for details, see [7]) and the m_{iz} are the eigenvalues of the S_{iz}. Each BMP is characterised by different values of B_+, B_-, A, and the b_i's. Our numerical investigations correspond to the case of $B_+=B_-=B$, and $b_i=b$ for any i. We assumed that this case was the generic case, or in another way that B and b are the averaged values over a large number of BMP's of the B_z's and b_i's. The averaging operation and the determination of the eigenvalues of H_{eff} would then have been interchanged. Let $\Omega=\sum_i m_{iz}$ be the polarisation of the BMP. Ω is proportional to the magnetic energy of the BMP in our model (which is the "box model" of reference[6]). H_{eff} admits two types of eigenstates.

The higher eigenstates $|+,m_{1z},m_{2z},\ldots\rangle$ with an eigenenergy

$$E_+(m_{1z},\ldots)=B+(A^2\Omega^2b^2)^{1/2} \qquad (6)$$

They are related to the situations where the spin S of the hole and the S_i's are mostly antiparallel.

The lower eigenstates $|-,m_{1z},m_{2z},\ldots\rangle$ with an eigenenergy

$$E_-(m_{1z},\ldots)=B-(A^2\Omega^2b^2)^{1/2} \qquad (7)$$

They are related to the situations where the spin S of the hole and the S_i's are mostly parallel.

Fig 2 shows the curves $E_\pm(\Omega)$. It is worthwhile to consider two limits to the study of the BMP dynamics. In the E_- branch. This branch admits two spin valleys and a stable point.

The transitions between the eigenstates of H_{eff} are due to a perturbation of the BMP by an external system which has to be specified during the relaxation of the BMP towards the bottom of the spin valleys. Its spin polarisation varies by many units. We assumed that the only efficient relaxation mechanism is the interaction of the S_i's involved in the BMP with others nuclear spins S_α which are not involved in the BMP but are close to it. The S_α's are in interaction with other nuclei which are remote from the BMP. If x is not lesser than a certain percolation threshold, all the In^{115} ions which are not involved in the BMP form clusters of infinite size, which gives rise to the spin relaxation of the BMP. This reservoir is coupled to the BMP by the following hamiltonian:

$$H_{coupl}=\alpha\sum_{i,\alpha} S_i S_\alpha \qquad (8)$$

The involved S_i and S_α are taken on the boundary of the BMP. In order to calculate the transition probability between the initial state a and the final state b of the BMP (the initial and final states of the reservoir are not specified), we use the Fermi golden rule:

$$W_{a\,c\to b\,d}=(2\pi/\hbar)|\langle a,c|H_{coupl}|b,d\rangle|^2\,\delta(E_f-E_i) \qquad (9)$$

E_i denotes the initial energy of the whole system and E_f its final energy. $W_{a,c\to b,d}$ must be summed over the final possible states of the reservoir, and averaged over its initial states with the Boltzmann probability [10]. Since the eigenstates of the reservoir are too intricate to be known, we have made the following assumption. The S_α are independant but each S_α experiences a random effective field h_α which is distributed with a gaussian probability law $P_h(h_\alpha)$:

$$P_h(h)=(1/2\pi\sigma^2)^{-3/2}\exp(-h^2/2\sigma^2) \qquad (10)$$

We are then able to calculate the transition probability $W_{a\to b}$ between the two states a and b of the BMP. The selection rules we found are the following. In the E- branch, a is the state $|-,m_{1z},m_{2z},\ldots,m_{iz},\ldots\rangle$, only the b states which are of the form $|-,m_{1z},m_{2z},\ldots,m_{iz}\pm1,\ldots\rangle$ can be reached. b differs from a in only one of its m_{iz} which becomes $m_{iz}\pm1$. m_i will in the following denote this m_{iz}. Instead of $W_{a\to b}$, we shall write $W_{m_i\to m_i\pm1}$. Our results are:

$$W_{m_i\to m_i\pm1}=C(\beta)\exp(-\beta(E_{m_i\pm1}-E_{m_i})/2)[(35/4)-m_i(m_i\pm1)] \qquad (11)$$

$$C(\beta)=(2\pi/\hbar)(4/3)(2\pi\sigma^2)^{-3/2}\exp(-b^2/2\sigma^2)b^2n^2\alpha^2[3\coth(3\beta b)-(1/2)\coth(\beta b/2)][(\coth(\beta b/2)+1)(\coth(\beta b/2)-1)]^{1/2} \qquad (12)$$

$\pm b=E_{m_i\pm1}-E_{m_i}$ denotes the difference between the final and initial energies of the BMP. n denotes the mean number of S_α's of a given S_i. In the following our energy unit will be b and our time unit τ will be (see [7]):

$$1/\tau=(2\pi/\hbar)(4/3)(2\pi\sigma^2)^{-3/2}\exp(-b^2/2\sigma^2)b^2n^2\alpha^2 \qquad (13)$$

A typical value of τ is 10^{-2}s. (11) allows to study the dynamics of the BMP. Let $P(m_{1z},\ldots,t)$ be the probability (at time t) the BMP in the state $|-,m_{1z},\ldots\rangle$ at time t. P can be seen as a vector with 6^V components which obeys:

$$dP/dt=\hat{A}P \qquad (14)$$

V is the number of S_i's involved in the BMP and the matrix elements of the operator $\hat{A}$ arises directly from (11). Let us point out the analogy of (14) with a problem of biased diffusion on a V-dimensionnal discrete hypercube with an inhomogeneous diffusion coefficient. We have numerically solved (14) in the case V=5 in order to obtain the time evolution of the averaged polarisation S(t) of the BMP:

$$S(t)=\sum_{m_{1z}}[P(m_{1z},\ldots)(\sum_i m_{iz})] \qquad (15)$$

In our model S(t) is directly proportionnal to the magnetic energy of the BMP. Results are plotted on Fig 3. S(t) exhibits a two times dynamics. It appears the more clearly at low temperatures. In a short time τ_S, it reaches a quasi stationnary value S(). Subsequently, it decays slowly to zero following an exponential law $\exp(-t/\tau)$. The part of the dynamics which is characterised by τ_S corresponds to the partial thermalisation of the BMP in the spin valley where its initial state was localised. The part of the dynamics characterised by τ corresponds to the equalisation of the two valleys through the saddle point, each valley being thermalised. Several experimental experiments have given us a justification of this assertion. For instance, let us before

$$P_{\pm}(t)=\sum^{\pm}P(m,t). \qquad (16)$$

Σ^{+} (Σ^{-}) denotes the summation over the states of the positive (negative) spin valley

P_{+} denotes the probability to find the BMP in the positive spin valley and P_{-} to find it in the negative spin valley. If our conceptions about the long time dynamics of the BMP are right, one should be able to write that for $t \gg \tau_S$

$$dP_{+}/dt=(1/\tau_1)(P_{-}-P_{+})$$
$$dP_{-}/dt=(1/\tau_1)(P_{+}-P_{-}) \qquad (17)$$

Then, in a situation where the initial state of the BMP is the bottom of the positive spin valley, one should have

$$S(t)=S_0\exp(-t/2\tau_1) \qquad (18)$$

while, if $t \ll \tau_1$

$$P_{-}=t/\tau_1 \qquad (19)$$

We have verified that the slope of P_{-} at medium times is the same as the slope of $-2\mathrm{Log}(S(t))$ at long times.

In order to be able to consider a BMP with a number V of S_1's greater than 4 or 5, we have carried out theoretical calculations. We will present a theoretical evaluation of τ_1.

One can write again (17) in the following form

$$d\Pi_{+}/dt=M\Pi_{+}+\mu\Pi_{-} \qquad d\Pi_{-}/dt=M\Pi_{-}+\mu\Pi_{+} \qquad (20)$$

The vector P has been split into the two vectors Π_{+} and Π_{-}. The components of Π_{+} (Π_{-}) are related to the states of the positive (negative) spin valley. M (μ) is related to the intravalley (intervalley) dynamics. μ couples the states which are on both sides of the saddle point. M admits a null eigenvalue corresponding to the thermodynamical equilibrium and several negative eigenvalues. Let $|p\rangle$ be the eigenvector of M related to the vanishing eigenvalue (note that the space of the P's is not hermitian). At large times there is

$$\exp(Mt)=|p\rangle\langle p| \qquad (21)$$

If $\Pi_{\pm}$ is written as $\exp(Mt)A_{\pm}$, one can write at large times

$$d\langle pA_{+}\rangle/dt=\langle p|\mu|p\rangle(\langle pA_{-}\rangle-\langle pA_{+}\rangle)$$
$$d\langle pA_{-}\rangle/dt=\langle p|\mu|p\rangle(\langle pA_{+}\rangle-\langle pA_{-}\rangle) \qquad (22)$$

which is a 2x2 scalar system analogous to (17). We therefore have

$$1/\tau_1=\langle p|\mu|p\rangle \qquad (23)$$

We were able to calculate the temperature dependence of τ_1 and to check that at low temperatures

$$1/\tau_1=(35/\pi\hbar^3)V^{-1}\exp(-\beta\varepsilon_2)(5V-4) \qquad (24)$$

V is the number of S_1's involved in the BMP. Fig. 4 shows the temperature dependence of the numerically computed $\ln(\tau_1)$ versus $\beta\varepsilon_2$. The straight line of slope 1 is in good agreement with the slope of the curve. The values of the activation energy are listed on Table 1. Table 2 presents the ratio $\tau_1(V)/\tau_1(V-1)$ for different values of β. The agreement between the numerical computations and the theoretical calculations is very good.

REFERENCES

1-A.K. Bhattacharjee, R. Planel, C. Benoit, à la Guillaume, ... Proceedings of the XVII International Conference on the Physics of Semiconductors (Springer-Verlag, New York).

2-T. Dietl, J. Spalek, Phys. Rev. Lett. 48 (...) 355.

3-D.R. Yakovlev, I.N. Uraltsev, W. Ossau, G. Landwehr, R.N. Bicknell-Tassius, A. Waag, S. Schmeusser, Surf. Sci. 623 (1992) 485.

4-C.E.T. Gonçalves Da Silva, Phys. Rev. B32 (1985) 6962.

5-A. Mauger, N.S. Almeida, D.L. Mills, Phys. Rev. B38 (1988) 1296.

6-P. Boudinet, G. Bastard, Europhys. Lett. 20 (1992) 149.

7-P. Boudinet, G. Bastard, To be published in Semicond. Sci. Technol.

8-A.V. Kavokin, Unpublished (1993).

9-D. Scalbert, M. Nawrocki, C. Benoit, à la Guillaume, J. Cernogora, Phys. Rev. B33 (1986) 4418.

10-C. Cohen-Tannoudji, J. Dupont-Roc, G. Grynberg, Processus d'interaction entre photons et atomes. Interéditions/Editions du CNRS (1988).

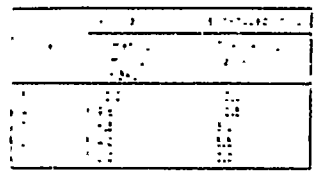

Table 1. Comparison between the theoretical and numerical values of the activation energy of the BMP for V = 2, 3, 4, 5.

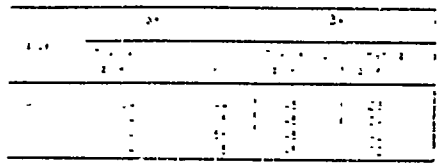

Table 2. Comparison between the theoretical and numerical values of $\tau_1(V)/\tau_1(V-1)$ for two different values of β, in reduced units $1/b$, and for V = 1, 2, 3, 4.

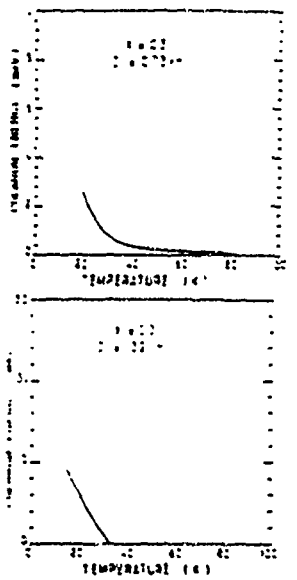

Fig 1 BMP magnetic energy versus the temperature for $z_{(w)}$ 33 nm and 132 nm

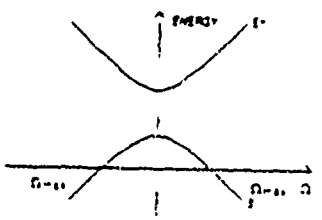

Fig 2 E'genenergies E_1 of the BMP versus its polarisation Ω

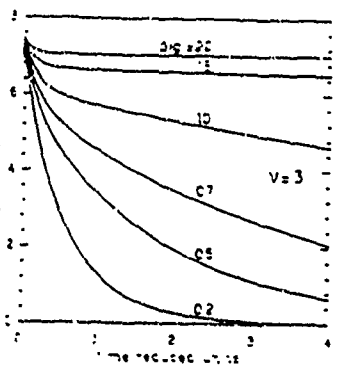

Fig 3 Calculated time evolution of the averaged polarisation S(t) of the BMP for several values of β g designs the energy unit b

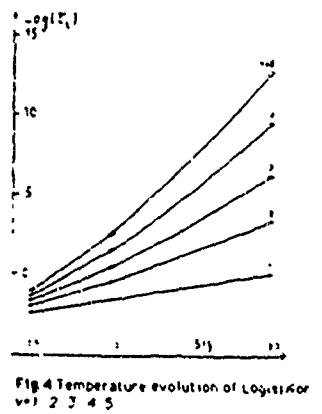

Fig 4 Temperature evolution of Log(I/I0) vol 2 3 4 5

ThP3

Time-resolved optical study of vertical transport in $Cd_{0.82}Mn_{0.18}Te/CdTe$ superlattices.

Ph. Roussignol(*)^, J. Martinez-Pastor(^)(+), A. Vinattieri(^), C. Delalande(*), and B. Lunn(#)

(*) Laboratoire de Physique de la Matière Condensée de l'Ecole Normale Supérieure, 24 rue Lhomond-75005 Paris, France.
(^) Laboratorio Europeo di Spettroscopie Non Lineari e Dipartimento di Fisica, Universita di Firenze, Largo E. Fermi 2- 50125 *Firenze, Italy*
(+) Departament de Física Aplicada, Universitat de València, 46100 Burjassot, València, Spain.
(#) Department of Engineering Design and Manufacture, University of Hull, Hull-HUGTRX, United Kingdom.

Abstract

We have performed cw and time-resolved photoluminescence measurements on a 30/30 $Cd_{0.82}Mn_{0.18}Te/CdTe$ superlattice containing two enlarged wells with different widths. Excitation above the alloy band gap allows to study the Bloch transport along the growth direction of the superlattice. Both ambipolar transport and hopping of carriers are observed in the 4-100K temperature range. At low temperatures (<20K), mobilities of the order of 4. 10^4 cm^2/Vs and 3. 10^2 cm^2/Vs are estimated for the two processes, respectively.

Introduction

In the last few years the improvement in molecular beam epitaxy growth has made possible the observation of vertical transport in superlattices [1]. Experimental evidences of this type of conduction first predicted by Esaki and Tsu [2] have been brought in heterostructures based on III-V semiconductors by using various optical or electric techniques [3-5]. Time-resolved photoluminescence in superlattices containing enlarged wells appeared to be one of the most powerful techniques and allowed an extensive study of the carrier transport in the AlGaAs/GaAs system [6]. In this paper, vertical transport is addressed by the same optical technique, in the case of the less investigated II-VI semiconductor heterostructures.

The sample was grown by molecular beam epitaxy on a *InSb* substrate. On this substrate are grown in succession, a 1000Å thick CdTe layer, a 2000Å $Cd_{0.82}Mn_{0.18}Te$ layer, 40 periods of 30/30 $Cd_{0.82}Mn_{0.18}Te/CdTe$ superlattice (SL) and a 60Å thick enlarged well (EW). The second EW, 200Å thick, is separated from the first one by 40 periods of SL, and followed by 160 periods of SL. Finally a 2000Å thick $Cd_{0.82}Mn_{0.18}Te$ cap layer completes the structure.

The excitation source for the time-resolved measurements was a Nd:YAG synchronously pumped dye laser, providing 5 ps pulses in the range 560-780 nm at the repetition rate of 76 MHz. Measurements have been also performed by using, for excitation, the second harmonics of the Nd:YAG laser (80 ps pulse duration at 532nm). The PL signal was dispersed through a 0.22 m double monochromator (spectral resolution : 1 meV) and detected by a synchroscan streak camera, with an overall time resolution of 20 ps. For decay times longer than 1 ns, the PL signal was analyzed by using a time correlated single photon counting system and a cavity dumper was inserted in the dye laser cavity in order to decrease the repetition rate; in this case the overall time resolution was of the order of 200 ps.

Experimental results

In order to study the Bloch transport over the SL minibands, the structure is excited at 2.33 eV (Nd:YAG second harmonics) or 2.18 eV (dye laser), far above the alloy band gap (1.869 eV at 4K). In this case all the carriers are photogenerated within the 2000Å thick CdMnTe cap layer. Typical PL spectra obtained at different temperatures are shown in Fig. 1. At 10K (lower curve in Fig. 1) the main peak at 1.722 eV corresponds to the excitonic recombination in the superlattice. The PL lines observed at 1.595 and 1.645 eV correspond to the excitonic recombination in the 200Å and 60Å EWs, respectively. The PL emission lines on the low energy side of the excitonic peaks are likely related to impurity assisted recombinations (A^0X, $e\text{-}A^0$, ...) [7]. As clearly shown in Fig. 1, at low temperatures (4-50K) the main peaks in the PL spectrum of the heterostructure correspond to the recombination in the SL. Excitonic recombination in the two EWs is also observed evidencing the vertical transport. Nevertheless, considering the rather low intensity of the EWs' PL peaks, transport along the growth axis of the heterostructure does not seem so efficient: most of the photogenerated carriers get localized and recombine in the superlattice region before reaching the enlarged wells. When the temperature increases the contribution at the PL emission of the EWs increases. However, above 80-90 K the PL line of the 60Å EW tends to disappear. As commonly observed [8], this behaviour is certainly due to a worse quality of the thinner well, which made it more sensitive to non radiative processes. Above those temperatures the luminescence from the 200Å EW is more important than that of the SL and becomes the dominant feature of the PL spectrum of the structure, indicating that the vertical transport is now more efficient than the localization process. An Arrhenius plot of the PL intensity ratio between the PL from the 200Å EW and that of the SL shows an activated behaviour above 50 K, with an activation energy of about 28 meV.

In the time-resolved measurements excitation powers of 20 - 200 mW were used corresponding roughly to excitation densities of about 10^{17}-10^{18} cm^{-3}. We report in Fig. 2 the PL decay curves of the 200Å EW at 4 and 40K obtained for two different excitation energies. Under resonant excitation of the E1H1 transition the PL decay (dotted lines in Fig. 2a and 2b) is fast with time constants of 20 and 50ps at 4 and 40K, respectively. Such a resonant excitation gives the recombination time of the isolated well. The PL decay of the 200Å EW is strikingly different when all the carriers are photogenerated in the cap layer (continuous lines in Fig. 2a and 2b). The long decay times obtained when exciting the heterostructure above the SL band gap are then characteristic of the vertical transport. In fact, the decay time of the isolated well, being much shorter, influences only the rise time of the measured PL signal as it can be seen in Fig. 2 (the apparent risetime is always related to the faster mechanism involved in the PL dynamics). A similar behaviour is observed for the 60Å EW.

At low temperatures (4-35K), the PL decay curves of the EWs under non resonant excitation (transport conditions and continuous line of Fig. 2a for the 200Å EW) can be decomposed as a sum of two exponentials with a risetime corresponding to the decay time of the isolated EW and two decay times characteristic of the transport mechanism which are shown in Fig. 3a for the whole temperature range investigated. In fact, the fast component dominates the PL decay curve: the intensity ratio between the slow and the fast component is of the order of 0.10. Moreover, when increasing the excitation power, this ratio tends to decrease. The two characteristic times of the EWs PL decay seem to be related to two different types of carrier transport, the fastest one being favoured by an increase of the excitation power.

Above 40 K a monoexponential decay is observed as shown in Fig. 2b.

The diffusion mobility, μ_D, can be deduced from the transport times according to [9]:

$$\mu_D = \frac{eD}{kT} = \frac{e\, v_D^2\, \tau_R}{kT} \qquad v_D = \frac{L_{SL}}{\tau_D} \qquad (1)$$

where D is the diffusion coefficient, τ_R the recombination time along the carrier path and v_D the drift velocity, determined by the path length (L_{SL}), and the diffusion time (τ_D).

The diffusion mobilities reported in Fig. 3b have been estimated using Eq. 1, with L_{SL} = 9600 Å and 12000Å (the distance between the cap layer and the EWs 200Å and 60Å, respectively) and τ_R = 350 ps. The PL decay time in the SL exhibits a weak temperature dependence: from 250ps to 350ps in the 4-100K temperature range. Therefore, this time, although influenced by the transport, can be mainly attributed to excitonic recombination in the SL. A τ_R value of 350ps will give the right order of magnitude for the recombination time of the SL, although somehow underestimated, in the whole range of temperature.

In the 4-25K temperature range, the fastest transport mechanism gives high diffusion mobilities ranging from 40000 cm^2/Vs to 2000 cm^2/Vs. Above 30K this mobility drops significantly to reach a value of 40 cm^2/Vs at 70K. The slowest mechanism gives much smaller mobilities, of the order of 300 cm^2/Vs. However, when the slow component is observable (4-20K) its decay time is not accurately determined (intensity ratio ~ 10%) and this mobility should be considered as an order of magnitude.

Discussion

Let us first consider the low temperature measurements (4-30K). At the large excitation intensities used in our experiments (10^{17}-10^{18} carriers per cm^{-3}) we can reasonably assume that the main contribution to the transport provided by the fast component is due to ambipolar Bloch transport of carriers [10]. Electron-hole pairs are created in the cap layer of the heterostructure and ambipolar band transport takes place. Nevertheless, for these temperatures, as it can be seen in Fig. 1, localization of carriers occurs. Carriers can be captured by ionized acceptors in order to give neutral acceptors or localized on defects before arriving to the large well. Due to the smaller width of the HH miniband, holes are certainly more sensitive to localization than electrons. The long time constant can then be related to an other transport mechanism, hopping through localized states, this mechanism being much slower than Bloch conduction [11].

As a matter of fact, PL spectra of the heterostructure obtained at high cw excitation power (150mW ≈ 10^{17}-10^{18} carriers/cm^3) are dominated by the excitonic recombinations in the SL and EWs; saturation of the finite number of the sites responsible for the localization of the carriers does occur. In time-resolved measurements a similar carrier density is photocreated, so we mainly see the band transport of free carriers. When the carrier concentration becomes sufficiently low, transport due to localized carriers begins to be observable. Moreover, when the excitation power is increased, due to the finite number of trapping sites, the ratio between free and localized carriers increases and the hopping process is less observable, as experimentally seen.

For temperatures higher than 30K we observe a monoexponential decay for the two EWs. Two main reasons make the observation of the slow component impossible. On one hand, as the temperature increases more and more carriers get detrapped from localized tail states of the SL and are thermally activated upwards the extended states [12]. The activation energy of 28 meV found for our heterostructure is consistent with the calculated localization energy on a two monolayers fluctuation (≈30meV). On the other hand, carrier scattering by acoustic and optical phonons takes place [13] and produces a large drop of the mobility (Fig. 3b). The transport time becomes longer than the hopping characteristic time and makes difficult the observation of the minor component.

At low temperature the mobilities in our 30/30 CdTe/$Cd_{0.82}Mn_{0.18}Te$ superlattice depicted in Fig. 3b are of the same order of magnitude as those reported for electrons in the GaAs/AlGaAs system [6, 14]. In fact, the ambipolar diffusion coefficient is expected to be close to the hole diffusion coefficient ($D_{amb} \approx 2\, D_h$) [15]. At 10K we estimate a diffusion coefficient of 15 cm^2/s which is intermediate between electron and hole diffusion coefficient

in a 30/30 GaAs/ $Al_{0.15}Ga_{0.85}As$ superlattice (30 cm^2/s and 2 cm^2/s, respectively) [10] Hole mobility seems then somewhat higher in the II-VI heterostructure. If we consider the small number of data available in the litterature for II-VI systems, the estimated value of 4 10^4 $cm^2/V.s$ seems also to be intermediate between the electron mobility (5 10^4 -10 10^4 $cm^2/V.s$ [13, 16, 17]) and the hole mobility (1 5 10^4 cm^2/Vs in a HgTe/CdTe superlattice [17]). At higher temperatures, the ambipolar mobility (= 20 cm^2/Vs at 100K) is lower than the values reported for holes in these materials (200 cm^2/Vs in a HgTe/CdTe superlattice [17] and 1200 cm^2/Vs in bulk CdTe [13] at 170K) However hole mobilities are much dependent on the valence band structure and can be hardly compared so directly, especially at high temperature, where acoustic and optical phonons scattering plays a major role and is also much sensitive to the valence band dispersion viz the Fröhlich potential

Conclusion

We have presented experimental results, obtained by means of time-resolved photoluminescence, on carrier transport in a II-VI $Cd_{0.80}Mn_{0.18}Te$/CdTe superlattice with two CdTe enlarged wells Excitation above the band gap of the superlattice allows us to excite the sample near its surface Band transport occurs but cw PL spectra show that localization of carriers plays an important role in this structure. A clear thermally activated behaviour is observed. In the time-resolved measurements two transport mechanisms with different time scales are individuated The faster one can be assigned to Bloch transport along the growth axis of the heterostructure, the slower one to hopping between localized states At low temperature, ambipolar mobilities of 40000 cm^2/Vs have been estimated for Bloch transport and 300 cm^2/Vs for hopping. The two order of magnitude difference between the two mobilities is consistent with calculations in the GaAs/AlGaAs system [11] These values can be compared and are in reasonable agreement with the values reported in similar systems [13, 16, 17]

References

1. see for example F. Capasso, K Mohammed and A Y Cho, IEEE, J Quant Electron QE-22, 1853(1986).
2. L. Esaki and R Tsu, IBM J Res Dev 14, 61(1970).
3. G Belle, J C. Maan and G Weimann, Sol. St Commun 56, 65(1985)
4. R.A Davies, M.J. Kelly and T M. Kerr, Phys Rev. Lett 55,1114(1985)
5. J F. Palmier, C Minot, J F Lieven, F Alexandre, J C Harmand, J Dangla, C Dubon-Chevallier and O Ankri, Appl Phys Lett 49,1260(1986).
6. B. Lambert, F Clérot, B Deveaud, A Chomette, G Talalaeff and A Regreny, B Sermage, J. Lumin 44, 277(1989)
7. A. Golnik, J Ginter and J A. Gaj, J Phys C 16, 6073(1983)
8. M Gurioli, A Vinattieri, M Colocci, C. Deparis, J Massies, G Neu, A. Bosacchi, and S Franchi, Phys. Rev. B 44, 3115(1991)
9. P Kireev, La Physique des Semiconducteurs, Ed Mir, Moscow (1975)
10. B. Lambert, B Deveaud, A Chomette, A Regreny and B Sermage, Semicond Sci Technol 4, 513(1989)
11. D Calecki, J F Palmier and A Chomette, J Phys C 17, 5017(1984)
12. A Chomette B Deveaud and A Regreny, G Bastard, Phys Rev Lett 57, 1464(1986)
13. B Segall, M R Lorenz and R E Halsted, Phys Rev 129 2471(1963)
14. B.F. Levine, W T Tsang, C G Bethea, and F Capasso, Appl Phys Lett 41, 470 (1982).
15. S M. Sze, Physics of Semiconductor Devices, J Wiley &Sons, New-York, 1981
16. S. Hwang, J F Schetzina, Properties of II-VI Semiconductors, Ed F J Bartoli, H F Schaake and J F. Schetzina, MRS Symposium Proc vol. 151, 245(1990)
17. C A Hoffman, J R Meyer, and F J Bartoli, Properties of II-VI Semiconductors, Ed F J Bartoli, H F. Schaake and J F Schetzina, MRS Symposium Proc. vol. 151, 403(1990)

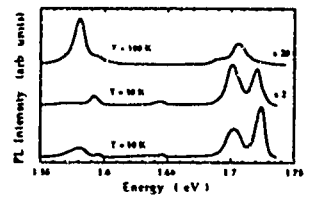

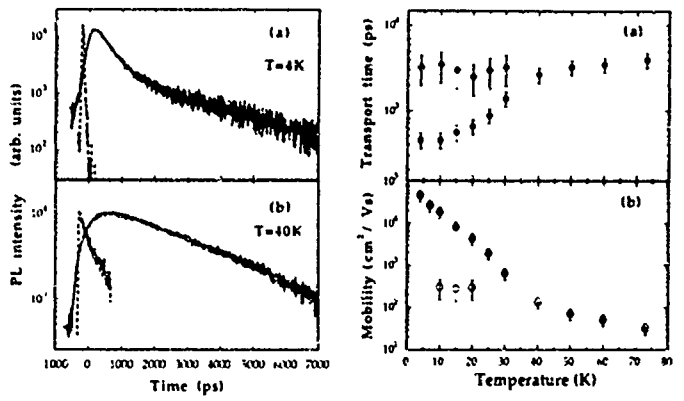

Figure 1 PL spectrum of the heterostructure excited above the SL band gap at different temperatures

Figure 2 Semilogarithmic plots of the PL decays of the 200Å enlarged well at 4K (a) and 40K (b) The dotted lines correspond to a resonant excitation of the E1H1 transition of the EW, the continuous lines are obtained when the excitation energy is higher than the CdMnTe barrier band gap and all the carriers generated in the cap layer of the heterostructure.

Figure 3 (a)Temperature dependence of the transport times obtained from the slow (◊) and the fast (•) component of the PL decay curve of the 200Å EW
(b)Log-log plot of the estimated carrier mobility (as explained in text) in the superlattice as a function of the temperature Estimation of the hopping mobility is also reported (◊)

ThP4

Electron Subband Structure of HgCdTe Metal–Insulator–Semiconductor Heterostructures

Junhao Chu[1], R Sizmann[2], Kun Liu[1], I Nachev[3], F Koch[2]

1) National Laboratory for Infrared Physics, Shanghai Institute of Technical Physics, Academia Sinica, Shanghai 200083, China
2) Physics Department E-16, T. U. München, 8046 Garchrug, F R Germany
3) Institute of Microelectronics, 1784 Sofia, Bulguria

Abstract

The doping and pressure dependence of surface layer capacitance has been investigated in this work for $Hg_{0.8}Cd_{0.2}Te$ with doping concentration N_A from 3.6×10^{16} to 1.1×10^{18} cm^{-3} and under hydrostatic pressure up to 7.3 kbar at temperature 4.2 K. By using a capacitance-voltage spectroscopy ($C-V$) fitting model, the subband structures such as the first subband energy E_0 as a function of the energy gap E_g and the variation of E_0 with doping have been determined. The second onset of the inversion in capacitance spectroscopy on HgCdTe MIS structure has been observed. By using an expanded $C-V$ fitting model several quantum parameters relating to the second subband of inversion layer electron can be determined quantitatively.

1. Introduction

The subband structure of n-type inversion layer of p-type HgCdTe metal-insulator-semiconductor (MIS) structures in quantum limit has been determined by a $C-V$ fitting model directly from the capacitance voltage relation, cyclotron resonance (CR) and magneto-conductivity oscillation (SdH) measurements [1]. Recently it becomes more generd after it was modified by taking account of the influence of resonant defect states on subband structures [2]. In order to investigate systematically the subband structures for the inversion layer of p-type $Hg_{0.8}Cd_{0.2}Te$ with different doping concentration and under different pressure, we have investigated the doping and pressure dependence of surface layer capacitance for $Hg_{1-x}Cd_xTe$ with doping concentration N_A from 3.6×10^{16} to 1.1×10^{18} cm^{-3} and under hydrostatic pressure up to 7.3 kbar at 4.2 K. By using the modified subband model, the subband structures such as the first subband energy E_0 as a function of the energy gap E_g and the variation of E_0 with doping have been determined.

The second onset of the inversion in capacitance spectroscopy on HgCdTe MIS structure has been observed for the first time. Several key points have been presented in this paper in order to expand the $C-V$ fitting model to determine the subband structures with two occupied subbands of n-type inversion layer in p-type HgCdTe MIS structures. By using the expanded $C-V$ fitting model to fit the measured $C-V$ relation, several quantum parameters relating to the second subband of inversion layer electron can be also determined quantitatively.

2. Model

We have presented a physical parameter fitting method to determine quantitatively the subband structure and its dependence on the inversion layer electron concentration in the electric quantum limit [1,2]. The basic idea is as follows: (i) the one-dimensional Poisson's equation is applied to give the relation between electric charge distribution and surface potential; (ii) the ground state energy E_0 is expanded into a series of surface electron concentration N_{s0} in the ground subband, $E_0 = E_{00} + E_{01}N_{s0} + E_{02}N_{s0}^2$, (iii) a characteristic parameter $j = Z_{cv}/Z_c$ is introduced for describing the wavefunction distribution of subband electrons, thus the electron gas in an inversion layer with depth Z_c can be regarded on the average as being distributed in the plane that is Z_{cv} distant from the surface, (iv) then from the calculations of capacitance-voltage relation of the MIS system to fit the measured $C-V$ curve, and the results of SdH and CR measurements, the subband structure can be obtained.

In the case of existing resonant defect states, several modification should be done. First, the charge density of chargeable resonant defect states should be involved in the one-dimensional Poisson's equation.

$$\frac{d^2\phi}{dz^2} = -\frac{1}{\varepsilon\varepsilon_0}[\rho_s(Z) + \rho_{dep}(Z) + \rho_R(Z)] \tag{1}$$

where $\rho_s(Z)$ is the charge density of subband electrons in the inversion layer, expressed as equation (8) in reference [1], $\rho_{dep}(Z)$ is the charge density in the depletion layer, $\rho_R(Z)$ is the charge density of resonant defect states.

$$\rho_R(Z) = -eN_R \qquad (0 < Z < Z_R) \tag{2}$$

where Z_R is the depth of chargeable resonant states. In the region $Z < Z_R$ the resonant level sinks down below the Fermi level. N_R is the density of resonant states. Secondly, semiconductor surface layer capacitance C_s can be redefined by taking account of the contribution of resonant defect states as

$$C_s = \frac{\partial Q_s}{\partial \phi_s} = -e\left(N_A\frac{\partial Z_d}{\partial \phi_s} + N_R\frac{\partial Z_R}{\partial \phi_s} + \frac{\partial N_s}{\partial \phi_s}\right)\cdot A \tag{3}$$

where ϕ_s is the surface potential, Q_s, the surface charge, A, the area of the capacitor; Z_d, the depletion width. N_s is the electron concentration in the inversion layer subband, the term of N_R is the contribution of resonant defect states to the semiconductor surface layer capacitance. Finally, the total induced charge can be separated into three parts: depletion charge, resonant defect state charge, and surface electron charge. Thus the relationship between surface electron concentration and gate voltage is

$$N_s = C_i(V_g - V_{FB})/e - N_A Z_d - N_R Z_R \tag{4}$$

For the heavily doped bulk p-type HgCdTe samples, the influence of resonant defect states on the subband structure should be taken into account in the calculation of subband structures. This is very important to get doping dependence of subband structure.

In the case of two occupied subbands of n-type inversion layer in p-type HgCdTe MIS structures the $C-V$ fitting model should be expanded. The main procedures are as follows.

(i) like the ground state energy E_0, the first excited state energy E_1 is also expanded into a series of electron concentration N_{s1} in the second subband.

$$E_1 = E_{10} + E_{11}N_{s1} + E_{12}N_{s1}^2 \tag{5}$$

where E_{10} can be obtained from the calculation of one-subband C—V fitting procedure at the second threshold voltage V_{T1}. E_{11} and E_{12} are two adjustable parameters in the two-subband C–V fitting calculation after the second onset. (ii) after the second onset, the total concentration of surface electrons is

$$N_s = N_{s0} + N_{s1} \tag{6}$$

The relation between N_s and the Fermi level E_F is

$$N_s = \int_{E_0}^{E_F} \frac{M_0^*}{\pi\hbar^2}\left[1 + \frac{2(E - jE_0)}{E_g}\right]dE + \int_{E_1}^{E_F} \frac{M_0^*}{\pi\hbar^2}\left[1 + \frac{2(E - j_1E_1)}{E_g}\right]dE \tag{7}$$

where j and j_1 are wave function distribution parameters for E_0 subband and E_1 subband, respectively. They can be obtained from the Fan-Howard wave function [3] (iii) in the calculation, all the combination and their derivatives change as

$$\begin{cases} N_sZ_i \to N_{s0}Z_{i0} + N_{s1}Z_{i1} \\ N_s\dfrac{\partial Z_i}{\partial\phi_s} \to N_{s0}\dfrac{\partial Z_{i0}}{\partial\phi_s} + N_{s1}\dfrac{\partial Z_{i1}}{\partial\phi_s} \\ Z_i\dfrac{\partial N_s}{\partial\phi_s} \to Z_{i0}\dfrac{\partial N_{s0}}{\partial\phi_s} + Z_{i1}\dfrac{\partial N_{s1}}{\partial\phi_s} \end{cases} \tag{8}$$

where Z_{i0} and Z_{i1} are depths of the first subband and the second subband, respectively.

By fitting to the measured C–V curve in the voltage region after the second onset we can get the second subband energy E_1 and other quantum parameters versus subband electron concentration

3. Results

In order to investigate the doping dependence of subband structure, we have measured the capacitance spectroscopy, magneto conductivity oscillation, and cyclotron resonance of subband electrons for p-type $Hg_{1-x}Cd_xTe$ ($x = 0.21$) samples with doping concentration N_A from 3.6×10^{16} to 1.1×10^{18} cm^{-3}. The sample preparation and the experimental details have been reported in our previous work [1,4]. By using the modified model described above, the one-subband C–V fitting calculation has been performed for all the measured samples. The subband energy coefficients E_{01} and E_{02} depend on N_s. The subband threshold energy E_{i0} varies with doping concentration N_A. From the best fit to the data, an empirical relation of E_0 can be derived as

$$E_0 = 4.97\times10^{-14}[\lg(N_A)]^{10} + 1.6\times10^{-13}N_s - 7\times10^{-26}N_s^2 \quad (\text{eV}) \tag{9}$$

which is applicable to $Hg_{1-x}Cd_xTe$ ($x = 0.21$) samples with different doping concentrations from 3.6×10^{16} to 1.1×10^{18} cm^{-3} for $N_s < 8\times10^{11}$ cm^{-2}. Table 1 shows the comparison of equation (9) with the results from theoretical calculation

Table 1 Comparison of subband energy E_0 in this work with that of theoretical calculation

samples	E_0(eV)	
	this work [eq. (9)]	theory
$N_A = 4.0\times10^{17}$ cm^{-3} $N_s = 6.3\times10^{11}$ cm^{-2}	0.215	0.220 Ref [5]
$N_A = 3.2\times10^{17}$ cm^{-3} $N_s = 2.0\times10^{11}$ cm^{-2}	0.163	0.170 Ref [5]
$N_A = 5\times10^{16}$ cm^{-3} $N_s = 3\times10^{11}$ cm^{-2}	0.126	0.122 Ref. [6]

The Fermi level and the effective mass of subband electrons at the Fermi level as well as the depths of inversion layer and depletion layer can be also obtained from the C–V fitting calculation. When $N_s = 3\times10^{11}$ cm^{-2}, as the N_A increases from 3×10^{16} to 1.1×10^{18} cm^{-3}, Z_d decreases from 90 nm to 30 nm, Z_i decreases slowly from 20 nm to 10 nm.

All of these data including subband energy E_0, Fermi level E_F, effective mass $M^*(E)$ and the sizes of depletion and inversion layers and their N_s-dependence are necessary for deriving the subband Laudau level fan chart and dispersion relation of subband electrons by combining the Kane's model and considering the contribution of k-linear term of spin-orbit interaction, so the obtained Laudau level fan chart is in good agreement with the data of magneto-optical resonance of subband electrons [7].

The one-subband C–V fitting model can also be applicable to determine the pressure dependence of subband. The pressure dependence of surface layer capacitance has been measured in this work for $Hg_{0.8}Cd_{0.2}Te$ at hydrostatic pressure up to 7.3 kbar at temperature 4.2 K. Figure 1 shows the capacitance spectroscopy for $Hg_{0.786}Cd_{0.214}Te$ at pressure of 0, 1.9, 2.9, 4.4, 5.8, and 7.3 kbar. It is obviously that the onset of inversion is delayed and the flat band voltage also moves towards the voltage-increasing direction as the pressure increases, i.e., as the energy gap E_g increases. The pressure dependence of energy gap for HgCdTe is $E_g(P) = E_g(0) + (9.5\,\text{meV/kbar})\cdot P$. From the C–V fitting model we get the subband energy E_0 and other quantities of subband as a function of energy gap E_g. Table 2 shows the related

Table 2 Related quantities of the C–V fitting calculation at different pressure

P (kbar)	C_i (pf)	V_{fb} (Volt)	V_{to} (Volt)	E_g (meV)	E_{00}(exp) (meV)	E_{00}(theory) (meV)
0	54.65	-.75	0	128	146	151
1.9	54.62	-65.3	11.5	146	148.6	154
2.9	54.61	-62.9	15.3	156	149.2	155.2
4.4	54.596	-59.7	20.5	170	151	156
5.8	54.603	-56	26.2	183	154	158
7.3	54.601	-52	32	197	155	159.4

quantities of the $C-V$ fitting calculation, where the values of $E_{00}(exp)$ are obtained by the $C-V$ fitting calculation, the values of E_{00} (theory) are from the self-consistant variation calculation [8,9]. Figure 2 shows the subband threshold energy E_{00} versus energy gap E_g and hydrostatic pressure P that was applied to the sample

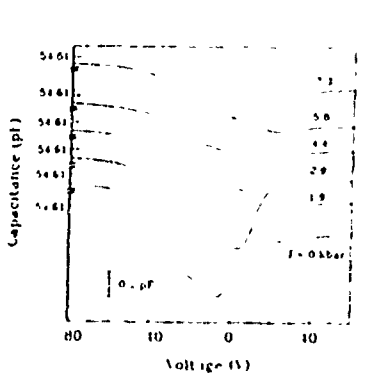

Fig 1 The measured capacitance spectroscopy for $Hg_{0.766}Cd_{0.234}Te$ at 4.2 K and hydrostatic pressure of 0, 1.9, 2.9, 4.4, 5.8 and 7.3 kbar, respectively

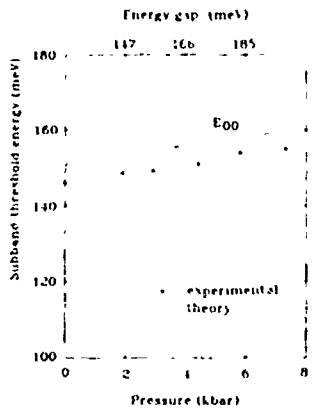

Fig 2 The subband energy E_0 versus energy gap E_g and pressure P for $Hg_{0.766}Cd_{0.234}Te$ at 4.2 K

Fig 3 The measured capacitance spectroscopy with the first and second onset of inversion for $Hg_{1-x}Cd_xTe$ samples with $x = 0.21$ and $N_A = 5.8 \times 10^{16}\,cm^{-3}$

The capacitance spectroscopy can be also used to study higher subband structures. In principle, the variation of C with V above the threshold should give evidence for higher subbands $E_1, E_2, \cdots$, etc and allows one to determine the density of states in the subbands. However, it is difficult to measure the higher onset of inversion due to the inhomogeneity. For measuring the second onset of inversion, a uniform sample or a relatively small area of gate is necessary. By a careful experiment we have measured the capacitance spectroscopy with the first and second onset of inversion for $Hg_{1-x}Cd_xTe$ samples with $x = 0.213$ and $N_A = 5.8 \times 10^{16}\,cm^{-3}$ at 4.2 K (Fig 3). In the figure we can see clearly the second onset of inversion. The second inversion threshold is reached when band bending equals an energy of $E_g + E_1$, and electrons start to occupy the bottom of the second subband. By using the $C-V$ fitting model that has been expanded to determine the subband structures with two occupied subbands of n-type inversion layer in p-type HgCdTe MIS structures, the energy E_1 and other quantum parameters relating to the second subband of inversion layer electron can be also determined quantitatively, which will be published elsewhere.

References

[1] J. H. Chu, Z. Y. Mi, R. Sizmann and F. Koch, *Phys. Rev.* **B44**, 1717(1991)

[2] J. H. Chu, Z. Y. Mi, R. Sizmann, F. Koch, R. Wollrab, J. Ziegler and H. Maier, *J. Vac. Sci. Technol.* **B10**(4), 1569(1992)

[3] F. F. Fang and W. E. Howard, *Phys. Rev. Lett.* **16**, 797(1966)

[4] J. H. Chu, R. Sizmann, R. Wollrab, F. Koch, J. Ziegler, and H. Maier, *Chin. J. IR Res.* **8**, 327(1989)

[5] R. Sizmann, Doctor Theses, T. U. München, (1989) p. 38, p. 50

[6] I. Nachev, *Semicond. Sci. Technol.* **3**, 29(1988)

[7] J. H. Chu, R. Sizmann, Z. Y. Mi, F. Koch, *21st Int'l. Conf. on Phys. of Semicond.* Beijing, Oct. 1992

[8] K. Liu, J. H. Chu, D. Y. Tang, to be published

[9] F. Stern, *Phys. Rev.*, **B5**, 4891(1972)

ThP5

Zeeman studies of CdTe-$Cd_{1-x}Mn_xTe$ multiquantum wells

S Jackson, S R Bayliff, I Stirner, W F Hagston,
P Harrison and J E Nicholls
Department of Applied Physics, University of Hull, HU6 7RX, U.K.

28th June 1993

Abstract

Various novel features of the magnetic field splitting associated with the photoluminescence excitation spectra (PLE) and the photoluminescence spectra (PL) for CdTe/$Cd_{1-x}Mn_xTe$ quantum well structures are described. Attention is focussed on those aspects of the data which reveal certain novel features of the physics involved. Sometimes these features are associated with observations that are the same for both the Faraday and Voigt configurations (isotropic effects) whereas at other times they involve observations that are markedly different for these two configurations (anisotropic effects). In this way evidence is presented for the existence of interface potentials together with anisotropic effects resulting from the rotation of the spin quantization axis by an external magnetic field. The latter leading to an admixture of the light and heavy hole states with increasing field in the Voigt configuration.

1 Introduction

Dilute magnetic semiconductors (DMS) such as the $Cd_{1-x}Mn_xTe$ system described here are characterized by large magneto optical effects resulting from the carrier magnetic ion exchange interaction [1]. In the multiquantum well system formed from CdTe wells and $Cd_{1-x}Mn_xTe$ barriers, this interaction gives rise to novel effects in the magnetic field dependence of the photoluminescence (PL) and photoluminescence excitation (PLE) spectra. In the following we describe the manner in which these effects manifest themselves and in particular we distinguish between those features that are similar in both the Faraday and Voigt configurations (isotropic effects) and those that are different (anisotropic effects).

2 Experiment

Since the effects to be described are characteristic of many different quantum well structures we present detailed results for only one sample. The latter was formed from 15 wells of CdTe of width 72 Å sandwiched between $Cd_{0.75}Mn_{0.25}Te$ barriers of width 156 Å. The sample was grown with a VG Semicon V80H molecular beam epitaxy (MBE) system on InSb (001) substrate. Layer thicknesses were determined from a calibration of the molecular flux rates and checked by double crystal X ray diffraction.

The zero field PL spectra consist of 3 emission bands shown in Figures 1 and 2 for the Faraday and Voigt configuration respectively. Two of these are free excitons of different intra well widths together with their associated donor bound excitons ≈ 3 meV lower in energy. The relative increase in the higher energy component of each pair (free or bound) at elevated temperatures is consistent with the assignment to intra well width (as opposed to inter well width) fluctuations. Similarly the energy separation between the free and bound excitons is consistent with the assignment of the latter as an exciton bound to a neutral donor, since envelope calculations we have carried out show that the binding energy of an electron to a donor varies from ~ 20 meV when the donor is in the centre of the well to ~ 5 meV when the donor is in the centre of the barrier. From this it follows that the peak separation ≈ 3 meV is consistent with an exciton binding energy ≈ 0.14 that of the donor electron, and agrees with calculations of this ratio for bulk material [2]. These same calculations also show that the donors are distributed throughout the well and barrier region, since this explains, for the Faraday configuration, the decrease in both the intensity of the bound exciton emission at all values of the applied field (as the latter successively destabilizes bound exciton formation [3] at donor positions moving from the centre of the barrier in toward the well region) and the change in the emission peak energies as a function of field shown in Figure 1.

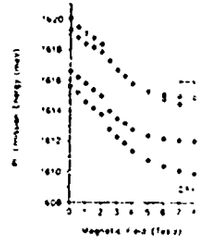

Figure 1 PL emission energy as a function of magnetic field in Faraday configuration

Figure 2 PL emission energy as a function of magnetic field in Voigt configuration

For this configuration the PL is associated with pure heavy hole exciton transitions. This is to be contrasted with observations of these lines in the Voigt configuration shown in Figure 2. Here the PLE spectra show, in agreement with the predictions of the theory to be described below, that an anti crossing will occur at a field of 2 to 3 Tesla between a light hole and a heavy hole state. Prior to this anti crossing there exists only a small splitting of the heavy hole state. Consequently the emission spectrum consists of two free exciton lines whose energy position is almost independent of the field up to ≈ 2 Tesla. Following the anti crossing, which leads to large energy shifts, only one line is ultimately resolved in the PL spectrum.

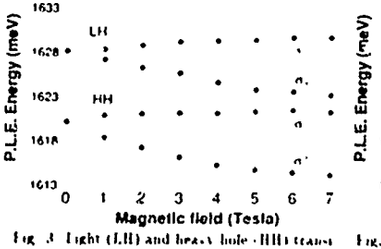

Fig. 3 Light (LH) and heavy hole (HH) transition energies as a function of magnetic field in Faraday configuration

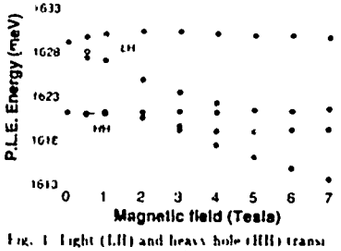

Fig. 4 Light (LH) and heavy hole (HH) transition energies as a function of magnetic field in Voigt configuration

The PLE spectra are quite complicated partially as a result of the existence of two effective well widths. For clarity we therefore display only those aspects of the data that illustrate novel features

and/or the asymmetry in the splittings between the Faraday and Voigt configurations. Within this restriction the relevant parts of the P.L.E. data for the Faraday and Voigt configurations are shown in Figures 3 to 5. Some of the important points of these spectra, as regards later discussion, are the following. The heavy hole exciton transitions in the barrier, which are almost identical for both configurations, are displayed in Figure 5. There is 'isotropy' with regard to the 'mean' Zeeman splitting of these lines in both the Faraday and Voigt configurations. It is to be noted however that there is an asymmetry in the σ^+ and σ^- splittings of the heavy hole exciton transitions. If the mean of the magnitude of these splittings is fitted to a Brillouin function for both the light and heavy hole states, it is found that the value of $N_0\alpha$, which characterizes the exchange interaction of the electrons in the conduction band, is typically 20 meV smaller than the bulk value [1].

With regard to the energy transitions in Faraday configuration in Figure 4, which are associated with excitons in the well region, one characteristic feature is the anomalously large splitting of the light hole exciton states compared with the heavy hole states. Likewise there is a marked anisotropy in the magnetic field splittings between Figure 3 and Figure 4. The heavy hole exciton states hardly split at all in the Voigt configuration until a field ≥ 2 Tesla when the anti crossing effect referred to earlier produces a significant splitting of these states. As opposed to this the light hole states show appreciable splitting in the magnetic field.

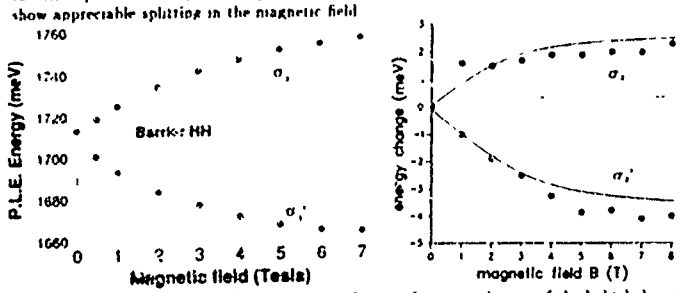

Fig. 5. Barrier heavy hole (HH) transition as a function of magnetic field

Fig. 6. Zeeman splitting of the light hole exciton transition together with theoretical fits in Faraday configuration

3 Discussion

The fact that the magnetic response of the first few monolayers in a magnetic barrier could differ from the rest of the barrier region has been noted by other workers [1]. Similarly the reduction in the value of $N_0\alpha$ has been seen in Faraday rotation experiments [3]. Coupling these features together shows, for example, that in the Faraday configuration the change in the potential profile for the light hole σ^- transition on application of a magnetic field could differ markedly from the normal square quantum well profile [6]. In this manner, by assigning a different Brillouin function response to the first few monolayers of the barrier region we have been able to obtain a theoretical fit to both the heavy hole and the light hole exciton splittings, where the light hole splitting in Faraday configuration together with the theoretical fit without (dashed lines) and with interface potentials (full lines) is depicted in Figure 6. I.e. we can account for the anomalously large light hole splittings we observe by making allowance for the anomalous magnetic response of the first few monolayers of the barrier region where the holes are effectively 'confined'. These same considerations can also account for the asymmetry in the splitting of the heavy hole barrier exciton, since the corresponding deviations in the magnetic response of the first few monolayers can be treated as a perturbation which effectively renormalizes the band gap of the material (which is why we chose the mean of the magnitude of the splittings earlier).

The theoretical analysis of the line splitting in the Voigt configuration is identical with that already described in the literature [7,8] and hence will not be described in detail here. It leads to results that give good overall agreement with regard to both the number of lines seen and their relative intensity as a function of the field. In particular it predicts the negligible splitting of the heavy hole states at low fields and the anti crossing of the light and heavy hole states in the field range 2 – 3 Tesla. Although there is good overall agreement with the observed light hole splittings the quantitative agreement is improved (exactly as in the Faraday configuration) by inclusion of interface potentials.

4 Conclusions

The observed asymmetry in the splitting of the barrier excitonic states is consistent with the existence of short range interface potentials resulting from the different magnetic response of the interface region. These same results also show that the magnetic exchange interaction of the conduction band electron with the Mn^{2+} ions is reduced in the finite barriers described here. A combination of both these effects can account for the anomalously large splitting of the light hole state in the Faraday configuration.

The energies and intensities of the bound exciton states are consistent with their being assigned to donors which are themselves distributed across the entire well and barrier region. Similarly the marked asymmetry in the field splittings in the Faraday and Voigt configuration of the light and heavy hole states associated with the well region is consistent with the rotation of the spin axis of quantization in the latter configuration. This also leads to an anti crossing of a light and heavy hole state which manifests itself clearly in both the P.L. and P.L.E. data.

Acknowledgements The authors wish to thank the Science and Engineering Research Council (U.K.) for supporting this work. One author (I.S.) would like to thank the University of Hull for the award of a Brynmor Jones Scholarship.

References

[1] Semiconductors and Semimetals, R.K. Willardson and A.C. Beer, Treatise Editors, J.K. Furdyna and J. Kossut, Volume Editors (Academic Press, Boston 1988) Vol. 25.

[2] Physics and Chemistry of II-VI Compounds, ed. J.S. Prener and N. Aven, North Holland Publishing Co. (1969).

[3] I.J. Gregory, J.F. Nicholls, J.J. Davies, J.O. Williams and N. Maung, Semicond. Sci. Technol. **3** 1193 (1988).

[4] D.R. Yakovlev, Festkorperprobleme, Advances in Solid State Physics **32**, ed. by U. Rossler (Vieweg, Braunschweig/Wiesbaden 1992) 251.

[5] M. Kohl, M.R. Freeman, J.M. Hong and D.D. Awschalom, Phys. Rev. B **43** 2181 (1991).

[6] I. Storner, P. Harrison, W.E. Hagston and J.P. Goodwin, J. Appl. Phys. **73** 5081 (1993).

[7] I.Z. Kachlishvili, Solid State Commun. **80** 283 (1991).

[8] P. Peyla, A. Wasela, Y. Merle d'Aubigne, D.E. Ashenford and B. Lunn, Phys. Rev. B **47** 1784 (1993).

ThP6

Time-resolved photoluminescence studies of stimulated emission and exciton dynamics in ZnSe/$ZnS_{0.18}Se_{0.82}$ superlattices

C J Stevens, R A Taylor & J H Ryan
University of Oxford Department of Physics
Clarendon Laboratory, Parks Road Oxford England OX1 3PU
M Dabbicco M Ferrara R Cingolani
Department of Physics, Universita Degli Studi Di Bari Bari Italy
Y Kunida, I Suemune
Faculty of Engineering, Hiroshima University, Higashihiroshima 724, Japan

We report measurement of time resolved photoluminescence from ZnSe/ZnSSe superlattices We observe an anomalous fast decay component in the luminescence at an energy corresponding to that at which stimulated emission is observed at highe pump densities From consideration of the lifetimes and spectral position of the lasing line we infer an excitonic scattering mechanism to be responsible for lasing in these samples

Introduction

Recent developments in the growth of II VI semiconductor heterostructures [1] have led to the fabrication of laser diodes operating at wavelengths in the green and blue [2] The physical processes which give rise to stimulated emission from these materials particularly in the low threshold lasers are not well understood and indeed are the subject of some controversy LO phonon assisted recombination [3] and excitonic inelastic scattering [4] have both been proposed as possible mechanisms In this paper we report pc time resolved photoluminescence measurements of stimulated emission and exciton dynamics in ZnSe/ZnSSe superlattices which have been shown to display low threshold lasing [5]

Experiment

The sample studied here is a 90-period ZnSe/$ZnS_{0.18}Se_{0.82}$ symmetric superlattice with 10nm layer widths grown on a GaAs substrate Electronic confinement for this ternary composition is not strong the conduction band offset is approximately 40meV while the valence band offset is 60meV [6] It is not clear yet whether the band alignment is type I or II [7] The exciton binding energy E_x = 19meV is of similar magnitude and so excitonic effects can be expected to play an important role in carrier dynamics and recombination

Photoluminescence was excited using a frequency doubled modelocked Ti:sapphire laser which produces a 76 MHz train of 150fs pulses at 400nm (3.1eV) with an average power of 150mW Luminescence was detected using a synchroscan streak camera and an intensified vidicon detector A subtractive dispersion double spectrometer with a bandpass of 1nm (7meV) was used to select different luminescence wavelengths The overall time resolution was 20ps The maximum carrier density generated in the time-resolved experiments was ~ $5x10^{17}cm^{-3}$ which is somewhat lower than that required for optically pumped lasing In order to study stimulated emission and time resolved spectra a frequency tripled Nd:YAG laser which produces a 10Hz train of 10ns pulses at 355nm (3.5eV)

The sample had cleaved faces forming a 800μm optical cavity Edge emission was monitored from a cleaved face the pump beam being focussed to a stripe 500μm x 200μm Neutral density filters were used to vary the excitation density while keeping the illuminated volume constant All of the measurements reported here were made with the sample mounted in a He gas flow cryostat with a base temperature of 8K

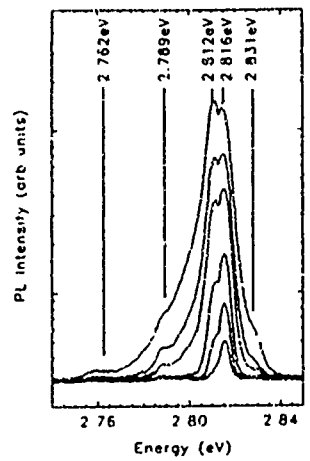

Figure 1 Edge emission spectra at pumping powers of 150 75 32 15 7.5 3.7mW focussed onto an area 200μm strip of the sample

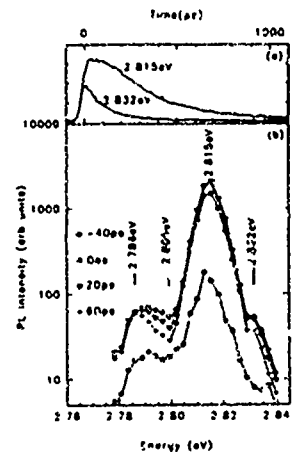

Figure 2 (a) Time resolved edge emission spectra at 8K (b) the time evolution of free and bound exciton recombination luminescence

Results

Time integrated edge emission measured at different excitation densities is presented in Fig 1 The dominant band (I) with peaks at 2.876 and 2.812eV is due to recombination of bound excitons these peaks correspond to the I_1 and I_2^0 peaks reported previously by Dabbicco and Lepore [6] The peak which develops on the high energy wing of the I band near 2.831eV is assigned to hot exciton recombination on the basis of the nonlinear dependence of its intensity on the excitation density At high excitation densities we detect weak recombination lines I_{LO1} at 2.789eV and I_{LO2} at 2.762eV the separation is close to the LO phonon energy (31meV) which suggests that the lines are phonon replicas of the bound exciton emission It is significant that the region between I and I_{LO1} fills in with increasing excitation density i.e. the luminescence intensity increases nonlinearly with the pump intensity The maximum carrier density generated here was ~$4x10^{17}cm^{-3}$ somewhat below the estimated Mott limit for this material ($10^{18}cm^{-3}$) and so is below the expected onset of stimulated emission

Time resolved spectra are shown in Fig 2 The I and I_{LO1} luminescence is weakly time dependent on the time scale of 600ps showing only a slight increase in intensity On the other hand the free exciton emission show a significant decrease in intensity on this timescale The inset to Fig 2 shows in more detail the temporal evolution of the signals the free exciton luminescence is prompt and decays on the time scale of 100ps the bound exciton signal rises for a longer time shows a plateau which extends for ~ 100ps, and then decays with a characteristic time of 250ps The duration of the plateau in the latter is a likely signature of free exciton trapping at defects More interesting however, is the behaviour of luminescence in the range I - I_{LO1} here the signal shows a relatively rapid decay on this time scale As we will show below stimulated emission occurs precisely in this spectral region

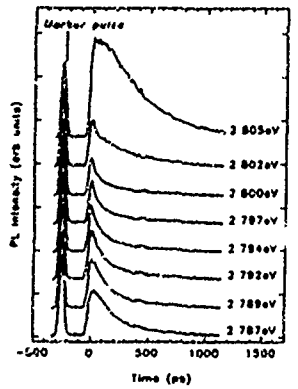

Figure 3 Time evolution of the PL signal in edge emission geometry at energies near the measured stimulated emission energy of 2 800eV

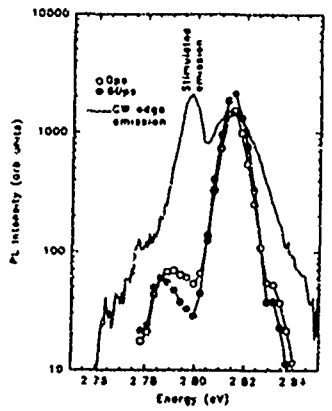

Figure 4 comparison of time resolved edge emission spectra and the quasi-CW edge emission spectrum, showing the above threshold stimulated emission line The latter was obtained with Nd YAG excitation

Fig 3 shows in more detail the time evolution of the signal at different energies in the range 2 787eV - 2 805eV where the fast recombination is observed At the upper and lower extremes the decay time is rather long, roughly equal to that of the I line (see Fig 2(a)) However, close to 2 80eV there is a very distinct fast component superimposed on the slower bound exciton recombination (the detection bandwidth here is 6meV) The rapid onset and decay of this component are very similar to that of the free exciton luminescence (see Fig 2 (a)) This observation is strongly suggestive that the recombination in this energy range originates from free excitons

Stimulated emission from the sample was measured under conditions of more intense excitation with long (10ns) laser pulses the laser intensity at the sample was ~100kWcm^{-2}, generating an estimated carrier density of 10^{18}cm^{-3} The time integrated luminescence spectrum presented in Fig 4 shows the I band together with strong stimulated emission at 2 80eV Also reproduced in the figure are the cw and 500ps time-resolved spectra obtained at lower excitation density, the comparison shows quite convincingly that the fast decay and the stimulated emission are related

Discussion

The time-dependence of the 2 80eV spontaneous emission (Fig 3) indicates that free excitons are involved since the temporal evolution of both signals are very similar The free exciton luminescence at 2 831eV(23meV) lies higher in energy by one LO phonon energy, which suggests that exciton scattering to the lower polariton branch by LO phonon emission is a possible mechanism However, the heavy hole exciton absorption peak in a similar sample has been measured to lie at 2 825eV [8], which would require that the luminescence involves hot exciton recombination, and that the phonon wavevector is approximately 3 82x10^{6}cm^{-1} The mechanism leading to stimulated emission, however, is not so clear not only must the optical field be coherent, but so also must the phonons Since the initial reports by Holonyak and co-workers [9] of lasing on phonon sidebands of electron-hole plasma recombination in GaAs it has not been possible to establish the presence of coherent nonequilibrium phonons, and so lasing mechanisms which involve phonon emission have remained in doubt

The results presented here clearly identify the energy for stimulated emission to lie in the low energy wing of the bound exciton luminescence. In addition to the possibility of free exciton phonon emission just mentioned, the obvious mechanisms for lasing involve the recombination of bound excitons, and free exciton-bound exciton scattering The first of these can most likely be ruled out on the basis of the low density of excited states, furthermore, the rate at which excitons can be trapped at the relevant sites is relatively slow, as we have seen above (Fig. 2), which further dictates against this mechanism An excitonic scattering mechanism in which the free exciton is ionised and the bound exciton recombines is energetically favourable, as the BE emission at 2 816eV lies approximately one exciton binding energy (19meV) above the 2 80eV emission However, it would seem that this process would saturate at high pump levels, determined by the trap density and exciton trapping kinetics Consequently, this excitonic mechanism would be expected to give way eventually to plasma formation and stimulated emission in the usual fashion So far this has not been observed

Conclusions

We have made time-resolved luminescence measurements of spontaneous emission in a $ZnSe/ZnS_{0.18}Se_{0.82}$ symmetric superlattice and found evidence of efficient exciton phonon-assisted recombination This emission occurs at the same energy as stimulated emission observed at much higher excitation density, which suggests that the lasing mechanism may involve exciton-phonon interactions

This work was supported by SERC in the UK and CNR in Italy

References

[1] Shahzad K, Olego D J, Van de Walle C G and Cammack D A 1990 *J Lumin* 46 109
[2] Nakanishi K, Suemune I, Masato H, Kuroda Y, and Yamanishi M 1990 *Japanese Journal of Appl Phys Part 2 Letters 29 Vol12*
[3] Nakanishi K, Suemune I, Fum Y, Kuroda Y, Yamanishi M 1991 *Appl Phys Lett* 59 1401
[4] Ding J, Jeon H, Ishihara I, Hagerott M, Nurmikko A V 1992 *Phys Rev Lett* 69 1707
[5] Shahzad K, Olego D J, Van de Walle C G 1988 *Phys Rev B* 38 1417
[6] Dabbicco M, Lepore M, Cingolani R, Scamarcio G, Ferrara M, Suemune I 1992 *Semicond Sci Technol* 7 681
[7] Landolt-Bornstein, Properties of II-VI & I-VII compounds, Semimagnetic Semiconductors p127
[8] Tommasi R, Lepore M, Nette K, *4th European Quantum Elect Conf* 1993 (to be published)
[9] Holonyak N, Kolbas R M, Dupuis R D, Dapkus P D, 1980 *IEEE J Quant Elect* QE-16 170

ThP7

STRAIN, CONFINEMENT, CARRIER DYNAMICS, AND HIGH DENSITY EFFECTS IN ZnSe/ZnMnSe-QUANTUM STRUCTURES

F Kreller, A Schulzgen, F Henneberger, J Puls, and U Streller

Humboldt-Universitat zu Berlin, Fachbereich Physik,
Sitz Invalidenstr 110 Unter den Linden 6, 10099 Berlin Germany

ABSTRACT

MBE grown ZnSe/ZnMnSe quantum structures are investigated using various spectroscopic techniques Conventional photoluminescence and excitation spectroscopy demonstrate an enhanced effective band offset due to tensile strain and a confinement induced shift of the excitonic resonances up to 100 meV Time-resolved luminescence reveals progressive localization of excitons on the 10 ps-time scale followed by rapid recombination within 100 ps Optical gain is observed under 400 kW/cm² excitation which is interpreted in terms of an eh-plasma

1. INTRODUCTION

Wide-gap II-VI semiconductor related quantum structures are very promising candidates for electro-optical and photonic devices operating in the blue-green spectral range Recent progress has occurred in heteroepitaxial and doping techniques, leading to profound improvement in material quality as well as proof-of-concept devices for blue-green light emitters in the ZnSe-based quantum well configuration [1, 2]

In this paper we focus on ZnSe/ZnMnSe quantum well structures Our aim is to study a binary quantum well with no alloy fluctuations In addition the emission wavelength can be tuned deeper into the blue range as compared with ZnCdSe/ZnSe mostly used until now for laser devices Early work on ZnSe/ZnMnSe structures was done by the groups of Brown and Pardue [3], but no systematic conclusions were achieved with respect to both growth perfection and optical properties

The structures of the present study were grown by molecular beam epitaxy on (001) GaAs substrates, on top of which a ZnSe buffer layer was first deposited Typically, a structure consists of 10 ZnSe quantum wells of the same thickness separated by about 100 nm wide ZnMnSe barrier layers The well widths studied range from 1 to 10 nm A manganese composition of 20 to 28 percent results in a total band offset of 90 to 120 meV [4] Steady-state photoluminescence (PL) and photoluminescence excitation (PLE) spectra demonstrate the reproducible growth of high quality type I quantum structures The low temperature PL spectra are dominated by a light hole (lh) emission band accompanied by a more or less distinct low energy shoulder which is typical for all quantum well samples investigated In the PLE spectra both the light and heavy hole (hh) exciton transitions are observed The FWHM of the excitonic resonances is on the order of 5 to 10 meV and a Stokes-shift between PL and PLE of 3 to 6 meV is found

2. STRAIN AND CONFINEMENT

In Fig 1 the energetic positions of the n=1 lh and hh exciton resonances for different well widths taken from PLE spectra are shown The data demonstrate the interplay between strain and confinement The structures are designed in a way (well width clearly smaller than both critical thickness and barrier width) so that the misfit induced strain is entirely and coherently assimilated by the ZnSe quantum well As the (001) lattice constant of ZnMnSe is the larger one this strain is tensile and for the present barrier composition (x=0.25) on the order of 5 to 10 ‰ A characteristic feature of a tensile in-plane strain situation is that the exciton resonances shift to lower energies and that the lh excitons occurs energetically below the hh one [5] As a consequence of this, the exciton structures of the larger wells in Fig 1 appear below the position of the ZnSe bulk exciton † Decreasing the well width the influence of the carrier confinement becomes increasingly important For the 1nm well a confinement induced high-energy shift of about 100 meV is found for the lh-exciton resonance

In consistency with the assignment based upon the above strain discussion the hh exciton with the heavier mass exhibits a weaker confinement shift so that the lh and hh structures eventually merge together for wells smaller than 2 nm A variational calculation of the lh and hh exciton energy using a trial function of the form [6]

$$\Phi_{ex} = \varphi_e(z_e)\,\varphi_h(z_h)\sqrt{\frac{1}{\pi a^3}}\,e^{-\frac{r_{eh}}{a}} \qquad (1)$$

(with a as parameter of variation) yields a reasonably good agreement with the experimental data The fit in Fig 1 relies on commonly accepted bandstructure parameters of ZnSe (γ_1=4.089, γ_2=1.404, m_e=0.16 m_0, ε_r=8.1, E_g=2.822 eV) and a total band offset of 70 meV between the unstrained materials taken from [4] We deduced from the calculation that 40 meV of this total offset stem from the conduction and 30 meV from the valence band The actual band offsets are enhanced by the strain The fit yields 5 meV for both electron and hh and 45 meV for lh, respectively Thus, the effective offset for the lh exciton of 120 meV is considerably larger than predicted without strain In addition to the offsets the calculation provides exciton parameters We find a maximum binding energy of 25 meV for d_z = 4.5 nm

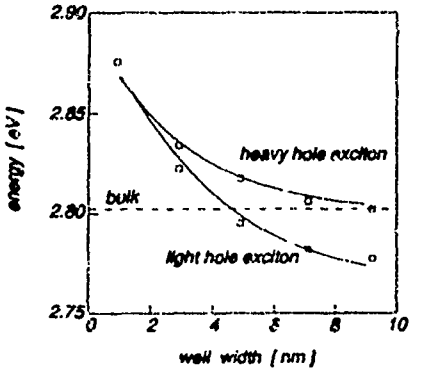

Fig 1 Energetic positions of the lh and hh exciton resonances deduced from PLE spectra of ZnSe/$Zn_{0.75}Mn_{0.25}Se$ MQWs at 5K ◻ experimental points, line calculation

† For superlattice structures of equal barrier and well width the exciton resonances occur at higher energies than those of the structures in Fig 1 with the same well width as an average strain across barrier and well is formed

3. TIME-RESOLVED PHOTOLUMINESCENCE

The exciton dynamics in the quantum structures are studied by time-resolved PL Tunable sub-ps pulses in the blue spectral range are used to excite eh-pairs resonantly at the transitions of the lh and hh exciton as well as in the barrier Decay curves at different spectral positions across the lh exciton band are recorded with a synchroscan streak camera yielding an overall time resolution after data deconvolution of 5 ps

The time behaviour of the lh exciton PL is practically the same for each of the three excitation wavelengths Thus, capture of the carriers by the well and subsequent relaxation into the lh exciton state is completed on a 1 ps-time scale In Fig 2 the rise and decay times for a sample of intermediate well width deduced from the PL decay curves are shown For comparison the time integrated PL measured under the same excitation conditions is given On the low-energy side of the lh exciton band a clearly resolved rise of the PL within some 10 ps is found followed by a decay within approximately 100 ps With increasing photon energy both time constants decrease continuously At the high-energy edge of the PL band the rise is not further resolved, whereas the decay time comes into the order of the rise time at the low energy tail We attribute this strongly inhomogeneous behavior to progressive localization of the excitons at barrier alloy fluctuations The interplay between spectral diffusion and rapid recombination leads to a non-thermal carrier distribution and causes the low energy structure in the steady-state PL lineshape of the lh exciton An exceedingly large radiative rate of the ZnSe quantum well is suggested by the 100 ps decay time A detailed study of the radiative yield is in progress

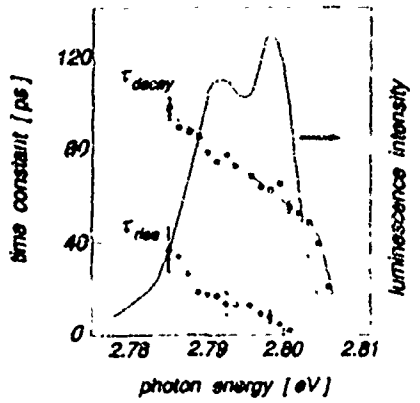

Fig 2 Left scale Photon-energy dependence of the PL rise and decay times of a MQW structure consisting of 10 periods of 5 nm ZnSe and 85 nm $Zn_{0.9}Mn_{0.1}Se$ layers Right scale Time-integrated PL

4. HIGH EXCITATION AND GAIN

Intensive sub-ns pulses from a dye laser are used to excite the samples in a quasi-steady state mode The emission signal is dispersed by a grating monochromator and subsequently detected with a MCP-photomultiplier

Spontaneous emission spectra were recorded in a backward geometry The data for the same sample used for the time-resolved measurements presented above are summarized in

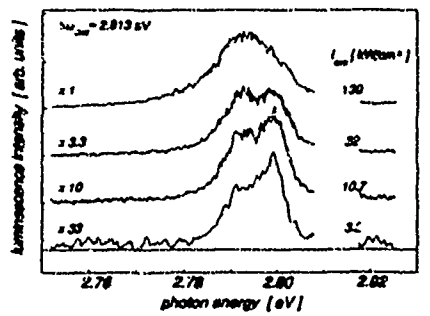

Fig 3 5K spontaneous emission spectra of the same ZnSe-MQW as in Fig 2 at various excitation intensities Excitation is at the hh exciton resonance

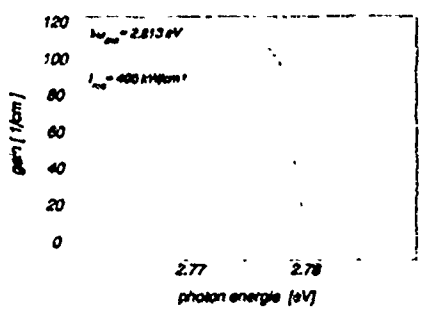

Fig 4 Gain spectrum of the same ZnSe-MQW sample as in Fig 3 obtained by the stripe-length method at 5K

Fig 3. For excitation intensities below 10 kW/cm² the spontaneous emission is very similar to the low-density (time-integrated) PL spectrum shown in Fig 2 Further increasing of the excitation intensity yields a growing contribution in the spectral range of the low-energy shoulder Simultaneously, the width of the structures increase At 130 kW/cm² only a broad band is seen with a pronounced low-energy tail For even higher intensities the spectra are distorted by stimulation effects

For gain measurements the method of stripe-length variation is applied [7] A rectangularly shaped spot of variable width l (50 350 μm) and fixed height (30 μm) is focused onto the sample at a cleaved edge along the natural (110) cleavage plane A typical unsaturated gain spectrum obtained at an excitation intensity of 400 kW/cm² is presented in Fig 4 The spectral gain is found to be very sharp with a FWHM of approximately 5 meV and a maximum value of 100 cm⁻¹

Different processes are known to explain stimulated emission at low temperatures in wide gap II-VI compounds At intermediate intensities exciton-phonon and exciton-exciton scattering processes dominate, whereas above the Mott-transition the gain is due to the population inversion in the degenerated eh-plasma Recently, it was shown that also excitons localized at alloy composition fluctuations in ternary quantum wells can give rise to gain at intermediate densities [8] Taking into account the carrier lifetime of about 100 ps determined above and an absorption coefficient of 10^5 cm⁻¹ an eh-pair density of $3 \cdot 10^{17}$ cm⁻³ is estimated at the excitation intensity used in the present gain studies This value is clearly above the Mott-density and a

renormalized bandgap of 2.768 eV follows from the theory [9]. The ... rather well with the low-energy onset of the gain spectrum, which supp... of the gain in terms of an eh-plasma.

In conclusion, the present study has demonstrated that the ZnSe/ZnMnSe system provides high-quality type-I quantum structures with robust confinement. We have observed exciton localization and very rapid recombination within 100 ps. Stimulated emission related to an eh-plasma yields gain in 100 cm^{-1} range.

Acknowledgements – The authors thank M. Hoffmann, J. Griesche, K. Jacobs for cooperation in the MBE growth. This work was partly supported by the Deutsche Forschungsgemeinschaft.

REFERENCES

1. M. A. Haase, J. Qiu, J. M. DePuydt and H. Cheng, *Appl. Phys. Lett.* **59**, 1272 (1991).

2. H. Jeon, J. Ding, W. Patterson, A. V. Nurmikko, W. Xie, D. C. Grillo, M. Kobayashi and R. L. Gunshor, *Appl. Phys. Lett.* **59**, 3619 (1991).

3. L. A. Kolodziejski, R. L. Gunshor, N. Otsuka, S. Datta, W. M. Becker and A. V. Nurmikko, *IEEE J. Quantum Electronics* **QE-32**, 1666 (1986).

4. R. L. Gunshor, L. A. Kolodziejski, N. Otsuka and S. Datta, *Surf. Sci.* **174**, 522 (1986).

5. G. L. Bir and G. E. Pikus, *Symmetry and Strain-Induced Effects in Semiconductors*, Wiley, New York (1974).

6. G. Bastard, *Wavemechanics Applied to Semiconductor Heterostructures*, Les editions de physique, Les Ulis, France (1988).

7. K. L. Shaklee and R. F. Leheny, *Appl. Phys. Lett.* **18**, 475 (1971).

8. J. Ding, H. Jeon, T. Ishihara, M. Hagerott, A. V. Nurmikko, H. Luo, N. Samarth and J. Furdyna, *Phys. Rev. Lett.* **69**, 1707 (1992).

9. S. Schmitt-Rink, D. S. Chemla and D. A. B. Miller, *Adv. Phys.* **38**, 89 (1989).

ThP8

PbSrS MQW LASERS AND THE EFFECT OF QUANTUM WELL ON OPERATION TEMPERATURE

A. Ishida, A. Sakurai*, K. Aikawa, and H. Fujiyasu
Faculty of Engineering, Shizuoka University,
Johoku 3-5-1, Hamamatsu 432, Japan
*Graduate School of Electronic Science & Technology,
Shizuoka University, Johoku 3-5-1, Hamamatsu 432, Japan

Abstract- Very few studies have been performed for IV-VI narrow gap semiconductor quantum well lasers especially for the laser with small well width, probably owing to the large diffusion of the constituents. In narrow gap semiconductor, it is considered that the free carrier absorption strongly affects the laser operation as well as Auger recombination, and that the multiple quantum well structure is very effective increasing the maximum operation temperature. We prepared PbSrS/PbS multiple quantum well (MQW) lasers with well width as large as 100Å using the *hot wall epitaxy technique*. The laser properties are compared with that of PbSrS/PbS and PbSrS/PbSrS DH lasers. The MQW laser showed small threshold current compared with that of DH laser, and pulsed laser operation was obtained up to 255k (2.80 μm). The operation temperature is the highest ever reported for PbS based semiconductor lasers. In this paper, properties of the PbSrS MQW lasers and effects of the quantum well on the laser properties, especially on the operation temperature, are discussed.

I. INTRODUCTION

IV-VI compounds are narrow gap semiconductors with the direct gap at L point in the brillouin zone. Various lasers have been prepared using the IV-VI compounds[1-5]. Band gaps of the PbSnTe and PbSnSe decrease with the Sn content, and they have been used as lasers of 6-20 μm range. Operation temperature of these lasers were usually less than 200K, owing to the large Auger recombination probability and strong free carrier absorption in the narrow gap semiconductors and also poor carrier confinement.[6] Recently, PbEuTe, PbSrSe, and PbSrS lasers have been reported[7-10]. The band gap of the film increases very rapidly with the Eu or Sr content, and they are very useful for cladding layers of the PbTe, PbSe, or PbS lasers. These lasers can cover the wavelength range of 2-8 μm[10-12], and many of the lasers operate above 200 K in pulsed condition owing to the effective carrier confinement and relatively small Auger recombination. However, room temperature operation is difficult owing to some large loss mechanisms of light and carrier in the narrow gap semiconductors. The multiple quantum well structure is considered to be very effective to increase the maximum operation temperature, because relatively small injected carrier density is needed to obtain population inversion and large optical gain, which exceeds strong free carrier absorption in the narrow gap semiconductor, is obtained by the MQW structure.

In this paper, first we describe and discuss operation condition of the DH and MQW lasers, then preparation and properties of the MQW and DH lasers are described and the effect of the quantum well on the operation temperature are discussed.

2. OPERATION CONDITION OF PbSrS DH and MQW LASERS

Figure 1 shows the joint density of states D(hν) and gain g(hν) of the PbSrS/PbS DH (a) and MQW (b) lasers at 300K. For the joint density of states of the MQW laser conduction band offset was assumed to be equal to that of valence band, and 1 μm thick optical confinement layer with 10 periods of PbSrS(200Å) / PbS (100Å) MQW active layer was assumed. In the gain calculation all the light was assumed to be confined in the optical confinement layer, so the real gain is somewhat smaller than this value. DN(hν) in the Fig.1 shows the joint density of states in which corresponding conduction band states are filled with electrons: The integral of the DN(hν) with respect to the photon energy hν represents electron concentration in the conduction band. Hole concentration was assumed to be equal to that of the electron in this gain calculation. In Fig.1 (a), the carrier concentration in the active layer is $6.5\times10^{18}cm^{-3}$, and the optical gain expected is as high as $300cm^{-1}$. In the narrow gap semiconductor main optical loss is free carrier absorption which can be estimated by the equation below:[6]

$$=q^3\lambda^2/4\pi^2\varepsilon_\infty^{1/2}c^3\xi_0 \propto (p/\mu_p m_{ch}^2+n/\mu_n m_{ce}^2). \quad (2)$$

where μ_p and μ_n are the mobility of the electron and hole, and the m_{ch} and m_{ce} the conductivity effective mass of the holes and electrons, respectively. The free carrier absorption is proportional to the carrier concentration and wavelength squared, and inversely proportional to the mobility. Free carrier absorption is calculated to be around 250 cm^{-1} for the electron and hole pairs shown in Fig.1(a) using the Eq.(1). Real free carrier absorption seems to be somewhat larger than this value, and it is understood that very high concentration carriers are needed obtaining sufficient optical gain. In calculating threshold current of the laser, life time of the carrier should be considered. Life time of the spontaneous emission of the PbS is about 1×10^{-8}s, and real life time of the carrier is much shortened by a carrier loss mechanism such as the Auger recombination, which increases strongly with temperature and carrier concentration. Taking the life time of the carrier as 1×10^{-9}s, and active layer thickness as 1um, the threshold current of the PbSrS/PbS DH laser becomes as high as 100kA/cm^2 at room temperature. For the MQW laser, carrier concentration needed to the laser operation is strongly decreased by the two-dimensional density of states as shown in Fig. 1 (b). In the model, band gap difference between PbS quantum well and PbSrS barrier or PbSrS optical confinement layer is assumed to be 170meV, and optical gain as high as $100cm^{-1}$ can be obtained by the carrier concentration of only 2.3×10^{18} cm^{-3}. It should be noted that only 7×10^{17} cm^{-3} of electrons are in the quantum well and the rest is overflowing to optical confinement layer. The ratio of the overflowing carriers to the carriers in the quantum well increases with the decrease of the number of quantum wells. Maximum gain obtained from one quantum well is as high as $120cm^{-1}$[13], and the gain for the single quantum well laser becomes very small increasing only overflowing current. Thus it is understood that the MQW structure is very effective for the laser with large free carrier absorption, and that the single quantum well laser is not effective for the narrow gap semiconductor laser with the large optical losses.

3. PREPARATION AND PROPERTIES OF PbSrS/PbS LASERS

Figure 2 shows the PbSrS/PbS multiple quantum well laser structure prepared. On p-type PbS substrate, PbS layer (2μm) and $Pb_{0.97}Sr_{0.03}S$ cladding layer (2μm), $Pb_{0.98}Sr_{0.02}S$ layer (0.35μm) for optical confinement and MQW active layer (0.3μm), which consists of 10 periods of $Pb_{0.98}Sr_{0.02}S$(200Å)/PbS(100Å) SL, were prepared. On the active layer, $Pb_{0.98}Sr_{0.02}S$ layer

(0.35μm) and $Pb_{0.97}Sr_{0.03}S$ cladding layer (2μm) were prepared successively. The room temperature band gap of the PbS is 410 meV. band gap of the cladding layer is 660meV, and that of the optical confinement layer is 580meV. Laser structure prepared is stripe contact laser with stripe width of 50μm and length of 300-400μm. Pulsed laser operation was measured for the laser with 1μs pulse width and 250Hz repetition. Figure 3 shows the dependence of the threshold current of the MQW laser (closed circle). $Pb_{0.97}Sr_{0.03}S$/PbS (open circle) and $Pb_{0.97}Sr_{0.03}S$/$Pb_{0.99}Sr_{0.01}S$ DH lasers (square for undoped active layer, and triangle for doped active layer) The PbSrS/PbS DH laser has PbS active layer of 0.5μm and this is the one which showed highest operation temperature[9] The thickness of the $Pb_{0.97}Sr_{0.03}S$ active layer of PbSrS/PbSrS DH laser is also 0.5 μm, and doping level of the doped p-type PbSrS active layer is the order of 10^{18} cm^{-3} Threshold current of the lasers with PbSrS active layer becomes somewhat higher than that of PbS active layer, and significantly increase for the laser with doped active layer This is considered to due to the free carrier absorption in the low mobility PbSrS active layer Since the mobility of the carrier strongly decreases with Sr content[11], the free carrier absorption effect becomes also important in the cladding layer of the DH laser and optical confinement layer in the MQW laser. For the MQW laser significant decrease of the threshold current was observed as expected and laser operation was observed up to 255K, which is the highest operation temperature ever reported for the PbS based lasers

Figure 4 shows the output photon energy of the MQW and DH lasers. Output photon energy of the PbSrS/PbS DH laser is about 20meV higher than the band gap of unstrained PbS This is due to the strain caused by the lattice mismatch between PbSrS cladding and PbS active layers[13] At high temperature, difference between heat sink and active layer is somewhat affecting the deviation of the output photon energy. Dashed line in the figure shows the energy between first conduction and valence subbands calculated for the MQW structure without strain Tensile strain of the PbS quantum well layer is increasing the band gap also. It should be noted that the temperature dependence of the output photon energy for the MQW laser and PbSrS laser with doped active layer is somewhat different from the others. Since the threshold current of the PbSrS laser with doped active layer is very large, this is considered to be due to the temperature difference between heat sink and the active layer For the MQW laser, hole and electron effective masses increase with the temperature as the band gap increases Thus the output photon energy of the MQW laser increases somewhat slowly compared with the band gap increase of the PbS bulk

In this experiment clear decrease of the threshold current was observed for the MQW laser, and significant increase of the operation temperature is expected for MQW lasers if optimum laser structure is taken From the threshold current densities of the PbSrS/PbS DH and MQW lasers, it is also estimated that the life time of the minority carrier is as high as 5×10^{-9}s

below 200k and the lifetime seems to be decreasing rapidly with the temperature above 200K. Free carrier absorption becomes significant at high temperature, but the absorption only can not explain the rapid increase of the threshold current. Other mechanism such as Auger recombination or recombination through crystal imperfection should be considered combined with the free carrier absorption. In our calculation band offsets of the conduction and valence band edges are assumed to be equal Real heterojunction may have different band offsets, so effect of the carriers overflowing to the cladding layer may also affecting the threshold current at high temperature

4. SUMMARY

PbSrS/PbS MQW laser was prepared by hot wall epitaxy, and pulsed laser operation was obtained up to 255K (2.80μm) This laser was compared with that of PbSrS/PbS and PbSrS/PbSrS DH lasers, and clear decrease of the threshold current was observed In the IV-VI compound laser, it was shown that the free carrier absorption becomes one of the main loss mechanism, and the MQW laser is useful for the reduction of the threshold current because the MQW structure gives large gain with relatively small carrier concentration injected

Acknowledgement- We would like to thank Mr K Matsushita for preparing PbS single crystal for the laser preparation

REFERENCES

1. H Preier, M.Bleicher, h.Riedel and H.Maier, Appl.Phys. lett. 28,669(1976)
2. J.N.Walpole, A.R.Calawa, T C.Harman and S H.Groves, Appl. Phys. lett. 28,552(1976).
3. K Shinohara, Y.Nishijima, H.Ebe, A.Ishida, and H.Fujiyasu, Appl.Phys lett.,47,1184(1985).
4. A.P.Shotov and Yu.G.Sellyanov, JETP Lett.,45,3(1987).
5. Y.Nishijima, J.Appl.Phys. 65,935(1989).
6. W.W.Anderson, IEEE J.Quantum Electron. QE-13,532(1977).
7. D.I.Partin, Superlattices and microstructures, 1,131(1985)
8. H Spanger, P.Schie▮l, A.Taabrecht, H.Böttner and M.Tacke, Appl. Phys. Lett. 53,2582(1988).
9. A.Ishida, K.Muramatsu, H.Takashiba and H Fujiyasu, Appl. Phys.Lett. 55,430(1989).
10. M.Tacke B.Spanger, A.Lambrecht, P.R.Norton and H.Böttner, Appl.Phys.Lett.,53,2260(1988).
11. D.L.Partin and C.M.Thrush, Appl.Phys.Lett., 45,193(1984).
12. S.Mohammadnejad, K.Afkasa, A.Ishida, and H.Fujiyasu, Jpn.J.Appl. Phys. 32,1658(1993).
13. A.Ishida, Y.Sase, T.Okamura, H.Fujiyasu, Y.Nishijima, and K.Shinohara, Superlattices and Microstructures, 6,27(1989).
14. A.Ishida, K.Muramatsu, K.Ishino, and H.Fujiyasu, Semicond Sci.Technol.5 S331(1990).
15. H.Böttner, P.Schie▮l, M.Tacke, Superlattices and Micro structures 7, 97(1990).

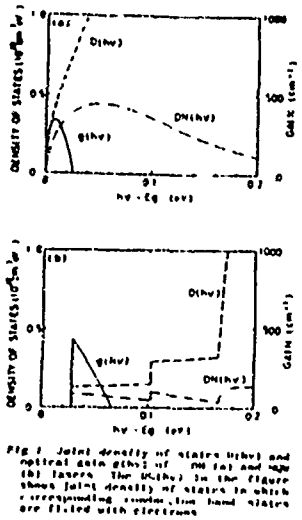

Fig.1 Joint density of states D(hν) and optical gain g(hν) of (a) DH (a) and MQW (b) lasers. The D(hν) in the figure shows joint density of states in which corresponding conduction band states are filled with electrons

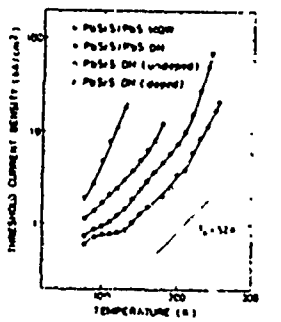

Fig.3 Threshold current densities of the PbSrS/PbS MQW laser (closed circle) PbSrS/PbS DH laser (open circle) and PbSrS/PbSrS DH lasers with undoped active layer (square) and doped active layer (triangle) as a function of temperature

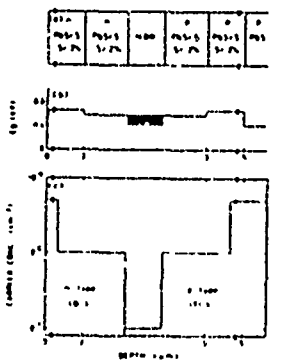

Fig.2 Structure (a) band gap profile (b) and doping profile (c) of the MQW laser prepared

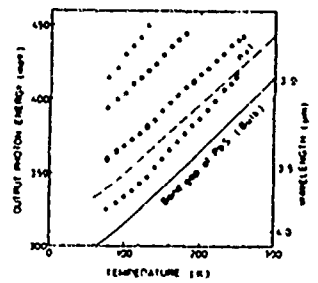

Fig.4 Dependence of the output energy of the PbSrS/PbS MQW (●), DH (▲) and PbSrS/PbSrS DH (■) lasers on temperature. Each symbols are in agreement with that of Fig.3

ThP9

Electronic structure of thin Si layers in CaF_2: hybridization versus confinement

A. Fasolino, Stefano Ossicini, F. Bernardini
Dipartimento di Fisica, Università di Modena, Via Campi 213/A, 41100 Modena, Italy

ABSTRACT

We present first principle calculations of thin (1-7 double layers) silicon (111) layers in CaF_2, a system with strong analogies to porous silicon. We show that the Si band gap opening is dominated by the valence band which follows the effective mass confinement picture, while the conduction band is found to flatten and shift very modestly due to hybridization effects between Si and Ca states which lead to bonding-antibonding interface states in the gap The relevance of these results for Si based low dimensional structures is discussed

The observation of *bright, visible light emission from porous Si [1] has* stimulated experimental [2] and theoretical effort [3-11] to understand both the energy shift and the increased efficiency of luminescence in porous Si, and in general of laterally confined Si structures, with respect to bulk Si. In fact, bulk Si has a 1.1 eV indirect gap resulting in luminescence in the near infrared with very low efficiency

All theoretical approaches, ranging from the effective mass approach [3] to tight binding [4-5] to ab initio LDA treatments [7-11], give a qualitative account of the shift of the band gap from the near infrared to the visible range as due to confinement and an enhancement of the dipole matrix element for radiative transitions resulting from the better overlap of confined wavefunctions. However, even assuming the persistence of crystalline order, both the *energy spectrum and the dipole matrix elements for radiative transitions* strongly depend on the model geometry chosen to represent porous Si The increase of luminescence efficiency has been attributed to the presence of a dipole allowed direct gap present in the energy spectrum of (100)-oriented wires [7-9]. The very recent observation of phonon assisted transitions in the photoluminescence of porous silicon [12] seems to contradict the hypothesis of a direct gap and of a columnar shape of the crystallites

The main problem for a quantitative description of porous Si is the still not characterized microscopic structure and shape This is why we have chosen to address the problem of Si crystallites embedded in CaF_2, as prototype of a Si-based system with known microscopic structure [13,14] Moreover, preliminary evidence of visible luminescence from Si layers in CaF_2 *has been reported* [15]

We show that the energy spectrum of Si layers is affected both by confinement and by hybridization effects with the saturating agent, be it the Ca atoms in our case and H or O in porous silicon Our results are compatible with the observation of luminescence in this system, since the band gap energy is found to increase for decreasing slab size Moreover, hybridization of the Si p-states with the Ca s-d-states leads to a high joint density of states all over the Brillouin zone

We present first principle calculations, performed by the Linear Muffin Tin Orbital method in the Atomic-Sphere Approximation (LMTO ASA) within the local density approximation (LDA), of the band structure of thin (1-7 double layers (dL's)) Si(111) slabs in CaF_2 CaF_2 is a good insulator, with a $\sim$ 12 1 eV band gap; crystalline CaF_2 and Si have similar fcc structures, with a room temperature lattice mismatch of only 0 6 %, allowing the growth of high quality epitaxial layers. The LMTO-ASA method has proven to describe correctly the interface properties of this system [13]. Due to the LDA we underestimate the energy gap: we obtain 0.56 eV and 6.96 eV for Si and CaF_2 respectively. We use supercells formed by thin Si layers of variable thickness and by CaF_2 layers large enough to make the central CaF_2 planes exhibit bulk-like properties. As shown in Fig 1, the first monolayer of CaF_2 looses half of its fluorine atoms leading to a Ca Si bond at the interface. The interface Ca atoms occupy the T_4 sites, the triangular filled sites on top of the *second layer Si* atoms, while the F atoms are located on the H_3 sites, the triangular hollow sites on top of the fourth layer Si atoms. We use the lattice constant of CaF_2 except for the interfacial Si-Ca distance, which is taken to be 3 15 Å The experimental Ca-Si bond length is $\sim 3\,1 \pm 0\,1$ Å [16,17]

In fig. 2 we show the calculated band structure for 2 and 4 dL's of Si in CaF_2 compared to that of bulk Si By taking the slab thickness as that between the Ca atoms on the two interfaces, the thicknesses of 2 and 4 dL's are 3 7 and 14 9 Å respectively. We show the bands projected along the Γ-M and Γ-K symmetry directions of the hexagonal two-dimensional Brillouin zone (BZ) of the (111) surface and along the (111) direction perpendicular to the surface BZ. The bulk BZ direction Γ-X, where the minimum of the Si conduction band occurs, is now projected along the Γ-M direction.

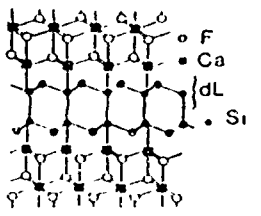

Fig. 1 Structural model for the Si CaF_2 interface; 1 dL is indicated.

Fig. 2 Band structure projected along two symmetry directions of the hexagonal two-dimensional Brillouin zone (BZ) of the (111) surface (Γ-M and Γ-K reaching *out one corner* and the middle of one side of the hexagon respectively) and along the (111) direction perpendicular to the surface BZ, indicated as z, for 2 dL Si 4dL Si in CaF_2 and bulk Si respectively Energies (in eV) are referred to the valence band maximum

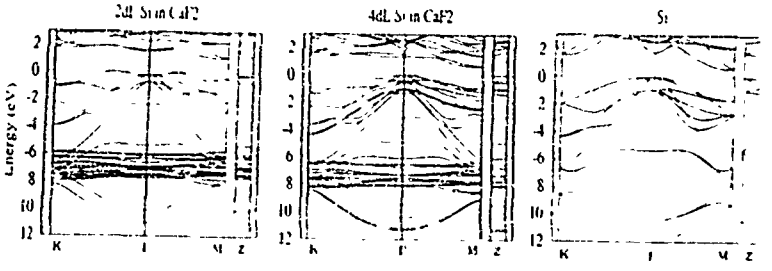

It can be seen that major changes occur in the energy region around the gap, in particular, the band gap increases and the width of the lowest conduction band is largely reduced. Even for thicker slabs, the bulk-like situation is not recovered: in fact interface states appear just below the conduction band at Γ and in the valence band region. The latter becomes the highest energy valence band state at finite wavevectors. These interface states are the bonding-antibonding states resulting from the Ca-Si bonds. In particular, at Γ, the bonding state has an upward curvature, since it results from an hybridization of the s-d-states of the Ca atoms (which constitute the conduction band of CaF_2) with the valence p-states of Si. It should be noted that the Si-Ca bond at the interface is somewhat intermediate between the covalent Si-Si bond and the ionic Ca-F bond. Therefore, the bonding-antibonding states are not removed from the gap as in the case of H-saturated Si structures. The H-Si bond, being mostly covalent, gives rise instead to a much larger bonding-antibonding energy separation and pushes the interface states inside the Si valence and conduction bands [18]. The Ca-Si bonding-antibonding interface states have a finite dispersion along the (111) growth direction, contrary to those related to the Si valence band which, as expected for confined states, are completely flat. Further evidence of the interface character of these states and of the confined nature of the state related to the bulk valence band comes from the calculated wavefunction along the (111) growth direction shown in Fig. 3.

Fig. 3 Squared amplitude of the wavefunction along the (111) growth direction. The dots indicate the position of the Si planes. The envelope is obtained by dressing the squared amplitude of the wavefunction on each plane (indicated by the vertical bars) with a Gaussian two inter plane spacing wide. Top panels: Double degenerate top valence state at Γ for 1, 2, 4 dL's Si in CaF_2. Note the confined character. Middle panels: same for the upper valence interface state at Γ. This state is spread both over the Si layer and the interface. Lower panels: same for the lowest conduction state at Γ. Note the pronounced interface character.

The previous results show that both hybridization and confinement play a role in the opening of the gap in laterally confined Si slabs. We can distinguish the two contributions by taking advantage of the possibility given by the LMTO method of fixing a single energy scale for all calculations. In Fig. 4, we have aligned the results for the different embedded (1-7 dL's) Si slabs by using the fluorine 2s core levels as a zero of energy. It can be seen that the opening of the gap is largely dominated by the Si valence band, which shifts to lower energies for thinner layers. The energy shift with layer thickness compares very well with that calculated within the effective mass theory, by taking the heavy hole mass as 0.281 m_0 for bulk Si, 0.3 m_0 in CaF_2 and a valence band offset of 0 eV, values estimated from LMTO calculations.

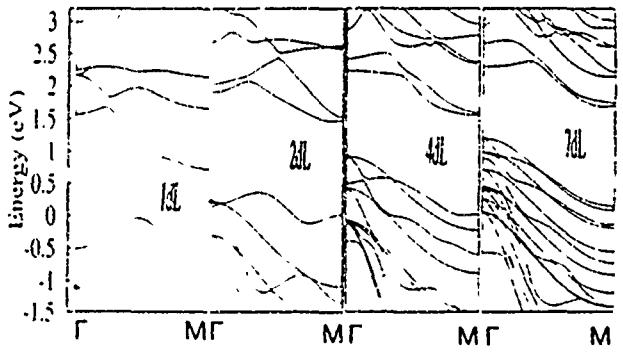

Fig. 4 Band structure along the Γ-M symmetry direction of the two-dimensional hexagonal (111) BZ on a single energy scale (see text) for 1 dL's, 2 dL's, 4 dL's and 7 dL's Si in CaF_2. The band gap opening is dominated by the confinement induced shift of the valence band of Si evidenced by dots.

Therefore, the quantum confinement picture accounts for the great part of the blue shift of the gap. The lowest conduction band level, instead, is dominated by hybridization effects which affect the dispersion, flattening it out; the symmetry properties, lifting the zone boundary degeneracy, and altering the original character, leading all over the BZ to a mixed s-p-d state with strong matrix element with both the Si valence band edge, and the interface bonding state which emerges, for thinner layers, from the Si valence band to become the highest occupied level.

In conclusion we have calculated the electronic properties of thin Si(111) slabs in CaF_2, a system which, due to its well characterized structure, is an ideal testing ground for experimental/theoretical comparisons. We have shown that, for laterally confined Si slabs,

confinement effects dominate the Si band gap opening, while Si-Ca hybridization effects lead to dipole allowed optical transition all over the Brillouin zone. These findings are compatible with the observation of visible luminescence in the Si-CaF_2 system. A more detailed calculation of dipole matrix elements for optical transitions is in progress. We hope that our results will also stimulate further experimental work on this system.

Acknowledgements: This work has been carried out within the European projects ESPRIT III n. 7220 EOLIS (S.O. and F.B.) and n. 7260 SOLDES (A.F.).

[1] L.T. Canham, Appl. Phys. Lett. 57, 1046 (1990);

[2] for a recent review see L.T. Canham in "Optical Properties of Low Dimensional Silicon Structures" ed. by D. Bensahel, L. T. Canham and S. Ossicini, Plenum Press, New York 1993

[3] M. S. Hybertsen, Mater. Res. Soc. Proc. 236, 179 (1992)

[4] J.P. Proot, C. Delerue, and G. Allan, Appl. Phys. Lett. 61, 1948 (1992)

[5] S. Y. Ren and J. D. Dow, Phys. Rev. B 45, 6492 (1992)

[6] G. D. Sanders and Y. C. Chang, Phys. Rev. B 45, 9202 (1992)

[7] A.J. Read, R. J. Needs, K. J. Nash, L.T. Canham, P. D. J. Calcott, and A. Qteish, Phys. Rev. Lett. 69, 1232 (1992)

[8] F. Buda, J. Kohanoff, and M. Parrinello Phys. Rev. Lett. 69, 1272 (1992)

[9] T. Ohno, K. Shiraishi, and T. Ogawa, Phys. Rev. Lett. 69, 2400-2403 (1992)

[10] F. Koch, V. Petrova-Koch, T. Muschik, A. Kux, F. Muller, V. Gavrilenko, F. Moller, Proc. 21st ICPS World Scientific (1993) in press

[11] C.G. Van de Walle and J.E. Northrup, Phys. Rev. Lett. 70, 1116, (1993)

[12] P. D. J. Calcott, K. J. Nash, L. T. Canham, M. J. Kane, and D. Brumhead, J. Phys. Condens. Matter 5, L91 (1993)

[13] S. Ossicini, C. Arcangeli, and O. Bisi, Phys. Rev. B 43, 9823 (1991), Surface Sci. 269/270, 743 (1992)

[14] J.C. Alvarez, K. Hirano, A. Yu. Kazimirov, M. V. Kovalchuk, A. Ya. Kremnev, N.S. Sokolov, and N.L. Yakoviev, Semicond. Sci. Technol. 7, 1432 (1992)

[15] A. P. Taylor, K. Stokes, P. D. Persons, L. J. Schowalter, and F. K. Legoues, Proceedings of MRS Conference (1992) Boston (USA), to be published

[16] R. M. Tromp and M. C. Reuter, Phys. Rev. Lett. 61, 1756 (1988)

[17] J. Zegenhagen and J. R. Patel, Phys. Rev. B 41, 5315 (1990)

[18] M. Buongiorno Nardelli, F. Finocchi, M. Palummo, R. De Felice, C. M. Bertoni, F. Bernardini, and S. Ossicini, Surface Sci. 269/270, 879 (1992)

ThP10

COULOMB ATTRACTION IN OPTICAL SPECTRA OF QUANTUM DISCS

B. Adolph, S. Glutsch and F. Bechstedt
Friedrich-Schiller-Universität, Max-Wien-Platz 1, 07743 Jena, Germany

Abstract

We present a theory which describes the influence of the Coulomb interaction on the optical spectra of quantum discs within the envelope function formalism. Starting from a non local Elliott formula luminescence is traced back to two particle wave functions and energies. They are solutions of the corresponding Schrödinger equation for an electron hole pair under the influence of the Coulomb attraction and confinement potentials determined by the spatial variation of the band edges of the considered microstructure.

1. Introduction

Novel crystal growth techniques together with nanometer lithographic techniques have made it possible to fabricate various semiconductor microstructures among them quasi 0D quantum dot systems. One interesting preparation technique is the focussed laser-beam induced thermal cation interdiffusion of narrow quantum well structures[1], whereby the form of the written laser lines determines the lateral shape of the resulting flat microstructure.

The spectroscopy of optical interband transitions across the band gap is a powerful tool to study these systems. In particular, photoluminescence spectra are governed by efficient intrinsic radiation of free excitons and exhibit a superior optical performance[1,2]. Studying the development of the corresponding line spectra one can learn somewhat about the mutual interaction of excited electrons (e) and holes (h) and its interplay with the vertical and lateral confinement potentials.

In this paper flat cylindrical quantum dots are studied. We solve the exciton problem for the ground state as well as excited states completely numerically. The solutions for wave functions and energies are used to calculate the exciton luminescence for flat dots i.e. discs, which has been observed recently[1]. In Sec. 2 the basic equations are given. The explicit solution of the electron hole problem in single quantum discs is described for different det confinements. We discuss exciton energies, wave functions and oscillator strengths versus the disc radius. Optical spectra are explicitly calculated in Sec. 4. The

variation of the shape of the spectra with the disc radius is discussed. The results are compared with recent luminescence measurements for discs fabricated by laser induced cation interdiffusion of narrow quantum wells.

2. Theory

For systems, for which the spatial variation of the photon propagator may be neglected, the optical properties can be expressed in terms of a frequency dependent optical susceptibility $\chi(\omega)$. It follows from the corresponding nonlocal function by two space integrations. The space dependent optical function can be directly related to the electron hole pair wave functions $\Phi_\nu(\mathbf{x}_e, \mathbf{x}_h)$ and energies E_ν, with ν as the complete set of quantum numbers for the two particle problem

$$\chi(\mathbf{x}, \mathbf{x}', \omega) = \frac{2}{\varepsilon_0} |\mu|^2 \sum_\nu \frac{\Phi_\nu(\mathbf{x}, \mathbf{x}) \Phi_\nu^*(\mathbf{x}', \mathbf{x}')}{E_\nu - \hbar\omega - i\Gamma_\nu} \tag{1}$$

ε_0 denotes the vacuum dielectric constant and Γ_ν indicates a certain damping of the electron hole pairs.

In the framework of the effective mass approximation and masses $m_e(m_h)$ of electrons (holes) the electron hole pairs obey a Schrödinger equation of the form

$$\left\{ E_g + \sum_{i=e,h} H_i(\mathbf{x}_i) - \frac{e^2}{4\pi\varepsilon\varepsilon_0 |\mathbf{x}_e - \mathbf{x}_h|} \right\} \Phi_\nu(\mathbf{x}_e, \mathbf{x}_h) = E_\nu \Phi_\nu(\mathbf{x}_e, \mathbf{x}_h). \tag{2}$$

where $H_i(\mathbf{x}_i)$ $(i = e, h)$ are the single particle Hamiltonians for electron and hole. E_g denotes the energy of the allowed optical transition in the underlying bulk material and ε is the relative static dielectric constant.

Following the preparation method described in Refs. 1 and 2 we can assume strong confinement in growth (z) direction. Therefore its sufficient to study only the most interesting spectral region of the first heavy hole to conduction band transition. As a result, the pair equation (2) can be rewritten for excitons in the xy plane with the quasi 2D Coulomb potential $v(\mathbf{r}) = -e^2/(4\pi\varepsilon\varepsilon_0 r)\,\mathrm{erf}(\alpha_{eh} r)$ with α_{eh} as the effective width of the underlying quantum well. Using center of mass (cm) and relative (rel) coordinates $(\mathbf{R}, \mathbf{r})$, E_g^{2D} as the energetical distance of first heavy hole and first electron well subband and a reduced set of quantum numbers λ the Schrödinger equation for the pair motion in the x,y plane follows from Eq. (2) to be

$$\left\{ E_g^{2D} - \frac{\hbar^2}{2M_0} \nabla_R^2 - \frac{\hbar^2}{2m_0} \nabla_r^2 + H_e(\mathbf{R} + \frac{m_h}{M_0}\mathbf{r}) + H_h(\mathbf{R} - \frac{m_e}{M_0}\mathbf{r}) + v(r) \right\} \Phi_\lambda(\mathbf{R}, \mathbf{r}) =$$

$$E_\lambda \Phi_\lambda(\mathbf{R}, \mathbf{r}) \tag{3}$$

With the dipole matrix element $|\mu|$ the optical susceptibility $\chi(\omega)$ can be written as a sum over oscillators

$$\chi(\omega) = \frac{2}{\varepsilon_0 A} |\mu|^2 \sum_\lambda \frac{f_\lambda}{E_\lambda - \hbar(\omega + i\Gamma_\lambda)} \quad \text{with} \quad f_\lambda = \left| \int d\mathbf{r}\, \Phi_\lambda(\mathbf{R}, 0) \right|^2 \tag{4}$$

In the quasi 0D case expression (4) replaces the Elliott formula well known for the 3D and 2D cases.

The excitons are considered to be optically excited in an isolated flat cylindrical quantum dot of characteristic lateral radius r_0, usually consisting of GaAs and embedded in a semiconductor layer with a higher energy gap (usually $Ga_{1-x}Al_xAs$), which itself is incorporated between barrier layers. The Al mole fraction x as a function of the distance from the disc center is responsible for the electron and hole confinement potentials in the xy plane. Two different types of potentials are used. In order to simulate infinite barriers by differentiable expressions we apply a power law

$$H_i(r_i) = a_{ni} (r_i / r_{i0})^n \tag{5}$$

We use typically values $n = 16$ for which convergence in energy eigenvalues is essentially reached with respect to the infinite barrier results. To model the effect of the finite barrier heights we study the potential form

$$H_i(r_i) = \Delta E_i \left[1 - e^{-(r_i/r_{i0})^n} \right] \tag{6}$$

A profitable result of such a potential choice is the unique splitting of the electron and hole confinement potentials

$$H_e(\mathbf{r}_e) + H_h(\mathbf{r}_h) = V_{cm}(R) + V_{rel}(r) + V_{int}(R, r, \Phi - \varphi) \tag{7}$$

into confining potentials for the center of mass motion, $V_{cm}(R)$, as well as the relative motion, $V_{rel}(r)$ and a coupling term of the two motions $V_{int}(R, r\,\Phi - \varphi)$. Therefore the exact solutions of the equation (3) can be expanded in terms of functions obtained without coupling

$$\Phi_\lambda(\mathbf{R}, \mathbf{r}) = \sum_{N,n} \sum_{M,m} c_{Mm}^\lambda(N, n) \Psi_{Nn}(R) \chi_{Mm}(r) \frac{1}{2\pi} e^{i(M\Phi + m\varphi)}, \tag{8}$$

where the radial parts with certain radial quantum numbers N and n as well as eigenvalues E_{Nn} and ε_{Mm} obey decoupled Schrödinger equations. We solve them by means of a Rayleigh Ritz Galerkin method[3] numerically. That procedure has been already successfully applied to describe the optical properties of flat quantum wires[4]. From the definition (4) of the oscillator strengths

$$f_{\lambda\nu} = \left| \sum_{N,n} c_{0n}^\lambda(N, n) c_{0n}^\nu(0) \int_0^\infty dR\; R \Psi_{Nn}(R) \right|^2 \tag{9}$$

it follows that only the s states of the two radial equations with zero angular momentum are needed. The unknown coefficients $c_{0n}^\lambda(N, n)$ are derived from a system of algebraic equations which results from Eq. (3) with the ansatz (8).

3. Discussion

Fig. 1 shows the imaginary part of the optical susceptibility (4) near the energy gap E_g^{2D} between the first electron and first heavy hole subband in the underlying quantum well structure. For numerical reasons a small line broadening $\hbar\Gamma = 0.05 E_B$ is assumed

independent of the certain two particle state. The spectra are plotted for different disc radii r_0 and the confinement potentials in (5). Calculations are done with and without coupling of center of mass and relative motion. For large dots (Fig. 1a) the excitonic spectrum of the underlying GaAs quantum well is reproduced. Decreasing the disc radius (Fig. 1b,c) strong quantization effects in the center of mass motion are observed. A series of blue shifted satellites with smaller oscillator strengths and belonging to higher quantum numbers N appear. In addition a finestructure, related to the influence of the disc confinement on the internal motion of the electron hole pairs, occurs (Fig. 1c). The Coulomb degeneracy is lifted. The coupling of the two motions becomes more and more important for the decreasing dot radii, and for radii close to the Bohr radius (Fig. 1d,e). The disc confinement leads to well separated peaks, which can be interpreted in terms of uncorrelated electrons and holes, i.e. the physical nature of the spectra changes qualitatively. The red shift of the spectrum without coupling in comparison to the correct one indicates that the neglect of the coupling of the two motions effectively acts as a decreasing of the disc confinement.

For very small discs the Coulomb attraction seems to be treated as a small perturbation. To check this assumption optical spectra with and without the Coulomb interaction of electrons and holes are plotted in Fig. 2. It can be seen that for $r_0 \leq a_B$ (a_B the Bohr radius of the bulk exciton) the peaks mainly arise from uncorrelated electron hole pairs and are only shifted by the Coulomb attraction. They can be nearly characterized by pairs of single-particle quantum numbers of electrons and holes. On the other hand, the Coulomb correlation strongly increases the oscillator strenghts and the Coulomb shift of the peaks does not follow clear rules.

The imaginary part of the optical susceptibility Eq. (4) is plotted in Fig. 3 for different effective dot radii r_0. To compare with experimental luminescence results some realistic features are introduced in the description. The spectra are cut at the high energy side by $6.32\ E_B$ above the lowest excitation peak to model the occupation due to the photoexcitation. The damping parameter Γ depends on the disc radius because of the thickness fluctuations in the underlying quantum well structure[4]. We assume a size dependence in the form $\Gamma = \frac{1}{2}E_B|1 - e^{-r_0/r_c}|$. The extent of the underlying quantum well is chosen as $r_c = 0.12 a_B$.

The series of theoretical spectra in Fig. 3 is in qualitative agreement (with respect to the position and the number of peaks) with the luminescence measurements of Brunner et al.[1,2]. To compare theoretical curves with experimental results one has to take into account the following facts: (i) Because of the finite height of the fabricated discs spectral lines cannot be observed up to arbitrary high energies. On the other hand, the spectra are truncated by the occupation of electron hole pairs. Therefore the magnitude of the band offsets is of minor influence on the observed spectra. (ii) Due to the thermodiffusion profile the dot radii entering the confinement potential differ from the distances of the laser-scan lines of about 200 nm. (iii) For small dot radii we are faced with a superposition of the diffusion tails from the left and the right side. Thus the potentials of the confinement potentials are shifted and the effective energy gap is decreased leading to a blue shift of the spectrum, as observed experimentally.

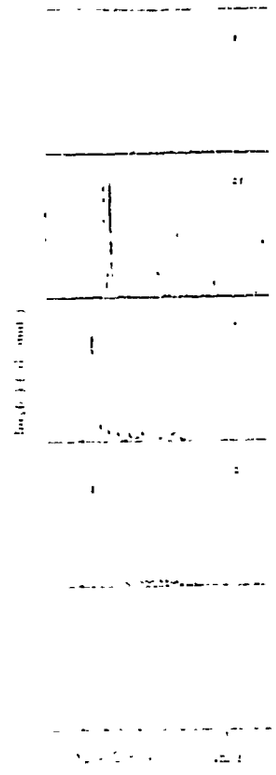

Fig. 3

Imaginary part of the optical susceptibility for different disc radii $r_0 = 100$ (a), 30 (b), 5 (c), 1 (d), and $0.5\ a_B$ (e). Solid lines represents full calculations, dashed ones such without the coupling of center of mass and relative motions.

Fig. 2

Imaginary part of the optical susceptibilities for different disc radii $r_0 = 100$ (a), 30 (b), 5 (c), 1 (d), and $0.5\ a_B$ (e). Solid lines represents calculations under inclusion of the Coulomb attraction, whereas dashed lines give the spectrum for uncorrelated electron hole pairs.

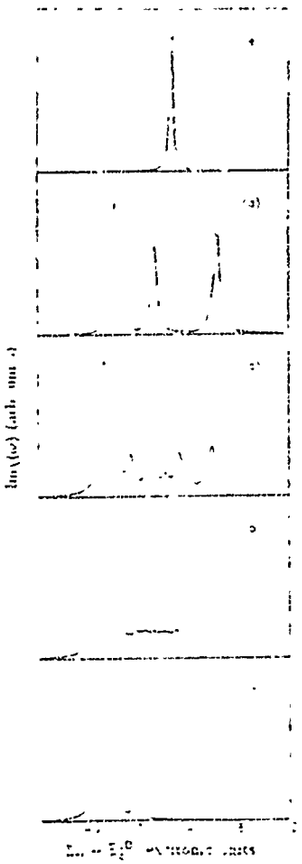

Fig. 3 Imaginary part of the optical susceptibility for different disc radii $r_0 = 160$ (a), 5 (b), 2 (c), 1 (d), and 0.5 a_B representing qualitatively with the measured spectra

Conclusions

In conclusion we have demonstrated the transition from the complete 2D exciton in an extremely narrow quantum well to quasi 0D excitons in well separated quantum discs prepared by laser induced cation interdiffusion. This transition is characterized by the interplay of the center of mass motion of the electron hole pair, its internal motion associated with exciton binding, and the confinement of electron and hole due to the disc potential.

In the case of flat discs with characteristic radii r_0 and high barriers in the disc plane the strengths of the different effects can be discussed comparing r_0 with the exciton Bohr radius a_B. In a wide range of disc sizes, $r_0 \gtrsim a_B$, the coupling of center of mass and internal motion plays a minor role. Only in the limit of strong confinement, $r_0 < a_B$, the consideration of this coupling is necessary. When the disc confinement effects overcome the Coulomb effects, i.e. when $r_0 < a_B$, the resulting spectra are similar to those obtained without excitonic effects. The Coulomb attraction gives rise to a divergent Coulomb shift $\sim 1/r_0$.

Our results are applied to explain qualitatively recent photoluminescence spectra of single discs with varying size. The development of the photoluminescence near the lowest heavy hole exciton of the underlying quantum well is interpreted in terms of the interplay of excitonic effects and disc confinement. However, a more quantitative analysis of the experimental spectra requires the inclusion of matrix element effects, the fluctuations in the vertical and lateral sizes, and, in particular, more realistic confinement potentials which more directly reflect the interdiffusion profile.

Acknowledgements

We would like to thank G. Abstreiter and K. Brunner for helpful discussions and leaving of unpublished photoluminescence spectra.

References

[1] K. Brunner, G. Abstreiter, M. Walther, G. Böhm, and G. Tränkle, Surface Sci. 267, 218 (1992).

[2] K. Brunner, U. Bockelmann, G. Abstreiter, M. Walther, G. Böhm, G. Tränkle, and G. Weimann, Phys. Rev. Lett. 69, 3216 (1992).

[3] J. Stoer and R. Bulirsch, Introduction to Numerical Analysis (Springer, New York, 1984).

[4] S. Glutsch and F. Bechstedt, Phys. Rev. B47, 16035 (1993).

ThP11

ELECTRONIC PROPERTIES AND ELECTRON-PHONON INTERACTION IN AN ARRAY OF ANISOTROPIC PARABOLIC QUANTUM DOTS IN THE PRESENCE OF A MAGNETIC FIELD

R Haupt and L. Wendler[1]

Institut für Festkörpertheorie und Theoretische Optik, Friedrich-Schiller-Universität Jena, Max-Wien-Platz 1, D-07743 Jena, Federal Republic of Germany

[1] *Fachbereich Physik, Martin-Luther-Universität Halle, Friedemann-Bach-Platz 6, D-06099 Halle, Federal Republic of Germany*

ABSTRACT

The electronic properties of a two-dimensional array of anisotropic parabolic quantum dots in the presence of a quantizing magnetic field is investigated in the tight binding approximation. The mini bands strongly depend on the superlattice periods, the eccentricity of the anisotropic parabolic quantum dot and the magnetic field. The electron-phonon interaction renormalizes the gaps between the mini bands, their widths and results in a resonant level splitting.

I. Introduction

In polar semiconductors the motion of an electron is coupled to the self induced polarization field of long wavelength optical phonons to form a quasi particle which is called polaron. Owing to this coupling the free electron properties are changed by (i) a shift in the energy, (ii) a mass renormalization and (iii) a polaron induced nonparabolicity. The most significant observations can be made in a cyclotron resonance experiment. The applied magnetic field quantizes the electron motion in the plane perpendicular to the magnetic field. With increasing magnetic field the phenomena of level crossing would appear in the absence of electron phonon interaction. The excited electronic levels can become degenerated with the lowest electronic level plus one optical phonon. Due to the electron phonon interaction the levels split at each resonance into two non crossing levels (resonant magnetopolaron). Hence, for strong magnetic fields the lower energy levels are pinned to the lowest level plus one optical phonon. Polarons ($B = 0$) and magnetopolarons ($B \neq 0$) have been extensively studied both theoretically and experimentally [1-4].

Advances of lithography and etching techniques make it possible to confine laterally a quasi-two-dimensional (Q2D) electron system into quantum dots (QD) of diameters $\sim 2\,\mu$m are less than the mean free path of the electrons. QD's have been fabricated by electrostatic confinement and deep-mesa etching techniques. The confining potential in such QD's is probably well represented by a parabolic potential. QD's can be viewed as artificial atoms with the atomic Coulomb potential replaced by the confinement potential of the QD. Polaronic effects are studied in Q2D systems [5-12] and more recently in Q1D quantum well wires [13], Q0D isotropic [14] and anisotropic [15] parabolic QD's. The reduced dimensionality changes the electronic and polaronic properties considerably. In Q1D and Q0D, for instance, it depends on the confinement potential of the resonant magnetopolaron exists or not [13-15].

In this paper we investigate the electronic and polaronic properties of a 2d array of anisotropic parabolic QD's. The electronic ground state will be described within the tight binding scheme because in the usual realized samples the QD's are well separated. The electron phonon correction will be calculated within second order perturbation theory for arbitrary magnetic fields.

II. Electronic Ground-State Properties

The superlattice system, a single electron confined to a zero thickness x-y plane along the z-direction at $z = 0$ and confined in the lateral direction in the potential of a 2D periodic array of anisotropic parabolic QD's in the presence of a quantizing perpendicular magnetic field $\vec{B} = (0, 0, B)$, is described by the Hamiltonian

$$H = \frac{1}{2m_e}(-i\hbar\vec{\nabla} + e\vec{A})^2 + V(\vec{r}). \tag{1}$$

The periodic confining potential is assumed to be $V(\vec{r}) = V(x + n_x l_x, y + n_y l_y) + V(z)$, $-\frac{N_x}{2} < n_x < \frac{N_x}{2}$, where l_x is the lattice period in x direction and l_y in y direction and N^2 is the number of QD's in the considered area. In Eq.(1) we ignore the Zeeman spin splitting, m_e is the effective conduction band-edge mass and $\vec{A}$ is the vector potential with $\vec{B} = \nabla \times \vec{A}$ for which we use the symmetric gauge $\vec{A} = (-y, x, 0)B/2$.

We first consider the single anistrope QD. The lateral potential of a single anisotropic QD is given by $V^{(0)}(x, y) = m_e/2(\Omega_x^2 x^2 + \Omega_y^2 y^2)$. The one electron Hamiltonian $H_e^{(0)} = H_e^{(0)} + H_e^{(1)}$ can be separated in an isotropic part

$$H_e^{(0)} = \frac{1}{2m_e}(\vec{p} + e\vec{A})^2 + \frac{m_e\Omega^2}{2}r^2 \tag{2}$$

with $\Omega = \Omega_x$ and $r^2 = x^2 + y^2$ and the deviation from it

$$H_e^{(1)} = \frac{m_e\Omega_\Delta^2}{2}r^2\cos^2\varphi \tag{3}$$

with $\Omega_\Delta^2 = \Omega_x^2 - \Omega_y^2$ and $x = r\cos\varphi$. The eigenenergies and corresponding single particle wave functions of the isolated isotropic parabolic QD are given by

$$\mathcal{E}_{N_r,m}^{(0)} = \hbar\omega_c(2N_r + |m| + 1) + \hbar\omega_c m/2 \qquad N_r = 0, 1, 2, \ldots \qquad m = 0, \pm 1, \pm 2, \ldots \tag{4}$$

and $\Psi_{N_r,m}^{(0)}(\vec{r}) = \chi_{N_r,m}^{(0)}(r,\varphi)\zeta_A(z)$ with

$$\chi_{N_r,m}^{(0)}(r,\varphi) = C_{N_r,m}\, r^{|m|} e^{im\varphi} \exp\left(-\frac{m_e\omega_c}{2\hbar}r^2\right) F(-N_r, |m|+1, \frac{m_e\omega_c}{\hbar}r^2) \tag{5}$$

respectively, where $\tilde{\omega}_c = (\omega_c/2)^2 + \Omega^2)^{1/2}$ is the hybrid frequency with $\omega_c = eB/m_e$ the cyclotron frequency and $F(a, b, z)$ is the confluent hypergeometric function. The normalization constant is

$$C_{N_r,m} = \left(\frac{(N_r + |m|)!}{\pi N_r!(|m|)!}\right)^{1/2}\left(\frac{m_e\omega_c}{\hbar}\right)^{\frac{|m|+1}{2}} \tag{6}$$

where N_r is the radial and m the azimuthal quantum number. According to the strict confinement assumed in z-direction $\zeta_A(z)^2 = \delta(z)$ is valid. In obtain the single particle energies and eigenstates of $H_e^{(0)}$ we express them in the representation of the states of the isotropic parabolic QD

$$\chi_\nu(r,\varphi) = \sum_{N_r,m} V_{N_r,m}\chi_{N_r,m}^{(0)}(r,\varphi) \tag{7}$$

The eigenenergies are determined from the algebraic system of equations

$$\sum_{N_r,m}\{\mathcal{E}_\nu - \mathcal{E}_{N_r,m}^{(0)}\}V_{N_r,m}\delta_{N_r,N_r'}\delta_{mm'} - \langle N_r'm'|H_e^{(1)}|N_r,m\rangle\} V_{N_r,m} = 0 \tag{8}$$

According to the spatial symmetry of the problem this system of algebraic equations splits into two separate ones, one for even m and the other for odd m. The eigenenergies can be found [16] to be explicitely

$$\mathcal{E}_{N_r,N_y} = \hbar\sqrt{(\omega_c/2)^2 + ((\Omega_x + \Omega_y)/2)^2}(N_r + N_y + 1) + \hbar\sqrt{(\omega_c/2)^2 + ((\Omega_x - \Omega_y)/2)^2}(N_y - N_r)$$
$$N_r, N_y = 0, 1, 2, \ldots \tag{9}$$

For vanishing anisotropy we can identify the quantum numbers $N_r = \min(N_r, N_y)$ and $m = N_y - N_r$. It is known [17] that $H_e^{(0)}$ is invariant under the unitary group $U(2)$ with the irreducible representation of the dimension $2N_r + |m| + 1$ corresponding to the degeneracy of this case. This dynamical symmetry [18] is broken by the anisotropy.

In Fig.1a) the first energy levels $\mathcal{E}_\nu$ of the anisotropic parabolic QD are plotted for a GaAs $Ga_{1-x}Al_xAs$ heterostructure (GaAs: $m_e = 0.0665\,m_0$, m_0 is the bare electron mass). In Fig.1a the electron energy levels $\mathcal{E}_{N_r,m}$ of the isotropic parabolic QD are shown. At vanishing magnetic field ($\omega_c = 0$) the energy levels are $(2N_r + |m| + 1)$ fold degenerated. In Fig.1b the anisotropy i.e. the deviation of the equipotential lines of $V^{(0)}(x,y)$ from circles is very weak and hence the energy spectrum is very similar to that of the isotropic parabolic potential. It is also seen that the $(2N_r + |m| + 1)$-fold degeneracy of the energy level $\mathcal{E}_{N_r,m}$ of the isotropic QD for vanishing magnetic field is lifted by the anisotropy. In Fig.1c the equipotential lines are more eccentric ellipses and following the energy spectrum deviates appreciably from that of the isotropic

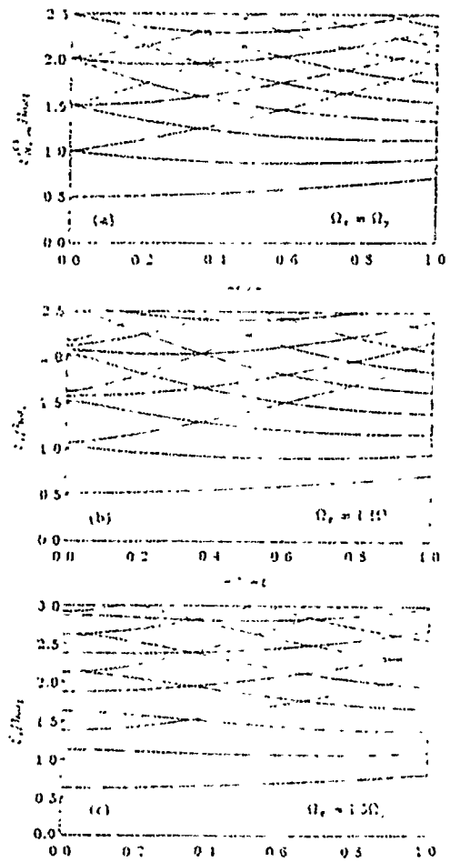

Fig 1 Energy levels $\mathcal{E}_i$ as a function of the magnetic field of an anisotropic parabolic GaAs-$Ga_{0.75}Al_{0.25}As$ QD with $\Omega/\omega_{LO} = 0.5$ (ω_{LO} = bulk energy of GaAs $\hbar\omega_{LO} = 36.17$ meV)

case. From Figures 1a–1b and 1c it is to be seen that level crossing at finite magnetic fields retains as in the case of the isotropic parabolic QD (Fig 1a).

For the potential of the 2D rectangular QD superlattice we assume

$$V(x,y) = \begin{cases} \frac{m^*}{2}[\Omega_x^2(x-n_xl_x)^2 + \Omega_y^2(y-n_yl_y)^2] & \frac{m^*}{2}[\Omega_x^2(x-n_xl_x)^2 + \Omega_y^2(y-n_yl_y)^2] < V_0 \\ V_0 & \frac{m^*}{2}[\Omega_x^2(x-n_xl_x)^2 + \Omega_y^2(y-n_yl_y)^2] > V_0 \end{cases} \tag{10}$$

The widths of a single QD in the 2D superlattice are W_x in the x-direction and W_y in the y-direction where $W_{x,y} = 2/\Omega_{x,y}\sqrt{2V_0/m^*}$. Assuming that the QDs are well separated, $W_x < l_x, W_y < l_y$, we can use the tight-binding approximation. In this case the single particle wave function reads

$$\Phi_{n\mu,k_x,k_y}(\vec{r}_{\vec{R}}) = \frac{1}{\sqrt{N}}\sum_{\vec{R}} C_{n\mu}(\vec{R}_{\vec{R}}) \sum_{\vec{R}_0} e^{i\vec{k}_0\vec{R}_0}\chi_\mu(\vec{r}_{\vec{R}} - \vec{R}_{\vec{R}}) \tag{11}$$

where μ denotes the nano-band, $\vec{r}_{\vec{R}} = (x,y,0)$ is the position vector in the x-y plane and $\vec{k}_{\vec{R}} = (k_x, k_y, 0)$ the wave vector, ranging through the N^2 values in the first nano-Brillouin zone consistent with the assumed Born-von Karman periodic boundary conditions. $\vec{R}_{\vec{R}} = (n_x l_x, n_y l_y, 0)$ is the lattice vector of the 2D Bravais lattice. Applying the Hamiltonian (1) with the potential (10) on the wave function (11) in the Schrödinger equation for an electron in the 2D array of anisotropic QDs, the eigenvalue equation system reads

$$\sum_{\vec{R}} [(E_n(\vec{k}_{\vec{R}}) - \mathcal{E}_i)\delta_{ij} - t_{ij} - 2\gamma_{ij}(l_x)\cos(k_x l_x) - 2\gamma_{ij}(l_y)\cos(k_y l_y))]C_{nj}(\vec{k}_{\vec{R}}) = 0 \tag{12}$$

where we have assumed for the integral $\int d^2r_{\vec{R}}\chi_i^*(\vec{r}_{\vec{R}})\chi_j(\vec{r}_{\vec{R}} - \vec{R}_{\vec{R}}) \approx \delta_{ij}\phi_{\vec{R}_{\vec{R}}0}$, which specifies the normalization constant of the wave function ($\alpha = \frac{1}{2}$) and we further include only the nearest-neighbour Hamiltonian matrix elements according to

$$t_{ij} = \int d^2r_{\vec{R}}\Delta V(\vec{r}_{\vec{R}})\chi_i^*(\vec{r}_{\vec{R}})\chi_j(\vec{r}_{\vec{R}}) \tag{13}$$

$$\gamma_{ij}(l_{x,y}) = \int d^2r_{\vec{R}}\Delta V(\vec{r}_{\vec{R}})\chi_i^*(\vec{r}_{\vec{R}})\chi_j(\vec{r}_{\vec{R}} - l_{x,y}\vec{e}_{x,y}) \tag{14}$$

with $\Delta V(\vec{r}_{\vec{R}}) = V(\vec{r}_{\vec{R}}) - V^{(n)}(\vec{r}_{\vec{R}})$. In the tight-binding approximation it is assumed that the nano-band $\mathcal{E}_n$ is very close to the dot level $\mathcal{E}_i$. Following, Eq (12) is to be solved assuming that for the calculation of the nano-band energy $\mathcal{E}_n(\vec{k}_{\vec{R}})$ the summation runs only through those dot levels with energies either degenerated with or very close to the corresponding dot level.

Figure 2 shows the three lowest nano-bands of the 2D array of QDs along ΓX, ΔM and MI of the square lattice where Γ, X and M are points in the nano-Brillouin zone that correspond to $(0,0)$ ($\frac{\pi}{l}$ 0) and ($\frac{\pi}{l}$ $\frac{\pi}{l}$), respectively with $l_x = l_y = l$. In Fig 2a the nano-bands are plotted for $\omega_c = 0$ and in Fig 2b for $\omega_c = 0.25\omega_{LO}$.

III. Electron-Phonon Interaction

Our interest is directed to QDs generated by nanostructured gate electrodes via the field effect in heterostructures of polar semiconductors. Hence the electrons occupying the nano-bands $\mathcal{E}_n(\vec{k}_{\vec{R}})$ interact with the optical phonons of the system. Neglecting the effects of interface phonons [19] the Hamiltonian of the electron-phonon interaction including only 3D bulk longitudinal optical (LO) phonons is the standard Fröhlich Hamiltonian and reads [20]

$$H_{e\nu} = \left(\frac{4\pi\alpha_{e\nu}(\hbar\omega_{LO})^3}{V_0}\right)^{1/2}\sum_{\vec{q}} e^{-i\vec{q}\vec{r}}\frac{1}{|\vec{q}|}(a_{\vec{q}} + a_{-\vec{q}}^+) \tag{15}$$

with α the dimensionless 3D polaron coupling constant (GaAs: $\alpha = 0.07$), r_p the corresponding 3D polaron radius (GaAs: $r_p = 3.98$ nm), $\hbar\omega_{LO}$ the energy of the LO phonon (GaAs: $\hbar\omega_{LO} = 36.17$ meV) and $\vec{q} = (q_x, q_y, q_z)$. The magnetic-polaron Hamiltonian is given by $H_e = H_e + H_{ph} + H_{e\nu}$ with $H_{ph} = \sum_{\vec{q}}\hbar\omega_{LO}a_{\vec{q}}^+a_{\vec{q}}(a_{\vec{q}}^+a_{\vec{q}} + 1/2)$. The first two terms represent the unperturbed electron and phonon system, $H_0 = H_e + H_{ph}$ and the electron-phonon interaction $H_{e\nu}$ is the perturbation H_1. The energy levels of an electron in the 2D array of anisotropic parabolic QDs are shifted over $\Delta E_n(\vec{k}_{\vec{R}})$ by the electron-phonon interaction with the LO phonons to $E_n(\vec{k}_{\vec{R}}) = \mathcal{E}_n(\vec{k}_{\vec{R}}) + \Delta E_n(\vec{k}_{\vec{R}})$. In the weak-coupling limit ($\alpha \ll 1$), valid

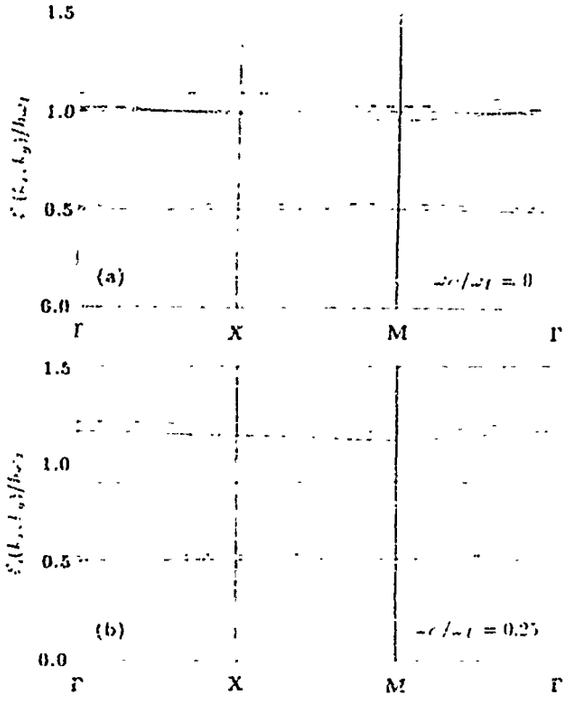

Fig. 2. The n bands $\tilde{\mathcal{E}}_n(\tilde{k}_\parallel)$ of a 2D array of QDs along Γ X M Γ of the square lattice where Γ, X and M are the points on the mini Brillouin zone that correspond to $(0,0)$, $(\pi/a, 0)$ and $(\pi/a, \pi/a)$, respectively. $a = l_x = l_y = 30\alpha_B$ and $V_0 = 1.5\hbar\omega_l$. Solid lines show mini bands for an isotropic QD array with $\Omega_x = \Omega_y = 0.5\omega_l$, long dashed lines for an anisotropic QD array with $\Omega_x = 0.5\omega_l$ and $\Omega_y = 0.55\omega_l$, and short dashed lines for $\Omega_x = 0.5\omega_l$ and $\Omega_y = 0.75\omega_l$. In Fig. 2a the first mini bands are plotted for $\omega_c = 0$ and in Fig. 2b for $\omega_c = 0.25\omega_l$.

for the n-th zero-dot materials $\tilde{\mathcal{E}}_n$ in which arrays of QDs are produced, as well as other potentials can be used to calculate $\Delta\mathcal{E}_n(\tilde{k}_\parallel)$. The energy shift of the mini band $E_n(\vec{k}_\parallel)$ reads

$$\Delta E_n(\vec{k}_\parallel) = -\sum_{n_x}\sum_{n_y}\sum_{l}\frac{|\langle \ldots|\ldots|\ldots\rangle|^2}{\ldots + \hbar\omega_l - \mathcal{E}_n(\vec{k}_\parallel)} \quad \text{(16a)}$$

with $M_{\ldots}(q) = \ldots \tilde{E}_q \ldots|H_{e-p}|\ldots\rangle$. The k-vector $\vec{k}_\parallel = \ldots \vec{k}_\parallel + \ldots$ corresponds to an eigenstate of H composed of an electron ... mini band ... 2D array ... polaron ...

momentum $\hbar\vec{k}_\parallel$ and n LO phonons with the energy $\hbar\omega_l$ and the momentum $\hbar\vec{q}$. The correction term we call n phonon unperturbed mini band in difference to the renormalized level, the magnetopolaron level containing n LO phonons. The value $\Delta_\nu(\tilde{k}_\parallel)$ depends on the type of the perturbation theory where is used [3]: (i) $\Delta_\nu(\tilde{k}_\parallel) = 0$ leads to the Rayleigh–Schrödinger perturbation theory (RSPT); (ii) $\Delta_\nu(\tilde{k}_\parallel) = \Delta E_n(\tilde{k}_\parallel)$ results in the Wigner–Brillouin perturbation theory (WBPT) and (iii) $\Delta_\nu(\tilde{k}_\parallel) = \Delta\mathcal{E}_n(\tilde{k}_\parallel) - \Delta E_0^{RSPT}(\tilde{k}_\parallel)$ gives an improved Wigner–Brillouin perturbation theory (IWBPT) with $\Delta E_0^{RSPT}(\tilde{k}_\parallel)$ the weak coupling electron–phonon correction to the electron ground state energy calculated within RSPT. For the ground state $\Delta E_0^{IWBPT}(\tilde{k}_\parallel) = \Delta E_0^{RSPT}(\tilde{k}_\parallel)$ is valid. It is well-known [3] that the RSPT describes the ground state correction for $B = 0$ quite well, but it fails for the excited states since it is possible that the denominator of (16) vanishes for certain B. This becomes possible if the zero-phonon unperturbed excited mini bands become resonant with the one phonon unperturbed ground state mini band. But the occurrence of a mini band crossing depends strongly on the relation between the LO phonon energy $\hbar\omega_l$ and the confinement energy of the weakly anisotropic QD [15]. If resonance occurs the electron–phonon interaction leads to splitting of the degenerated mini bands. Further for large magnetic fields the lower energetic mini bands become pinned to the energy $\hbar\omega_l + \tilde{\mathcal{E}}_0(0) + \Delta E_0^{RSPT}$ well described by IWBPT. The crossing of the unperturbed mini bands is shifted to lower magnetic fields for increasing eccentricity of the anisotropic QDs forming the 2D lattice. From (16) it is seen that the polaron corrections to the mini-bands are different for different mini bands even in the case of $B = 0$. This behaviour is different from the well known 3D and 2D magnetopolaron [3] for which the polaron corrections at $B = 0$ are independent of the quantum numbers. The electron–phonon interaction decreases the gaps between the mini bands and also the width of the mini band.

References

1 *Polarons and Excitons* Ed. C. Kuper and G. Whitfield (Oliver and Boyd, Edinburgh (1963)
2 *Polarons in Ionic Crystals and Polar Semiconductors* Ed. J. T. Devreese (North-Holland, Amsterdam (1972)
3 G. Lindemann, R. Lassing, W. Seidenbusch and E. Gornik, *Phys. Rev.* B 28, 4693 (1983)
4 H. Sigg, H. J. A. Bluyssen and P. Wyder, *Solid State Commun.* 48, 897 (1983)
5 F. M. Peeters and J. T. Devreese, *Phys. Rev.* B 31, 3689 (1985)
6 S. Das Sarma and A. Madhukar, *Phys. Rev.* B 22, 2823 (1980)
7 D. Larsen, *Phys. Rev.* B 30, 4595 (1984)
8 W. Seidenbusch, G. Lindemann, R. Lassing, J. Edlinger and E. Gornik, *Surface sc.* 142, 375 (1984)
9 M. Horst, U. Merkt and J. P. Kotthaus, *Phys. Rev. Lett.* 50, 754 (1983)
10 C. J. G. Langerak, J. Singleton, P. J. van der Wel, J. A. A. J. Perenboom, D. J. Barnes, R. J. Nicholas, M. A. M. A. Hopkins, and C. T. B. Foxon, *Phys. Rev.* B38, 13 133 (1988)
11 R. Haupt and L. Wendler, to be published in *J. Phys. Condens. Matter* (1993)
12 R. Haupt and L. Wendler, to be published in *Z. Phys.* B (1993)
13 L. Wendler, A. V. Chaplik, R. Haupt and O. Hipolito, *J. Phys. Condens. Matter* 5, 2 (1993)
14 L. Wendler, A. V. Chaplik, R. Haupt and O. Hipolito, to be published in *J. Phys. Condens. Matter* (1993)
15 R. Haupt and L. Wendler, *Physica* B184, 291 (1993)
16 B. Schuh, *J. Phys. A: Math. Gen.* 18, 841 (1985)
17 C. C. Martens, G. S. Ezra, *J. Chem. Phys.* 87, 284 (1987)
18 B. G. Wybourne, *Classical Groups for Physicists*, John Wiley, New York (1974)
19 L. Wendler, *phys. stat. sol. (b)* 129, 513 (1985)
20 H. Fröhlich, *Adv. Phys.* 3, 325 (1954)

ThP12

Monte-Carlo Calculation of Few-Electron Systems in Quantum Dots

F. Bolton
Institut für Theoretische Physik,
Universität Regensburg,
D-93040 Regensburg, Germany

Selected eigenstates are calculated for 1–10 electrons in a quasi-2-dimensional harmonically confined dot as a function of magnetic field. This includes a detailed look at the ground state of three electrons and a more general calculation for 1–10 electrons carried out in the lowest Landau level for different spin configurations. The results provide an outline of the N-electron ground state as a function of magnetic field, enabling a comparison to be made with recent experiments involving capacitance measurements on quantum dots. The calculations are made using the fixed node quantum Monte-Carlo method which can accurately estimate electron correlation and easily extends to large numbers of electrons.

1 Introduction

Basic to our understanding of quantum dots is the ability to calculate spectra in the few-electron regime (0–50) particles. In particular, experimental probes of quantum dots require the calculation of dipole excitations, in the case of optical spectroscopy, and ground state energies in the case of tunneling experiments. Since the few-particle regime is numerically quite taxing, there have only been a few examples of such spectra calculated[1–5]. Experimental work on tunneling, however, has already reached the point where ground state spectra for 0–50 electrons are measurable[6]. Also the possibility of different spin states, although not often considered, remains a relevant effect up to magnetic fields of about 3T in GaAs.

From the theoretical side what is required is a method whose computational difficulty rises gently with respect to the number of electrons N. One such method is the fixed node Monte-Carlo algorithm whose computational effort grows only as N^3. The basic method is described in detail in the article by Reynolds et al[7] and the modifications appropriate to the present application are discussed in Bolton[8]. Here we give just a brief outline of the method. Consider a general N particle Hamiltonian

$$H = -\frac{\hbar^2}{2m^*}\left(\sum_{j=1}^{N}\nabla_j^2\right) + V(\vec{r}) \qquad (1)$$

where $V(\vec{r})$ is a general potential which includes any interactions and $\vec{r} = (\vec{r}_1 \ldots \vec{r}_N)$ denotes a many particle configuration. In the fixed node approximation we consider the propagation of $f(\vec{r},t) = \Psi^*(\vec{r},t)\Psi_T(\vec{r})$ in imaginary time t. Here $\Psi_T(\vec{r})$ is a trial function approximation to the solution and, in the limit as t goes to infinity, $\Psi(\vec{r},t=\infty)$ is the sought after solution to H. The advantage in considering the propagation of the product $f = \Psi^*\Psi_T$ is that f remains a positive real function and this is a basic requirement of the quantum Monte-Carlo algorithm. The equation for the propagation of $f(\vec{r},t)$ in imaginary time is

$$-\frac{\partial f(\vec{r},t)}{\partial t} = -\frac{\hbar^2}{2m^*}\left(\sum_{i=1}^{N}\nabla_i^2 f\right) + (E_L(\vec{r}) - E_T)f + \frac{\hbar^2}{2m^*}\sum_{i=1}^{N}\nabla_i\cdot(f\,\mathbf{F}_i(\vec{r})) \qquad (2)$$

where $E_L(\vec{r}) = H\Psi_T/\Psi_T$ defines the local energy and the gradients $\mathbf{F}_i(\vec{r}) = 2\nabla_i\Psi_T/\Psi_T$ introduce a drift term to the equation (see [7,8]). The constant E_T is a parameter which is adjusted during the run until the distribution $f(\vec{r},t)$ becomes stable — neither growing nor shrinking in imaginary time. This procedure finds the lowest energy eigenstate of the Hamiltonian H which is consistent with the nodal structure of the trial function Ψ_T. With a suitable choice of trial function we can find the eigenenergies of fermionic states and even excited states. The use of a trial function only partly restricts the solution as is seen by considering the nature of the constraints. The solution Ψ is constrained to vanish on the same nodal surfaces and maintain the same complex phase as Ψ_T. Within these constraints, however, the Hamiltonian is solved exactly, including the effects of electron correlation.

The model considered here is that of a quasi two-dimensional quantum dot so that only degrees of freedom in the plane of the dot are considered. The problem is solved in the effective mass approximation with effective mass m^* and in a cylindrically symmetric harmonic confinement $\frac{1}{2}m^*\omega_0^2 r^2$. The Hamiltonian considered is thus

$$H_0 = -\frac{\hbar^2}{2m^*}\sum_{j=1}^{N}\nabla_j^2 + \frac{1}{2}m^*\omega^2\sum_{j=1}^{N}r_j^2 + \frac{\omega_c}{2}\sum_{j=1}^{N}L_{j,z} + \frac{1}{4\pi\varepsilon\varepsilon_0}\sum_{i<j}\frac{1}{r_{ij}} \qquad (3)$$

where a magnetic field B enters via the hybrid oscillator strength $\omega^2 = \omega_0^2 - (\omega_c/2)^2$, with $\omega_c = eB/m^*$ and $L_{j,z}$ is the z-component of orbital angular momentum. The introduction of a magnetic field into the model Hamiltonian does not cause any great difficulties for the Monte-Carlo procedure. Our trial functions Ψ_T now have to be complex but, as noted above, this can be accomodated in the algorithm [8]. The only significant alteration to H is the addition of the angular momentum term. Since the total angular momentum is conserved under the Hamiltonian, this term evaluates to just a constant.

In the next three sections we take a detailed look at the ground state of a three particle system and then look at selected eigenstates of between one and ten electrons. A possible comparison of these results with capacitance experiments is indicated in section §4.

2 Three-Particle Problem

For the special case of three particles we are able to compute a rather complete spectrum of the Hamiltonian H. There is available in this case a particularly convenient coordinate system (see [1,3]) and we restrict our attention here to states in the lowest Landau level. For three particles the relative motion can be specified with the complex coordinates

$$\begin{aligned} \rho_1 &= z_1^* + e^{i\pi/3}z_2^* + e^{-i\pi/3}z_3^* \\ \rho_2 &= z_1^* + e^{-i\pi/3}z_2^* + e^{i\pi/3}z_3^* \end{aligned} \qquad (4)$$

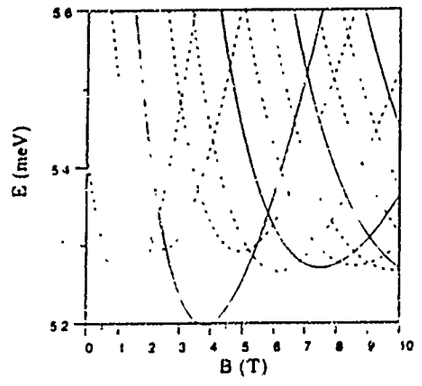

Figure 1 The complete ground state spectrum of three particles as a function of magnetic field, plotted with GaAs parameters and $\hbar\omega_0 = 1.37meV$. Energies E are shown with respect to the lowest Landau level energy as $E - 3\hbar\omega(B)$. The dashed lines are for spin $S = \frac{1}{2}$ states and the solid lines for spin $S = \frac{3}{2}$ (spin polarised) states.

where $z_i^* = x_i - iy_i$. It turns out that a complete basis of correctly symmetrised states is easily written down for three particles[5]. Restricted to the lowest Landau level these are given by

$$\Psi_m = (p_0^m - p_1^m)p_m^m p_2^m \, e^{-(r_0^2+r_1^2+r_2^2)/2l^2} \qquad (5)$$

Here we have introduced the harmonic oscillator length $l = \sqrt{\hbar/m^*\omega_0}$. For $(m \bmod 3) = 0$ this represents a spin $S = \frac{3}{2}$ state and for $(m \bmod 3) = 1$ or 2 it represents a spin $S = \frac{1}{2}$ state. Given that we are interested in finding the ground state as a function of magnetic field we may further restrict our attention to states for which $m = 0$. This is because, as noted some time ago by Laughlin[1], the modes associated with non-zero m are energetically unfavourable. We can easily understand this by noting that the product $p_0 p_1 p_2$ vanishes whenever the three particles occupy the vertices of an equilateral triangle. Since an equilateral triangle is in fact the most energetically favourable configuration of three particles it is clear that forcing Ψ_m to vanish at this point is characteristic of an excited state. Thus we consider only trial functions Ψ_m for which $m = 0$ and we are left with just the quantum number n.

In fig. 1 the results of calculations for $n = 1, 2, 3, \ldots$ in a GaAs quantum dot are shown with $m^*/m_e = 0.067$, permittivity $\epsilon = 12.9$ and the confinement strength is given by $\hbar\omega_0 = 3.37$meV. Here we have plotted the energy per electron against the magnetic field. The energies are plotted with respect to the lowest Landau level $E - 3\hbar\omega(B)$ and Zeeman spin-splitting is omitted. The dashed lines indicate states with spin $S = \frac{3}{2}$ and the solid lines $S = \frac{1}{2}$. Note that the sequence of states for $n = 1, 2, 3, \ldots$ have their minima at steadily increasing values of the magnetic field. It is interesting to make a comparison with the calculations of Hawrylak and Pfannkuche[5]. With the symmetric basis set they use the problem simplifies sufficiently to solve via straightforward diagonalisation of the Hamiltonian. Qualitatively fig. 1 is in good agreement with those results, however the average energy level of the ground state in fig. 1 lies about 4% lower than that of Hawrylak and Pfannkuche. The difference is significant since the Monte-Carlo results are converged to within 1%. It is possible that the Monte-Carlo result has in fact converged closer to the ground state since the algorithm obeys a variational principle and thus ought to find an upper bound to the eigenenergy.

3 Trial Functions

We now turn to the choice of trial function. As we are interested in the ground state as a function of magnetic field we confine our attention once again to the lowest Landau level (see Girvin and Jach[9]). Using a harmonic oscillator basis the states in the lowest Landau level have the form

$$p^{(m)}(z_1^*, \ldots, z_N^*) \, e^{-(1/2l^2)\sum_i z_i z_i^*} \qquad (6)$$

where $p^{(m)}$ is a polynomial of degree m in the N complex variables. The subspace of polynomials $p^{(m)}$ of degree m form a complete basis for states of total angular momentum m in the lowest Landau level. A good choice of trial function is given by a polynomial which correctly correlates the motion of the electrons. Denoting the set of electrons with up spin by S_1 and those with down spin by S_1, we propose as a trial function

$$\Psi_T = \Big(\prod_{i,j\in S_1}(z_i^* - z_j^*)\Big)\Big(\prod_{k,l\in S_1}(z_k^* - z_l^*)\Big)\exp\Big\{-\frac{1}{2l^2}\sum_{i=1}^{N} z_i z_i^*\Big\} \qquad (7)$$

This incorporates the lowest order polynomial which satisfies the condition that the co-ordinates of like-spin electrons be fully anti-symmetric amongst themselves. In the case of a spin polarised state this reduces to the well known Laughlin function. Note that this choice of trial function is quite logical since the polynomial of minimum order satisfying spin symmetry is unique.

4 Few-Electron Ground States

In fig. 2 the result of carrying out the Monte Carlo procedure with the above trial functions is shown for 1-10 electrons. The system is GaAs with confinement strength given by $\hbar\omega_0 = 3$meV. Zeeman splitting of the spins is not included and it makes no significant difference to these results. Note that, in contrast to fig. 1, we have plotted here

the absolute energies Solid curves are drawn to mark the lowest calculated eigenenergy in each case for systems of 1-10 electrons For example the upper group of six states

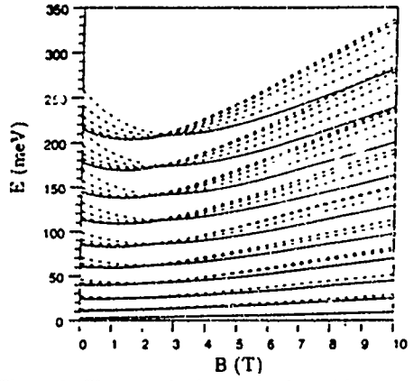

Figure 2 The energy levels given by the trial functions of equation (7) are plotted for 1-10 electrons with a solid line indicating the lowest N-electron energy in each case Parameters are for GaAs with confinement $\hbar\omega_0 = 3meV$ and zero Zeeman splitting

is composed of eigenstates of ten electrons with total spin $S = 0$ 5 Clearly, as the spectra are incomplete, we cannot infer that the lowest of the calculated energies correspond to the ground state for all values of the magnetic field B However these eigenstates provide us with a skeleton of the lowest Landau level in each case It is also a reasonable assumption that for zero magnetic field the lowest N-electron eigenenergy thus calculated is indeed that of the ground state since the corresponding trial function is chosen to have minimal kinetic energy

To facilitate comparison with capacitance experiments we have plotted in fig 3 the energy required to add electrons to the dot as a function of magnetic field The lowest curve shows the energy required to add the first electron, the next curve the second electron and so on. The curves in fig 3 thus show effective "single particle" energy levels and are calculated simply by taking the differences between successive N-particle ground states in fig 2 It is interesting to compare these results with the experiments of Ashoori et al[6] In their capacitance experiments they measured a similar sequence of N-electron ground states as a function of magnetic field Our choice of confinement strength of $\hbar\omega_0 = 3meV$ differs from the value of $\hbar\omega_0 = 5.4meV$ suggested in[6] as a fit to a two dimensional confinement potential In their paper it is not indicated that allowance has been made for the contribution from confinement in the growth direction Therefore we suppose that the confinement energy of 5 4meV consists partly of a contribution from confinement in the

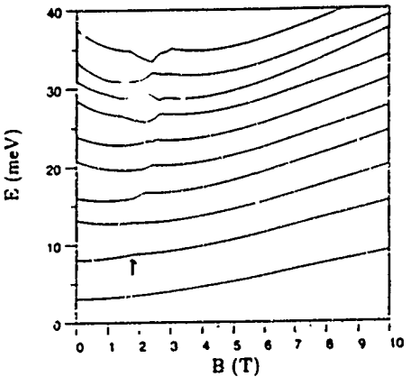

Figure 3 This graph shows the effective "single-electron" energy levels derived by plotting the differences between successive N-electron ground states in fig. 2 as a function of magnetic field. The arrow indicates the position of the spin singlet-triplet crossover in the two particle ground state.

z-direction We have preferred to use the spectrum of two electrons as a guide to choosing $\hbar\omega_0$ since the two electron system is theoretically very well understood (see Merkt et al[10]) The appearance of a slope discontinuity in the two-particle ground state can be taken as a clear sign of the first spin-triplet crossing[11]. Thus we have chosen $\hbar\omega_0$ so that this slope discontinuity occurs in approximately the same place in our fig 3 as in fig. 2(a) of [6] Comparing theory and experiment more closely now we observe a similar spacing of energies at $B = 0$ for the first four levels. The most interesting feature of fig. 3 is the sequence of irregular bumps occurring in different levels over the range 1.5T to 3T Their resemblance to the features highlighted in [6] is striking and the two may turn out to be related. However there are some significant differences between the calculations and experiment. In fig. 3 the energies for $N > 4$ show a distinct drop as the magnetic field increases from zero whereas the energy levels in [6] remain nearly constant over the same range of B Also the range of energies at $B = 0$ spans roughly 0 to 38meV in fig. 2 compared with 0 to 30meV in[6] These discrepancies might be explicable as being due to mixing of the given states with higher quantum well subbands (an effect not considered in the model) The relatively broad well width of 175Å makes this a likely factor.

5 Conclusion

Results have been presented of ground state spectra calculated using a quantum Monte Carlo algorithm We have been able to make a tentative comparison with ca-

pacitance measurements of N-electron ground states. The limitations to this comparison probably stem from the quasi-two dimensional nature of the model. Finally these calculations show that the fixed node Monte-Carlo method has the potential to be a flexible and accurate tool in the calculation of few-electron spectra in quantum dots.

Acknowledgements: The author wishes to thank U. Rössler for helpful discussions and his critical reading of the manuscript. Support is gratefully acknowledged from the Deutsche Forschungs-Gemeinschaft, SFB348.

References

[1] R. B. Laughlin, *Phys. Rev. B* 27, 3383, (1983)
[2] S. M. Girvin and T. Jach, *Phys. Rev. B* 28, 4506, (1983).
[3] P. A. Maksym and T. Chakraborty, *Phys. Rev. Lett.* 65, 108, (1990)
[4] A. Kumar, S. E. Laux and F. Stern, *Phys. Rev. B* 42, 5166, (1990)
[5] P. Hawrylak and D. Pfannkuche, *Phys. Rev. Lett.* 70, 485, (1993)
[6] R. C. Ashoori, H. L. Stormer, J. S. Weiner, L. N. Pfeiffer, K. W. Baldwin and K. W. West (to be published in *Phys. Rev. Lett.*)
[7] P. J. Reynolds, D. M. Ceperley, B. J. Alder and W. A. Lester Jr., *J. Chem. Phys.* 77, 5593, (1982)
[8] F. Bolton (to be published).
[9] S. M. Girvin and T. Jach, *Phys. Rev. B* 29, 5617, (1984)
[10] U. Merkt, J. Huser and M. Wagner, *Phys. Rev. B* 43, 7320, (1991)
[11] M. Wagner, U. Merkt and A. V. Chaplik, *Phys. Rev. B* 45, 1951, (1992)

ThP13

Spectral luminescence enhancement in three-dimensional optical microcavities formed by GaAs-microcrystals

S. JUEN, K. F. LAMPRECHT, R. RODRIGUES, R. A. HÖPFEL,
Institute of Experimental Physics, University of Innsbruck, Technikerstr. 25/4, A-6020 Innsbruck, AUSTRIA.

Abstract

The photoluminescence of GaAs microcrystallites with average sizes in the range of 0.35 μm to 1.3 μm has been studied experimentally. The observed spectral blue-shift and line-broadening of the luminescence are explained by spectral enhancement and inhibition of spontaneous emission due to a modified photonic density-of-states in the dielectrically confined microcrystallites. The emission spectra calculated for rectangular particles via their photonic density-of-states agree well with the experimental results. Theoretical emission spectra obtained from Mie theory for spherical GaAs microcrystals yield similiar results. Furthermore, the internal and surface fields of GaAs microspheres calculated via Mie theory reveal field enhancement factors of up to 20 for optical excitation at resonance frequencies of the microcavity.

1. INTRODUCTION

Recently, there has been a strong interest in the control of spontaneous emission in microscopic resonators [1-7]. In these structures the coupling between electronic states and the radiation field is restricted to a small number of electromagnetic field modes. Resonant coupling enhances the spontanous emission rate and ultimately allows zero-threshold laser action by the spatial and spectral overlap of a single field mode with the gain medium [2]. Increased light emission efficiencies and spectral alterations were demonstrated in one- and two-dimensional semiconductor microcavities based on III-V quantum well structures [3-7]. Theoretical calculations predict a drastic reduction of the threshold current for microcavity surface emitting lasers with sub-micron lateral dimensions [8].

In this paper we report on anomalies in the photoluminescence spectra of size-selectively fabricated sub-micron GaAs crystallites. The microcrystals are strongly dielectrically confined due to a change in the index of refraction of $\Delta n \approx 2.4$ at their surface. The observed spectral characteristics are shown to be consistent with the expected light emission from a three-dimensional optical microcavity. The emission spectra are calculated for rectangular GaAs microcrystals via the photonic density-of-states of these microresonators. For comparison, the emission spectra are calculated on the basis of Mie theory by estimating the absorption efficiency of spherical GaAs crystals. Finally, numerical results for the internal field distribution of GaAs microspheres are presented.

2. PHOTOLUMINESCENCE EXPERIMENTS

The GaAs microcrystallites investigated in the photoluminescence experiments were fabricated and characterized as reported previously by pulverization of monocrystalline bulk GaAs, particle separation by sedimentation techniques, and sample deposition on Si-substrates

[9, 10]. The average microcrystallite diameters and standard deviations are (a) $D_A = 0.35\ \mu m$ ($\pm 0.12\ \mu m$) (sample (A)), (b) $D_B = 0.55\ \mu m$ ($\pm 0.19\ \mu m$) (sample (B)), and (c) $D_C = 1.3\ \mu m$ ($\pm 0.48\ \mu m$) (sample (C)). The luminescence spectra were measured from microcrystals adhered on polished Si-substrates (immersed in liquid nitrogen) using a He-Ne laser (632.8 nm) and a Ti:Sapphire laser for cw-excitation with a maximum power density of 200 W/cm^2 and a CCD detection system with a spectral resolution of 1.4 meV.

Fig. 1 shows photoluminescence spectra from the smallest GaAs crystallites (sample (A)) at a temperature of 77 K. The spectra represent the integrated emission of roughly 20 ($\pm$ 10) particles and were recorded from two different excitation areas to demonstrate the inhomogeneity of the emission spectrum within one sample. The luminescence spectra in Fig. 1 and, similarly, that of samples (B) and (C), are broadened and their maxima are shifted to higher energies as compared to the reference GaAs spectrum. The luminescence linewidth $\Delta E_{1/2}$ and the blue-shift of the luminescence maximum ΔE_m are smaller for samples (B) and (C), i.e. $\Delta E_{1/2}$ and ΔE_m decrease with increasing average crystal size. The photoluminescence intensity scales with the square of the excitation power density for all samples, indicating bimolecular band-to-band recombination. The spectral position and shape of the luminescence is independent of the excitation power density.

Fig. 1: Experimental photoluminescence spectra from GaAs crystallites with an average diameter of 0.35 μm (sample (A)) at a temperature of 77 K. Spectra (a) and (b) were recorded from two different excitation areas within the same sample. Dashed curve: bulk GaAs photoluminescence spectrum.

Fig. 2 summarizes the experimental results for samples (A), (B), and (C). The observed spectral blue-shift ΔE_m and the luminescence linewidth $\Delta E_{1/2}$ are plotted as a function of the microcrystallite size. The theoretical results plotted in Fig. 2 (open circles) are described below.

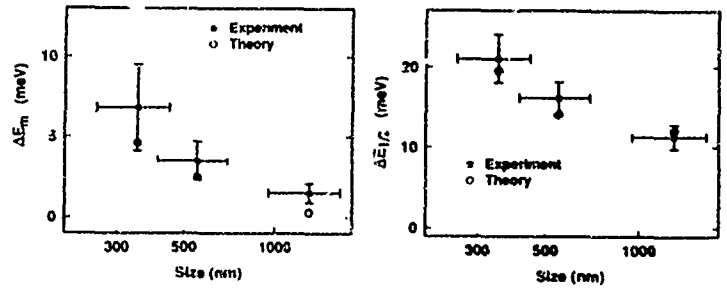

Fig. 2: Experimental results for the spectral blue-shift ΔE_m and the luminescence linewidth $\Delta E_{1/2}$ as a function of the microcrystallite size for samples (A), (B) and (C) (filled circles). Theoretical results from the microcavity model are plotted as open circles.

3. MICROCAVITY MODEL

In the following, we use the concept of the photonic density-of-states, i.e. the optical mode density, to describe the light emission from semiconductor microcrystals. The spontaneous emission rate per unit volume and unit energy is given by [11]

$$\gamma_{sp}(h\nu) = \frac{c}{n}\rho_c(h\nu)\alpha_0(h\nu)f_e f_h \qquad (1)$$

where c is the vacuum velocity of light, n is the real part of the refraction index, ρ_c is the local photonic density-of-states (i.e. the number of optical modes at $h\nu$ per unit energy and unit volume), α_0 is the absorption coefficient of the unexcited bulk semiconductor, f_e is the electron occupation probability in the excited state (conduction band), and f_h is the hole occupation probability in the ground state (valence band) at the corresponding transition energy. Due to the strong dielectric confinement of the GaAs microcrystals (change of the index of refraction $\Delta n \approx 2.5$, critical angle of reflection $\phi_c = 17°$) most of the internally generated light is totally reflected and redistributed to allowed modes determined by the geometry.

Fig. 3 illustrates the effect of a modified local photonic density-of-states in a microcavity on the emission spectrum. The dashed line shows the band-to-band luminescence spectrum from bulk GaAs with the continuum photonic density-of-states $\rho_0(\nu) = 8\pi\nu^2 n^3/c^3$ (dotted line). The thick solid line represents the emission spectrum for an oscillating mode density ρ_c (thin solid line). The radiative decay rate is increased ("enhanced"), if $\rho_c > \rho_0$, and decreased ("inhibited") in the opposite case.

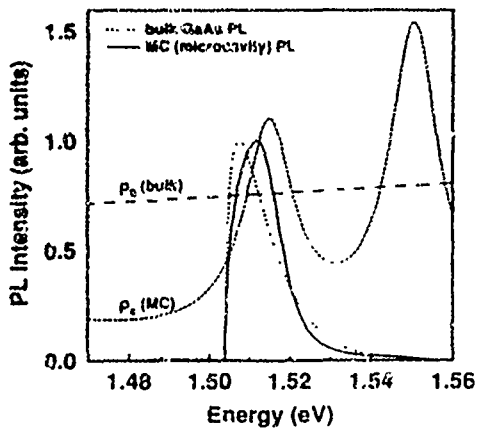

Fig. 3: Dotted line: band-to-band luminescence spectrum from bulk GaAs with the continuum photonic density-of-states ρ_0 (dashed line). Thick solid line: band-to-band luminescence spectrum caused by an oscillating photonic density-of-states ρ_c (thin solid line). The radiative decay rate is increased ('enhanced'), if $\rho_c > \rho_0$, and decreased ('inhibited'), if $\rho_c < \rho_0$.

The photonic density-of-states of a square box microcavity can be approximated by [10, 12]

$$\rho_c(\nu) \cong \frac{1}{8L^3} \sum_{jkl} \frac{\Gamma_{n,t}/2}{(\nu_{jkl}-\nu)^2 + (\Gamma_{n,t}/2)^2} \qquad (2)$$

$$\Gamma_{n,t} = \frac{c}{2\pi n} \left(\alpha_0(\nu) + \alpha_s - \frac{1}{L} \ln R_{n,t}\right) \qquad (3)$$

where L is the length of the cube, ν_{jkl} is the resonance frequency of mode (jkl), and losses $\Gamma_{n,t}$ are determined by the bulk material absorption coefficient $\alpha_0(\nu)$, scattering losses α_s due to surface roughness, and propagating modes (subscript 'n' for propagating modes with $R_n = 0.32$, subscript 't' for total internal reflection with $R_t = 1$).

The photonic density-of-states and the luminescence spectrum were calculated from Eqs (1)-(3) for GaAs microboxes with the cavity lengths (A) L = 0.35 µm, (B) L = 0.55 µm, and (C) L = 1.0 µm. The output coupling from individual modes in Eq (2) was taken into account by multiplying them with the corresponding average transmission coefficient (including losses due to surface roughness) [10]. The estimated luminescence linewidths and blue-shifts of the emission maximum are plotted in Fig. 2 (open circles).

4. MIE THEORY

The photonic density-of-states given by Eq (2) does not take into account the spatial mode distribution inside the microcrystal. The microscopic photonic density-of-states has been

calculated in Ref.[12] for spherical particles and is related to the efficiency factors for scattering and absorption defined in Mie theory [14]. Starting from Mie theory, analytical expressions were derived for the internal and scattered electromagnetic fields of spherical particles [14]. Furthermore, the angle-averaged external emission rate per unit energy is given by

$$r_s(h\nu) = c\rho_f(h\nu) f_{BE}(h\nu) Q_{abs}(h\nu) \pi a^2 \qquad (4)$$

for a spherical particle with radius a and the absorption efficiency Q_{abs}, defined as the ratio of the absorption cross section to the geometrical cross section [14]. Eq (4) was derived for thermal equilibrium of the particle with a radiation field described by the Bose-Einstein distribution function f_{BE} and the free space photonic density-of-states ρ_f. The absorption efficiency of a sphere with radius a is given by

$$Q_{abs} = 2\left(\frac{\lambda}{2a\pi}\right)^2 \sum_{n=1}^{\infty} (2n+1)\left\{\mathrm{Re}\{a_n + b_n\} - |a_n|^2 - |b_n|^2\right\} \qquad (5)$$

where λ is the wavelength in the surrounding medium, and a_n and b_n are the complex scattering coefficients [14].

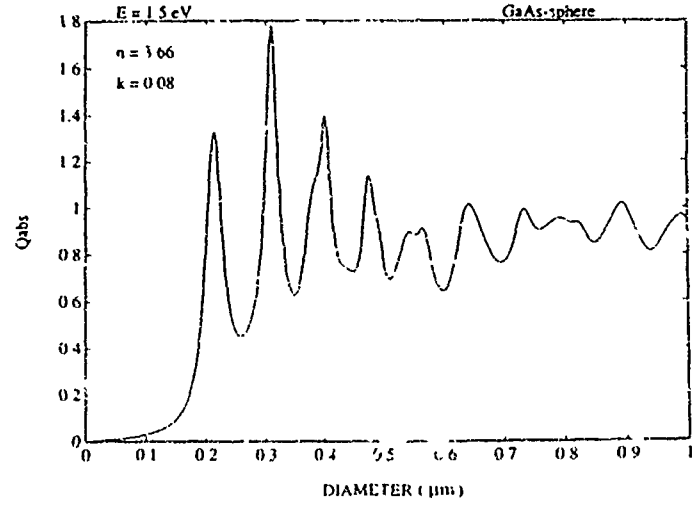

Fig. 4: Calculated absorption efficiency Q_{abs} of a spherical GaAs microcrystal as a function of the sphere diameter for optical excitation at the bandgap energy (indices of refraction for bulk GaAs: $N_1 = 3.66 + i0.08$ for E = 1.5 eV (T = 77 K); surrounding medium: $N = 1.2 + i0.0$)

In Fig. 4 the calculated absorption efficiency Q_{abs} of spherical GaAs microcrystals is plotted as a function of the sphere diameter for optical excitation at the bandgap energy. The calculation was performed after Ref.[14]. The curve shows an oscillatory behavior with several size ranges where the absorption efficiency exceeds unity, leading to an increased emission rate according to Eq.(4). Since Q_{abs} scales with the ratio of sphere diameter to wavelength, the energy dependence of Q_{abs} for a given particle size is qualitatively similar to the size dependence at a given wavelength [14].

Fig. 5 shows the emission spectra from GaAs microspheres calculated from Eq.(4) as a function of energy at a temperature of 77 K. The spectra were estimated for the sphere diameters 400 nm, 550 nm, and 900 nm, where $Q_{abs}(E_{gap})$ reaches a maximum, respectively (see Fig. 4). The dashed curve in Fig. 5 shows the bulk GaAs luminescence spectrum for comparison. The microsphere luminescence spectra reveal a size- and energy-dependent enhancement that leads to a spectral blue-shift of the luminescence maximum and a line-broadening.

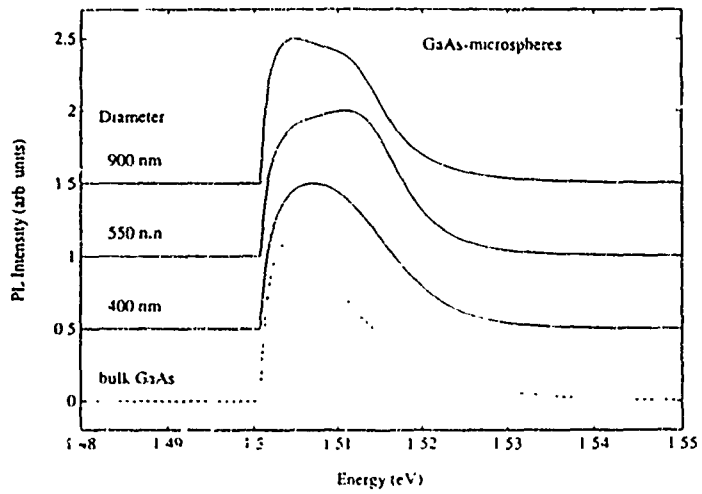

Fig. 5: Calculated luminescence spectra from GaAs microspheres as a function of energy at a temperature of 77 K. The spectra were estimated for the sphere diameters 400 nm, 550 nm, and 900 nm, where $Q_{abs}(E_{gap})$ reaches a maximum, respectively (see Fig. 4). Dashed curve: bulk GaAs luminescence spectrum.

The internal electric field of GaAs microspheres was calculated after Ref.[15] for optical excitation at the bandgap ($E_0 = 1.5$ eV at 77 K) by a plane wave with a field amplitude E_0. Fig. 6 shows the normalized angle-averaged electric field $<E>/E_0$ as a function of the normalized radius r/a for different sphere diameters $2a$. The values for the radii were chosen from Fig. 4 at 'resonant' ($Q_{abs} > 1$) and 'nonresonant' ($Q_{abs} < 1$) positions. At resonant sizes ($2a = 0.214$ µm, 0.31 µm, and 0.89 µm) the averaged internal field is enhanced up to $<E>/E_0 \sim 20$ near the surface, whereas at nonresonant sizes (e.g. $2a = 0.26$ µm) the field maximum occurs at the sphere center and is less pronounced. Similarly, an estimation of the surface field following the treatment in Ref.[16] revealed resonant enhancement of the radial field component at the surface [17].

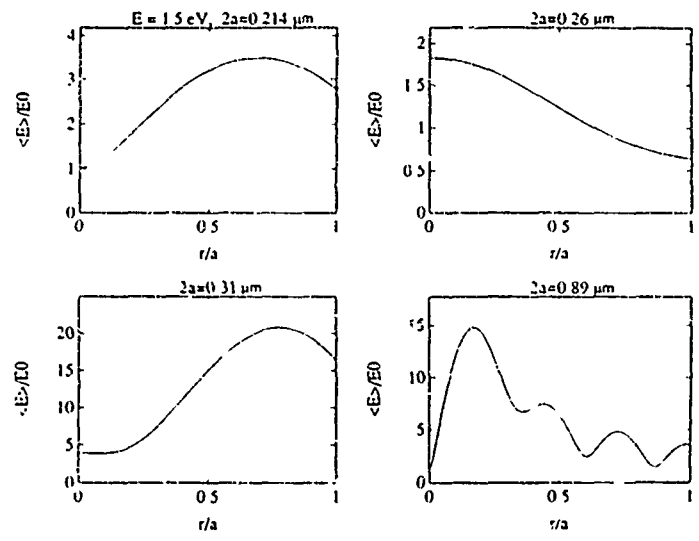

Fig. 6: Calculated angle-averaged electric field $<E>/E_0$ in GaAs microspheres (laser excitation at the bandgap with a field amplitude E_0) as a function of the normalized radius r/a for different sphere diameters $2a$ (given in micrometers). The values for the radii were chosen from Fig. 4 at resonant ($Q_{abs} > 1$) and 'nonresonant' ($Q_{abs} < 1$) positions.

5. DISCUSSION

The experimentally observed photoluminescence spectra from GaAs microcrystallites exhibit a line broadening and a blue-shift of the luminescence maximum which both increase with decreasing average crystal size (Fig. 2). This anomalous behavior is consistent with the calculated effects due to dielectric light confinement in semiconductor microcrystals.

The theoretical results for a threedimensional optical microcavity show that a resonance in the photonic density-of-states above the band gap energy enhances the emission rate and thus

modifies the shape of the luminescence spectrum Due to the asymmetry of the luminescence spectra and the statistical size distribution of the crystals, a blue-shift of the total luminescence maximum is expected, and the spectral changes get more pronounced with decreasing crystal size, i.e. increasing mode spacing [10]. The optical excitation process of the microcrystals and the interaction with the Si-substrate are not included in our model However, the results from similiar experiments show only a minor effect of different substrates (insulator or metal) on the emission spectrum [18]. In these experiments structural resonances were observed in the fluorescence spectra of dye-doped dielectric microspheres [18].

Similiar theoretical results for the luminescence spectra are obtained from an analysis based on Mie theory for GaAs microspheres. The emission spectrum is determined by the absorption efficiency, which is implicitly related to the photonic density-of-states [19]. Since the absorption efficiency is resonantly enhanced as a function of both the sphere size (Fig. 4) and the excitation wavelength, size-selective excitation is expected. Therefore, the relative luminescence intensity from spheres with different sizes (Fig 5) depends on the absorption efficiency both at the excitation and the emission wavelength.

The strength of the internal field enhancement (Fig 6) reaches remarkable values of up to a factor of 20 at resonant excitation. This field enhancement near the surface corresponds to the 'whispering gallery' modes that have been reported in disklike semiconductor structures [6]. The resonant field enhancement on the microcrystal surface should lead to surface-enhanced Raman scattering as already observed on GaP microcrystallites [20] The internal field enhancement depends strongly on the imaginary part of the index of refraction and reaches several orders of magnitudes below the bandgap of GaAs Therefore, strong optical nonlinearities or even intrinsic optical bistability might be possible at spectrally narrow optical transitions below the bandgap or at indirect transitions in different materials

The agreement of the calculated spectral characteristic in Fig 2 and Fig. 5 with the experimental results in Fig 2 leads us to the conclusion, that the observed photoluminescence spectra result from *spectral enhancement and inhibition of spontaneous emission in dielectrically confined GaAs microcrystallites*

6. CONCLUSION

Spectral alterations in the photoluminescence of GaAs microcrystallites have been investigated experimentally The observed behavior is in agreement with the calculated effects of dielectric light confinement in three dimensional semiconductor microcavities The consequences of enhanced spontaneous emission in this kind of microcavity are promising for applications in nonlinear optics and optoelectronics

This work has been supported by the Fonds zur Forderung der Wissenschaftlichen Forschung (FWF), Austria, under projects number P7558 and P8704

REFERENCES

1. E. Yablonovitch, *Phys Rev Lett* 58, 2059 (1987)
2. F. De Martini, G Innocenti, G R Jacobovitz, P Mataloni, *Phys Rev Lett* 59, 2955 (1987)
3. Y. Yamamoto, S Machida, K Igeta, G Björk, in *Coherence Amplification and Quantum Effects in Semiconductor Lasers*, edited by Y Yamamoto (Wiley, New York, 1991)
4. T. J. Rogers, D G Deppe, B G Streetman, *Appl Phys Lett* 57, 1858 (1990)
5. T Yamauchi, Y Arakawa, M Nishioka *Appl Phys Lett* 58, 2339 (1991)
6. S L McCall, A F J Levi R E Slusher, S J Pearton, R A Logan, *Appl. Phys. Lett.* 60, 289 (1992)
7. E. F. Schubert, Y.-H. Wang, A. Y Cho, L.-W. Tu, G. J. Zydzik, *Appl Phys. Lett* 60, 921 (1992)
8. T Baba, T. Hamano, F Koyama, K Iga, *IEEE J Quantum Electron* 28, 1310 (1992)
9. S Juen, K Uberbacher, J. Baldauf, K F Lamprecht, R. Tessadri, R Lackner, R A. Höpfel, *Superlattices&Microstructures* 11, 181 (1992).
10. S Juen, K. Überbacher, J Baldauf, K F Lamprecht, R A Höpfel, *Appl Phys Lett* 62, 1958 (1993)
11. H B. Bebb, E. W Williams, in *Semiconductors and Semimetals*, Vol. 8, ed. by R K. Willardson and A C. Beer (Academic Press, 1981)
12. D P. O'Brien, P. Meystre, H Walther, in *Advances in Atomic and Molecular Physics*, Vol. 21, ed. by D. Bates and B Bederson (Academic Press, Orlando, 1985)
13. S. C. Ching, H. M. Lai, K Young, *J Opt Soc. Am B* 4, 1995 (1987).
14. C F Bohren, D R Huffman, *Absorption and Scattering of Light by Small Particles* (John Wiley, New York, 1983)
15. P R Conwell, P. W Barber, C K Rushforth, *J Opt Soc Am A* 1, 62 (1984)
16. B J. Messinger, K. U von Raben, R K Chang, P W Barber, *Phys Rev. B* 24, 649 (1981)
17. S Juen, K. F Lamprecht, R. Rodrigues, R A Höpfel, unpublished
18. S C Hill, R E Benner, C K Rushforth P R Conwell, *Appl. Opt.* 23, 1680 (1984)
19. A J Campillo, J D Eversole, H-B Lin, *Phys Rev Lett* 67, 437 (1991).
20. S Hayashi, R Koh, Y Ichiyama, K Yamamoto, *Phys Rev. Lett.* 60, 1085 (1988)

ThP14

Tailoring of the carrier capture efficiency of a quantum well

J M Gerard
France Telecom CNET/PAB, 196 av Henri Ravera, 92225 Bagneux Cedex FRANCE
and
B Deveaud
France Telecom, CNET/LAB, 22301 Lannion FRANCE

Abstract:
A GaAs quantum well (QW) placed in an AlGaAs barrier layer of linearly graded composition has been studied by photoluminescence, so as to estimate experimentally the carrier capture efficiency of a QW in an electric field. The capture probability can be drastically enhanced or reduced, by introducing a slight compositional asymmetry (3 to 5% Al) between both sides of the QW. This tuning is efficient for temperatures as high as 77K. Our experimental results, supported by a quantum mechanical calculation of the capture probability, suggest novel routes for optimizing QW infrared photodetectors and QW lasers.

The efficiency of carrier capture processes often define the ultimate performance of quantum well (QW) based devices. For instance, the capture of photoexcited carriers by subsequent QWs limits the optical gain, and therefore the responsivity and detectivity of QW infrared photodetectors (QWIPs) [1], whereas the capture time of electrons in the optical cavity by the QWs limits the modulation bandwidth of separate confinement QW lasers [2]. The capture efficiency of a quantum well (QW) markedly depends on its design. For instance, the oscillatory dependence of the capture time as a function of the QW thickness, predicted theoretically some years ago [3], has found recently a clear experimental confirmation from time resolved photoluminescence (PL) studies [4,5]. It is therefore necessary (and possible) to take into account capture processes in a global attempt to optimize optoelectronic QW devices. Up to now, only a transmission of the electron capture time in undoped seperate confinement multi QW heterostructures has been conducted [6]. It appears now more generally highly desirable 1) to study the capture efficiency of a QW for electrons drifted by an E-field (which is the relevant situation for vertical transport optoelectronic devices such as QWIPs or electrically pumped lasers), 2) to be able to adjust independently such electronic properties of the structure as its operating wavelength and the QW capture efficiency.

We show for the first time that the capture probability p of a drifted electron to be captured by a QW can be tuned very efficiently by introducing a slight asymmetry of the barrier heights of the QW. For moderate E fields the dominant capture mechanism presumably relies on LO phonon scattering as in absence of E field. In order to avoid the capture of a carrier (e.g. an electron), we raise the upstream barrier height V_u with respect to the downstream barrier height V_d by typically $\hbar\omega_{LO}$, even after emission of a single LO phonon the electron still occupies a delocalized quantum state and can be drifted by the electric field. Electron capture then requires multiple phonon emission, and is therefore drastically less probable. On the other hand, the capture probability p can also be drastically enhanced by raising V_d with respect to V_u. If the barrier height difference $V_d - V_u$ is larger than the typical kinetic energy of incoming electrons, the capture probability will become close to unity.

Since time resolved PL experiments cannot be easily conducted for QWs under E field, we introduced a novel approach which permits an optical investigation by cw PL of the influence of the QW barrier asymmetry on p. We mimic the presence of an E field by inserting the QW whose capture efficiency is studied in a barrier of linearly graded composition. The PL intensity of the QW under continuous excitation of the upstream barrier is then proportionnal to the probability for injected electrons to be captured by the QW. We describe hereafter two series of experiments which highlight the efficient tuning of p resulting from a slight asymmetry of the QW composition profile.

Our GaAlAs/GaAs test structures have been grown by molecular beam epitaxy (MBE) on GaAs (001) substrates; there design is plotted in the inserts of figures 1 and 2 for the first and second series of experiments respectively. Each sample comprises, from surface to buffer layer, a thick surface absorbing $Ga_xAl_{1-x}As$ cap layer (0.4 µm), the upstream $Ga_xAl_{1-x}As$ graded barrier: (dx/dz = 1 µm^{-1}) the GaAs QW "C", whose capture efficiency is studied, the "downstream" $Ga_xAl_{1-x}As$ graded barrier (dx/dz = 1 µm^{-1}) and a broad GaAs QW "T". A low MBE growth rate (0.3 µm/h) has been implemented in order to ensure a perfect control of the composition profile. Finally, the structure is entirely Be-doped low p-type ($5\ 10^{16}$ cm^{-3}).

Our cw PL experiment is performed at 8K under excitation with the blue 476.5 nm line of an argon ion laser. For this wavelength the absorption coefficient in the cap layer A is α=60000 cm^{-1}, so that we have no significant direct excitation of QWs T and C. The generated electron-hole pairs diffuse in layer A, and the electrons are drifted in the apparent electric field of the graded barrier layer. The valence band configuration of this p type heterostructure is essentially flat in our power density range (typically 500 W cm^{-2}), so that this apparent electric field is close to 15 kV/cm in the graded layers, i.e. in the useful range for QWIPs. On the other hand, majority holes move nearly freely throughout the structure. A fraction p_c of the injected electrons is captured by QW C, whereas transferred electrons are collected in QW T. At such a low temperature (8K), thermoemission of electrons out of QW C can be neglected, since GaAs/GaAlAs structures have furthermore a radiative efficiency close to unity at low temperature, the PL intensity of QWs C and T respectively reflect the proportions of incoming electrons which have been captured or not by QW C, i.e. p_c and $1-p_c$.

We study in a first experiment a 65 Å thick $Ga_{0.7}Al_{0.3}As$ QW. In our reference sample R_0, the downstream barrier of QW C has a 0.7% lower Al composition than the upstream barrier, in order to mimic the potential drop across the QW for a 1.5 kV/m electric field. In a series of "modified" samples, the Al composition of the upstream barrier has been uniformely lowered (or raised) by a variable Δx. The PL spectra obtained at 8K for three samples (Δx = 0, 0.05 and -0.05) are shown on figure 1. We observe for each sample two PL peaks, easily attributed to the thin QW C and to the large QW T. The relative intensity of these peaks is drastically affected by the introduction of a small barrier (Δx = 0.05) or a small "jump" (Δx=-0.05) for the drifted electrons: the PL intensity of QW T is reduced by a factor of 10 in the first case, and enhanced by a factor of 2.5 in the second case, which reveals a similar change for the proportion $1-p_c$ of the transferred electrons.

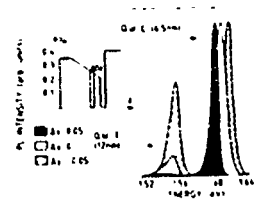

fig. 1 Normalized 8K PL spectra for the reference sample R_0 (Δx = 0), and for two modified samples, for which the electron capture by QW C is enhanced (Δx = -0.05) or inhibited (Δx = 0.05). The Al composition profile of these GaAs/GaAlAs heterostructures is sketched in insert, by solid and dashed lines respectively.

This efficient tuning of $1-p_c$ is obtained for a moderate change of the composition profile (Δx = 0.03 corresponds to 45 meV change of the upstream barrier height, i.e. in the energy range of the (higher energy) AlAs-type LO phonons of the GaAlAs barrier (≈ 47 meV). In this experiment however, the capture efficiency of QW C is always very large: p_c, equal to 0.85 for the reference sample, remains larger than 0.5 for all samples. The comparison with our second experiment will indicate that this large capture probability is essentially related to the presence of a high barrier on the substrate's side of QW T, i.e. in the vicinity of QW C (distance: 37 nm).

A second series of samples which mimics more closely the conduction band configuration in QWIPs, has also been grown. Their structure sketched in figure 2, differs of the first series in that 1) the high barrier on the substrate's side of QW T has been suppressed, 2) the width of the downstream barrier has been enlarged up to 100 nm, 3) our reference QW C is now a 5nm thick $GaAs/Ga_{0.7}Al_{0.3}As$ QW. Furthermore, the "modified" samples are now obtained by changing the height of the downstream barrier.

The PL spectra obtained for the reference sample R_0 (Δx=0) and two modified samples (Δx = 0.03 and 0.03) are displayed in figure 2. The capture probability p_c for the reference sample

is now 0.4. Here again a drastic modification of the intensity ratio of QWs *C* and *T* emissions is observed when a slight QW asymmetry is introduced. It is worth being emphasized that the total PL intensity remains, as expected, essentially constant. p_c becomes close to 0.85 when the composition of the Al composition of the downstream barrier is raised by 0.03, whereas capture probabilities as low as 0.15 and 0.10 are observed when it is lowered by 0.03 and 0.06 respectively. On the other hand, the PL peak energy of QW *C* is essentially unaffected for the "modified" samples: capture characteristic and other electronic properties of QWs can by optimized independently by using this technique.

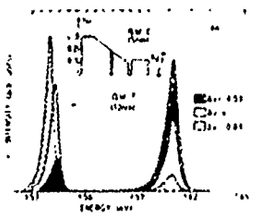

fig. 2: Same as fig. 1, for the reference sample R_2 ($\Delta x = 0$), and two modified samples ($\Delta x = -0.03$ and 0.03). The Al composition profile of these GaAs/GaAlAs heterostructures is sketched in insert, by solid and dashed lines respectively. The PL intensity scale is the same for all samples.

As required for any practical application to QWIPs, this effect is also observed at 77K: we obtain p_c= 0.20, 0.45 and 0.70 respectively for Δx= -0.03, 0 or +0.03. Thermoemission of electrons from QW *C* totally blurs the data obtained at 300K (by strongly enhancing the PL intensity of QW *T*), and presumably accounts for the slight differences observed between 8K and 77K results.

No quantum mechanical calculation of p has been conducted up to now for carriers drifted in an electric field. We propose here a novel approach, which gives, despite its roughness, a good estimate of p_c in QWIPs and describes satisfyingly the influence of Δx on p_c.

Two major problems are the difficulty to describe the overall relaxation of the electrons in the graded layer and the fact we need to take into account the finite coherence length of the electron wave function when calculating p. To overcome these difficulties, we consider an electron "just arriving" at QW *C*. We attribute to this electron a wave-paquet Ψ, which typical extension is defined by the electron mean free path. We then compute the bound states $|k>$ of the heterostructure comprising both QWs, the graded layer and a semi-infinite barrier on the substrate's side of QW *T*, and the scattering rate rate W_{ij} for single LO phonon emission processes for all possible initial and final electron minibands, by using Fermi's golden rule and a Fröhlich matrix element. Retaining these dominant energy relaxation processes only, we estimate p_c as:

$$|\Psi> = \sum_k a_k |k> \qquad p_c = \sum_i |a_i|^2 \frac{W_{i,c}}{\sum W_{i,.}}$$

where c labels the miniband originating from the single bound state $|c>$ of QW *C*.

Figure 3 displays for both series of samples the influence of Δx on the calculated capture probability, for a 20 nm broad real square wave-paquet (This size corresponds to the typical mean-free path of the electron for a $1.5\ 10^5$ V/m electric field and a μ_n=2000 $cm^2\ V^{-1}\ s^{-1}$ electron mobility in $Ga_{0.7}Al_{0.3}As$ [6]). For the reference samples R_1 and R_2, we respectively estimate p_c to be 0.085 and 0.4. (For a lower quality barrier material, p_c is somewhat larger, e.g. p_c = 0.1 and 0.35 for a 15 nm broad wave paquet). On the one hand, this clear difference confirms the drastic influence of the proximity of a high barrier on the capture efficiency of QW *C*, already observed experimentally. On the other one, our theoretical estimate for p in sample R_2 is in correct agreement with previous measurements of p_c (p_c =0.13) by admittance spectroscopy [7] and accounts particularly well for the p_c = 0.08 average estimate which has been extracted from

the measurement of the optical gain of numerous QWIPs [8]. Though rather crude, our model is therefore very likely to describe accurately the influence of a QW asymmetry on p_c. The theoretical dependance of p_c on Δx is plotted on figure 3. For the second series of samples (as well as QWIPs), a small Δy (Δx<0.05) allows to reduce by a factor of three (down to 0.03) or enhance p_c up to 0.95.

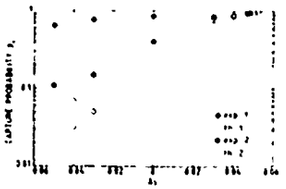

fig. 3: The experimental and theoretical values of p_c are plotted as a function of Δy for both kind of heterostructures, whose composition profiles are sketched in the inserts of fig. 1 and 2 respectively.

Though the experimental *relative* dependance of p_c on Δy is well described for both series of samples, differences are observed between experimental and calculated values of p_c. This effect is presumably related to the ambipolar character of the transport and capture in our samples. At the initial stage of the illumination, the capture probability by QW *C* is much larger for the holes than for the electrons. A photoinduced electric field E_{ph} appears *between QW C and QW T* under steady state illumination [9], in order to favor the transport of holes across the structure toward QW *T*. Consequently, the capture probability of the incoming electrons by QW *C* is enhanced (E_{ph} is such that electron and hole currents flowing from QW *C* to QW *T* are equal, as such, E_{ph}, and the capture probability of electrons are independent of the excitation power). We therefore do not expect our experiment on the reference sample to give a *quantitative estimate* for p_c in conventional QWIPs, but reflect only qualitatively the dependance of p_c on Δy. The determination becomes however quantitative when p_c is large, since nearly all photocreated electron-hole pairs then recombine in QW *C*.

To conclude, the introduction of a slight compositionnal asymmetry for QW barriers allows to tune very efficiently the probability for electrons, drifted by an electric field, to be captured by this QW. This opens the way to an independant optimisation of capture characteristics and optical properties of numerous QW based optoelectronic devices.

The authors gratefully acknowledge J.Y. Marzin, G. Bastard, J.F. Palmier, A. Regreny, B. Lambert, F. Clérot, D. Morris, M. Veos and M. Quillec for stimulating discussions.

References:

[1] *Intersubband Transitions in Quantum Wells*, edited by E. Rosencher, B. Vinter and B.F. Levine (Plenum, London 1992)
[2] P.W.M. Blom, J.E.M. Haverkort and J.H. Wolter, Appl. Phys. Lett. 58, 2767 (1991)
[3] J.A. Brum and G. Bastard, Phys. Rev. B33, 1420 (1985)
[4] B. Deveaud, A. Chomette, D. Morris and A. Regreny, Solid State Comm. 85, 367 (1993)
[5] P.W.M. Blom, C. Smit, J.E.M. Haverkort and J.H. Wolter, Phys. Rev. B47, 2072 (1993)
[6] Stringfellow G.B., J. Appl. Phys. 50, 4178 (1979).
[7] F. Luc, E. Rosencher and B. Vinter, Appl. Phys. Lett. 62, 1143 (1993)
[8] H.C. Liu, Appl. Phys. Lett. 60, 1507 (1992)
[9] C.T. Liu, J.M. Liu, P.A. Garbinski, S. Luryi, D.L. Sivco and A.Y. Cho, Phys. Rev. Lett. 67, 2231 (1991)

ThP15

Stark-Wannier states in nanostructures

E.A.M. Fagotto, P.A. Schulz and J.A. Brum
IFGW-DFESCM, UNICAMP, Cx. 6165, 13081 - Campinas (SP) - Brazil

Abstract

We study the effects of a longitudinal-external-electric field on the electronic properties of an open-quantum-dot superlattice. These structures present the formation of two different gaps, one associated with the periodicity of the structure imposed upon the 1D mode and the other associated to the destructive interference between the 1D mode and the quantum-dot states. The transmission coefficients between two quasi-two dimensional reservoirs through these structure are calculated. The electric field presents different regimes: at weak fields the transmission peaks associated to the tunneling through the confined dot states show an energy shift and a progressive decline of the transmission. At moderate fields the transmission bands become sharp and the transmission peaks to one. As the electric field increases the anti-resonance gaps widen. Finally, at large electric fields, the Wannier-Stark levels are completely formed and the transmission is characterized by a series of relatively equally spaced peaks.

Mesoscopic systems have been intensively studied in the recent years [1]. With the improvement of nano-scale fabrication techniques, it has been possible to design a whole new kind of structures based on the high-mobility two-dimensional (2D) electron gas formed in GaAs-(Ga,Al)As heterojunctions. The physics behind these systems is based on the lateral confinement which binds the carriers in one or two additional dimensions besides the epitaxial one. Recently, the interplay between one- and zero-dimensional levels has been considered. Particularly, an open-quantum-dot superlattice was built and transmission gaps were observed [2]. The existence of carrier confinement in open cavities was first discussed by van der Marel [3] and Peeters [4]. Ulloa et al. [5] discussed for the first time the effects of a periodic quantum-dot structure superimposed on a one-dimensional channel. Brum [6] discussed the effects of the interplay between the cavity confined states and the superlattice states. More recently, other structures based on the same principles have been considered [7,8]. The effects of a longitudinal-external-electric field, F, in a single constriction and quantum chains have been studied by Castaño et al. [9]. Their emphasis was on the nonlinear transport characteristics in these nanostructures.

An electric field superimposed on a periodic potential leads to the replacement of the band structure by a ladder of spatially localized states (Wannier-Stark states) equally spaced in energy by eFd, where d is the periodicity of the structure [10]. Recently, these states have been observed in one-dimensional semiconductor superlattices [11,12]. The coupling among Wannier-Stark levels originated from different subbands has also been considered [13,14].

In this work, we discuss the effects of an external electric field, applied along an asymmetric-multiple-open-quantum-dot structure (AMOQDS). Our main interest is on their electronic properties. They will be probed by the transmission coefficient through the structure enclosed by two quasi-two-dimensional reservoirs. Our structure is similar to the one discussed previously by one of us [6]. A laterally patterned GaAs/(Ga,Al)As heterojunction is considered. We assume a strong confinement along the z-direction so that the system is in the Electric Quantum Limit with respect to quantization of motion in this direction. The lateral confinement is sketched in Figure 1. Two structures are studied: one with a single quantum dot and the other with three quantum dots. We perform a multi-mode transmission calculation following the same lines as in previous work [6]. We approximate the electric field effects by considering only the potential drop from one layer respective to the other. Inside each layer, a flat band is assumed. Our calculations for a large number of dots have shown that three dots are already enough to reflect the main superlattice effects. Basically, they are formed by periodic indentations superimposed on one side of a one-dimensional (1D) channel. The carriers are assumed to be ballistic in the channel. They are linked to the two wide regions which behave as quasi-two dimensional reservoirs. The indentations give origin to a zero-dimensional confinement potential. At least one zero-dimensional state is energetically below the first 1D mode. The excited dot states will then be resonances in the 1D modes.

In the absence of electric field, the transmission probability is rich in structures [6]. At energies below the first-1D mode, it shows a narrow band of energy with unitary transmission. This is associated with the tunneling through the confined-quantum-dot levels. At energies above the first-1D mode, transmission gaps are superimposed on the transmission-step quantization. These gaps have two different origins: one is associated to the superlattice gaps, due to the periodicity introduced in the 1D channel. The other comes from the destructive interference between the 1D mode and the quantum-dot levels. The latter can also be seen as the anti crossing between two bands: a wide band, the 1D mode, and a narrow band, formed by the small overlap among the quantum dot levels. Due to the one-dimensionality of the transmission channel, the anti crossing creates a gap in the transmission, associated with the anti resonance gap on the band structure [6]. The character of the 1D mode levels is well illustrated with the wave-functions. Fig. 3(a) shows the wave-function probabilities for an one-open-quantum-dot for an energy at the second transmission maximum in the absence of electric field. Fig. 5(a) and Fig. 6(a) show the wave-function probabilities for a three-open-quantum-dot structure, for an energy at the third peak of the first transmission band maximum and at the second peak of the second transmission band maximum, respectively, in the absence of the electric field. Figures 3(a) and 6(a) show maxima of probability of finding the electron at the narrow constrictions characterizing the states as 1D mode-like. On the other hand, the third peak of the first transmission band maximum, Figure 5(a), shows the maximum of the wave-function probability at the wide constriction, i.e., at the quantum dot.

In the presence of an electric field applied along the AOQDS the two bands present a quantitative different behavior. This is reflected at the gaps formed in the transmission probability. On one side, the Wannier-Stark states are evenly spaced in energy in both bands. This implies that the narrow band will largely widen with the electric field in comparison to the wide band in order to accommodate the Wannier-Stark levels. At the same time, the coupling of these bands is responsible for the anti resonance gap. These effects may be separated in three ranges of values for the electric field showing qualitative different behavior. In the following, we compare the effects for the one dot and the three dot case for the different electric fields.

Figures 2 (a-i) shows the transmission probability for the one-dot case as a function of the electron incoming energy for several values of electric field. At weak electric fields, we clearly observe a linear shift in energy of the first transmission peak. This peak is associated with the tunneling through the fundamental quantum dot state below the first 1D mode. The anti resonance gap, associated to the second dot state, shows an identical shift, as it is expected. For

the same range of electric field, the transmission maxima fall to values lower than one. This is a consequence of the break of symmetry in the barriers through which the electron has to tunnel [15]. As the electric field increases, the first peak is suppressed since it shifts to energy values below the emitter minimum.

At intermediate fields, we observe the evolution of the transmission band towards a sharp peak. Originally, this band is associated with the first 1D mode. The electric field breaks the degeneracy between the modes from the two narrow constrictions. The first 1D mode hybridizes with the dot state given origin to a sharp transmission. When these states are resonant one with the other, the hybridization is maximum and the transmission reaches the unitary value. As the electric field further increases, the dot state falls below the energy of the 1D mode. The transmission is then due to the tunneling through a confined state, in a similar behavior as the fundamental dot state at the zero electric field. The difference to the latter case is that now, the confined state is a hybrid one. This is illustrated in Figures 3(a) and 3(b) where the wave-function probability for the second transmission maximum is plotted for zero electric field and for $F=0.53$ kV/cm. We clearly observe its evolution from a 1D mode toward a 1D-0D hybrid state. As a consequence of this hybridization, the energy shift of this maximum has a weaker dependence with the electric field than the dot levels. Its position gets close to the anti resonance gap and their wave-function probabilities are quite similar.

For higher electric fields (not shown here), the above behavior repeats in a quite similar way for the higher dot levels.

Figure 4 (a-i) shows the three-dots structure transmission probability as a function of the electron incoming energy for several electric fields. The three-dots case presents a quite different behavior. As mentioned before, the superlattice effects are already present. The first series of maxima in the transmission are associated to the narrow band formed by the confined-fundamental dot states. The second transmission band is associated with the 1D mode. After that we observe a strong reduction in the transmission probability which is related to the gap formed by the periodicity of the structure. The next gap is due to the anti crossing between the 1D mode and the dot bands. This gap is strongly marked even for a small number of periods [6].

At weak electric fields, the first band shows a similar behavior as the single dot case: a linear energy shift is observed accompanied by the fall of the transmission probability. At higher electric fields ($F > 0.02$ kV/cm) the transmission peaks again for a single level, reaching the unitary value for the last level of the band. The other levels have practically disappeared. This behavior is similar to the transmission band associated to the first 1D mode in the single dot case and it is a common characteristic to the transmissions through a set of levels. Here, due to the discreteness of the states, the sharpening of the band is replaced by the peak at a single level. The same behavior can be observed for the other bands, with the sharpening of the transmissions and remaining at unitary value at least for one level. Only at higher electric fields ($F > 0.04$ kV/cm) these transmissions start to fall below one. In Figures 5 (a) and (b) we plot the wave-function probabilities for the third peak at the first transmission band for F=0 kV/cm and F=0.06 kV/cm, respectively. We clearly observe the extended state to localize into a discrete state, typical of a Wannier-Stark level. Figures 6 (a) and (b) show the wave-function probabilities for the second peak at the second transmission band at the same values of electric field as in Figures 5. As in Figures 3, we clearly observe the 1D mode and the dot level hybridization.

We also observe in Figures 4 (a-i) a different behavior for the transmission gaps. The superlattice gap practically does not change. This is not surprising since the electric field splits the wide 1D mode bands into discrete levels. For the electric fields considered here, the band width can accommodate the Wannier-Stark levels without modifying the gap width. At the higher fields shown here, we observe a slight narrowing of the superlattice gap. This reflects the limit of the 1D mode band to accommodate the Wannier-Stark levels within its energy width. A complete different behavior is shown by the anti resonance gap. Here, the gap is formed by the anti crossing of the narrow dot band with the wide 1D band. As the Wannier-Stark levels are formed, they further contribute to prevent the transmission. At intermediate electric fields ($F \sim 0.04$ kV/cm), the transmission gap broadens significantly. This is due to the increasing separation in energy of the dot levels. They are, however, close enough to each other in order to prevent almost entirely the transmission in this energy range due to the anti resonance effect. At higher fields, the Wannier-Stark levels are too separated in energy and some transmission is possible for the energies between two different levels. Actually, for these and higher values of electric field, the concepts of gap and band start to break down.

A direct observation of the above effects depends on several additional effects. Conductance measurements have been one of the most powerful experimental tools to probe similar effects [1,2]. However, some aspects remain to be cleared: charge effects, such as Coulomb blockade, may hamper their observation for the state-of-art of the mesoscopic systems. Another difficulty is in the connection among transmission probabilities and conductance measurements, particularly in the presence of nonlinear effects. A complete solution of the transport problem in these systems is beyond the scope of this work. Nevertheless, we believe that the effects discussed here should be reflected in the electronic properties of actual systems and should be considered whenever confined cavity states are coupled to 1D modes.

Acknowledgments: E.A.M.F. is supported by the Brazilian Agency CAPES. P.A.S. and J.A.B. are partially supported by the National Council for Research and Development (CNPq, Brazil).

1. For a review see Beenakker and van Houten, *Quantum Transport in Semiconductor Nanostructures*, in *Solid State Physics*, p. 1, edited by H. Ehrenreich and D. Turnbull, Academic Press, New York, 1991.
2. L.P. Kouwenhoven, C.W.J. Hekking, B.J. van Wees, C.J.P.M. Harmans, C.E. Timmering, and C.T. Foxon, Phys. Rev. Lett. 65, 361 (1990).
3. D. van der Marel, in *Nanostructures Physics and Fabrication - 1989*, College Station, Texas, p. 149, ed. by M.A. Reed and W.P. Kirk, (Academic Press, New York, 1989).
4. F.M. Peeters, *Science and Engineering of 1- and 0-Dimensional Semiconductors*, p. 107, ed. by S.P. Beaumont and C.M. Sotomayor Torres (Plenum, New York, 1990).
5. E. Ulloa, E. Castaño, and G. Kirczenow, Phys. Rev. B41, 12350 (1990).
6. J.A. Brum, Phys. Rev. B43, 12082 (1991).
7. K. Nakazato and R.J. Blaikie, J. Phys. Condens. Matter 3, 5729 (1991).
8. H. Wu and D.W.L. Sprung, Phys. Rev. B47, 1500 (1993) and H. Wu, D.W.L. Sprung, and J. Martorell, J. Phys. D Appl. Phys. 26, 798 (1993).
9. E. Castaño, G. Kirczenow and S.E. Ulloa, Phys. Rev. B42, 3753 (1990).
10. G.H. Wannier, Rev. Mod. Phys. 34, 645 (1962).
11. E.E. Mendez, F. Agullo-Rueda, and J.M. Hong, Phys. Rev. Lett. 60, 2426 (1988).

12 P Vouin, J Bleuse, C Bouche, S Gaillard, C Alibert, and A Regreny Phys Rev Lett 61, 1639 (1988)
13 S R Andrews, C M Murray, R A Davies, and T M Kerr, Phys Rev B37,8198 (1988)
14 H Schneider, H T Grahn, K v Klitzing, and K Ploog, Phys Rev Lett 65, 2720 (1990)
15 B Ricco and M Ya Azbel, Phys Rev B29, 1970 (1984)

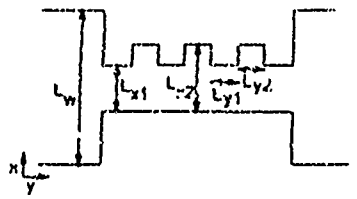

Fig 1 - Top view of the potential of the asymmetric open-quantum dot structure

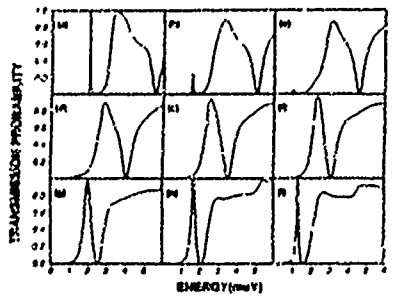

Fig 2 - Transmission probabilities for an asymmetric open quantum dot structure as a function of the incoming energy. L_W = 4000 Å, L_{x1} = L_{y2} = 195 Å, L_{x2} = 500 Å, L_{y1} = 995 Å. a) F = 0 kV/cm, b) F = 0.567 kV/cm, c) F = 0.334 kV/cm, d) F = 0.2 kV/cm, e) F = 0.267 kV/cm, f) F = 0.334 kV/cm, g) F = 0.4 kV/cm, h) F = 0.4673 kV/cm and i) F = 0.534 kV/cm

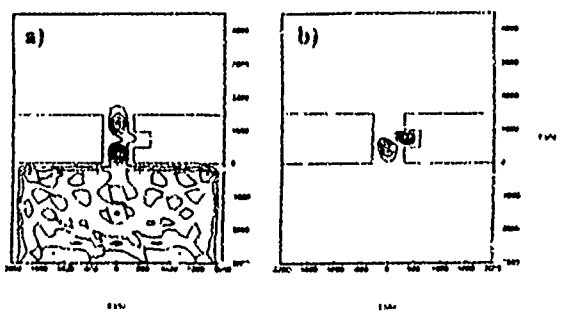

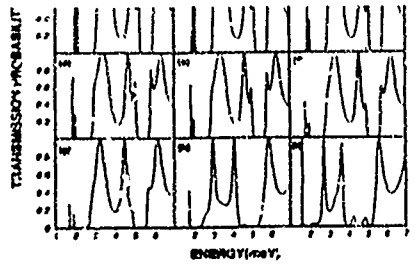

Fig 4 - Transmission probabilities for a three-terminal open quantum dot structure as a function of the incoming energy. a) F = 0 kV/cm, b) F = 0.004 kV/cm, c) F = 0.008 kV/cm, d) F = 0.01 kV/cm, e) F = 0.012 kV/cm, f) F = 0.014 kV/cm, g) F = 0.02 kV/cm, h) F = 0.04 kV/cm and i) F = 0.06 kV/cm. The other parameters are the same as in Figure 2

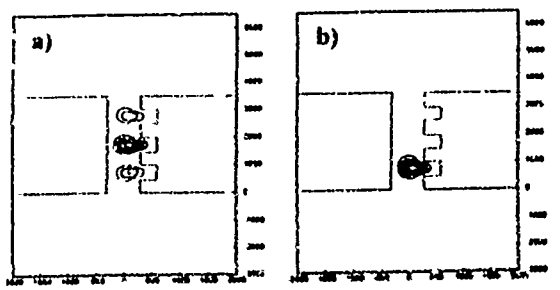

Fig 5 - Wave-function probabilities for the same structure as Figure 4 for a) F = 0 kV/cm, E = 2.1 meV b) F = 0.04 kV/cm and E = 1.8 meV

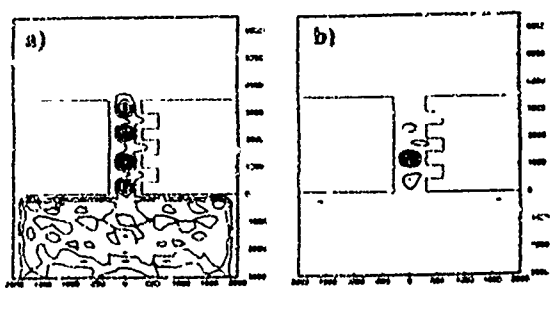

Fig 6 - Wave-function probabilities for the same structure as Figure 4 for a) F = 0.1 kV/cm, E = 1.5 meV, b) F = 0.04 kV/cm and E = 2.7 meV

ThP16

Multi-phonon Relaxation of Electrons in a Semiconductor Quantum Dot

T. Inoshita and H. Sakaki

Quantum Wave Project, IRDC

1-14-302 Komaba, Meguro-ku

Tokyo 153, Japan

Intra-band electron relaxation via phonon emission is an important process that governs the light emission efficiency of semiconductor lasers. Using a perturbation theory, electron relaxation rate in a GaAs quantum dot is calculated to the second order in electron-phonon interactions. If first order processes only are included, rapid relaxation in a small (<1000 Å) dot is impossible unless the intersubband separation is exactly tuned to the LO phonon energy. Two-phonon (LO+LA) processes significantly alleviate the tuning condition by creating a window of rapid (subnanosecond) relaxation around the LO phonon energy. Based on this finding, prescriptions are given for the achievement of highly-efficient quantum dot lasers.

1. Introduction

It was predicted a decade ago that the use of 1D (quantum wire) and, in particular, 0D (quantum dot) structures will produce semiconductor lasers with high efficiency due to their highly peaked (1D) or δ-function-like (0D) density of states [1]. This prediction has given considerable impetus to the research of these low-dimensional systems and seems to have been generally accepted. Experiments, however, have so far shown evidence of photoluminescence *degradation*, rather than enhancement, for dot size below ≈ 1000Å [2]. Damage introduced during the fabrication process has been suspected as the cause of this degradation.

A different and intrinsic mechanism was recently put forward by Benisty, Sotomayor-Torres and Weisbuch [3]. Its main points can be summarized as follows. In the usual process of light emission in a laser, electrons and holes, first created in higher energy continuum, relax down to the ground level in cascade emitting phonons and finally recombine to emit light. Thus, relaxation rate is an important factor dominating emission efficiency. In a quantum dot, longitudinal-optical (LO) phonon emission, which is by far the most efficient relaxation mechanism in higher dimensional systems, is forbidden due to the very discrete nature of the levels, unless the level separation equals the zone center LO phonon energy $\hbar\omega_{LO}$. Deformation potential interaction with longitudinal-acoustic (LA) phonons, which is already weak in the bulk, weakens further as the dot size is reduced, due to decreasing form factor [3,4]. Hence carriers are unable to reach the ground level and compelled to stay in excited levels, whose radiative lifetime is long (due to orthogonality between electron and hole levels with different level index [3]).

Although the above argument is convincing, one would still have to ask, 'Is this the whole story? Is there no way out of this dilemma which can point the way to achievement of efficient light emission?' In an effort to answer this question, we have calculated the electron relaxation rate with both one- and two-phonon processes included [5].

2. Method of calculation

We take a GaAs dot and consider the relaxation of a single electron. (*Hole* relaxation should be much faster due to smaller level separation.) The electron is assumed to be confined in the dot by a parabolic potential $= x^2 + y^2 + z^2$. (It should be stressed that this parabolic model is used here only to facilitate the calculation of matrix elements.) The energy of electrons in this potential is of the harmonic oscillator form $E_n(=m+n)$, where $l,m,n = 0,1,2 \cdots$. The transition rate between the lowest two electronic levels, $\psi(l,m,n) = (1,0,0)$ and $(0,0,0)$, with energy separation of E_0, is calculated by the standard perturbation theory (first and second order). As for the phonons, we take into account bulk LA and LO phonons of GaAs [6], which interact with electrons via deformation potential and Fröhlich interactions, respectively.

This bulk approximation for the phonons may need some explanation. Although no detailed study of the phonon modes in quantum dot structures has been made yet, phonon modes in GaAs/AlAs multi-layer structures are well understood by now [7,8]. The LA modes are delocalized and can be treated as bulk modes. The LO modes, in contrast, are well localized and are classified into confined LO (CLO) modes and interface LO (ILO) modes. In spite of the localized nature of these modes, the relaxation rate calculated in the simple bulk approximation agrees fairly well with that obtained in a fully microscopic calculation [8]. Thus, the bulk approximation is valid for both the LA and LO modes. We will assume that the same is true of our quantum dot structure.

Our calculation was carried out for a total of five processes: LO and LA (one-phonon), and LO±LA and 2LA (two-phonon), where + (-) denotes emission (absorption). The result indicates that LO and LO+LA are the most important. Thus, we will confine our discussion hereafter to these three processes. (For the discussion of LA and 2LA processes, see [5].)

Since an electron-phonon matrix element is proportional to the form factor $\langle n_1 m_1 l_1 | e^{iq\cdot r} | l_0 m_0 n_0 \rangle$ which decays rapidly to zero as q goes beyond $Q = \pi/L$ (where L is the dot diameter and hence $Q << \pi$/zone edge wave vector), only long-wavelength phonons are important. Combining this with energy conservation ($\hbar\omega_q = E_0$ or $\hbar\omega_q \pm \hbar\omega_L = E_0$), we can deduce that rapid relaxation by the LO and LO±LA processes is possible only when E_0 is in the vicinity of $\hbar\omega_{LO} = 35.9$ meV.

3. Results

The calculated relaxation rate $1/\tau$ at $T = 0$ K is shown in Fig. 1 as a function of level separation E_0. As expected, relaxation rate due to the LO (one-phonon) process is sharply peaked immediately below $\hbar\omega_{LO}$. The peak value is as large as 10^{15} s^{-1} (independent of temperature for $kT << \hbar\omega_{LO}$) but the peak is so sharp that $1/\tau$ drops to only 10^{8} s^{-1} for a slight detuning of $\Delta E_0 = -0.05$ meV. (Note that we have taken into account the dispersion of the LO mode.) Thus one cannot take advantage of the large peak value unless E_0 is precisely tuned to $\hbar\omega_{LO}$, far more precise than is possible with today's microfabrication technology.

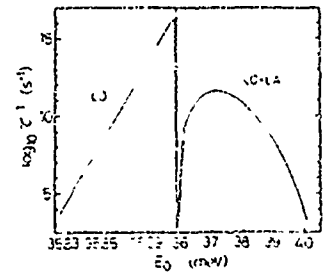

Fig. 1. Calculated electron relaxation rate $1/\tau$ at T=0K. Note that the scale in abscissa is different above and below $\hbar\omega_{LO}$, which is indicated by the vertical dotted line.

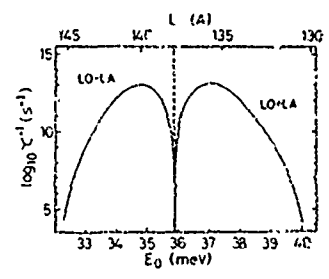

Fig. 2. Calculated electron relaxation rate $1/\tau$ at T=30K. Dot diameter L corresponding to E_0 is shown across the upper part. Note the uniform scale in the abscissa.

The inclusion of the second-order LO+LA process drastically improves the situation. As seen from Fig 1, LO+LA produces a rather broad peak on the high energy side of $\hbar\omega_{LO}$, with the peak value exceeding 10^{11} s^{-1} (corresponding to $\tau \approx 10$ ps). This peak, although smaller than the LO peak, is large enough for our purpose of achieving efficient light emission. (The radiative recombination lifetime τ_{rad} of electrons and holes in their ground levels is estimated by the golden rule to be on the order of 1 ns. Hence $\tau < 1$ ns is required for efficient luminescence.) Moreover, the large peak width considerably alleviates the tuning condition. For example, $\tau < 1$ ns if E_0 is in a broad window of 36.1 meV $< E_0 <$ 38.8 meV.

The tuning condition is further alleviated at higher temperatures. Figure 2 illustrates calculated $1/\tau$ at T = 300K. Now the LO-LA process, which is totally absent at T=0K, contributes another broad peak on the low energy side of $\hbar\omega_{LO}$. Also, the LO+LA peak is enhanced by a factor of 10^3 compared to T = 0K. This is due to the enhanced Bose distribution function of LA phonons. Thus, at finite temperatures, the enhanced Bose function and the emergence of the LO-LA peak act to increase detuning tolerance. For τ to satisfy $\tau < 1$ ns, the tolerable range of E_0 is now 33 meV $< E_0 <$ 39.1 meV. (The narrow dip in $1/\tau$ on the immediate high-energy side of $\hbar\omega_{LO}$ should be smeared out by phonon broadening, which is neglected in our calculation.) The LO peak is not shown in Fig. 2 since it is essentially the same as in Fig 1 in this logarithmic scale.

The level separation E_0 can be translated into dot diameter L by the relation $L \sim 2\sqrt{\langle g|x^2+y^2+z^2|g\rangle}$ where $|g\rangle$ denotes the ground state wavefunction. The L thus determined is shown in Fig.2 across the top. (Due to the parabolic confinement, this definition of L is rather arbitrary.) It is seen that L must be on the order of 100 Å to achieve rapid relaxation.

4. Discussion

In our calculation, we have simulated the real LO mode (CLO and ILO modes) in our structure by a single "bulk" LO mode. By doing so, we have implicitly assumed that CLO and ILO have the same energy. If we take account of the energy difference between CLO and ILO, there are two windows of rapid relaxation (corresponding to CLO±LA and ILO±LA processes) centered around CLO and ILO energies, respectively. Now the level spacings are required to fall into either of these two energy windows.

We can further increase the number of windows by using a mixed-crystal of multi-LO-mode type, such as $Al_xGa_{1-x}As$, as barrier material. There are now two types of ILO modes (GaAs-like and AlAs-like) that differ in energy by over 10 meV. We can alternatively use such a mixed crystal as dot material, which results in two CLO modes.

Although the introduction of more than one relaxation window considerably eases level tuning, additional level tuning may be required to fully adjust the level separations to these windows. This can be accomplished by introducing a localized (i.e., with extent smaller than the dot size) potential into the dot. Placing a small domain of a different semiconductor material serves this purpose [9,10]. How this affects the energies of various levels depends on the position and sign of the localized potential. For example, if the dot has an inversion symmetry and this domain is located at the center of the dot, then electron levels of even-parity are pushed up (if the localized potential is positive) or down (negative), the change being largest for the ground state (Fig.3). Odd-parity states, in contrast, remain unchanged, since the wavefunctions vanish at the localized potential.

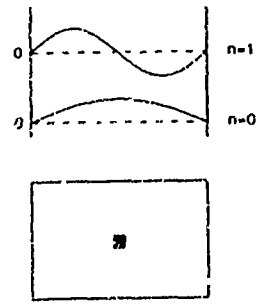

Fig 3 Introduction of a localized potential in a dot (grey rectangle) by means of a small domain of a different semiconductor material (shaded area) placed at the center. The upper part shows unperturbed wavefunctions. The ground state (n=0) has a finite amplitude at the potential and is perturbed, whereas the first excited state (n=1) vanishes there and is unaffected.

In our calculation, many-body correlation between carriers such as exciton and Auger effects was totally neglected. It is possible that these effects further enhance relaxation. In fact, Bockelmann and Egeler [11] recently calculated electron relaxation rate via the Auger effect in the random-phase approximation, and concluded that it strongly enhances relaxation at high optical excitation. More study seems necessary to fully clarify the role of many-body effects in carrier relaxation in a dot.

5. Conclusion

We have studied the effects of multi-phonon processes on electron relaxation in a GaAs dot. The results indicate that, in spite of the general slowing down of relaxation, efficient light emission is still possible by adjusting the level separations to the windows of rapid relaxation created by LO±LA processes. To be able to do this, there should not be more than several bound states. Hence the barrier height should not greatly exceed 100 meV.

References

[1] Y Arakawa and H.Sakaki, Appl. Phys. Lett. 24, 195 (1982).
[2] See, for example, M Notomi, M.Naganuma, T.Nishida, T.Tamamura, H.Iwamura, S Nojima and M Okamoto, Appl. Phys. Lett. 58, 720 (1991).
[3] H.Benisty, C.M Sotomayor-Torres and C.Weisbuch, Phys. Rev. B44, 10945 (1991).
[4] U Bockelmann and G.Bastard, Phys. Rev. B42, 8947 (1990).
[5] T Inoshita and H.Sakaki, Phys. Rev. B46, 7260 (1992).
[6] K.C.Rustagi and W.Weber, Solid State Commun. 18, 673 (1976).
[7] M.V Klein, IEEE J.Quantum Electron. QE-22, 1760 (1986).
[8] H Rücker, E. Molinari, and P. Lugli, Phys. Rev. B45, 6747 (1992).
[9] W Trzeciakowski and B.D.McCombe, Appl. Phys. Lett. 55, 891 (1989).
[10] J.M Gerard and J.Y.Marzin, Phys. Rev. B40, 6450 (1989).
[11] U Bockelmann and T.Egeler, Phys. Rev. B46, 15574 (1992).

ThP17

Ground state properties of interacting electrons in semiconductor quantum dots: Exact and Unrestricted Hartree-Fock results.

I. Martín Moreno

Instituto de Ciencias de Materiales (CSIC), Universidad Autónoma de Madrid, Cantoblanco 28049, Madrid, Spain

J. J. Palacios and C. Tejedor

Departamento de Física de la Materia Condensada, Universidad Autónoma de Madrid, Cantoblanco 28049, Madrid, Spain

G. Chiappe and F. Louis

Departamento de Física Aplicada, Universidad de Alicante, Apartado 99, 03080 Alicante, Spain

(July 9, 1994)

The ground state properties of up to 8 interacting electrons confined to square quantum boxes are calculated by exact diagonalization of the full Hamiltonian. The behavior with the magnetic field is analyzed as well as its possible implications on the measurables properties of such systems. Results comparison with an Unrestricted Hartree-Fock approach reveals the latter one to be an excellent candidate to go beyond the few electrons limit of exact calculations.

Properties of quantum dots (QD's) have been extensively studied in the last couple of years, both experimental and theoretically [1]. Measurements have been performed mainly on the transport properties (see some ref), has appeared, as well on the capacitance of such systems [2]. In both cases it has been shown that the properties of QD are greatly altered by adding or removing a single electron. The calculations that have appeared in the literature on the properties of such systems can be classified in two groups: large number of electrons and small number of electrons in the QD. In the first case, the approximation of representing the electron-electron interaction by a classical capacitive term has proved to be qualitatively satisfactory [3-4]. On the other hand, when the number of electrons is small and correlations are strong, this model is expected to fail. This has been shown in exact calculations performed in this regime, considering the full electron-electron interaction, for small number of electrons ($N \leq 5$) in one-dimensional QDs [5] and in two-dimensional (2D) QD's with high symmetry in the confining potential [6-8]. Two quantities related to the isolated dot are of special interest, due to their relation to measurable properties (e.g., the conductance): the energies and the spectral weights [9,10]:

$$\Delta_{ij}^{\sigma}(N) = \langle \Phi_i^{N-1} | d_{i\sigma} | \Phi_j^{N} \rangle \langle \Phi_j^{N} | d_{j\sigma}^{\dagger} | \Phi_i^{N-1} \rangle \qquad (1)$$

where i,j index one-electron eigenstates of σ, I index many-body eigenstates at fixed N, and $d_{i\sigma}(d_{i\sigma}^{\dagger})$ is the annihilation (creation) operator for the one-electron eigenstate i.

The purpose of this paper is double: a) To show the changes that a perpendicular magnetic field induces on the electronic properties of QDs, i.e., on eigenenergies, eigenstates and spectral weights (in this paper we concentrate on $\Delta(N) = \sum_{ij\sigma} \Delta_{ij}^{\sigma}(N)$) and b) to show that the Unrestricted Hartree-Fock (UHF) approach can be used as an accurate way to calculate properties of dots, especially in the intermediate and high N regime. We present exact calculations for N up to 8 for different magnetic fields. We compare these exact results with those obtained with the UHF approach and, given the good agreement found, we extend the study to higher N.

We consider electrons confined in a 2D square box, under the influence of a perpendicular magnetic field B (B was represented by a symmetric gauge vector potential) and interacting via the Coulomb interaction, which has been cut off in order to take into account the finite width of 2D gas in real semiconductor systems. In order to obtain eigenvalues and eigenfunctions, the Hamiltonian is first expressed in a second quantization form in the base set of one-electron wave functions. The calculation of each matrix element of the interacting part of the Hamiltonian in this base set reduces to the calculation of four-dimensional integrals involving single particle wave functions. The ground state wave function and those of the first excited states for N fixed were calculated by using Lanczos method. The UHF approximation consist of finding the self-consistent one-electron wave functions that are eigenfunctions of the Hamiltonian

$$H_{HF} = \sum_{ij\sigma} \epsilon_{i\sigma}^{0} d_{i\sigma}^{\dagger} d_{j\sigma} +$$

$$+ \sum_{ijkl\sigma} V_{ijkl}(d_{i\sigma}^{\dagger} d_{k\sigma})\langle d_{j\sigma}^{\dagger} d_{l\sigma}\rangle - \tfrac{1}{2}\langle d_{i\sigma}^{\dagger} d_{k\sigma}\rangle) +$$

$$+ \sum_{ijkl\sigma} V_{ijkl}(d_{i\sigma}^{\dagger} d_{k\sigma})\langle d_{j\bar{\sigma}}^{\dagger} d_{l\bar{\sigma}}\rangle -$$

$$- \sum_{ijkl\sigma} V_{ijkl}\langle d_{i\sigma}^{\dagger} d_{k\sigma}\rangle (d_{j\bar{\sigma}}^{\dagger} d_{l\bar{\sigma}}) -$$

$$- \sum_{ijkl\sigma} V_{ijkl}\langle d_{i\sigma}^{\dagger} d_{k\sigma}\rangle \langle d_{j\bar{\sigma}}^{\dagger} d_{l\bar{\sigma}}\rangle \qquad (2)$$

where σ labels the electron spin, $\epsilon_{i\sigma}^{0}$ are the eigenenergies for noninteracting electrons, V_{ijkl} are matrix elements of the Coulomb interaction in the one-electron basis set, and the expectation values, and therefore the Hamiltonian, have to be recalculated at each iteration until convergency is reached.

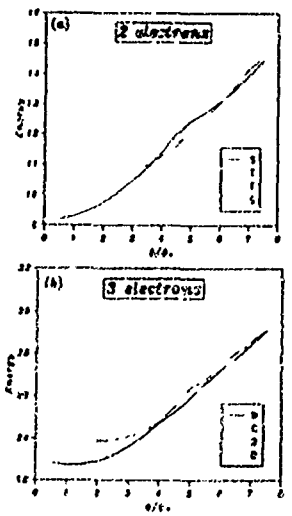

FIG. 1. *Exact low-lying many-body energies for a square quantum dot as a function of the magnetic flux through the dot for (a) two electrons in the dot (S: Singlet and T: Triplet) and (b) three electrons in the dot (D: Doublet and Q: Quadruplet). For the dot considered (see text), the unit of energy, $\hbar^2\pi^2/(2mL^2)$, is 36 meV.*

All parameters, as dielectric constant and effective mass, are taken to have the values in the 2D electron gas formed in AlGaAs/GaAs. The results presented in this paper are for a square dot of area $L^2 = 1100\,\text{nm}^2$. Figure 1 shows the calculated eigenvalues as a function of the magnetic flux Φ through the dot [for the dot considered, this corresponds to a perpendicular magnetic field $B = 0.51\Phi/\Phi_0$ (T), with $\Phi_0 = h/e$, h being the Plank constant and e the electron charge] for (a) $N = 2$ and (b) $N = 3$. 12 one-electron wave functions (21 including spin) were used throughout the calculations. In both figures there are cusps and anticrossings between energy levels. Crossings occur between eigenvalues corresponding to levels with different total spin (as the Zeeman energy term has not been taken into account in the calculations, spin multiplets are degenerate), while anticrossings occur between levels with the same total

spin and are reminiscent of the crossings between states with different angular momentum that have been found in parabolic 2D QD. Both after a crossing or anticrossing between the two lowest lying eigenstates the character of the ground state wave function changes abruptly. As we show later on, this abrupt change is going to be reflected on the values of spectral weights.

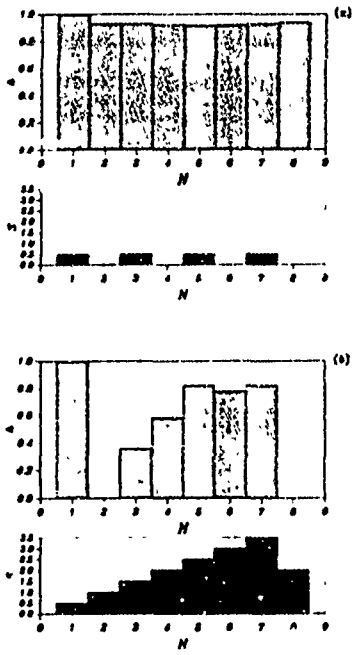

FIG. 2. *Spectral weight $\Delta(N)$ and total spin $S(N)$ for (a) $\phi = 3\phi_0$ and (b) $\phi = 15\phi_0$ for a square quantum dot calculated from the exact many-body ground state wave functions.*

Figure 2 shows $\Delta(N)$ and the spin total $S(N)$ up to $N = 8$ for two different magnetic fluxes: a) $\phi = 3\phi_0$ and b) $\phi = 15\phi_0$ ($\phi_0 = h/e$, h being the Plank constant and e the electron charge) which are typical representatives of the low- and high magnetic field regimes respectively. In the low B case the ground state eigenfunctions have minimum total spin: that is $S(N) = 0$ for N even and $S(N) = 1/2$ for N odd. In this case $\Delta(N)$ is a very smooth, although not monotonous, function of N. For high B, the ground state eigenfunctions are spin polarized for small N. Even when, in order to obtain the results shown in Fig. 2(b) the electron-electron interaction has been fully taken into account, this may be understood so as to minimize the exchange energy (the relevance of the kinetic energy contribution to the total energy decreases with B, as a consequence of the condensation of one electron energy levels into Landau levels). Spectral weights change rapidly as function of N for N small, in this regime. For example, while $\Delta(1) = 1$ always, $\Delta(2)$ decreases as ϕ increases, reflecting the fact that the occupancy of the first one electron eigenstate decreases for $\phi > 3.9\phi_0$ (i.e., after the first crossing between the ground and the first excited state). The reason for this is that the charge is more spread out when occupying one electron edge states than when occupying the first one-electron state, which is localized at the center of the QD. Eventually, for large enough N, all the firsts one-electron levels are occupied and, after that, $\Delta(N)$ seems to tend to 1 for large N. Notice that Kinaret *et al.* [9] predict a quenching of $\Delta(N)$ in a different situation: they calculated $\Delta(N)$ for states such that the filling factor remains constant, and these are not necessarily the ground states of the many-body system. It is also worth mentioning the *disappearance of $\Delta(8)$ due to the change of S for $N = 8$ electrons (in comparison with $N = 7$) by more than 1/2.*

Our UHF calculations produce an excellent approximation to the ground state energy, as well as to the wave function as shown in table I. The UHF ground state energy approximates better than 2% the exact ground state energy, and it is always in between the energies of the ground state and the first excited state in the exact many-body calculation. The excellent agreement found for the UHF calculations leads us to extend the calculation of both the many-body energies and spectral weights to large N. The $\Delta(N)$ and $S(N)$ calculated from the UHF wave functions are shown in Fig. 3 for $\phi = 15\phi_0$. Hartree-Fock reflects qualitatively all the features found in the exact calculations and the agreement between them is quantitatively rather good for $\Delta(N)$ when $N \geq 3$. UHF calculation supports the idea that $\Delta(N)$ tends to 1 for large N for the dot considered, while showing a clear paramagnetic trend of the ground state. *An observation that deserves a more detailed investigation in the future is that the overlaps between the exact and the UHF ground state wave functions remain above 0.9 in all cases, except close to the fractional filling factors ν considered (defining $\nu = N/o$) suggesting a very correlated groundstate for these cases. A more detailed description of these effects for different geometries and of the intermediate B regime, where $\Delta(N)$ presents abrupt changes as a function of B, will be published elsewhere.*

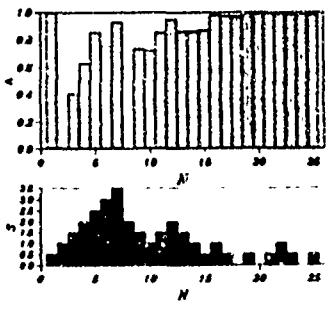

FIG. 3. *As for Fig. 2b, but using the ground state wave functions obtained from the Unrestricted Hartree-Fock method and extended to 25 electrons.*

To conclude, we have calculated the many-body low lying eigenenergies and their correspondent eigenstates in a square 2D QD for up to 8 electrons and different magnetic fields. While for small B the spectral weights are a smooth function of N, for high B they are strongly modulated. A similar effect is expected to appear in the conductance through these systems at low temperatures. Finally, it has been shown that Hartree-Fock is an excellent approximation for the calculation of properties on a typical class

defined in the AlGaAs GaAs electron gas

TABLE I *Ground state energies in meV (Exact and UHF) N electrons on a square box of 0.1μm of side with a transversal magnetic flux φ (in units of the flux quanta $\Phi_0 = h/e$). The overlap between the exact and UHF wavefunctions is also given. 16 nonelectronic wave functions are included in the calculations (2L including spin). The Zeeman contribution has been neglected*

φ/Φ₀	N	2	4	6	8	10	12	14
	Energy (UHF)	6.10021	23.951	51.809	91.279	141.459	202.425	274.010
0	Energy (Exact)	5.9191	23.111	52.952	93.978	145.212	207.423	279.958
	$\langle \Phi_E \vert \Phi_{UHF} \rangle$	0.9939	0.972	0.9559	0.9558	0.9559	0.9681	0.978
	Energy (UHF)	12.884	32.851	65.022	109.219	165.410	233.658	313.55
1/2	Energy (Exact)	12.774	32.326	64.991	109.615	166.219	234.525	314.32
	$\langle \Phi_E \vert \Phi_{UHF} \rangle$	0.936	0.915	0.991	0.958	0.933	0.919	0.936

[1] M. A. Kastner, Phys. Today, January 1993, p. 24, and references therein
[2] R. C. Ashoori *et al.*, Phys. Rev. Lett. **68**, 3088 (1992)
[3] C. W. J. Beenakker, Phys. Rev. B **44**, 1646 (1991)
[4] P. L. McEuen *et al.*, Phys. Rev. Lett. **66**, 1926 (1991)
[5] A. Haussler, B. Kramer, and J. Masek, Z. Phys. B **85**, 435 (1992)
[6] P. A. Maksym and T. Chakraborty, Phys. Rev. Lett. **65**, 108 (1990); also Phys. Rev. B **45**, 1947 (1992)
[7] U. Merkt, J. Huser, and M. Wagner, Phys. Rev. B **43**, 7320 (1991); M. Wagner, U. Merkt, and A. V. Chaplik, Phys. Rev. B **45**, 1951 (1992)
[8] D. Pfannkuche and R. R. Gerhardts, Phys. Rev. B **44**, 13132 (1991)
[9] J. M. Kinaret *et al.*, Phys. Rev. B **45**, 9489 (1992); also **46**, 4681 (1992)
[10] J. J. Palacios, L. Martin-Moreno, and C. Tejedor, Surface Science, in press

ThP18

Strong lateral quantization effects in the luminescence of InGaAs/InP quantum wires

P. Ils, M. Michel, A. Forchel
Technische Physik, Universität Würzburg, Am Hubland,
97074 Würzburg, Germany;

I. Gyuro, M. Klenk, E. Zielinski
Alcatel SEL AG Research Center, Lorentzstr. 40, 70435 Stuttgart, Germany

Abstract

We have fabricated $In_{0.53}Ga_{0.47}As/InP$ quantum wires with lateral widths down to 8 nm by high voltage electron beam lithography and deep wet chemical etching. The wires were studied by photoluminescence spectroscopy at room temperature and at 2K. We observe only a weak decrease of the luminescence yield with decreasing wire width, which indicates that no significant damage has been induced at the sidewalls of the wires during the fabrication process. For wires with widths smaller than about 60 nm an increasing blue shift of the photoluminescence energy up to about 75 meV (for 8 nm wide wires) is observed indicating a strong lateral quantization. The photoluminescence emission of the wires is strongly polarized parallel to the wire orientation with increasing polarization degree for decreasing wire width

Introduction

One- and zero dimensional structures have been raised considerable interest in the last years regarding novel physical properties as well as the potential for applications in optoelectronic devices [1-4]. A number of techniques involving different physical mechanisms have been used recently to obtain structures with lateral confinement and to study their specific physical properties [5-9]

A strong lateral carrier confinement requires sh deep lateral potentials In order to observe the properties of a one-dimensional sys energetic splitting between the lateral subbands should be significantly larger than the characteristic energy describing the carrier distribution (e.g. thermal energy or Fermi energy) The analysis of the experimental results should be based on well defined sample quantities like semiconductor parameters and geometrical data Damage free fabrication processes are required to avoid the formation of optically inactive regions

In the present work we report on the results obtained from photoluminescence studies of ultranarrow $In_{0.53}Ga_{0.47}As/InP$ quantum wires with lateral dimensions down to 8 nm, which were fabricated by the combination of high resolution electron beam lithography at 200 kV and wet chemical etching Down to the smallest widths obtained the $In_{0.53}Ga_{0.47}As/InP$ wires show a good luminescence yield even at room temperature due to the absence of damage in our fabrication processes. The photoluminescence emission of wires with widths down to 8 nm shows energy shifts up to more than 70 meV indicating the streng lateral carrier quantization in our wire structures Furthermore the photoluminescence emission is strongly polarized parallel to the wire orientation

Technology

The starting material for the wire fabrication are metal organic vapor phase epitaxy grown $In_{0.53}Ga_{0.47}As/InP$ single quantum well layers with a 200 nm InP buffer layer, a 5 nm $In_{0.53}Ga_{0.47}As$ layer and an InP cap layer with a thickness of 8 nm. The samples are coated with a 100 nm thick layer of polymethylmetacrylat (PMMA) electron beam resist. The high resolution electron beam exposure is performed with a transmission electron microscope at an accreleration voltage of 200 kV in order to reduce the proximity effect [10]. Using a lift-off process gold wires with lateral widths down to about 15 nm are obtained, which serve as a mask for deep wet chemical etching with a $Br_2/HBr/H_2O$ etchant. Fig. 1 shows a scanning electron micrograph of wet etched $In_{0.53}Ga_{0.47}As/InP$ wires delineated parallel to the [011] direction after the removal of the gold mask. Here the lateral width of the $In_{0.53}Ga_{0.47}As$ layer in the wires, which is located below the 8 nm thick InP cap layer, is about 15 nm.

As a result of the lithography process we have obtained wet etched $In_{0.53}Ga_{0.47}As/InP$ wires with SEM measured lateral widths of the $In_{0.53}Ga_{0.47}As$ layer down to 8 nm. The wire width fluctuations arising from the roughness of the gold masks and the roughness caused by the etching process amounts to about ± 5 nm. The lateral dimensions realized in our structures are in general comparable to the thickness of typical quantum well layers. Therefore strong lateral confinement effects should be observable in our structures.

Optical Studies

The wires were investigated by photoluminescence spectroscopy at temperatures of 300 K and 2 K. The experiments were carried out on wire arrays of 50 x 50 μm^2 size. Beside these wire arrays some mesa structures of the same size were placed on the samples serving as two-dimensional references. The distance between the different arrays was about 200 μm. For the excitation the 514 nm line of an argon ion laser was used at normal incidence. The laser beam was focused to a diameter of about 40 μm to obtain a sufficiently high spacial resolution. The photoluminescence signal was detected by a liquid nitrogen cooled germanium detector and lock-in technique.

The $In_{0.53}Ga_{0.47}As/InP$ quantum wires show a good photoluminescence yield down to the smallest wire widths even at room temperature. This demonstrates the high quality of our wire structures. Fig. 2 displays photoluminescence spectra for different lateral wire widths taken at room temperature. The wire widths indicated in the figure have been determined by a high resolution scanning electron microscope. The relative intensities are normalized. The position of the photoluminescence peak remains unchanged down to geometrical wire widths about 60 nm. For wire widths smaller than 60 nm an increasing blue shift of the photoluminescence signal is observed, which amounts to about 60 meV for the 11 nm wide wires displaying a strong lateral quantization.

Both, the absence of a shift for wire widths above 60 nm and the strong emission energy shifts observed in narrower structures indicate that a steep lateral confinement potential is obtained by the $In_{0.53}Ga_{0.47}As$/vacuum transition at the etched surfaces leading to one-dimensional quantum effects for wire widths smaller than 60 nm. The observed photoluminescence energy shift fits well theoretical calculations for the lateral quantization based on the geometrical wire widths [11]. This indicates that in contrast to dry-etched wires [12] there exist no pronounced dead layers at the sidewalls of the wires. The increase of the spectral halfwidth of the photoluminescence signal with decreasing wire width is predominantly due to wire width fluctuations and is consistent with the lateral quantization itself. From the measured increase of the spectral halfwidth as a function of wire width a typical wire width fluctuation ΔL_x of about ±5nm is estimated, consistent with the value determined from the SEM micrographs.

The wire width dependence of the photoluminescence intensity at room temperature is shown in Fig. 3. Here the integrated intensities of the wire spectra, corrected by the area filling factor and normalized with respect to the quasi-two-dimensional mesa reference are displayed as a function of the measured wire width. The wire widths were obtained from high resolution scanning electron micrographs. The error in the determination of the geometrical wire width is about 5 nm. Taking the nonradiative surface recombination into account the wire structures show good quantum efficiencies for wire widths down to 8 nm. The 200 nm wide wires show nearly the same luminescence yield as the two-dimensional reference, for 20 nm wide wires it amounts to about 5% of the 2D value. At room temperature the 8 nm wide wires still have a quantum efficiency of about 0.6%.

Compared to dry-etched wire structures the decrease in quantum efficiency with decreasing wire width is clearly weaker [8]. In particular the photoluminescence does not vanish abruptly for wire widths smaller than 60 nm. This strong decay of the quantum efficiency in narrow dry-etched wires has been attributed to the formation of optically inactive ('dead') layers at the dry-etched sidewalls [8,12]. A dead layer of 20 nm as observed in these dry-etched structures would lead to vanishing quantum efficiency at a wire width of about 40 nm in clear disagreement with our data. Quantum efficiencies greater than 1 observed for wire widths greater than 100 nm are due to efficient carrier capture from the InP barriers. Carriers excited by the laser in the InP layers can diffuse into the $In_{0.53}Ga_{0.47}As$ layer in the wires and thus contribute to the photoluminescence signal of the $In_{0.53}Ga_{0.47}As$ wires.

The photoluminescence emission of the $In_{0.53}Ga_{0.47}As$ wire structures at a temperature of 2 K was also studied for different polarization directions. As shown in Fig. 4 the luminescence signal is preferentially polarized parallel to the wire direction. The polarization degree increases significantly with decreasing wire width and amounts to about $(60\pm5)\%$ for wire widths of about 10 nm, which is roughly comparable to theoretical expectations [13]. The polarization dependence of absorption and photoluminescence emission is determined by the heavy-hole and light-hole character of the one-dimensional valence subbands. The strong mixing of heavy-hole and light-hole states in one-dimensional structures reflects itself in the anisotropy of the optical transitions involved. This anisotropy increases with decreasing wire width due to the increasing mixing of heavy-hole and light-hole states [13].

Additionally to this intrinsic anisotropy based on the electronic band structure a further electrodynamic effect may play an important role. As our experiments are performed on arrays of wires, these periodic configurations of deep etched wires act as grating structures. Due to the lateral modulation of the dielectric constant in these wire gratings the magnitude of the local electric field induced by the incoming electromagnetic wave is different for different polarizations [14]. This may be the reason for the fact that we observe a strong polarization of the photoluminescence parallel to the wire orientation already for relatively wide wires with widths in the region between 1000 nm down to about 80 nm, where the electronic effect on the polarization of the e_{11}-hh_{11}-transition due to the band mixing of heavy-hole and light-hole states can practically be neglected [13].

Conclusions

By means of high voltage electron beam lithography and deep wet chemical etching we have developed $In_{0.53}Ga_{0.47}As/InP$ quantum wires with pronounced lateral quantization effects. $In_{0.53}Ga_{0.47}As/InP$ quantum wires with widths down to 8 nm have been fabricated. The wires show strong optical emission at T=2K and at room temperature even without having been overgrown. The photoluminescence signal from the $In_{0.53}Ga_{0.47}As$ wires is polarized parallel to the wire orientation with significantly increasing polarization degree for decreasing wire width. In contrast to previous studies on dry-etched structures we found no indications for the existence of an optically inactive 'dead' layer at the sidewalls of the wires, which clearly demonstrates the advantage of the damage free wet etching process. The photoluminescence energy of the $In_{0.53}Ga_{0.47}As$ wires is independent of the wire dimensions down to widths of about 60 nm. For the narrowest structures the energetic blue shift of the photoluminescence peak amounts to about 70 meV. Our results indicate that by electron beam lithography and wet

chemical etching of quantum well layers quantum wires with comparable quantization in the vertical and lateral direction can be obtained

We are grateful to S. Kuhn for expert technical assistance and to A Wolf for preparing the SEM micrographs The financial support of the Volkswagen Stiftung is gratefully acknowledged

References

[1] Y Arakawa and P Sakaki, Appl. Phys. Lett. 40, 939 (1982).
[2] Y. Arakawa, K. Vahala, and A. Yariv, Appl. Phys. Lett. 45, 950 (1984).
[3] M. Asada, Y Miyamoto, and Y. Suematsu, Jap. Jour. Appl. Phys. 24, L95 (1988).
[4] S Schmitt-Rink, D.A.B. Miller, D.S. Chemla, Phys. Rev. B 35, 8113 (1987).
[5] M Notomi, M. Nagamuma, T. Nishida, T Tamamura, H. Iwamura, S Nojima, and M Okamoto, Appl. Phys. Lett. 58, 720 (1991)
[6] A. Izrael, J.Y. Marzin, P Sermage, L Birotheau, D Robein, R Azoulay, J L. Benchimol, L. Henry, V. Thierry-Mieg, F R. Ladan, and L. Taylor, Jap Jour. Appl Phys. 30, 3256 (1991).
[7] Y. Nagamune, Y. Arakawa, S. Tsukamoto, M. Nishioka, S. Sasaki, and N. Miura, Phys Rev. Lett. 69, 2963 (1992).
[8] B.E. Maile, A. Forchel, R. Germann, D. Grützmacher, H.P Meier, and J -P Reithmaier, J. Vac. Sci. Technol. B7, 2030 (1989)
[9] Ch. Greus, L. Butov, F. Daminger, A Forchel, P.A. Knipp, and T.L. Reinecke, Phys Rev. B 47, 7626 (1993).
[10] P. Ils, M. Michel, A. Forchel, J. Gyuro, P Speier, and E. Zielinski, Mat Res. Soc Symp. Proc. Vol. 283, 777 (1993)
[11] P Ils, M Michel, A. Forchel, J. Gyuro, M Klenk, and E. Zielinski, is to be published
[12] E.M. Clausen Jr , H.G. Craighead, J M Worlock, J P Harbison, L M Schiavone, L Florez, and B Van der Gaag, Appl Phys Lett 55, 1427 (1989).
[13] U. Bockelmann and G. Bastard, Phys Rev B 45, 1688 (1992).
[14] U. Bockelmann, Europhys. Lett. 16, 601 (1991)

Figure Captions

Fig. 1
SEM micrograph of wet etched $In_{0.53}Ga_{0.47}As/InP$ wires delineated parallel to the [011] direction after mask removal. The optically active $In_{0.53}Ga_{0.47}As$ layer (thickness 5 nm) is located 8 nm below the top of the semiconductor structures The lateral width of the $In_{0.53}Ga_{0.47}As$ layer is about 15 nm

Fig. 2
Photoluminescence (PL) spectra of the $In_{0.53}Ga_{0.47}As/InP$ wires for different lateral wire widths taken at room temperature (laser power 2mW)

Fig. 3
Wire width dependence of the photoluminescence (PL) intensity of the $In_{0.53}Ga_{0.47}As/InP$ wire structures at room temperature. Here the integrated intensities of the photoluminescence signal, corrected by the area filling factor and normalized with respect to the quasi two dimensional mesa reference are displayed as a function of the geometrical wire width as obtained from SEM micrographs.

Fig. 4
Wire width dependence of the polarization degree of the photoluminescence emission parallel to the wire orientation at a temperature of 2 K

Fig 1

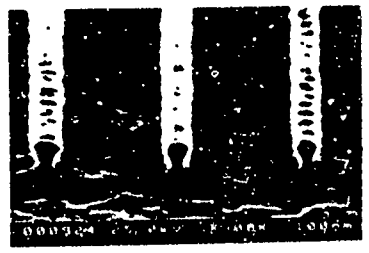

Fig. 2

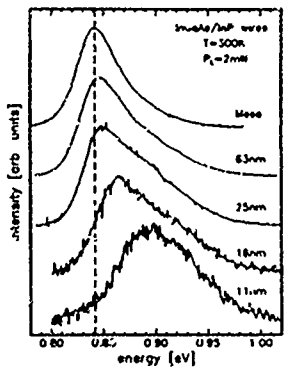

Fig 3

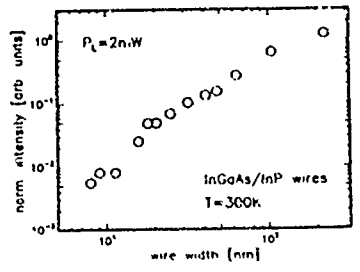

Fig. 4

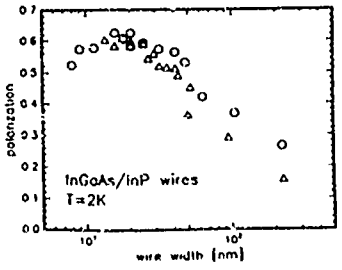

ThP19

GaAs/AlGaAs Quantum Well Infrared Photodetectors

T. Miyatake, S. Honbata, T. Ezaki, P. Kubo, N. Mori
K. Taniguchi and C. Hamaguchi
Department of Electronic Engineering, Faculty of Engineering
Osaka University, Suita City, 565, Japan

Abstract

We fabricated GaAs (Si doped 40 Å)/$Al_{0.25}Ga_{0.75}As$ (undoped 500 Å) multi-quantum well infrared photodetectors to realize a high efficiency. The detector is based on the intersubband transition from a bound state in the GaAs quantum well to extended continuum states above the AlGaAs barrier so that the excited electrons can flow easily. In order to improve the detectivity the incident surface is polished at 45° off the quantum well layers, to provide multireflection of the light in the device. The photocurrent was observed at $T = 77$ K in the incident photon wavelength region of $6 \sim 10\,\mu m$ with peak photocurrent at $8.3\,\mu m$. Since the operation mechanism is based on the photocurrent carried by the electrons in the extended continuum states excited from the bound state in GaAs wells, the band width is expected to be broader than the devices which utilize the transition between the bound states in the well. We calculated the absorption coefficient of photons by using the energy band structures obtained from *Kronig Penney model* and photocurrent with a simplified model. The results well explain the band width of the detectivity and also a weak structure (weak peaks) in the photocurrent.

Introduction

In recent years, a lot of interests have been placed on intersubband absorption in GaAs/AlGaAs quantum wells [1, 2]. For example, infrared detection using intersubband absorption in doped quantum wells has been a subject of much current interest. Up to now, many studies on GaAs/AlGaAs multiquantum well (MQW) infrared (IR) photodetector with high performance have been reported [3] [16].

Concentional IR photodetectors for the long wavelength of 5 ~ 10 μm have been fabricated using narrow band gap semiconductor materials such as HgCdTe. However, with the use of an intersubband process rather than an interband process, it is possible to fabricate an IR detector of wide band gap materials such as GaAs/AlGaAs MQWs instead of narrow gap materials. The major advantage of GaAs/AlGaAs MQW IR photodetectors with respect to HgCdTe devices is that the range of detective wavelength can be controlled with the GaAs quantum well width L_z, the AlGaAs barrier width L_b, or the Al alloy composition x [3] [16].

The GaAs/AlGaAs MQW IR photodetector we discuss here is based on an electron transition between the localized bound state and the extended continuum states. In such quantum well photodetectors, two-dimensional electron gas is in the bound state at thermal equilibrium. Under IR illumination, electrons at the bound state are excited to the extended continuum states, and photo-excited electrons are inside in the conduction band and contribute to the photocurrent. Therefore, such a photodetector is expected to have a higher detectivity, as compared with photodetector based on bound to bound state absorption in quantum wells [8-12, 15]. In addition, the AlGaAs barrier width L_b can be increased without affecting the sensitivity of the photodetector, resulting in the significant reduction of an undesirable dark tunneling current [8-12, 15].

In the present work, we fabricate GaAs/AlGaAs MQW IR photodetectors as described above. Photocurrent measurement of the photodetectors is carried out and the photocurrent spectrum is calculated with a simplified model. By comparing both results, we clarify the mechanism of IR detection.

Experimental Results and Discussions

The MQW detector structure is grown on a semi-insulating GaAs substrate by molecular beam epitaxy, consisting of 50 periods with 40 Å wells of GaAs (Si doped $N_d = 1.0 \times 10^{18}$ cm^{-3}) and 500 Å barriers of $Al_{0.25}Ga_{0.75}As$. The MQW layers are sandwiched between a 0.5 μm top and 1 μm bottom contact layers of GaAs with donors $N_d = 3.0 \times 10^{18}$ cm^{-3}. Thicknesses of the GaAs quantum well and AlGaAs barrier layers and Al alloy composition are measured by the X-ray rocking curve method. Subband energy levels are calculated for this structure by solving the Schrodinger equation and the Poisson equation self-consistently. In this analysis, exchange interaction and depolarization effects are ignored for simplicity. The exchange interaction and depolarization effects are very important in a device with very high doping density but not so important in our samples with low doping concentrations of 1.0×10^{18}cm^{-3}. The effective mass of $0.067m_0$ is used both in the GaAs quantum wells and in the $Al_{0.25}Ga_{0.75}As$ barriers. The other physical parameters used in the present calculation are as follows [17]: the static dielectric constant of GaAs of 12.9ε_0, the difference of the band gap between GaAs and $Al_{0.25}Ga_{0.75}As$ of 312 meV and the quantum well barrier height of 208 meV appropriate to $x = 0.25$. We confirmed that the GaAs/$Al_{0.25}Ga_{0.75}As$ MQW has only one bound state in the well from the result of the calculations. The bound state is formed at 95 meV *above the GaAs conduction band minimum*. The first excited state, which lies in the continuum states is located just above the edge of the $Al_{0.25}Ga_{0.75}As$ barrier. The energy difference between the bound state and the first excited state is 115 meV, corresponding to the wavelength $\lambda = 10.8\,\mu m$.

Figure 1 shows a GaAs/AlGaAs MQW IR photodetector used for photocurrent measurements. The sample was partly etched off to the bottom contact layer and formed in such shape as shown in Fig. 1 by polishing *the backside and the edge at the angle 45° in order to get an electric field component of the incident* light perpendicular to the quantum wells and to make the optical coupling in the MQWs more efficient [14, 6, 18]. As a final step in the processing, ohmic contacts were made to the top and bottom contact layers.

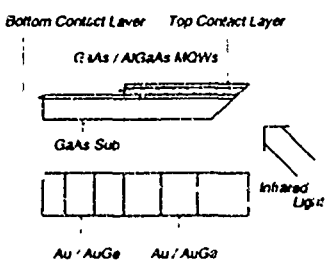

Figure 1 Schematic illustration of the GaAs/$Al_{0.25}Ga_{0.75}As$ MQW IR photodetector.

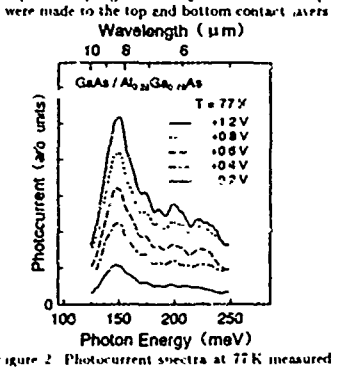

Figure 2 Photocurrent spectra at 77 K measured at applied bias voltages from +0.2 to +1.2 V with respect to the bottom contact layer.

The photocurrent is measured using a infrared radiation source and a single grating monochromator with a standard lock-in technique. The measurement is performed at 77 K with the sample mounted on a cold finger in the liquid nitrogen cooled cryostat. Figure 2 shows the photocurrent spectra versus the incident *IR photon energy, where the photocurrent was normalized* by the light intensity spectrum of the infrared radiation source. The electric field of unpolarized incident IR light is parallel to the 45° polished facet. The bias voltages applied to the sample are changed from +0.2 to +1.2 V with respect to the bottom contact layer. The spectra demonstrate that all the photocurrent curves have a peak at 8.3 μm regardless of the applied voltage and the photocurrent increases with the applied bias voltage. We found however that the measured photocurrent saturates at *high applied bias voltages. This may be interpreted* in terms that the continuum excited states above the barriers are localized in the well region in the presence of such a high electric field.

We calculate absorption spectra of IR radiation and induced photocurrent in a GaAs/AlGaAs MQW structure to clarify the origin of the peaks in the photocurrent spectra. Electronic states in the structure are calculated by the Kronig Penney model since the band bending due to doped Si is *found to be negligibly* small in our samples from the self-consistent calculation. The effective mass of the electrons is assumed to be equal ($0.067m_0$) in each layer. We find a good agreement of the lower two energy levels between the self-consistent calculation and the result of the Kronig Penney model.

Only the ground state is occupied in the thermal equilibrium and thus the absorption coefficient α is expressed by the transition probability W_{if} of electrons in the ground state by absorbing photons of ω as follows:

$$\alpha = \hbar\omega W_{if} / \tfrac{1}{2} c\varepsilon |F| \qquad (1)$$

where ϵ is the dielectric constant, c the light velocity and E is the electric field of the radiation. Using the Fermi's golden rule, the transition probability is given by

$$W_{i} = \frac{2\pi}{\hbar} \sum_{f} |\langle \Psi_f | H' | \Psi_i \rangle|^2 \delta(\epsilon_f - \epsilon_i - \hbar\omega) \tag{2}$$

where $|\Psi_i\rangle$ is the initial state, $|\Psi_f\rangle$ the final states, H' the electron photon interaction Hamiltonian

$$H' = -\frac{e\hbar}{m} A \cdot \nabla \tag{3}$$

and A is the vector potential of the incident photons. The states $|\Psi_i\rangle$ and $|\Psi_f\rangle$ are calculated without considering the effect of the applied electric field on the electron wave functions [18]. In the following analysis, we replace the delta function in the Fermi's golden rule, which represents the energy conservation by the Lorentzian function with the broadening Γ to take into account the broadening phenomenologically. The calculated results of absorption spectra of P polarized (normal to the growth direction) IR radiation are shown in Fig. 1, where the broadening energy is assumed to be 5 meV. Absorption spectra show a maximum value $\alpha = 1.8 \times 10^3 \text{cm}^{-1}$ at the photon energy of $\hbar\omega = 128$ meV. There are several peaks of absorption spectra, which arise from the miniband structure above the AlGaAs barrier. The spacing between two neighboring peak positions is larger at higher energies. This is interpreted in terms that the band width of the two consecutive superlattice minibands increases monotonously with the energy.

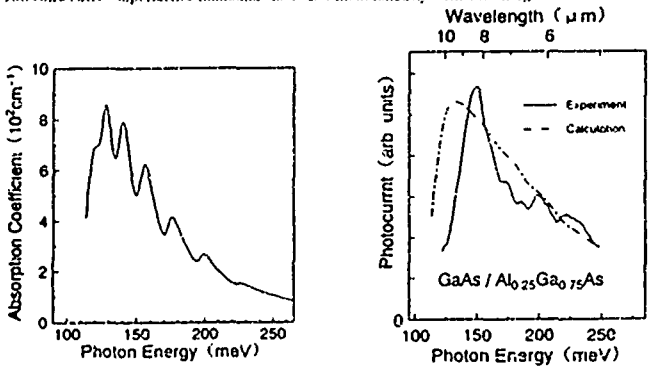

Figure 1 Calculated infrared absorption coefficient by electrons in the MQW structure. The level width of density of states of electrons Γ is assumed to be 5 meV.

Figure 2 Calculated photocurrent of the MQW photodetector is compared with the measured photocurrent, where the full width at the half maximum of incident IR light is assumed to be 20 meV in the calculation.

In order to evaluate the photocurrent from the absorption coefficient, we consider a simplified rate equation. For electrons of density n in the excited states, which are excited from the ground state by absorbing photons and relaxed into the ground state by a certain relaxation process, the rate equation is written as

$$\frac{dn}{dt} = \frac{n_0 - n}{\tau_E} - \frac{n}{\tau_L} \tag{4}$$

where n_0 is the two dimensional electron density in the ground state at the thermal equilibrium, $1/\tau_E$ the excitation rate and $1/\tau_L$ is the relaxation rate. The excitation rate $1/\tau_E$ is equal to W_i.

We estimate τ_L taking optical phonon scattering into account. The optical phonon scattering probability W_{op} is given by

$$W_{op} = \frac{\pi e^2 \omega_0 (N_0 + 1)}{\sqrt{2m^*\hbar\omega}} \sqrt{\frac{\hbar\omega - \varepsilon_{Nz}}{\hbar\omega}} \tag{5}$$

where α_F is the Frohlich coupling constant, N_0 is the phonon number with energy ω_0 (36.2 meV), ε_{Nz} represents the energy difference between the Nth subband and the ground state energy at the wave vector k_z, and L_z and L_B are the periodic length of the MQW and quantum well width respectively. Using Eq. (5), the value of τ_L is estimated to be longer than a few pico second.

At the steady state we have $dn/dt = 0$, and the electron density n which contributes to photocurrent is given by

$$n = n_0 \frac{\tau_L}{\tau_E + \tau_L} \tag{6}$$

Then the photocurrent J_{ph} reduces to

$$J_{ph} = q n_0 \mu E \frac{\tau_L}{\tau_E + \tau_L} \tag{7}$$

where μ is the electron mobility and E is the applied electric field.

The calculated results of the photocurrent J_{ph} along the growth direction for $n_0 = 4.0 \times 10^{11} \text{cm}^{-2}$ are shown in Fig. 4, together with the measured photocurrent spectrum at 77 K. In this calculation, μ is taken to be a constant and the spectrum of incident IR light is assumed to be a Gaussian with a width of 20 meV. As seen in Fig. 4, the peak of the photocurrent appears at $\hbar\omega = 133$ meV, and is about 20 meV higher than the calculated energy difference between the first excited state and the ground state in the GaAs/AlGaAs MQW. Comparing the calculated photocurrent spectrum with the measured spectrum, the peak position of the calculated photocurrent is located at a little lower energy side. However, the overall feature shows a good agreement with the measured photocurrent spectrum. From the present analysis we conclude that the excited electrons into higher states play an important role in carrying the photocurrent in addition to the electrons in the first excited state just above the $Al_{0.25}Ga_{0.75}As$ barriers in the GaAs/$Al_{0.25}Ga_{0.75}As$ MQW structure. It should be noted here that the calculated photocurrent with a smaller broadening energy exhibits several peaks at higher energy sides, reflecting the miniband structure.

In summary, we fabricated the GaAs/$Al_{0.25}Ga_{0.75}As$ MQW IR photodetector which utilizes the intersubband absorption which has a photocurrent peak at 8 μm. From the calculation of photocurrent spectrum we confirmed that the higher states will contribute to the photocurrent in the MQW IR photodetector in addition to the excitation into the first excited state just above the $Al_{0.25}Ga_{0.75}As$ barriers.

References

[1] J. C. West and S. L. Gilbert, Appl. Phys. Lett. 46, 1156 (1985).
[2] B. F. Levine, R. J. Malik, J. Walker, K. K. Choi, C. G. Bethea, D. A. Kleinman and J. M. Vandenberg, Appl. Phys. Lett. 50, 273 (1987).
[3] G. Hasnain, B. F. Levine, C. G. Bethea, R. A. Logan, J. Walker and R. J. Malik, Appl. Phys. Lett. 54, 2515 (1989).
[4] B. F. Levine, S. D. Gunapala, J. M. Kuo, S. S. Pei and S. Hui, Appl. Phys. Lett. 59, 1864 (1991).
[5] A. Kock, E. Gornik, G. Abstreiter, G. Bohm, M. Walther and G. Weimann, Appl. Phys. Lett. 60, 2011 (1992).
[6] J. Y. Andersson, L. Lundqvist and Z. F. Paska, Appl. Phys. Lett. 58, 2264 (1991).
[7] L. S. Yu, S. S. Li, Y. H. Wang and Y. C. Kao, J. Appl. Phys. 72, 2105 (1992).
[8] B. F. Levine, A. Zussman, S. D. Gunapala, M. T. Asom, J. M. Kuo and W. S. Hobson, J. Appl. Phys. 72, 1129 (1992).
[9] Y. H. Wang, S. S. Li and P. Ho, Appl. Phys. Lett. 62, 93 (1993).
[10] B. F. Levine, C. G. Bethea, K. K. Choi, J. Walker and R. J. Malik, J. Appl. Phys. 64, 1591 (1988).
[11] B. F. Levine, S. D. Gunapala and R. E. Kopf, Appl. Phys. Lett. 58, 1551 (1991).
[12] B. F. Levine, C. G. Bethea, K. G. Glogovsky, J. W. Stayt and R. E. Leibenguth, Semicond. Sci. Technol. 6, C114 (1991).
[13] T. J. Kozlowski, G. M. Williams, G. J. Sullivan, C. W. Farley, R. J. Anderson, J. Chen, D. T. Cheung, W. E. Tennant and E. DeWames, IEEE Trans. Electron Devices 38, 1124 (1991).
[14] S. R. Andrews and B. A. Miller, J. Appl. Phys. 70, 993 (1991).
[15] A. Zussman, B. F. Levine, J. M. Kuo and J. de Jong, J. Appl. Phys. 70, 5101 (1991).
[16] B. K. Janousek, M. F. Dougherty, W. F. Bloss, M. F. Rosenbluth, M. J. O'Loughlin, B. Kramer, J. J. De-Succa and E. E. Perry, J. Appl. Phys. 67, 7608 (1990).
[17] S. M. Sze, J. Appl. Phys. 58, R1 (1985).
[18] D. Ahn and S. L. Chuang, Phys. Rev. B 35, 4149 (1987).

ThP20

New type of photoconductivity induced by continuum-confined states in intersubband transitions

Carlo Sirtori, Jerome Faist, Federico Capasso, Deborah L. Sivco and Alfred Cho

AT&T Bell Laboratories,
Murray Hill, NJ 07974 (908) 582 2731

Bound states above the barrier height confined by Bragg reflectors have been recently detected via intersubband transitions[1]. A new asymmetric structure, where the confinement in the classical continuum arises from a Bragg reflector on one side and a field-induced barrier on the other, has been investigated by means of photocurrent spectroscopy. Our AlInAs/GaInAs sample consists of 40 periods, each period comprises a GaInAs quantum well (32 Å, n-type doped $1.5X10^{18}$ cm^{-3}) sandwiched between an AlInAs barrier (280 Å) and an AlInAs/GaInAs electron quarter wave stack. A strong narrowing of the photocurrent spectra demonstrates the effect of confinement. For small electric fields however a unique feature has been observed: the photocurrent changes polarity as a function of the photon energy. We can understand this result considering that in the range of energies where the quarter-wave stack act as an electron reflector, quasi-bound states at energies higher than the barrier height extend above the doped well plus thick barrier combined. For small electric fields the centroids of these states is located above the thick barrier. The electrons which are photoexcited from the ground state to one of these quasi-bound states can either scatter back into the center well and therefore do not contribute to the transport or scatter in the next λ/4 stack and give rise to a current against the direction of the electric field. Transitions at energies above the continuum-confined states will instead generate a photocurrent in the direction of the electric field and therefore produce a change of sign in the photocurrent spectra

[1] F. Capasso, C. Sirtori, J. Faist, D.L. Sivco, A.Y.Cho, Nature 358, 565 (1992)

ThP21

Landau Levels of Bragg Confined Electrons and Holes

M. Zahler, E. Cohen, J. Salzman and E.Linder
Solid State Institute
Technion-Israel Institute of Technology, Haifa 32000, Israel
and L.N. Pfeiffer
AT&T Bell Laboratories, Murray Hill, NJ. 07974, U.S.A.

Abstract

We report on the observation of the electronic Landau level splitting in Bragg confining structures (BCS) under an applied magnetic field at T=2K. The BCS consists of finite $GaAs/Al_{0.32}Ga_{0.68}As$ superlattice (SL) sections that clad $Al_{0.32}Ga_{0.68}As$ spacer layers. The SL sections act as Bragg reflectors that give rise to confined electron and hole states in the spacer layers (e_B, hh_B and lh_B). The Landau levels are observed in the photoluminescence excitation spectra in the Faraday configuration. The electron and hole cyclotron frequencies correspond to a two - dimensional motion in the Bragg confining barrier. We use the magnetic field dependence in order to determine the $e_B - hh_B$ and $e_B - lh_B$ band gaps and from these we find the Bragg confined exciton binding energy.

In semiconductor Bragg confining structures (BCS) the carriers are confined in the quantum barrier [1][2], or in the well with an energy higher than that of the barrier [3,4]. The confinement mechanism is then based on two requirements: a. The carrier wavefunction must be coherent over a long distance (in the confinement direction, that is, the growth direction (z) of the structures discussed below); b. The carrier de Broglie wavelength along the confinement direction must fulfill a certain Bragg reflection condition [5,6], so that its wavefunction amplitude outside the barriers is greatly reduced. In such BCS, properly designed superlattice (SL) sections act as Bragg reflectors [6]. This results in a discrete energy level, corresponding to the barrier - confined state that falls within the first SL mini stop-band.

Undoped BCS have been studied by photoluminescence (PL) and its excitation (PLE) spectroscopy [4], as well as by LO-phonon resonant Raman scattering [7]. n doped BCS were studied by intersubband absorption [3]. In this paper we present a study of the Landau level splitting of the Bragg - confined electrons and holes in undoped BCS under a magnetic field applied along the z - direction.

The BCS studied here was grown by molecular beam epitaxy on (001) - oriented GaAs substrates. It consists of SL - sections, each one has 5 periods of 6 monolayers (ml's) of GaAs wells and 22 ml's of $Al_{0.32}Ga_{0.68}As$ barriers. Between these SL sections there are $Al_{0.32}Ga_{0.68}As$ spacers, 66 ml's thick. The 'unit cell' of this BCS is schematically shown in Fig. 1, by the band gap variation of the constituent materials along the growth direction. (It is repeated 66 times). The band offset is taken as $\Delta E_c : \Delta E_v = 6 : 1$. The

calculated Bragg confined energy levels (e_B, hh_B and lh_B),1 are shown together with their associated envelop- functions.

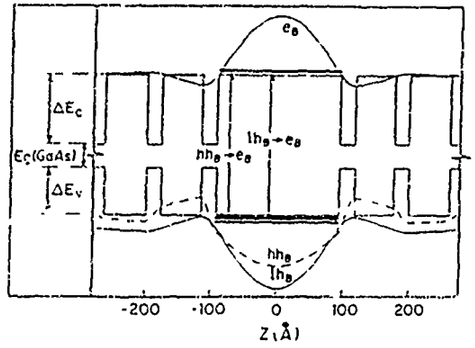

Fig.1: A schematic description of the "unit cell" of the Bragg confining structure studied here. e_B, hh_B and lh_B are the Bragg confined electron, heavy hole and light hole states, respectively. They are represented by the energy levels (heavy horizontal bars) and envelope functions.

For the spectroscopic measurements, the sample was placed in an immersion type dewar (at T=2K), in the bore of a superconducting magnet (Faraday configuration). It was excited by cw dye lasers pumped with an Ar^+ laser. The dye laser linewidth was 0.1 meV and the intensity at the sample surface was varied in the range of 0.1-5W cm^2. A backscattering geometry was used, and the scattered radiation was dispersed by a double monochromator (resolution of 0.05 meV).

The PL spectrum of the BCS, at $B = 0$, is shown in Fig. 2a. The two PL bands with peaks at 1.981eV and 1.991eV are identified as the $(e_B - hh_B)1S$ and $(e_B - lh_B)1S$ excitonic transitions 1. The PLE spectra (Figs. 2b - e) are monitored in the $(e_1 - hh_1)1S$ excitonic transition of the SL sections (at 1.75eV, not shown here 1). The PLE spectrum, for $B = 0$, shows the same Bragg confined exciton transitions as observed in PL, but blue - shifted by $\sim 3meV$. This shift is probably due to exciton dynamics within its inhomogeneously broadened band, as in other alloy semiconductors. The PLE band at 2.02eV is shifted by $\sim 35meV$ from the $(e_B - hh_B)1S$ band. This is the energy of the GaAs - like LO phonon in $Al_{0.32}Ga_{0.68}As$. It is thus assign to a phonon sideband of the $(e_B - hh_B)$ excitonic transition.

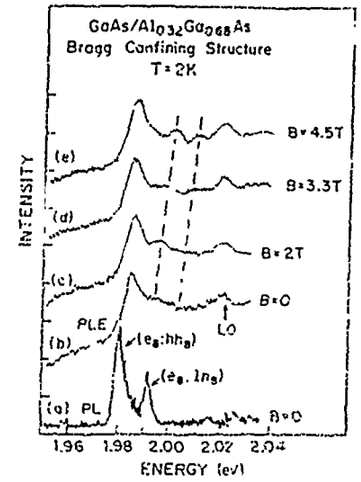

Fig.2: The photoluminescence (a), under a cw excitation at 2.1eV, and the magnetic field dependent photoluminescence excitation spectra (b - e), of the Bragg confining structure described in Fig. 1. The emission (in the PLE spectra) was monitored at 1.75eV, at the $(e_1 - hh_1)1S$ exciton transition of the superlattice sections. The band denoted LO, in the PLE spectra, is the GaAs - like LO phonon sideband of the $(e_B - hh_B)1S$ exciton band.

Under a magnetic field ($B \sim 5T$), applied along the direction perpendicular to the BCS plane, the PL spectrum does not change. Nor do the $(e_B - hh_B)1S$ band (at 1.981eV) and its LO - phonon sideband, observed in the PLE spectra (Figs. 2b - 2e). This is expected, as the 1S exciton shows only a diamagnetic shift that is much smaller than its inhomogeneous width. The PLE spectra show two bands that shift linearly to higher

energies with increasing magnetic field, according to:

$$E_i = E_{0i} + \frac{1}{2}\hbar\omega_c \qquad (i = 1,2) \tag{1}$$

E_{01} and E_{02} are the extrapolated (to $B = 0$) energies of the two field dependent bands. We identify these two bands as the transitions between the lowest electron Landau level ($N_{eB} = 0$) and the highest heavy and light hole Landau levels ($N_{hhB} = N_{lhB} = 0$), which are Brillouin confined. Therefore, E_{01} and E_{02} correspond to the $e_B - hh_B$ and $e_B - lh_B$ band gaps, respectively. The difference between these energies and the energy measured by PLE of the 1S exciton bands, yields the exciton binding energies, $Ry(e_B - hh_B)$ and $Ry(e_B - lh_B)$. The cyclotron frequency, ω_c, is given by:

$$\omega_c = \frac{2\mu_B B}{\hbar(m_\parallel^* m^0)} \tag{2}$$

where μ_B is the free electron Bohr magneton, m^0 is the free electron mass and $m_\parallel^*$ is the reduced electron - hole in plane effective mass:

$$\frac{1}{m_\parallel^*} = \frac{1}{m_{e\parallel}} + \frac{1}{m_h} \tag{3}$$

The reduced masses are determined from the dependence of the respective cyclotron frequencies on the magnetic field, i.e., from the field dependent slopes of E_1 and E_2 (as shown in Fig. 2).

In Table 1 we compare the calculated values of the $e_B - hh_B$ and the $e_B - lh_B$ band gaps [1], effective in-plane masses [9][10] and exciton binding energies [11], with the measured quantities. As one can see, there is an excellent agreement, between theory and experiment, for both the band gaps and the exciton binding energies. For the calculated reduced effective masses, the in plane values, $m_{eh} = 0.07m^0$, $m_{elh} = 0.15m^0$ and $m_{hh} = 0.23m^0$ are taken from Refs. [9] and [10]. The agreement with the measured values is lower. This may be due to both experimental errors and inadequacy of the assumption of uncoupled hole states [8].

Table 1: Calculated and experimental BC transition energies, in plane masses and exciton binding energies.

		calculated*	experimental
$e_B - hh_B$	band gap (E_{01})	1.995eV	1.993eV
	$m_\parallel^*/m_0$	0.046	0.038
	Ry ($e_B - hh_B$)	8.5meV	9meV
$e_B - lh_B$	band gap (E_{02})	2.003eV	2.003eV
	m^*/m_0	0.053	0.013
	Ry ($e_B - lh_B$)	9meV	8.5meV

* See Refs. [1],[9],[10] and [11].

The observation of the Landau levels proves that the Bragg confined electrons and holes are free to move in the $Al_{0.35}Ga_{0.65}As$ spacer layers (planar motion). The high values of the Bragg confined exciton binding energies confirm its two dimensional character, as was recently deduced from the LO-phonon RRS profiles [7] and predicted theoretically by Grundmann and Bimberg [11].

Acknowledgments: The research at the Technion was supported by the U.S Israel Binational Science Foundation (BSF), Jerusalem, Israel, and was done in the Center for Advanced Opto- Electronics. E.Linder acknowledges the support of the Center for Absorption in Science, Ministry of Immigrant Absorption, State of Israel.

References

[1]: M Zahler, I.Brener, G Lenz, J Salzman and E Cohen, Appl Phys Lett 61, 949 (1992)
[2] F.C Zhang, N.Dai, H.Luo, N Samarth, M Dobrowolska, J K Furdyna and L R Ram Mohan, Phys Rev Lett. 68, 3220 (1992)
[3]: C Sirtori, F.Capasso, J.Faist, D.L.Sivco, S n.G Chu and A Y Cho, Appl. Phys Lett 61, 638 (1992).
[4]: F Capasso, C Sirtori, J Faist, D.L Sivico, S.Nee G Chu and A Y Cho, Nature 358, 565 (199.)
[5]: F H.Stillinger, Physica B 85, 270 (1977).
[6]: G Lenz and J Salzman, Appl. Phys Lett 58, 871 (1990).
[7]: M.Zahler, E.Cohen, J.Salzman and E Linder, *to be published in Phys. Rev. Lett*
[8]: D Heimc in *The spectroscopy of Semiconductors* V2B, Ed by D J Seilk, ... C L Littler (Academic Press, New York (1992)),p 16-18
[9]: S.Datta *Modular Series on Solid State Devices, Vol VIII: Quantum Phenomena*, Ed by R F Pierret and G W Neudeck, (Addison-Wesley Publishing Company, 1989), p 200
[10]: L C.Andreani and A.Pasquarello, Phys Rev B42, 8928 (1991), L C Andreani, *Ph D thesis* (Scuola Normale Superiore, Pisa, 1989), p 11-25
[11]: M Grundmann and D Bimberg, Phys Rev B38 13486 (1988)

ThP22

Long Lived Photoexcited Electron-Hole Pairs in Modulation Doped GaAs/AlGaAs Quantum Wells Studied by Intersubband Spectroscopy

Y. Garini,[a] E. Ehrenfreund[a], E. Cohen,[a] and Arza Ron[b]
Solid State Institute Technion Israel Institute of Technology, Haifa 32000, Israel
([a] Department of Physics, [b] Department of Chemistry)

K K Law, J L. Merz and A.C. Gossard
Center for Quantized Electronic Structures (QUEST)
University of California, Santa Barbara, CA 93106, U S A

Abstract

We present a study of the e1-e2 intersubband absorption in modulation doped $GaAs/Al_{0.3}Ga_{0.7}As$ MQW's that are photoexcited by interband radiation A comprehensive study of the photoinduced absorption (PIA) strength as a function of exciting (laser) intensity and modulation frequency indicates that only a subgroup of the photoexcited electrons contribute to the PIA. These electrons are long lived in MQW's with a 2DEG density in the range of $1 - 3 \times 10^{10}$ cm^{-2}. The existence of long lived electrons is explained by a model based on localized, photoexcited holes, that have a reduced radiative recombination rate with the 2DEG. We calculate this recombination rate and show that it is much longer than that of free electrons and holes

Introduction

The optical properties of doped quantum wells (QW's) strongly depend on the interaction of the photoexcited electron-hole pairs with the two dimensional electron gas (2DEG) [1, 2]. This is mainly due to phase space filling and screening [3, 4] Most of the experimental work aimed at studying photoexcitation of doped QW's is based on interband transitions [5, 6] However, the intensity, spectral shape and decay time of the interband transitions vary gradually with n_D (the electron areal density) in the low 2DEG density range, and therefore, they are not sensitive enough to small variations in n_D
In this work we report on a study of the (e1-e2) intersubband absorption in modulation doped $GaAs/Al_{0.3}Ga_{0.7}As$ QW's, under interband photoexcitation We show that the photoinduced intersubband absorption (PIA) is strongly dependent on both n_D and the density of photoexcited e-h pairs. These observations are compared with the dependence of the photoluminescence (PL) on the excitation intensity The results are analyzed in terms of a model based on the existence of long lived electrons in the photoexcited 2DEG. These are due to localized holes that have a small recombination probability with the electrons

Experimental

Several $GaAs/Al_{0.3}Ga_{0.7}As$ modulation doped MQW's with different n_D were studied. They were grown by molecular beam epitaxy on (001) oriented GaAs substrates Each MQW consists of 50 GaAs wells of 50Å nominal thickness, separated by ≈100Å thick barriers. Each barrier is Si doped in the middle 40Å and the densities were in the range of $n_D = 1 \times 10^{10} - 1 \times 10^{12}$ cm^{-2} (in each well) The samples were cut and polished at 45° to the QW plane. This 'waveguide configuration' provided a finite electric field of the infrared radiation along the normal to the QW plane (z direction). Most studies were done in the range of 2-100K, by placing the samples in an immersion-type dewar. The infrared beam passed through a Bruker IFS-66V Fourier transform infrared spectrometer. It was modified in order to record small changes in the absorption, which were induced by excitation with an Ar^+ laser or a Pyridine 2 dye laser. The intersubband transitions were measured with a spectral resolution of 2 meV The PIA spectra were obtained by measuring $(-\Delta T/T)$, where T is the sample transmission and ΔT is its photoinduced change The sensitivity in measuring the PIA was better then 10^{-4} The exciting laser beam was chopped with an acousto optic modulator in the range of $10^2 - 10^6$ Hz. For the PL measurements we used a double grating monochromator with a resolution better than 0.1 meV
The PL spectrum of the MQW with $n_D = 1 \times 10^{10}$ cm^{-2} is shown in Fig. 1a. The measured integrated intensity of this PL band as a function of exciting laser intensity, in the intensity range of $I_L = 0.01 - 1$ W/cm^2 is found to be linear However, the band shape varies slightly with increasing excitation intensity In order to study this effect we obtained the differential PL (DPL) spectra by first normalizing each spectrum by its integrated intensity. Then we subtract the normalized spectra taken under two excitation intensities. Figs. 1b-1d show three such DPL spectra. ($I_L - I_{0.03}$ denotes the spectrum obtained by subtracting the normalized spectrum for $I_L = 0.03$ W/cm^2 from that of $I_L = 1$ W/cm^2). Fig. 2 shows the absorbance and PIA spectra for two MQW's with $n_D = 1 \times 10^{10}$ and 7×10^{10} cm^{-2}). The observed absorption band is due to the e1-e2 intersubband transition [3, 9]. Its integrated intensity is proportional to the doping level and to the optical path of the infrared beam in the sample The PIA spectra were observed under interband excitation energy of 2.41 eV and intensity of 0.64 W/cm^2 (at the sample surface). It is clearly seen that while the PIA is relatively strong ($[-\Delta T/T]_{max} = 6 \times 10^{-3}$) for $n_D = 1 \times 10^{10}$ cm^{-2}, it is unobservable for $n_D = 7 \times 10^{10}$ cm^{-2}. No PIA signal could be observed for the MQW's with higher doping levels It should be noted that the direct absorption and PIA of the same MQW have the same spectral shape, and are polarized along the growth direction. Fig. 3 shows the dependence of the integrated PIA intensity, $I_A = \int(-\Delta T/T)d\epsilon$, on the exciting laser intensity, for two MQW's with $n_D = 1 \times 10^{10}$ and 3×10^{10} cm^{-2}

Analysis

The PIA spectrum (observed only for the lightly doped samples, $n_D < 3 \times 10^{10}$ cm^{-2}) has the same shape as that of the absorption spectrum Therefore, the PIA is due to electrons added to the 2DEG with the same energy distribution The fact that the integrated PL intensity dependence on exciting laser intensity is linear, means that the total density of photoexcited electron-hole pairs depends linearly on the laser intensity On the other hand, the PIA saturates with increasing laser intensity (Fig. 3) We thus conclude that the electrons contributing to the PIA are only a finite subset of the total photoexcited electron population We have measured the dependence of I_A on the exciting laser modulation frequency [10] and found that the lifetime of these electrons is of the order of a few μsec. We also found that while the PIA intensity depends very strongly on both n_D and I_L, the DPL intensity (Fig. 1b-d) varies very weakly with I_L (for a given n_D) This supports the conclusion that only a subgroup of photoexcited electrons contributes to the intersubband absorption, while all these electrons contribute to the interband PL

This suggestion can be tested by fitting the PIA intensity on I_L using a phenomenological approach. Following Ref. 1, we propose that the generation rate of the electrons contributing to the PIA (with a density of N_{PIA}) is given by $g(1 - N_{PIA}/N_0)$. Here g is the photogeneration rate ($g \propto I_L$) and N_0 is the saturation density of the electrons contributing to the PIA. If we further assume that these electrons have a lifetime τ, then the rate equation is:

$$\frac{dN_{PIA}}{dt} = g(1 - N_{PIA}/N_0) - \frac{N_{PIA}}{\tau} \qquad (1)$$

Its steady state solution is

$$N_{PIA}^{ss} = \frac{g\tau N_0}{g\tau + N_0} \qquad (2)$$

The experimentally measured I_A is directly proportional to N_{PIA}^{ss}: $I_A = I_0 N_{PIA}^{ss}$, where I_0 contains various constants including the infrared optical path in the sample. The fit of this model to the data of Fig. 5 is shown by the solid lines. The parameters obtained by this fit are: $N_0 = 1.2$ and $0.36 \times 10^{10} cm^{-2}$ and $\tau = 12$ and $1.8\ \mu sec$ for the $n_D = 1$ and $3 \times 10^{10} cm^{-2}$ MQW's, respectively. For comparison, we show in Fig. 3 the linear dependence of I_A on laser intensity, as measured for undoped MQWs. It is clear that the PIA in the doped MQW's is due to a different mechanism than in undoped MQW's (long lived electrons vs short lived excitons). In order to account for the existence of long lived photoexcited electrons in doped MQW's with $1 \times 10^{10} \leq n_D < 7 \times 10^{10}$ cm^{-2}, we propose the following model: a subgroup of the photoexcited hole population consists of localized holes, whose wavefunction weakly overlaps with the 2DEG wavefunctions. It is assumed that the hole localizing centers do not localize electrons. It is conceivable that such hole localization can occur due to interface roughness together with a random distribution of the Si dopant atoms (which are located only 40Å from the interfaces). A finite density of such hole localizing sites results in a measurable density of long lived photoexcited electrons, because the localized holes will have a reduced recombination rate with the 2DEG. We estimate this rate by the following calculation. The z-dependent part of the electron wavefunction is obtained by self consistently solving the Schrödinger and Poisson equations, for a given n_D. Using the resulting electrostatic potential, the z dependent part of the hole wavefunction, $\chi_A(z)$, is obtained. Then, following Bastard [11], we assume a cylindrical localization potential on the interface and solve the Schrödinger equation for the in plane hole wave function ($f_h(\vec{r})$)

$$\left[\frac{p_x^2 + p_y^2}{2m^*} - V_h\Theta(a - r)P_h\right] f_h(\vec{r}) = (\epsilon - E_{h1}) f_h(\vec{r}) \qquad (3)$$

where $p_{x,y}$ are the in-plane momentum operator components, m^* is the hole effective mass in the well, $\Theta(a - r)$ is a step function that defines a cylindrical well with radius a and a potential of V_h. P_h is the probability of finding the hole on the interface. E_{h1} is the lowest confined hole energy level and ϵ is the localized hole energy level. Assuming $f(\vec{r}) = \frac{1}{\lambda}\sqrt{\frac{2}{\pi}}e^{-r/\lambda}$, $n_D = 1 \times 10^{10}\ cm^{-2}$, a valence band offset of $V_h = 0.37$ eV and $a = 200$Å, we obtain $\epsilon = 3.5$ meV and $\lambda = 100$Å for the binding energy and the wavefunction extension radius, respectively. The extension radius and the density of localizing sites that we have found are in reasonable agreement with other works done on interface roughness [12, 13]

Now, assuming that the electrons in the 2DEG have a 2D free particle wavefunction, we can calculate the recombination rate (in comparison to that of a free electron recombining with a free hole) by using Fermi's golden rule (Fig. 4). The result (which is approximated for the case where $n_D\lambda^2 >> 1$) is: $\tau_f/\tau_b \approx n_D\lambda^2$, where τ_b^{-1} is the radiative recombination rate of a free electron with a localized hole and τ_f^{-1} that of a free e and h. Taking $n_D = 1 \times 10^{10}$ cm^{-2} and the parameters quoted above we find:

$$\frac{\tau_b}{\tau_f} \sim 300 \qquad (4)$$

This result leads to a lifetime of the localized holes and corresponding excess electrons in the order of $0.5\mu sec$. Moreover, since $\tau_b \propto 1/n_D$, the density of electrons contributing to the PIA will be greatly reduced with increasing n_D, resulting in a very weak PIA spectrum (as observed).

Summary

We find that the (e1-e2) PIA is strongly dependent on the density of the 2DEG and on the exciting (laser) intensity. This absorption is only observed for $1 \times 10^{10} \leq n_D < 7 \times 10^{10}$ cm^{-2}, and is non-linearly dependent on I_L. The intensity of the interband PL, on the other hand is linearly dependent on I_L, with very small variations in its shape. We show that these results are well explained by a model based on the existence of a subgroup of long-lived photoexcited holes. We present a model of hole localization centers that are due to interface potential fluctuations. The calculated hole wavefunction leads to a radiative recombination rate with the 2DEG, that is much smaller than that of a free hole. Our study shows that the interband spectroscopy of low density 2DEG is a much more sensitive tool than interband spectroscopy.

Acknowledgments The work at the Technion was supported by the US-Israel Binational Science Foundation (BSF), Jerusalem, Israel, and was carried out in the Center for Advanced Opto-electronics. The work at UCSB was supported by the National Science Foundation Science and Technology Center, QUEST.

References

[1] S. Schmitt-Rink, D.S. Chemla and D.A.B. Miller, Adv. Phys. 38, 89 (1989).

[2] G.D. Sanders and Y.C. Chang, Phys. Rev. B35, 1300 (1987).

[3] G. Livescu, D.A.B. Miller, D.S. Chemla, M. Ramaswamy, T.Y. Chang, N. Sauer, A.C. Gossard and J.H. English, IEEE Journal of Quantum Electronics, 24, 1677 (1988).

[4] D. Huang, H.Y. Chu, Y.C. Chang, R. Houdre and H. Morkoc, Phys. Rev. B38, 1246 (1988).

[5] D.A. Kleinman, Phys. Rev. B32, 3766 (1985).

[6] H.W. Liu, C. Delalande, G. Bastard, M. Voos, G. Peter, R. Fischer, E.O. Gobel, J.A. Brum, G. Weimann and W. Schlapp, Phys. Rev. B45, 8469 (1992).

[7] C.D Delalande, G Bastard, J Orgonasi, J.A. Brum, H.W Liu, M. Voos, G Weimann and W. Schlapp, Phys Rev Lett. 59, 2690 (1987)

[8] L.C. West, S.J. Eglash, Appl. Phys. Lett. 46, 1156 (1985).

[9] Y. Garini, M. Olszakier, E. Cohen, E Ehrenfreund, Arza Ron, K-K Law, J.L. Merz and A.C. Gossard, Superlattices and Microstructures 7, 287 (1990).

[10] Y. Garini, E Ehrenfreund, E. Cohen, Arza Ron, K-K. Law, J.L. Merz and A.C. Gossard, Phys. Rev. B48 (Aug. 1993).

[11] G Bastared, "Wave Mechanichs Applied to Semiconductor Heterostructures", (Les editions de physique, Les Ulis, 1988), Chap. 4

[12] J Christen and D. Bimberg, Phys. Rev. B42, 7213 (1990).

[13] C.A. Warwick, R.F. Kopf, Appl. Phys Lett 60, 386 (1992).

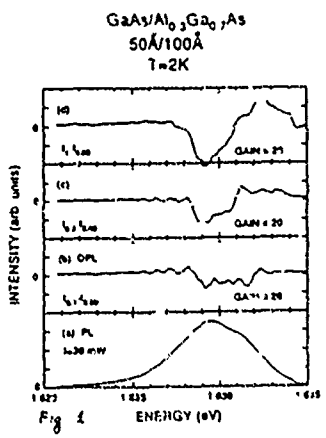

Fig. 1

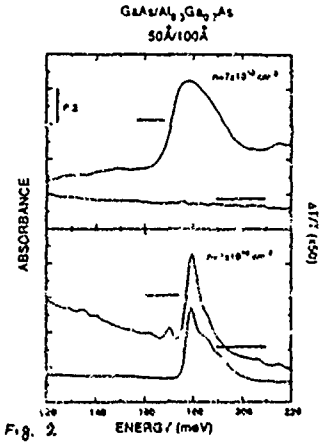

Fig. 2

Figure Captions

Fig. 1 : a. The photoluminescence (PL) spectrum of the MQW with $n_0 = 1 \times 10^{10}$ cm^{-2}. b. The differential photoluminescence (DPL) spectrum obtained by subtracting the (area-normalized) PL spectrum for excitation intensity of $I_{ex} = 3.03$ W/cm² from that excited by $I_{ex} = 0.1$ W/cm². (c), (d) are the same as (b) but with different excitation intensities.

Fig. 2 : The absorbance and photo induced (σ_1-σ_2) absorption ($-\Delta T/T$) of two MQW's with the indicated areal electron densities, observed at liquid He temperature.

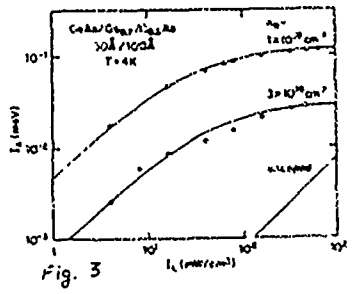

Fig. 3 : The integrated photoinduced (σ_1-σ_2) absorption strength of two MQW's as a functio of excitation intensity Also shown is the measured photoinduced absorption strength of an undoped MQW.

Fig. 4 : A schematic description of the localized hole - free electron recombination model (see text)

ThP23

Electron Transport in InAs-$Ga_{1-x}In_xSb$ Superlattices

C A Hoffman, J R Meyer, E R Youngdale, and F J Bartoli

Code 5613, Naval Research Lab, Washington, D C 20375

R H Miles

Hughes Research Laboratories, Malibu, CA 90265

L R Ram-Mohan

Worcester Polytechnic Institute Worcester, MA 01609

We will discuss a magneto-transport and quantum transport investigation of InAs-$Ga_{1-x}In_xSb$ strained layer superlattices, which are of great current interest as a potentially more producible alternative to $Hg_{1-x}Cd_xTe$ in infrared detector applications Despite a crucial role in photovoltaic device operation, the transport properties of electrons and holes in this system have received almost no previous attention The present data will be correlated with theoretical band structures from an 8-band *k·p* calculation

Temperature-dependent electron mobilities have been determined for a series of n-type superlattice with constant $Ga_{1-x}In_xSb$ barrier thickness (d_2 = 25 Å) but a range of InAs well thicknesses (d_1 = 25-86 Å) Interface roughness scattering is found to dominate μ_n in all samples and most temperatures up to ambient ($T \leq 200$ K) However, the dependence on d_1 is found to be much weaker than the d_1^6 relation observed in other heterostructure systems with larger d_2 This is, in fact, consistent with the theoretical prediction of a weaker sensitivity of the energy levels to monolayer fluctuations in the well width Theory also predicts that the low-temperature mobility should abruptly drop when d_1 is increased to the point where the energy gap vanishes and the superlattice becomes a semimetal Not only is this confirmed experimentally, but the observed decrease in μ_n is much larger than that predicted The calculations show that when d_2 is thin, the E1 and HH1 bands strongly repel one another Semimetallic InAs-$Ga_{1-x}In_xSb$ thus has much more in common with semimetallic HgTe-CdTe superlattices than with semimetallic InAs-GaSb (for thick d_2) The experimental observation of two coexistent electron species whose relative populations shift with T is a predicted consequence All of the samples in this series display quantum oscillations in both the diagonal and Hall conductivities Since the system has a strongly 3D rather than 2D character, it is surprising that in several superlattices the oscillations in σ_{yy} are considerably *stronger* than those in σ_{xx}

ThP24

Comparison of Far-Infrared- and DC-Conductivity of Electron-Systems Laterally Patterned by Low-Energy Ion Beam Exposure

C. Lettau[a], M Wendel[a], A. Schmeller[a], W Hansen[a], J P. Kotthaus[a], G. Böhm[b], G. Weimann[b], and M. Holland[c]

(a) Sektion Physik, Ludwig-Maximilians-Universität München, D-80539 München
(b) Walter Schottky Institut, TU München, D-85748 Garching
(c) DEEE, University of Glasgow, GB-Glasgow G128QQ

We investigate the electronic properties of quantum wires that are prepared in AlGaAs-GaAs heterojunctions with a low energy ion beam irradiation technique. Magneto-transport measurements on single wire structures reveal that diffuse scattering at the lateral boundaries is enhanced in these structures compared to wires prepared by split gates or etching techniques. Furthermore, the lateral depletion width is relatively small, i. e. the electronic width is only 40nm smaller than the width of the lithographically defined mask. In addition we study the far-infrared conductivity of these quantum wires. We find that the boundary roughness scattering has a dramatic impact on the resonance linewidths at low magnetic fields. The 1D intersubband plasmon is found to be much more affected than the 1D intrasubband plasmon reflecting highly anisotropic scattering.

Low-dimensional electron systems such as quantum wires and quantum dots are preferably prepared by lateral patterning of a two-dimensional electron systems (2DEG) in semiconductor heterostructures Different patterning techniques have been employed of which the most widely used are etching into the sample surface or patterned field effect electrodes [1] The properties of wires generated with these methods are thus intensively investigated and it is found that, generally, the external charges that define the electrostatic binding in lateral direction are separated from the electron system by relatively large depletion widths. This leads to smooth potential walls, i. e. channel boundaries with roughness that can be characterised by a correlation length comparable to the depletion width. A less thoroughly characterized technique is the lateral patterning by low energy ion beam irradiation although existing experiments show intriguing results. [2-5] In particular, these results indicate that the depletion widths in ion beam defined quantum wires are considerably smaller than in field effect-defined samples and that the boundary scattering is considerably more diffuse reflecting more roughness Here we focus on the impact of enhanced diffuse boundary scattering on the dynamic conductivity in ion beam defined quasi-one-dimensional (1D) electron systems.

Two conventional HEMT-structures are used for the preparation in which the hetero-interfaces are 70nm and 55nm below the sample surface. At T=4.2K the 2DEGs have electron densities of n_s=4 $10^{15}m^{-2}$ and 5 $10^{15}m^{-2}$ and mobilities of $17m^2/Vs$ and $50m^2/Vs$, respectively. The ion beam irradiation results in a depletion of mobile electrons except from those areas that are protected by mask. As irradiation mask a resist pattern defined by optical or electron beam lithography was used

For DC magneto transport measurements we have prepared single quantum wires by electron beam lithography The geometries of the Ni-AuGe ohmic contacts are defined with PMMA positive resist, whereas the ion beam irradiation masks are made of 100nm thick negative resist (Hoechst AZ PN 114) stripes connecting the previously prepared ohmic contacts. Quantum wires with resist stripe widths between 100nm to 1000nm have been fabricated Three pairs of voltage probes for measurements of the Hall resistance are arranged along the wires with 7.5µm separation between each pair The samples for FIR) transmission measurements are multiple quantum wire arrays defined with a holographically exposed positive photoresist layer

(Shipley AZ1805) of 140nm thickness. Periods of the wire arrays range from 300nm to 700nm. The widths of the photoresist stripes are typically less than half the period, e.g. 300nm for a sample with period 700nm.

The ion beam exposure is performed in a commercial ion-milling-machine modified to use low ion dose rates (typically 5-6μA/cm^2) with low acceleration voltages (200-300V). The use of low energy Ne ions results in low sputtering rates when irradiating the sample surface. This is verified with an atomic force microscope with which a material removal of 2-3nm height has been measured after irradiating the sample with a typical dose (3.5mC/cm^2) necessary to pattern the electron system. Detailed investigations concerning the confinement mechanism in these ion beam defined wires will be published elsewhere [6]. We note that the small surface corrugation makes the ion beam irradiation technique very advantageous for combination with additional patterning techniques like, e. g., additional metal gates on the sample surface. Thus, as described later, a metal grating coupler for the investigation of 1D plasmons can easily be fabricated on top of the sample after the ion beam exposure. The irradiation effect on the 2DEG is monitored during the ion beam exposure by measuring the increase of the resistance between two ohmic contacts during ion beam exposure. Additionally, in the single wires the vanishing of the low temperature resistance measured at B=0 in Hall geometry serves as an independent test for the successful isolation of the unmasked regions. On the other hand in the wire arrays for FIR transmission measurements the successful isolation of the wires can be judged from the frequency of the dimensional resonance as described below.

The inset of Fig. 1 shows typical traces of the longitudinal DC resistance in ion beam defined quantum wires as function of the magnetic field applied perpendicular to the sample surface for various wire widths. At low fields a pronounced maximum of the longitudinal resistance is observed, with a position that depends on the electronic widths of the quantum wires. This maximum arises from diffuse scattering at the boundaries of the 1D channels on the longitudinal magneto-resistance. [3] At zero magnetic field the channel resistance is dominantly determined by electron trajectories that reflect from the channel boundaries under glancing angles. A small magnetic field bends the trajectories towards the boundaries and thus intensifies contact to the channel boundaries. Diffuse scattering processes then lead to an enlarged resistance. At higher fields the opposing channel boundaries become decoupled, i. e. an electron trajectory is either bound to one of the boundaries or in the sample center. The magneto-resistance decreases accordingly at high magnetic fields. The strength of the magneto-resistance anomaly indicates the importance of boundary roughness in our samples.

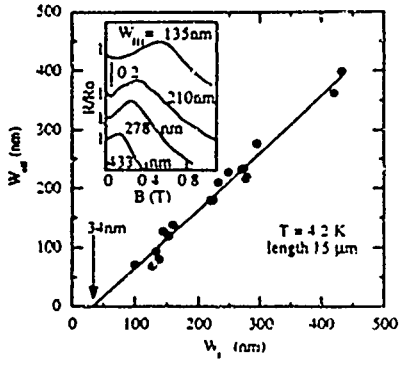

Fig. 1. Effective widths of electron wires defined by ion beam exposure plotted vs. the lithographic width of the mask. W_{eff} is calculated as explained in the text. Inset: Longitudinal magneto-resistance of those wires at small magnetic fields, showing the resistance anomaly that arises from diffuse boundary scattering.

The magnetic field position B_{max} of the resistance maximum can be used to determine an effective width of the electron wire. [3] A numerical model for description of the magneto-resistance anomaly [7,8] relates the classical cyclotron radius $R_c=\hbar k_F/eB_{max}$ to the effective width W_{eff} of the 1D electron system according to: $W_{eff}=0.55\cdot R_c$. In Fig. 1 the effective widths determined from the resistance anomaly are plotted as a function of the lithographic width of the mask as determined from SEM-pictures. The straight line is a least square fit to the data. The intercept with the abscissa reflects twice the depletion width, i. e., the amount by which the effective widths of the electron channels are smaller than the lithographic width of the mask. We thus have a lateral depletion length smaller than 20nm, a very low value compared to those found with other patterning techniques. The slope of the line is close to one as expected if the depletion width does not depend on the lithographic width.

The thus determined effective width W_{eff} together with the electron density determined from the high field quantum oscillations of the magneto-resistance are used to determine an electron mobility from the longitudinal resistance at B=0. In Fig. 2 the mobility is depicted vs. the effective wire width. We consider the modification of the phase space for scattering processes arising from the reduced dimensionality in our quantum wires as unimportant. If scattering is 100% specular the as-grown mobility represents an upper limit for the electron mobility in the 1D channels as indicated by the upper solid line. The lower solid line is calculated with a model

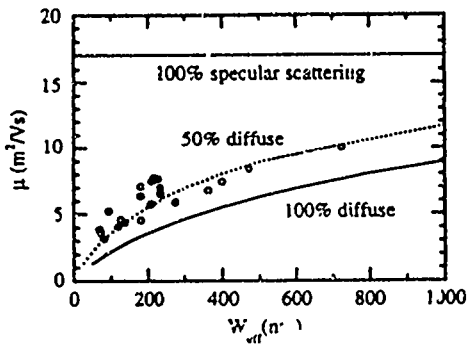

Fig. 2. Electron mobilities in ion beam defined quantum wires determined from the zero field resistance as function of the effective wire width. Solid lines are calculated for 100% specular and 100% diffuse scattering, respectively (see text).

of Beenaker et al. [9] assuming 100% diffuse scattering. The dashed line demonstrates that the mobilities found in our ion beam defined quantum wires are best described assuming about 50% diffuse boundary scattering.

The FIR-transmission-spectra are measured with a rapid scan Fourier-transform-spectrometer at T=2K. We first discuss measurements on wire arrays that have periods of 700nm, 500nm and 300nm and no additional grating coupler on the sample surface. With the FIR radiation polarized perpendicular to the wires we excite the intersubband plasmon at wave vector q=0, the so-called dimensional resonance. Dimensional resonances of a wire array with 700nm period recorded at different magnetic fields are shown in Fig. 3 along with the resonance linewidths as function of magnetic field (inset). Whereas the linewidth is low at high magnetic fields it strongly increases with decreasing magnetic field. The resonance oscillator strength remains roughly constant. The magnetic field dependent broadening is even more drastic in samples

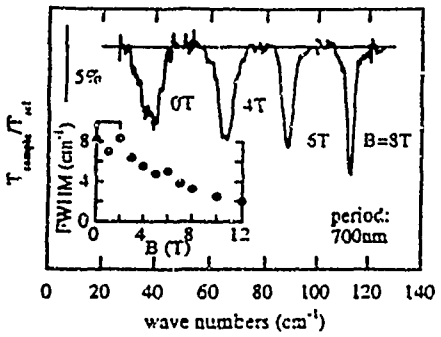

Fig. 3: Dimensional resonances of an ion beam defined wire array with period 700nm. The inset shows the FWHM of the resonances vs. magnetic field.

with 500nm period and different from line widths of dimensional resonances in wire arrays fabricated with more conventional techniques Here the linewidth increases with decreasing magnetic field so strongly that at B=0 no dimensional resonance can be resolved. The resonance position follows the magnetic field dispersion $\omega_{res}^2=\omega_0^2+\omega_c^2$ as shown by the crosses in Fig. 4a [1] The dashed line is calculated according to this formula Since ω_0 is an additional measure of lateral confinement we can use the ω_0 extracted from the measured resonance positions as another indicator for successful ion beam patterning. In wire arrays with 500nm and 700nm resist gratings the resonance shifts by about 15cm^{-1} at B=3T after ion beam exposure In samples with a resist mask of 300nm period and exposed to a successively increasing ion dose to meet this criterium at B=3T it was found that the resonance vanishes before a significant shift of the resonance position could be resolved.

A small increase of the resonance linewidth is often also observed in field effect defined wire arrays. This, generally, is discussed in terms of fluctuations of the wire width and an associated inhomogeneous broadening of the resonance position. In our experiments on field effect defined quantum wires [1] we used the same fabrication process for the resist masks as is used here. Thus in both cases the roughness of the resist masks should be comparable. The drastic increase of the resonance FWHM in ion beam defined wires at small magnetic fields can be understood in terms of boundary roughness created by the ion beam exposure. This is in agreement with the enhanced boundary roughness found in above DC transport experiments. A simple argument considering the classical electron trajectories connected with the dimensional resonance shows that diffuse scattering can effectively smear the dimensional resonance. At B=0 the dimensional resonance is associated with electron motion perpendicular to the channel boundaries and thus can be broadened by diffuse boundary scattering. In a magnetic field this situation changes since the magnetic field localizes the electron wave function within the channel. In the classical picture the majority of the classical electron trajectories have reduced boundary contact. Accordingly, the FWHM decreases with increasing magnetic field

After successful investigation of wire arrays with 700nm period a grating coupler was prepared on the sample surface The grating coupler consists of an gold grid of period b=1μm The gold strips have 35nm thickness and a width of approximately 700nm With unpolarized FIR radiation we now observe in addition to the dimensional resonance an intrasubband plasmon at

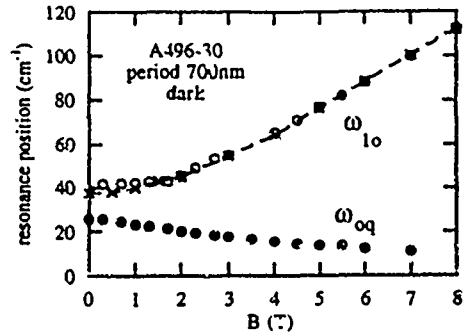

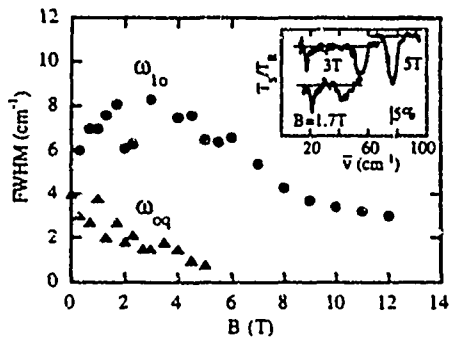

Fig. 4: (a) resonance positions of intersubband plasmons $\omega_{1,o}$ and intrasubband plasmons $\omega_{o,q}$ of the sample in Fig.3 as function of the magnetic field. The dashed line is calculated as described in the text. Crosses denote resonance positions measured before the grating coupler was prepared on the sample surface. Circles are measured with a grating coupler consisting of stripes oriented perpendicular to the electron wires and period b=1μm. (b) Resonance linewidth of the $\omega_{o,q}$ (triangles) and $\omega_{1,o}$ mode. The inset shows three typical FIR transmission spectra

lower frequency. The magnetic field dependence of the resonance positions are shown in Fig. 4a together with the resonance positions of the dimensional resonance in this sample before fabrication of the grating coupler. The resonance position of the intersubband plasmon is only slightly shifted with respect to the dimensional resonance measured without grating coupler.

The negative magnetic field dispersion of the low frequency mode unambiguously identifies this mode as the intrasubband plasmon. [10,11] In the experimental spectra the FWHM of the intrasubband plasmon is remarkably small compared to the linewidths of the intersubband plasmon as demonstrated by the data in Fig. 4b and the spectra in the inset of the same figure. This behaviour can be understood with the assumption that the effectivity of the diffuse boundary scattering process is anisotropic with respect to the angle between channel boundary and direction of electron motion. Since at B=0 the electron motion associated with the intrasubband plasmon is along the channel the small resonance linewidth suggests that glancing angle scatte-

ring processes much less effectively damp the resonances in contrast to the large angle scattering processes associated with the intersubband resonance. We note that the direction of electron motion probed in DC transport experiments again is preferentially along the channel as in the case of intrasubband plasmons

In conclusion, we investigate the DC as well as FIR conductivity of quantum wires defined by low-energy ion beam exposure. DC transport measurements demonstrate that diffuse boundary scattering processes are important in such wires. The resonance linewidth of the FIR-conductivity reflects the high anisotropy of these scattering process.

Acknowledgements: We like to thank A Wixforth and A. Huber for valuable discussions and gratefully acknowledge financial funding by the Deutsche Forschungsgemeinschaft.

References

1. W. Hansen, U. Merkt, and J. P. Kotthaus, in Semiconductors and Semimetals, ed. R K. Williardson, A. C. Beer, E R Weber,Vol. 35, ed. M. Reed, (Academic Press, San Diego 1992) p. 279
2. M. L. Roukes, A. Scherer, S. J Allen,Jr., H. G. Craighead, R. M. Ruthen, E. D. Beebe, and J. P Harbison, Phys. Rev. Lett. 59, 3011 (1987).
3. T. J. Thornton, M L. Roukes, A. Scherer, and B P. Van de Gaag, Phys. Rev Lett. 63. 2128 (1989).
4. M. L Roukes, A. Scherer, and P Van der Gaag, Phys Rev. Lett. 64, 1154 (1990)
5. T. J Thornton, M. L. Roukes, A. Scherer, and B. van der Gaag, in "Science and Engineering of 1- and 0-Dimensional Semiconductors", ed. S. P. Beaumont and C. M. Sottomayor-Torres (Plenum)
6. C. Lettau, M. Wendel, A. Schmeller, W Hansen, J P. Kotthaus, G Böhm, G. Weimann, and M. Holland, to be published.
7. E. Ditlefsen and J. Lothe, Philos Mag 14, 759 (1966).
8. A. B. Pippard, "Magnetoresistance in Metals", (Cambridge University Press, Cambridge 1989)
9. C.W. J. Beenakker and H. van Houten, Phys Rev. B38, 3232 (1988)
10. G. Eliasson, J.-W. Wu, P. Hawrylak, and J J. Quinn, Solid State Commun. 60, 41 (1986).
11. T. Demel, D. Heitmann, P Grambow, and K. Ploog, Phys Rev. Lett. 66, 2657 (1991)

ThP25

Novel Tunable Far Infrared Detector Based on a Quantum Ballistic Channel

L.Fedichkin,* ..Ryzhii** and V.V'yurkov*

*Institute of Physics and Technology,
25A Krasikov str., Moscow, 117218, Russia
** University of Aizu, Tsuruga, Ikki-machi,
Aizu-Wakamatsu-City, 965 JAPAN

Abstract

A new tunable far infrared detector based on a quantum ballistic channel in the asymmetric split-gate structure is proposed and considered theoretically. The asymmetric split-gate provides a long constant width channel with a rather sharp asymmetric narrowing at its end. It is supposed that only the lowest 1st subband in a wide channel is occupied by electrons. There is a thick barrier for these electrons in the narrow channel, so the dark current reduces almost to zero. Due to the asymmetric variation of the of the channel width the electrons can pass the narrow region of the channel under illumination with the photon energy close to subband separation.
The Ampere-Watt responsivity of the photovoltaic detector under is evaluated. The advantage of the proposed detector is a possibility of tuning by a gate voltage and the small response time

[illegible] with a constant [illegible] and the varying of [illegible] is not [illegible] for infrared detector applications because [illegible] is very small. This is due to the conservation [illegible] of an electron absorbing photon [illegible] the current through the

ballistic channel under illumination is almost the same as in darkness. We offer the split-gate structure like that in Fig.1. The essential feature of the electrode shape is that it provides a long constant width channel with a rather sharp asymmetric narrowing at its end so that the subband bottom vs longitudinal coordinate diagram is alike to that in Fig.2.

The main idea is the following. Suppose that only lowest 1st subband in a wide channel is occupied by electrons, i.e. 1st subband is under the Fermi level in a two-dimensional electron gas (2DEG) reservoir. There is a thick barrier for these electrons in a narrow channel so the dark current reduces almost to zero. A dark current caused by a thermal activation or tunneling is very small. When a photon has an energy $\hbar\omega$ close to subband separation $\hbar\omega_0$ in the wide channel and is polarized perpendicular to the channel axis an electron can absorb a photon and be excited to the 2nd subband. When the channel width variation is rather sharp and asymmetric the transition to the 1st subband is possible. In this way the electron can pass the narrow channel if its energy surmounts the 1st subband barrier height E_b. It occurs at least when E_b is higher than Fermi energy ε_f and lower than subband separation $\hbar\omega_0$. In reality there is a simultaneous photon assisted transition rather than two sequential processes of absorption and transition. To evaluate the responsivity of the structure we have used a common perturbation theory for electron-photon interaction in a long wave limit because we assumed the wave length (about 50-250 μ) to be much greater then all geometrical parameters of the structure. Practically gate electrodes are semitransparent for wave length

50-250 μ. As usual the constrictive potential caused by split-gate is supposed to be parabolic [1]

$$U(x,y) = \frac{m}{2}\Omega^2(x)(y_c(x)-y)^2, \qquad (1)$$

where x-axis is directed along the channel, y-axis lies in a plane of the structure, y_c is a channel center coordinate. In the wide part of the channel $\Omega(x) = \omega_0 = \text{const}$, so the subband energy spectrum has oscillatory equidistant form. X-dependence of Ω and y_c describes respectively narrowing and bending of the channel.

The probability of a transition from a state (n,k) with a subband number n and a wave number k in x-direction to a state (n',k') was calculated. It differs from zero only for transitions to adjacent subband with conservation of a wave number k and only for y-polarization of incident light.

Provided there is an asymmetric narrowing in the channel an excited electron can transform into another subband electron, pass the channel and contribute to a photocurrent. To evaluate the transformation efficiency $T_{nn'}$ from n-th to n'-th subband we have used a weak bent channel model which assumed that $(kR)^{-1} \gg 1$ where $\hbar k$ is a longitudinal momentum and R is a radius of channel bending. For the 2nd to 1st subband transformation efficiency T_{21} a simple estimation is valid when the electron energy $\frac{\hbar^2k^2}{2m}$ is not too small compared with subband separation $\hbar\omega$:

$$T_{21} \sim \frac{h}{\omega R^2} \qquad (2)$$

When the narrow split (Fig.1) is more than twice or so less than the wide split the bending radius R is about half average split width. The transformation efficiency according to (2) attains a value about 0.1 for $\hbar\omega \approx 5$ meV and split width 0.1 μ. Really for this conditions the transformation efficiency can be

much greater (about unity as in [2]).

For the low temperature limit responsivity R_λ was obtained

$$R_\lambda = \frac{4\pi L e^3}{h^2 S c \omega_0 n_0} v_f T_{av} \delta(\omega-\omega_0) \qquad (3)$$

where L is a channel length, S is a structure area, v_f is the Fermi velocity, T_{av} - averaged transfer coefficient. For real channels a broadening $\Delta\omega$ should be taken into account. So the δ-function in (3) should be replaced by the Lorentz function

$$f_L(\omega-\omega_0) = \frac{1}{\pi} \frac{\Delta\omega}{\Delta\omega^2 + (\omega-\omega_0)^2} \qquad (4)$$

A finite channel length L leads to a broadening $\frac{\Delta\omega}{2\pi}$ about a reciprocal transit time $\tau = \frac{L}{v_f}$. In this way a simple expression for the peak sensitivity of the detector was obtained

$$R_\lambda = \frac{2}{\pi n_0} \frac{e}{\hbar\omega_0} \frac{e^2}{hc} \frac{L^2}{S} T_{av} . \qquad (5)$$

Supposing $S = L^2$, $\hbar\omega_0 = 5$ meV and T_{av} about unity this expression gives R_λ about 0.2 A/W which is close to that achieved previously [3]. However the advantage of the proposed detector is a convenient tuning by a gate voltage. The response time is limited by a transit time τ. The sensitivity peak can be operated by a gate voltage. The detector is photovoltaic and rather fast.

References

1. F.Stern, S.E.Laux, D.J.Frank, *Surface Science*, 196, 101 (1988)
2. J.C.Wu, M.N.Wybourne, W.Yindeepol, A.Weisshaar, S.M.Goodnick, *Appl Phys. Lett* , 59, 102 (1991)
3. E.Dießel, G.Müller, D.Weiss, K.von Klitzing, K.Ploog, R.Losch, H.Nickel, W.Schlapp, *Appl Phys Lett* , 58, 2231 (1991)

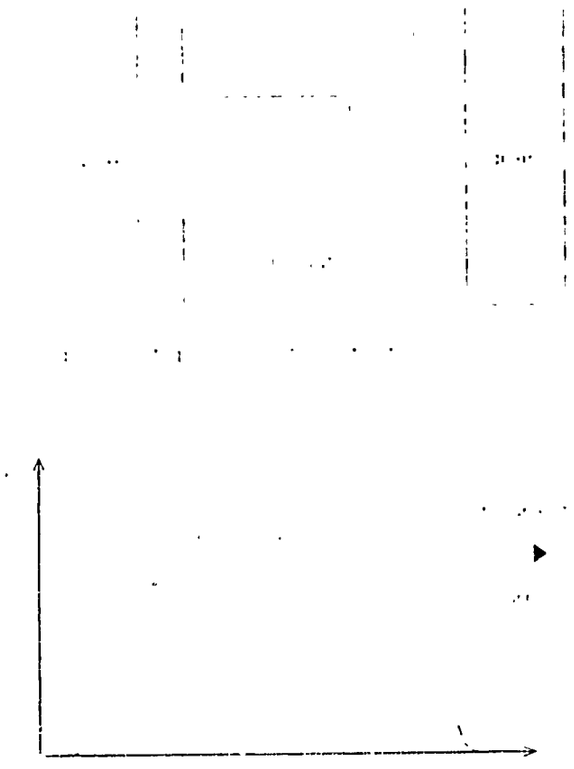

ThP26

Cyclotron FIR Emission from Hot Electrons in GaAs-GaAlAs Heterostructures

W. Zawadzki, C. Chaubet, D. Dur, W. Knap, and A. Raymond
Groupe d'Etudes des Semiconducteurs
Universite Montpellier II
34095 Montpellier, France

We study far infrared emission from GaAs-GaAlAs heterostructures, induced by electric pulses in the presence of a magnetic field and a hydrostatic pressure. Cyclotron masses are measured as functions of 2D electron density in the strong electron heating regime at pressures P=0 and P=7kbar and the detection energy of 4.43 meV. The results are described by an effective two-level $\vec{k} \cdot \vec{p}$ theory, which takes consistently into account the effect of band's nonparabolicity in GaAs on electric and magnetic quantisation. It is shown that the observed emission spectrum is due to eight transitions between Landau levels (populated up to the optic phonon energy), since under the strong heating conditions the 2D electron gas is nondegenerate. This is independently confirmed by magnetotransport measurements. Very good theoretical description of emission experiments at pressures P=0 and P=7 kbar is achieved with the use of bulk GaAs parameters. Theoretical estimations of the heating conditions in crossed magnetic and electric fields indicate that the electric field in our GaAs-GaAlAs structures is highly inhomogeneous.

ThP27

Resonant Magneto-Polarons in Strongly-Coupled Superlattices

F.M. Peeters*, J.M. Shi*, J.T. Devreese*, J.P. Cheng *, B. McCombe+ and W. Schaff‖

* Departement Natuurkunde, Universiteit Antwerpen (UIA), B-2610 Antwerpen, Belgium
+ Department of Physics and Astronomy, SUNY at Buffalo, , NY 14260, USA
+ Presently at: Francis Bitter National Magnet Laboratory, MIT, Cambridge, MA 02139
‖ Cornell University, Ithaca, NY 14853, USA

Abstract

Impurity bound magneto polarons are studied experimentally and theoretically in a strongly coupled GaAs/AlGaAs superlattice. The $1s \rightarrow 2p_0$ transition of well center donors is tuned through resonance with the GaAs optical phonon mode. An anti-level crossing behavior and three different peaks are clearly observed at the LO phonon energy. The theoretical analysis shows that the size of the magneto polaron effects: 1) are very close to those for the bulk system and 2) no direct evidence is found for non-bulk LO phonon interaction.

1 Introduction

High magneto field cyclotron resonance experiments are a sensitive probe to investigate: 1) the coupling strength between electrons and optical phonon modes and 2) the frequency of the relevant optical phonons which are involved in the coupling. We use such experiments to investigate the polaron coupling in confined structures and in particular in strongly-coupled superlattices.

Recently there has been considerable interest in polaron effects in confined structures. One of the key questions is *whether or not coupling of electrons to different phonon modes* like bulk phonons, confined phonons, interface phonons, etc... are observable. In previous work [1] on cyclotron resonance of free electrons in GaAs heterostructures no such coupling had to be introduced in order to explain the available experimental results. But in those experiments polaron effects were considerably weakened by many body effects like screening and the occupation effect [2]. In the case of low density impurity bound polarons no such complications are present and the system is effectively a one-particle problem.

In the present work, which is partly experimental and partly theoretical, thin-barrier superlattices are investigated. Such strongly coupled superlattices are different from the earlier quantum well systems in the sense that: 1) the electron wavefunction is more extended, 2) propagating phonon modes exist when the AlGaAs barriers are thinner than about 2 nm [3], 3) large interface effects may be present, and 4) zone folding of LO phonons should occur [4].

We have carried out a far infrared photoconductivity spectroscopical study of impurity bound magneto polarons in a $GaAs/Al_xGa_{1-x}As$ superlattice consisting of 80Å wide wells and 9Å wide barriers and Si donors planarly doped at the center of each well. The $1s \rightarrow 2p^+$ transition was tuned through the resonant interaction region with GaAs optical phonons by magnetic fields up to 24T. An anti-level crossing behavior has been clearly observed at the energy of the GaAs LO phonon. Different peaks are identified in the spectrum. This is the first study of a GaAs/AlGaAs system in which the lower branch can be traced into the reststrahlen band, in contrast to the case of isolated quantum wells (QW), where the transition vanishes at much lower energies.

A detailed theoretical analysis is made of the experimental results. Effects like 1) tunneling of the bound electron into the adjacent wells, 2) band non parabolicity, and 3) the coupling of the electron with bulk LO phonon modes are included in the calculation. Good agreement is obtained with the experimental results.

2 Experiment

The sample used was a $GaAs/Al_xGa_{1-x}As$ superlattice grown by molecular beam epitaxy (MBE). It consists of 40 periods of 80Å GaAs wells separated by 9Å $Al_xGa_{1-x}As$ barriers. The wells were planar doped with Si donors at the center with a concentration of $10^{10} cm^{-2}$. The superlattice structure was sandwiched between two thick (~ 2000Å) $Al_xGa_{1-x}As$ cladding layers and the whole structure was grown on a GaAs buffer layer on top of a semi-insulating GaAs substrate and capped by a ~ 100Å thick GaAs layer.

A capacitively coupled photoconductivity technique was used to enhance the signal to noise ratio and to reduce the dielectric effects near the reststrahlen band region in comparison to normal transmission measurements[5]. In this technique two semi-transparent chromium electrodes separated by a small gap were evaporated on the top surface of the sample. A low frequency (~ 100Hz) ac voltage was applied to the two electrodes coupled capacitively to the resistively conducting superlattice planes and the ac current through the sample was detected with a current sensitive preamplifier / lock-in amplifier. Far infrared magneto-optical spectra were obtained in a 9T superconducting magnet (Buffalo) or a 23T Bitter magnet (Francis Bitter National Magnet Laboratory) using Fourier transform spectrometers. All data presented in this paper were taken at liquid helium temperatures in the Faraday geometry (magnetic field parallel to the propagation direction of FIR light and normal to the sample surface).

Results. Photothermal ionization spectra of the impurity $1s \rightarrow 2p_+$ transition are shown in Fig. 1 near the resonant polaron region for several magnetic fields. At low magnetic fields the $1s \rightarrow 2p_+$ transition is a sharp and symmetric line and it moves to higher energies with increasing magnetic field. At about 15T a new line appears around the GaAs LO phonon energy ($\hbar\omega_{LO} = 296 cm^{-1}$ at low temperatures) which is the upper branch of the resonant process. It increases in relative intensity and moves to higher energies as the field increases. Meanwhile the lower branch loses intensity and nearly disappears as it approaches the GaAs LO phonon ($\hbar\omega_{LO} = 296 cm^{-1}$ e.g. see the 19T spectrum). At slightly higher fields it reappears inside the reststrahlen band and finally vanishes at the highest magnetic fields. In the highest field region an additional transition at about $430 - 450 cm^{-1}$ growing in intensity with increasing magnetic field is clearly observable. This line is attributed to the mixing of the $2p_+$ state with the virtual $(2p_+ + \text{one LO phonon})$ state through the electron-LO phonon interaction.

In Fig. 2 we display the magnetic field dependence of the impurity transition energy (dots), and compare the results with the theoretical calculations (curves). In the non-resonant field region (low fields), the $1s \rightarrow 2p_+$ transition for this sample shows a slightly smaller slope (hence larger CR mass) as a function of magnetic field as compared to bulk GaAs[5] or MQW structures [6] due to the finite probability of the electrons being inside the barrier [7]. In the resonant magnetic field region the lower branch shows a clear sublinear behavior as it approaches the resonance condition, $E(2p_+) - E(1s) = \hbar\omega_{LO}$, and it can be traced into the reststrahlen band, in contrast to the case of isolated QWs [6], where the transition vanishes at much lower energies. Typical anti-level crossing behavior has been observed in this field region with three branches separated by two resonant interaction gaps involving the $2p_+$ state interacting with the $(1s + \text{one-phonon})$ state (the so-called two-level resonance) and the $(2p_+ + \text{one phonon})$ state (three-level resonance), respectively.

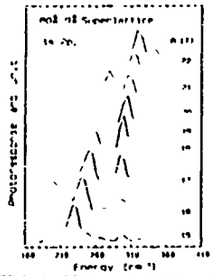

FIG. 1. Photoconductivity spectra at several magnetic fields.

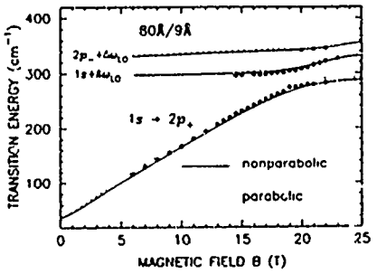

FIG. 2. Transition energy as function of magnetic field. The solid dots are experimental data and the curves are the results from a variational calculation of magneto polaron effects on shallow impurities with (solid curves) and without (dotted curves) inclusion of band nonparabolicity.

3 Theory

In the present system of a strongly coupled superlattice it is no longer possible to approximate the system by a *single* quantum well [8]. In previous work we found that even for relative thick barriers (e.g. a 100/100Å superlattice) the corrections due to the tunneling of the electron to the adjacent wells leads to observable corrections in the transition energies. The first step in our calculation is to find the energies of the lowest lying electron states of a shallow donor at the center of the quantum well of a strongly interacting superlattice placed in a magnetic field directed perpendicular to the interface. This system is described by the Hamiltonian

$$H = \frac{p_z^2}{2m^*} + \frac{1}{2m^*}(p_x + \frac{eB}{c}y)^2 + \frac{1}{2}m^*\omega_c^2 y^2 - \frac{e^2}{\sqrt{\rho^2 + z^2}} + V(z) \qquad (1)$$

where we exploited the cylindrical symmetry of the problem by using the polar coordinates (ρ, ϕ, z), with the z direction chosen along the magnetic field. We use the following units: 1) the effective Bohr radius $a_0^* = \hbar^2\varepsilon_0/m^*e^2 = 100.7$ Å for the length with $\varepsilon_0 = 12.75$ the static dielectric constant and $m_e/m^* = 0.067$ the electron band mass of GaAs, $-e$ the electron charge and m_e the electron mass in vacuum, 2) the effective Rydberg $R^* = e^2/2\varepsilon_0 a_0^* = 15.2\,\mathrm{meV} = 123\,\mathrm{cm}^{-1}$ for the energy, and 3) $\gamma = \hbar eB/2m_e cR^* = 0.1534B$ (B in T) is a dimensionless measure for the strength of the magnetic field. $L_z = -i\partial/\partial\phi$ is the z component of the angular momentum operator in units of $\hbar$, which is still a good quantum number in the present system. The superlattice potential is modelled by a series of square well potentials of height V_0 with barrier width b and well width a. The barriers are made out of the material $Al_xGa_{1-x}As$ which has $V_0 = 0.691x + 0.322x^2$ (in eV) and $m_e = m_e = 0.067 + 0.083x$.

The Schroedinger equation corresponding to the Hamiltonian (1) cannot be solved exactly and therefore we relied on a variational calculation of the donor states with the trial wave functions given by

$$\psi_{nm}(\rho, \phi, z) = f_n(z)\,\rho^{|m|}\exp(-\zeta\rho^2 - \eta\rho)\,e^{im\phi} \qquad (2)$$

where $f_n(z)$ is the lowest energy solution in the absence of the magnetic field and the Coulomb potential. ζ, η are two variational parameters which are chosen in such a way that they minimize the unperturbed energy of the n state of the donor. $E_{nm} = \langle H_0 \rangle_{nm} = \langle \psi_{nm} | H_0 | \psi_{nm} \rangle$.

The results of such a calculation are given in Table I for the binding energy (in units of R^*) of the $1s$ and $2p$ states and the $1s \rightarrow 2p$ transition energy at $B = 0$T. We compare the results of 1) the present system under study (80/90 Å) of a strongly coupled superlattice, 2) a weakly coupled superlattice (100/100 Å), 3) a broad multi quantum well structure (450/125 Å), and 3) the bulk system. Notice that the results of the present system are very close to those of the bulk, while the two other cases have an appreciable larger coulomb energy which is a result of the strongly confinement of the donor states to quasi two dimensions.

TABLE I. Binding energy of a shallow donor for a parabolic band at $B = 0$ and in the absence of electron phonon interaction.

state	80Å/90Å	100Å/100Å	450Å/125Å	3D
$1s$	1.0521	1.2177	1.2512	1.0000
$2p$	0.2551	0.3596	0.3257	0.2500
$1s \rightarrow 2p$	0.7970	1.3581	0.9656	0.7500

Since GaAs is a weakly polar material, the polaron correction to the energy of the n state of the donor can be calculated within second order perturbation theory

$$\Delta E_n = -\sum_{\vec{q}}\sum_{n'} \frac{|\langle n', \vec{q}|H_{FC}|n, 0\rangle|^2}{\hbar\omega_{LO} + E_n - E_{n'}} \Delta \qquad (3)$$

where $H_{FC}(r)$ is the Fröhlich electron LO phonon interaction Hamiltonian given by

$$H_{FC}(r) = \sum_{\vec{q}} \left(\frac{4\pi\alpha}{\Omega}\right)^{1/2} \frac{\hbar\omega_{LO}}{q} e^{i\vec{q}\cdot\vec{r}} (b_{\vec{q}} + b_{-\vec{q}}^\dagger) \qquad (4)$$

where $b_{\vec{q}}^\dagger$ ($b_{\vec{q}}$) is the creation (annihilation) operator of a LO phonon with wave vector $\vec{q}$ and frequency ω_{LO}, Ω is the volume of the system, $\alpha = 0.068$ the dimensionless electron phonon coupling constant. In the calculation only the 10 LO phonon modes of GaAs are included, $\hbar\omega_{\vec{q}} = \hbar\omega_{LO} = 296.1\,\mathrm{cm}^{-1} = 36.75\,\mathrm{meV}$. In Eq (3) $\Delta_n = 0$ for the non resonant states and $\Delta_{2p_\pm} = \Delta E_{2p_\pm} - \Delta E_{1s}$ for the $2p_\pm$ state. Away from the magneto polaron resonant region the sum over the donor states in Eq (3) converges very slowly and the incorporation of only the lowest few states is insufficient. Therefore we relied on a different method, which is described in detail in [2], in which *all* intermediate donor states are included in an approximate way. One outcome of such a calculation, is that it is possible to proof that in the case of $m_e = m_e$ the polaron correction satisfies $\Delta E_n/\hbar\omega_{LO} < -\alpha$.

The results of such a calculation are given in Fig. 3a where we depict the polaron correction to the $1s$ and the $2p_+$ states for the present system (solid curves) and compare them with the results for the 3D system. Notice that the polaron correction to the $1s$ state is slightly larger for the stronger coupled superlattice while the one for the $2p_+$ state is almost the same as for the bulk case. The resulting polaron correction to the transition energy is given in Fig. 3b. Notice that for small magnetic fields ($B < 10 - 15$T) the polaron correction is very small and shortly positive i.e. it increases the transition energy. Near the resonance region $\omega_c = E_{2p_+} - E_{1s} \approx \hbar\omega_{LO}$, the amplitude of the polaron correction decreases appreciably the transition energy. Notice that for the strongly coupled superlattice the result for the polaron correction to the transition energy is very close to the one for the bulk case. Only for the weakly coupled superlattice (100/100Å) we find that the polaron correction is appreciably different from the 3D situation.

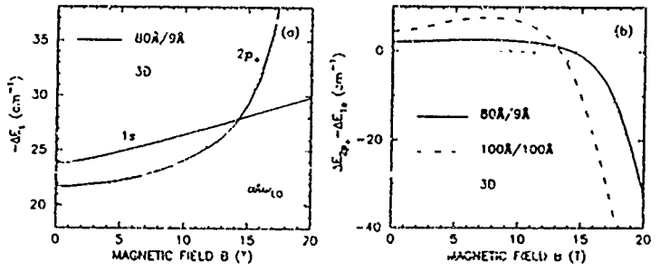

FIG. 3. Polaron correction (a) to the $1s$ and $2p_+$ states and (b) to the transition energy $1s \rightarrow 2p_+$ for different systems.

Before we are able to compare our theoretical results with experiment we must include another correction: band nonparabolicity. We use the standard Kane model, which was successfully applied to describe second nonparabolicity in GaAs: $E_n = (E_n/2)\{-1 + \sqrt{1 + (4E_n/E_g)}\}$, where E_n and E_n are the donor energies with and without the effect of band nonparabolicity respectively, $E_g = 1.52$meV is the energy gap of GaAs.

4 Comparison and conclusions

In Fig. 2 the present theoretical results for the $1s \rightarrow 2p_+$ transition (solid curves) are compared to the present experimental results (solid dots) for donors located at the center of the wells of a GaAs/$Al_b$$Ga_{0.7}$As superlattice with $w = 80$Å and $b = 9$Å . The dotted curves are the theoretical results where the effect of band nonparabolicity is excluded. Near resonance the polaron correction and the correction due to band nonparabolicity are largest. There the energy difference $E_{1s} - E_{2p_+}$ is relevant, which is appreciably large and this implies that the two different corrections to the energy of the 1s and to the $2p_+$ state are different and thus do not cancel.

The agreement between experiment and theory is very good. Nevertheless there are two small discrepancies: 1) below the LO phonon energy the experimental results are between the results with (solid curve) and without (dotted curve) band nonparabolicity. This may indicate that the effect of band nonparabolicity is slightly overestimated; 2) the gap at the anti-crossing point is theoretically slightly overestimated as compated to experiment. Nevertheless one should keep in mind that in this energy region one is in the reststrahlen band of GaAs and that radiation is strongly absorpted by the lattice.

Acknowlegments: The high magnetic field measurements were carried out at the Francis Bitter National Magnet Laboratory; we thank all staff, especially B. Brandt and L. Rubin for assistance. JPC and BDM thank the Office of Naval Research for support under grant No. N00014-89-J-1671. One of us (FMP) is supported by the Belgian National Science Foundation and part of the theoretical work is supported by "Diensten voor de Programmatie van het Wetenschapsbeleid" under contract No. IT/SC/24.

References

1. F.M. Peeters, X.G. Wu, J.T. Devreese, C.J.G.M. Langerak, J. Singleton, D.J. Barnes and R.J. Nicholas, Phys. Rev. **B43**, 4206 (1992).
2. J.M. Shi, F.M. Peeters and J.T. Devreese, Phys. Rev. **B48** (1993).
3. D.-S. Kim, N. Bouchalkha, J.M. Jacob, J.F. Zhou, J.J. Song, and J.F. Klem, Phys. Rev. Lett., **68**, 1002 (1992).
4. A.K. Sood, J. Menendez, and M. Cardona, Phys. Rev. Lett. **54**, 2115 (1985).
5. J.-P. Cheng, B.D. McCombe, and G. Brozak, Phys. Rev. **B43**, 9124 (1991), and Surf. Science **267**, 188 (1992).
6. J.-P. Cheng, B.D. McCombe, J.M. Shi, F.M. Peeters, and J.T. Devreese, Phys. Rev. **B48** (1993).
7. G. Brozak et al., Phys. Rev. Lett. **64**, 471 (1990); M.J. Yang et al., Phys. Rev. **B47**, 1691 (1993).
8. M. Helm, F.M. Peeters, F. DeRosa, E. Colas, J.P. Harbison, and L.T. Florez, Phys. Rev. **B43**, 13983 (1991), Surf. Sci. **236**, 518 (1992).

ThP28

Far infrared response of quantum dots: from few electron excitations to magnetoplasmons

D. Pfannkuche[1], Vidar Gudmundsson[2], P. Hawrylak[3], R.R. Gerhardts[1]

[1] *Max-Planck-Institut für Festkörperforschung, Heisenbergstr.1, 70506 Stuttgart 80, Germany.*
[2] *Science Institute, University of Iceland, Dunhaga 3, IS-107 Reykjavik, Iceland.*
[3] *Institute for Microstructural Sciences, National Research Council of Canada, Ottawa, K1A 0R6, Canada*

(July 1, 1993)

We study the far infrared (FIR) response of quantum dots with a variable number N_e of electrons and a non-parabolic confinement in a magnetic field B. For few electrons we compare the results of a Hartree (H) and a Hartree-Fock (HF) approach with those obtained by an exact diagonalization of the few-particle Hamiltonian. A good qualitative agreement is found between the HF approximation and the exact calculation. The resonance spectra are fingerprints of the ground state of the electron system and depend therefore strongly on N_e and B. With an increasing number of electrons, the H- and the HF-calculations show new features evolving in the FIR spectra. These features resemble the non-local mode coupling effects observed in the magnetoplasmon dispersion of two- and one-dimensional systems marking the transition to a quasi-classical hydrodynamic behaviour

I. INTRODUCTION

The experimental study of quantum dots is proceeding rapidly [1-5], often producing FIR spectra differing from the simple spectrum predicted by Kohn's theorem for harmonically confined electrons [6-9]. The simple spectrum for parabolically confined electrons can be obtained analytically due to the decoupling of the center of mass (CM) and relative motion (RM). In order to understand the more complex spectra it is therefore important to have reliable methods to calculate the properties of electrons in quantum dots where the CM and RM excitations couple and simple analytical calculations cannot be performed. Recently, for few electrons, an 'exact' numerical diagonalization [6,10-15] has been performed and for many electrons a H-approximation has been used [7,16,17]. A comparison between the results of an exact numerical diagonalization and those of a H- and a HF-approximation has established that exchange and correlation effects are of great importance for the *ground state properties* when the electrons are not spin polarized [18].

In the present work the *FIR spectra* obtained in the HF-approximation are compared to the spectra from the exact diagonalization and the H-approximation. In the light of the good qualitative agreement between the models, the HF- and H-approximation are used to investigate the evolution of the spectra with increasing number of electrons.

II. MODELS

N_e Electrons in a quantum dot are described by the Hamiltonian

$$H = \sum_{i=1}^{N_e} \left[\frac{1}{2m^*} \left(\vec{p}_i + \frac{e}{c} \vec{A}(\vec{r}_i) \right)^2 + V_{conf}(\vec{r}_i) + \frac{g^* \mu_B}{\hbar} \vec{B} \cdot \vec{S}_i \right] + \sum_{i<j}^{N_e} \frac{e^2}{\epsilon |\vec{r}_i - \vec{r}_j|}$$

$$= \sum_{i=1}^{N_e} \hat{H}(i) + \sum_{i<j}^{N_e} \frac{e^2}{\epsilon|\vec{r}_i - \vec{r}_j|} \tag{1}$$

The confining potential $V_{conf}(\vec{r})$ is composed of a harmonic part and an anharmonic one proportional to r^4, $V_{conf}(r) = \frac{1}{2}m^*\Omega_0^2 r^2 + br^4$, and we assume the electrons to be strictly confined to the plane perpendicular to the magnetic field B. The Coulomb interaction between the electrons is modified by the dielectric constant ϵ of the bulk material, m^* and g^* denote the bulk effective mass and g-factor, respectively. The vector potential $\vec{A}$ is chosen in the symmetric gauge, $\vec{A} = \frac{1}{2}\vec{B} \times \vec{r}$. According to the rotational symmetry the eigenfunctions $|\Theta\rangle$ of the system

$$\mathcal{H}|\Theta\rangle = \epsilon_\Theta|\Theta\rangle, \tag{2}$$

can be classified by the total angular momentum $\mathcal{L} = \hbar\mathcal{M} = \hbar\sum_i m_i$, the total spin $\mathcal{S}$, the spin component parallel to the magnetic field, $\mathcal{S}_z$, and an energy quantum number which labels the eigenenergies ϵ_Θ for given $\mathcal{M}$, $\mathcal{S}$, and $\mathcal{S}_z$ in ascending order, i.e. the ground state for fixed $\mathcal{M}$, $\mathcal{S}$, and $\mathcal{S}_z$ is labeled by $|\Theta\rangle = |\mathcal{M}, \mathcal{S}, \mathcal{S}_z; 0\rangle$.

FIR radiation incident on a quantum dot (in the regime where linear response holds) induces transitions between the ground state and excited states, if the FIR frequency corresponds to the energy difference between those states. The oscillator strength f_Θ given by

$$f_\Theta = \frac{2m^*}{\hbar}(\epsilon_\Theta - \epsilon_0)\left|\langle\Theta|\mathcal{H}^{ext}/\mathcal{E}^{ext}|0\rangle\right|^2, \tag{3}$$

is a measure for the likelyhood of this transition. (In this equation $|0\rangle$ denotes the ground state and $\mathcal{H}^{ext}$ is the interaction Hamiltonian of the FIR field $\vec{\mathcal{E}}^{ext}$ with the electron system.)

For two and three electrons we calculated the few-particle energy spectra and wave functions by diagonalising the Hamiltonian matrix numerically [13,18,19]. Due to the small size of the quantum dots (< 200nm) the FIR radiation field is spatially constant throughout a single dot. Therefore, it only couples to the center-of-mass (CM) motion of the electrons,

$$\mathcal{H}^{ext} = \sum_{i=1}^{N_e} e\vec{\mathcal{E}}^{ext} \cdot \vec{r}_i e^{i\omega t} = eN_e\vec{R} \cdot \vec{\mathcal{E}}^{ext} e^{i\omega t}, \tag{4}$$

where $\vec{R}$ is the CM coordinate.

Out of the rich spectrum only those transitions are excited which occur between states with non-vanishing overlap of the internal (relative) wave functions. In a strictly parabolic quantum dot (where the wave functions factorize into the CM part and the relative wavefunction [10,20,21]) only two transitions are allowed. The corresponding resonance frequencies are given by $\omega_\pm = |\sqrt{4\Omega_0^2 + \omega_c^2} \pm \omega_c|/2$, regardless of the number of electrons in the dot and their mutual interaction (Kohn's theorem). ω_c is the cyclotron resonance frequency. However, even a small anharmonicity allows the coupling to the internal degrees of freedom and additional resonances can be observed [23].

In the HF-approximation the interacting many-body problem is reduced to a problem of non-interacting particles subjected to an effective external potential. The HF-single particle states $|\alpha\rangle$ together with their eigenenergies ϵ_α are found by iterating the HF-equations [18] in the basis of the non-interacting states $|u\rangle$ (the eigenstates of H in (1)). The total energy of the system E can then be found by summing up the single electron contributions and carefully counting the interaction energy of each electron pair only once [18].

The FIR-absorption of the system is calculated as a self-consistent linear response to an external potential ϕ^{ext}. In this so-called time-dependent HF-approximation the change of the density matrix due to an adiabatically switched total electrostatic potential ϕ^{ext} is calculated within a linear approximation. The total potential consists of the external potential and the induced potential $\phi^{ind} = \phi^H + \phi^F$ due to the direct and the exchange interaction of the electrons. The induced potential in turn depends on the density matrix, thus closing the circle and allowing for a self-consistent evaluation of the total potential together with an expression for the frequency dependent dielectric tensor $\epsilon_{\alpha\beta,\delta\gamma}(\omega)$. The power absorption is then calculated from the Joule heating of the system due to ϕ^{ext}

$$P(\omega) = e\mathcal{E}^{ext}\sum_{\alpha\beta}\frac{(E_\beta - E_\alpha)}{\hbar}\langle\beta|r|\alpha\rangle 2\pi\delta_{M_\beta, M_\alpha \pm N_p}\mathrm{Im}\left\{f^{\alpha\beta}(\omega)\langle\alpha|(-e\phi^{ext})|\beta\rangle\right\}, \tag{5}$$

where $\mathcal{E}^{ext}$ is the strength of the external field and

$$f^{\alpha\beta}(\omega) = \frac{1}{\hbar}\left\{\frac{f_\alpha^0 - f_\beta^0}{\omega + (\omega_\alpha - \omega_\beta) + i\eta}\right\} \tag{6}$$

with the fermi distribution f^0. $N_p = \pm 1$ corresponds to left or right circular polarization of ϕ^{ext}. The HF-calculations are done for the temperature $T = 1.0$ K, but since the ratio of the thermal and the confinement energy is very small the results can be compared with the exact calculations for $T = 0$ K.

III. FIR RESPONSE OF FEW ELECTRONS

For quantum dots with two and three electrons we calculated the FIR response within the diagonalization approach as well as in the HF approximation. The results for quantum dot helium are shown in Fig. 1. Lines mark the Hartree and HF results, and symbols mark those obtained by the 'exact' method. Within the shown magnetic field range, the ground state changes from the spin-singlet state $|0,0,0;0\rangle$ for low magnetic fields (B <2.6T) to the spin-triplet state $|-1,1,1;0\rangle$ for higher magnetic fields. The figure shows the FIR resonances from both initial states within the whole magnetic field range. The upper resonance in the spin-triplet state is split due to the non-parabolicity [13]. The HF approximation reproduces this line splitting as well as the resonance position to a very high accuracy. This is in accordance with the good agreement between the HF and the exact ground state in the spin-triplet state for two electrons [18]. More remarkable is the coincidence of the results for the spin-singlet state. Here the HF ground state deviates strongly from the exact one [18] due to correlations which are important in this state. Nevertheless, the FIR resonances agree very well in both approaches. The two models predict different values for the magnetic field where the spin-singlet spin-triplet transition occurs. Accordingly, the HF approximation predicts the splitting of the upper resonance for $B > 0.6$T instead of $B > 2.6$T.

The resonances calculated in the *Hartree* approximation do not show the line splitting of the upper mode. Moreover, they are blueshifted with respect to the spin-singlet resonance. A similar blueshift appears for the lower spin-triplet mode with respect to the spin-singlet resonance. This is a consequence of the larger spatial extent of the spin-triplet states which leads to a stronger influence of the r^4-potential. Accounting for this blueshift by an effective confining frequency Ω_0 which depends on the strength of the confining frequency as well as the actual ground state

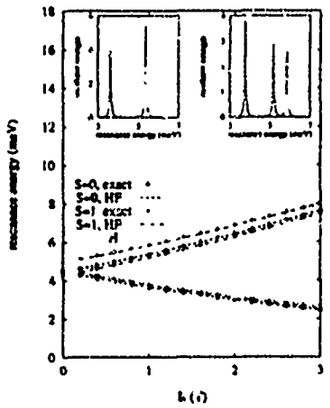

FIG. 1. FIR resonances as function of the magnetic field for a dot occupied by two electrons. Resonances are shown for the spin-singlet state $|0,0,0;0\rangle$ (which is the ground state for $0T < B < 2.6T$) and the spin-triplet state $|-1,1,1;0\rangle$. Symbols and solid lines mark results of the diagonalization approach, HF results are shown as dashed ($S = 0$) and dash-dotted ($S = 1$) lines, and dotted lines refer to Hartree results. Left inset: oscillator strength of the spin-singlet transitions. The exact and HF results are nearly indistinguishable. Right inset: oscillator strength of spin-triplet transitions. Parameters: $\hbar\Omega_0 = 3.3$meV, $\delta = 2.5 \times 10^{-10}$meV/Å^4, GaAs bulk parameters: $m^* = 0.067m_0$, $\epsilon = 12.4$, $g^* = -0.44$.

wave function, the resonances can even in the presence of the anharmonicity be well described by $2\omega_{\pm\sigma} = \sqrt{4\Omega_c^2 + \omega_c^2} \pm \omega_c$, i.e. Ω_c replaces the bare confining frequency Ω_0.

The resonance patterns for three electrons (Fig. 2 and Fig. 3) show even more clearly that the FIR excitation spectra for few electrons are fingerprints of the actual ground state of the quantum dot. The resonances of the spin-doublet ground state $|-1,\frac{1}{2},\frac{1}{2};0\rangle$ (Fig. 2) resemble those of the 2-electron triplet state $|-1,1,1;0\rangle$. The HF approximation yields a single lower mode and two upper modes with nearly the same oscillator strength. As for two electrons, the ω_+-resonance splits due to the coupling of the CM excitation to a RM excitation which in the harmonic potential has the same energy. This line splitting which is due to an internal symmetry of the system is equally well described in the HF and the 'exact' treatment. The exact approach shows a weak additional resonance below these modes, which also appears in the H-approximation. This additional mode is due to ground state contributions (linear combinations of Slater determinants) which are not allowed in the HF-ansatz. They witness the existence of ground state correlations which are strong

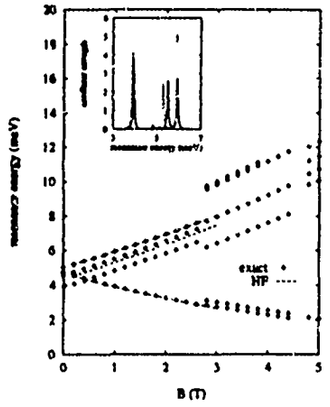

FIG. 2. FIR resonances as function of the magnetic field for a dot occupied by three electrons. Resonances are shown for spin-doublet transitions from $|-1,\frac{1}{2},\frac{1}{2};0\rangle$ ($B < 2.6$T) and $|-2,\frac{1}{2},\frac{1}{2};0\rangle$. Inset: corresponding oscillator strengths in exact (solid line), HF (dashed), and H approach (dotted). Parameters as in Fig. 1.

in the non-spin polarized states.

At $B = 2.6$T the ground state changes to the spin-doublet $|-2,\frac{1}{2},\frac{1}{2};0\rangle$ which cannot be found in the HF approximation. Here, a small splitting of the lower mode appears, while the upper one is single. The upper resonance shows very weak satellites. These additional resonances occur due to the mixing of CM and relative wave functions in the r^4-potential. It becomes the more important the more the electrons test the steeper (than harmonic) confining potential in states with higher angular momentum.

For even higher magnetic fields ($B > 3.6$T) the 3-particle ground state is the spin-quartet state $|-3,\frac{3}{2},\frac{3}{2};0\rangle$ (Fig. 3). It clearly shows two upper resonances which in the HF approximation have similar oscillator strengths. The origin of these two modes is not a line splitting, but the strong mixing of different CM and internal wave functions in the ground state. These distinct contributions are differently affected by the r^4-potential giving rise to distinct frequencies Ω_c. Due to correlation effects the different contributions to the ground (and excited states) have different weight in the diagonalization and HF results. This is most obvious from the differences in the oscillator strengths of the corresponding resonances which are much more sensitive to the actual wavefunctions involved than the resonance positions

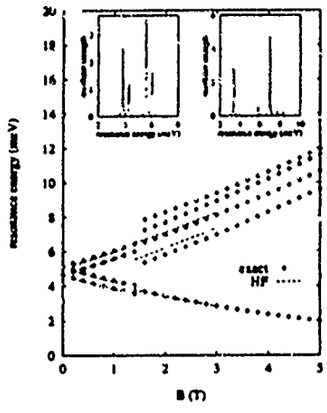

FIG. 3. FIR resonances as function of the magnetic field for a dot occupied by *three* electrons. Resonances are shown for spin-quartet transitions from $|0,\frac{3}{2},\frac{3}{2};0\rangle$ ($B < 1.6$T) and $|-3,\frac{3}{2},\frac{3}{2};0\rangle$. Left inset: oscillator strength at $B = 1$T ($\mathcal{M} = 0$), right inset: oscillator strength at $B = 2$T ($\mathcal{M} = -3$).

IV. FIR RESPONSE OF MANY ELECTRONS

In 2D electron systems, quantum wires [22], and dots [23] a splitting of the plasmon dispersion curve (or the upper excitation branch, $\omega_+(B)$ in quantum dots) has often been observed when the frequency $\omega_+(B) \propto \omega_c$ (the $2\omega_c$-splitting). In contrast to the anticrossing caused by deviations from circular symmetry [13], this line splitting is independent of the form of the dots. Instead it shows a strong dependence on the number of electrons in the system, becoming clearer the more electrons occupy the dot. It has not been observed in small dots with few electrons ($N_e \sim 1 - 10$). Theoretically, the coupling to the second harmonic of the cyclotron frequency has been predicted for a 2DEG when the interaction between the electrons and the electromagnetic field is considered to a higher order than in the dipole approximation, thus being called a non-local correction [24]. The $2\omega_c$-splitting has also been found in a Hartree-calculation (H-calculation) for many electrons in a quantum dot [17], where the confinement of the 2DEG causes modes with different wave vectors to be mixed and the deviation from the parabolic confinement makes these mode crossings visible.

Since this mode coupling appears only for a high number of electrons and in larger systems, it can best be described in terms of magnetoplasmons rather than by excitations of a specific quantum dot atom. Therefore, this spectral feature is expected to be adequately treated by a mean field theory such as the H and the HF approximation, especially since even for few-particle systems the time-dependent HF-method qualitatively well reproduces the main FIR resonances. Accordingly, the H and HF calculations show no $2\omega_c$-splitting (for the used confinement of $\Omega_0 = 3.37$ meV) for less than ten electrons, but the first sign of it develops for $N_e = 10$ and the splitting is almost complete for $N_e = 16$ as is seen in Fig. 4. This is accompanied by the density of electrons $n_e(r)$

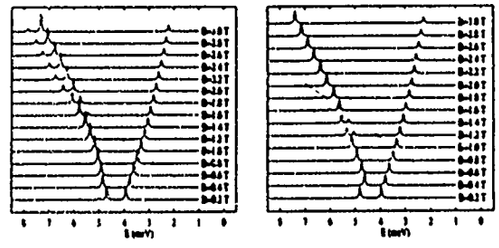

FIG. 4. The absorption $P(\hbar\omega)$ as a function of the magnetic field B in the H-approximation with $N_e = 16$ (left figure), and in the HF-approximation with $N_e = 20$ (right figure). The dashed lines represent the energy $2\hbar\omega_c$. $\hbar\Omega_0 = 3.37$ meV, $b = 30 \times 10^{-12}$ meV/Å^4, $m^* = 0.067 m_0$ $\epsilon = 12.4$, $g^* = -0.44$, $\eta = 0.01\hbar\Omega_0$, and $T = 1.0$ K

becoming homogeneous within a region larger than the effective magnetic length [18] λ inside the dot. We, therefore, believe the splitting to indicate a transition from a 0DEG to a confined 2DEG. In contrast to the infinite 2DEG, where the mode coupling to the second harmonic of the cyclotron resonance is due to deviations from a constant external electric field, in the confined 2DEG it is caused by the anharmonicity of the confining potential. For few electrons a region with homogeneous density can never develop as the dot diameter is of the order of λ, thus inhibiting the pronounced occurrance of the $3\omega_c$-splitting. Nevertheless, we found a precursor of this feature in a wide dot with a strongly anharmonic confinement occupied by three electrons only.

An analysis of the participating single electron transitions for the two peaks occurring for $N_e = 16$ at $B = 1.8$T shows that the lower one represents the normal stiff oscillations of the mass center predicted by Kohn's theorem, while the upper peak includes only transitions of electrons in states with high values of M. This reflects the characteristics of a radial mode which affects only the relative coordinates of the electrons (breathing mode). The mutual Coulomb interaction of the electrons is essential for the occurrance of the $2\omega_c$ splitting. Without the interaction the r^4-anharmonicity causes the $\omega_R(B)$ branches to be split into many parallel lying modes without any crossings. Changes in the ground state can be observed when $\omega = 2\omega_c$ as well as for other values of the magnetic field. These changes manifest themselves as a change in the number of parallel resonance lines.

A careful evaluation of the H-approximation for different strengths of the anharmonic part

of the confinement shows that the occurrance of the splitting can deviate slightly from the field where $\omega_+(B) = 2\omega_c$, just as has been observed in experiments. The 2ω splitting is independent of the exact form of the deviation from the parabolic confinement, it occurs for r^4 as well as for r^6 deviations over a wide range of strength of the anharmonicity.

The HF-calculation also shows this $2\omega_c$ splitting when N_e increases, however, since $u_s(r)$ does never develop a totally flat region, but maintains small modulations, the splitting is never as clear as in the II approximation (see Fig. 4).

V. SUMMARY

Anharmonicities in the confinement potential introduce features in the FIR resonance spectra of quantum dots which cannot be explained by pure excitations of the CM of the electron system, i.e. deviations from Kohn's theorem arise. While the magnetodispersion $\omega(B)$ of the modes can still be described by a formula of the type $\omega(B) = (\sqrt{4\Omega_o^2 + \omega_c^2} \pm \omega_c)/2$, the effective confining frequency Ω_o is no longer given by the bare confining frequency, but strongly depends on the number of particles, the Coulomb interaction, and the strength of the anharmonicity. Moreover, beside the pure CM excitations, which are the only ones to occur in parabolically confined quantum dots, additional modes appear due to a mode coupling between the CM excitations and those of the internal (relative) degrees of freedom.

The few particle spectra not only differ for dots occupied by different numbers of electrons, but are also fingerprints of the actual ground state which changes with increasing magnetic field. We compared the few particle resonances obtained by diagonalizing the Hamiltonian matrix and by a time-dependent HF approach. Even though the ground states calculated by both methods differ considerably, the FIR resonance positions agree very well. Differences, of course, appear in the results for the oscillator strength of the resonances, since this quantity is much more sensitive to the features of the initial and final wave functions.

For quantum dots with many particles (more than 10) the fine structure of the resonance spectra, reflecting transitions which are unique for the actual quantum dot atom, vanishes. Simultaneously, the anticrossing of the upper CM resonance, ω_+, with another non-dipole active mode appears, when $\omega_+ = 2\omega_c$. The crossing mode is an excitation of the internal degrees of freedom only (breathing mode). Its occurrence is coupled to the existence of a mesoscopic region with homogeneous particle density inside the dot. Since the mode coupling does not occur for a non interacting electron system, we consider this mode to be the dot-analogue of the non local resonance in pure two-dimensional systems.

ACKNOWLEDGMENTS

We would like to thank D. Heitmann, P. Grambow, E. Vasiliadou, and B. Meurer for fruitful discussions about experimentally observed FIR spectra on various quantum dots. Two of us (D.P. and V.G.) very much appreciate the intense and instructive discussions with A.H. MacDonald about the origin of the $2\omega_c$-mode.

This research was supported in part by the Icelandic Natural Science Foundation and the Bundesminister für Forschung und Technologie under contract number ITK0375/2 as well as a NATO Collaborative Research Grant CRG921201.

[1] C. Sikorski and U. Merkt, Phys. Rev. Lett. **62**, 2164 (1989).
[2] T. Demel, D. Heitmann, P. Grambow, and K. Ploog, Phys. Rev. Lett. **64**, 788 (1990).
[3] A. Lorke, J. Kotthaus, and K. Ploog, Phys. Rev. Lett. **64**, 2559 (1990).
[4] B. Meurer, D. Heitmann, and K. Ploog, Phys. Rev. Lett. **68**, 1371 (1992).
[5] J. Alsmeier, E. Batke, and J. Kotthaus, Phys. Rev. B **41**, 1699 (1990).
[6] P. Maksym and T. Chakraborty, Phys. Rev. Lett. **65**, 108 (1990).
[7] D. Broido, K. Kempa, and P. Bakshi, Phys. Rev. B **42**, 11404 (1990).
[8] L. Brey, N. Johnson, and B. Halperin, Phys. Rev. B **40**, 10647 (1989).
[9] W. Kohn, Phys. Rev. **123**, 1242 (1961).
[10] U. Merkt, J. Huser, and M. Wagner, Phys. Rev. B **43**, 7320 (1991).
[11] Q. Li *et al.*, Phys. Rev. B **43**, 5151 (1991).
[12] T. Chakraborty, V. Halonen, and P. Pietiläinen, Phys. Rev. B **43**, 14289 (1991).
[13] D. Pfannkuche and R. Gerhardts, Phys. Rev. B **44**, 13132 (1991).
[14] M. Wagner, U. Merkt, and A. Chaplik, Phys. Rev. B **45**, 1951 (1992).
[15] P. Maksym and T. Chakraborty, Phys. Rev. B **45**, 1947 (1992).
[16] A. Kumar, S. Laux, and F. Stern, Phys. Rev. B **42**, 5166 (1990).
[17] V. Gudmundsson and R. Gerhardts, Phys. Rev. B **43**, 12098 (1991).
[18] D. Pfannkuche, V. Gudmundsson, and P. Maksym, Phys. Rev. B **47**, 2244 (1993).
[19] P. Hawrylak and D. Pfannkuche, Phys. Rev. Lett. **70**, 485 (1993).
[20] P. Bakshi, D. Broido, and K. Kempa, Phys. Rev. B **42**, 7416 (1990).
[21] N. Johnson and M. Payne, Phys. Rev. Lett. **67**, 1157 (1991).
[22] H. Drexler *et al.*, Phys. Rev., to be published (1993).
[23] B. Meurer, Ph.D. thesis, Universität Stuttgart, 1992.
[24] N. Horing and M. Yildis, Annals of Physics **97**, 216 (1976).

ThP29

Cyclotron and intersubband resonance studies in [001] and piezoelectric [111] InAs/(Ga,In)Sb superlattices

M. Lakrimi, T.A. Vaughan, R.J. Nicholas, D.M. Symons, N.J. Mason, and P.J. Walker

Clarendon Laboratory, The Department of Physics, The University of Oxford, Parks Road, Oxford OX1 3PU, U.K.

Abstract

Cyclotron resonance and inter subband excitation experiments have been performed on superlattices of the semimetallic, strained type II system InAs/(Ga,In)Sb. We observe *simultaneously one cyclotron resonance from* the 2D electrons located in the InAs and two resonances from the 2D holes in the (Ga,In)Sb layers. The two hole resonances originate from the $M_J = |3/2>$ states. We have found a strong crystallographic anisotropy in the hole masses between structures grown along [001] and [111]A orientations attributed to the strain decoupling of the heavy and light hole levels in the $Ga_{1-x}In_xSb$ valence band. In addition, we demonstrate for the first time that intersubband resonances can be directly seen for the electrons at large tilt angles.

1. Introduction:

The InAs/GaSb combination is a type-II crossed gap system, characterised by a *semiconductor-semimetal* transition when the InAs layer thickness exceeds 45 Å [1] and a small lattice mismatch of ~0.6%. In the semimetallic regime, the system contains both two-dimensional electrons in the InAs and holes in the GaSb. Further interest has arisen from growth in directions *different* to the conventional <001>. Due to the lack of inversion symmetry and non-zero off-diagonal tensor strain components, [111] oriented zincblende structures contain a strain-induced piezoelectric field which modifies the optical and electronic properties [2]. This has led to the observation of novel phenomena [3], such as enhanced carrier densities and optical absorption.

Cyclotron resonance (CR) and resonant subband Landau level coupling (RSLC) have been extensively studied in single carrier type systems. CR has mainly been used for the determination of the effective mass and its dependence on energy with infra red light and magnetic field applied parallel to the growth direction. RSLC, however, is a convenient way of determining the electric subband energy separation [4] when resonant coupling between the cyclotron and subband motion is induced by tilting the sample with respect to the direction of the magnetic field.

Previous far infra-red studies on the InAs/GaSb system concentrated mainly on the cyclotron resonance (see Ref. [5] for a review). While recently Sundaram and co workers [5] observed both the electron and hole resonances, Maan *et al* [6] mostly observed electron and interband transitions between the electrons and hole subbands along with two CR transitions from two electron subbands. Tilted field experiments were initially performed by Maan and co-workers [7]. Recently, CR studies have been extended to pulsed magnetic fields [8], thus bridging the semimetallic-semiconducting regimes.

We report on cyclotron resonance experiments performed on nine 20 period InAs/(Ga,In)Sb superlattices grown along [001] and [111]A orientations. First, we compare the effective masses of the carriers and then tilt the samples at large angles with respect to the direction of the magnetic field to determine the energy separation between subbands.

2. Experimental details:

The superlattices are not intentionally doped and are simultaneously grown on [001], [111]A, and [111]B oriented GaAs substrates, put side by side, at atmospheric pressure in an MOVPE reactor [9]. The indium content was varied from 0 to 10%. Thick GaSb buffer layers (at least 2 μm) were used to accommodate the misfit dislocations originating from the large lattice mismatch (~ 7%) between GaAs and GaSb. The novelty of these structures, grown by MOVPE, lies in the high quality of the interfaces and the very high proportion of intrinsic carriers. Magnetotransport measurements have shown that all layers are electrically conducting. Some typical sample parameters can be found in table 1.

The measurements have been performed at 2 K and 130 mK in magnetic fields up to 16 Tesla using a Bruker 113 fast Fourier transform spectrometer.

3. Effective mass anisotropy:

We have measured a total of eighteen 20 period superlattices (nine per orientation). Typically, one electron and two hole resonances are observed. Some typical spectra can be found in *Ref [5]. All these resonances extrapolate to zero energy* at zero magnetic field. The electron mass is isotropic, as shown in figure 1a, and is larger than that of the InAs bulk band edge due to the conduction band non-parabolicity.

The relative strengths of the two hole resonances are found to be strongly carrier concentration dependent, and the mass values are also found to be strongly orientation dependent, as illustrated in figure 1b (plots of the resonance positions as a function of magnetic field are shown in figure 3). The electron and hole masses are summarised in table 1. Typically, [001] oriented structures show hole effective masses of 0.09 and 0.20m_0, compared to 0.08 and 0.20m_0 for [111]. Furthermore the hole masses are found to get lighter as the amount of indium is increased.

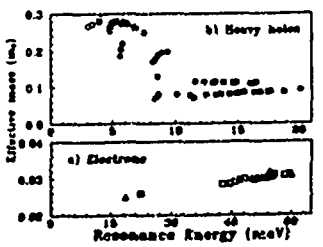

Fig. 1: Electron and hole effective mass for [001] (empty symbols) and [111]A (filled symbols) orientations for sample 1265 (similar growth parameters to 1266)

It is well known that in a strained system the $M_J = |3/2>$ heavy hole states in the valence band (of the $Ga_{1-x}In_xSb$) are decoupled from the $M_J = |1/2>$ light hole states (for $Ga_{0.9}In_{0.1}Sb$, the uniaxial strain is about 1%). For a well under compression, the holes occupy the $M_J = |3/2>$ states [10]. *k.p* theory predicts the in-plane heavy hole masses in a strained quantum well, in the limit where there is a strong decoupling between the light and heavy hole bands, to be given by $m_0(\gamma_1 + \gamma_2)^{-1}$ and $m_0(\gamma_1 + \gamma_3)^{-1}$ for [001] and [111] orientations, respectively [11]. Conversely, the bulk in-plane heavy hole masses are given by $m_0(\gamma_1 - 2\gamma_2)^{-1}$ and $m_0(\gamma_1 - 2\gamma_3)^{-1}$ for [001] and [111], respectively [11].

Sample	Period Å	In %	N_e	N_h	m_{e0} m_0	m_{hh1} m_0	m_{lh1} meV	E_F meV	E_0 meV	E_1 meV	E_2 meV	E_3 meV	HH_0 meV	HH_1 meV
1132 [001]	200/200	0	6.7	3.0	0.028	0.28	0.11	125.7	55.8	156.5	313.2		128.2	121.8
[111]A	150/300*		10.9	3.3	0.032	0.20	0.06	217.0	104.1	264.6			210.9	200.9
1249 [001]	220/120	0	6.3	6.6	0.036	C.23	0.070	116.1	51.0	130.3	268.9		121.2	99.8
[111]A	150/120		10.9	5.4	0.040	0.13	0.09	209.2	93.3	207.8			200.8	180.5
1266 [001]	150/100	10	9.1	9.5	0.026	0.25	0.095	125.8	66.8	80.1	117.3	167.5	134.5	104.2
[111]A	110/207		13.6	4.2	0.031	0.19	0.084	238.8	129.1	176.9	245.6	346.5	244.3	216.8
1270 [001]	150/85	1	6.9	5.6	0.029	0.25	0.095	121.0	62.2	79.4	124.0	184.2	127.8	85.7
[111]A	155/110		11.5	4.3	0.030	0.19	0.084	213.8	120.6	150.0	192.4	256.4	218.4	190.6

* estimated

Table 1: Measured effective masses and calculated electron (E_n) and heavy hole energy (HH_n) levels along with the sample parameters for three superlattices. The superlattice period is given with the InAs thickness first. The *carrier densities* listed to magnetotransport data are given in units of 10^{11} cm^{-2}

For GaSb, the Luttinger parameters γ_1, γ_2, *and* γ_3 *are* 11.3, 5.3, and 6.5, *respectively* [12], giving quantum well(bulk) in plane masses of $0.051(0.27)m_0$ and $0.018(0.77)m_0$ for [001] and [111] orientations, respectively. In practice such low values for the hole masses are only seen for the lowest Landau level, due to the rapid onset of level interactions with higher states. This probably leads to the dominance of the relatively heavy hole mass which is seen in the samples with higher hole densities, due to their high Fermi energy levels. It is clear, however, that the [111]A oriented samples show consistently lower values for the in-plane mass. Such a difference has also been observed recently in p-type GaSb/(Ga,In)Sb strained quantum wells [13]. Our *light* heavy-hole mass of $0.05m_0$ is quite close to the decoupled limit and the values seen in the GaSb/(Ga,In)Sb structures of Ref. [13].

One further significant factor which may influence the observation of lighter hole resonances in the case of [111]A is the significantly enhanced band overlap which has recently been reported for this orientation. Symons *et al* [14] have found that [111] structures have a band overlap of over 80 meV larger than [001] structures and this may lead to an enhanced decoupling.

Another complicating factor is the possible influence of magnetoplasmon effects. Das Sarma and Quinn [15] have derived an expression for the collective mode excitations for an electron-hole system. In the limit of $qL << 1$, where L is the period of the superlattice and q the wavenumber, the coupled magnetoplasmons, of frequency ω, are given by:

$$\frac{\omega_{pe}^2}{\omega^2 - \omega_{ce}^2} + \frac{\omega_{ph}^2}{\omega^2 - \omega_{ch}^2} = 1 \qquad (1)$$

where the plasmon and cyclotron frequencies are $\omega_{pi} = \sqrt{N_i e^2/(\varepsilon\varepsilon_0 L m_i)}$ and $\omega_{ci} = eB/m_i$, respectively. The index i refers to electrons or holes. We have calculated the magnetoplasmon resonances with the electron mass and both the *light* heavy hole mass and the *heavy* mass separately and these plasmon branches are plotted in figure 3. It is clear that the observed electron transitions at least are not associated with plasmons and by inference this is also true for the holes.

4. Resonant subband Landau level coupling:

We have used tilted field experiments to study the resonant subband Landau level coupling (RSLC). Given that the energy range between 230 and 329 cm^{-1} is inaccessible due to the GaAs and GaSb reststrahlen bands, sample *1266 (or samples with similar growth parameters)* was best suited for the RSLC experiment. This sample and others were measured at a tilt angle of 0, 10, 30, and 60 degrees with respect to the magnetic field and light propagation directions. Figure 2 shows typical experimental spectra at 60 degrees.

Figure 3 shows the data for sample 1266 for both orientations at 0, 10, and 60 degrees plotted against the perpendicular component of the magnetic field. There are two groups of different resonances: three low energy resonances following a $B\cos(\theta)$ dependence and high energy resonances at around 400 cm^{-1} which become stronger on tilting.

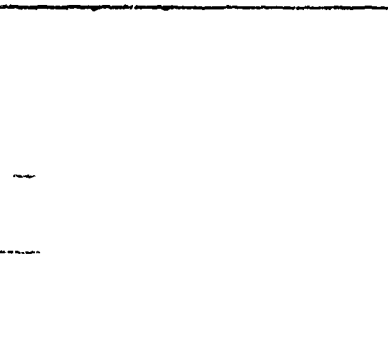

Fig 2: Raw transmission spectra for sample 1296 [001] ratioed against the zero field spectrum at a tilt angle of 60 degrees. The magnetic field is decreased in 1 Tesla steps from 11 T (top trace).

The three resonances that are shown to obey the well-established $B\cos(\theta)$ dependence for two-dimensional systems at low energies originate from the low energy branches of the CR: one from the 2D electrons and the other two from the 2D holes. As the tilt angle increases they show increasingly strong subband coupling, pushing the lower branch of the electron resonance down in energy.

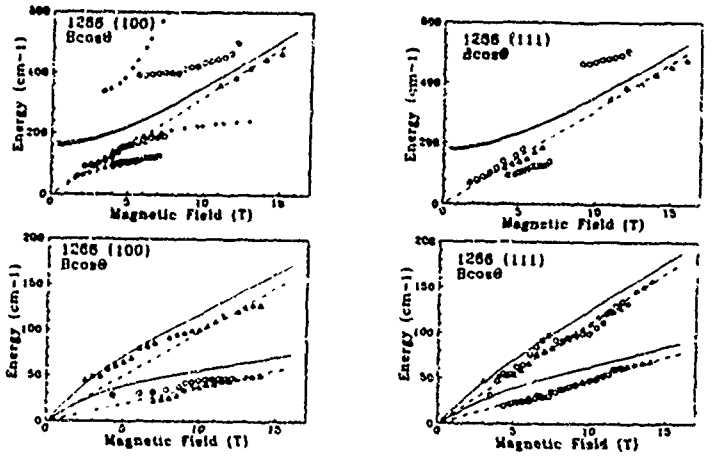

Fig. 3: Plot of the observed resonances at 0 (△) 30 (○), and 60 (□) degree angles for both 1266 [001] and [111]A. The dashed lines represent the bare cyclotron resonances for the electrons and holes whilst the solid lines correspond to the plasmon coupled resonances. Calculations for the [001] orientation at 30 and 60 degree tilts are shown by ∘ and + respectively.

The highest energy resonances, extrapolating at zero magnetic field to about 400 cm^{-1} for both orientations, are attributed to the upper branch of the resonant subband Landau level coupling from the electrons. To interpret these tilted sample experiments, we solve the Schrodinger equation in the presence of a magnetic field for any arbitrary angle with respect to the growth direction. The calculation is performed self-consistently taking into account the band bending due to charge transfer and the experimentally determined electron to hole density ratio (but not the actual densities). However, electron to hole and hole to hole band mixing have been neglected. To a first order, the agreement between theory and experiment is rather good. For example, the theoretically calculated electron and hole densities are within 5% of values obtained by fitting the magnetotransport traces. Table 1 lists the superlattice parameters and the electron and hole confined energy levels. The energies are given with respect to the lowest point in the InAs conduction band and the change of band overlap between [100] and [111]A has been included in the calculation.

Assuming that transitions take place between a filled and a partially filled or empty level, we expect to see RSLC for the [001] superlattice 1266 at 400 and 237 cm^{-1} corresponding to E_1-E_3 and H_0-H_1 transitions, respectively. Similarly, the RSLC is expected to occur in the [111]A superlattice 1266 at 386 and 205 cm^{-1} corresponding to E_1-E_0 and H_0-H_1 transitions, respectively.

Figure 3 demonstrates excellent agreement with theory for the lower electron branch at both 30 and 60 degrees, and quite good agreement for the upper branches. Considerable non-parabolicity effects occur at the higher energies, and we expect that mixing of the electron and hole bands should also be taken into account for the theory to agree quantitatively with experiment. By 60 degrees the two branches of the resonance observed for the electrons at high field have moved to 120 and 350 cm^{-1}, as shown in figure 2. In contrast to the electron behaviour, we see no evidence of significant hole subband coupling in the data at 30 degrees, and by 60 degrees the hole resonances are very difficult to resolve underneath the lower electron branch. This result is rather surprising, since we expect stronger subband coupling for holes [16], due to the anisotropic nature of the valence band, although the field range used does not fully approach the coupling condition $\hbar\omega_c = \hbar\omega_0 - \hbar\omega_1$ even for the lighter of the two hole resonances.

5. Conclusion:

In summary we have measured the electron and heavy hole masses for both [001] and [111] orientations. We find that the heavy hole masses are anisotropic. The *light* heavy hole resonance is attributed to the strain and quantisation induced decoupling of the valence band. Large angle tilts allowed us to determine the electron subband energy separation: the agreement between experiment and theory was very good.

6. Acknowledgements:

We gratefully acknowledge Drs. T.Y. Seong and G.R. Booker for transmission electron microscopy studies and the Science and Engineering Research Council (UK) for continued financial support. One of us (TAV) would like to acknowledge the National Science Foundation for financial support.

References

[1] L.L. Chang, *J. Phys. Soc Jpn* **49**, 997 (1980).

[2] D.L. Smith and C. Mailhiot, *Rev. Mod Phys.* **62**, 173 (1990).

[3] M. Lakrimi, R.W. Martin, C. López, D.M. Symons, E.T.R. Chidley, R.J. Nicholas, N.J. Mason, and P.J. Walker, *Semicond. Sci. Technol* **8** S167 (1993) and references therein.

[4] G.L.J.A. Rikken, H. Sigg, C.J.G.M. Langerak, H.W. Myron, J.A.A.J. Perenboom, and G. Weimann, *Phys. Rev. B* **34**, 5590 (1986).

[5] G.M. Sundaram, R.J. Warburton, R.J. Nicholas, N.J. Mason, and P.J. Walker, *Semicond. Sci. Technol.* **7** 985 (1992) and references therein.

[6] J.C. Maan, Ch. Uihlein, L.L. Chang, and L. Esaki, *Sol St Commun.* **44**, 653 (1982); Y. Guldner, J.P. Vieren, P. Voisin, M. Voos, J.C. Maan, L.L. Chang, and L. Esaki, *Sol. St. Commun.* **41**, 755 (1982).

[7] J.C. Maan, M. Altarelli, H. Sigg, P. Wyder, L.L. Chang, and L. Esaki, *Surf Sci.* **113**, 317 (1982); H. Bluyssen, J.C. Maan, P. Wyder, L.L. Chang, L. Esaki, *Phys Rev B* **25**, 5364 (1982).

[8] R.J. Nicholas, K.S.H. Dalton, M. Lakrimi, C. Lopez, R.W. Martin, N.J. Mason, G.M. Summers, G.M. Sundaram, D.M. Symons, P.J. Walker, R.J. Warburton, M.I. Eremets, D.J. Barnes, N. Miura, L. van Bockstal, R. Bogaerts, and F. Herlach, *Physica B* **184** 268 (1993). D.J. Barnes, R.J. Nicholas, N. Miura, R.J. Warburton, N.J. Mason, P.J. Walker, *Physica B* **184** 268 (1993).

[9] M. Lakrimi, R.W. Martin, N.J. Mason, R.J. Nicholas, and P.J. Walker, *J. Cryst. Growth* **124** 395 (1992).

[10] R.W. Martin, R.J. Nicholas, G.J. Rees, S.K. Haywood, N.J. Mason, and P.J. Walker, *Phys. Rev B* **42** 9237 (1990).

[11] For a review see C. Wiesbuch and B. Vinter *Quantum semiconductor structures physics and applications*. Academic Press 1991, pp15-19.

[12] A.P. Roth and E. Fortin, *Can. J. Phys* **56**, 1168 (1978).

[13] R.J. Warburton, R.A. Lewis, R.J. Nicholas, N.J. Mason, and P.J. Walker, *Physica B* **184** 154 (1993).

[14] D.M. Symons, M. Lakrimi, R.J. Warburton, R.J. Nicholas, N.J. Mason, P.J. Walker, and M.I. Eremets, *to be published* (1993).

[15] S. Das sarma and J.J. Quinn, *Phys. Rev. B* **25**, 7603 (1982).

[16] A.D. Wieck, F. Thiele, U. Merkt, K. Ploog, G.L.J.A. Rikken, H. Sigg, C.J.G.M. Langerak, H.W.G. Weimann, and W. Schlapp, *Phys. Rev. B* **39**, 3785 (1989).

ThP30

MAGNETIC FIELD TUNED TRANSITION OF AHARONOV-BOHM OSCILLATIONS FROM hc/e TO hc/2e PERIODICITY IN THE ARRAY OF AlGaAs/GaAs RINGS.

G M Gusev*, P Basmaji, D I Lubyshev*
Instituto de Fisica e Quimica de São Carlos,
Universidade de São Paulo, SP, Brasil

J C Portal
Service National des Champs Intenses, Centre National
de la Recherche Scientifique, F-38042, Grenoble
and INSA-Toulouse, 31077, France

L.V Litvin, Yu V Nastaushev and V I Toropov
Institute of Semiconductor Physics Russian Academy of Sciences,
Siberian Branch, Novosibirsk, Russia

Abstract.

The variation of Aharonov Bohm oscillation periodicity and persistent magnetoconductivity have been observed in the array of AlGaAs/GaAs rings with diameter of 0.3 μm. Magnetic field tuned impurity levels were suggested to be responsible for this behavior. It can be a result of the local electron density variation due to the influence of the weak magnetic field on the interference effect in mesoscopic samples.

Magnetooscillations in the normal metal ring with small diameter due to the Aharonov-Bohm effect is one of the remarkable phenomena that demonstrated the quantum behavior of an electron in solids. These Aharonov-Bohm (AB) oscillations are very sensitive to impurities, because defects introduce the additional shift to the electron wave function phase and, consequently, to magnetooscillations of a small single ring at nearly zero magnetic field [1,2]. In small samples, whose size are comparable to the phase coherence length L_φ the conductance fluctuations are random because of the interference among all possible trajectories. The results of interference are not averaged, but rather depend on the specific arrangement of the scattered centers in the given samples [3]. The change in the configuration of the random potential in microstructures gives rise to variation of the mesoscopic fluctuation pattern in a specific sample. This configuration can be changed as a result of spontaneous switching [4,5] under the interband irradiation [6,7] and after application of a strong electric field pulse [5,6]. Magnetic field also can influence the impurity level, and change in the switching time of a single impurity with magnetic field was observed [8]. However, it's difficult to see the influence of magnetic field on the conductance fluctuations because of their random pattern. Another situation exists in the single submicron ring. In this case AB oscillations with the periodicity given by the flux quantum $\Phi_0 = hc/e$ are dominant. Introduction of an additional shift in the magnetic field can change an apparent periodicity of AB oscillations.

In this paper we report the variation from hc/e to hc/2e AB oscillation periodicity in the array of rings tuned by magnetic field. We suggested that the impurities are responsible for this behavior. We've firstly observed also nonmonotonic behavior of the impurity energy which can be connected to a mechanism based on the influence of the electron local density on the defect [9].

The test samples were Hall bridges based on AlGaAs/GaAs heterostructures with 2D electron gas. In the initial heterostructures the electron density was $n_s = 1 \times 10^{11} cm^{-2}$ and electron mobility $\mu = 2 \times 10^5 cm^2/V \cdot s$. The samples with area $500 \times 200 \mu m^2$ were split off, and in the middle part between the potentiometric probes the square bridge was formed with size $2 \times 2 \mu m^2$. In this bridge a periodic lattice of holes (antidots) was patterned using electron lithography. The lattice period d was 0.3 μm, lithography antidot size $c = 0.15 \mu m$. Next, the lithographic samples were etched using reactive plasma etching, which was stopped before the AlGaAs spacer. The antidot size was larger than the geometric diameter because of the depletion region around the antidots, therefore we have $a = c + t$, where t is the width of this depletion region. Thus, our system is different from other antidot lattices, which have been studied previously and for which $d/a >> 1$ [10]. Also our samples have a small size L_φ, where l - mean free path in the initial heterostructures, therefore the electron transport was quasi ballistic. The geometry of our array is closer to the geometry of the connected rings with diameter 0.3 μm.

The magnetoresistance was measured by the four probe method at frequencies 70-700 Hz in a magnetic field up to 0.5 T at temperature 1.7-4.2 K. We measured two samples with identical parameters.

We found the magnetoresistance oscillations which can be connected most clearly with AB effect, however their behavior was unusual. The typical curves of this magnetoresistance are shown in fig 1a. Fig 1b shows the periodicity of AB oscillations. The periodicity is varied from Φ_0/S to $\Phi_0/2S$, where $S = \pi d^2/4$ is the ring area with diameter d. The envelope of the magnetoresistance curve, correlated with periodicity variation is observed. After several sweepings of B the oscillation picture is slightly changed, in particular, the second minimum of the resistivity moves to the higher magnetic field (curves 3), and oscillations with periodicity h/e move to the higher B too. We swept B 16-20 times and found that the sample begins to reveal hysteresis behavior. The same situation was observed when we swept B up with low velocity (0.3 T/min) and switched off B after the approach of B_{max} with high velocity (2 T/min). Fig. 2 shows some typical magnetooscillation curves when the magnetic field was swept up and down. We observe two features differ from AB oscillations in a single AlGaAs/GaAs ring, decrease of the periodicity and hysteresis of the magnetoresistance oscillations. For curves 1,2 the resistivity did not return to the initial state when B was turned off. The sample resistivity was relaxed to this state during 80 s. The magnetic field B was swept up and down 15 times, and magnetooscillations were slightly transformed into the curves 3,4 which also reveal hysteresis. For these curves after 40-80 s at zero magnetic field the sample returned to the first state. This behavior was repeated several times. Oscillation periodicity for curves 3,4 is changed from hc/eS to hc/2eS (fig 2). Maximum amplitude of the conductance oscillation was found to be $0.8e^2/h$.

We believe, that the impurities are responsible for this behavior. For the dynamic study of this effect we measured the resistance as a function of time during a sweeping of the magnetic field. Fig 3 shows the resistance as a function of time for these oscillations. At zero magnetic field the sample state was stable during expectation time 10 min. Next we swept the magnetic field up and down. As can be seen in fig 3 the oscillation with hysteresis was observed, and when the magnetic field was swept down, the sample resistance was found to be higher, than for the initial state. The relaxation of the resistivity to the initial state was observed. The relaxation time was found to be 60 s. We did not see any spontaneous switching of impurities during the record of the magnetoresistance curves (magnetofingerprints), which can change the oscillation picture. Thus, all results give evidence, that the magnetic field influences the impurity level, and changes AB oscillations.

In mesoscopic samples telegraph noise connected to switching of the two level impurity state has been observed [4,5]. This switching is related to tunneling in a double well energy potential with slight assymmetry or activation over this internal barrier [11], and thus, with the motion of the scatterer from one place to another. In this case the interference electron pattern can be affected by this motion [3]. If defect hopping is activated by the temperature (we believe that this mechanism is dominant in our case), activation energy is responsible for the switching time. When the activation energy is larger than the temperature the impurity spends all time in the lower state. The proposed mechanism of the impurity switching influence on the AB oscillations is illustrated

in fig.4 . When the magnetic field increases, impurities hop to the other state (fig 4b). Configuration of the random potential is changed, therefore the new phase shift to AB oscillations is introduced. In our case magnetic field changes the state of many impurities (a long relaxation time tail was found). Therefore AB oscillation phase is not changed abruptly, but smooth transition is observed (fig 4c). As magnetic field increases further, impurities can hop back to the initial state (fig 4c) or defects with higher hopping barrier height switch to the second state. As a result of the change in the configuration of the random potential AB oscillations periodicity is slightly randomized - it is varied between hc/e and $hc/2e$. We also believe, that the envelope of magnetoresistance oscillations on fig 1 can be connected with impurity hops to the other state. In this case it is a new kind of magnetoresistance due to the changing in the configuration of the random potential. We see also this magnetoresistance for curve 1 (fig 2), however because the oscillations are smeared, analysis of their periodicity is difficult. For the two level system the living time t_u and t_d spent in up and down states can be introduced. For the system with a barrier when the activation mechanism is dominant $t_d/t_u = exp(E_a/kT)$, where E_a -activation energy. In our case at $B = 0$ $t_d >> t_u$ and $E_a > kT$, in a magnetic field this situation is reversed $t_d << t_u$, i.e. E_a decreases and changes the sign. The magnetic field influence on the telegraph noise in a mesoscopic sample was observed in ref.[8], however the mechanism of this effect was not clear. It is well known that the activation energy increases with B for the conduction band Γ valley. Also it is necessary to apply high magnetic field (>3 T) to shift the impurity energy to the value kT due to the Zeeman splitting, if g -factor is equal 2, and magnetic momentum is different for these two levels in a double well defect. Another mechanism has been proposed by Al'tshuler and Spivak [9]. Interference of the electron waves is responsible for the local electron density. Magnetic field influences the interference due to AB effect, and thus, electron local density is changed, therefore the energy of the nearly located impurity is varied too. The Al'tshuler Spivak mechanism should lead to a random fluctuation of the local impurity energy, because of the random pattern of the electron density in the disordered scattering potential. The autocorrelation function of the impurity energy is equal [9]

$$< I(B)I(0) > \approx (\hbar\omega_c/\pi)^2/L \approx (\hbar\omega_c)^2 \qquad (1)$$

for $L \gtrsim l_\omega$, ω_c - cyclotron frequency. In the array of rings the electron interference is determined by the ring geometry and not by the specific impurity configuration as in mesoscopic samples. Therefore the impurity energy should oscillate with periodicity Φ_0, and the amplitude of this oscillation should increase linearly with magnetic field. As can be seen from fig.1,2 transition of AB periodicity is observed at $B \approx 0.2$ T, therefore $E_a \approx \hbar\omega_c \approx 0.35meV$. It is comparable to temperature , therefore $t_u \approx t_d$. As we mentioned above, when the magnetic field was swept down with high velocity, the sample resistance hopped to the other state. A similar effect exists in a heavy doped GaAs and AlGaAs alloy system after illumination of the sample by light at low temperature - persistent photoconductivity [12]. In our case impurity switching time lies in the interval 1-50 s, therefore when the magnetic field is turned off at a high rate some defects were staying in the metastable state due to the barrier. The sample was switched to the state with another resistivity in a zero magnetic field and we observed persistent magnetoconductivity and hysteresis behavior (fig 1,2,4). This persistent magnetoconductivity can be positive (fig 2) or negative (fig 3). We also see the long tail of the impurity relaxation arising from the different switching time in the ensemble of impurities. Some defects have a longer relaxation time, therefore the picture of the magnetooscillations differs from the initial. However, after irradiation by light or heating of the sample up to room temperature, we turned off the device to the initial state. These experiments were carried out during two months, and all time we observed the impurity switching induced by the weak magnetic field.

It should be noted that recently new magnetooscillations with periodicity hc/ea^2 have been observed in samples which contain 10^7 antidots [13,14]. As was suggested in

[14], it is not due to AB effect, and quantization of the periodic orbits (QPO) is responsible for these oscillations. The next difference in our experiments can be emphasized: QPO oscillations appear only at B>0.5 T and T<1.5 K in contrast to AB oscillations which are seen at smaller magnetic field and at T≈4.2 K. The thermal broadening of energy levels, which depends on the magnetic field value, is responsible for the behavior of QPO oscillations.

In summary, we have observed the influence of the weak magnetic field on the impurity state in the system with an array of submicron rings. Novel magnetoresistance appeared because of the changing in the configuration of the random potential by magnetic field. Metastability of these states is responsible for the hysteresis of the magnetoresistance and persistent maggetoconductivity. A more delicate effect connected with sensitivity of the AB oscillation periodicity to the impurity state has been found: variation of periodicity between hc/eS to $hc/2eS$. The Al'tshuler Spivak mechanism because of the change in the local electron density which leads to the impurity energy shift is responsible for this behavior.

Two of us (G.M.G. and D.I.L.) are supported by CNPq (Brazil).
This work is supported by funds CNPq and FAPESP.

*Permanent address: Institute of Semiconductor Physics, Russian Academy of Sciences, Siberian Branch, Novosibirsk, Russia.

REFERENCES

[1] S.Washburn, R.A.Webb, Rep.Pr.Phys. **55**, 1311 (1992).

[2] A.D.Benoit, S.Washburn, C.P.Umbach, R.B.Laibowitch, R.A.Webb, Phys.Rev.Lett., **57**, 1765 (1986).

[3] B.L. Al'tshuler, B.Z.Spivak, JETP Lett., **42**, 447 (1985).

[4] M.J.Kirton, M.J.Uren, Adv.Phys., **38**, 367 (1989); K.S.Ralls, R.A.Buhrman, Phys.Rev.Lett., **60**, 2434 (1988); D.E.Beutler, T.J.Meisenheimer, N.Giordano, Phys.Rev.Lett., **58**, 1240 (1987).

[5] G.M.Gusev, Z.D.Kvon, E.B.Olshanetskii, V.Sh.Aliev, A.M.Kudryashov, S.V.Palesskii, J.Phys.:Cond.Matter, **36**, 6507 (1989).

[6] G.M.Gusev, Z.D.Kvon, E.B.Olshanetskii, Sov.Phys.JETP, **74**, 735 (1992).

[7] S.J.Klepper, O.Millo, M.W.Keller, D.E.Prober, R.N.Sacks, Phys.Rev.B, **44**, 8389 (1991).

[8] N.M.Zimmerman, B.Golding, W.H.Haemmerle, Phys.Rev.Lett., **67**, 1322 (1991).

[9] B.L. Al'tshuler, B.Z.Spivak, JETP Lett., **49**, 671 (1989).

[10] K.Lassila, P.Petroff, Phys.Rev.B, **41**, 12307 (1990); G.M.Gusev, V.I.Dolgopolov, Z.D.Kvon, V.V.Shashkin, V.M.Kudryashov, L.V.Litvin, Yu.V.Nastaushev, JETP Lett., **54**, 364 (1991); A.Lorke, J.P.Kotthaus, K.Ploog, Phys.Rev.B, **44**, 3447 (1991).

[11] C.J.Rogers, R.A.Buhrman, Phys.Rev.Lett., **55**, 859 (1985).

[12] D.V.Lang, R.A.Logan, Phys.Rev.Lett., **39**, 635 (1977).

[13] I.Ishii, K.Nakamura, Physica B, **184**, 398 (1993).

[14] D.Weiss, K.Richter, A.Menschig, R.Bergmann, H.Schweizer, G.Lütjering, Proc. 20th Int.Conf. on LT2DS, Newport, 26 (1991).

Figure captions

Fig 1 a) Magnetoresistance as a function of magnetic field T = 1.2 K. Insert Schematic view of the sample

b) Periodicity of oscillations for the different magnetoresistance curves

Fig 2 a) Magnetoresistance with hysteresis as a function of B 1.1 B sweep up, 2,4 B sweep down

b) Periodicity of AB oscillations for curves 3,4

Fig 3 Resistivity as a function of time during a magnetic field sweeping and following relaxation

Fig 4 Schematic illustration of the AB periodicity variation due to the changing in the impurity state Insert left impurity potential at different magnetic field

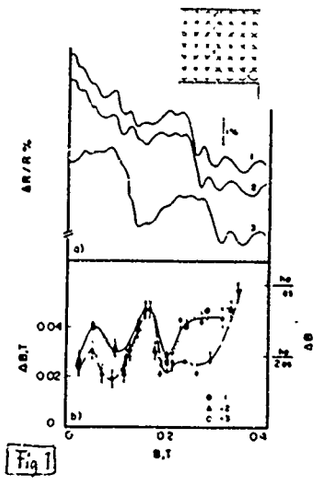

Fig 1

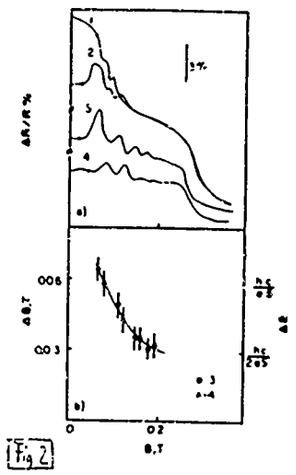

Fig 2

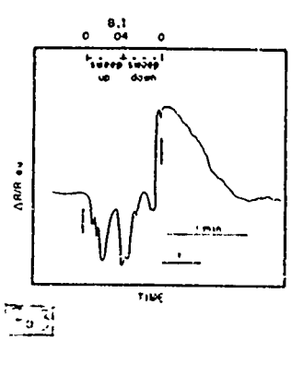

Fig 3

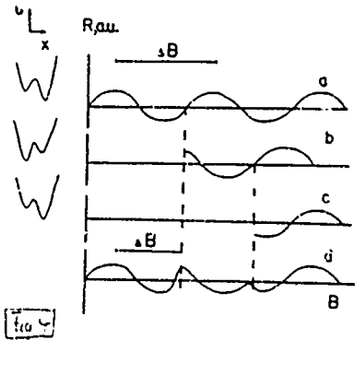

Fig 4

ThP31

Negative Conductance at THz Frequencies in Multi-well Structures

W S. Truscott
Department of Electrical Engineering and Electronics, University of Manchester Institute of Science and Technology, PO Box 88, Manchester, M60 1QD, UK

Abstract

An algorithm by which the exact first order ac response of quantum electronic devices, including tunnelling structures, may be calculated rapidly is described. Novel multi-well tunnelling structures with negative conductance maxima at 1.4×10^{12} Hz (1.4 THz) and 14 THz at temperatures of 80 K and 300 K respectively are presented. Devices of this sort are expected to operate as power sources, mixers and amplifiers between 0.5 and 20 THz. The effects of bias and departures from the ideal geometry are discussed as are the factors which indicate that such devices are realisable in practice.

Three new aspects of the response at extremely high frequencies of electronic transport structures, particularly tunnelling and other quantum devices, are presented in this paper: first, an algorithm to calculate both the terminal currents and the internal carrier displacement currents that are induced when an external ac potential is applied to a structure; second, a novel device structure which may operate as a power source or amplifier at frequencies in the range 0.5 - 20 THz (5×10^{11} - 2×10^{13} Hz); and, third, experimental and theoretical considerations related to the practical production and utilisation of these devices.

This work is based on exact solutions to Schrodinger's equation for systems in uniform time dependent fields [1]. The solutions are inherently self-consistent, i.e. where one of these solutions applies, the additional time dependence caused by the ac field is independent of the carrier - carrier interactions. Full details of, and justification for, their use in the calculation of the ac response of semiconductor devices will be reported later; here the method is outlined. The response of a wave function to a time dependent field is close to the motion of a classical particle in that field, in addition there is a time-dependent phase modulation. As a specific example, $A\exp(ikx)$ is a wave function for a particle of mass m in a region of constant potential, when the potential $-Fx\cos(\omega t)$ is added an exact wave function is:

$$A\exp\left\{ik\left[x+\frac{F\cos(\omega t)}{m\omega^2}\right]-\frac{iEt}{\hbar}+\frac{iFx\sin(\omega t)}{\hbar\omega}-\frac{iF^2[2\omega t-\sin(\omega t)]}{2\hbar m\omega^3}\right\} \quad (1)$$

Exact solutions also exist for regions in which the potential is a linear or parabolic function of distance. A semiconductor device subject to an ac bias may be divided into regions within each of which there are many time dependent wave functions that will be exact solutions of Schrodinger's equation; however, most of these will not satisfy the continuity equations at regional boundaries since the adjoining wave functions will have different time dependencies for their amplitudes and phases. For the above example, this will always occur if either F or k changes at a boundary. In a seminal paper concerned with a transit time for tunnelling which has acted as a major stimulus to this work, Büttiker and Landauer have given a solution [2]: for any wave function with energy E that describes the device with a static potential, there is a related one for the structure subject to an additional sinusoidally time dependent field of period $2\pi/\omega$ which has a similar wave function at energy E together with a series of functions with time dependences which differ from it by $\exp(in\omega t)$ where n is any integer. The latter are wave functions for the local potential with energies $E+n\hbar\omega$ selected so that their sum satisfies the continuity equations and the boundary conditions at all times. The first order response is associated solely with the components identified with $\exp(\pm i\omega t)$; a total of three functions in any region are sufficient to describe the linear behaviour of a device.

To first order, the time dependent continuity equations at any boundary divide into two parts separating the effects of the ac field in adjacent regions. The algorithm used for this paper calculates the effect of the ac field on each region of the potential having an exact solution: with this approach the waves generated at the two boundaries of a region tend to cancel outside it. First order forms for the amplitude and spatial derivative of the wave function of equation (1) for a boundary at $x=a$ may be found by multiplying the function $A\exp\left[ika-\frac{iEt}{\hbar}+\frac{iFa}{\hbar\omega}\sin(\omega t)\right]$ by $\left[1+\frac{ikF}{m\omega^2}\cos(\omega t)\right]$ and $\left[ik-\frac{k^2}{2}\cos(\omega t)+\frac{ik}{k}\sin(\omega t)\right]$ respectively. If the ac potential is continuous then the original function will also be continuous at $x=a$ and it is only the time dependence associated with the multipliers that has to be counterbalanced by wave functions at energies $E\pm\hbar\omega$; waves of the required amplitude and derivative are added at one side of the boundary with respect to the other. They propagate through the region to the second boundary at $x=b$ where a similar set of functions describe the amplitude and derivative. For small values of ω the latter at $E\pm\hbar\omega$ will almost exactly cancel those required for the boundary at $x=a$: the residual sum of the waves satisfying the boundary conditions at $x=a$ and at $x=b$ propagates into the rest of the structure and gives rise to the time dependent terminal current. The carrier displacement current in any region of the structure is found by summing the net current due to all other regions, the current associated with the initial time dependent wave function and that associated with the waves within the region generated at its boundaries.

The results in this paper are from a computer programme which uses the above algorithm. This programme can analyse any structure which is composed of a sequence of regions of constant potential separated by abrupt steps in potential. There are many advantages in restricting the structures in this way: all the functions within the algorithm are analytical and any result may be checked (in simple structures) by an independent calculation; because the functions involved are either exponential or trigonometrical the calculation is much faster than it would be if the functions had to be numerically integrated; the programme is simple and has been checked and verified over a long period of time, the probability of error in these results is very small. This algorithm is readily extended to include regions with a linear or parabolic variation of potential and programmes have been developed to analyse structures including such regions: the results from these are not different in kind from those presented here. The modulation of the current emerging from a double barrier resonant tunnelling diode structure (DBRTS) calculated using this programme is consistent with results published elsewhere [3],[4],[5]: the overall response is that of a system with a single resonance for which a characteristic time, τ, is defined by the ratio of Plank's constant to the half width of the transmission peak.

The limitations on the frequency response intrinsic to the DBRTS are overcome in structures with two of more quasi-bound levels which have spacings corresponding to the operating frequency, f_o. The algorithm has allowed the behaviour of many different structures

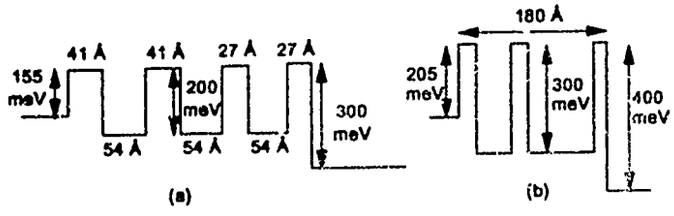

Figure 1: Conduction band energy diagrams of two structures exhibiting negative conductance. They are optimised for 1.4 THz (a) and 14 THz (b) respectively.

to be investigated; the overall pattern of phase and amplitude variation is characteristic of spatially distinct states whose coupling through an external potential is characterised by a resonant response. The argument that this resonant modulation of a unidirectional particle flux by an external field is a novel quantum effect will be given in a later paper; this is concerned with the practical implications of the effect. The pattern of the results that have been obtained allows optimised device structures to be evolved; examples of the conduction band diagram of two of these are shown in Figures 1(a) and 1(b). The key features of these are the wider barriers on either side of the left hand well and the nearly uniform spacing in energy of the three lowest quasi-bound levels when the device is biased at the optimum operating point. The wider barriers cause the tunnelling transmission to be dominated by the quasi-bound state at energy $E2$ associated with the left hand well. There will be a significant accumulation of carriers in this well when a tunnelling current flows. The rest of the structure is designed so that the energies of two other levels, $E1$ and $E3$ satisfy $E3\text{-}E1 = 2hf_c$. The calculated response to an applied field when $E2 = \frac{1}{2}(E1+E3)$ is very small because the effects of the coupling to levels 1 and 3 are equal and opposite. This is shown by Figure 2 which illustrates for electrons with energies corresponding to the transmission window at E2, the reactive and conductive parts of the terminal current as a function of the energy $E \pm hf$ of the state to which the tunnelling electrons are coupled by the ac field. The reactive currents are opposite in sign for coupling to the states at E1 and E3, as are the conductive currents for a given modulation frequency if $E2 = \frac{1}{2}(E1+E2)$; these two parts always vary with energy in accordance with expectations based on the Kramers-Kronig relationships. However if $E2 > \frac{1}{2}(E1+E3)$, the case shown in Figure 2, the coupling between levels 2 and 3 occurs at lower frequencies than that between 2 and 1; it is the overlap between the two responses which gives the large negative terminal conductance which is constant over a substantial bandwidth. Figures 3(a) and 3(b) show the frequency dependence of the real and imaginary parts of the admittance of the structures in Figures 1(a) and 1(b) respectively when bias is applied so that $E2 > \frac{1}{2}(E1+E3)$.

The quantities plotted in Figure 3(a) are the real and imaginary components of the ac

terminal current produced by unit field across the device structure for an incident electron spectrum at the left hand side of Figure 1(a) that is characterised by a temperature of 80 K, while those plotted in Figure 3(b) are the identical quantities for the structure of Figure 1(b) with an incident electron temperature of 300 K; in both cases an effective mass one tenth the electron mass has been assumed. The algorithm described above is used to calculate at a fixed frequency and incident electron energy the magnitude and phase of the modulation of the tunnelling current produced by the ac field. The observable admittance at that frequency is found by integrating the modulation weighted by the transmission probability over the electron spectrum: this integration extends over the range of incident energies that cover the transmission peaks $E1$, $E2$ and $E3$. For some structures and frequencies there is significant cancellation between the response of the electrons with the highest energies in the central transmission peak and those with the lowest energies. The structure shown in Figure 1(a) minimises this with barrier widths designed so that the major transmission peak at energy $E2$ is about half the width of those at energies $E1$ and $E3$, in which case the phase of the modulation produced by the ac field does not vary significantly over the transmission peak at $E2$.

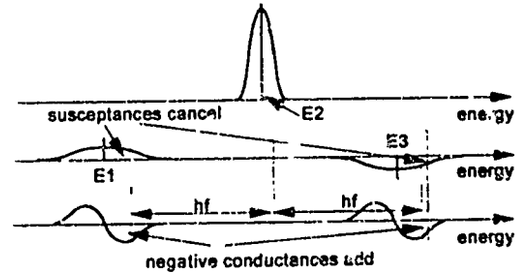

Figure 2: An explanation of the calculated admittance frequency curves of Figure 3. The upper curve shows the transmission peak at energy E2. The lower curves are sketches of the susceptance and conductance for any electron with energy close to E2 coupled to energies close to E1 or E3 by the applied ac field at a frequency f.

The total current flowing through any device similar to those shown in Figure 1 is composed of two parts, first, the tunnelling current which passes through the right hand barrier into the contact and second, the displacement current associated with the electrical polarisation of the material and carriers within the structure. The dielectric polarisation is a fixed function of the device geometry, the carrier polarisation normally adds to this, increasing the overall structural capacitance. In these devices however, the negative

resistance is the result of the reduction in the density of carriers adjacent to the final barrier when the ac field is directed towards it; the carrier displacement within the device under optimum operating conditions is therefore inductive. These new devices therefore exhibit an effect of great importance in THz applications, namely that the capacitance of the device is reduced below its structural value by the carrier displacement currents within the active region of the device. Calculation of the combined structural and carrier capacitance is possible using the above theory but, since this effect is of the same order as the variation in the applied field over the device due to carrier accumulation, such a calculation will only be valid in a model which includes these effects.

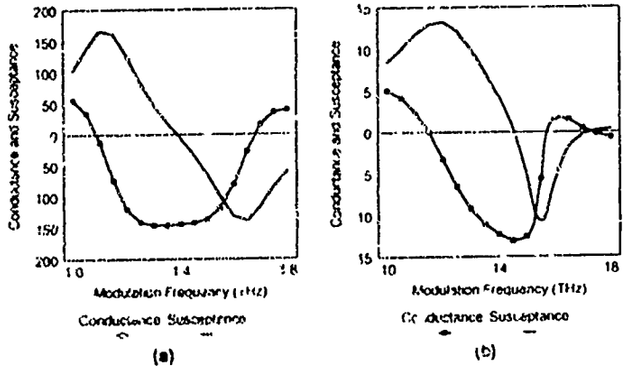

Figure 3: The calculated conductance and susceptance (arbitrary scales) as a function of frequency for the two device structures of Figure 1

Devices using this new concept can only be realised experimentally and exploited commercially if the range of parameters such as structural width, barrier height and device bias over which the effect is exhibited covers the probable range of deviations that may occur in the normal manufacturing processes and operating conditions for such structures. The effect on the negative conductance characteristic of changing the energy offset between the barriers and the wells for the structure in Figure 1(a) by 5% is shown in Figure 4(a), as is the effect of changing the overall width scale by 2%. It can be seen that, as a result of the bandwidth over which the device has a constant negative conductance, devices with either of these departures from the designed structure would still perform as oscillators or amplifiers at the design frequency of 1.4 THz. Since these variations are in excess of the degree of control which can be achieved in MBE growth, normal structural variations will not restrict the performance of these devices. Figure 4(b) shows the negative resistance characteristic with three different values of forward bias, the effect of reducing the bias by

a few mV over the active region of the device to the condition that $E2 < \frac{1}{2}(E1 + E3)$ is to switch the sign of both the conductance and susceptance at the operating frequency. This device may therefore be used as a modulator. Changing the bias by a similar amount in the opposite direction splits the features in the device response associated with the coupling between E2 and E3 from that between E2 and E1 giving a reduced magnitude for the negative conductance, but an increased bandwidth and a correspondingly less rapid change of susceptance with frequency. A single device may therefore be used in high gain narrow bandwidth and low gain wide bandwidth applications depending on the applied bias.

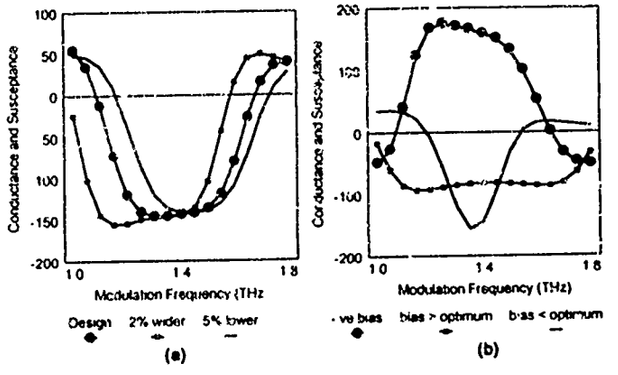

Figure 4: Variation of the conductance for the device in Figure 1(a) with (a) device geometry and (b) applied bias. The design conductance curve is compared those for devices with a 5% decrease in barrier height and a 2% increase in geometrical widths, and curves are presented for forward biases which are larger and smaller than the optimum bias and also for a small negative bias.

The band structure diagrams shown in Figure 1 are significantly different from those for real devices fabricated in GaAs/AlGaAs, a material system which minimises the broadening of the quasi-bound levels, subject to a dc bias prompting an electron flow. The bias will cause an electric field over the whole structure; in addition the accumulation of carriers, particularly in the left hand well, will make this field vary over the active region. The problem of designing a structure which has the required energies for the three quasi-bound levels when a forward bias is applied is considerable and must be overcome before the negative conductance can be demonstrated. This design process needs to combine theoretical modelling with experimental assessment as a means of empirical optimisation of the model. Although it might seem a very difficult task to produce a structure with three energy levels whose relative energies are correct within 0.5 meV, there are two factors that are a considerable assistance for structures similar to that of Figure 1(a): first, levels *E1* and

$E3$ are associated with the mixed states of right hand wells; the minimum value of $E3$-$E1$ as the dc bias is varied is determined only by the barrier between these wells, and it changes slowly with this field about this condition because of the mixing. There will therefore be a useful range of applied bias over which the $E3$-$E1$ will be close to $2hf_0$. Second, the position of $E2$ with respect to $E1$ and $E3$ is controlled by the bias, a suitable value can always bring their energies into the correct relation to show negative conductance at some frequency. Because $E3$-$E1$ varies slowly over a certain range of applied bias, the design requirements reduce to establishing an appropriate barrier thickness between the right hand wells and choosing the widths of these wells so as to ensure that the bias at which $E2$ is in the correct relative position is close to that at which $E3$-$E1$ reaches its minimum value.

An important factor determining the practical applications of these devices is temperature at which they can be operated. The negative conductances shown in Figures 3(a) and 3(b) have been calculated for electrons at 80 K and 300 K; the structures therefore have the potential to operate at practical temperatures. The other factor which will determine the maximum operating temperature is the broadening of the quasi-bound levels by phonon scattering. Roskos et al. [6] have reported the observation of up to 15 cycles of radiation at a frequency of 1.5 THz caused by coherent electron oscillations in an optically excited double well structure at a temperature of 10 K. The basis for this phenomenon is closely related to that giving rise to the negative conductance; this observation strongly suggests that the high frequency negative conductance will be observed in suitable structures at practical temperatures as does the observation at temperatures up to 185 K of maxima in the tunnelling current - voltage curve associated with a 38 meV miniband spacing in a multi-well structure [7].

The author wishes to thank his colleagues for the stimulating environment which has led to this work. It has been supported solely by research element of the Higher Education Funding Council for England recurrent grant to UMIST. The author believes that the future exploitation of these ideas is a fruitful area for international collaboration.

1. W.S. Truscott, Phys Rev. Lett. 70, 1900, (1993).

2. M. Büttiker and R. Landauer, Phys Rev Lett. 49, 1710 (1982).

3. W.R. Frensley, Appl. Phys. Lett. 51, 448 (1987)

4. H C. Liu, Appl. Phys Lett. 52, 453 (1988)

5. V. Kislov and A. Kamenev, Appl Phys. Lett. 59, 1500 (1991).

6. H.G. Roskos, M.C Nuss, J. Shah, K. Leo, D.A.B. Miller, A.M. Fox, S. Schmitt-Rink and K Köhler, Phys. Rev. Lett 68, 2216 (1992)

7. P.C. Harness, Ph.D Thesis, "Resonant-Tunnelling Structures incorporating Finite Superlattice Energy Filters", Faculty of Technology, University of Manchester, UK pp. 170 - 177, (1992)

ThP32

Perpendicular Transport Through Rough Interfaces in the Metallic Regime

Arne Brataas [*] and Gerrit E.W Bauer
Faculty of Applied Physics and DIMES. Delft University of Technology
Lorentzweg 1, 2628 CJ Delft, The Netherlands

June 28, 1993

Abstract

Perpendicular transport through an interface in the metallic regime is considered. The semiclassical theory presented is based on the Landauer-Büttiker formalism, it generalises previous work by taking into account an effective mass mismatch at the interface and a non-zero average of random scattering potentials. The transmission probability for a given mode is found in terms of the effective mass and the conduction band profile to the left and to the right of the interface, the Fermi energy, the self-energy of the electron, and the transverse wave vector of the electron. The diffuse and specular contributions to the interface roughness scattering are shown to be equally important in the weak scattering limit. Predictions for the transport properties of interfaces with a low concentration of strongly scattering defects should be accessible to verification by experiments. The theory is applied to the spin-valve effect in magnetic multilayers

The importance of interface scattering in many areas of metal and semiconductor physics is reflected by numerous papers since the seminal work by Fuchs [1]. The overwhelming majority of the work is concerned with transport parallel to an impenetrable rough interface, e.g. in the two-dimensional electron gas [2]. Here, a theory of interface scattering based on the Landauer-Büttiker formalism [3] is presented which is concerned with transport normal to the interfaces in the metallic regime. The relation between diffuse and specular scattering at an interface is usually described by introducing a factor p which is determined empirically or derived from a microscopic model of the interface roughness [1, 4]. We will show that diffuse scattering is uniquely connected to the so-called vertex correction. Our approach gives a simple relation between the specular and diffuse part of the transmitted wave and a simple formula for the specularity parameter. The conductance for a system of multiple interfaces can be found by a semiclassical concatenation of a single interface. The theory is applied to find the magnetoconductance in magnetic multilayers, where spin-dependent interface scattering is generally believed to be responsible for the "giant" magnetoconductance or spin valve effect [5, 6, 7, 8, 9, 10, 11, 12]. The

magneto-conductance is well described by a simple formula in terms of the mean free number of traversed interfaces for the majority and minority spin electrons. The mathematical details are presented in Ref. [13]. Here, these results are generalised to include the effect of different effective mass mismatch at the interface and non-vanishing average of the random scattering potential.

Let us first consider scattering at a single interface. The interface roughness is modeled by short-range scatterers that are randomly distributed over the interface with density n_{IR}. The incoming and outgoing electron states are taken to be Bloch waves and are approximated by plane waves. Heterostructures are described by means of spin-dependent potential steps and effective masses. The wave function at an energy E is determined by the Schrödinger equation

$$\left[-\frac{\hbar^2}{2}\nabla\frac{1}{m^*(x)}\nabla + U_C(x) + V(x,y,z)\right]\psi(x,y,z) = E\psi(x,y,z). \tag{1}$$

The conduction band profile, $U_C(x)$, and the effective mass of the electron $m^*(x)$, are simply step functions at $x = 0$. The interface roughness gives rise to the potential $V(x,y,z)$. By integrating out the transverse coordinates (y and z), a one-dimensional equation is obtained [14]. We assume that the particles are incident from the left with transverse momentum k_y^i. To the left of the interface the longitudinal part of the wave function consists of the incoming and reflected waves and to the right side of the interface there are only transmitted right-going waves. For propagating modes, the longitudinal wave function is

$$\varphi_{\xi_y}(x) = \begin{cases} \sqrt{\frac{m_L^*}{\hbar k_\perp^L}}\delta_{\xi_y,\xi_y^i}e^{ik_\perp^L x} + \sqrt{\frac{m_L^*}{\hbar k_\perp^L}}r_{\xi_y,\xi_y^i}e^{-ik_\perp^L x} & x \lesssim 0 \\ \sqrt{\frac{m_R^*}{\hbar k_\perp^R}}t_{\xi_y,\xi_y^i}e^{ik_\perp^R x} & x \gtrsim 0 \end{cases} \tag{2}$$

where ξ_y and $k_\perp$ are the transverse and longitudinal components of the wave vector and $k_\perp^L = [\frac{2m_L^*}{\hbar^2}(E_F - U_C) - k_y^{i2}]^{1/2}$, $k_\perp^R = [\frac{2m_R^*}{\hbar^2}(E_F - U_R) - k_y^{i2}]^{1/2}$. Note that we have normalised the longitudinal parts of the wave function, $\varphi_{\xi_y}(x)$, so that they carry unit flux. The transmission (reflection) coefficient from state k_y^i to state k_y is t_{ξ_y,ξ_y^i} (r_{ξ_y,ξ_y^i}). Evanescent modes correspond to complex longitudinal wave vectors, which should be treated as in Ref. [13]. For low temperatures, the conductance can now be found from the Landauer-Büttiker formalism [3]

$$G = \frac{e^2}{h}\sum_{\xi_y,\xi_y^i}^{propag.}|t_{\xi_y,\xi_y^i}|^2, \tag{3}$$

where the summation is over propagating modes. In matrix notation the transmission coefficients are determined by the equation [14] $(1+\Gamma)t = \Lambda$ where $\Lambda_{\xi_y,\xi_y^i} = \delta_{\xi_y,\xi_y^i}\sqrt{k_\perp^L k_\perp^R}/k_\perp$ and

$$\Gamma_{\xi_y,\xi_y^i} = \sum_n \frac{im^*\gamma_n}{\hbar^2}\frac{\sqrt{k_\perp^R}e^{ik_\perp^R x_n}}{k_\perp}\frac{1}{\sqrt{A}}\frac{1}{\sqrt{k_\perp^R}}\frac{e^{-ik_\perp^L x_n}}{\sqrt{A}}. \tag{4}$$

with $m^* = \sqrt{m_L^* m_R^*}$ and $k_\perp = (m_R^* k_\perp^L + m_L^* k_\perp^R)/2m^*$. This result generalises Eq. (4) in Ref. [13] for the case of different effective mass to the left and to the right of the interface. Current conservation and the continuity of the wave function relate the transmission probabilities and the transmission coefficients as

$$\sum_{\xi_y}^{propag.}\frac{k_\perp}{k_\perp^R}|t_{\xi_y,\xi_y^i}|^2 = \sqrt{\frac{k_\perp^L}{k_\perp^R}}\mathrm{Re}(t_{\xi_y,\xi_y^i}), \tag{5}$$

which has the same form as Eq. (5) in Ref. [13].

The transmission probabilities of present interest are given by the ensemble average of all impurity configurations, which cannot be treated exactly. We have chosen a perturbation approach. The relevant perturbation series are obtained by inverting the matrix relation for t, expanding $(1+\Gamma)^{-1}$ as a power series in Γ and by taking the configurational average. Green functions can be introduced to identify the terms in the expansion and as a tool to understand the nature of the approximations ([13] and references therein). The diagrams contributing to the transmission probability can be classified as crossing or non-crossing. The crossing diagrams describe phase coherence and are e.g. responsible for weak (Anderson) localisation of the wave function [16]. Neglecting crossing diagrams, i.e. phase coherent scattering between different defects, it is possible to find the transmission probability in terms of the irreducible self-energy Σ [13],

$$\langle|t_{\xi_y,\xi_y^i}|^2\rangle = \delta_{\xi_y,\xi_y^i}\frac{k_\perp^R k_\perp^L}{|k_\perp + i\frac{m^*}{\hbar^2}\Sigma|^2} + \frac{k_\perp^R}{|k_\perp + i\frac{m^*}{\hbar^2}\Sigma|^2}\frac{-\frac{m^*}{\hbar^2}Im(\Sigma)}{\sum_{\xi_y^i}^{propag.}\frac{k_\perp^L}{|k_\perp^L + i\frac{m^*}{\hbar^2}\Sigma|^2}}\frac{k_\perp^L}{|k_\perp^L + i\frac{m^*}{\hbar^2}\Sigma|^2}. \tag{6}$$

Quantum interference between different scattering centers is neglected. The approximation can therefore be labeled as semiclassical and breaks down when the distance between dephasing inelastic collisions becomes larger than the average separation between scatterers. Electrons are scattered specularly at the interface if the transverse component of the wave vector is conserved, which is the first term on the right hand side of Eq. (6). The second term clearly represent the diffuse scattering contribution, which vanishes if the vertex correction is not taken into account.

In the following we set $\Delta U_C = 0$ and $\Delta m^* = 0$, which considerably simplifies the analytical treatment. It is interesting to make contact with the traditional treatment of interface roughness in terms of the specularity factor p. The factor p_i defined as the fraction of electrons transmitted specularly is found to be

$$p_i(\theta) = \frac{\cos(\theta)}{\eta_{IR} + \cos(\theta)}, \tag{7}$$

where $\eta_{IR} = -m^*\mathrm{Im}(\Sigma)/\hbar^2 k_F$ is a scattering parameter and θ is the angle of incidence of an electron wave vector measured from the surface normal. This expression is exact for

semiclassical transport and the specularity factor is independent of the real part of the self energy. Diffuse scattering increases for larger incoming angles as shown in Fig. (1) Electrons with wave vector perpendicular to the interface are scattered purely specularly, and electrons with wave vector parallel to the interface plane will be completely diffused. A similar relation can be derived for reflected electrons.

To lowest order in the self-energy $m^*\Sigma/\hbar^2 k_F$ the conductance is

$$G = \frac{2e^2}{h}\frac{Ak_F^2}{4\pi}[1 - 4\eta_{IR} + 2\eta_{IR}], \tag{8}$$

and is independent of the real part of the self energy. The first term is the Sharvin conductance which is proportional to the sample cross section A. The second term reduces the conductance due to specular scattering. The third, diffuse term increases the conductance by opening additional channels for electron transport.

The self-energy is

$$\Sigma^D = n_{IR}\gamma - i\frac{m^*}{\hbar^2}\frac{n_{IR}}{\pi}\gamma^2 k_F[1 - i\sqrt{\alpha^2 - 1}] \tag{9}$$

in the Born approximation, where the average scattering strength $\bar{\gamma} = \sum_n \gamma_n/n_{IR}A$ and the mean square value of the scattering strength $\gamma^2 = \sum_n \gamma_n^2/n_{IR}A$ are introduced. Here a ultraviolet divergence in the summation over intermediate evanescent states has been cut-off at a wave-vector αk_F to account for the finite range of the potential. $\alpha \geq 1$, but not much larger than unity for magnetic multilayers, since the range can not be shorter than a d orbital radius. The Born approximation is valid in the weak scattering limit. $|m^*\Sigma^D/\hbar^2 k_F| \ll 1$ and $m^*\gamma k_F/\pi\hbar^2 \ll 1$, which means that the probability of strong scattering by a single impurity is small. The scattering parameter is in this approximation $\eta_{IR} = n_{IR}\gamma^2/\pi$. The specularity factor is not affected by the non-zero average of the scatterers. In the weak scattering limit, the non-zero average of scatterers has also no effect on the conductance.

We will now study the situation where all scatterers have equal magnitude of strength, such that $|\gamma_n| = \gamma$. The self-energy is calculated in the single-site approximation, i.e., using the exact cross-section for isolated defects but neglecting crossed diagrams which stand for quantum interference between different defects

$$\Sigma^D = \frac{n_{IR}\gamma - i\frac{m^*}{\hbar^2}\frac{n_{IR}}{\pi}\gamma^2 k_F(1 - i\sqrt{\alpha^2 - 1})}{1 + (\frac{m^*\gamma k_F}{\pi\hbar^2}(1 - i\sqrt{\alpha^2 - 1}))^2}. \tag{10}$$

This result reduces to the Born result in the weak scattering limit ($m^*\gamma k_F/\hbar^2\pi \ll 1$). For strong scattering ($m^*\gamma k_F/\hbar^2\pi \gg 1$), but to lowest order in n_{IR}, we obtain the interesting result that

$$G = \frac{e^2}{h}(\frac{2Ak_F^2}{4\pi} - \frac{N_{IR}}{\alpha^2}). \tag{11}$$

Here $|m^*\bar{\gamma}k_F/\hbar^2\pi| \ll (m^*\gamma k_F/\hbar^2\pi)^2$ in the present regime has been used. The conductance is reduced by a factor proportional to the number of defects, $N_{IR} = An_{IR}$. Each scatterer effectively blocks one channel and the conductance becomes independent on the scattering strength. This blocking is somewhat reduced by a factor $1/\alpha^2$ via a "leak" of evanescent states. An experiment is proposed to test this expression: Insert a layer (or a multilayer, see below) with strong short-range scatterers between two perfect leads. By measuring the conductance and the number of impurities the theory can be checked and the "leaking factor" α can be determined which provides information about the scattering potential. A non-zero average of scatterers has no effect on the conductance.

Results for a single interface can be generalised to a multilayer situation where interface scattering and bulk impurity scattering is taken into account. Semiclassical concatenation of transmission probabilities [14] is consistent with the neglect of crossing diagrams in the single interface scattering. The transmission properties do not change with the distance between the interfaces in this approximation. By allowing the interfaces to be infinitesimally close to each other, one can convince oneself that the relation between the transmission probabilities and the transmission coefficients, Eq. (5), still holds for the N-interfaces configuration. Concatenation of the *diagonal* transmission coefficients is straightforward and the conductance for transport through N interfaces is

$$\frac{G^{(N)}}{G^0} = 1 - 2(N\eta_{IR}) + 2(N\eta_{IR})^2\ln(1 + \frac{1}{N\eta_{IR}}). \tag{12}$$

This equation has been verified by comparison with numerical results for the concatenated total transmission probabilities Eq. (6). The conductance obtained by neglecting the diffuse scattering in Eq. (6) gives a similar result, but the scattering parameter is increased by a factor 2. The diffuse contribution due to the vertex correction is therefore important. The conductance calculated with and without the diffuse part is shown in Fig. (2). A bulk system is modeled by N interfaces with an interface scattering parameter η_{BI}^{2D}. Letting $N \to \infty$ and $\eta_{BI}^{2D} \to 0$ but keeping $N\eta_{BI}^{2D} = L\eta_B$, where L is the length of the bulk material and η_{BI} is the scattering parameter for the bulk system. The conductance for a multilayer is

$$\frac{G^{(N)}}{G^0} = 1 - 2(\frac{N}{\hat{N}}) + 2(\frac{N}{\hat{N}})^2\ln(1 + \frac{\hat{N}}{N}), \tag{13}$$

where $\hat{N}$ is the mean free number of traversed interfaces given by $\hat{N} \equiv [\eta_{IR} + L\eta_{BI}]^{-1}$. This relation agrees with Eq. (11) in Ref. [9] for $\Delta U_C = 0$. In the large N limit a Drude-like (Ohm's law) expression is obtained for the conductivity of a thick multilayer

$$\sigma_\infty = \lim_{N\to\infty} NLG^{(N)}/A = \frac{2e^2}{3\pi}k_F^2\hat{N}L, \tag{14}$$

which agrees with the results of Zhang and Levy [8]. The Drude result is approached rather slowly.

For a magnetic multilayer it is now straightforward to find the conductance by including spin-dependent interface scattering and bulk scattering. The difference in mean free number of traversed interfaces between both spin channels is $\Delta\hat{N}$ and the spin-averaged result is $\hat{N}$. The relative magnetoconductance of an antiferromagnetically coupled multilayer $\Delta G/G$ is shown in Fig. (3), where $\Delta G = G^F - G^{AF}$ and $G = (G^F + G^{AF})/2$.

The relative magnetoconductance depends on the ratios $\Delta\hat{N}/\hat{N}$ and $N/\hat{N}$. The spin-valve effect increases with the number of bilayers and saturates at the Drude limit for $N \gg \hat{N}$ as given by Zhang and Levy [8]. In this limit of a magnetic superlattice the relative magnetoconductance is $(\Delta G/G)^{Drude} \propto (\Delta\hat{N}/2\hat{N})^2$.

The effect of the potential steps and different effective masses in the materials on the conductance can be found by concatenation of Eq. (6). This should be done numerically since the expression for the N-layer conductance is very complicated.

In summary, we have derived semiclassical expressions for perpendicular transport through disordered interfaces which are exact for the present model. The effect of a different effective mass to the right and to the left of the interface is included in the formalisme. In the weak scattering limit the effect of a non-zero average of the random potential on the conductance is found to be of a higher order in the concentration of scatterers n_{IR} and can be neglected in most cases. An experiment to check the theory is proposed which might lead to a deeper understanding of the scattering process and the microscopic structure of disordered interfaces. A simple, semiclassical formula for the giant magnetoconductance of antiferromagnetically coupled magnetic multilayers in terms of the mean free number of traversed interfaces for the majority and minority spins is derived.

This work is part of the research programme of the "Stichting voor Fundamenteel Onderzoek der Materie (FOM)", which is financially supported by the "Nederlandse Organisatie voor Wetenschappelijk Onderzoek (NWO)".

References

[*] Permanent address: University of Trondheim, The Norwegian Institute of Technology, Faculty of Physics and Mathematics, Division of Physics, N-7034 Trondheim.

[1] K. Fuchs, Proc. Philos. Camb. Soc. 34, 100 (1938).

[2] T. Ando, A.B. Fowler, and F. Stern, Rev. Mod. Phys. 54, 437 (1982).

[3] R. Landauer, Z. Phys. B 68, 217 (1987).

[4] S.B. Soffer, J. Appl. Phys. 38, 1710 (1967).

[5] M.N. Baibich, J.M. Broto, A. Fert, F. Nguyen van Dau, and F. Petroff, Phys. Rev. Lett. 21, 2472 (1988); G. Binasch, P. Grünberg, F. Saurenbach, and W. Zinn, Phys. Rev. B, 39, 4828 (1989). For a recent review see R. Coehoorn, Europhysics News 24, 43 (1993).

[6] W.P. Pratt, S.F. Lee, R. Loloee, P.A. Schroeder and J. Bass, Phys. Rev. Lett. 66, 3060 (1991).

[7] M.A.M. Gijs, S.K.J. Lenczowski and J.B. Giesbers, preprint.

[8] S. Zhang and P.M. Levy, J. Appl. Phys. 69, 4786 (1991); S. Zhang and P.M. Levy, Phys. Rev. 45, 8689 (1992); H.E. Camblong, S. Zhang, and P.M. Levy, Phys. Rev. B 46, 4735 (1993).

[9] G.E.W. Bauer, Phys. Rev. Lett. 69, 1676 (1992). The Erratum 70, 1733 (1993) is superseded by the present results.

[10] R.Q. Hood and L.M. Falicov, Phys. Rev. B 46, 8287 (1992).

[11] T. Valet and A. Fert, preprint.

[12] Y. Asano, A. Oguri and S. Maekawa, preprint.

[13] A. Brataas and G.E.W. Bauer, preprint.

[14] M. Cahay, M. McLennan and S. Datta, Phys. Rev. B 37, 10125 (1988).

[15] P.M. Bagwell, Phys. Rev. B 41, 10354 (1990).

[16] P.A. Lee and T.V. Ramakrishnan, Rev. Mod. Phys. 57, 2 (1985).

[17] J. Inoue, A. Oguri, and S. Maekawa, J. Phys. Soc. Jpn. 60, 376 (1990).

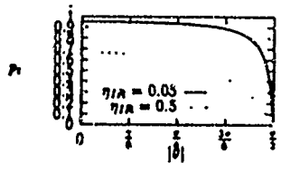

Figure 1: Fraction of electrons transmitted specularly as a function of incoming angle to the normal of the interface. The specularity factor is shown for η_{IR} = 0.05 and η_{IR} = 0.5 (dotted line).

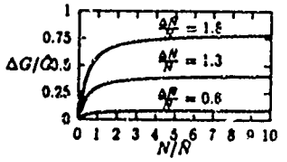

Figure 2: Conductance for a metallic multilayer. The dotted line is the conductance where only specular scattering is considered. The solid line shows the conductance where diffuse scattering is included.

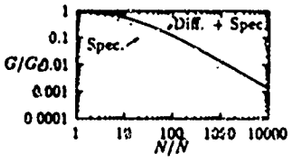

Figure 3: Magnetoconductance for an antiferromagnetically coupled magnetic multilayer. The curves illustrate the effect of spin dependent mean free number of traversed interfaces

ThP33

Giant third-order nonlinear susceptibilities for in-plane far-infrared excitation of single InAs quantum wells

A. G. Markelz, E.G. Gwinn, M. S. Sherwin
Center for Free Electron Laser Studies, University of California, Santa Barbara

C. Nguyen and H. Kroemer
Electrical and Computer Engineering, University of California, Santa Barbara

Third order, free carrier nonlinear susceptibilities, $\chi^{(3)}$, have been measured between 19 cm^3/esu and 23 cm^3/esu for three InAs/AlSb quantum wells with sheet densities between 2.5×10^{12} cm^{-2} and 8×10^{12} cm^{-2}. We find that these wells are strongly nonlinear at far infrared frequencies. odd harmonics to seventh order have been observed at high incident intensities, and the peak value of $\chi^{(3)}$ reaches ~ 1 esu. This is several orders of magnitude larger than previously reported values for $\chi^{(3)}$ in bulk n-GaAs (10^{-4} esu[1]) and in quantum well GaAs (10^{-7} esu[2]). The large magnitude of $\chi^{(3)}$ is attributed to the high carrier density in the InAs wells and to the strong non-parabolicity of the conduction band in InAs. However, the free carrier $\chi^{(3)}$ for bulk InAs predicts a density dependence different from that observed, and the measured decrease in $\chi^{(3)}$ with increasing intensity indicates non perturbative response. We find that the anisotropy of $\chi^{(3)}$ displays the expected 4-fold symmetry.

Recently, high quality InAs/AlSb wells have been grown with 3D electron densities as high as $\sim 10^{19}$ cm^{-3} in the InAs wells[3]. The density-, mass-, and frequency-dependence of the free-carrier, third-order susceptibility $\chi^{(3)}$ due to non-parabolicity in narrow-gap semiconductors leads one to expect that these wells should be strongly nonlinear materials at far-infrared frequencies. For degenerate, bulk material, $\chi^{(3)}$ is,

$$\chi^{(3)}(\omega = \omega + \omega - \omega) = -\frac{ne^4}{m^{*3}} \frac{1}{F_4(\omega - \frac{i}{\tau})^2 (3\omega - \frac{i}{\tau})(1 + \frac{\frac{3\hbar^2}{5E_g}}{1 + \frac{4\hbar^2}{E_g}})^{3/2}} \qquad (1)$$

where τ is the momentum relaxation time[4, 5]. This relation, which is derived assuming a perturbative fundamental field, has been confirmed experimentally in *bulk*, n-type InAs [6]. However, we find that the density-dependence of $\chi^{(3)}$ for InAs quantum wells cannot be described solely by bulk nonparabolicity as in Eq. 1, and that $\chi^{(3)}$ depends on the incident intensity, indicating non-perturbative response.

The sketch on the left side of Fig. 1 shows the structure of the MBE-grown, 150 Å-wide InAs quantum wells studied here. The 1.35 eV conduction-band offset between the InAs and the AlSb barrier allows large sheet densities. Samples with $n_s = 2.5 \times 10^{12}$ cm^{-2} and $n_s = 4 \times 10^{12}$ cm^{-2} are δ-doped by Te sheets set back 500 Å from the top side of the wells. For the $n_s = 8 \times 10^{12}$ cm^{-2} sample, the Te sheets are set back by 100 Å from each side of the well. Table 1 gives the effective mass at the Fermi energy and the 300 K mobility. Mobilities and n_s were measured in a Van-der-Pauw geometry. The effective masses for two of the samples were determined from 4.2 K cyclotron resonance measurements, and in both cases agreed well with the Kane model[7,8]. Because n_s is nearly independent of temperature, we expect these masses

to apply to our 300 K experiments. The effective mass for the lowest density sample was calculated using the Kane model [8].

The right side of Fig. 1 shows the optical set-up. After a small fraction of the power in the incident beam is split off to a reference detector, the radiation is focussed at normal incidence on the sample. We vary the power by inserting plexiglass attenuators before the beam splitter. The radiation from the sample is collimated over a short section, and focussed onto a cooled bolometer through a high-rejection, low-pass waveguide filter, which prevents the fundamental radiation from reaching the bolometer. A Fabry-Perot etalon in the collimated beam is used to measure the frequency content of the radiation from the sample.

Table I. Physical Parameters of the tested wells

n_s (x 10^{12}/cm^2)	2.5	4.0	8
m*	0.051	0.0521	0.057
μ (x 10^3cm^2/Vs)	1.9	2.2	1.9

* Effective mass calculated from Kane model for this sample only

In preliminary experiments, we used a CO_2 TEA - pumped methyl fluoride molecular gas laser (MGL) at 29.5 cm^{-1}. The MGL provides short pulses with peak power to several MW/cm^2. For the $n_s = 8 \times 10^{12}$ cm^{-2} sample, Fabry Perot scans showed that the sample emitted odd harmonics up to the 7th order [9]! To our knowledge, this is the highest order harmonic generation seen from a semiconductor sample. Because our MGL has complex, erratic pulse structure, it is unsuitable for quantitative measurements of nonlinear susceptibilities. To determine $\chi^{(3)}$ for the InAs wells, we have used the UCSB Free-Electron Laser (FEL), which provides lower peak powers than the MGL (to ~50 kW/cm^2), but which has much cleaner pulse structure. All of the following discussion concerns measurements made with the FEL. In these experiments, the experimental area was enclosed with a large glove bag, and purged with dry N_2 gas to prevent loss of signal due to water vapor absorption. The harmonic content in the FEL radiation is removed with a low pass capacitive mesh filter (3dB at 25 cm-1), followed by a fluorogold filter. Using the FEL, we have detected only third harmonic radiation from the electron gas in the InAs wells. Improved FEL peak power may make observable the higher-order harmonics found with the MGL.

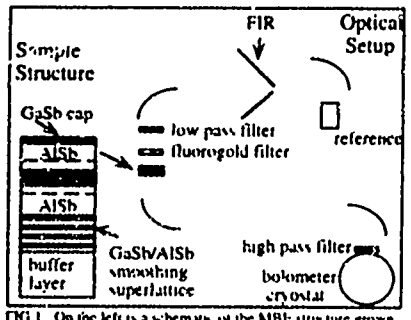

FIG 1. On the left is a schematic of the MBE structure grown. The dashed lines in the AlSb regions are for the Te δ-doped regions. On the right is the optical setup for the harmonic generation experiment.

For all of the samples studied, and for all frequencies investigated (from 19 cm^{-1} to 23 cm^{-1}), we find that the intensity of the third harmonic emitted by the samples, $I(3\omega)$, has a *sub-cubic* dependence on the fundamental intensity, $I(\omega)$, to the lowest $I(\omega)$ that produces a detectable signal. In the most commonly studied regime of nonlinear response, the fundamental field can be treated perturbatively, and the intensity of the n^{th} harmonic scales as the n^{th} power of the fundamental: $I(n\omega) \propto I(\omega)^n$. Thus, the observed sub-cubic dependence of $I(3\omega)$ on $I(\omega)$ may indicate that our wells are in a non-perturbative regime. Mayer and Keilmann have also shown sub-cubic power dependence in experiments on free-carrier third harmonic generation from n-GaAs[1], at the much higher peak powers provided by a MGL. They ascribed this behavior to intervalley scattering from the Γ valley to the L valley, where $\chi^{(3)}$ should be much smaller. For InAs, the Γ to L valley energy difference is 1.17 eV, compared to ~ 0.3 eV in GaAs. Thus, it is not likely that intervalley scattering can explain the power dependence that we observe.

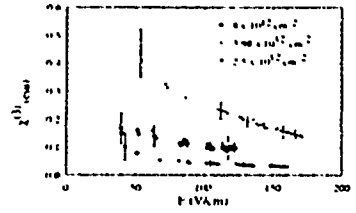

FIG 2. $\chi^{(3)}$ measured at 22 cm^{-1} for the three samples vs field at the well.

To compare our results on InAs quantum wells to earlier results on bulk InAs[6], we have made an absolute determination of $\chi^{(3)}$, which is proportional to $[I(3\omega)/I(\omega)^3]^{1/2}$. Reference materials with known $\chi^{(3)}$ are unavailable at the frequencies used here. The fundamental intensity incident on the sample is found from the spot size measured at the sample plane, and from the incident power, which is measured with an electrically-calibrated photo-acoustic detector (Thos. Keating). The collected third harmonic intensity is calibrated by tuning the FEL to 3ω and measuring the bolometer response through the high pass filter, relative to the response of the photo-acoustic detector.

We find a bulk $\chi^{(3)}$ by treating the InAs well as a bulk slab with $n_{1D} = n_s/150$ Å. To account for etalon and phase matching effects, we use Bethune's method for calculating the harmonic field for a multilayer system[10]. This gives a calculated linear transmission that agrees well with the transmission measured with an FTIR. $\chi^{(3)}$ is calculated as:

$$\chi^{(3)} = \sqrt{\frac{c}{(8\pi)} \frac{I(3\omega)}{I(\omega)^3 |F|^6}} \qquad (2),$$

where $|F|^2$ is a factor that corrects for phase-matching and standing-wave effects[9].

Figure 2 shows the dependence of $\chi^{(3)}$ on the fundamental field at the plane of the electron gas, for all three samples, at 22 cm^{-1}. The incident polarization is along ⟨110⟩. The decrease in $\chi^{(3)}$ with increasing fundamental field reflects the sub-cubic behavior discussed above. The dependence of $\chi^{(3)}$ on carrier density shown in Fig. 2 does not agree with Eq. 1: the sample with the middle charge density has the largest $\chi^{(3)}$. However, for the lowest density

sample, the magnitude of $\chi^{(3)}$ is comparable to that expected from scaling the bulk susceptibility calculated by Jha and Bloembergen for bulk InAs [3] to our frequencies and mobilities We calculate a bulk $\chi^{(3)}$ of 0 06 esu for $n_{3D} = 1x10^{18}$ cm^{-3}, which corresponds to a sheet density $n_s = 1.5x10^{12}$ cm^{-2} for a 150 Å slab This reasonable agreement with the range of $\chi^{(3)}$ observed for our lowest density sample may be fortuitous, due to the apparent non-perturbative response, and the unusual density-dependence of $\chi^{(3)}$

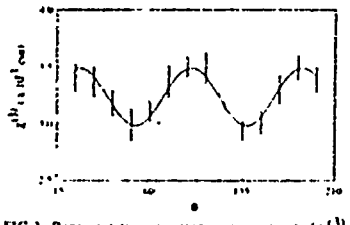

FIG 3 Representative anisotropy measurement of $\chi^{(3)}$ The measurement shown is for $n_s = 2.5 \times 10^{12}$ cm^{-2} and frequency 23 cm^{-1} The solid line is a fit to the data giving $\sigma = 1.18 \pm 0.03$ All of the above data is for the same incident electric field 3 9 ± 0 1 kV/cm

Finally, we show that the measured anisotropy in $\chi^{(3)}$ is consistent with the crystal symmetry of InAs. Figure 4 shows the dependence of $\chi^{(3)}$ at fixed incident intensity on the polarization of the incident field, for the $n_s = 2.5x10^{12}$ cm^{-2} sample. The maxima in $\chi^{(3)}$ occur when the polarization is aligned with the (110) axis, and $\chi^{(3)}$ has the expected 90 degree periodicity. A cosine-squared fit to the data gives an anisotropy of 1.18 ± 0.03, comparable to the measured value for GaAs at 45 cm^{-1}[1] All samples and all frequencies measured give comparable anisotropy .

In conclusion, we have found that electrons in single, remotely-doped InAs wells produce large, 300 K $\chi^{(3)}$ to ~ 1 esu, relative to a GaAs/ $\chi^{(3)} \sim 10^{-9}$ esu[1]) and n-polyacetylene ($\chi^{(3)} \sim 10^{-7}$ esu[2]). It may be that a useful device can be fabricated from a superlattice of InAs wells Future work requires extending our sensitivity to lower powers, at which we expect to recover a cubic power dependence, and cooling the sample to help elucidate the scattering contribution to $\chi^{(3)}$

The authors would like to thank S J Allen Jr , J Heyman, N G Asmar and K C Craig for many useful discussions, and Mani Sundaram for providing us with the results of his cyclotron resonance experiments In addition we are grateful for the assistance of the staff at the Center for Free Electron Laser Studies Work at the Center for Free Electron Laser Studies was supported by the Office of Naval Research (N00014-92-J 1452) Clean room use was supported by the NSF Center for Quantized Electronic Structures Grant No DMR88 *1430

[1] A. Mayer and F. Keilmann, Phys Rev B 33, 6962 (1986).
[2] C Halvorsen, D Moses, T W. Hagler, Y Cao, A H. Heeger, Syn Met. 49-50, 49 (1992)
[3] C Nguyen, B Brar C R. Bolognesi, J. J. Pekarik, H. Kroemer, J H English, J Elec. Mat. 22, 253 (1993)
[4] S S. Jha and N. Bloembergen, Phys Rev 171, 891 (1968)
[5] P A Wolff and G A Pearson, Phys Rev. Lett 17, 1015 (1966).
[6] J J Wynne, Phy Rev 178, 1295 (1969)
[7] M Sundaram, S J Allen Jr , C Nguyen, H Kroemer to be published
[8] E. O. Kane, J. Phys Chem Solids 1, 249 (1957)
[9] A G. Markelz et al, to be published
[10] D S Bethune, J Opt Soc Am B 6, 910 (1989)

ThP34

Enhancement of Free-to-bound Transitions due to Resonant Electron Capture in Be-doped AlGaAs/GaAs Quantum Wells

K.Muraki, Y.Takahashi*, A.Fujiwara, S.Fukatsu, and Y.Shiraki

Research Center for Advanced Science and Technology (RCAST), The University of Tokyo, 4-6-1 Komaba, Meguro-ku, Tokyo 153, Japan
**IBM Research, Tokyo Research Laboratory, 1623-14, Shimo-Tsuruma, Yamato, Kanagawa 242, Japan*

We report a new phenomenon concerning the photoluminescence from $Al_{0.3}Ga_{0.7}As$/GaAs quantum wells with Be-delta-doping at the well center For excitation photon energy larger than the barrier band gap, the relative intensity of the free-to-bound and the excitonic transitions was found to display a strong oscillation as a function of the well width For "resonant" well widths, the free-to-bound transition was observed to be 2 times as strong as the excitonic transitions. We correlate this phenomenon with the electron capture efficiency from the barrier into the well, which also exhibits a similar oscillation as a function of the well width.

Photoluminescence (PL) spectra of undoped quantum wells are usually dominated by intrinsic, i e , free exciton transitions even at very low temperatures. This makes a sharp contrast to bulk materials, in which extrinsic luminescence dominates the low-temperature spectra even in samples of highest purity This difference has been attributed to the enhanced radiative transition rate of free excitons in quantum wells which results from the increased binding energy and the broken translational symmetry along the quantization axis, i e , the lack of polarion effect [1] Thus, in undoped quantum wells most of the photogenerated carriers recombine as free excitons before they are captured by residual impurities To this end, studies of impurity-related luminescence in quantum wells have been done mainly on intentionally doped samples. Various spectral features originating from heavy-hole excitons bound to neutral and ionized donors [2-4] and neutral acceptors [5] have been identified Free-to-bound transitions, however, are usually very weak or absent even in doped samples [5] Holtz et al have reported that the resonant excitation at the heavy- or light-hole exciton energy enhances the free-to-bound transition in Be-doped quantum wells [6] For above-barrier excitation, however, they have reported that the free-to-bound transition was not observed for Be doping concentration of $5x10^{18}$ cm^{-3} per well

In this paper, we report a new phenomenon concerning the photoluminescence from $Al_{0.3}Ga_{0.7}As$/GaAs quantum wells with Be-delta-doping at the well center ($[Be] = 10^{19}$ cm^{-2}) Under excitation by light with photon energy larger than the barrier band gap, we have observed a significant enhancement of the free-to-bound transition for particular well widths Furthermore, the relative intensity of the free-to-bound and the excitonic transitions displayed a strong oscillation as a function of the well width, featuring a series of resonance peaks appearing periodically For these "resonant" well widths, the free-to-bound transition was observed to be 2 times as strong as the excitonic transitions We correlate this phenomenon with the electron capture efficiency from the barrier into the well, which also exhibits a similar oscillation as a function of the well width [7-9]

Samples are $Al_xGa_{1-x}As$/GaAs (x = 0.3) quantum well structures grown at 580 °C on semi-insulating GaAs (100) substrates in a molecular beam epitaxy reactor (VG semicon V80H) Each sample contained several GaAs quantum wells separated by 50-nm AlGaAs barriers Be was delta-doped at the well center to an areal density of 10^{19} cm^{-2} per well Delta-doping was employed to minimize the spectral broadening due to the variation of the bound exciton energy with the doping position [10] Photoluminescence was measured at 6 8 17 K using an Ar^+-ion laser as the excitation light source The excitation power density was about 0 3 W cm^{-2}

Figure 1 shows the 17 K photoluminescence spectra of a sample containing four quantum wells with various well widths. Peaks labeled FE and BE are due to the radiative decay of free excitons and excitons bound to neutral acceptors, respectively. The energy separation between FE and BE, i.e., the binding energy of an exciton to a neutral acceptor, is 4.1 and 4.3 meV for the 9.0- and 6.3-nm wells, respectively. These values compares favorably with the reported value [5]. For narrower two wells, FE and BE are not resolved because of the increased inhomogeneous broadening. The peaks at 1.529 and 1.587 eV, labeled F-B, are assigned to the free-to-bound transitions associated with the 9.0- and 4.5-nm wells, respectively, in which electrons in the $n = 1$ conduction subband recombine with holes bound to neutral acceptors. It is surprising that such intense peaks are observed for the free-to-bound transition in quantum wells with low doping concentration. More interesting is that the free-to-bound transition is absent for the 6.3- and 3.2-nm wells though the doping concentration is the same. These observations lead us to speculate that the relative intensity of the free-to-bound and the excitonic transitions is a strong function of the well width.

In order to investigate the well-width dependence in more detail, we adopted the following procedure; in the molecular beam epitaxy of the samples the substrate rotation was deliberately interrupted during the growth of the quantum well layer, thereby allowing the well width to vary across the wafer due to inhomogeneous Ga beam flux. Thus, by scanning the laser spot on the sample, one can systematically investigate the PL spectrum as a function of the well width. In Fig. 2 photoluminescence spectra taken at 6 or 8 K are shown for various well widths. The well width was calculated from the transition energy of the $n = 1$ heavy-hole free exciton. It is seen that the relative intensity of the free-to-bound transition and the excitonic transitions drastically changes with the well width. Meanwhile the total intensity remains the same.

In Fig. 3 the PL intensity ratio of the free-to-bound transition to the excitonic (free exciton plus bound exciton) transitions is plotted as a function of the well width. The PL intensity ratio exhibits a strong oscillation as a function of the well width. Up to five peaks labeled M_n ($n = 2$-6) are clearly observed, accompanied by subsidiary peaks labeled L_n ($n = 2$-5). (The peaks L_5 and M_6 are overlapped.) It is noteworthy that the M_n peaks appear almost periodically with a period of about 3.7 nm.

We have further carried out the PL mapping experiments with various excitation photon energies from below and above the barrier band gap using an Ar^+-ion laser pumped dye (DCM) laser and a Ti:sapphire laser. The results were almost the same as that in Fig. 3 when the excitation photon energy is larger than the barrier band gap. In contrast, the oscillation was not observed for the below-barrier excitation [11]. These results strongly suggest that the capture of carriers from the barrier into the well is the controlling process causing the oscillation. According to the effective-mass calculation taking the conduction band nonparabolicity [12] into account, the position of the M_n peak corresponds to the well width for which the energy of the n-th conduction subband in the quantum well coincides with the conduction band-edge of the barrier. And that of the L_n peak compares favorably with the well width for which the energy of the n-th conduction subband lies one LO-phonon energy (36 meV) below the barrier band-edge. Brum and Bastard [7] have calculated the capture time of carriers as a function of the well width, and predicted that for such well widths the electron capture efficiency is resonantly enhanced. The experimental evidence for this, the resonant electron capture, has been first given by Fujiwara et al. using ex-photoluminescence [8]. And recently, the resonant electron capture time has been successfully measured by Blom and co-workers using subpicosecond luminescence technique [9]. Therefore, it is reasonable to consider that the free-to-bound transition is enhanced when the electron capture efficiency is high.

We explain this by considering the charge build-up in the quantum well induced by the different capture time of electrons and holes. Photoexcitation creates an equal number of electrons and holes in the barrier, however, one of these two types of carriers can be captured preferentially depending on their capture time. In the steady-state, *the number of electrons and holes captured per unit time must be equal*. It should be noted, however, that *the number of electrons and holes present in the well can be different* even in the steady-state. Thus, the negative charge will build-

up in the quantum well if the capture time of an electron is shorter than that of a hole. In the usual off-resonant condition, the capture time is shorter for holes due to the larger density of states in the valence band [7]. In this hole-rich condition the excess holes will immediately neutralize the ionized acceptors, if present. Thus, all the acceptors remain neutral at low temperatures. Since the radiative lifetime of the free-to-bound transition is much longer than that of the excitons [13], most of the carriers recombine as excitons in this case. In the resonant condition, on the other hand, the capture efficiency becomes larger for electrons. In this electron-rich condition the excess electrons, which can not participate in exciton formation, will recombine with holes bound to acceptors, thereby creating ionized acceptors. These ionized acceptors are subsequently neutralized by trapping free holes, which decreases the number of holes available for the exciton formation. As a result, the exciton formation is quenched and excess electrons are left in the conduction subband. These electrons recombine with holes bound to neutral acceptors as in the first step. Since this continues like a chain reaction, only a slight excess of electrons can lead to a drastic enhancement of the free-to-bound transition. This qualitatively explains the correlation between the enhancement of the free-to-bound transition and the electron capture efficiency.

In summary, we have reported a new phenomenon concerning the photoluminescence from quantum wells doped with Be. For above-barrier excitation, a strong oscillation of the relative intensity of the free-to-bound and the excitonic transition was observed as a function of the well width. This phenomenon has been tentatively attributed to the charge build-up in the quantum well induced by the resonant capture of electrons, and the resultant ionization of the acceptors. These ionized acceptors quench the exciton formation by trapping free holes out of the photogenerated electron-hole pairs and enhance the free-to-bound transition. Since this charge build-up is not specific to Be-doped quantum wells and considered to occur generally in quantum well structures, we expect that it might shed light on some aspects of the carrier/exciton dynamics in intrinsic quantum wells. However, further investigation is required to confirm this assertion.

One of the authors (K.M.) was supported by Fellowships for Japanese Junior Scientists (JSPS). The authors thank to S. Ohtake for his technical assistance.

References

1 J. Feldmann, G. Peter, E. O. Göbel, P. Dawson, K. Moore, C. Foxon, and R. J. Elliott, Phys. Rev. Lett. **59**, 2337 (1987).
2 Y. Nomura, K. Shinozaki, and M. Ishii, J. Appl. Phys. **58**, 1864 (1985).
3 X. Liu, A. Petrou, B. D. McCombe, J. Ralston, and G. Wicks, Phys. Rev. B **38**, 8522 (1988).
4 D. C. Reynolds, C. E. Leak, K. K. Bajaj, C. E. Stutz, R. L. Jones, K. R. Evans, P. W. Yu, and W. M. Theis, Phys. Rev. B **40**, 6210 (1989).
5 P. O. Holtz, M. Sundaram, K. Doughty, J. L. Merz, and A. C. Gossard, Phys. Rev. B **40**, 12338 (1989).
6 P. O. Holtz, M. Sundaram, J. L. Merz, and A. C. Gossard, Phys. Rev. B **41**, 1489 (1990).
7 J. A. Brum, and G. Bastard, Phys. Rev. B **33**, 1420 (1986).
8 A. Fujiwara, S. Fukatsu, Y. Shiraki, and R. Ito, Surf. Sci. **263**, 642 (1992).
9 P. W. M. Blom, C. Smit, J. E. M. Haverkort, and J. H. Wolter, Phys. Rev. B **47**, 2072 (1993).
10 G. C. Rune, P. O. Holtz, M. Sundaram, J. L. Merz, A. C. Gossard, and B. Monemar, Phys. Rev. B **44**, 4030 (1991).
11 For below-barrier excitation, the PL intensity ratio depends on the excitation photon energy rather than the well width, which is far beyond the scope of this study and will be published elsewhere.
12 T. Ruf and M. Cardona, Phys. Rev. B **41**, 10747 (1990).
13 We have performed time-resolved measurements and observed the radiative decay time of the free to bound transition as long as 34 ns, which will be published in the Future.

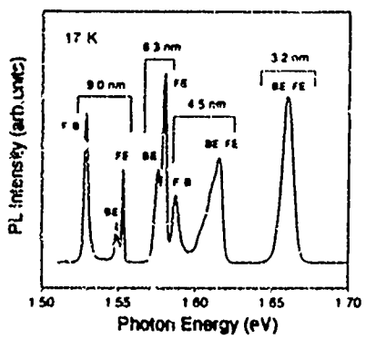

Figure 1

17-K PL spectra of an $Al_{0.3}(Ga_{0.7}As/GaAs$ quantum well structure with various well widths. Each well is doped with Be to an areal density of $(2)10^{11}$ cm^{-2}.

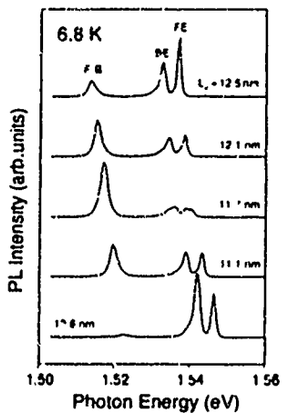

Figure 2

6.8-K PL spectra of Be-doped $Al_{0.3}(Ga_{0.7}As/GaAs$ quantum wells with various well widths.

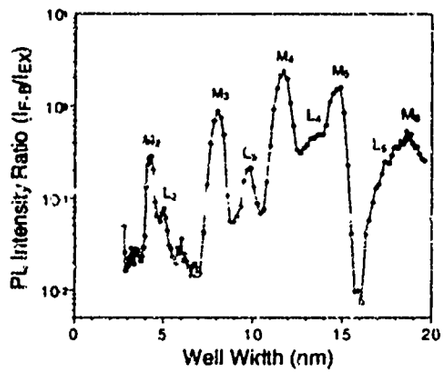

Figure 3

PL intensity ratio of the free to-bound transition to the excitonic three exciton plus bound exciton transition as a function of the well width.

ThP35

Constructive Superposition of Field- and Carrier induced Absorption Changes in Hetero-n-i-p-i Structures

M. Kneissl, K.H. Gulden, P. Kiesel, A. Luczak, S. Malzer, G.H. Döhler
Institut für Technische Physik, Universität Erlangen,
Erwin-Rommel-Str. 1, 91058 Erlangen, Germany

X. Wu and J.S. Smith
University of California at Berkeley, Berkeley, CA 94720, USA

By applying a voltage U_{pn} to hetero-n-i-p-i structures with n- and p-contacts, both the internal fields in the intrinsic layers and the carrier concentrations in the quantum wells are changed. Therefore, large changes of the absorption coefficient can be achieved simultaneously by field effects and phase space filling. In this paper we demonstrate that a constructive superposition can be achieved by shifting the bandfilling contribution to lower photon energies in type-I-hetero-n-i-p-i crystals. A 25 period δ-doped InGaAs/GaAs hetero-n-i-p-i structure with 10 nm pseudomorphic $In_{0.07}Ga_{0.93}As$ quantum wells was grown by "shadow mask MBE" in order to obtain selective contacts to the n- and p-layers. At room temperature a relative transmission change of more than 2:1 at photon energies of 1.39 eV with a voltage swing from -2.5 V to +0.8 V could be demonstrated. This corresponds to a total change of the absorption coefficient of about 2000 cm^{-1} referred to the total sample thickness of 3.55 µm. These large absorption changes (Δα) are a consequence of the constructive superposition of the Franz-Keldysh effect in the intrinsic layers and phase space filling in the InGaAs quantum wells. Comparing our experimental results with theory we deduce a maximum Δα of more than 10000 cm^{-1} (referred to the total quantum well thickness) by bandfilling, whereas the Franz-Keldysh effect contributes a Δα of about 1450 cm^{-1} (referred to the total intrinsic layer thickness).

I. Introduction

Recently much effort has been devoted to the study of electro-optic effects in semiconductor crystals for applications in modulators and switches [1,2]. The absorption changes are based either on field effects or on carrier induced phase space filling [3]. In n-i-p-i

crystals both effects are present [4]. Strong changes of the absorption coefficient up to 8000 cm^{-1} have been achieved by bandfilling in hetero-n-i-p-i structures [5,6]. However, the active region in such structures is very small, which limits the performance of modulator devices. In homo-n-i-p-i doping superlattices field induced changes of the absorption coefficient due to the Franz-Keldysh effect of about 2000 cm^{-1} have been demonstrated [7]. The active region in these structures can extend over almost the whole sample thickness especially in δ-doped n-i-p-i devices. Both phenomena, field and bandfilling effects, contribute simultanously to the absorption changes in n-i-p-i structures. However, in homo-n-i-p-i crystals a significant contribution of both effects occurs just above the bandgap where the two effects have opposite signs. Therefore, a reduction of the pure Franz-Keldysh induced absorption changes above the bandgap is observed as a result of the destructive superposition of these two effects. On the other hand the maximum field and bandfilling induced absorption changes in hetero-n-i-p-i devices so far occur at different photon energies. In this paper we demonstrate that in a type-I-hetero-n-i-p-i structur the bandfilling contributions can be shifted to lower photon energies, so that a constructive superposition of the two effects is achieved.

II. Experiment

The investigated InGaAs/GaAs-hetero n-i-p-i crystal consists of 25 pseudomorphic $In_{0.07}Ga_{0.93}As$ quantum wells imbedded in a GaAs δ-doped n-i-p-i structure. The 10 nm wide QW's are modulation doped on both sides with $\delta n^{(2)} = 4.5\,10^{12}$ cm^{-2} and 7 nm thick GaAs spacer layers. The width of the intrinsic GaAs layer is 50 nm, the $\delta p^{(2)}$-doping is $1.1\cdot10^{13}$ cm^{-2}. The total sample thickness is 3.55 µm. The n-i-p-i crystal was grown by a new epitaxial "shadow mask MBE" technique which allows the *in situ* lateral structuring of the doping profile on a µm scale. This enables the fabrication of n-i-p-i doping superlattices with built in highly selective and ohmic contacts [8,9]. By applying an external voltage U_{pn} to the n- and p-layers, the electric field in the intrinsic GaAs region and the carrier density in the InGaAs quantum wells is tuned simultanously. Figure 1 shows the calculated real space conduction band diagram for the investigated sample. At a certain threshold voltage, in this case $U_{pn} = -2.5$ V, the quantum wells in the n-layers are completely depleted. Therefore, the absorption coefficient of the InGaAs-QW's is expected to be very high for photon energies near and above the lowest QW excitonic transition. At the same time the electric field in the intrinsic GaAs layers reaches its maximum value of $6.3\,10^5$ V/cm. At such high fields, the absorption coefficient below the GaAs bandgap which is due to the Franz-Keldysh effect, is also very large (see Fig. 1 a). By applying a forward bias of $U_{pn} = +0.8$ V the electric field decreases to

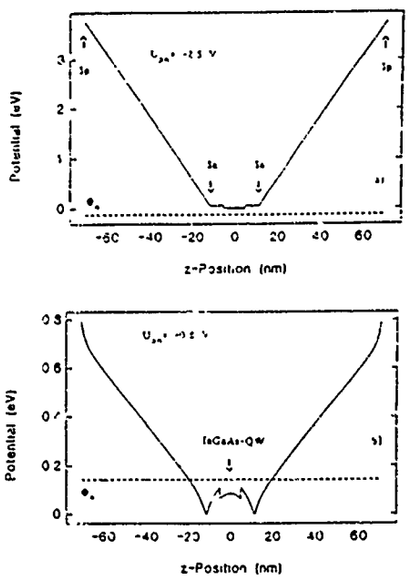

Figure 1 Calculated real space conduction band diagram for the investigated hetero n-i-p-i structure. a) At the threshold voltage $U_{pn}^{th} = -2.5$ V the case where the QW's in the n-region are completely depleted. b) At a forward bias of $U_{pn} = +0.8$ V with $\delta n^{(2)} = 4.5\cdot10^{12}$ cm^{-2} free carriers in the QW's. Note very different energy scale in part a) and b).

1.3 10^5 V/cm and at the same time the carrier concentration in the InGaAs quantum wells rises to $7.4\,10^{12}$ cm^{-2} (see Fig. 1 b). This leads simultanously to a reduction of the absorption coefficient in the intrinsic GaAs layers, due to the Franz-Keldysh effect and also in the QW's, due to phase space filling. By using a suitable sample design we succeded in shifting the bandfilling contribution to lower photon energies, so that a constructive superposition of field and carrier induced absorption changes is achieved.

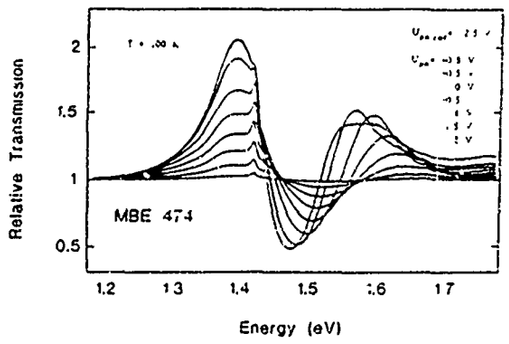

Figure 2 : Measured relative transmission spectra for 25 periods of a pseudomorphic $In_{0.27}Ga_{0.73}As/GaAs$ type I hetero n-i-p-i structure. The Quantum wells (d_{QW} = 10 nm) are modulation doped on both sides with $2x10^{12}$ = $8.5\,10^{12}$ cm^{-2} ($d_{barrier}$ = nm). The width of the intrinsic region is 59 nm the $1p^{18}$-doping is $1.1\,10^{13}$ cm^{-2}. The total sample thickness is 3.55 µm

Fig. 2 shows the measured relative transmission spectra for the investigated n-i-p-i structure. At room temperature a maximum relative transmission change of more than 2:1 around photon energies of 1.39 eV with a voltage swing from -2.5 V to +0.8 V is observed. Note that the contrast ratio remains larger than 2:1 over an energy range of more than 26 meV, implying very good stability against temperature variations or wavelength detuning, which is important for device applications. The low switching bias of only 3.2 V is also an attractive feature for applications in integrated optics. The large transmission changes correspond to an absolute change of the absorption coefficient of more than 2000 cm^{-1} referred to the total sample thickness of 3.55 µm. Figure 3 shows the measured absorption changes (solid lines) and the corresponding calculated $\Delta\alpha$ due to the Franz-Keldysh effect in the intrinsic GaAs layers (dotted lines). All curves are related to the total intrinsic layer thickness of $d_{i\,tot}$ = 2.95 µm. Comparing our results with the calculated Franz-Keldysh data, these large absorption changes can only be explained by the superposition of field effects in the intrinsic regions and phase space filling in the InGaAs-QWs. At photon energies below the GaAs bandgap (E_{gap} = 1.424 eV) the superposition is constructive as the field induced absorption changes are enhanced due to the bandfilling contributions of the quantum wells. Above the GaAs bandgap the field and bandfilling absorption changes

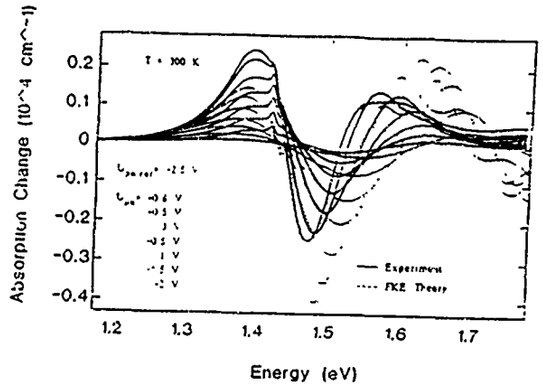

Figure 3 : The solid curves show the absorption changes for different voltage swings derived from the transmission measurement in Fig. 2. The dotted lines exhibit the calculated absorption changes due to the Franz-Keldysh effect for the corresponding different electric fields in the intrinsic GaAs regions. All curves are related to the total intrinsic layer thickness ($d_{i\,tot}$ = 2.95 µm). Below the GaAs bandgap (E_{gap} = 1.424 eV) the bandfilling and the field contributions superpose constructive. This leads to an enhancement of the absorption changes for photon energies below the bandgap. Above the GaAs bandgap both effects superpose destructive and therefore the absorption changes are reduced.

have opposite signs. Therefore, the observed absorption changes for photon energies above the bandgap are reduced, compared to the Franz-Keldysh changes. Figure 4 shows the difference spectra between the measured and the calculated Franz-Keldysh-absorption changes related to the total QW thickness of $d_{QW\,tot}$ = 250 nm. The resulting curves should only contain the absorption changes due to phase space filling, providing that the non-uniformity of the field in the intrinsic GaAs layers and its influence on the Franz-Keldysh-absorption can be neglected. For photon energies below the GaAs bandgap maximum absorption changes of almost 15000 cm^{-1} due to phase space filling are deduced. As can be seen in Fig. 1 b) bandfilling does not only occur in the InGaAs-QW's but also in the adjacent GaAs region, which also leads to large absorption changes above the GaAs bandgap. In this energy region, however, the Franz-Keldysh and the bandfilling induced absorption changes have opposite signs which results in a destructive superposition of the two effects.

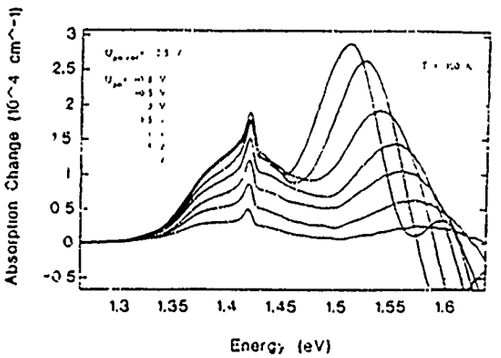

Figure 3 : Measured absorption changes due to the bandfilling contributions related to the total quantum well thickness ($d_{QW\,tot}$ = 250 nm) for different voltage swings. The carrier concentration in the quantum wells is varied by the external bias U_{pn} from $n^{(2)} = 0$ ($U_{pn,th}$ = -2.5 V) up to $n^{(2)} = 7 \times 10^{18}$ cm^{-3} (U_{pn} = +0.8 V).

III. Summary

In summary we have reported on a novel electro-optic modulator device based on the contructive superposition of field and bandfilling absorption changes. A type-I InGaAs/GaAs hetero-n-i-p-i structure was grown by a new shadow mask MBE technique in order to obtain built in highly selective contacts. By applying a voltage U_{pn} to the n-i-p-i crystal, both, the fields in the intrinsic GaAs regions and the carrier concentration in the InGaAs quantum wells are varied simultanously. At room temperature a relative transmission change of more than 2:1 at photon energies of 1.39 eV with a voltage swing from -2.5 V to +0.8 V has been demonstrated. Comparing our experimental results with theory these large absorption changes are the consequence of the constructive superposition of the absorption changes due to field effects of 1500 cm^{-1} (related to the total intrinsic layer thickness) and bandfilling contributions of the InGaAs-QWs of more than 10000 cm^{-1} (referring to the total QW thickness). By optimizing the design of the hetero-n-i-p-i structure it will be possible to improve on the performance of the modulator device furthermore.

This work was partly supported by the Volkswagen-Stiftung under contract number I/68 042

References

1. B.S. Ryvkin, Phys. Stat. Sol. (b), 150, 567 (1988)
2. D.A.B. Miller, D.S. Chemla, T.C. Damen, A.C. Gossard, W. Wiegmann, T.H. Wood, and C.A. Burrus, Phys. Rev. B 32, 1043 (1985)
3. M. Wegener, J.E. Zucker, T.Y. Yang, N.J. Sauer, K.L. Jones and D.S. Chemla, Phys. Rev. B, 41, 3097 (1990)
4. S. Malzer, N. Linder, K.H. Gulden, A. Hofler, P. Kiesel, M. Kneissl, X. Wu, J.S. Smith and G.H. Dohler, Phys. Stat. Sol. (b) 173, 459 (1992)
5. A. Larsson and J. Maserjian, Appl. Phys. Lett. 58, 1946 (1991)
6. X. Wu, K.H. Gulden, P.J. Thomas, J.S. Smith and J.R. Whinnery, S. Malzer, P. Kiesel, M. Kneissl, and G.H. Dohler, Appl. Phys. Lett. 62, 152 (1993)
7. P. Kiesel, K.H. Gulden, A. Hofler, M. Kneissl, B. Knupfer, N. Linder, P. Riel, X. Wu, J.S. Smith and G.H. Dohler, Appl. Phys. Lett. 62 (25), (1993)
8. G.H. Dohler, G. Hasnain, and J.N. Miller, Appl. Phys. Lett. 49, 704 (1986)
9. K.H. Gulden, X. Wu, J.S. Smith, P. Kiesel, A. Hofler, M. Kneissl, P. Riel and G.H. Dohler, Appl. Phys. Lett. 62, (1993)

ThP36

POLARIZATION OF THE SPONTANEOUS EMISSION OF STRESSED LASER HETEROSTRUCTURES

A.A.Ptashchenko, M.V.Deych, N.V.Mironchenko, F.A.Ptashchenko
Odessa University
ul.Petra Velikogo 2, 270100 Odessa, Ukraine

Abstract--Measurement system with a polaroid was constructed allowing to detect the degree of the light polarization (ρ) of 0.1%. ρ as a function of driving current(I) and axial stress (σ) was studied for spontaneous output of the AlGaAs lasers at low pumping levels. It was found that in the range of sufficiently small currents ρ linearly depends on I and σ. When extrapolated to I=0, the ρ depends not only on σ, but also on the light amplification parameters of the individual laser structure. These observations must be taken into account when one attempts to estimate the strain in the active layer of a diode laser through the polarization measurments. The Cassidy's one-dimensional model of the polarization effects in diode lasers was modified to include modulation of the optical absorbtion by the stimulated emission in the active region at very low pumping intensities.

Introduction

Axial stress in the active region of the semiconductor lasers essentially affects the spectra of the spontaneous and stimulated emission, modifies the threshold current value [1,2]. Mechanical stress in heterostructures enhances degradation processes in diode lasers [3]. The most sensitive method of detecting the anisotropical deformation in semiconductor structures is based on the polarization-resolved measuring of the recombination radiation [4,5]. Polarization technique was succesfully used for estimating the strain in the active layer of semiconductor lasers [6,7]. The degree of polarization of the subthreshold emission from the active region, defined as

$$\rho = (L_1 - L_2)/(L_1 + L_2), \qquad (1)$$

where L_1 and L_2 are the light intensities with transverse electric (TE) and transverse magnetic (TM) polarization, was shown to depend on the difference in reflectivity ΔR at the facet mirrors as well as on the variation in the single-pass gain for the TE and TM modes [6]. This dependence generally is nonlinear, making difficulties in its using for detecting the strain in semiconductor lasers.

In [6] was postulated that in the range of pumping current $I \ll I_{th}$, where I_{th} corresponded to the lasing threshold, ρ was approximately independent of current. This assumption allowed the authors [6] to estimate the proportionality coefficient between the ρ and the axial stress σ and, using the nonlinear part of the dependence $\rho(I)$, to obtain the difference in reflectivity ΔR for the TE and TM modes. But the degree of polarization of the spontaneous emission in the range of low pumping levels was not detailed studied. The minimal magnitude of ρ, detected with the accuracy of ±20%, was 0,01 [4-6].

The purpose of this work was detailed study of the spontaneous light polarization of diode lasers at low pumping levels in order to prove the tecnique [3] of stress detecting. For this purpose the sensitive polarization measurement system was constructed; the depences $\rho(I)$ and $\rho(P)$, where P denotes external pressure, were studied; the one-dimensional laser model [6] was more detailed analyzed for the case of low driving levels.

Our measurments were performed on the AlGaAs double-heterostructure lasers with stripe geometry. We found that at low pumping intensities the degree of polarization of the spontaneous output of diode lasers was not constant, but linearly depended on the driving current. And the rate of change in ρ with I depended on the individual parameters of a laser. And finally, the proportionality coefficient between $\rho(I)$, extrapolated to I=0, and σ was observed to depend on the amplification properties of the individual laser structure.

2. Measurement system

The measurement system is schematically depicted in Fig.1. Laser diode LD was mounted on the massive copper cooler and pumped by the current source S_1. Axial stress in the perpendicular direction to the laser active layer was produced by a metallic plane, pressed to the upper metallized surface of the heterostructure. The pressure was hydraulically regulated. The light output of the laser was collimated with a lens, passed through the polaroid P, rotating with a fixed frequence, and detected by photodiode PD_1. The dc component of the photodiode signal V_d, was proportional to the averaged light intensity $(L_1+L_2)/2$ in Eq.(1). The ac component of the signal V_a, being proportional to the difference between the intensities of TE and TM polarized light $|L_2-L_1|$, was detected by the selective amplifying system SA. The ρ was determined as $\rho = V_a \alpha / V_d$, where α was a calibrating coefficient. In order to determine the sign of ρ, the additional optical circuit was used. The output of the light-emitting diode LED was passed through the modulator M, coupled to the rotating polaroid P, and then directed on the photodiode PD_2. The phases of the signals from the photodiodes PD_1 and PD_2 were compared by the phase analyser PA, giving the sign of ρ. The constructed experimental system allowed measuring the degree of polarization of 0.001 (with the error less than 20%).

3. Experimental results

Fig.2 represents the degree of polarization of the spontaneous emission ρ, measured under various external pressures as a function of the driving current. The upper three curves correspond to the diode laser DL №451 with $\rho > 0$, and the lower curves were measured on the DL №484 with $\rho < 0$. One can see that ρ is not constant at low biasing currents. It means that estimation the mechanical stress in the active region of a laser, as basing on the spontaneous emission polarization measurements, is more delicate problem than it was supposed in [6], assuming $\rho = \text{const}$. It is also seen that the axial pressure in the perpendicular direction to the active layer shifts all the curves $\rho(I)$ down in the both cases of positive and negative signs of ρ. It confirms the conclusion of [1,2,6] that the

compressive stress in this direction increases the intensity of the TM mode and induces the TE mode. Comparison of the data, presented in Fig.2 shows that the external pressure decreases the derivative $d\rho/dI$. In the most interesting for this work range of low currents, the curves of the Fig.2 can be approximated by

$$\rho = \rho_0 - \rho_1 I, \qquad (2)$$

where ρ_0 and ρ_1 are independent of current, but are different for the individual samples. Both the coefficients ρ_0 and ρ_1 decrease with the axial pressure.

Fig.3 represents the degree of polarization of the spontaneous emission from a facet mirror of the laser N°451, measured

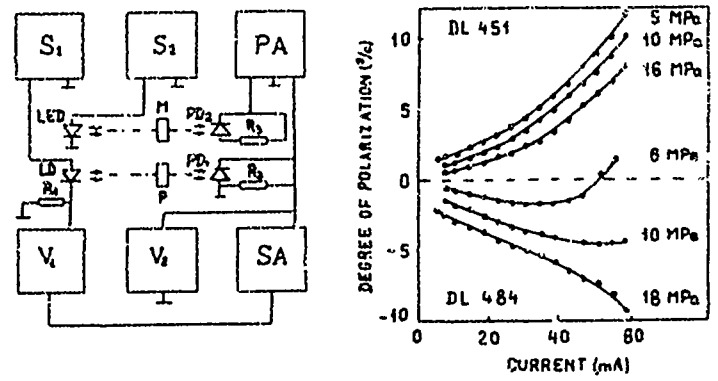

Fig.1. Schematic diagram of the measurement system.
Fig.2. Degree of polarization of the lasers as a function of I

at various driving current as a function of the external pressure. The presented data show that this dependence $\rho(P)$ generally is nonlinear, in agreement with the results [6]. In the range of driving current $I \leq 0.1 I_{th}$, where I_{th} is threshold current, the curves $\rho(P)$ were practically linear for all the investigated laser diodes. Deviations from the linear dependence $\rho(P)$ in this range of I were less than 10%. These observations corraborate the conclusion of Cassidy et al [6] that the range of small pumping currents is most suitable for estimating the strain with the help of the polarization measurements.

4. Comparison with the model [6]

In analysing the obtained experimental data we used the one-dimensional laser model [6]. This model gives for the intensity of the spontaneous emission, partly amplified in the active region,

$$L = \frac{B\tau(1-R)(G-1)}{\ln G(1-GR)}, \qquad (3)$$

where B is the radiative recombination rate in the active layer of the lenght of l; R is the reflectivity at the facet mirrors; G is single-pass gain

$$G = \exp(gl), \qquad (4)$$

g denotes the gain coefficient. For the most interest (in respect to measuring the strain in the active layer) $\rho \ll 1$ assuming that the axial stress produces the difference ΔB and Δg in values of B and g between the TE and TM modes, and that $\Delta g/g = \delta = \Delta B/B$ [5] and supposing that difference in reflectivity between the TE and TM modes $\Delta R \ll R$ for $gl \ll 1$ one can obtain

$$\rho = 0.5\delta + 0.5[\delta \cdot \Delta R/(1-R^2)]g_1 I. \qquad (5)$$

where

$$g_1 = gl/I \qquad (6)$$

is fixed parameter for a given sample.

Eq.(5) predicts a linear dependence of ρ on I in the range of very small pumping intensities, which agrees with the empirical form (2) describing the experimental curves $\rho(I)$ in the range of small I. Analysing the experimental data on $\rho(I)$,

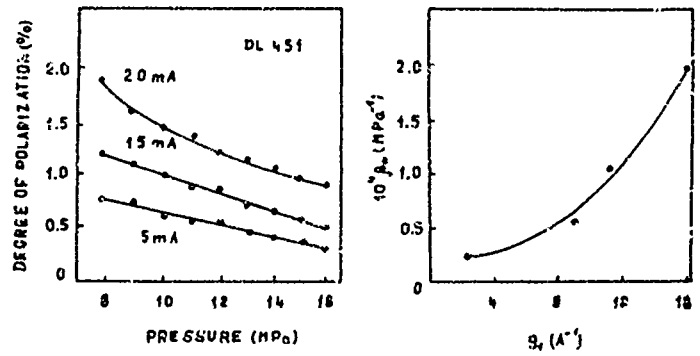

Fig.3. Plot of the degree of polarization vs. external pressure. The driving currents are given at the curves.
Fig.4. Correlation between the pressure-sensitivity of the polarization β_0 and the value g_1, defined Eq.(6).

measured on the lasers under various external pressures, we can obtain $\delta(P)$ and ΔR in Eq.(5). The magnitude of g_1 as well as the ratio B/g can be estimated; analysing the experimental curve L(I) with the help of Eq.(3). Such analysis, made for all the studied diode lasers assuming $\delta \sim \sigma$, where σ is the axial stress in the active region, yielded σ in the $-2\cdot10^8$–$+2\cdot10^8$Pa range. ΔR was found to be practically independent on I and lying in the interval 0.04–0.06. Independence of ΔR of I indicates that the guiding properties of the active layer in the double heterostructure lasers remain at very low pumping currents below threshold.

Our data indicated that the stress-sensitivity of polarization, as defined by

$$\beta_0 = d\rho_0 / d\sigma, \qquad (7)$$

where ρ_0 was the degree of the laser output polarization, extrapolated to I=0, variated in the range of one order of the magnitude among the studied samples. Fig.4 plots the magnitudes of β_0, obtained in the above described manner, versus g_1, defined Eq.(6) and estimated on the same lasers. The presented data show that there is a definite correlation between these values. Laser, having g_1, i.e. larger gain coefficient at the fixed current, revealed stronger sensitivity of ρ_0 to the axial stress. On the other hand, the difference in the spontaneous light intensity among the studied lasers at a current $I \ll I_{th}$ was much less than the variation in g_1. The pressure-sensitivity of ρ_0 was higher for those samples which revealed larger ratio g/B.

5. Modification of the model [6]

The most probable origins of the variation in the gain coefficient g among lasers, having approximately the same quantum yield of the spontaneous emission, are [8] : a) difference in the doping level; b) variation in the thickness of the active layer. This factor leads to a difference in the pumping density among lasers at the same driving current; c) difference in the absorption coefficient α.

In order to study the effect of the doping level on ρ_0 we measured the spectrum shift of the spontaneous emission with current. No correlation was found between the individual values of the rate of this shift, depending on the doping level [9], and β_0.

Absorbtion of the spontaneous emission in the active region of a laser can be taken into account, using the expression for the total gain coefficient [3]

$$g_t = g_0(I - I_0) - \alpha, \qquad (8)$$

where α is the absorbtion coefficient, g_0 and I_0 are parameters, depending on the active layer thickness and the doping level in a given laser. It means that quantum amplification in the active layer begins not from I=0, but from

$$\bar{I}_1 = I_0 + \alpha/g_0 . \qquad (9)$$

At $I \leq I_0$ there are no quantum amplification effects, so that $g_t = -\alpha$; in the range $I_0 < I < \bar{I}_1$ resonant light is not amplified in the active region, but the total absorbtion coefficient ($-g_t$) is modulated by the pumping current, according to Eq.(8).

This modified model gives for the degree of the polarization in the range $I < I_0$

$$\rho = \frac{\Delta\delta}{2\delta} - \frac{1-G}{2(1-R)(1+RG)}\Delta R, \qquad (10)$$

where $G = \exp(-\alpha l) < 1$. Eq.(10) indicates that, contrary to the authors [6], the degree of polarization of the spontaneous output must depend on ΔR at very small pumping currents.

In the range $I_0 < I < \bar{I}_1$, when $G \ll 1$, Eqs. (1),(2) and (3), supposing after [6] $\Delta B/B = \Delta g_0/g_0$, lead to

$$\rho = \frac{1}{2}\left(\frac{\Delta g_0}{g_0} - \frac{\Delta\alpha}{\alpha}\right)\frac{\alpha}{\alpha - g_0(I - I_0)} - \frac{\Delta R}{1-R}, \qquad (11)$$

where $\Delta g_0/g_0$ and $\Delta\alpha/\alpha$ are the relative differences in g_0 and α between the TE and TM polarized photons, caused by the axial stress. The magnitude of the stress-sensitivity of polarization, as defined by Eq.(7), can vary among lasers because differences in α, g_0 and I_0. More effective lasers, having higher g_0 and lower α and I_0, must reveal higher polarization-sensitivity to the stress.

Conclusions

Detailed study of the degree of polarization (ρ) of the spontaneous emission of AlGaAs double-heterostructure lasers as a function of current (I) and axial pressure (P) in the range of low driving intensities showed that using these measurements for the estimation of the mechanical stress in the laser active region is more delicate problem than it seemed previously [6]. The ρ is not constant at low pumping currents, but linearly depends on I. This dependence, when expolated to I=0, gives ρ_0 which can be used as a measure of the stress (σ) in the active layer. The magnitude of ρ_0 depends not only on the σ, but also on the difference ΔR in the reflectivities at the facet mirrors between the TE and TM polarized photons, as well as on the g_0, the proportionality coefficient between the gain coefficient g and I. The last effect takes place in the range of low I, where the spontaneous emission is partly absorbed in the active region, but the absorbtion coefficient is modulated by the stimulated emission. In this case the axial stress causes not only the difference ΔB between the rates of the radiative recombination, producing TE and TM polarized photons, but additionally modulates (differently for the TE and TM modes) the effective lenght of the portion of the active layer suplying the registered output photons. Therefore, in order to applying the polarization measurements for the estimation of the value of the strain in the laser active region, one must study the influence of the laser structure on the difference in reflectivities ΔR

between the TE and TM modes, as well as the influence of the quantum amplification parameters of the actual lasers on ρ_0.

Acknowledgments

The authors gratefully acknowledge Prof. P.G.Eliseev and Prof. D.T.Cassidy for the presentation of the reprints and preprints of their works; we would like to thank Dr. V.Ya.Filipchenko and M.I.Sverdlov for supplying the heterostructures and L.P.Prokopovich for the assistance in assembling of the measurement system.

REFERENCES

1. P.G.Eliseev, B.M.Sverdlov, I.Ismailov, and N.Shokudzhaev, Sov. J.Quantum Electron., 16, 1046 (1986).
2. P.G.Eliseev, B.M.Sverdlov, I.Ismailov, and N.Shokhudzhaev, Sov. J.Quantum Electron., 16, 1051 (1986).
3. R.J.Nelson, A.K.Dutta, J.Appl. Phys., 54, 2923 (1983).
4. Z.I.Vekua, R.I.Dzhioev, B.P.Zakharchenya, S.L.Ivchenko, and V.G.Fleysher, Sov. Solid State Physics, 17, 1096 (1975).
5. M.S.Averkiev, M.P.Gorelenok, and I.S.Terasov, Sov. J. Physics and Technics of Semiconductors, 17, 1997 (1983).
6. D.T.Cassidy and C.S.Adams. IEEE J. Quantum Electron., 25, 1156 (1989).
7. P.M.Peters, D.T.Cassidy, Applied Optics, 28, 3744 (1989).
9. O.V.Bogdankevich, S.A.Darznek, and P.G.Eliseev, Poluprovodnikowye lasery, P.415. Nauka, Moscow (1976).

ThP37

Bistability Effect in Laser-Transistor Resonant-Tunneling Structure

V.Ryzhii and I.Khmyrova
The University of Aizu,
Tsuruga, Ikki-machi, Aizu-Wakamatsu-City,
Fukushima Prefecture, 965 JAPAN

Abstract

We report laser-bipolar transistor incorporating a resonant-tunneling structure (RTLBT) operation analysis. An analytical model of RTLBT is proposed and used. It is shown that RTLBT can exhibit bistable operation, so in a certain range of collector voltage ($V_{C'}<V_C<V_{C}$) the collector and the base currents, and the stimulated photon emission intensity, are double-valued. The physical nature of the bistability effect is associated with a mobile electron space charge in the collector that influences the electron transparency of the resonant-tunneling structure and the pumping conditions of the laser active region.

Introduction

Modulated semiconductor heterostructures have recently attracted considerable attention as important components for optical preprocessing and photonic switching functions (see, for example [1,2]). In this paper we report a laser-bipolar transistor incorporating resonant-tunneling structure (RTLBT) as an optoelectronic switching device. The RTLBT has electrical and optical switching characteristics exhibiting a bistable operation in a certain range of the collector voltage. The band structures of the RTLBT in both the on and off states are shown in fig.1. The narrow-gap p^+-layer plays the role of the laser active region and the transistor base simultaneously. The double-barrier resonant-tunneling (RT) structure placed between the base and the collector plays the role of the electron filter controlled by the electric field which is created by the mobile electron space charge in the collector region. The origin of the bistability effect in the RTLBT under consideration is associated with the mobile electron space charge being accumulated in the collector layer behind the RT-structure. The variation of the electron concentration in the base (laser active region) because of different electron transparency of the RT-structure admits of control of the stimulated radiative recombination and photon emission in the base. In the closed state the collector current (J_C) and the electron space charge in the collector (Q) are negligible ($J_C\approx0$, $Q\approx0$) and the base electron concentration exceeds the laser generation threshold concentration. In this case the intensity of emitting light $N_\omega \neq 0$. In the opened state the electron leakage through the RT-structure ($J_C \neq 0$, $Q\neq0$) suppresses the stimulated emission ($N_\omega = 0$). In order to switch

on the collector current and switch off the stimulated light emission it is necessary to store the mobile electron space charge which opens the RT structure by reducing the applied collector voltage to a value lower than a certain threshold value ($\bar{V}_{th}$).

If current flows through the RT structure and collector region and thereby creates the mobile electron space charge in this region, to switch off the current and to switch on the stimulated light emission, it is necessary to increase the collector voltage over another threshold value ($\bar{V}_{th}$). Since $\bar{V}_{th} > \bar{V}_{th}$ this results in double-valued current-voltage and intensity voltage (Watt-voltage) characteristics. Recently the similar bistability effect in the resonant-tunneling bipolar transistor (operating only as an electronic device) was predicted and discussed by one of the authors and S Khrenov in [3].

Model

A simple one-dimensional model of RTLBT was utilized to evaluate its performances. This model includes the following assumptions:

(i) There is a single RT level in the double-barrier collector structure. The RT level energy shift is proportional to the electric field within the double-barrier structure (E_r).

(ii) The base (laser active region) is equipotential due to a significant hole concentration; the electron density is uniform within the base.

(iii) The electron nonradiative recombination in the base is linear, so the recombination time (τ_R) may be introduced.

(iv) Spontaneous light emission is negligible. Spatial distribution of the light is not essential; the photon life time (τ_ω) approximation is valid.

With these assumptions one can write down the following equations for the electron concentration in the base (n) and the photon density (N_ω)

$$\frac{dn}{dt} = \frac{j_E - j_C}{eW_B} - \frac{n}{\tau_R} - G(n)\, N_\omega \qquad (1)$$

$$\frac{dN_\omega}{dt} = G(n)N_\omega - \frac{N_\omega}{\tau_\omega} . \qquad (2)$$

Here j_E and j_C are the emitter and collector current densities, W_B is the base (laser active region) width, τ_R is the electron recombination time, τ_ω is the photon life time, G(n) is the stimulated emission function which can be expressed usually as $G = K(n - n_{th})$, if $n \geq n_{th}$ and $G = 0$, if $n < n_{th}$, where n_{th} is the threshold electron density, K is the coefficient. The emitter current density j_E depends on the applied base-emitter voltage and it is treated as a given value. The collector current density j_C may be represented as

$$j_C = ev_T n\, (t_r \exp(-\varepsilon_r/T)\, \theta(\varepsilon_r) + t_n \exp(-\varepsilon_n/T)) , \qquad (3)$$

where v_T is the thermal electron velocity, e is the electron charge, ε_r is the energy of the RT level with the respect to the emitter conduction band edge, ε_n is the height of the double barrier, t_r and t_n are the coefficients characterizing the electron transport via RT level (resonant part of the collector current) and electron transport over the barriers (thermionic part of the collector current), respectively. (t_r, $t_n < 1$), $\theta(x)$ is the step-like function. In the simplest case it can be taken as follows.

$\theta(x) = 1$, if $x > 0$ and $\theta(x) = 0$, if $x < 0$.

Naturally, $\varepsilon_r < \varepsilon_n$. For appropriate RT structure with high peak-to-valley ratio the following unequality is valid

$$\frac{t_r}{t_n} \exp((\varepsilon_n - \varepsilon_r)/T) > 1$$

According to the accepted assumptions one can use the following expression

$$\varepsilon_r = \varepsilon_{0r} - eE_r w,$$

where ε_{r0} is the RT level energy in the absence of electric field ($E_r = 0$). Taking into account the electron space charge $Q = \frac{j_C}{v_s}$ in the collector region and its drift nature one can rewrite (see [5]) the last formula as

$$\varepsilon_r = \varepsilon_{r0} - \frac{ew}{W_C}(V_C + V_{bi}) + \frac{2\pi e w W_C}{\kappa v_s} j_C \qquad (4)$$

Here w is the effective width of the double barrier RT structure, W_C is the width of the collector region (in reality $w < W_C$), V_C and V_{bi} are the applied collector voltage and the collector built-in voltage, v_s is the electron saturation velocity, κ is the dielectric constant of the collector material.

Stationary Characteristics

For the stationary states of the RTLBT one can get from eq.(1) and (2) the following expressions

$$N_\omega = 0, \quad n = \frac{\tau_R}{eW_B}(j_E - j_C), \qquad (5)$$

if $j_E < j_C + j_{th}$, and

$$N_\omega = \frac{\tau_\omega}{eW_B}(j_E - j_C - j_{th}), \quad n = n_{th} + \frac{1}{K\tau_\omega} , \qquad (6)$$

if $j_E \geq j_C + j_{th}$, where $j_{th} = \frac{eW_B}{\tau_R}(n_{th} + \frac{1}{K\tau_\omega})$.

Substituting expressions (5) and (6) into formula (3) and using

formula (4) one can obtain

$$j_C = j_E \left(\frac{v_T \tau_R}{W_B}\right) \frac{t_r \{\exp[(\bar{j} - j_C)/j_T]\, \theta[(j_C - \bar{j})/j_T] + t_n \exp(-c_n/T)}{1 + \frac{v_T \tau_R}{W_B}\left(t_r \exp\left(\frac{\bar{j} - j_C}{j_T}\right) \cdot \theta\left(\frac{j_C - \bar{j}}{j_T}\right) + t_n \exp(-c_n/T)\right)} \qquad (7)$$

if $j_E < j_{th} + j_C$,

and

$$j_C = j_{th}\left(\frac{v_T \tau_R}{W_B}\right)\left[t_r \cdot \exp\left(\frac{\bar{j} - j_C}{j_T}\right) \theta\left(\frac{j_C - \bar{j}}{j_T}\right) + t_n \exp(-c_n/T)\right], \qquad (8)$$

if $j_E \geq j_{th} + j_C$.

Here $j_T = \frac{\kappa v_s}{2\pi e w W} T$, $\bar{j} = \frac{\kappa v_s}{2\pi W_C^2}(V_C - \bar{V}_C)$,

where $\bar{V}_C = \frac{c_{0r}}{e}\frac{W_C}{W} - V_{bi}$.

By introducing dimensionless variables and parameters such as

$$n_\omega = N \frac{eW_B}{\omega \tau j_T}, \quad i_C = \frac{J_C}{j_T}, \quad i_E = \frac{J_E}{j_T}, \quad u_C = \frac{eV_C}{T}\frac{W}{W_C},$$

and $i_{th} = \frac{j_{th}}{j_T}$, $\bar{u}_C = \frac{e\bar{V}_C}{T}\frac{W}{W_C}$, $\alpha = \frac{v_T \tau_R}{W_B} t_r$,

one can rewrite equations (7) and (8) in the form

$$n_\omega = 0, \qquad (9)$$

$$i_C = i_E \frac{\alpha \cdot \exp(u_C - \bar{u}_C - i_C)\, \theta(\bar{u}_C - u_C + i_C) + \beta}{1 + \alpha \cdot \exp(u_C - \bar{u}_C - i_C)\, \theta(\bar{u}_C - u_C + i_C) + \beta}$$

for $i_E < i_{th} + i_C$, and

$$n_\omega = i_E - i_C - i_{th}, \qquad (10)$$

$$i_C = i_{th}\left[\alpha \exp(u_C - \bar{u}_C - i_C)\, \theta(\bar{u}_C - u_C - i_C) + \beta\right]$$

for $i_E \geq i_{th} + i_C$.

Here $\beta = \frac{v_T \tau_R}{W_B} t_n \exp(-c_n/T)$.

This set of equations gives rise to dependencies of the dimensionless collector current i_C and dimensionless photon density n_ω via dimensionless applied voltage u_C under a given value of the dimensionless emitter current i_E. The quantity $\bar{u}_C = \frac{c_{0r} - e(w/W_C)V_{bi}}{T}$ is definded by the RTLBT material and structure parameters (c_{0r}, V_{bi}, w and W_C), and the temperature. Typical current-voltage ($i_C = i_C(u_C)$ and $i_B = i_E - i_C = i_B(u_C)$) and photon-density-voltage ($n_\omega = n_\omega(u_C)$) characteristics are shown in fig.2. In many cases the dependencies of the values α and β upon u_C can be considered as weak. Neglecting these dependencies one can obtain the analytical expressions for critical points $i_C^{(A,B,C,D)}$ and $n_\omega^{(A,B,C,d)}$ (see fig.2). There are three different modes of the RTLBT operation:

(a) If $i_E < i_{th}(1 + \beta)$ the RTLBT operates as a bistable transistor. Thus only the current-voltage characteristic exhibits the bistability (see fig.2a), so $n_\omega = 0$. In this case

$$\bar{u}_{th} = \bar{u}_C + i_E \frac{\beta}{1+\beta}, \qquad \bar{u}_{th} = \bar{u}_C + i_E \frac{\alpha + \beta}{1 + \alpha + \beta},$$

$$i_C^{(D)} = i_C^{(C)} = i_E \frac{\beta}{1+\beta}, \qquad i_C^{(B)} = i_E \frac{\alpha + \beta}{1 + \alpha + \beta}.$$

The value $i_C^{(A)}$ may be determined from a transcendental equation

$$\text{as } i_C = \frac{\alpha e^{-i_C} + \beta}{1 + \alpha e^{-i_C} + \beta}, \quad \text{so } i_C^{(A)} < i_C^{(B)}.$$

(b) In the case $i_{th}(1 + \beta) < i_E < i_{th}(1 + \alpha + \beta)$ the RTLBT operates as a transistor and a laser simultaneously exhibiting the bistability in a certain range of collector voltages ($\bar{u}_{th} < u_C < \bar{u}_{th}$). Moreover the laser generation arises if $u_C > \bar{u}_C$ (fig.2b). Provided the emitter current densities satisfy the above unequalities one can obtain from eqs.(9) and (10):

$$\bar{u}_{th} = \bar{u}_C + i_E \frac{\beta}{1+\beta}, \quad \bar{u}_C = \bar{u}_C + i_E \frac{\alpha + \beta}{1 + \alpha + \beta},$$

$$i_C^{(D)} = i_C^{(C)} = i_{th}\beta < i_C^{(A)} < i_C^{(B)} = i_E \frac{\alpha + \beta}{1 + \alpha + \beta}.$$

In this case

$n_\omega^{(D)} = n_\omega^{(C)} = i_E - i_{th}(1 + \beta)$ and $n_\omega^{(A)} = n_\omega^{(B)} = 0$.

(c) Finally, if $i_E > i_{th}(1 + \alpha + \beta)$ the RTLBT can operate in both the transistor and laser modes under all collector voltages being considered. Moreover in the range $\bar{u}_{th} < u_C < \bar{u}_{th}$ it exhibits the bistable characteristics (see fig.2c). As for critical points they are $i_C^{(D)} = i_C^{(C)} = i_{th}\beta < i_C^{(A)} < i_{th}(\alpha + \beta)$.

$n_\omega^{(B)} = i_E = i_{th}(1 + \alpha + \beta) < n_\omega^{(A)} < n_\omega^{(D)} = n_\omega^{(C)} = i_E - i_{th}$.

In this case $\bar{u}_{th} = \bar{u}_C + i_{th}\beta$, $\bar{u}_{th} = \bar{u} + i_{th}(\alpha + \beta)$.

Discussion

It is seen in fig.2 that both collector current and photon density are double valued functions of the collector voltage. Thus the RTLBT can be considered as an electronic and photonic

device simultaneously. The bistability effect of this type appears if $i_E > i_{th}$. The difference between "on" and "off" voltages $\bar{u}_{th} - \bar{u}_{th}$ (and certainly $\bar{V}_{th} - \bar{V}_{th}$) is proportional to the emitter current density (for cases (a) and (b) in fig.2) and to the value j_{th} (for case (c) in fig.2). Returning to the dimensional variables we get

$$\Delta V_{th} = \bar{V}_{th} - \bar{V}_{th} = \frac{2\pi}{\kappa} \frac{W_C^2}{v_s} \frac{\alpha}{(1+\alpha+\beta)(1+\beta)} j_E \qquad (11)$$

if $i_E < i_{th}(1 + \alpha + \beta)$, and

$$\Delta V_{th} = \frac{2\pi}{\kappa} \frac{W_C^2}{v_s} \alpha j_{th} \qquad (12)$$

if $i_E > i_{th}(1 + \alpha + \beta)$.

In the most interesting case ($\beta < 1$, $\alpha > 1$) formulae (11), (12) ca be rewritten as $\Delta V_{th} = \frac{2\pi}{\kappa} \frac{W_C^2}{v_s} j_E$ and $\Delta V_{th} = \frac{2\pi}{\kappa} \frac{v_T}{v_s} \frac{W_C^2}{h_B} \tau_R \tau_r j_{th}$.

If $\kappa = 12$, $v_s = 10^7$cm/s, $W_C = 5\ 10^{-5}$cm, $j_E = 10^4$ A/cm^2 one can obtai from above formula $\Delta V_{th} = 1$ V.

1. G.W.Taylor and P.W.Cooke. IEEE Trans.Electron Dev., 39, 2529(195
2. M.Mastrapasqua, S.Luryi, F.Capasso, A.I.Hatchinson, D.L.Sivco ar A.Y.Cho. IEEE Trans.Electron Dev., 40, 250 (1993).
3. V.Ryzhii and G.Khrenov. Semiconductor Sci.and Techn., 7,1178, (1992).

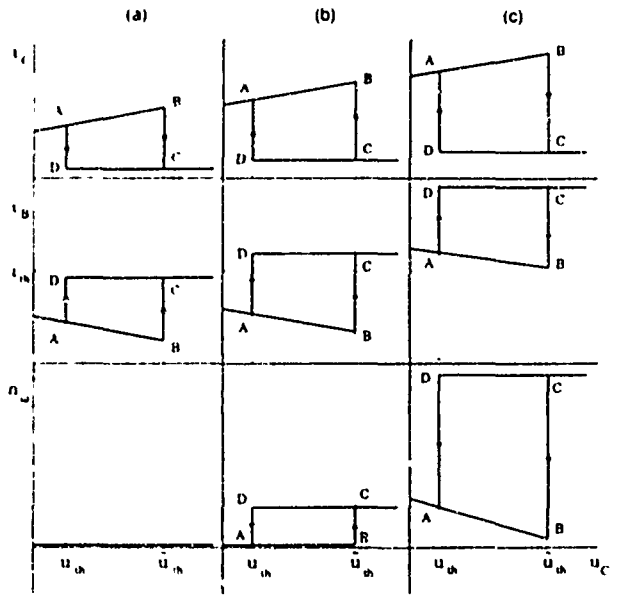

Fig 2 Qualitative view of current-voltage and photon density-voltage characteristics under different emitter current densities (a) $i_E < i_{th}(1+\beta)$, (b) $i_{th}(1+\beta) < i_E < i_{th}(1+\alpha+\beta)$, (c) $i_E > i_{th}(1+\alpha+\beta)$

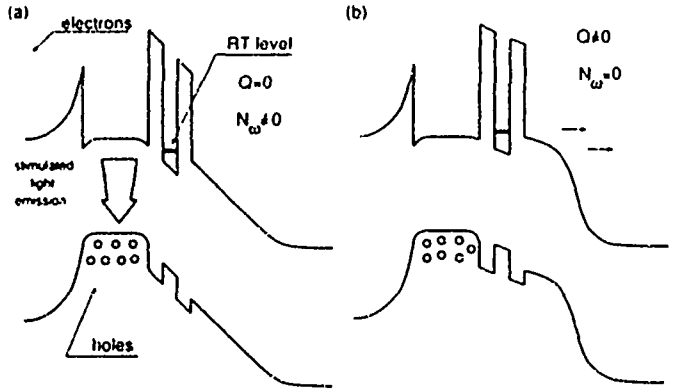

Fig 1 Band diagrams of the RTLBT in closed collector state (a) and opend collector state (b)

ThP38

Optoelectronic Properties of (001) and (111) Lattice-Matched and Strained Quantum Wire Lasers - Comparison with Quantum Well Lasers

Igor Vurgaftman and Jasprit Singh
Solid State Electronics Laboratory,
Department of Electrical Engineering and Computer Science,
The University of Michigan, Ann Arbor, MI 48109-2122

June 18, 1993

Abstract

We investigate the optoelectronic properties of GaAs wires along the [001] and [111] directions for a range of cross sections and compare these with the corresponding parameters for optimized quantum wells. The relative benefits of built-in strain in quantum wire and quantum well systems are also studied. We find that the threshold current density in the $130\mathring{A} \times 50\mathring{A}$ wire is 80 A/cm^2 compared with 560 A/cm^2 in a $50\mathring{A}$ GaAs well. The differential gain in quantum wires is increased by an order of magnitude in comparison with quantum wells, and can be as high as 10^{-13} cm^2. The narrow gain spectrum is calculated for quantum wire lasers ensuring high mode selectivity and strong damping of relaxation oscillations. We also consider the issue of carrier relaxation in quantum-confined structures, which may impose an upper limit on the laser modulation frequency. Performing a Monte Carlo simulation of the relaxation process, we find that the electron relaxation time in quantum wires is increased to above 100 ps in comparison with $\approx$ 10 ps in quantum wells. Within our model, this unusually slow relaxation process may limit the small signal modulation frequency of quantum wires to several GHz. Since modulation frequencies of over 20 GHz have been achieved in quantum wells, we conclude that although quantum wires possess superior optoelectronic properties as compared with those of quantum wells, the degraded small-signal response can make the use of quantum wire lasers for high speed applications undesirable.

1 Introduction

The rapid development of the quantum well laser technology is the direct consequence of the advantages that the 2D density of states offers over the 3D density of states in the conventional double heterostructure laser [1] [3]. However, the 2D density of states is not ideal in terms of laser applications. What is desired is the highest possible concentration of available states near the bandedge, which will result in the lowest necessary injection level to overcome the cavity losses. While quantum wire fabrication presents many more difficulties than the fabrication of quantum wells [4],[5], there also purely theoretical concerns that may reduce the expectations for quantum wire speed and efficiency Non-parabolicities in the bandstructure and heavy-light hole mixing may affect negatively the threshold current and modulation speed. The efficiency of the carrier capture and relaxation mechanisms in quantum wells has been a matter of some concern[6],[7] The situation in quantum wires is even less optimistic, since the absence of intrasubband electron electron scattering may lead to bottlenecks in the relaxation process due to lack of thermalization in the electron gas which loses energy primarily by emitting monoenergetic LO phonons [8]. In both cases, a detailed numerical simulation is the only solution taking into account the complexity of the underlying mechanisms and the number of interacting particles.

In this paper, we present the results of a detailed theoretical analysis of the optoelectronic properties of the (001) and (111) strained and lattice-matched quantum wire lasers as well as the relaxation characteristics for electrons injected in a thermal distribution at the potential well edge and carry out a thorough comparison of these with similar properties in the quantum well structures. In Section 2, we examine the considerations affecting primarily laser efficiency as quantified by the notion of the threshold current, and in Section 3, we cover the properties which influence high speed modulation in quantum wire lasers. We summarize the results and offer our conclusions in Section 4. The list of symbols used in this work and their numerical quantities, where appropriate, is given in Table 1.

2 Optoelectronic Properties

The optoelectronic properties of GaAs quantum well and quantum wire lasers can be studied directly on the basis of the bandstructure The conduction band structure can be computed quite accurately in the effective mass approximation by solving the one-band Schrödinger equation for s-type states, while the procedure for solving for the valence band structure is to diagonalize the Kohn-Luttinger four band Hamiltonian. Both problems can be solved by the finite difference method in which the appropriate derivative terms in the differential equations are approximated as difference terms on a mesh in the wire or well region. The resulting matrix equation is then solved by the standard eigenvalue technique In Fig.1 we show the bandstructure and the density of states for the valence band in a $100\mathring{A} \times 100\mathring{A}$ wire Although the conduction band structure is approximately parabolic, the valence band structure is much more complex owing to the non-parabolicities and heavy light hole mixing. The effect of the non-parabolicities on the density states is to broaden or smear the sharp peak at the bandedge which may be expected from the parabolic dispersion relation analysis. The strain is incorporated into our formalism by calculating the splitting between the heavy and light holes by the method found in Ref.[2]. Compressive strain is obtained by adding In into the well region, and the lattice mismatch ϵ is related to the In mole fraction by $\epsilon = -(0.07)x$. Tensile strain is obtained by adding P into the well region. The resulting bandstructure for the $100\mathring{A} \times 100\mathring{A}$ $In_{0.2}Ga_{0.8}As$ wire is shown in Fig.2.

The material gain can be calculated from the Fermi Golden Rule yielding (in Gaussian units)

$$g(\hbar\omega) = \frac{4\pi^2 e^2 \hbar}{n_0 c m_0^2 \hbar\omega} \frac{1}{A} \frac{2}{2\pi} \int dk_z \sum_{n,m} |\hat{\varepsilon} \cdot \vec{P}_{nm}(k_z)|^2 \delta(E_n^e(k_z) - E_m^h(k_z) - \hbar\omega)[f^e(E_n^e) - f^h(E_m^h)], \tag{1}$$

where $f^e(E_n^e)$ and $f^h(E_m^h)$ are the electron and hole quasi-Fermi functions respectively The light experiences optical gain only in the well region, therefore, we characterize the laser optical gain by multiplying the material gain by an optical confinement factor $\Gamma = \gamma/W$, where γ is the optical confinement per unit width and W is the width of the quantum wire in the direction of the current flow.

The differential gain is given as the partial derivative of the material gain with respect to the carrier concentration. The recombination rate is also necessary in order to determine the threshold current and is given by the dipole transition rate for carrier-confined states

$$R_{sp} = \int d(\hbar\omega) \frac{4e^2 n_r \hbar\omega}{3m_0^2 c^3 \hbar^2} \frac{2}{2\pi} \int dk_z \sum_{n,m} |\vec{P}_{nm}(k_z)|^2 \delta(E_n^e(k_z) - E_m^h(k_z) - \hbar\omega)[f^e(E_n^e)][1 - f^h(E_m^h)] \tag{2}$$

Note that the above expressions are applicable to quantum wires. The formalism for quantum wells can be found in Ref [3] In order to provide a theoretical estimate of the threshold carrier density we set up the optical loop gain for the cavity losses, resulting in the transparency condition

$$\Gamma g(n_{th}, E_{peak}) = \frac{1}{L_c} \ln \frac{1}{R} + \alpha_i, \tag{3}$$

where $g(n_{th}, E_{peak})$ is the material gain at the peak mode E_{peak}, L_c is the length of the cavity, R is the reflectivity of the mirrors, and α_i is the intrinsic cavity loss. We assume a total loss of 48 cm^{-1} for the Fabry-Perot laser cavity. Below threshold, the current is completely due to spontaneous recombination, and the threshold current density is given by.

$$J_{th} = eR_{sp}(n_{th}). \tag{4}$$

The transparency carrier density and maximum differential gain are shown for a number of lattice-matched and strained wires in Table 2 The same parameters are shown in Table 3 for a variety of quantum well structures Reduction in the transparency density

can be achieved by built-in strain compressive as well as tensile, or orienting the wire axis along the [111] direction. Growth along [111] offers a more than 50 % decrease in the transparency density due to the greater separation between the subbands resulting in a more nearly parabolic dispersion relation. The effect of strain is similar, but less pronounced (see Fig. 2). The transparency densities in quantum wells are 30-40 % greater than those in quantum wires for optimized wire and well sizes. A lower transparency density normally corresponds to a lower threshold current for identical optical cavities provided the recombination rates are comparable for different structures. We have calculated a threshold current density of 80 A/cm^2 for the 100$\AA$ × 100$\AA$ GaAs wire, and that of 30 A/cm^2 for the $In_{0.2}Ga_{0.8}As$ wire of the same cross section. This corresponds to a threshold density of 560 A/cm^2 for the 50$\AA$ GaAs well and 150 A/cm^2 for the 50$\AA$ $In_{0.2}Ga_{0.8}As$ well. While the threshold currents are found to be much smaller in quantum wires than in quantum wells, we note that the reduction achieved by incorporation of strain is not as drastic.

The gain spectrum found as a result of our calculations is much more narrow than that calculated for quantum well lasers explicable by the sharpness and narrowness in the density of states function in a quantum wire. The narrow gain spectrum not only insures excellent mode selectivity and ease of single mode operation at low injected currents, but also provides substantial damping of the relaxation oscillations observed as the response to a step in the driving current since the side-mode power is very low. Also shown in Tables 2 and 3 is the maximum differential gain achievable in each structure. The differential gain is an important parameter for high speed modulation of semiconductor lasers. It is clear that quantum wire lasers are capable of significantly higher differential gains than quantum wells, in some cases of the order of 10^{-13} cm^2. Higher differential gains may lead to a much lower linewidth of emission in quantum wires. However, high speed modulation in quantum wires may be degraded by the extremely slow relaxation processes as discussed in the following section.

3 Relaxation Processes

The modulation speed for a semiconductor laser is normally calculated with the assumption of a quasi-Fermi distributions for both electrons and holes. This assumption is excellent for bulk lasers, in which the intraband relaxation times are of the order of one picosecond. In quantum wells, however, the relaxation time increases by as much as an order of magnitude due to the reduction in the momentum space and difficulty in coupling of the extended states in the barrier to the confined states in the well. While the capture time in quantum wells depends on the width [7] and structure, the relaxation time for electrons injected into the well is of the order of picoseconds. The relaxation time for holes is expected to be much lower than that for electrons primarily due to the higher density of states and a greater number of subband levels in the valence band.

In quasi one-dimensional systems, the only intrasubband electron-electron scattering process allowed by the requirement of simultaneous conservation of energy and momentum is the exchange of states by the colliding electrons. The main mechanism for energy loss in quantum wires is expected to be emission of polar optical phonons whose energy is nearly constant near the zone center. The lack of randomization by electron-electron scattering may result in bottlenecks in the relaxation process, in which the temperature of the electron distribution significantly exceeds that of the lattice up to time scales of 100 ps. The bottlenecks are eventually overcome owing to the small, yet finite, inelasticity of the acoustic phonons, but the relaxation times may range, depending on the wire size, from 100 ps to 1 ns [9]. With such long relaxation times, the assumption of the Fermi-Dirac distribution for electrons in the small-signal analysis is no longer correct. In fact, laser modulation with frequencies exceeding the reciprocal of the relaxation time is problematic. In this sense, we say that electron relaxation sets the upper limit on the laser modulation frequency.

We calculate the electron relaxation times for a number of quantum wire cross sections by an ensemble Monte Carlo simulation. A large number of electrons (5,000-10,000) are injected in a thermal distribution at the edge of the potential well formed by the barrier region. They are allowed to interact with the reservoir of acoustic and polar optical phonons, as well as between themselves, and their progress is recorded as a function of time. The scattering rates are calculated in the Born approximation as follows:

$$W_{n,n'} = \frac{2\pi}{\hbar} \sum_{q} |M_{n,n'}(q)|^2 \delta(E_{n'} - E_n \pm \hbar\omega), \tag{5}$$

where the upper sign corresponds to absorption and the lower sign to emission of a phonon. Since we consider quantum wires of cross sections from 100$\AA$ × 100$\AA$ up, we assume that the coupling between the confined electronic states and localized electronic states is significantly smaller than that between electrons and confined bulklike phonons, and perform our calculations only for the latter interaction. The Fröhlich coupling between polar optical phonons and electrons is much stronger than the deformation-potential coupling between acoustic phonons, the POP scattering rates are on the order of 10^{12} s^{-1} with sharp peaks corresponding to the peaks in the density of states, while the AP scattering rates are smaller by an order of magnitude. The effect of screening is incorporated using the Thomas-Fermi theory. The details of the formalism are presented elsewhere [10].

In Fig 3, we plot the electron relaxation times for two electron concentrations for the 100$\AA$ × 100$\AA$ quantum wire. At a high screening carrier density characteristic of laser operation, the relaxation time ranges from 120 ps for the 100$\AA$ × 100$\AA$ wire to 30 ps for the 200$\AA$ × 200$\AA$ wire (Fig 4). However, for large wire sizes, the threshold current approaches that in quantum wells, therefore, we must conclude that based on the model described above, the relaxation times in quantum wires exceed those in quantum wells by at least an order of magnitude. The theoretical limit on the modulation frequency for 100$\AA$ × 100$\AA$ quantum wire laser is thus calculated to be less than 10 GHz. That is well below the highest modulation frequencies obtained for some quantum well lasers.

4 Conclusions

We have made a comparative analysis of the optoelectronic properties in lattice-matched and strained quantum well and quantum wire systems. We have found that in quantum wires the transparency carrier density is reduced considerably in comparison with quantum wells, which leads to significantly lower threshold currents. The maximum differential gain is increased in quantum wires by an order of magnitude in comparison with quantum wells, which may lead to a lower linewidth for emission. However, a consideration of the relaxation processes with the inclusion of electron-phonon and electron-electron interaction leads us to believe that the electron relaxation time in quantum wires may be increased to over 100 ps and may constitute the upper limit on the modulation frequency. Therefore, although the quantum wire laser requires a significantly lower threshold current than a comparable quantum well laser, high speed operation in quantum wire lasers may be degraded in comparison with quantum wells due to exceedingly slow carrier relaxation processes.

References

1. Y. Arakawa and A. Yariv, *IEEE J. Quant. Electron.* **22**, 1887 (1986)
2. J.P. Loehr and J. Singh, *IEEE J. Quant. Electron.* **27**, 708 (1991)
3. Y. Lam, J.P. Loehr and J. Singh, *IEEE J. Quant. Electron.* **28**, 1218 (1992)
4. P.M. Petroff, A.C. Gossard, R.A. Logan and W. Wiegman, *Appl. Phys. Lett.* **41**, 635 (1982).
5. M. Tsuchiya, J.M. Gaines, R.H. Yan, R.J. Simes, P.O. Holtz, L.A. Coldren and P.M. Petroff, *Phys. Rev. Lett.* **62**, 466 (1989)
6. S.M. Goodnick and P. Lugli, *Phys. Rev. B* **37**, 2578 (1988)
7. J.A. Brum and G. Bastard, *Phys. Rev. B* **33**, 1420 (1986).
8. J.P. Leburton, *Phys. Rev. B* **45**, 11922 (1992).
9. I. Vurgaftman and J. Singh, *Appl. Phys. Lett.* **62**, 2251 (1993)
10. I. Vurgaftman and J. Singh, submitted for publication

List of Figures

Fig. 1 The valence band structure (a) and density of states (b) for the $100\text{Å} \times 100\text{Å}$ $GaAs/Al_{0.3}Ga_{0.7}As$ quantum wire

Fig. 2 The valence band structure (a) and density of states (b) for the $100\text{Å} \times 100\text{Å}$ $In_{0.2}Ga_{0.8}As/Al_{0.3}Ga_{0.7}As$ quantum wire.

Fig. 3 The energy averaged over a large number of electrons as a function of time after injection for a $100\text{Å} \times 100\text{Å}$ GaAs quantum wire for low and high injected carrier concentrations. The horizontal line corresponds to the expectation value of the energy for the equilibrium Fermi distribution.

Fig. 4 The electron relaxation time as a function of the wire cross section. A square cross section is considered, the length of the side is given for carrier concentrations of 10^{16} cm^{-3} and 10^{18} cm^{-3}

Symbol	Physical Meaning	Numerical Quantity
ϵ	Lattice Mismatch	$\sim(0.07)x$ for $In_xGa_{1-x}As$
n_o	Refractive Index	3.6 in GaAs
$\hbar\omega$	Photon Energy	
A	Wire Cross-Sectional Area	
$\hat{e}$	Light Polarization	
$\vec{P}_{nn'}$	Momentum Matrix Element	$\frac{2}{m_o}\lvert < s\lvert p_x\rvert x > \rvert^2 = 25.7$ eV
$f^c(E_n^c),\ f^v(E_{n'}^v)$	Electron and Hole Quasi Fermi Functions	
γ	Optical Confinement per Unit Width	0.00025 1/Å
W	Width in Direction of Current Flow	
L_z	Cavity Length	500 μm
R	Mirror Reflectivity	0.32
α_i	Internal Cavity Loss	10 cm^{-1}
$W_{nn'}$	Scattering Rate between States n and n'	
$M_{nn'}$	Overlap Matrix Element between n and n'	

Table 1 The list of symbols with numerical quantities used in calculations (where appropriate)

Structure		Transparency Density	Differential Gain
GaAs (001)	$50\text{Å} \times 100\text{Å}$	1.10×10^{18} cm^{-3}	3.0×10^{-15} cm^2
	$100\text{Å} \times 100\text{Å}$	1.25×10^{18} cm^{-3}	2.0×10^{-15} cm^2
GaAs/ (001)	$50\text{Å} \times 100\text{Å}$	0.90×10^{18} cm^{-3}	5.0×10^{-15} cm^2
	$100\text{Å} \times 100\text{Å}$	1.00×10^{18} cm^{-3}	1.2×10^{-15} cm^2
InGaAs (001)	$50\text{Å} \times 100\text{Å}$	0.95×10^{18} cm^{-3}	4.7×10^{-15} cm^2
	$100\text{Å} \times 100\text{Å}$	1.05×10^{18} cm^{-3}	1.2×10^{-15} cm^2
GaAs (111)	$50\text{Å} \times 100\text{Å}$	0.50×10^{18} cm^{-3}	7.0×10^{-15} cm^2
	$100\text{Å} \times 100\text{Å}$	0.60×10^{18} cm^{-3}	4.5×10^{-15} cm^2

Table 2 The transparency carrier density and the maximum differential gain for a number of quantum wire structures

Structure	Transparency Density	Differential Gain
50Å GaAs (001)	1.80×10^{18} cm^{-3}	3.0×10^{-16} cm^2
50Å InGaAs (001)	1.25×10^{18} cm^{-3}	1.0×10^{-15} cm^2
50Å GaAs (111)	0.75×10^{18} cm^{-3}	2.0×10^{-16} cm^2

Table 3 The transparency carrier density and the maximum differential gain for a number of quantum well structures

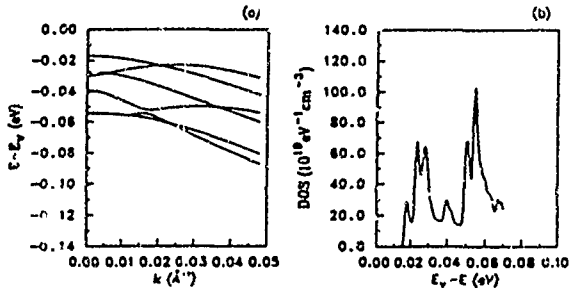

Figure 1.

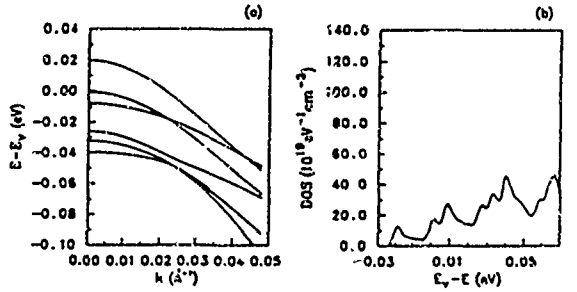

Figure 2.

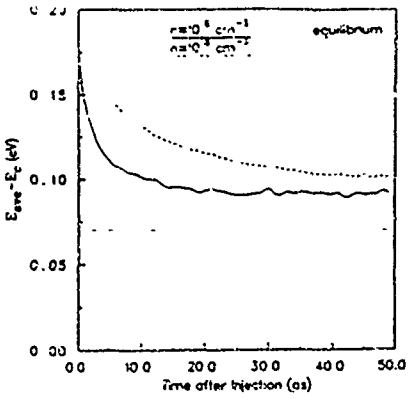

Figure 3.

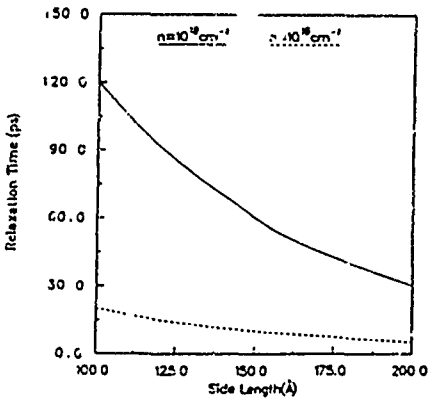

Figure 4.

ThP39

Photomodulation Spectroscopy of Narrow Minibands in the Continuum of Multi Quantum Wells

J. Oiknine-Schlesinger, E. Ehrenfreund, D. Gershoni and D. Ritter
Solid State Institute, Technion-Israel Institute of Technology,
Haifa 32000, Israel

R.A Hamm, J.M. Vandenberg and S-N.G. Chu
AT&T Bell Laboratories, Murray Hill, NJ 07974, USA

Abstract

Photomodulation technique is utilized to spectroscopically resolve minibands structure in the energy "continuum" above the barriers of a *InGaAs/InP* multi quantum-well structure. Above-bandgap radiation is used to continuously pump electrons into the first electronic level, which is confined in each well. Infrared radiation is used to probe the optical transitions of these electrons to higher subband levels. The transition to the second electronic level, which is also confined, is observed together with higher order transitions to extended states. By comparison between the experimental observations to calculations based on the $\vec{k}\cdot\vec{p}$ model, we account for the energy, the lineshape and temperature dependence of the newly observed minibands.

Introduction

A discrete set of energy levels characterizes the energy spectrum of a quantum-well (QW) bellow its barrier's energy. The wavefunctions associated with these levels are confined to the well. Above the barrier, the energy spectrum evolves into a continuum of levels with extended wavefunctions which are no longer confined to the well. Right above the barriers, however, the continuum is not uniform and the variations in the density of states still resemble the discrete spectrum at lower energies. In a multi quantum-well (MQW) structure, at energies lower than the energy of the barriers, the spectrum is discrete and is similar to that of a single QW, since wavefunctions of neighboring wells do not interact. However, right above the barriers, minibands of finite width, separated by forbidden minigaps, where the density of states vanishes, are formed. The wavefunctions associated with these minibands, are not confined to an individual well, and they extend over the whole structure (similar to a superlattice (SL)). At yet higher energy above the barrier, the forbidden gaps between the minibands diminish, and a continuum of states is restored.
Intersubband absorption in MQWs and superlattices (SL) has been intensively studied in recent years, following the pioneering work of West and Eglash [1]. Most of the works reported intersubband absorption between the first two confined states (n=1 to n=2) in a MQW structure [1-4]. The characteristic width of the absorption line at low temperatures, due to this optical transition was found to be 10-20 meV. This width was attributed to inhomogeneous broadening caused by interface roughness and structural fluctuations of the samples studied. Considerably broader absorption lines were found in narrow MQW structures, where only one confined state exists in each QW. In these structures the second level is pushed above the barrier, and a miniband of extended states is formed. The spectral width of the absorption line in these structures reflects the finite width of this second (n=2) miniband [5, 6]. These latter structures are used as efficient infrared (IR) detectors [6]. Recently, confined electronic states above the barrier were reported in special structures where a "Bragg reflector" was used to confine carriers to the barrier region [7, 8].
In this work we study the continuum minibands that correspond to truly propagating states in MQW structures. We focus our attention here to intersubband transitions studied by the photoinduced absorption (PIA) technique. This is a two beam method, in which we continuously pump electrons into the lowest n=1 level, using interband excitation, while probing the changes in intersubband absorption by weak IR radiation [9]. Using this technique, we have observed transitions between the n=1 and n=2 confined levels [10], and between the *n=1 confined level and the continuum minibands*. We analyze our experimental results by means of an eight band $\vec{k}\cdot\vec{p}$ theoretical model [11], which is used to calculate the electronic band structure and wavefunctions of the MQWs. The matrix elements for optical transitions between the various states are calculated by the dipole approximation using the calculated wavefunctions[12]. The absorption is then calculated by summing over all the allowed optical transitions from occupied to unoccupied states. The distribution of carriers within our one-electron band structure is calculated using the estimated carrier concentration, and assuming thermal equilibrium [12].

Experimental

The optical measurements were performed on a sample of InGaAs quantum well lattice matched to InP. The sample was grown by metal organic molecular beam epitaxy (MOMBE) as described elsewhere [13]. It consists of 15 periods of nominally undoped 65 Å $In_{0.53}Ga_{0.48}As$ ternary wells separated by 367 Å InP binary barriers. The sample dimensions were determined by high resolution x-ray diffraction and transmission electron microscopy [13]. Carrier concentration is estimated from Hall measurements performed on thick ($> 1\mu m$) ternary layers grown under the same conditions. The estimated unintentional n-doping concentration in our sample is $< 1 \times 10^{16} cm^{-3}$. To allow for an IR electric field component parallel to the MQW axis the sample was fabricated as a multipass waveguide by polishing a 45° angle on both edges. The changes, ΔT, in the IR transmission, T, through the waveguide due to above-bandgap optical excitation of the sample surface were measured using a lock-in technique and a step-scan Fourier transform IR spectrometer. The photoinduced changes in the absorbance of the whole waveguide is then equal to $-\Delta T/T$. An all-lines Ar^+ laser was used for the pump and incandescent Nernst glower source for the probe. The sample was placed in a Helium immersion cryostat, with variable temperature capability.

Results

The PIA results are presented as $\Delta\alpha$, the average change in the absorption coefficient per period. $\Delta\alpha$ is obtained from the measured $-\Delta T/T$ by taking into account the number of passes the IR beam makes inside the waveguide, the number of wells, the direction of the IR beam and the period of the MQW. The solid (dashed) line in Fig. 1a is the photoinduced absorption spectrum, $\Delta\alpha$, for IR light polarized parallel (perpendicular) to

the growth direction. The lowest optical band centered at 0.155 eV, is identified as the e1-e2 transition [10]. It is polarized along the growth direction. Its shape is distinguishably asymmetric. It can be described as composed of two components: a relatively narrow line of 7 meV full width at half maximum, characteristic of intersubband absorption between two confined states, and a broad shoulder in the high energy side. Three additional bands, around energies of 0.18, 0.20 and 0.22 eV, respectively, are clearly resolved (solid line). Since the barrier in this sample is estimated to be at energy of 0.165 eV above the n=1 level, these additional absorption bands are due to optical transitions between the n=1 confined state to states above the barrier. This conclusion is in perfect agreement with our model calculations as displayed in Fig. 1b. The absorption spectra in Fig. 1b are calculated for a uniform background electron concentration of $\simeq 2 \times 10^{18} cm^{-3}$ per period. The intensity of the laser pump in these experiments was 1 Watt/cm^2, for which we estimate the steady state photoexcited electron density as $\simeq 6 \times 10^{8} cm^{-2}$ per period [14], in addition to the background electron density. Since we have found that the absorption spectrum is nearly linear with the electron density, we have calculated the changes in the absorption due to laser beam, $\Delta\alpha$, by dividing the absorption calculated for the actual background density by a factor of 15. The solid line is the calculated changes in the absorption for the nominal width of the well, 65 Å. Apart from the strong e1-e2 transition (at 0.15 eV), there appear several distinct weaker bands, at 0.17, 0.18, 0.20 and 0.22 eV, which we identify as the e1-e3, e1-e4, e1-e5 and e1-e6 transitions, respectively. The bands are identified by the optical transition which contribute the most to their oscillator strength. From the agreement between the measured and calculated spectra both in spectral positions and relative intensities we conclude that the observed spectral bands at energies above the e1-e2 transition, are due to optical transitions into the continuum minibands. Moreover, the typical asymmetric shape of the absorption lines can be understood by monolayer fluctuations in the QW widths. In order to show this, we have plotted the absorption spectra for identical samples having 62 and 68 Å well width and the same periodicity (broken lines, Fig. 1b). The sharp rise at low energies and the slower fall at the high energy side, can be reproduced by averaging over the three spectra shown in Fig. 1b.

In Fig. 2a we show the experimental PIA spectrum at various temperatures in the range 3-200 K. Since the experimental spectra are polarized along the growth direction (see Fig. 1), these experimental spectra were taken with unpolarized IR radiation in order to increase the signal to noise ratio. Two features are apparent in the evolution of the PIA spectra as the temperature increases: (a) There is additional absorption in the low energy side of the e1-e2 transition, which makes this line more symmetric in shape. (b) The "continuum" minibands become weaker relative to the e1-e2 band and are barely observable above 130 K.

Discussion

In order to discuss our results, it is instructive to consider the conduction subband structure relevant to our sample. Fig. 3a shows the calculated subbands energies *vs* the in plane wavevector, $\vec{k}_t$ [11]. In addition to the two discrete confined levels e1 and e2, there are also very narrow minibands at energies above the barrier. The widths of these minibands result from the finite overlap between wavefunctions of neighboring periods. The overlap becomes more significant for higher subbands and at high enough energies a continuum of states is formed. Thus, it is only the spectral region in the close vicinity to the barrier which distinguishes between the MQW and the single QW case. The absorption spectra shown in Figs. 1b and 2b, were all calculated using the band structure and wavefunctions (not shown) of Fig. 3a. Fig. 3b shows the population density of the e1 level in thermal equilibrium, $n(E)$, as a function of the energy E. It is seen that, as the temperature increases, a larger portion of the Brillouin zone is occupied by electrons. This, in turn, gives rise to lower energy optical e1-e2 transitions due to the difference in curvature (effective mass) between the two subbands. This qualitatively explains the evolution of the low energy tail of the e1-e2 transition as the temperature increases. A more quantitative description is given in Fig. 2b, where the intersubband absorption spectra are calculated for various sample temperatures.

The relative decrease of the observed e1 to minibands absorption as a function of temperature, can only be partially accounted for by our model. In the temperature range, 3-90 K, the reduction in the relative intensity of the measured minibands absorption is somewhat larger than what we calculate (see Fig. 2). We believe that this discrepancy, has to do with important extrinsic contributions to the PIA signal. These contributions explain also the saturation of the PIA at large laser intensities [15]. Since our model does not take any extrinsic effects into account, it cannot explain all the experimental details.

Finally, we have also studied these intersubband transitions in n-doped samples by measuring their dark absorption (without interband excitation). Under these conditions there could not be any effect of photoexcited holes on the intersubband absorption. Detailed account of this study is reported separately [16].

Summary

We have studied, by means of photoinduced absorption spectroscopy, optical transitions between confined electronic states of a MQW to minibands in its continuum. By comparison with a theoretical model we identify all the observed transitions, explain their strength, spectral shape, polarization selection rules, and temperature dependence.

Acknowledgments The work was carried out in the Center for Advanced Optoelectronics, and was supported by the Technion Vice President Fund-the Sydney Goldstein Research Fund and by the Basic Research Foundation Administered by the Israel Academy of Sciences and Humanities, Jerusalem, Israel.

References

[1] L.C. West and S.J. Eglash, Appl. Phys. Lett. 46, 1156 (1985).

[2] B.F. Levine, R.J. Malik, J. Walker, K.K. Choi, C.G. Bethea, D.A. Kleinman and J.M. Vandenberg, Appl. Phys. Lett. 50, 273 (1987).

[3] A. Seilmeier, H.J. Hubner, G. Abstreiter, G. Weimann and W. Schlapp, Phys. Rev. Lett. 59, 1345 (1987).

[4] H. Asai and Y. Kawamura, Phys. Rev. B 43, 4748 (1991).

[5] G. Abstreiter, T. Egeler, S. Beeck, A. Seilmeier, H.J. Hübner, G. Weimann and W. Schlapp, Surface Science 196, 613 (1988).

[6] S D. Gunapala, B F. Levine, R A.Logan, T Tanbun Ek and D A. Humphrey, Appl Phys. Lett 57, 1802 (1990).

[7] M. Zehler, J Brener, G. Lenz, J. Salzman, E Cohen and L. Pfeiffer, Appl Phys. Lett 61, 949 (1992)

[8] F. Capasso, C Sirtori, J Faist, D L Sivco, S N G Chu and A.Y Cho, Nature 358, 565 (1992)

[9] M Olszakier, E. Ehrenfreund, E Cohen, J Bajaj and G.J Sullivan, Phys Rev Lett 62, 2907 (1989).

[10] J Oiknine-Schlesinger, E Ehrenfreund, D. Gershoni, D. Ritter, M B. Panish and R.A. Hamm, Appl Phys. Lett 59, 970 (1991)

[11] G A. Baraff and D. Gershoni, Phys. Rev. B 43, 4011 (1991)

[12] D Gershoni, C.H. Henry and G A. Baraff, IEEE Journal of Quantum Electronics (in press, 1993).

[13] D. Ritter, R.A. Hamm, M B. Panish, J.M. Vandenberg, D Gershoni, S.D Gunapala and B.F. Levine, Appl Phys Lett 59, 552 (1991)

[14] I. Brener, D. Gershoni, D. Ritter, M.B. Panish and R.A. Hamm, Appl. Phys. Lett 58, 965 (1991).

[15] E. Ehrenfreund, J. Oiknine-Schlesinger, D. Gershoni, D. Ritter, M.B. Panish and R.A Hamm, Surface Science 267, 461 (1992)

[16] D. Gershoni, J Oiknine-Schlesinger, E Ehrenfreund, D Ritter, R A. Hamm and M B. Panish, submitted for publication

Figure Captions

Fig. 1 (a) The photoinduced absorption $\Delta\alpha$, per well for infrared light polarized along the growth direction (solid line) and perpendicular to it (dashed line) (b) The calculated $\Delta\alpha$, for light polarized along the growth direction. Solid line - nominal well width thickness of 25 monolayers. Dashed (dotted) line - well width of 23 (21) monolayers

Fig 2 Measured (a) and calculated (b) $\Delta\alpha$ for various temperatures The spectra are vertically displaced for clarity The calculated spectra are averaged over ±1 monolayer fluctuations

Fig. 3 (a) Calculated conduction subband structure plotted as energy vs. the in plane wavevector, $k_\perp$ The energy is measured from the top of the $In_{0.53}Ga_{0.47}As$ QW valence band. (b) The calculated electron occupation density $n(E)$, in thermal equilibrium, for T=3 and 200 K.

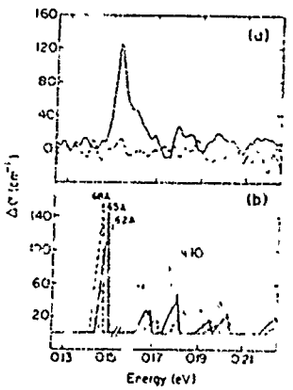

Fig. 1

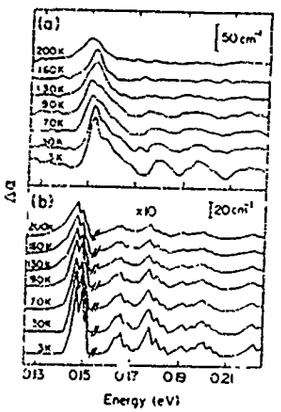

Fig. 2

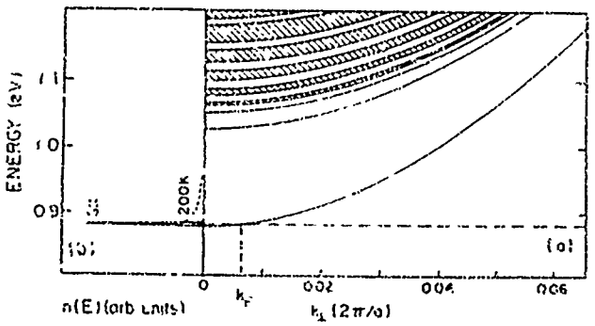

Fig. 3

ThC1

Intersubband lifetime in quantum wells with transitions energies above and below the optical phonon energy

Jerome Faist, Federico Capasso, Carlo Sirtori, Deborah L. Sivco, Alfred Y. Cho, Loren Pfeiffer and Ken West

AT&T Bell Laboratories, Murray Hill, NJ 07974 (908) 582 2336

A new measurement of the intersubband lifetime is presented. In a first set of experiments, electrons are pumped from the ground state to the first excited state of a n-doped quantum well using a c.w. CO_2 Laser. A Fourier transform infrared spectrometer beam probes the absorption cross-section between the first and second excited state, measuring the *population* of optically excited electrons. From this cross-section, we find a lifetime equal to $\tau_2 = 0.65 \pm 0.15$ps for a 85 Å GaAs quantum well and $\tau_2 = 0.8 \pm 0.3$ps for a 100 Å $Ga_{0.47}In_{0.53}As$ quantum well, in good agreement with the theoretical predictions of Ferreira and Bastard. In a second set of experiment we investigate a asymmetric modulation-doped GaAs/AlGaAs coupled quantum well in which the spacing between the ground and first excited state E_{01} = 18.6meV is below the optical phonon energy. Electrons are optically pumped on the short-lived second excited state (E_{02} = 115meV) and some of them, cascading down, are trapped on the first excited state. A measurement of the differential absorption between the first and second excited state proves the existence of a bottleneck effect and we estimate an electron lifetime of about τ_2 = 300fs. The extremely narrow (FWHM = 2.6meV) lorentzian line of the (0-2) transition corresponds to a time τ = 0.5 ps, very close to the lifetime (0.65ps) measured in the first experiment. This is a clear indication that we are able to observe the ultimate broadening mechanism of intersubband transitions: lifetime broadening.

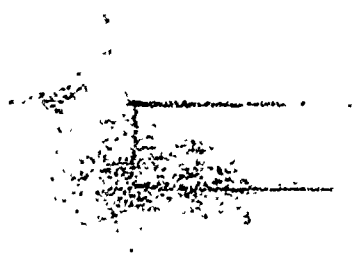

ThC2

MINIBAND DISPERSION, CRITICAL POINTS, AND IMPURITY BANDS IN SUPERLATTICES: AN INFRARED ABSORPTION STUDY

M. Helm, W. Hilber, T. Fromherz
Institut für Halbleiterphysik, Universität Linz, A 4040 Linz, Austria

F. M. Peeters
Department of Physics, University of Antwerp (UIA), B 2610 Wilrijk, Belgium

K. Alavi, R. N. Pathak
Center for Advanced Electron Devices and Systems, Department of Electrical Engineering, The University of Texas at Arlington, Arlington, TX 76019

ABSTRACT

Infrared absorption is employed to study the structure of the minibands in GaAs/AlGaAs superlattices. The miniband dispersion is directly revealed through two absorption maxima, related to the singularities of the density of states at the center and the edge of the mini-Brillouin zone. The total lineshape is strongly asymmetric and can be quantitively explained, when the k_z-dependent transition matrix elements are taken into account. It is argued that the asymmetry follows from the oscillator sum rule. When the doping is low, so that the Fermi energy lies in the first miniband, the $k_z=\pi/d$ peak can be suppressed at low temperature due to thermal depopulation, which reflects the curvature of the lowest miniband. At low temperature another absorption line is observed, identified as $1s\text{-}2p_z$ impurity transition. The existence of this transition implies that the impurity band has not merged with the conduction band despite the metallic behavior.

1. INTRODUCTION

Despite the impressive recent progress in the physics of semiconductor superlattices, as is evidenced by the observation of the Wannier-Stark ladder [1] and of Bloch oscillations [2], the number of experiments directly revealing the curvature of the minibands is rather scarce. In transport experiments, the measured current-voltage characteristics has to be simulated with a complicated model [3], and in optical experiments [4] one has to deal with holes in addition to the electrons, and also with excitons [5].

In the present paper we show that infrared absorption between minibands is a way of directly probing the miniband dispersion. Since all minibands within the conduction band have the same in plane curvature (leaving nonparabolicity aside), the joint density of states has one-dimensional character and shows δ function like singularities. This is in contrast to interband transitions, where the joint density of states contains electron and hole states and is much less divergent due to their different curvatures. In the here reported experiment the miniband dispersion is directly evidenced through strong absorption maxima resulting from the critical points at the mini-zone edges [6]. A strong asymmetry is observed and can be explained, if the k_z-dependent transition matrix elements are taken into account. At low temperature thermal depopulation of the first miniband is reflected in the absorption spectrum through the disappearance of the $k_z=\pi/d$ peak. Furthermore an impurity transition ($1s\text{-}2p_z$) contributes to the absorption at low temperature.

2. EXPERIMENTAL DETAILS

Two $GaAs/Al_{0.3}Ga_{0.7}As$ superlattices with different doping concentrations were studied. They were grown by molecular beam epitaxy on semi-insulating GaAs (100) substrates and a 2000 Å

nuite, undoped GaAs buffer. In both cases the nominal width of the GaAs quantum wells was 75 Å and the width of the AlGaAs barriers 25 Å, corresponding to a superlattice period of d= 100 Å. Superlattice No 1 was homogeneously doped n type, to give an electron concentration of $6x10^{17}$ cm^{-3}, with a total thickness of 2 µm (200 periods), superlattice No 2 was doped to n = $6x10^{16}$ cm^{-3} and had a thickness of 5 µm (500 periods). Due to the homogeneous doping, band bending can be assumed to be rather small. Sample characterization was performed by X-ray diffraction and Hall measurements, yielding a period of 96.5 Å for both superlattices and a peak mobility of 3000 cm^2/Vs (at 200 K) for sample No 1 and 6000 cm^2/Vs (at 100 K) for No 2, respectively.

Infrared absorption measurements were performed with a Bruker IFS 113v rapid scan Fourier transform spectrometer. The samples were mounted in a liquid helium flow cryostat, where the sample temperature could be varied between 5 K and 300 K. In order to achieve an active polarization for the intersubband absorption (electric field perpendicular to the layers), the samples were prepared in a multi pass waveguide geometry [7]. Then the ratio of active and inactive polarization was measured for the superlattice and a reference substrate in the same geometry. In order to obtain data which were completely free of any system artifacts, a metallic grate (Ti/Au) was deposited on the waveguide samples and was used to modulate the electron density in the top section of the sample.

3 THEORY

Fig. 1 shows the band structure for the nominal parameters of the superlattices, calculated within the one-band effective mass approximation. For sample No.1 the Fermi energy at low temperature is calculated to be 67 meV, that is between the first and second miniband, and for sample No 2 at 43 meV, which is approximately in the middle of the first miniband (depolarization effects neglected). In addition, the 1s and $2p_z$ donor states are shown schematically. Although the binding energy of impurities in superlattices depends on the position of the impurity atom [8,9], this variation is smaller than 3 meV in the present case, and can therefore be neglected compared to the other energies involved. Moreover, since the doping level is well above the metal-insulator transition (n_M=1.5x10^{16}cm^{-3} for bulk GaAs), the donors will form impurity bands rather than isolated energy levels. These two donor states can be regarded as bands for band width of delocalized states sitting at the bottom of or marginally below each miniband.

Within a single-particle approximation the absorption coefficient for transitions between the two lowest minibands can be expressed as

$$\alpha = \frac{\pi^2\hbar^2}{\varepsilon_0 c n \hbar^2 \pi m^* \omega} \int_0^{\pi/d} dk_z |\langle \psi_2 | p_z | \psi_1 \rangle|^2 \cdot n \left\{ \frac{1+\exp[(E_F - E_1(k_z))/kT]}{1+\exp[(E_F - E_2(k_z))/kT]} \right\} \left\{ \frac{\Gamma/\pi}{(E_2(k_z) - E_1(k_z) - \hbar\omega)^2 + \Gamma^2} \right\} \quad (1)$$

Here, k is Boltzmann's constant and n is the refractive index. The other quantities have their usual meaning. The dispersions of the first and second minibands $E_1(2)(k_z)$, as well as the momentum matrix elements (also k_z-dependent) are calculated within the above model. Note that for atomic periodic systems, the A·p interaction has to be used for the electron radiation coupling, whereas the $\vec{E}\cdot\vec{r}$ interaction leads to wrong results if the wavefunction does not vanish in the barriers [10]. The Fermi energy, E_F, has to be determined from the electron concentration for each temperature. It is assumed that each transition at wave vector k_z is broadened in a Lorentz an fashion with the broadening parameter Γ. There are basically three factors determining the absorption coefficient. The joint density of states, the Fermi Dirac distribution already integrated over k_x and k_y, and the squared momentum matrix element. The latter can be expressed through the oscillator strength by $f_{12} = (2/m^*\hbar\omega_{21})|\langle 1|p_z|2\rangle|^2$. The joint density of states for the present superlattices is shown in Fig. 2 (dashed line). The slight asymmetry stems from the fact that Kronig-Penney-like bands have a weaker curvature at their bottom edges than at their top edges. For tight-binding bands the shape would be exactly symmetric [9]. The second contribution to α, the thermal occupation factor, has the opposite effect: since at k_z = 0 there are more occupied states with finite in-plane wavevectors than at k_z = π/d, the high frequency peak is enhanced. The third, and most important contribution to α is the oscillator strength. For the present system we calculate f_{12} = 0.3 at the zone center (k_z=0) and f_{12} = 2.3 at the zone edge (k_z = π/d), which is a variation by a factor of 7.5 (the physical reason for this will be discussed later). This behavior strongly enhances the low frequency peak. The resulting absorption coefficient (for sample 1 at T=5K) is also shown in Fig. 2 (solid line).

4 EXPERIMENTAL RESULTS AND DISCUSSION

In Fig. 3 the measured absorption spectrum for the highly doped sample (No. 1) is shown for T = 5 K and T = 300 K. The lineshape remains essentially the same at both temperatures, since the thermal smearing of the distribution function occurs well above the top of the first miniband. Contributions from both critical points in the Brillouin zone are clearly resolved, a peak at 106 meV (at 5K, 103 meV at 300K) and a shoulder at about 180 meV. Comparison with the calculated absorption (Fig. 2) shows that the shape of the absorption, in particular the relative strength of the two peaks is predicted surprisingly well *without adjustable parameters*.

In the lower-doped sample the situation is more complex. Absorption spectra for five different temperatures between 5 and 300 K are shown in Fig. 4. At high temperatures, when kT is larger than the width of the lowest miniband, the absorption is similar to the one of the high-doped sample. On decreasing the temperature, the peak at 106 meV disappears, because the top of the miniband at k_z=π/d becomes thermally depopulated. This demonstrates clearly the well-developed curvature of the first miniband. In addition, a new peak at 126 meV occurs at low temperature, which can readily be identified as the $1s\text{-}^3p_z$ donor transition [9]. Since the 1s and $2p_z$ level are pinned to the bottom of the first and second miniband respectively, the spectral position of the $1s\text{-}2p_z$ transition can be used to determine the *individual* widths of the first and second miniband (and not only the sum of both) in the following way: Δ_1 = E_1(top) - E_1(bottom) = E(1s-$2p_z$) - $E_{21}(k_z=\pi/d)$, and similarly Δ_2 = E_2(top) - E_2(bottom) = $E_{21}(k_z=0)$ - E(1s-$2p_z$). This gives Δ_1 = 17 meV and Δ_2 = 54 meV. Whereas Δ_1 agrees well with the theoretical value (18 meV), Δ_2 is predicted to be 74 meV. This is however not surprising, since our above calculation does not include nonparabolic effects, which are definitely important at energies of ≈200 meV B.z introducing an energy dependent effective mass and fitting the Al content in the barrier (fitted Al-content =35%) we can get a good agreement of both the miniband widths and the absolute energetic positions.

The occurrence of the impurity transition at low temperature is remarkable in itself, since our sample is doped four times higher than the critical density for the Mott-metal insulator transition. We have also checked the metallic nature of the sample by low temperature transport measurements. Our observations imply that (1) the Fermi energy is located in the first miniband (since the k_z=0 miniband peak remains visible), but (2) the impurity band has not merged completely with the conduction band (since the impurity peak is visible).

Finally we want to make a few remarks on the variation of the oscillator strength along the superlattice Brillouin zone. It is well known that the oscillator strength obeys the so-called f-sum rule, which for a superlattice can be expressed as [10]

$$\sum_n \sum_{k_z} f_{nn'}(k_z, k_z) = 1 \quad (2)$$

Here, n (n') and k_z (k_z') are the initial (final) miniband index and wavevector along the superlattice axis, respectively. For absorptive transitions f is positive, for emission it is negative. The sum has to be performed over *all* possible final states, even if this involves non-direct transitions ($k_z' \neq k_z$), where the momentum transfer is provided by phonons or impurities. If $n'=n$, such transitions correspond to *intra* miniband absorption (Drude-like one-dimensional free-carrier absorption [11]). Now for $n=1$, $k_z=0$ is the ground state of the system from which only absorptive processes are possible. Therefore, in order to fulfill Eq. (2), all individual terms of the sum have to be *smaller* than unity, including the most important term $f_{12}(k_z=k_z'=0)$. In contrast, at $k_z=\pi/d$ intra-miniband *emission* processes are possible, which count negative in Eq. (2). Therefore the inter-miniband oscillator strength at the *zone edge* has to be *greater* than unity, $f_{12}(k_z=k_z'=\pi/d) > 1$. This tendency becomes more substantial for larger miniband widths. Besides the asymmetry of the absorption spectrum there is second manifestation of this effect. As can be seen in Fig. 4 the area under the absorption curve is not constant, but increases at low temperature. Following the above arguments, the "missing" area is contained in the intra-miniband absorption at very low frequency (< 10 meV, not measured in the present experiment). At high temperature, when the whole miniband is populated, this absorption vanishes as has been demonstrated recently [11]. Thus the asymmetry of the miniband absorption spectrum is a generic feature which follows from fundamental physical reasons.

5 SUMMARY

We have demonstrated that infrared spectroscopy is a powerful tool to study the electronic structure of superlattices, and more specific, the nature of the minibands. The critical points at the mini-zone edges manifest themselves as strong absorption maxima. The asymmetry between the two maxima is an intrinsic feature which follows from an as basic principle as the oscillator sum rule. The dispersion of the lowest miniband is further evidenced through thermal (de)population of the zone edge. Finally, the impurity-band transition enables determination of the individual widths of the two lowest minibands. The same techniques can be applied to investigate the metal - insulator transition in superlattices, which will be attempted in future experiments.

ACKNOWLEDGMENT

This work has been supported by the "Fonds zur Förderung der wissenschaftlichen Forschung," Vienna, by the Texas Advanced Technology Program (Nos. 003656-141, 003656-042), and Texas Advanced Research Program (No. 003656-107). One of us (F.M.P.) acknowledges support by the Belgian National Science Foundation.

REFERENCES

1. E. E. Mendez, F. Agullo-Rueda, and J. M. Hong, Phys. Rev. Lett. 60, 2426 (1988); P. Voisin, J. Bleuse, C. Bouche, S. Gaillard, C. Alibert, and A. Regreny, Phys. Rev. Lett. 61, 1639 (1988).
2. Ch. Waschke, H. G. Roskos, R. Schwedler, K. Leo, H. Kurz, and K. Köhler, Phys. Rev. Lett. 70, 3319 (1993), and H. G. Roskos et al., this volume.
3. P. England, J. R. Hayes, E. Colas, and M. Helm, Phys. Rev. Lett. 63, 1708 (1989); A. Sibille, J. F. Palmier, H. Wang, and F. Mollot, Phys. Rev. Lett. 64, 52 (1990).
4. B. Deveaud, J. Shah, T. C. Damen, B. Lambert, and A. Regreny, Phys. Rev. Lett. 58, 2582 (1988); H. Schneider, K. von Klitzing, and K. Ploog, Europhys. Lett. 8, 575 (1989); H. T. Grahn, K. von Klitzing, K. Ploog, and G. H. Döhler, Phys. Rev. B 43, 12094 (1991).
5. J. J. Song et al., Phys. Rev. B 19, 5562 (1979); B. Deveaud et al., ibid. 40, 5802 (1989); K. Moore, G. Duggan, A. Raukema, and K. Woodbridge, ibid. 42, 1326 (1990).
6. M. Helm, W. Hilber, T. Fromherz, F. M. Peeters, K. Alavi, and R. N. Pathak, Phys. Rev. B 48, 15 July 1993.
7. N. Hertle, G. Schobert, E. Gornik, G. Abstreiter, and F. Schäffler, Appl. Phys. Lett. 59, 3077 (1991).
8. F. Lane and K. L. Greene, Phys. Rev. B 33, 5871 (1986).
9. M. Helm, F. M. Peeters, F. DeRosa, E. Colas, J. P. Harbison, and L. T. Florez, Surface Sci. 263, 518 (1992).
10. F. M. Peeters, K. Matuda, M. Helm, T. Fromherz, and W. Hilber, submitted for publication.
11. G. Brozak, M. Helm, F. DeRosa, C. H. Perry, M. Koza, R. Bhat, and S. J. Allen, Jr., Phys. Rev. Lett. 64, 3163 (1990).

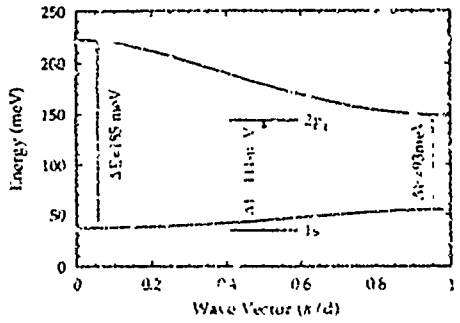

Fig. 3 The calculated dispersion of the two lowest minibands. The 1s and $2p_z$ impurity states are included schematically. The transition energies at the center and the edge of the Mini-Brillouin zone as well as the impurity transition energy are indicated.

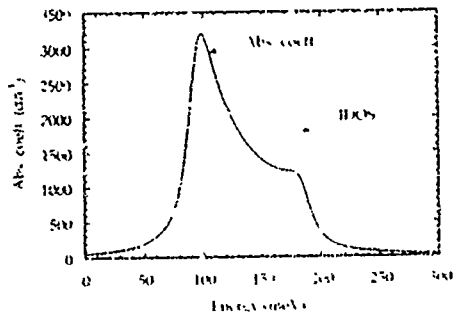

Fig. 2 One-dimensional joint density of states (dashed line) and absorption coefficient according to Eq. (2) for Γ = 10 meV, $n=6\times10^{17}cm^{-3}$, and T=5K (full line) for the minibands of Fig. 1. The units of the joint density of states are arbitrary.

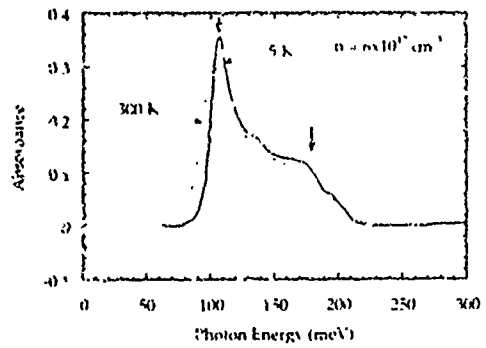

Fig 3 Experimental absorption spectrum of superlattice No 1 (n_s=6x10^{17}cm^{-3}) at T=5K and T=300K. The peaks resulting from the critical points at k_z = 0 and k_z = π/d are indicated. (Absorbance = $-\log_{10}$(Transmission))

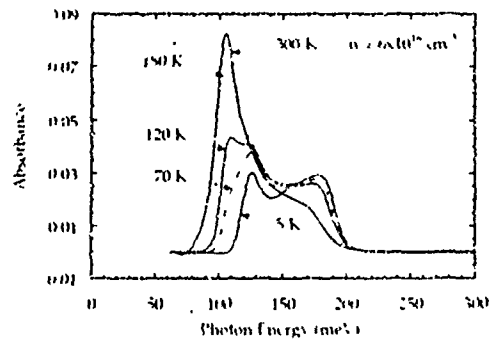

Fig 4 Experimental absorption spectra of superlattice No 2 (n_s=6x10^{16}cm^{-3}) at different temperatures as indicated.

ThC3

Inelastic Light Scattering by Electrons in GaAs Quantum Wires: Spin-Density, Charge-Density and Single-Particle Excitations.

A.Schmeller*,A.R.Goñi†,A.Pinczuk,J.S.Weiner,J.M.Calleja◊,B.S.Dennis, L.N.Pfeiffer and K.W.West.
AT&T Bell Laboratories, Murray Hill, New Jersey, USA

In inelastic light scattering experiments we observe for the first time clearly resolved one dimensional (1D) intersubband spin-density excitations. Together with new structure at energies close to the 2D intersubband transitions, these observations display the formation of 1D subbands. The depolarization shift (W_{dep}) and the excitonic shift (W_{xc}) can be deduced approximately from our experiments. These shifts are of special interest because they are related to the direct and exchange-correlation terms of the electron-electron interaction. We find ratios of the shifts (W_{xc}/W_{dep}) of up to 55 %.

Since the first observation of one-dimensional intersubband plasmons (charge-density excitations, CDEs) in far infrared (FIR) transmission experiments by Hansen et al. [1] there has been an enormous body of work devoted to the study of collective excitations in low-dimensional electron systems (1DES or quantum wires) [2,3]. Most of this work was done by FIR transmission. The study of manybody effects by this technique, however, is hampered by three inherent limitations. Firstly, due to the generalized Kohn's theorem [4] only the lowest intersubband CDE couples to the far infrared light for a parabolic bare potential and only recently it was possible to realise 1DES structures with a sufficiently non parabolic confinement to observe higher intersubband plasmons in FIR transmission [3]. Secondly, a different experiment, usually magneto transport measurements [6,7], has to be performed to compare the observed collective CDE energy to the single particle spectrum. Thirdly a different kind of collective excitation involving changes in spin-density (spin-density excitations, SDE) can not be observed. These excitations are of special interest, because, unlike the CDE, they are only affected by the exchange and correlation part of the electron-electron interactions (excitonic shift) and therefore their observation allows separation of contributions of direct and exchange-correlation interactions [8].

These limitations are overcome by measuring the light scattered inelastically by the electrons. Charge-density and spin-density excitations of two-dimensional (2D) electron systems have been observed and identified by simple polarization selection rules [8]. Besides the collective excitations, light scattering also allows the direct observation of single-particle excitations (SPE), which are not affected by many-body corrections [9].

present addresses:
* Sektion Physik, Universität München, München, GERMANY.
† Max-Planck-Institut für Festkörperforschung, Stuttgart, GERMANY.
◊ Universidad Autónoma, Madrid, SPAIN.

inelastic light scattering was only recently applied to 1DES [3,10-13]. The results of Egeler et al. [13] obtained in a system with many occupied one-dimensional subbands could be explained in a semi-classical effectively two dimensional picture of confined plasmons. The work by Gofii et al. [3,10] revealed the characteristic linear dispersion of the one-dimensional intrasubband plasmon. They also found indications for an enhancement of the excitonic shift that could be evidence of stronger correlations in one dimension. However separate SDEs were not observed leaving uncertainties in the contributions of exchange and correlation.

Here we report the first observation of one-dimensional intersubband spin-density excitations in GaAs quantum wires. These excitations as well as intersubband CDE are identified by clear polarization selection rules. Transitions from the occupied states of the 1D-subbands to the first excited 2D-subband (quasi-2D transitions) also give an indication of the 1D-subband spacing. As the Fermi wave vector of our system can be inferred from the wave vector dispersion of intrasubband spin-density excitations, we achieve a complete characterisation of the sample parameters and the basic electron excitations. Our experiments show that the contributions of exchange electron-electron interactions are comparable to the ones of direct electron-electron interactions.

One-dimensional structures were fabricated from a modulation doped, 250Å wide GaAs/AlGaAs single quantum well (SQW) grown by MBE. The top barrier was silicon-delta-doped. The mobility and carrier density of the as-grown SQW at 4.2 K was 2.4 10^5 cm^2/Vs and 3.12 10^{11} cm^{-2}. 700Å wide lines with 2000Å period patterned into PMMA by electron beam lithography served as mask for the subsequent etching in an Plasmatherm SL700 electron cyclotron resonance reactive ion etcher (ECR-RIE). The BCl_3-Ar mixture was found to give good etching characteristics, low damage and a well reproducible etching rate of about 170 Å/minute under the selected operating conditions [14]. Therefore the etching

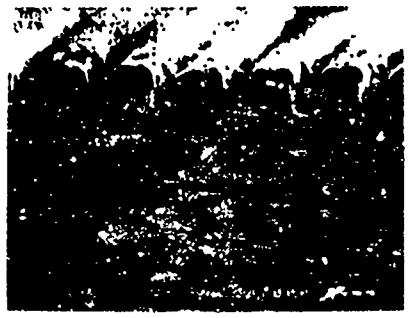

Figure 1: SEM photograph of the cleaved edge of a sample

time could be chosen to remove the Si dopant in the gaps between the lines. This confines the carriers in the SQW electrostatically into a type II lateral superlattice. Figure 1 shows an SEM photograph of the cleaved edge of the quantum well.

Figure 2 compares photoluminescence spectra of asgrown and patterned regions on a quantum wire sample. Figure 2a shows the well-known features of a SQW containing electrons: The signal peaks at the fundamental edge and displays a long high energy tail with a cutoff at the Fermi energy. The formation of quantum wires strongly changes the light emission as shown in figure 2b. The photoluminescence peak becomes broad, rather symmetric and red shifted. Its energetic position now depends on the intensity of the exciting laser light. This effect is well known from nipi structures [15] and has also been seen in shallow etched quantum wire samples [16,17]. It is due to spatially indirect electron-hole recombination in the type II superlattice. Photo induced carriers tend to screen the confinement potential and therefore cause a shift of the PL peak as a function of incident light intensity. The energy difference between the Fermi edge in the unstructured regions and the peak position of the structured regions gives an indication of the lateral potential modulation, because the indirect recombination is most likely to occur from the Fermi edge of the quantum wires due to the

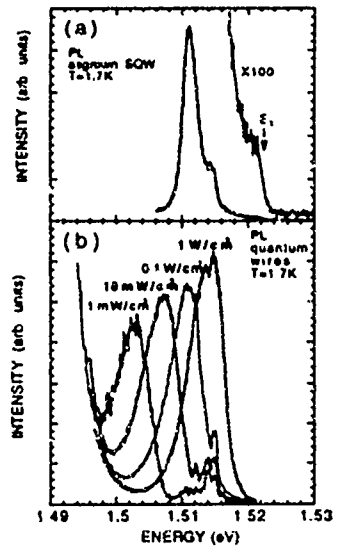

Figure 2:
(a) PL spectrum taken in an unpatterned region of the sample showing the light emission from the asgrown SQW. The part containing the cutoff at the Fermi energy is enlarged by a factor of 100.
(b) PL spectra taken in the quantum wire region. Parameter is the power density of the incident laser light.

enhanced electron hole overlap. We find a modulation of approximately 10 meV even under an illumination of 1W/cm², which was the power density used in the light scattering experiments. The quantum wire Fermi energy was deduced from the wave vector dispersion of intrasubband spin-density excitations to be 5.0±0.2 meV. Together with a subband spacing of 2.5±0.5 meV this results in two occupied subbands (n_0=6.1±0.1·10⁵ cm⁻¹, n_1=4.3±0.4·10⁵ cm⁻¹).

Figure 3 shows the effect of the quantum wire formation on intersubband transitions between subbands due to confinement in growth direction. The upper panel displays spectra taken in an unstructured region. Polarized and depolarized spectra, i.e. spectra taken with the polarization of incident and scattered light parallel or crossed, show strong peaks of charge- and spin-density excitations, respectively (labelled CDE and SDE). A peak due to single particle excitations (SPE) is apparent in both spectra [9]. In the quantum wire region we also observe main peaks at energies similar (but not identical) to the spectra of the as grown SQW. These peaks labelled $CDE_{00,1}$ and $SDE_{00,1}$ in the polarized and depolarized spectrum, respectively, are assigned to charge-density and spin-density excitations associated with the transition between the lowest 1D subband and the first excited 2D subband. The small peak on the high energy side of the $SDE_{00,1}$, energetically coincident with the low-energy shoulder of the $CDE_{00,1}$ peak is assigned to the corresponding single-particle transition ($SPE_{00,1}$). Furthermore new features appear at energies below 20 meV in both spectra labelled $CDE_{01,1}$ and $SDE_{01,1}$. They are assigned to charge-density and spin-density excitations corresponding to transitions between the first excited 1D subband and the first excited 2D subband. From these observations it is possible

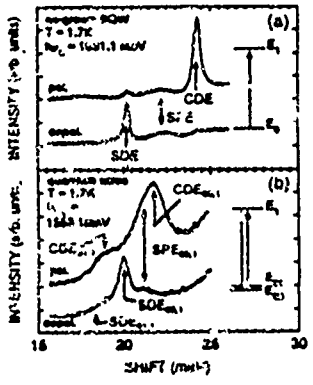

Figure 3: Inelastic light scattering spectra taken in an as grown (a) and quantum wire (b) region. The insets show the transitions schematically.

to deduce the 1D subband spacing to be larger then 2 meV, assuming that the difference of the single-particle excitation energies is given by the splitting of the 1D subbands (inset of fig. 3b). Given a Fermi energy of ~5 meV we conclude to have at least 3 well confined 1D subbands of which two are occupied with electrons. There are two 1D intersubband transitions with a change in subband index of one (Δn =1) and one transition with a change of two (Δn =2).

The 1D intersubband excitations are also observed. Figure 4 shows depolarized and polarized low energy spectra for different incident photon energies. Observations of the electronic excitations of the 1DES are possible due to strong

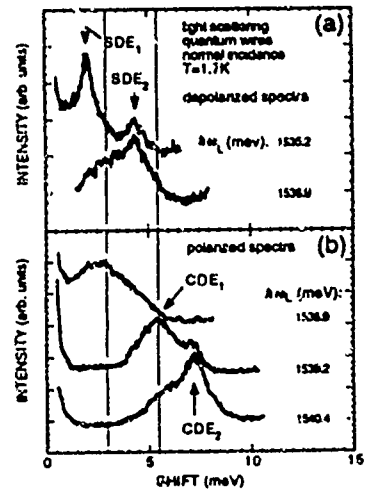

Figure 4. Depolarized (a) and polarized (b) inelastic light scattering spectra showing 1D intersubband excitations. Parameter is the incident light energy.

resonant enhancements, if the energy of the scattered light matches an excitonic transition of the sample (outgoing resonance) [18]. The polarized spectra (fig. 4b) exhibit a strong peak at 7.4 meV and weaker features at around 5.5 meV and 3 meV. The weak features occur at energies expected for single particle transitions according to the 2D-like spectra (fig. 3b) and the assumption of nearly equally spaced 1D electron levels. The sharp peak at 7.4 meV is most likely to be a collective charge-density excitation. Being the highest energetic feature we assign it to the Δn =2 CDE (labelled CDE_2). We believe that the Δn =1 CDEs are not as pronounced and merge with the Δn =2 SPE in the 5.5 meV feature. One possible reason might be parity conservation, because for a symmetric potential a

two photon process such as inelastic light scattering is only sensitive to even transitions (Δn=2,4,...).

Figure 4a shows depolarized spectra in the same energy range. We observe two well defined peaks at 2.0 and 4.4 meV which are assigned to the SDEs with Δn=1 and Δn=2 (labelled SDE_1 and SDE_2). The clear polarization selection rule identifies these peaks as spin-density excitations. This is the first observation of intersubband SDEs in a 1DES. However the approximate parity selection rule seen for CDEs seems to be absent for the SDEs. Intersubband SPEs are on the contrary not clearly resolved in figures 4a. Nevertheless, changes in line shape of the spectra as a function of incident laser wavelength again suggests additional features around 3 meV and 5.5 meV (indicated by vertical lines).

The energies of the collective modes can be connected to the single-particle energy (E_{SPE}) and the depolarization (W_{dep}) and excitonic (W_{xc}) shifts by writing $(E_{CDE})^2=(E_{SPE})^2+(W_{dep})^2-(W_{xc})^2$ and $(E_{SDE})^2=(E_{SPE})^2-(W_{xc})^2$ [3]. This leads to ratios of the shifts (W_{xc}/W_{dep}) of up to 55 % in the case of the Δn=2 transition (E_{SDE} = 4.4 meV, E_{SPE} =5.5 meV, E_{CDE} =7.4 meV), a value close to the ratio of 68% deduced from the 2D intersubband excitations of figure 3a. However due to experimental uncertainties the exact number can not yet be deduced from our experiments.

In conclusion we have investigated the transition from a 2D to a 1D system in light emission and light scattering experiments. The spatially indirect nature of the electron-hole recombination is apparent in the emission line shape and a shift of the emission peak energy with incident light intensity. The formation of 1D subbands produces new structure in light scattering spectra in the energy range of transitions to the first excited 2D subband. Our light scattering data show the first measurements of 1D intersubband spin-density excitations. Consequently, it is possible to observe the basic excitations of a 1DES by inelastic light scattering. The energetic position of the intersubband SDEs is shifted from the SPEs by a correction due to exchange and correlation electron-electron interactions (excitonic shift). Similar to the two-dimensional case this shift appears to be comparable to the depolarization shift in one-dimensional electron systems in GaAs.

One of us (A.S.) would like to thank H.Drexler and W.Hansen for many important discussions. He also acknowledges financial support by the Deutsche Forschungs Gemeinschaft.

References

[1] W.Hansen, M.Horst, J.P.Kotthaus, U.Merkt, C.Sigorski and K.Ploog, Phys. Rev. Lett. *58*, 2586 (1987)

[2] W Hansen, J.P.Kotthaus and U.Merkt in *Semiconductors and Semimetals*, Vol. 35 (1992), edited by R.K.Willardson and A.C.Beer

[3] A.R.Goñi et al in *Phonons in Semiconductor Nanostructures*, edited by J.P.Leburton, J.Pascual and C.M.Stomajor-Torres (Kluwer, New York, 1993), to be published.

[4] S.K.Yip Phys. Rev. B *43*, 1707 (1991), and references therin.

[5] H.Drexler,W.Hansen,J.P.Kotthaus,M.Holland and S.P.Beaumont Phys. Rev. B *46*, 12849 (1992).

[6] F.Brinkop, W.Hansen, J.P.Kotthaus und K.Ploog, Phys. Rev. B*37*, 6547 (1987)

[7] T.Demel, D.Heitmann, P.Grambow and K.Ploog, Phys. Rev. B *38*, 12732 (1988).

[8] A.Pinczuk and G.Abstreiter in *Light Scattering in Solids V*, edited by M.Cardona and G.Güntherodt (Springer,Berlin1969) p. 153.

[9] A.Pinczuk, S.Schmitt-Rink, G.Danan, J.P.Valladares, L.N.Pfeiffer and K.W.West, Phys. Rev. Lett., *63*, 1633 (1989).

[10] J.S.Weiner,G.Danan, A.Pinczuk, J.Valladares, L.N.Pfeiffer and K.W.West Phys. Rev. Lett. *65*, 1641 (1989).

[11] A.R.Goñi, A.Pinczuk, J.S.Weiner, J.M.Calleja, B.S Dennis, L.N.Pfeiffer and K.W.West, Phys. Rev. Lett. *67*, 3298 (1991).

[12] A.R.Goñi, A.Pinczuk, J.S.Weiner, B.S.Dennis, L.N.Pfeiffer and K.W.West, Phys. Rev. Lett. *70*, 1151 (1993).

[13] T.Egeler, G.Abstreiter, G.Weimann, T.Demel, D.Heitmann, P.Grambow and W.Schlapp, Phys. Rev. Lett. *65*, 1804 (1990).

[14] J.S.Weiner, J.M.Calleja, A.Pinczuk, A.Schmeller, B.S.Dennis, A.R.Goñi, L.N.Pfeiffer and K.W.West, submitted to APL.

[15] G.H.Döhler,H.Künzel,D.Olego,K.Ploog,P.Ruden,H.J.Stolz and G.Abstreiter, Phys. Rev. Lett. *47*, 864 (1981).

[16] F.Hirler,R.Küchler,R.Strenz,G.Abstreiter,G.Böhm,J.Smoliner, G.Tränkle and G.Weimann Surf. Sci. *263*, 536 (1992).

[17] M.Fritze,A.V.Nurmikko and P.Hawrylak in Proceedings of the tenth International Conference on Electronic Properties of 2-Dimensional Systems (EP2DS-10), Newport, USA 1993 (in press).

[18] G.Danan,A.Pinczuk,J.P.Valladares,L.N.Pfeiffer,K.W.West and C.W.Tu Phys. Rev. B *39*, 5512 (1989).

ThC4

Tunable far infrared absorption in logarithmically graded quantum wells

P. F. Hopkins,(1) M. Sundaram,(2) K. L. Campman,(1) G. Bellomi,(1) E. L. Yuh,(2)
S. J. Allen, Jr.,(2) and A. C. Gossard(1)
(1)*Materials Department and Department of Electrical and Computer Engineering*
(2)*Quantum Institute, University of California, Santa Barbara, CA 93106*

Compositional grading in the growth direction z is used to simulate a potential well of the form $V(z) = -a^2 \ln(abz+1) + abz$, where a and b are constants. Using both a front gate and an epitaxially grown back gate, we observe a giant Stark shift from 35 cm^{-1} to 125 cm^{-1} in the collective electronic resonance response by moving the electron gas through the asymmetric well.

In this paper, we present the first experimental evidence of dramatically tunable far infrared (FIR) absorption in wide graded quantum wells in zero magnetic field. The weak quantum confinement in remotely n-doped wide (~1000 Å), compositionally graded, GaAs/$Al_xGa_{1-x}As$ quantum wells leads to collective electronic excitations at FIR frequencies (0.4 THz < $\omega/2\pi$ < 3 THz) [1-8]. With scattering of carriers strongly reduced by remote doping, the FIR resonances in these wells are sharp ($\omega\tau >> 1$) and strong at the low temperatures studied ($T < 10$ K). In structures with near perfect parabolic confinement and in zero magnetic field, optical excitation causes transitions at only a single frequency $\hbar\omega_0$, corresponding to the electronic harmonic oscillator frequency [1-3]. To study additional FIR collective modes in wide graded wells, periodic perturbing wells and barriers [4] and grating couplers [5] have been added to parabolic wells, and biparabolic well structures have been studied [6,7]. In the present work, following concepts presented in reference 8, we have fabricated wide graded well structures with the specific goal of a tunable far infrared response in zero magnetic field. By using both a front gate and an epitaxially grown back gate to controllably position the electron gas in a "logarithmic" well, we observe a giant Stark shift that tunes the electronic resonance over a frequency range of more than 350% (from 35 cm^{-1} to 125 cm^{-1}). By comparison, previous work on narrower (~100 Å) asymmetric step wells has yielded much weaker shifts in the frequency of the intersubband optical absorption [9, 10].

We study a bare well potential V(z) in which the harmonic oscillator frequency $\hbar\omega_0$ at the potential minimum varies linearly with applied electric field $E(z) = E$ across the well:

$$\omega_o(z_{min}) = a\left\{\frac{1}{m^*}\left[\frac{\partial^2 V_T(z_{min})}{\partial z^2}\right]\right\}^{1/2} = \frac{a}{\sqrt{m^*}}(aeE + b) \quad (1)$$

where a and b are constants, e is the electronic charge, $V_T(z) = V(z) + eEz$ is the total potential in the absence of electrons in the well, and the second derivative is evaluated at the minimum point of $V_T(z)$. A solution of Eq. (1) is the bare well potential $V(z) = -a^2 \ln(abz+1) + abz$. In this paper, we study such a "logarithmic" well design in which $a = 0.0751$ $(meV)^{-1/2}$, $b = 0.0263$ $(meV/Å^2)^{1/2}$, $z = -450$ Å and $z = 1005$ Å are the well edges, and the empty well tunability $\hbar\,\partial\omega_o/\partial E$ is 2.0 cm^{-1}/(kV/cm).

To investigate the theoretical absorption properties of this well filled with electrons, we followed the example of Brey et al. [3] and first calculated the ground state energies and wavefunctions by self-consistently solving Poisson and Schrödinger's equations [7] for the well, including exchange-correlation in the local density functional approximation (LDA). The calculations were done for zero temperature, assumed a constant effective mass $m^* = 0.07$ and relative dielectric constant $\varepsilon = 13$, added an infinite potential barrier at the well edges, and included an electric field by adding the potential eEz to the bare well potential. The inset to Fig. 1 shows the charge density n(z) and total self-consistent potential $V_T(z) = V(z) + ecn_{2d} + V_H(z) + V_{x-c}(z)$, where $V_H(z)$ is the electrostatic potential of the electron gas and $V_{x-c}(z)$ is the exchange-correlation potential [3], for $n_s = 1 \times 10^{11}$ cm^{-2} and for an applied electric field of +13.5 kV/cm. The net applied electric field is V_g / eW, where $V_g = V_T(z = -450\ Å) - V_T(z = 1005Å)$ is the potential drop across the well of width $W = 1455$ Å.

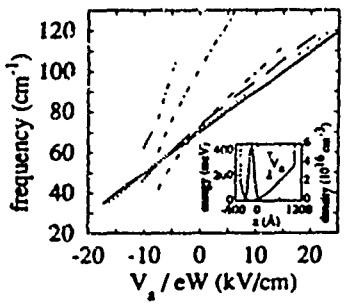

FIG. 1. Calculated absorption peak frequencies for the logarithmic well versus applied field V_g / eW for a series of electron fillings: $n_s = 1 \times 10^{10}$ cm^{-2} (solid line), 5×10^{10} cm^{-2} (short dashed line), 1×10^{11} cm^{-2} (long dashed line) and 2×10^{11} cm^{-2} (dashed dotted line); inset: self-consistent potential $V_T(z)$ and electron density n(z) for the case $n_s = 1 \times 10^{11}$ cm^{-2} and $V_g / eW = 13.5$ kV/cm.

The optical absorption was calculated using the time-dependent LDA [3,11]. Fig. 1 shows the calculated absorption peaks for the logarithmic well as a function of V_g / eW. The peak frequencies are shown for four fillings of the well, $n_s = 0.1$, 0.5, 1, and 2×10^{11} cm^{-2}. For $n_s = 1 \times 10^{10}$ cm^{-2}, the calculated peak frequencies agree with Eq. (1) within the linewidth used. For small n_s, the well region occupied by the narrow electron gas is essentially parabolic, and the absorption frequency is to a good approximation given by Eq. (1) [1,3]. For larger n_s, the wider electron gas occupies a well region which contains substantial nonparabolicities. In this case, the frequency of the center-of-mass mode shifts from Eq. (1) and additional peaks are clearly seen [3]. For these higher densities, the center-of-mass of the electron gas $\bar{z} = n_s^{-1}\int z n(z) dz$ shifts accurately from the well minimum. Using Eq. (1) to determine $\hbar\omega_o(\bar{z})$ qualitatively explains the peak shifts. Increasing the electron gas width at fixed n_s by applying a more negative voltage V_g / e can similarly result in multiple observed peaks in the absorption. Calculated spectra for $n_s = 1 \times 10^{11}$ cm^{-2} and 2×10^{11} cm^{-2} at large negative fields show complicated peak structure, and these frequencies were not plotted.

The sample presented in this paper is one of a series of samples grown by molecular beam epitaxy on semi-insulating GaAs (100) substrates. To simulate the potential $V(z)$ studied above, a 1455 Å well was constructed from a 15 Å period digital alloy superlattice [12] of GaAs and $Al_{0.3}Ga_{0.7}As$, with the average Al composition x per period varied so that:

$$x(z) = \left(\Delta E_c / z\right)^{-1}\left[\frac{-1}{a^2}\ln(abz+1) + z\frac{b}{a}\right] + 0.01; \quad -450Å \le z \le 1005Å \quad (2)$$

where we have assumed that the $Al_xGa_{1-x}As$ / GaAs conduction band offset $\Delta E_c / x$ is constant and equal to 877 meV, and a and b are given above. Electrons for the well came from Si δ-doped $Al_{0.3}Ga_{0.7}As$ barrier regions located at $z = -1065$ Å and $z = +1205$Å. A highly doped ($N_D = 2 \times 10^{18}$ cm^{-3}) 150 Å quantum well was grown at $z = -3.5$ μm below the asymmetric well to serve as a back gate electrode. Included in the 3.5 micron barrier was a 5000 Å low temperature grown ($T_{substrate} = 230$ °C) GaAs layer. After etching a mesa, AuGeNi and In ohmic contacts were annealed to separately connect the 1455Å well and the 150Å well, respectively. In addition, a 4 mm dia. 50Å/500Å Ti/Au front gate was e-beam evaporated onto the sample surface, ~2700 Å above the 1455 Å well.

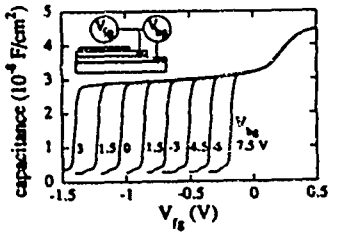

FIG. 2. Front gate to electron gas small-signal capacitance data for a series of DC back gate voltages V_{bg} with the sample cooled in the dark at $T = 4.2$ K.

In Fig. 2 we demonstrate complete modulation of the electron filling n_s in the logarithmic well with either the front gate or the back gate. Plotted is the front gate to electron gas capacitance-voltage (CV) data for the sample while immersed in liquid helium at 4.2 K in the dark. A DC gate voltage (V_{fg}) and small (10 mV peak-peak) 400 Hz AC signal were

applied between the front gate and the ohmic contacts to the electron gas, at a series of different DC voltages applied between the back gate and the electron gas (-7.5V ≤ V_{bg} ≤ +3.0 V). The CV data show a monotonic decrease in the capacitance with decreasing V_{fg} as the depletion edge is moved down from the top doping layer through the asymmetric well and to the back gate. Likewise, the front gate depletion voltage V_{fd} increases almost linearly as V_{bg} is decreased, indicating that the back gate depletion edge is sweeping up through the well. Integrating each capacitance curve from V_{fd} to V_{fg} gives $n_s(V_{fg},V_{bg})$, so that the carrier density in the well is known for each combination of gate voltages.

Far-infrared absorption measurements were made using a Bomem Fourier transform infrared spectrometer (FTIR), with the sample and bolometer detector cooled to 4.2 K under illumination. A stripline geometry was used (inset of Fig. 3) with radiation coupled into the edge of the sample to provide a z-polarized electric field. FTIR scans were taken at a series of different V_{fg} biases, with V_{bg} fixed. After each FTIR scan at V_{fg}, a scan at V_{fg}= -2.5V was taken to normalize the data. After the scans at the V_{fg} biases were completed, the back gate voltage was changed, a CV measurement was made (similar to a single curve in Fig. 2), and a new series of scans was taken. Absorption data were collected for 2 separate cooldowns of the sample. A series of V_{fg} CV curves similar to Fig. 2 were found on both cooldowns, although the corresponding values of V_{bg} had shifted.

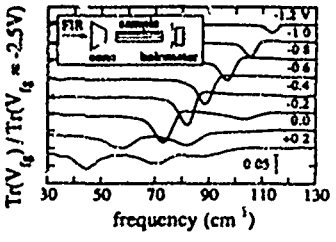

FIG. 3. T = 4.2K normalized transmittance spectra for V_{bg} = 0 V and several V_{fg} values. Inset: experimental setup for the absorption measurements.

The large tunable absorption in the logarithmic well is demonstrated in Fig. 3, which shows a typical set of spectra for V_{bg} = 0 V and several V_{fg} values. From the CV data we determined the well density n_s = 1.0 x 10^{11} cm^{-2} at V_{fg} = 0 V. Plotted versus frequency is the normalized transmittance $Tr(V_{fg})$ / $Tr(V_{fg}$ = -2.5V). A dip in the transmittance corresponds to a peak in the absorption by the electrons in the well. With large negative V_{fg}, there are electrons only in the higher curvature part of the well, and the observed absorption frequency is high. As V_{fg} increases, the electron gas extends into well regions with lower curvature, decreasing the observed frequency. In addition, n_s increases and so the integrated absorption strength increases [3]. Additional peaks are clearly observed for V_{fg} ≥ -0.2 V.

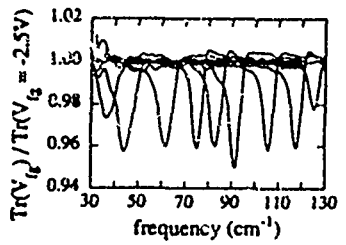

FIG. 4 T = 4.2 K normalized transmittance spectra for combinations of gate voltages in which the density in the well was approximately the same $n_s(V_{fg},V_{bg})$ ~ 5 ± 2 x 10^{10} cm^{-2}. The corresponding gate biases and CV derived n_s for each absorption peak are listed in Table I.

Although the three terminal device allows great flexibility in adjusting n_s and the well tilt on either side of the electron gas, it is difficult to determine the exact V_{fg} and V_{bg} to apply a uniform Stark tilt, as in the calculations of Fig. 1. Instead, we present in Fig. 4 a compiled series of scans (over the 2 cooldowns) in which the density in the well was approximately the same $n_s(V_{fg},V_{bg})$ ~ 5 ± 2 x 10^{10} cm^{-2}. The corresponding gate biases and CV derived n_s for each absorption peak are listed in Table I. In this device it is possible to Stark shift the single sharp absorption peak from 35 cm^{-1} to 125 cm^{-1} by moving the electron gas through the logarithmic well. From Table I we estimate $d^{-1}\hbar\,\partial\omega_o/\partial(V_{bg} - V_{fg})$ ~ 1.9 ± 0.4 cm^{-1}/ kV/cm where d ~ 3.9 μm is the distance between the front and back gates. This rough estimate of the tunability of the well is close to the theoretical empty well value of 2.0 cm^{-1}/kV/cm).

In conclusion, we have used linear FIR spectroscopy to study the collective electronic excitations of remotely doped, wide, logarithmically graded quantum wells. We observe a giant Stark shift of the resonances in these slowly varying potential wells. Harmonic generation and other nonlinear properties of these anharmonic potentials could also be studied, using high intensity FIR excitation. Similar graded well structures have been proposed as tunable, narrow band, FIR solid state oscillators, which do not require the application of magnetic fields [8,13].

We thank J. Maserjian for proposing the concept of tunable emitters based on wells with graded curvature [8]. We also thank K. Ensslin, E. G. Gwinn, J. Ibbetson, P. R. Pinsukanjana, G. Robinson, G. L. Snider, and A. Wixforth for useful discussions. We thank N. G. Asmar for use of his Poisson-Schrödinger program. This work was supported by the Air Force Office of Scientific Research under grant AFOSR-91-0214, by the NSF Science and Technology Center for Quantized Electronic Structures (QUEST) DMR-91-20007, by the NSF DMR90-02491, and the ONR N000-14-92-J1452.

TABLE I. Gate voltages and calculated densities n_s for spectra in Fig. 4.

Peak frequency (cm^{-1})	36.5	44.1	61.7	75.1	82.9	91.3	106	118	124
V_{fg} (V)	0.2	0.0	-0.2	-0.5	-0.7	-0.8	-1.0	-1.4	-1.4
V_{bg} (V)	-14	-12	-10	-8	-6	-2	0	+2	+6
n_s (10^{10} cm^{-2})	4.9	4.3	4.8	4.3	4.7	5.8	6.1	5.0	4.1
cooldown #	2	2	2	2	2	1	1	1	1

References:

1. L. Brey, N. F. Johnson, and B. I. Halperin, Phys. Rev. B40, 10647 (1989).
2. K. Karrai, X. Ying, H. D. Drew, M. Santos, M. Shayegan, Phys. Rev. B40, 12020 (1989); A. Wixforth, M. Sundaram, J.H. English, and A.C. Gossard, *The Physics of Semiconductors*, ed by E. M. Anastassakis and J. D. Joannopoulos (World Scientific, 1990), Vol II, p. 1705.
3. L. Brey, Jed Dempsey, N. F. Johnson, and B. I. Halperin, Phys. Rev. B42, 1240 (1990).
4. K. Karrai, X. Ying, H. D. Drew, M. Santos, M. Shayegan, G.-R. E. Yang, and A.H. MacDonald, Phys. Rev. Lett. 67 (1991) 3428.
5. P. R. Pinsukanjana, G. G. Gwinn, John F. Dobson, E. L. Yuh, N. G. Asmar, M. Sundaram, and A.C. Gossard, Phys. Rev. B46, 7284 (1992); A. Wixforth, M. Kaloudis, M. Sundaram, and A.C. Gossard, Sol. St. Comm. 84, 861 (1992).
6. N. F. Johnson and J. E. Vargas, Appl. Phys. Lett. 62, 627 (1993).
7. N. G. Asmar and E. G. Gwinn, Phys. Rev. B46, 4752 (1992).
8. J. Maserjian and A. C. Gossard, "Tunable quantum-well submillimeter-wave oscillators", Nano Tech Briefs 14, 7 (July 1990).
9. E. Martinet, F. Luc, E. Rosencher, Ph. Bois, and S. Delaitre, Appl. Phys. Lett. 60, 895 (1992).
10. R. P. G. Karunasiri, Y. J. Mii, Kang L. Wang, Appl. Phys. Lett. 55, 1986 (1990).
11. A. G. Eguiluz, Phys. Rev. Lett. 51, 1907 (1983); W. L. Schaich, Phys. Rev. B 37, 6711 (1988); for the calculations, a small (300 cm^{-1}) in-plane wavevector was used.
12. M. Sundaram, A. Wixforth, A. Wixforth, R. S. Geels, A C. Gossard, and J. H. English, J. Vac. Sci. Technol. B 9, 1534 (1991).
13. M. Helm, E. Colas, P. England, F. DeRosa, and S. J. Allen, Jr. Appl. Phys. Lett. 53, 1714 (1988).

ThC5

Widely Tuneable Quantum Wire Arrays in MISFET-type Heterojunctions with a Stacked Gate

G. Hertel[a], H. Drexler[a], W. Hansen[a], A. Schmeller[a], J.P. Kotthaus[a],
M. Holland[b], and S.P. Beaumont[b]
(a) Sektion Physik, Ludwig-Maximilians-Universität München, D-80539 München
(b) DEEE, University of Glasgow, GB-Glasgow G128QQ

A stacked gate technique is applied to study electronic excitations in electron quantum wire, quantum dot and antidot arrays in GaAs/AlAs MISFET-type heterojunctions at far-infrared frequencies. The gate configuration consists of a finely (period a≥250nm) patterned bottom electrode on the surface of the heterostructure, a dielectric spacer and a homogeneous top gate. An electron grating is induced at the heterostructure interface either beneath the strips or beneath the gaps of the grating gate. With the fields induced by the top gate the confining potential can be controlled nearly independently of the electron density in quantum wires below the bottom gate. This is demonstrated by far-infrared studies of the dimensional resonances in the wires. In a perpendicular magnetic field we observe a very pronounced splitting of the dimensional resonance. We study this behaviour as a function of wire separation and potential form and find this splitting to reflect the anharmonicity of the confining potential.

Currently the investigation of laterally microstructured electron systems attract much interest. Suitable metal oxide semiconductor (MOS) structures and heterostructures are very good systems to study the properties of electron wires and dots. On MOS structures it was demonstrated that the transition between electron systems of different topology and dimensionality can be studied by using a stacked gate technique to generate the superlattice potential.[1-3] Here we have succeeded in developing such a stacked gate configuration on GaAs/AlAs heterostructures. Thereby we obtain a nearly independent control of the electron density and the confining potential in quantum wires and dots.

The collective excitations of electron systems with lateral dimensions of about 100nm are in the far-infrared (FIR) spectral region. If the so-called bare confining potential of the electron systems is parabolic the FIR response of a quantum wire has only one resonance according to the generalized Kohn theorem,[4] corresponding to the center-of-mass motion of all electrons in the bare potential. Here the bare potential is understood to be generated by all external charges, e.g. charges on the gates or charged surface states, excluding the electrons that occupy the low-dimensional electron system. Then the resonance energy solely depends on the bare potential and the applied magnetic field. It was found that in many of the experimentally realized electron wires or dots the assumptions of the generalized Kohn theorem are valid in good approximation. Here we focus on the FIR conductivity if the Kohn theorem becomes invalid. This is the case if e. g. there are non-harmonic terms in the bare confining potential or there is a strong mutual influence of adjacent electron systems. In previous experiments by Drexler et al [5] strong deviations from the predictions of the Kohn theorem were observed in electron wire arrays prepared in a novel type of MISFET (metal-insulator-semiconductor-field-effect-transistor) heterojunctions. There the fundamental resonance shows a pronounced splitting at a magnetic field at which the cyclotron resonance energy $\hbar\omega_c$ becomes equal to the energy of the dimensional resonance at B=0T. In these previous experiments the electron wires were field-effect-induced by a metal grid on the sample surface. Here we use more elaborate gate configurations to study the dependence of this splitting on the wire separation as well as the form of the confining potential.

Like in the previous experiments[5,6] we use MISFET heterojunctions that consist of an undoped AlAs/GaAs superlattice barrier grown by molecular beam epitaxy on an undoped GaAs

spacer. A highly conducting layer buried about 1.5μm beneath the heterojunction interface serves as back electrode with respect to which the gate voltage is applied. A grating gate of parallel strips or a mesh-type gate with period a≥250nm are fabricated on the surface of the heterojunction crystal. The metal grid is lithographically defined either by optical holography or by e-beam exposure. In latter case we can easily fabricate gratings that have a rather large aspect ratio of gate width to period.

Furthermore, in order to gain additional control over the potential in the gaps of the bottom gate we use a so-called stacked gate configuration. A second homogeneous top gate is evaporated onto a dielectric spacer deposited on top of the bottom gate. Similar stacked gates were previously realized on silicon MOS structures.[7]

As illustrated in the inset of Fig. 1 the stacked gate configuration allows to induce electron systems in two different modi. In the so-called sub-grating mode a positive voltage is applied between the bottom gate and back electrode and electrons are induced beneath the bottom gate. The top gate bias controls the lateral barriers between the electron wires. In the sub-gap mode the two gates are biased such, that the electron system now resides beneath the gaps of the bottom gate. Then the bottom gate biased below threshold voltage controls the barriers between the electron systems. The data in Fig. 1 depict the resonance frequency of the dimensional resonance as function of the magnetic field in a sample that is operated in either the sub-gap (circles) or sub-grating (rhombi) mode with corresponding gate voltages as indicated in the figure. The bottom gate consists of metal strips of width w=200nm arranged in an array of period a=800nm. The FIR transmission of the sample was also studied before the preparation of the top gate. Squares in Fig. 1 denote the positions of the dimensional resonance without top gate. In all three cases resonances of about equal oscillator strength are observed at different resonance frequencies, demonstrating that with the stacked gate configuration it is possible to induce electron wires in the sub-gap as well as in the sub-grating mode.

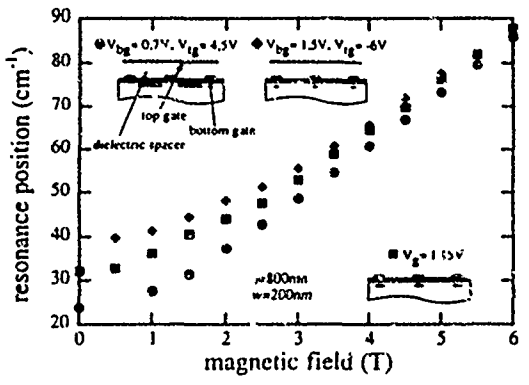

Fig. 1 Positions of the dimensional resonance in a MISFET heterojunction with stacked gate as function of a perpendicular magnetic field. As indicated in the insets the three sets of data are recorded before preparation of the top gate (squares), in the sub-grating mode (rhombi) and in the sub-gap mode (circles).

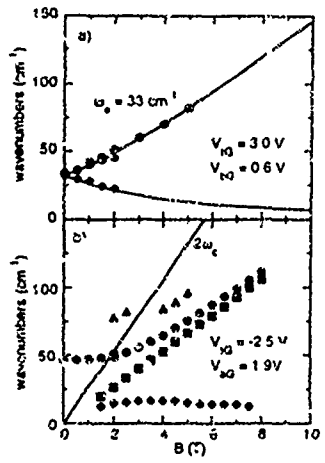

Fig. 2: Resonance positions measured on a MISFET heterojunction with stacked gate. The bottom gate is a metal mesh with period of 500nm. The gates are biased in the (a) sub-gap mode and (b) sub-grating mode, respectively.

We have also prepared stacked gate samples with a metal mesh serving as a bottom gate. In this case a dot matrix can be induced in the sub-gap mode and an antidot superlattice in the sub-grating mode. In Fig. 2 we depict the magnetic field dependence of the FIR resonance frequencies measured on such a sample with a metal mesh of period a=500nm in both lateral directions. In the sub-gap mode electrons are field-effect-induced by the positively biased top gate beneath the holes in the bottom gate. Fig. 2a depicts representative results for the resonance frequencies in the sub-gap mode. The magnetic field dispersion of the resonance frequency is typical for dimensional resonances excited in electron dots. At zero magnetic field one mode is observed that splits at finite fields into two modes, which monotonically increase (circles) or decrease (rhombi) with the magnetic field, respectively. Straight lines are calculated assuming a parabolic bare potential, i. e. the resonance positions are determined by the center-of-mass motion in a harmonic oscillator potential with characteristic frequency ω_0: $\omega_\pm = (\left[4\omega_0^2 + \omega_c^2\right]^{1/2} \pm \omega_c)/2$.

In the sub-grating mode an antidot superlattice is induced beneath the bottom gate (see Fig. 2b). We can use the top gate to tune the potential landscape and thus vary the size of the antidots. Four distinct modes are observed in the FIR transmission spectra of our antidot superlattices. The prominent difference of the modes as compared to the dot case is the absence of a mode with negative magnetic field dispersion at low magnetic fields (B<3T in the case of Fig. 2b). Instead, at low magnetic fields below the cyclotron resonance frequencies (squares) a strong resonance occurs with positive magnetic field dispersion. The positive dispersion saturates at higher fields exhibits a maximum at about 3.5T and then decreases with increasing fields beyond 4T. At the same time the oscillator strength is gradually transferred to the high frequency mode (dots). A very similar behaviour has been observed on etched antidots in InGaAs.[8] It has been suggested[8] that at high magnetic fields the low frequency mode corresponds to classical motion of electrons around a single antidot. Correspondingly, the mode becomes an edge magneto-plasmon at high magnetic fields with frequency $\omega_{mp} \sim 1/R$ determined by an effective antidot radius R. Such edge modes in an antidot superlattice are difficult to observe on etched GaAs structures. In such structure the antidot size usually is considerably enlarged by the depletion length and therefore the absorption frequency lies below the spectral region easily accessible to Fourier spectroscopy. The stacked gate allows us to vary the size of the antidots and thus to observe the edge mode by FIR spectroscopy.

The fundamental dimensional resonance in the electron wire arrays of Fig. 1 shifts in a perpendicular magnetic field and at low electron densities as predicted by the generalized Kohn theorem $\omega_{res}^2 = \omega_0^2 + \omega_c^2$. However, a very pronounced splitting of the fundamental mode into several branches is observed at higher electron densities [5,9] Here we study this behaviour as function

of wire separation and shape of the confining potential. In order to investigate the influence of the inter-wire interaction on the splitting, we have employed electron beam lithography to fabricate samples with large aspect ratios (t=a/w) between grating period a and width w of the metal stripes. In Fig. 3 the resonance frequencies of a wire array in the sub-grating mode with an aspect ratio t=10 are shown as function of the magnetic field. The sample has a grating gate of period a=1.5μm and width w =150nm so that the wire separation is very large as compared to the wire width. A clear splitting is observed implying that inter-wire interaction is not responsible for the splitting. Furthermore, we note that here three branches appear in the magnetic field region (ω_c=ω_0) where the splitting occurs, whereas in previous experiments[5] only two modes have been resolved.

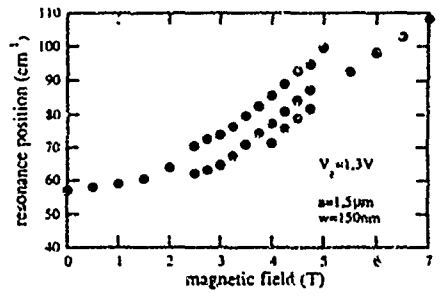

Fig. 3: Resonance positions vs. magnetic field of the dimensional resonance measured on a sample with large aspect ratio t=a/w between array period a=1.5μm and gate width w=150nm.

The stacked gate technique enables us to modify the shape of the potential in the electron wires. This is demonstrated in Fig. 4 where the frequency of the dimensional resonance in a sample with a stacked gate is plotted vs. the magnetic field for three different gate voltage configurations. These are chosen so that the electrons are induced beneath the bottom gate and the oscillator strengths of the resonances are about equal. The bottom gate of the sample has a period of a=400nm and aspect ratio t=2. The B=0T resonance position (ω_0) shifts clearly from 25cm^{-1} to 45cm^{-1} with decreasing top gate voltage. The dashed lines in Fig. 4 indicate the magnetic field at which the cyclotron frequency equals the B=0T resonance frequency in the wire array (ω_c=ω_0). The magnetic field region at which the splitting occurs increases systematically with the strength of the bare confining potential and is roughly at the field where ω_c=ω_0.

To extract more information on the bare lateral potential as function of the voltages applied at bottom and top gate we have calculated the potential distribution from the Poisson equation, assuming that no electrons occupy the potential minima. If Kohn's theorem is valid the second derivative V'' at the potential minima reflects the resonance frequency according to ω_0^2=V''/m*. Here we neglect image charges that result from the polarization of the surrounding material by the charge in the electron wires. If we compare the potential form with the experimental resonance positions with the assumption that no surface charges occupy the gaps in the bottom gate, we find that the calculated resonance frequencies are always significantly lower. They are roughly described by above calculations if we assume that an additional negative areal charge densitiy of 5 10^{11} cm^{-2} resides in the gap areas of the bottom gate. A further indication for importance of surface charges in the gap regions is found if the samples are illuminated. After illumination with band gap radiation the potential modulation is found to be reduced so strongly that the frequency of the dimensional resonances do not deviate from the cyclotron resonance frequency of a homogeneous two-dimensional electron system. Surface charges may also be responsible for the fact that in some of our samples no splitting is observed in the whole gate voltage regime investigated

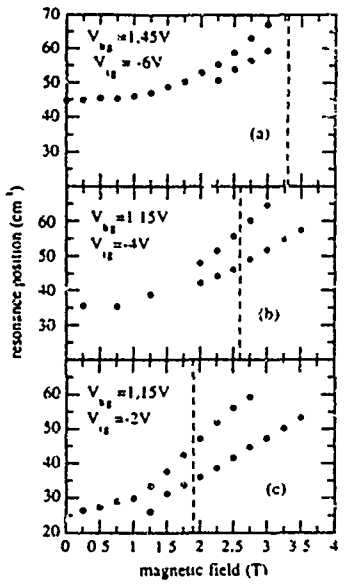

Fig. 4: Resonance positions vs. magnetic field of a MISFET heterojunction with stacked gate. The bottom gate is an array of metal stripes with period a=400nm and aspect ratio t=2. In (a) - (c) different gate voltages are applied at the top and bottom gate. The dashed lines indicate the magnetic fields where the cyclotron frequency is equal to the B=0T resonance frequency.

The lateral potential distribution as derived from the Poisson equation contains in addition to parabolic terms also considerable terms with 4th and 6th power. Our finding that the splitting becomes stronger at higher electron densities might be explained by the fact that the non-parabolic terms become more effective at higher densities. Dempsey and Halperin calculated the FIR absorption spectrum of an electron system in a two dimensional parabolic well, that is truncated at both sides by steep potential walls, and compare it to the spectrum of a perfect parabolic well [10]. The calculations show a fundamental mode according to the generalized Kohn theorem for a well with perfect parabolicity. A splitting of the fundamental mode similar to ours appears in calculations for the truncated well at sufficiently high electron densities so that the electrons in the well sense the steep potential walls. Similarly to our experimental data on one dimensional electron channels, the oscillator strength of the splitting shifts with increasing magnetic field from the upper to the lower branch. The oscillator strengths are about equal in the region $\omega_0 \approx \omega_c$.

The similarity of the results obtained by Dempsey and Halperin with our experimental data as well as of the Voigt geometry in a two-dimensional parabolic well with a one-dimensional wire in a perpendicular magnetic field suggests that a corresponding calculation for our wires will explain our data. Indeed, power spectra that numerically average over classical trajectories[5] indicate already that the behaviour of the oscillator strength at $\omega_0 \approx \omega_c$ can be caused by a change in the character of the combined density of states in this magnetic field region. The FIR excitations in the region $\omega_c < \omega_0$ ($\omega_{res} > \sqrt{2}\omega_c$) are mainly determined by the electrostatic confinement potential of the electron channel, whereas the magnetic field is dominant in the region $\omega_c > \omega_0$ ($\omega_{res} < \sqrt{2}\omega_c$). With increasing magnetic field the electrons become more and more localized in the wire center, i.e. the number of electron trajectories influenced by the wire wall decreases. Therefore the importance of the non-harmonic terms of the confinement potential decreases with increasing field and the transitions become cyclotron-resonance-like. A detailed calculation of the influence of non-harmonic terms in the bare potential on the dimensional resonances in one dimensional electron wires still needs to be done.

Acknowledgements: We gratefully acknowledge financial support of the Deutsche Forschungsgemeinschaft.

References.

1. A. C. Warren, D. A. Antoniadis, and H. I. Smith, Phys. Rev. Lett. **56**, 1858 (1986).

2. J. Alsmeier in "High Magnetic Fields in Semiconductor Physics III", Ed. G. Landwehr (Springer, Berlin, 1992) p. 614.

3. A. Lorke, I. Jejina, and J. P. Kotthaus, Phys. Rev. **B46**, 12845 (1992).

4. L. Brey, N. F. Johnson, and B. I. Halperin, Phys. Rev. **B40**, 10647 (1989).

5. H. Drexler, W. Hansen, J.P. Kotthaus, M. Holland, and S. P. Beaumont, Phys. Rev. **B46**, 12849 (1992).

6. H. Drexler, W. Hansen, J. P. Kotthaus, M. Holland, and S. P. Beaumont, Semicond. Sci. Technol. **7**, 1008 (1992).

7. J. Alsmeier, E. Batke, and J. P. Kotthaus, Phys. Rev. **B40**, 12 574 (1989).

8. K. Kern, D. Heitmann, P. Grambow, Y. H. Zhang, and K. Ploog, Phys. Rev. Lett. **66**, 1618 (1991).

9. W. Hansen, H. Drexler, J. P. Kotthaus, M. Holland, and S. P. Beaumont, Proc 21st Int. Conf. "Physics of Semiconductors" (Beijing, 1992), in press.

10. J. Dempsey and B. I. Halperin, Phys. Rev. **B47**, 4674 (1993).

ThC6

Infrared Spectroscopy of Lateral-Density-Modulated 2DES in InAs/AlSb Quantum Wells

M. Sundaram and S. J. Allen, Jr.
Quantum Institute, University of California, Santa Barbara, CA 93106, USA
&
C. Nguyen, B. Brar, V Jayaraman, and H. Kroemer
Dept. of Electrical & Computer Engg., University of California, Santa Barbara, CA 93106, USA

In infrared transmission experiments through a two-dimensional electron system with substantial lateral density modulation in an InAs quantum well, we directly observe plasmon absorption without the mediating help of a surface metallic grating. The plasmon frequency is determined by the average density, and its strength by the amplitude of the density modulation. It disperses in a magnetic field in predicted fashion

We have observed plasmon absorption in lateral-density-modulated two-dimensional electron systems (2DES) in InAs quantum wells in far infrared spectroscopy. Its location and strength agree well with the dynamic conductivity $\sigma(q,\omega)$ that we explicitly derive for such a system. The dispersion of the plasmon frequency ω_p in a magnetic field agrees well with existing theory.

Far infrared plasmon experiments on 2DES have traditionally relied on the fabrication of a surface metallic grating (of period a) to couple to plasmons with fixed wave vectors $q = n\pi/a$ ($n = 1,2,\ldots$) [1] in 2DES residing as inversion layers in Si MOSFETs or as accumulation layers in GaAs/AlGaAs heterojunctions and quantum wells [1, 2]. Such measurements have shown the position, width, and strength of the plasmon resonance, and also its dispersion in a magnetic field B to agree with theory in detail Non-local effects have manifested themselves in the plasmon B field dispersion via a coupling between the magnetoplasmon and the second harmonic of the cyclotron frequency $2\omega_c$ [3]. Most of these experiments have been on 2DES with lateral uniformity. Measurements on 2DES with electron density laterally modulated with submicron spatial periodicity in both the Si MOSFET [4] and the GaAs/AlGaAs [3] systems reveal the resultant creation of minigaps in the plasmon dispersion, manifested as a splitting of the plasmon peak. Increase of the periodicity to micron levels appears to shift the plasmon to higher frequencies and cause the splitting to vanish [5]. Density modulation was achieved with modulated oxide thickness in the former material system [4]; it was a side-effect of a surface metallic grating [3] enhanced by illumination [5] in the latter system.

The InAs/AlSb system offers certain unique advantages in the study of laterally modulated 2DES. The electron density n_s in an InAs quantum well sandwiched between AlSb barriers is extremely sensitive to both the composition of the cap layer and its separation from it [6]. Firstly, its 1.35 ev depth allows deep donors in the barriers and surface to drain electrons into it resulting in typical n_s values of 10^{12} cm^{-2}. Secondly, the absence of a surface depletion layer allows the quantum well to be located closer to the surface than in the GaAs/AlGaAs system, resulting in substantially more sensitivity to it. Thirdly, the selection of a cap layer, either InAs or GaSb, can result in a difference of n_s in excess of 100% by virtue of the difference in the surface Fermi level pinning in each cap [6]. Growing and laterally patterning a bilayer InAs/GaSb cap [7] and thereby modulating the surface Fermi level suggests itself as a logical means of impressing large lateral modulation on the 2DES residing in the quantum well a short distance below (Fig. 1)

The sample for this experiment had the following epilayer sequence: on a semi-insulating (100) GaAs substrate were grown a GaAs buffer, AlAs and AlSb nucleation layers, a 1 μm AlSb buffer, a 10 x (2.5 nm GaSb + 2.5 nm AlSb) short-period smoothing superlattice, a 20 nm AlSb bottom barrier, followed by the 15 nm InAs quantum well, a 15 nm AlSb top barrier, a 5 nm GaSb cap, a 10 nm AlSb cap separator, and a 3 nm InAs cap (sufficiently thin that it contains no electrons, due to the large quantization of the ground state). The sample was not intentionally doped. More details on the growth procedure for this material system can be found elsewhere [8]. The periodic patterns of alternating InAs and GaSb cap layers were fabricated by conventional photolithography and selective etching. For the two samples investigated here, the period a is 4 μm, and the duty cycle t/a (t = opening in InAs cap) 0.5 and 0.75 (Fig 1)

The samples were characterized by low-temperature (4.2K) magnetotransport on conventional Hall bars both before and after the lateral patterning. The as-grown sample with the InAs cap had a 2DES with density $n_s = 5.2\times10^{11}$ cm^{-2} and mobility $\mu = 170{,}000$ cm^2/Vs. Stripping this cap and exposing the GaSb cap caused these values to rise to 9.2×10^{11} cm^{-2} and 250,000 cm^2/Vs, respectively. For the sample with t/a = 0.5, the low-field Hall resistance both along and across the lateral superlattice (LSL) gave an electron density $n_s = 7.2\times10^{11}$ cm^{-2}, exactly the average of the two unpatterned values. The mobilities dropped to 80,000 cm^2/Vs across the LSL and 160,000 cm^2/Vs along it. The

high-field magnetotransport differed drastically in the two directions. From these measurements the amplitude of the lateral potential modulation is calculated to be 30 meV [7].

Transmission measurements were performed with a conventional rapid-scan Fourier transform spectrometer with the radiation light-piped through the sample immersed in a cryostat at 4.2K. The transmission T(B) was measured with a resolution of 1 cm^{-1} at various magnetic fields B up to 8 Tesla in steps of 0.2 Tesla.

Several absorption features are observed in a T(B)/T(0) trace. The 2D plasmon (B = 0) is observed only when the radiation is polarized perpendicular to the LSL (Fig. 2). Cyclotron resonances with identical lineshapes are observed in both polarizations; so also are the magnetoplasmons (since the B field mixes polarizations). The fractional change in transmission -ΔT/T = 1 - T(0)/T(B) for both samples show the high-frequency Drude tails with plasmon absorptions at ω_p = 49 cm^{-1} and ω_p = 52.5 cm^{-1} for the samples with t/a = 0.5 and 0.75, respectively (Figs. 3). The peak absorption is ~ 10% for the former sample, ~ 4% for the latter. The polarization-dependence and the fit to theory (developed below) leave no doubt about the identification of these peaks as 2D plasmon resonances.

-ΔT/T directly measures the real part of the dynamic conductivity of a 2DES [9]

$$-\Delta T/T = 2\,\mathrm{Re}\,\sigma(\omega)/(Y_0 + Y_s) \qquad (1)$$

where Y_0 and Y_s are the wave admittances of free space and the host semiconductor, respectively. For a 2DES with lateral density modulation $n_s = n_{s0} + \Delta n_{s0}\cos(qy)$, where $q = 2\pi/a$, on the surface of a semiconductor with dielectric constant ε_s, we derive $\sigma(\omega)$ explicitly as

$$\sigma(\omega) = \frac{\sigma_0}{1 + i\omega\tau} - \frac{\Delta\sigma_0\,\Delta\omega_p^2}{2\left[(\omega_p^2 - 2\omega^2) + \frac{i\omega}{\tau}\left\{1 + \tau^2(\omega_p^2 - \omega^2)\right\}\right]} \qquad (2)$$

where

$$\omega_p = \sqrt{\frac{n_{s0}\,e^2\,q}{m^*(\varepsilon_0 + \varepsilon_s)}}, \quad \Delta\omega_p = \sqrt{\frac{\Delta n_{s0}\,e^2\,q}{m^*(\varepsilon_0 + \varepsilon_s)}} \qquad (3)$$

where ω_p is the plasmon frequency, m^* the electron effective mass, τ the relaxation time, $\sigma_0 = en_{s0}\mu_0$ is the dc (ω = 0) conductivity, $\Delta\sigma_0 = e\Delta n_{s0}\mu_0$, and μ_0 is the dc electron

mobility. The first part on the right hand side of (2) is the Drude part and is determined solely by the average electron conductivity, the second part is the plasmon part: its pole determines the plasmon frequency to be ω_p given by the classic expression (3) for a 2DES with uniform density n_{s0} [10] and its strength and shape are determined by Δn_{s0} and τ respectively. From (1) and (2) for $\omega_p\tau >> 1$, the peak absorption at ω_p simplifies to

$$-\frac{\Delta T}{T}(\omega = \omega_p) = \frac{e\,\Delta n_{s0}\,\mu_0}{Y_0 + Y_s}\,\frac{\Delta n_{s0}}{n_{s0}} \qquad (4)$$

and is seen to be directly fixed by the size of the density modulation. As expected, it also vanishes as the density modulation is tuned to zero.

For a rectangular density modulation of period a and duty cycle t/a, with low and high (in the region t) density values of n_{s1} and n_{s2}, the average density $n_{s0} = n_{s1}(1-t/a) + n_{s2}(t/a)$, and the amplitude of the first Fourier component $\Delta n_{s0} = (2/\pi)(n_{s2} - n_{s1})\sin(\pi t/a)$. Using the values of n_{s1}, n_{s2}, and μ_0 measured above, an effective mass $m^* = 0.037m_0$ (from the cyclotron resonance), and $\varepsilon_s = 10.5\varepsilon_0$ for the thick AlSb cladding layer, we calculate ω_p to be 49 cm^{-1} and 52.2 cm^{-1} for t/a values of 0.5 and 0.75, in exact agreement with measurement. Furthermore, the peak absorption strengths from (4) are respectively 10% and 5% for the two cases, again in close agreement with experiment. The detailed absorptions from (1) and (2) are plotted along with the measured spectra in Figs. 3. There are no adjustable parameters in the calculated trace in Fig. 3a. For Fig. 3b, the calculated trace assumes the dc mobility along the LSL to be 100,000 cm^2/Vs to get a better fit to the Drude tail.

The positions of all resonances for the sample with t/a = 0.5 are plotted as a function of magnetic field up to 8 Tesla in Fig. 4. From the cyclotron resonance frequencies we calculate an electron mass $m^* = 0.037m_0$. The magnetoplasmon resonances obey the relation [11]

$$\omega_{mp}^2 = \omega_p^2 + \omega_c^2 \qquad (5)$$

very well, as indicated (Fig. 4). No evidence is seen in these samples for the coupling of the magnetoplasmon resonance with harmonics of the cyclotron resonance. Measurements on LSLs with two-dimensional modulation yielded results identical to the 1D LSLs.

In summary, we observe the absorption of 2D plasmons in one-dimensional and two-dimensional lateral density-modulated 2DES in an InAs quantum well sandwiched between AlSb barriers. The density modulation is achieved by lateral modulation of the surface

Fermi level with a periodic alternation of the composition of the cap layer between InAs and GaSb. In a LSL with 4 μm period we observe up to 10% peak absorption at 49 cm^{-1}. Both the location and strength of the plasmon absorption, as well as the dependence of these quantities on the duty cycle, agree well with theory. Sub-micron periodicities achieved with holographic lithography should lift the plasmon absorption to higher frequencies, and make possible the observation of non-local effects, which, in first order, are proportional to a^*q, where a^* is the Bohr radius. The higher Bohr radius for a 2DES in InAs together with a higher q should make this interaction appear in far infrared transmission measurements on such samples. These investigations will be reported elsewhere.

It is a pleasure to thank P. Pinsukanjana, A. Lorke, and A. Wixforth for many illuminating discussions. This work was supported in part by the Office of Naval Research (ONR grant #N000 15-92-J-1452) through the Quantum Institute, and by the National Science Foundation (NSF grant #DMR-91-10430) through QUEST, a National Science and Technology Center, at the University of California, Santa Barbara.

1. S. J. Allen, Jr., D. C. Tsui, and R. A. Logan, *Phys. Rev. Lett.* 38, 980 (1977).
2. D. Heitmann, *Surf. Sci.* 170, 332 (1986), and references therein.
3. E. Batke, D. Heitmann, J. P. Kotthaus, and K. Ploog, *Phys. Rev. Lett* 54, 2367 (1985).
4. U. Mackens, D. Heitmann, L. Prager, J. P. Kotthaus, and W. Beinvogl, *Phys. Rev. Lett.* 53, 1485 (1984).
5. P. Pinsukanjana, E. L. Yuh, E. G. Gwinn, M. Sundaram, P. F. Hopkins, and A. C. Gossard, *to be published.*
6. C. Nguyen, B. Brar, and H. Kroemer, *to be published*
7. C. Nguyen, B. Brar, V. Jayaraman, A. Lorke, and H. Kroemer, *to be published*
8. C. Nguyen, B. Brar, C. B. Bolognesi, J. J. Pekarik, H. Kroemer, and J. H. English, *J. Electron. Mater.* 22, 255 (1993).
9. S. J. Allen, Jr., D. C. Tsui, and F. DeRosa, *Phys. Rev Lett* 35, 1359 (1975)
10. For a comprehensive review on electronic properties of a 2DES, see: T. Ando, A. B. Fowler, and F. Stern, *Rev. Mod. Phys.* 54, 437 (1982).
11. F. Stern, *Phys. Rev. Lett.* 18, 546 (1967).

Figure Captions

Fig. 1. Lateral composition modulation of the cap layer can result in substantial lateral density modulation in an InAs quantum well. t/a is the duty cycle. Figure not to scale.

Fig. 2. Relative transmission spectra at B = 5.6 Tesla for the lateral superlattice with t/a = 0.75 for both polarizations. The lower trace has been vertically offset for clarity.

Fig. 3. Relative transmission for the sample with t/a = 0.5 (a) and for the sample with t/a = 0.75 (b). Dashed curves are obtained from Eq. (2). The reference spectrum is T(B = 8.4 Tesla).

Fig. 4. Absorption frequencies at different magnetic fields, for the sample with t/a = 0.5. Closed circles denote cyclotron resonance, open ones the 2D plasmon resonance. The dashed line fit for the CR line assumes $m^* = 0.037 m_0$. Dashed curve for the plasmon dispersion is calculated from Eq. (5).

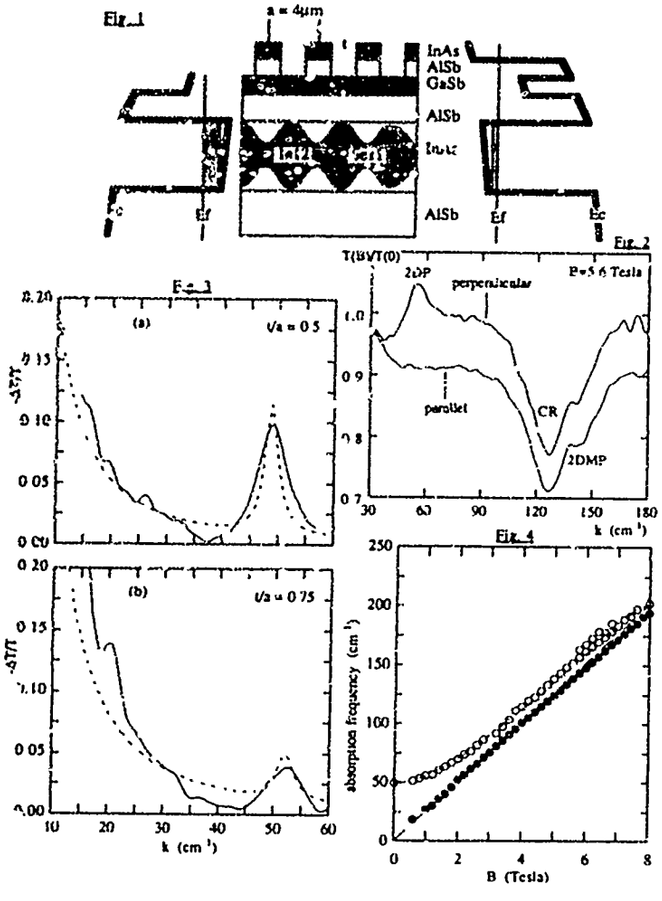

ThC7

Middle Infrared (λ=2-5.5 μm) High Quantum Efficiency Luminescence in GaSb/InAs II-type Multi-Quantum Well Structures.

S.V. Ivanov, B.K.Kuminkov, N.N.Ledentsov, B.Ya.Meltser, A.A.Monakhov, A.A.Rogachev, S.V.Shaposhnikov, and P.S.Kop'ev

A.F.Ioffe Physico-Technical Inst., Academy of Sciences of Russia, Politekhnicheskaya 26, St.Petersburg 194021, Russia

The paper reports for the first time a high radiative recombination yield within the range of 2 - 5.5 μm in II-type GaSb/InAs multi-quantum well (MQW) structures grown by molecular beam epitaxy (MBE) on lattice matched (100)GaSb substrates. Earlier these superlattices were developed by L.Esaki et al [1].

The investigated structures include the buffer layer sequence, consisting of 0.2μm-GaSb layer followed by ten period 50Å-AlSb/50Å-GaSb superlattice and a top 0.3μm-GaSb layer, and GaSb/InAs MQW structure. The GaSb barrier thickness was always constant of 100Å, while the InAs QW thickness varied from 10 to 35Å. The details of substrate preparation, growth regime have been reported elsewhere [2,3]. The growth temperature was chosen of 520°C. Special care were taken in forming the GaSb/InAs interface [4].

The double crystal differential x-ray diffraction (XRD) and transmission electron microscopy (TEM) data indicate very high structural quality of the structures. Their luminescence spectra are dominated up to room temperature by the very intensive line which is assumed to be associated with the recombination of electrons and holes in InAs/GaSb II-type MQW because of the pronounced red shift of luminescence band maximum position with the InAs QW thickness increase. The 300K to 77K integral luminescence intensity ratio was observed to be 3-4 at 3.5μm (17Å QW) and ~25 at 5.5μm (35Å QW) at 1W/cm^2 excitation density. These structures seem to be very promising for optoelectronic applications.

[1] L.Esaki and L.L.Chang, Thin Solid Films 36 (1976) 285

[2] S.V.Ivanov et al., Semicond. Sci. Technol. 8 (1993) 347

[3] P.S.Kop'ev et al., Sov. Phys. Semicond. 24 (1990) 450

[4] G.Tuttle et al., J. Appl. Phys. 67 (1990) 3032

Friday, August 27

FrA Optical Properties - Lasers

FrB Ultrafast Processes - New Optical Phenomena

FrA1

Microdisk Lasers

A F J Levi
Department of Electrical Engineering and Electrophysics
University of Southern California
Los Angeles, CA 90089-1112, USA

Abstract

InGaAs/InGaAsP quantum well microdisk lasers 0.8μm in radius and 0.18μm thick with emission at $\lambda = 1.542\mu m$ can be fabricated and operated at room temperature. Optical mode spacing in such structures is so large that a significant fraction (~20%) of spontaneous emission feeds into the lasing line resulting in superlinear output over a wide pump range.

Introduction

A conventional laser diode consists of an electrically driven semiconductor optical gain medium such as InGaAs placed within a resonant optical cavity. A Fabry Perot cavity, defined by the presence of two parallel mirror faces, results in definite longitudinal optical resonances called cavity modes. Figure 1(a) shows the geometry of such an edge emitting laser. The optically active gain medium is typically 300-500 μm long, approximately 1 μm wide, and 0.1 μm thick. When electrically pumped, the number of electrons (holes) injected into the conduction (valence) band of a direct band gap semiconductor may be large enough to result in optical gain over a small spectral region near the band edge. Optical gain will approach total optical loss first for the high Q (low loss) Fabry-Perot cavity mode nearest the peak in the gain spectrum. Lasing emission should occur predominantly into this cavity mode because the cavity resonance ensures optical losses are low. However, due to their relatively large size, these devices tend to be power hungry with threshold current for lasing greater than 10 mA. One way to reduce threshold current is to decrease the size of the device and increase the Q of the optical cavity. To some extent the advent of semiconductor microlasers was inspired by such goals.

15 years ago Iga and co-workers at the Tokyo Institute of Technology invented the Vertical Cavity Surface Emitting Laser (VCSEL) [1]. Since then designs have been refined [2] so that today dielectric mirror stacks of the order one micrometer thick above and below a quantum well active region form the high-Q resonant cavity with lasing light emission possible from the surface of the semiconductor substrate. Figure 1(b) shows a schematic diagram of a VCSEL. The optically active gain medium typically consists of one or more approximately 100Å thick quantum wells placed at an anti-node of the cavity resonance. Small lateral dimensions in the range 3-20 μm give a potentially superior optical beam profile for launching into optic fiber as well as low threshold currents in the range of 1 mA. Threshold currents would be even lower if more of the optical field were more tightly confined to the gain medium. Never-the less, while many practical issues still need to be addressed such as the high series resistance for current flowing though the mirror stacks, initial results are encouraging enough that some companies are considering developing VCSEL arrays for use in high speed parallel optical data links.

Recently very small laser diodes have been fabricated using a different type of resonant cavity in which light is very tightly confined to the gain region and emission is in the plane of the semiconductor substrate [3, 4]. The device consists of an InGaAs/InGaAsP multiple quantum well structure formed into a 1.5-10 μm diameter disk approximately 0.1 μm thick. Electrical current and mechanical support is provided by n- and p-type InP structures above and below the disk. Figure 1(c) shows a schematic diagram of this type of laser and figure 2 shows a scanning electron micrograph of such a microdisk laser. Total internal reflection for photons traveling around the perimeter of the semiconductor disk result in high Q whispering-gallery resonances. The term "whispering-gallery" is taken from Lord Rayleigh's explanation of sound propagation in the dome of St. Pauls Cathederal, London [5]. In the microdisk laser, the low optical losses associated with high Q whispering-gallery modes allow room temperature lasing action with a measured submilliamp threshold current [4]. Improved designs should result in threshold currents as low as a few tens of microamps. Of course, a consequence of using very high Q resonators is that not much lasing light radiates out into free space. However, it is possible to use light output couplers which slightly spoil the Q and yet allow the emitted light to be increased and redirected in or out of the substrate plane [6]. Other structures which make use of whispering gallery modes, such as the "microcylinder laser laser diode [7], are also being investigated.

Submicron radius disk laser

It is natural to consider how small a microlaser can be made and still function as a laser. In this context it is useful to focus on the microdisk laser since very small gain volumes and high Q cavities may be simultaneously achieved using this geometry. Figure 3 shows a scanning electron micrograph of a very small optically pumped InGaAs/InGaAsP quantum well microdisk of radius $R = 0.8 \pm 0.05\mu m$ and thickness $L = 0.18\mu m$. The disk is composed of six 120Å thick quantum wells of InGaAs material lattice matched to InP. Five barriers 120Å thick of InGaAsP separate the quantum wells, and InGaAsP layers 240Å thick enclose the quantum well-barrier structure. The InGaAsP material has a band-edge corresponding to $1.1\mu m$ wavelength radiation. After post growth fabrication the device is measured with the sample maintained at room temperature. Optical pump power from a diode laser with emission at wavelength $\lambda = 0.85\mu m$ is focused onto the disk laser top surface using a 0.5 numerical aperture (N.A.) lens, so that at best only about 80% of total incident pump light is intercepted by the $R = 0.8\mu m$ radius disk. The total incident pump power, P_{in}, is delivered during an 8 ns period at a repetition period of 100 ns. It is observed that heating becomes significant for pulse widths of 30 ns (30% duty cycle) or greater as evidenced by a decrease of both laser and total light output. The radiation emitted by the microdisk is collected by the same 0.5 N.A. lens, and directed to a spectrometer. The lens collects lasing light scattered by disk imperfections into the vertical direction. The spectra shown in figure 4 were obtained with 5 nm resolution. The figure shows a luminescent background, a lasing line at $\lambda = 1.542\mu m$, and a resonance at $\lambda = 1.690\mu m$.

The power in the lasing line versus total incident pump power, P_{in}, is shown in figure 5. It is clear from this data that output lasing power is superlinear with input. This is in accord with simple models for very small semiconductor lasers and is most readily explained by considering the steady state intensity, S, in the lasing mode: $S = r_{sp}^{mode} / (\kappa - g^{mode})$ where r_{sp}^{mode} is the spontaneous emission rate into the lasing mode, κ is the optical loss rate in the cavity and g^{mode} is the modal gain. For S to reach a given threshold intensity S_o when r_{sp}^{mode} is small requires a much smaller value of $(\kappa - g^{mode})$ than when r_{sp}^{mode} is relatively large. Hence, superlinear behavior extends over a larger range of pump power for r_{sp}^{mode} large, because the rate of change in S with P_{in} around S_o is larger when r_{sp}^{mode} is small.

Mode counting

It is possible to construct a straight-forward mode counting argument to calculate the fraction, β, of total spontaneous emission that feeds into the lasing mode. For an ideal disk the whispering mode frequencies ω_M may be calculated to an accuracy of a few percent by solving the equation $2\pi R n_{eff}(\omega) R = x_M^1 c$, where c is the speed of light in vacuum, $n_{eff}(\omega)$ is the (two-dimensional) effective refractive index, and x_M^1 is the smallest positive root of $J_M(x) = 0$, where J_M is the usual Bessel function with integer index M. Larger roots are denoted by x_M^q. The effective refractive index is found from

$$\tan(kL\sqrt{\varepsilon - n_{eff}^2}/\lambda) = \sqrt{(n_{eff}^2 - 1)/(\varepsilon - n_{eff}^2)}$$

where ε is the real part of the semiconductor dielectric constant. The small discrepancy between the calculated ($\lambda_1 = 1.480\mu m$ and $\lambda_2 = 1.634\mu m$) and experimentally measured ($\lambda_1 = 1.542\mu m$, $\lambda_2 = 1.690\mu m$) values of λ_M is in part due to uncertainties in the exact physical dimensions of the disk.

The spontaneous emission rate into a mode may be expressed as

$$r_{sp}^{mode} = \int r_{sp}(\omega)\Gamma(\omega)d\omega$$

where

$$\Gamma(\omega) = \frac{\gamma(\omega)/\pi}{(\omega - \omega_c(\omega))^2 + \gamma(\omega)^2}$$

is the cavity function and $\gamma(\omega)$ describes the frequency dependent line shape of the resonance centered at $\omega_c(\omega)$. For simplicity we consider the case where both ω_c and γ are independent of ω. Clearly, if γ is small, it follows that Γ is a δ-function and so $r_{sp}^{mode} = r_{sp}(\omega_c)$. Even though the cavity line width γ may be small and the spontaneous emission into the mode originates from the frequency interval $\omega_c \pm \gamma$, such emission is enhanced by $1/\gamma$ so that the principle of mode partition is preserved. However, when γ becomes larger than the luminescence width, r_{sp}^{mode} is usually reduced below $r_{sp}(\omega_c)$ by an overlap factor.

Spontaneous emission within a dielectric slab of the disk's thickness ($0.4 \times \lambda$ in the material) and composition is about 75% into trapped transverse electric modes (evanescent above and below the dielectric), 10% transverse magnetic modes and about 15% into free modes propagating outside the dielectric [Ref 8]. Very little goes into trapped transverse magnetic modes because most of the corresponding modal energies are outside the dielectric. If one assumes these properties of dielectric slabs also apply to disks then about 75% of spontaneous emission is into two-dimensional disk modes of transverse electric character describable by scalar forms $J_M(n_{eff}\omega r/c)e^{-iM\theta}$, where θ is the polar coordinate angle and r is the radial coordinate. There are four roots x_M^q of Bessel functions J_M

between $x_6^1 = 9.936$ and $x_5^1 = 7.588$, namely $x_5^1 = 8.771$ (corresponding to the $M = 5$ whispering-gallery mode lasing emission measured at $\lambda_1 = 1.542\mu m$), $x_6^1 = 8.654$, $x_5^2 = 8.417$, and $x_4^2 = 9.761$. Thus, in this region, there are about (2 + 2.5) modes in an interval centered on the $M = 5$ whispering mode and with endpoints halfway to the adjacent whispering modes. The factor 2.5 is from counting half of the 5 modes corresponding to x_6^1, x_5^2, and x_4^2, taking into account the degeneracy factor of two for $M > 0$. The factor 2 is from x_5^1 and its degeneracy of two. The separation of the $M = 4$ and $M = 5$ whispering modes is about 150 nm and the measured spectral width of luminescence (full-width half-maximum) is about 220 nm for $P_{in} = 1mW$. Including the 75% factor mentioned above, one may therefore estimate that the fraction of spontaneous emission which goes into one of the $M = 5$ whispering gallery modes is $\beta(P_{in} = 1mW) = (150 \times 0.75)/(220 \times 4.5) = 0.106$, or 0.212 into both $M = 5$ whispering modes.

This result for β appears to be inconsistent with the measured emission shown in figure 4. However, it should be noted that in an ideal disk geometry, radiation from whispering modes is emitted into directions near the plane of the disk, not towards the vertical direction and into the detection apparatus. In addition, the measured smooth luminescence background has a substantial and perhaps dominant contribution from free modes. Furthermore, below transparency, light emitted into whispering modes is substantially absorbed before it escapes the laser structure and is detected. Overall, these effects reduce the apparent β value as determined by casual inspection of the vertically emitted emission spectrum. It is worth mentioning that disk modes other than whispering gallery modes are expected to have relatively low Q values. If a mode width exceeds the luminescence width, the amount of spontaneous emission into such a mode is reduced by an overlap factor. In that case, low Q modes with central frequencies outside the luminescence region experience some spontaneous emission. Never-the-less, the sum of modes times their overlap factor should still give the fraction, β, calculated above.

Device physics

The above results and discussion are representative of present knowledge of microlaser operation. In fact, it is remarkable that, while very small laser diodes have been fabricated, our understanding of how such devices work is manifestly inadequate. Much of what is interesting about microlasers cannot be modeled with the commonly used rate equations for carrier and photon density in the device. In fact, efforts to parameterize microlaser effects with such an unjustifiably simplistic approach are somewhat pointless and bound to fail. The weakness of such modeling motivated the use of mode counting (described above) to establish a value for β. Clearly, it is necessary to examine every relevant aspect of the physics governing device operation before developing a new model for microlasers.

The spacing between the mirrors of a standard Fabry-Perot laser is relatively large so that several hundred longitudinal cavity modes overlap the optical gain spectrum. It follows that only a small fraction ($\beta \sim 10^{-4} - 10^{-5}$) of spontaneous photon emission feeds into the longitudinal lasing mode. This combined with the large difference between stimulated and spontaneous recombination rates gives rise to an abrupt increase in lasing light output with increasing drive current above threshold. However, below threshold there is extra photon intensity in cavity modes. In fact, the formal mathematical analogy which exists between a nonequilibrium Landau-Ginzburg phase transition and photon field statistics around

threshold allows us to describe all photons in cavity modes below threshold as (unsustainable) fluctuations [Ref. 9]

In a very small resonant cavity, such as those used in microcavity lasers, it is possible that only one optical mode overlaps the semiconductor's gain and spontaneous emission spectrum. In such a situation every spontaneous emission event fluctuates into the lasing mode and there is no abrupt increase in average lasing light level with which to define a laser threshold. Similarly, it is no longer possible to define a threshold by considering moments of the statistical distribution in photon number [Ref. 10]. Apparently, the concept of a laser threshold along with the implicitly mean-field language of Landau Ginzburg phase transitions is no longer useful and a full quantum mechanical description may become necessary [Ref. 11].

It is also worth mentioning that fluctuations in photon number may also be driven directly by fluctuations in electron number. This may become important in microlasers which are so small they operate using only a few thousand electrons. In such a situation the influence of variations in electron chemical potential can be modified depending on whether the laser is driven by an external voltage or current source.

Of course, the above relates to only one aspect of the problem which, unfortunately, is overshadowed by the more fundamental concern of optical gain in a resonant cavity. Even after several decades of effort, physicists have failed to develop a satisfactory quantitative model of optical absorption and gain in *bulk* intrinsic semiconductors. Such a poor state of affairs is perhaps understandable when one begins to consider the complexity of the problem [Ref. 12]. If one specializes to the case of electron distributions in thermal equilibrium with the semiconductor lattice, then, under low drive current conditions, the semiconductor's band-edge absorption spectrum shows strong conduction/valence band many electron interaction effects in the form of spectrally sharp exciton features. Under high drive current the semiconductor may contain of order 10^{18} cm^{-3} excess electrons and display optical gain over a small spectral range near the band-edge and absorption elsewhere. Electron interaction effects redistribute and broaden the spectral weight in the exciton features and a significant band tail develops in the semiconductor's renormalized band gap. Even if many-electron interaction effects could be evaluated beyond the mean field (random phase) approximation and a satisfactory quantitative explanation of band tails be established we would still be limited to the case of thermal equilibrium. It seems unlikely, however, that the electron distribution in a microlaser is, in fact, at thermal equilibrium with the semiconductor lattice. The reason for this is that the calculated time scales for various optical and electronic relaxation processes in microlasers are comparable. For example, a microlaser of radius $R = 1\mu m$ with emission wavelength $\lambda = 1.5\mu m$ has a calculated cavity round trip time of 40 fs, a cavity photon lifetime of 150 fs, and an electron electron scattering rate in the range of 100 fs. In these circumstances one is tempted to speculate that lasing photons remove electrons from the system at such a fast rate that the electron distribution is unable to equilibrate. The resulting spectral hole burning [Ref. 13] in the electron distribution reduces the spontaneous emission into the lasing mode modifying both the intensity and spectral purity of the microlaser output characteristics. In practice however, except for devices with disk radius less than $1\mu m$ this situation is somewhat masked by spatial diffusion of charge carriers from regions of low photon field intensity in the microstructure.

The short and comparable characteristic time scales for cavity round trip time, photon lifetime, and electron scattering rate in microcavity lasers raises the interesting issue of distinguishing between optical and electronic processes on short time scales. One is tempted to speculate that, since electron scattering is mediated via emission and absorption

of a photon, on very short time scales one ultimately cannot distinguish between optical and electronic phenomena.

Conclusion

In summary, room temperature lasing action in a very small InGaAs/InGaAsP quantum well microdisk of radius $R = 0.8\mu m$ and thickness $L = 0.18\mu m$ has been demonstated. It is estimated that, for this device, approximately 20% of the spontaneous emission feeds into the $M = 5$ whispering gallery modes at wavelength $\lambda = 1.542\mu m$. Although it should be possible to fabricate even smaller structures which lase into the $M = 4$ whispering gallery mode, there is still much to be understood about the physics of microlaser operation.

REFERENCES

1. H. Soda, K. Iga, C. Kitahara, and Y. Suematsu, *Japn. J. Appl. Phys.* **18**, 2329 (1979), and K. Iga, S. Kinoshita, and F. Koyama, *Electron. Lett.* **23**, 134 (1987).

2. For a review, see J. L. Jewell, editor of special issue *Microresonator devices*, *Quantum Electronics* **24** (1992).

3. S. L. McCall, A. F. J. Levi, R. E. Slusher, S. J. Pearton, and R. A. Logan, *Appl. Phys. Lett.* **60**, 289 (1992).

4. A. F. J. Levi, R. E. Slusher, S. L. McCall, T. Tanbun-Ek, D. L. Coblentz, and S. J. Pearton, *Electron. Lett.* **28**, 1010 (1992).

5. Lord Rayleigh, *Scientific Papers*, p. 617, Cambridge University, Cambridge England (1912).

6. A. F. J. Levi, R. E. Slusher, S. L. McCall, J. L. Glass, S. J. Pearton, and R. A. Logan, *Appl. Phys. Lett.* **62**, 561 (1993).

7. A. F. J. Levi, R. E. Slusher, S. L. McCall, S. J. Pearton, and W. S. Hobson, *Appl. Phys. Lett.* **62**, 2021 (1993).

8. S. J. Ho, S. L. McCall, and R. E. Slusher, *Quant. Electron. Laser Sci. Tech. Dig.* **11**, 54 (1991).

9. This description is discussed by H. Haken, *Light*, Vol. 2, *Laser Light Dynamics*, North Holland, Amsterdam (1986) also see V. DeGiorgio and M. O. Scully, *Phys. Rev.* **A2**, 1170 (1970), R. Graham and H. Haken, *Z. Physik.* **273**, 3; (1970), S. Grossmann and P. H. Richter, *Z. Physik.* **242**, 458 (1971), M. Corti and V. DeGiorgio, *Phys. Rev. Lett.* **36**, 1273 (1976).

10. H. J. Charmichael, *Lasers and Quantum Optics*, editors L. M. Narducci, P. J. Quel, and J. R. Tredicce, World Scientific, Singapore (1991).

11. M. Lax, *1966 Brandeis University Summer Institute of Theoretical Physics*, Vol. II, editors M. Chretien, E. P. Gross, and S. Deser, Gordon and Breach, New York (1968), also V. Korenman, *Annals of Physics* **39**, 72 (1966).

12 For an overview see *Quantum theory of the optical and electronic properties of semiconductors*, H. Haug and S. W. Koch, World Scientific, Singapore (1990).

13 For a recent discussion on spectral hole burning see K. Henneberger, F. Herzel, S. W. Koch, R. Binder, A. L. Paul, and D. Scott, *Phys. Rev.* A45, 1853 (1992).

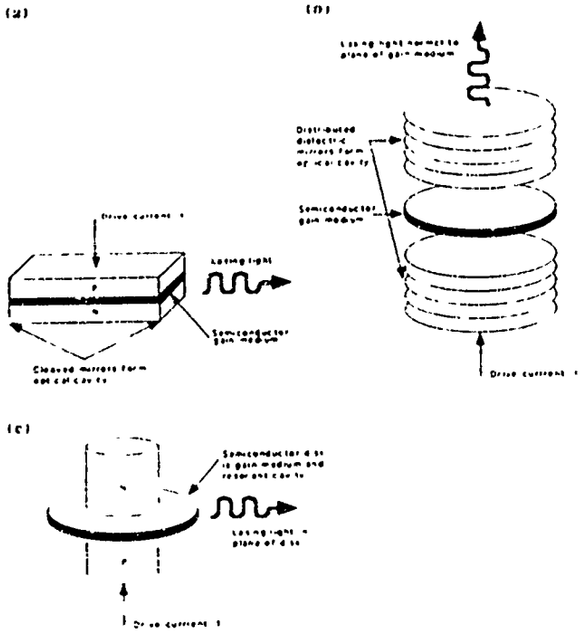

Fig. 1 Schematic diagram of (a) an edge emitting Fabry-Perot laser diode, (b) a VCSEL and (c) a microdisk laser. Drive current I is indicated.

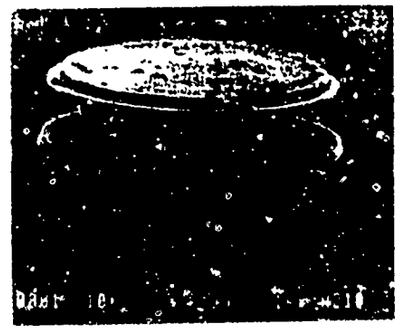

Fig. 2 Scanning electron microscope image of an approximately 10μm diameter microdisk laser diode similar to the device discussed in Ref. 4.

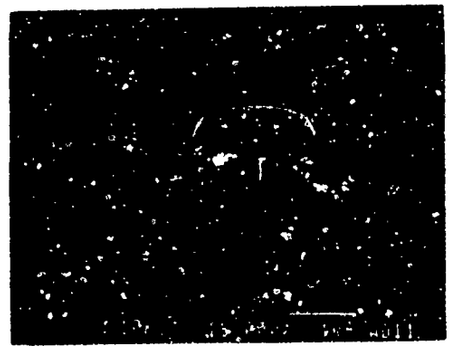

Fig. 3 Scanning electron micrograph of an InGaAs/InGaAsP multiple quantum well microdisk laser with $R = 0.8\mu m$ and $L = 0.18\mu m$. The $1\mu m$ bar provides a scale.

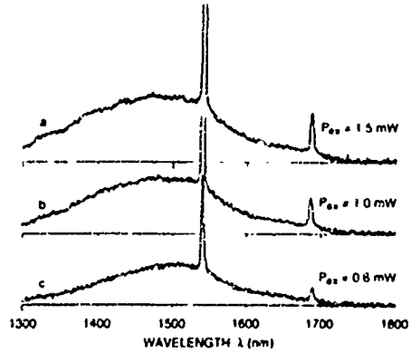

Fig 4 Room temperature photoluminescence spectra of a $R = 0.8\mu m$ radius microdisk laser. Excitation is by a pulsed AlGaAs/GaAs laser diode emitting at $\lambda = 0.85\mu m$. Pump power incident on the device is P_{ex}.

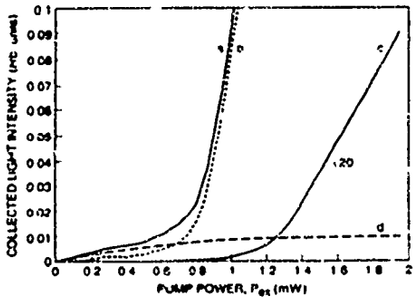

Fig 5 Room temperature power at the lasing wavelength versus incident pump power, P_{ex}, for the $R = 0.8\mu m$ microdisk laser of Fig 3 and 4. (b) Power in the lasing line versus pump power. (c) Power at the lasing wavelength versus pump power. Vertical scale is divided by 20. (d) Power in the spontaneous emission background at the lasing wavelength versus pump power. Resolution is 5 nm.

FrA2

GaAs-AlAs and Si-SiGe Quantum Well Structures For Applications in Nonlinear Optics.

M.J.Shaw, K.B.Wong, and M.Jaros

Physics Department, The University, Newcastle upon Tyne, England, NE1 7RU.

Both, GaAs-AlAs and Si-SiGe quantum well structures have been considered for applications as infrared detectors, modulators and switching devices. The miniband structure in these systems covers a wide range of energies (e.g.1-200 meV) and offers an opportunity to design optical devices that would operate in the far infrared range of wavelengths. An external electric field and triangular wells have been used to modify the structure of confined states. This enhances optical nonlinearities (e.g. the second order susceptibility). In this paper we present the first full scale evaluation of GaAs-AlAs and Si-SiGe quantum well structures in which the nonlinearity arises due to virtual optical transitions between valence minibands. We aim at structures which could operate in the 10-15 micrometer range. We present both the magnitude and the frequency dependence of the second order susceptibility. We show that the valence band structure offers several advantages compared to the conduction band. We find that - contrary to commonly held views - the strongest contributions to the second order response originate from regions in momentum space lying farther from the zone centre. Also, the frequency of the peak response does not correspond to that expected from simple models.

FrA3

Charge Transfer and Electroabsorption in an Electric Field Tunable Double Quantum Well Structure

K. Bernhard, A. Zrenner, G. Böhm, G. Tränkle and G. Weimann
Walter Schottky Institut, Technische Universität München,
85748 Garching, Germany

Abstract

An optical modulator based on electric field induced charge transfer in a double quantum well structure is introduced. The modulator is configured as a n-i-n diode for waveguide applications at a wavelength of ≈1μm. Dark currents caused by thermionic emission are suppressed by introducing specially designed InGaAs/AlGaAs hetero barriers. Room temperature operation with negligible dark current up to internal electric fields of 1.7×10^5V/cm is demonstrated. Electric field tuneable absorption is obtained by both band filling and Stark effect in a GaAs/InGaAs double quantum well unit which has been repeated five times in the i-region of the n-i-n structure. Absorption spectroscopy is performed in waveguide geometry and applications as optical modulators are demonstrated.

The introduction of III/V quantum well (QW) structures opened a variety of new perspectives in semiconductor optoelectronics. Deliberate control over individual layer composition and thickness allows the construction of highly optimised optoelectronic devices. In this contribution we describe an optical modulator based on charge transfer[1,2] and quantum confined Stark effect[3] in a pseudomorphic GaAs/InGaAs double QW structure. The present structure is configured as an electric field tuneable n-i-n hetero diode for optical waveguide applications. In contrast to the related InP-based BRAQWET device[1,2] our structure is designed for a wavelength in the range of 1μm to match to the emission lines of strained layer InGaAs QW lasers.

The overall band diagram of our layer sequence is shown in Fig. 1. The electro-optically active parts of the structure are the double QW (DQW) units in the centre of the AlGaAs i-region. Five DQW units have been introduced into the i-region to obtain sufficient electroabsorption and optical confinement on one hand and to avoid problems with the overall critical layer thickness of the strained layer InGaAs system on the other hand. The layer sequence of a single unit is indicated in the left bottom part of Fig. 1. The modulator is operated near the fundamental band gap of the 80Å i-$In_{0.15}Ga_{0.85}As$ QW. This optically active QW is separated on one side by a 10Å GaAs interface layer and a 150Å i-$Al_{0.10}Ga_{0.90}As$ barrier from a 120Å n-doped GaAs QW, which acts as a charge reservoir. On the other side a 102Å p-$Al_{0.45}Ga_{0.55}As$ layer is separated by a 10Å GaAs interface layer and a 100Å i-$Al_{0.45}Ga_{0.55}As$ spacer. The basic purpose of this layer sequence is twofold: The charge reservoir first of all has been designed to provide electrons for an electric field induced transfer over the AlGaAs barrier into the InGaAs QW. The p-AlGaAs layer on the other hand has been introduced to increase the effective barrier height in order to minimise thermionic emission of electrons out of the DQW region. Without loss due to thermionic emission and tunnelling each single unit is by itself

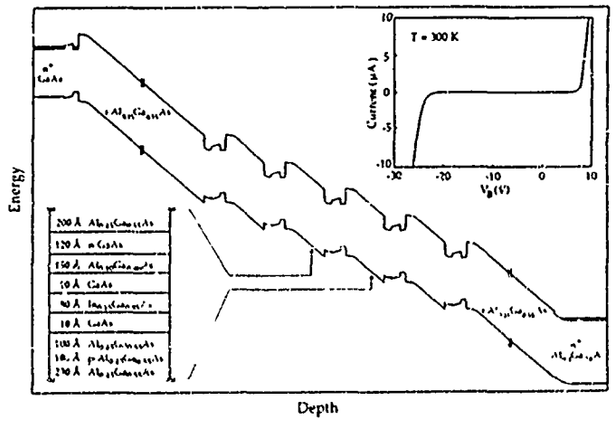

Fig. 1: Calculated band diagram of the n-i-n double QW modulator structure. The layer sequence of one out of the five active double QW units is shown on the left. The insert on the right shows the room temperature I-V characteristic of the structure as measured on a 200μm×300μm mesa diode.

neutral. The net number of free electrons N_e in each unit is given by $N_e=N_D\times d_D-N_A\times d_A=1\times10^{12}cm^{-2}$, where N_D (N_A) is the doping concentration of the n-layer (p-layer) and d_D (d_A) the corresponding layer thickness. As shown in Fig. 1 the additional dipole field between the n- and p-doping layer leads to a saw-tooth like potential drop throughout the structure. Although thermionic emission currents are suppressed by the presence of the p-doped AlGaAs barriers and by the introduction of the InGaAs/AlGaAs hetero interface, additional care has been taken to avoid the depletion of individual units even on a long time scale. If electron depletion happens in a given unit, the electric field on the right hand side of the unit is reduced, while the field on the left hand side is increased (for the bias conditions shown in Fig. 1). This in turn has an influence on the thermionic depletion of the neighbouring units. A homogenous potential drop throughout the structure as indicated in Fig. 1 can only be obtained if the effective barrier heights of all built in hetero barriers are identical. The first hetero barrier on the top left part of Fig. 1 (n-i junction) has therefore been chosen to be identical to those used in the optically active DQW units. From those considerations it is also quite obvious, that a unipolar charge transfer device as described here can only be implemented as n-i-n structure. Attempts to introduce the active DQW units in the intrinsic region of a p-i-n structure would result in a depletion of the active units and in an inhomogenious potential drop throughout the structure.

The room temperature I-V characteristic of a 200μm×300μm mesa diode processed from our n-i-n layer sequence is shown in the insert of Fig. 1. The introduction of the InGaAs/AlGaAs hetero interface and the p-type doping layer in the AlGaAs barrier results in a maximum bias voltage V_B of

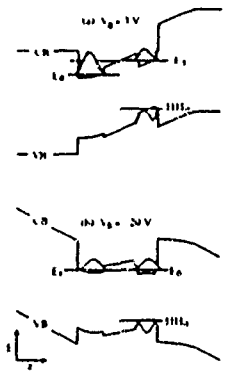

Fig. 2. Band diagram of a double QW unit for (a) V_B=3V and (b) V_B=-20V. Occupied subband levels are shown in gray. Besides the occupied levels only the relevant subbands for optical absorption in the InGaAs QW are indicated.

about 25V with negligible dark current. This means that electric fields up to 1.7×10^5V/cm can be controlled without significant current flow.

Such a tuning range is sufficiently high to cause an appreciable electric field induced charge transfer within the DQW units. The individual layer width and composition of the DQW units have been calculated to allow for a transfer of 5×10^{11}cm^{-2} electrons from the GaAs into the InGaAs QW within the available tuning range of the electric field. With our design parameters and tuning range the inter-well charge transfer is expected to happen on a psec time scale[4]. For realistic applications the modulation bandwidth of our structure will be therefore RC-limited. The band diagrams and charge distributions as calculated with a self consistent model calculation for room temperature are shown in Fig. 2 for two different bias conditions. The results in Fig. 2 have been obtained by treating the DQW unit as a coupled QW system. Only the relevant subband levels are indicated. All subbands are shown with their probability distribution. Levels with significant electron occupancy are shown in gray and are scaled proportionally to the individual electron occupancy in order to visualise the field induced charge transfer. At V_B=3V all electrons are confined in the doped GaAs QW. The InGaAs QW is empty and biased by the dipole field which builds up between the n-doped GaAs QW and the p-type doping layer in the $Al_{0.45}Ga_{0.55}As$ barrier. At V_B=-20V half of the original charge in the n-GaAs reservoir has transferred into the now unbiased InGaAs QW. What the optically active InGaAs QW is concerned, both the changes in electric field in terms of the QCSE and the changes in charge accumulation (band filling) lead to a blue-shift in the absorption spectrum of the lowest spatially direct transition in the InGaAs QW as V_B is decreased from 3V ($E_3\rightarrow HH_0$) to -20V ($E_0\rightarrow HH_0$)[5].

All optical investigations on our structure have been performed in waveguide geometry for TE polarisation. The optical transmission as a function of wavelength is shown in Fig. 3 for different bias conditions. The spectra have been recorded with a stabilised Ti-saphire laser and a Si p-i-n detector diode. Both facets of the waveguide remained uncoated. The dimensions of the electric field tuneable waveguide structure are shown in the insert of Fig. 3. The high frequency Fabry-Perot oscillations caused by the internal reflections at the facets have been removed for clarity by a numerical filtering process. The data clearly confirms the predicted blue-shift of the absorption which appears here as a blue-shift of the transmission for decreasing V_B (7V→-20V). The observed blue-shift is considerably stronger in the regime of the bare QCSE (V_B>3V) as compared to the regime of band filling (V_B<0V), where part of the blue shift is compensated by the red shift which originates from band gap

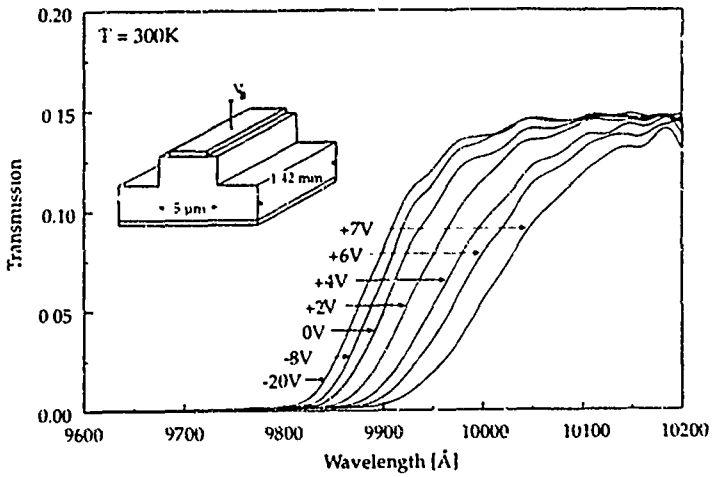

Fig. 3: Optical transmission in waveguide geometry as a function of wavelength for different V_B. The dimensions of the optical waveguide are indicated.

renormalisation[6,7]. From the displayed data it is difficult to clearly separate the regimes of band filling and QCSE. In the transition region between those two regimes an interesting enhancement of the blue-shift is observed (compare data for 0, 2, 4 and 6V). From the QCSE alone a monotonic increase of the incremental blue-shift with decreasing V_B would be expected, as observed for V_B=7, 6 and 4V. Between V_B=4 and 2V however again an increase of the incremental blue-shift is observed, just before the regime of band filling at V_B<0V. We tentatively attribute this behaviour to the appearance of an excitonic regime which is quenched by the QCSE on one side and by the transition to a charged plasma due to band filling on the other side[7].

The electric field induced changes of the absorption spectrum can be directly applied in a modulator which is operated in the electro-absorptive mode in the region around 9900Å. The on/off ratio for this operation mode is shown in Fig. 4 as a function of wavelength. The bias voltage V_B was switched between a fixed reference voltage of 7V and the indicated values. The set of data demonstrates that the electro-absorptive straight waveguide version of this n-i-n structure can be directly used for device applications at room temperature. The propagation loss for V_B=-20 at the operation wavelength of 9900Å is only 2dB as shown in the insert of Fig. 4. If a lower on/off ratio can be tolerated in a system design, also high speed operation with reduced voltage swing is possible (for example 0V↔2V). This relaxes the requirements of the digital driver circuit. The bare RC time constant (50Ω system without parasitic capacitance) of the investigated waveguide structure is only 20psec.

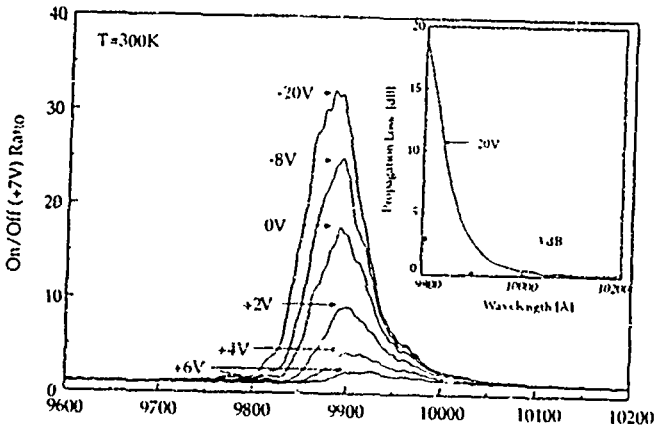

Fig. 4: On/Off ratio of the transmitted light intensity as a function of wavelength for various V_B. The reference bias voltage for all the data is 7V. The propagation loss is shown in the insert.

In conclusion we have introduced an optical modulator based on electric field induced charge transfer and QCSE in a DQW unit. The modulator is configured as a n-i-n type tuneable waveguide structure for applications at wavelength around 1μm. Thermionic emission at room temperature is controlled by introducing InGaAs/AlGaAs hetero interfaces. Electric field tuneable absorption is obtained by both band filling and Stark effect in a GaAs/InGaAs double quantum well unit. Absorption spectroscopy is performed in waveguide geometry and the application as optical modulator is demonstrated. This work has been supported by the BMFT Photonics project.

References:

[1] M. Wegener, J. E. Zucker, T. Y. Chang, N. J. Sauer, K. L. Jones and D. S. Chemla, Phys. Rev. B 41, 3097 (1990)

[2] J. E. Zucker, M. Wegener, K. L. Jones, T. Y. Chang, N. Sauer and D. S. Chemla, Appl. Phys. Lett. 56, 1951 (1990)

[3] D. A. B. Miller, D. S. Chemla, T. C. Damen, A. C. Gossard, W. Wiegmann, T. H. Wood and C. A. Burrus, Phys. Rev. Lett. 53, 2173 (1984)

[4] Jun Wang and J. P. Leburton, Appl. Phys. Lett. 59, 2709 (1991)

[5] The indicated transitions are the energetically lowest transitions in the InGaAs QW. Both transitions are dipole allowed

[6] H. Sakaki, H. Yoshimura, and T. Matsusue, J. Appl. Phys. Japan 26, L1104 (1987)

[7] A. Pinczuk, J. Shah, R. C. Miller, A. C. Gossard and W. Wiegmann, Solid State Commun. 50, 735 (1984)

FrA4

Strained InAs/$Ga_{0.47}In_{0.53}As$ quantum-well heterostructures grown by molecular-beam epitaxy for long-wavelength laser applications

F. Fournier[a], P. Grunberg[a], C. Fouillant, A. Baranov, A. Joullie[a] and K. H. Ploog

[a] Max Planck Institut fur Festkorperforschung, D-70506 Stuttgart (Germany)
LA2, URA CNRS 102, Universite de Montpellier II, F-34095 Montpellier (France)
Paul Drude-Institut fur Festkorperelektronik, D-10117 Berlin (Germany)

Abstract

Strained InAs single quantum wells (SQWs) embedded in a $Ga_{0.47}In_{0.53}As$ matrix are studied by photoluminescence spectroscopy. Spontaneous emission is obtained up to 2.1 μm at 300 K, which is the longest wavelength achieved so far with QWs grown on InP substrates. Laser diodes based on a 10 ML wide InAs SQW confined by $Ga_{0.47}In_{0.53}As$ layers are characterized. At 80 K the emission spectrum of broad area diodes is centered at 1.846 μm and the threshold current density is 175 A/cm². Continuous wave operation is achieved with narrow stripe devices but at shorter wavelength due to increased losses and filling of the QW energy levels.

Introduction

The study of strained-layer heterostructures (SLHs) attracts currently much attention because they exhibit unique physical properties [1] which find applications in microwave as well as optoelectronic devices. One of the most remarkable benefits of SLHs manifests itself in the quantum-well (QW) laser field where the peculiar valence band configuration of compressively strained layers [2, 3] results in superior laser performances as compared to lattice matched devices [4]. Strained InAs QWs confined by $Al_{0.48}In_{0.52}As$ lattice matched to InP have theoretically been credited a high potential for laser emission near 1.5 μm [5]. Substituting the $Al_{0.48}In_{0.52}As$ confining layer by a $Ga_{0.47}In_{0.53}As$ layer, which has a much narrower band gap energy (0.75 eV versus 1.45 eV at 300 K), should in principle allow emission to be obtained at longer wavelengths, where a number of interesting applications exist. However stimulated emission has not yet been reported in these materials systems because the high strain (1.2 %) experienced by InAs renders the epitaxy of high quality structures very difficult.
In this work we demonstrate that the InAs/$Ga_{0.47}In_{0.53}As$ QW materials system is suited for emission above 1.6 μm and we report the first operation of laser diodes made from this system.

Growth Procedure

The samples under investigation are InAs SQWs embedded in a $Ga_{0.47}In_{0.53}As$ matrix which are grown on n⁺ (100) oriented InP substrates by solid source MBE in a Riber 32P system. The detailed growth procedure can be found in Ref. [6]. The key point is that the InAs SQWs are grown under virtual surfactant conditions [6] which allow superior quality QWs to be obtained and enhance the critical thickness before defect generation [7]. The InAs SQW width lies between 2 and 23 ML in different samples. High resolution double-crystal x-ray diffraction (HRXRD) was used to check the structural properties of the samples and to demonstrate that the epitaxial structures are actually pseudomorphic.

[a] Present address: Paul Drude Institut fur Festkorperelektronik, Hausvogteiplatz 5-7, D-10117 Berlin (Germany)

Photoluminescence Spectroscopy

For the PL experiments the excitation source was the 647.1 nm line of a Kr^+ laser and the emitted signal was detected by a cooled InAs detector. We have plotted in Fig. 1 the PL spectra taken at low temperature (6 K) from 3 representative SQWs. Note that they span the 1.6 μm to 2.2 μm wavelength range. The vertical arrows indicate the positions of the transitions between the confined electron state e_1 and the confined heavy hole state hh_1 calculated with the envelope function model [8] assuming fully strained InAs QWs and using the parameters given in Ref. [9]. Excellent agreement between calculated and experimental values is obtained except for the thinnest wells which are more sensitive to any interface fluctuation. However when increasing the SQW width above 15 ML the PL line broadens and becomes less intense. This result is indicative of a slight structural deterioration as also observed by HRXRD. Nevertheless the excellent agreement between experimental and calculated positions indicates that even the widest SQWs are elastically strained as also confirmed by transmission electron microscopy [7]. It has to be noted that we have measured the narrowest PL lines ever reported for InAs QWs grown on InP substrates [10] which reveals the superior quality of our samples.

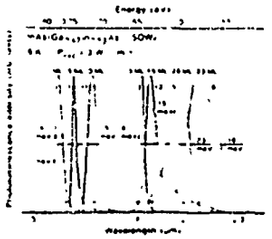

Fig. 1: PL spectra taken at 6 K from representative InAs/$Ga_{0.47}In_{0.53}As$ SQWs.

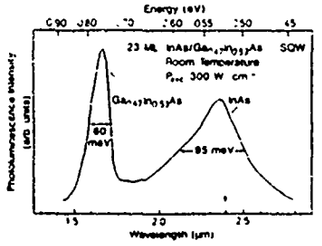

Fig. 2: PL spectrum taken at 300 K from the 23 ML wide InAs/$Ga_{0.47}In_{0.53}As$ SQW.

To further evaluate the potential of the InAs/$Ga_{0.47}In_{0.53}As$ QW materials system for light emitter application we have studied the variation of the PL emission as a function of the temperature. PL could be obtained up to 300 K from all samples investigated in this study. As an example we show in Fig. 2 the RT spectrum taken from the widest (23 ML) InAs/$Ga_{0.47}In_{0.53}As$ SQW sample. Although the QW line is rather broad, its peak position (2.48 μm) fits very well with the calculated value indicated by the vertical arrow (any structural relaxation of this QW would give a red shift by as much as 0.28 μm). This wavelength of 2.48 μm is, to our knowledge, the longest wavelength achieved up to now with QWs grown on InP substrates.

Laser diode characteristics

Laser diodes were fabricated from a 10 ML InAs / $Ga_{0.47}In_{0.53}As$ SQW clad by stepped $Al_{0.35}Ga_{0.24}In_{0.52}As$ / $Al_{0.48}In_{0.52}As$ barriers. Fig. 3 shows the output power versus current injection for a typical broad area (200 μm x 500 μm) diode under pulsed current injection (500 ns pulse length, 1 kHz repetition rate) at 80 K. The threshold current density is 1.475 kA/cm². The inset in Fig. 3 shows a spectrum taken from the same diode at $I = 1.1\ I_{th}$. It is centered at 1.816 μm with about ten clearly resolved longitudinal modes. This is the first observation of laser emission from InAs QWs grown on InP substrates. The peak position well fits the value of the e_1 - hh_1 transition calculated for a 10 ML InAs/$Ga_{0.47}In_{0.53}As$ SQW (1.815 μm). Planar narrow stripe devices (7 μm x 380 μm) were also fabricated from the same epitaxial wafer. In this case the threshold current intensity at 80 K is 10 mA ($J_{th} = 1.2$ kA/cm²) which allows continuous wave (cw) operation to be achieved. Quantitative measurements of the light emitted in cw operation under 100 mA current injection yield an output power of 5 mW and a differential quantum efficiency of ≈15 % both per uncoated facet.

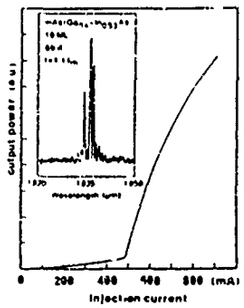

Fig. 3: Output power versus drive current measured at 80 K from a broad area (200 μm x 500 μm) laser diode. The inset shows a spectrum taken at $I = 1.1\ I_{th}$.

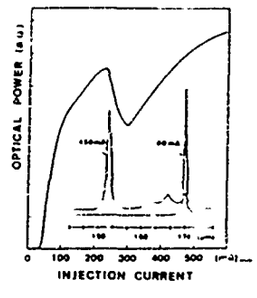

Fig. 4: Output power versus drive current measured at 80 K from a narrow stripe diode (7 μm x 380 μm). The inset shows two spectra taken under 60 mA and 450 mA current injection respectively.

The lasing characteristics of the present diodes strongly depend on the stripe width the injection current and the heat sink temperature. Fig. 4 shows the output power versus drive current measured at 80 K from a narrow stripe device. Two spectra taken under pulsed current injection of 60 mA and 450 mA are displayed in the inset of Fig. 4. Several features have to be noted. First under low injection (60 mA) the spectrum is centered at 1.74 μm instead of the 1.81 μm obtained with a broad area diode (Fig. 3) although both devices were made from the same epitaxial wafer. Second under high injection the main laser emission occurs at 1.57 μm i.e. at the $Ga_{0.47}In_{0.53}As$ barrier wavelength. Finally we have also noted that when increasing the temperature above 80 K the threshold current density increases as $\exp(T/T_0)$ with a low characteristic temperature of $T_0 \approx 40$ K for the broad area diodes and $T_0 \approx 35$ - 40 K for the narrow stripe devices. Above 110 K the main laser mode in both cases corresponds to the $Ga_{0.47}In_{0.53}As$ barrier emission. To understand these a priori puzzling findings one has to consider the band structure of the 10 ML InAs/$Ga_{0.47}In_{0.53}As$ SQW displayed in Fig. 5. The well is rather shallow the heavy hole and electron levels lie only 42 meV and 86 meV below the barrier band edges respectively. In addition InAs has

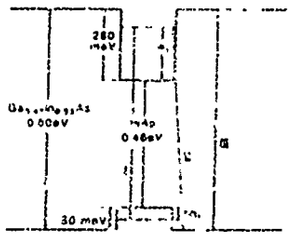

Fig. 3: Band structure of the 10 ML InAs/Ga$_{0.8}$In$_{0.2}$As SQW. (1) - (2): broad area laser emission; (1) narrow stripe laser emission - no inversion; (2) high injection; (3)

a low *in plane* heavy hole effective mass which leads to rapid filling of the hole subbands as previously demonstrated by PL spectroscopy [9]. As for the laser structure reducing the stripe width leads to large lateral losses [11] and the high gain required to overcome them leads then to band filling. In our case the broad area diodes lase on the ev 1dh SQW transition (Fig. 3, arrow 1). For a narrow stripe device under low injection (60 mA) we observe a laser emission at 1.71 μm which coincides with the transition between the SQW electron level e_1 and the $Ga_{0.8}In_{0.2}As$ valence band edge (Fig. 3, arrow 2). Finally when increasing the pump current the emission from the well saturates (Fig. 3) before gain is achieved on the $Ga_{0.8}In_{0.2}As$ barrier levels (Fig. 3, arrow 3).

Conclusion

We have shown by PL spectroscopy that the InAs/Ga$_{0.8}$In$_{0.2}$As materials system is suited for light emission above 1.6 μm. The first laser emission with this system was reported at 80 K from a 10 ML InAs/Ga$_{0.8}$In$_{0.2}$As SQW structure. However the poor confinement of the carriers in the InAs QW results in a filling of the SQW levels detrimental to the laser performances.

Acknowledgements

Part of this work was sponsored by the GSI Darmstadt and by the Bundesministerium für Forschung und Technologie of the Federal Republic of Germany.

References

1 See e.g. F.F. Pearsall (ed.) Semicond. and Semimet. Vols. 12A-B *Strained Layer Superlattices* Academic San Diego 1990)
2 M. Adams Electron. Lett. 26, 239 (1986)
3 E. Yablonovitch and E.O. Kane J. Light. Technol. LT-4, 504 (1986); LT-4, 963 (1986)
4 P.J.A. Thijs in *14th IEEE Int. Semicond. Laser Conf.* September 21-25, 1992, Takamatsu Kagawa (Japan), paper A1 and references therein
5 E. Yablonovitch and E.O. Kane J. Light. Technol. LT-6, 1292 (1988)
6 E. Fourrow and K.H. Ploog Appl. Phys. Lett. 62, 858 (1993)
7 E. Fourrow, O. Brandt, K.H. Ploog and M. Hohenstein Appl. Phys. A 58, 91 (1994)
8 G. Bastard, *Wave Mechanics Applied to Semiconductor Heterostructures*, (Les Editions de Physique Les Ulis, 1990)
9 E. Fourrow, O. Brandt and K.H. Ploog Appl. Phys. A 58, 109 (1994)
10 E. Fourrow, R.P. Schonhoff, K.H. Ploog C. Guanmin and L. Tapfer Appl. Phys. Lett. 61, 486 (1992)
11 C. Shieh, J. Mantz, H. Lee, D. Ackley and R. Engelmann Appl. Phys. Lett. 54, 2521 (1989)

FrA5

Feasibility of Room-Temperature Operation of Tunable Coupled-Quantum-Well Lasers

M. Ogawa* and E.E. Mendez

IBM Research Division, T.J. Watson Research Center, P.O. Box 218, Yorktown Heights, New York 10598

Abstract

We have calculated the gain of laser heterostructures whose active regions consist of two strongly coupled quantum wells subjected to an electric field. The results demonstrate that by using two 40 Å GaAs wells separated by an 11 Å $Ga_{0.7}Al_{0.3}As$ barrier a field induced wavelength tunability of over 7 nm is possible at room temperature.

Realization of field controlled tunable semiconductor lasers is considerably attractive since it would be applicable, for instance, to tunable coherent light sources for optical heterodyne communication systems.

The idea of field controlled light emission from quantum well devices was proposed some time ago [1],[2], but few experimental works have been reported so far. The devices would operate on the principle of the Stark effect by which both the optical transition energies of a quantum well and the electron-hole overlap inside the active area are modulated by an electric field applied perpendicular to the well. Both wavelength tunability and intensity modulation would be expected. The latter effect has been demonstrated in light-emitting diodes up to 200 K[3], but, there had been no report of tunable lasers based on the Stark effect. This absence is probably due to the practical difficulty of effectively applying large fields to the well in the presence of electric field screening induced by the large number of carriers needed for lasing.

Recently, Liu et al. suggested that a pair of coupled quantum wells embedded in a conventional quantum well laser structure could offer, for comparable electric fields, a larger tunability of stimulated emission than that in a single (or several isolated) well(s). They used a structure with an active region consisting of two 50 Å GaAs wells and a 20 Å $Ga_{0.77}Al_{0.23}As$ barrier and demonstrated stimulated emission tunabilities of over 7 nm (~ 3 THz) at a temperature of 5 K[4]. However, the red shift of the emission spectrum saturated and the gain decreased drastically beyond a certain bias, moreover, tunable laser operation above 77 K was not attained. In order to break through those limitations on both tunability and operation temperature and to find out an improved design, we have carried out self-consistent simulation.

In this paper we present calculations of the gain in CQW lasers under an electric field that explain quantitatively those previous results including the absence of laser emission at room temperature. More important, we conclude that in an improved laser design with an

*On leave from Department of Electrical and Electronics Engineering, Kobe University, Rokkodai, Nada, Kobe 657, Japan

active region consisting of two 40 Å GaAs wells and an 11 Å $Ga_{0.7}$-$Al_{0.3}As$ barrier a tunability of over 7 nm can be achieved at room temperature

Figure 1(a) shows the band diagram and the electron and heavy hole squared wave functions of the lowest subbands under flat-band condition in a symmetric CQW laser structure consisting closely coupled two quantum-wells separated by a thin barrier layer When carriers are pumped and lasing occurs, the optical transition between these two subbands is dominant, since the transition probability between them is the largest of the possible transitions When an electric field perpendicular to the wells is applied, the energy levels are modified and the wave functions are increasingly localized in separate wells, as sketched in Fig 1 (b) The energy of the lowest transition decreases as the field increases, which tunes the lasing wavelength The transition, indicated by the arrow on Fig 1 (b), can be considered as spatially indirect, since the electron wave function is mostly localized in one well while the hole wave function is fully confined in another one The degree of localization depends on the field strength

There are several possible aspects which would limit the tuning characteristics of this device First, the gain coefficient would decrease as the field increases because it strongly depends on the overlap integral between the electron and hole wave functions. Second, the wavelength tunability would be limited by the effect of field screening due to the pumped carriers in the wells The concentration of pumped carriers decreases the effective strength of the applied external field, reducing the shift of the quantized levels, and correspondingly the tunability of the device Third, at room temperature, carriers can exist in subbands higher than the lowest subbands. The population of carriers in higher states would contribute to the spatially direct transition Consequently, a larger number of carriers is needed to exceed the threshold gain for stimulated optical transition between the lowest subbands Fourth, at high fields pumped carrier in the wells can tunnel out, which would increase the screening effect since the tunneling rates of electrons and holes are different due to the difference in the masses

Considering these important aspects, we have simulated the feasibility of the operation of CQW laser diodes (LDs) at room temperature mainly from the stand point of the gain coefficient

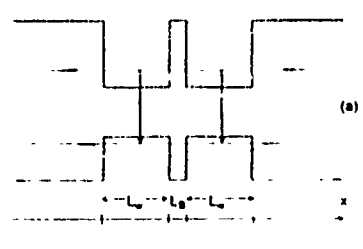

Fig 1 Schematics of potential profile and electron and heavy hole squared wave functions for a CQW (a) under flat band conditions and (b)for application of an external electric field Figure 1(b) also shows the definitions and relations of physical quantities used in the text The arrows show the lowest optical transitions dominant in emission

The linear gain g in a CQW LD structure depends on applied fields through the dipole moment μ_{mn} formed by the field-induced separation of electrons in subband n and holes in subband m We consider the magnitude of the dipole moment for the TE mode oscillation, since in this structure it is much larger than that for the TM mode If we choose the z-axis along the direction of quantization, and the y-axis along the direction of light propagation, the unit polarization vector lies along the x-axis Then the magnitude of the matrix element of the dipole moment is written as

$$|\mu_{mn}|^2 = \frac{|R|^2}{2}\left\{\left|\int_{well}\Psi_{cn}^*(x)\Psi_{vm}(x)\cos\theta(x)dx\right|^2 + \left|\int_{well}\Psi_{cn}^*(x)\Psi_{vm}(x)dx\right|^2\right\} \qquad (\text{TE } c \rightarrow hh), \tag{1}$$

where $\Psi_{cn}(x)$ and $\Psi_{vm}(x)$ are the envelope functions of the n-th subband in the conduction band and the m th subband in the valence band, respectively and θ is the angle between k and k_z-axis The magnitude of the optical matrix element $|R|$ in this equation is given by [5]

$$|R|^2 \approx \frac{q^2}{4\omega_0^2\varepsilon_0}\left[\frac{E_g(E_g+\Delta_0)}{(E_g+2\Delta_0/3)m_c^*}\right], \tag{2}$$

where Δ_0 is the spin-orbit splitting energy and m_c^* is the conduction edge effective mass

In previous reports [6], [7], the dipole moment was averaged over all possible directions since no external field was applied On the other hand, in the present theory, we have taken into account the effect of the external field on the dipole moment We obtain the relationship between the transition energy $E_{cv} = \hbar\omega_{cv}$ and the angle θ using the parabolic-band approximation and the k -selection rule as

$$\cos\theta(x) = \frac{k_z}{k} = \sqrt{\frac{E_{cnz}(x)}{\epsilon_{cn}(x)}},$$
$$\sin\theta(x) = \frac{k_{\parallel}}{k} = \sqrt{\frac{E_{c\parallel}(x)}{\epsilon_{cn}(x)}}, \tag{3}$$

where $\epsilon_{cn}(x)$ is the total energy of subband n in the conduction band, $E_{cnz}(x)$ the quantized energy, and $E_{c\parallel}$ is the energy perpendicular to the x-direction given by

$$\epsilon_{cn}(x) = E_{cnz}(x) + E_{c\parallel},$$
$$E_{cnz}(x) = E_{cn}(F) - U_c(x),$$
$$E_{c\parallel} = \frac{m_c^*}{m_{\parallel}^*}[E_{cn} - E_g - E_{cn}(F) - E_{vm}(F)]. \tag{4}$$

where $U_c(x)$ is the energy of the conduction band, and $m_{\parallel}^*$ is the reduced mass defined by

$$m_{\parallel}^* = (m_c^{*-1} + m_{hh}^{*-1})^{-1} \tag{5}$$

The gain coefficient g of a CQWLD subjected to electric fields is then similarly calculated as developed for QW lasers [6], [7] and conventional lasers [8] and given by

$$g = \sqrt{\frac{\mu_0}{\varepsilon_0}}\frac{\omega}{\hbar n_r}\times\frac{m_c^*}{\pi\hbar^2 L_W}\sum^{MAX}\int_{E_{cn}+E_{vm}}^{\infty}|\mu_{mn}|^2\frac{(f_c-f_v)\hbar^2/\tau_{in}}{(E_{cv}-\hbar\omega)^2+\hbar^2/\tau_{in}^2}dE_{cv}. \tag{6}$$

where μ_0 and ϵ_0 are the permeability and dielectric constant of air, respectively, ω the angular frequency of light, n_r the refractive index of the material, L_W the total width of the coupled wells($= 2L_w + L_B$), and T_2 the intra band relaxation time. E_{cv} is the transition energy between the electron E_{cn} and hole E_{vm} energies given by $E_{cv} = E_{cn} - E_{vm}$. MAX is the number of levels relevant to the optical transition, and f_c and f_v are the Fermi-Dirac distribution functions. The origin of energy is at the cross point of the center of the CQW structure and the bottom of the GaAs conduction band minimum. For holes, E_{vm}'s are measured from the cross point of the center of the CQW structure and the top of the GaAs valence band down into the valence band (Fig. 1(b)). The quasi Fermi levels E_{fc} and E_{fv} are related to the injected surface carrier density N_s into the wells as

$$N_s = \frac{m_c^* k_B T}{\pi \hbar^2 L_W} \sum_{n=1}^{MAX} \ln\left[1 + \exp\left(\frac{E_{fc} - E_{cn}(F)}{k_B T}\right)\right]$$
$$= \frac{m_{hh}^* k_B T}{\pi \hbar^2 L_W} \sum_{m=1}^{MAX} \ln\left[1 + \exp\left(\frac{E_{fv} - E_{vm}(F) - E_g}{k_B T}\right)\right] \quad (7)$$

Here we have neglected the contribution from the light hole band, since the density of states of this band is much smaller than that of the heavy hole band.

In the calculation of the gain coefficient, subband energies E_{cn} and E_{vm} and the wave functions Ψ_{cn} and Ψ_{vm} are obtained by solving Schrodinger's and Poisson's equations self consistently, taking into account the spatial dependence of such parameters as the effective masses and permittivity.

We have finally obtained the gain coefficient of a CQWLD, where the effect of the external electric field on the dipole moment, and the screening effect are taken into account through eqs. (5) and (6). When the electric field is set to zero and eqs (1) and (6) are averaged over all possible directions of θ, the results coincide with those in the literature [6,7].

We have applied the calculation to two hetero structures with different material parameters: structure A consisting of two 50 Å GaAs wells and a 20 Å $Ga_{0.77}Al_{0.23}As$ barrier, which is identical to that used in Ref. 4 and structure B consisting of two 40 Å GaAs wells and an 11 Å $Ga_{0.7}Al_{0.3}As$ barrier. We have used standard band parameters for the calculation [9].

In Figs. 2(a) and (b), we show the low temperature ($T = 5$ K) gain spectra of structures A and B, respectively, at various applied fields for an injected surface carrier density of $N_s = 4.0 \times 10^{11}$ cm^{-2}. The threshold gain, indicated by a dashed line in each figure, is estimated as 146 cm^{-1} for an optical confinement factor of 0.021 and a cavity loss of 45 cm^{-1}. These parameters are typical for a laser structure with high reflection coating (90%) on its facets whose length is 300 μm and core width is 2000 Å.

As seen in Fig. 2(a) and (b), under flat band condition ($F = 0$ kV/cm), even for a relatively low injection of carriers, the gain far exceeds lasing threshold. This is because at low temperature most carriers reside on the lowest subbands and the overlap between the lowest electron and hole states is maximum under flat-band condition. As the electric field increases, the gain peak shows red shift, which corresponds to the tunable operation, simultaneously, the gain decreases, eventually dropping below threshold. From the peak shift, the tunability can be estimated for each laser structure. Figure 2(c) shows the dependence of the oscillation wavelength (tunability) and the gain coefficient on applied fields in each structure. Structure A shows a tuning range of 7 nm, which is comparable to the tunability in the reported experiment [4] when a high reflection coating (90 %) on the facets was used. On the other hand, with structure B a tunability of more than 20 nm can be achieved, if we can apply an electric field up to 140 kV/cm.

As seen in Fig. 2(c), structure A loses its gain more drastically than structure B with increasing electric field. This is due to the fact that with the field the electron and hole wave functions are well localized at opposite wells and this localization is much enhanced in structure A as the field becomes stronger, since the barrier width L_B is larger than in structure B. At low temperature, the magnitude of the overlap between the wave functions of the lowest electron and hole subbands is so sensitive to the field that the gain curves show a drastic decrease with an increase of the field. This explains the saturation of the red shift and the drastic decrease of the gain beyond a certain bias voltage in the experiment of Ref. 4.

At low temperatures, a relatively low density of carriers is enough to surpass the threshold gain. However, at room temperature, carriers can exist in subbands other than the lowest ones, and a larger number of carriers is needed to exceed the threshold gain. For structure A, a carrier density of at least 2.8×10^{12} cm^{-2} is needed for lasing at 300 K, but in this case the field screening effect would prevent any significant tunability. At lower densities, lasing would not occur. These results are consistent with the absence of stimulated emission at 300 K in the experimental device of Ref. 4.

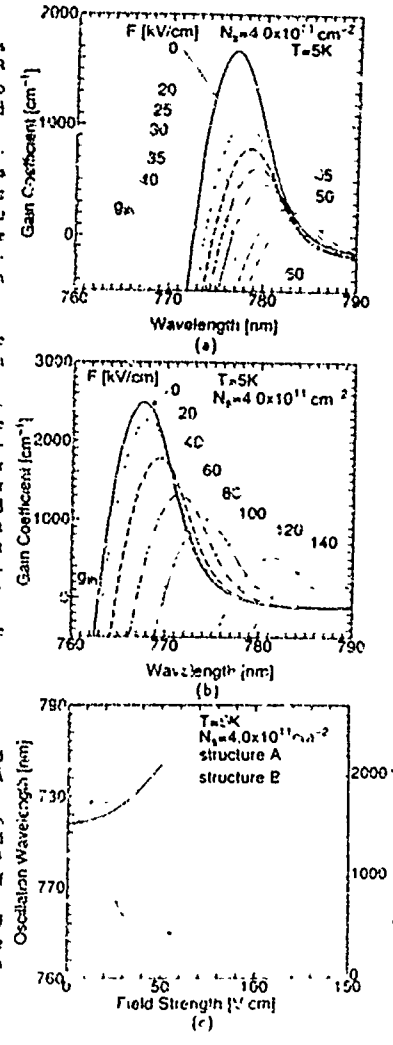

Fig. 2 Linear gain spectra of CQW laser structures at 5 K as a function of the external field F calculated for (a)structure A with two 50 Å GaAs wells and a 20 Å $Ga_{0.77}Al_{0.23}As$ barrier and (b)structure B with two 40 Å GaAs wells and an 11 Å $Ga_{0.7}Al_{0.3}As$ barrier. The injected surface carrier concentration $N_s = 4.0 \times 10^{11}$ cm^{-2} and the intraband relaxation time T_2 of 1×10^{-13} sec are assumed in the calculation. The threshold gain is indicated by the dashed line in each figure. (c)Field dependence of the tunability and the peak gain coefficient in each structure.

On the other hand, as shown in Fig. 3 (a), in structure B, gain above threshold can be maintained for a density of 2.0×10^{12} cm^{-2} and tunability is possible. In this structure, the gain coefficient is mainly from the contribution of the transition between the lowest subbands e_1, e_2, spatially indirect transition. In this structure tunability of up to 7 nm would be possible if a field of 105 kV/cm were applicable. Our calculation has not taken into account the likely tunneling of carriers through barriers at such a high field, but such a limitation could be overcome by incorporating multi-quantum barriers[10] on both sides of the CQW.

For comparison we have also calculated the gain spectra for a single quantum well laser diode whose well width is 91 Å. This structure corresponds to the case where the barrier L_B is removed from structure B, keeping constant the total width of the CQW. The results are shown in Fig. 3(b). This figure shows slightly higher gain coefficient than that of structure B. However, this structure shows a reduction of tunability, to 4 nm, since the lowest subband in the valence band disappears at fields higher than $F \approx 100$ kV/cm, thus preventing the transition between the lowest subbands. Therefore, the CQW structure B is a more favorable structure than either structure A or a single quantum well for the successful room-temperature operation of the tunable LDs using Stark effect. A systematic study of CQWs with various well and barrier widths around the parameters of structure B should yield the optimum design point.

In summary, we have simulated the operation of the CQW LDs from the standpoint of gain coefficient and shown that a CQW LD whose active region consists of two 40 Å GaAs wells separated by an 11 Å $Ga_{0.7}Al_{0.3}As$ potential barrier is favorable to lase at room temperature and is tunable over a wavelength range of 7 nm.

One of the authors (M. Ogawa) would like to acknowledge Prof. T. Kimoshi of Kobe University for his continuous encouragement. He also would like to acknowledge the staff of IBM Research Division for their hospitality and thank IBM Japan for financial support. This work has been partially supported by the Army Research Office.

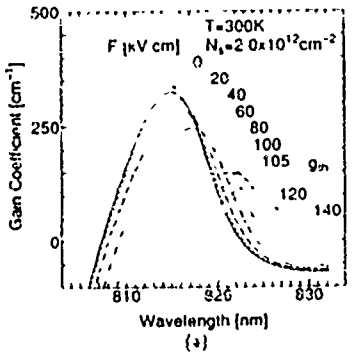

Fig. 3 (a) Calculated linear gain spectra at 300 K of structure A with $N_s = 2.0 \times 10^{12}$ cm^{-2}. (b) Comparison of tunability and gain coefficient between structure B and a single quantum well (SQW) laser structure with the well width of 91 Å. In the SQW structure the electric field is applicable only up to 100 kV/cm where the lowest subband in the valence band disappears. The injected surface carrier density is assumed to be same as in Fig. 3(a).

References

[1] E. E. Mendez, G. Bastard, L. L. Chang, and L. Esaki, Phys. Rev. B 26, 7101 (1982).

[2] M. Yamanishi, and I. Suemune, Jpn. J. Appl. Phys. 22, L22 (1983).

[3] Y. Kan, M. Yamanishi, M. Okuda, K. Mukaiyama, T. Ohnishi, M. Kawamoto, and I. Suemune, Appl. Phys. Lett. 55, 1149 (1989).

[4] L. Y. Liu, E. E. Mendez, and H. Meier, Appl. Phys. Lett. 60, 2971 (1992).

[5] E. O. Kane, J. Phys. Chem. Solids 1, 249 (1957).

[6] M. Asada, A. Kameyama, and Y. Suematsu, IEEE J. Quantum Electronics QE-20,745 (1984).

[7] M. Yamanishi, and I. Suemune, Japan. J. Appl. Phys. 23, L35 (1984).

[8] W. E. Lamb, Jr., Phys. Rev. 134,A1429 (1961).

[9] We have used the following values throught the text: for GaAs, $0.067m_0$ (m_0 is the free electron mass) for: the conduction-edge effective mass, $0.34m_0$ for the heavy-hole effective mass, 1.424 eV for: the energy gap at 300 K, 1.519 eV at 5 K, 13.1 for the dielectric constant, and 0.34 eV for the spin splitting of the valence band, for $Ga_{0.77}Al_{0.23}As$, $0.086m_0$ for the conduction edge effective mass, $0.355m_0$ for the heavy hole effective mass, 1.71 eV for the energy gap at 300 K, 1.81 eV at 5 K, 12.4 for the dielectric constant, for $Ga_{0.7}Al_{0.3}As$, $0.092m_0$ for the conduction edge effective mass, $0.36m_0$ for the heavy-hole effective mass, 1.80 eV for the energy gap at 300 K, 1.69 eV at 5 K, 12.2 for the dielectric constant. They are taken from the literatures: H. C. Casey, Jr., and M. B. Panish, *Heterostructure Lasers*, Part A, Chap. 4, Academic Press, New York (1978) and W. Batty, U. Ekenberg, A. Ghiti, and E. P. O. O'Reilly, Semicond. Sci. Technol. 4, 901 (1989).

[10] K. Iga, H. Uenohara, and F. Koyama, Electron. Lett. 22, 1008 (1986).

FrB1

Detection of Bloch Oscillations in a Semiconductor Superlattice by Time-Resolved Terahertz Spectroscopy and Degenerate Four-Wave Mixing

Christian Waschke, Patrick Leisching, Peter Haring Bolivar, Ralf Schwedler, Frank Brüggemann, Hartmut G. Roskos, Karl Leo, Heinrich Kurz
Institut für Halbleitertechnik II, Rheinisch-Westfälische Technische Hochschule (RWTH) Aachen, Sommerfeldstr. 24, 52074 Aachen, Germany

Klaus Köhler
Fraunhofer-Institut für Angewandte Festkörperphysik, Eckerstr. 27, 79106 Freiburg, Germany

We have studied the spatial dynamics of coherently excited wave packets of charge carriers in a semiconductor superlattice structure by both time-resolved THz spectroscopy and degenerate four-wave mixing. In the Wannier-Stark hopping regime, we observe electron Bloch oscillations with a frequency that depends linearly on the electric bias field and can be tuned between a few hundred GHz and 5 THz.

I. Introduction

In the last few years, four-wave mixing (FWM) and THz wave emission [1-7] spectroscopy have been established as powerful means to study the dynamics of wave packets in semiconductors. Resonant excitation of an ensemble of eigenstates in a quantum system creates a wave packet by the coherent superposition of wave functions. The temporal evolution of this wave packet is studied either by time-resolved detection of the electromagnetic radiation emitted as a result of the wave packet oscillations or by tracing the associated macroscopic interband polarization in degenerate four-wave mixing (DFWM) measurements.

Recently, these spectroscopic techniques have enabled the first observation of Bloch oscillations (BO) in semiconductor superlattice structures [3-5]. In the terminology for the description of coherent phenomena, BO are quantum beats between the eigenstates of a periodic potential subjected to a uniform electric bias field [8,9]. The theory of BO predicts in its simplest form that a wave packet composed of eigenstates of the periodic potential will undergo periodic spatial oscillations. The BO with a frequency $\nu_{BO} = eFd/h$. Here, F is the applied bias field and d the lattice constant of the periodic potential [10,11]. For many decades, attempts to observe BO in conventional bulk solids have failed. For all practical fields, F, the oscillation frequency turns out to be much smaller than the dephasing rate. In 1970, Esaki and Tsu pointed out that it should be possible to observe BO in superlattice structures. The larger lattice constants allow to reach oscillation frequencies in the THz range at modest fields [12]. Esaki and Tsu proposed superlattices as sources for bias-tunable submillimeter wave radiation. In fact, photoabsorption and photocurrent measurements have revealed resonant localized Wannier-Stark (WS) states as the eigenstates of superlattices [13,14]. In 1990, observation of negative differential velocity (NDV) of electrons in superlattice structures was reported [15]. This phenomenon is closely related to BO because, in k space, both rely on reaching the upper part of the miniband where the real space velocity decreases with field. Later, the simultaneous observation of NDV and WS localization finally confirmed the analogy between WS states in frequency space and BO in the time domain [16].

For the direct observation of BO in Ref. [3,4,7] it turned out to be important that optical excitation and detection of BO are decoupled from the dc biasing circuit of the superlattice. Hence, unlike in all electrical transport measurements, no sophisticated ultra-high frequency circuitry is needed for the generation and observation of BO. Furthermore, DFWM and THz wave emission spectroscopy are only sensitive to coherent transport processes in the structure. Incoherent processes do not evoke a background signal.

In this paper, we summarize our main results related to the observation of BO in a GaAs/AlGaAs superlattice structure. We demonstrate THz wave emission by BO from 800 GHz to more than 2 THz and demonstrate by DFWM that oscillations at frequencies as high as 5 THz can be generated.

II. Experimental setup

The superlattice structure used for both types of experiment (THz emission and DFWM) consists of 15 periods of GaAs wells (97 Å, i.e. 31 monolayers) and $Al_{0.3}Ga_{0.7}As$ barriers (17 Å, i.e. 6 monolayers). The undoped superlattice structure is grown by molecular beam epitaxy on an n-doped GaAs substrate with a 2500 Å thick undoped $Al_{0.3}Ga_{0.7}As$ buffer layer beneath the superlattice region and a 3500 Å thick undoped $Al_{0.3}Ga_{0.7}As$ buffer on top. A reverse bias field can be applied between the doped substrate and a semitransparent 7 or 3 nm Schottky contact on the sample surface. For the DFWM transmission measurements, a substrate window is etched into the sample to enable experiments in transmission geometry.

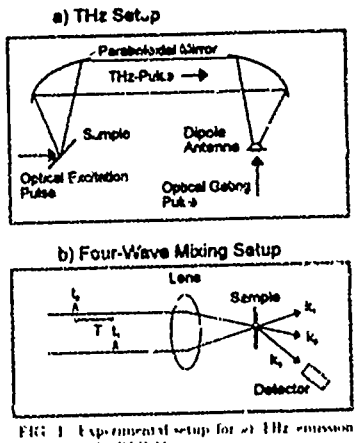

FIG. 1. Experimental setup for a) THz emission spectroscopy, b) DFWM.

In both experiments, we use a self-modelocked Ti:sapphire laser (pulse repetition rate: 76 MHz) for the optical excitation of the superlattice samples. The duration of the optical pulses is about 100 fs with a full width at half maximum (FWHM) bandwidth of 20 meV. We tune the center wavelength of the laser to 802 nm close to the heavy hole exciton transition - flatband.

The experimental setup for the time-resolved THz measurements, as shown schematically in Fig. 1a [5-7], the laser beam is split into two parts. One part excites the superlattice sample mounted in a closed cycle cryostat cooled down to temperatures as low as 10 K. Corresponding to the generalized Drude equations, a THz wave is emitted in a direction nearly collinear with the reflected optical beam. The THz pulse leaves the cryostat through a silicon window (resistivity > 10 kΩcm) and is focussed with a pair of off-axis parabolodial mirrors onto a 50 μm sized nonlinear dipole antenna that is gated by the second time-delayed part of the femtosecond laser pulse. Its ringing antenna current as a function of delay time allows measurement of both the amplitude and the phase of the electromagnetic transients.

In the sample, a single laser pulse generates excitons at a density of 1×10^9 cm^{-2} per quantum well (average laser power: 18 mW, diameter of the illuminated spot: 350 μm). The dipole moment associated with the optically excited charge oscillations is directed normal to the surface allowing THz-wave emission only in directions off the surface normal. In this experiment, we have chosen an excitation and emission angle of 45°.

Figure 1b shows the experimental setup used for DFWM measurements [1-4]. The laser beam is split into two copolarized beams of equal intensity (average laser power: 1.3 mW per beam). The first pulse is focussed onto the sample (100 μm spot diameter) inducing a macroscopic polarization that is probed by the second time-delayed pulse in a self-diffraction geometry. The time-integrated nonlinear DFWM signal emitted into the background-free direction $k_S = 2k_2 - k_1$ is traced as a function of the delay time $\tau = t_2 - t_1$ between the two pump pulses.

III. Wannier-Stark ladder formation

At low reverse bias close to flatband (+0.6 V), strong inter-well coupling leads to delocalization of the wave functions over many periods of the superlattice [17]. The eigenstates of the superlattice overlap and form minibands. For our superlattice structure, we calculate a width of 19 meV (2 meV) for the lowest electron (heavy-hole) miniband using a Kronig-Penney model. Increasing the bias voltage reduces the coupling between the wells and leads to a stronger localization of the wave functions [13,14,17]. The minibands split into a series of discrete levels, the WS ladder. To lowest order, the energy separation between ladder states increases linearly with the bias voltage (for a more precise description taking into account excitonic effects see Ref. [18]).

Figure 2 shows low-excitation photocurrent spectra of our structure at $T = 4$ K for different bias voltages. An increase of the voltage by 1.0 V raises the internal electric field by 10 kV/cm. Close to flatband, in the miniband bias regime, the spectra are weakly structured revealing three exciton transitions. We assign them to the fundamental 1s heavy-hole (hh) exciton, the light-hole (lh) exciton, and excited hh excitons (hh2) at the onset of the continuum [19]. Increasing the reverse bias voltage above +0.4 V results in a break-up of the minibands into WS ladders. In Fig. 2, we have marked the predominant transitions for the hh ladder. We assume that the heavy holes are completely localized even at low internal fields [14,17]. The indicated exciton lines hence involve transitions originating from localized hh states into conduction band states with partially delocalized wave functions. 0hh denotes transitions to a conduction band state with the highest probability density in the same well (intra-well transitions), +1hh and -1hh mark transitions to conduction band states with wave functions peaked in adjacent wells

and so forth

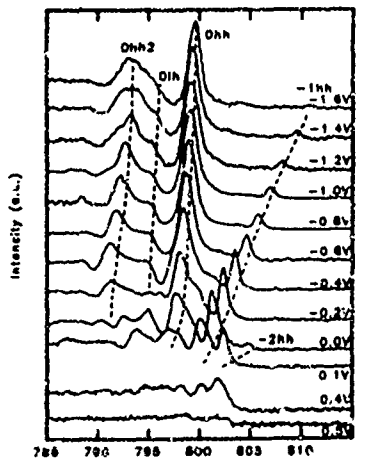

FIG. 2 Photocurrent spectra at $T = 1$ K

IV. Results: THz wave emission

In the time resolved experiments electron wave packets are created by the coherent excitation of several hh transitions of the WS ladder. The resulting wave packet motion can lead to the emission of a THz transient. It is important to note that charge oscillations that have just the proper phase do not contribute to the detected THz signal. The same holds for incoherent emission processes such as spontaneous transitions between ladder states. These contributions suffer destructive interference or are averaged out over many duty cycles of the high repetition rate (76 MHz) measurement system.

In Fig. 3 detected THz transients are shown as a function of bias voltage for a sample temperature of 15 K. Time delay zero is chosen arbitrarily. The data are not corrected for the spectral characteristics of the detection system. In the low voltage regime from +0.8 V to 1.2 V the amplitude of the THz transients increases gradually with increasing bias. The waveform reveals three maxima and does not change significantly with bias. In the bias regime between 1.0 V to 1.5 V the second maximum disappears. Above a reverse bias of 1.5 V both the amplitude and the waveform change considerably with voltage. The number of oscillations rises with increasing reverse bias, whereas the oscillation period decreases continuously. The amplitude of the measured transients passes through a maximum at 2.9 V.

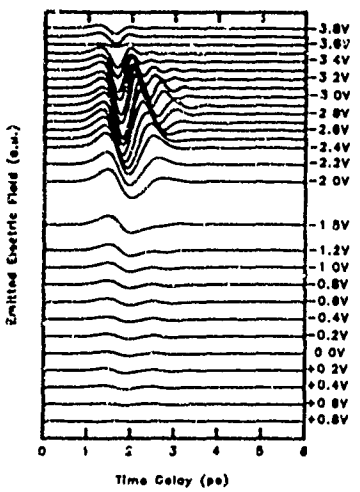

FIG. 3 Measured coherent electromagnetic transients

Fig. 4 shows Fourier transforms of the data shown in Fig. 3. From flatband up to a reverse bias of 1.0 V the Fourier spectra consist of two lines: a signal around 300 GHz (photon energy 1 meV) and a contribution of similar strength that gradually shifts from 300 GHz at flatband to 1.1 THz (photon energy about 4 meV) at 1.2 V. Above 1.2 V the high frequency signal disappears. The signal originally peaked at 300 GHz begins to gain strength and shifts gradually from 300 GHz to higher frequencies. We can trace the signal up to more than 2 THz before the limited bandwidth of the measurement system cuts off detection. The decline of the amplitude for reverse voltages above 2.9 V results from the sensitivity decrease of the antenna. In the upper part of Fig. 5 the voltage dependence of the THz emission frequency is plotted. For a reverse bias above 2.5 V the emission frequency depends linearly on the applied voltage. As discussed in the next section, we can assign this bias tunable radiation to coherent Bloch wave packet oscillations.

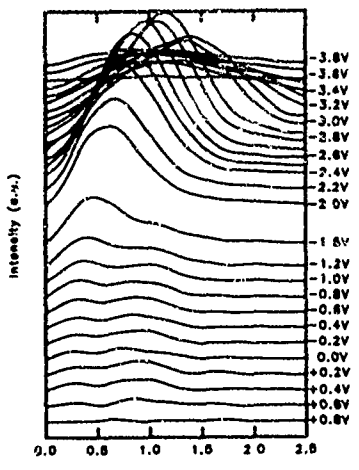

FIG. 4 Fourier transforms of the time domain data of Fig. 3. The data are not corrected for the spectral characteristics of the detection system.

V. Field screening

To relate the THz radiation to the energy band structure of the superlattice, in particular the WS ladder formation, we take time resolved transmission and cw electroreflectance spectra under excitation conditions identical to those of the THz wave emission measurements (for details see Ref. [7] and a forthcoming publication [20]). From these measurements we draw the following conclusions: (i) Even modest excitation of the samples as in our experiments leads to screening of the electric field across the superlattice by accumulation of photogenerated charge carriers over many duty cycles of the 76 MHz laser system. (ii) Time resolved measurements indicate that a single optical pulse generally does not affect the screening significantly. (iii) The screening shifts the onset of the WS regime to higher bias. (iv) In the WS regime the bias dependence of the energy separation between WS ladder states is, within the accuracy of the measurements, linear and *identical* to the slope obtained without field screening.

For the excitation conditions relevant for the data in Fig. 3 we observe the onset of the WS regime at a bias of 2.5 V. The onset is shifted by 2.9 V relative to the cw photocurrent spectra, i.e., excitation of Fig. 2. If we relate these results to the THz emission data of Fig. 3, it is striking that above -2.5 V a linear bias dependence of the emission frequency is observed. This linear bias dependence serves as primary proof that the radiation originates from BO of electron wave packets.

VI. Results: Four-wave mixing

The THz measurements discussed above detect directly the *intraband* polarization associated with the dipole moment of the Bloch wave packet. In the DFWM experiment we trace the complementary nonlinear *interband* polarization of third order. Recently we have conclusively shown by frequency resolved DFWM that the BO signals observed in our samples are due to quantum interference [21]. The damping of the oscillatory part of the polarization in the DFWM measurements is given by the damping of the polarization between the electronic states forming the wave packet, and the valence band transitions. The intraband dipole moment is damped by relaxation processes between the states the wave packet consists of. These are the same relaxation processes that determine the dephasing in pump/probe experiments (i.e., a detection of the polarization emitted in the direction k_3). Using both experiments, DFWM and THz wave emission, we can thus (at least in principle) obtain a complete picture of the relaxation dynamics of the system.

Figure 5 shows a three dimensional plot of the DFWM signal as a function of the delay time and the applied electric field. One can basically distinguish two different regions: (i) For bias fields close to flatband (+0.6 to 0.0 V) the signal shows (as a function of the delay time) a decay which has a strong oscillation superimposed. The period of the oscillations is virtually field independent. We ascribe this signal to quantum beats between the excitonic states of the electron and the heavy-hole and light hole miniband respectively. The field independence of the signal can be expected for the low field regime. (ii) For somewhat higher reverse bias field (0 to -0.2 V) the DFWM signal becomes very weak. The photocurrent spectra show no distinct peaks in this field range. (iii) For even higher bias fields the DFWM signal increases again to a strength similar to the flatband regime. The signal decay is again superimposed with a strong oscillation. These oscillations show the dependence of the period on the bias field expected from Bloch theory. This is clear evidence that they originate from Bloch wave packet oscillations.

Semi logarithmic plots of DFWM transients (not shown) yield six to seven oscillation periods before the Bloch wave packet is damped away. For very high fields, when the oscillation frequency reaches about 1 THz, the oscillatory modulation starts to weaken, due to the finite pulse duration of the laser. Recent

experiments with shorter laser pulses indicate that frequencies in excess of 10 THz are achievable with this particular sample. For even higher frequencies one would need samples with larger miniband width since the maximum frequency is limited by field localization.

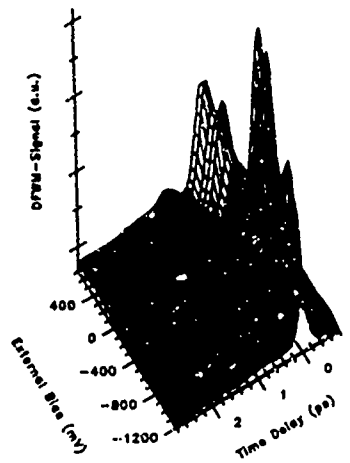

FIG. 5. Three dimensional plot of the DFWM data. Flatband: +0.4 V.

The overall decay time of the DFWM signals is on the order of 1.5 ps and rather independent of the electric field in the bias range measured here. The relative field independence is an indicator that tunneling processes to higher minibands (the present sample has a second miniband) or the continuum are rather unimportant in this field range. It is indeed a prerequisite for the observation of BO that such tunneling processes are slow compared to the BO frequency.

VII. Discussion

Comparing the THz emission and the DFWM results we find general agreement between the data. In the miniband regime we observe with both techniques a signal around 1 THz that we associate with hh/lh quantum beats. In the transition regime from the miniband to the WS regime this signal disappears. In the WS regime both experiments reveal BO as strong signals with bias tunable frequency. The dependence of the observed oscillation periods on the applied electric field is linear. We find the same slope for both experimental methods (see Fig. 6). The slope follows closely BO theory where the oscillation frequency is given by $f = eEd/(hL)$ with e the electron charge, h Planck's constant, d the lattice constant, L the thickness of the electrically biased region, and E the applied bias voltage plus a constant offset to account for screening.

There are, however, some differences in the data of the two experiments. The THz emission measurements reveal a signal at 300 GHz in the miniband regime that is not found in the DFWM data. At present, the origin of this signal is speculative. The Fourier spectra of the THz data give the impression that the Bloch emission at low bias develops out of the 300 GHz signal. This suggests that the 300 GHz signal results from quantum beats of miniband states, i.e. is of similar origin as the BO in the WS regime. We can rule out that the signal is caused by quantum beats between free and bound excitons or involves biexcitons because the signal has the same dependence on sample temperature as the BO in the WS regime. It is not clear at the moment why the signal is not visible in the DFWM data. It may well be that DFWM measurements with longer time delay may reveal a feature around 300 GHz.

VIII. Temperature variation

We finally discuss results obtained for different sample temperatures. Increase of the temperature leads to a reduction of the peak amplitude of both the THz radiation and the modulated DFWM signal. At 60 K the amplitude of the THz wave is about a third of that at 10 K. The DFWM amplitude decreases to 20 % when the temperature is raised from 10 K to 77 K. Together with the signal amplitude the dephasing time of the signals decreases with rising temperature.

Here we want to report another thermal effect: a temperature dependence of the bias offset needed to reach the WS regime even under weakest optical excitation. Figure 6 shows the oscillation frequency in terms of a photon energy of the tunable THz wave (upper part of Fig. 6) and the DFWM signal (lower part) for different sample temperatures. In the THz emission experiment the wavelength of the laser beam is fixed after it has been verified that up to a temperature of 60 K it is not necessary to readjust the laser wavelength for the maximum THz radiation amplitude. In the DFWM experiment the wavelength is adjusted to yield the maximum oscillation amplitude at 77 K. In both cases an increase of the temperature gradually shifts the onset of the WS regime to higher voltages even though the laser pulse energy is fixed. In the THz wave emission experiment the onset of the WS regime shifts gradually from 1.2 V at 10 K to -1.2 V at 60 K. In a DFWM experiment at very low excitation we find a shift from 0.2 V at 10 K to -1.2 V at 77 K. In the WS regime the bias dependence of the oscillation frequency remains linear for all temperatures. The slope of the curves is temperature independent. These results indicate that screening affects the superlattice more severely at higher temperatures. Currently, the temperature dependence of screening is under detailed investigation, results will be published elsewhere [20].

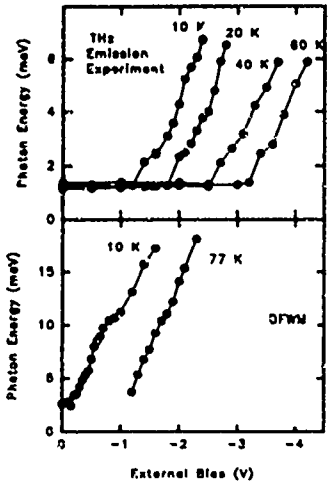

FIG. 6. Voltage dependence of the oscillation frequency (in terms of a photon energy) for THz emission (upper part) and DFWM (lower part).

IX. Conclusion

In summary we have studied the electron wave packet dynamics in a superlattice structure by both THz emission and degenerate four wave mixing spectroscopy. Both techniques give complementary information because THz emission experiments probe the *interband* polarization associated with the dipole moment of the wave packets, whereas DFWM is sensitive to the corresponding third order *intraband* polarization. In both experiments we observe Bloch oscillations of the charge carriers when the sample is biased into the Wannier Stark regime. The DFWM measurements reveal bias tunable Bloch oscillations from a few hundred GHz to more than 5 THz. In the THz emission experiments we detect the electromagnetic radiation from Bloch oscillations in the frequency range from 300 GHz to more than 2 THz *before* the bandwidth limitation of the receiver antenna cuts off detection.

X. Acknowledgments

We are very much indebted to J. Shah for many discussions. We thank H. Bakker, K. Victor, S. L. Chuang, G. Bastard, P. Voisin, and M. Luban for helpful comments. This work was supported by the DFG and the Volkswagen-Stiftung.

[1] K. Leo, J. O. Göbel, T. C. Damen, J. Shah, S. Schmitt-Rink, W. Schäfer, J. F. Müller, K. Köhler, and P. Ganser, Phys. Rev. B **44**, 5726, (1991).

[2] K. Leo, J. Shah, J. O. Göbel, T. C. Damen, S. Schmitt-Rink, W. Schäfer, J. F. Müller, K. Köhler, Phys. Rev. Lett. **66**, 201 (1991).

[3] J. Feldmann, K. Leo, J. Shah, D. A. B. Miller, J. E. Cunningham, T. Meier, G. von Plessen, A. Schulze, P. Thomas, and S. Schmitt-Rink, Phys. Rev. B **46**, 7252 (1992).

[4] K. Leo, P. Haring Bolivar, F. Brüggemann, R. Schwedler, and K. Köhler, Solid State Commun. **84**, 943 (1992).

[5] H. G. Roskos, M. C. Nuss, J. Shah, K. Leo, D. A. B. Miller, A. M. Fox, S. Schmitt-Rink, and K. Köhler, Phys. Rev. Lett. **68**, 2216 (1992).

[6] P. C. M. Planken, M. C. Nuss, I. Brener, K. W. Goossen, M. S. C. Luo, S. L. Chuang, and L. Pfeiffer, Phys. Rev. Lett. **69**, 1800 (1992).

[7] Chr. Waschke, H. G. Roskos, R. Schwedler, K. Leo, H. Kurz, and K. Köhler, Phys. Rev. Lett. **70**, 3319 (1993).

[8] J. B. Krieger and G. J. Iafrate, Phys. Rev. B **33**, 5494 (1986).

[9] G. Bastard and R. Ferreira, in Spectroscopy of Semiconductor Microstructures, NATO ASI Series (Plenum, New York, 1989), p. 111.

[10] F. Bloch, Z. Phys. **52**, 555 (1928).

[11] C. Zener, Proc. R. Soc. London Ser. A **145**, 523 (1934).

[12] L. Esaki and R. Tsu, IBM J. Res. Dev. **14**, 61 (1970).

[13] J. Bleuse, G. Bastard, and P. Voisin, Phys. Rev. Lett. **60**, 220 (1988).

[14] E. E. Mendez, F. Agulló-Rueda, and J. M. Hong, Phys. Rev. Lett. **60**, 2426 (1988).

[15] A. Sibille, J. F. Palmier, H. Wang, and F. Mollot, Phys. Rev. Lett. **64**, 52 (1990).

[16] A. Sibille, J. F. Palmier, and F. Mollot, Appl. Phys. Lett. **60**, 457 (1992).

[17] F. Agulló-Rueda, E. E. Mendez, and J. M. Hong, Phys. Rev. B **40**, 1357 (1989).

[18] M. M. Dignam and J. E. Sipe, Phys. Rev. B **43**, 4097 (1991).

[19] F. Agulló-Rueda, J. A. Brum, E. E. Mendez, and J. M. Hong, Phys. Rev. B **41**, 3678 (1990).

[20] P. Leisching, Chr. Waschke, et al., in preparation.

[21] P. Leisching, et al., in preparation.

FrB2

Femtosecond Degenerate Four-Wave-Mixing on unstrained (InGa)As/InP Multiple-Quantum-Wells Usit.g an Optical Parametric Oscillator

T.F. Albrecht, J.H.H. Sandmann, S T Cundiff, J Feldmann, W Stolz and E O Göbel
Fachbereich Physik und Wissenschaftliches Zentrum für Materialwissenschaften, Philipps-Universität Marburg Renthof 5, D-35032 Marburg, Germany

Abstract

We have constructed a femtosecond optical parametric oscillator in order to perform transient four wave mixing experiments on (InGa)As/InP quantum well superlattice structures in the 1160 - 1300 nm wavelength region. The dependence of the low temperature exciton dephasing rate on sample parameters and temperature is investigated. The observed temperature dependence indicates disorder induced localization of excitons, which is consistent with inhomogeneous broadening of the exciton emission and absorption lines In addition, we observe quantum beats in the FWM decay and attribute them to localized and bound excitons

Semiconductor heterostructures based on the Ga-In-As-P material system have gained considerable interest recently due to their potential for optoelectronic applications, especially in fiber communications [1] The effective bandgap of (InGa)As quantum wells (QW) lattice matched to InP can be tuned from 1 2 eV to 0.75 eV by varying only the QW thickness For many device applications high quality of the interfaces and the ternary well material is essential However, standard characterization methods like photoluminescence (PL), absorption or x-ray diffraction techniques often do not provide sufficient information to fully determine the properties of these structures Transient four-wave mixing (FWM) experiments on (AlGa)As/GaAs [2,3] and II/VI compounds [4,5] have been used to study interface and alloy disorder via its contribution to exciton dephasing FWM experiments allow a distinction to be made between the different contributions to the dephasing of excitonic excitations in semiconductors and semiconductor quantum wells, which includes, interface , alloy-, phonon and exciton-exciton-scattering [6].

Measurement of excitonic dephasing by FWM requires resonant excitation with picosecond (ps) or femtosecond (fs) laser pulses While such lasers are currently available for GaAs based heterostructures, no tunable, high repetition rate fs pulse sources were available for experiments on (InGa)As/InP QWs Recently, femtosecond optical parametric oscillators (fs-OPOs) synchronously pumped by a fs-Ti sapphire laser have been developed [7-9] They can be continuously tuned through the entire energy range of the (InGa)As/InP QW system In this paper we present the first FWM experiments carried out with such a fs-OPO

The dephasing of the exciton is sensitive to interactions between the exciton and its environment, including interaction with excitations such as phonons or other excitons and interaction with static disorder The broadening of the excitonic resonance in the linear optical spectra for these samples indicates the presence of strong disorder, which we attribute to a combination of interface roughness and alloy fluctuations. The temperature dependence of the excitonic dephasing rate displays the functional form associated with thermal activation of disorder localized excitons, consistent with the interpretation of the linear spectra. The dephasing rate is observed to increase sharply with decreasing barrier width, in agreement with the broadening of the exciton resonances due to miniband formation One of the samples displays quantum beats in the FWM signal, which are attributed to the simultaneous excitation of disorder localized excitons and defect bound excitons.

We used an OPO based on that reported in Ref [9] and described in more detail elsewhere [10]. The OPO is synchronously pumped by 110 fs pulses from a commercial, Kerr-lens modelocked Ti:sapphire laser (Coherent Mira 900). Because the OPO-spectrum is extremely sensitive to length changes of only a few 100 nm, the length of the resonator is actively stabilized The OPO uses a 2 mm thick, antireflection coated KTP crystal cut for type II (e $\rightarrow$ eo) noncritical phase matching in the xy-plane ($\phi = 0°$, $\theta = 90°$) This enables a collinear pump-geometry resulting in high conversion efficiency and relatively easy alignment and operation, compared to non-collinearly pumped OPOs [7,8]. The emission wavelength is tuned via the pump wavelength and small adjustments of the OPO-resonator length Under optimized operating conditions transform limited pulses of 160 fs (FWHM) duration with more than 1 nJ pulse energy are generated. An energy conversion efficiency into the signal beam of 30% was achieved for non-transform limited pulses. Currently this is the highest value reported for a fs-OPO. The experimentally determined tuning range is from 1060 nm to 1330 nm using two mirror sets. Additional mirror sets should extend OPO operation to 1640 nm with the Ti:sapphire laser as the pump source [11]. The FWM experiments described below represent the first application of a fs-OPO and demonstrate its potential for time resolved spectroscopy in a spectral regime which has been difficult to access

The unstrained (InGa)As/InP multiple quantum well (MQW) samples were fabricated by standard low pressure metal organic vapour phase epitaxy [12] in commercial equipment (Aix 200, Aixtron Corp.) The semi-insulating InP substrates were Fe doped and exactly (100) oriented. They were prepared for growth as described in Ref. [13]. The growth temperature was 640°C, the pressure was 20 mbar and the gas velocity in the reactor was approximately 1.6 m/s. A growth interruption of 5 s under PH_3 was used during switching from InP to (InGa)As-growth. At the As terminated interfaces growth was not interrupted The growth rates were 3.3 Å/s and 6 6 Å/s for the InP and (InGa)As layers, respectively

We have grown a set of MQWs with thin wells (1 6 nm and 3 0 nm) and several barrier widths between 40 nm and 5 nm. This allows us to study phenomena related to the transition from a MQW to a superlattice (SL), i e , phenomena due to the delocalization of the electronic wavefunctions and the formation of minibands. The samples were characterized by low temperature photoluminescence (PL), absorption spectroscopy and high resolution x-ray diffraction (HRXRD) All samples consisted of a 390 nm thick InP buffer layer, a MQW and a 525 nm thick (InGa)As caplayer. The caplayer was used to calibrate the (InGa)As-composition through the HRXRD spectra, which cannot be unambiguously determined from the MQW itself It was removed by selective etching prior to the optical experiments.

The HRXRD measurements (not shown here) exhibit sharp peaks for both zero order and satellite reflections of the MQW for all samples, indicating high quality epilayers. Details of the structural sample properties and the analysis of the HRXRD spectra will be reported elsewhere [14]. The absorption and PL spectra of two typical MQWs with well widths of 1 6 nm and 3 0 nm are shown in Fig 1

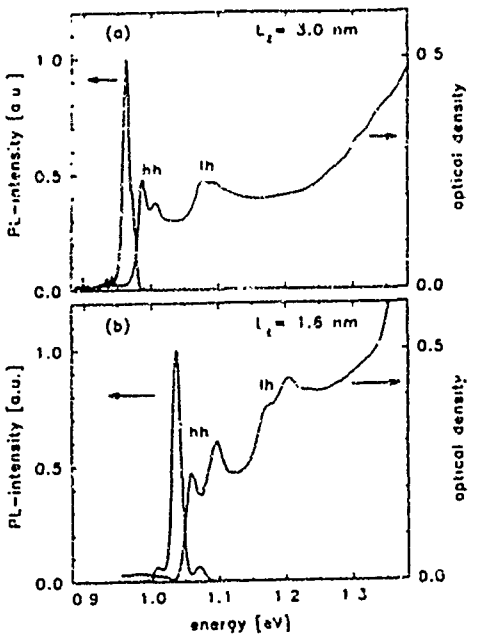

FIG. 1 Absorption and photoluminescence spectra of two MQWs with L_z = 1.6 nm and L_z = 3.0 nm. Both absorption spectra show ML splitting of the heavy hole (hh) and light hole (lh) resonances. The luminescence spectra are Stokes shifted by approximately the value of the inhomogeneous broadening. ML splitting is resolved only in the PL of the 1.6 nm well.

Both samples consist of 50 periods with a barrier thickness of approximately 40 nm. The absorption and PL spectra are inhomogeneously broadened and exhibit a Stokes shift on the order of 20 meV. This can be partly ascribed to the high quantization of the electronic levels in connection with interface roughness, but also reflects the presence of alloy fluctuations. Therefore, we expect that the excitons will be localized. A monolayer (ML) splitting of the heavy and the light hole exciton resonances is observed in the absorption spectra of both samples and in the luminescence spectrum of the thinner well. For the thicker well, the splitting is smaller and not clearly resolved in luminescence. The FWM experiments use the degenerate two-pulse self diffraction technique [15]. The sample is excited by two laser pulses with wave vectors $\vec{k}_1$ and $\vec{k}_2$ with a time delay Δt. The Δt-dependent diffracted FWM signal

is detected in the phase matched direction $2\vec{k}_2 - \vec{k}_1$ using a slow germanium photodiode. If a single resonance is excited, the signal decays with a time constant τ. This allows the determination of the dephasing time T_2 and thus the homogeneous linewidth $\Gamma_h = 2\hbar/T_2$ irrespective of inhomogeneous broadening effects. For inhomogeneously broadened transitions the dephasing time is $T_2 = 4\tau$ [15].

All FWM experiments were done with parallely polarized beams and photon energies corresponding to the low energy side of the lowest energy heavy hole absorption peak of the respective sample. For higher energies the diffracted signal becomes very weak and its decay time approaches our time resolution. Although we estimate carrier sheet densities in the order of 10^9 cm^{-2}, the density dependence of the measured dephasing times is very weak. We attribute this to the strong inhibition of exciton-exciton scattering due to their localization. For all experiments shown here, the exciton-exciton scattering contribution to the dephasing rate is less than 10%.

Localization modifies the exciton-phonon interaction and hence the temperature dependence of the homogeneous linewidth. The homogeneous linewidth, as determined from the FWM measurements, is plotted as a function of temperature, T, in Fig. 2. This data is for the heavy hole exciton resonance in the sample for which the linear spectra are shown in Fig. 1.

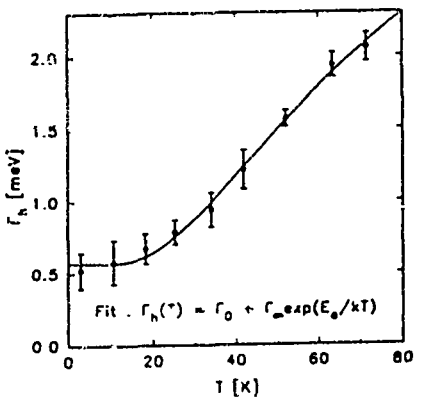

FIG. 2 Temperature dependence of the homogeneous linewidth of the 3 nm well MQW for which the spectra are shown in Fig. 1. The photon energy was 2.3 meV below the absorption peak. The fit is discussed in the text.

The homogeneous linewidth, Γ_h, clearly does not exhibit the linear temperature dependence expected for single phonon scattering of free excitons. The data is well fit by the functional form expected for thermal activation [2].

$$\Gamma_h(T) = \Gamma_0 + \Gamma_\infty \exp(-E_a/kT)$$

where Γ_∞ is the high temperature limit for dephasing due to activated behavior, E_a is the activation energy, k is Boltzman's constant and Γ_0 is additional dephasing due to non-activated processes. Γ_0 includes possible contributions due to exciton-exciton interactions and tunneling or hopping relaxation channels. Although relaxation due to tunneling or hopping is temperature dependent [16], the dependence is relatively weak and so determination of the pertinent process(es) is not possible. The fit yields an activation energy of (7.3 ± 0.5) meV. This value is quite large compared to the values observed in GaAs/AlGaAs MQWs [2,3] where the activated behavior was attributed to a mobility edge. However, the similarity of the activation energy to the exciton binding energy suggests that acoustic phonon ionization of the exciton may contribute due to a lifting of the crystal momentum conservation selection rules because of exciton localization. The large activation energy, compared to the inhomogeneous width, is consistent with earlier observations in (InGa)As MQW that all optically active excitons are localized [17].

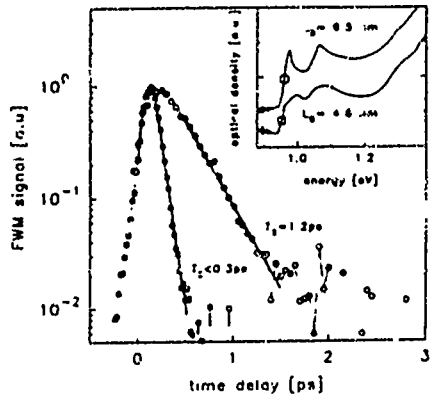

FIG. 3 FWM-transients for samples with L_B = 9.5 nm (circles) and L_B = 4.6 nm (squares) with the fitted decays. The inset shows the corresponding absorption spectra and the respective spectral positions for these measurements (0.960 eV and 0.954 eV).

When the barrier thickness L_B is decreased so that the quantum wells become strongly coupled and as the electronic levels are broadened to minibands a drastic change in dephasing time is observed. The inset of Fig. 3 shows absorption spectra of two samples with 100 periods, L_z = 3.6 nm and barrier widths of 9.5 nm and 4.6 nm. The calculated widths of the minibands are 3.7 meV and 39 meV, respectively, for the electrons and below 0.1 meV for the heavy holes, i.e. the holes remain localized in these samples. These values agree well with the observed broadening of the prominent absorption structures. To compare the dephasing of the two samples, the measurements must be carried out at equivalent spectral positions. We have chosen the half maximum points of the absorption edges as the excitation photon energy in both cases, as indicated in the inset. The measurements were carried out

under the conditions described above. Fig. 3 shows the FWM-signal as a function of delay time. While T_2 = 1.2 ps for the sample with nearly uncoupled wells (L_B = 9.5 nm), which is the same value as for samples with thicker wells, T_2 of the L_B = 4.6 nm SL is considerably shorter and actually below our time resolution (T_2 < 0.3 ps).

There are several phenomena which should modify the excitonic dephasing rate at the transition from a QW to a superlattice is made. While the delocalization of the wavefunctions increases the probability density of the exciton at the interface, resulting in an increased scattering this is counteracted by the increased probability density within the barriers, which should reduce the alloy scattering within the well regions. Probably the most important effect is the modification of the excitonic wavefunction itself. The exciton binding energy is reduced [18] as is the electron-hole overlap [19]. The exact contributions of these competing effects are difficult to distinguish and require further, more extensive investigation.

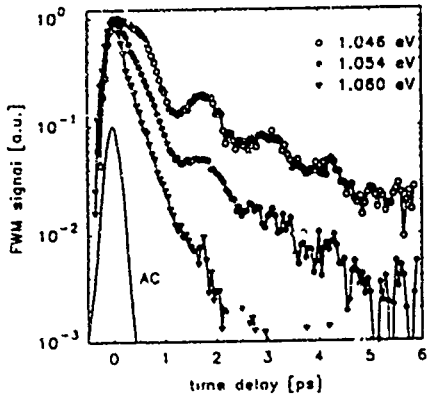

FIG. 4 FWM traces of a MQW sample with 1.6 nm wells and 20.5 nm barriers for photon energies of 1.046 eV, 1.054 eV and 1.060 eV. A typical autocorrelation curve is also shown (AC). With the exception of the 1.060 eV curve, pronounced quantum beats with a period of 1.2 ps are observed.

In one particular sample with 1.6 nm well width and 20.5 nm thick barriers we have observed quantum beats [20] at a temperature of 4 K. Fig. 4 shows three transient FWM signals for different photon energies along with an autocorrelation curve. The beating phenomenon is only observed for energies lower than 1.058 eV. The beating period is 1.3 ps corresponding to an energy splitting of ΔE = 3.2 meV between the interfering quantum mechanical states. This energy spacing is considerably smaller than any structure resolved in the absorption or luminescence spectra. Yet, as mentioned before, FWM is able to resolve transitions which are obscured in the linear spectra by the considerable inhomogeneous broadening. We attribute the beating to the simultaneous excitation of excitons localized in alloy or well width fluctuations and excitons that are bound to an impurity or defect [21,22]. A

definite identification of the state involved is not possible on the basis of the present results The beats are absent or very faint in the other samples, suggesting that this defect might be related to the particular epitaxy run

The dephasing times obtained from the transient FWM traces shown in Fig 4 drop from about 6 ps at 1.060 eV to 1 2 ps at 1 046 eV. This result is in qualitative agreement with similar investigations on inhomogeneously broadened exciton lines in other structures [3,5] It reflects the decrease of the exciton hopping rate at lower energy due to the decrease in density of states and thus larger seperation of sites with lower energy

In conclusion we have investigated the dependence of the dephasing times of excitons in unstrained (InGa)As/InP MQWs on energy, temperature and barrier thickness The temperature dependence of the dephasing could be explained with a model for localized excitons that dephase via thermal activation with an activation energy of E_a = 7.3 meV We furthermore demonstrate that the transition from a MQW to a SL by lowering the barrier width results in the drastic reduction of T_2 by more than a factor of 4 In one sample pronounced quantum beats were found that are attributed to the coherent excitation of localized and bound excitons. The binding energy of this bound exciton is 3 2 meV, yet its identification is still open. Altogether our experiments have demonstrated the great potential of a fs-OPO operating in the near IR-spectral regime for time resolved, nonlinear spectroscopy

We thank A. Nebel, C. Fallnich and R. Beigang for support with the construction of the OPO and making available to us their results prior to publication We are grateful to T Marschner for help with the sample characterisation, G von Plessen, U. Lemmer and M Koch for stimulating discussions and M Preis and T Ochs for expert technical support This work has been supported by the Deutsche Forschungsgemeinschaft

REFERENCES

[1] e g N Pütz, J. Cryst. Growth 107, 806 (1991) and references therein
[2] see e g Hegarty and M.D. Sturge, J Opt. Soc. Am. B. 2, 1143 (1985) and references therein.
[3] M.D. Webb, S.T. Cundiff, and D.G. Steel, Phys Rev. B 43, 12658 (1991).
[4] G. Noll, U. Siegner, E.O. Göbel, and S Shevel, Phys. Rev. Lett. 64, 792 (1990).
[5] U. Siegner, D. Weber, E.O. Göbel, D. Bennhardt, V. Heukeroth, R. Saleh, S. Baranovski, P. Thomas, H. Schwab, C. Klingshirn, J.M. Hvam, and V.G. Lyssenko, Phys. Rev. B 46, 4564, (1992).
[6] J. Kuhl, A Honold, L Schultheis, and C.W. Tu in : Festkörperprobleme / Advances in Solid State Physics, Vol 29, ed by U Rössler, (Vieweg, Braunschweig 1989), p 157 and references therein
[7] Q Fu, G. Mak, and H.M van Driel, Opt. Lett , 17, 1006 (1992)
[8] W S. Pelouch, P.E Powers, and C.L Tang, Opt. Lett., 17, 1070 (1992)
[9] A. Nebel, U Socha, R. Beigang, in Ultrafast Phenomena 8, ed. by J -L. Martin, A Migus, G A Mourou, A H Zewail, Springer Verlag (1993), p.187
A. Nebel, C Fallnich, R. Beigang, R. Wallenstein, accepted for publication in J Opt Soc Am B, spec issue on optical parametric oscillators and amplifiers
[10] T F Albrecht, J H H Sandmann, J Feldmann, W. Stolz, E.O Göbel, A Nebel, C Fallnich and R. Beigang, submitted to Appl. Phys Lett.
[11] The idler pulse that is simultaneously produced with the signal pulse provides even longer wavelengths between 2 15 μm and 3 3 μm
[12] M. J Ludowise, J Appl Phys 58, R31 (1985) and references therein
[13] Y. Nishitami, T Kotani, J Electrochem Soc.: Solid-State Sc and Techn , 126, 2269 (1979)
[14] T.F Albrecht, T. Marschner, W. Stolz, E.O. Göbel unpublished
[15] T Yajima, Y. Taira, J. Phys. Soc. Jpn 47, 1620 (1979)
[16] T. Takagahara, Phys. Rev. B 32, 7013 (1985).
[17] J Hegarty, K. Tai, W T Tsang, Phys Rev B 38, 7843 (1988)
[18] M.M Dignam and J E Sipe, Phys Rev B 43, 4097 (1991)
[19] G. Peter, Ph.D thesis, Marburg (1990)
[20] see e g.: K. Leo, E O Göbel, T C Damen, J Shah, S. Schmitt-Rink, W Schäfer, J F Muller, K Kohler, P Ganser, Phys Rev B 44, 5726 (1991)
[21] K Leo, T.C Damen, J Shah, K Köhler, Phys Rev B 42, 11359 (1990).
[22] M Koch, D Weber, J. Feldmann, E O Göbel, T. Meier, A. Schulze, P Thomas, S Schmitt-Rink, and K Ploog, Phys Rev B 47, 1532 (1993)

FrB3

Time Resolved Spectroscopy of Electron Decay in Coupled Quantum Wells - Observation of Relaxation Induced Slow-Down

I Bar-Joseph[1], G Cohen[1], B Deveaud[2], P Bergman[2] and A Regreny[2]

(1) Department of Physics, The Weizmann Institute of Science, Rehovot 76100, Israel
(2) Emav Telecom, CNET, Tannion, 22301 Tannion, France

Abstract

Electron decay from symmetric coupled quantum wells through a potential barrier to a continuum is studied using time resolved optical spectroscopy. We find that at the limit of a thin barrier the decay rate decreases with decreasing barrier thickness and the energy splitting between the electron levels disappears. We show that this behavior is general for systems where resonant tunneling is coupled to a relaxation channel.

Introduction

Optical spectroscopy was successfully implemented in recent years in studying the resonant tunneling process of electrons and holes in coupled quantum wells (CQW) [1-6]. The system on which those studies were performed is *asymmetric* CQW, consisting of a narrow and a wide well. A theoretical analysis of the electron decay process in these structures has revealed that it is affected by quantum interference phenomena in an unexpected way [7]. It was shown that when a CQW system is in contact with a relaxation channel, the electron decay rate through this channel can be sometimes slowed down with increasing relaxation rate. In fact, it was suggested that the excessively long decay time, which was measured for resonant tunneling of holes in CQW, is due to inelastic relaxation processes which suppress the decay rate.[1]

Unfortunately, it is rather difficult if not impossible to experimentally vary the coupling to phonons and study the dependence of the decay process on Γ_0, the relaxation rate. An alternative system, which exhibits a similar behavior, is *symmetric* CQW, where one of the wells is coupled via a thin barrier to a continuum. It was shown in Ref. [7] that the asymmetric CQW, where the decay is through phonon emission, and the symmetric CQW, which decays by tunneling, are described by the same effective Schrodinger type equation, with Γ_0 being the relaxation rate due to coupling to phonons or to the continuum states, respectively. The advantage of such a system as a model for experimentally studying the coupling between quantum tunneling and relaxation is obviously the ability to change the relaxation parameter in a controlled manner.

In this paper we experimentally investigate the symmetric CQW system. Using time resolved photoluminescence (PL) and differential transmission (DT) spectroscopy, we monitor the decay rate of photo excited electrons in these structures. We investigate 3 samples, each having a different thickness of the outer barrier which separates the CQW from the continuum, while all the other parameters are kept constant. We show that the decay rate varies in a non monotonic way as a function of outer barrier width, such that the decay rate from the sample with the medium barrier width is the fastest. Studying the spectral line shape we find a splitting of the electron levels only in the wide barrier sample, and explain the collapse of the splitting at the other samples as representing a transition from an oscillatory to a two exponential decay.

Samples and experimental set-up

Three samples have been grown by molecular beam epitaxy. Their structure consists of 10 repetitions of the following structure: Two 80 Å quantum wells with a 50 Å $Al_{0.3}Ga_{0.8}As$ barrier between them (designated by L_1), which on one side are coupled to a continuum (800 Å wide GaAs layer) by a thin $Al_{0.3}Ga_{0.8}As$ outer barrier of thickness L_2, while on their other side there is a thick (200 Å) $Al_{0.3}Ga_{0.8}As$ barrier. The values of L_2 in the three samples are 50, 20, and 10 Å. Hereafter the samples will be labelled by the width of their outer barrier.

Two complimentary experimental techniques were used in this work, time resolved PL and DT spectroscopy. In the first, the system is excited at an energy which is larger than the gap and the recombination rate of the photo excited free electrons and holes is monitored using non linear optical gating in the up conversion mode. In the DT measurement the sample is excited at the energy of the lowest exciton and the photo induced changes in the absorption spectrum are measured. The experimental system is a conventional pump probe set-up. The measurements were conducted at relatively low densities, $5 \times 10^{-5} - 5 \times 10^{9}$ cm^{-2}, at liquid helium temperature, with a time resolution of 0.6 ps.

Results

A typical PL spectrum taken at a constant delay is shown in Fig. 1a. The decay time of the large peak at 1.52 eV is relatively slow, of the order of 1 ns, while the decay of the small peak at 1.57 eV, corresponding to the CQW, is much faster in all 3 samples. Fig. 1b shows the temporal evolution of the CQW luminescence in the three samples. It is seen that the decay time is very short, and depends on the thickness of L_2. The measured decay time decreases from 11 ps in the 50 Å sample to 3 ps in the 20 Å sample and then increases to 5 ps in the 10 Å sample. These results show very clearly that the decay rate varies non monotonically with the coupling strength, and demonstrate the anomalous decay behavior of the system.

To get a deeper insight into the behavior of the system and to determine the influence of extrinsic processes, such as hole tunneling and possible energy mismatch between the symmetric wells, we shall examine now the DT measurements. The DT signal is generally composed of two components. The first is associated with the electrons escape from the CQW and lasts a few picoseconds. The second component is related to the holes and is much slower. The tunneling time of the holes from the inner well is very long, and is comparable with the time elapsing between two consecutive pulses (13 ns). Consequently, there is a persistent contribution to the DT signal, which does not appear in the PL measurements, and is seen in all three samples as an early time signal. In the following we shall concentrate on the fast component.

Fig. 2a displays a spectral DT measurement of the 50 Å sample. In this measurement the probe pulse is kept at a constant time delay with respect to the pump pulse and the excitation energy is scanned. This scan is performed for a set of time delays, between 0 to 11 ps. Two spectral features, 1 meV apart, are clearly observed: a high energy peak, centered at 1.570 eV, and a lower one, centered at 1.566 eV. A similar line splitting is seen at the cw PL of this sample. These two features are associated with the splitting of the electronic levels in CQW. It is seen that the two features decay in magnitude as time elapses at different rates. Just after the excitation by the pump (dashed line) the two are of similar height. However, 10 ps later

(dotted dashed line) the low energy peak has strongly decayed while the high energy peak only slightly decreased in magnitude. The corresponding decay times of the low and high energy components are 7 and 16 ps respectively. This line splitting is not observed in the DT and cw PL measurements of the other two samples. We shall later show that the absence of the splitting in these two samples is well explained by the theory.

Turning to the 20 Å sample two decay times are observed throughout the excitonic line, a very fast one of 3 ps and a slower one - of 35 ps (Fig. 2b). Since only the fast component is found in the PL measurement we can attribute it to the electrons escape from the CQW and conclude that the slow component is due to holes escape from the outer well. This conclusion is further supported by the fact that the measured time constant of 35 ps for the slow component agrees with the computed time for tunneling of holes through a 20 Å barrier.

Figure 2b gives also the results of the temporal measurement for the 10 Å sample. A single component, of 6 ps decay time, is measured throughout the excitonic line. As found in the PL measurement, the observed decay time is longer than that of the 20 Å sample. The holes that are created in the outer well escape through the 10Å barrier very fast, and are not apparent in the DT signal.

Discussion

Let us turn now to a quantitative analysis of the results. Following Ref. [7] the electron wave function in the CQW is given by the solution of an effective Schrodinger equation of the form.

$$i\hbar\frac{d}{dt}\begin{pmatrix} c_1(t) \\ c_2(t) \end{pmatrix} = \begin{pmatrix} E_1 & \frac{1}{2}\delta \\ \frac{1}{2}\delta & E_2 + \Delta_0 - i\frac{\Gamma_0}{2} \end{pmatrix} \times \begin{pmatrix} c_1(t) \\ c_2(t) \end{pmatrix} \qquad (1)$$

where $|c_i(t)|^2$ is the probability of finding the system in the i-th well with an energy E_i, Δ_0 and Γ_0 are the level shift and width due to coupling to the continuum respectively, and δ is the energy splitting due to tunneling between the levels of the different wells. The two eigenvalues of the matrix are

$$\lambda_{1,2} = E_1 + \frac{\Delta}{2} - \frac{i\Gamma_0}{4} \pm \frac{1}{2}\sqrt{\Delta^2 + \epsilon^2 - \left(\frac{\Gamma_0}{2}\right)^2 + i\Delta\Gamma_0} \qquad (2)$$

where $\Delta = \Delta_0 + i\frac{\Gamma_0}{2}$, $\epsilon = E_2 - E_1$. Let us assume for the moment that $\Delta = 0$. It can easily be seen that when $\Gamma_0/2 < \delta$ (weak relaxation) we get two *non degenerate* levels, with an energy splitting which is equal to $\sqrt{\delta^2 - (\Gamma_0/2)^2}$. In the opposite case of $\Gamma_0/2 \geq \delta$ (strong relaxation), we get two *degenerate* energy levels and the energy splitting disappears. Further insight into the behavior of the system is obtained by inspecting the imaginary part of the eigenvalues which represents the decay time. In the weak relaxation regime we get approximately the same value $\Gamma_0/2$ for both energy levels. In the strong relaxation regime, however, the imaginary part of the eigenvalues bear two different values $\Gamma_0/2$ and $\delta^2/2\Gamma_0$, representing a fast and a slow decay, respectively. Thus, in the strong relaxation regime the overall time evolution of the system is a two exponential decay. Including of a finite Δ_0 would obviously change the situation, and there will be an energy splitting also in the strong relaxation regime. However, since $\Delta_0 \ll \Gamma_0$ this splitting, which is $\sim \sqrt{\Gamma_0\Delta_0}/2$, is much smaller than the width of the broad resonance $\Gamma_0/2$, and is therefore not very significant.

Let us turn now to a quantitative comparison of the system behavior with theory. Examining the parameters of the three samples we find that in the 50 Å sample, where $L_2 = L_1$, the condition $\Gamma_0/2 \ll \delta$ is satisfied, and we are in the weak relaxation regime. The 20 Å sample is chosen to be at the transition between the weak to strong relaxation, where $\Gamma_0/2 \approx \delta$. In the 10Å sample, where $L_2 < L_1/2$, we are in the regime of strong relaxation where $\Gamma_0/2 \gg \delta$. Thus the observed collapse of the energy splitting in the 20 and 10 Å is well explained by the theory. Our temporal resolution does not enable us to resolve the fast component of the two exponential decay, which in the 10 Å sample is 10 fs. We therefore measure the time evolution of the slower component only. Since the decay time of this component scales like $1/\Gamma_0$, it is clear that in the 10 Å sample the measured time for the depletion of the system is expected to be longer then in the 20 Å sample.

There are, however, some discrepencies between the observed the decay times and the calculated ones are observed. Most noticable is the the existance of different decay rates for the two electron levels at the 50 Å sample (7 and 16 ps), whereas theory predicts that there should be a single decay rate for both levels. We could exclude well width fluctuations and level misalignment (due to the coupling to the continuum) as the possible source of the different decay rates. A possible explanation is that in steady state the holes density is larger in the outer well due to Coulomb attraction to the electrons in the continuum. This results in lowering the electron energy level in the outer well and consequently in a slower decay time of the higher energy component. It should be emphasized, however, that the shortest measured decay time (7 ps) is shorter than the one that should have been measured in an ideal case, with a zero energy mismatch, and is, therefore, a low limit for it.

In conclusion, we have shown that decay rate of CQW to continuum depends in a non trivial way on the coupling strength between the two. In the weak relaxation limit the decay rate increases with increasing the coupling strength. However, in the strong relaxation limit it decreases with increasing the coupling strength. This result is applicable to any system in which resonant tunneling is coupled to a relaxation channel.

This work was supported by the Minerva foundation, Munich, Germany.

References

1. D. Y. Oberli *et al.* Phys. Rev. B 40, 3028 (1989).
2. M. G. W. Alexander *et al.* Phys. Rev. B 41, 12295 (1990).
3. I. Matsutsune *et al.*, Phys. Rev. B 42, 5719 (1990).
4. K. Leo *et al.*, Phys. Rev. B 42, 7065 (1990).
5. A. P. Heberle, W. W. Rühle, C. Kohler, Phys. Stat. Sol. B 173, 81 (1992).
6. B. Deveaud *et al.*, Phys. Rev. B 42, 7021 (1990).
7. S. A. Gurvitz, I. Bar-Joseph, and B. Deveaud, Phys. Rev. B 43, 14703 (1991).

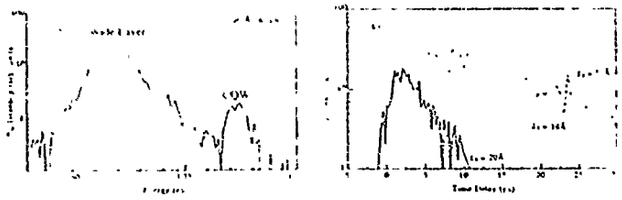

Fig. 1. (a) Luminescence spectrum of the 50 Å sample at a delay time of 10 ps. (b) Decay behavior of the QQW luminescence in the 3 samples.

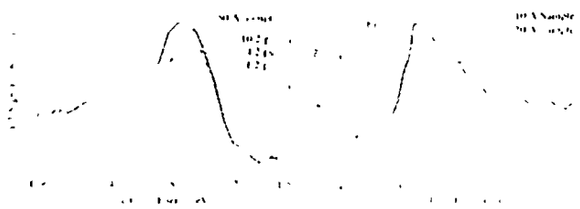

Fig. 2. [illegible]

FrB4

Modulation of Wannier Stark Transitions by Miniband Franz Keldysh Oscillations in Strongly Coupled GaAs AlAs Superlattices

K H Schmitt W Gedeltbrecht N Linder G H Döhler
Institut für Technische Physik, Universität Erlangen-Nürnberg, Erwin-Rommel-Str. 1, D-91058 Erlangen, Germany

H T Grahn K Ploog
Paul Drude Institut für Festkörperelektronik, Hausvogteiplatz 5-7, D-10117 Berlin, Germany

H Schneider
Fraunhofer Institut für Angewandte Festkörperphysik, Tullastr. 72, D-79108 Freiburg, Germany

We present calculations and optical experiments performed at 77 K on a GaAs AlAs superlattice with only one monolayer AlAs barriers and a combined miniband width of 180 meV. In particular the field dependent transition from the three dimensional miniband system to the two dimensional Wannier Stark (WS) regime is investigated. Using Differential Photocurrent Spectroscopy we are able to resolve WS transitions with indices n between 1 and 29. At the same time Franz Keldysh (FK) oscillations are observable at the lower and for the first time even at the upper miniband edge. A modulation of the WS transitions by the FK oscillation can also be clearly visible. Our theory describes in detail the competition of the linear WS fan originating at the center of mass energy with the non linear fans of the FK oscillations evolving from the lower and upper miniband edges.

I. INTRODUCTION

In type I semiconductor superlattices the well known Wannier Stark (WS) ladder dominates the field dependent absorption [1,2]. At high applied electric fields the electron and hole wavefunctions are strongly localized. Therefore only spatially direct transitions are allowed. The two distinct 3D combined density of states is reflected in a step like absorption coefficient. With decreasing electric field F the delocalization of the wavefunctions increases. Due to their different effective mass the heavy hole remains localized even at rather weak applied fields while the electron wavefunction may extends over several wells. Thus the heavy hole wavefunction acts as a detector for the electron one and spatially indirect WS transitions appear in the absorption spectra (Fig. 1). These transitions shift linearly towards the center of mass energy F according to

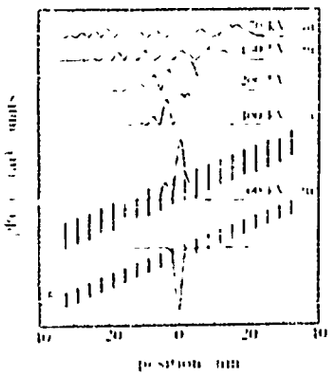

FIG. 1. Field dependent behavior of the squared electron wavefunction. The lower part of the figure shows the superlattice potential and the heavy hole wavefunction at 500 kV/cm.

$$\hbar\omega_n = E + \hbar\omega_c(n+\delta) \qquad n = \pm 0, 1, 2 \qquad (1)$$

where ω_c is the superlattice period. The two dimensional combined density of states gradually transforms into a three dimensional one.

If there is no field applied all wavefunctions are completely delocalized. The resonant subbands split into minibands with a three dimensional combined density of states and three dimensional critical points M_0 [1]. Similar to bulk material these critical points show a square root lineshape at each miniband edge in the superlattice absorption. The field dependent absorption of a three dimensional system is described by the well known Franz Keldysh (FK) effect [2-6]. It is characterized by oscillations beside the band region moving away from the critical point with increasing field according to

$$\hbar\omega_{FK} = E + \left(\frac{e^2F^2\hbar^2}{2\mu_\parallel}\right)^{1/3} \cdot \gamma_i^{2/3} \qquad (2)$$

Here γ_i is the ith zero crossing of the Airy function $Ai(z)$ which describes the envelope function near the lower and upper miniband edge in the low field limit, $\mu_\parallel$ is the effective mass in field direction and E the energy of the critical point M.

In this paper we report about theoretical and experimental investigations of the field induced transition from the three dimensional miniband system to the WS regime with its two dimensional character which is reflected by steps of the WS ladder in the superlattice absorption. Using differential photocurrent spectroscopy (DPCS) a special wavelength modulation technique we are able to resolve a symmetric WS fan up to an index of ± 9. At the same time FK oscillations appear at the lower and even at the upper miniband edge shifting towards the center of the miniband with the frequency according to Eq. 2. Our theory describes in detail this competition of the linear WS fan with the non linear fans of

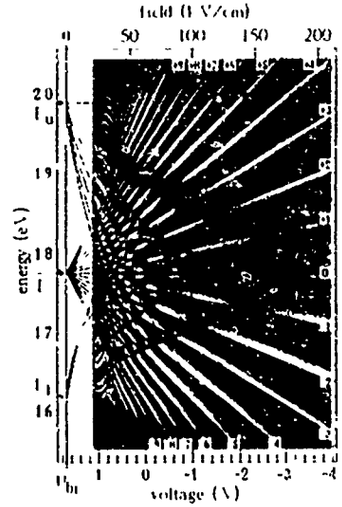

FIG. 2. Calculated wavelength derivative of the field-induced change of the superlattice absorption $\alpha(F, \lambda)$ ($\alpha d = 0.92$). λ is depicted in a grey scale graphic (small amplitude=white, large amplitude=black, cp. Fig. 1). The linear WS fan (black numbers) is evaluated with respect to Eq. 1 ($\delta = 1.772$, $eV = eF \cdot \gamma \cdot d$ + built in voltage ($V_{bi} = 1.7$ V, intrinsic region $d_i = 2748$ Å). The non linear FK fan (white numbers) is calculated according to Eq. 2 ($E_g = 1.610$ eV, $\mu_\parallel^{hh} = 0.065 m_0$).

the FK oscillations resulting in a modulation of the WS transitions and vice versa.

II. THEORY

In our calculations (Eq. 1) we used the Kane formalism which gives a crystal momentum representation of the wavefunction [7, 8]. The theoretically investigated superlattice is composed of 11 monolayer (ML = 2.8 Å) GaAs wells and one monolayer AlAs barriers. The combined width of the lowest electron and heavy hole miniband is 881 meV. The energy dispersion is determined by the Kronig Penney model. Because of the strong coupling between the wells the tight binding model is not appropriate for our theoretical considerations. In particular the miniband dispersion is strongly asymmetric with respect to the lower and upper miniband edges. The field dependent superlattice absorption is given by the overlap of the electron and heavy hole wavefunction. Due to a three times smaller oscillator strength and a larger delocalization of the wavefunctions light hole transitions are negligible.

To compare our theory with our experimental data we do not calculate simple absorption spectra but the wavelength derivative of the field induced change of the absorption $\partial^2\alpha / \partial\lambda\partial F$. In Fig. 2 WS ladder transitions (labelled by black numbers) are clearly observable shifting linearly away from E with increasing electric field according to Eq. 1. Originating at the lower and upper miniband edge the non linear FK fans modulate the intensity of the WS levels while the oscillations move towards E with the period proportional to $F^{2/3}$.

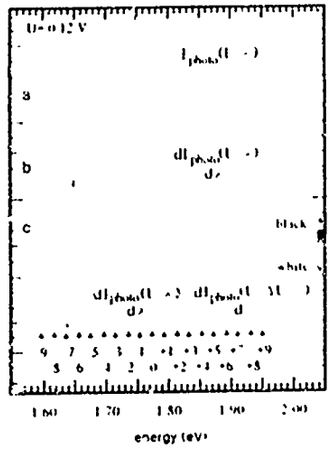

FIG. 3 Comparison between PC (a) DPC (b) and DDPC (c) spectra ($\Delta U = 0.02$ V). The lower part of Fig. 3c shows the calculated WS transition energies according to Eq. 4.

Due to the asymmetric miniband dispersion the field dependence of the FK oscillations at the lower miniband edge (marked by thick lines and white numbers) is much better described by the effective mass m^* connected with the Kronig Penney model in contrast to the upper edge. The small lines, which describe the field dependent shift of the FK oscillations at the upper miniband edge, are calculated with Eq. 2 using a fitted effective mass $m^*_{exciton} = 0.2\,m_0$, $E_g = 2.031$ eV. (Therefore these lines are only guide lines for the eyes.) Due to a larger effective mass the FK oscillation period is smaller at the lower miniband edge compared to the upper one, cp. Eq. 2. In the low field limit the energetic distance eFd between adjacent WS states is too small to be resolved and the WS features add only a fine structure to the FK oscillations. At intermediate fields the WS structure becomes increasingly coarse. The competition of the WS and FK fans produces a checkered pattern in Fig. 2. For higher fields when the first FK absorption maxima corresponding to the lower and upper miniband edges would formally merge with each other the "FK picture" becomes meaningless. This is the extreme WS regime where the spatially direct transition becomes more and more dominant while all other levels of the WS ladder gradually disappear [1–3].

III. EXPERIMENT

In our experiments we have studied a GaAs/AlAs superlattice which was grown on a GaAs n^+-substrate with molecular beam epitaxy. The superlattice consists of 50 periods of 11 monolayer GaAs wells and only one monolayer AlAs barriers. The superlattice is sandwiched between 0.6 μm wide $Al_xGa_{1-x}As$ ($x \approx 0.3$) undoped regions followed by 0.2 μm Si doped GaAs on the n-side and 400 Å Be doped GaAs layers on the p-side of the sample.

We used DPC – a new wavelength modulation technique [10] which is much more sensitive compared to normal photocurrent spectroscopy. Fig. 4a shows the photocurrent of our sample measured at 77 K and an applied voltage of 0.12 V. Only the lower confined heavy hole miniband edge and wide field independent Fabry–Perot oscillations above the fundamental gap energy lying on top of a huge background signal are clearly observable. In the wavelength derivative of the photocurrent (Fig. 4b) a sharp peak at the lower miniband edge and again wide Fabry–Perot oscillations appear. However, in contrast to Fig. 4a the huge background signal is suppressed by the first derivative character and a small fine structure becomes visible caused by field dependent WS ladder transitions. To remove the field independent structure it is useful to study the difference of two DPC spectra measured at different applied fields (Fig. 5c). The investigation of the field induced change of the photocurrent allows a detailed and very sensitive study of the field dependent superlattice absorption (Fig. 6–11).

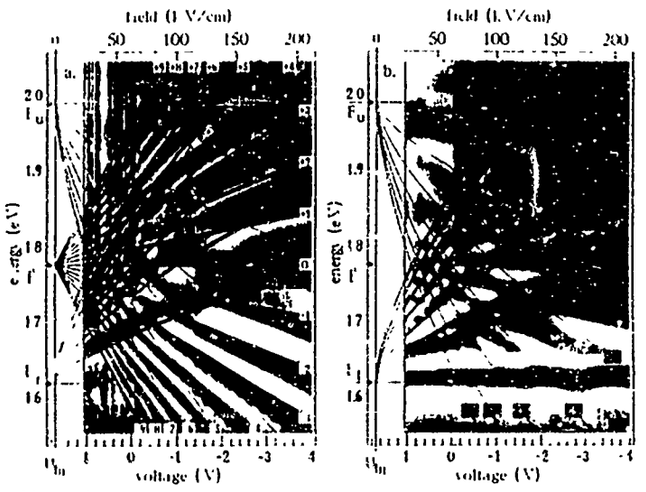

FIG. 4 Experimentally observed wavelength derivative of the field induced change of the PC. Part (a) shows $\partial I_{PC}(F,U,\lambda)/\partial\lambda = \partial I_{PC}(F,U=0.24\text{ V},\lambda)/\partial\lambda$ and is the experimental counterpart to Fig. 2. The WS and FK fans are identical. In part (b) DPC spectra at higher fields are related to the DPC spectrum measured in the very low field limit, $\partial I_{PC}(F,U=0.24\text{ V})/\partial\lambda = \partial I_{PC}(F=0, U=0.24\text{ V})/\partial\lambda$. The lower and upper miniband edge (E_1 and E_2) and FK oscillations labelled 1 to 6 and 1' to 6' dominate in the spectra.

Depending on the magnitude of the electric field, WS features (Fig. 1a) or FK oscillations and band edge structure (Fig. 1b) dominate in such double differential photocurrent spectra (DDPCS). In Fig. 1a WS transitions from $\nu = 0$ up to $\nu = 9$ are clearly visible. Their intensity is modulated by FK oscillations which is in very good agreement with our theory (cp. Fig. 2) although excitonic effects are not included in our calculations. The small deviations at high fields can be explained by the quantum confined stark effect which is not included in our calculated spectra. In order to see the FK oscillations and the miniband edges more clearly it is advantageous to relate DPC spectra measured at higher fields to a DPC spectrum taken in the very low field limit (Fig. 1b). Now FK oscillations appear at the lower and upper miniband edge reflecting the field dependence of Eq. 2. All difference spectra exhibit a field independent band edge structure caused by the zero field limit spectrum with its characteristic peak at each miniband edge. The experimentally observed upper miniband edge energy is slightly smaller than expected from theory. This deviation can be explained by conduction band non parabolicities. At higher fields WS levels occur again.

IV. SUMMARY

We have studied the transition from the miniband to the WS regime, i.e. from a three dimensional density of states to a two dimensional. The difference of two DPC spectra measured at different applied fields shows a symmetric WS fan up to an index of 29 and for the first time FK oscillations across the whole lowest confined miniband have been observed. In our experiments as well as in our theoretical results a modulation of the WS transitions by FK oscillations is clearly visible. In conclusion there is no sharp transition from a three dimensional system to a two dimensional one but rather a coexistence of the FK and the WS regime over a wider field range.

REFERENCES

[1] P. Voisin, Superlattices Microstruct. 8, 323 (1990).
[2] F. E. Mendez, F. Agullo-Rueda, and J. M. Hong, Phys. Rev. Lett. 60, 2426 (1988).
[3] J. Bleuse, G. Bastard, and P. Voisin, Phys. Rev. Lett. 60, 220 (1988).
[4] D. E. Aspnes, Handbook on Semiconductor, edited by T. S. Moss, Vol. 2, ch. IV, 109.
[5] B. Schneider, A. Fischer, and K. Ploog, Phys. Rev. B 45, 6429 (1992).
[6] C. Corrasso, D. Campi, C. Caccatore, C. Velluti, S. Gaillard, B. Lambert, and A. Regreny, Europhys. Lett. 16, 591 (1991).
[7] E. O. Kane, J. Phys. Chem. Solids 12, 181, 1959.
[8] M. Satoh, J. Phys. C: Solid State Phys. 5, 914 (1972).
[9] E. E. Mendez, and F. Agullo-Rueda, J. Lum. 44, 223 (1989).
[10] K. H. Schmidt, A. D'Intino, N. Linder, M. Luna, G. H. Dobler, H. T. Grahn, K. Kawashima, and K. Fujiwara, Superlattices Microstruct. 12, 281, 1992.

FrB5

Photonic bandgap of two-dimensional dielectric crystals

J.M. Gerard, A. Izrael, J.Y. Marzin and R. Padjen
France Telecom/CNET/PAB, 196 av. Henri Ravera, F-92220 Bagneux, FRANCE
and F.R. Ladan
Laboratoire de Microstructures et Microelectronique (CNRS), 196 av. Henri Ravera, F-92220 Bagneux, FRANCE

Abstract

The existence of an absolute photonic bandgap in the near infrared for two dimensional periodic dielectric structures is discussed for photons propagating in the plane of such 2D crystals. A special emphasis is put on the influence of the shape and size of the filling pattern on the absolute bandgap formation. Very large absolute photonic bandgaps are predicted for 2D crystals formed by etching in a semiconductor slab periodic arrays of large vertical cylindric voids of circular cross section arranged in a triangular lattice. The technological feasibility of such optimum air/GaAs 2D crystals by standard processing techniques (electron beam lithography and reactive ion etching) is demonstrated.

Tailoring the spontaneous emission of a semiconductor active medium is particularly challenging, for fundamental reasons as well as in the view of a further optimisation of optoelectronic devices. The insertion of the emitting center in a microstructured material with three dimensional (3D) periodicity potentially allows to inhibit optical transitions within the photonic bandgap (PBG) energy range of this material, or to couple the emission to a single, or a few, defect modes [1-3]. Though optimum 3D air/semiconductor crystals are very attractive due to their large theoretical PBG in the near infrared, it is presently very difficult to process such structures. In this respect, it seems presently easier to fabricate air/semiconductor crystals with 2D periodicity. After discussing potential applications of such crystals, we will present the results of a large scale study of the influence of the shape, symmetry and size of the pattern on the existence of a photonic bandgap. Among those which have been considered, a single class of structures (large circular holes on a triangular lattice) allows to get a large PBG, common for both polarisations. Preliminary results concerning the microfabrication of such crystals are presented.

Bidimensional air/semiconductor crystals, formed by a periodic array of cylindric vertical semiconductor rods or of vertical cylindric holes in a semiconductor matrix, can in principle be produced by standard processing techniques. Due to the strong periodic modulation of the dielectric constant in this material, large PBGs appear in the photonic dispersion curves as soon as the direction of propagation of the photons is different of the direction z of the rods (or holes). It is important to note however that these PBGs appear generally in different energy ranges for the two polarizations, E parallel to z and E perpendicular to z. Two classes of interesting applications are opened for such a material.

In a guided wave geometry (as is the case for most optoelectronic devices and integrated circuits), a 2D crystal displaying a PBG for photons propagating in its plane (x,y) can be used as a low loss (eventually polarization dependent) mirror (having no cut off incidence angle, unlike Bragg mirrors). The application to photon recycling in a laser is particularly attractive.

Since (for appropriate patterns) a large PBG exists, which is common to all directions of propagation in or close to the x,y plane, a full control of optical transitions could be obtained by inserting a slab of this material between two Bragg mirrors, or by orienting preferentially the optical transition dipole in a direction (as is the case for strained quantum wells under strong biaxial tension). The full control of spontaneous emission is here clearly the main challenge.

We will essentially discuss hereafter the results of our calculations in terms of a maximization of the width W of the PBG of the crystal for photons propagating in the x,y plane. Focusing our attention on the second class of applications indeed, we see that a PBG width W at least larger than Of the typical spectral width of the emission in a semiconductor is required. Considering an energy E within the PBG, a large W means also a large range of incidence angles (with respect to the crystal normal) for which the propagation of photons with energy E is forbidden.

It has already been shown that 2D arrays of circular rods (or holes) on a triangular lattice exhibit, for appropriate parameters, a large PBG for either *E* or *H* polarizations (i.e. electric or magnetic field parallel to *z*) [4]. Up to now however, the fundamental question of whether the PBGs for *E* and *H* polarizations overlap (i.e. the existence of an 'absolute' PBG) has not been adressed to our knowledge.

2D crystals obtained for a circular pattern and a triangular lattice are particularly favorable to the appearance of a large PBG. Such a crystal (and therefore its photonic band structure) retains the full symmetry of the triangular Bravais lattice, which makes easier the overlap, all around the edge of the first Brillouin zone, of the photonic gaps relevant for each direction of propagation. We plot for instance in figure 1 the calculated photonic band structure of a crystal formed by large circular vertical holes in a GaAs matrix (dielectric constants: $\varepsilon_{air}=1$, $\varepsilon_{GaAs}=13.6$). The filling factor *f*, defined as the fraction of the (x,y) plane which is covered by the cross section of the circular cylinders, is here 0.78. Details of the calculation, based on a plane wave expansion of the solutions of Maxwell's equations, have been presented elsewhere [4,5]. Since the band structure scales with the lattice parameter *a* of the crystal, we plot here $\omega a/2\pi c$ (ω: photon pulsation, c: velocity of light) as a function of the Bloch vector $\vec{k}$. Numerous band degeneracies occur at high symmetry points of the Brillouin zone, so that only two large PBGs exist for the lower energy bands. *H*, and *E* (We refer from now on to *H*, (*E*,) in order to design the PBG, at any, between the 1st and the 2nd bands in *H* (*E*) polarization). Fortunately, *E* and *H*-PBGs widely overlap for this set of parameters, which will be shown hereafter to be an exceptionnal feature for 2D crystals. The absolute PBG is, for instance, 280 meV large, it centered near the 1.42 eV electronic gap of GaAs at room temperature, which will in principle be the case for $a\approx0.4$ μm. Note that for this lattice parameter and a 0.78 filling factor, nearest neighbour holes are separated by a semiconductor wall as thin as 300Å.

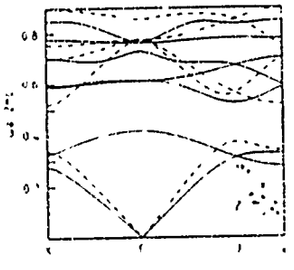

Fig 1: Photonic band structure for the *E* (solid line) and *H* (dashed line) polarizations, for a 2D array of circular holes in a GaAs crystal (ε=13.6). The filling factor is here 0.78. The first brillouin zone of the 2D crystal, and the Γ-X-M-Γ path along which the dispersion curves have been calculated are shown in the insert.

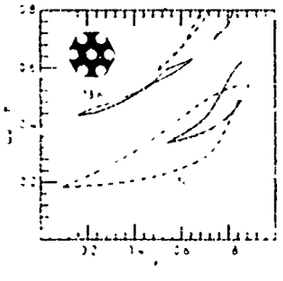

Fig 2: Plot of the energy range of all PBG existing for the first seven bands in *E* (or *TM*) or *H* (or *TE*) polarization, for a 2D crystal with triangular Bravais lattice, and formed by an array of vertical circular holes in GaAs, as a function of the fraction *f* of the medium occupied by the holes.

In an attempt to optimize both *B* and the technological feasability of the crystal, we have investigated the photonic band structure for various patterns conforming to the crystal the full symmetry of the triangular Bravais lattice. All bandgaps appearing for the nine lower energy bands have been plotted for all possible values of the filling factor ($0 \le f \le 0.86$) for an array of circular holes in GaAs (figure 2) or of GaAs circular rods in air (figure 3). For holes, the only possible significant PBGs are *H*₁ and *E*₂. *E*₂ opens only for $f\ge0.6$, so that a large absolute PBG is observed only when *f* is close to the maximum filling factor of a plane by disks ($f_{max}=0.86$). As in the previous exemple, neighbour voids are separated by a very thin dielectric sheet, which makes the microprocessing of such crystals somewhat delicate, even for state of the art etching techniques. It is more generally easier to etch semiconductor rods rather than drill holes in a semiconductor slab. Considering figure 3 however, we see that arrays of circular GaAs rods on a triangular lattice never display an absolute PBG. Though large *E*₂ PBGs exist for most values of *f*, *H*₁, the single PBG observed in *H*₁ polarization never overlaps one of these.

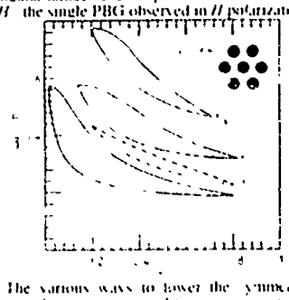

Fig 3: Same as figure 2 for an array of GaAs vertical rods with circular cross section. *f* is here the fraction of the medium occupied by the rods.

The various ways to lower the symmetry of the crystal have been systematically investigated in an attempt to lift some symmetry induced degeneracies, and open novel gaps [5]. When actually achieved, this result is generally obtained at the expense of a reduction of the *E*₂ or *H*₁ PBGs observed for circular patterns for the same filling factor. Furthermore, these novel gaps generally have a small width, so that no interesting absolute PBG can be obtained. To understand this result, one should keep in mind that large PBGs are the more likely to appear in a medium which is as close to an in plane isotropy as possible: arrays of circular rods, or holes on a triangular lattice are optimum in this respect. Similarly, the marked anisotropy of 2D crystals (between Γ-X and Γ-M directions) is the intrinsic reason why *E*-gaps and *H*-gaps so rarely overlap. For optimum 3D crystals [6,7] (with face centered cubic lattice), *E* and *H* polarizations play rather similar roles, and an absolute PBG results from the overlap of *E*₁ and *H*₁ PBGs. For 2D crystals on the opposite, *E* and *H* polarizations intrinsically play very different roles. Coupling coefficients in the eigenvalue problem being systematically smaller for the *H* than for the *E* polarization [4,5], the *n*th band lies, for instance at a much lower energy for *E* than for *H*, in particular *E*₁ and *H*₁ (which both open) never overlap.

Finally, the calculation has also been conducted for an array of holes with hexagonal cross section (this pattern having the same orientation as the Wigner-Seitz unit cell of the triangular lattice). The interest is here twofold. Firstly, it is possible to test to some extent the sensitivity of the absolute PBG of arrays of circular holes to deviations of the pattern for an ideal circular shape. Secondly, it is possible for such a pattern to study the photonic band structure for the whole range of filling factors ($0<f<1$). The energy location of the *E*₂ and *H*₁ PBGs is plotted as a function of *f* on figure 4, which should be compared to figure 2, relevant for circular holes. No more PBG appears for this hexagonal pattern, since both corresponding 2D crystals exhibit the same symmetry. As expected also, all gaps pinch off for *f* close to 0 (or 1, i.e. in the limit of a uniform medium). The location and width of the PBGs are remarkably similar for both crystals for the smaller filling factors ($f\le0.5$). The photonic band structure is indeed hardly modified (for a given *f*) as long as pattern modifications occur at a scale much smaller than the wavelength of the electromagnetic waves in the medium ($a/\lambda \le 0.3$). When *f* approaches

the critical filling factor for which circular holes get in touch however, the repartition of the dielectric material becomes very different for circular and hexagonal holes. We observe a drastic shrinking of the PBG if - for an hexagonal pattern, whereas H_1 is essentially unaffected. As a result, this crystal has a very small absolute PBG. For regular polygons with a higher number n, of sides, we recover the limit of circular holes rather quickly ($n_c \approx 8$ or 10) in good approximation (the width and position of PBG 1 is the same within 10 per cent).

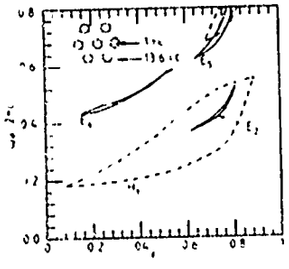

Fig 4 Same as figure 2 for an array of vertical voids in GaAs with hexagonal cross section. f is here the fraction of the medium occupied by the voids.

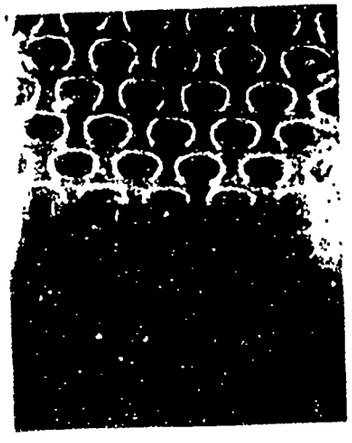

Fig 5 Scanning electron micrograph obtained for a view with 45°incidence of the cleaved edge of a 2D air/GaAs crystal. Note the

Etching deep holes with submicronic diameter and vertical walls is still a major technological challenge. Preliminary experiments have been conducted so as to demonstrate the feasibility of optimum 2D air/GaAs crystals and test their degree of perfection. Our test structures are arrays of circular holes in GaAs arranged on a triangular lattice of submicronic parameter (a=0.36 µm). For this lattice parameter, the absolute PBG is theoretically centered near 1.4 eV for optimum structures (0.7 < f < 0.8). Various crystals have been processed, for hole diameters in the 0.26 µm (f=0.47) to 0.32 µm (f=0.72) range. The holes are drilled by $SiCl_4$ reactive ion etching (RIE), under conditions which optimize the verticality of the etched walls. For that etching procedure, we use a Ni mask defined by electron beam lithography in a JEOL 5DIIU machine. Figure 5 displays a typical scanning electron micrograph obtained on the cleaved edge a 2D air/GaAs crystal there, f=0.63 after 0.6 µm deep holes have been etched. The shape and depth of the holes seem pretty homogeneous. It is important to note that their bottom (essentially flat) do not exhibit the round shape typical of an inefficient etching process. Etching deeper holes with a good verticality seems therefore realistic, at least up to a 0.8 or 1µm depth (which would be enough for most applications). Finally, the cross-section of the holes at the surface is close to a perfect disk. This is the combined result of a careful definition of the circular pattern at the lithography step, and also of the intrinsic tendancy of resist patterns to smooth at the revelation step.

To conclude, the photonic band structure of some 2D air-semiconductor crystals has been studied as a function of the shape and size of the same simple crystal patterns. A detailed his review of the performance of some simple 2D PBG crystals highlights some design rules for obtaining large absolute PBG's. A wide absolute PBG has only been obtained for arrays of large voids etched in the semiconductor matrix. Circular voids lead (for 0.7≤f≤0.8 typically) to the largest absolute PBG attainable, resulting (unlike in the 3D case) from the overlap of H_1 and E_2 PBGs. Any deviation from this perfectly symmetric pattern reduces the width of the absolute PBG; elongated shapes (rectangles for instance) are particularly detrimental in this respect. This final design rule qualitatively indicates that the medium must be as isotropic as possible for the crystal to have a large absolute PBG. Finally, we have shown that state of the art lithography and etching techniques allow to produce such 2D air/GaAs crystals which theoretically display a large absolute PBG in the near infrared. An optimization of the etching procedure, so as to obtain deeper vertical holes, and the optical study of the photonic band structure have still to be performed.

References

[1] E. Yablonovitch, Phys. Rev. Lett. 58, 2059 (1987).

[2] S. John, Phys. Rev. Lett. 58, 2486 (1987).

[3] E. Yablonovitch, T.J. Gmitter, R.D. Meade, A.M. Rappe, K.D. Brommer, J.D. Joannopoulos, Phys. Rev. Lett. 67, 3380 (1991).

[4] M. Plihal, A. Shambrook, A.A. Maradudin and P. Sheng, Opt. Communications 80, 199 (1991); M. Plihal and A.A. Maradudin, Phys. Rev. B 44, 8565 (1991).

[5] R. Petit, J.M. Gerard and J.Y. Marzin, to be published in the Review of Modern Optics special issue on photonic band gaps.

[6] K.M. Ho, C.T. Chan and C.M. Soukoulis, Phys. Rev. Lett. 65, 3152 (1990).

[7] E. Yablonovitch, T.J. Gmitter and K.M. Leung, 67, 2295 (1991).

Author Index

Abstreiter, G	MoC7	319
	TuP22	559
	TuP24	572
	ThB5	790
Adachi, A	MoP9	102
Adolph, B	ThP10	846
Agulló-Rueda, F	TuC4	424
Aihara, K	MoP35	248
Aikawa, K	ThP8	834
Akiyama, H.	MoC1	281
Alavi, K	ThC2	1016
Albrecht T F	FrB2	1081
	TuP13	515
Albrektsen, O	WeB2	712
Allen Jr., S J	ThC4	1029
	ThC6	1039
	TuA5	360
Alperovich, V L.	MoP23	181
Andersson, T G	MoP40	275
André, J P	WeA5	694
André, J P	MoP18	151
Aoyagi, Y	MoP36	252
Apetz, R.	TuP26	581
Arakawa, Y	MoP5	73
	MoA1	1
Aristone, F.	TuP40	658
Aschauer, M	TuP24	572
Asmar, N. G	MoP32	234
Atmani, H.	MoP2	54
Austing, D G	TuP31	613
Badoz, P A	TuP25	576
Baldwin, K W	MoB2	23
Bar-Joseph, I	FrB3	1089
Baranov, A	FrA4	1064
Baranov, P G.	TuP15	523
Bardorff, S R	ThP5	821
Barnes, D J	WeA2	675
Bartoli, F J	ThP23	915
Basmaji, P	ThP30	949
Bass, S J	TuC2	411
Bastard, G	TuP2	446
	TuP3	454
	ThP2	803
Bauer, G	TuP22	559
	MoP17	144
	ThA2	738
Bauer, G E W	ThP32	962
Beaumont, S P	ThC5	1033
Bechstedt, F	ThP10	846
Bedel, E	MoP2	54
Behr, D	MoP11	110
Belitsky, V I	MoP12	119
Bellomi, G	ThC4	1029
Bending, S J	TuP39	652
Bennett, B R	MoC2	290
Bergman, P	FrB3	1089
Bernardini, F	ThP9	841
Bernhard, K	FrA3	1059
Bernussi, A A	MoP22	175
Berrour, J M	TuP25	576
Bertram, D	MoP8	94
Beton, P H	TuP30	605
	TuP28	593
Bhat, R	ThB2	773
Bicknell, R N	ThA5	756
Bimberg, D	ThB2	773
Bird, J. P	MoP36	252
Birotheau, L	ThB1	763
Bloch, J	MoA2	9
Bockelmann, U	MoA2	9
	ThB5	790
Bogaerts, R	TuA5	360
Bohm, G	ThP24	916
	MoP28	206
	FrA3	1059
Bois, P	TuA2	338
Bolognesi, C	MoP4	68
Bolton, F	ThP12	859
Boudinet, P	ThP2	803
Brar, B	ThC6	1039
Brasil, M J S P	MoP22	175
Brataas, A	ThP32	962
Brehmer, D	TuA5	360
Brill, B	MoB1	21
Brown, C V	TuP38	645
Bruggemann, F	FrB1	1075
Brugger, H	TuP37	640
	TuB2	377
Brum, J A	MoP22	175
	ThP15	879
Brunt, M R	MoP19	157
Brunner, K	ThB5	790
Buckle, P D	TuP35	634
	MoP39	268
Buhmann, H	TuP30	605
Bungaro, C	MoC8	324
Butov, L V	MoP40	275
Bykov, A A	MoP37	261
Calleja, J. M	ThC3	1022
Campbell, P M	MoP6	80
Campman, K L	ThC4	1029
Caneau, C	ThB2	773
Capasso, F	ThC1	1015
	ThP20	903
Capizzi, M	MoP19	157
Cardona, M	MoP12	119
	MoC6	314
Carmona, H	TuP38	645
De Carc, L	MoC5	307
Cerva, H	WeB1	700
Chang, K H	MoP27	200
Chang, Y H	MoP27	200
Chaubet, C	ThP26	927
Cheeks, T L	WeA3	680
Chen, J J.	ThA2	738
Chen, T C	MoP27	200
Cheng, J P	ThP27	928
Chi, V. S	TuP11	502
Chiappe, G	ThP17	889
Cho, A	ThP20	903
Cho, A. Y.	ThC1	1015
Chow, D H	TuP32	617
Christen, J	ThB2	773
Chu, J	ThP4	5
Chu, S N G	MoP22	175
	ThP39	1009
Cingolani, P	ThP6	825
Cockburn, J W	TuP35	634
Cohen, E	ThP21	904
	ThP22	909
Cohen, G	FrB3	1089
Cotta, M A	MoP22	175
Cundiff, S T	FrB2	1081
D Intino, A	TuC4	424
Dabbicco, M	ThP6	825
David, J P R	MoP20	165
Davis, J L	MoC2	290
Daweritz, L	MoP11	110
	TuA4	354
DeBoeck, J	WeA3	80
Delalande, C	ThP3	810
Dennis, B S	ThC3	1022
DeRosa, F	TuA5	360
Deveaud, B	FrB3	1089
Deveaud, B	ThP14	875
Devreese, J T.	ThP27	928
Deych, M [illegible]	ThP36	985
Dietrich B	TuP23	565
Dietsche, W	MoP31	228
Dilger, M.	MoA3	13
Diniz, R	TuB2	377
Dmowski, L H	MoP28	206
Dohler, G H	TuC4	424
	ThP35	978
	FrB4	1094
Dottling, R	MoP30	220
Dresselhaus, G	ThA2	738
Dresselhaus, M S	ThA2	738
Drexler, H	ThC5	1033
Dur, D	MoP25	188
	ThP26	927
Dutartre, D	TuP25	576
Dutisseuil, E	MoP33	238
Dzyubenko, A B	TuP14	522
Eaves L	TuP23	593
	TuC6	435
	TuP30	605
	TuP27	585
	MoP39	268
Eberl, K	MoP31	228
	MoA3	13
Ehrenfreund, E.	ThP39	1009
	ThP22	909
Eisele, I	TuP29	600
Ekenberg, U	MoP24	182
Engelhardt, C M	TuP24	572
Ensslin, K	MoP4	68
Evans, H B	MoP39	268
Ezaki, T	ThP19	899
Fagotto, F A M	ThP15	879
Fani, Z	TuP33	625
Faist, J	ThC1	1015
	ThP20	903
Faller, F	ThB3	777
Fasolino, A	TuP34	629
	ThP9	841
Fedichkin, L E	ThP25	922
Feldmann, J	FrB2	1081
Ferrara, M	ThP6	825
Ferreira, R	TuP2	446
	TuP3	454
Fischer, A	TuP6	471

Fischer, A MoC5 307
Fisher, T A MoP20 165
MoP39 266
TuC2 411
Fontaine, C MoP2 54
Forchel, A ThB3 777
ThP18 894
Forster, A TuB2 377
Foster, T J TuP38 645
TuP28 593
Fouillant, C FrA4 1064
Frankenfeld, H TuP23 565
Fromherz, T TuP22 559
ThC2 1016
Frost, J E F TuP31 365
Frova, A MoP19 157
Fu, Y TuB5 396
Fujii, M MoP9 102
Fujiwara, A ThP34 974
Fujiwara, K TuP1 442
TuP4 460
TuP10 496
Fujiyasu, H ThP8 834
Fukatsu, S MoA4 17
TuP20 553
TuC1 403
ThP34 974
Furdyna, J K ThA1 729
Gadaleta, C MoP16 199
Garini, Y ThP22 909
Geim, A K TuP38 645
TuP39 652
TuP28 593
Geißelbrecht, W FrB4 1094
Gerard, J. M ThP14 875
FrB5 1100
Gerhardts, R R ThP28 934
MoP29 213
Gershoni, D. ThP39 1009
de Gironcoli, S MoC7 319
MoP15 131
Glutsch, S ThP10 846
Gmachl, C TuC5 431
Gnezdilov, V P MoP14 124
Göbel, E O MoP8 94
TuP13 515
FrB2 1081
Goiran, M MoP- 54
Goldoni, G TuP34 629
Goñi, A R ThC3 1022
Gorczyca, I MoP28 206
Gornik E. TuP24 572
TuC5 431
TuB2 377
MoP28 206
Gossard, A C ThP22 909
ThC2 1029
MoP32 234
Grahn, H T TuC4 424
FrB4 1094
Grambow, P MoA3 13
Grey, R MoP20 165
TuP35 634
Grimmeiss, H G TuP23 565
Grunberg, P FrA4 1064
Grundmann, M ThB2 773
Guasch, C MoP2 54
Gudmundsson, V ThP28 934
Gulden, K. H ThP35 978
Guldner, Y. TuP25 576
Gusev, G M ThP30 949
Gwinn, E G ThP33 970
MoP32 234
Gyuro, I Th' 18 894
Haacke, S TuP18 541
Hagston, W E ThP5 821
Hamaguchi, C TuC5 431
TuP19 899
Hamberger, P MoP17 144
Hamm, R. A ThP39 1009
MoP22 175
Han, H-X TuP9 492
Hansen, W ThP24 916
ThC5 1033
Hara, K MoP21 170
Harbison, J P WeA3 680
Haring Bolivar, P FrB1 1075
Harle, V MoP26 192
Harmand, J C MoP33 238
Harriot, L. R MoP22 175
Harris, J J TuP39 652
Harrison, P A ThP5 821
MoP39 268
Hartmann, A TuP26 581
Hasenberg, T C TuP32 617
Hashimoto, Y MoC4 302
Haug, R J TuP36 635
Haupt, R ThP11 853
Hawrylak, P ThP28 934
Heath, M. TuP30 605
Heberle, A MoC3 298
TuP18 541
Heiblum, M MoB1 21
Heime, K MoP7 88
Heitmann, D MoA3 13
Helm, M TuP22 559
ThC2 1016
Henini, M TuC6 435
TuP30 605
TuP28 593
MoP39 268
Henneberger, F ThP7 829
Herlach, F TuA5 360
Hertel, G ThC5 1033
Hessman, D TuP12 509
Hey, R MoP11 110
TuA4 354
Hilbet, W ThC2 1016
Hill, G TuC6 435
TuP31 613
MoP20 165
TuP35 634
TuP28 593
MoP39 268
Hiyamizu, S MoP9 102
Hoffman, C A ThP23 915
Hofmann, D M MoP26 192
Hogg, R A MoP20 165
Hohenstein, M. MoA3 13
Holland, M ThP24 916
ThC5 1033
Holy, V MoP17 144
Hopfel, R A ThP13 866
Hopkins P F ThC1 1029
MoP32 234
Höricke, M TuA4 354
Horihata, S ThP19 899
Hosoda, M TuP1 442
Hu, E L WeA1 665
Huang, Y-S TuP11 502
Hughes, O H MoP39 268
Hunt, A W WeB3 714
Hwang, D M ThB2 773
Ichimose, H MoC1 281
Ikoma, T MoC4 302
Ilg, M MoC3 298
Ils, P. ThP18 894
Inata, T TuB4 389
Inoshita, T MoC1 281
ThP16 885
Inoue, K. MoP9 102
MoB4 35
Ishibashi, K. MoP36 252
Ishida, A ThP8 834
Ishikawa, T MoP1 48
Ito, R. TuP16 527
Ito, T. MoP10 104
Itskevich, I E ThB3 777
MoP40 275
Ivanov, S V ThC7 1046
Ivchenko, E L TuB5 396
Izrael, A. ThB1 763
FrB5 1100
Jackson, S ThP5 821
Jaros, M. FrA2 1058
Jaroshevich, A. S MoP23 181
Jayaraman, V ThC6 1039
Johnson, M B WeB2 712
Johnson, M D WeB3 714
Jones, G A C TuB1 365
de Jong, M J M MoB3 29
Joullié, A FrA4 1064
Juen, S ThP13 866
Jungk, G MoP11 110
Kamal-Saadi, M MoP25 188
Kang, W MoB2 23
Kapon, E ThB2 773
Kasper, E MoC7 319
MoP17 144
Kawashima, K TuP1 442
TuP4 460
TuP10 496
Kelly, M J TuB1 365
Keramidas, V G WeA3 680
De Keyser, A TuA5 360
Khan-Cheema, U M TuP31 613
Khmyrova, I ThP37 992
Kibbel, H MoC7 319
MoP17 144
Kiesel, P ThP35 978
Kiselev, A A TuB5 396
Kitamura, J MoP21 170

Klunke, W	TuP29	600
Klehn, B	TuP29	600
Klenk, M	ThP18	894
Klipstein, P C	TuP31	613
von Klitzing, K	MoP31	228
	MoA3	13
	TuP36	635
Knap, W	MoP25	188
	ThP26	927
Kneissl, M	ThP35	978
Knipp, P A	ThB4	783
Knott, R	MoP31	228
Kobbi, F	MoP25	188
Kochi, F	ThP1	815
	TuP37	640
Kochereshko, V P	ThA4	749
Koenraad, P	WeB2	712
Koidl, P	WeA4	687
Kop'ev, P S	ThC7	1046
Koppensteiner, E	TuP22	559
	MoP17	144
Koshiba, S	MoC1	281
	MoP3	60
Kostial, H	TuA4	354
Kotthaus, J. P	ThP24	916
	ThC5	1033
	MoP4	68
Kowalski, B.	MoP26	192
Kreller, F	ThP7	829
Kroemer, H	MoP4	68
	ThC6	1039
	ThP33	970
	WeA1	665
Kubo, H	TuC5	431
	ThP19	899
Kuhn, O	TuC6	435
Kukimoto, H	MoP21	170
Kulakovskii, V D	MoP40	275
Kulik, L V	MoP40	275
Kunze, U	TuP29	600
Kurinkiev, B. K	ThC7	1046
Kuroda, Y	ThP6	825
Kurtenbach, A	MoA3	13
Kurz, H	FrB1	1075
Kvon, Z D	MoP37	261
La Scala Jr., N	TuP28	593
Lakrimi, M	ThP29	943
Lambrecht, A	ThP1	796
Lamprecht, K F	ThP13	866
Landwehr, G	ThA4	749
Langheinrich, W	MoP7	88
Laruelle, F	MoA2	9
	TuP33	625
Lavallard, P	TuP15	523
Law, K -K	ThP22	909
Law, V J	TuB1	365
Le Person, H	MoP33	238
Leadbeater, M L.	TuP27	585
Ledentsov, N N	ThC7	1046
Lee, C I	MoP27	200
Lehmann, A	MoA3	13
Leisching, P	FrB1	1075
Leo, K	FrB1	1075
Lerch, M L F	TuP27	585
Leroux, G	MoP33	238
Lettau, C	ThP24	916
Leuther, A	TuP26	581
Levi, A F J	FrA1	1049
Li, G-H	TuP9	492
Linder, E	ThP21	904
Linder, N	FrB4	1094
Lindolt, J.	TuP29	600
Litvin, L V	ThP30	949
	MoP37	261
Litwin-Staszewska, E	MoP25	188
Liu, K	ThP4	815
Liu, X	TuP12	509
Liu, Z-X	TuP9	492
Lockwood, D J	MoP14	124
Lomsadze, A V	MoP40	275
Loo, R	TuP26	581
López, M	MoP1	48
Lorke, A	MoB5	44
Louis, E	ThP17	889
Lu, W	ThA5	756
Lubyshev, D I	ThP30	949
Luc, F	TuA2	338
Luczak, A	ThP35	978
Lugagne-Delpon, E	MoP18	151
Lugli, P	MoC8	324
Lunn, B	ThP3	810
Lutgen S	TuP13	515
Luth, H	TuB2	377
	TuP26	581
Maan, J C	TuP17	533
	TuP18	541
Maier, M	WeA4	687
Maile, B E	TuP37	640
Main, P. C	TuP38	645
	TuP28	593
	ThP35	978
Malzer, S	TuP30	605
Mansouri, L	MoP37	261
Mansurov, V G	TuP11	502
Maracas, G N	ThP33	970
Markelz, A G	MoP32	234
Marschner, T	TuP13	515
Martelli, F	MoP19	157
Martin, A D	TuP27	585
Martin, P M	MoP39	268
Martín-Moreno, L	ThP17	889
	TuB1	365
Martinez-Pastor, J	ThP3	810
Marzin, J Y	FrB5	1100
	TuB1	763
Mashkov, I.V	TuP15	523
Mason, N. J	TuP31	613
	WeA2	675
	ThP29	943
Mathine, D L	TuP11	502
Matsuyama, T	MoP1	48
Maude, D K	TuC6	435
	TuP40	658
McCombe, B	ThP27	928
McMarr, P J	MoP6	80
Mehr, W	TuP23	565
Meiners U	TuP37	640
	TuB2	377
Meltser, B Ya	ThC7	1046
Mendez, E E	FrA5	1068
	TuA3	347
Merkulov, I A	ThA4	749
Merz, J L	ThP22	909
	TuP17	533
Mestres, N	TuP7	479
Meyer, B K	MoP26	192
Meyer, J R	TuP23	915
Michel, M	ThP18	894
Michels, J G	TuC3	416
Migal, V P	MoP37	261
Milekhin, A	MoP13	123
Miles, R H	ThP23	915
Mine, T	MoA4	17
Minot, C	MoP33	238
Mironchenko, N V.	ThP36	985
Miura, N	WeA2	675
	TuC2	411
Miyatake, T	ThP19	899
Mizutani, T	MoP35	248
Molenkamp, L W	MoB3	29
Molinari, E.	MoC7	319
	MoC8	324
	MoP15	131
Moliot, F	TuP40	658
Monakhov, A. A	ThC7	1046
Mori, N	ThP19	899
Morifuji, M.	TuC5	431
Morni, A	MoP21	170
Moschenko, S P	MoP37	261
Mosser, V	MoP25	188
Motohisa, J	MoP3	60
Mowbray, D J	MoP20	165
	TuC2	411
Muggelberg, C	TuA4	354
Muñoz, L	TuP7	479
Muraki, K.	ThP34	974
Murase, K.	MoP9	102
Muto, S	TuB4	389
Nachew, I	ThP4	815
Nagamune, Y	MoP5	73
Nakamura, Y	MoC1	281
	MoP3	60
Nakata, S	MoP35	248
Nakayama, M	TuP4	450
Nakayama, T	ThA3	742
Nash, K J	TuC2	411
Nastaushev, Yu V	MoP37	261
	ThP30	949
Nayak, D K	TuP20	553
Newbury, R	TuP1	365
Nguyen, C	MoP4	68
	ThC6	1039
	ThP33	970
	WeA1	665
Nicholas, R J.	WeA2	675
	TuC3	416
	ThP29	943
Nicholls, J E	ThP5	821
Nicholls, J T	TuB1	365
Nishida, A	MoB4	35
Nishimura, H	TuP4	460
Nishioka, M.	MoP5	73

Nocera, J.	TuA3	347	Pinczuk, A	ThC3	1022	Robert J L	MoP25	188	Schmeller, A	ThP24	916
Noge, H.	MoC1	281	Pistol, M-E	TuP12	509	Robson, P. N	MoP20	165		ThC5	1033
	MoP3	60	Planel, R	TuP15	523	Rocher, A	MoP2	54	Schmidt, A	ThB3	777
Nomura, Y	MoP1	48	Ploog, K	MoP12	119	Rodrigues, R	ThP13	866	Schmidt, G.	MoP7	88
Nötzel, R.	MoC6	314		MoC6	314	Rodriguez, F J	TuP5	466	Schmidt, K H	TuC4	424
	MoC5	307		TuP6	471	Rogachev, A A	ThC7	1046		FrB4	1094
Nützel, J. F.	TuP24	572		TuP8	485	Romanov, N G	TuP15	523	Schmitz, J	WeA4	687
	TuP22	559		TuC4	424	Ron, A.	ThP22	909	chneider, H	TuP6	471
Oakeshott, R B S	TuP38	645		TuP39	652	Rosencher, E	TuA2	338		TuP8	485
Ogawa, M.	FrA5	1068		MoP31	228	Roskos, H G.	FrB1	1075		FrB4	1094
Ohmori, Y.	MoP16	199		TuP10	496	Rossi, F.	MoC8	324	Scholl, E.	MoP30	220
Ohno, T	MoP10	104		MoP16	199	Rota, L	MoC8	324	Scholz, F	MoP26	192
Oiknine-Schlesinger, J	ThP39	1009		TuP17	533	Roussignol, Ph	ThP3	810	Schorer, R.	MoC7	319
Okamoto, H	MoP16	199		MoP34	244	Rucker, H	TuP23	565	Schulman, J N	TuP32	617
Omling, P.	MoP26	192		TuP36	635	Ruf, T	MoP12	119	Schulz, P A	ThP15	879
Onabe, K	TuP16	527		FrB4	1094		MoC6	314	Schulzgen, A	ThP7	829
Orr, B G.	WeB3	714		MoC5	307	Ruhle, W. W	TuB4	389	Schwedler, R	FrB1	1075
Ossau, W	ThA4	749		MoC3	298		TuP18	541	Seidel, W	WeA5	694
Ossicini, S	ThP9	841		FrA4	1064	Ryan, J F	ThP6	825	Seifert, W	TuP12	509
Osten, H.J	TuP23	565	Polato[illegible]u, H M	TuP21	558	Ryzhii, V I	ThP37	992	Selbmann, P E	MoP38	262
Ota, K	TuP16	527	Polimeni, A	MoP19	157		ThP25	922	Shanabrook, B V	MoC2	290
Ozanyan, K B	MoP19	157	Pollak, F H.	TuP11	502	Sagnes, I	TuP25	576	Shaposhnikov, S V	ThC7	1046
Pabla, A. S	MoP20	165	Popovic, Z V	MoC6	314	Saito, T	MoC4	302	Shaw, M J	FrA2	1058
Padjen, R	FrB5	1100	Portal, J. C	ThP30	949	Sakai, J W.	TuP28	583	Shen, S C.	ThA5	756
Palacios, J. J	ThP17	889		TuC6	435	Sakaki, H.	MoC1	281	Sherwin, M S	ThP35	970
Palmier, J F	TuP40	658		TuP40	658		MoP3	60	Sheu, Y. M	MoP27	200
	MoP33	238	Potemski, M	TuP17	533		ThP16	885	Shi, J M	ThP27	928
Palmstrom, C J	TuA5	360		TuP18	541	Saker, M. K	TuC2	411	Shi, Z.	ThP1	796
Panish, M. B	MoP22	175	Pothier, H	TuP36	635	Sakurai, N.	ThP8	834	Shimizu, A	MoC1	281
Pate, M	TuC6	435	Pozina, G R	ThA4	749	Salemink, H W M	WeB2	712	Shimomura, S	MoP9	102
	MoP20	165	Presting, H	MoP17	144	Salzman, J	ThP21	904	Shiraishi, K	MoP10	104
	TuP35	634	Ptashchenko, A A	ThP36	985	Samuelson, L	TuP12	509	Shiraki, Y	TuP16	527
	TuP28	593	Ptashchenko, F A	ThP36	985	Sanchez-Rojas, J L	MoP20	165		MoA4	17
Pathak, R N	ThC2	1016	Puls, J	ThP7	829	Sandmann, J H H	FrB2	1081		TuP20	553
Peck, A J	TuP39	652	Pusep, Yu	MoP13	123	Sands, T	WeA3	680		ThP34	974
Peeters, F M	ThP27	928	Qiang, H.	TuP11	502	Sano, N	MoP9	102	Shtrikman, H	MoB1	21
	ThC2	1016	Ralston, J D	WeA4	687	Sapega, V F	MoP12	119	Shumin, W	MoP40	275
	TuA5	360	Ram-Mohan, L R	ThP23	915	Sasaki, S	TuC2	411	Sibari, H.	MoP25	188
Peggs, D W	TuC2	411	Ramsteiner, M	MoP11	110	Scamarcio, G	MoP16	199	Sibille, A	TuP40	658
Pepper, M	TuB1	365	Raymond, A	MoP25	188	Schaff, W	ThP27	928	Simeone, M G	MoP19	157
Petroff, P M	MoB5	44		ThP26	927	Schaffler, F	TuP24	572	Simmonds, P E	TuP27	585
Peyla, P	TuC3	416	Rees, G J	MoP20	165		TuA1	333	Singh, J	ThP38	1000
Peyrade, J P	MoP2	54	Regreny, A	FrB3	1089	Schapers, T.	TuP26	581	Sirtori, C	ThC1	1015
Pfannkuche, D	ThP28	934	Reinecke, T L	ThB4	783	Scheibler, H F	MoP23	181		ThP20	903
Pfeiffer, L N	ThC1	1015	Richards, D	TuP6	471	Schley, P	TuP23	565	Sivachenko, A Yu	TuP14	522
	ThC3	1022		MoP24	182	Schlosser, T	MoP4	68	Sivco, D L	ThC1	1015
	ThP21	904	Ritchie, D A	TuB1	365	Schmalz, K	TuP23	565		ThP20	903
	MoB2	23	Ritter, D	ThP39	1009	Schmeller, A	ThC3	1022	Sizmann, R	ThP4	815

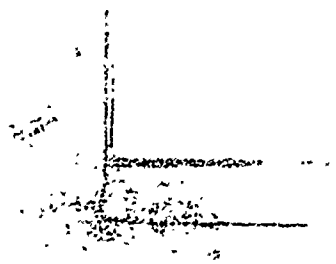

Skierbiszewski, C	MoP25	188
Skolnick, M S	MoP20	165
	TuP35	634
	MoP39	268
	TuC2	411
Smith, G W	TuP35	634
Smith, J M	TuP31	613
Smith, J S	ThP35	978
Smith, R S	TuC2	411
Smolner, J	MoP28	206
Snow, E S	MoP6	80
Someya, T	MoC1	281
Spill, B	MoP8	94
Spitzer, J	MoP12	119
	MoC6	314
Springholz, G	ThA2	738
Staley, T W	MoP22	175
Stevens, C J	ThP6	825
Stirner, T	ThP5	821
Stoddart, S T	TuP39	652
Stolz, W	MoP8	94
	TuP13	515
	FrB2	1081
Stormer, H L	MoB2	23
Straub, U	TuB4	389
Streller, U	ThP7	829
Sudijono, J	WeB3	714
Suemeune I	ThP6	825
Sugano, T	MoP36	252
Suhrke, M	MoP38	262
Sunamura, H	TuP2.	553
Sundaram, M	ThC4	1029
	ThC6	1039
Suski, T	TuB2	377
	MoP28	206
Symons, D M	ThP29	943
Taboryski, R	TuP38	645
Tacke, M	ThP1	796
Tackeuchi, A	TuB4	389
Tagliente, A	MoP16	199
Tagliente, M A	MoC5	307
Takahashi, Y	ThP34	974
Takano, T	MoP21	170
Tanaka, I	TuP4	460
Tanaka, M	WeA3	680
	MoP9	102
Tanaka, N	MoP1	48
Taniguchi, K	TuC5	431
Taniguchi K	ThP19	899
Tapfer, L.	MoP16	199
	MoC5	307
Taylor, R A	ThP6	825
Tejedor, C	TuP5	466
	ThP17	889
Temkin, H	MoP22	175
Terekhov, A S	MoP23	181
Tewordt, M	TuB3	365
Theodoron, G	TuP19	548
Thibaudeau, I	TuA2	338
Titkov, A	WeA5	694
Tobben, D	TuP24	572
Tominaga, K	TuP1	442
Toropov, A I	MoP13	123
	ThP30	949
Tournie, E	FrA4	1064
Trankle, G	FrA3	1059
Truscott, W S	ThP31	955
Tserbak, C	TuP19	548
Tsuchiya, M	MoP3	60
Tsukamoto, S	MoP5	73
Tuerck, V	ThB2	773
Turner, T S	MoP39	268
Twigg, M E	MoC2	290
Uraltsev, I N	ThA4	749
Usami, N	MoA4	17
	TuP20	553
Utzmeier, T	MoP4	68
V'yurkov, V V	ThP25	922
Vandenberg, J M	ThP39	1009
Vasiliev, A	ThB3	777
Vaughan, T A	ThP29	943
Veje, E	TuP38	645
Vescan, L	TuP26	581
Vieren, J P	TuP25	576
Viña, L	TuP7	479
Vinattieri, A	ThP3	810
Vinter, B	TuA2	338
Voillot, F	MoP2	54
Voisin, P	TuP3	454
	WeA5	694
	MoP18	151
Voos, M	WeA5	694
	TuP25	576
de Vries, D K	MoP34	244
Vurgaftman I	ThP38	1000
Waag, A	ThA4	749
Wada, K	MoC1	281
Wagner, J	TuP6	471
	WeA4	687
	MoP11	110
	TuP8	485
Wagner, R J	MoC2	290
Walker, P J	TuP31	613
	WeA2	675
	ThP29	943
Wang, C C	MoP27	200
Wang, H	MoP33	238
Wang, J	TuP30	605
Wang, W I	TuP7	479
	TuA3	347
Wang, Z-P	TuP9	492
Wang, Z H	ThA2	738
Warburton, R J	WeA2	675
	TuC3	416
Warren, P	TuP25	576
Waschke, C	FrB1	1075
Watanabe, T	MoP9	102
Waterman, J R	MoC2	290
Webb, J B	MoP14	124
Wegscheider, W	MoB2	23
Weimann, G	ThP24	916
	TuP18	541
	MoP28	206
	FrA3	1059
Weiner, J S	ThC3	1022
Weis, J	TuP36	635
Wendel, M	ThP24	916
Wendler, L	ThP11	853
West, K W	ThC1	1015
	ThC3	1022
	MoB2	23
Wetzel, C	MoP26	192
Whittaker, D M	MoP20	165
	TuP35	634
	MoP39	268
	TuC2	411
Wieck, A D	MoP34	244
Willander, M	TuB5	396
Willcox, A R K	MoP20	165
Wilson, R A	TuB3	383
Wisniewski, P	MoP28	206
Wolk, C	TuP37	640
Wong, K B	FrA2	1058
Woodbridge, K	TuC3	416
Woodhead, J	MoP20	165
Worren, T	MoP19	157
Wu, X	ThP35	978
Yaguchi, H	TuP16	527
Yakovlev, D R	ThA4	749
Yamaguchi, M	TuC5	431
Yamamoto, M	MoP35	248
Yamamoto, T	TuP10	496
	MoP9	102
Yang, C. H	TuB3	383
Yassievich, I N	TuP23	565
Yasuda, T	MoP21	170
Yeh, J J	MoP27	200
Yoh, K	MoB4	35
Yoshino, J.	MoP21	170
Youngdale, E R	ThP23	915
Yuh, E L.	ThC4	1029
Zahler, M	ThP21	904
Zastrow, U	TuP26	581
Zawadzki, W	ThP26	927
Zekentes, K	MoP25	188
Zhang, L J	ThA5	756
Zhang, Y-H	TuP17	533
Zielinski, E	ThP18	894
Zrenner, A.	FrA3	1059

END

10-94